A BRIEF PREHISTORY OF TIME

By

Martin Jones

SUBMITTED IN PARTIAL FULFILLMENT OF THE
REQUIREMENTS FOR THE DEGREE OF
PHD
AT
UNIVERSITY OF AUCKLAND
AUCKLAND
JUNE 2002

Abstract

In this thesis we develop an approach to using obsidian hydration date (OHD) chronometric data as a chronology building tool. A Bayesian interpretive framework is developed that enables archaeological chronology to be outlined through OHD data. This is implemented both for OHD as a stand-alone dating system, and for OHD in combination with convention radiocarbon age (CRA) chronometric measurements. On the basis of this development we assess the current utility of OHD as a chronology building tool, and evaluate its future potential. The purpose of this research is two-fold.

At a general level the research presented here illustrates how the Bayesian calibration frameworks that have been extensively developed over the past decade (e.g., Naylor and Smith 1988; Buck and Litton 1995; Buck et al. 1991, 1992, 1994a, 1994b, 1994c, 1996; Christen 1994a, 1994b; Christen and Buck 1998; Christen and Litton 1995; Christen et al. 1995; Litton and Buck 1995, 1996; Litton and Leese 1991; Nicholls and Jones 1998, in press; Zeidler et al.1998) can be extended to incorporate other types of chronometric data — OHD in this case. To-date the implementation of Bayesian calibration frameworks have principally focussed on combining CRA data with non-metric temporal data such as the relative ordering of events implied by super-position. However, while radiocarbon is the most widely used chronometric technique in the world other types of chronometric data are more suited to addressing particular tem-

poral questions than radiocarbon assays. In the example considered in this thesis we identify obsidian hydration dating as having the potential to provide chronometric data that can address questions relating to the fine grained relative timing of events, which is identified as a particular weakness of the radiocarbon chronometric largely due to the non-monotonic nature of the radiocarbon calibration curve.

At a New Zealand specific level the research presented in this thesis seeks to provide an advance in the ability to resolve the type of temporal questions that are central to the understanding of New Zealand's archaeological record. By world standards New Zealand's prehistory is short– potentially spanning only 600 years. Thus the temporal resolution of archaeological investigation is typically high. In this thesis we seek to combine radiocarbon and OHD chronometric data within a suitable statistical framework that leverages the benefits of both techniques, enhancing our ability to explore archaeological chronology in New Zealand.

Thus the research presented in this thesis outlines the development of an approach to chronometric enquiry that is of general interest and in the process make an advance for archaeological enquiry in New Zealand.

Contents

List of Figures

List of Tables

Chapter 1

Introduction

1.1 Introduction

Dating the absolute, or relative, timing of events in the past is a problem common to many disciplines. In archaeology it is fundamental. Dating forms the basis for archaeological chronology building and without a reliable chronology the discipline is largely reduced to antiquarianism. As put by Renfrew (1973: p. 21)

> Dating is crucial to archaeology. Without a reliable chronology the past is chaotic: there is no way of relating or ordering people, events and cultures into the coherent narrative which the prehistorian seeks to construct.

Thus dating is not in itself a direct goal of archaeology. We wish to construct event chronologies that allow the anthropological exploration of the archaeological record. The construction of these chronologies, however, is reliant upon temporal data. The relationship between the two can be very complex, and in many cases the link between dating data and associated chronologies — implicit in Renfrew's comments quoted above — is very poorly considered (*e.g.* Jones 2001). The research presented in this thesis is directed at that link; the construction of chronology from temporal data. Here we will concentrate on the use of temporally correlated measurements (hereafter *chronometrics*) — such as the residual ^{14}C concentration used in radiocarbon dating — for chronology building.

Chronometric data are very widely employed in archaeological research. However, without an approach to analysing these data in a sound statistical fashion, and within an archaeological context, they remain largely meaningless numbers that have little value for chronology building. Thus a central theme of this thesis is establishing meaning for chronometric data within the context of chronology building. This means establish-

ing precisely what inferences can be drawn regarding chronology on the basis of a particular set of chronometric data in an objective and mathematically sound manner.

Our particular focus in this thesis is the obsidian hydration chronometric (OHD). Here we will explore the OHD chronometric and establish approaches to chronology building using this data type. Additionally we will develop a method for combining radiocarbon chronometric data (the CRA) with obsidian hydration chronometric data in a fashion that draws upon the strengths of both data types. This combination is considered here as it represents a particularly useful outcome for New Zealand archaeology. The results, however, will be equally useful to archaeological research in other parts of the world. Currently chronology building is typically limited to a single chronometric data type. The combination of multiple data types within a suitable analytic framework leads to a more powerful method of enquiry. For example, consider the combination of OHD and radiocarbon chronometrics explored in this thesis. Radiocarbon dating is well suited to determining the absolute date at which a biological sample died. However, the technique cannot directly date many events of cultural interest and even where it can be employed radiocarbon dating is relatively weak at being able to discriminate the relative age of events (largely due to the non-monotonic nature of the radiocarbon calibration curve). In contrast, the OHD chronometric can be used as a powerful measure for the relative timing of certain cultural events, in spite of being relatively weak in providing absolute age estimates. By combining these two chronometric data types in an appropriate fashion we can address temporal questions in a manner that draws upon the strengths of both. The general approach to this type of combined analysis is discussed here and can be readily applied to the combination of other types of chronometric data. Thus the research presented here is in a general sense a case study in the development of chronology from chronometry that will be of global interest.

For New Zealand, the research presented in this thesis seeks to provide an advance in our ability to resolve the type of temporal questions that are central to the understanding of New Zealand's archaeological record. By world standards New Zealand's prehistory is short — potentially spanning only 600 years (Anderson 1991). Thus the temporal resolution of archaeological investigation needs to be high. In particular, as acute processual models of New Zealand's prehistoric sequence are advanced (*e.g.* Anderson *et al.* 1996; Higham *et al.* 1999), it is becoming increasingly important to determine the absolute time differences between events of interest. However, the chronometric data currently employed derives almost exclusively from ^{14}C measurements. While the radiocarbon chronometric is extremely powerful, it has limited ability to resolve questions of relative timing at a high temporal resolution, and can only be brought to bear on a little over half of New Zealand's prehistoric sequence. Thus a chronometric tool that address these issues and can be brought to bear on chronology building for archaeology in New Zealand would be a significant advance. Ideally such a tool would both extend the period over which dating assays are available and extend the range of temporal questions that can be readily addressed. Here, OHD is identified as a chronometric method that potentially meets these requirements. In theory OHD can be applied to events from throughout New Zealand's entire prehistoric period, can provide powerful data regarding the relative timing of archaeological events and dates an event ubiquitous within New Zealand's archaeological record. Further, OHD has been use to date artefacts in New Zealand at various times over the past 40 years with some success (*e.g.* Stevenson *et al.* 1995). Thus we would expect that OHD can be used to augment the radiocarbon chronometric and extend the range of chronological questions our chronometric data can address.

In the remainder of this chapter we will first consider what approaches we can take to build chronologies from chronometries in a sound fash-

ion. Then we will present an outline of the steps required to assess and develop the OHD chronometric as a chronology building tool; both as a stand-alone technique and in conjunction with radiocarbon dating.

1.2 Chronometry vs Chronology

As outlined previously, in time related research a description of the timing, temporal relationships and duration, or chronology, of processes is attempted. What is usually produced is a series of temporally dependant data, or a chronometry. In order to define a chronology that is based upon, or constrained by, chronometry it is necessary to articulate the chronology and chronometry. This is brought about by modelling the temporal structure and relationships of the events of interest and their relationship to the chronometric data.

The same basic process applies in all cases of chronometric dating. A quantity related to the elapsed time is measured (a *chronometric*), and this in turn is related to the event(s) of interest, either relatively or on some normalised absolute time scale (most commonly the Christian calender). However, in most dating applications the primary interest is in some phenomenon or phenomena associated with the dated event, rather than the event itself. For instance, an archaeologist may submit a sample of shell from a site for ^{14}C dating, with the intention of dating the time of formation of the cultural layer, or perhaps by association other aspects of the archaeological record. In this case the actual dated event is a biological process related to the age of the shell fish at death, and in order for the ^{14}C data to be of any use the archaeologist must make assumptions (either implicit or explicit) about the temporal association of the dated event and the phenomena (in this case cultural) of interest. The same case applies in the application of dating in other fields such as environmental research. For instance the ^{14}C dating of pollen cores ex-

tracted from swaps is common. In this case the phenomena of interest are features of the pollen record such as the date(s) of environmental disturbance rather than the death of the organic matter actually dated.

In light of the fact that the actual events dated are often not those that are of interest, inferences must be drawn about the association of the dated event and those under study. The purpose of this section is to develop and outline a consistent frame work for making these inferences explicit. In order to develop this frame work it is necessary to briefly define some central terms and concepts.

When material is dated, a temporally dependant attribute(s) is measured. These measurements are the *chronometric data*. The assumption is that the measured attributes are related in some predictable way to the time elapsed between present and the dated event. In the case of the most widely applied dating method, radiocarbon dating, the primary measured attribute is the residual ^{14}C content. Here the assumption is that organic material will stop exchanging atmospheric ^{14}C at death, and due to radioactive decay of the ^{14}C isotope, ^{14}C levels of dead organic material will decrease through time and thus serve as a measure of the time elapsed since the death.

In order for the chronometric data to be of use in dating applications, it must be possible to compare the chronometric data with reference to a common time scale. Further, for absolute dating the chronometric data must be transformed to a common absolute time scale. Here we refer to these processed data as *event dates* and the transformation process as *calibration*. Calibration is typically complex, frequently requiring measurement of many additional sample attributes, and for many materials is an active area of research — even for a well developed technique such as radiocarbon dating. However, as outlined previously the date of related events are often of more interest than the actual event dates themselves.

In order to relate different events a useful concept is the *context date*. The context date is the age of the archaeological context within which the dated sample is incorporated. The context date is fundamental to chronology building as we really seek to date the cultural processes manifest in the archaeological record. For example, in the archaeological midden dating example described previously it is the context of the dated shell that relates the event date to phenomena such as the formation date of the midden or the duration of occupation at that location. In a similar manner all event dates exist within some context of interest. In order to produce a context date it is necessary to understand the temporal relationship between the context formation and event; this is the *event-context relationship*. In the absence of a sound understanding of the event-context relationship a chronometric is effectively useless as a chronology building tool. It is often implicitly assumed that the event and context dates are the same. In practice this will often be incorrect, though the extent of the error may be insignificant in many applications. An example common to ^{14}C dating is the question of inbuilt age in charcoal samples (*e.g.* Anderson 1991). Here a sample of wood may be dated from an archaeological site where considerable time has elapsed between the dated event (the death of the wood) and the deposition of the sample in the archaeological record. Thus any assumptions about concurrence of the event date and context date in this case would be significantly wrong. Thus a clear understanding of the event-context relationship is fundamental to meaningful chronology building.

A related concept is that of the *temporal envelope*. When an artefact (of any type) is used within a cultural context it will remain in use for a finite period of time. This period is the temporal-envelope of the artefact. At any given time within any cultural context a number of different artefacts with differing temporal envelopes will exist. Thus even if we can associate a dated event with a particular cultural context this does not necessarily relate the dated event to the particular archaeological

context within which it is observed. As an example consider a wooden artefact. With this artefact there will most probably be a difference in time between the dated event (the death of the wood) and the use of the material within a cultural context. However this is further confounded by the temporal envelope of the artefact. As a piece of firewood the temporal envelope of the artefact will be small. The wood will be burnt and then will in most cases cease to be used within a cultural context. However, if the wood was used to make a carving or something similar the artefact may remain in use for many centuries. Thus the event-context relationship for the archaeological record describes both the relationship between the event-date and the initial cultural use of the artefact and the temporal-envelope of the artefact. It follows that the most precise dates for particular archaeological contexts will derive from artefact types that have typically small temporal-envelopes. However, the range of dates from a particular archaeological context can be used to assess the temporal envelope of particular artefacts and artefact types which is useful cultural information.

The final basic concept that needs to be introduced is that of *process parameters*. As archaeologists, our ultimate interest is in the cultural actions that have given rise to the observed archaeological record — our chronology is the narrative of these actions. At a general level the elements of the chronological narrative are not events, but rather processes. Colonisation for example — while often referred to as an event — is a (probably quite complex) process that will occur over a finite period of time. In a similar fashion all of the cultural actions that we wish to study are some form of temporally finite process. In describing these processes in a chronology we describe temporal parameters of the particular process. So for example we might talk about when people initially began living in an area, or when a particular artefact type ceased to be manufactured. These concepts while nominally events are really temporal parameters of higher order cultural processes of inter-

est; in the two examples just given, the settlement history of a particular region and the history of a particular type of material culture respectively. Clearly there may be a complex interaction of cultural processes of interest so that we may talk about when humans initially began living in an area as a temporal parameter of the human settlement history of the region but also talk about when a particular group may have subsequently invaded. In that case we refer to a temporal parameter of a process occurring within the broader scope of human settlement within a region.

In order to build a chronology from chronometric data we have to able to explicitly resolve the relationships between chronometric data, event dates, context dates and temporal parameters. Any chronology based upon chronometric data must address these issues, implicitly or explicitly. It is certain that the arguments advanced in many dating applications adopt implicit warrants[1] associated with the prevailing paradigm that are not necessarily true. In New Zealand for example it is relatively common to see a statement that goes along the lines

> ... the date for this site is X ...

Such a statement makes the following implicit assumptions;1) the event date can be summarised by a small number of parameters (rarely true for multimodal events date distributions such as typically arise from radiocarbon data) 2) the event date and the context date are isochronous 3) The archaeological record at said site corresponds to a sufficiently brief instant in time that it can be assumed to be an event. These may or may not be valid assumptions, however in any real chronology building exercise it is most appropriate that these relationships are made explicit and justifications for these assumptions are made. On that basis it is possible to be sure that any chronological narrative developed

[1] as in the logical bridge of an argument; analogous to the major premiss in a conditional syllogism

actually reflects what is known and or believed about the articulation of chronometry and chronology for the particular case in question. This both ensures that unwitting errors of chronometric interpretation do not violate the chronometry, and makes it possible to review and assess the conclusions inherent in a chronological narrative in an objective manner. This serves to ensure that debate regarding chronology can develop in an objective and constructive fashion.

Having defined the elements of articulation chronometry and chronology we next need to establish how precisely this may be achieved. Essentially we need some form of interpretive framework which allows us to perform the articulation in a mathematically sound manner. Fortunately such a framework exists in the form of the temporal Bayesian models that have been widely applied to radiocarbon data over the past 5–10 years (*e.g.* Naylor and Smith 1988; Buck *et al.* 1991; 1992; 1994; 1996; Christen 1994*a*;*b*; Christen and Buck 1998; Christen *et al.* 1995; Christen and Litton 1995; Jones and Nicholls 2001; Litton and Buck 1996; Litton and Leese 1991; Nicholls and Jones 1998; 2001; Zeidler *et al.* 1998). In the next section we will briefly outline the Bayesian modelling approach and show how it fits with the elements of chronology building defined above.

1.2.1 Bayesian Analysis

Bayesian methods allow chronometric data and models defining the relationships among the elements of a chronology building exercise to be combined, in an explicit way, in the chronometric analysis. A good overview of Bayesian models in Archaeology is given in Buck *et al.* (1996) and a very good outline of a temporal Bayesian modelling approach that treats most of the elements of chronology building defined above is given by Christen (1994*a*). In the following we will introduce the

Bayesian approach to chronology building and identify the implications for OHD as a chronology building tool.

To provide an introductory context for Bayesian analysis it is useful to review the question(s) we wish to ask based upon chronometric data. In terms of the chronology building elements outlined in the preceding section we want to ask something along the lines of

Statement 1 *"what are the dates of the events, observed archaeological contexts and associated cultural process parameters in light of the available chronometric data and our understanding of the relationships among these parameters"*

This is a form of conditional probability statement. In a conditional probability statement we ask

Statement 2 *"what is the probability of x given y"*

Clearly the development of chronology from chronometry fits this form, and we can summarise Statement 1 above as

Statement 3 *"what is the probability distribution of our temporal parameters of interest given the available data"*

The standard notation of a conditional probability uses the operator "|" to denote the concept "given" or "conditional upon". Thus statement 3 can be rewritten as

$$P(\text{parameters}|\text{data}) \tag{1.1}$$

i.e. what are the probability distributions of the parameters of interest given the available chronometric data.

The Bayesian method is useful in addressing this question as Bayes theorem gives us a method for manipulating conditional probabilities in a

suitable manner. In a simplified form Bayes theorem states

$$h(x|y) \propto \ell(y|x)f(x) \tag{1.2}$$

And this simple relationship allows us to cast our questions regarding the relationship between chronology and chronometry in computationally tractable manner. Basically this breaks the problem down into three components as expressed in Equation 1.3 below

$$\text{Posterior} \propto \text{likelihood} \times \text{prior} \tag{1.3}$$

Thus the *posterior* — which defines our understanding of the chronological parameters after the analysis — is the product of a probability distribution known as the *likelihood* which is defined by the chronometric data and another known as the *prior* which expresses our understanding of the temporal relationships amongst the chronology building elements, prior to the analysis taking place.

To illustrate how this allows us to articulate chronometry and chronology in a suitable fashion it is useful to define some notation. Here we will use the standard notation generally used in Bayesian temporal models (*e.g.* Buck *et al.* 1996; Christen 1994*a*; Nicholls and Jones 2001). Let y represent the chronometric data, θ represent an event date, ϕ represent a context date and ψ represent a process parameter. As outlined previously we are interested in the distribution of θ,ϕ and ψ on the basis of the measured chronometric data y (*i.e.* $h(\theta, \phi, \psi|y)$). Following Bayes theorem this gives us

$$h(\theta, \phi, \psi|y) \propto \ell(y|\theta, \phi, \psi)f(\theta, \phi, \psi)$$

as y is independent of ϕ and ψ this reduces to

$$h(\theta, \phi, \psi|y) \propto \ell(y|\theta)f(\theta, \phi, \psi)$$

Again making reference to Bayes theorem we can break this up as follows (Nicholls and Jones 2001)

$$h(\theta, \phi, \psi|y) \propto \ell(y|\theta)f(\theta|\phi)f(\phi, \psi) \tag{1.4}$$

which is a direct mathematical representation of Statement 1 given at the start of this section.

Here the term $f(\theta|\phi)$ defines the event context relationship and the term $f(\phi,\psi)$ models the relationship among and between the context dates and temporal parameters. The density $f(\phi,\psi)$ requires careful model building which may well need to be case specific. However, general classes of models have been developed that will probably be appropriate for many archaeological applications (*e.g.* Nicholls and Jones 2001).

The critical point to note is the fact that the chronometric data only enters the model in the definition of the likelihood $\ell(y|\theta)$. Thus if we can define the likelihood for any chronometric data type then we can implement a Bayesian analyses on these data in an identical manner to those now routinely applied to radiocarbon data. In fact as the analysis of multiple chronometric data is simply conducted by calculating the product of the various likelihood and prior terms we can compute a Bayesian posterior for any combination of data types for which suitable likelihoods have been defined.

It is apparent that the general Bayesian framework described above meets our requirements for articulating chronometry and chronology. The relationship between the chronometric and the event date is defined in the likelihood $\ell(y|\theta)$. The event context relationship is defined in the density $f(\theta|\psi)$ and the density $f(\phi,\psi)$ models the relationship among and between the context dates and temporal parameters. The most complex component of this model building process is in the definition of the density $f(\phi,\psi)$. However various models for this density have been developed (*e.g.* Nicholls and Jones 1998; 2001) and it is possible to use these existing models where one that suits the type of problem under consideration exists.

The major complication of this type of analysis lies in the fact that the

parameters given in Equation 1.4 almost always represent vectors. This means that the posterior, likelihood and prior will be multi-dimensional distributions. Accordingly the individual distributions of parameters of interest within the posterior (typically the process parameters defined above) need to be integrated out of the full posterior distribution. These distributions are known as *marginal* posterior distributions. The integration of marginal posterior distributions from a full posterior is typically very difficult and usually requires specialised software. A system that implements the scheme described here for the radiocarbon chronometric has been produced by Jones and Nicholls (submitted; 2002) and a good overview of this computation is presented by them. However, the software packages that currently exist are primarily designed to analyse the CRA chronometric and in order to analyse the OHD chronometric within a Bayesian framework suitable software will have to be developed (*supra vide*:§13).

Thus to use chronometrics other than radiocarbon data, or in addition to radiocarbon data, to develop chronologies based around suitable Bayesian methodologies we simply need to develop the appropriate likelihood and software that can perform the calculation. Accordingly the major focus of the remainder of this thesis is in defining an appropriate likelihood for the OHD chronometric and developing software that allows the analysis to be performed.

1.3 The OHD Chronometric

Obsidian hydration has been used to date tens of thousands of artefacts since it was initially demonstrated by Friedman and Smith (1960). And while there is some debate as to whether the technique actually works (*e.g.* Anovitz *et al.* 1999; Ridings 1996) apparently useful results have been obtained for a number of different archaeological contexts (*e.g.* Am-

brose 1994; Katsui and Kondo 1976; Meighan and Scalise 1988; Michels 1971; Stevenson *et al.* 1995; Webster *et al.* 1993). Excellent overviews of the general OHD process are given by Ambrose (2001) and Stevenson *et al.* (1998) so only a very brief summary will be presented here.

OHD is based upon the fact that obsidian reacts with the environment and converts to a water rich form known as perlite (8-9 % water for perlite vs 0.1-1 % water for obsidian). This reaction, known as hydration, begins as soon as a fresh obsidian surface is exposed and gradually propagates into the body of the obsidian from a freshly exposed face forming a zone of perlite known as the *hydration rim*. Obsidian hydration dating exploits this fact by seeking to model the relationship between the amount of perlite that has formed (hereafter the *hydration extent*) and time. Thus the obsidian hydration extent is the base chronometric data for OHD.

As outlined in the preceding section in order to use the OHD chronometric as a chronology building tool we need to be able to define the likelihood for this chronometric. A likelihood is a statement of the probability of observing measured data given particular values of the parameters governing the measured process. So, for example, with an OHD the likelihood would pose the question "what is the probability that the measured hydration extent is associated with an event that took place in the year X?". It will be appreciated that in order to quantify this expression we need to be able to clearly define a temporally dependent model for the hydration process. This is known as the *observation model*. An observation model is central to developing an appropriate likelihood. It defines the parameters that govern the measured process and expresses our understanding of the relationship between that parameter set and the data we observe.

In the case of OHD a variety of models for this relationship have been proposed. While there is some debate over the correct form of the tem-

poral model, the general relationship

$$t = kx^2 \tag{1.5}$$

(t = hydration duration; k is the hydration rate; and x is the measured hydration extent) first defined by Friedman and Smith (1960) has proved to be suitable in many applications (Ambrose 2001). A relationship such as this can be used to define an observation model and hence the required likelihood. However, in order to employ OHD as chronology building tool within a Bayesian framework such as that outlined in §1.2 we also need to be able to define prior distributions for the observation model parameters (these are t and k in Equation 1.5 above). This is the real limitation for OHD. The rate (k) is very sensitive to small changes in the environment, particularly the ambient temperature. This means that to use OHD as an absolute dating tool we need to be able to accurately take account of small fluctuations in the ambient environment over the lifetime of an artefact. Clearly this is a very difficult proposition in most circumstances particularly for old samples.

While various models for the relationship between hydration duration and hydration extent have been expressed, few complete observation models have been proposed for the OHD chronometric and no likelihoods have yet been formulated. In part this derives from the fact that there is no standard method for measuring the OHD chronometric. As discussed in Chapter 2 many methods have been employed to measure obsidian hydration extent, and there is no guarantee that they have all measure exactly the same attributes of the hydration process. This makes development of a likelihood difficult as to an extent the specific form of a likelihood depends upon how the data is actually observed (*i.e.* measured). The development of a complete OHD observation model has been further hindered by the fact that almost no consideration has been given to meaningfully quantifying the uncertainties associated with hydration extent measurements and the associated parameters of any

proposed hydration mechanisms. This also limits our ability to specify prior distributions for parameters of the OHD observation model.

Thus any consideration of OHD as a chronology building tool requires that a complete observation model for hydration extent is developed along with properly formulated prior densities for the parameters of this model. This in turn requires a thorough examination of all components of the OHD chronometric. This is a substantial undertaking and at this point it is worth outlining the potential benefits of the OHD chronometric that warrant this level of research.

1.3.1 Potential Benefits of the OHD chronometric

Perhaps the most powerful attribute of the OHD chronometric is the potential that this data type holds for making assessments of the relative time difference between flaking events. In reality OHD is unlikely to prove as useful an absolute dating tool as Radiocarbon, due to limitations in our ability to accurately model the hydration rate. However, OHD holds great potential as a tool for absolute relative dating. This is distinct from the simple process of relative dating which simply seeks to place artefacts in some temporal order. With absolute relative dating the effort is directed at quantifying exactly how much older or younger one sample is than another. This is extremely important information in chronology building, and as discussed previously this is an area in which the radiocarbon chronometric is relatively weak. In theory OHD can draw some absolute relative inferences without having to fully explain the hydration rate (*supra vide*:§8.1.1). This is a powerful concept as it makes the conditions under which the OHD chronometric can be useful much easier to meet than if absolute dating is attempted. The drawback is that OHD employed in the capacity of absolute relative dating typically needs to be analysed in conjunction with other types of

chronometric data. The case of OHD in conjunction with CRA data is considered in this thesis.

Another primary benefit of the OHD chronometric is the fact that it directly dates a cultural event and the temporal envelope associated with this artefact type will typically be small. Thus there should be fewer problems with describing an association between the dated event and the observed cultural context than is the case for Radiocarbon dating. This attribute makes the OHD chronometric particularly useful in conjunction with CRA data as it means that many of the problems associated with spurious associations in the CRA event-context relationship can be identified. As this is a particularly problematic aspect of radiocarbon dating in New Zealand (Anderson 1991), chronometric data that addresses this issue would be of real benefit.

A further benefit of using OHD in conjunction with CRA is that the two dating methods are based around completely different mechanisms. Thus factors contaminating one chronometric are unlikely to contaminate the other chronometric in an identical fashion. This means that contamination problems can be identified by significant discrepancies between the event dates returned by the two different chronometrics. Obviously this is not unique to OHD and CRA chronometric but will be a feature of any dating exercise drawing upon multiple chronometric data types that are based around different temporal mechanisms. Nonetheless this is a potential benefit of developing the OHD chronometric to allow combined dating exercises with the CRA chronometric. Again this addresses one of the major problems identified with the application of radiocarbon dating in New Zealand.

Finally, OHD offers the potential to date events falling within the past 250 years — a period which cannot be reliably data via radiocarbon yet comprises a substantial part of New Zealand's archaeological record.

Thus the OHD chronometric potentially represents a suitable secondary

chronometric to augment radiocarbon dating. This is useful for both archaeological investigations in areas such as New Zealand, and as a general case study in the articulation of chronometric and chronological data.

1.4 Summary

Chronology development is fundamental to archaeology and this development typically relies upon analysis of chronometric data. In order to build chronometrically informed chronologies it is necessary to be able to explicitly articulate the chronometric data set and the chronological sequence. This requires that an appropriate inferential framework is employed, and that the chronometric data can address the particular temporal questions asked. Bayesian statistics can provide a suitable framework, however there are some limitations the sole use of radiocarbon chronometric data for the purposes of chronology building. This is particularly so when addressing the types of temporal questions typically posed by New Zealand's archaeological record. The OHD chronometric — especially in conjunction with the radiocarbon chronometric – has been identified as having the potential to address some of these. Thus we seek to try and develop the OHD chronometric as a tool that can be used within a Bayesian temporal model, and to assess the utility of this tool. This both serves to provide a useful methodology for archaeological landscapes such as that seen in New Zealand and as a general case study in the development of chronology building on the basis of chronometric data.

In the remainder of this thesis we will consider the specifics of obsidian hydration dating both from a general viewpoint and with a specific focus on applying the technique in New Zealand. In particular we need to address the following:

1. At the most fundamental level we need to be able to measure and define the base chronometric data; the hydration extent. In spite of the fact that OHD has been applied for over 40 years there is no standard definition of the OHD chronometric serving in the same capacity that the CRA performs for radiocarbon dating. As a result of this the observation models that are defined for one type of measurement are not necessary appropriate for another. Thus as an initial step we must define the base chronometric for OHD and establish the distributional form of this measurement. This is considered in Chapter 2.

2. Once we have defined the base OHD chronometric we need to define the observation model. That is to define the functional relationship between time and the OHD chronometric. It is possible that the optimal form of this model will be unique to New Zealand obsidian, or even that the form varies among New Zealand obsidian as a function of different glass chemistry. This step is considered in Chapter 4.

3. Following the definition of the observation model we need to develop models to take account of any glass specific and environment specific parameters of that observation model. This involves: establishing any glass specific parameters for the different obsidian sources within New Zealand (Chapters 5 and 6); identifying some method for discriminating between glasses that exhibit different hydration properties (Chapter 7); taking account of key environmental variables identified in the observation model (Chapters 8–12).

4. A final step in the desired development of the OHD chronometric is the definition of the OHD likelihood and posterior for inclusion in Bayesian analyses, the development of software to allow the analysis and calibration of OHD chronometric data, and the assessment

of the utility of the OHD chronometric as a tool for chronology building. This is considered in Chapter 13.

Chapter 2

Measuring the OHD Chronometric

2.1 Introduction

In this chapter we will consider the measurement of the OHD chronometric. Both from a general measurement perspective, and with a focus on identifying and developing a measurement system that can provide a suitable OHD chronometric for use throughout the remainder of this thesis, and as a more general archaeological tool. The goal is a reproducible measurement of a precisely defined temporal phenomenon with properly quantified measurement uncertainty. As outlined through this chapter there are a number of different approaches that could be used to provide such a measurement. The approach adopted here is a development of the digital image analysis approach initially proposed by Ambrose (1993). This system can be adapted to provide suitable chronometric data within the economic and time constraints of the current research programme. As this system is based around optical imaging, it is necessary to consider all relevant elements of the optical measurement process and establish the optimum sample processing and measurement protocol.

Thus in this chapter I will consider a general overview of hydration measurement followed by an in depth discussion of relevant aspects of optical hydration measurement. Starting from the fundamentals we will begin with a consideration of the measured phenomenon; most commonly referred to as the *hydration rim*.

2.2 The Hydration Rim

Measurement of an "hydration rim" is the primary step in OHD. This is analogous to the measurement of residual ^{14}C activity in a sample to be radiocarbon dated, and forms the basic chronometric upon which any individual date is based. The measured "hydration rim" is basically an

estimate of the extent of perlite formation on the surface of an obsidian artefact (Figure 2.1), and while this can be estimated in a number of different ways, it is standard to reference the measurement to a thickness in μm. "Hydration rim" thickness typically ranges in depth from 0.5 to 10 μm in archaeological contexts, though this range is obviously a function of the length of prehistory for any given region. In New Zealand, with slow hydrating obsidian and a short prehistory, the typical archaeological "rim" thickness ranges between 0.5 and 1.2 μm roughly corresponding to ages of 100-1000 years B.P.

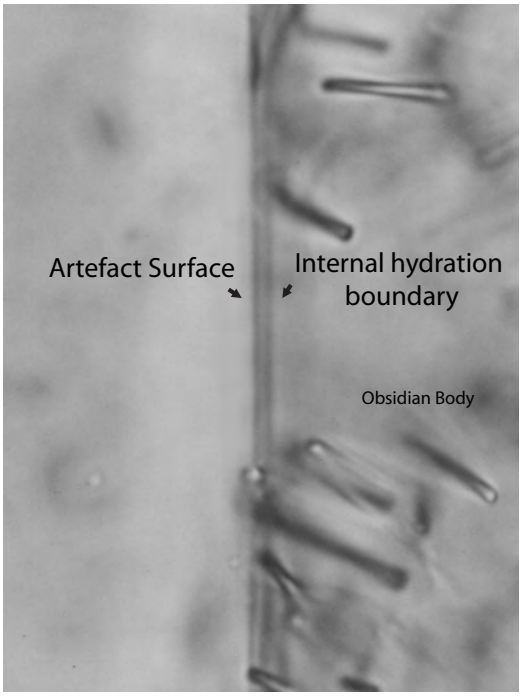

Figure 2.1: Diagram of perlite zone on the surface of artefacts

modify and enhance this Figure

In any discussion of "hydration rim" measurement it is vital that the term "hydration rim" is defined. What is commonly referred to as the "hydration rim" is in fact a set of separate phenomena related to a zone of perlite formation on the surface of obsidian artefacts, which is why

I have placed the term in quotation marks. To clarify this concept it is important to look at the basics of obsidian hydration dating and develop a definition of "hydration rim" in terms of the actual dating process.

Obsidian hydration dating is based around the regular and predictable conversion of obsidian into perlite. The idea is that by establishing the rate of this conversion, and the extent of the perlite formation, we can determine the reaction duration for any given artefact. The ambiguous nature of the term hydration "rim" lies in the fact that the various methods used for measuring the extent of perlite formation estimate this quantity by measuring related, but different, phenomena. For example, when measuring the hydration rim optically there are two phenomena that can be used to identify the hydration zone. Under normal transmitted light the hydrated perlite appears as a dark grey band and due to the differing refractive indexes of perlite and obsidian a dark line is visible at the junction between the hydrated zone and obsidian body. Here the hydration rim is defined by the dark edge boundary and the dark perlite obsidian junction (Figure 2.3).

A second phenomenon can be observed under crossed polars where the hydration rim appears as a bright band. This effect results from stress in the perlite fabric due to an increase in density, which induces birefringent or double refractive properties to the hydration zone (Friedman and Smith 1960).

Both of these optical phenomena are functions of the perlite zone on the edge of a piece of obsidian, however they occur to different depths. This appears to be as the strain induced birefringence propagates beyond the immediate hydration zone and into the body of the obsidian.

The preceding example is obviously a simple demonstration, but it can be appreciated that in a similar manner all techniques measure distinct but related phenomena. This is not in itself a problem if a distinction is

made between the different measurements, as the requirement for OHD is simply a quantifiable time dependant phenomenon. However, it must be recognised that measurement phenomena may be different, and thus produce different chronometrics.

It becomes apparent that the *"hydration rim"* is a zone of chemically altered material that has formed at the surface of an obsidian artefact. The "rims" that are measured are in fact phenomena related to this zone of interest. Thus a suitable definition of an hydration rim in terms of OHD is:

Rim definition 1 (phenomenon) *a consistent, quantifiable, phenomenon associated with the zone of perlite formation on the surface of obsidian artefacts.*

This raises some complications for the dating technique if comparisons are made between measurements of different hydration phenomena. This problem extends beyond the simple case of individual dates and impacts upon the development of universal measures such as rate constants. Date errors are bound to occur when rate constants developed with one measurement system are used to produce dates with another, unless appropriate measurement calibration is applied. This is analogous to the case of comparing ^{14}C dates from marine and terrestrial reservoirs. If the same calibration data were used universally for all reservoirs, marine samples would appear systematically older than isochronous terrestrial samples. In a similar fashion, different measurement systems will produce different chronometrics in OHD.

A similar problem occurs in the comparison of measurements of the same phenomenon when the measurements are not made according to the same measurement protocol. It is possible for different attributes of any rim phenomenon to be defined as the measurement boundaries. Thus it is possible that different rim boundary definitions can give rise to

different measurements of any given rim phenomenon. Worse still, measurements may be made with no precise definition of the measurement boundaries giving rise to the potential for considerable measurement variation. It is clear that measurement of any hydration phenomenon should be made according to a specific protocol and a precise definition of the hydration extent. It is only under these circumstance that consistent chronometrics can be generated, and any hope of comparison between different operators and measurement systems can be meaningfully pursued. Thus I would define an appropriate obsidian hydration measurement as:

Rim definition 2 (Measurement) *The measurement of a rim phenomenon according to a precise definition of rim boundaries and following a precise measurement protocol.*

This definition ensures measurement consistency, however the problem of different measurements due to different measurement phenomena and protocols still exists. The logical resolution to this problem is the development of standards allowing calibration of measurements amongst different facilities.

2.2.1 Calibration standards

At present there are no internationally accepted standards for the calibration of obsidian hydration measurements. Various approaches exist for calibrating the measurement techniques used, but in general these are not specifically designed for hydration measurement, nor are they necessarily comparable between measurement techniques.

As an example, again drawing on optical measurement techniques, it is common practice to calibrate the measurement system with a stage micrometre. While this is fine in principle, in practice the optical hydration

phenomena measured are quite different to those used for calibration. Unfortunately this does not ensure that the actual measured hydration phenomena are calibrated among the various facilities. It can be similarly appreciated that the calibration of results between different measurement approaches is equally problematic.

Thus it makes sense that the standards used to calibrate measurements are actual hydration rims. As long as all measurements conform to these standards then the measurements are consistent and any universal rates will actually be *universally* applicable with reference to the standards. The rims used for the standards can be arbitrarily set to any value though it makes sense to refer the standards to S.I. length units, μm being the most appropriate for measurements of the size encountered in OHD.

The use of a set of standards such as these would enable any facility to calibrate their measurements to a common standard thus making all hydration "rim" measurements comparable, and we could then talk about hydration rim as opposed to "rim" measurements. The application of this type of approach would require the establishment of precise measurement protocols. Without these, standards would be spurious.

As no internationally accepted standards currently exist, a set of standards have been developed that will be used throughout this thesis and which will be consistently applied in any work carried out in the Auckland OHD laboratory. Any facilities wishing to compare results should calibrate their measurements to these same standards. To facilitate the use of these standards by other facilities the standards are based around samples induced at 95 - 125 ^{0}C for varying amounts of time using a specific source of obsidian (Hall's Pass #2, *supra vide*:§3). This source has been chosen as it is an homogenous high quality glass that exists in quantity and produces very clear hydration rims. These standards (the NZ97 OHD standards) are detailed in Table 2.1

Table 2.1: NZ97 OHD standards

Rim thickness μ m	1 σ Error μ m	Induction temperature °K	Run duration Hours
0.600	0.075	368.16	720
0.741	0.038	368.16	1296
0.710	0.075	385.66	341
1.005	0.105	380.16	984
1.574	0.062	398.16	840

These figures are based around inductions conducted in a saturated vapour environment on samples of freshly flaked obsidian. The underlying measurements were generated following the section preparation protocol outlined in §2.5 and according to the digital rim measurement protocols outlined later in this chapter (§2.6.4).

Having developed a consistent definition for the measurement of hydration rims, it is now possible to present an overview and assessment of the measurement systems that have been applied to OHD. These can be broadly divided into two categories, optical and non-optical. This division is principally one of application. Optical measurement is by far the most widely used approach in OHD, while the non-optical techniques have principally been the focus of experimental work. In this section a broad overview of the major published measurement approaches is given in order to outline the real current measurement capabilities and prospects for OHD.

2.3 Non-Optical Hydration Rim Measurement

Relatively few non-optical measurement techniques have been applied in actual dating applications. Only nuclear resonance profiling (RNR Leach and Naylor 1981), sputter induced photon spectrometry (SIPS Leach 1983; Tsong *et al.* 1978), interferometry (Kondo and Matsui 1992) and tritium exchange (Lowe 1977) have actually been applied in dating applications. Although techniques such as RNR (Neve and Barker 1997; Lanford 1978; Laursen and Lanford. 1978; Coote and Nistor 1982; Tsong *et al.* 1978; 1981; Lee *et al.* 1974) SIPS (Tsong *et al.* 1978; Bates *et al.* 1988), scanning electron microscopy (Bates *et al.* 1988), secondary ion mass spectrometry (SIMS Anovitz *et al.* 1999; McGrail *et al.* 1988; Tsong *et al.* 1980; 1981), forward recoil profiling (Duerden *et al.* 1982) and laser ellipsometry (Ericson 1988) have been tested or used in experimental contexts, and techniques such as Rutherford forward/backscattering should also be suitable. In practice the application of a new technique to hydration measurement requires considerable effort and while approaches such as SIMS/SIPS and laser ellipsometry, in particular, offer great potential as measurement systems they do not yet represent viable approaches for routine dating applications, principally due to the cost involved.

The non-optical techniques that have been develop for, or adapted to, OHD have unique characteristics and it is useful to outline the application of these techniques to OHD and evaluate their utility. In the following sections the main techniques by which published measurements have been made are outlined. The list is not exhaustive and techniques such as ellipsometry and interferometry have not been included. The intention is to assess those techniques that have been most widely used, and to present an overview of the range of measurement phenomena that are associated with the hydration zone.

2.3.1 Resonant Nuclear Reaction Profiling (RNR)

RNR analysis of obsidian hydration profiles was first demonstrated by Lee *et al.* (1974), and as a non-destructive technique is useful in situations where samples cannot be destroyed. However, the technique is expensive and time consuming, and as a result is unlikely to ever be a routine measurement approach.

The general principle by which RNR profiling operates is that an ion beam directed at an artefact will, under certain conditions, undergo a nuclear reaction with an element(s) of interest within the artefact. The reason that this phenomenon is of use is that these reactions only occur at precise energies (Resonant energy). As the incident beam energy drops on travelling through the artefact matrix, the resonant energy is only achieved at a point some depth inside the artefact that is a function of the initial beam energy and the stopping power of the artefact matrix. Thus by varying the energy of the incident ion beam it is possible to produce the resonant nuclear reaction at a series of depths from the artefact surface. As the reaction rate is proportional to the concentration of the reacting element within the artefact matrix it is possible to build a depth profile of the relative elemental concentration by measuring the reaction rate. Thus the RNR profile consists of incident beam energy/reaction rate data pairs.

By using different ion beams it is possible to promote different reactions and hence measure concentration profiles for different elements. Some reactions that have been used for elemental profiling are presented in Table 2.2.

One of the primary limitations of this technique is due to secondary reactions. As any ion beam may react with a number of different elements (at different resonant energies) there may be confounding signals that need to be removed from the data (Neve and Barker 1997; Lee *et al.*

Table 2.2: Examples of RNR's applied to elemental profiling in obsidian

Element	Reaction	References
Fluorine	$^{1}H(^{19}F,\alpha\gamma)^{1}6O$	(Lee *et al.* 1974)
Hydrogen	$^{1}H(^{15}N,\alpha\gamma)^{12}C$	(Lanford 1978)
	$^{1}H(^{7}Li,\gamma)^{8}Be$	(Leach and Naylor 1981) (Neve and Barker 1997)
Sodium	$^{23}Na(p,\gamma)^{24}Mg$	(Lee *et al.* 1974)
	$^{2}3Na(p,\alpha\gamma)^{20}Ne$	(Coote and Nistor 1982)

1974). This can limit the profile depth as the incident beam energy necessary for a reaction with one element at 3 μm depth may produce a surface reaction with another, and vice versa. It is possible to provide some control over these sorts of problems, and (as examples) this technique has been used to measure Fluorine (Leach and Naylor 1981; Lee *et al.* 1974), Sodium (Lee *et al.* 1974; Coote and Nistor 1982) and Hydrogen (Lee *et al.* 1974; Leach and Naylor 1981; Lanford 1978; Neve and Barker 1997) profiles in obsidian.

Other than technical details the main problem in the application of RNR profiling to obsidian hydration measurements is the interpretation of the results. The depth measurement in a RNR profile is most properly referred to as a measurement in MeV, as the data actually consists of reaction intensity/beam energy pairs. The conversion of these data into a depth profile expressed in μm requires the stopping power of the artefact matrix to be known. In practice, a general stopping rate constant for material of obsidian's density is used to map the MeV scale to μm, resulting in errors of approximately $\pm$ 0.04 μm (Neve and Barker 1997).

A more significant problem is the comparison of the profile results with the measurements from other techniques. For instance, it is not obvious which point on a constructed resonance profile corresponds to an optical measurement. This issue has been addressed previously (Lee *et al.* 1974; Leach and Naylor 1981) and at least three different approaches to correlating optical and RNR measurements are published (Lee *et al.* 1974; Tsong *et al.* 1981; Leach and Naylor 1981). A common approach is to describe the full profile width at the point where resonance intensity falls to half maximum (FWHM) as corresponding to the optical measurement. There is no real discussion of why this should be an appropriate measurement and it's use is based on the assumption that the diffusion front is very steep with the maximum profile gradient falling halfway between the maximum hydration value and the level of the bulk glass. This position is based around an unproven model of the hydration profile, and could quite well result in systematic discrepancies between optical and RNR measurements. The use of FWHM as the comparison point of RNR and optical measurements has been questioned by Leach and Naylor (1981) who also assume that the visible internal rim boundary corresponds to the point of maximum profile gradient. They use the diffusion model proposed by Haller (1963) to calculate that this gradient maximum should occur at a point where hydrogen concentration is at 1/10 maximum (WTM). Again this is based on an unproven model of the hydration front. It is quite possible that the exact form of the hydration profile will be dependant on the chemistry of the glass, and the hydration environment. There are a number of possible hydration reactions (*supra vide*:§5) and it is reasonable to expect that there may be a corresponding range of possible concentration profiles. As a result the point of maximum profile gradient may vary according to the specific glass and/or hydration environment, rendering any simple ratio definition inappropriate. In this case an approach such as that adopted by Lee *et al.* (1974), who directly identify the maximum profile gradient from

the analysis results, may be most suitable.

There are benefits to using RNR as a measurement technique, the primary being that it is non-destructive and there will always be situations in which non-destructive techniques are necessary. The realised measurement precision available through this system is acceptable with a realised measurement error of approximately ± 10-15% (Neve and Barker 1997).

In spite of this, RNR profiling does not represent a viable measurement system for routine OHD. As can be appreciated, RNR measurements are expensive. A particle accelerator, specially designed reaction chamber and specialised software are required to make the measurements. A further consideration is that the measurements made are slow, further increasing cost. As an example, a semi- automated system has been developed at the AURA-II accelerator (university of Auckland), it is designed to process 20 samples in 5 12 hour days (Neve, pers comm.; UOA-511 1997 FoRST report), that is 3 hours of accelerator and personnel time per sample plus the materials cost of producing the ion beam, maintaining the necessary vacuums etc. In practice processing rates such as these are not achieved and sample processing rates of 5 a week are more likely. This leads to prohibitively expensive measurements, and as it is very unlikely that an OHD facility could have sole use of an accelerator, the measurements must be made to fit around the other work being conducted on the facility. The conclusion then is that while RNR profiling represents a useful avenue in situations where other techniques may not be appropriate (*i.e.* a non-destructive technique is required) it does not present a viable option for routine dating purposes.

2.3.2 Sputter Analysis: SIMS and SIPS

Sputter analysis operates by the principle that a surface under bombardment by an ion beam will emit charged atomic and molecular species. The ion bombardment products include electron and photon emission and the emission of surface particles. With secondary ion mass spectrometry (SIMS) the secondary ions are separated and analysed by mass analysers. With sputter induced photon spectroscopy (SIPS) the method consists of detection of optical line spectra emitted by sputtered ions. In essence SIMS and SIPS are measuring the secondary ion emission via different emission phenomena.

There a two general types of SIMS/SIPS analysis, static and dynamic. In static analysis the primary ion beam current is low resulting in a long life for the surface monolayer (in the order of some hours) and the intention is to derive information on the composition of the uppermost monolayer with minimal disturbance. In dynamic analysis a high primary beam current is applied resulting in a short lifetime of the surface monolayer ($\approx 10^{-3}s$), this erosion continuously moves the actual surface into the bulk material thus allowing a depth profile of compositional data for the material to be built up. Through the use of dynamic SIMS, depth profiling of element concentration can be achieved with a sensitivity down to the ppb range. Given the ability of SIMS to measure hydrogen concentration, dynamic SIMS is potentially very useful for studying and measuring the obsidian hydration process.

For SIPS measurements a number of chromators are used to obtain a wavelength spectrum for light emitted by excited sputtered atoms. In this manner the concentration is continuously monitored as the surface is sputtered away.

Problems can arise in the use of these sputtering techniques due to migration of atomic species (in particular Na and H). While this may handi-

cap certain applications, SIMS/SIPS represent a very useful tool for high precision measurements of multi elemental profiles in obsidian. In theory as both SIMS and SIPS only deal with the very surface layers the detection limits are in the order of nm. In practice the sputtering rate of the material is imprecisely known and this limits the ultimate precision of the measurement. However, measurements of the order $\pm$ 0.01 μm should be possible on archaeological material, and further, these techniques can measure thickness profiles in the *nm* range which holds the possibility for very useful experimental work.

The work that has been conducted in applying SIPS and SIMS to surface layer measurement has demonstrated that these two techniques hold great potential for the measurement of hydration rims and in particular, as multiple elements can be profiled simultaneously, these techniques represent great research tools for the study of obsidian hydration mechanisms.

As with all of the techniques covered here, the application of SIPS or SIMS requires that calibration is carried out to ensure the results are consistent with those derived from other techniques.

2.3.3 Tritium Exchange

The tritium exchange measurement system seeks to measure the extent of perlite formation by exchanging tritiated water from solution with water in the hydrated zone. Measurement of hydration extent is then made by measuring the amount of tritiated water that has been exchanged into the hydration rim. This can either be carried out by direct counting of the emissions from the surface of the obsidian (obsidian is a natural scintillator) or by back-exchanging from a tritiated sample and measuring tritium content of aliquots in a scintillation counter.

This technique was pioneered by Lowe (1977) and has not been widely used. The basic assumption underlying this technique is that water exchange will be rapid in the hydrated region compared to the rate of rim growth. Thus when an obsidian artefact is placed in a bath of tritium enriched water at elevated temperatures the hydrated zone will become tritium enriched without artificially enlarging the hydration rim. If this underlying assumption is correct then the measurement of the quantity of tritium enriched water in the tritiated sample will be a function of the age of the sample, and it is merely necessary to measure the tritium content of the tritiated sample and use appropriate calibration constants to produce an age estimate.

This measurement is either carried out by a surface counting method or by a back-exchange method. In the surface counting method the natural scintillation properties of obsidian are made use of with or without the aid of additional scintillators, and a standard scintillation counter is used to count the emissions. This process has met with limited success due to a number of reasons, among those cited are:

1. Due to the stopping power of obsidian only rims of depth approximately 1.3 μm or less will produce surface counts for the full depth of the rim (Lowe 1977)

2. Irregularities in the surface of the obsidian have meant that the distance from the counter window to the surface of the obsidian will introduce variable results (Lowe 1977)

3. Some obsidian already exhibit significant levels of activity naturally (Leach and Naylor 1981)

In response to some of these problems the back exchange measurement method was developed. This method is based around placing a tritiated artefact in a bath of tritium free water and back- exchanging the tritium

enriched water. Aliquots are then taken and measured in a standard scintillation counter to estimate the extent of perlite formation on the artefact.

As can be appreciated measurements produced via tritium exchange (direct counting or back-exchange methods) differ fundamentally from those produced by the other methods outlined. However, the use of appropriate calibration standards and the development of a sound definition of the measured phenomenon would ensure that any comparisons are sensible, and that the use of universal rate constants are possible.

The tritium exchange technique has some attractive features, it is cheap and if the samples were processed in bulk it should be relatively rapid. However, there are some serious drawbacks in the development of the technique and while it shows some promise, tritium exchange is not yet at the stage where it can be readily used for dating purposes.

The primary problem lies in the lack of any definition of the relationship between measured tritium uptake and hydration duration. That is, no model of the hydration process is used. On the face of it this may be attractive, but it means that there is no mechanism by which variation in environmental or glass specific hydration parameters (*e.g.* temperature) can be incorporated into the dating process. These factors must be accounted for in the dating process, or the precision of the dates are reduced to such a coarse level that the dates are effectively useless (*supra vide*:§4).

Some attempt has been made to provide a general empirical rate equation, however there may be problems with this development. One problem is that during the development of tritium exchange measurement, the experimenters did not check that the differences in tritium uptake were not a function of phenomena other than time. They simply assumed that their underlying assumptions were correct and then used a set of archaeological controls to develop the measurement technique to

generate the assumed ages of the controls. There is some evidence that hydrogen concentration may be inversely related to the environmental hydration temperature (*supra vide*:§4). Thus samples that have hydrated at a cooler environmental temperature may uptake a larger amount of tritium, simply as a function of a higher concentration of hydrogen in the hydrated zone, than if they had developed an identical hydration extent in a warmer environment. This potentially confounding factor has been ignored so far, as has any question about the security of the cross-dating exercise.

Other problems due to factors such as fractionation may also arise. As the proposed diffusion mechanism is a thermodynamic process it would be expected that there would be an isotopic differentiation in the diffusion process, especially given the large difference in weight of tritium and hydrogen. This could possibly confound effects arising from differences in hydrogen concentration of the hydration zone.

In conclusion the tritium exchange technique is not currently a viable measurement approach. Future research may fully address the use of tritium-exchange techniques for rim measurement purposes, until then it must remain a potentially useful technique.

2.3.4 Conclusion

A variety of non-optical techniques have been applied to the measurement of hydration rims, yet none of these are currently routine, nor do any yet represent viable methods for the basis of an ongoing dating method. The most promise is shown by SIMS/SIPS, and if these techniques are developed to a level where they represent a readily available and economically cost-effective measurement system, they will be of great use to obsidian hydration dating. At the moment they must be classed, at best, as useful research tools.

2.4 Optical Hydration Rim Measurement

Optical techniques are based around the measurement of hydration phenomena observed in obsidian thin sections. This is a two step process. Initially a thin section perpendicular to the artefact surface (30-60 μm thick) must be produced. Secondly, an hydration rim must be identified in the thin section through a transmitted light microscope and measured. This primary optical train is common to all optical measurement systems with the principal differences occuring in the processing of the hydration phenomena visible in the thin section.

Optical measurement techniques used with OHD fall into four main categories: microscope based, photogrammetric, video and digital image analysis. Measurements made via techniques from within the first three categories are fundamentally the same, with the implementation simply varying. These three approaches require that the operator defines the rim boundaries and measures the rim thickness against some scale. With microscope based techniques the measurements are made through the microscope, usually with a filar micrometre or an image splitting eye piece. Photogrammetric techniques operate in an identical manner except the measurement is made on a photomicrograph of the image as opposed to through the microscope, and the measurement is made with any calibrated scale (Findlow and DeAtley 1976). Video techniques again operate in a similar manner, except this time the measurement is made on a video image either via specialised hardware or software. The only technique that is fundamentally different is digital image analysis (Ambrose 1993; *supra vide*:§2.6). In this approach a digital image of the hydration rim is captured to a computer and the measurement of the hydration rim is made by analysis of this image according to a specific definition the hydration phenomena. In the original approach proposed by Ambrose (1993) an integrated pixel intensity histogram running perpendicular to a portion of the rim image is generated. In this manner

the rim boundaries can be defined as the points of lowest intensity and the measurement is made in terms of a pixel count between the two intensity minima (*e.g.* Figure 2.2).

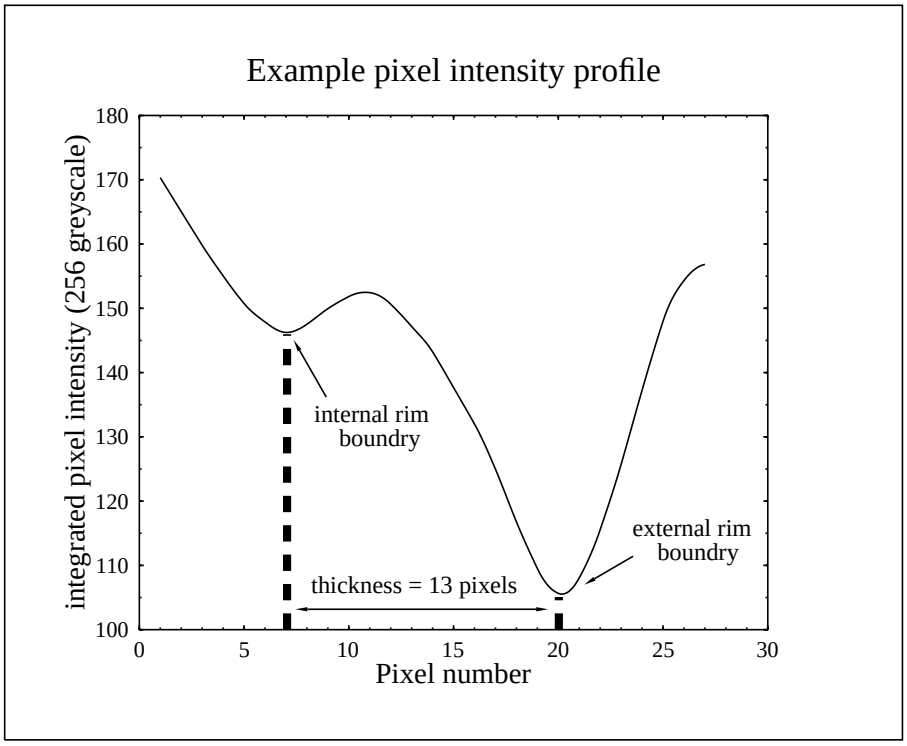

Figure 2.2: Example of intensity profile following the simple pixel count method (Ambrose 1993)

Optical measurement techniques are potentially inferior in accuracy to the non-destructive techniques such as argon milling, nuclear resonance profiling or interference spectrometry. Yet the effective measurement precision of properly designed optical techniques (0.03-0.2 μm), as discussed later (*supra vide*:§2.6), is not greatly different to the non-optical techniques (0.03-0.1 μm). The major difference lies in the fact that most optical techniques can not provide objective, and therefore consistent,

measurement results. This introduces considerable ambiguity into the measurement process reducing the effective precision, and is bound to reduce confidence in the technique. Measurement uncertainty arises from the nature of the hydration rim. As can be appreciated when looking at a rim image (Figure 2.3) the internal and external boundaries are not sharply defined. The visible rim boundaries is are simply dark zones and at high magnifications there are no obvious measurement points. If it is left to the operator to define the rim boundaries, there is considerable scope for variation in rim measurements. For instance in Figure 2.3 it is apparent that the true rim thickness lies somewhere between the length of lines d1 and d2, a range of 0.8 μm which corresponds to a measurement range of $\approx$ 75%. Using a technique where the operator is responsible for choosing the appropriate rim limits, the measured length would lie somewhere in this interval, with a certain degree of variation between successive measurements by the same operator, and certainly between different operators. It is not difficult to see why there have been problems in the consistency of optical rim readings (*e.g.* Stevenson *et al.* 1989*b*).

A further problem with current approaches to optical hydration measurement is the fact that there has been very little consideration toward quantifying the uncertainty associated with any quoted measurements. Without a meaningful measurement error the measurements can not represent useful chronometric data.

This section is an overview of fundamental optical measurement issues common to all optical measurement approaches. It considers the basic optical train used in hydration rim measurements and forms the basis for the application of all optical measurement techniques, including the digital image analysis techniques presented later (§2.6). The major factors common to all measurements are microscope resolution, system set-up and confounding optical phenomena. Additionally the perfor-

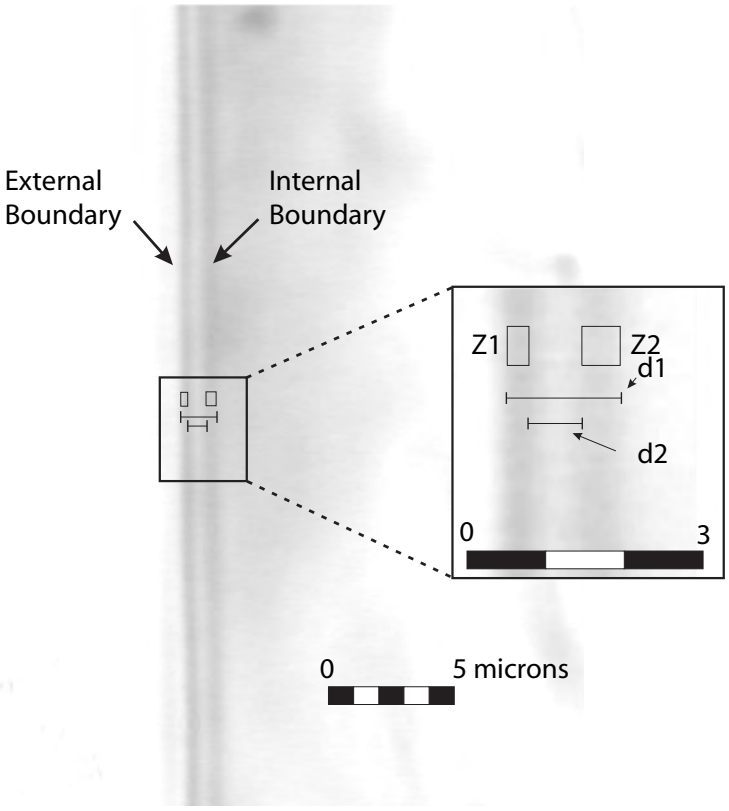

Figure 2.3: A digital hydration rim image

The figure shows the difficulty of making an objective measurement of the rim thickness. It is apparent that the rim thickness lies somewhere between the lengths of the lines d1 ($\approx 1.5\mu m$) and d2 ($\approx 0.7\mu m$). This range arises as the rim boundaries cannot be precisely discriminated optically and each rim boundary appears to correspond to a zone of apparently uniform intensity (Z1 & Z2).

mance of the human eye is an important consideration in all techniques other than digital image analysis. In the following we consider each of these factors separately.

2.4.1 Microscope Resolution

While microscope resolution has been the object of discussion with respect to OHD in the archaeological literature, it seems to have been used synonymously with perception limit and measurement precision (*e.g.* Scheetz and Stevenson 1988). A dangerous practice as these terms mean different things and describe different quantities. Microscope resolution is simply the smallest distance that can be resolved between two objects (Pluta 1988). There is no ultimate limit to how small an object can be detected given sufficient illumination (Spencer 1982; Pluta 1988), and this perception limit is not the same as system resolution which simply quantifies how far apart two objects have to be in order to be distinguishable as separate objects (Klein 1970). Archaeological literature seems to take the attitude that microscope resolution represents the ultimate limit to measurement accuracy (*e.g.* Scheetz and Stevenson 1988). This is only the case if the hydration rim thickness approaches the system resolution, which is very rare. Microscope resolution merely limits how small a rim can be measured. The limit to rim measurement precision lies in how accurately the separation of two precisely defined points can be measured. To pursue this discussion further it is necessary to outline some basic principles of microscopy.

Resolution

The resolution of a system is governed by diffraction at the aperture of the objective lens (Pluta 1988). Due to this diffraction the light from a

luminous object doesn't focus at a point, but forms a diffraction pattern consisting of an intense central maximum flanked by weak secondary maxima (Pluta 1988). If the optical system is perfect or suffers from very small aberrations then the image of any point object follows that of the ideal Airy pattern

The ideal Airy pattern has a symmetrical circular form, and the normalised light intensity I across the image is expressed by (Pluta 1988):

$$I' = \left(\frac{2J_1(Y)}{Y}\right)^2 \tag{2.1}$$

Where $J_1(Y)$ denotes the first order Bessel function of the first kind, and Y is a parameter known as the Airy optical unit and defined by (Pluta 1988):

$$Y = \frac{2\pi n sin\sigma y'}{\lambda M_{ob}} \tag{2.2}$$

Where λ is the light wavelength, n the refractive index of the space between the object point and the objective, σ the object-side aperture angle, M_{ob} the magnification of the objective and y' the distance from the centre of the Airy pattern. From this it can be derived that the point is viewed as a small patch of radius

$$r_{Airy} = \frac{1.22\lambda}{2nsin\sigma} \tag{2.3}$$

Thus for a given magnification (M_{ob}) the radius r_{Airy} is smaller the larger the numerical aperture $nsin\sigma$ of the objective and the smaller the wavelength λ. So for a system using a 100x objective with $NA = 1.3$ and $\lambda = 0.55\mu m$, the Airy disk will have a radius of $0.26\mu m$.

This phenomenon is directly related to the resolution of the optical microscope (Spencer 1982). While there is no lower limit to the size of an

object that can be detected in isolation given adequate illumination, if two objects are in close proximity, the Airy pattern that each produces will overlap. There comes a point when the overlap is so bad that it becomes impossible to say whether there are two objects or only one. The resolution of the system defines how great a distance two points must be apart before the overlap of diffraction patterns is small enough that the points can be distinguished (Pluta 1988). The definition of this distance is somewhat arbitrary (Spencer 1982), but a measure that is widely used is Rayleigh's criterion (Pluta 1988). This states that two objects can be distinguished when the central maximum of one pattern overlays the first minimum of the other. In this situation the separation (Q) between the two points must be equal to the radius of the Airy disk viewed in the object plane. Thus

$$Q = \frac{1.22\lambda}{2nsin\sigma} = \frac{0.61\lambda}{NA} \tag{2.4}$$

Where λ is the wavelength and NA is the numerical aperture of the objective ($NA = nsin\sigma$).

In this situation the intensity midway between the two points falls to approximately 74% of the maximum value at the Airy centre. All of this theory is based upon the assumption that the object is illuminated with incoherent light. As we work at very high magnifications in OHD the distance we wish to resolve is less than the transverse coherence of the light, and as such the light should be treated as coherent. In order to achieve the same 74% intensity drop between two points under coherent illumination the separation must be greater, namely

$$Q = \frac{1.63\lambda}{2nsin\sigma} = \frac{0.82\lambda}{NA} \tag{2.5}$$

As can be seen the resolving power is worse for coherent than for incoherent illumination.

In the case of OHD we are more interested in the two line resolution of the system than the two-point resolution. Based upon the same principles as the two-point resolution the two- line resolution according to Rayleigh's criterion is given by

$$Q = \frac{0.5\lambda}{NA} \tag{2.6}$$

for resolved images in incoherent illumination, and

$$Q = \frac{0.75\lambda}{NA} \tag{2.7}$$

for coherent illumination.
Thus the resolving power for lines is better than for points.

An alternative definition of microscope resolution in mainstream use is Sparrow's criterion (Pluta 1988). This states that two points can be treated as already separated if the second derivative of the intensity function (d^2I/dx^2) is zero at the midpoint between the centres of the Airy disks. According to this definition the two-line resolution is given by

$$Q = \frac{0.41\lambda}{NA} \tag{2.8}$$

for incoherent light, and

$$Q = \frac{0.66\lambda}{NA} \tag{2.9}$$

for coherent light

The above values are considerably smaller than those derived via Rayleigh's criterion, so it is probably more conservative to use Rayleigh's criterion in the estimation of system resolution. Similarly it is also more conservative to assume that the illuminating light is fully coherent. In practice

the transmitted light falls somewhere between fully coherent and fully incoherent on the basis of the condenser aperture (Pluta 1988).

The numerical aperture can be made as high as 1.6 for the immersion objectives used at high magnifications (Klein 1970). Thus with $NA = 1.6$ & $\lambda = 500$ nm, $x_{s,min} = 0.156\mu m$ is the maximum theoretical resolution of an optical microscope operating in the visible light spectrum. In all systems the effective NA will fall below the value of 1.6 and the maximum resolution will decrease accordingly. In order to further improve resolution it would be necessary to reduce λ , though this would mean the light passing out of the visible spectrum. In theory this could be accomplished by using an UV light source and an UV sensitive video camera attached to the microscope. This is an approach being used in other fields, particularly biology. However, as the resolution in visible light is sufficient for the purposes of OHD there is little point in investing the time and money for the increased resolution of an UV system.

Another gain in resolution can be made through the use of digital image analysis. Image analysis can be used to deconvolve the diffraction patterns arising from the objective and thereby increasing the effective NA of the objective. This super-resolution when combined with other analysis techniques such as VEC (video enhanced contrast) can result in a tenfold increase in effective resolution (Weiss and GaGlfe 1986). Weiss and GaGlfe (1986) report the use of computer imaging to increase effective resolution to 0.02 μm in biological applications. Applications of this sort could be made to OHD measurements, but as microscope resolution is not a significant barrier for the purposes of OHD this type of process is not necessary.

Having outlined the basis of the calculation of system resolution it is important to note again that this does not represent a limit to the precision with which rim measurements can be made. The resolution will only have a significant effect on measurement precision if the rim width

approaches system resolution and it becomes impossible to resolve the rim boundaries. This will very rarely be the case. As noted previously; in a typical oil immersion system with a 100× objective of $NA = 1.3$ and $\lambda = 0.5$ the system resolution is 0.26 μm . The only practical limit this sets on rim thickness measurement is that the rim thickness must be greater than 0.26 μm for the rim boundaries to be resolved. We are not interested in resolving the rim boundaries into components. We are merely interested in being able to consistency locate a precisely defined point on each of the optical phenomena that demark the hydration rim. If this condition can be satisfied then we have a basis for producing high precision rim measurements.

As stressed previously, for the purposes of OHD we are interested in a detectable time dependant phenomena. The intensity distribution associated with the hydration boundary is such a phenomenon. For the purposes of OHD it is not necessary to resolve the elements that produce this intensity distribution. Rather it is sufficient that we can detect and measure this distribution. In light of this, if we can accurately locate precisely defined points on the intensity distribution associated with an hydration rim, then we have an accurate measurement system suitable for the purposes of OHD. This can be demonstrated by looking at Figure 2.4. In terms of OHD we are interested in accurately locating the two intensity minima associated with the optical hydration phenomenon. As this intensity profile corresponds to a 1000× magnification we are working at the resolution limits of the microscope. Therefore if we increase the magnification of the image we do not resolve any more detail of the rim components, rather we simply achieve a magnification of the already resolved continuous intensity distribution associated with the optical hydration phenomenon. This is shown in the figure where each of the intensity minima are shown magnified to a 10,000× magnification, which does not reveal any further detail of the hydration rim. In the case of OHD this fact is irrelevant, as we only wish to locate the

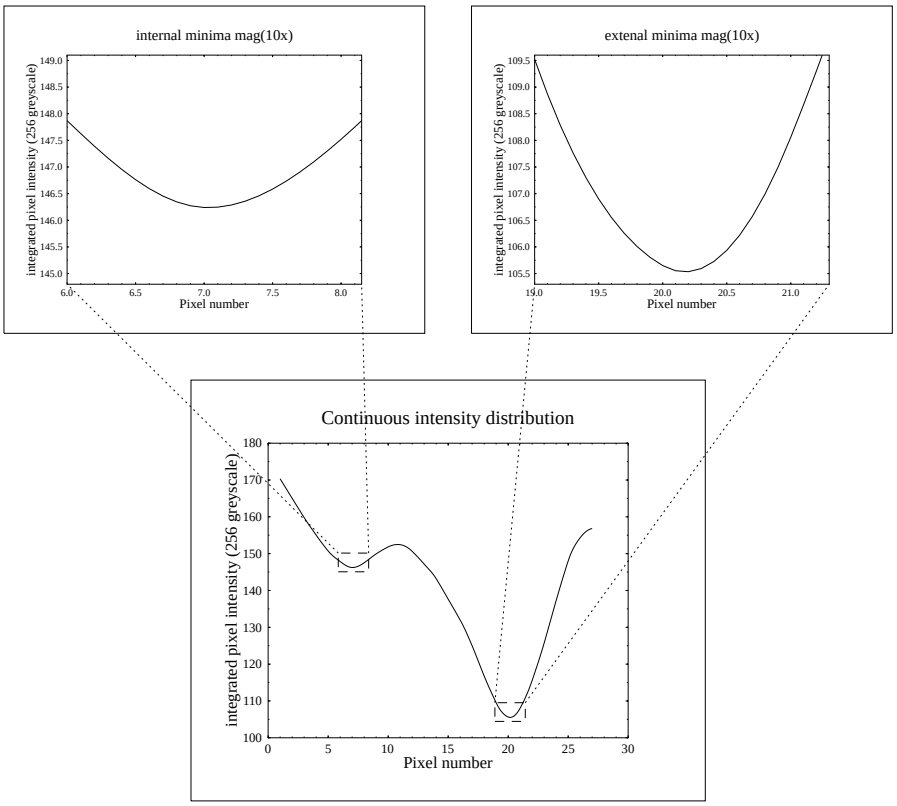

Figure 2.4: Example of the difference between resolution and precision of point location: In the magnified portions of the two intensity minima we do not resolve any further structure of the object creating the optical intensity distribution. However we can locate the location of the visible minima with greater precision in the magnified portions

intensity minima, we do not need to resolve greater detail of the rim image. Thus, as long as the system resolution is sufficient to resolve the intensity distribution corresponding to the optical hydration phenomena, microscope resolution should not make any difference to hydration measurements.

However, we do need to ensure that a correct and consistent microscope

set-up is used. This ensures that the maximum resolution is used for any given measurement, and also ensures that the measured optical intensity distributions remain consistent between samples.

2.4.2 Microscope Set-up

Correct and consistent microscope set-up is an important measurement step, as this ensures that any images are being compared according to the same measurement process, and also influences the measurement by affecting the quality of the image. Techniques for accurately setting microscopes are discussed in detail elsewhere (*e.g.* Pluta 1988; Spencer 1982), though it is worth noting that correct set-up is vital as this will enhance image quality. As OHD measurement is all conducted via Kohler illumination, only simple procedures are necessary. Of primary importance is keeping the microscope system clean and free of dust. Beyond this basic step, the condenser setting plays an important role in producing clear sharp images. It is important that the condenser is correctly focussed, and that the condenser aperture is correctly set, as the condenser setting effects the contrast, resolution and depth of field of an image. This is important, as in OHD we would like to produce as high a contrast image as possible in order to aid in identification of the rim boundaries, yet we would also like to ensure that the resolution is sufficient to resolve the rim boundaries, and further that the depth of field is as small as possible in order to identify any non-normality that may be present. Unfortunately there is a trade off between these measures, and the ideal high contrast, high resolution, low depth of field image cannot be readily achieved. Though a suitable compromise can be established. There is a direct trade off between contrast and resolution/depth of field. A high contrast image will reduce the resolution and increase depth of field. In many respects this is not a difficult problem to resolve, as we merely need enough image contrast to make the rim boundaries

out from the background. If the minimum contrast is used to achieve this situation then depth of field will be minimised and resolution maximised.

Table 2.3: Standard microscope set-up

Step 1	Close the field diaphragm until it is in the field of view
Step 2	Close the condenser aperture to minimum
Step 3	Focus the condenser until the field diaphragm is in sharp focus
Step 4	open the condensers aperture until there is a distinct haze around the visible field diaphragm
Step 5	open the field diaphragm until it is just out of the field of view

Table 2.3 outlines an appropriate set-up procedure. If a procedure such as this is followed as a basic step for every section portion viewed then all images will correspond to a common process. This will avoid many of the problems that may occur due to confounding optical phenomena if the microscope is incorrectly set. Once this set-up procedure has been carried out the condenser focus should not be changed for any given rim portion, though it is often desirable to open the condenser aperture wider once the rim image is in focus in order to reduce the depth of field and contrast.

Correct setting of the microscope also helps identify and minimise the impact of confounding optical phenomena.

2.4.3 Confounding Effects

Correct sample processing protocols and equipment set-up as discussed previously will help ensure the quality of the optical hydration rim mea-

surement. However, there are other potential sources of error. In particular it is possible that confounding optical phenomena may be incorrectly identified as hydration phenomena. This would be principally expected to arise through Fresnel diffraction or Becke lines.

Fresnel diffraction patterns can be seen off sharp edges (Lipson *et al.* 1995; Fowles 1968) and are apparent off the edges of some obsidian samples. The ideal Fresnel pattern generated by a straight edge results in a very similar optical phenomenon to that of the optical hydration phenomenon. A visible intensity minimum occurs off the edge of the obsidian away from the body of the sample. In practice when measuring hydration rims usually only the first Fresnel minima (if any) can actually be seen. This minimum occurs at a consistent distance from a diffracting edge dependant upon the microscope set up (Fowles 1968). When rim thickness is comparable to the separation of the first two Fresnel minima there is potential for confusion as the two dark bands due to the sample edge and the Fresnel minima may be mistaken for an hydration rim. This can raise problems when observing an edge where no rim is present and the operator mistakenly measuring the rim, or secondly causing confusion as to which phenomena to measure. As this effect will not be noticed under crossed polars, the obvious solution is to establish where and if the actual rim occurs under crossed polars if the measurement is to be made under normal transmitted light. Another way of reducing the impact of Fresnel diffraction is to reduce the contrast by opening the condenser aperture.

Uncertainty arising from Fresnel effects will be particularly prevalent in situations where the hydration rim is small, especially where the rim is optically difficult to detect. In these situations it is vital that the rim is checked under crossed polars before any measurement is made under normally transmitted light, and also that it is established that the hydration phenomena remain visible as the condenser aperture is opened and

the image contrast drops.

Becke lines also occur at the boundary between media of differing refractive indices and have been previously identified as a potentially confounding phenomenon (*e.g.* Anovitz *et al.* 1999). However it is easy to identify confounding Becke phenomena. Becke lines form due to a lens effect where materials of differing refractive index are in contact. A particular feature of Becke lines is the fact that as the field of focus is moved up or down through the image the Becke line will move (Nesse 1991). A correct hydration phenomena will not move as the field of focus is moved through the image. Thus this constitutes a simple test to Identify potentially confounding Becke phenomena.

The fact that hydration rim images should remain stationary as the field of focus is moved through the image also relates to section non-normality. While the gross surface of a flake section may be normal, at a microscopic level there will be variations in the normality of the section along the rim image. However if the immediate section is normal, the rim boundaries will remain in the same place as the focal plane is moved through the image. If the rim appears to change in size or the boundaries move as the focal plane is moved through the image then the section is not normal at that point and the section should not be measured. Thus moving the focal plane through the rim image constitutes a useful test for establishing the integrity of any rim image.

Thus if a well prepared section is observed through a properly set-up microscope confounding optical phenomena and poor quality portions of the rim image should be readily identified.

As a final aspect of this discussion for non-digital techniques we need to consider the final element of the optical train — the human eye.

2.4.4 Function of the Eye

High precision measurements require that measurements are made between points that can be exactly located according to a precise definition. And secondly, and perhaps less importantly, that the separation of these points can be accurately determined. Thus high precision rim measurements rely on the accuracy of two separate processes. As systemic errors are additive the overall precision of the measurement is limited by the least accurate component of the measurement process. Accordingly, very high resolution measurement scales are useless without a consistent and precise method of locating measurement points.

In most optical systems the operator must locate the measurement points, and the function of the human eye introduces a degree of error into how precisely these points can be defined and located. As outlined previously any point or optical phenomena is composed of an intensity distribution. Thus when we make a measurement between any objects we must select points on the associated intensity distributions to make the measurement from. High precision measurements require that these points can be precisely defined and accurately located. Therefore it makes sense to chose either an intensity maximum or minimum, as these points are easily defined, and should therefore be able to be relocated. In all optical techniques bar one (digital image analysis) the eye must be capable of determining where these maxima or minima occur, and, as will be outlined in the following, this can result in errors.

Contrast Sensitivity of the Eye

The degree to which this discrimination can take place is defined by the contrast sensitivity function of the human eye (Inoué 1986; Schiffman 1990). This describes the contrast threshold for different spatial frequencies, where the spatial frequency is the number of luminance

changes per degree of visual angle. Using this function we can define the contrast necessary for a given spatial frequency to be detectable to the eye.

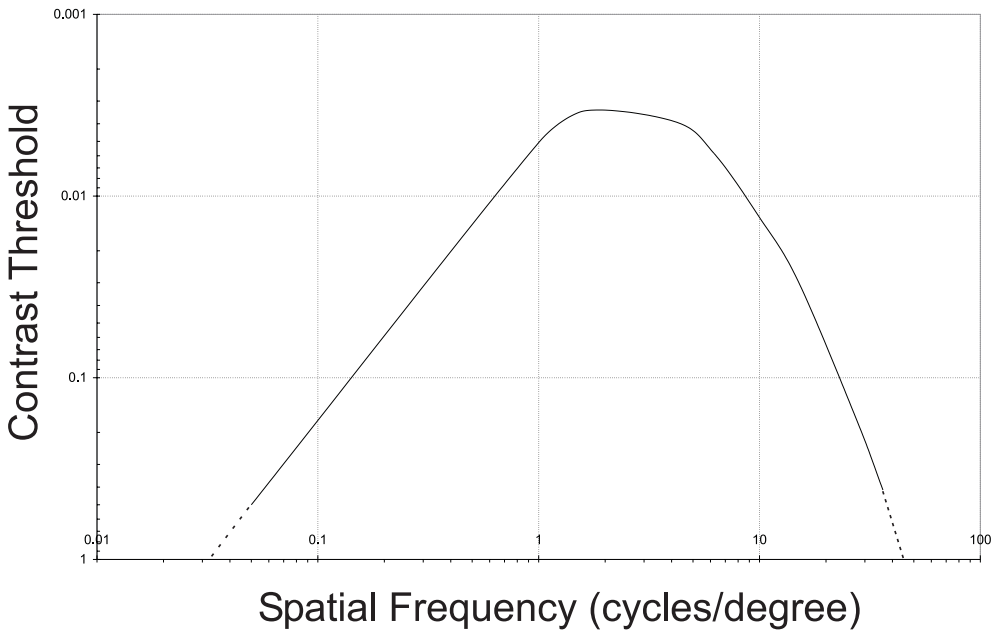

Figure 2.5: Contrast sensitivity function after Schiffman (1990) pp. 281.

In a standard microscope a visual angle of 1° corresponds to an image size of approximately 4.5 mm (Pluta 1988). Thus the spatial frequency of an intensity distribution equals 4.5 mm divided by the cycle size (image distance across the contrast change of interest). For instance with an idealised Airy disk the cycle size is the system resolution × the system magnification. So for a system with a resolution of 0.26 μm the image(cycle) size of the Airy disk will be 0.26 mm and the spatial frequency will be

$$\frac{4.5}{0.26} = 17.3 \tag{2.10}$$

Using the contrast sensitivity function (Figure 2.5) the contrast threshold

at this spatial frequency is approximately 0.09. Where contrast is

$$C = \frac{Max(I') - Min(I')}{Max(I') + Min(I')} \tag{2.11}$$

As the contrast over the cycle of an ideal Airy disk is 1 we should, and can, easily discriminate the pattern. However, the discrimination of the point of highest intensity within the central luminous portion of the Airy disk is more difficult. If we take a point 0.5 r_{Airy} each side of the point of highest intensity the spatial frequency is exactly twice that of the full Airy disk (*i.e.* 34.6) and as the Intensity at 1/2 r_{Airy} is 0.37 of the max, the contrast is

$$C = \frac{(1 - 0.37)}{1.37} = 0.46 \tag{2.12}$$

Again using the contrast sensitivity function the contrast threshold for a spatial frequency of 35 is approximately 0.5. Thus the image contrast falls below the contrast threshold, and the eye is incapable of differentiating the contrast in the internal luminous portion of the Airy disk which appears to be of uniform intensity.

In this manner the location of precise measurement points is limited by the ability of the eye to discriminate a precise location on an intensity distribution. In the case of an ideal Airy disk there is a range of the system resolution centred on the Airy disk centre over which the eye cannot discriminate the highest intensity. So the measurement of the distance between the intensity maxima of two ideal airy disks is limited by the inability to consistently visually locate the same measurement points.

A similar case arises in measuring the hydration rim. Under normal transmitted light two hydration bands are visible. The most sensible points to make the measurements from are the two intensity minima as these points can be precisely defined (Ambrose 1993). The problem arises in precisely locating the minima. The dark band on each side of the hydration rim is again an intensity distribution (*e.g.* Figure 2.4)

and measurement accuracy is limited by the ability of the eye to locate intensity minima in what appears to be a uniform intensity field.

While it is very difficult to define the exact error likely to occur due to this effect[1] it is possible to outline the likely degree. This can be achieved by measuring the contrast change per degree of visual angle for a series of measured rim intensity profiles such as that presented in Figure 2.4. From this it is possible to calculate the size of the intensity minima zone associated with each rim boundary over which contrast cannot be discriminated, and thus provide a measure of the degree of error that may be introduced into measurements. This process can be

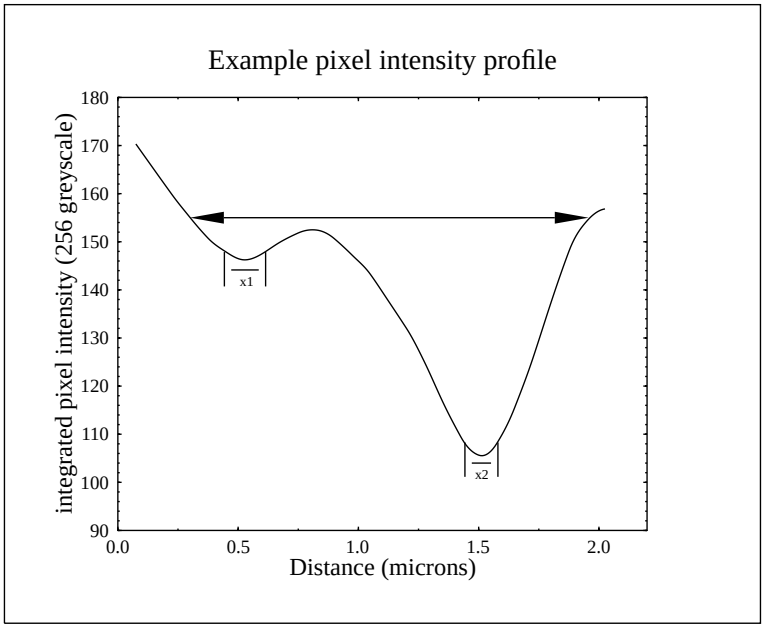

Figure 2.6: Diagram of apparent uniform intensity zones

described with reference to Figures 2.3 & 2.6. It is apparent that there

[1] due to the fact that it will vary according to a number of factors such as microscope set up, and we have no precise model of the actual underlying optical phenomena associated with hydration rims

will be two zones (x1 & x2) in Figure 2.6 around the two intensity minima over which the image intensity may appear to be uniform. This is shown in Figure 2.3, where it is apparent that the hydration rim boundaries, which appear clear at normal magnifications, in fact represent zones of apparently uniform intensity (zones Z1 & Z2 in Figure 2.3) despite the fact that the intensity distribution actually corresponds to a distribution like that in Figure 2.6. We can use the contrast sensitivity function of the human eye to calculate how wide the zones x1 & x2 in Figure 2.6 will be. For instance if we consider the length x1 in Figure 2.6 a length of $0.15\mu m$ would mean that the contrast (equation 2.11) would be

$$c = \frac{147.8 - 146.2}{147.8 + 146.2} = 0.005$$

at a spatial frequency of $2.5/0.15$ which is below the contrast threshold and hence an x1 of $0.14\mu m$ would appear to be a zone of uniform intensity. In contrast to this, the overall intensity distribution represents a contrast of 0.23 over at a spatial frequency of 1.25 which, unsurprisingly, is above the contrast threshold. By repeating this process it is possible to calculate threshold values for x1 and x2 below which the zone would be perceived as of uniform intensity. If this is repeated for a number of intensity distributions it is possible to outline the magnitude of potential error arising from limitations in the contrast discrimination of the human eye.

In an attempt to provide some measure of the extent of this problem x1 & x2 have been measured for a number of images. As the measured intensity curves are only approximations (as is the contrast sensitivity diagram) it is a little spurious to try and precisely calculate x1 & x2, so this has simply involved a process of subjectively fitting zones of apparently uniform intensity similar to those shown in Figure 2.3. As a result the figures given correspond to the microscope set up used (Nikon photomic II with panchromatic oil immersion objective, NA 1.4. and the contrast sensitivity of my eyes). So these figure should be regarded as

simply an estimate of the extent of variation likely to occur due to this factor. The figures presented in Table 2.4 are the estimated zones of uniform intensity measured in pixels from 50 random digital rim images. The pixel counts are presented as an Euclidean measure as is the estimated rim thickness, and the total error that may result. As can be seen from the data it is possible that significant differences in measurement may be expected if these zones were measured subjectively by different operators, or a number of times.

Table 2.4: Uniform intensity zones

x1 (pixels)	x2 (pixels)	x1 (μm)	x2 (μm)	rim thickness (μm)	% error
1	2	0.075	0.15	0.825	27
3	6	0.225	0.45	1.2	56
4	6	0.3	0.45	1.125	67
2	3	0.15	0.225	0.7875	48
2	2	0.15	0.15	0.8625	35
4	6	0.3	0.45	1.125	67
5	6	0.375	0.45	1.125	73
1	2	0.075	0.15	0.6375	35
1	1	0.075	0.075	0.7875	19
4	6	0.3	0.45	1.2	63
2	5	0.15	0.375	0.9375	56
3	6	0.225	0.45	1.125	60
2	2	0.15	0.15	0.9	33
2	5	0.15	0.375	0.9	58
1	1	0.075	0.075	0.675	22
2	3	0.15	0.225	0.75	50
2	5	0.15	0.375	0.9	58

continued on the next page

Table 2.4: *continued*

x1 (pixels)	x2 (pixels)	x1 (μm)	x2 (μm)	rim thickness (μm)	% error
1	2	0.075	0.15	0.7875	29
5	6	0.375	0.45	1.35	61
4	6	0.3	0.45	0.8625	87
5	6	0.375	0.45	1.125	73
1	1	0.075	0.075	0.6375	24
2	2	0.15	0.15	0.825	36
2	5	0.15	0.375	1.0125	52
2	3	0.15	0.225	0.825	45
1	2	0.075	0.15	0.825	27
2	2	0.15	0.15	0.7875	38
2	2	0.15	0.15	0.7875	38
2	2	0.15	0.15	0.8625	35
3	6	0.225	0.45	1.1625	58
3	4	0.225	0.3	0.975	54
3	4	0.225	0.3	0.9	58
2	2	0.15	0.15	0.75	40
3	6	0.225	0.45	1.35	50
2	2	0.15	0.15	0.8625	35
3	4	0.225	0.3	0.825	64
2	3	0.15	0.225	0.975	38
5	6	0.375	0.45	1.275	65
1	2	0.075	0.15	0.675	33
2	2	0.15	0.15	0.9	33
1	1	0.075	0.075	0.75	20
1	1	0.075	0.075	0.6375	24
2	5	0.15	0.375	1.125	47

continued on the next page

Table 2.4: *continued*

x1 (pixels)	x2 (pixels)	x1 (μm)	x2 (μm)	rim thickness (μm)	% error
3	4	0.225	0.3	0.7875	67
3	6	0.225	0.45	1.1625	58
5	6	0.375	0.45	1.2375	67
3	4	0.225	0.3	0.8625	61
2	2	0.15	0.15	0.75	40
4	6	0.3	0.45	0.9	83
2	3	0.15	0.225	0.8625	43
mean		0.1875	0.2775		
min		0.075	0.075		
max		0.375	0.45		
range		0.3	0.375		

This demonstrates that optical techniques which rely on operators to locate the precise rim boundary points will suffer from errors due to functional limitations of the human eye. The human eye is not capable of contrast discrimination with sufficient resolution to enable measurement of optical hydration phenomena according to precise rim boundary definitions. This will result in inconsistent measurements and consequently a true measurement precision well below that which may be achieved with an objective technique such as digital image analysis.

2.4.5 Conclusion

Optical hydration rim measurement is a relatively simple process. It involves measuring the separation of two precisely defined points on a rim image. As long as a well prepared sample is observed through a correctly set-up microscope and a protocol to identify confounding op-

tical phenomena is employed, an image suitable for consistent objective hydration rim measurement is available. Unfortunately, subjective measurement approaches that require an operator to visually locate the hydration rim boundaries will suffer inconsistencies in measurement due to functional limitations of the human eye. It is apparent that an objective optical measurement protocol such as digital image analysis needs to be adopted to ensure consistent measurements. Further there needs to be a meaningful quantification of the uncertainty associated with any measurement. This is currently lacking from any of the measurement approaches that have been adopted to date.

Thus while there are a number of techniques that can be used to measure hydration rim thickness the majority of these cannot make suitable measurements. This is because most approaches are not based around a precise and consistent definition of the measurement points of the optical hydration phenomena, and further there has been almost no consideration of measurement uncertainty. Clearly this is not desirable for the base chronometric data of a dating system and it is necessary to establish an approach that can provide suitable measurements results.

In the following we will examine some aspects of digital image measurement with a view to developing an objective optical hydration measurement protocol that meets the requirements for producing a suitable OHD chronometric (§2.6). This is based around an adaptation of the computer imaging approach proposed by Ambrose (1993). However, the first step in producing an optical rim measurement is the thin sectioning process. As the quality of the thin section effects any subsequent measurements a consideration of the thin sectioning process is an appropriate point to begin.

2.5 OHD Thin Section Preparation

Thin section production is an integral part of optical rim measurement and constitutes the principal sample preparation step. Accordingly it is important to identify what factors govern the quality of thin sections for the purposes of OHD, and to establish a suitable section production protocol.

The general process of producing a thin section is to cut a cross section from the surface of an artefact, then mount and grind this sample to a suitable thickness for rim measurement. In light of this there are three aspects of thin section production that need to be addressed:

1. Thin section normality: As optical measurements are based on the size of a rim cross-section, non-normal thin sections are problematic as the thin section does not present a true cross section of the hydration rim. Non-normality of the thin section will result in inflated apparent rim thickness. It is important to quantify this problem and establish methods to control it (*supra vide*:§ 2.5.1).

2. Rim protection during the thin section making process: It is important to protect the rim surface during the, at times, aggressive thin section making process. Damage to the rim can result in poor image quality and inaccurate rim measurements. Some simple steps can greatly improve rim protection and therefore greatly improve image quality and measurement confidence (*supra vide*:§ 2.5.2).

3. Optimum section thickness: Section thickness effects optical clarity and to some extent contrast. It is important that sections are not so thick as to reduce image clarity, yet sections that are too thin may result in reduced contrast, and in some cases result in the total obliteration of the sample during section production. It is

useful to establish an appropriate routine section thickness (*supra vide*:§ 2.5.3)

These general areas are addressed in the following three sections (§2.5.1–2.5.3).

2.5.1 Thin Section Normality

If a thin section is produced where the section is not perfectly normal to the immediate artefact surface then the apparent rim thickness (T) will be greater than the "true" value (x) (Figure 2.7). This rim inflation can be easily quantified by considering the geometry of the rim to be read. Any non- normality of the edge section-surface angle will result in the apparent rim being the hypotenuse of a triangle with base x (the true rim thickness) and angle θ (the angle between the surface normal and the actual section cut). This means that the apparent rim thickness (T) of any non-normal sample will be a cosec(θ) percent inflation of the true rim thickness x. Since our interest is in OHD, the significance of any inflation should be referred to the resulting date error. The inflation of apparent rim thickness due to section non-normality is purely a function of the true age of the artefact and the non-normality angle, this is easily established as

$$\begin{aligned}
\text{apparent age} &= \frac{T^2}{k} \\
\text{true age} &= \frac{x^2}{k} \\
\text{Age error} &= \text{apparent age} - \text{true age} \\
&= \frac{T^2 - x^2}{k} \\
&= \frac{x^2(\text{non} - \text{normality inflation} - 1}{k} \\
&= t \times (\text{non} - \text{normality inflation} - 1) \qquad (2.13)
\end{aligned}$$

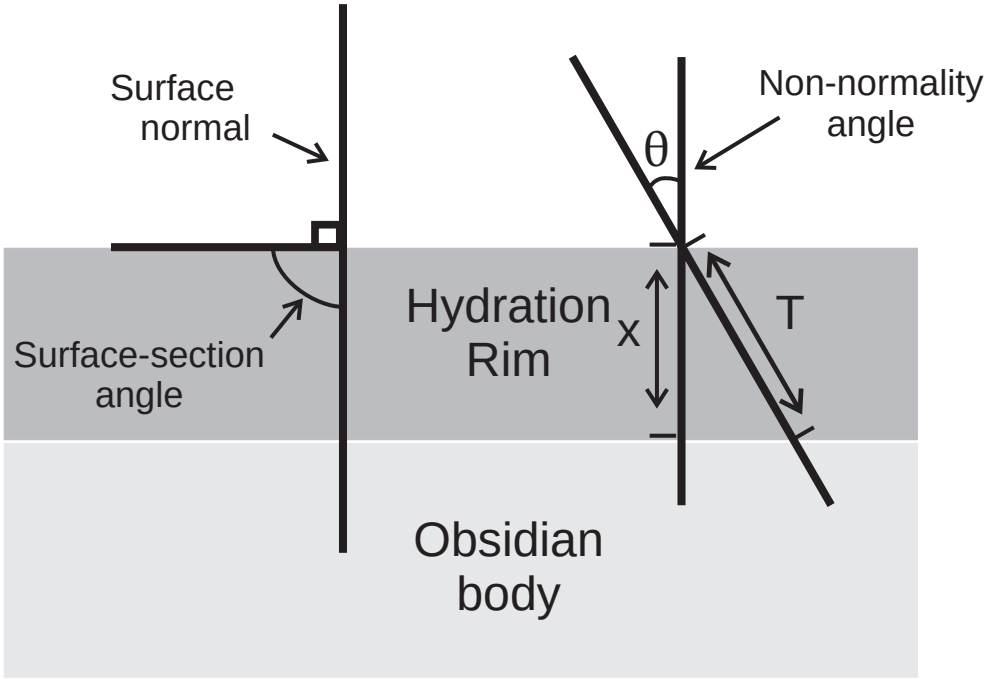

Figure 2.7: The geometry of non-normal rim inflation

Presented in Figure 2.8 are the inflation error and date error curves for samples of 250, 500 & 1000 years age. Obviously, for small values of θ the inflation is small and does not constitute a significant error. Looking at Figure 2.8 we can see that θ 's of approximately 5^o or less constitute insignificant levels of error. Though errors rise rapidly after this, and if we have no *a priori* evidence about the age of the artefact it is difficult to use the calculated age to estimate the possible degree of non-normality date error. It is apparent that if we can keep the normality deviation angle to below 5^0 we will be incurring errors of less than 10 years for samples from throughout New Zealand's prehistory. Nevertheless, it must be appreciated that this type of error could have very significant effects on samples of considerable age as the effects will be pro-rata those presented in Figure 2.8. For instance a sample 5000 years old will experience $5\times$ the error plotted for the 1000 year line.

Variation in rim measurements due to non-normality can occur at two stages of the rim measurement processes. Initially, inadequate thin section preparation techniques may result in a non-normal thin section being produced or read. A second source of non-normal rim variation can arise from a poorly designed rim reading protocol. It is important to eliminate any potential non-normality inflation from both of these processes. As a starting point we can define four points where non-normality errors may arise in the thin sectioning and reading process:

1. A non normal initial section cut
2. Incorrect face identification
3. Angle introduced during grinding and polishing
4. Incorrect rim reading protocol

As outlined in the sections that follow simple procedures can ensure that any potential errors are eliminated during these steps.

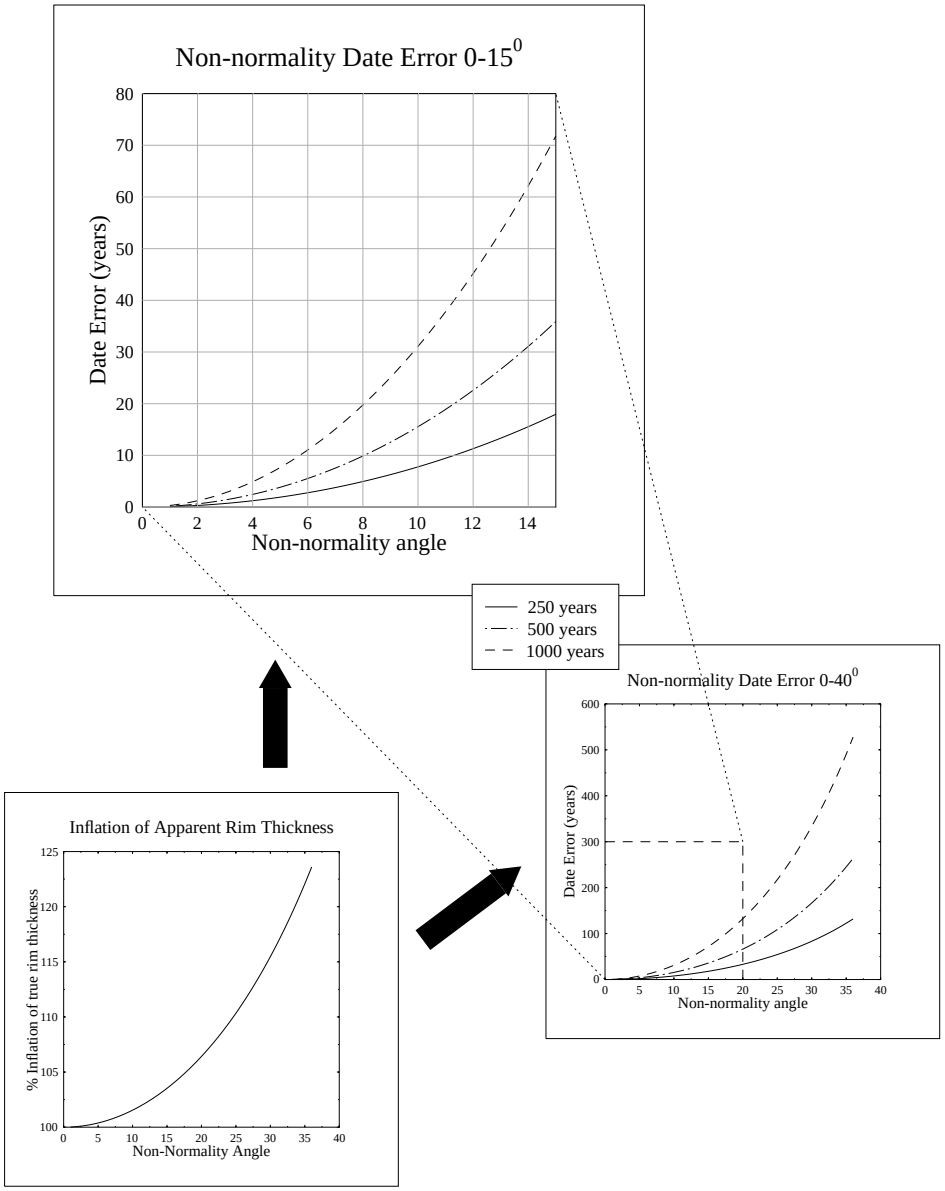

Figure 2.8: Non-normality errors

Normal Section Cuts

Given the potential error introduced into the dating system by non-normal rim inflation it is imperative that the surface section cut is as normal as possible. As a study into the degree of non-normality introduced into the surface section angle by the initial section cut, two different cutting approaches were compared. The approaches tested were (i) cutting the sample by holding the flake manually and orienting the flake visually (ii) setting the flake in a plasticine bed, and orientating the flake visually.

The test data for approach (i) has been generated from samples processed by the Auckland OHD lab 1993-1994. In this test the angles have been measured by taking a video image of the cut in the flake and measuring the surface section angle on each face (*e.g.* Figure 2.9). To make the measurement conservative the most normal angle was measured in each case, even though there was no face identification protocol in place (*supra vide*:§2.5.1) when these sections were cut and it is possible that the actual reading was taken from the less normal face. Thus this data is a conservative measure of the error introduced from this rim cutting process.

The samples to test approach (ii) were cut as a specific test set, the section surface angle being measured as for (i). In these samples a face identification protocol was in place and the measurements are a true representation of the normality variation of this rim cutting process.

In total 50 flake angles were measured from approach (i) with an average normality deviation in the surface section angle of 8.5^o ($\sigma = 6$). As can be appreciated this represents a significant source of error in the final dates. Additionally, this cutting approach introduces a high degree of damage to the rim surface as is outlined in the following section.

The results of approach (ii) were not much better. In total 50 surface

section angles were measured with an average normality deviation angle of 4^o ($\sigma = 6$). Again extensive surface damage resulted through this cutting process.

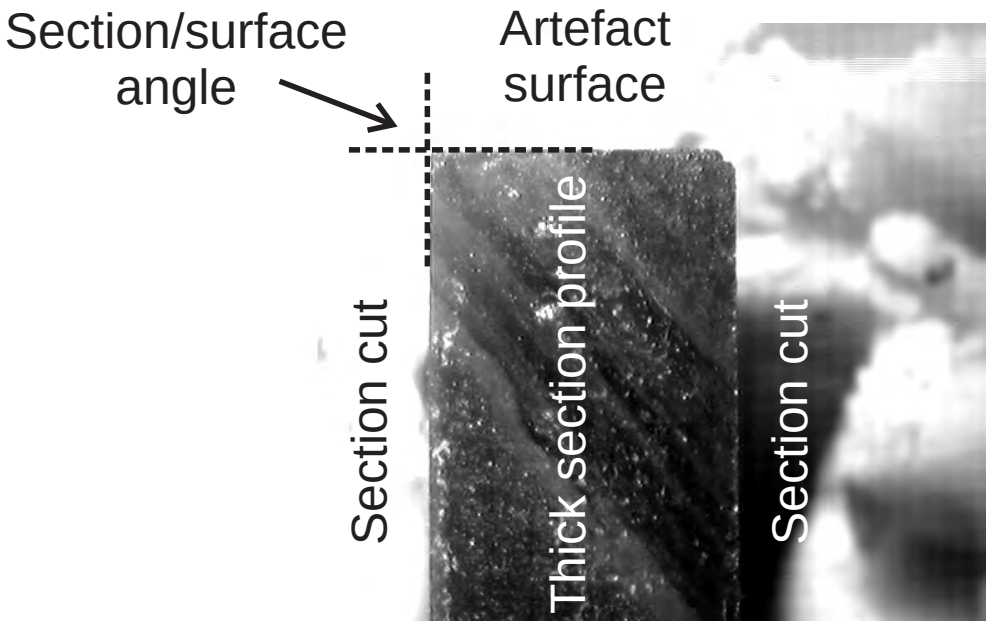

Figure 2.9: Example of video measurement of the surface/section angle apparent in the thick section profile

As can be appreciated, neither of these approaches can generate the normality control desired. While the average deviation angle is below the 5^o tolerance limit for the plasticine bed approach, a high percentage of the flakes will be well above the 5^o tolerance limit (due to the high standard deviation of normality angles for this technique).

The results of these two tests provided the motivation to produce a section cutting process that provided better normality control. The approach that has been adopted is to mount a portion of the artefacts' ventral surface on a slide. By applying heat and pressure this surface will set parallel to the slide. A normal section cut can then be made by running the glass slide along a bed set at right angles to the saw blade. This

ensures that the cut is normal to both the glass slide and the mounted artefact surface. This process is cheap, quick and produces consistently normal section cuts. As a test of this procedure, the section angle was measured for 60 samples via video imaging of the x-section. The results returned an average normality deviation angle of 2^o ($\sigma = 0.5$), and the angles were well within the 5^o tolerance limits outlined earlier.

Face Identification

Face identification is necessary, as in general only one of the flake faces can be normal to the section[2]. Therefore when a section is cut only one of the flake surfaces can be normal to the cut (*e.g.* Figure 2.11).

In the example given in Figure 2.11 a section has been cut normal to the upper surface of the flake leaving the bottom surface at an angle of $\approx 30^0$ ($\theta = 31.6$) to the section cut. This means that the apparent thickness of the rim on the non-normal side will be inflated by a value of cosec(30) or 115%. This could correspond to date errors of up to 300 years (see Figure 2.8) in dating samples from New Zealand's prehistory. Clearly this source of error must be controlled for.

Errors of this sort can easily be avoided by only measuring the rim from the face that is normal to the cut. In selecting the face to be read it makes sense to make the cut perpendicular to the ventral surface of the flake. As we know that this is the most recently exposed face, and therefore is the most sensible temporal marker of the archaeological context. Additionally, we can be sure that the ventral surface is a cultural surface. Ensuring the correct face is read is a simple matter of cutting a notch into the non-normal face that will be apparent in the final thin section (Figure 2.13)

Ignoring this source of error in rim measurement can result in significant

[2] as the faces of an obsidian flake are rarely parallel

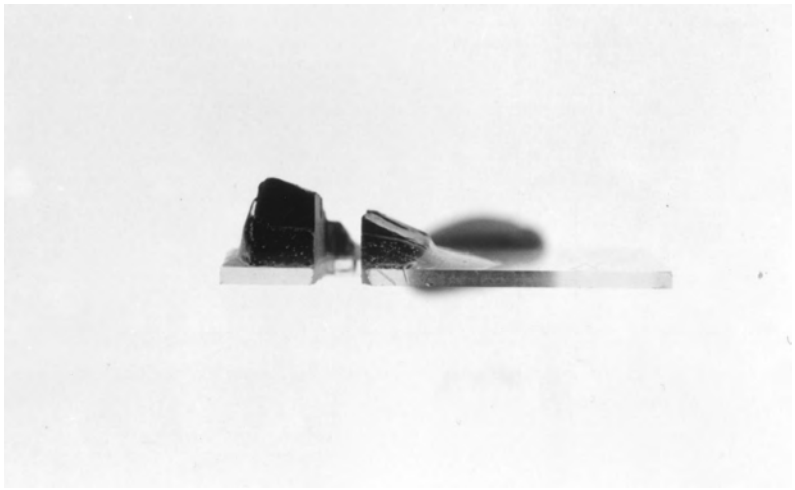

(a) One

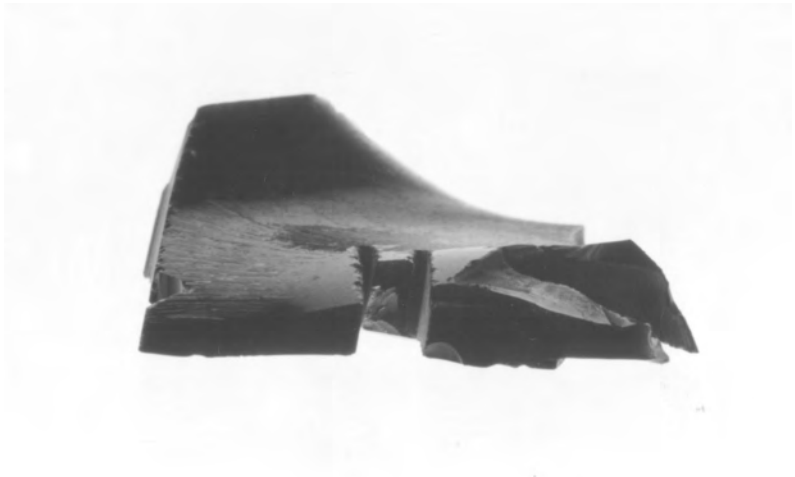

(b) Two

Figure 2.10: Non-normality photos

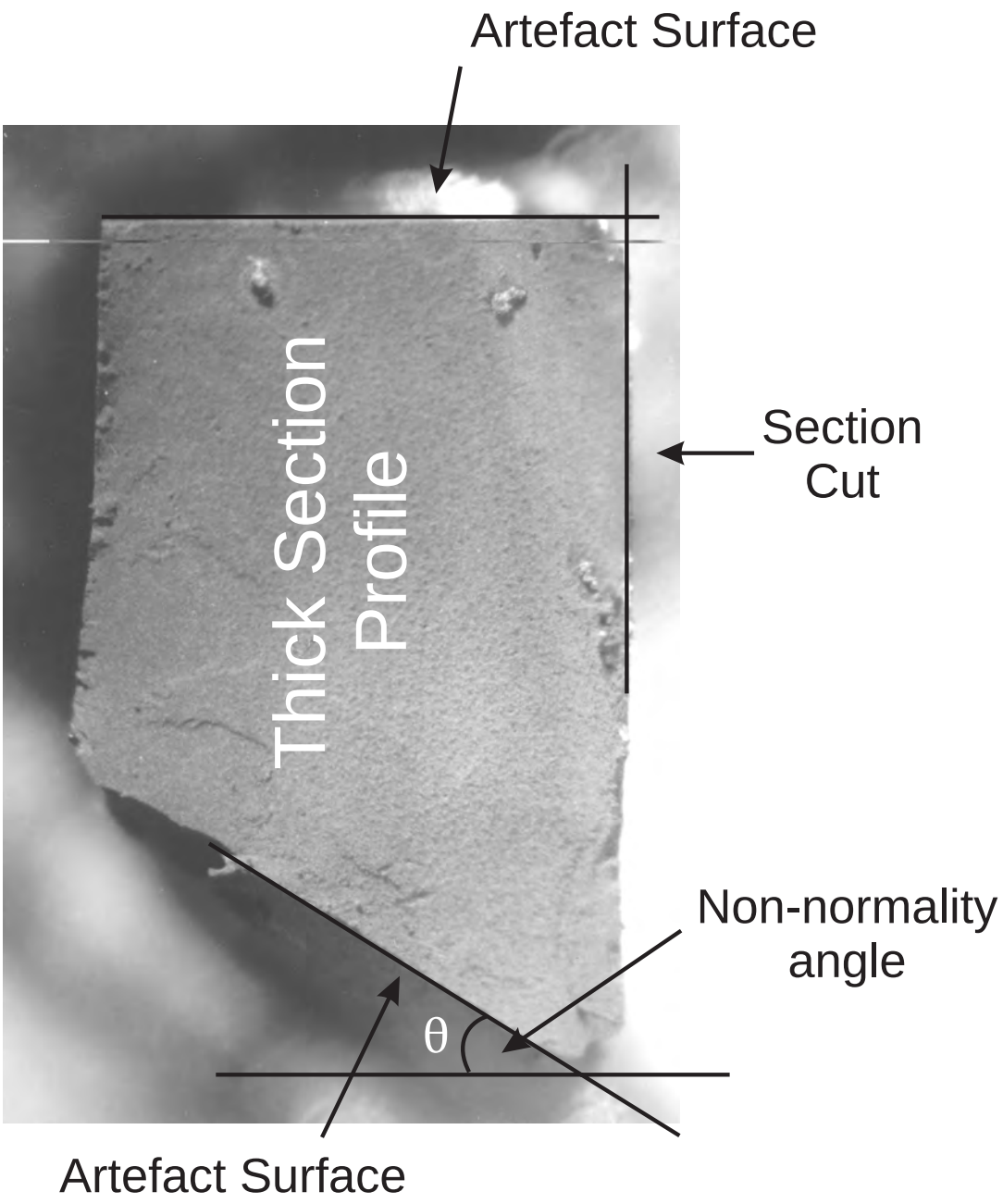

Figure 2.11: Face identification non-normality

In the example above the profile of an obsidian thick section is shown. The upper artefact surface, which corresponds to the ventral surface of a flake, is effectively normal to the section cut, incurring insignificant non-normality inflation error. The lower artefact surface is at an angle of 30^0 to the section cut, which would result in an apparent rim thickness of 115% of the true value.

and avoidable date errors. As a measure of the magnitude of variation introduced into the system by this source of error 200 slides were cut from 50 obsidian artefacts. The slides where read for rim thickness with a comparison between the face cut parallel to the slide and the opposite face. In total 10 readings were taken on each face to establish the effects of non-normality introduced into the system by ignoring the non-parallel nature of obsidian flake surfaces. Of these, 8 samples where removed from the test due to poor rim quality which would have resulted in rim inflation due to unrelated causes. In total 1640 readings were used in the test. For each sample the smallest reading on each of the faces (face 1 cut normal to the surface, face 2 opposite face) was chosen to give a conservative measure of the rim measure and avoid any excessive rim inflation due to confounding variables. Normality to face 1 was judged visually and the cut was made by setting the sample in a plasticine bed normal to the saw blade. As this will result in some rim inflation of face 1 (*infra vide*:§2.5.1) the comparison between face 1 and face 2 should be considered a conservative measure (Table 2.5). In 74% of the samples the face 2 rim was measurably larger, and on average the Face 2 rims were 19% larger than those on Face 1 with a percentage difference between the two faces ranging between 0 and 80%. A paired samples t-test returned a significant difference between the face means at α=99%. None of the face 2 rims were smaller than the face 1 rims.

Table 2.5: Non-normality error due to incorrect face identification

Sample	Face 1 measurement	Face 2 measurement measurement	Rim Inflation (%)
548	0.9	0.9	0
549	0.97	1.05	8.25

continued on the next page

Table 2.5: *continued*

Sample	Face 1 measurement	Face 2 measurement measurement	Rim Inflation (%)
550	0.8	1.12	40
550	0.8	1.05	31.25
551	0.9	1.02	13.33
551	0.72	0.79	9.72
552	0.9	1.09	21.11
553	0.72	0.72	0
553	0.67	0.99	47.76
554	0.78	0.87	11.54
555	0.7	0.7	0
555	0.7	0.75	7.14
556	0.92	0.92	0
557	0.72	1	38.89
558	0.87	1	14.94
559	0.9	1	11.11
560	1	1	0
561	0.79	0.9	13.92
562	0.62	0.81	30.65
563	0.67	0.67	0
564	1.02	1.05	2.94
566	1.1	1.1	0
567	0.65	0.65	0
568	0.7	0.87	24.29
569	0.97	1	3.09
569	0.9	1.1	22.22
570	0.64	0.88	37.5
570	0.67	1	49.25

continued on the next page

Table 2.5: *continued*

Sample	Face 1 measurement	Face 2 measurement measurement	Rim Inflation (%)
571	0.83	1.01	21.69
572	1	1	0
573	1	1	0
574	0.95	1.02	7.37
576	0.72	1.29	79.17
578	0.64	0.94	46.87
578	0.65	0.85	30.77
579	0.7	0.85	21.43
580	0.8	0.92	15
581	0.95	1.12	17.89
583	0.65	0.65	0
585	0.95	1.12	17.89
586	0.85	1.1	29.41
586	0.58	0.9	55.17

As can be appreciated it is vital that a face identification protocol is integral within any thin sectioning process. This basic and simple step can avoid significant measurement error.

Summary

By dealing with the issues just outlined, it is possible to effectively remove non-normality errors from the optical rim measurement process. This results in a far less variable measurement than would be observed if non-normality errors were not taken account of.

A second issue in the production of thin sections is protecting the hydration rim during processing.

Martin Jones 2002

2.5.2 Rim Protection

Cutting and grinding the sample is an aggressive process and can result in extensive micro-damage to the rim (see Figure 2.12). It is important to reduce this as much as possible as this ensures that image quality is good and that the measurements made actually correspond to the full archaeological rim. With fragile rims protection is vital as this may make the difference between being able to make a measurement or not. Rim protection needs to occur during both the cutting and grinding/polishing steps of section production.

Protection During Cutting

When the initial section is cut, shatter occurs on the upper and lower faces of the artefact and the resultant thick section (Figures 2.12 & 2.13). This shattering is particularly pronounced on the lower face of the section, and it is important to ensure that a rim section free from this damage is read. This can be accomplished either by cutting a very thick initial section, which is highly destructive and incurs a high time cost, or by reducing the degree of damage during the cut. The degree of damage can be dramatically reduced by setting the sample deeply in cement during the cutting process and backing the sample with a piece of "sacrifice" glass (Figure 2.12(a)). That is, if the sample is mounted on a glass slide then the shattering occurs on the glass slide leaving the obsidian surface free of any shatter (Figure 2.13(b)). If the ventral flake surface is mounted face down on a glass slide in this manner the surface section of interest is preserved and suffers minimal damage during the cutting process. Compare the artefact surface on the thick sections shown in Figures 2.13(a) and 2.13(b).

This protection occurs by default when the method for ensuring normal section angles described earlier is followed (*infra vide*:§ 2.5.1).

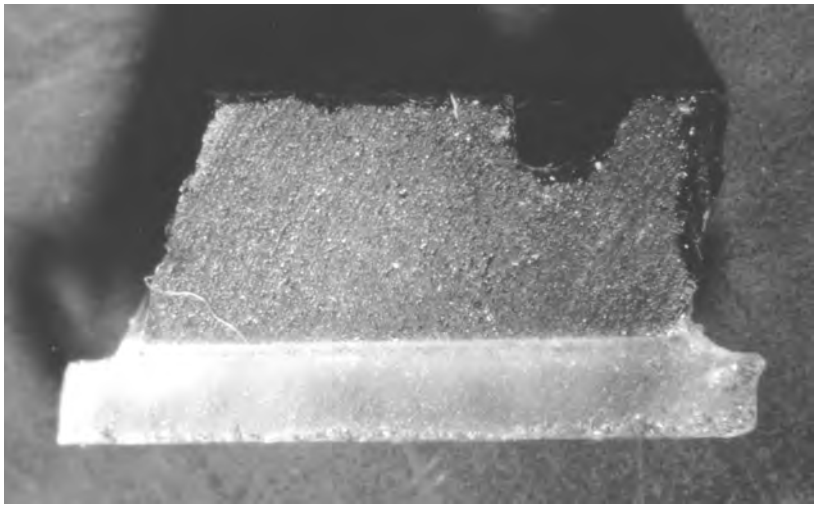

(a) Protected thick section: the shatter occurs on the sacrifice glass

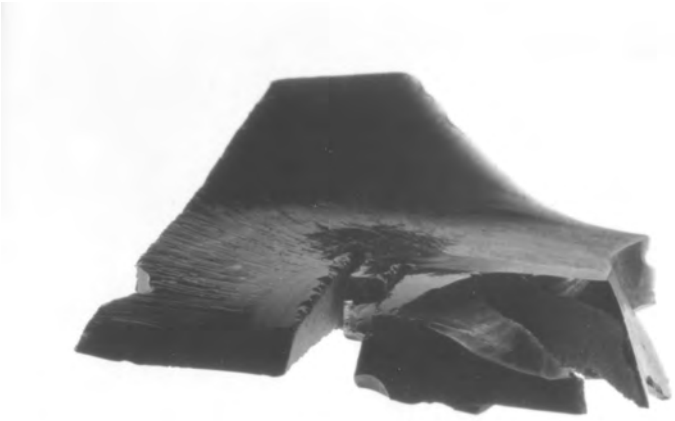

(b) Shatter on the artefact following an un-protected section cut

Figure 2.12: Example of edge shatter location on thick section

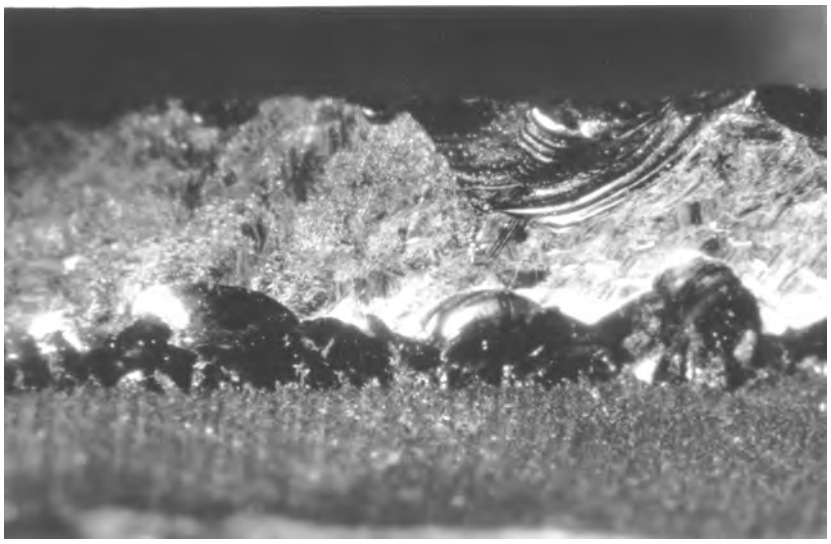

(a) Un-protected surface

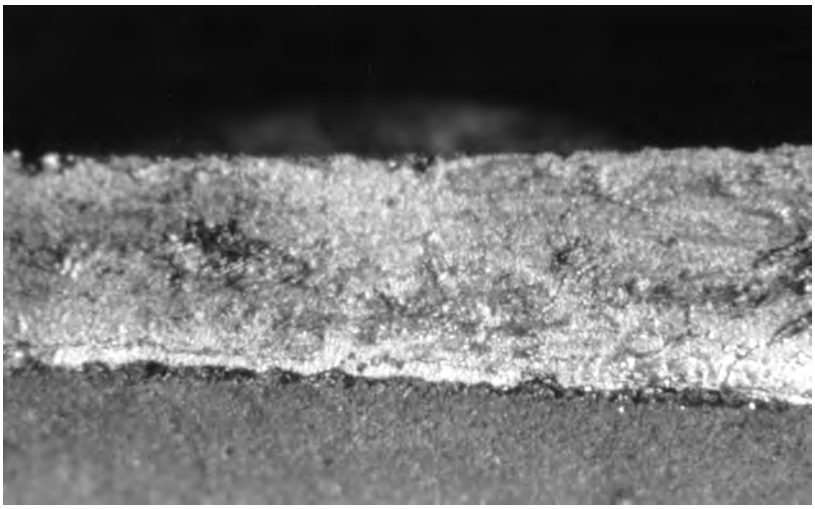

(b) Protected surface

Figure 2.13: Comparison of shatter on the thick section surfaces under protected and un-protected section production

Protection During Grinding/Polishing

The second process that can introduce rim damage into the thin sectioning process is the grinding and polishing step. If an exposed rim is ground there is the potential for damage to the surface. This can result in both poor quality rims and a reduced apparent rim thickness. It is best to protect the rim during this process, and a simple method of achieving this is to leave the glass section bonded to the obsidian during the cutting process (Figure 2.13) in place during the grinding/polishing process. If the samples are deeply set in cement then the rim is protected from any potential damage. As a further safety measure it is a good idea to orient the surface to be measured toward the centre of the slide. This means that it is practically impossible to accidentally damage one of the rims due to chipping or over pivoting during grinding.

The measurement of Samoan Basalt Rims: A Case Study in Rim Protection

Clark *et al.* (1998) report measurements made on weathering rims of basaltic glass from Samoa as an argument in support of recent ceramics in the region. In the case of these measurements rim protection was paramount as the weathering rims were very fragile. Standard petrographic sectioning procedures failed to produce thin sections with any intact weathering rim evident, presumably because the fragile weathering rim was destroyed during the section making process. When the sectioning process previously described was used with these samples, intact weathering bands were apparent. A contrast between these methods is evident in Figure 2.14. Figure 2.14(a) shows a typical result of standard sectioning procedures, which left a shattered poorly intact surface zone. In contrast Figure 2.14(b) shows a typical rim protected example with an visible weathering band. The adoption of a sectioning protocol

designed to maximise rim protection allowed the measurement of useful archaeological data in this case.

2.5.3 Thin Section Thickness

The final issue we need to address with regard to thin section production is the optimum section thickness. Thin section thickness should not be of great importance, as in general the image depth of field will be less than the section thickness. However, the thickness will have an influence on image quality and it is important to establish the optimum thickness range. If too thin a section is produced, there is the danger of totally obliterating the slide during the grinding process, and if the slides are too thick image quality will suffer.

As part of an effort to produce high quality slides an experiment designed to outline appropriate section thicknesses was run. As standard petrographic thin sectioning procedures can be hard to perform on obsidian due to the fact that there are often no crystals present in a sample suitable for determining section thickness, an initial set of experiments were conducted to determine actual section thickness from the measured mounted thickness. In these experiments three separate tests were conducted to determine section thickness from mounted thickness. In effect this process took the form of measuring the cement thickness between the petrographic slide and obsidian section. In each experiment the petrographic slides were ground to a standard thickness of 0.8 mm, in all cases the reported mounted thickness is the total sample thickness minus petrographic slide thickness. The experiments were

1. Measuring the mounted thickness of 10 samples and then slowly grinding the samples to obliteration. The thickness at obliteration was assumed to be slide thickness plus mounting cement thickness.

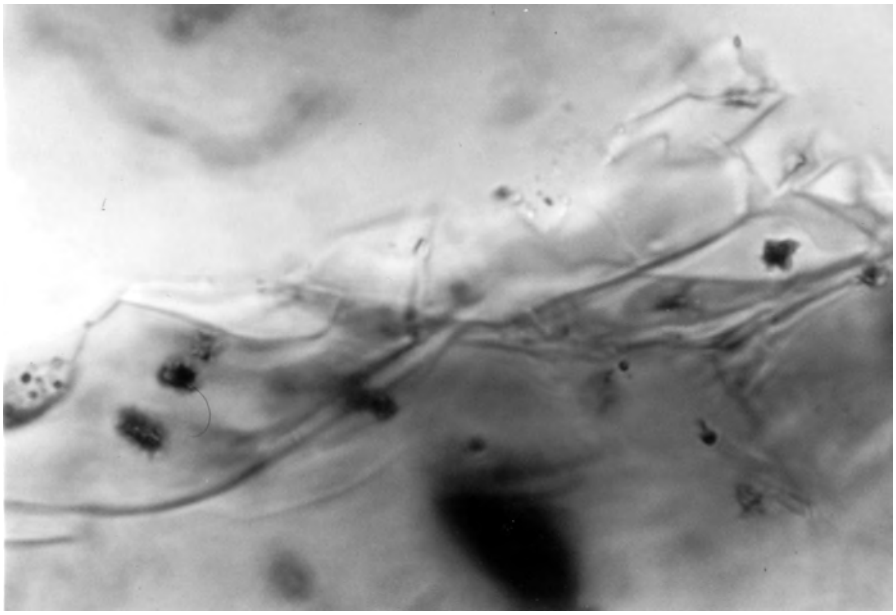

(a) Standard petrographic sectioning process

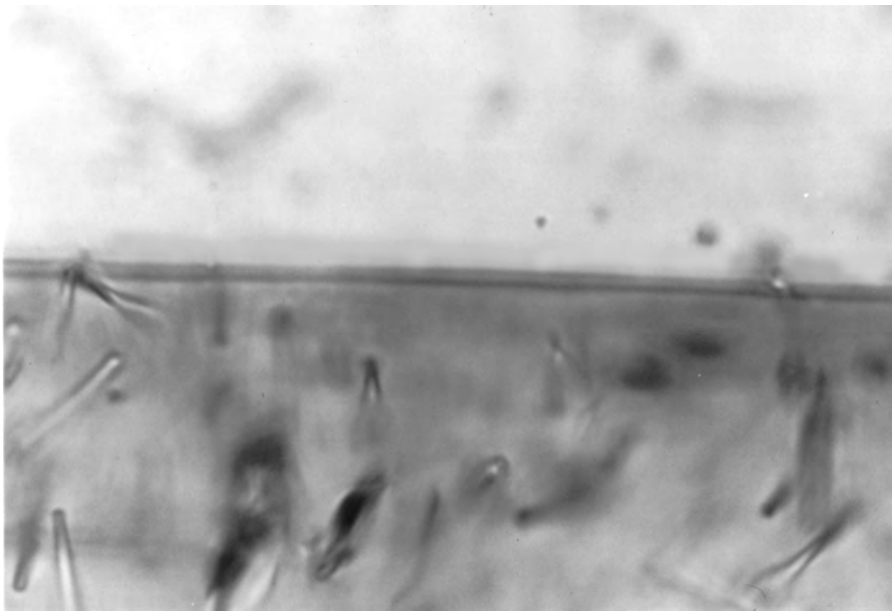

(b) Rim protection sectioning process

Figure 2.14: Samoan glass examples

2. Measuring the mounted thickness of 10 samples of known section thickness. The glue thickness simply being the difference between mounted thickness and section thickness.

3. Using standard thin sectioning techniques on 10 samples with feldspar present to produce a section of 30 μm and then measuring mounted thickness.

The results of these experiments (Table 2.6) showed that a standard cement thickness of $\approx$ 30 μm results from the mounting process used here (overall mean = 30.3 $\pm$ 3.78μm). This enables the actual section thickness to be approximated by simply subtracting 30 μm from the mounted thickness. Using a vernier micrometre this process gives section thickness to $\pm$ 10 μm . Once this had been established an exper-

Table 2.6: Mounted thickness experiments

sample	Thickness (μm)		
	exp 1	exp 2	exp 3
1	25	30	25
2	30	25	34
3	25	32.5	32.5
4	30	30	30
5	35	30	35
6	30	30	25
7	40	35	30
8	30	32.5	35
9	30	30	32.5
10	25	25	30
mean	30	30	30.9
σ	4.7	3.1	3.7

iment was run to establish the optimum section thickness for the purposes of hydration measurement. For this experiment 5 samples were selected and sections of each of these were produced with section thicknesses ranging from 20 μm to 100 μm in 10 μm steps. The samples were subjectively judged for optical clarity, and it transpired that within the limits 30- 70 μm section thickness made no detectable difference, and quite frequently outside these limits there was little difference. On the basis of this it has been decided to produce sections with a mounted thickness of 70 μm which produces a section thickness of $\approx 40\ \mu m \pm 10\ \mu m$. This thickness produces consistently clear sections and is unlikely to result in a sample being ground to obliteration.

2.5.4 Conclusion

Thin section production is an integral part of optical hydration rim measurement, and it is important that the thin sectioning process is optimised for the purposes of OHD. Failure to follow a suitable section production protocol can give rise to significant errors in hydration rim measurement. Standard petrographic sectioning procedures are not adequate in themselves as the needs of petrography and OHD differ. In particular, sections for OHD must offer a section normal to the surface of interest. It has been outlined in this section that significant errors can arise due to section non-normality. A simple, effective, protocol has been outlined in order to maintain the appropriate section normality.

Another area particular to the purposes of OHD is the importance of the sample edge. In contrast to petrography, interest in OHD sections is almost exclusively on a very fine band of potentially fragile material at the extremes of the section. It is easily appreciated that this area should be protected as well as possible. Standard petrographic sectioning procedures do not offer optimised protection to the very edges of the section,

as this is not of primary interest to petrography. It has been shown that the section normality protocol outlined in this section has the added benefit of offering a high degree of rim protection.

Following the discussion presented in this section a suitable sectioning protocol for the purposes of OHD is as follows:

Sample preparation : bond a small plane section of the ventral flake surface to a clean piece of petrographic slide. This must be done with a heat proof epoxy such as Hillquist cement, so that the glass remains in place during the entire thin sectioning procedure (Figure 2.10,2.13).

Face identification : cut a notch in the side opposite to that which will be read. This should be cut so that it will be visible in the resulting thin section (Figure 2.12(a)).

Sample cut : place the bonded slide on a saw bed set at 90° to the saw blade and cut a thick section.

Sample Mounting : place four thick sections on a single petrographic slide, with the faces to be read oriented toward the centre of the petrographic slide.

Sample Grinding : initially grind the samples on a thin sectioning lathe so that all section surfaces are in the same plane, and then polish the exposed face with grinding powder. Following this mount the polished surface on a second slide and repeat the grinding and polishing on the second side until the mounted section thickness is 70 μm as measured by vernier micrometre.

This section production protocol that has been employed for the analyses presented in this thesis.

Having established a protocol for the production of thin sections we can now consider the details of measuring the hydration phenomena present in these samples.

2.6 Digital Rim Measurement

The measurement of rim thickness by digital image analysis involves the manipulation of digital image data to identify and quantify optical hydration rim phenomena. For the purposes of OHD we wish to locate precisely defined points on the optical rim phenomena, accurately measure their separation and quantify a meaningful error associated with this measurement. This allows consistent, re-producible and objective measurement results. In order to do this it is necessary to understand the relationships between the digital data under analysis and the actual optical hydration phenomena of interest, and to establish what inferences can be drawn regarding the real-world size of optical hydration phenomena on the basis of digital image data. In the remainder of this chapter we will consider the analysis of digital image data for the purposes of measuring an hydration rim, and outline a method for making suitable hydration rim measurements.

2.6.1 The Digital Image

A digital image is essentially a matrix of integer values that correspond to the intensity of an underlying continuous optical image. Thus a digital image is a mosaic of image elements (pixels), and the production of a digital image loses some of the structure in the corresponding optical image. This can be demonstrated with reference to Figure 2.15. This figure shows the letter ‘a’ represented in both continuous and pixelised formats. While the pixel representation (A) is clearly recognisable

it is easily appreciated that this is only an approximation to the continuous image (B). It is also clear that if there were more pixels in the array (higher pixel density) represented in Figure 2.15(A) then the pixelised version would more closely approximate the continuous version. This can be demonstrated by the observation that the 'a' in Figure 2.15(B) is also pixelised (due to the printing process), though is represented by a much larger number of pixels (higher resolution). The phenomenon of

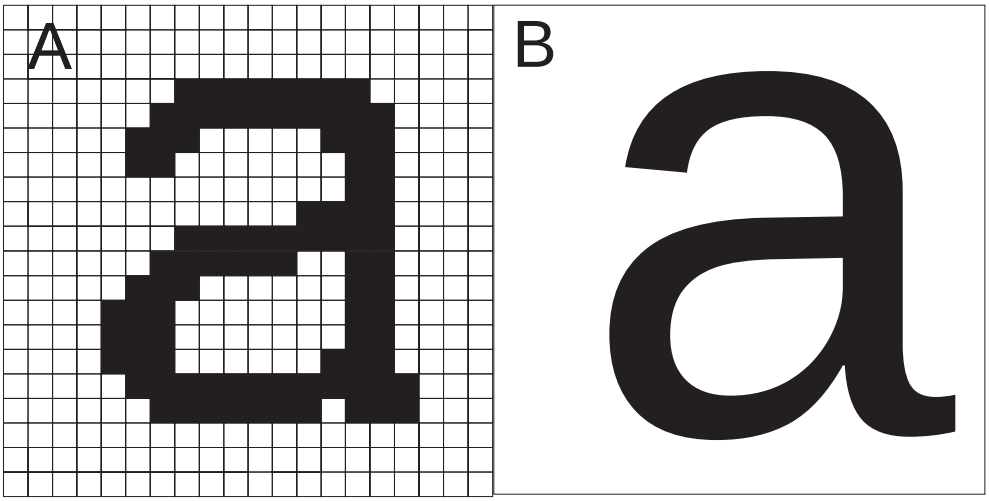

Figure 2.15: Raster vs vector images

discrete pixels in a digital image is mirrored by the intensity or colour values that each pixel can be set to. In a digital image the pixels can only be set to an integer value. Thus while the underlying optical intensity distribution may take an infinite number of intensity values, the digital image can only represent a limited number of these.

Thus a digital image is an approximation of an optical image. While we need to consider how this approximation can be used to draw inferences regarding the actual optical image, it is important to first ensure that the image digitisation process does not bias the data. That is we wish to ensure that the spatial relationships in the optical image are preserved (*i.e.* there is no distortion in the digitisation), and that the underlying

intensity values mapped to each pixel are represented as accurately as possible (*i.e.* effects such as noise are minimised). Therefore for the purposes of OHD we need to consider the image capture process (the initial data measurement), any subsequent image manipulations that may be performed (data polishing) and the actual analysis of the final data set. In the following we address each of these steps.

2.6.2 Image Capture

Here we will exclusively consider the issue of capturing a digital image from a microscope. In general the issues dealt with will equally apply to images acquired by other means of digitisation such as the flatbed scanning of photomicrographs.

The process of image capture involves converting visible optical phenomena into an array of intensity values I_{ij} which are then stored in computer memory as an array of a certain number of bytes[3]. In standard video applications capture involves the use of a CCD (charge coupled device), which is essentially an array of light sensitive elements that respond to the number of photons striking them. Circuitry in the CCD continuously scans each element and outputs the intensity value of the element array. Thus at best, each element in the CCD array corresponds to a picture point or pixel in the final digital image.

Effective image pixel density can be increased by magnification of the optical phenomena projected onto the CCD, which simply increases the effective CCD density for any portion of the optical phenomena. This does raise some problems at high magnifications due to low light intensity which increases noise, though this can be reduced by image aver-

[3] 1 byte = 8 bits, so number of intensity values = 2 raised to the power of nbytes*8. Thus in a standard 1 byte greyscale image there are 256 intensity values possible for each pixel

aging (*supra vide*:§2.6.3) and also limits the extent of the optical image that can be captured. For the purposes of OHD it is best to use as high a density CCD as possible and project the optical image onto this CCD at the highest practical magnification, as this facilitates optimum measurement precision.

Digital vs Analogue video

The output from a CCD device can either be a direct digital signal, such as would be produced by modern digital video cameras, or as an analogue (most commonly RS 170) signal. The initial CCD image capture process is identical for both of these devices, though analogue systems broadcast the captured intensity data as an analogue voltage signal which must subsequently be re-digitised by hardware onboard a computer to produce the digital pixel array. Digital CCD cameras are becoming very affordable and are obviously preferable to analogue systems, though many applications will still be using analogue cameras with video capture cards.

Analogue Signal Capture

In analogue signal capture a time variable voltage signal must be converted to intensity values. This is achieved by the use of flash ADC's (Analogue to Digital Converters) known as frame grabbers. These devices measure a series of equally spaced voltages along the incoming analogue signal by generating a series of voltages and matching them to the voltage to be measured. The measured voltage is then equated to a previously defined intensity value. In this manner a series of pixel intensities are generated. The pixel location is defined by the scan timing, which is crucial, and standard analogue video formats broadcast timing information at the start of each CCD array scan.

Many frame grabbers offer options to define the voltage/intensity conversion, which enables a sub range of the incoming voltage range to be mapped to the intensity value range. This has the effect of electronically enhancing the contrast of a particular intensity band in the digitised image and is often referred to as VEC (video enhanced contrast). This is one of the most useful features of analogue systems as it allows the microscope to be set for maximum resolution, which minimises contrast, and to then electronically enhance the contrast. This allows microscope imaging at a higher resolution to contrast ratio than can be achieved optically. A great deal has been written on video enhanced contrast (VEC) and it is not useful to go into to depth here, but good references on VEC microscopy are Inoué (1986), Pluta (1988) & Häder (1992).

Image Storage

There are also issues involved in storing digital images. For our purposes the principal consideration is the format which the image is stored in. Many image formats use built in compression routines (*e.g.* GIF's and JPEG's). Some of these compression routines do not store the exact image but rather store a close approximation of the image. These are known as "lossy" formats. Thus lossy compression formats such as JPEG should be avoided. Any compression approach used must be able to re-produce the exact analysis image. So for example TIFF and Bitmap formats would be suitable.

2.6.3 Image Processing

The final product of a digital image acquisition is an array (I_{ij}) of intensity values stored in computer memory, which can be graphically displayed on the computer screen in some image format (e.g. as a DIB in

windows based applications). It is this array of intensity values that will be processed and analysed to produce the final rim thickness measurements.

Once an array of pixel intensities has been transferred to the computer, capture is complete and it is at this stage that any necessary image processing is performed. While on some systems it may be possible to simply capture a single image frame and measure the rim thickness, this will rarely be the case. In practice there are a number of artefacts introduced to an image during capture that may influence the final result. In particular, pixel scanning devices such as CCD's often encounter problems such as variation in sensitivity between the CCD elements, directional distortion of the final image, unwanted optical interference from dust in the optical train or the presence of background noise. These problems can all be ameliorated by various image processing techniques. It is not my intention to go into an in depth discussion of image processing here, rather to outline those techniques that are relevant to the measurement of hydration rims.

Noise Reduction

Image noise can arise due to a wide number of processes ranging from CCD and/or capture card imprecision through to external electrical interference. The effect of noise is to randomly vary the observed pixel values and this obviously results in degradation of the image. Amelioration of image noise can easily be achieved by averaging pixel values over a number of images. The assumption is that any noise present is random and thus successive image averaging will reduce noise and render a clearer picture of the underlying image. This process takes a number (n) of captured frames $I(x)_{(ij)}$ ($x \in \{1, 2 \ldots n\}$) and averages them to produce a noise reduced averaged image $A_{(ij)}$. The averaging can be achieved in a number of ways such as continuous averaging and expo-

nential averaging, though the simplest approach is to average the pixel array as:

$$A_{(i,j)} = \frac{\sum_{x=1}^{n} I(x)_{(i,j)}}{n} \tag{2.14}$$

The standard deviation of the averaged value will be given by:

$$\sigma = \sqrt{\frac{\sum I(x)^2_{(i,j)} - n * A^2_{(i,j)}}{n-1}} \tag{2.15}$$

thus the measurement precision is approximately proportional to the square root of n, or the number of averaged images. This essentially means that precision increases at a power of two, so halving the current residual noise will take double the current value of n (e.g. halving the noise for an n of 16 would require an n of 32).

Background Removal

Another improvement upon image integrity can be made by producing an image that represents the deviations from a perfectly uniform background field. This background image can then be automatically subtracted from any image being captured to produce a final image free from any artefacts in the optical train or bias in the CCD. An easy way to accomplish this is to take an averaged image of a blank field (B), and then generate a pixel intensity ($\hat{I}$) averaged over the entire frame. The intensity correction ($C_{(i,j)}$) image can then take the form

$$C_{(i,j)} = B_{(i,j)} - \hat{I} \tag{2.16}$$

Thus the $C_{(i,j)}$ represent deviation from the uniform intensity field, and the background intensity correction can be applied as follows

$$D_{(i,j)} = A_{(i,j)} - C_{(i,j)} \tag{2.17}$$

This correction can be carried out to remove any unwanted disturbance from the image analysis. It is probably best that this correction be applied before geometric de-calibration takes place in order to ensure that no bias is introduced into the system.

Geometric De-calibration

Another improvement in image integrity can be brought about by correcting the image for any geometrical distortions caused by aberrations in the optical or electrical train. The correction or geometrical de-calibration for geometric image distortion can be accomplished by imaging a regular test pattern of known proportions and measuring the distortion (if any). In this manner a function ($MF_{(i,j)}$) that maps the ideal pixel location to the distorted location can be developed to describe the distorting properties of the imaging system. An efficient approach to the geometric de-calibration of an image is outlined by Walter & Burns (1986). In this approach a pixel location in the corrected image is chosen and the corresponding pixel in the distorted image is chosen via the mapping function. The intensity value of the pixel in the corrected image is then replaced by the value of the corresponding pixel in the distorted image. Thus the relationship takes the form

$$F_{(i,j)} = D_{(m,n)} \tag{2.18}$$

Where $F_{(i,j)}$ is the pixel intensity in the corrected image at row i and column j, and $D_{(m,n)}$ is the corresponding pixel in the distorted image, where the indices are related by

$$(m,n) = MF(i,j) \tag{2.19}$$

Where $MF(i,j)$ is the mapping function. A problem arises in the fact that the indexes m & n will almost certainly be non- integers, and thus there must be a method for deciding which pixel to assign to the corrected image. The simplest approach is to assign the pixel closest to the fractional position $MF(i,j)$, though this could cause artefacts in the final image. A preferable approach is to use a simple bi-linear interpolation, *i.e.*

$$F_{(i,j)} = \frac{Interp(m) + Interp(n)}{2}; \tag{2.20}$$

$$Interp(m) = D_{(int(m)-1,int(j))} + (m - int(m) + 0.5)$$
$$(D_{(int(m)+1,int(j))} - D_{(int(m)-1,int(j))}); \tag{2.21}$$

$$Interp(n) = D_{(int(m),int(j)-1)} + (j - int(j) + 0.5)$$
$$(D_{(int(m),int(j)+1)} - D_{(int(m),int(j)-1)}) \tag{2.22}$$

The application of geometric de-calibration may not be necessary in all systems. In particular it may well be the case that the central portion of any captured image is distortion free as distortion tends to be most pronounced at the edges of images. For the effective use of digital image analysis in OHD any systematic geometric distortion in image capture must be established, and either a distortion free image boundary must

be defined or automatic geometric de-calibration must be incorporated as part of standard image capture.

Conclusion

Digital image capture and processing are important steps in the analysis and measurement of hydration rim images. Simple and logical analytic procedures will ensure that optimum clarity, distortion free, images are captured and measured. While there is no barrier to analysis taking place if these steps are not followed, it is very probable that the analysis will incur (unpredicted) errors due to measurement deviation and geometric distortion resulting in complications in verification of results.

The general processing steps that should be followed, or at least considered and influence determined, are as follows:

Captured pixel intensity array(s) $I(x)_{(ij)}$
$\Downarrow$ *Noise Removal; Equation 2.14*
Averaged pixel intensity array $A_{(ij)}$
$\Downarrow$ *Background Removal: Equation 2.17*
Uniform Averaged pixel intensity array $D_{(ij)}$
$\Downarrow$ *Geometric De-calibration: Equation 2.18*
Final analytic pixel intensity array $F_{(ij)}$

2.6.4 Image Analysis

Digital image hydration rim measurement involves analysing a processed pixel intensity array F(ij) to determine the distance between the hydration rim boundaries and quantify the uncertainty of this estimate. As previously described, accurate rim thickness measurement requires that the measurement boundaries are precisely defined and can be accurately located (*infra vide*:§2.2). This can be achieved to a high degree of preci-

sion in digital image measurement, where the boundaries can be defined as the optical intensity minima associated with visible hydration phenomena. Thus the implementation of digital hydration rim thickness measurement involves the location and measurement of the distance between the two optical intensity minima associated with the hydration rim. However, while we are seeking to make measurements of continuous phenomena in real-world Euclidean co-ordinates our data are discrete raster entities. In order to establish what inferences we can draw regarding rim thickness we need to consider the relationship between our discrete raster data and the underlying euclidean intensity distribution we are analysing.

Let the true euclidean intensity distribution be described by the function

$$\xi(x, y) \tag{2.23}$$

For the raster image $F_{i,j}$ corresponding to $\xi(x, y)$ we define two vectors $X[i]$ and $Y[j]$ respectively such that $(X[i], Y[j])$ corresponds to the Euclidean location for the centroid of pixel $F_{i,j}$. During rasterisation $\xi(x)$ is averaged over the area of a pixel assumed to be a square with an area of Δp^2. Following this the observed pixel intensity is given as follows

$$F_{i,j} = \frac{\int_{X[i]-\frac{\Delta p}{2}}^{X[i]+\frac{\Delta p}{2}} \int_{Y[j]-\frac{\Delta p}{2}}^{Y[j]+\frac{\Delta p}{2}} \xi(x, y) dy dx}{\Delta p^2} + \epsilon_{i,j} \tag{2.24}$$

Where $\epsilon_{i,j}$ is the noise associated with the imaging process.

let the hydration rim image be oriented vertically and the analysis be confined to a sub region of the full image of height J pixels. If J is sufficiently small that there is no systematic vertical intensity variation in $\xi(x, y)$ over this analysis region then Equation 2.24 reduces to

$$F_i = \frac{\int_{X[i]-\frac{\Delta p}{2}}^{X[i]+\frac{\Delta p}{2}} \xi(x) dx}{\Delta p} + \epsilon_i \tag{2.25}$$

Where each F_i represents the average

$$F_i = \frac{1}{J}\sum_{j=1}^{J} F_{i,j} \tag{2.26}$$

and the noise term is given by

$$\epsilon_i \sim N(0, \sigma_i^2) \tag{2.27}$$

where

$$\sigma_i = \sqrt{\frac{\sum_{j=1}^{J} F_{i,j}^2 - J \times F_i^2}{J-1}}$$

In digital image analysis for the purposes of OHD we are trying to infer the location of minima in the distribution of $\xi(x,y)$ ($min(\xi(x))$) from the observed digital data $F_{i,j}$. If we choose a sufficiently small portion of the rim image it is always possible to reduce the problem to inferring $min(\xi(x))$ on the basis of F_i (*i.e.* Equation 2.25), which simplifies the process. However, the relationship given in Equation 2.25 is insufficient to directly identify $min(\xi(x))$. The problem is that due to the loss of information incurred in the rasterisation process we cannot uniquely identify $\xi(x)$ on the basis of the observed F_i. This is because there are an infinite number of distributions that could give rise to the observed F_i data. However, we can use the observed F_i data to place constraints on the set Ω of possible underlying distributions from which $\xi(x)$ derives. If we can then draw inferences regarding the minima associated with members of Ω we can use these to describe a distribution for $min(\xi(x))$.

In the following we will consider two approaches to inferring the location of $min(\xi(x))$. The first of these, the Simple Pixel Count method, was originally proposed by Ambrose (1993). This method allows bounds to be set on the location of $min(\xi(x))$ under certain conditions. However, in some cases the Simple Pixel Count method will fail and accordingly we will consider an extension to this method, the intensity reconstruction approach, which is more general.

In the Simple Pixel Count method an averaged intensity histogram of a region of the rim image is produced, and the rim thickness is measured by counting the number of pixels between the two pixels of lowest intensity (Ambrose 1993). The rim boundaries can be objectively defined as the minima on graphs such as Figure 2.2. Measurement then becomes the simple objective task of performing a pixel count between the two minima. The real world rim thickness is calculated with reference to the calibrated pixel size Δp. The assumption that the actual optical intensity minima falls somewhere within the identified pixel minima means that the error of a measurement of this type will be uniform over the interval $\pm\Delta p$.

With reference to the terms defined above, the Simple Pixel Count method calculates F_i after Equations 2.25 and makes the assumption that the set of underlying intensity distributions from which $\xi(x)$ derives (Ω) is constrained such that the minima of member distributions fall within the bounds of the pixel for which F_i is a local minima ($min(F_i)$).

In the case that the confidence intervals of pixel intensity values for neighbouring pixels do not overlap that of $min(F_i)$ this assumption is valid. However, where the confidence intervals of pixel intensity values for neighbouring pixel values do overlap it is possible that the minima for $\xi(x)$ does not fall within the boundary of the pixel where a minima for F_i is observed. This is because the set of possible distributions which could give rise to the observed F_i data are not sufficiently constrained to exclude distributions which have minima falling outside the bounds of $min(F_i)$. This is illustrated in Figure 2.16.

Under the circumstance that simple pixel counts are not valid we need to adopt another method for making the measurement. One approach is to extend the underlying logic used in the Simple Pixel Count method. As just discussed, the Simple Pixel Count method makes the assumption that the set of intensity distributions from which $\xi(x)$ derive are

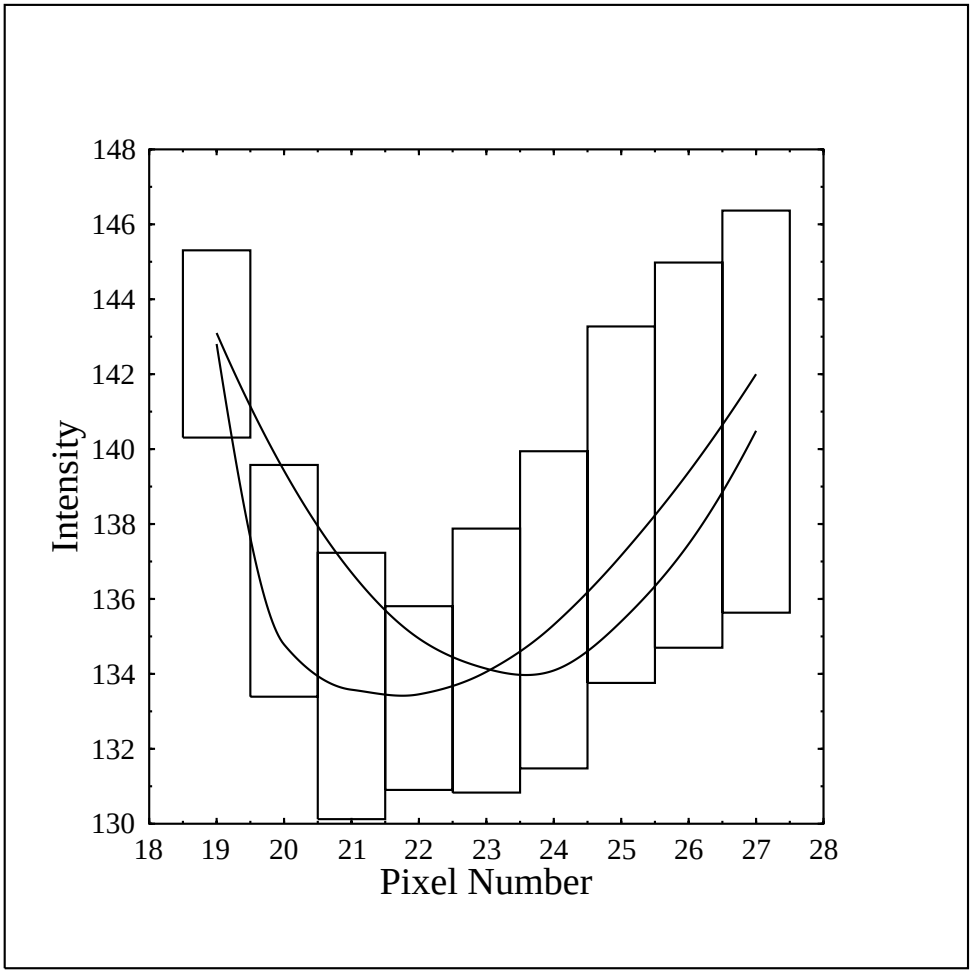

Figure 2.16: Demonstration of Simple Pixel Count limitations: In the example given above the rectangles represent the 95% C.I distribution for individual pixel intensity values. These data derive from minima 1 in the analysis illustrated in Figure 2.20. As will be appreciated, many curves can be fitted to this data in which the curve minima and the minimum mean pixel intensity value to not coincide. Under this circumstance the minimum mean pixel value cannot be used to approximate the minimum of $\xi(x)$ and the Simple Pixel Count approach fails. For example, the minima of the two arbitrary curves plotted above are separated by 2 pixels.

constrained so that $min(\xi(x))$ and $min(F_i)$ coincide. We can extend this to situations where the simple pixel counting approach is invalid by using similar logic. If we can place bounds on the set of intensity distributions that could give rise to the observed F_i data then we can ask what is the distribution of intensity minima that could arise from this set. As $\xi(x)$ is a member of this set we know that $min(\xi(x))$ falls within such a distribution thus the distribution acts as an estimate for $min(\xi(x))$. So we want to estimate the distribution of minima in set Ω. One approach to calculating this estimate is to randomly sample the minima in set Ω. Under this simple analysis the samples will tend to the same distribution as the underlying distribution of minima in set Ω (Press *et al.* 1992). The question is how do we actually make this random sample? Sampling the set of underlying intensity minima can be performed in a relatively straightforward manner as we know that the set of underlying intensity distributions must conform to Equation 2.25. Thus we simply need to sample minima from the set of functions that observe Equation 2.25. That is if we can randomly generate intensity distributions that could give rise to the observed data then we can sample the associated minima. As an example, Figure 2.17 shows an intensity minima pixel and its four closest neighbours with a possible continuous intensity line fitted. In this case the exact Euclidean location of the distribution minima can be calculated, and this represents a sample from the underlying minima distribution for functions in the set Ω. If a series of these lines, such as shown in Figure 2.18, are fitted, a number of these minima can be sampled and a distribution such as that shown in Figure 2.19 can be generated. This acts as a distribution for the location of $min(\xi(x))$. In order to calculate a rim thickness we simply sample a distribution for the location of each minima and calculate the distribution of the separation of these two.

This raises the question how we randomly sample distributions from Ω? Firstly to simplify this a little we will treat each of the two inten-

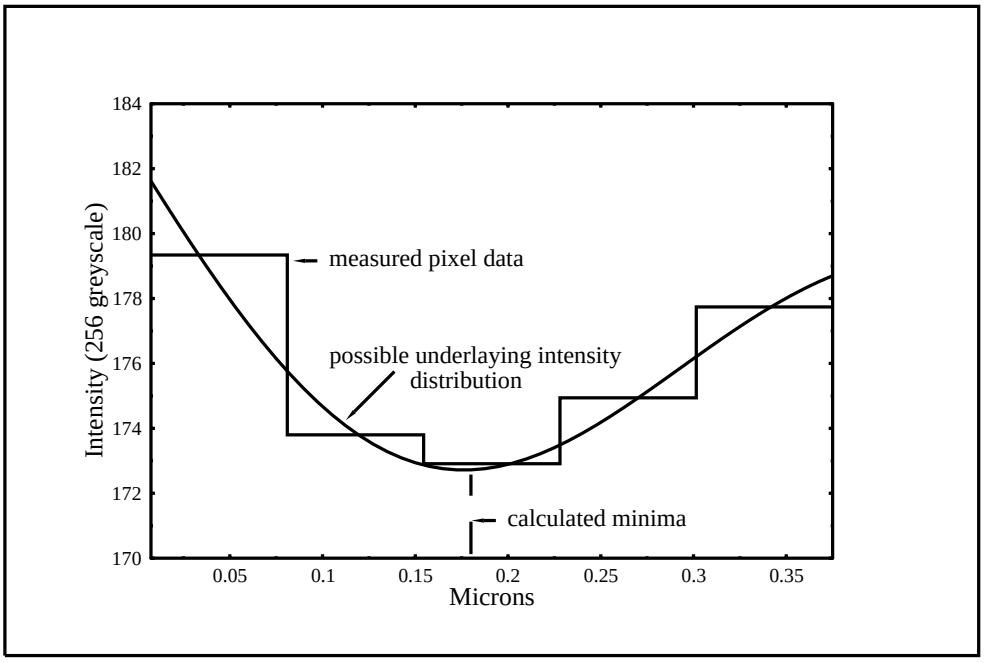

Figure 2.17: Possible intensity distribution corresponding to measured pixel intensity data

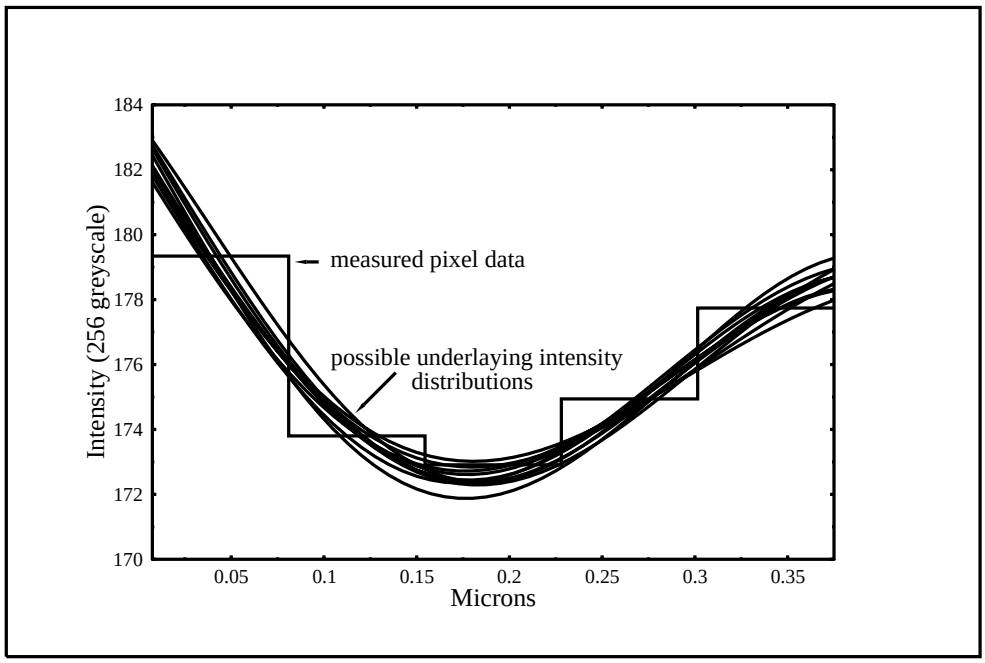

Figure 2.18: Example of multiple intensity distributions

sity minima in $\xi(x)$ separately and make the assumption that $\xi(x)$ is closely approximated by some simple function in a region (the analysis zone) surrounding each minima. Secondly we use the approximation that this curve is linear over any given pixel. Under this approximation the observed pixel intensity acts as an estimate of $\xi(X[i])$ at the centroid of pixel i. Thus by fitting the approximating function to the observed pixel intensity values we can estimate a local minima $\xi(x)$. Unfortunately, we do not know the precise pixel intensity value. However we can estimate the distribution for the observed pixel intensity values (*e.g.* Equation 2.27). We can randomly generate possible sets of data (candidate data) from these distributions and fit the approximating function to each data set. If these fitted functions observe Equation 2.25 then they act as samples for minima in Ω.

Thus the general algorithm for sampling local minima in Ω is

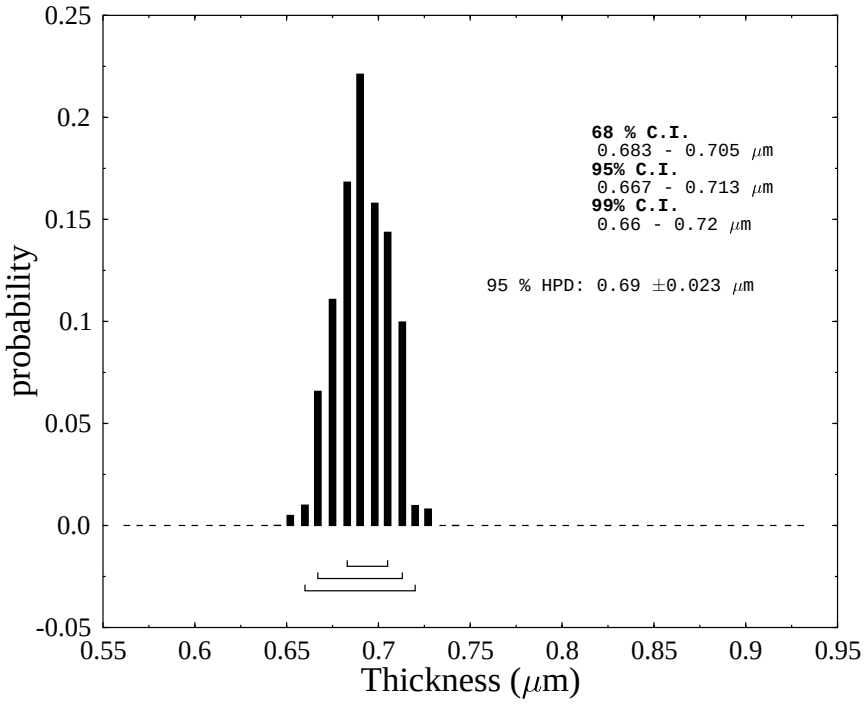

Figure 2.19: Posterior probability distribution for euclidean location of $min(\xi(x))$

1. randomly generate a set of candidate data for true mean pixel value from the observed pixel intensity distributions.

2. fit an approximating function to the candidate data for each analysis zone.

3. determine if Equation 2.25 is true for this candidate function, if true goto step 4 else goto step1.

4. calculate the minima for the candidate function and add to the sampled set. If sufficient samples have been collected finish else goto step 1.

A distribution for the thickness of the hydration rim (the distance between the intensity minima) can then be generated from the distributions calculated for the individual minima.

The intensity reconstruction measurements generated through this process are more generally applicable than Simple Pixel Counts. They also have the advantage over SPP measurements that the sampled distribution directly corresponds to the quality and nature of the image being analysed.

In order to implement this measurement it is necessary to be able to describe the intensity probability distribution for any given pixel, to be able to fit an approximating curve for candidate pixel data sets, and to implement the algorithm given above. Software designed to perform this analysis is presented and tested in the following section.

2.7 The Rim Buster Software

The implementation of the digital image measurement approach outlined in the preceding sections is not trivial, and requires specialised

software. While simple pixel counting can be performed using standard scientific image analysis software (*e.g.* Mocha, Jandel Scientific;V2, Digital Optics) intensity reconstruction measurements are not implemented in currently available software. Additionally, the type of routine image processing necessary for digital hydration rim measurement may not be available in some packages. In light of this I have written a software package (Rim Buster) to implement digital hydration rim measurement according to the approaches and routine image processing requirements outlined in the previous section. The software is presented and tested in this section.

Currently the overall application is still in alpha development[4] but it is functional as an OHD analysis package. Rim Buster is designed to run on Intel platforms running windows NT 4.0/95/98 or later. It is not intended to go into the syntax in depth, rather the relevant units are reproduced in Appendix A for reference, and the source code and an installation package can be found on the companion CD under the directory /software/rim buster.

To introduce, outline and test the Rim Buster software we need to initially describe the interface (§2.7.1). Following this we will define and test the sampling procedure used in Rim Buster (§2.7.2), establish an appropriate measurement protocol (§2.7.3), and finally we will test the reproducibility, precision and accuracy of this type of measurement approach (§2.7.4).

[4]This means that there are almost certainly some bugs in the system that will cause error messages and may even cause the system to crash. However, these are problems with the interface code rather than the far simpler analysis code.

2.7.1 Rim Buster interface

The basic Rim Buster interface consists of an application window containing the Rim Buster window. Images are opened into the application within child windows. Currently only the Bitmap format is supported. In order to use rim buster it is simply necessary to marquee an area of a rim image for analysis (this defines the analysis region) and select the **`bust rims`** option from the **`tools`** menu. The available menu is context sensitive, so different menu options will be available depending upon which window is active.

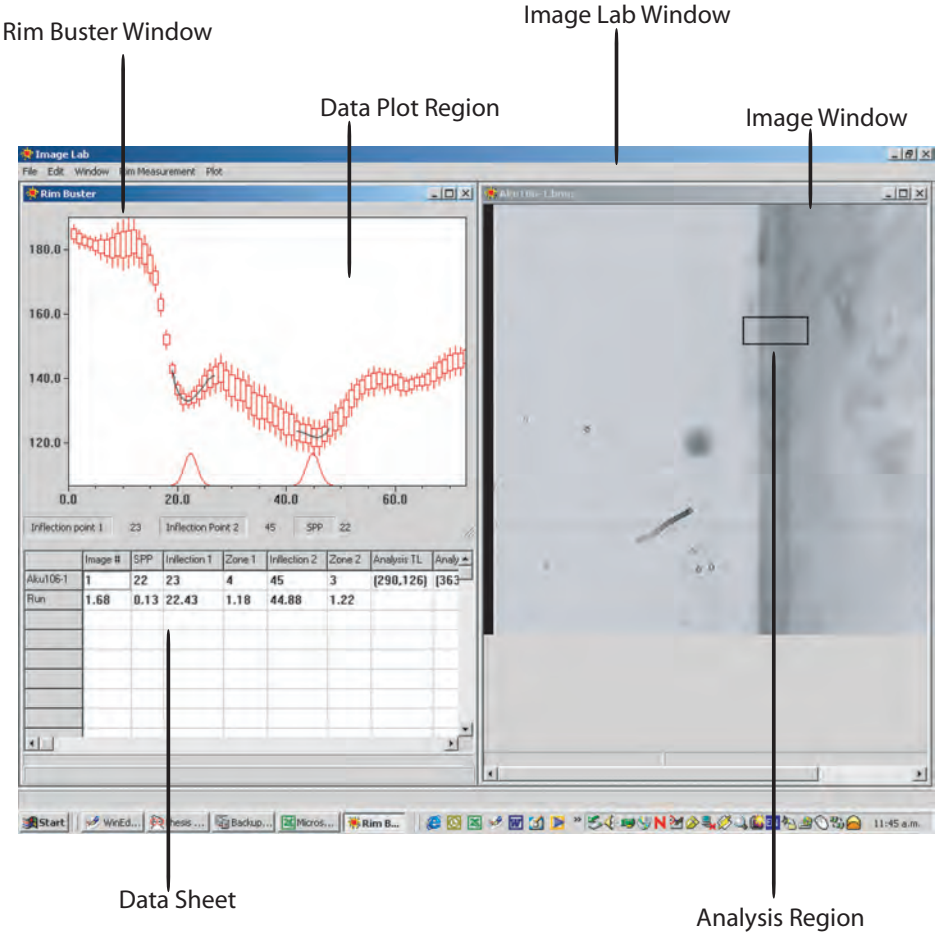

Figure 2.20: The rim buster interface

Some basic image processing options are available. Image averaging following Equation 2.14 can be performed through averaging a set of images within a given directory. This is offered as an option through the individual image widow under the **tools** menu. Additionally, background subtraction following Equation 2.17 is offered. In order to use this option it is necessary to first load a blank background image.

Analysis is performed by selecting an analysis region on any open image. An analysis region is selected by using the left mouse button to marquee a region of the rim image. Clicking the right mouse button clears the marquee. Once a suitable analysis region has been established an initial analysis is performed by selecting the **bust rims** menu option from the **tools** menu. This calculates the values F_i and σ_i according to Equations 2.26 and 2.27 respectively. These data are then reported in the data sheet and plotted graphically in the data plot region. Three different data plot formats are available these can be selected through the plot menu.

To perform further analysis the left minima is selected by clicking the minima on the plot with the left mouse button and the right minima is similarly selected by clicking the plot with the right mouse button. As the minima are selected the pixel locations are recorded in the data sheet. Once the location of both pixel minima have been identified the simple pixel count is automatically calculated.

In order to perform the intensity reconstruction analysis it is necessary to identify a zone around each minima over which an approximating curve will be fitted. By default 3 this zone is 3 pixels either side of the identified minima. However, other values can be used. The zone is either selected by holding down the ALT key while left clicking for the left minima or right clicking for the right minima, or by directly entering a value in the data sheet.

So for example, we may identify the left minima as occurring in pixel 12.

Thus we would left click on pixel 12 in the graph. Further we may wish to perform an intensity reconstruction analysis. In this case we identify the number of pixels either side of the minima we wish to include in the analysis (the appropriate number is discussed in §2.7.2); this defines the analysis zone for that particular minima. So we may decide that we want to include 4 pixels either side of the minima in the zone. Thus in our current example we would hold down the ALT key and left click on either pixel 8 or pixel 16. We would then repeat the process for the right minima. These values can also be directly edited in the datasheet.

The datasheet can hold up to 500 analysis entries. The plot of any analysis data in the datasheet can be displayed by selecting the appropriate entry (left click the leftmost column of the sheet). Entries in the datasheet can be deleted, saved or copied to the clipboard through a popup menu accessed by right clicking the datasheet. This enables data to be copied and pasted into applications such as Excel.

Two rows of the data sheet are used per analysed data set. The actual analysis data are recorded in columns 9–2000 (column headers 1 to 1991), with the pixel count corresponding to the column header. The mean intensity values are reported in the upper row, and the standard deviation of the intensity values are reported in the lower row. The pixel locations of each minima are reported under the inflection 1 and inflection2 columns, and the co-ordinates of the analysis region within the analysed image are recoded in the columns Analysis TL and Analysis BR which record the top left and bottom right co-ordinates of the analysis region respectively.

Once the data are entered into the datasheet and the pixel minima and analysis zones have been set it is possible to perform an intensity reconstruction analysis. To perform the analysis simply select the **`run analysis`** item under the **`rim analysis`** menu. This analysis will sample minima and calculate the rim thickness for all entries in the data

sheet. The mean and standard deviation for each minima and the rim thickness are reported in the datasheet as the analysis is completed. The minima location means are reported under the associated inflection location with the standard deviation being given under the zone data. The actual rim measurement is reported in column 1 with the associated standard deviation in column 2. These data are reported in μm according to the settings for pixel size. The default pixel size is 0.075 μm , this can be reset through the **`Rim Measurement|pixel size`** menu item. Additionally, once the run is complete the sampled minima distribution will be plotted under the pixel intensity plot as illustrated in Figure 2.20.

Three curve approximations are available and can be selected through the rim analysis menu. Prior (and subsequent to) analysis an example fitted curve can be plotted over the pixel intensity plot via the **`fit curve`** item under the **`rim analysis`** menu.

In addition to the overview given here, a simple tutorial covering the basic operations of Rim Buster is available in Appendix A (§A.1).

Having given a basic overview of Rim Buster operations we will now have a look at how well the intensity reconstruction approach performs as a general tool for digital hydration rim measurement. As a first step we will examine the sampling process; we need to establish what functions might act as suitable approximations for $\xi(x)$, and we need to establish some measure of how many samples are required to estimate the distribution for $min(\xi(x))$. Following this we then need to assess the accuracy, precision and stability of the general measurement approach.

2.7.2 Sampling $\xi(x)$

A central component of the measurement approach implemented in Rim Buster involves sampling the minima associated with Ω. As outlined previously this requires that we can define a suitable approximating function for $\xi(x)$ over the analysis zone; a small region surrounding each local minima(*infra vide*:§2.6.4). Also of importance is the question of how many samples we need to take. If the sample size is too small then the results will be an imprecise estimate of the distribution of minima associated with curves from Ω, yet we want to choose a sample size that is a small as possible to speed processing. We will consider both of these questions in this section.

Curve models

There are a huge number of different curve functions that could be employed to approximate $\xi(x)$. However, from the available data it is qualitatively possible to observe that the intensity curve at each minima is approximately parabolic (*e.g.* Figure 2.4). In light of this we would assume that a quadratic equation (this describes the shape of a parabola) would be a reasonable first approximation of $\xi(x)$ at each local minima. Thus we would model $\xi(x)$ as

$$y := \beta_0 + \beta_1 x + \beta_2 x^2 \tag{2.28}$$

Higher order polynomials would also be useful in that the extra degrees of freedom would allow a closer approximation to a non-parabolic $\xi(x)$. However, too many degrees of freedom would be undesirable as this would allow the possibility of many minima within the analysis zone. By definition there is only one minima for $\xi(x)$ within the analysis zone. In light of this a cubic model would seem to be a suitable extension of the

quadratic model; *i.e.*

$$y := \beta_0 + \beta_1 x + \beta_2 x^2 + \beta_3 x^3 \tag{2.29}$$

Another simple model that has approximately the same form as the observed data is the Gaussian model. The Gaussian model has the form

$$y = \beta_0 exp\left(\frac{x - \beta_1}{\beta_2}\right) \tag{2.30}$$

It may appear that the question we are addressing here could also be regarded as an interpolation problem. Thus we could apply some form of interpolation scheme such as a cubic spline. However, interpolation schemes will explicitly fit each data point. Given the typically noisy data that we need to analyse this gives rise to the possibility of implausible approximations for $\xi(x)$ that exhibit features such as multiple minima within each analysis zone. Accordingly we should only employ explicit approximating functions such as those defined above. However, for the purposes of evaluating the performance of the three $\xi(x)$ approximations given above we will consider a trigonometric interpolation via a fourier series analysis. This will provide an independent evaluation of the measurement estimates via the proposed $\xi(x)$ approximations.

A full fourier series curve involves solving for a_i & b_i in (Chatfield 1996)

$$y = \frac{1}{2} + \sum_{j=1}^{m} (a_j cos\alpha_j x + b_j sin\alpha_j x) \tag{2.31}$$

where

$$\begin{aligned} a_0 &= \bar{y}, \\ na_j &= 2\sum I_i \cos\alpha_j x, \quad j = 1, \ldots, m; \\ nb_j &= 2\sum I - i \sin\alpha_j x, \quad j = 1, \ldots, m. \end{aligned} \tag{2.32}$$

which corresponds to a weighted average of sin waves for the $n = 2m+1$ intensity values. Here the α_j terms define the frequency of the particular wave. For an analysis region of n pixels wide the frequency α_j is given as

$$\alpha_j = \frac{2\pi j}{360}$$

As discussed above fourier series is not an ideal approximation as this is likely to give rise to multiple minima within the analysis zone. Thus in the current analysis we will only use the first two wave frequencies to minimimise this problem; *i.e.*

$$y = \beta_0 + \beta_1 \sin(\alpha_1 x) + \beta_1 \cos(\alpha_1 x) + \beta_2 \sin(\alpha_2 x) + \beta_2 \cos(\alpha_2 x) \quad (2.33)$$

The general suitability of the four models defined above can be illustrated by fitting these different curve functions to intensity data from optical hydration phenomena. In Table 2.7 summary R^2 statistics for the fit of the different models to 100 different data sets is presented. As can be seen all of these models describe the observed data well. This provides quantitative support for the qualitative observations that have identified those four curve functions being potentially suitable $\xi(x)$ approximations.

Table 2.7: R^2 data for these models fitted to 100 minima from different slides

Model	Mean R^2	Max R^2	min R^2	σ
Cubic	0.988	1.000	0.920	0.014
Quadratic	0.935	1.000	0.628	0.079
Gaussian	0.931	0.999	0.628	0.079
Fourier	0.81	0.901	0.405	0.082

Having established a set of curves which appear to be suitable candidates for approximating $\xi(x)$ we need to establish how sensitive the modelling procedure is to the actual function employed. Ideally the results should not be too sensitive to the approximating function chosen. A comparative test of the different interpolation schemes was run in the interests of determining how sensitive the results are to the type of interpolation used. In this test, 100 random sections were analysed. The measurement analysis was performed using each of the models defined

above and a summary of the observed measurement differences is presented in Table 2.8.

Table 2.8: Summary statistics for measurement contrasts under different $\xi(x)$ approximations

Comparison	mean		standard deviation	
	$\bar{x}$	σ	$\bar{x}$	σ
Cubic vs Quadratic	0.148	0.492	0.193	0.643
Cubic vs Gaussian	0.244	0.425	0.259	0.956
Cubic vs Fourier	-0.130	0.526	-0.164	0.755
Quadratic vs Gaussian	0.117	0.264	-0.505	0.402
Quadratic vs Fourier	0.262	0.407	-0.416	0.59
Gaussian vs Fourier	0.44	0.322	-0.618	0.92

None of these comparisons is significant at $\alpha = 0.05$. The same result is returned for the estimated measurement variance. Thus there are no systematic differences in the reported measurement results between the four proposed models.

These results show that the measurement results should not be dependant upon which of the four proposed approximating functions are used. This indicates that the proposed functions are suitable approximations for $\xi(x)$ as there appears to be no systematic bias in the measurement result. However, to ensure consistency between measurements it is probably most appropriate that the reported measurement relates to a consistent approximating function. This ensures that the measurement results are consistent and comparable. In practice the cubic curve model has the highest R^2 values of the proposed models and tends to be the most stable. Thus the suggestion is that reported results through the intensity reconstruction measurement approach should relate to the cubic $\xi(x)$ approximation. As a general rule of thumb, however, it is a good idea to run the analysis under multiple $\xi(x)$ approximations. This allows the integrity of the measurement result to be checked. If the re-

sults are not consistent under different $\xi(x)$ approximations then there are problems with the analysis.

The fourier model is not implemented as an ongoing analysis option within the Rim Buster interface. As discussed above this model has some undesirable properties and it will tend to be unstable. The primary reason for implementing the fourier model was for the model checking exercise as the fourier model provided a suitably independent comparison to the other models. Thus only the Cubic, quadratic and gaussian models are implemented as routine measurement functions within Rim Buster. However, the fourier code (along with other models) is present in the source and could be re-implemented if desired.

Having identified the approximating functions for routine analysis it is important to comment upon the size of the analysis zone for each minima. Basically, we want the analysis zone to incorporate the region surrounding a pixel minima where the intensity distribution is approximately parabolic. At a minimum the zone should span two pixels either size of the local pixel minima (*i.e.* a total of five data points for the curve fitting exercise). The default value in Rim Buster is 3 pixels which should be suitable for most applications. However, where very high resolution images have been captured the zone may need to be enlarged. The suitability of any given zone can be visually assessed by plotting the approximating curve through the **`Rim Measurement | fit curve`** menu item. This will also report the R^2 statistic for the fit.

Sample size

As well as identifying suitable $\xi(x)$ approximations it is important to establish a suitable sample size for the measurement analysis. If we sample too few points then the collected sample will not act as a realistic approximation of the distribution of minima in Ω. However, if

we set the number of samples too high then we will incur unnecessary computing costs. In order to establish a suitable sample size a series of repeat measurement experiments were run. In these experiments each measurement analysis was conducted 100 times at sample sizes of 5000 to 150000 in steps of 5000 (thus 3000 repeat measurement analyses per data set) in order to assess the variability of the measurement result as a function of sample size. An example of the type of result achieved for each repeat run experiment is given in Figure 2.21. In this figure

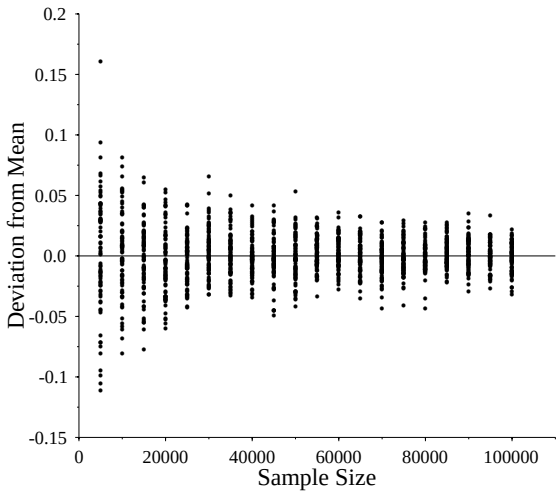

Figure 2.21: Deviation of measurements from the mean value for a repeat run experiment

the deviation of each measurement result from the overall experimental mean value is plotted against total sample size. As can be seen the variance of the measurement results decrease as sample size increases. This is asymptotic and it is apparent that for the example given in Figure 2.21 the measurement variance stabilises at around a sample size of 60000. Thus for this analysis a sample size of around 60000 would be an appropriate compromise between limiting measurement variance and minimising sample size. If we repeat this exercise for a number of images then we can plot the variance statistics derived from analyses

such as that graphed in Figure 2.21 against total sample size to establish the sample size at which measurement variance typically stabilises. In

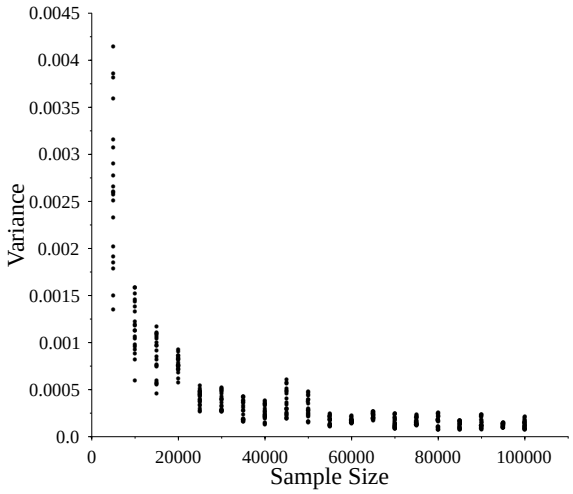

Figure 2.22: Plot of variance in measurement deviation versus sample size for the repeat run experiments

Figure 2.22 the results from 20 repeat run experiments are plotted and it can be seen that measurement variance has stabilised by a sample size of 60000. In Figure 2.23 the same exercise is repeated for variance in the reported measurement standard deviation. From this figure we can see that variance in the reported measurement standard deviation has stabilised by a total sample size of 100000. These experiments suggest that a total sample of 100000 should represent a reasonable compromise between measurement variance and sample size. Accordingly the routine Rim Buster analysis collects a sample of 100000 minima per measurement.

Summary

We have established that various functions can act as suitable $\xi(x)$ approximations. In particular we have identified a cubic model as being a

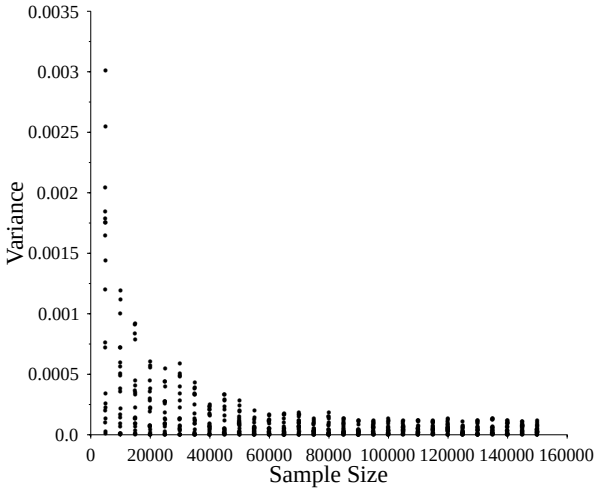

Figure 2.23: Plot of variance in reported measurement standard deviation versus sample size for the repeat run experiments

useful approximation that is shown to closely model optical hydration data, typically explaining around 99 % of the observed data structure. Following this it is suggested that the standard result reported for intensity reconstruction measurement should derive from an analysis using a cubic $\xi(x)$ approximation. This result should be checked against the quadratic and gaussian models to ensure that the result under each $\xi(x)$ approximation is consistent. Further, to minimise variance in measurement results a total sample size of around 100000 should be used. This represents a suitable balance between minimising measurement variance and minimising computational costs.

While this has established that consistent intensity reconstruction measurements are possible for any given individual set of data, we need to establish how much variability arises in the measurement result due to differences in the exact rim image data chosen for analysis. This is considered in the following section and a protocol for digital rim measurement is proposed.

2.7.3 Measurement Protocol

When a measurement analysis is conducted an essentially random data set is chosen for analysis; a range of analysis data could be chosen for any given image, and the actual image could derive from many locations on an obsidian thin section. While we have established that consistent measurement results are possible for any given data set, we need to establish how variable the measurement results are in response to different data sets. That is, how much influence does the precise choice of analysis data have upon the measurement result. This involves both specification of the analysis region from within a given rim image, and the process of image capture. Thus we need to test how consistent measurement results are for any given image, and how consistent the measurement result is for any given slide. To address these issues two experiments were conducted as described in the following sections.

Image Variation

The first experiment was designed to test the degree of variation in measurement results that may arise from selecting different analysis regions from within a single image. In this experiment 20 images were chosen at random from an image data base. These images were then randomly presented 10 times each, and at each presentation only one analysis region was selected for analysis. The purpose of this experimental design is to assess the degree of variation that is likely to arise through an experienced operator deliberately selecting optimal analysis regions.

The results show that in general the comparisons are excellent (Figure 2.24). Of the 200 measurements 198 of the calculated 95% C.I. overlap within the measurement group.

As we would expect that only 95% of the 95% C.I. intervals would overlap

within the measurement groups these results may be taken to suggest that the calculated 95 % C.I. is conservative; *i.e.* the results are under-dispersed. However this is unlikely to be the case as the calculated measurement uncertainty principally reflects data loss during image digitisation;remembering that the actual data measurement is the digitisation process. Thus this comparison is an assessment of how consistently the system calculates the uncertainty given similar analysis data. Given the fact that an experienced operator should be able to consistently identify high quality portions of the rim image, the selected analysis data should be very similar, and hence the results should be highly consistent. However, there are two cases where measurements significantly deviate from the measurement group (*i.e.* measurement sets 4,12). This indicates that outliers due to the selection of different analysis regions are possible. Following this observation it is important to establish the potential range in rim thickness represented in each image.

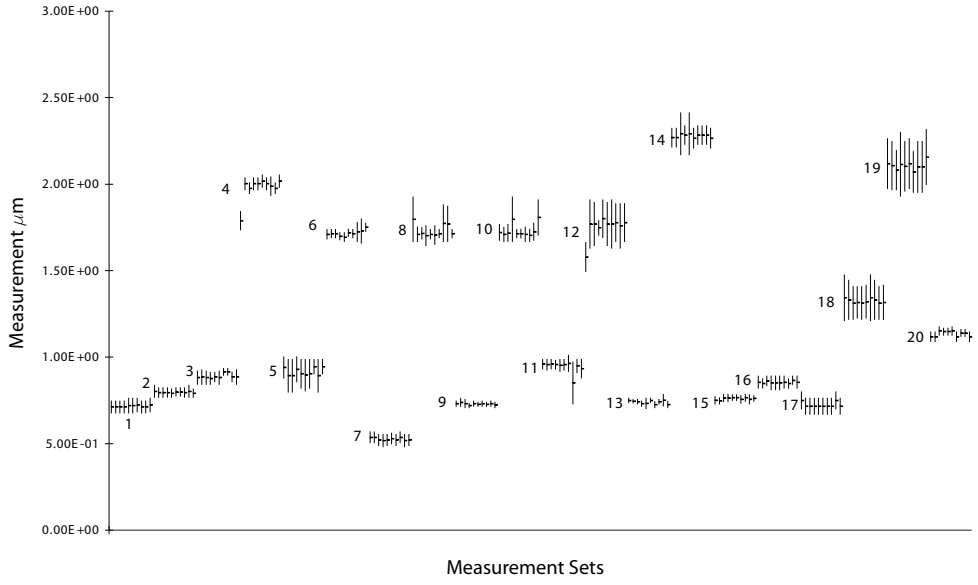

Figure 2.24: Image variation data set 1

Capture Variation

Having established that consistent measurement results can be generated for any given image the next test was to establish the consistency of the rim identification and capture process. That is, given an obsidian thin section how consistent are the measurement results. To test this variation an experiment was run by randomly selecting 18 sample sections and then randomly presenting these ten times each.

The results of this test (Figure 2.25) show that there is good correspondence between the measurements for any given section. Again the high degree of correspondence within measurement sets might suggest that the data are under-dispersed. However, just as for the experimental results presented in the previous section, this is to be expected. The reported measurement uncertainty principally reflects the loss of data arising through the rasterisation process. Thus we would expect similar uncertainty in the observation process for all of the captured data sets. Additionally, it would be expected that an experienced operator would select similar portions of the rim section for analysis. This is because in practice many portions of a rim section are not ideal for analysis as the image is not of suitable quality. Thus it is likely that similar portions of a rim image will be consistently re-selected. However, it is apparent that wild results can occur as evidenced in measurement 4 set 15.

This suggests that an appropriate protocol is to capture images from multiple rim points to establish the degree of variation in rim thickness present and enable the identification of any outlying measurements.

Conclusion

In general, repeat analyses of rim images return consistent measurement results. However this probably relies upon an experienced operator be-

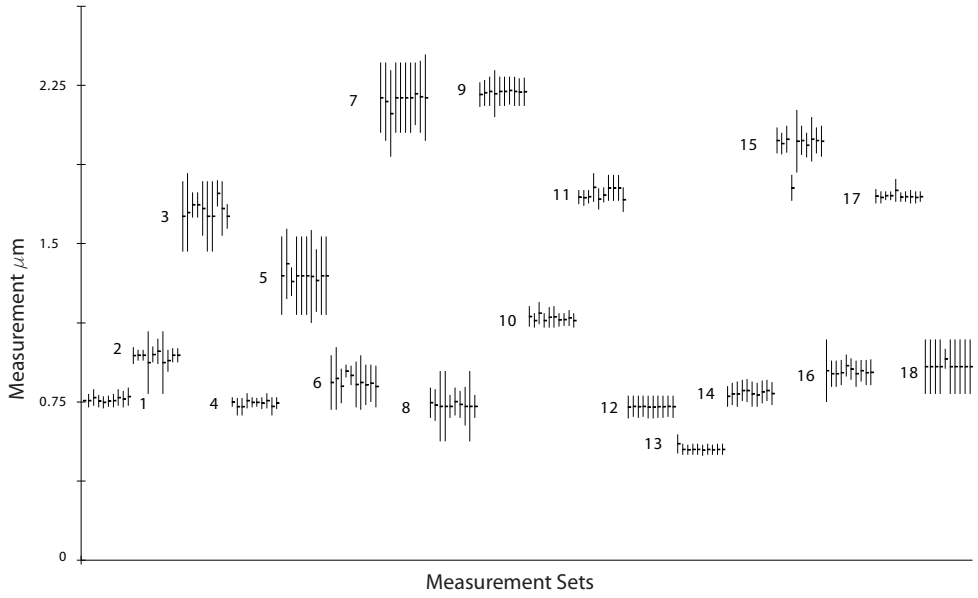

Figure 2.25: Capture variation

ing able to consistently identify analysis regions of suitable quality, and even then wild readings are possible. In light of this a sensible protocol is to collect multiple rim images from different portions of the actual obsidian section, and to analyse multiple regions on each of these images. This will allow the consistency of the measurement result to be established and will identify problematic measurement results.

Having established that consistent measurement results are possible for any sample given a suitable measurement protocol, we need to evaluate the performance of the measurement estimates; both as absolute values and in terms of reproducibility under real measurement conditions. This evaluation is discussed in the following section.

2.7.4 Measurement Tests

Two tests of the intensity reconstruction measurements made via Rim Buster were conducted. In the first, comparisons were made between RNR hydrogen profiles measured at the AURA II accelerator and the optical measurements produced through Rim Buster. This enables an assessment of the absolute measurement values. In the second experiment a double blind repeat measurement test was conducted to assess the reproducibility of the measurement system.

Comparative RNR measurements

As a test of the absolute measurement values produced via the intensity reconstruction procedure implemented in Rim Buster, comparative measurements have been made on six obsidian artefacts subjected to RNR hydrogen profiling analyses at the AURA II accelerator. The AURA II facility and RNR measurements produced there are described by Neve and Barker (1997). The six comparative artefacts are all samples of Mayor Island obsidian deriving from New Zealand archaeological contexts. Thus the nature of the hydrogen profiles is typical of that likely to be observed in New Zealand and forms a sound comparative test.

As discussed earlier there is no clear definition of how optical and RNR measurement data are related (*infra vide*:§2.3.1). A common approach is to describe the full profile width at the point where resonance intensity falls to half maximum (FWHM) as corresponding to the optical measurement. However, the use of FWHM as the comparison point of RNR and optical measurements has been questioned by Leach and Naylor (1981) who propose that optical equivalence occurs at 1/10 maximum (WTM). They have tested this via RNR measurement made at AURA II (Leach and Naylor 1981).

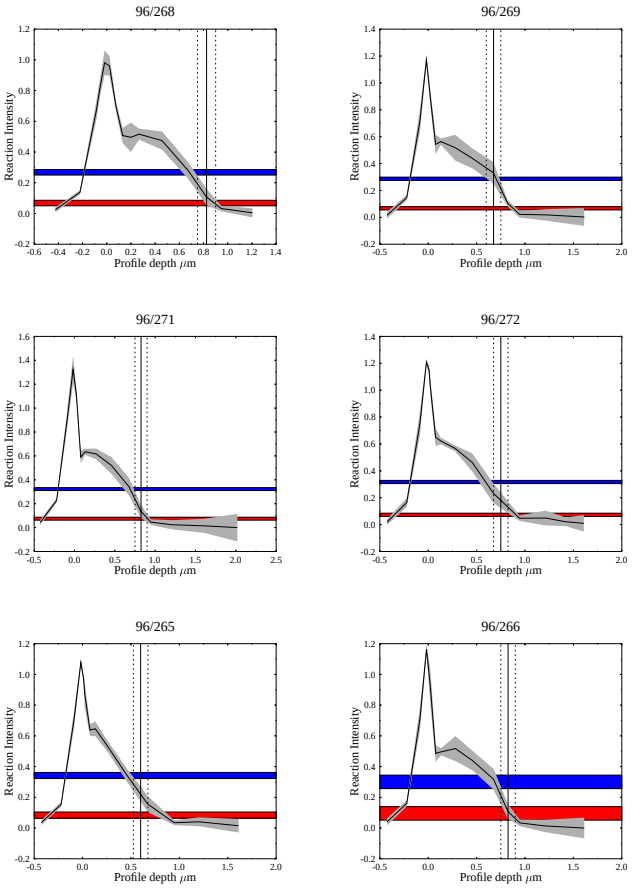

Figure 2.26: Comparative RNR and optical measurements: RNR measurements conducted at AURA II; Optical measurement made via digital rim image analysis through Rim Buster. The blue zone represents the FWHM level and the red zone represents the WTM zone. The solid vertical line represents the corresponding optical measurement with the dashed lines marking the 2σ limits of the optical measurement.

In light of this, the optical measurements have been compared to both the FWHM and WTM levels (Figure 2.26). Conveniently the optical measurements overlap both the WTM and FWHM levels as can be seen in Figure 2.26. Thus there is a correspondence between the optical measurements and those performed via RNR. This provides independent support for the validity of the absolute values produced through the intensity reconstruction measurement approach. This supports the notion that digital image measurements are absolute and can act as OHD chronometric data.

Double Blind Measurement Test

A final test was designed to assess the reproducibility of measurements made via the Rim Buster system under actual measurement conditions. This comprised a double blind experiment based around five runs of ten samples which were selected from a pool of 500 sections. The experimental structure is presented in Table 2.9.

In this experiment the contrasts of interest are:

- sample 58 three repeats
- sample 398 two repeats
- sample 432 two repeats
- sample 286 three repeats
- sample 332 two repeats

These measurement contrasts are presented in Table 2.10 and Figure 2.27. While these results are not in perfect correspondence, they do show that a high degree of reproducibility can be achieved in optical hydration rim measurements when a suitable measurement protocol is employed. It

Table 2.9: Double blind experiment structure

Run 1	Run 2	Run 3	Run 4	Run 5
205	332	180	286	92
407	73	58	214	113
58	163	311	64	283
107	384	432	375	191
111	455	119	360	286
398	316	193	135	332
354	122	288	441	218
161	287	286	58	56
87	95	316	402	141
239	398	78	32	532

Table 2.10: Double blind experimental results

Sample	Reading	$\bar{x}$	σ
58	1	1.145	0.039
58	2	1.155	0.03
58	3	1.160	0.03
398	1	0.608	0.031
398	2	0.589	0.027
432	1	0.732	0.025
432	2	0.708	0.02
286	1	1.485	0.035
286	2	1.47	0.05
286	3	1.53	0.02
332	1	0.769	0.042
332	2	0.742	0.021

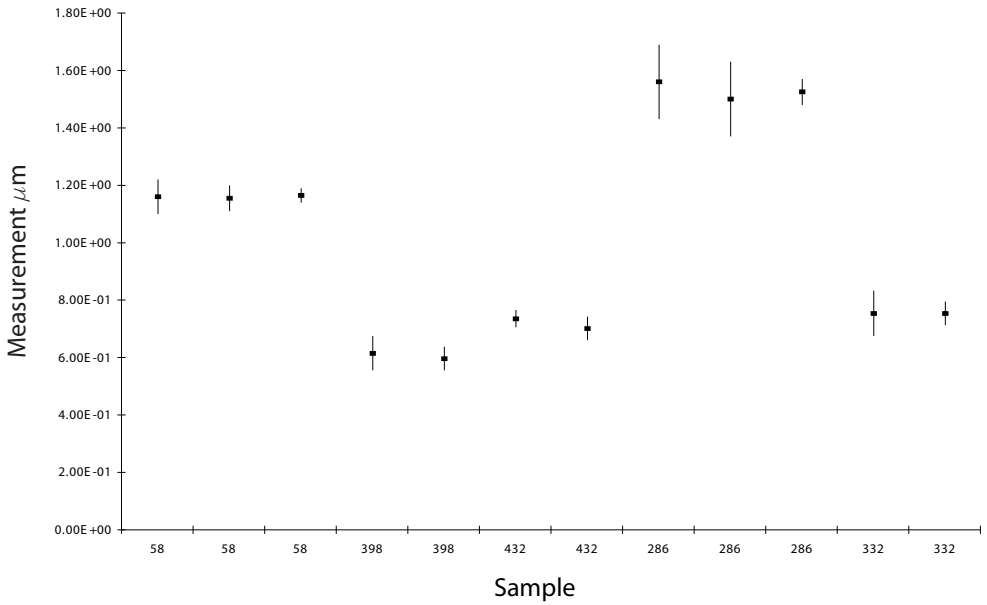

Figure 2.27: Double blind experimental results

may appear that these comparisons are under-dispersed. However, as discussed with the measurement variation tests (*infra vide*:§2.7.3) the principal uncertainty in the measurement result derives from data loss during the digitisation process. This uncertainty will be reflected in all of the measurements.

2.7.5 Conclusion

The Rim Buster software that has been presented and tested in this section provides an implementation of the simple pixel count and intensity reconstruction methods discussed previously (*infra vide*:§2.6.4). The intensity reconstruction approach, in particular, provides a general method for measuring the extent of optical hydration phenomena via digital image analysis. This system has been shown to generate consistent, reproducible absolute measurements of hydration extent. Thus

this system can be used to generate base OHD chronometric data on the basis of optical hydration phenomena. However the use of this system does require an experienced operator and also requires that a suitable measurement protocol is adopted.

On the basis of the measurement tests that have been presented in this section critical elements of a suitable measurement protocol are (this assumes the section production, microscope set up and image identification protocols described previously are used):

1. analysis of multiple images for any given obsidian thin section
2. analysis of multiple image regions for each image
3. comparative measurement analyses under multiple $\xi(x)$ approximations
4. assessment of measurement consistency between the results from 1–3 above.

2.8 Summary

A measured hydration rim thickness is the basic OHD chronometric. Accordingly it is vital that this measurement is made as accurately and precisely as possible, and that the distribution of the measurement estimate is properly developed. While a number of different approaches and technologies can be employed in order to make this measurement (*infra vide*:§2.3; §2.4), measurement consistency is to a large extent dependant upon suitable definitions of the measured hydration phenomena and precise measurement protocols based around these definitions (*infra vide*:§2.2). In most cases these conditions are not met. However, these issues that need to be resolved in the application of any measurement approach to hydration rim thickness measurement. In the absence

of an appropriate development suitable chronometric data do not exist and there is no basis for a dating system.

A measurement system based around the digital analysis of optical images initially proposed by Ambrose (1993) has been designed to meet these requirements (*infra vide*:§2.6.4). It has been demonstrated that this system can produce consistent measurement results associated with realistic measurement errors (*infra vide*:§2.7). Thus the use of this system will allow valid hydration rim thickness measurements to be made and consequently provide the basis for a useful dating system. This is largely unique amongst optical measurement approaches and represents a useful development for OHD.

Measurements of hydration extent made though Rim Buster following a protocol that meets points 1–4 defined in §2.7.5 will provide valid OHD chronometric data. In order to use data such as these in a chronology building exercise we need to be able to define a likelihood and priors for the OHD chronometric — this is considered in the chapters that follow.

The measurements that are presented in the remainder of this thesis follow the section production (*infra vide*:§2.5) and optical microscopy (*infra vide*:§2.4) protocols outlined previously. Two different image capture systems have been used. The experimental hydration rate data reported in Chapters 4–6 are based around an analogue video head mounted on a Nikon photomtic II base using a Nikon oil immersion panchromatic 100 x objective (NA 1.26) and universal condenser (NA 0.9). The analogue video signal is captured as a 620 X 540 256 greyscale bitmap (pixel size 0.075 μm) using a pcVision plus frame grabber. The remainder of the reported measurements use a higher resolution capture system. In this case a Nikon E600 base with a panapocromat 100 x objective (NA 1.6) and apocromat condenser (NA 1.6) with an optical step up of 2.5 magnification via a Nikon VMC-2.5 video relay lens and a Pixera Pro digital camera enable capture of a 1260x960 bitmap (pixel size 0.015 μm).

Chapter 3

Obsidian Reference Collection

3.1 New Zealand Obsidian Sources and Reference Samples

In this chapter the development of an obsidian reference collection for New Zealand is described. The purpose of generating this reference collection is to develop a set of securely provenanced obsidian samples. This enables both experimental control over variables such as glass geochemistry, and the use of experimental results in providing parameters for the hydration behaviour of different geological sources. This is important as in following chapters a number of experiments into obsidian hydration are presented. In order for appropriate experimental designs to be constructed it is necessary to be able to select experimental samples which allow precise control over factors such glass chemistry. Thus the obsidian reference collection described in this chapter provides the base samples for all of the experiments and source rate controls presented and used throughout the remainder of this thesis. As the application of the current research is primarily focussed on New Zealand, the reference samples all derive from New Zealand. This does not compromise the overall experimental program as the experimental questions relate to general hydration behaviour, however it ensures that the results are most directly applicable to the New Zealand context.

As there are a large number of potential sources in New Zealand it was decided that the primary basis of the reference collection in terms of experimental hydration results should be material deriving from Mayor Island. This is as Mayor Island material is all but ubiquitous in the New Zealand archaeological context and is relatively easily differentiated from most other sources on the basis of transmitted colour. This means that the use of experimental results in an archaeological context is facilitated as identification of the source material is greatly simplified.

For the development of this reference collection we need to establish

where obsidian may arise throughout New Zealand, establish what is known about obsidian from these sources, identify those sources that need to be included within the reference collection, and finally to collect the necessary samples. Each of these steps is considered through the remainder of this chapter.

3.1.1 Identification of Potential Source Areas

While natural glasses such as pitchstones and dacites are found throughout New Zealand, obsidian is found exclusively on the eastern coast of the upper North Island associated with tertiary and quaternary rhyolitic volcanism. A large number of New Zealand obsidian sources have been identified to date (*supra vide*: D.1), and it is most likely that all significant source areas that were exploited prehistorically have been identified. That some exposures are yet to be identified is probable. However these will almost certainly correspond to material from source areas already identified. In order to establish the degree to which obsidian deposits in New Zealand have been identified, it is useful to outline the potential source areas.

A preliminary outline of where obsidian may be expected to be found can be made with reference to the geological history of New Zealand. In defining these "source areas", the intention is to identify volcanically discrete rhyolitic groups. Such groups may be geographically or temporally discrete, and represent generally consistent geochemical groups. In establishing potential sources of obsidian it is only necessary to identify locations of rhyolitic volcanism that may have occurred during the tertiary or quaternary, any older episodes will now be de-vitrified (Challis 1978*a*).

The early tertiary (Palaeocene-Eocene) was not a period of wide spread volcanism in New Zealand and there are no rhyolitic volcanics associ-

ated with this period (Challis 1978*a*). The Oligocene appears to have continued as a period of relative volcanic quiescence, though there are several areas of basaltic tuff and thin flows of basalt ranging from glassy varieties to almost doleritic which occur near Mount Somers in Mid-Canterbury (*Ibid.*). Pitchstone but no obsidian is found in this area (Thornton 1985).

During the Miocene, volcanic activity was quite wide spread in both the North and South Islands (Watters 1978*b*). During this period the rhyolitic volcanics where principally confined to Northland, and the Parahaki Volcanic Group is believed to have been formed during this period (Ferrar 1925). There are three recognised formations of the Parahaki Volcanic Group (Watters 1978*b*), the most northerly of these are the Putahi Rhyolites. These consist of rhyolitic lava's at Te Pene, South of Pungarae and immediately south of Lake Omapere (Source Area 1: Figure 3.1 and Figure 3.2). Further south are the Whangerei Parahaki volcanics, consisting of the Maungarei Dacite and Pukekaroro Dacite formations (Source Area 2: Figure 3.1 and Figure 3.2). Also during the Miocene there was a single instance of rhyolitic volcanic activity in the South Island. A small area at the head of the Lyttleton Harbour is covered by the Gebbies rhyolite (Liggett and Gregg 1965). Rocks present are rhyolite , breccia and tuff. Minor pitchstone is associated with this outcrop but no obsidian, thus it is not a relevant source area.

Volcanism continued on into the Pliocene in both Northland and the Coromandel (Watters 1978*b*). However only Coromandel experienced significant rhyolitic volcanism, though it is possible that limited rhyolitic volcanism continued in Northland through to the Pleistocene (Kear and Thompson 1964) (Source Area 1: Figure 3.1). In Coromandel the Miocene was characterised by andesitic volcanism, this was succeeded by rhyolitic volcanism in the Pliocene which resulted in the development of extensive rhyolitic domes and ignimbrite sheets down the East Coast

of Coromandel (Schofield 1967). The Coromandel rhyolites have been aggregated into two general groups. The Whitianga Rhyolites (Schofield 1967) form part of the mainly rhyolitic rocks of the "third period volcanics" described by earlier authors (Henderson and Bartrum 1913; Fraser and Adams 1907). Thompson (1960; 1961) includes the small areas of rhyolitic rock forming Mount Hobson and Te Ahumata (GB) and the Mokohinau and Poor Knights islands in this group. Cutting the older volcanic rocks and resting upon them in the southern part of the Coromandel range and its extension through the Kaimai range to the Bay of Plenty are the Minden rhyolites (Source Area 4: Figure 3.1). The Minden rhyolites in the Coromandel range comprise part of the "third period volcanics" and, in the Bay of Plenty, the "rhyolite series" of Henerson and Bartrum 1913. These Coromandel rhyolites represent a general source area (Source Area 3: Figure 3.1). Contemporaneous with the oldest Minden rhyolites are the first of the great ignimbrite sheets of the Bay of Plenty and central volcanic regions.

During the Quaternary there was extensive Volcanic activity throughout the North Island (Watters 1978*a*; Challis 1978*b*). However, rhyolitic volcanism was restricted to two, possibly three zones. In Northland, the predominant Quaternary volcanism is associated with the Basalt's of the Kerikeri volcanic group, though there is the possibility that there was some Rhyolitic activity as recently as the late Pleistocene among the Putahi Rhyolites (Kear and Thompson 1964). Other than this the focus of rhyolitic volcanics during the quaternary has been in the Taupo Volcanic Zone (TVZ) and at Mayor Island (Challis 1978*b*).

A zone of quaternary volcanism termed the Taupo Volcanic Zone (TVZ) (Source Area 4: Figure 3.1; Figure 3.4) extends for about 250 km in a north-east direction between Ohakune and White Island (Thornton 1985). The region is a linear depression controlled by faults and bounded to the east and west by basement rocks and extensive ignimbrite covered

plateaus. Within the zone there are a number of major rhyolitic volcanic centres. The majority of the material in the TVZ is rhyolitic and it has been estimated that around 10,000 cubic kilometres of rhyolitic material has erupted since the Pliocene (Healy 1962). Rhyolite lavas, as opposed to ash deposits and ignimbrites are concentrated in four main volcanic centres; the Taupo Volcanic, Maroa Volcanic and Okataina Volcanic Centres, plus the Rotorua Caldera (Challis 1978*b*). In general the composition of rhyolite is consistent among each of these centres, though there is some variation with the Taupo Volcanic Centre being the most geochemically distinct(*Ibid.*). The eruptive history of these centres is complex, however it is possible to say that there have been a number of flows over a range of time associated with each centre. Additionally it is considered that an eruption of ignimbrite preceded the extrusion of rhyolite. These ignimbrites are widespread throughout the TVZ, and very extensive plateau's flank the zone on either side. Individual ignimbrite flows may extend over hundreds of square k's, many have flowed at least 70 km from source and reach thicknesses of up to 200 m (Kear 1960). It is assumed the sources of the larger ignimbrite flows are the major rhyolitic volcanic centres of the TVZ, though no definite feeding vents have been identified. In general the ignimbrites are very similar in their chemistry to the extruded rhyolites of the TVZ (Challis 1978*b*).

The final source area identified on the basis of volcanic history is Mayor Island (Source Area 5: Figure 3.1). This is an isolated soda rhyolite volcano lying about 26 k offshore in the north-west Bay of Plenty (Challis 1978*b*). Extensive obsidian deposits have been described for this location, and geochemical analysis has shown the chemistry of the rhyolites here to be distinct from the TVZ and other locations (*Ibid.*).

Thus there are five general source areas in New Zealand within which obsidian sources may be expected to be located (Figure 3.1). It is essential that the nature of any exposed obsidian deposits in these areas are

properly described.

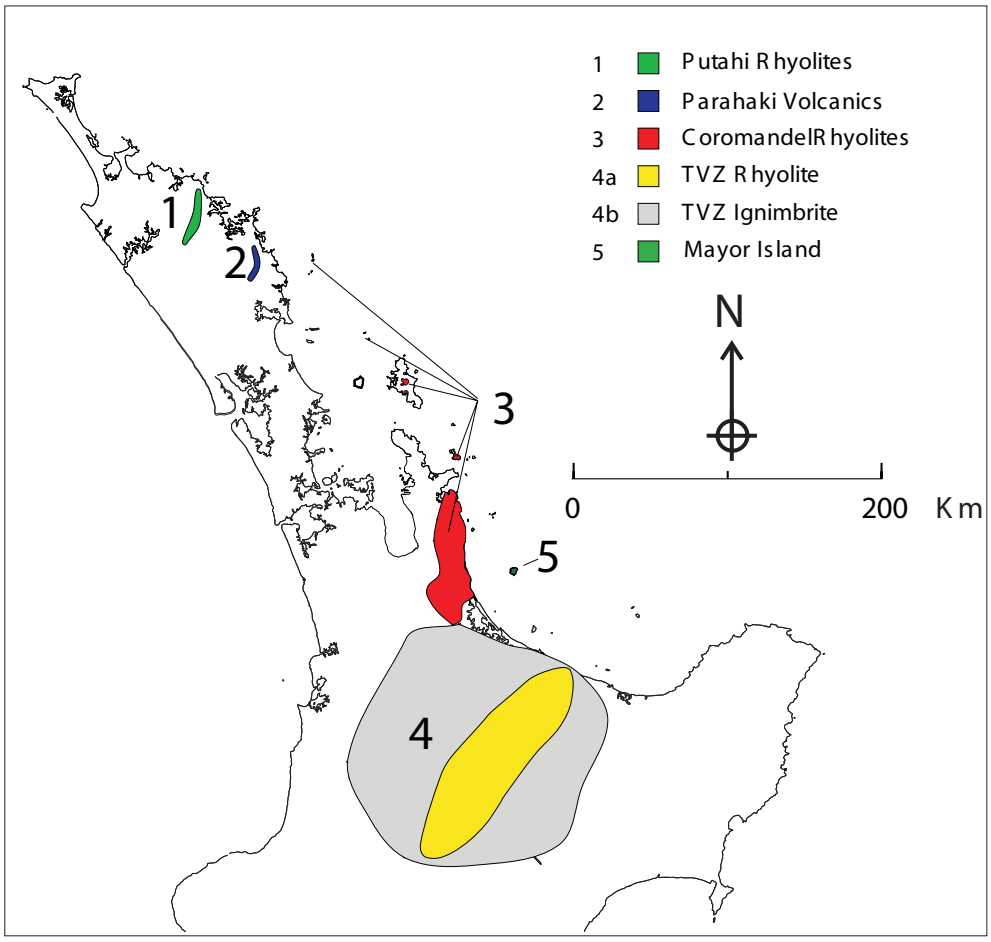

Figure 3.1: General source areas within which obsidian may be located

3.1.2 Identified Sources

In total approximately 26[1] sources of obsidian have been identified for New Zealand (Bird *et al* 1981; Duerden *et al* 1987; Moore n.d.; Neve *et al* 1994; Ward 1972: *supra vide*:§D.1). While there are definitely deposits that are not identified in this list (*e.g* Northland *supra vide*:§3.3), these

[1] this treats Mayor Island as a single source

samples will allow a general description of the obsidian deposits associated with each source area. In the current context the primary interest is in describing Mayor Island obsidian and other sources in which green obsidian may be found.

Northland Source Area

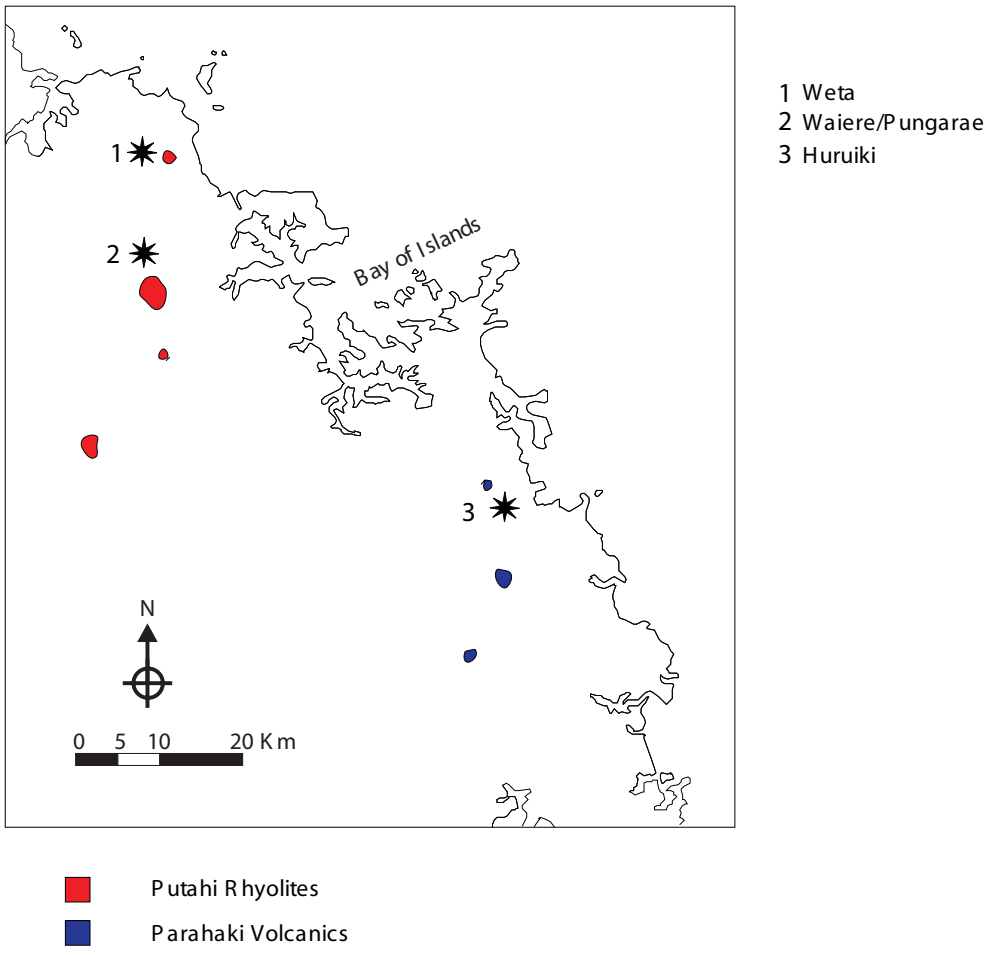

Figure 3.2: Northland obsidian locations (base geological data after Challis 1978*a*)

Three general source groups have been described for the Northland area

(Ward 1972), and these correspond to the expected zones. In addition to these sources there is a report of an obsidian source that occurs in a

> . . . large dyke-like mass *[at]* a spot thirteen miles from Kaitaia

(Morgan 1927). This deposit has not been re-located, and there must be some doubt about its existence given that Morgan's (1927) account is second hand. While there are certainly more deposits in Northland than these (*supra vide*:§3.3), descriptions of the sampled sources show that "green" obsidian does derive from deposits in the Northland area. Accordingly it is necessary to establish a protocol that distinguishes between the Northland "green" sources and those from Mayor Island.

Coromandel Source Area

The Coromandel sources have been the subject of thorough research and ten general outcrop zones have been identified (Moore 1983; 1985; Moore and Coster 1984*a*; 1989*a*). While other outcrops may yet be identified, it is highly probable that these would simply represent additional exposures of already sampled sources. The descriptions of the available sources (*supra vide*:§D.1) again demonstrate that with the exception of Waihi obsidian no "green" obsidian is to be found within the Coromandel source area.

Taupo Volcanic Zone

In the Taupo Volcanic zone the rhyolites associated with three of the main volcanic centres (Rotorua Caldera, Okataina Volcanic Centre and the Maroa Volcanic Centre) have been sampled (Bird *et al.* 1981, Duerden *et al.* 1987, Leach *et al.* 1978, Leach and Warren 1981, Moore n.d., Ward 1972; Figure 3.4). These samples will allow the general characteris-

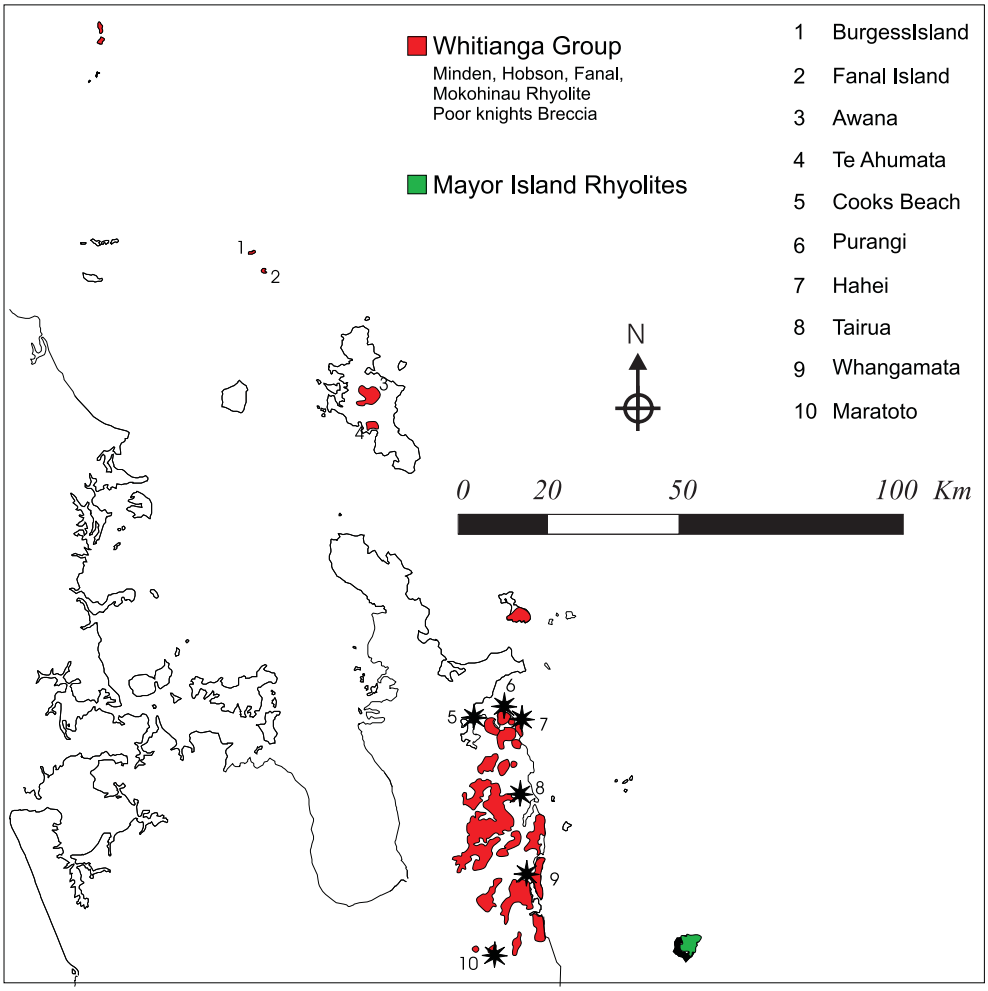

Figure 3.3: Coromandel obsidian locations (base geological data after Challis 1978*a*)

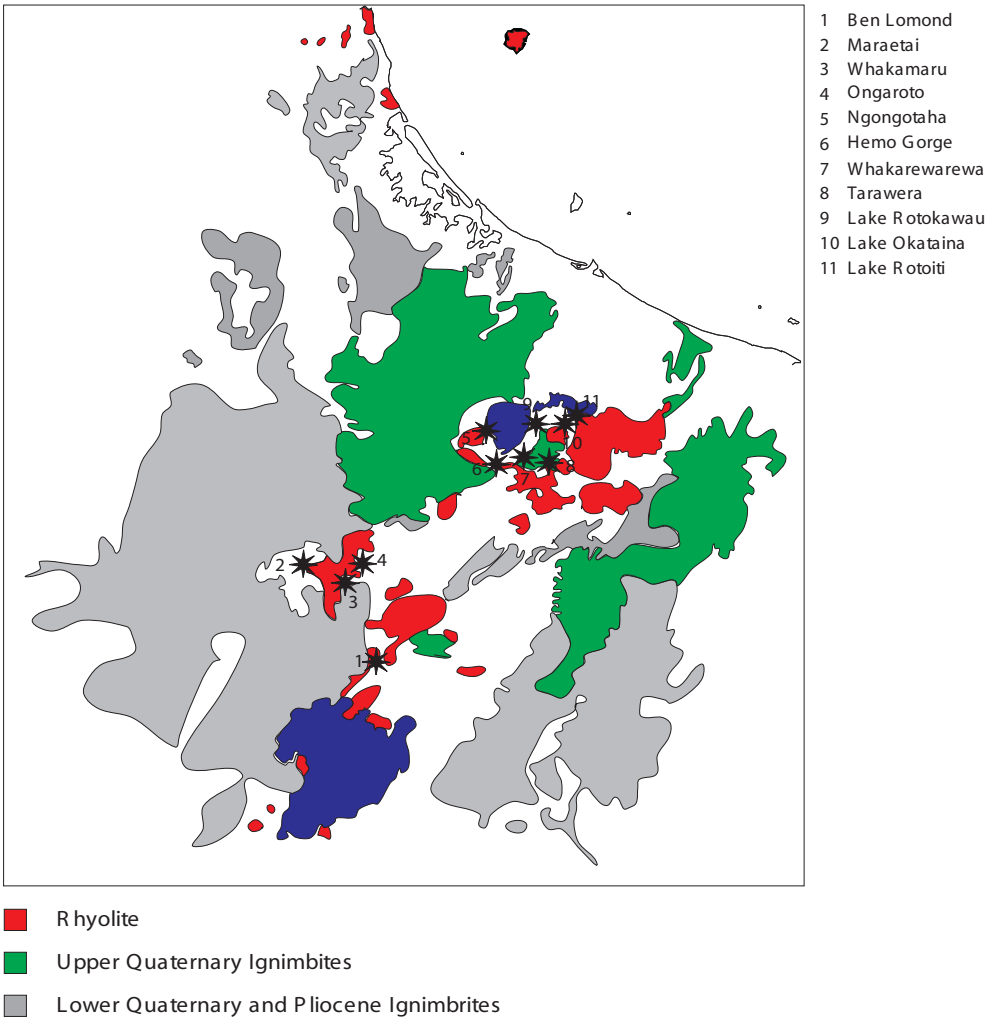

Figure 3.4: TVZ obsidian locations (base geological data after Challis 1978*b*)

tics of the obsidian associated with each of these volcanic centres to be described. Any obsidian related to the Taupo Volcanic Centre has not yet been identified or described in available literature. This is of some limited concern as the rhyolites from the Taupo Volcanic Centre are identified as being geochemically distinct from the otherwise fairly compositionally uniform rhyolites of the Taupo Volcanic Zone. The available material from the Taupo Volcanic Zone is characterised by being grey in transmitted and reflected light (*supra vide*:§B.1). There is no chance that material from this zone would be visually confused with any of the "green" sources. However this needs to be confirmed for any material associated with the Taupo Volcanic Centre.

3.1.3 Key Reference Sources

While there will possibly be further sources identified in the future, as more detailed work is done on the individual source localities, the currently identified sources do act as sample of the source areas and allow some observations to be drawn with respect to identifying suitable reference sources. First, it is apparent that material associated with some source groups, the TVZ in particular, may be distributed over a wide geographical range and potentially exhibit significant intra source geochemical differences due to the presence of a large number of eruptive centres in the area. This is particularly so in locations such as the southern Coromandel where it is possible that rhyolitic ignimbrites associated with both the TVZ and Coromandel source areas are present. In this case identifying a specific deposit, providing source specific hydration parameters for the deposit, and identifying archaeological material deriving from this source may be difficult.

Mayor Island obsidian represents the optimal source group for primary hydration control. This is for several reasons:

- Mayor Island obsidian derives from a geochemically distinct volcanic zone
- the Mayor Island obsidian sources will not be intermixed with material from other source zones
- Mayor Island obsidian is the most frequently represented source in archaeological deposits, with Mayor Island obsidian being found in almost every archaeological site containing obsidian (Davidson 1981; Seelenfreund-Hirsch 1985)
- Mayor Island obsidian is characteristically green in transmitted light, a characteristic only shared by two other source locations. Thus the archaeological identification of Mayor Island obsidian will be simplified. This ensures that the experimental results will be more readily applicable to archaeological dating than for other sources.

In light of this the most sensible focus of the experimental hydration program should be the control of the "green" obsidian, that is the Mayor Island, Northland and Waihi obsidian sources. The field sampling of these sources to generate a reference collection is detailed in the following sections. However, it is important to include samples from the other source zones in order to establish some basis for assessing the degree of variation in hydration behaviour among all of the New Zealand sources. In light of this a rhyolite flow (Ben Lomond) from within the TVZ was selected as a type sample from this location. Additionally the Whitianga rhyolites were sampled at Whitipirorua (Coromandel) and Te Ahumata (Great Barrier) and the Parahaki Rhyolite group was sampled with the Huruiki source. In addition to the sources that were directly sampled in the field, some source samples were extracted from the Auckland university Reference Collection, these are as follows:

Source	Accession Number	reference collection
Fanal Island	#2949/1, #2949/5	#39
Onemana / Whitiporua	#1690,#2866	#34
Awana	#679/7, #679/11	#35
Te Ahumata	#680	#36
Cook's Beach	#2189	#37
Purangi	#917	#38

3.2 Mayor Island Field Survey

3.2.1 Introduction

Mayor Island is the summit of a peralkaline rhyolite volcano lying approximately 26 km offshore in the Western Bay of Plenty. The island is roughly circular, approximately 4km in diameter and is dominated by an ≈ 3 km diameter circular caldera in the centre. Being peralkaline rhyolites, the composition of the Mayor Island rocks differ from the other rhyolitic zones in New Zealand, and accordingly the obsidian deriving from Mayor Island is geochemically and (generally) visually distinct from other sources. Mayor island is a composite volcanic cone, with the present form being produced by a number of eruptive events occurring over a period of ≈ 120 K years (Houghton *et al.* 1992). Accordingly, obsidian related to distinct eruptive episodes exists on Mayor Island and as such the island should be treated as a source area, rather than a homogenous source.

A number of studies have been conducted into the volcanic history of Mayor Island *e.g.* (Brothers 1957; Buck *et al.* 1981*a*; Houghton *et al.* 1992) and on the basis of these it is possible to outline a basic eruptive

Figure 3.5: NZMS 260 map of Mayor Island

history that can be used to identify potential subsources. This indicates that Mayor Island is made up of five major physiographic units: the main cone, the caldera fault blocks, the Ohineiti dome, the young dome and the coastal flats (Figure 3.6).

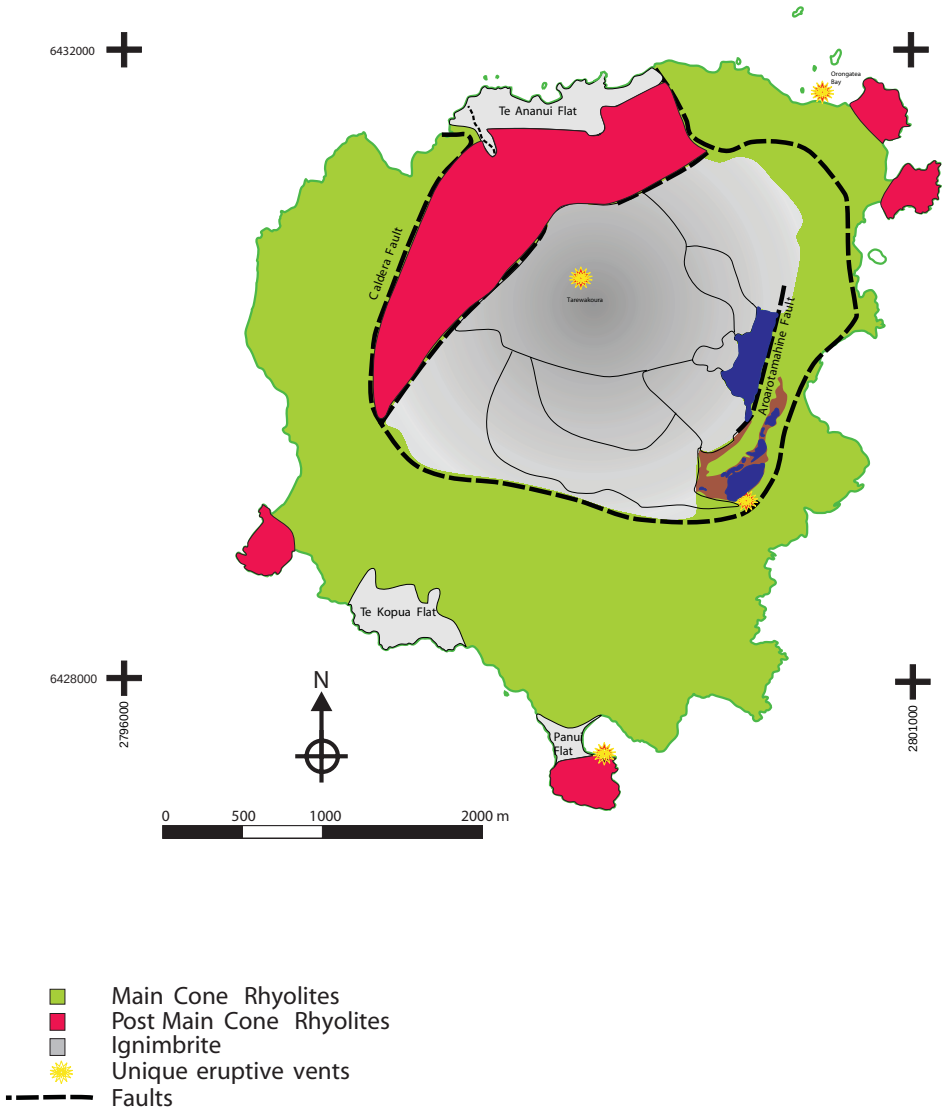

Figure 3.6: Generalised map of the major physiographic units on Mayor Island after Buck *et al.* (1981*a*) and Houghton *et al.* (1992)

Main Cone

The main cone forms the principal outer-slopes of the island and is predominantly constructed of vesicular rhyolite flows up to 40 m thick with obsidian selvages on the upper and lower surfaces, interbedded with pyroclastic deposits. Over most of the island's outer-slopes the main cone is covered by pyroclastic deposit. There are five broad rhyolitic flows that have been identified (Buck *et al.* 1981*a*), and these are exposed either on the coast, or in the caldera fault blocks.

Caldera Fault Blocks

The caldera wall delimits a near-circular ring fracture approximately 3km in diameter. Within the caldera there are a number of faults across the crater floor. Five have been identified (Buck *et al.* 1981*a*), although some of these may in fact relate to successive dome building episodes rather than faulting (Houghton *et al.* 1992). It appears most likely that there are two superimposed caldera faults (Houhton *et al.*'s 1992 Caldera A and Caldera C) and possible a third intermediate fault (Houhton *et al.*'s 1992 Caldera B). These faults serve to expose the main cone rhyolite flows in section, and hence expose the associated obsidian selvages. Thus it is important to locate where unique selvage exposure may occur in the fault blocks. In terms of the current study, only the Te Ohineiti fault which may expose obsidian associated with the pre-caldera C Ohineiti dome is of significance as the other fault faces are not exposed.

Coastal Flats

There are three coastal flats. The Te Ananui and Te Kopua flats are comprised of epiclasic sediments. The Panui flat is built up of a succession

of eruptive events associated with a parasitic dome.

Ohineiti Dome

After the initial caldera was formed a second dome grew within the caldera. This was fractured in subsequent caldera ring fault episode (Houghton *et al.*'s 1992 Caldera C). The remnants of this dome are present in the western caldera region, and form part of the valley within which the Opuhi Springs lie.

The Young Dome

The final physiographic unit is the young dome that lies within the caldera. This relates to the most recent phase of volcanic activity at Mayor Island and consists of a series of block lava flows. At least eight flows occur and there is no associated airfall pyroclastic deposit.

3.2.2 Sampled Locations

Previous field sampling of the obsidian sources at Mayor Island has been under taken by archaeologists who have identified a number of subsources (Holroyd 1993; Seelenfreund-Hirsch 1985; Ward 1972) (Figure 3.7). However, it is unclear how these sources have been sampled in terms of distinguishing between flows and sampling within flows. It is also apparent that potentially unique sources have not been sampled (*e.g.* Orongatea). In light of this, two further field surveys of Mayor Island obsidian have been conducted in conjunction with a sampling programme.

On the basis of the available geological evidence it is possible to produce a preliminary outline of what source areas need to be sampled. It is ap-

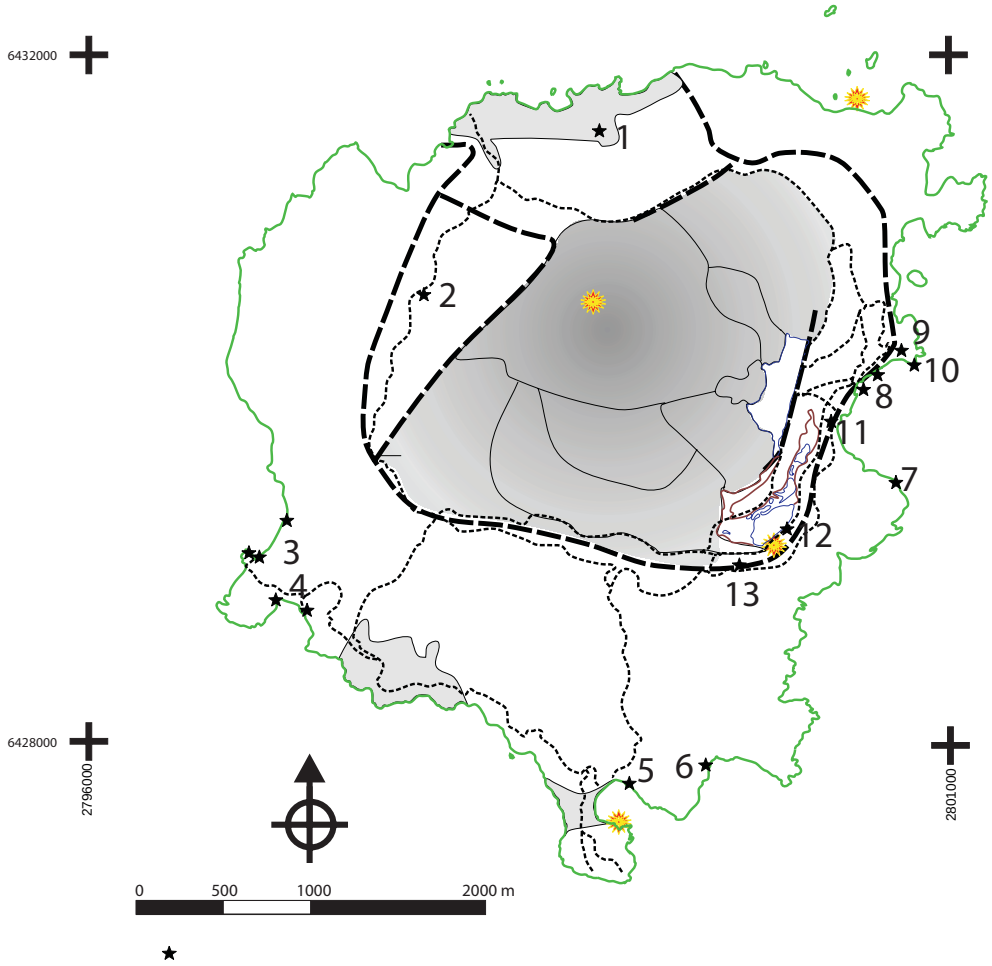

Figure 3.7: Published obsidian sample locations

1, (Holroyd 1993);2, (Holroyd 1993; Seelenfreund-Hirsch 1985);3, (Holroyd 1993; Seelenfreund-Hirsch 1985; Ward 1972);4, (Holroyd 1993; Seelenfreund-Hirsch 1985; Ward 1972);5, (Holroyd 1993; Seelenfreund-Hirsch 1985; Ward 1972);6, (Holroyd 1993);7, (Seelenfreund-Hirsch 1985);8, (Holroyd 1993; Seelenfreund-Hirsch 1985; Ward 1972);9, (Holroyd 1993; Seelenfreund-Hirsch 1985);10, (Ward 1972);11, (Holroyd 1993; Seelenfreund-Hirsch 1985; Ward 1972); 12, (Holroyd 1993); 13, (Holroyd 1993; Seelenfreund-Hirsch 1985; Ward 1972)

parent that around the coast there are a number of potentially unique sources arising from selvages associated with the exposed main cone rhyolites. As there are a number of these flows (*infra vide*:§3.2.1) multiple selvages may be exposed at any point. Additionally, it is also possible that early pre-caldera rhyolites not present on the coast are exposed in the caldera fault blocks (*i.e.* the Caldera, Te Ohineiti and Aroarotamatine Faults).

Post main-cone eruptive episodes in the Caldera (Tarewakoura and Te Paritu), Northern Coast(Orongatea Bay, Wharenui Point), Opo bay, Raumata Point and the flow mantling Parikoura point (Buck *et al.* 1981*a*; Houghton *et al.* 1992) may also give rise to unique localised sources. Thus it is important to sample exposed main-cone selvages in order to determine both the degree of homogeneity within and between each flow event. Additionally, it is important to sample the possibly unique material associated with the identified vents, and further any material that maybe associated with pyroclastic deposits on the coastal flats, Ruawaipiro Pass and Opuhi Springs area.

The sampled sources (Figure 3.8; *supra vide*:§B.2) represent a sample of obsidian from both the selvages and pyroclastics that would have been available resources prehistorically. This collection makes it possible to identify the degree to which there are subsources within Mayor Island in terms of hydration behaviour and to define a protocol to distinguish any such sub-groups. In total, field samples were taken from 36 spatially discrete areas within 17 general locations (Figure 3.8). The coastal exposures were sampled on the west and east coast in order to account for any variation due to a possible east west dip (Buck *et al.* 1981*a*). Additional to this, exposures were sampled in areas associated with the Caldera fault blocks and those associated with possibly unique vents at Opo Bay, Orongatea Bay and Te Paritu. The sample areas are as described below:

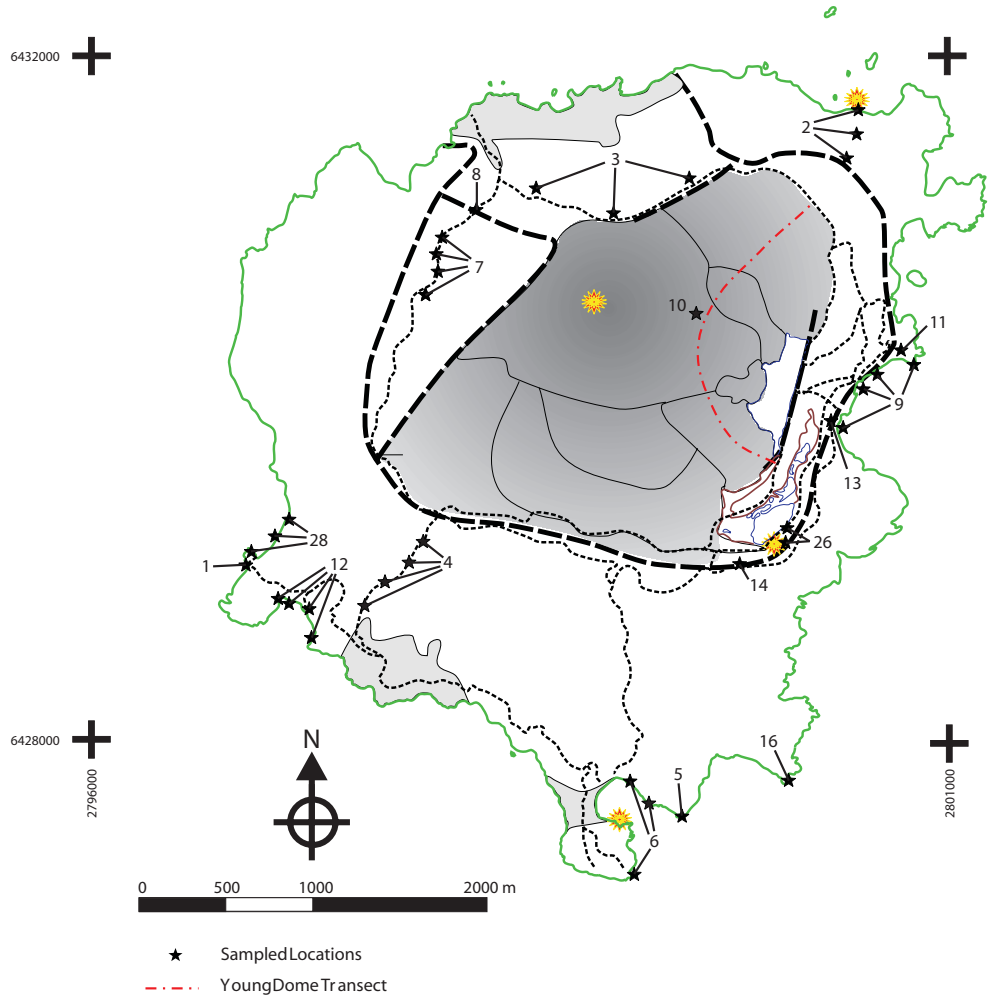

Figure 3.8: Locations from which field samples have been collected

Raumata Point (Source 1, *supra vide*:§B.2)

On the southern side of Raumata Point there is a small beach. Obsidian is present in the form of beach cobbles and twin selvages in the headland that are continuations of those exposed to the south of Oira Bay. Both selvages were sampled (Samples 1.5.x-1.7.x; Table B.2, *supra vide*:§B.2.1) and samples were taken from each of four beach cobbles (Samples 1.1.x-1.4.x; Table B.2, *supra vide*:§B.2.1).

Martin Jones 2002

Orongatea (Source 2, *supra vide*:§B.2)

The vertical Orongatea seams were reached by land. There are three vertical seams visible in the cliff face at Orongatea Bay and samples were taken from each of these (Samples 2.1.x-2.3.x; Table B.2, *supra vide*:§B.2.2). Additionally a sample of material present in the internal caldera wall was collected in a transect over the crater rim (Samples 2.4.x-2.11.x; Table B.2, *supra vide*:§B.2.2). This will represent a comparative sample of obsidian associated with the main cone rhyolites.

Te Ananui Flat (Source 3, *supra vide*:§B.2)

There is a fairly uniform low density scatter of obsidian cobbles and boulders over the area to the North of the caldera and on Te Ananui flat proper. No visible vents or in situ selvages were located, though it is assumed that the material has eroded out of in situ seams, or exists as rubble deposited during the various formation processes of the island. The deposits in this area were randomly sampled at six locations in a west east transect running along the Te Ananui Flat path (Samples 3.1.x-3.9.x; Table B.2, *supra vide*:§B.2.3).

Ruawaipiro Pass (Source 4, *supra vide*:§B.2)

A zone of pyroclastic material is present through the Ruawaipiro Pass area. The obsidian in this area is present as loose material in the form of cobbles and boulders. No particular density of location has been identified and it appears that the material is present in relatively uniform density throughout the region. Samples of material were taken from four locations along the vertical extent of the pass area.

Te Matawhero Point (Source 5, *supra vide*:§B.2)

The twin selvages that are continuously visible running from Opo Bay to Taratimi have been sampled at Te Matawhero Point.

Opo Bay (Source 6, *supra vide*:§B.2)

At Opo bay there are two primary exposures of obsidian, present in the western and eastern headlands. The western exposure probably relates to a unique eruptive event, and accordingly may correspond to a unique type of glass. The obsidian is exposed as a selvage in the face of the cliff at this point. Several samples were taken from a single location in this exposure (Samples 6.1.x, 6.4.x; Table B.2, *supra vide*:§B.2.6).

To the east of Opo bay there is a twin selvage of obsidian typical of the general coastal exposures. As stated previously, this exposure is continuous through to Taratimi Bay. Both seams have been sampled at two locations in the headland to the east of Opo Bay (Samples 6.2.x, 6.3.x; Table B.2, *supra vide*:§B.2.6).

Opuhi Springs (Source 7, *supra vide*:§B.2)

Opuhi Springs lie in the valley formed by the Te Ohineiti dome and Caldera A Fault. Approximately 300 m north of the springs an almost continuous scatter of obsidian cobbles and debitage is present through to the where the Te Ohineiti fault cuts the end of the valley. The material present is presumably remnants from disturbance during the faulting process and ongoing erosion of nearby exposed selvages. The highest concentration of obsidian rubble occurred in four distinct areas (Figure 3.9). In each of these areas the valley narrowed to the north and south leaving a bounded area with significant widening. The obsid-

ian from each area was systematically sampled separately. As it was possible that the western most obsidian rubble derives from the extant caldera cliff, and that the eastern most obsidian derives from material eroded from the upper layers of the Te Ohineiti dome, a distinction was drawn between the Eastern and Western obsidian samples.

Opuhi A lies approximately 300m from the Opuhi Springs. This area is approximately 40 m long and encompasses a valley running to the east. The samples were collected along three transects (upper slope, mid slope, lower slope) on each of the western (Samples 7.8.x,7.9.x,7.24.x,7.25.x; Table B.2, *supra vide*:§B.2.7) and eastern sides (Samples 7.17.x-7.19.x; Table B.2, *supra vide*:§B.2.7). The material from the eastern side is predominantly small, poor quality, irregularly shaped material that appears to be eroding out of loose pumice and soil. Some larger pieces (≈ tennis ball) are present on the lower eastern slopes. In contrast, the western slope material occurs in higher concentration and appears less weathered, whether this is a function of the material being higher lustre or not is unclear.

Opuhi B lies about 100m from Opuhi A and runs approximately 60 m to the north. There is considerable widening to both the east and west of the valley at this point. There appear to be cultural structures in this area, so it is difficult to distinguish between the cultural and geological distribution in this location. There are extensive scatters of obsidian over the valley floor in this area, though it is possible that some or all of this is cultural. A random sample of this material was collected (Samples 7.21.x,7.23.x; Table B.2, *supra vide*:§B.2.7). Transects were walked on the eastern and western slopes of this area. There was no material apparent on the eastern slope. Extensive deposits of high quality material occur as fractured cobbles and boulders over the western slopes (Samples 7.3.x-7.5.x; Table B.2, *supra vide*:§B.2.7). A valley lying approximately 10m above the path rises to the west of Opuhi B. This leads towards the

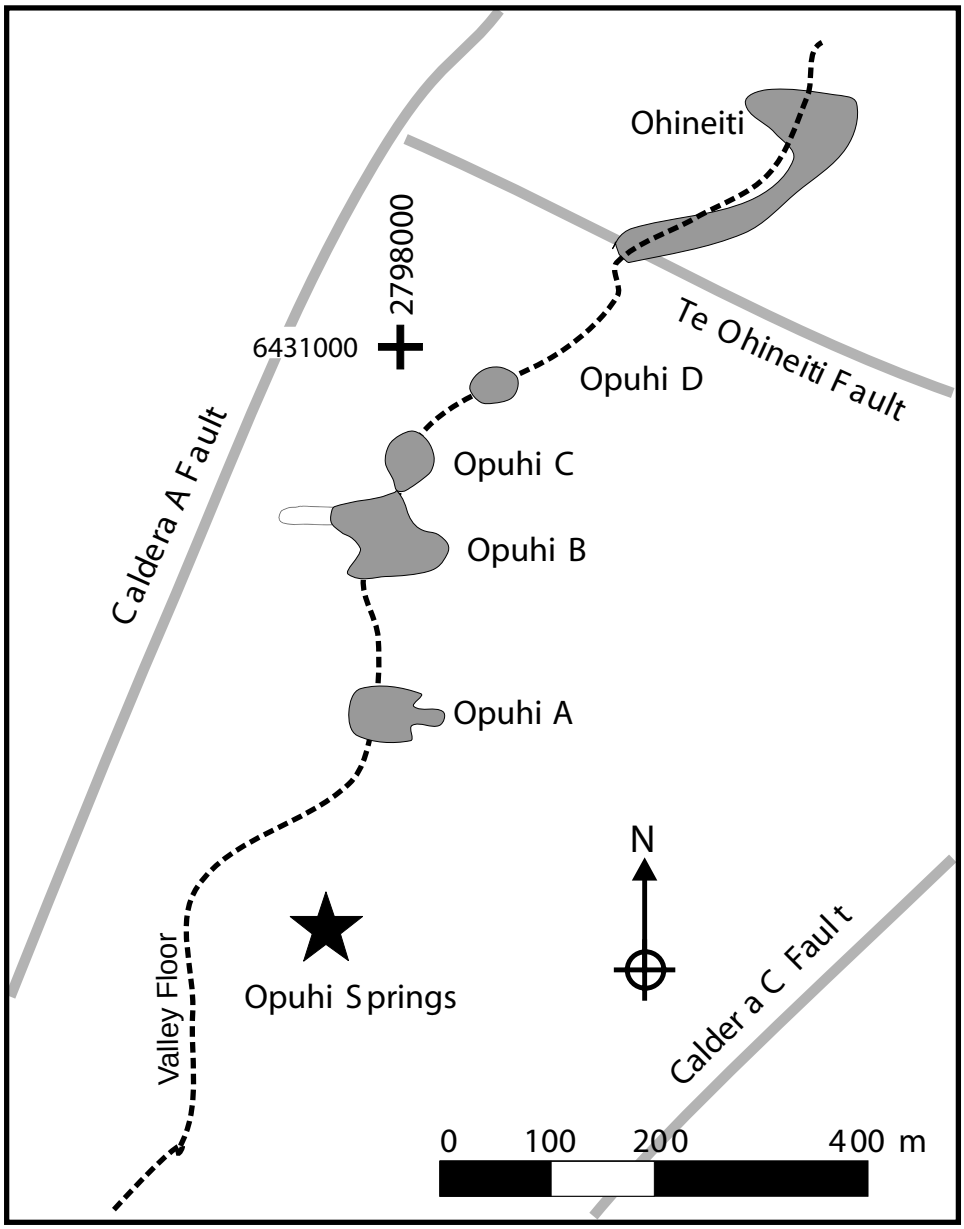

Figure 3.9: Locations of the opuhi springs samples

caldera crater wall and contains extensive obsidian boulders and rubble scatter. A sample was collected from the western valley scatter (Samples 7.20.x; Table B.2, *supra vide*:§B.2.7) and a separate sample was collected from the western valley head (Samples 7.26.x-7.28.x; Table B.2, *supra*

vide:§B.2.7).

Opuhi C is immediately adjacent to Opuhi B and is approximately 35 m in length. There is considerable obsidian rubble on the valley floor around the path in this area, and again there is the possibility that some of this material is in a cultural rather than geological context. A random sample of this material was collected (Samples 7.10.x-7.14.x; Table B.2, *supra vide*:§B.2.7). There is extensive material on the western slopes of this area and it again occurs as fractured cobbles and boulders in a soil matrix. Samples were collected from throughout the distribution (Samples 7.1.x, 7.2.x, 7.6.x, 7.7.x, 7.29.x,7.30.x; Table B.2, *supra vide*:§B.2.7).

Opuhi D lies 50 m beyond Opuhi C, and in this area the valley widens out to the west. Extensive deposits of fractured boulders and cobbles are present on the western slopes of this area. Samples were taken along three transects walked into the western embayment (Samples 7.16.x, 7.22.x; Table B.2, *supra vide*:§B.2.7).

Te Ohineiti (Source 8, *supra vide*:§B.2)

At the mouth of the valley caused by the Te Ohineiti fault the fault block ends and the path drops down the exposed fault face. An obsidian selvage is exposed in this fault face which tends east at this point for approximately 50m. Associated with this selvage are a number of boulders and cobbles lying below the face. The exposed selvage is composed of multiple bands of material and at most extensive is 2m thick. Samples were taken from along the extent of the exposed selvage and each substrata was sampled (Samples 8.2.x,8.6.x-8.12.x,8.17.x-8.19.x,8.46.x-8.49.x,8.51.x-8.52.x; Table B.2, *supra vide*:§B.2.8). Flakes lying on the floor beneath the “quarry” face were also sampled (Samples 8.13.x-8.15.x,8.19.x-8.34.x,8.50.x; Table B.2, *supra vide*:§B.2.8) Additionally the associated cobble and boulder scatters were sampled (Samples

8.1.x, 8.3.x-8.5.x,8.16.x,8.35.x-8.45.x; Table B.2, *supra vide*:§B.2.8).

Taratimi Bay (Source 9, *supra vide*:§B.2)

There are a number of obsidian exposures in the Taratimi Bay area. In general the Beach at the base of the cliff surrounding Taratimi Bay comprises boulders and cobbles, some of which are composed of obsidian. There are no visible exposures of obsidian in the cliff backing the beach which appears to be composed of pumacious tuff. Obsidian seams are exposed at the two headlands to the south and north of Taratimi Bay, and at a small point in the centre of the Bay.

The central seam is identified as the Southern Taumou Beach source by Holroyd 1993. Samples were taken from along this exposure (Samples 9.7.x; Table B.2, *supra vide*:§B.2.9). The southern Taratimi Bay seam corresponds to Seelenfreund's 1985 Te Rangiora Bay Quarry. It was not possible to sample this source on either of the field trips due to problems with access. However, this seam is continuously exposed from Southern Taratimi Bay through to Opo Bay, and it is possible to sample the seam elsewhere (*e.g.* Te Matawhero and Ruakikeno points). A sample has been obtained from the flow in the headland to the north of Taratimi Bay (Samples 9.9.x,9.10.x; Table B.2, *supra vide*:§B.2.9). In addition to the exposed seams there is considerable loose material available on the beach. This material obviously derives from seams above the bay and there is considerable variation in the type of material present. A sample of this material has been taken (Samples 9.1.x-9.6.x, 9.8.x, 9.11.x-9.13.x; Table B.2, *supra vide*:§B.2.9). The basic composition appears to correspond to the vitreous material present in the Staircase and Taumou selvages and the banded green material found in the Taumou *pā* outcrop.

Young Dome (Source 10, *supra vide*:§B.2)

On the basis of previous descriptions there are no true obsidian associated with the young dome rhyolites as the glassy material found in this vicinity has a phenocryst level exceeding 35% (Houghton *et al.* 1992). In order to sample the type of deposit associated with the young dome rhyolites a single transect was walked as shown on Figure 3.7. The material observed on this transect was universally of poor quality and of uniform visual appearance. Representative samples were collected at three points along the transect.

Taumou *pā* (Source 11, *supra vide*:§B.2)

There are several exposures of obsidian in the Taumou *pā* area. A small seam of obsidian is exposed in the caldera rim adjacent to the *pā* (Samples 11.10-11.12; Table B.2, *supra vide*:§B.2.11). This probably corresponds to Seelenfreund's (1985) "quarry". There is also obsidian exposed in weathered outcrops at the top of the *pā* ridge, which possibly correspond to an ignimbrite layer. The obsidian in this context occurs as medium sized cobbles. This outcrop was sampled over it's spatial extent (Samples 11.1-11.9; Table B.2, *supra vide*:§B.2.11).

Otiora Bay (Source 12, *supra vide*:§B.2)

Selvages are exposed in the headlands to the north and south of Otiora Bay, and there is an exposure in the central part of the beach immediately to the south of the path. In each case it is apparent that there are twin flows present. Each flow was sampled along its extent (South samples 1.5.x-1.7.x, Central samples 12.5.x,12.13.x-12.15.x, North samples 12.10.x-12.12.x; Table B.2, *supra vide*:§B.2.12). In addition to the exposed selvages, there are numerous cobbles and occasional boulders

of obsidian present on the beach. Samples were collected from each of eight randomly selected cobbles (Samples 12.6.x-12.12.x; Table B.2, *supra vide*:§B.2.12).

Staircase (Source 13,15,27 *supra vide*:§B.2)

As the path follows the eastern Caldera rim, the crater becomes very narrow and drops in altitude making access to the interior of the caldera possible. This section is known as the Devil's Staircase and along this portion of the Caldera rim there are a number of exposed main-cone selvages. There are three broad bands of exposed obsidian in this area in stratigraphic sequence. We have termed these the upper, middle and lower staircase exposures.

The upper exposure (Source 13 *supra vide*:§B.2.13) consists of poor quality obsidian formed in thin sheets (< 10 cm) interbedded with non-vitreous material. In total the exposure is about 1 metre deep. Six spatially discrete samples were collected from this exposure.

About 10 m below this the middle staircase layer is exposed (Source 15 *supra vide*:§B.2.15). The middle Staircase exposure is the most extensive in this area, and consists of complex interbanded selvages. We have identified five discrete obsidian seams in this area, which occur interbanded with rhyolite. The exposure occurs over a depth of about 3-4 m. An upper layer (Layer 3) is separated from the middle layer (layer 2) by a zone of heavily weathered, inconsistently banded, semi-vitreous material. Samples were taken from along the spatial extent of this exposure (Samples 15.4.x; Table B.2, *supra vide*:§B.2.15) . The layer 2 deposits were further divided into three sub-strata. These substrata consist of high quality vitreous obsidian seams banded with poor quality semi-vitreous material and occasional honey coloured obsidian. It is at this location that the "Staircase Quarry" (Seelenfreund-Hirsch 1985;

Ward 1972) is located. Samples were taken from along the spatial extent of each of the sub-strata in this layer (strata A samples 15.1.x; strata B samples 15.2.x, 15.10.x-15.25.x; strata C 15.3.x; Table B.2, *supra vide*:§B.2.15). The lower layer (Layer1) is less extensive than the other two layers and occurs as a contiguous zone of obsidian. Again samples were taken from along the spatial extent of this exposure (Samples 15.5.x; Table B.2, *supra vide*:§B.2.15).

The lower staircase exposure (Source 27 *supra vide*:§B.2.21) lies approximately 5 m below the middle exposure and is not extensive. The exposure consists of a contiguous exposure of high quality obsidian $\approx$ 2-3 m^2 in area. Samples were taken from throughout the areal extent of the exposure.

Hall's Pass (Source 14, *supra vide*:§B.2)

At Hall's Pass it is possible to navigate the internal caldera cliff. Along this cliff most of the main-cone rhyolites are exposed, and it is possible to sample the associated selvages. Some of the stratigraphically superior main-cone rhyolites (Buck *et al.* 1981*a*) do not appear to be present in the Hall's Pass section, as only three principal flows could be seen. However, the stratigraphically superior flows will be present in the coastal sections and the Hall's Pass section allows the stratigraphically inferior range of main-cone obsidian selvages to be sampled. In the Hall's Pass section The obsidian was present as massive selvages in the Caldera wall. Three flows (Lower, Middle and Upper) where present and these were sampled in the immediate Hall's Pass area (Lower Samples 14.1.x, Middle Samples 14.2.x 14.4.x-14.11.x, Upper Samples 14.3.x; Table B.2, *supra vide*:§B.2.14).

Ruakikeno Point (Source 16, *supra vide*:§B.2)

The twin selvages that are continuously visible running from Opo Bay to Taratimi have been sampled at Ruakikeno Point.

Te Paritu (Source 26, *supra vide*:§B.2)

Immediately below the Caldera cliff along the side of Lake Te Paritu there are extensive deposits of boulders and cobbles. These almost certainly derive from seams higher in the caldera cliff, rather than insitu exposures at this location. A random sample was made along the length of the scatter (Samples 26.5.x-26.7.x; Table B.2, *supra vide*:§B.2.20). In order to sample the in situ material from the area supposed to correspond to a discrete vent, the cliff base and slope was searched for in situ selvages. A single seam was found at the base of the caldera cliff. While contiguous, the seam is only exposed in discrete locations and only for small expanses. This seam was sampled along the exposed length (Samples 26.1.x-26.4.x; Table B.2, *supra vide*:§B.2.20).

Oira Bay (Source 28, *supra vide*:§B.2)

There are a number of locations from which obsidian is available in the general Oira Bay area. At the headlands to the north and east of the beach selvages associated with the main cone rhyolites are exposed. The northern exposure consists of at least two flows. Samples were taken from along the length of each flow exposed in the headland (Samples 28.4.x; Table B.2, *supra vide*:§B.2.22).

To the south of the beach there are twin selvages exposed in the headland leading out to Raumata Point. Samples were taken from both selvages along their spatial extent (Samples 28.2.x,28.3.x,28.5.x,28.6.x; Ta-

ble B.2, *supra vide*:§B.2.22).

Obsidian is also present as small pebbles in the tephra cliff backing the beach. A sample of this material was collected (Samples 28.1.x; Table B.2, *supra vide*:§B.2.22).

3.2.3 Summary

Obsidian associated with main-cone rhyolites has been sampled at a number of locations. Along the coast, twin obsidian selvages are almost continuously visible around the entire coast. Except for the possibly unique flows at Opo east and Orongatea, it would be expected that the exposed coastal seams correspond to a similar compositional group. Thus the sampled coastal exposures should be representative of the coastal selvages. Related to these samples will be the selvages exposed in the internal fault blocks. The samples from stratigraphically superior selvages associated with the Staircase and Taumou *pā* (possibly also Opuhi Springs west) sources should also be a representative sample from these flows, and may be expected to correspond to the exposed coastal selvages. The stratigraphically inferior selvages exposed in the Hall's pass section and possibly in scatters at Te Paritu and Opuhi would be expected to be similar to the other main-cone selvages, though as they relate to an earlier phase in the islands eruptive history may exhibit a distinct geochemical and hydration signature. The flows corresponding to unique events in Ohineiti, Orongatea and Opo Bay may also exhibit distinct geochemistry and hydration behaviour.

In general the obsidian associated with the rhyolite selvages is extremely uniform in visual appearance (*supra vide*:§ B.2). The glass is typically highly vitreous with little or no flow banding and low levels of crystalline inclusion. With the exception of the tan and honey obsidian found around Taratimi Bay, these sources are typically black in trans-

mitted light and have a characteristic deep green with a hint of yellow colour in transmitted light.

It appears that pyroclastic deposits have definitely been sampled at four locations, and possibly at seven. In situ pyroclastic material has been sampled at Ruawaipiro Pass, and the samples from the Taumo *pā* outcrop and Opuhi east are interpreted as associated with pyroclastic eruption. It is apparent that some of the Taumou *pā* pyroclastic has been re-deposited on the coast at Taratimi Bay where this has also been sampled. The material from these sources is visually distinctive from that associated with the pre-caldera rhyolites in hand specimen. This material is typically greenish in reflected light, flow banded, opaque and of only moderate lustre.

The detrital coastal sources could correspond to material either eroded from selvages, or deposited during pyroclastic eruptions. Both situations are probably present. It is apparent that the bulk of the detrital material found in Taratimi bay derives from the exposures on the Caldera rim above the bay, and as such most probably corresponds to secondary deposits of obsidian associated with both selvages and pyroclastic deposits. The cobbles sampled at Oira Bay, Raumata Point and Otiora Bay may also correspond to either type, though those sampled are visually most similar to the pyroclastic material.

3.3 Northland

There are three general source areas that have been identified in Northland: Kaeo (Green *et al.* 1967; Bell and Clark 1909; Ward 1972); Weta (Ward 1972; Moore n.d.); and Huruiki (Ferrar 1925; Moore 1982). Though there is the possibility of other sources in the area.

The reports of the Northland sources with the exception of Huruiki

(Moore 1982) are unclear and confusing. With the deposits located near Kaeo, up to five occurrences have been noted (Brassey 1985), though the reports appear to be contradictory. As an example, Ward (1972) identifies a deposit located adjacent to the Pungarae settlement which is not noted in the geological survey of the area (Bell and Clark 1909) yet fails to identify the sources located during Bell and Clarke's 1909 geological survey. The Weta deposit is similarly unclear. In light of this it was decided to conduct a field survey of the obsidian deposits in the Northland region in conjunction with the source sampling.

3.3.1 Waiere/Pungarae (Source 17, *supra vide*:§B.2)

Four general deposits have been described for this area. In the original geological survey Bell and Clark (Bell and Clark 1909) noted the presence of obsidian scattered over an area "... one to two miles north of the Pungarae settlement ..." and also in the bed of the Waiarewau stream. A later survey (Green *et al.* 1967) identified obsidian boulders eroding out of white sediments in the headwaters of the Okaihau stream. A fourth location is reported by Ward (1972) as occurring in the Pungarae settlement itself. This reference is confused, as the actual reported location and that indicated in Ward's map do not correlate. Each of these locations were visited in an attempt to clarify the relationships among the exposures and to generate a suitable sample of material from the source(s).

The first location visited was Pungarae (Location 1: Figure 3.10; *supra vide*:§B.2). The area around the Pungarae settlement and the reference given by Ward (1972) was systematically searched. Stream beds, exposed sections and recently turned earth were examined. No obsidian was identified. The local residents reported never having seen any obsidian in this location, though they were aware of the material on the table-

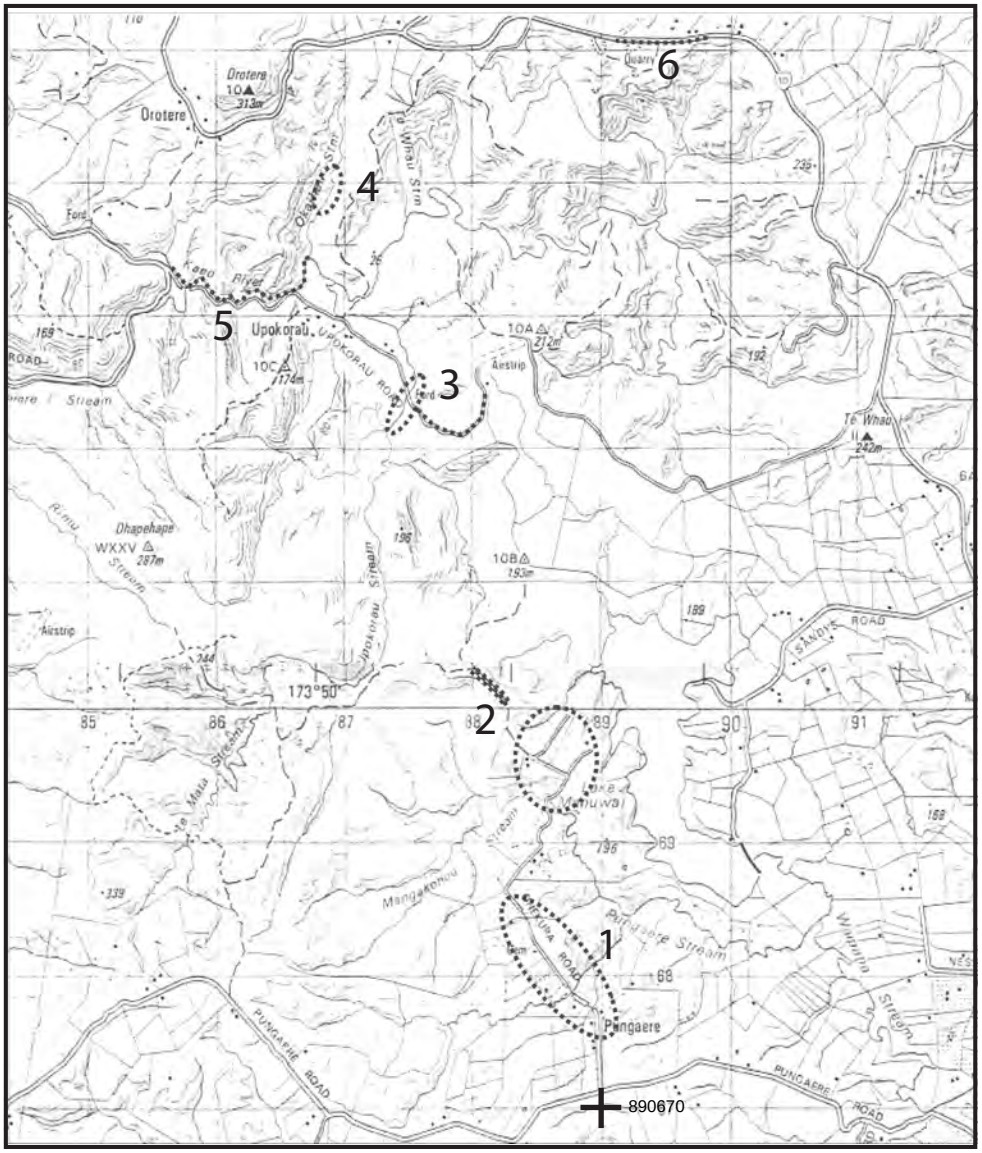

Figure 3.10: Location of samples in the Kaeo source area (base map NZMS 260 P04

Martin Jones 2002

lands to the north of Pungarae. The actual Pungarae settlement area can be ruled out as a source of obsidian in Northland, and it is probable that this source has arisen due to an incorrect map reference given by Ward (1972).

The second location visited was the material referred to by Bell and Clark (1909) as lying several kilometres to the north of Pungarae (Location 2: Figure 3.10). Obsidian is widely scattered over an area that begins several hundred metres down Caprine Road, and is visible in cuttings and in areas were the top soil has been removed such as watercourses and farm tracks. This is presumably the location that was also sampled by Ward (1972). The obsidian in this area is found in a friable white material approximately 20 cm below the topsoil. It is apparent that this white layer readily erodes when exposed, which explains the visibility of obsidian in situations where rain can wash away the surrounding matrix. The obsidian at this location typically occurs in small rounded cobbles which have a well weathered cortex. A sample of the obsidian from this area was collected along three transects parallel to Caprine Road; one transect along Caprine Road and one $\approx$ 20 m each side (Samples 17.1.x; Table B.2, *supra vide*:§B.2.17).

The lower lying region to the west of lake Manuwai and immediately adjacent to the Caprine Road source was also searched in the same manner as described for the Pungarae settlement. No in situ obsidian or equivalent of the white ashy layer was identified. A single angular cobble was found imbedded in a farm track at the location marked in Figure 3.10 (Sample 17.7; Table B.2, *supra vide*:§B.2.17). This sample may either derive from in situ material in the area that is either deeply buried or completely eroded away, or may be an artefact of the road gravelling process.

The third location visited (Location 3: Figure 3.10) was the Landslip Creek vicinity described by Bell and Clark (1909). In this area there

are extensive deposits of obsidian in the bed of the Upokorau stream, and also in the surrounding hillsides where obsidian is visible in slips and cuttings in an identical context to that of the Caprine Rd material described previously. The obsidian found in the stream bed has obviously eroded out of the surrounding slopes. The obsidian in this area was sampled along the transects shown in Figure 3.10 (Samples 17.2.x-17.3.x; Table B.2, *supra vide*:§B.2.17-B.2.17).

The fourth location sampled (Location 4: Figure 3.10) was the Okaihau deposit described by Green *et al.* (1967). The material in this area is again present in an identical context to that seen in the other deposits in this location (Sample 17.8; Table B.2, *supra vide*:§B.2.17).

A fifth sample group was collected from a transect walked down the Kaeo River. Three samples were collected at intervals along the transect shown in Figure 3.10 (Samples 17.4.x-17.6.x; Table B.2, *supra vide*:§B.2.17-B.2.17). This was primarily collected to establish the degree of water rounding and size of samples along the transect, which gives some measure of how far the material has been moved from source. Thus the sub-samples collected from along the transect allow some inferences to be drawn regarding how far any source material may extend along the transect. In the samples collected there was a distinct drop in size and increase in water ware down stream which suggests that no new material is eroding into the river along the transect, implying that the transect lies outside the available source area.

On the basis of the evidence seen in this field survey it seems likely that these three deposits correspond to a the same volcanic episode. From the condition of the in situ material it seems most likely that the obsidian in this area corresponds to a heavily weathered rhyolite. Thus the base matrix of the rock has rotted to a fine powder and only the more resistant obsidian has remained. This explains the association of the obsidian and the fine white “ashy” material within which it is found and the

heavily weathered cortex that characterises material from this location. It is very unlikely that the deposits correspond to reworked sediments because:
1) the Pungarae material is at the highest point in the surrounding landscape and thus deposits would be eroded from rather than to this location
2) the terrestrial material tends to be sharply angular in locations other than the Pungarae deposit. This tends to argue against reworking as this would have the effect of rounding the material down.

The conclusion is that the exposures in the Waiere/Pungarae area correspond to the same phase of rhyolitic eruption. Thus the various exposures would be expected to be relatively homogenous. This is in fact the case; PIXE analysis of the sources (Neve *et al.* 1994) found no consistent geochemical difference between the Pungarae and Waiere sources. A wider distribution of obsidian than is indicated by the three sources identified is expected. The characteristic white layer associated with the obsidian deposits was identified along State Highway 10 between Te Whau and Orotere with occasional small obsidian pebbles (Location#6: Figure 3.10). Further to the west, the name of the Te Mata stream suggests further deposits are likely[2]. In terms of a representative sample for the purposes of providing hydration control the three in situ exposures sampled will provide a basic outline of the hydration parameter variability from within this general source area.

3.3.2 Weta (Source 24,25, *supra vide*:§B.2)

The nature of the Weta source is unclear. No geological surveys have reported obsidian in this area, and the archaeological reports are conflicting. Ward 1972 reports a second hand account of obsidian in an

[2] matā is a generic maori term for chert or obsidian

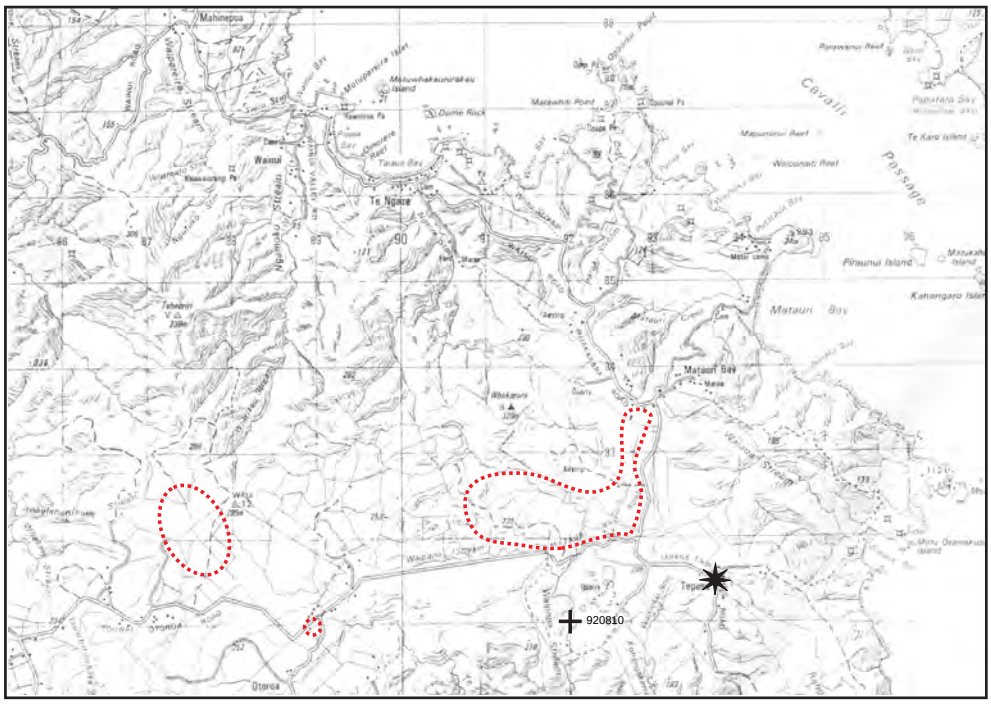

Figure 3.11: Location of samples in the Weta trig area (base map NZMS 260 P04

area that Holroyd 1993 reports second hand that there is no obsidian. The only first hand account is that given by Moore (n.d.) who identifies obsidian occurring in Otoroa. However, Moore's survey was brief and was intended as a preliminary field trip prior to a possibly more extensive survey that has not yet taken place (Moore pers. comm. 1998). In light of this, the area surrounding Weta was investigated via field survey.

Geological survey has identified rhyolitic lava's at Te Pene near Matauri Bay. Any obsidian in the area would be expected to be related to this outcrop and accordingly the area around Te Pene was surveyed. This principally involved asking farmers if obsidian was present on their property and then finding specimens in areas where obsidian had been observed by them. Obsidian is identified occurring in an area to the north of Te Pene, primarily around the base of the Whakarara Trig(Samples 24.1.x-24.2; Table B.2, *supra vide*:§B.2.18). I will identify this source as the Whakarara deposit. In general the material is highly vitreous, has abundant inclusions and exhibits good translucency with a brownish tinge (*supra vide*:§B.2.18). This material is visually identical to the deposit Ward (1972) refers to as Weta, and that Moore (n.d.) refers to as Otoroa. Also occurring in the same area, though less frequently, is a glass with a different visual appearance (*supra vide*:§B.2.18). This glass is identical in visual appearance to the Wiaere material.

The Weta Trig area was also surveyed. There is a deposit of material that lies to the North/North East of Weta trig. This material is identical in visual appearance to the Waiere material (Samples 25.1.x; Table B.2, *supra vide*:§B.2.19) . In this area there is no glass of the type typically associated with the Whakarara deposit.

Thus it is apparent that there are at least two general deposits in the Weta trig area. One of these deposits is of significance to the current study as it corresponds to a previously undescribed source of glass that is green in transmitted light, and that could very easily be visually con-

fused with the separate Waiere deposit.

In addition to the Kaeo and Weta sources, samples were collected from the Huruiki source (Samples 31.1.x-31.6.x; Table B.2, *supra vide*:§B.2.25) corresponding to the HU-1 deposit as described by Moore (1982).

3.4 Taupo Volcanic Zone

As the primary focus is on providing hydration control for "green" obsidian, little field sampling of the Taupo Volcanic zone was necessary. However a sample from this zone is of interest in providing an initial comparative baseline, and it is also necessary to survey the Taupo Volcanic Centre. No obsidian deposits in this centre have been identified, yet it is quite probable that some deposits do exist. As the rhyolites from this centre are relatively distinct from those of other centres within the TVZ it is important to establish that there are no confounding sources that lie within the Taupo Volcanic Centre. To this end two field surveys were carried out.

3.4.1 The Whangamata Fault (Source 29, *supra vide*:§B.2)

A sample of Obsidian was collected from along the Whangamata Fault as a general reference sample providing a basic characterisation of the material from the TVZ. There are extensive deposits of obsidian in this area, occurring in two general contexts; flows and surface scatters.

Obsidian flows are exposed at various points along the Whangamata fault. Ward (1972) has identified and sampled five of these. I have sampled insitu obsidian from alongside the road adjacent to Ben Lomond Station (Samples 29.1.x ;*supra vide*:§B.2.23), labelled Ben Lomond in the reference collection.

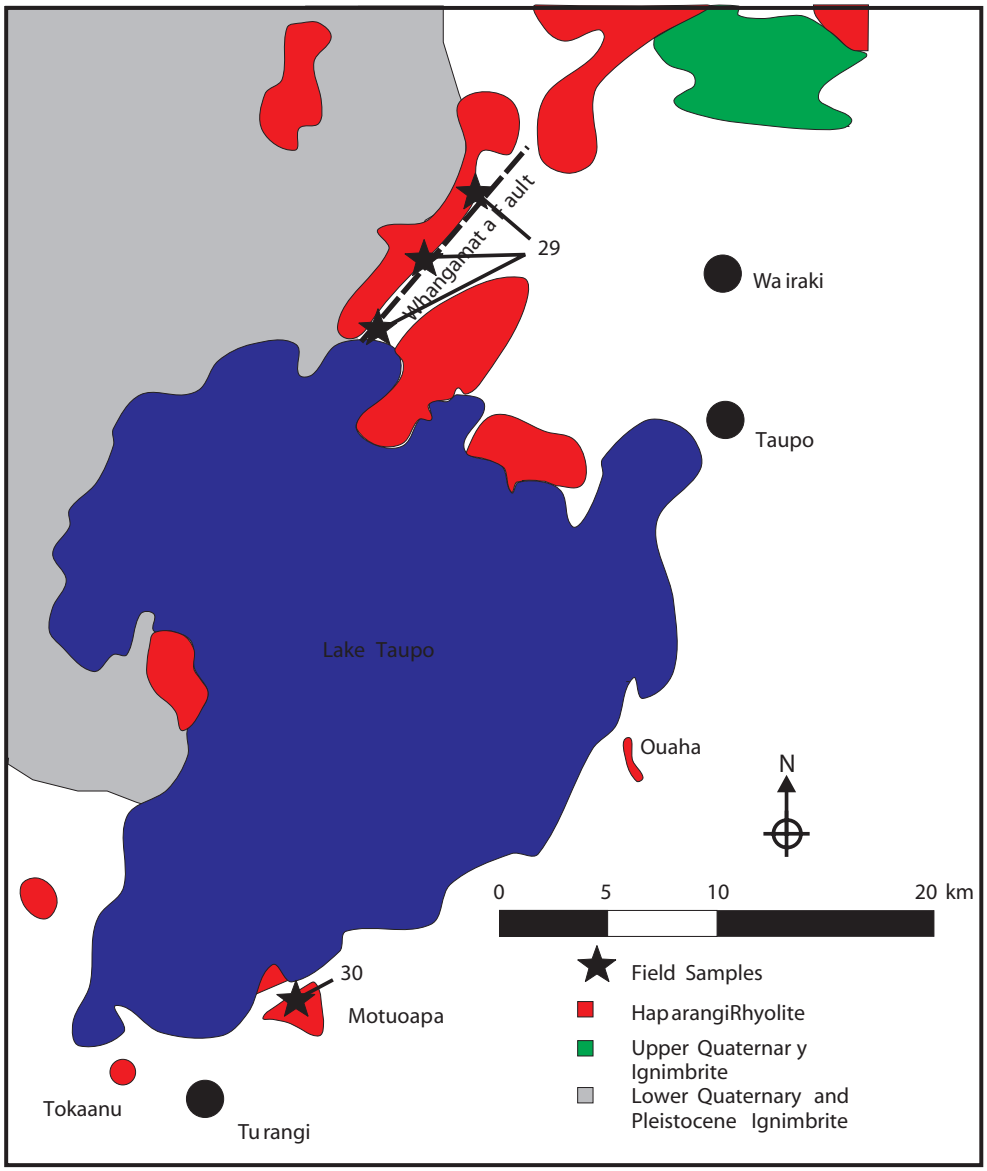

Figure 3.12: Sampled and surveyed locations in the Taupo Volcanic Zone

In each of the areas surveyed along the Whangamata fault obsidian scatters have been identified. The obsidian occurs as cobbles ≈ 2-20 cm diameter. This type of material was collected in the vicinity of the in situ Ben Lomond source (Samples 29.2.x,29.3.x,29.5.x ;*supra vide*:§B.2.23) and in the area of the Otaketake State Park along the Whangamata road (Samples 29.4.x ;*supra vide*:§B.2.23). These collections will provide a representative sample of the obsidian that is associated with the Haparangi rhyolites along the Whangamata fault, which in its turn acts as a type source for the TVZ in general. These samples will provide first approximation baseline data for the hydration properties of TVZ obsidian in general.

3.4.2 The Taupo Volcanic Centre (Source 30, *supra vide*:§B.2)

A second survey was carried out in the Taupo Volcanic Centre. Here the zones of Haparangi rhyolite were surveyed for evidence of obsidian. There are three primary occurrences in the Taupo Volcanic Centre; Tokaanu, Motuoapa and Ouaha (Figure 3.12).

The Tokaanu dome (Maunganamu, E2750400 N6242900) was searched, and while extensive rock outcrops were present there was no indication of obsidian in the area. A search of disturbed soils and exposed sections in the surrounding area also failed to reveal any traces of obsidian. The conclusion is that there is no available obsidian located in the Tokaanu Haparangi Rhyolite dome.

The Ouaha outcrop (E2774200 N625890) again revealed no evidence of obsidian. It is in difficult terrain and the survey was not as comprehensive as wished, and it may yet prove that obsidian is associated with this outcrop. However no evidence of obsidian was found in the outcrop or surrounding area.

Extensive obsidian deposits are associated with the Motuoapa Outcrop (*supra vide*:§ B.2 sample # 30). Small fragments of obsidian (0.5-15 cm diameter) are scattered over the flats in front of the Parikarangaranga cliffs at the back of Motuoapa Bay. No in situ seams are apparent in the Parikarangaranga Cliffs, but extensive seams and scattered boulders are present on the flanks of the Whakamoanga dome rising to the back of the Cliffs. Samples were taken from the material scattered to the front of the Parikarangaranga Cliffs (Samples 30.1.x; Table B.2, *supra vide*:§B.2.24), and from along a transect along the flanks of the Whakamoanga dome (Samples 30.2.x; Table B.2, *supra vide*:§B.2.24). Further exposures of obsidian associated with this outcrop are likely. However, the sample that has been obtained will provide a baseline for the geochemical and visual characteristics of the obsidian associated with this outcrop.

There are limited obsidian sources associated with the Taupo Volcanic Centre. The samples available from the single source identified are all of moderate to very poor quality, tending to have a very high phenocryst level. In visual appearance the material ranges from Black to red in reflected light, and the samples translucent enough to transmit light are all grey in transmitted light. The conclusion is that obsidian from the Taupo Volcanic Centre, and by extension the TVZ, will not confound the "green" sources.

3.5 Coromandel

The Coromandel sources have been the subject of comprehensive surveys and the general physical attributes of the material from these sources are well controlled (Moore 1983; 1985; Moore and Coster 1989*a*; Ward 1972) (*supra vide*:§ B.1). With the exception of Waihi material, Coromandel obsidian will not confound the identification of "green" obsidian. Thus the Waihi source was sampled.

The Waihi samples were collected from the Waimata Stream at a position that corresponds to Moore and Coster's 1989*a* location WI-2 (Samples 32.1.x-32.3x; Table B.2, *supra vide*:§B.2.26).

A representative sample for providing basic hydration reference data for the Coromandel region was extracted from the Auckland University reference collection as described previously, though field samples were also collected from Tairua.

The Tairua source samples were collected from Tanehua Road (Samples 33.1.x-33.7.x; Table B.2, *supra vide*:§B.2.27) at locations corresponding to Moore and Coster's 1989*a* deposits TA3,TA5,TA6,TA8.

3.6 Summary

The obsidian samples that have been described in this chapter represent a securely provenance reference collection for New Zealand obsidian. While this reference collection is not comprehensive it will provide a secure basis for describing the geochemical and hydration properties of the green obsidian, and also for providing first approximation baseline geochemical and hydration parameters of all New Zealand obsidian.

The samples that are used in the following hydration experiments, and to generate basic parameters describing the hydration behaviour of New Zealand obsidian all derive from the reference collection described in this chapter.

Chapter 4

Obsidian Hydration

4.1 Introduction

In order to make use of OHD it is necessary to relate the measured hydration rim thickness (x) to the amount of time (t) that has passed since the flake surface was first exposed. To achieve this we need to be able to accurately describe the relationship between hydration duration and hydration extent. This is the observation model discussed in Chapter 1 (*infra vide*:§1.3) More formally, we need to be able to specify a model $x(t)$ which is defined as:

$$\text{hydration extent} = x(t) \tag{4.1}$$

Thus $x(t)$ is any model that can be used to describe hydration rim thickness on the basis of the amount of time that has passed since the onset of hydration. It is clear that without a suitable model for $x(t)$ OHD is impossible. Thus it is vital that suitable models for $x(t)$ are identified. Any such model must take into account the influence that both the archaeological environment and specific artefact composition may have on $x(t)$.

The purpose of this chapter is to examine the nature of potential reactions between obsidian and the environment, and to establish a suitable model(s) for $x(t)$ that will take into account the significant factors governing the relationship between hydration duration and hydration extent in archaeological environments. As detailed in the following sections, various approaches have been used to provide control for $x(t)$. However it is vital that these are critically examined with regard to how well they might actually perform in applied OHD.

This development proceeds by assessing previous experimental results, models and conclusions on the basis of a basic outline of the hydration process. From the conclusions drawn in this assessment aspects of current models for $x(t)$ that require further consideration are identified. These are addressed via an experimental program that allows the defi-

nition of a baseline empirical model for $x(t)$ that is suitable for applied OHD.

4.1.1 Modelling Obsidian Hydration Rates

Since OHD was first proposed by Freidman and Smith in 1960 a variety of methods have been employed to describe and estimate $x(t)$, ranging from simple regional definitions of hydration velocity (Friedman and Smith 1960) through to more complex theoretically based models (Doremus 1994). Currently it is standard to produce an estimate of $x(t)$ that fits the following relationship.

$$x(t) = (kt)^{1/y} \tag{4.2}$$

Where: k is the hydration rate; x is the measured rim thickness and t is the hydration duration

Almost exclusively equation 4.2 is written with $y = 2$ (*e.g.* Ambrose 1976; Friedman 1976; Friedman and Long 1976), representing a classic diffusion controlled process (*supra vide*:§4.4.1). However, there is no clear consensus on what is actually diffusing other than it involves hydrogen in some form (*supra vide*:§4.4.1).

As $x(t)$ is known to be temperature dependant (Friedman and Smith 1960), the rate (k) in Equation 4.2 is usually modelled by an Arrhenius type function of the form (Friedman and Long 1976)

$$k = Aexp\left\{-\frac{E}{RT}\right\}. \tag{4.3}$$

Where: A is the pre-exponential component; E is the gas activation energy; R is the universal gas constant and T is the absolute temperature of the reaction (^{o}K)
Here the variables A and E are specific to the artefact. Thus this model

for $x(t)$ describes the hydration duration as a function of hydration extent, artefact specific chemistry and environmental temperature. The question is whether this model for $x(t)$ is suitable. While some archaeological applications have produced apparently sensible results (*e.g.* Stevenson *et al.* 1995), and by association effectively modelled $x(t)$, there have been some problematic results (*e.g.* Tremaine and Fredrickson 1988) which raise the possibility that $x(t)$ has been inappropriately modelled. Thus it is important to critically evaluate the available evidence relating to obsidian hydration processes in order to assess the suitability of potential models for $x(t)$. In order to pursue this assessment, it is useful to develop an understanding of what reactions may occur between obsidian and the environment. This provides a basis for evaluating the suitability of any proposed model for $x(t)$, and makes it possible to identify what (if any) further experimental work needs to be undertaken. In order to develop this understanding of the potential reactions between obsidian and the environment it is useful to consider the basic structure of obsidian and identify the chemical nature of the different compositional elements. On this basis it is possible to generate an idea of what reactions may occur.

4.2 Obsidian: Structure

Obsidian is a natural volcanic glass derived from rhyolitic melts with significant variations in chemistry, structure and appearance among different groups of obsidian. Strictly, obsidian is an alumino-silicate (70-71 % Si, 12-15 % Al) glass with low body water content (0.05-0.2 %), typically varying in density between 2.3-2.44 gcm^{-3}. The vitreous ground mass of obsidian may contain inclusions which vary according to source, but as a general guide the main inclusions in obsidian are:

- Crystallites

- Microlites (Feldspar, Pyroxene & Magnetite being the most common)
- Trichites
- Spherulites
- Gas vesicles

As the properties of "glass" in general apply to obsidian, it is useful to consider the nature of glasses as a background to the structure, and potential chemical reactions, of obsidian.

4.2.1 Glass

Glasses are essentially amorphous solids (Doremus 1994) and in the case of obsidian we are dealing with a silicate glass that has formed by cooling a melt below it's freezing point without crystallisation occurring. The classic explanation of this state is that as the fluid is cooled its' viscosity increases — approaching infinity below the freezing point — thus the liquid becomes rigid (Paul 1990).

The standard description of glass structure follows the random network hypothesis first proposed by Zacharisen (1932). In this theory glasses are viewed as extended 3-D networks formed around a backbone of polyhedral oxides. The difference between a glass and the corresponding crystal is that the crystalline network is symmetric and periodic, whereas it is random in glass. Basically this means that there is no long range order in glasses as opposed to crystals. In the case of a silicate glass the relative orientation of adjacent silicon-oxygen tetrahedra is variable, whereas it is constant in the crystal. An alternative view known as the *crystallite theory* has been proposed (Porai-Koshits 1990). According to this theory glasses are composed of small crystalline regions. However,

it has been demonstrated that any such crystalline regions must be less than 10 Å (Warren 1937; Warren and Biscoe 1938). A consensus view of the available evidence suggests that the random network theory describes an "average" picture of the glass structure, and there may be areas of short range order in the glass and compositional inhomogeneity not described by the random network. However, the random network hypothesis can be used to model the basic properties of a glass, and here we will use this theory to develop a basic outline of the structure of obsidian.

4.2.2 Glass Network Elements

As outlined above the random network hypothesis describes glass as 3-D networks of polyhedral oxides. We can form some understanding of the properties of glass by considering the elements of such a network and identifying the type of reactions that might take place between the network and the environment.

The oxygen ions that link the backbone polyhedra are an important element of the glass network, and exist in two basic states. Oxygen ions that link adjacent polyhedra are known as *bridging oxygen ions* and account for the majority of oxygen ions found within the glass network. In some cases oxygen ions are only bonded to one silicon ion resulting in an excess negative charge which needs to be balanced by the presence of a cation. These ions are known as *non-bridging oxygen ions*. The presence of non-bridging oxygen ions serves to both break (de-polymerise) the glass network, and to provide a potential reaction site of different chemical nature to the main network. Thus the quantity of non-bridging oxygen ions in the glass can have a large influence on the chemical durability.

Most glasses do not consist solely of a single oxide and there are various

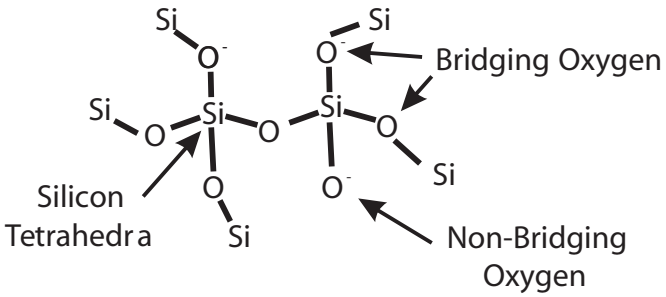

Figure 4.1: Silicate network

other elements incorporated within the glass network. The random network theory describes certain oxides which when present in the glass melt result in the formation of non-bridging oxygen ions. These oxides are known as *network modifiers* and are typically the oxides of low charge cations (eg K^+, Na^+ & Ca^+). In the glass structure these ions may exist bound to non- bridging oxygen ions.

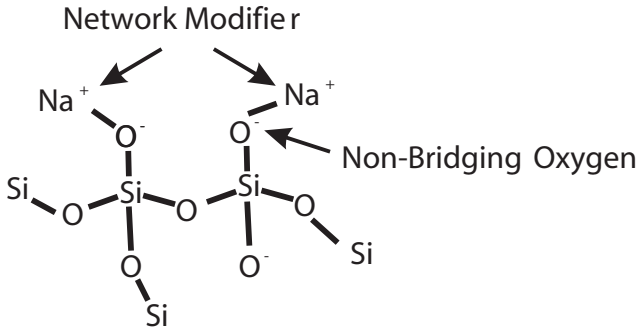

Figure 4.2: Depolymerisation of the network by network modifiers

Some oxides, which can exist as both network modifiers and network formers, are termed *intermediates*. It is possible for intermediates to act as formers and modifiers within the same glass network, the extent to which they perform either role being a function of the glass chemistry. In obsidian the main intermediate is Al^{3+} (Fe^{3+} also acts in this capacity) and the presence of Al^{3+} as an intermediate is important to the structure

and chemical durability of obsidian.

In summary, glasses can be described as rigid non-crystalline solids formed around a network of randomly orientated polyhedra oxides. Within this basic network there are usually a variety of oxides, some of which serve to de-polymerise the network by promoting the formation of non-bridging oxygen ions (modifiers), others that form part of the polyhedra backbone (formers) and those that can act in both capacities (intermediates).

4.2.3 Obsidian Glass

The primary network forming element of obsidian is the silica tetrahedra, thus obsidian is a silicate glass. Specifically, due to a high aluminium content, obsidian is an alumino-silicate. This high aluminium content is important to the structure and chemical durability of obsidian, as in high alumina glasses Aluminium may act as both a modifier and a network former. The influence Aluminium has on glass structure depends to what extent it serves as a modifier as opposed to a network former. This varies depending on the relative proportions of modifiers, intermediates and formers within the glass network.

As network formers, small highly charged ions such as Al^{3+} (Fe^{3+} is also important in natural glasses, though is present in much smaller concentrations) enter the network as tetrahedral units. These units share corners with silica tetrahedra through bridging oxygen ions (*i.e.*, through an Al-O-Si bond). As Al^{3+} has one less charge than Si^{4+} the aluminium tetrahedra will have a net negative charge, requiring that a cation is located in an interstitial site in the neighbourhood. In this manner network modifiers such as Na^{+} can play the role of providing charge balance without disrupting the glass structure through de-polymerisation of the network. It has been shown that when the molecular ratio between

alkali oxide and Aluminium oxide (γ) is unity or more, Aluminium exists as a network former (White 1988). Furthermore, when $\gamma = 1$ the glass contains mainly bridging oxygen ions, with aluminium acting purely as a network former and potential modifiers such as Na^+ providing charge balance within the glass structure. In obsidian γ approximately equals 1 (White 1988) suggesting that obsidian should contain mainly bridging oxygen ions, and should exhibit a high degree of polymerisation. This is supported by the work of White and Minser (1984), who have used Raman Spectra on obsidian to demonstrate that obsidian contains mainly bridging oxygen ions, and by Okuno *et al.* (1996) who have used X-ray diffraction to establish that aluminium and silicon occur almost exclusively as tetrahedral units in obsidian.

Thus obsidian is a highly polymerised glass containing few non-bridging oxygen ions, which implies that most of the cations in obsidian serve to provide charge balance for network forming ions rather than acting as network modifiers.

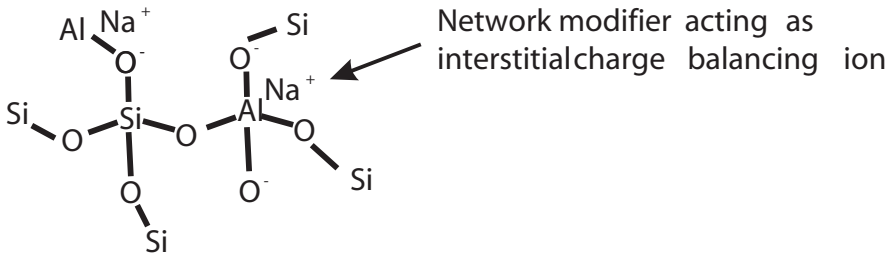

Figure 4.3: Alumino-silicate framework

In addition to the basic structure just outlined, obsidian exhibits inhomogeneity at various scales (McPherson *et al.* 1984; Ryan and Brown 1985). Crystalline inclusions may occur throughout the vitreous ground-mass described above and these have different chemical properties to the glass network. Additionally, as described previously, there may be compositional inhomogeneity throughout the vitreous ground-mass. For

instance Ryan and Brown (1985) have noted that there appears to be Na^+ depletion in the glass structure immediately surrounding the Na^+ rich feldspars and trichites where the K^+ seems to have been substituted for Na^+.

In summary, obsidian is an alumino-silicate glass with a highly polymerised vitreous phase. It is clear that obsidian is not purely homogenous and there are potentially a number of elements within obsidian that may undergo different environmental reactions. Taking this basic obsidian structure as a starting point it is possible to present an outline of the potential reactions between obsidian and the environment.

4.3 Potential Environmental Reactions With Obsidian

On the basis of the preceding section it can be seen that there are several sites of a different chemical nature within the basic obsidian structure. To effectively model $x(t)$ we need to consider how reactions between the different elements of the glass structure and the environment may influence the observed hydration process. In terms of OHD the potential reactions fall into two basic categories:

Rim Formation This is brought about by any reaction that increases the hydrogen concentration in the surface zone of the artefact. This could arise through two primary mechanisms:

1. The diffusion of molecular water species into the glass network. This process would involve the movement of water molecules through the glass network, and would quite possibly be associated with secondary reactions between the diffusing water molecules and various elements of the glass network

and or inclusions.

2. Ion exchange. Here hydrogen bearing ions from the environment may exchange with charge balanced ions from within the glass network. In terms of the glass structure outlined previously, this type of exchange would be most likely to occur with network modifiers either attached to non-bridging oxygen ions or those providing charge balance for network forming intermediates such as Al^{3+}. It is possible that the nature of the ion exchange reaction may differ for interstitial charge balancing ions as opposed to those attached to non-bridging oxygen ions.

Rim Removal This is brought about by any reaction that promotes surface dissolution. Thus any reaction that directly dissolves the glass network or inclusions within the glass matrix or abrades the glass surface, will result in rim removal.

Therefore there are three primary processes that we need to consider: Molecular diffusion of water species, Ion exchange reactions and processes that may dissolve or abrade elements of the glass structure.

4.3.1 Molecular Diffusion of Water

As water can hydrolyse the silica network, diffusion of molecular water is a multi component process. The exact mechanics of water diffusion into obsidian are not yet established, but some broad observations can be made.

There has been the suggestion that water diffusion in silica glass proceeds by a lattice diffusion mechanism (Doremus 1995). That is, a proton from one silonol group jumps to a neighbouring Si-O-Si bridge followed by a jump of a hydroxyl group. Doremus (1995) disputes this mecha-

nism pointing out that if a lattice diffusion mechanism was valid then similar diffusion would be observed in fused silica and quartz. In actuality no diffusion is observed in quartz under conditions where water readily diffuses in fused silica. The conclusion is that the most likely model of water diffusion in vitreous silica is one of molecular diffusion followed by reaction with the silica lattice, where the silonol groups produced are immobile (Doremus 1994). Thus this is a multiple process reaction, and an equilibrium is established within the glass between dissolved molecular water and silonol groups that is a square root function of the ambient vapour pressure (Doremus 1994). As hydrolysis of the glass network may influence the net hydration rate (*supra vide*:§4.4.1) it is possible that the rate of diffusion of molecular water into glass will be influenced by the ambient vapour pressure, and further that the effective diffusion coefficient of water may be related to the concentration of silonol groups in the glass. If this result is extrapolated to obsidian we would expect that obsidian with higher bulk silonol contents would permit a faster effective diffusion coefficient of molecular water, as has in fact been observed in some high temperature induction experiments (Stevenson *et al.* 1998).

There is the possibility that the diffusion of molecular water in obsidian may not be significant at ambient temperatures. It has been observed that the diffusion of molecular water is insignificant in alkali-silicate glasses below 100 ^{0}C except as a part of the hydronium ion (Doremus 1995). This situation may or may not extend to obsidian. Studies of experimentally hydrated obsidian have shown that the diffusion of water is significant at higher temperatures (Bates *et al.* 1988) and recent SIMS profiles of archaeological hydration rims have shown that the diffusion of molecular water is dominant in at least some obsidian (Anovitz *et al.* 1999). This would tend to suggest that diffusion of molecular water in obsidian proceeds similarly to that of fused silica, and that the diffusion of molecular water is a potentially significant mechanism in producing

the visible hydration rim at ambient temperatures.

4.3.2 Ion exchange

The second class of reactions outlined above is leaching or ion exchange processes. Basically these involve the exchange of protons from solution with cations in the glass structure. This type of reaction is possibly a significant mechanism driving the development of visible archaeological hydration rims. SIMS profiling of the hydrated zone in artificial glasses has shown that the zone is depleted in Na in exchange for H with a molecular ratio of 1:3 suggesting that the hydration of this outer zone is primarily accomplished by the exchange of sodium and hydronium ions (Doremus 1995). It is not clear whether a similar situation exists for obsidian. While it has been established that there is ionic depletion at the surface of obsidian artefacts (Coote and Nistor 1982), some results have suggested that the depletion zone is shallower than the observed hydration rim (Bates *et al.* 1988; Anovitz *et al.* 1999). Thus while ion exchange does occur it may be a secondary phenomena in obsidian hydration.

In silicate glasses, ion exchange typically occurs between water species (most probably hydronium) and either Na^+ or K^+. There has been experimental evidence which suggests that only one of the cation species is active at any one time during the ion exchange process, and researchers describe the exchange as principally taking place between hydronium and sodium (Doremus 1995). In the case of an alkali alumino-silicate such as obsidian this ion exchange reaction most probably takes the form of a direct ion exchange between a proton (or hydronium ion, H_3O^+) and a cation, this can either be between modifiers attached to non-bridging oxygen ions, or between interstitial charge balancing ions.

As demonstrated in Figure 4.4 the ion exchange reaction can be described simply as

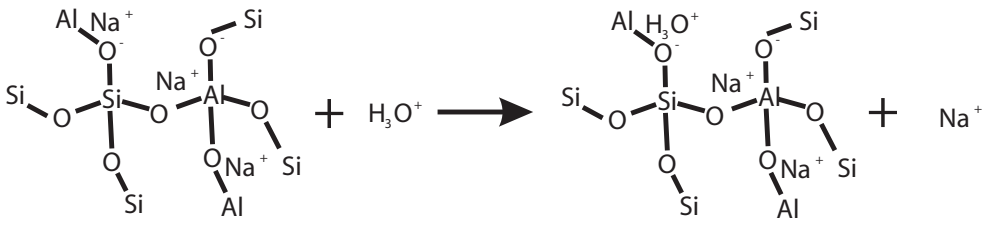

Figure 4.4: Proposed Na^+ H_3O^+ ion exchange reaction

$$Na^+_{gl} + H_3O^+_{aq} \rightarrow Na^+_{aq} + H_3O^+_{gl}$$

It is probable that the reaction energy required for the exchange of an interstitial charge balancing cation differs to that of a modifier attached to a non-bridging oxygen ion. This may mean that if the exchange reaction is at all significant as a rate limiting factor the relative proportion of charge balancing cations to oxygen bonded modifiers may influence the overall hydration rate.

A point to note is that if ionic interdiffusion is a significant hydration mechanism in terms of OHD, then hydration velocity may be influenced by the cation concentration and pH of the solute. That is, raised cation concentrations in the solute may lower the effective concentration gradient and therefore result in a decreased interdiffusion (and hence hydration) rate. Similarly raised solute pH levels could increase the interdiffusion rate. It is unclear to what extent this would influence the visible depth of hydration as distinct from the concentration gradient of the diffusing species.

4.3.3 Surface Dissolution

Dissolution is the process of surface removal. This can occur in a number of ways, but most usually through direct attack on the glass network or crystal inclusions. Dissolution is of real importance in OHD as the dissolution reaction competes with the hydration mechanisms that produce a visible rim. The fact that a hydration rim is visible and hydration thickness is time dependant suggests that the dissolution reaction is considerably slower than the hydration process under most hydration conditions.

Experiments have demonstrated that obsidian is one of the most corrosion resistant glasses (Ericson *et al.* 1975), which is very likely due to the high degree of polymerisation apparent within obsidian (White 1988). Modelling of glass dissolution has shown that there is a direct relationship between the thermodynamic stability of the glass and dissolution rate, and this stability has been correlated with the relative number of non-bridging oxygen bonds in the glass (Jantzen 1988). Theoretically, highly polymerised glasses such as obsidian should be thermodynamically stable, and this tends to explain the low dissolution rate observed for obsidian.

There are a series of dissolution reactions possible between the obsidian surface and the environment, and a lot of theoretical and experimental work has been directed at this question (for glass as a whole). Much of this is overly technical for the purposes of the current discussion and I'll simply present a summary of the important results here.

pH

Solution pH has a strong influence on the dissolution rate of glasses in general. Glasses dissolve more rapidly in basic solutions, and most

glasses experience a minimum dissolution rate at an acidic pH. In highly acidic conditions (pH below 1) and alkaline solutions above 9 the rate of dissolution of silicate glasses become rapid and dominates rim growth. However, Alumino-silicates exhibit a greater alkaline durability than other glasses.

In acidic solutions less than pH 3.2 the hydrated alumina sites on the glass surface are leached into solution as $Al^{3+}_{(aq)}$, and in high alkaline conditions $AlO_{2\,(aq)}$ is leached. Both processes result in surface dissolution (Paul 1990).

In addition to the glass bulk, dissolution of the crystal inclusions can take place via a series of pH dependant reactions. White (1988) has outlined 3 potential pH dependant reactions that will cause dissolution of feldspars within the glass.

$$NaAlSi_3O_8 + 4H^+ + 4H_2O \rightarrow Na^+ + Al^{3+} + 3H_4SiO_4 \quad \text{Acidic}$$

$$NaAlSi_3O_8 + 8H_2O \rightarrow Na^+ + Al^{3+} + 4OH^- + 3H_4SiO_4 \quad \text{Neutral}$$

$$NaAlSi_3O_8 + 3OH^- + 5H_2O \rightarrow Na^+ + Al(OH)_4^- + 3H_3SiO_4^- \quad \text{Basic}$$

Thus surface dissolution of obsidian is expected to be a pH dependant process. Fortunately obsidian is a very corrosion resistant glass and in theory should be relatively stable over a pH range of 3-9. This pH range is unlikely to be exceeded in most archaeological conditions, though in some high alkaline tropical contexts it is quite possible that alkaline dissolution will be significant. The influence of pH attack would also be expected to relate to the degree of crystalline inclusion in the glass. Glasses with a high crystal content would be expected to be more vulnerable to surface attack in acidic or alkaline solutions.

Water

Another dissolution reaction is that between water and the silicon network. As a general scheme, water reacts with the bridging silicon oxygen bond creating two non-bridging silonol groups. This reaction appears to

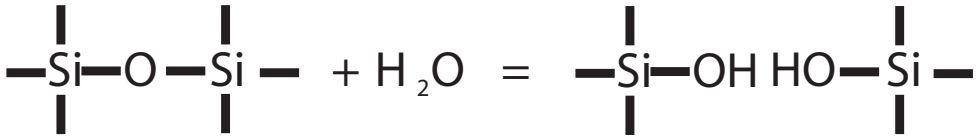

Figure 4.5: Water break down of the silicate framework

proceed by an intermediate step (Charles 1958), where the silicon network initially reacts with an hydroxyl ion forming a non-bridging oxygen ion which then can react with a water molecule. This reaction at the glass surface serves to break down the surface glass network and may render the glass structure more vulnerable to other forms of chemical attack. Build up of silica in solution reduces the rate of dissolution and as the solution approaches saturation this dissolution mechanism essentially ceases. Though in a field situation where solution flow occurs, silica saturation is unlikely.

In addition to the processes outlined above, surface removal can result from confounding influences such as biochemical attack (Thorseth *et al.* 1992) or simple surface removal due to abrasion, anthropogenic or otherwise.

From this discussion it is apparent that there are a number of potential environmental reactions that may cause surface dissolution. It is quite possible that in a highly corrosion resistant material such as obsidian the effect of these reactions will be insignificant in terms of OHD in most environments. Though it is vital that surface dissolution is considered in the development of $x(t)$.

4.3.4 Conclusion

The reaction of obsidian with the environment proceeds via of number of different, often interrelated, reactions. To produce a suitable model for $x(t)$ it is necessary to evaluate the influence and, where necessary, account for the effect of these. In general it is expected that the hydration of obsidian in archaeological environments will be dominated by a combination of ionic-interdiffusion and direct diffusion of molecular water. It is unclear to what extent each of these will dominate the ambient hydration process, and it is possible that the dominant hydration mechanism will be temperature dependant as is the case for some at least some alkali-silicate glasses (Doremus 1994). However, recent studies have suggested that the ionic interdiffusion zone occurs to a shallower depth than the visible hydration zone (Anovitz *et al.* 1999) in obsidian and this suggests that obsidian hydrates in a similar manner to fused silica where the diffusion of molecular water occurs at any temperature.

In terms of providing an effective model for $x(t)$ it is necessary to consider both how the progress of these reactions can be related to time, and how glass specific and environmental factors may influence the general reaction rate. To a large extent this assessment can be made on the basis of experiments conducted into obsidian hydration over the past 30 years.

4.4 Obsidian Hydration Current Parameters

An assessment of the degree to which current models for $x(t)$ take into account significant factors governing ambient hydration can be made with reference to experimental work that has been conducted over the past 30 years (*e.g.* Ambrose 1976; 1993; Ericson 1989; Friedman and Long 1976; Friedman 1976; Friedman *et al.* 1994; Leach and Naylor 1981;

Mazer *et al.* 1991; Michels *et al.* 1983; Stevenson *et al.* 1987; Stevenson and Scheetz 1989*a*;*b*; Tremaine and Fredrickson 1988; Tsong *et al.* 1981). In the following discussion the data are almost exclusively extracted from archaeometric experimental data. While a lot of glass corrosion research *per se* has taken place, much of it is not applicable to OHD except in a general context. This is primarily as glass corrosion research is focussed on different phenomena to obsidian hydration, and on glasses of different structure.

The general result of previous experimental programmes has been to establish that rim formation proceeds as a function of the square root of time and exhibits an Arrhenius type temperature dependency (Ambrose 1976; Friedman and Long 1976; Friedman 1976; Mazer *et al.* 1991; Michels *et al.* 1983; Stevenson *et al.* 1987). However, there have been some significant differences in induction results and interpretation (*e.g.* Tremaine and Fredrickson 1988; Stevenson and Scheetz 1989*b*). In part this may have arisen due to a lack of any measurement calibration standards or standard experimental protocols. In addition, non-explicit modelling has resulted in quite different interpretations of the same data (*e.g.* see the linear, square root & cubic relationships proposed for the same data set by Meighan *et al.* (1968), Friedman and Evans (1968) and Kimberlin (1976)).This suggests that it is most appropriate to conduct a conservative evaluation of the previous research.

As outlined previously the basic issues to consider in this review are:

- What is the relationship between hydration extent and time.

- What influence do environmental variables have on hydration rates

4.4.1 Rim Thickness vs Time

As has been outlined previously, it would be expected that the predominant hydration process is one of diffusion (*infra vide*:§4.3.4). If the obsidian matrix is regarded as a semi-infinite homogenous material, then diffusion can be described according to Fick's laws as (Crank 1975)

$$\frac{\partial C}{\partial t} = D\frac{\partial^2 C}{\partial x^2} \tag{4.4}$$

where C is the concentration of the diffusing species, t is the duration of the diffusion, x is the distance from the diffusion source and D is the rate of diffusion. If the rate of diffusion D is constant during the diffusion process then Equation4.4 can be solved analytically to calculate the concentration C of the diffusing species at any distance x and time t as

$$C = C_1 + (C_0 - C_1)erfc\left(\frac{x}{2\sqrt{Dt}}\right) \tag{4.5}$$

where C_1 is the initial diffusant concentration and C_0 is the surface concentration of the diffusant.

This relationship might be expected to hold for ionic interdiffusion in obsidian as Ryan and Brown (1985)have demonstrated that the ionic diffusion rate does not differ between hydrated and non-hydrated glasses. In contrast, it would be expected that the diffusion of molecular water into obsidian would be accompanied by reaction between the water and the glass network (*infra vide*:§4.3.3). Crank (1975) has considered this type of problem, and in this case the diffusion process is modelled as

$$\frac{\partial C}{\partial t} = D\frac{\partial^2 C}{\partial x^2} - \frac{\partial s}{\partial t} \tag{4.6}$$

where S is the concentration of reacted diffusant.

Solutions to this problem can become complex. However where the concentration of the diffusant is much lower than the reaction product, the

problem reduces to one of simple diffusion with a concentration dependant diffusion coefficient (Crank 1975; Doremus 1994);*i.e.*

$$\frac{\partial C}{\partial t} = \frac{\partial}{\partial x}\left(D\frac{\partial C}{\partial x}\right) \tag{4.7}$$

Doremus (1994) suggests that this model is appropriate for diffusion of molecular water into fused silica, and it is reasonable to expect a similar situation for obsidian. The solution of the concentration dependant diffusion equation is analytically complex and needs to be solved numerically (*supra vide*:§C.2).

The two general diffusion scenarios presented above give different concentration distance curves. Simple constant diffusion profiles follow an error function type distribution and are of the form shown in Figure 4.6. The form of concentration dependant diffusion profiles depend on the functional dependency of diffusion rate and concentration. Three general classes of concentration dependant diffusion rates that have been applied to sorption reactions are shown in Table 4.1, and the typical diffusion profiles are shown in Figure 4.7.

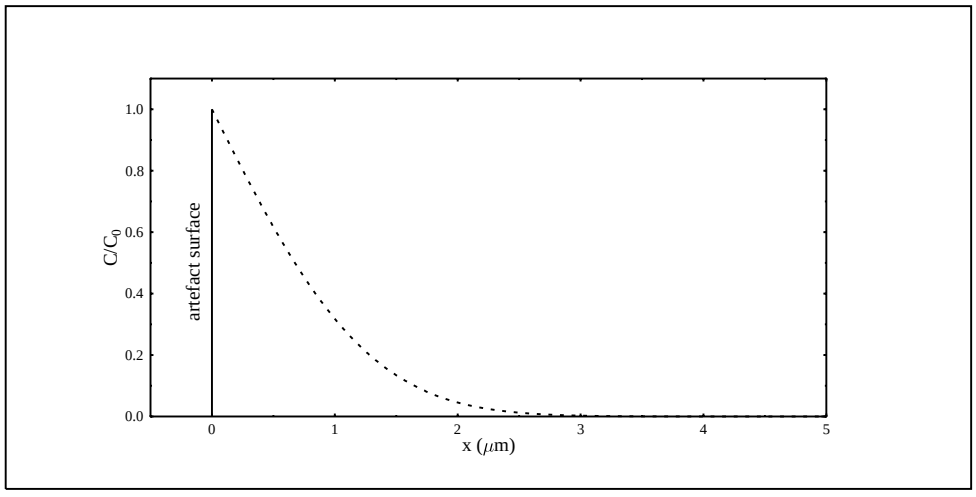

Figure 4.6: Concentration-distance curve according to Equation 4.5

Table 4.1: Generalised concentration dependant diffusion functions after (Crank 1975)

Model	concentration dependance rate ratio
$D = D_0(1 + \alpha(C/C_0)^{\gamma})$	$D(c_0)/D(0) = 1 + \alpha$
$D = D_0 exp(kC/C_0)$	$D(c_0)/D(0) = e^k$
$D = \frac{D_0}{(1-\alpha(c/c_0)^{\gamma})}$	$D(c_0)/D(0) = 1/(1-\alpha)$

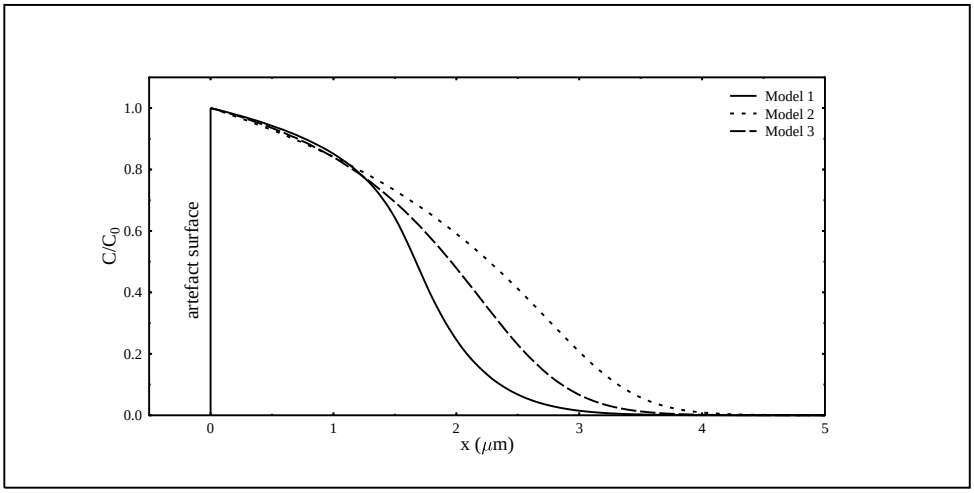

Figure 4.7: Concentration-distance curve according to Equation 4.5

It is immediately apparent that the concentration profiles of the two different diffusion processes are distinct and it needs to be clarified what implications this has for OHD.

It follows from Equation 4.5 that the concentration at any t and x for a system with a constant diffusion rate is dependant on the parameter

$$\frac{x}{2\sqrt{Dt}} \tag{4.8}$$

and accordingly

1. The distance of penetration of any given concentration is proportional to the square root of time
2. the amount of diffusant entering the glass varies as the square root of time

Thus the extent of any hydration phenomena that arises due to concentration independent diffusion will be proportional to the square root of total diffusion duration.

A similar analytically tractable result is not easily obtained for concentration-dependant diffusion processes, though it is possible to solve the diffusion equation numerically. In the results presented here the solution is obtained via both Crank-Nicholson and fully explicit finite difference schemes (*supra vide*:§C.2). A solution has been obtained for each of the general classes in Table 4.1, and for each curve the distance of penetration of 0.1,0.50.9 % concentration, $max\left(\frac{dc}{dx}\right)$ and $max\left(\frac{d^2c}{dx^2}\right)$ against time has been calculated (Figures[1] 4.8-4.10;*supra vide*:§C.3). In all cases the distance of penetration of any given concentration against time is proportional to the square root of time. Additionally if the concentration

[1] all examples have been calculated assuming that D(c_0)/D(0)≈ 17and that D(0)= 0.0005

curves obtained at each time step are integrated, the calculated quantity of diffusant entering the glass is proportional to the square root of time (Figure 4.11;*supra vide*:§C.3).

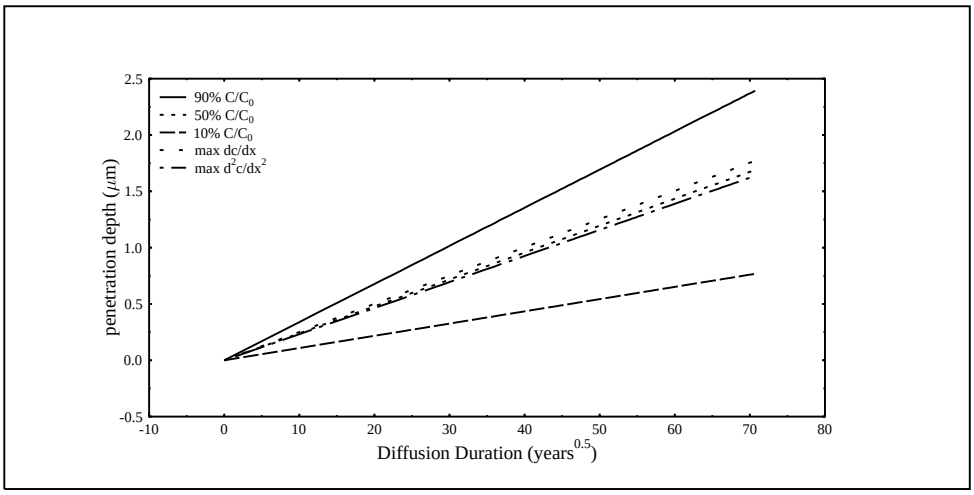

Figure 4.8: Relationships of concentration curve markers against time for model 1, Table 4.1

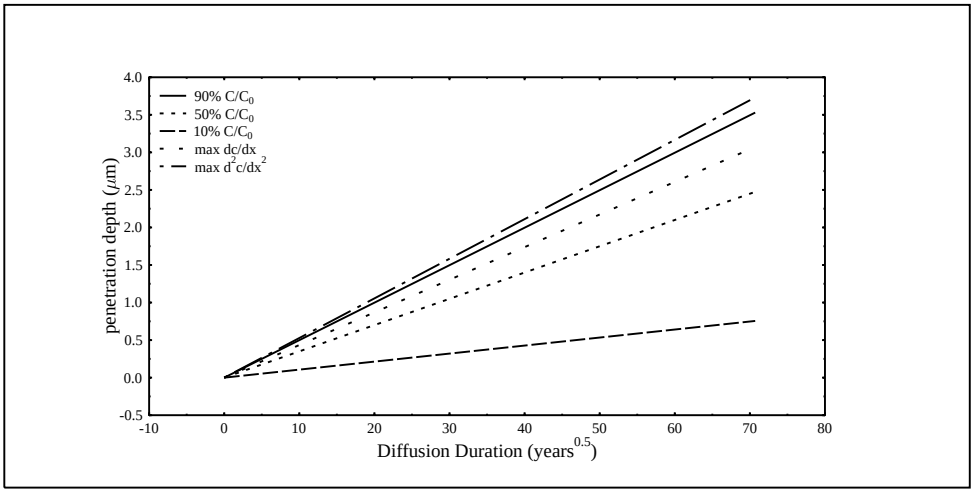

Figure 4.9: Relationships of concentration curve markers against time for model 2, Table 4.1

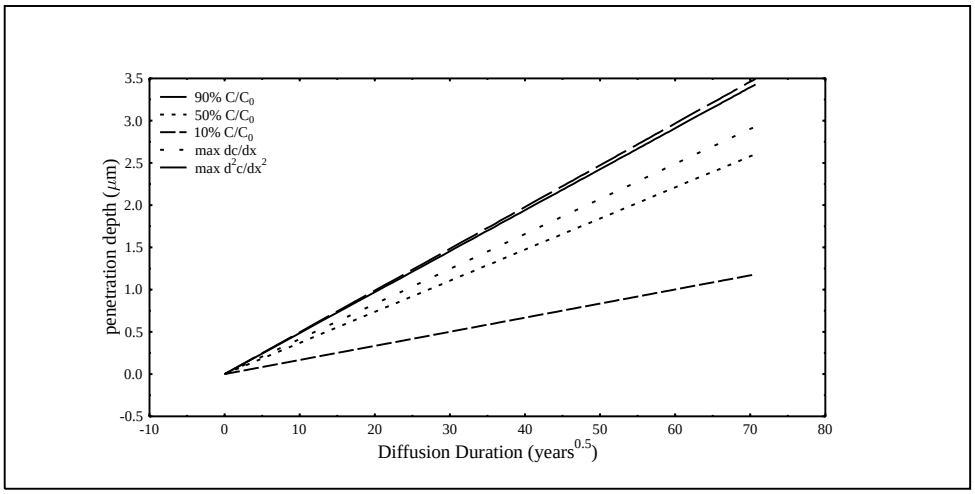

Figure 4.10: Relationships of concentration curve markers against time for model 3, Table 4.1

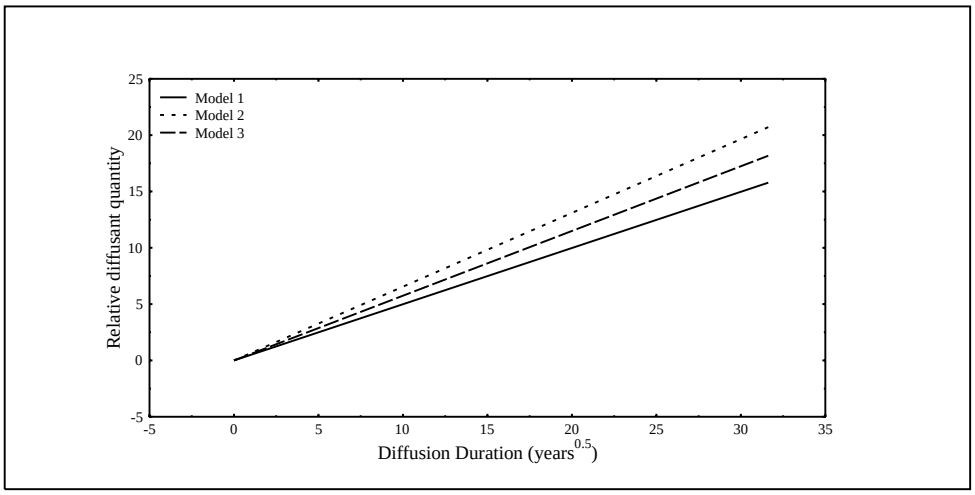

Figure 4.11: Relationship of diffusant quantity against time for the models presented in Table 4.1

Thus the conclusion is that the extent of hydration phenomena associated with both concentration-independent and concentration dependant diffusion will be proportional to the square root of time, allaying some of the concerns expressed by Anovitz *et al.* (1999). In the case of obsidian hydration it is certain that diffusion-dependant diffusion is the dominant hydration process. Most hydrogen profiles that have been produced for obsidian artefacts previously (*e.g.* Anovitz *et al.* 1999; Leach and Naylor 1981; Lee *et al.* 1974; Tsong *et al.* 1978) show a characteristic curve convex away from the distance axis as opposed to the constant diffusion curve which is concave to the distance axis.

While this theory suggests that we might expect a general root time dependence for hydration rim growth, it has been based around the generalisation of obsidian as a homogenous medium. As has been pointed out previously this is not the case and it is possible that inhomogeneities such as crystalline inclusions may influence the rate of the hydration process. Thus a pure root time dependence

$$x(t) = \sqrt{kt} \tag{4.9}$$

must initially be regarded as a first approximation to modelling $x(t)$.

A number of induced hydration experiments have examined Equation 4.9 (*e.g.* Ambrose 1976; Doremus 1995; Friedman 1976; Mazer *et al.* 1991; Michels *et al.* 1983; Stevenson *et al.* 1998) and concluded that the relationship is valid. As outlined above this result is a little surprising. The net hydration rate (k in this model) is the overall result of a number of, sometimes competing, reactions. Not all of these reaction rates would be expected to be proportional to the square root of time, nor would the reaction rates be expected to be the same, so the result that the net reaction rate is proportional to the square root of time means that either the reaction rate is dominated by a single hydration mechanism or that the experiments and analysis are biased towards a single mechanism. If this result can be validly applied to ambient OHD, this means

that mechanisms such as dissolution or secondary reactions within the glass body are not significant rate controlling factors. The interpretation is that hydration is purely driven by ion exchange and/or the diffusion of molecular water into the glass body, as both reaction rates should be proportional to the square root of time.

However it is difficult to accept this conclusion on the basis of the current evidence as there several potential problems with the current interpretation. In part these arise as there has never been a real attempt to explore the parameters of equation 4.9, nor have the experimental data been critically examined in terms of $x(t)$. The original proposition by Friedman and Long (1976) that there is a root relationship between hydration extent and time seems to have been accepted as a null hypothesis in induction experiments and the data have been interpreted on this basis, rather than in a more critical capacity. This is not a satisfactory situation. As I have pointed out previously, hydration is the result of a number of potential reactions and the uncritical acceptance of a model that is based on the most simple mechanism of one of the reactions is dangerous. A far more satisfactory approach is the acceptance of the null hypothesis that hydration extent is a function of time and evaluating the data to define the optimum form and parameterisation of this relationship. It is quite probable that an empirical model of the general form presented in equation 4.2 (of which equation 4.9 is a specific representation) is suitable for describing obsidian hydration, but it is possible that the optimum parameters of this model would vary among different obsidian types depending on how well they fit the approximation of a homogenous media. Thus a fully polymerised, crystal free glass with no phase separations may exhibit hydration behaviour very closely modelled by Equation 4.9, whereas the hydration of a less homogenous glass may not be so well modelled. It may be the case that $x(t)$ varies for different glasses.

Another problem with the available experimental data, particularly for applications of OHD to events falling within the past 1000 years, is the size of the induced rims. With the exception of Ambrose (1976) who has conducted experiments using the weight gain of finely powdered obsidian to explore the relationship between hydration extent and time at ambient temperatures, and who has run a long term experimental induction program at ambient temperatures, all published induction programmes have produced large hydration rims (2-20 μm) at temperatures well above the ambient.

As an example, Friedman (1976) has conducted induced experiments on 12 different obsidian sources at temperatures ranging from 95-245 ^{0}C for time periods of up to 3 years, and in a separate set of experiments (Friedman and Long 1976) conducted experiments at 100 ^{0}C for up to 4 years. They concluded from these sets of experiments that obsidian hydrates as a function of the square root of time. The published rim thicknesses are all larger than 1 μm and appear to extend out into the range of approx 20 μm. While these results may not reject a square root relationship with time, there has to be a question of whether they represent archaeological reality in terms of hydration extent and whether the fitted model is optimal. Certainly these thicknesses do not represent the expected rim thicknesses for events falling within the past 2000 years or so, which is most probably towards the archaeologically useful limit for OHD (*supra vide*:§11).

Another, potentially key, problem with the experimental results produced so far is the fact that they are generated at temperatures significantly higher than that experienced in archaeological contexts. This problem is highlighted by the fact that while most of experimental data published so far has been interpreted as supporting the notion of a square root relationship between rim thickness and time, there have been other relationships suggested on the basis of cross-dated archae-

ological samples. These range between a cubic relationship suggested by Kimberlin (1976) for the hydration of a particular obsidian source to the stance by Meighan (1988) that the relationship is linear. However, these propositions have to be evaluated in terms of how well any potentially confounding glass specific or environmental factors have been controlled as well as the precision of the cross-dating program. This type of control is largely ignored and accordingly the results cannot be used to interpret fine scale model discrimination.

In fact the data is equivocal. For instance the data from Kimberlin who suggested a cubic relationship is shown in Table 4.2.

Table 4.2: Kimberlin's rate data

sample	^{14}C age	rim
308	2050 ± 200	7.5
123	2750 ± 300	8.2
237C	1456 ± 340	6.5
4118A	2100 ± 230	7.5
4118D	2100 ± 230	6.8

If we look at the actual plots of rim thickness versus time (Figures 4.12-4.14) we can see that there is no reason to choose a cubic relationship over a squared or linear one. Thus the data presented by Kimberlin does not reject nor confirm the model for $x(t)$ presented in equation 4.9. This observation is highlighted by the fact that Kimberlin's 1976 data is a subset of that used by Meighan (1983) to infer a linear model for $x(t)$.

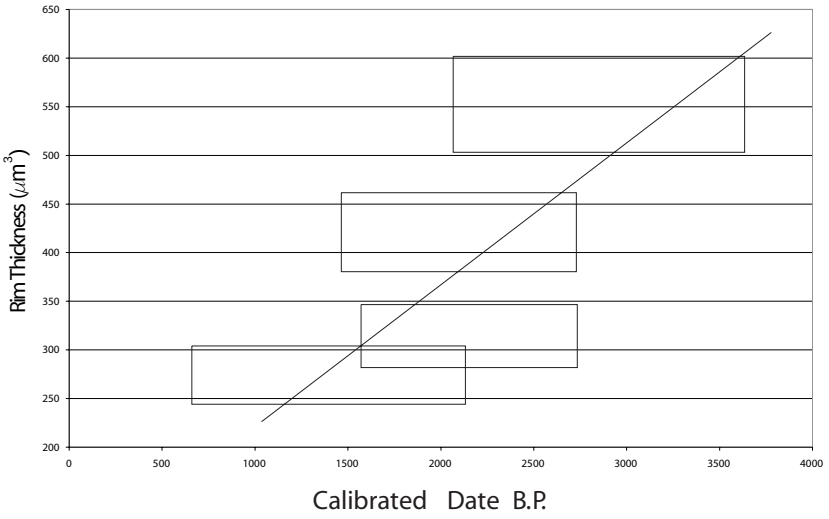

Figure 4.12: Cubic relationship for Kimberlin's data

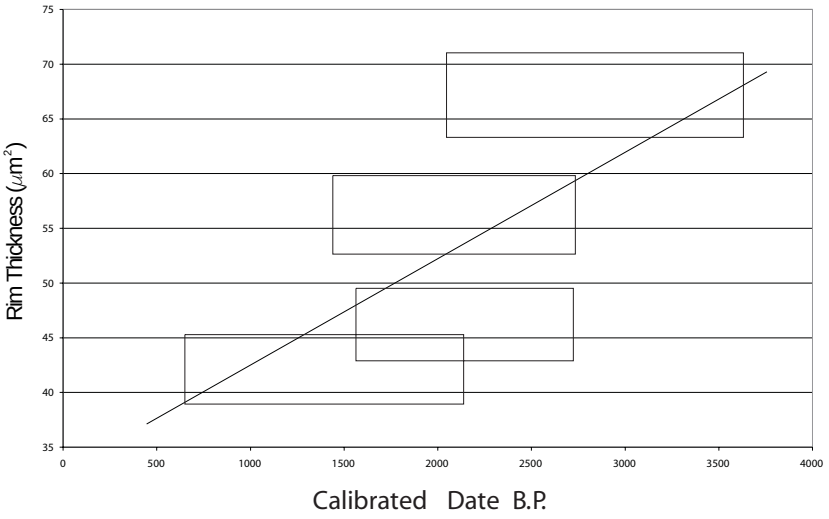

Figure 4.13: Squared relationship for Kimberlin's data

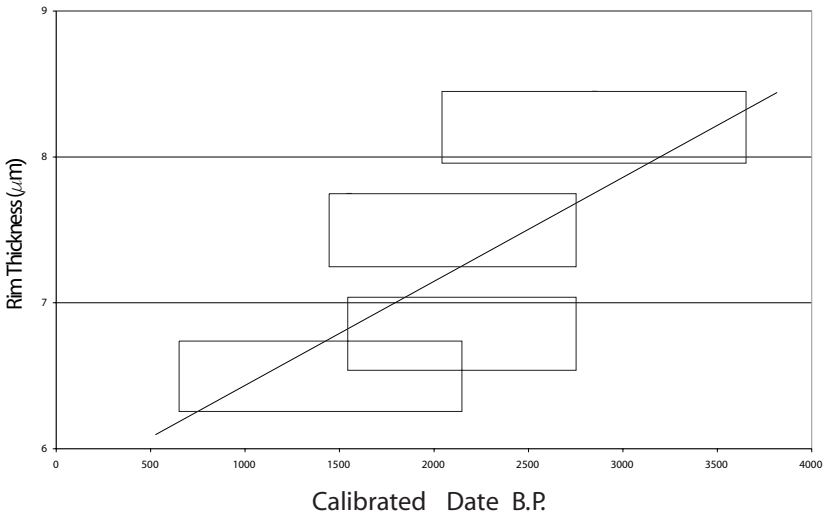

Figure 4.14: Linear relationship for Kimberlin's data

Model Summary

The overall result of various experimental induction programmes is an acceptance that obsidian hydration extent is closely approximated by a root time relationship. Couched in terms of reaction chemistry outlined previously (*infra vide*:§ 4.3) this square root relationship describes the hydration process as a diffusion controlled process; *i.e.* a mixture of ion exchange processes;

$$Na_g^+l + H_3O_{aq}^+ \rightarrow Na_{aq}^+ + H_3O_{gl}^+$$

and diffusion of molecular water. Further it is apparent that the diffusion is concentration-dependant and given Ryan and Brown's (1985) result that ionic diffusion rates are constant in the hydrated and dry zones we would expect that hydration is dominated by the diffusion of molecular water.

There are some problems with this conclusion. The analysis and interpretation has been based around an implicit acceptance of molecular

diffusion being the only significant glass reaction mechanism, which has lead to very limited critical examination of experimental results. In light of the fact that the data associated with much of the published analysis incorporate significant errors a number of models can be fitted to the data. This means that adopting the model presented in equation 4.9 as a null hypothesis and uncritically testing the model form is unacceptable.

Further problems may arise from relying on the results of induction experiments conducted at temperatures elevated well above archaeological reality. It is possible that the nature of the hydration process in high temperature induction experiments differs from that in an ambient archaeological environments. This raises the real possibility that over reliance on high temperature induction results will produce a systematic error in modelling ambient hydration.

Another problem with the experimental induction data is the size of the induced hydration rims, which in most instances are well in excess of those on artefacts produced within the past 2,000 years. The problem with this practice is that if the induced rims are of a size in excess of archaeological reality then this runs the risk of over emphasising mechanisms that may be rate controlling with large rims and ignoring the archaeological reality. While the results may demonstrate that rim formation ultimately proceeds as a diffusion controlled process, the question is does this necessarily describe the initial stages of rim formation? It has been suggested that the initial stages of hydration in some artificial glasses could follow a linear relationship with time (Sullivan and Machiels 1984), and it is possible that obsidian may behave in a similar manner. The basic reasoning behind this is that when the rim is thin the actual ion exchange and de-polymerisation reaction rates are significant in comparison to the diffusion rates over the small initial hydration thicknesses. This consideration is particularly important in archaeological situations where rim thickness will be small ($< 1\mu m$). Such as the

case in New Zealand where hydration rates are slow and the prehistory is short.

In conclusion, the current description of the relationship between hydration extent and time needs to be tested further. It is apparent that the existing corpus of experimental data needs to be critically re-examined in order to define the most appropriate model form for $x(t)$, and that further research is necessary in order to establish the influence of reactions not explicitly modelled in previous research.

4.4.2 The Environment

In addition to describing the form of models for $x(t)$ it is necessary to understand how the parameters of these models are influenced by environmental factors. This has been apparent since the initial applications of Obsidian Hydration Dating, and the two environmental variables that have been most closely studied are temperature and Humidity. Other factors such as environmental pH, biochemical attack and soil composition have been suggested as potential influences (Ambrose 1993; 1994) but little examination of these problems has taken place (Ambrose 2001).

Temperature Dependence

It has been assumed that the hydration rate of obsidian is influenced by temperature since the technique was first proposed (Friedman and Smith 1960). The form of this relationship was not specified at first, and temperature control was effected by defining broad global climatic regions and producing a hydration rate for these regions. However it became apparent that finer temperature controls were needed and further experimental research (Friedman 1976) led to the proposal that the

rate of hydration should follow a general Arrhenius type dependence on temperature such as that presented in equation 4.3.

Friedman (1976) on the basis of the experiments described earlier, demonstrated that his experimental data did not reject the linearity of $\ln(k)$ vs $1/T$ and thus concluded the Arrhenius relationship was valid. These results have been confirmed in subsequent experiments (Ambrose 1976; Mazer *et al.* 1991; Michels *et al.* 1983; Stevenson *et al.* 1987) and this experimental relationship has been applied to archaeological material with seemingly good results (e.g. Michels *et al.* 1983; Stevenson *et al.* 1987; 1995). Therefore it seems reasonable to accept the general relationship.

This relationship also makes some sense in terms of theories relating to molecular diffusion. A random-walk treatment of diffusion (Doremus 1994) represents the diffusion coefficient (*i.e* D in Equation 4.4, k in Equation 4.9) as

$$D = \gamma\bar{\lambda}^2 \frac{kT}{h} exp\left(\frac{\Delta S}{R} - \frac{\Delta H}{RT}\right) \tag{4.10}$$

where T is the absolute temperature; k is Boltzmann's constant; h is Planck's constant; R is the gas constant; ΔS is the entropy of activation and ΔH is the enthalpy of activation or activation energy (E).

In terms of temperature dependence Equation 4.10 can be reworked as

$$D = T\alpha exp\left(\frac{-E}{RT}\right) \tag{4.11}$$

where α is a temperature independent constant

Equation 4.11 is an Arrhenius type model of basically the same form as that proposed by Friedman (1976) incorporating a pre-exponential temperature factor. If this theory applies to diffusion in obsidian it would suggest that $\ln(k)$ vs $1/T$ is non-linear. While this tends to be rejected by the published experimental obsidian hydration results there are potential problems with the results. These mainly arise due to the reliance

upon high temperature induction experiments, generally conducted over a narrow temperature range.

An exploration of the temperature response of gas diffusion rates over a wide temperature range (25 ^{0}C to 1000 ^{0}C) showed that ln(k) versus $1/T$ was non-linear in fused silica (Swets *et al.* 1961). This study demonstrated that a pre-exponential factor of temperature is valid in fused silica and possibly other glasses as well. It may be that as a relatively small temperature range is used in most archaeometric induced experiments the relationship ln(k) vs $1/T$ appears locally linear, and may not bear linear extrapolation over more extensive temperature ranges. The question is whether local linearity can be assumed over the temperature range ambient to $\approx$ 250 ^{0}C, which represents the approximate relevant extrapolation limits for obsidian induction experiments. The only study conducted at ambient conditions that examines the Arrhenius behaviour of obsidian hydration are the powder experiments conducted by Ambrose (1976), and while these demonstrate Arrhenius linearity over the temperature range 10-40 ^{0}C there are complications in comparing this powder data to other higher temperature rate data (*e.g.* Leach and Naylor 1981) and this comparison has not yet been satisfactorily made. It is vital that this issue is resolved for OHD.

Humidity

The question of whether obsidian hydration is influenced by relative humidity has been evaluated in several experiments (Ambrose 1976; Mazer *et al.* 1991; Friedman *et al.* 1994) which have demonstrated that hydration is influenced by rH. This also follows on the basis of glass science theory as outlined previously (*infra vide*:§ 4.3.1). Before continuing this discussion any further it is important to draw a distinction between rH and vapour pressure. rH is the ratio of partial water vapour pressure to saturated water vapour pressure at any given temperature and pressure.

So while this discussion is nominally about rH, hydration of species such as molecular water is governed by the ambient partial vapour pressure of water. Thus while it may be possible to talk about rH at standard atmospheric temperatures, comparison between rH levels at different temperatures and pressures is a little misleading as the actual vapour pressure regimes are different and there is no guarantee that the influence is linearly comparable.

When OHD was first proposed it was thought that there should be sufficient water in any environment to produce normal hydration as the obsidian hydration occurs so slowly (Friedman and Smith 1960). Subsequent induction experiments (Ambrose 1976; Mazer *et al.* 1991; Friedman *et al.* 1994)have shown this assumption to be incorrect, all demonstrating that hydration velocity is dependant upon the rH.

The initial experiments were conducted by Ambrose (1976) on powders at 20 ^{0}C for 240 days under rH's of 12, 54 and 92 %. From these results Ambrose concluded that hydration proceeded normally at an rH of greater than 50 % *at ambient temperatures*.

Further experiments on the influence of rH have been conducted by Mazer *et al.* (1991) & Friedman *et al.* (1994). These studies confirm Ambrose's initial findings and demonstrate a dependence of hydration rate on rH. However, the nature of this dependence is equivocal. In a series of high temperature inductions Mazer *et al.* (1991) found that there was a very rapid change in hydration rate corresponding to rH changes between 90- 100%, but that below 90 % rH hydration dependence on rH was less marked. These results appear to contradict the results of Ambrose (1976) & Friedman *et al.* (1994), both of whom find marked hydration rate dependence at rH's below 90 % rH. Further, Ambrose's (1976) conclusion that there is no significant effect above an rH of 50 % is contrary to the findings of later research.

This lack of consensus may well arise due to confounding experimental

conditions. That is the differences between Ambrose's (1976) results and those of later researchers could well be due to differences in the experimental temperature and pressure regimes.

The overall result of the experiments is to demonstrate that hydration is influenced by ambient rH. Though the extent of this variation and it's implications for hydration at ambient temperatures are not clear. The most useful evidence is from the Ambrose powder inductions that suggest no humidity dependence at rH above 50%. These results are most applicable to modelling ambient hydration as the experiment is conducted under temperature and pressure conditions similar to actual archaeological conditions.

It should be noted that in many archaeological contexts rH is unlikely to be significant, as the effective rH in soils that can support plants is almost always greater than 95% (Hanks and Ashcroft 1980), and as Ambrose (1976) points out, the conditions of an obsidian flake in archaeological context are likely to promote higher surface moisture at the surface of the obsidian than in the surrounding air. This is due to contact with contaminants from the soil and the leaching of salts onto the surface of the obsidian. Certainly there is a relationship between rH and hydration velocity under experimental conditions, but it may be the case that the effective rH is very close to 100 % in archaeological conditions and this will be the case in most New Zealand contexts (*supra vide*:§8).

Solution Chemistry

The effects of different chemical environments have not been explored experimentally by archaeologists but some effects have been demonstrated through archaeological data (Ambrose 2001) and others may be inferred from general glass corrosion research (*e.g.* Strachan 1984; Lokken and Strachan 1984). Different chemical environments may influ-

ence both surface dissolution rates and hydration mechanisms, and it is important to assess the significance of both of these effects.

In some archaeological situations it is apparent that excessive corrosion of the glass surface has occurred, leading to significantly smaller rims than would otherwise be expected (Ambrose 2001). For instance, Ambrose (1994) has found that in some Pacific contexts a high degree of surface corrosion is apparent and has suggested the use of hydration zones in fissures as a means of avoiding surface corrosion.

There is also experimental evidence that soil conditions may effect the hydration rate of obsidian. Though to be more correct these environmental variables effect the "apparent" hydration rate of obsidian. This is as these variables will affect the dissolution rate of the glass surface. It has been demonstrated that high pH and brine conditions will result in corrosion of nuclear waste glasses (Clark 1984), and similarly it has been shown that microbes and fungi will attack glass surfaces (Thorseth *et al.* 1992). There is also some suggestion that ion exchange between clay minerals and the glass surface will result in accelerated corrosion rates (Aertsens 1997).

The effects of environmental variables that may accelerate surface dissolution have not been thoroughly treated in the archaeometric experimental programs to date, and this may have an impact on the variability of the dating process. While obsidian is a very corrosion resistant material it is important to define the effects that different environments may have on the surface dissolution and actual hydration rates. In this manner a protocol to ameliorate any potential problems can be developed and implemented (*e.g.* Ambrose 1994). Typically this treatment will be specific to a particular region as the environmental conditions will vary from location to location.

In addition to affecting the rate of surface dissolution the chemical environment may also influence some hydration mechanisms. For instance,

ionic inter-diffusion may be influenced by the concentration of diffusing species in the immediate environment. Thus raised environmental levels of cations such as Na^+ may serve to slow down ionic inter diffusion, while raised pH levels may accelerate the process. This sort of effect is potentially significant in comparing results between saline and non-saline environments, as well as confounding the effects of environmental pH.

In conclusion, it has been demonstrated that the hydration environment is a significant factor in determining hydration rates under both experimental and archaeological hydration regimes.

The archaeological temperature regime has been identified as a universal environmental factor governing hydration rates. The thermal response of experimental obsidian hydration has been successfully modelled using an Arrhenius equation and ambient temperature inductions have demonstrated that this model is valid for archaeological hydration, though it is still not clear whether the extrapolation from high to ambient temperatures is linear, or if the thermal response characteristics of high temperature hydration reactions can be applied to hydration in archaeological contexts.

Additionally it is apparent that environmental variables other than temperature can influence both the surface dissolution rate and the actual hydration rate. In particular, the environmental rH and pH have been identified. The influence of these factors is not well understood and there are currently no clear protocols for taking them into account for the purposes of OHD. It is possible that soil composition and biochemical attack may also influence net hydration rate, though no studies have been conducted on these problems. In light of this, further work is needed to define the potential influences of these “other” environmental factors.

4.4.3 Conclusion

The effective hydration rate of obsidian is the net result of a number of different reactions, and in order for OHD to represent a viable dating system it is necessary to model this composite reaction process.

From the outline of obsidian structure that has been presented (*infra vide*:§ 4.2.3) it is apparent that a number of different reactions may take place between obsidian and the environment, and that the significance of any one of these reactions may vary from obsidian to obsidian depending on the particular glass structure and chemistry. It is similarly possible that differences in hydration may occur at the spatial scale of an artefact due to inhomogeneity with any sample of obsidian. An example of this can be graphically observed in Figure 4.15. Here flow banding of the glass is apparent. These bands correspond to a change in the quantity of crystalline inclusion in the glass. As can be seen, corrosion of the glass on this sample varies between the different flow bands. We would expect that the apparent hydration behaviour may vary similarly.

Thus in spite of a large corpus of experimental data, many issues are still unclear. This is partially due to the potential for different primary hydration mechanisms in high temperature experimental inductions versus ambient hydration. This has implications for both the conclusions about hydration mechanisms drawn from high temperature induction experiments, and for the extrapolation of model parameters from high to low temperatures. In terms of our current understanding of obsidian hydration this issue clouds the influence of environmental rH; the validity of chemically indexed rate equations based on high temperature data; and the validity of extrapolating thermal response over wide temperature ranges.

Further factors such as soil pH, soil composition and biochemical attack have been shown to influence corrosion in either obsidian or other

Figure 4.15: Photograph of a sample showing the correspondence between corrosion rates and flow banding

volcanic glasses, and are potentially significant net hydration rate governing factors in certain archaeological environments. Currently the influence of these factors is poorly understood and no protocols exist for providing any necessary controls.

So, while much research has been conducted and a very useful baseline of experimental data is available, it is clear that the current understanding of obsidian hydration is founded on some simple, non-critical, assumptions and that this may have a detrimental influence on the final application of the dating system. The most obvious example of this is the acceptance of a purely diffusion controlled relationship between hydration extent and time. There is no doubt that the experimental data produced to date does not reject a diffusion controlled rate, though there has been no critical evaluation of the optimum model form. It is reasonable that an exponential model of the form presented in equation 4.2 would closely approximate obsidian hydration as this is ex-

pected to be a diffusion dominated reaction. However, there are very real grounds to expect deviations from this behaviour that may necessitate a change in parameterisation and\or form of the model. In particular the quantity of crystalline inclusion, porosity, degree of polymerisation and degree of hydrolysis would be expected to influence the overall hydration process with the influence of some factors being linearly related to time and others involving more complex temporal relationships. Thus it may well be the case that different empirical models are necessary for different obsidian.

From the overview presented in this section it is apparent that further work needs to be conducted into obsidian hydration. The next section of this chapter is directed at this process, with a view to generating working models and parameters for the prediction of archaeological hydration in general and the development of models for use within the past 2,000 years in particular.

4.5 Hydration Experimental Dataset

4.5.1 Introduction

As outlined in the previous section, various issues need clarification in order to provide a secure empirical basis for the estimation of $x(t)$, and as a basis for designing future, effective, obsidian hydration research programs. The most significant areas requiring clarification are:

- The relationship between hydration extent and time (*infra vide*:§4.4.1)
- The dependence of hydration model on hydration extent (*infra vide*:§4.4.1)
- Thermal dependence of the hydration reactions (*infra vide*:§4.4.2)

- The influence of environmental variables other than temperature (*infra vide*:§4.4.2)
- Glass specificity of hydration models (*infra vide*:§4.4.3)

These issues need examination with reference to both obsidian hydration dating in general, and its application in New Zealand specifically. Obviously most of the issues outlined above may need to be specifically resolved for each particular glass source and environment within which OHD is applied. Thus in the context of the current thesis it is important to consider OHD in New Zealand specifically, though the results will have implications for OHD in general.

In order to pursue this resolution it is necessary to develop a suitable experimental data set. The purpose of this section is to outline the development of an experimental programme designed to address some of these issues. It is intended that analysis of this data set will resolve the issues highlighted above to the extent that reasonable bounds can be placed on models for obsidian hydration in New Zealand specifically, and that a realistic appraisal of what is understood about obsidian hydration in general can be made.

The majority of the data considered are derived from the hydration experiments described below (*supra vide*:§4.5.3). The intention was to conduct a series of induced hydration experiments on compositionally characterised samples of obsidian incorporated within a structure that allowed resolution of the issues highlighted above. Some data could not be obtained within the course of this research due to time constraints (*e.g.* Raman Spectra data: *supra vide*:§5.2) though these are being pursued as part of an ongoing hydration research program. Additional data were obtained from published sources (*supra vide*:§C.7 Ambrose 1976; Ericson 1989; Friedman 1976; Mazer *et al.* 1991; Michels *et al.* 1983; Stevenson and Scheetz 1989*a*; Tsong *et al.* 1981; Tremaine and Fredrick-

son 1988) and from measurements on samples that were part of the long term induction program being conducted by Wal Ambrose (Ambrose pers. comms. 1997).

4.5.2 The Obsidian Sources

The obsidian sources used in this experimental induction programme were selected from the sources throughout New Zealand that are either known to be exploited prehistorically or produce artefact grade material, with a strong emphasis on material from Mayor Island which was the major source of industrial obsidian in prehistory (*infra vide*:§3). Thus the samples used allow a comparison of the relative hydration rates of obsidian from major prehistoric sources of New Zealand obsidian. As an induction program encompassing an intensive evaluation of every potential source of obsidian within New Zealand would be beyond the scope of what could be achieved within the time frame of the current research, the major experimental focus has been on "green" obsidian. This is as the number of sources of obsidian that are green in transmitted light in New Zealand are limited and fairly easily provenanced (*infra vide*:§3). In comparison, the other sources are more numerous, less well described and considerably more difficult to provenance (*supra vide*:§3). Thus this means that the results are more easily applied to OHD in New Zealand. In order to cover the full compositional range of obsidian in New Zealand two "grey" sources *Ben Lomond* and *Te Ahumata* (*infra vide*:§3) were also extensively used. The samples were extracted from the reference set of obsidian defined in Chapter 3.

In total, results were obtained for twelve[2] sources of New Zealand obsidian with principle focus on 4^2 sources. Each source used was given an

[2]here Mayor Island in general is counted as a single source, in total 35 sub-sources on M.I. were examined

experimental number from 1-92 as described in Table C.4.

4.5.3 Experimental Structure

Introduction

In total 15 experimental induction runs were conducted (Tables 4.3 & 4.4). These resulted in the induced hydration of 300 samples of obsidian at temperatures ranging from 95-160 ^{0}C. The experiments were designed to produce induced hydration rims of a similar size to what would be expected in archaeological samples from New Zealand, which effectively means detectable rims of less than $\approx 1.2\ \mu m$. This limit was observed for two reasons; 1) this ensures that any inferred hydration models are applicable to New Zealand archaeology 2) this allows a comparison to be made with the data obtained from the more extensive hydration's conducted in previously published studies.

While the primary focus of this experimental program was to study obsidian hydration, it was also necessary to evaluate the induction process in order to ensure that the results were not being confounded by sample preparation or induction environment. Additionally it was necessary to build an evaluation of the experimental precision into the experiment in order to define how precisely the results could be inferred.

The analysis presented in this thesis cannot reasonably attempt to resolve all questions associated with obsidian hydration, and the questions to be addressed are as follows.

- Is there a significant deviation from the $t^{\frac{1}{2}}$ relationship for hydration extent
- Is the form of $x(t)$ dependant on hydration extent

Table 4.3: Induction experiments

Run No	Induction Media						
	Temperature ^{0}C	Run Length (days)	Vapour #1	Distilled water #2	Silica #3	Soil #4	Sand #5
1	100 ^{0}C	10	✓	✓	✓	✓	✓
2	95 ^{0}C	30	✓	✓	✓	⊗	⊗
3	95 ^{0}C	54	✓	✓	✓	✓	✓
4	95 ^{0}C	54	✓	✓	✓	⊗	⊗
5	95 ^{0}C	30	✓	✓	✓	⊗	⊗
6	95 ^{0}C	30	✓	✓	⊗	⊗	⊗
7	112.5 ^{0}C	14	✓	✓	✓	⊗	⊗
8†	112.5 ^{0}C	9	✓	✓	✓	⊗	⊗
9	112.5 ^{0}C	5	✓	✓	✓	⊗	⊗
10	107 ^{0}C	21	✓	⊗	⊗	⊗	⊗
11	125 ^{0}C	35	✓	⊗	⊗	⊗	⊗
12	160 ^{0}C	0.5	✓	⊗	⊗	⊗	⊗
13	95 ^{0}C	nil	⊗	⊗	⊗	⊗	⊗
14	160 ^{0}C	0.666·	✓	⊗	⊗	⊗	⊗
15	160 ^{0}C	1	✓	⊗	⊗	⊗	⊗

† an additional experimental structure was employed in Run 8 to explore the influence of environmental variables on hydration as outlined in Table 4.4

- Is the form of $x(t)$ dependant on glass composition
- Is the form of $x(t)$ dependant on ambient temperature and pressure

Precision of the Results

The precision of the induction process is designed to be inferred as part of the results of Runs 2-6. In these runs two sets of replicate measurements were made. The 30 day 95 ^{0}C run was repeated 3 times (Runs 2,5,6; *supra vide*:§C.4) within each run there were 6 paired replicates in each of two induction media (Distilled water, Water Vapour). Thus there are twelve paired replicate conditions each replicated three times. This entire experimental structure was repeated in the 54 day 95 ^{0}C runs (Runs 3 and 4; *supra vide*:§C.4) except there were only two replicates of each of the twelve paired replicate conditions.

Thus these comparisons represent a set of 120 experimental replicates of intra experimental block variation and 48 replicates of inter experimental block variation. The intra experimental block variation will test the precision of the induction results, while the interblock variation will test the precision of the experimental procedure.

Influence of Induction Environment

In addition to testing the precision of the experimental results it was important to ensure that the results are not confounded by the experimental procedure. It has previously been demonstrated that under certain experimental conditions different induction protocols give rise to different results (Stevenson and Scheetz 1989*b*). In order to test the influence of induction environment under the current experimental conditions, samples were induced in 3 primary induction media; distilled

water, silica saturated water and water vapour. This comparison was made within induction runs 1-9. In total the comparison between these three induction media was made with 87 triplicate samples (*i.e.* 261 samples total).

Relationship Between Time and Hydration Extent

The key relationship between time and hydration extent was explored at three temperature regimes, 95 (runs 2-6),112.5 (Runs 7-9) & 160 ^{0}C (Runs 12,14 & 15). At each of these temperatures, induced hydrations of varying duration were conducted. In each case the absolute hydration extent was kept approximately equal among the three temperature regimes, thus the hydration duration varied considerably, ranging from 0.5 days for the shortest duration 160 ^{0}C induction to 54 days for the longest 95 ^{0}C induction. The hydration extents were kept approximately constant amongst the temperature regimes to ensure that the comparisons are a function of temperature and not confounded by hydration extent or similar. The glasses included in these inductions were chosen to represent the range of source chemistry represented by glasses in the reference collection (*infra vide*:§4.5.2,§5.2).

The results of this experiment will allow

1. an assessment of an appropriate model for $x(t)$
2. whether $x(t)$ is temperature dependant
3. whether $x(t)$ is glass dependant

to be established for New Zealand obsidian

Thermal Response of the Net Hydration Reaction

The thermal response of the net hydration reaction is explored at seven different temperatures ranging from 40 ^{0}C to 160 ^{0}C. Experimental hydration's were conducted at six different temperatures ranging from 95 ^{0}C to 160 ^{0}C (Runs 1-15) on glasses that are chemically representative of the reference collection (*infra vide*:§4.5.2,§5.2). Additional data has been obtained from samples of a subset of the sources that have been induced at 40 ^{0}C by Wal Ambrose (*supra vide*:§C.1). These data will allow the temperature dependence of $x(t)$ to be examined. Of particular significance is the ability to examine the utility of extrapolating high temperature induction behaviour to ambient temperatures. This issue is central to establishing whether high temperature induction experiments are suitable for estimating archaeological hydration, and also is of significance in inferring temperature dependency of hydration mechanism.

Influence of Non Thermal Environmental Variables

A very basic examination of the influence of non-thermal environmental variables is incorporated within the experimental structure. As previously outlined the hydration environment may influence net hydration rate, and in particular environmental pH, cation concentration and soil composition may have an influence (*infra vide*:§4.4.2). The major experimental results were generated during Run 8 where the influence of environmental pH and cation concentration were explored (Table 4.4). In this experiment, inductions were performed in solutions with pH varying between 3.5 & 10.5 and a solute Na^+ concentration of 0.05-3 M. The glasses included in these inductions were chosen to represent the range of source chemistry represented by glasses in the reference collection (*infra vide*:§4.5.2,§5.2). Additional to this experiment a comparison of hydration behaviour in soil and silica sand has also been made (Runs

2-9). In all cases the experiments are compared against samples in the same run induced in water vapour. The results of these comparisons will allow an assessment of the influence of the environment on net hydration.

Table 4.4: Environmental experiments

Glass	pH 3.5	pH 6.2	pH 6.8†	pH 8	pH 10.5	0.1M NaCl	0.5M NaCl	2M NaCl
	#9	#10	#3	#11	#12	#6	#7	#8
7	✓	✓	✓	✓	✓	✓	✓	✓
14	✓	✓	✓	✓	✓	✓	✓	✓
16	✓	✓	✓	✓	✓	✓	✓	✓
30	✓	✓	✓	✓	✓	✓	✓	✓
42	✓	✓	✓	✓	✓	✓	✓	✓

† Saturated silica solution

Archaeological Hydration Rate Controls for New Zealand

Incorporated within this experimental programme is an exploration of the hydration behaviours of different New Zealand obsidian sources. As outlined previously (*infra vide*:§4.5.2) the main focus is on examining the "green" sources. Accordingly the sources on Mayor Island and in Northland have been extensively sampled (*infra vide*:§3) and an effort has been made to establish the degree of intra-source hydration variability. In addition to these, a range of different source samples have been examined (*infra vide*:§3), primarily with a view to establishing the degree of variation in hydration behaviour among rather than within the sources. The primary inter and intra source hydration comparisons were conducted at 95 ^{0}C (Runs3 & 4) 112.5 ^{0}C (Run 7) and 125 ^{0}C (Run 11). These results are discussed in more detail in Chapter 6

4.5.4 Experimental Method

Inductions

The inductions were performed in either 20 L Aluminium pressure cookers, or 0.75 L Parr pressure bombs. Only the high temperature inductions (160 ^{0}C: runs 12,14 & 15) were induced in the pressure bombs, as the internal pressure of these inductions exceeded the safety specifications of the pressure cookers. Where possible the pressure cookers were the preferred induction vessel as the much larger vessel volume enables a greater number of samples to be induced in any given run, and also the experiment was considerably easier to set up due to greater accessibility of the internal vessel space. The temperature was held constant by either placing the cooker on a hot plate and holding the internal pressure at a constant level (runs 7,8,9), or by placing the cooker in an oven held at a constant temperature (runs 1-6,10-15). Periodic temperature measurements were conducted on the first runs in both experimental set-ups to determine the temperature fluctuation of the cooker.

In the incubation oven the temperature was held constant to $\pm$ 0.1 ^{0}C. It is assumed that the thermal inertia of water (due to the large thermal capacity of water relative to air) would ensure that the actual internal pressure vessel temperature would vary by an amount considerably less than this. Though as a conservative estimate the figure of $\pm$ 0.1 ^{0}C is used.

The temperature of the cooker held on the hot plate was more variable. The measured temperature extremes fell in the range $\pm$ 0.2 ^{0}C, and while the temperature was more constant than this for the majority of the induction $\pm$ 0.2 ^{0}C is conservative for these runs.

The pressure vessels were filled with distilled water at the beginning of an induction run and a perforated bottom plate was fitted above the wa-

ter to keep the induction samples out of direct contact with the pressure cooker body water. The samples to be induced in a vapour environment where suspended from a thin copper rod in the centre of the pressure cooker, with the water vapour being provided by the heated body water. The samples to be induced in aqueous solutions or soil and sand environments were placed in Pyrex beakers filled with the appropriate matrix. Prior to use the Pyrex beakers were autoclaved at 120 ^{0}C for 4 weeks and then washed in distilled water to ensure that any potential reactions between the solution and the Pyrex that might influence the experiment were minimised.

Media

The media used in the inductions where prepared as follows:

1. Water Vapour (#1)simply derived from heated body water.
2. Distilled water (#2) was produced via a standard scientific still. The water was not polished after stilling.
3. The silica saturated solution (#3) was prepared by the adding of powdered amorphous silica to distilled water. Many orders of magnitude of silica beyond ambient saturation where added to ensure saturation at higher temperatures where the solubility of silica increases.
4. The soil (#4) was a sample of field loam.
5. The sand (#5) was washed silica sand.
6. The NaCl solutions (#6-8) where diluted to the appropriate concentration with distilled water from a bulk sample of 5 M NaCl.
7. The solution held at a pH of 3.5 in run 8 (#9) was a solution of dilute HCl.

8. The solutions held at a pH's of 6.2 and 8 in run 8 (#10,11) were buffered with TRIS.

9. The solution held at a pH of 10.5 in run 8 (#12) was a solution of dilute NaOH.

Sample Preparation

The samples where prepared by producing a fresh flake of obsidian and inscribing it's sample number on the dorsal surface with a diamond pen. Cut and polished samples for comparison between the induced flaked material and the polished material were produced following the method described by Mazer *et al.* (1992). After production the samples to be induced in a vapour environment were drilled with a 2 mm diamond coring bit in order to permit suspension.

After preparation the samples were placed in the preheated pressure vessel and reaction time was measured from when the temperature stabilised. Typically this was 10 minutes for the oven heated samples and 15 minutes for the samples on the hot plate. The inductions conducted in the 20L pressure cookers where brought to reaction temperature rapidly on a gas stove in order to ensure that temperature stabilisation was rapid. The use of two different heating systems was made necessary by the long induction times and the need to run inductions at different temperatures simultaneously. Each experimental temperature group was maintained constant within a single experimental set-up.

Sample Measurement

At the termination of an induction run the pressure vessels were removed from the heating environment and the internal vessel pressure was reduced to atmospheric by venting. The vessels were then opened

and the samples were reduced to room temperature by immersion and washing in distilled water. At this stage the samples were bagged and the measurement process began.

4.6 Analysis of the Experimental results

4.6.1 Precision of the Results and Influence of Induction Protocol

Experimental Precision

The experimental precision has been tested by 82 replicate pairs from within an experimental model consisting of six experimental conditions (three induction environments by two induction duration's) a subset of which are replicated 2-3 times. Nine glasses that are compositionally representative of the reference collection have been used within this experimental structure in order to ensure that any inferences are not confounded by inter glass effects.

Table 4.5: Experimental precision data

Glass	Run	Time (days)	Temp (^{0}K)	Cond	x1 (μm)	x2 (μm)
7	2	30	368.15	D	0.68	0.71
7	5	30	368.15	D	0.64	0.71
7	3	54	368.15	D	0.9	0.86
7	4	54	368.15	D	0.86	0.86
5	3	54	368.16	D	0.75	0.68
5	4	54	368.16	D	0.75	0.68
9	3	54	368.16	D	0.86	0.79
9	4	54	368.16	D	0.86	0.94

continued on the next page

Table 4.5: *continued*

Glass	Run	Time (days)	Temp (^{0}K)	Cond	x1 (μm)	x2 (μm)
11	2	30	368.16	D	0.68	0.68
12	2	30	368.16	D	0.68	0.71
11	3	54	368.16	D	0.86	0.79
12	3	54	368.16	D	0.86	0.79
11	4	54	368.16	D	0.86	0.86
12	4	54	368.16	D	0.83	0.86
13	2	30	368.16	D	0.56	0.60
13	5	30	368.16	D	0.56	0.60
13	3	54	368.16	D	0.68	0.71
13	4	54	368.16	D	0.68	0.75
4	3	54	368.16	D	0.79	0.71
4	4	54	368.16	D	0.75	0.68
10	2	30	368.16	D	0.79	0.75
10	3	54	368.16	D	1.05	0.97
10	4	54	368.16	D	0.97	1.05
8	3	54	368.16	D	0.98	0.79
8	4	54	368.16	D	0.83	0.87
7	2	30	368.15	S	0.68	0.71
7	5	30	368.15	S	0.71	0.68
7	3	54	368.15	S	0.86	0.9
7	4	54	368.15	S	0.86	0.86
5	3	54	368.16	S	0.68	0.71
5	4	54	368.16	S	0.68	0.71
9	3	54	368.16	S	0.86	0.79
9	4	54	368.16	S	0.86	0.83
11	2	30	368.16	S	0.68	0.71
12	2	30	368.16	S	0.68	0.71

continued on the next page

Table 4.5: *continued*

Glass	Run	Time (days)	Temp (^{0}K)	Cond	x1 (μm)	x2 (μm)
11	3	54	368.16	S	0.83	0.86
12	3	54	368.16	S	0.79	0.79
11	4	54	368.16	S	0.83	0.83
12	4	54	368.16	S	0.83	0.79
13	2	30	368.16	S	0.56	0.64
13	5	30	368.16	S	0.53	0.56
13	3	54	368.16	S	0.75	0.71
13	4	54	368.16	S	0.68	0.68
4	3	54	368.16	S	0.71	0.68
4	4	54	368.16	S	0.79	0.68
10	2	30	368.16	S	0.75	0.79
10	3	54	368.16	S	1.01	1.09
10	4	54	368.16	S	1.01	1.09
8	3	54	368.16	S	0.83	0.94
8	4	54	368.16	S	0.83	0.94
7	2	30	368.15	V	0.68	0.71
7	5	30	368.15	V	0.68	0.64
7	6	30	368.15	V	0.68	0.68
7	3	54	368.15	V	0.86	0.94
7	4	54	368.15	V	0.9	0.86
5	3	54	368.16	V	0.75	0.75
5	4	54	368.16	V	0.75	0.71
9	3	54	368.16	V	0.86	0.90
9	4	54	368.16	V	0.86	0.83
11	2	30	368.16	V	0.64	0.64
12	2	30	368.16	V	0.64	0.64
11	5	30	368.16	V	0.68	0.64

continued on the next page

Table 4.5: *continued*

Glass	Run	Time (days)	Temp (^{0}K)	Cond	x1 (μm)	x2 (μm)
12	5	30	368.16	V	0.64	0.64
11	6	30	368.16	V	0.64	0.60
12	6	30	368.16	V	0.64	0.64
11	3	54	368.16	V	0.83	0.83
12	3	54	368.16	V	0.86	0.79
11	4	54	368.16	V	0.83	0.86
12	4	54	368.16	V	0.86	0.86
13	2	30	368.16	V	0.53	0.60
13	5	30	368.16	V	0.60	0.53
13	6	30	368.16	V	0.60	0.60
13	3	54	368.16	V	0.75	0.68
13	4	54	368.16	V	0.71	0.68
4	3	54	368.16	V	0.75	0.71
4	4	54	368.16	V	0.71	0.75
10	2	30	368.16	V	0.75	0.71
10	3	54	368.16	V	1.01	1.05
10	4	54	368.16	V	1.05	1.01
8	3	54	368.16	V	0.90	0.83
8	4	54	368.16	V	0.90	0.79

The primary interest lies in establishing:

1. are the replicate pairs significantly different
2. are the replicated inductions within each experimental condition significantly different
3. are the induction environments significantly different
4. is there a significant difference between the glasses

The data shown in Table 4.5can be analysed using a GLM type analysis to assess the significance of the different factors. The following analysis was run using the SPSS 7.5.1 GLM procedure using the following syntax:

```
GLM
  x1 x2 BY run time glass cond
  /WSFACTOR = f1 2 Polynomial
  /METHOD = SSTYPE(3)
  /CRITERIA = ALPHA(.05)
  /WSDESIGN
  /DESIGN time run(time) glass cond cond by glass cond by time glass by time by cond.\\
```

We can use the within factor effects to test the consistency among replications. As can be seen in Table 4.6 there is no significant difference between the replicate pairs within the experiment as a whole at $\alpha = 0.05$ (source F1). It is also apparent that this result is consistent for all of the glasses, experimental conditions and induction durations. Thus we can conclude that the experimental protocol will produce consistent results for replicates within the tested experimental conditions. The consistency of induction results can be tested by examining the Between-Subjects effects (Table 4.7). As would be expected there is a significant effect due to hydration duration and glass source, though there is no

Table 4.6: Tests of within-subjects effects

Source	df	Sig.
F1	1	0.227199666
F1 * TIME	1	0.775381553
F1 * RUN (TIME)	3	0.091937965
F1 * GLASS	7	0.525337907
F1 * COND	2	0.09607458
F1 * GLASS * COND	14	0.015789429
F1 * TIME * COND	2	0.979466089

significant effect due to either the induction conditions or the replicated runs nested within each hydration duration condition. Thus we would

Table 4.7: Tests of between-subjects effects

Source	df	Sig.
Intercept	1	1.11022E-16
TIME	1	1.11022E-16
RUN(TIME)	3	0.442932455
GLASS	7	0
COND	2	0.678820427
GLASS * COND	14	0.423705237
TIME * COND	2	0.057117183

conclude that the results of any of the experimental conditions tested, using glasses from the reference collection, will be reproducible.

These results can also be demonstrated by generating descriptive statistics for the experimental contrasts of interest. For instance Table 4.8 shows the average, std, max, min and range of the absolute difference between replicates grouped by glass and induction condition. So for example, the replicates of Ben Lomond obsidian across all induction environments had an average absolute difference of 0.033 μm with an std of 0.024 μm. That is, we would expect that 95% of the replicates would fall within 0.08 μm of one another, which is what we observe as the maximum range for this set of readings.

As the measurement error associated with the experimental results is $\pm 0.075 \mu m$ the replicates should deviate by less than $0.15 \mu m$ if there is no experimental effect. It is apparent that this is the case for all of the glass sources other than Waihi. The Waihi source is the most highly compositionally variable glass in the test set, and this probably accounts for the poor reproducibility of the Waihi samples. So while there is no

statistically significant inter glass difference it is apparent that there are possibly some real differences for compositionally variable glasses.

Table 4.8: Replicate descriptive statistics

Glass	$\bar{x}$	σ	MAX	MIN
7	0.033076923	0.024284637	0.08	0
4	0.04	0.026832816	0.07	0
9	0.053333333	0.022509257	0.08	0.03
11,12	0.027954545	0.026136505	0.0725	0
13	0.045192308	0.026109975	0.08	0
5	0.068333333	0.027913557	0.1075	0.0325
10	0.057777778	0.021081851	0.08	0.04
8	0.103333333	0.050464509	0.19	0.04
Condition Comparisons				
D	0.0563	0.038202585	0.19	0
S	0.0447	0.032781791	0.11	0
V	0.039274194	0.028782182	0.1	0
Overall	0.046203704	0.033496994	0.19	0

The conclusion from the tests of experimental protocol is that the experimental procedure produces repeatable results. We can therefore conclude that any effects observed during the experimental program are not a function of experimental procedure.

4.6.2 The Relationship Between Rim Thickness and Time

While this relationship has been tested in many previous experiments there may be problems with the results and analysis of particular significance for archaeology in New Zealand (*infra vide*:§4.4.3). Most previous

research has focussed on producing and analysing hydration rims that are many orders of magnitude larger than those found in archaeological samples of less than 1,000 years of age. Additionally, there has been an uncritical acceptance of a model based on only one potential hydration reaction component. Here the intention is to assess model and parameter estimates for archaeological hydration in general, and that of events occurring within the last 1,000 years in particular.

As outlined in chapter 4 the relationship between hydration rim thickness and time is usually described by a squared relationship of the form:

$$x^2 = kt \tag{4.12}$$

and should provide a close first approximation for $x(t)$.

The induction experiments that have been run in this piece of work are designed to test four aspects of this relationship:

1. If the parameter values of this relationship are optimum for obsidian hydration in general. This involves evaluating the available data to determine the optimum fit for y in the relationship

$$x^y = kt \tag{4.13}$$

2. If the model and/or model parameters hold for temperatures below 100 ^{0}C where it has been suggested that different hydration mechanisms may be in operation than at higher temperatures.

3. If there is any functional relationship with glass composition that may have significance for OHD in new Zealand.

4. If there is any deviation from this relationship as a function of rim thickness for rims smaller than 1 μm.

The experimental inductions to test this relationship have been run at 95 ^{0}C ,112.5 ^{0}C & 160 ^{0}C producing hydration rim thicknesses ranging

from 0.4-1.05 μm (experimental runs 2-9,12,14,15). In addition to the data produced during these experimental inductions other published experimental results (*supra vide*:§C.7) have been included in the analysis where necessary. In general only the data presented in this thesis have been used, as other experimental data sets have been measured using different protocols and involve rims induced under different conditions, all of which raise the possibility of confounding the analysis. As an example compare the induction results produced by (Michels 1986) and Tremaine and Fredrickson (1988) on the same glasses as presented in Table 4.9. In this case a completely different interpretation of $x(t)$ is drawn from the two data sets. This arises directly due to experimental method, and if the results were on different source materials the erroneous conclusion may be drawn that $x(t)$ varied due to fundamental differences in hydration between the glasses.

Table 4.9: Comparative induction data

Source	Rim max (μm)	R^2	N	$\hat{y}$	s.e.
Michel's Napa glass 200 C	6.6	0.999	4	1.98	0.02
Michel's Annadel farms 200 C	6.2	0.999	4	1.95	0.01
Michel's Casa diablo 200 C	6.6	0.999	4	1.96	0.02
Michel's Otumba 200 C	7	0.999	4	2.02	0.03
Michel's Hawkins-malad 200 C	6	0.998	4	1.98	0.06
Tremaine Borax lake 200 C	5.9	0.972	4	3.08	0.37
Tremaine Napa glass 200 C	5.1	0.949	4	2.56	0.42
Tremaine Konociti 200 C	5.2	0.965	4	2.54	0.34
Tremaine Annadel 200 C	3.6	0.904	4	2.92	0.67

The first step in this analysis is to evaluate the conventional model (Equation 4.12) in light of the new induction data, it is then proposed to establish the optimum model parameters.

The results of these experiments have been tested by fitting the following model to the data

$$x_{it}^2 = k_i t + \sigma_{it}(\sigma_{it} i.i.d) \tag{4.14}$$

which is essentially a set of independent regressions through the origin of each experimental block (blocks of glass x temperature). Overall the model r^2 is 0.88 and the analysis is statistically significant, though of more interest are the residuals. If the relationship is valid then the residuals should be normally distributed, and more importantly, show no structure.

Residual normality was established using a 1 sample K-S test which returned a p-value of 0.16. We can therefore accept the null hypothesis that the residuals are normally distributed. The plot of residuals versus hydration rim thickness (Figure 4.16) does not suggest any systematic deviation of the fitted model as a function of rim thickness, and this can be tested by fitting a regression to the residuals and evaluating the significance of the fitted slope. The fitted slope for the residuals from the overall model (Equation 4.14) is insignificant (pval 0.5) and we can therefor accept the null hypothesis that there is no significant linear structure in the residuals.

The average absolute residual is 0.023 with a σ of 0.018. Thus we would expect that 95 % of absolute residuals would lie below 0.059. This is approximately what is observed, with 96 % of the absolute residuals lying below 0.59 and a maximum absolute residual of 0.78. Thus the observed residuals fall within the expected measurement precision of 0.075 and could possibly arise due to measurement rather than model imprecision.

These results demonstrate that a root time model for $x(t)$(*i.e.* Equation 4.9) describes the experimental results to a high precision. However, it should be noted that exploratory data analysis returns some individ-

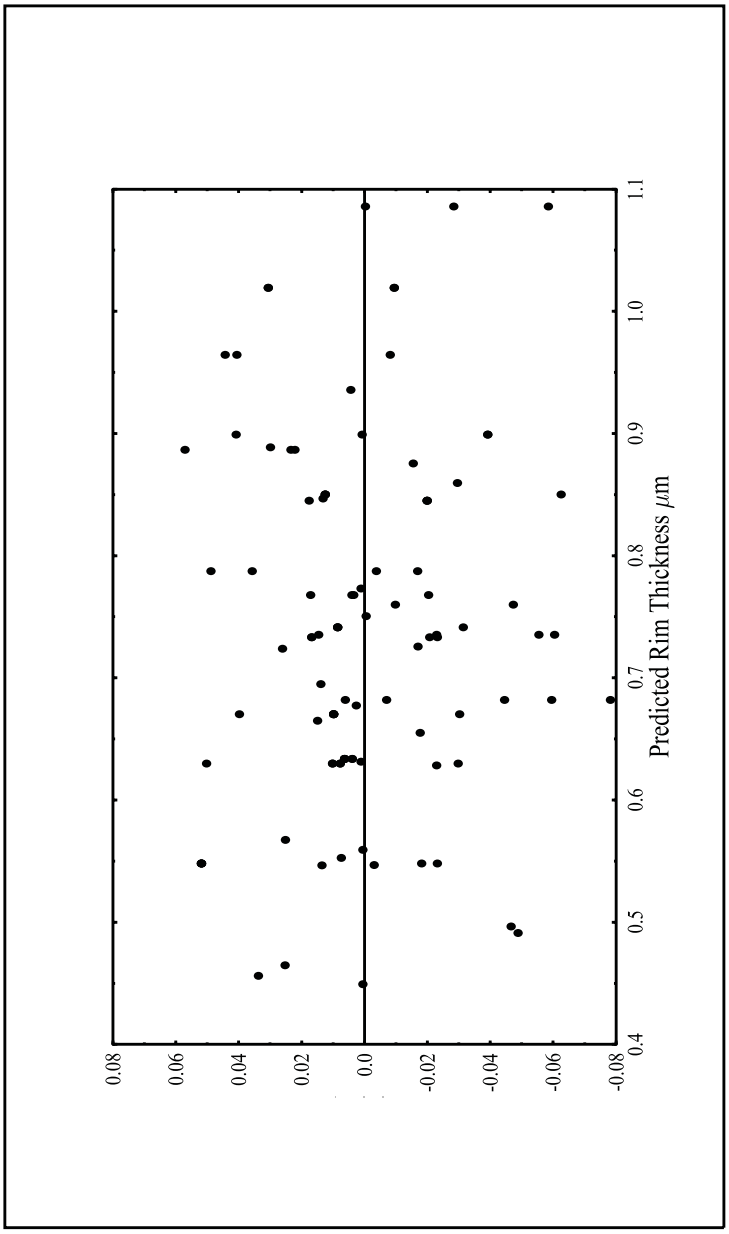

Figure 4.16: Residuals versus rim size for experimental results fitted to Equation 4.14

ual block fits with a higher r^2 when x is raised to a power higher than 2, which suggests that the parameters in Equation 4.12 may not be optimum. That is that the optimum exponent of x may be some (probably non-integer) value other than 2.

To test the optimum fit of y in the relationship presented in Equation 4.13 the induction data produced in this piece of work were analysed by re-arranging Equation 4.13 as

$$ln(Time) = yln(x) - ln(k) \tag{4.15}$$

and fitting the following model to the data

$$ln(Time)_i = \beta_{0i} + \beta_{1i} ln(x_{it}) + \sigma_{it} \tag{4.16}$$

Here the β_{0i} are the fitted $-ln(k)$ for each experimental block i and β_{1i} is the fitted $\hat{y}$ for each experimental block. The results of this analysis are presented in Table 4.11.

A comparison of these results show that there is no significant parameter difference among the sources at any given temperature, though as presented in Table 4.10 there is a possible temperature related trend with the 160 ^{0}C results tending to suggest an optimum parameter falling below 2, in contrast to the lower temperature results which suggest a figure indistinguishable from 2.

Regression of Probability Distributions

A difficulty with the current analysis is that the data are not points, but rather probability distributions. In this case regressing the mean of the probability distribution makes the assumption that the "true" measurement is most likely to correspond to the mean of the probability distribution which, is not the case. It is preferable to use an analysis that treats the data as probability distributions.

Table 4.10: Mean $\hat{y}$ for the different induction temperatures

Temperature ^{0}C	$\hat{y}$
95	2.032441301
112	2.072260593
160	1.726051023
total	1.951695759

Table 4.11: Fitted $\hat{y}$ for the experimental induction data

Glass	Temperature	r^2	n	$\hat{y}$	se
7	95	0.941	10	2.04	0.18
7	112	0.999	3	2.26	0.03
7	160	0.938	12	1.51	0.12
5	95	0.965	5	2.04	0.22
14	112.5	0.999	3	2.39	0.07
11	95	0.948	10	2.09	0.17
12	95	0.967	10	2.05	0.13
12	160	0.998	3	1.65	0.07
16	112.5	0.996	3	1.96	0.13
13	95	0.771	10	2.24	0.43
13	160	0.946	3	1.42	0.34
4	95	0.952	5	2.11	0.27
6	95	.	2	2.01	.
34	160	0.999	3	1.96	0.03
30	112.5	0.988	3	1.68	0.19
10	95	0.982	6	1.68	0.11
10	160	0.953	10	2.08	0.16

One approach to this, is to systematically sample from throughout the possible solutions for $\hat{y}$. In this manner it is possible to produce a probability distribution for $\hat{y}$ from the uniform distributions that are represented by the measurements. This can be illustrated with reference to Figure 4.17.

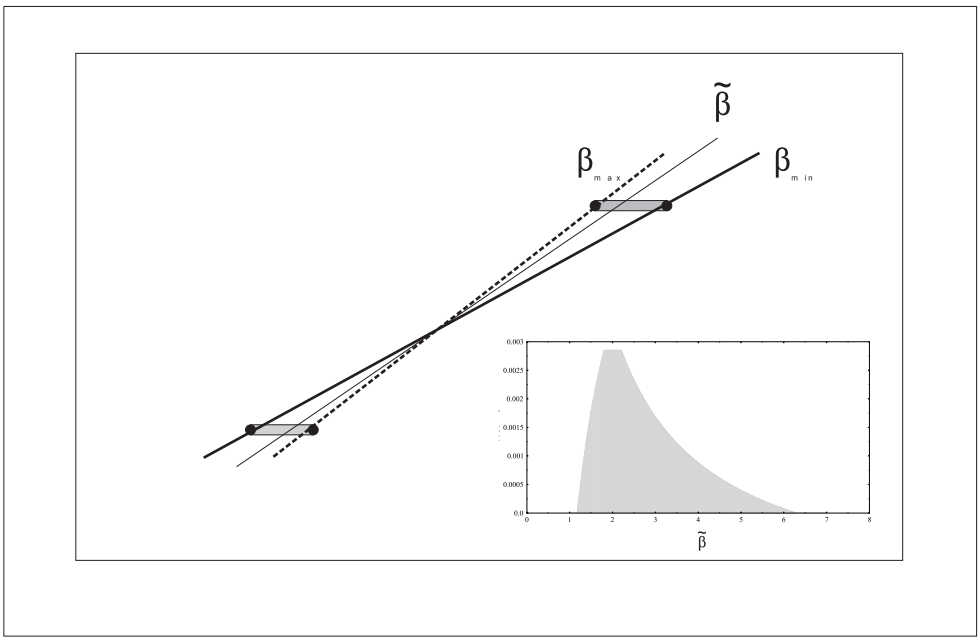

Figure 4.17: Diagram of the relationship between $\hat{\beta}$, β_{max} and β_{min}

In this example the data represented are two probability distributions. It is apparent that a number of lines can be fitted that will pass through the two probability distributions, though the gradient of these lines ($\tilde{\beta}$) will fall between the maximum (β_{max}) and minimum(β_{min}) possible for the data represented. If every possible candidate line is fitted to these data, then it is possible to build up a probability distribution for the "true" gradient of the line represented by the data. A typical distribution is shown in Figure 4.17.

In practice there are an infinite number of $\tilde{\beta}$ that can be fitted to such

data, and some method for estimating the probability distribution needs to be implemented. In the analyses that follow the distribution for $\tilde{\beta}$ has been fitted by incrementally generating $\tilde{\beta}$ over 1000 steps in the interval (1,4). For each $\tilde{\beta}$ 1000 possible lines each with an intercept incrementally generated over 1000 steps in the interval (intercept$_{min}$,intercept$_{max}$) were fitted to the data. In this manner the relative probability of any $\tilde{\beta}$ can be generated and a normalised probability distribution produced.

In the case at hand the $\tilde{\beta}$ corresponds to $\hat{y}$, and we can therefore use the data to infer distributions for the $\hat{y}$. As we are dealing with distributions any analysis will not return tight estimation intervals, and as an example of the type of distributions we may expect it is useful to conduct a simulation of what would be observed if the data observed a perfect root time relationship. Figures 4.18-4.20 show the probability distributions for data that have been generated using Equation 4.9 over the same temperature and duration as the experimental data. In each case the data correspond to a uniform distribution of width $0.15\mu m$. Table 4.12 shows the range of distribution we may expect from the three sets of experimental data, and it is apparent that the 95 ^{0}C data will show the highest range.

Table 4.12: Expected distribution limits for $\hat{y}$ if the reaction was exactly $\propto \sqrt{t}$

temperature ^{0}C	lower limit	upper limit
95	1.18E+00	6.27E+00
112	1.40E+00	3.32E+00
160	1.28E+00	4.38E+00

The same analysis has been conducted on the induction data presented here, and the resulting probability distributions (*supra vide*:§C.6) can be used to draw inferences regarding the nature of $x(t)$. Table 4.13 presents the absolute limits of the $\hat{y}$ inferred for each experimental

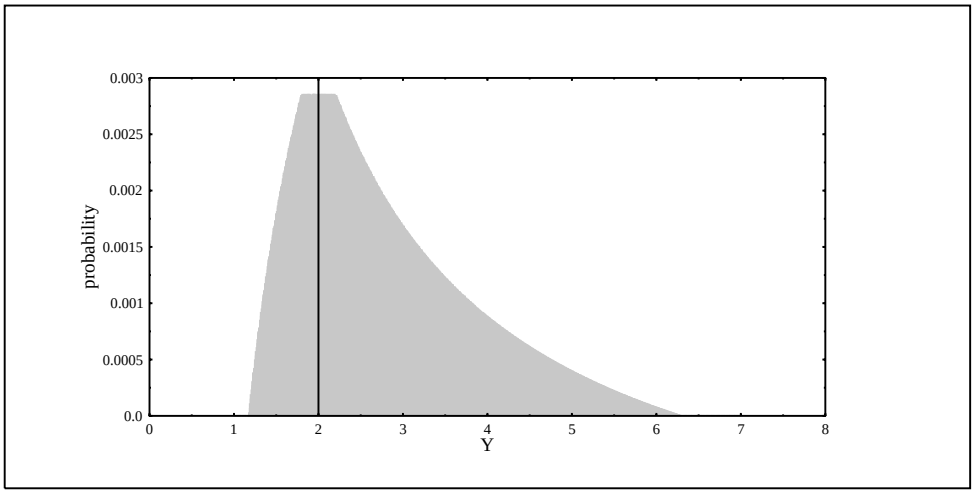

Figure 4.18: Expected probability distribution for 95 ^{0}C induction data conforming to an exact root time dependency

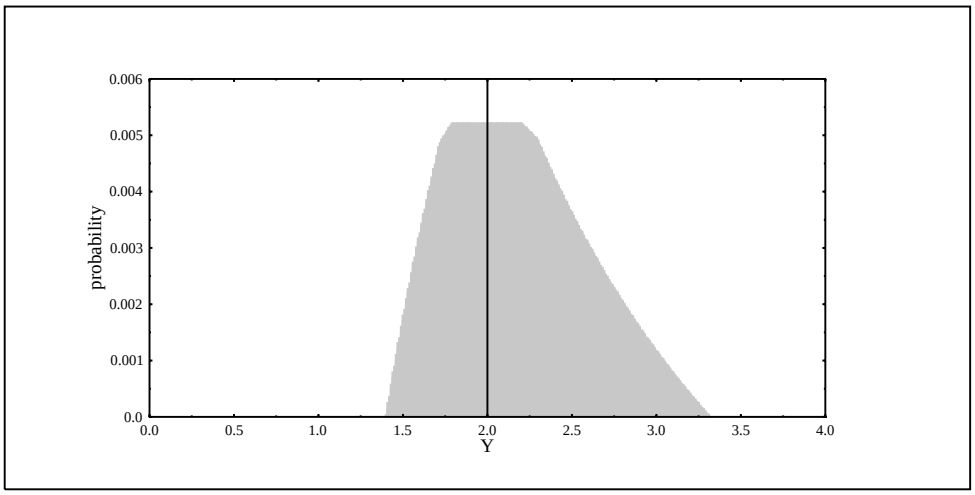

Figure 4.19: Expected probability distribution for 112.5 ^{0}C induction data conforming to an exact root time dependency

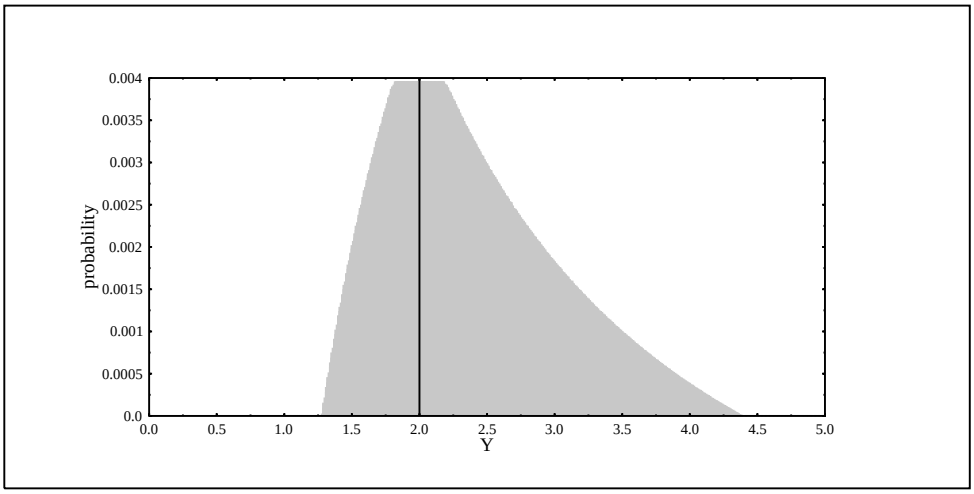

Figure 4.20: Expected probability distribution for 160 ^{0}C induction data conforming to an exact root time dependency

group, and it is apparent that none of the results reject the possibility that $y = 2$. It is also apparent that none of the experimental groups are statistically different at $\alpha = 0.95$.

If the assumption that y is the same for any given set of experimental groups is made, then it is possible to combine the distributions and produce a tighter estimation interval. The combined probability distribution for $\hat{y}$ arising from any set of distributions $\hat{y}_i$ can be calculated using the following equation

$$p(\hat{y}) = \frac{1}{v} \prod p(\hat{y}_i)$$

Where v is a normalising factor and the $p(\hat{y}_i)$ are the distributions calculated in the analysis described above.

Table 4.13: Estimated $\hat{y}$ for each experimental group

Experimental Group	Lower 95 % C.I.	Upper 95 % C.I.
Ben Lomond 95	1.52	3.09
Ben Lomond 112.5	1.56	3.85
Ben Lomond 160	1.48	2.22
Hall's Pass	1.33	9.62
Huruiki	1.63	4.37
Kaeo 11	1.51	3.92
Huruiki 12 95	1.43	5.51
Huruiki 12 160	1.29	2.34
Waiere	1.39	3.15
Mayor Island 95	1.69	4.70
Waiere 160	0.94	2.22
Raumata	1.22	9.62
sc 95	1.11	9.62
sc 160	1.18	5.22
Taumou	1.27	2.54
Te Ahumata 95	1.25	2.73
Taumou Raumata 160	1.74	2.86

Temperature Dependence of $x(t)$

The data presented here allow a test of the form of $x(t)$ over the range 95-160 ^{0}C. The data presented in Table 4.13 show that there is no significant difference between the temperature regimes within any glass type. If the data for each temperature regime is combined under the assumption that $x(t)$ is the same for the glasses used in the experiments at any given temperature then the resulting distributions (Figures 4.21-4.23;Table 4.14) return no significant difference.

Table 4.14: $\hat{y}$ inference intervals testing temperature dependence of $x(t)$

Temp(^{0}C)	L 95 % C.I.	U 95 % C.I.	L 68 % C.I.	U 68 % C.I.
95	1.79	2.48	1.92	2.29
112.5	1.75	2.41	1.86	2.21
160	1.76	2.1	1.8	1.99

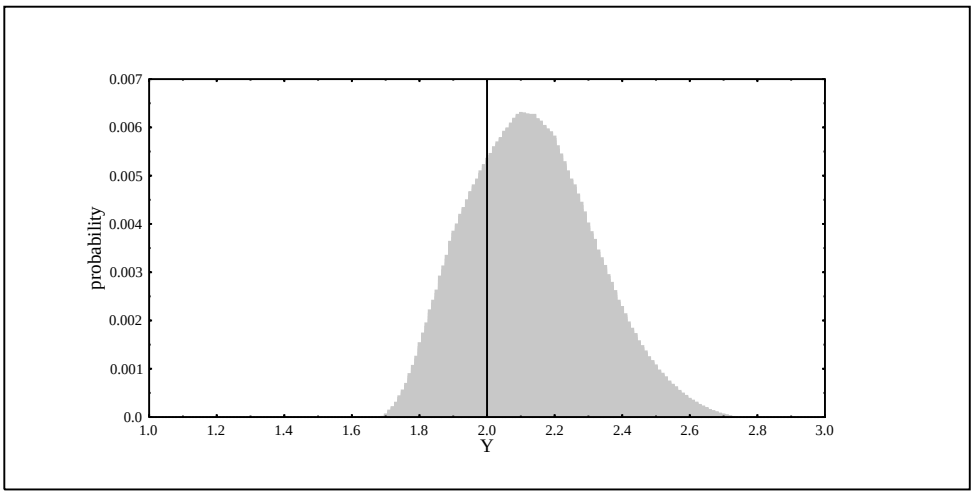

Figure 4.21: Probability distribution of $\hat{y}$ using combined 95 ^{0}C induction data

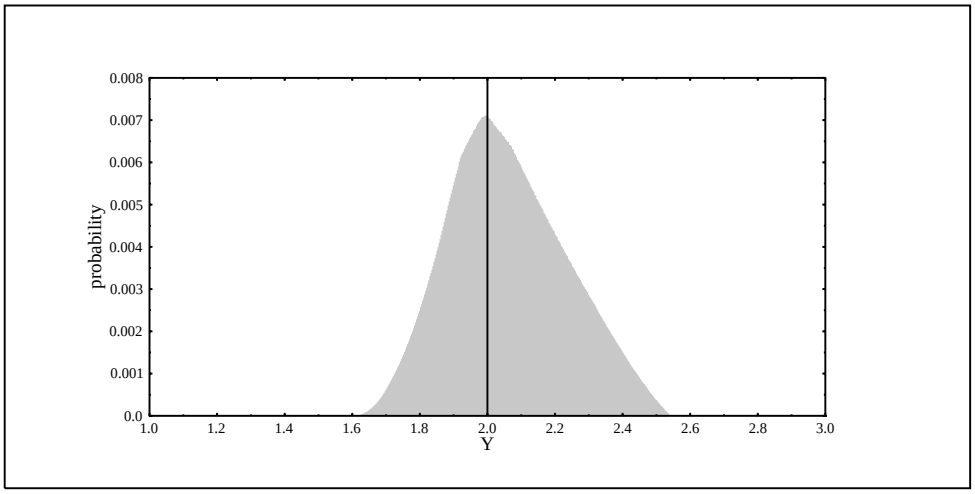

Figure 4.22: Probability distribution of $\hat{y}$ using combined 112.5 ^{0}C induction data

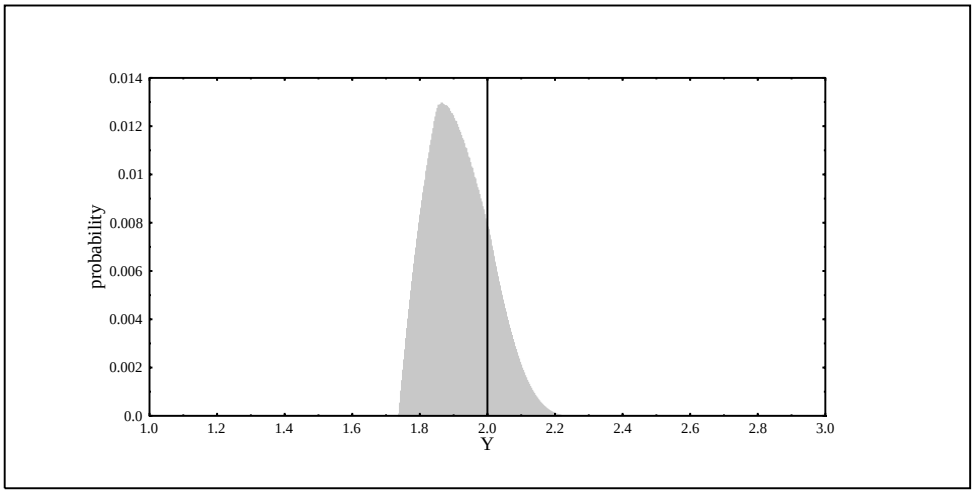

Figure 4.23: Probability distribution of $\hat{y}$ using combined 160 ^{0}C induction data

There does appear to be a trend, with the higher temperature data tending to infer a $\hat{y}$ that falls below 2, in contrast to the lower temperature data that tends to fall above 2. There is no statistical significance to this trend, and none of the results reject a y of 2 at $\alpha = 0.05$. However, the 68% C.I. of the 160 ^{0}C $\hat{y}$ distribution does fall below 2 and it is possible that there is some temperature dependency to the optimal form of $x(t)$. A further examination of this trend can be made with reference to low temperature powder inductions that have been conducted by Wal Ambrose (1976). Ambrose presents a set of data on powdered New Zealand obsidian (Ben Lomond and Mayor Island) that have been induced at temperatures ranging from 20-45 ^{0}C (*supra vide*:§C.7). If these data are regressed using the model presented in Equation 4.16 the estimated $\hat{y}$ are larger than 2 (Table 4.15), in most cases this is significant at $\alpha = 0.05$. This result tends to support the observed trend, though there is the confounding factor that $x(t)$ may vary between hydration in powder and flakes. Thus the observed difference may not purely be a function of temperature, and this possibility should be explored in further experimental work.

In summary, the results do not reject the idea that $x(t)$ is temperature invariant. There is some suggestion of temperature dependency with a trend of $\hat{y}$ rising at lower temperatures and this should be explored in further experimental work. If this tend is a real phenomenon then it would suggest that a simple power relationship of the form presented in Equation 4.2 is insufficient to model $x(t)$.

Glass Dependence of $x(t)$

Under the assumption that $x(t)$ is effectively temperature invariant for the data presented here, it is possible to combine data from within each glass set to examine any potential difference in $x(t)$ between the glasses. The results of this analysis (Table 4.16;Figures 4.24-4.27) show that there

Table 4.15: Estimated $\hat{y}$ for the Ambrose (1976) powder induction data

Source	Size	Temperature	r^2	N	$\hat{y}$	s.e.
Taupo	$< 44\mu m$	40 ^{0}C (NZ)	0.999572	7	2.23189	0.02067
Taupo	$< 44\mu m$	30 ^{0}C (NZ)	0.993734	7	2.28182	0.08104
Taupo	$< 44\mu m$	20 ^{0}C (NZ)	0.998388	7	2.77575	0.04988
Taupo	$44 - 63\mu m$	40 ^{0}C (NZ)	0.854701	7	2.13828	0.394278
M.I.	$38 - 63\mu m$	45 ^{0}C (NZ)	0.997722	7	2.24348	0.04795
M.I.	$38 - 63\mu m$	25 ^{0}C (NZ)	0.992735	6	2.28373	0.09769
M.I.	$44 - 63\mu m$	45 ^{0}C (NZ)	0.993025	7	2.35811	0.08838
M.I.	$44 - 63\mu m$	20 ^{0}C (NZ)	0.9008	7	2.07896	0.308534

is no significant difference in $x(t)$ among the glasses used, and that none of the glass sets reject $\hat{y} = 2$. There does appear to be some contrast between the Te Ahumata results and those from the other sources, with the Te Ahumata data tending toward higher $\hat{y}$, though this is not statistically significant.

These results are on a representative sample of "green" obsidian from New Zealand, and it is reasonable to accept that the form of $x(t)$ is effectively the same for these sources and that there is no reason to adopt a more complex model than presented in Equation 4.9 for these glasses at least. While the results are less representative for "grey" obsidian the data do suggest that $x(t)$ model form is constant for these glasses also. It is difficult to extrapolate these results to glasses of significantly different chemical and physical structure. While the suggestion is that $x(t)$ model form is effectively constant for most New Zealand obsidian, and by association glasses of similar composition, this is not guaranteed for other glasses.

Table 4.16: $\hat{y}$ inference intervals testing glass dependence of $x(t)$

Source	U 95 % C.I.	L 95 % C.I.	U 68 % C.I.	L 95 % C.I.
Ben Lomond	1.69	2.16	1.8	2.1
Kaeo	1.62	2.22	1.71	2.05
Mayor Island	1.75	2.19	1.82	2.08
Te Ahumata	1.78	2.46	1.88	2.26

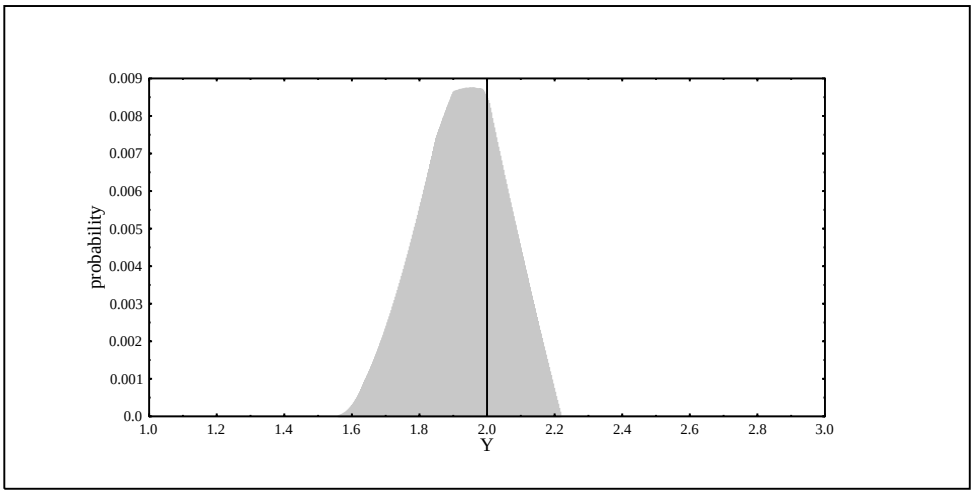

Figure 4.24: Probability distribution of $\hat{y}$ using combined Ben Lomond induction data

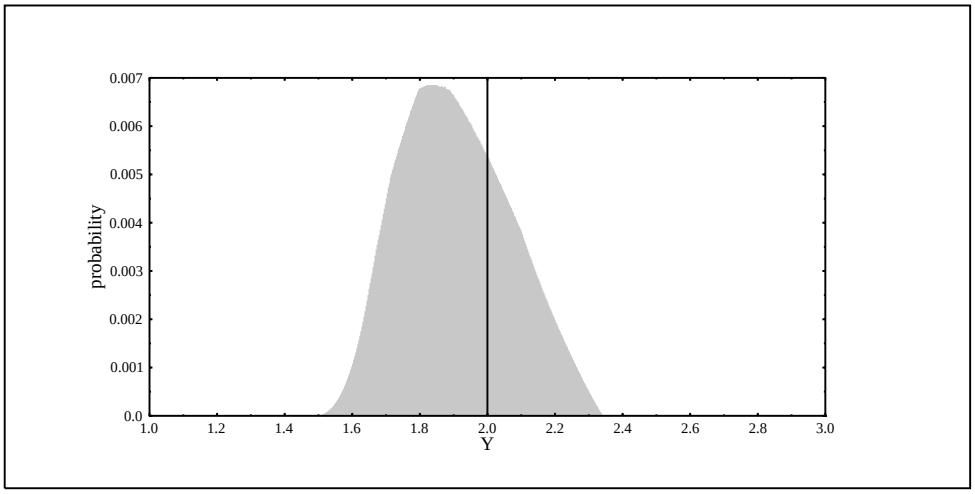

Figure 4.25: Probability distribution of $\hat{y}$ using combined Kaeo induction data

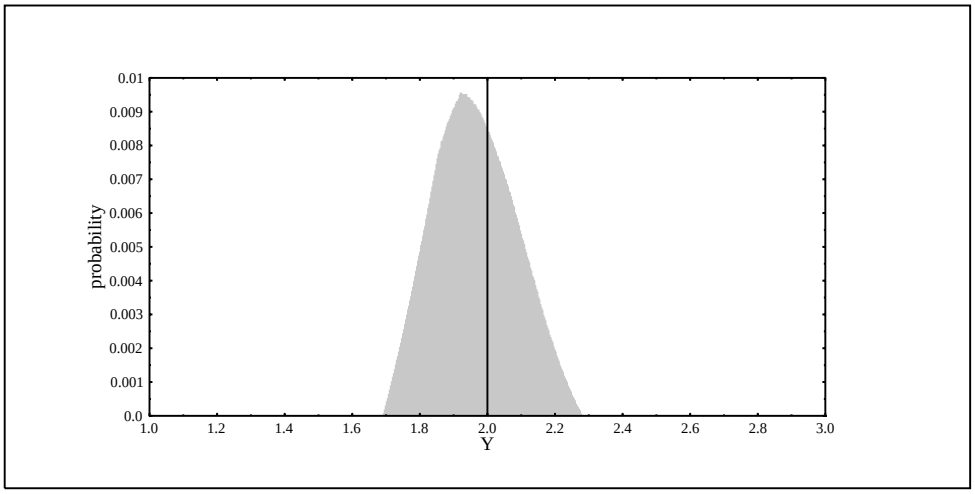

Figure 4.26: Probability distribution of $\hat{y}$ using combined Mayor Island induction data

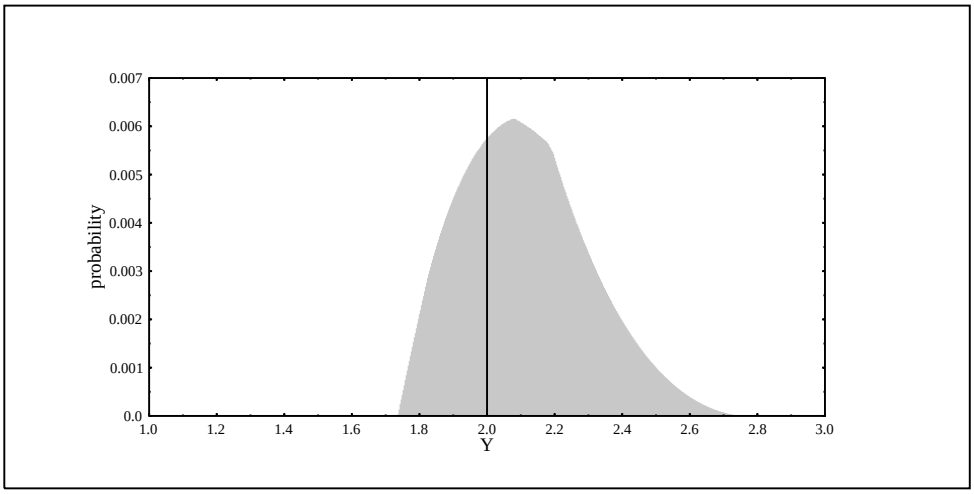

Figure 4.27: Probability distribution of $\hat{y}$ using combined Te Ahumata induction data

Small Rims

In order to use the available data to examine any relationship between $x(t)$ and hydration extent it is useful to make reference to previously published experimental data (Table 4.17;*supra vide*:§C.7).

As it is unclear how the associated measurement errors have been obtained I have treated the available data as point estimates and conducted a regression using the model presented in Equation 4.16. If we use this data in combination with the similar small rim data presented in Table 4.11 we can assess the dependence of $\hat{y}$ on hydration extent by creating a "large" rim group ($x_{max} > 1.5\mu m$) and a "small" rim group ($X_{max} \leqslant 1.5\mu m$) and testing the significance of any difference in fitted $\hat{y}$ between the two sets. In this analysis the two datasets divide into a "small" rims set of the data presented in this thesis plus the results published by Tsong *et al.* (1981), and a "large" set consisting of the remaining data presented in Table 4.17. I have tested for statistical difference in fitted $\hat{y}$ using an independent samples t-test which returned the

Table 4.17: Results of fitting $\hat{y}$ to previously published induction data

Source	Size	r^2	N	$\hat{y}$	s.e.
Tsong[a]	0.25	0.987965482		2.272303161	0.144793516
Iceland 100 ^{0}C [b]	7	0.950336723	12	1.51889698	0.109801241
Iceland 95 ^{0}C [b]	3	0.904475988	5	1.587764409	0.297908704
Iceland 150 ^{0}C [b]	5.4	0.988854415	7	2.203214082	0.104606085
Iceland 195 ^{0}C [b]	11.7	0.995128719	4	1.958966219	0.096915646
Sugar loaf ^{0}C [c]	14.7	0.982284993	4	1.891840089	0.179647563
SugarLoaf ^{0}C [d]	7.1	0.993218713	5	1.835108793	0.087545698
Government Mountain 200 ^{0}C [e]	5.4	0.562445312	4	1.38655804	0.864766935
Rio Grande gravel group II 200 ^{0}C [e]	5.2	0.948306302	4	2.098504192	0.346449012
Vulture 200 ^{0}C [e]	4.52	0.94326769	4	1.791501286	0.310670403
antelope wells 150 ^{0}C [e]	3.62	0.992295415	5	2.1193596	0.107819712
Sugar Loaf flow 2-1 [f]	6.9	0.995032887	3	1.802405451	0.127346138
Sugar Loaf flow 2-2 [f]	6.2	0.984423712	3	1.594838675	0.200612372
Sugar Loaf flow 2-3 [f]	9.2	0.99479773	3	1.682253041	0.121652318
Sugar Loaf flow 2-4 [f]	6.8	0.972683073	3	1.987326135	0.33304229
Sugar Loaf flow 2-5 [f]	8.6	0.96581652	3	1.824685477	0.343280263
Sugar Loaf flow 2-6 [f]	7.2	0.88986656	3	1.831060859	0.644169174
Sugar Loaf [g]	8.9	0.994941648	4	2.078319919	0.104785965
Sugar Loaf [g]	5.3	0.971606872	4	2.09352694	0.253060806

[a] (Tsong *et al.* 1981)

[b] (Friedman 1976)

[c] (Mazer *et al.* 1991)

[d] (Michels *et al.* 1983)

[e] (Stevenson *et al.* 1987)

[f] (Ericson 1989)

[g] (Stevenson and Scheetz 1989*a*)

following results:

Group Statistics

	$\hat{y}$	N	Mean	Std. Deviation	Std. Error Mean
Rim Size	"Small"	18	1.969507281	0.272777408	0.064294252
	"Large"	27	2.009722009	0.387982984	0.07466736

Independent Samples Test

		t-test for Equality of Means		
		t	df	Sig. (2-tailed)
Rim Size	Equal variances assumed	-0.380819931	43	0.705211862
	Equal variances not assumed	-0.408130128	42.83421208	0.685211157

These results show that there is no statistical difference between the fitted $\hat{y}$ for the "large" or "small" rims set, The conclusion from this is that $x(t)$ is effectively size invariant for rims in the range $\approx (0, 10)\mu m$.

This result is useful as it allows us to make use of the $\hat{y}$ presented in Tables 4.11 & 4.17 to further explore the question of whether the fitted $\hat{y}$ exhibit temperature dependency. We can regress the fitted $\hat{y}$ from Tables 4.11 & 4.17 against the temperature of the induction experiment to determine if there is a significant temperature dependency. The results from this regression (Table 4.18) show that there is a statistically insignificant temperature dependency exhibited by the fitted $\hat{y}$ for this overall data set. While this result is valid for obsidian in general it may well be the case that different glasses deviate slightly from this pattern, and it would still be sensible to conduct a further examination of the temperature dependency of $x(t)$ for New Zealand obsidian.

Table 4.18: Results of regressing fitted $\hat{y}$ against temperature

Regression Statistics	
Multiple R	0.266361466
R^2	0.070948431
Adjusted R^2	0.037768018
Standard Error	0.263474486
Observations	30

ANOVA

	df	SS	MS	F	Significance F
Regression	1	0.148435622	0.148435622	2.138262425	0.154798905
Residual	28	1.943726531	0.069418805		
Total	29	2.092162153			

Model

	Coefficients	Standard Error	t Stat	P-value
Intercept	2.17695234	0.173086008	12.57728668	4.87786E-13
X Variable 1	-0.001785527	0.001221057	-1.462279872	0.154798905

Summary

The previous analysis has demonstrated that $x(t)$ is effectively size and temperature invariant for obsidian in general. For New Zealand obsidian specifically it has been established that $x(t)$ is glass independent for the "green" obsidian, and most likely for the majority of the "greys" as well (certainly Ben Lomond and Te Ahumata). There is some suggestion of a temperature dependency to the $x(t)$ model form for New Zealand obsidian, but this is statistically insignificant and there is no overall trend for obsidian in general. This possibility should be examined in further research.

In terms of New Zealand obsidian the preceding analysis allows us to make the assumption that we can combine all of the $\hat{y}$ probability distributions (*infra vide*:§4.6.2) generated for the experimental inductions presented in this thesis in order to produce a tight estimate for the optimum parameter in Equation 4.13. The results (Table 4.19;Figure 4.28) show that the optimum parameter for Equation 4.13 falls in the interval 1.82-2.11 ($\alpha = 0.05$) and that we cannot reject $y = 2$ as the optimum parameter when modelling $x(t)$ using Equation 4.13. Thus on the basis of the current evidence we accept that $x(t)$ can be usefully modelled by the theoretically motivated relationship

$$x^2 = kt$$

and further that this model is at worst applicable to all "green" and some "grey" obsidian in New Zealand and is of an effectively temperature invariant form.

4.6.3 The Temperature Dependence of Hydration Rates

As outlined previously it has been experimentally demonstrated that the rate of hydration is temperature dependant and that there is a theoret-

Table 4.19: Probability distribution for $\hat{y}$ using all induction data combined

Lower 95% C.I.	Upper 95% C.I	Lower 68% C.I	Upper 68% C.I
1.82	2.11	1.88	2.03

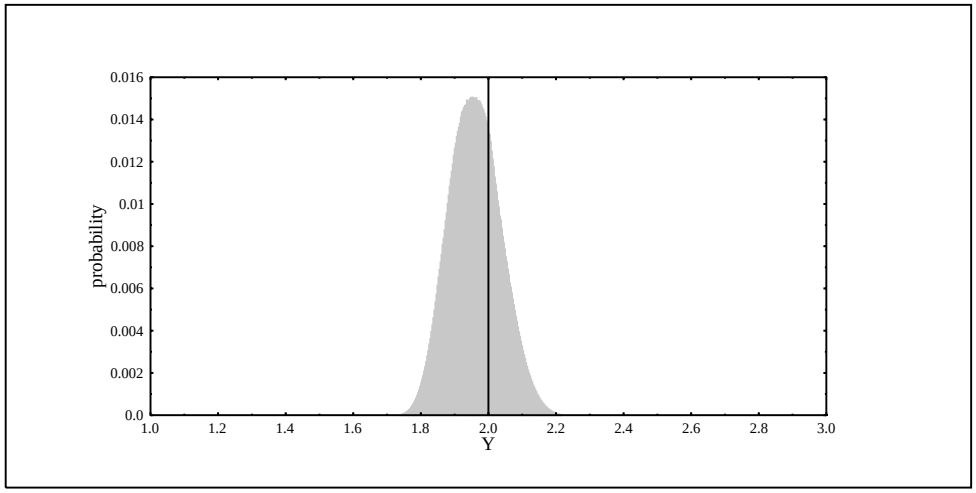

Figure 4.28: Probability distribution of $\hat{y}$ using all induction data combined

ical basis for describing this relationship (*infra vide*:§4.4.2). Thus while it has been established that the form of $x(t)$ is effectively temperature invariant (*infra vide*:§4.6.2) the parameters used to model $x(t)$ won't be. In terms of the model discussed in the preceding section; *i.e.*

$$x^2 = kt$$

this means that k will vary as a function of temperature, and for the purposes of OHD it is necessary to be able to model this temperature dependence for any dated artefact. As outlined previously (*supra vide*:§4.4.2) we would expect the temperature dependence of k to be modelled by an Arrhenius type relationship of the form

$$k(T) = TAexp\left(\frac{-E}{RT}\right) \tag{4.17}$$

though a simplified model without a pre-exponential temperature factor such as

$$k(T) = Aexp\left(\frac{-E}{RT}\right) \tag{4.18}$$

has been proposed as an accurate model of $k(T)$ for obsidian hydration (Ambrose 1976; Friedman 1976).

The primary purpose of this section is to establish whether a model for $k(T)$ such as presented in Equation 4.17 or 4.18 is valid over the temperature range occurring between ambient and high temperature induction's ($\approx$ 0-160 ^{0}C). Establishing this validity has two purposes

1. if the model is accurate over this temperature range, then it is reasonable to apply the model to estimating $k(T)$ for the purposes of OHD; This is fundamental to estimating $x(t)$.

2. if the model for $k(T)$ is valid over this temperature range, then it is possible to use the results of high temperature induction experiments to estimate ambient hydration rates.

Appropriate models for $k(T)$ can be examined through the experimental data presented in this thesis in conjunction with measurements on low temperature samples induced by Wal Ambrose (*infra vide*:§C.1). In total this combined dataset corresponds to k measured for 51 experimental conditions. A number of these conditions are essentially replicates where different glass samples from the same source have been hydrated. In this circumstance the results from within each general source have been combined resulting in a dataset comprising 38 estimated k on ten general sources of obsidian over a temperature range of 40-160 ^{0}C (Table 4.20). k has been estimated for each experimental condition as uniformly distributed between $k_{min} = max\left(\frac{Time}{x^2_{lower}}\right)$ and $k_{max} min\left(\frac{Time}{x^2_{upper}}\right)$[3], with a point source estimate ($\bar{k}$) being generated as $\bar{k} = \frac{k_{min}+k_{max}}{2}$.

Table 4.20: Measured parameters for $k(T)$

Source	T (^{0}C)	k_{min}	k_{max}	$\bar{k}$
Ben Lomond	95	0.014	0.016	0.015
Ben Lomond	112.5	0.043	0.062	0.052
Ben Lomond	160	0.851	0.911	0.881
Hall's Pass	95	0.008	0.011	0.010
Hall's Pass	125	0.064	0.081	0.073
Huruiki	95	0.013	0.015	0.014
Huruiki	107	0.029	0.045	0.037
Huruiki	112.5	0.043	0.058	0.050
Huruiki	125	0.088	0.131	0.109
Kaeo	95	0.012	0.014	0.013
Kaeo	107	0.03	0.035	0.033
Kaeo	112.5	0.044	0.057	0.050

continued on the next page

[3] $x_{lower} = x-$ measurement error; $x_{upper} = x+$ measurement error

Table 4.20: *continued*

Source	T (^{0}C)	k_{min}	k_{max}	$\bar{k}$
Kaeo	125	0.108	0.124	0.116
Kaeo	160	0.744	0.822	0.783
Mayor Island	95	0.009	0.01	0.010
Te	107	0.02	0.03	0.025
Te	112.5	0.028	0.043	0.036
Te	160	0.569	0.658	0.614
Te (Ambrose)	40	4.92E-05	6.50E-05	5.711E-05
Raumata	95	0.008	0.011	0.010
Raumata	112.5	0.028	0.043	0.036
Raumata	125	0.073	0.081	0.077
Staircase	95	0.008	0.013	0.011
Staircase	125	0.072	0.08	0.076
Staircase	160	0.518	0.689	0.603
Tairua	112.5	0.04	0.053	0.046
Tairua	125	0.092	0.115	0.103
Taumou	107	0.033	0.052	0.042
Taumou	112.5	0.054	0.069	0.061
Taumou	125	0.115	0.136	0.125
Te Ahumata	95	0.018	0.021	0.019
Te Ahumata	107	0.035	0.058	0.047
Te Ahumata	112.5	0.056	0.077	0.067
Te Ahumata	125	0.117	0.199	0.158
Te Ahumata	160	1.095	1.216	1.155
Whitipourua	107	0.051	0.057	0.054
Whitipourua	112.5	0.073	0.096	0.084
Whitipourua	125	0.152	0.194	0.173

Similar to the data treated in the previous section, the data analysed

here represent distributions rather than points. Though as the current interest is in establishing the validity of the relationships presented in Equations 4.17 & 4.18 rather than parameter estimation it is sufficient to treat the data as point estimates. The experimental results have been tested by fitting the following models to the data:

$$ln\left(\frac{k_{iT}}{T}\right) = \beta_{0i} + \frac{\beta_{1i}}{T} + \sigma_{iT} \tag{4.19}$$

$$ln(k_{iT}) = \beta_{0i} + \frac{\beta_{1i}}{T} + \sigma_{iT} \tag{4.20}$$

which correspond directly to the relationships presented in Equations 4.17 & 4.18 and allow for a difference in model parameters among the sources. Here the β_{0i} represent glass specific pre-exponential components (A in Equations 4.17 & 4.18) and the β_{1i} represent the glass specific activation energy (E in Equations 4.17 & 4.18) as

$$\beta_{1i} = \frac{E_i}{R = 8.314}$$

As the low temperature Ambrose results are on different glasses[4] to those used in the higher temperature induction experiments an initial analysis was made by fitting Equations 4.19 & 4.20 to the results arising from induction's conducted in this thesis (Table 4.21; Figures 4.29 & 4.30). In both cases the analysis R^2 was 0.999, indicating an excellent model fit. The normality of the residuals in each analysis were tested via a 1 sample K-S test, and in both cases no significant residual non-normality is indicated (Equation 4.19 pval=0.82; Equation 4.20 pval=0.56).

These results show that an Arrhenius type relationship describes $k(T)$ to a high degree of precision over the temperature range 95-160 ^{0}C. It is apparent from the preceding analyses that there is very little difference in activation energy ($\propto \hat{\beta}_{1i}$ and slope in Figures 4.29 & 4.30) among New

[4] different samples as opposed to sources

Table 4.21: Results of fitting equations 4.19 & 4.20 to the high temperature data from Table 4.20

Source	$\hat{\beta}_0$	s.e.	$\hat{\beta}_1$	s.e.
		Equation 4.19		
Ben Lomond	15.91515395	0.153367005	-9576.297593	60.26075928
Huruiki	16.1148653	1.323283295	-9665.924145	506.2482249
Kaeo	15.92276767	0.60156783	-9609.944424	235.3760391
Tairua	15.40448994	0	-9421.238299	0
Te Ahumata	16.38017606	0.228657869	-9654.427537	89.46719035
Whitipirorua	15.65647094	1.945353771	-9309.343568	754.3429932
Taumou	9.121458252	1.98593689	-6914.489931	770.0797663
Hall's Pass	14.251455	0	-9120.066031	0
Mayor Island	14.26592537	0.631582369	-9102.571293	246.0684277
Raumata	16.13225929	0.475146114	-9809.332043	182.1647133
Staircase	15.40941887	0.498693727	-9533.434222	198.0754915
		Equation 4.20		
Source	$\hat{\beta}_0$	s.e.	$\hat{\beta}_1$	s.e.
Ben Lomond	22.9104891	0.134677927	-9976.863294	52.91747162
Huruiki	23.06248274	1.31536714	-10048.61251	503.2197429
Kaeo	22.91700322	0.587191981	-10010.35385	229.7511865
Tairua	22.37545425	0	-9813.071846	0
Te Ahumata	23.3744116	0.216916085	-10054.83696	84.87297079
Whitipirorua	22.62144253	1.939850512	-9698.809517	752.2090135
Taumou	16.08642985	1.98043363	-7303.95588	767.9457866
Hall's Pass	21.199626	0	-9502.824419	0
Mayor Island	21.26298761	0.617815527	-9503.914984	240.7047803
Raumata	23.07891881	0.464423628	-10191.60511	178.0538541
Staircase	22.40025042	0.522241532	-9932.301546	207.4284126

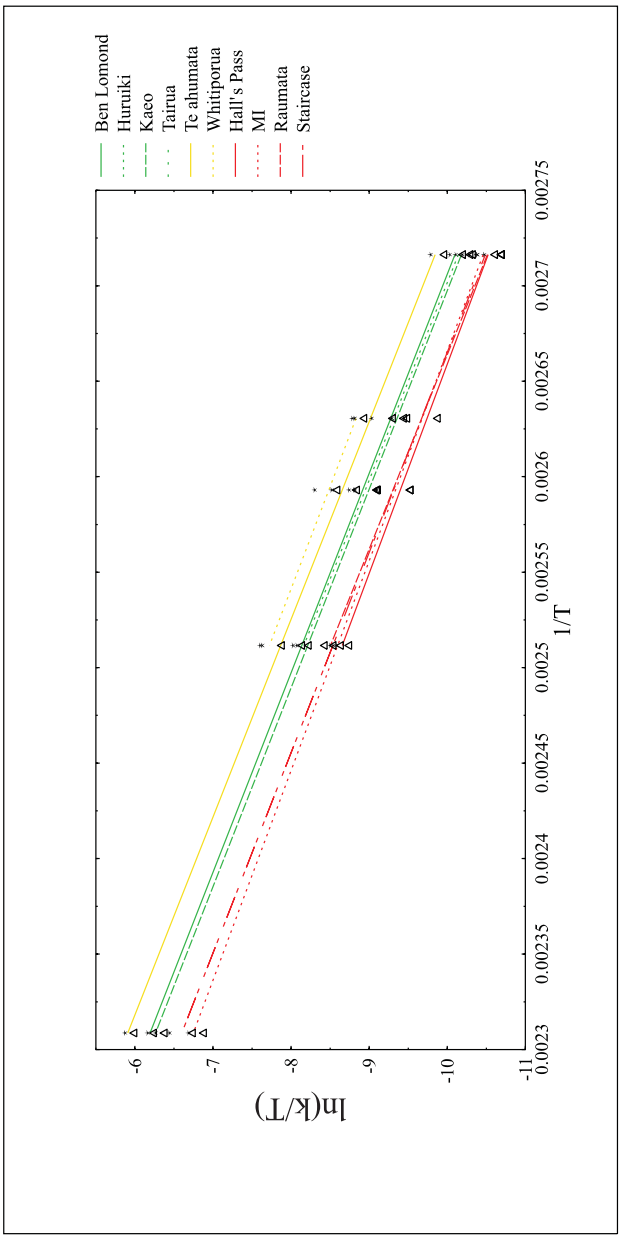

Figure 4.29: Data and fitted regression line for $ln(k/T)$ vs $1/T$ for induction data 95-160 ^{0}C

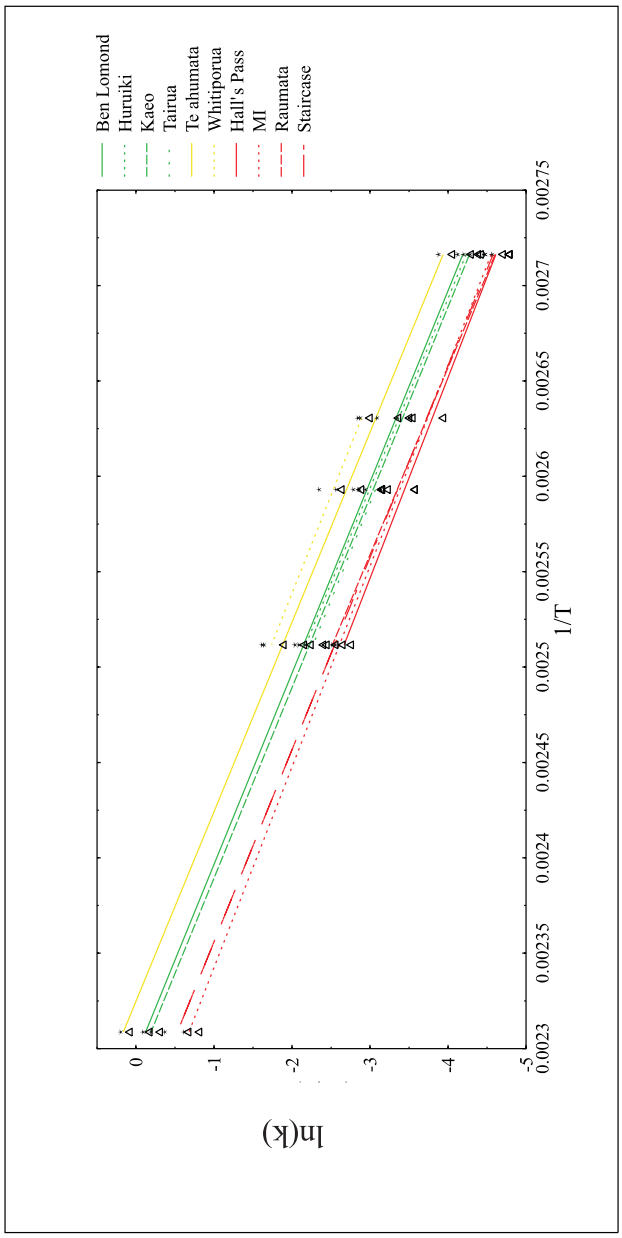

Figure 4.30: Data and fitted regression line for $ln(k)$ vs $1/T$ for induction data 95-160 ^{0}C

Zealand obsidian, and it is also apparent that the pre-exponential term ($\hat{\beta}_{0i}$ and intercept in Figures 4.29 & 4.30) falls into three broad clusters (coded yellow, green and red in Figures 4.29 & 4.30). One of these (red) corresponds to Mayor Island sources, and it is apparent that there is no significant difference in activation energy (E) or pre-exponential component (A) among these at $\alpha = 0.05$ (Table 4.21). Thus it is reasonable to combine the overall Mayor Island results with the low temperature Ambrose results to examine $k(T)$ over a wider temperature interval for the Mayor Island source in general. Analysis of these combined results (Figures 4.31 & 4.32) again demonstrates that an type model describes $k(T)$ to a high precision. Under both models the R^2 is 0.999, and a 1 sample K-S test does not indicate any significant residual non-normality under either model (Equation 4.19 pval=0.59; Equation 4.20 pval=0.70). Thus this result indicates that $k(T)$, for Mayor Island obsidian at least, can be described with high precision over the temperature range 40-160 ^{0}C by the relationships presented in Equations 4.17 & 4.18. As this result is derived from a dataset incorporating readings from a range of glass samples the result is conservative.

Summary

Analysis of the available data has shown that the Arrhenius type relationships presented in Equations 4.17 & 4.18 describes $k(t)$ to a high precision over the temperature range 95-160 ^{0}C for all obsidian samples examined. Further, these models have been demonstrated to apply to Mayor Island obsidian over the temperature range 40-160 ^{0}C. As the observed $k(T)$ for all obsidian samples in the temperature range 95-160 ^{0}C is highly similar, and there is no theoretical basis for expecting any difference in the form of $k(T)$ between the glasses, we can accept that Equations 4.17 & 4.18 model $k(T)$ over the temperature range ambient-160 ^{0}C for obsidian in general. As both relationships model $k(T)$ to

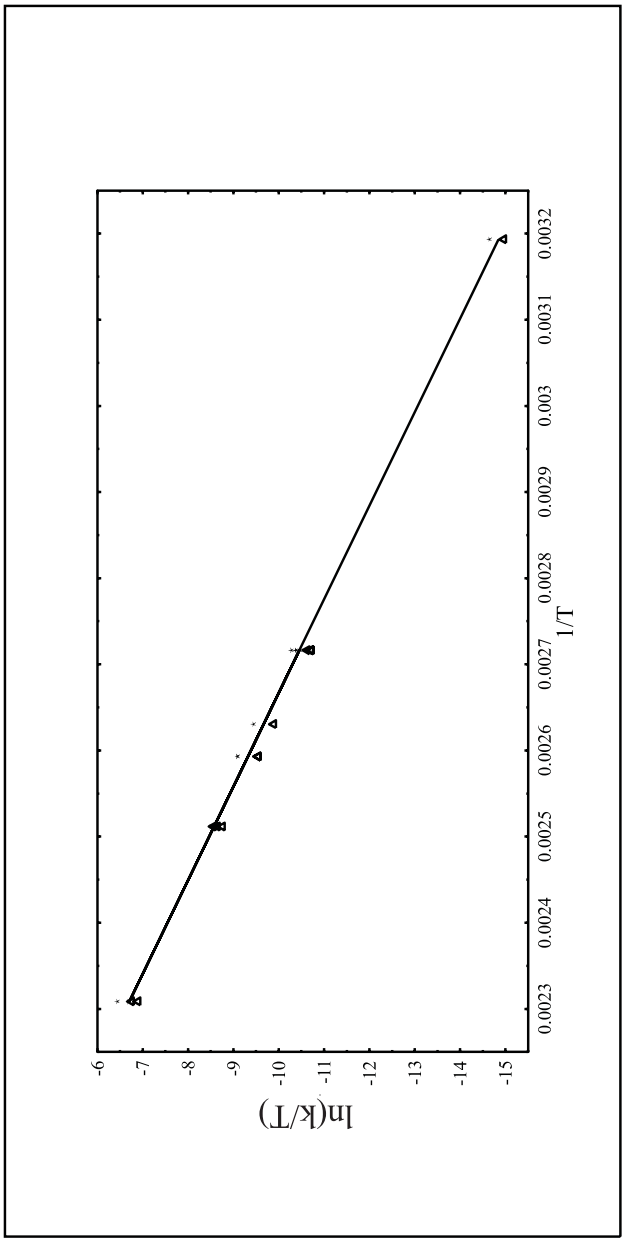

Figure 4.31: Data and fitted regression line for $ln(k/T)$ vs $1/T$ for combined Mayor Island data 40-160 ^{0}C

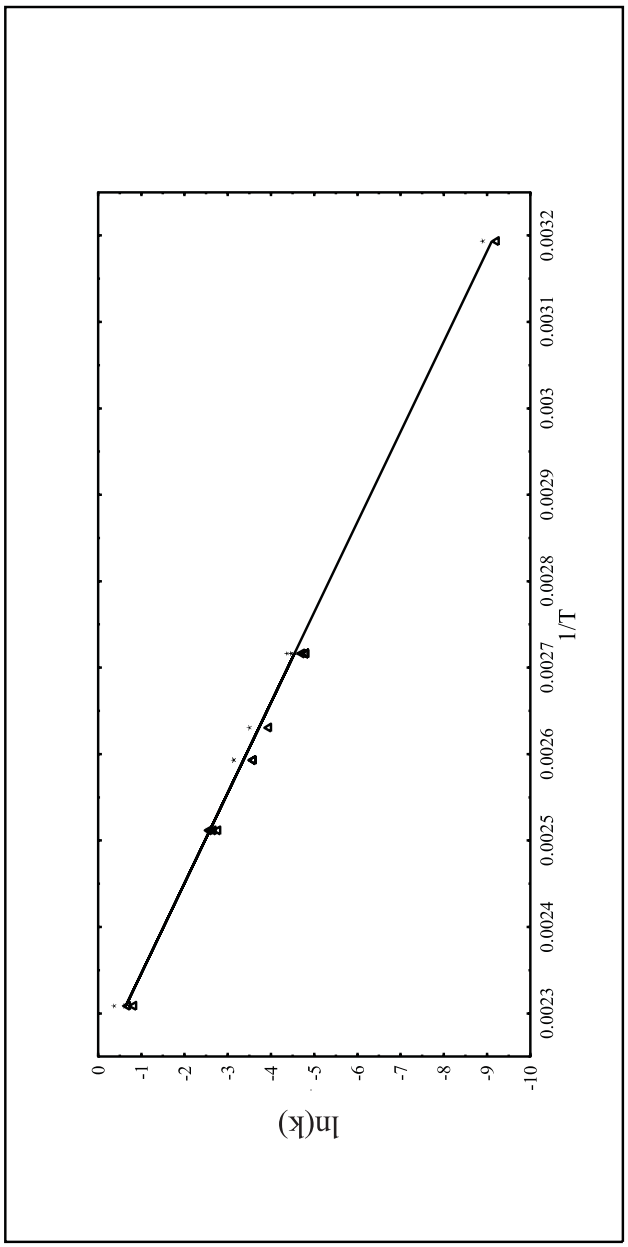

Figure 4.32: Data and fitted regression line for $ln(k)$ vs $1/T$ for combined Mayor Island data 40-160 ^{0}C

a similar precision over a temperature range that approximately corresponds to the range seen between ambient and experimental hydration it is probably most convenient to use the simpler relationship presented in Equation 4.18. This result demonstrates that the proposed model can be used to estimate $k(T)$ in applied OHD, and that high temperature induction data such as that presented in this thesis can be extrapolated to estimate model parameters for $k(T)$ at ambient temperatures.

4.6.4 The Influence of Environmental Variables

Environmental variables other than temperature can exert a significant influence on the apparent hydration rate of obsidian (*infra vide*:§4.4.2). In order to assess the effects of the principal environmental factors that may influence apparent hydration rate, experimental hydration's were conducted in 10 different environments, allowing a comparison of the effects of these conditions.

The principal environmental variable tested was solution pH. Ambient pH will affect the rate of dissolution of the glass surface and additionally if ionic inter-diffusion is a significant hydration mechanism, solution pH may affect the diffusion gradient and hence hydration rate. The interest in this experiment was in establishing whether a significant pH effect was noticeable for obsidian within the extremes likely to occur in an archaeological environment, thus five pH conditions were tested pH 3.5, 6.2, 6.8, 8, 10.5 (*infra vide*:§4.5.3).

A second environmental variable of interest is the solute cation concentration. If ionic inter-diffusion is a significant hydration mechanism then solute cation concentration, particularly Na^+ concentration, may affect the diffusion gradient and hence hydration rate. It is important to establish any influence this environmental variable may have, as coastal locations may be expected to experience elevated Na^+ levels due to ex-

posure to sea brine, either through direct contact or via spray. Three Na^+ concentration levels were tested 0.1M, 0.5M, 2M with the 6.8 pH condition acting as a 0M control.

The final contrast tested was whether interaction with the archaeological matrix exerted any influence on the hydration rate. Only two environments were tested. One was a sample of pure silica sand, and the other was a sample of organic clay/loam.

All of the test environments were compared to the results of a vapour induction conducted during the same run. Five sources of glass were used in these experiments (*supra vide*:§C.4). However one of these sources has produced aberrant results in previous induction's and will not be considered here.

An analysis of the influence of the environments was conducted via fitting the model

$$x_{cg} = G + C + \sigma \tag{4.21}$$

Where the fitted G are differences observed due to the type of glass, and C is the effect due to the environmental condition. Thus the fitted C represent a measure of the influence of the environment on the hydration rate. This is a factorial model with no interactions and can be analysed via any general factorial method. In this case I used the GLM procedure on SPSS 7.5.1 with the following syntax

```
GLM
  rim  BY glass condition
  /METHOD = SSTYPE(3)
  /INTERCEPT = INCLUDE
  /PRINT = DESCRIPTIVE ETASQ PARAMETER
  /CRITERIA = ALPHA(.05)
  /DESIGN = glass condition .
```

The parameter estimates associated with this analysis (Table 4.22) show that while there is the expected difference in rim thickness between the glasses there is no significant trend arising from induction condition at $\alpha = 0.05$. Though it should be noted that the high pH condition(pH 10.5) is significant at $\alpha = 0.1$ suggesting that smaller rims have been produced in this environment.

The results of this experiment have all been derived from readings on crystal free portions of the respective rims. This step was taken after it became apparent that the optical rim boundaries were blurred on portions of the rim containing crystallites. This resulted in a variable measurement in these locations in comparison to the measurements made on the clear glass portions. I conclude that this effect is due to differential environmental attack on the glass matrix and crystalline inclusion, with the crystalline inclusions being susceptible to high pH, low pH and 2M brine conditions. On two of the glasses (Ben Lomond, Huruiki) there was no visible rim and a noticeably degraded surface in areas of high crystallite density in contrast to the clear glass sections. This is in contrast to the Kaeo sample which did not show the same degree of crystalline dissolution in spite of a similar level of inclusion. This may have something to do with the nature of the inclusion. In the Ben Lomond and Huruiki samples the crystallites are aligned and the long axis is many orders of magnitude greater than the short axis. In contrast the Kaeo crystallites are randomly oriented and the axis dimensions are far more even. The result of this observation is that crystallite free portions of the flake surface should be analysed where possible, as this will minimise environmental dissolution of the artefact surface.

The result that the only potential trend is due to matrix dissolution in high pH conditions is interesting. It follows on the basis of glass theory that obsidian should be invulnerable to all but extreme pH attack (*infra vide*:§4.4.2) but other trends would have been expected if ionic

exchange is a significant component of the hydration reaction. This is as ionic interdiffusion rates may have been affected by the solute cation concentration and pH. There is no effect of this nature, which suggests that either ionic interdiffusion is not a significant hydration mechanism, or that the surface reaction sites for the ions are limited and become quickly saturated so the effective ionic diffusion gradient is essentially solute concentration and pH independent. The only affect noted due to the solute concentration was that portions of the surface with a high crystallite density experienced dissolution in the 2M brine.

There was no influence apparent due to either of the soil conditions. This was expected for the silica sand, though it was expected that exchange with clay minerals in the soil may have had some influence. Again this effect was not apparent.

Surface Damage

In addition to environmental variables that may influence the actual hydration mechanism, factors that promote surface damage will also influence the apparent hydration rate (Ambrose 2001). Fortunately it is easy to detect surface damage by examination of the artefact surface under a microscope. In this case the sensible protocol is to check each artefact for surface damage, and only analyse damage free portions of hydration rim. An example of this type of factor is biochemical attack. While it was not possible to conduct a simulated biochemical attack experiment, the influence is purely one of surface attack. There is no reason to suspect that biochemical attack would promote apparent rim growth, and as biochemical attack is apparent as surface damage under a microscope it is easy to ensure that the measured rim is not influenced by this factor. In a similar manner we would expect that surface damage may arise from:

- chemical dissolution

Table 4.22: Results of fitting equations 4.19 & 4.20 to the combined Mayor Island data from Table 4.20

Parameter Estimates

Dependent Variable	Parameter	B	Std. Error	t	Sig.
rim	Intercept	0.696	0.020	34.037	0.000
	[glass=7]	-0.005	0.017	-0.300	0.767
	[glass=9]	0.019	0.017	1.115	0.276
	[glass=13]	-0.087	0.017	-5.225	0.000
	[glass=16]	0.000[a]	.	.	.
	[cond.=0.5 M NaCl]	-0.028	0.025	-1.123	0.272
	[cond.=0.1 M NaCl]	-0.019	0.025	-0.749	0.461
	[cond.=2 M NaCl]	-0.039	0.025	-1.572	0.129
	[cond.=pH 8]	-0.008	0.025	-0.324	0.748
	[cond.=pH 10.5]	-0.047	0.025	-1.872	0.073
	[cond.=pH 3.5]	0.016	0.025	0.649	0.523
	[cond.=pH 6.2]	-0.027	0.025	-1.073	0.294
	[cond.= pH 6.8]	-0.001	0.025	-0.050	0.961
	[cond.=V]	0.000[a]	.	.	.

[a] This parameter is set to zero because it is redundant.

- biochemical attack
- in situe abrasion
- damage during excavation
- curatorial damage (*e.g.* "bag wear")

The high pH results also showed an elevated surface dissolution rate for the glass. Fortunately high pH conditions will not be experienced in New Zealand though this may be a factor in some Pacific contexts.

Of final interest in the environment results is the lack of influence of distilled water in comparison to water vapour or silica saturated hydrations. It may well be the case that at lower temperatures the corrosive effect of distilled water on obsidian surfaces diminishes. In light of this it would seem fair to suggest that at ambient temperatures the dissolution of the glass surface by water will be insignificant.

Environmental Summary

The available results have shown that the apparent hydration rate within crystallite free portions of an obsidian surface is fairly independent of environmental conditions. The only trend observed was a slower apparent rim growth under high pH conditions which is almost certainly due to dissolution of the glass matrix and concurs with archaeological observations of the same phenomenon (*e.g.* Ambrose 1994). Other effects may be apparent due to surface damage, but this can be avoided by only analysing damage free surfaces.

Thus the results suggest that if undamaged, crystallite free, rim portions are analysed and ambient pH is not high then no significant environmental influence other than environmental temperature and humidity should be apparent.

4.7 Hydration Parameters: Conclusion

This needs to expand to specify the definition of $x(t,g,e)$ and define the programme through to the end of chapter 12. The fundamental conclusion of this experimental programme is that $x(t)$ can be modelled as

$$x(t) = \sqrt{k(T)t} \tag{4.22}$$

and that the temperature dependant variable $k(T)$can be modelled as

$$k(T) = Aexp\left(\frac{-E}{RT}\right) \tag{4.23}$$

The form of both of these relationships appears to be glass and temperature invariant. There is the possibility of a trend in $x(t)$ model form with temperature. This needs to be examined further, and an appropriate experiment would be based around powder induction's at temperatures ranging from 20-160 ^{0}C. This would enable a consistent examination of $x(t)$ model form as a function of temperature.

The result that an Arrhenius type function can model $k(T)$ over a temperature range that encompasses both ambient and experimental hydration is important. This suggests that it is possible to conduct experimental hydration experiments that can be validly used to estimate ambient hydration rates, and also that the model is appropriate for use in applied OHD.

Unfortunately a similar conclusion cannot yet be drawn regarding the validity of high temperature humidity experiments. The current evidence is equivocal. However, this will not be of significance to the application of OHD in most contexts as effective rH in most archaeological environments is $\approx$ 100% (*supra vide*:§11).

The secondary conclusion of this experimental programme is that if an appropriate measurement protocol is followed then environmental variables other than elevated pH should not be significant. This conclusion

should be re-checked via further experimental work conducted at different temperatures to ensure that none of the effects are temperature dependant, and also a larger number of pH conditions should be tested to set limits on what environmental parameters constitute an insignificant effect to a higher resolution than is currently possible.

Following the conclusions drawn in this chapter the relationships given in Equations 4.22 and 4.23 can be used to define an observation model for obsidian hydration extent. As discussed in Chapter 1 (*infra vide*:§1.2) this allows us to form a likelihood for the OHD chronometric data. However, in order to employ this likelihood in a chronology building exercise we need to be able to choose an appropriate prior term. This basically means developing models that describe the distribution of the parameters governing k. Following Equation 4.23 these are A, E and T. In Chapters 5 –12 that follow we will consider models for these parameters.

Chapter 5

Estimating Hydration Rates

5.1 Introduction

For OHD it is necessary to accurately relate hydration extent to hydration duration for each artefact analysed. While it is possible to define a general model for this relationship $x(t)$ (*infra vide*:§4.7), the parameters will vary depending on the archaeological environment and specific structure of the glass (*infra vide*:§4.7). That is $x(t)$ should most properly be written $x(t,g,e)$; modelling hydration extent as a function of hydration duration(t), glass structure (g) and the ambient environment (e). Thus for each dated artefact it is essential to accurately estimate the specific parameters of the function $x(t,g,e)$. In this chapter and Chapters 6 & 7 that follow we will consider the estimation of glass specific hydration parameters.

As it is not practical to directly measure the artefact specific hydration rate for each sample analysed we must employ some method to estimate the artefact specific hydration parameters g for each artefact dated. The most common approach is to try and define some form of source specific hydration rate and estimate the artefact specific rate by association with a particular source. The use of this approach requires that the nature of the intra-source variability in hydration behaviour is well understood, and further that it is possible to reliably associate artefact and geological source. An improvement upon this base method may be achieved through the use of empirical models describing either variation within sources or within obsidian in general (*e.g.* Stevenson *et al.* 1998). Here these are referred to as attribute rate estimates.

Attribute rates are estimated hydration rates that have been calculated on the basis of measured attributes of an obsidian artefact. Strictly speaking any estimate of hydration parameters for an artefact is an attribute rate, as some attribute of the artefact must be used in the estimation process. In this discussion an attribute rate is an estimation

calculated according to an empirical or theoretical rule that defines a hydration rate based on some measured attribute(s) of an artefact.

In theory attribute rates are attractive. They allow direct estimation of hydration rates based on the measured attributes of an individual artefact. This is particularly useful where the hydration rate of a source may be highly variable, and an improvement in rate estimation may be possible over a simple source rate estimation. However, by the same token it is possible that an inadequately developed attribute index may introduce spurious rate estimates to samples from highly consistent sources. It is important that attribute index estimation methods are developed against a comprehensive reference set of material and that analysis incorporates the measurement uncertainty of both the reference hydration rates and the attribute measurements. If this is not the case then there is the very real risk that the attribute index will reduce rate estimation precision (*e.g. supra vide*:§5.3.4).

The purpose of this chapter is to assess rate indices as general rate estimation models, and for application to New Zealand obsidian in particular. This assessment is based on a set of attribute data (Tables D.1,D.2) generated for a subset of the hydrated samples derived from the experimental program outlined previously (*infra vide*:§4.5).

5.2 The Experimental Dataset

The data set for testing the performance of the rate indices examined here was produced by measuring a suite of factors for a sub-set of the glasses used in the induction program described previously (*infra vide*:§4.5). For this exercise the comparison was amongst the measured hydration rates (k) at 125 ^{0}C for the glasses listed in Table D.1. The comparison has been conducted amongst the 125^{0}C induction results

as a single temperature comparison represents the most simple case of relative predictive model evaluation. The only variation in k should be due to glass composition g as the environmental conditions have been held constant.

The actual samples included within this set were chosen to give both a representative coverage of the range in measured k for the 125^0C induction data and to give a detailed evaluation of intra-source variation within the Mayor Island samples. The evaluation of the Mayor Island samples was conducted as this source is of primary interest in the New Zealand archaeological context, and secondarily as this set acts as a control for the predictive power of the models with respect to intra-source variation.

For each sample the bulk chemical composition has been measured via XRF. As obsidian almost always has crystal inclusions the results of any bulk elemental analysis will be a combination of the vitreous groundmass and crystal components. In order to understand hydration, these components may need to be treated separately as each will have a different influence on hydration rates, and this may be significant for certain glasses. For example, it is possible that the extent and type of crystal inclusion has an influence on hydration. It has been demonstrated that there is sodium depletion in the groundmass surrounding trichites and microlites for instance (Ryan and Brown 1985), and this may well influence ion exchange. Additionally the crystal component can undergo various chemical reactions in addition to those that may take place with the vitreous groundmass. In light of this, measures of the relative volume of crystals and microlites have been made for each of the glasses, and a test has been made to assess whether the bulk elemental XRF data is sufficient to describe the geochemical data, or whether a correction needs to be made in allowance for any crystal inclusions. As a final component of the data base the density of each of the glasses has been

measured.

This data base is not complete for such an analysis, and in particular it would be useful to have Raman spectra for each of the glasses in order to provide a measure of the degree of polymerization for each glass (ratio count of bridging to non-bridging oxygen within the vitreous groundmass). It is possible that the degree of polymerisation will ultimately prove to be a significant factor in controlling hydration rate, as the average energy required for an interstitial jump during diffusion may be lower for a glass of exhibiting a low degree of polymerisation versus a highly polymerised one. The Raman spectra have not been included as there has not been time during the course of this research to develop and implement an appropriate protocol for the analysis. This will be pursued as part of a continuing program of research into obsidian hydration. An additional lack is the absence of data on intrinsic water species content of the different glasses. Again there has been insufficient time to develop a suitable measurement system. Initially the infra-red spectroscopic approach proposed by Newman *et al.* (1986) was attempted, and while results were possible, the precision was insufficient as it rapidly became apparent that there is very little variation in intrinsic water contents in New Zealand obsidian. It will be necessary to adopt a more precise technology for this measurement, and again this will be pursued in ongoing research.

In spite of this apparent lack, the test database does represent a useful tool for the evaluation of many aspects of the hydration process in general, and for that of New Zealand obsidian in particular. The data collection methods are detailed in the following sections.

5.2.1 Sample Density

Stevenson *et al.* (1995) have suggested that density can be used to di-

rectly predict the hydration behaviour of obsidian. They based this on an observed correlation between density and intrinsic hydroxyl content of obsidian. In light of this the density of each sample in the test dataset has been measured. The density measurements were eventually made in distilled water using a surfactant to lower the surface tension.

As an initial step to making the comparative density measurements three repeat measurement experiments were run to determine the measurement accuracy and optimum measurement system for producing consistent ongoing density measurements. An initial experiment was conducted to compare density measurements made Perflouro-Methyldecalin[1] versus distilled water with a surfactant.

The experiment consisted of producing 10 flakes from one homogenous piece of obsidian and then measuring the density of each flake once on each of five consecutive days. In theory all of the flakes should have the same density, though measured density will vary slightly due to effects introduced by size and geometry. Additionally air buoyancy of the samples will vary over time due to relative temperature and air pressure. The experiment conducted in this manner allows a comparison between the two measurement set-ups and an evaluation of the actual measurement precision of the apparatus. This experiment was conducted on using a 4 dp Mettler Balance fitted with a density measurement device.

The results are given in Tables 5.1 & 5.2

The overall standard deviation for the water measurements was 0.0057 versus 0.0024 for those made in the PFMD, though if the results of the very small flake in sample 4 are excluded the standard deviation for the water results drops to 0.0043 vs 0.0024. A paired samples t-test between the water and PFMD results is not significant at $\alpha = 0.05$.

[1] high density low surface tension fluid that has been used to produce high precision density measurements.

Table 5.1: Distilled water repeat measurement results

		Density Measurement (g/cm^3)						
Sample	Weight	#1	#2	#3	#4	#5	$\bar{x}$	σ
1		2.3566	2.3531	2.3410	2.3430	2.3384	2.3464	0.0080
2		2.3549	2.3524	2.3436	2.3460	2.3411	2.3476	0.0059
3		2.3475	2.3474	2.3479	2.3461	2.3455	2.3469	0.0010
4		2.3437	2.3303	2.3333	2.3355	2.3298	2.3345	0.0056
5		2.3430	2.3416	2.3467	2.3446	2.3433	2.3438	0.0019
6		2.3541	2.3413	2.3408	2.3478	2.3495	2.3467	0.0057
7		2.3524	2.3498	2.3425	2.3508	2.3491	2.3489	0.0038
8		2.3518	2.3506	2.3399	2.3497	2.3459	2.3476	0.0048
9		2.3450	2.3495	2.3440	2.3442	2.3414	2.3448	0.0030
10		2.3463	2.3418	2.3447	2.3453	2.3472	2.3450	0.0021

Table 5.2: Perflouro Methyldecalin repeat measurement results

		Density Measurement (g/cm^3)						
Sample	Weight	#1	#2	#3	#4	#5	$\bar{x}$	σ
1		2.3451	2.3444	2.3463	2.3469	2.3436	2.3453	0.0013
2		2.3493	2.3468	2.3459	2.3477	2.3473	2.3474	0.0012
3		2.3453	2.3432	2.3454	2.3462	2.3460	2.3452	0.0012
4		2.3419	2.3434	2.3413	2.3436	2.3432	2.3427	0.0010
5		2.3399	2.3412	2.3412	2.3442	2.3417	2.3417	0.0016
6		2.3454	2.3465	2.3447	2.3452	2.3419	2.3447	0.0017
7		2.3498	2.3476	2.3474	2.3481	2.3495	2.3485	0.0011
8		2.3494	2.3480	2.3476	2.3470	2.3485	2.3481	0.0009
9		2.3426	2.3452	2.3449	2.3440	2.3446	2.3443	0.0010
10		2.3443	2.3449	2.3450	2.3452	2.3448	2.3449	0.0003

The results of this experiment show that there is little to be gained from using PFMD over distilled water except in the case of very small flakes. The variation using both liquids suggest that use of a 4 d.p. balance is unjustified. Given the non-toxic, cheap, nature of water versus the expensive carcinogenic nature of PFMD I don't feel that the PFMD is sufficiently more precise to warrant it's use. The use of distilled water ensures that anyone can readily compare results with those presented here. The use of PFMD limits the use of ongoing density measurements to those who can get access to PFMD.

In light of the preceding trial, routine density measurements have been made using a 3 d.p. system and distilled water. Prior to measuring the full set of obsidian, a further repeat measurement experiment was performed using the 3 d.p. system. In this experiment 16 new flakes were struck from the same block of obsidian used in the initial repeat density experiments. These samples were measured once on each of four consecutive days. This measurement was conducted to evaluate the measurement precision of this system (Table 5.3). The overall standard deviation for this set of measurements is 0.003, which can be used to represent the variability in density measurements under this system.

The density for each induced sample was measured via this system using the calculated system error of $\pm 0.003\ gcm^{-3}$ (*supra vide*: Table D.1).

5.2.2 Bulk Elemental Data (XRF)

The chemical characterisation has proceeded by performing a bulk elemental XRF analysis of each glass for both majors and minors. In this analysis the samples were measured in a Siemens SRS 3000 using Spectra 3000 (V2.0) software. The major elemental composition was measured using fusion disks of finely ground glass powder ($< 5\mu m$) in a lanthanum based heavy absorber flux. Prior to fusion the glass powder

Table 5.3: 3 d.p. density system measurement results

	Measurement					
sample	1	2	3	4	$\bar{x}$	σ
1	2.347	2.347	2.351	2.352	2.349	0.003
2	2.341	2.354	2.348	2.349	2.348	0.005
3	2.340	2.348	2.341	2.351	2.345	0.005
4	2.340	2.348	2.347	2.348	2.346	0.004
5	2.347	2.345	2.345	2.346	2.346	0.001
6	2.350	2.351	2.346	2.351	2.350	0.002
7	2.343	2.351	2.353	2.349	2.349	0.004
8	2.347	2.350	2.350	2.353	2.350	0.002
9	2.342	2.349	2.345	2.350	2.346	0.003
10	2.346	2.347	2.347	2.349	2.347	0.001
11	2.349	2.344	2.350	2.348	2.348	0.003
12	2.344	2.341	2.346	2.348	2.345	0.003
13	2.349	2.341	2.346	2.350	2.347	0.004
14	2.343	2.350	2.349	2.354	2.349	0.005
15	2.347	2.350	2.348	2.344	2.347	0.002
16	2.347	2.356	2.353	2.354	2.352	0.004
17	2.341	2.342	2.339	2.351	2.343	0.005
18	2.348	2.345	2.342	2.351	2.346	0.004
19	2.350	2.351	2.351	2.350	2.351	0.000

was maintained at 100 ^{0}C for 48 hours in order to measure the adsorbed water loss and was then heated at 850 ^{0}C for 4 hours to drive of any radicals. The minor elemental composition was achieved by measurement of standard powder briquettes.

The standard output of major elemental composition from this analysis is in the form of percentage weight composition of the standard oxides. In order to render the data more meaningful in terms of hydration mechanisms and as a comparison to the PIXE data base generated by Neve *et al.* (1994) the elemental data was reworked to provide elemental molar ratios. Prior to this analysis the major data were normalised with respect to +H2O and radicals loss.

As the XRF analysis simply measures bulk glass composition which includes both the vitreous ground mass and crystalline inclusion, it is necessary to establish what degree of deviation from this composition would be induced by the crystal component, and where necessary to generate separate measures of the groundmass and crystal component composition. This check is necessary as the crystalline and vitreous components of the glass will influence hydration in a different manner.

5.2.3 Phenocryst Counts

Relative volume measurements of the phenocryst component were made using purpose written software included as an analytic function within the Rim Buster software (*infra vide*:§2.7). Low depth of field video images of obsidian thin sections were captured and image classification was carried out to define the crystal and groundmass components in the image. Geometrically calibrated images were produced following the process outlined in Chapter 2, and automatic identification of crystals was accomplished by simple thresholding. The proportion of crystal to ground mass measurement was made by performing a pixel count of the

thresholded image and measuring the proportion of crystal to groundmass pixels (C and M in Table D.2).

For optically active crystals imaging at 100x magnification under x-polars was used. For each sample 4 images were captured with the x-polars rotated 45 degrees at each capture and a final image was produced by combining the 4 process images. This process ensured that any crystals or crystal portions in extinction at any given orientation were included in the final image. If this process had not been followed the phenocryst volume would have been systematically underestimated. The optically active crystal proportion is identified as C in the following.

For the microlites an oil immersion objective at 1000 x magnification under normal transmitted light was used as these micro crystals do not polarised light. For each of these samples a single low depth of field image was generated. The microlites were again identified by simple thresholding and measurement was by pixel count. The microlite proportion is given as M in the following.

The generated count statistics cannot be directly used to estimate the volume of crystal inclusion without further calibration of the process. This is because the image depth of field is significant thus the plan count of visible crystalline inclusions will systematically over estimate the volume of crystal relative to vitreous groundmass. However, the count statistics will provide a measure of the relative volume of crystalline inclusion amongst the analysed glasses.

5.2.4 The Vitreous Groundmass

In order to test whether the XRF data is suitable for analysis of the geochemical influence on hydration rates, direct microprobe analysis of the vitreous groundmass for several glasses was conducted. The purpose

of this analysis was to determine if the bulk XRF data effectively described the vitreous geochemistry or whether the crystalline inclusion had a significant influence on these results. The glasses for this analysis were chosen to be representative of the range in phenocryst counts as described in the previous section (*supra vide*: Table D.2). The overall results of this analysis are presented in Table 5.4. As can be seen there is no significant difference between the two sets of results in correlation with the phenocryst count data, with the correlation between average diff and crystal counts being with a p-val of . The most extreme average deviation (Huruiki) is $\approx$ 0.27 %, which is not of a great concern. This is particularly so in light of the Te Ahumata results which exhibit a comparable variance in spite of a very low crystalline inclusion level. This suggests that there is a detectable level of heterogeneity within the vitreous groundmass of at least some samples. This variation will be better accounted for by a bulk technique such as XRF, rather than a spot technique such as the microprobe. The conclusion from the comparison is that the XRF data are suitable for assessing the influence of geochemistry on hydration rates for the current sample set.

5.3 Rate Indices

There are a number of attribute estimation models that have been proposed through time. Those published in the archaeological/OHD literature are:

1. S-Value silicon/oxygen ratio (Ericson *et al.* 1976)

2. Zeta structural factor (Ericson *et al.* 1976)

3. The chemical index (Friedman 1976)

Table 5.4: Comparative bulk and spot geochemical results

Source		SiO2	Al2O3	Fe2O3	CaO	Na2O	K2O	TiO2	average diff
Ben Lomond	xrf	76.94	12.48	1.41	1.12	4.15	3.46	0.18	
	mp	76.82	12.74	1.36	1.16	3.92	3.59	0.26	
	diff	0.12	0.26	0.06	0.04	0.23	0.13	0.07	0.131
Huruiki	xrf	75.87	13.11	1.36	0.78	4.58	3.92	0.10	
	mp	76.30	13.47	0.88	0.68	4.43	4.24	0.00	
	diff	0.42	0.36	0.48	0.09	0.15	0.33	0.10	0.275
Kaeo	xrf	74.32	10.05	4.62	0.14	5.92	4.17	0.14	
	mp	74.16	10.26	4.80	0.10	5.84	4.36	0.00	
	diff	0.16	0.21	0.18	0.03	0.08	0.19	0.14	0.141
Staircase	xrf	74.40	10.33	4.53	0.19	5.61	4.39	0.23	
	mp	74.35	10.53	4.73	0.17	5.46	4.53	0.24	
	diff	0.05	0.19	0.20	0.02	0.15	0.15	0.01	0.110
Te Ahumata	xrf	76.55	12.71	1.36	0.76	3.80	4.70	0.11	
	mp	76.61	12.80	1.20	0.65	3.58	5.06	0.00	
	diff	0.06	0.09	0.15	0.11	0.22	0.36	0.11	0.159

4. The intrinsic OH- content in the unaltered glass (Stevenson *et al.* 1993)

5. Glass density (Stevenson *et al.* 1995)

Of these only the Chemical Index (Friedman and Obradovich 1981; Stevenson and Scheetz 1989*a*) and the glass density/ intrinsic OH- (Stevenson *et al.* 1995; 1998) approaches have been applied in actual published rate estimations.

5.3.1 S-Value

The S-value model was one of two attribute models proposed by Ericson *et al.* (1976). They suggested that obsidian diffusion may be controlled by the general glass structure and proposed using the silicon oxygen bond ratio in the glass, the S-value, calculated as:

$$S - value = \frac{Silicon(mole\%)}{Oxygen(mole\%)} \tag{5.1}$$

As can be appreciated this model takes a very simplified view of the hydration reaction. Though this index does make sense in terms of the overview of hydration mechanisms that has been presented previously. If the glass network is fully polymerised then the s-value should be maximised as only bridging oxygen will be present. Therefore, the s-value may represent a measure of the degree of polymerisation of the glass network. Obviously this is a simple model which ignores significant factors such as the role of Aluminium within the glass network. This model has not been applied in any published rate estimates. Due to the limited nature of this model the necessary data has not been collected, and the S-value is not calculated in Table D.2.

5.3.2 Zeta Factor

The second model proposed by Ericson *et al.* (1976) was the Zeta structural Factor

$$Z = 100\frac{Al_2O_3 - (CaO + Na_2O + K_2)}{Al_2O_3 - (CaO + Na_2O + K_2)} \tag{5.2}$$

using the mole percent of each oxide. Relating this score back to theory outlined previously (*infra vide*:§4), it makes sense that the Zeta value should be related to the hydration rate. This score will be a basic index into the degree of polymerisation of the glass structure. As outlined in Chapter 4 the degree of polymerisation may relate to the energy required to deform the glass network to allow hydration to proceed. The Zeta factor has been calculated for each of the samples in the reference set and the results are presented in Table D.2.

5.3.3 Chemical Index

The third attribute rate estimator listed above is the Chemical Index proposed by Friedman and Long (1976). This empirically determined index estimates the hydration rate from an index value at temperature T and is calculated as:

$$CI = SiO_2 - 45(CaO + MgO) - 20(H_2O+) \tag{5.3}$$

where the values are in weight percent. While this index has been applied with apparently useful results it is empirical and there is the possibility that this index is specific to the sources used in its' generation (*supra vide*:§5.3.5). Therefore this index may not be generally applicable.

5.3.4 OH-/ Density index

The final set of attribute rates listed above are the OH-/density rates (Stevenson *et al.* 1995). I am treating these two index rates together as the density index is an estimate of the OH- index. The OH- index was proposed by Stevenson *et al.* (1993) who found that their high temperature induced hydration results were strongly correlated with the bulk glass OH- content (r^2 = 0.95). Thus they defined a relationship that allowed the hydration rate constants indexed at 160 ^{0}C to be defined by the measurement of bulk glass OH- content as measured by the FTIR procedure outlined by Newman *et al.* (1986).

The high correlation observed makes sense in terms of the theory outlined in §5.3, where it was suggested that for molecular diffusion of water an equilibrium would be established between bulk OH- and H_2O content such that the water content of the dry glass bulk should influence the rate of molecular diffusion of water.

Stevenson (pers comm.) found problems with this technique in that the FTIR spectroscopic technique used to measure the bulk OH- concentration required that the specimen is translucent and free of interfering crystalline inclusions, which is a condition often not met in artefacts. A solution to this problem was brought about by the suggestion that bulk OH- content could be predicted on the basis of glass density (Stevenson *et al.* 1995). In this way it is proposed that the density of an individual artefact can be measured and used to estimate the necessary water species content of the glass and from these estimates an estimate of the glass hydration constants indexed at 160 ^{0}C can be produced.

While there is reason to expect a correlation between hydration behaviour and intrinsic hydroxyl content, the extension of this reasoning to glass density is less secure. Glass density varies due to a range of factors such as the degree of non-vitreous inclusion, extent of vesicle formation etc.

To suggest that bulk glass hydroxyl concentration can be predicted on the basis of density also implies that factors such as the degree and type of crystal inclusion can also be predicted on the basis of glass density.

5.3.5 Further models

In addition to the models described above, further models can be generated on a theoretical basis. It is possible to derive equations empirically as Friedman and Long (1976) did with the Chemical Index. The problem with this type of approach is that there is a very real chance of confounding the results with source specific effects. That is, sources are likely to be geochemically distinct and also likely to exhibit fairly consistent hydration behaviour. Thus it may be possible to describe the observed differences in hydration behaviour on the basis of geochemical data, where the model is simply defining a source rather than a geochemically moderated hydration process. Thus source distinction could confound the empirical model. In light of this it is most appropriate to generate such models on a theoretical basis. Unfortunately the underlying theoretical basis for obsidian hydration is poorly developed (*infra vide*:§4) thus it is not possible to generate fully factored models. However a model can be proposed on the basis of the function Aluminium and Iron play as network formers as opposed to modifiers within the glass. As described previously, when the ratio of intermediates to modifiers in the glass is unity then the glass should be highly polymerised. Thus this ratio could be a useful index. I have proposed two models based on this ratio; MI 1 which is a straight quantification of the ratio:

$$MI1 = \frac{Al + Fe}{Ca + Na + K} \tag{5.4}$$

As we would expect hydration rates to be minimised when MI 1 = 1 a further index (MI 2) which measures the absolute deviation of MI 1 from

unity as

$$MI2 = abs(1 - MI1) \tag{5.5}$$

may also be a useful predictor.

5.4 Rate Index Evaluation

The available reference dataset (Table D.2; Table D.1) allows the utility of any proposed chemical index to be assessed. While the reference results all relate to New Zealand obsidian, valid indices will still apply as the base hydration mechanism should remain constant. The fundamental conclusion from the available dataset is that none of the proposed indices perform adequately. As is shown in Table 5.5 there is significant correlation between hydration rate and all of the measured variables, with up to 85 % of the variation in hydration rate amongst the samples being explained by Ti alone. However this correlation is confounded by the fact that primary variation is between source groups. This is graphically demonstrated in Figures D.1-D.18, which show that there is significant variation in rate for any potential predictor. The predominant feature of Figures D.1-D.18 is that the rate and index clusters are source specific. This means that the index variables are simply serving to discriminate amongst sources rather than describe any fundamental parameters underlying the hydration process. Thus a simple assignation of an artefact to source and the application of a general source specific rate provides more precise rate estimation than any of the proposed indices.

This conclusion can be shown on the basis of intra source variation in hydration rates. If the subset of reference data that applies to Mayor Island sources is analysed, it is apparent that there is no predictive power to the proposed indices (Figures D.19-D.35). As shown in Table 5.6 there are no

Table 5.5: Correlation between sample attributes and hydration rate for total reference set

Attribute	Correlation	Sig	N
AL	0.620	4.22E-05	37
C	0.258	1.23E-01	37
CA	0.595	1.01E-04	37
CI	-0.597	9.59E-05	37
DENSITY	-0.675	4.69E-06	37
FE	-0.686	2.81E-06	37
H2O	0.219	1.94E-01	37
K	-0.444	5.94E-03	37
M	0.346	3.57E-02	37
M1	0.612	5.72E-05	37
M2	0.667	6.60E-06	37
MG	0.562	2.96E-04	37
MN	-0.745	8.90E-08	37
NA	-0.627	3.33E-05	37
P	0.212	2.08E-01	37
SI	0.695	1.85E-06	37
TI	-0.858	3.46E-16	37
ZETA	0.643	1.81E-05	37

significant correlations between hydration rate and any of the available variables. For this set of data the confounding effects of geochemical and hydration rate variation correlated with source will be ameliorated. This analysis lends further weight to the conclusion that none of the proposed or available variables can provide an index to hydration rates.

Table 5.6: Correlation between sample attributes and hydration rate for Mayor Island sub-set

Attribute	Correlation	Sig	N
AL	0.587	0.002	25
C	0.122	0.56	25
CA	-0.13	0.536	25
CI	-0.018	0.931	25
DENSITY	-0.108	0.608	25
FE	0.064	0.761	25
H2O	0.154	0.463	25
K	-0.161	0.443	25
M	0.254	0.221	25
M1	-0.132	0.529	25
M2	0.132	0.529	25
MG	-0.282	0.172	25
MN	0.058	0.782	25
NA	0.059	0.778	25
SI	0.023	0.915	25
P	-0.16	0.444	25
TI	-0.142	0.499	25
ZETA	-0.102	0.628	25

The implication of this analysis is that some of the published rate estimation indices are invalid and may give rise to spurious results. However, the high correlation between hydration rate and bulk hydroxyl con-

tent described by Stevenson *et al.* (1993) has not been tested. This index looks the most promising of those so far proposed and it is important to establish whether Stevenson *et al.*'s 1993 results are repeated for New Zealand obsidian to establish the universality of the index.

None of the other indices proposed so far appear to be globally applicable. Freidman and Long's 1976 Chemical Index appears to have been useful in describing the hydration behaviour of certain American obsidian deposits, but the result is empirically derived and appears to have been confounded by spurious correlation between geochemistry and hydration behaviour of the analysed deposits. This is apparent as the Chemical Index is incapable of describing the hydration behaviour of New Zealand obsidian, and hence the index is not universal.

The only other index that has been actually used is the density calibration method (Stevenson *et al.* 1995). There are some serious drawbacks to the OH- / density rate estimation model. As discussed previously obsidian density is likely to vary in response to a number of factors in addition to those that may have some theoretical influence on the hydration rate. That is factors such as the type and quantity of inclusions within the glass body will influence the density in addition to factors such as the bulk hydroxyl content. Thus it is quite possible to have two glasses with the same bulk hydroxyl content but with differing densities. This is highlighted by the experimental data presented here which show no significant correlation between density and hydration rates for New Zealand obsidian (*supra vide*:Figure D.1).

5.5 Conclusion

In terms of the initial problem of providing a method for accurately estimating glass specific hydration parameters, the chemical index methods

are not of great use as they currently stand. It seems probable that an OH- index may provide some universal control. However, the application of this index is problematic, as precise measurement of intrinsic OH- content is difficult. This is precisely the problem that motivated the density calibration approach. It is apparent that other approaches to maximising hydration prediction efficiency must be employed. Certainly on the basis of the current results it is apparent that the optimal universal approach is to define source specific hydration parameters on the basis of high precision primary experimental data and estimate artefact specific parameters on the basis of assigned source. In the following chapter we will develop base source specific hydration rate data for New Zealand.

Chapter 6

New Zealand Hydration Rates

6.1 Introduction

The purpose of this chapter is to outline the development of primary source hydration rate data for New Zealand obsidian. This data can be directly used for providing artefact specific hydration parameters for obsidian deriving from the analysed sources, as discussed in the preceding chapter, and also serve as a basis for developing and refining hydration parameter estimates for other sources via secondary methods (*supra vide*:§6.1.2).

In terms of the standard model for hydration of obsidian (*infra vide*:§4.7) this development means calculating parameters for modelling k, where:

$$k = Aexp\left\{\frac{-E}{RT}\right\} \tag{6.1}$$

That is, estimating the distribution of the pre-exponential component A and gas activation energy E values for each source location. These parameter values derive from analysing measured hydration rate (k) data.

The gas activation energy E is related to the temperature dependence of the hydration rate k. Accordingly, E for any particular sample can be calculated by measuring the hydration rate at several temperatures and re-arranging Equation 6.1 as:

$$ln(k) = ln(A) - \frac{E}{RT} \tag{6.2}$$

Here k and T are variables so this relationship is of the form

$$ln(k) = \beta_0 + \beta_1\left(\frac{-1}{T}\right) \tag{6.3}$$

i.e. the equation of a line. The parameters β_0 and β_1 can be estimated via various methods, producing estimates of A and E. Thus estimates for A and E are simply derived from the line relating $ln(k)$ to $-1/T$, where $ln(A)$ is the intercept and E/R is the slope. These parameters can

be calculated by standard regression according to Equation 6.3[1].

Thus in order to generate primary source hydration rate data for a subset of New Zealand obsidian sources we need to be able to make measurements of k for a number of samples over a range of temperature conditions. Here the method used for developing these data is to perform induced hydration experiments, which is a fairly standard approach to this problem. However, there are practical limitations on the number of samples that can be experimentally hydrated. Accordingly it is important to consider how experimental design influences the ultimate precision of the final E and A parameter estimates so that we can design the optimal induction experiment.

6.1.1 Induction Rates

Induction rate estimates are based around the k data measured through induced hydration experiments such as those described in Chapter 4. Ideally we would like to produce the highest precision estimates for A and E possible. However the nature of the experimental data dictates the precision of any estimates for A and E. While such experiments are relatively easy to perform there are limitations on the number of sam-

[1] An alternative method for calculating A is to conduct a single induction run over a series of temperatures in order to estimate E as just described, and then to make the following re-arrangement of Equation 6.1:

$$\begin{aligned} k(T_1)exp\left\{\tfrac{E}{RT_1}\right\} &= k(T_2)exp\left\{\tfrac{E}{RT_2}\right\} \\ \therefore \quad k(T_1) &= k(T_2)exp\left\{\tfrac{E}{R}\left(\tfrac{1}{T_2}-\tfrac{1}{T_1}\right)\right\} \end{aligned} \tag{6.4}$$

Thus $k(T_1)$ can be extrapolated from a known $k(T_2)$. This calculation has been used in various published studies (*e.g.* Michels *et al.* 1983; Stevenson *et al.* 1995). While this approach is computationally valid, it results in higher associated errors (assuming they are calculated) as less information is used to estimate A, thus calculation of A and E according to Equation 6.3 is preferred.

ples that can be analysed, due to both time and equipment constraints. Accordingly it is useful to outline how the structure of an induction programme will influence the estimation precision of A and E so that we can optimise the power of the data set that is generated. In the following some simple guidelines to maximising the estimation precision of A and E through induced hydration experiments are outlined.

Following a purely geometric argument, the wider the induction temperature range the smaller the error interval for E and A. This follows as the slope of the line used to calculate E is calculated by the change in $ln(k)$ over a base line of $1/T$. Obviously the greater the $1/T$ baseline, the less variation that will be introduced into E by uncertainty in the $ln(k)$ measurement. As the base line is a function of inverse absolute temperature range, this means that smaller baselines and hence greater errors in E are generated over high temperature induction intervals in comparison to intervals of the same magnitude but at lower temperatures. The same argument obviously applies to calculating A.

As an example, consider a sample of obsidian with an E of 85705 $Jmol^{-1}$ induced over a range of 180 ^{0}C to 150 ^{0}C in comparison to the same material induced over a range of 120 ^{0}C to 90 ^{0}C. Both inductions extend over a 30 ^{0}C temperature range, yet the lower temperature induction baseline is 134% the size of that in the higher temperature induction. This results in a tighter distribution for the estimated E. For instance, if inductions are carried out over the ranges described above to produce rims of 2 μm which are measured with an error of $\pm$ 0.0375 μm, then the 180-150 ^{0}C induction will estimate E as $\sim$ U[81717,89693] $Jmol^{-1}$ as opposed to the lower temperature results where E would be estimated as $\sim$ U[82736,88674] $Jmol^{-1}$. The lower temperature induction range would produce an estimation interval that is approximately 30% smaller than an interval of the same magnitude but at a higher temperature. Thus optimum experimental design maximises the induction tempera-

ture baseline.

However, maximising the temperature baseline can involve significant time costs. A basic guide to minimum experimental duration is presented in Table 6.1. This shows the length of the temperature baseline arising from differing induction temperature regimes. Table 6.1 is read by intersecting the lower temperature row and upper temperature column. Thus an induction conducted over the temperature range 40-160 ^{0}C would have a temperature baseline of 0.0009 $^0K^{-1}$. The minimum induction time associated with each lower temperature (assuming measurement via an optical system) is also presented in Table 6.1. As can be seen, low temperature inductions can be very time consuming $\approx$ 50-60 years minimum for a 20 ^{0}C induction. A base line 2/3 the size can be produced in a more manageable time frame (60-180 ^{0}C: 0.8 years), and accordingly may be a more suitable choice.

Table 6.1: % Error in k as a function of induced hydration extent

Temp	Upper Temperature ^{0}C									Duration
^{0}C	20	40	60	80	100	120	140	160	180	years
20	0	0.0002	0.0004	0.0006	0.0007	0.0009	0.0010	0.0011	0.0012	56.3230†
40		0	0.0002	0.0004	0.0005	0.0006	0.0008	0.0009	0.0010	5.9160
60			0	0.0002	0.0003	0.0005	0.0006	0.0007	0.0008	0.8145
80				0	0.0002	0.0003	0.0004	0.0005	0.0006	0.1404
100					0	0.0001	0.0003	0.0004	0.0005	0.0292
120						0	0.0001	0.0002	0.0003	0.0071
140							0	0.0001	0.0002	0.0020
160								0	0.0001	0.0006
180									0	0.0002

† This is the minimum induction time (years) required for a 0.4 μm hydration rim to be produced for a sample of obsidian with E=86600 $Jmol^{-1}A$ = 19443992661days μm^{-2}

A second increase in k estimation precision can be made by increasing the experimental hydration extent. For a constant measurement error,

the calculated k becomes more precise with increasing hydration extent (*e.g.* Table 6.2). Thus it is optimum to induce as large a rim as possible in order to maximise k estimation precision. It should be noted however, that the production of rims significantly exceeding archaeological hydration extents may not produce valid data, and it is necessary to establish that the linearity of x^2 vs kt is preserved throughout the range of induced hydration extents. As will be appreciated maximising the hydration extent will significantly extend the minimum experimental durations given in Table 6.1.

A third increase in k measurement precision can be achieved by increasing the number of data used in its calculation. As k is calculated from data relating hydration extent to time for any particular temperature, the more data collected for each induction run the more tightly constrained and hence more precise k will be.

Thus k estimation precision is increased by:

1. high precision measurements of hydration extent
2. induction over a wide temperature range
3. induction at the lowest temperature possible
4. induction of large hydration extents
5. collection of multiple datum points for each k

While these points allow us to design programmes that will maximise E and A estimation precision for any given sample, we also need to consider definition of source parameters.

For the purposes of defining source specific hydration parameters the analysis a single source sample is insufficient. For the experimental hydration data to be of use in applied OHD we need to be able to quantify

Table 6.2: % Error in k as a function of induced hydration extent

Hydration rim Thickness	% error in $k^{\dagger}$
0.1	0.700
0.2	0.350
0.3	0.233
0.4	0.175
0.5	0.140
0.6	0.117
0.7	0.100
0.8	0.088
0.9	0.078
1	0.070
1.1	0.064
1.2	0.058
1.3	0.054
1.4	0.050
1.5	0.047
1.6	0.044
1.7	0.041
1.8	0.039
1.9	0.037
2	0.035
2.1	0.033
2.2	0.032
2.3	0.030
2.4	0.029
2.5	0.028
2.6	0.027
2.7	0.026
2.8	0.025
2.9	0.024
3	0.023

† error calculated assuming a constant uniformly distributed measurement error of $\pm 0.035 \mu m$.

the degree of variation in hydration behaviour within a source and to be able to take account of any systematic component. So, while it is possible to calculate the specific hydration parameters for any sample experimentally, a single result does not give information on variation in hydration behaviour within the general source area. It is not acceptable to simply assume that variation in hydration behaviour within any source will be insignificant. Accordingly any induction program must establish the intra source variation in hydration parameters. In the absence of this type of examination there is a very real chance that there will be significant uncontrolled variation in hydration parameters and consequently, in the resulting dates. Thus while the analysis of a single source sample may involve the induced hydration of a large number of discrete sub-samples under a wide range of temperature conditions this analysis needs to be repeated for sufficient samples to control for any intra-source variation. This means that the proper definition of source specific hydration parameters will require the experimental analysis of a large number of discrete samples over a considerable period of time. It follows that the generation of high precision rate data for a wide range of distinct obsidian sources may be impractical via induced hydration experiments alone. The cost, both economic and time, of producing the number of samples required would be substantial. In light of this, methods that generate secondary data allowing the improved precision of primary hydration rate data and the definition of hydration rate parameters for other sources would be very useful. Two options that offer great potential are the use of hydration analogues and suitable cross-dated cultural material.

Analogues to the hydration reaction that provide k data over a shorter time span than standard obsidian hydration would provide useful secondary data. The most obvious analogue is the induction of obsidian powder (*e.g.* Ambrose 1976). With this approach it is practical to produce high precision measurements of a k analogue at ambient tempera-

tures over a wide temperature range. It is probable that the gas activation energy (E) for both flake and powder hydration will be the same. If this can be established, then it should be possible to make use of powder induction data to complement other hydration data which would allow longer temperature baselines to be used.

6.1.2 Cross Dating Data

Cross-dated samples also offer a method for complimenting direct experimental hydration data. While it is not practicable to experimentally hydrate as many samples as would be optimal, under certain conditions it is possible to treat archaeological samples as long term induction experiments. The case is often encountered where a number of obsidian flakes are recovered from an essentially isochronous context. In this situation the flakes will have been hydrating for the same duration in an identical environment. Thus these flakes represent an ambient hydration experiment that tests the degree of inter-glass hydration variability.

The results from an analysis such as this are by nature relative, though can be applied in two manners. First, it is possible to compare the variation in hydration extent among samples from within the same source. This allows the intrinsic variation in source hydration behaviour to be more fully explored than would be possible with laboratory based experimental inductions alone. One artefact specific hydration rate (k_2) can be related to another (k_1) by

$$k_2 = k_1 \frac{x_2^2}{x_1^2} \tag{6.5}$$

Where x_1 and x_2 are the respective measured hydration extents. Thus the ratio $\frac{x_2^2}{x_1^2}$ can be used as a measure of the intra source variation for samples from an isochronous context.

The second use that can be made of such sets of flakes is to produce

more precise calculations of absolute hydration rates for sources which are currently poorly controlled. The relative hydration extent of two flakes can be expressed as follows

$$\frac{x_1^2}{x_2^2} = \left(\frac{A_1}{A_2}\right) \exp\left(\frac{E_2 - E_1}{RT}\right) \tag{6.6}$$

or by taking logarithms as

$$\ln\left(\frac{x_1^2}{x_2^2}\right) = \ln\left(\frac{A_1}{A_2}\right) + \frac{E_2 - E_1}{RT} \tag{6.7}$$

This reduces to the following linear equation

$$y = \beta_0 + \beta_1 (RT)^{-1} \tag{6.8}$$

where $y = \ln\left(\frac{x_1^2}{x_2^2}\right)$; $\beta_0 = \ln\left(\frac{A_1}{A_2}\right)$; and $\beta_1 = E_2 - E_1$. If samples from contexts of differing EHT's are analysed it is possible to establish the parameters β_0 and β_1 through regression or some such similar analysis. following this we can establish the value of the unknown parameters A_2 and E_2 on the basis of the known parameters A_1 and E_1 as

$$A_2 = A_1 e^{-\beta_0} \tag{6.9}$$

and

$$E_2 = \beta_1 + E_1 \tag{6.10}$$

This requires that samples with high precision hydration rate parameter estimates exist within an isochronous context that contains samples from other source groups.

The use of appropriate cross-dated archaeological samples is potentially a very useful research tool for analysing obsidian hydration rates, particularly with reference to analysing intra-source variation. Appropriate cross-dated archaeological samples act as long term experimental inductions, and the results can be used to extend and refine the primary reference hydration data on which artefact specific estimates are based. Estimation of cross-dated rate data is re-visited later as part of the Bayesian analysis of OHD chronometric data presented in Chapter 13.

6.1.3 Summary

The most general method to providing artefact specific hydration rate parameters is to associate each artefact with a known source group for which the hydration behaviour has been defined. Thus for the purposes of OHD in New Zealand we need to define the hydration behaviour of key source locations with the highest possible precision. However, while it is possible to experimentally define glass specific hydration parameters for any $x(t,g,e)$ to practically any degree of accuracy given sufficient time and money, it is not practical to experimentally induce the optimum number of samples, nor to conduct inductions over the ideal temperature or time range, to fully estimate parameters for a large number of sources. The conclusion is that initial induced hydration experiments should concentrate on producing high precision primary data for a small range of sources, rather than low precision data for a larger range of sources. The ideal application of this approach is to produce high precision primary hydration rate data for a single source of material that is relatively abundant in archaeological assemblages and readily identified. This enables both the dating of artefacts deriving from this source group and the development of further rate data via secondary methods.

Following this conclusion the Mayor Island obsidian source is the most appropriate focus of the induced hydration programme presented here. Mayor Island material is all but ubiquitous in archaeological collections that contain obsidian (Davidson 1981; Seelenfreund-Hirsch 1985), and additionally, the majority of Mayor Island material is readily identifiable to source on the basis of colour in transmitted light (*supra vide*:§7.1). However there are other potentially confounding "green" sources (*i.e.* Waihi and Kaeo) and in practice it is necessary to conduct a similar analysis of these other sources. In this manner we can establish to what extent there is variation in hydration properties of "green" obsidian in general, and establish what procedures need to be adopted in order to

associate “green” obsidian with the appropriate hydration source group. Additionally, it is possible that there is no real variation in obsidian hydration behaviour among the New Zealand source areas at all. Thus we need to include additional source types within the analysis to establish how much variation there may be among New Zealand obsidian in general.

Thus we have identified two components to the experimental hydration programme presented here:

1. the description and quantification of glass specific hydration parameters for each of the “green” obsidian source regions, with a particular focus on Mayor Island.
2. the preliminary description and quantification of variation in glass specific hydration parameters among New Zealand obsidian in general

Following these goals the four general obsidian source areas identified in Chapter 3 (Coromandel,Mayor Island, Northland and the Taupo Volcanic Zone) have each been incorporated in the experimental hydration program at some level as outlined in the following. The exact sources of obsidian used throughout the experimental programme and their experimental tags are presented in Table C.4 and the specific experimental structures are detailed in the following sections.

6.2 Mayor Island

6.2.1 Experimental Design

The Mayor Island experimental structure has been designed to examine the regional intra and inter source variation in hydration behaviour as

well as providing base line estimates of generic Mayor Island hydration parameters. In this sense "source" refers to distinct units within the broader Mayor Island geological structure as identified on the basis of geological history and geochemical characterisation.

Primary Source Groups

As outlined previously there are five broad physiographic units within Mayor Island from which obsidian derives (*infra vide*:§3; Main Cone Rhyolites, the Houghton *et al.* (1992) post A shield and domes, Ignimbrites, the Houghton *et al.* (1992) 8ka Lava Flow), and it is sensible to compare material from within and between each of these. It is obvious that one of the Major physiographic units the "Young Dome" (*infra vide*:§ 3.2.2) should not be included within the analysis as this obsidian is of insufficient quality to have been exploited prehistorically. In light of this we can define 4 Potentially distinct sub source regions that need to be considered in terms of defining the hydration parameters of Mayor Island obsidian as a general source region. Further sub-groups can be identified from the results of geochemical analyses.

An extensive Pixe/Pigme program by Neve *et al.* (1994) has identified four geochemically distinct obsidian groups within the broader Mayor Island area. However there are likely to be more geochemical groups than these as some physiographic units such as the unique vents at Orongatea were not sampled by Neve *et al.* (1994). Further, is unclear what sampling strategy they employed at locations such as Opuhi Springs, Te Ananui Flat, Te Paritu or Taratimi Bay where obsidian is present as detrital material that may derive from a number of sources. Similarly, there are unique obsidian selvages within some of the identified sub-sources considered by Neve *et al.* (1994) and it is not clear to what extent their analysis takes account of this fact both at the level of primary sampling of reference material and in the statistical definition of geochemically

distinct sub sources within their sample areas. However, the analysis presented by Neve *et al.* (1994) does show that we need to consider the possibility of inter-source differences within the broader physiographic units. For example Neve *et al.* (1994) identify 3 geochemically distinct groups associated with obsidian that would be expected to derive from the main cone rhyolites (Neve *et al.* (1994) groups 1,3&4 their p. 104), which would otherwise be classed together.

Thus on the basis of basic geological structure and the analysis of obsidian deposits conducted by Neve *et al.* (1994) we can define six sub source regions within the broader Mayor Island area that need to be considered in terms of hydration behaviour. These would be expected to show the greatest degree of variation and hydration behaviour, and accordingly identify representative sample sources for assessing the degree to which hydration behaviour varies amongst the discrete sub sources within Mayor Island. Multiple sources within each identified unit have been selected to provide a representative sample from each unit.

Structure

The experimental structure employed to assess the hydration parameters of obsidian deriving from Mayor Island comprises two components. The first is designed to assess the degree to which significant intra source variation in hydration behaviour occurs. These primary intra flow comparisons were conducted at 125 ^{0}C. At this temperature the intraflow comparisons were made for six representative obsidian subsources (Table 6.4).

The second component of experimental program is designed to assess the degree to which hydration behaviour varies among the different subsource areas within Mayor Island. Interflow variation in hydration parameters was investigated at five different temperatures (95, 107, 112.5,

Table 6.3: Potential hydration-subgroups within Mayor Island

Group	Source Locations
1 Main Cone Rhyolites (the Houghton *et al.* (1992) pre-A lava shield)	
	Opuhi west
	Ruakiki
1.1 Neve *et al.* (1994) group 1	
	Taratimi
	Taumou (seam)
	Oira
1.2 Neve *et al.* (1994) group 3	
	Opo
1.3 Neve *et al.* (1994) group 4	
	Halls Pass
2 Post A shields and domes after Houghton *et al.* (1992)	
	Te Ananui
	Ohineiti
	Orongatea
	Opuhi
	Raumata
	Otiora
3 Pyroclastics	
	Opuhi east
	Taumou loose
	Taratimi
4 8ka Lava flow after Houghton *et al.* (1992)	
	staircase

Table 6.4: Intraflow comparisons for Mayor Island obsidian

Location	Discrete samples	Significant intraflow hydration variation
Ohineiti	7 ×	nil
Orongatea	5 ×	nil
Opuhi Springs	4 ×	nil
Staircase	5 ×	nil
Raumata	3 ×	nil
Taratimi	3 ×	nil

125 & 160 ^{0}C; Table 6.5). The focus of this comparison was in establishing the degree of variation in hydration behaviour among obsidian selvages, though a secondary comparison was made with sources deriving from pyroclastic deposits. In total, the hydration behaviour of twelve obsidian selvages have been compared, and a secondary comparison has been drawn between selvage and pyroclastic deposits at Taumou, Otiora and Oira (Figures 6.1,6.2; Table 6.5).

6.2.2 Results

As can be seen in Figure 6.1 no significant intra flow variation is indicated by the experimental results. This result strongly suggests that there is no significant intraflow variation in hydration behaviour among obsidian Mayor Island obsidian selvages. It is also apparent from Figure 6.1 that there is no significant intersource variation in hydration behaviour among the Mayor Island obsidian selvages. However, the obsidian samples associated with pyroclastic deposits exhibit distinct hydration results, and do not appear to conform to such uniformity in hydration behaviour. This result is repeated with interflow comparisons at

Table 6.5: Inter-Source comparisons for Mayor Island obsidian

Location		Temperature ^{0}C			
Name	Group	95	107	112.5	125
Teananui	2				1
Hall's Pass	1.3	1			1
Ohineiti	2				7
Orongatea	2				5
Opuhi Springs	2				4
Staircase	4	1			5
Ruakiki	1				1
Raumata	2	1		1	3
Otiora(seam)	2				1
Taratimi	1,2,3			1	3
Opo Bay	1.2				1
Otiora (cobble)	2				1
Taumou(seam)	1.1			2	1
Taumou(pyroclastic)	3		1	1	1
Oira	1.1				1

other temperatures as shown in Figure 6.2 where inter flow comparisons at three further temperatures are shown. The 95 ^{0}C results show tight correspondence between four selvages. At 107 ^{0}C there is a comparison between a sample associated with a selvage and one associated with a pyroclastic deposit. This comparison is consistent with the pattern of obsidian related to pyroclastic deposits exhibiting more rapid hydration than that associated with selvages. At 112.5 ^{0}C five sources are compared. Four of these relate to selvages and exhibit uniform hydration behaviour. In contrast, the single sample associated with pyroclastic deposits exhibits a more rapid hydration rate in line with the previous comparisons of this type.

6.2.3 Discussion

The conclusions from these results are:

- There is no significant intraflow variation in hydration behaviour for Mayor Island obsidian selvages[2].
- There is no significant interflow variation in hydration behaviour among Mayor Island obsidian selvages
- Obsidian associated with pyroclastic deposits exhibit more variable, and generally more rapid, hydration behaviour than that associated with the pre-caldera selvages.

Thus the basic conclusion is that the Mayor Island obsidian selvages (*i.e.* Groups 1,2,4 Table 6.3) represent an effectively uniform hydration source group. On this basis it is appropriate to treat the experimental results related to this source as replicates and use these to generate generic hydration parameters for the Mayor Island obsidian selvages, here after the Mayor Island Hydration Group (Figure E.1; "pooled" data in Table E.1). Analysis of these data results in tight estimates for source specific hydration parameters associated with the Mayor Island Hydration Group (Tables 6.6,6.7 :Figures E.2, E.3). These results act as a direct estimate of glass specific hydration parameters for Mayor Island obsidian artefacts, and form a primary reference for further refinement of MIHG parameters and the development of hydration parameters for other source groups via secondary methods (*infra vide*:§5);

It is not possible to develop meaningful estimates for the hydration parameters of sources associated with pyroclastic deposits on Mayor Island as the available data are of limited extent, and suggest that there

[2] within available measurement precision

is significant variation in hydration behaviour among obsidian associated with these sources. There is no real benefit in pursuing further researched directed at generating hydration parameters for these sources as the obsidian associated with them is typically of poor quality, particularly so within the Mayor Island context, and is highly unlikely to have been utilised as a lithic resource prehistorically.

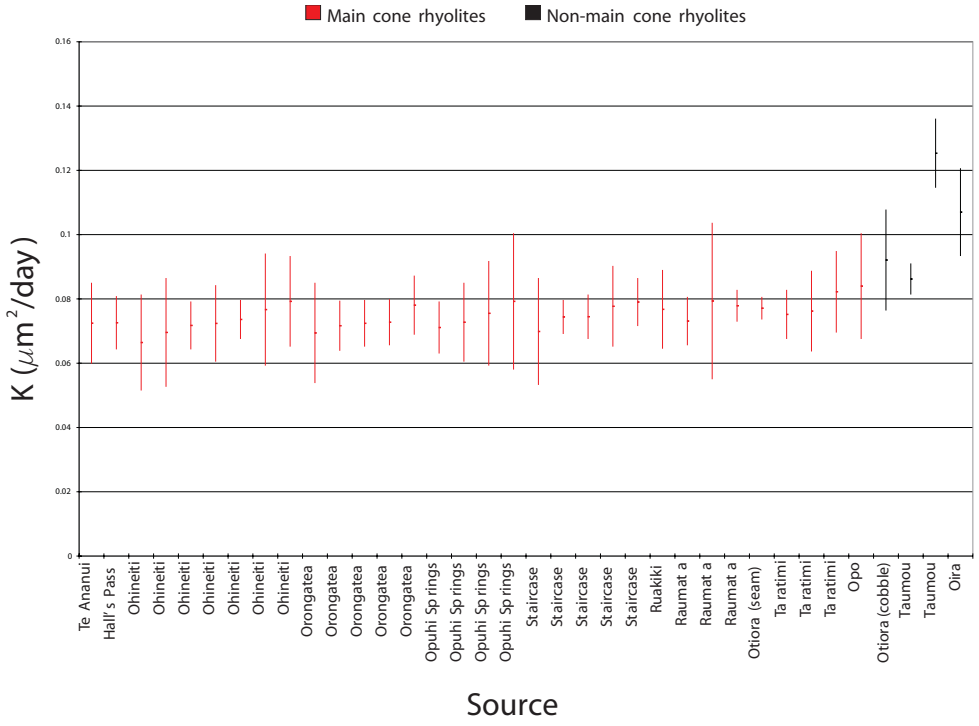

Figure 6.1: Comparative hydration rates for Mayor Island source samples at 125 ^{0}C

6.3 Northland

The definition of hydration parameters for Northland obsidian is a central component of the current experimental hydration program as there

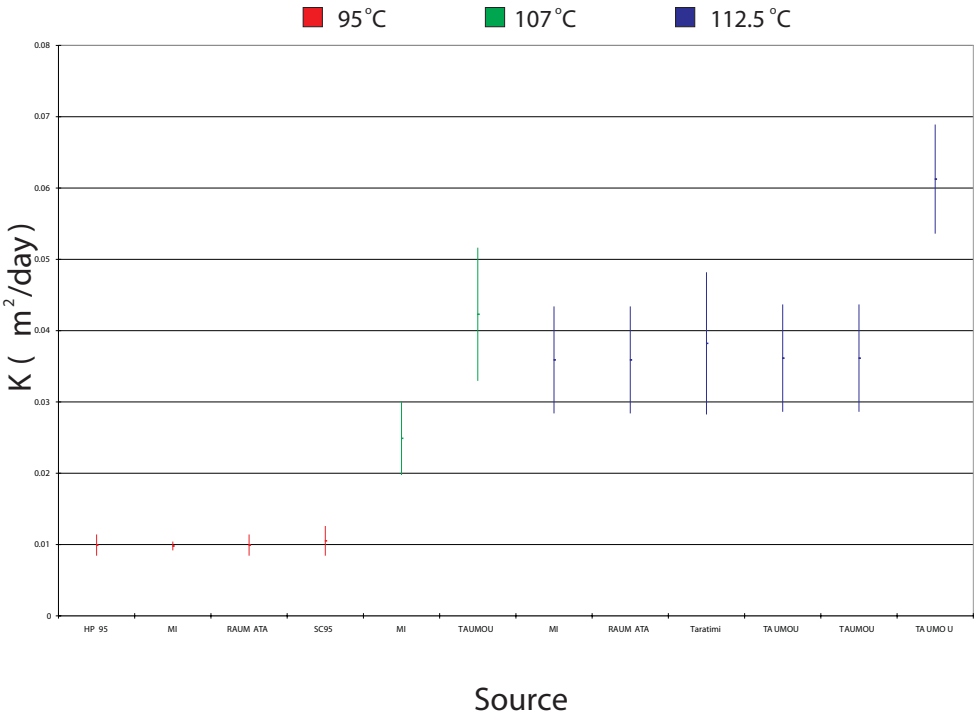

Figure 6.2: Comparative hydration rates for Mayor Island source samples at 95, 107 and 112.5 ^{0}C

are sources of obsidian in this region that are green in transmitted light and potentially confound identification of material deriving from the Mayor Island hydration group. It is important to establish the extent to which green material from the Northland region differs from material from Mayor Island in terms of hydration behaviour. This also provides primary hydration data for material associated with the general Kaeo source area. Thus the primary focus of the experimental programme with regards to the Northland sources was to establish the variation in hydration behaviour within the general Kaeo source, however Huruiki samples were also investigated as part of the general New Zealand wide comparison.

6.3.1 Experimental Design

In order to investigate the range of variation in hydration behaviour within the wider "Kaeo" source area, samples have been examined from four discrete spatial locations corresponding to the main exposures identified in this area previously (*infra vide*:§3.3.1; Table C.4). The experimental focus is on identifying the range of hydration behaviour within, and establishing base hydration estimates for, material from this source area. To this ends comparative hydrations have been conducted at 95, 107, 112.5 and 125 ^{0}C as outlined in Table E.2.

Base hydration data has also been generated for a sample from the Huruiki source. Hydration data have been generated at 95, 107, 112.5 and 125 ^{0}C (Table E.2; Figure E.7). These data have been collected to provide a comparative result from the Huruiki source group with a view to making inferences about the variation in hydration rates among New Zealand obsidian in general, and as an initial basis for defining the hydration behaviour of Huruiki obsidian.

6.3.2 Results

The Kaeo results (Figure 6.3) indicate no systematic differences in hydration results among the Kaeo source samples detectable at the available measurement precision. As the analysed samples derive from spatially discrete deposits this strongly suggests that the Kaeo material exhibits uniform hydration behaviour[3] thus the data can be treated as replicate measurements of a general Kaeo source hydration rate, and generic source hydration parameters have been generated from the grouped data (Figure E.4 : "pooled" data in Table E.2). The conclusion that there is little systematic variation within the Kaeo source area is in keeping with geochemical analyses which have indicated that there are no geochemically discrete sub sources of obsidian within this area (*e.g.* Neve *et al.* 1994; *supra vide*:§D).

In addition to providing baseline hydration data for the Kaeo region this analysis provides direct estimates of glass specific hydration parameters for the general Kaeo source (Tables 6.6,6.7 :Figures E.5, E.6) that can be directly applied in the dating of artefacts associated with this group.

The Huruiki hydration results (Table E.2; Figure E.7) provide relatively broad estimates for the hydration behaviour of the sample analysed (Tables 6.6,6.7 :Figures E.8, E.9). As these results relate to a single specimen they do not provide control over the degree of intrasource variation that may be present, and accordingly these data cannot be used to meaningfully infer glass specific hydration parameters for artefacts deriving from Huruiki. While these results cannot be used to directly infer hydration parameters of artefacts associated with the Huruiki source area, they do provide baseline for further resolution of Huruiki hydration parameters via secondary techniques such as cross dating and hydration analogue experiments.

[3] within the available measurement precision

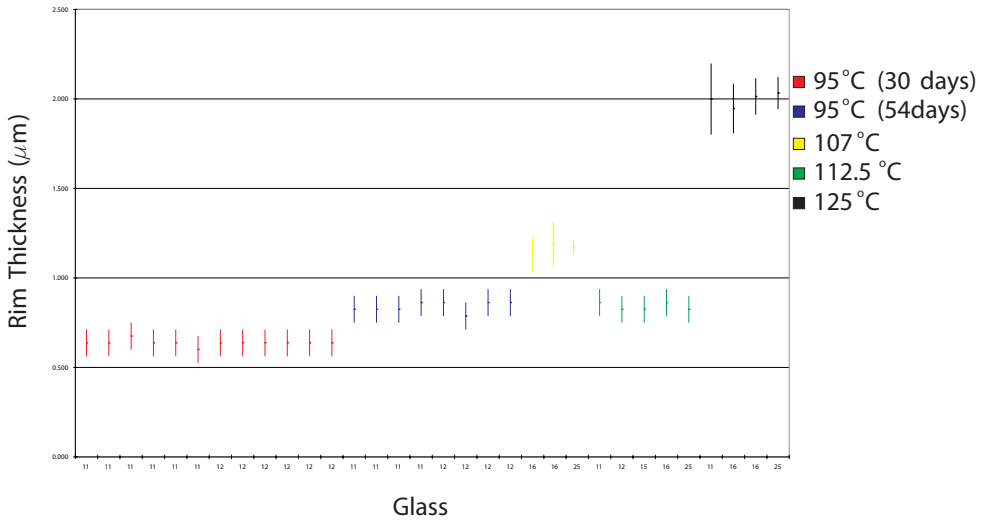

Figure 6.3: Comparative experimental hydration rates of Kaeo source material

6.4 TVZ

As no green obsidian is associated with the TVZ source area the definition of hydration parameters for TVZ material has not been a high priority in the current experimental program. However, it is useful to define baseline hydration parameters for material deriving from this source area for the purposes of both defining the degree of variation in hydration behaviour amongst New Zealand obsidian general, and to act as a reference for further resolution via secondary techniques. A single source location (Ben Lomond) has been arbitrarily chosen as the base TVZ material for this purpose.

6.4.1 Experimental Design

As this component of the experimental program is simply designed to provide a reference control for the hydration of TVZ obsidian, the ex-

perimental data all derive from samples obtained from a single block of obsidian hydrated at temperatures ranging from 95-160 ^{0}C (Table E.3; Figure E.10). The intention is to generate a single high precision hydration reference point for the TVZ.

6.4.2 Results

The hydration parameters generated by analysis of these data provide a reasonable precision estimate of the hydration parameters for the sample analysed (Tables 6.6,6.7 :Figures E.11, E.12). However, these do not in themselves provide any control over the degree of intrasource variation throughout the TVZ. Thus the results presented here simply represent baseline data for hydration rates of obsidian from the TVZ and should not be used to directly estimate glass specific hydration parameters for TVZ obsidian. This does however represent a geochemically characterised hydration datum for the TVZ which can be used as a base to establishing a more secure description of the hydration parameters of TVZ obsidian in general via secondary techniques.

6.5 Coromandel

The Coromandel source area was initially targeted as a primary focus of the experimental program as “green” obsidian derives from this source region (Waihi *supra vide*:§B.1). Accordingly a series of inductions were designed for the Wahi samples. However, it has become apparent that the inherent variation within any given sample deriving from the Waihi source is of a magnitude to render any such program useless. In some cases three flakes from the same specimen hydrated in the same experimental run have returned hydration extents varying by up to 200 % of the minimum rim size. This variation is also apparent in any given flake,

where there may be significant variation in size along the measured rim. In light of this the extensive hydration program initially pursued for the Waihi samples has produced only limited, low quality, results. The only results reported are those for which the rim size remained constant over the measured section.

In addition to the aborted definition of Waihi hydration parameters, the experimental inductions have been designed to provide both base hydration parameters for obsidian deriving from the Coromandel source area and an outline of the degree of variation in source hydration rates from within this general source area. A sample from Te Ahumata has been arbitrarily selected as the type source for the Coromandel zone.

6.5.1 Experimental Design

Samples from Te Ahumata have been hydrated at temperatures ranging from 95-160 ^{0}C (Figure E.13), in order to generate the highest possible precision definition of hydration parameters for the sample analysed. The results of these inductions can be compared with samples from five additional Coromandel zone sources induced at 112.5 and 125 ^{0}C (Table E.4). This comparison provides base data relating to the degree of variation in hydration rates of sources from within the general Coromandel zone as well as initial estimates for the individual sources.

6.5.2 Results

A comparison of the rate data from the six Coromandel zone sources analysed shows that there is significant variation in hydration behaviour within this source zone (Figure 6.4). There is a consistent trend of the Te Ahumata and Whitipirorua samples exhibiting more rapid hydration behaviour than the otherwise fairly uniform hydration behaviour exhibited

by the other sources. This suggests that the calculated hydration parameters for the Te Ahumata sample (Tables 6.6,6.7 :Figures E.14, E.15) cannot be used as a generic estimate for the glass specific hydration parameters of artefacts sourcing to the Coromandel zone.

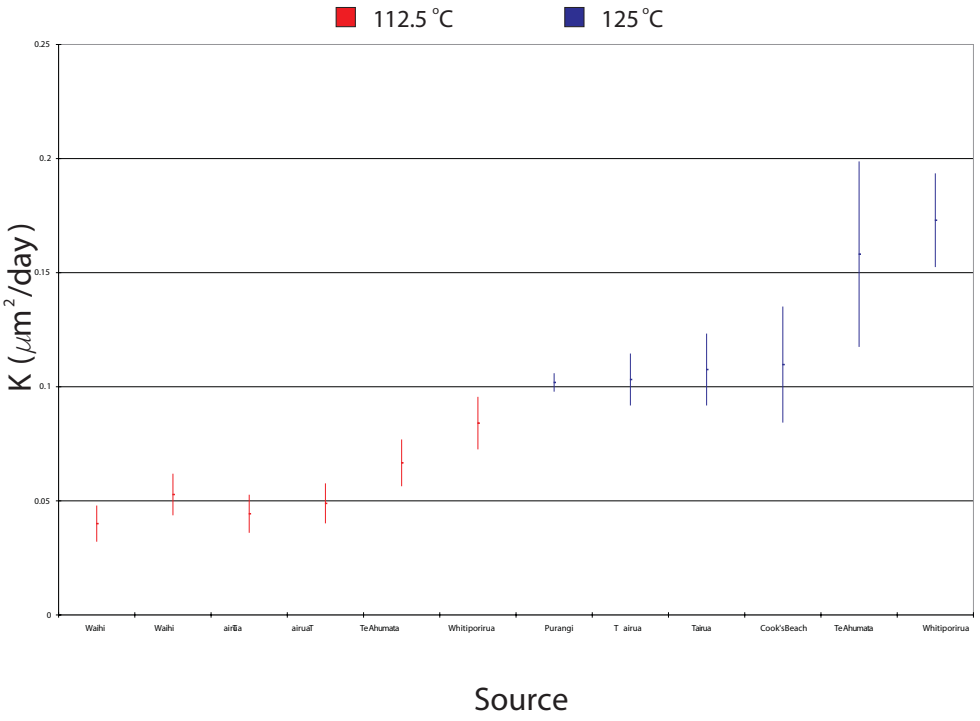

Figure 6.4: Comparative experimental hydration rates for the Coromandel zone samples at 112.5 and 125 ^{0}C

6.6 Conclusion

The most general method to providing artefact specific hydration rate parameters is to associate each artefact with a known source group for which the hydration behaviour has been defined. However, it is not practical to generate high precision experimental results for a wide range of

source groups through experimental hydration alone. In light of this induced hydration experiments should (initially at least) concentrate on producing high precision primary data for a small range of sources, rather than low precision data for a larger range of sources. This enables both the dating of artefacts deriving from the analysed source groups and the development of further rate data via secondary methods.

Following this there have been two components to the experimental programme presented here. First there has been a concentration on establishing the hydration behaviour of "green" obsidian for New Zealand, with a particular focus on the Mayor Island source. Secondly there has been an effort in establishing the degree to which there may be variance in hydration behaviour amongst New Zealand obsidian sources in general.

The experimental results have shown that there is significant variation in hydration behaviour among New Zealand obsidian (Figures 6.5 & 6.6; *supra vide*:§E.2 - Figures E.16, E.17, E.18, E.19 and E.20). Comparisons of all analysed source groups at 95-160 ^{0}C reveal a consistent pattern of three broad hydration groups. It is apparent that the Mayor Island hydration group hydrates at a significantly slower rate than all other sources. With the exception of the Whitipirorua and Te Ahumata samples, the remaining sources exhibit apparently uniform hydration behaviour. This suggests that it may be possible to expand the Kaeo hydration group to incorporate the majority of non-Mayor Island sources in New Zealand. However this hydration group is potentially confounded by sources such as Te Ahumata, and it is necessary to develop a protocol for the identification of hydration group membership.

The data that has been generated via this experimental program only represents an initial baseline for describing the hydration behaviour of New Zealand obsidian. Further resolution is necessary, particularly for the "grey" obsidian, and this would most profitably be pursued via

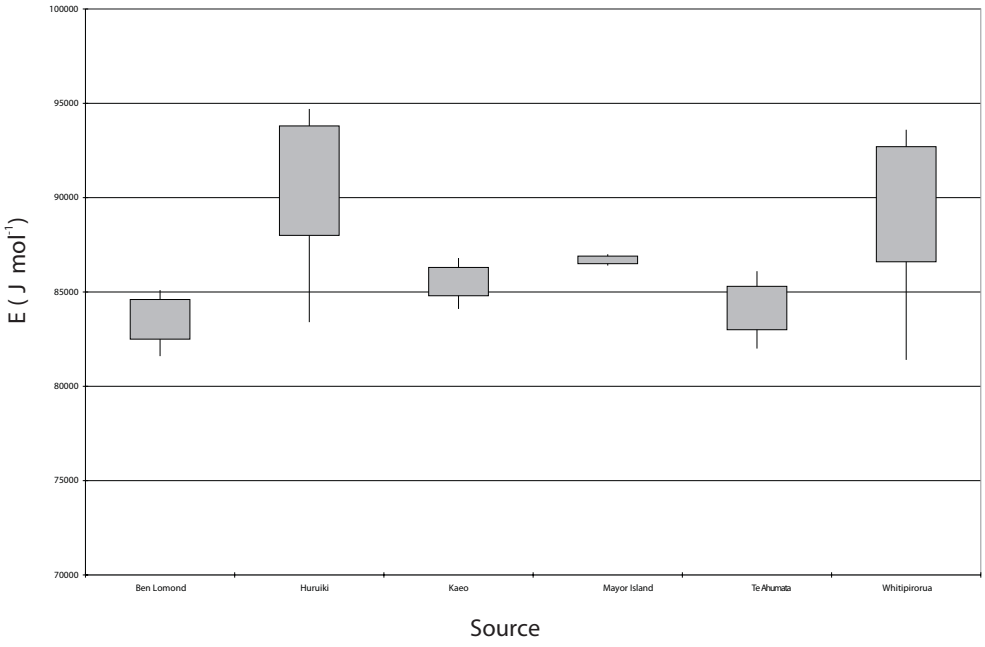

Figure 6.5: Comparison of estimated gas activation energy (E) distributions for some New Zealand obsidian groups; solid rectangles represent the 68% HPD, lines represent the 95 % HPD

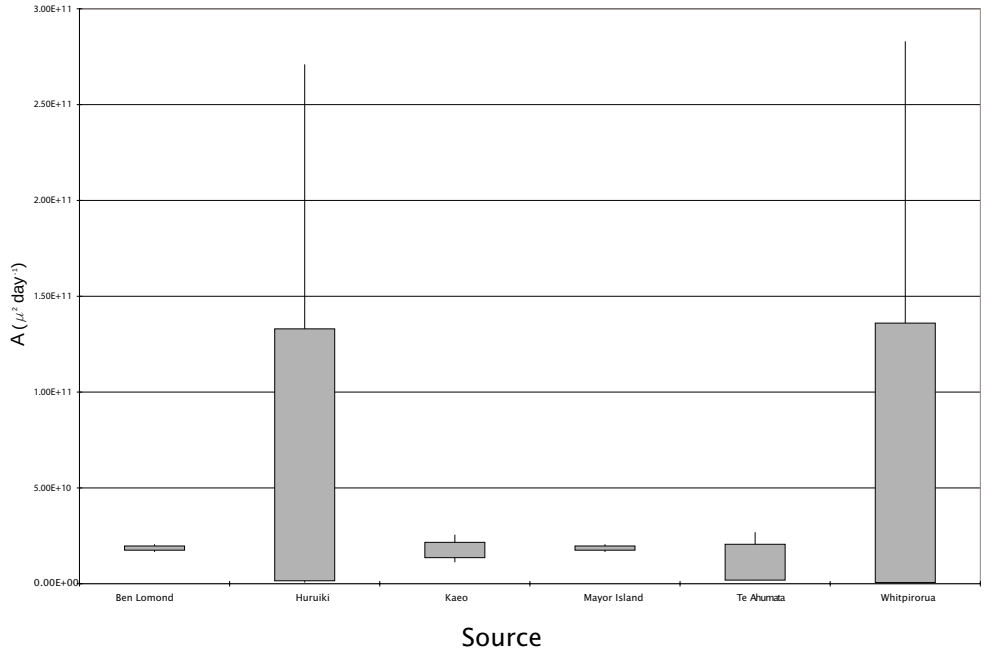

Figure 6.6: Comparison of estimated pre-exponential component (A) distributions for some New Zealand obsidian groups; solid rectangles represent the 68% HPD, lines represent the 95 % HPD

Table 6.6: Estimated gas activation energies (E J mol^{-1}) for some New Zealand obsidian groups

Source	Lower 95% C.I.	Upper 95% C.I.	Lower 68% C.I.	Upper 68% C.I.
Ben Lomond	81600	85100	82500	84600
Huruiki	83400	94700	88000	93800
Kaeo	84100	86800	84800	86300
Mayor Island	86400	87000	86500	86900
Te Ahumata	82000	86100	83000	85300
Whitipirorua	81400	93600	86600	92700

Table 6.7: Estimated pre-exponential components (A μ^2 day^{-1}) for some New Zealand obsidian groups

Source	Lower 95% C.I.	Upper 95% C.I.	Lower 68% C.I.	Upper 68% C.I.
Ben Lomond	1.66E+10	2.06E+10	1.75E+10	1.97E+10
Huruiki	6.46E+08	2.71E+11	1.54E+09	1.33E+11
Kaeo	1.12E+10	2.56E+10	1.36E+10	2.16E+10
MayorIsland	1.66E+10	2.06E+10	1.75E+10	1.97E+10
Te Ahumata	7.51E+09	2.69E+10	1.87E+09	2.06E+10
Whitipirorua	6.11E+08	2.83E+11	6.11E+08	1.36E+11

further primary induction experiments in tandem with secondary techniques such as cross-dating controls and induction analogues that are targeted at defining the degree of intra-source variation.

At the current juncture, artefact specific hydration control is possible for both the Kaeo and Mayor Island hydration groups, and this is sufficient to apply OHD in most archaeological contexts if a suitable method for associating artefacts and hydration groups can be defined. As the Mayor Island hydration group (MIHG) is the most precisely controlled source, and also the most widely distributed source within the archaeological record, this group acts as a primary hydration rate control for New Zealand obsidian. The distribution of the hydration rate parameter estimates for the MIHG are normal (Figures E.2 and E.3) with E $\sim N(86700, 150^2)$ and $A \sim N(1.86E+10, (1E+9)^2)$. These estimates enable both the development of secondary hydration rate data for other

sources through cross-dating exercises, and the dating of artefacts that derive from the MIHG. However, in order to do this it is necessary to be able to confidently identify archaeological samples that derive from the MIHG. This problem is considered in the next chapter.

Chapter 7

Sourcing New Zealand obsidian

7.1 Introduction

As concluded in the preceding chapter one of the most important components of establishing rate controls for New Zealand obsidian is being able to determine the source of any given flake. If this cannot be achieved then there is no benefit in defining rates more precisely than generating a generic "New Zealand" rate. However, for the purposes of OHD, sourcing is only necessary to the extent of associating artefacts with hydration groups. Currently only two hydration groups have been defined, the Mayor Island Hydration group (MIHG) and the Kaeo group (KHG). Thus we wish to establish the most efficient and cost effective method of identifying artefacts that derive from each of these two groups. The problem can be further simplified by the fact that it is not necessary to be able to associate every artefact with an hydration group. It is only necessary to be able to source sufficient material for the dating application. In consideration of these points a sourcing protocol that is optimal in terms of the requirements of OHD may not be suitable for general provenance studies, and vice versa.

In this chapter general approaches to sourcing obsidian artefacts are considered and a protocol that meets the requirements of applied OHD is outlined.

7.2 Previous Approaches to Sourcing New Zealand Obsidian

There have been various programs directed at establishing methods for sourcing New Zealand obsidian ranging from basic physical descriptions (Moore n.d.) to simple attribute studies such as the R.I. measurements conducted by Green (1962) through to comprehensive PIXE-PIGME char-

acterisation studies (*e.g.* Neve *et al.* 1994). These approaches can be classed into two general groups:

1. Chemical characterisation studies
2. Discriminating attribute studies

The chemical characterisation group of sourcing approaches are directed toward defining characteristic chemical signatures of each of the sources. Sourcing of an artefact is then accomplished via selecting the source that most closely matches the chemical signature of the artefact. The discriminating attribute studies have been based around defining a set of characteristic attributes (ie Density, Colour *etc.*) associated with each source. Sourcing is then accomplished via matching artefact attributes with known source attributes. The distinction between these two approaches is rather fine. Chemical characterisation is obviously based around the chemical attributes of source and artefact, but the distinction is valid in the context of the application of these two general approaches. In general chemical characterisation is more amenable to statistical treatment and certainly the typical application of this type of sourcing approach has been treated in a more quantitative fashion than those I've classed attribute approaches. However, this is a distinction in the typical application of the two approaches and chemical characterisation is no more inherently objective nor "scientific" than any other attribute sourcing technique. Objectivity and reproducibility in sourcing is brought about by sound, precise, protocols.

Whatever approach is employed, it is apparent that the results of any sourcing analysis are only meaningful in terms of a sound set of reference data. If the reference data for the source material are not representative of either the individual source or the broader source groups available prehistorically, then the results of the analysis may well be misleading. Thus any sourcing protocol should provide a sound, sys-

tematic and reproducible method for source assignation and must take into account the extent to which the available reference data actually represents the true distribution of material that was available for exploitation prehistorically.

There are a wide variety of analytic techniques in use through the sciences that could be employed to source artefacts, and a number of these have been used in New Zealand obsidian studies. The approaches that have been applied in New Zealand range through Emission spectroscopy (Green *et al.* 1967; Leach *et al.* 1978*b*), Atomic absorption spectroscopy (Armitage *et al.* 1972), Neutron Activation Analysis (Leach and Warren 1981), thermoluminescence (Leach *et al.* 1978*b*), XRF (Ward 1972; 1974*a*; Seelenfreund-Hirsch 1985; Bollong 1983; Leach 1977) and PIXE/PIGME (Leach *et al.* 1986*a*; Neve *et al.* 1994; Duerden *et al.* 1987). As a result of the large number of characterisation studies that have been conducted an extensive corpus of reference geochemical data exists. However, in order to make use of this data it is necessary to employ one of the techniques outlined above, which can be expensive, of limited accessibility and/or completely destructive. While there is no doubt that chemical characterisation studies can provide a very reliable means of sourcing archaeological material (*e.g.* Neve *et al.* 1994), the techniques referred to above are of limited suitability in terms of routine OHD.

It is important for the ongoing use of OHD that it is possible to quickly and economically associate artefacts with the appropriate hydration group. Ideally the technique should be as non-destructive as possible. Of the techniques outlined above Pixe-Pigme is ideal for the purposes of OHD but the expense and time cost of characterising every sample to be dated would be taxing. This is not to mention the fact that most facilities capable of doing such work will not give volume archaeological provenance studies high priority.

In addition to the chemical characterisation studies there have been several discriminating attribute studies used in New Zealand archaeology. An initial study was conducted by Green (1962) who measured the R.I. of several New Zealand obsidian sources. Green's study showed that there was not sufficient discrimination between sources in terms of R.I. to provide an accurate protocol, other than the discrimination of Mayor Island material from other sources. The other major attribute that has been used as a sourcing index is the relative density of obsidian samples from different sources (Reeves and Armitage 1973*a*; Stevenson *et al.* 1995). Again this attribute suffers in that there is too great a degree of overlap between the sources to provide sufficient discrimination. A third approach is that used by Moore (n.d.) where the physical characteristics of the different sources are described. Here the sample is sourced by relating features visible in the hand specimen to the described features from the different sources. This approach is limited by the requirement of a reasonable degree of familiarity with the material (not an insurmountable problem) and the fact that small flakes may not contain sufficient visual indicators to enable sourcing. Another problem with this approach is that in its current form there is no possibility of quantifying the certainty of the fit.

7.3 Routine sourcing protocol

In terms of sourcing for the purposes of OHD it is only necessary to identify artefacts to hydration groups, and it is only necessary to be able to identify sufficient material to enable OHD to be applied. The optimal sourcing protocol then, is the one that can most rapidly and reliably meet these requirements. Thus if there were some simple discriminating attribute that enabled association of the majority of artefacts with hydration groups this would be sufficient. It is clear that the range of

techniques that may be employed to enable sourcing vary considerably in complexity and cost. Thus the most efficient system to employ should be based around the stepwise application of successively more sophisticated techniques until sufficient material has been associated with an hydration group. This sort of top-down system will minimise the cost and time involved with any sourcing program, and increase the power of any discrimination technique through combination.

The application of such an approach involves the stepwise sub setting of the assemblage by successive discriminating attributes. That is the sample is initially split into general sub-groups, and these subgroups are discriminated into further subsets as necessary until either all or a sufficient number of samples have been associated into a sub-group that corresponds to a hydration group. In this type of approach it is obviously most efficient to employ the most rapid, cost effective, techniques first. This means that only the approaches necessary to discriminate sufficient artefacts need to be employed resulting in a more efficient system than would arise from the global application of all techniques. An additional benefit of this approach is that it maximises discrimination efficiency as any given technique is only required to discriminate amongst samples within existing subsets.

The application of visual identification is the most rapid and economic option described above, and accordingly should be the first approach employed. If visual identification is insufficient then it is possible to employ more time consuming and expensive techniques such as PIXE/PIGME. For the current purposes of associating the appropriate artefacts with the Kaeo and Mayor Island hydration groups it is only necessary to employ visual discrimination. For the extension of this protocol into further hydration groups it may be necessary to follow visual subsetting with other discrimination procedures.

7.4 Visual Indicators

Visual attributes are present in both hand specimen (Macro-visual attributes) and petrographic section (micro-visual attributes), and it is possible to use these attributes to successively exclude potential hydration groups from possible association with the artefact. In the current situation only two hydration groups (Kaeo and Mayor Island) have been defined, thus the attribute identification protocol only needs to identify these two groups. However, as further hydration groups are defined, appropriate exclusion characteristics can be added to enable association of the appropriate artefacts with these sources.

With most visual attributes there is considerable scope for subjectivity in the description. Accordingly it is essential that the attributes are explicitly defined in order to ensure that descriptions are consistent. The visual attributes defined in the following sections are designed to provide a preliminary subsetting protocol for any archaeological assemblage and are sufficient to define the current hydration groups. However, they will not provide sufficient discrimination for general archaeological sourcing applications such as those discussed by Moore (n.d.).

7.4.1 Macro-visual

There are an almost infinite number of macro-visual attributes that could be used in describing artefacts. However there is no benefit in defining more attributes than are necessary to associate artefacts and hydration groups. In the following sub-sections a series of attributes that allow definition of key features are described. In each case the application of the visual indicators described requires the use of a suitable reference set of hand-specimens.

Transmitted Colour

This is the colour of the glass in transmitted light. As the colour arises due to differential absorption of various wavelengths the thickness of any glass sample will influence the apparent colour. Thus there will be some variation in transmitted light colour for samples from the same source purely as a function of sample thickness. This attribute is designed to be the primary discriminating variable for initial subgrouping, and in terms of providing control for the current hydration groups it is only necessary to distinguish between green and non-green. However, as further hydration groups are defined the categories will change. The current categories are:

1. Green
2. Other

In this case the definition of "green" is to some extent subjective. The classification requires that suitable hand specimens are present in the reference set.

A more formal definition of "green" can be made with reference to the typical transmitted light spectra. This can be accomplished via digital colour images of the sample under transmitted light. If a digital image capture device is calibrated to a common standard then the RGB band intensities of the captured image can be used to objectively define the transmitted light colour. In this most simple application the results are not directly comparable between image capture systems, however will be consistent within any given system. If we use a Pixera Pro camera and with white calibrated to a standard blank glass target then the transmitted light colour characteristics of the different sources can be defined. Here the band intensities are defined in the total intensity (greyscale intensity) region of 40-120 which roughly corresponds to the second dark-

est quarter of the image intensity range. In order to take into account variation in the absolute intensity of any given image it is necessary to define band intensity ratios, in this case given the interest in green the two intensity ratios defined are Green/Blue and Green/Red. On the basis of these ratios green is hereby defined as samples exhibiting an average G/B and G/R measure of greater than 1.57 and 0.6 respectively. It is most probably possible to produce more exact measures of these attributes and define what are in some cases source specific parameters via an extension of this approach. However, the current interest is simply in defining "green". In practice this definition limits the definition of "green" solely to samples deriving from the Kaeo and MI source regions.

Reflected Colour

This is the colour of the glass under reflected light in front of a matt black background. Samples may vary in reflected colour and this attribute should describe the predominant surface colour. In this definition only the primary colour is defined. Thus while there may be a number of different shades of grey they would all be defined as grey under this definition. The current categories are:

1. Black
2. Grey
3. Green
4. Red
5. Yellow
6. Brown
7. Other

Again a reference set of type specimens is required in order to assign artefacts to the correct categories.

Lustre

This is the appearance of the glass surface. I have currently defined four general classes of Lustre; vitreous, pitted, waxy and other. Where samples are of a mixed composition they are described as mixed with a suffix of the appropriate categories. This attribute requires an appropriate set of reference samples. The type specimens are as follows:

Viteous	Mayor Island staircase (source 15 Table B.2)
Pitted	Kaeo (source 17.1 Table B.2)
Waxy	Waihi (source 32.1 Table B.2)

Translucency

The attribute of translucency qualifies the degree of translucency in the sample. This attribute is subjective and any consistent description must be made with reference to a standard definition. I will adopt the basic categories defined by Moore (n.d.) as follows:

- Excellent: it is possible to read this text through the sample.
- Good: can just make out letters through sample
- moderate: sample transmits light, but no detail can be discerned through the sample
- poor: sample only just transmits light or is completely opaque

Banding

Banding can be visible on both the surface of obsidian flakes and internally when viewed in transmitted light. In this definition internal and external banding are described separately, though the nature of each type of banding is described identically. Four elements of banding are described as follows.

A) Composition describes the visible appearance of the composite elements making up the band. In most cases the composite elements of bands are not visible. In this case the band composition is described as continuous. In some cases however, it is possible to detect the individual elements within a band. In this case the band composition is described as discrete.

B) Intensity describes the ease with which the band can be visually detected. This attribute is obviously highly subjective and classification needs to be made with reference to comparative samples. I have defined three categories; weak, moderate and strong and these are classified with reference to two type samples held as part of the obsidian reference collection described in Chapter 3.

C) Size quantifies the width of any banding present. In the case that the banding is of an irregular size then the range of band size is stated.

Crystals

This attribute describes the degree of visible crystalline inclusion in the glass surface. This inclusion can be present either as phenocrysts or spherulites. Each of these are described separately though the same

two characteristics (size and abundance) are quantified for each type of inclusion.

A) Size simply describes the approximate size or range of sizes of the inclusions. This is defined as a longest axis measurement.

B) Abundance simply describes the abundance of the inclusion as a percentage surface coverage figure. This measurement can be made with reference to tables such as the chart for visual percentage estimation reprinted in the Munsell soil colour charts.

It should be noted that the macro-visual attributes defined above will not in themselves allow reliable discrimination between sources. The degree of intra-source variability is such that it is possible to find specimens from almost any source that could be confused with other sources on the basis of the attributes just defined. These attributes are simply defined to allow initial subsetting of the artefacts.

7.4.2 Micro-visual

In addition to the macro-visual attributes of the specimen, visual features of the sample are apparent in petrographic section. There are a number of micro-visual features that discriminate amongst different source groups (*e.g.* Wilson 1988) and the explicit definition of these will most probably allow consistent provenancing of most artefacts to source. In terms of applied OHD this is currently unnecessary and only two micro-visual attributes are currently defined. These are the pheoncryst counts described previously (*infra vide*:§5). As outlined it is possible to quantify the relative abundance of optically active crystals and non-optically active microlites in each glass. These two variables allow a further level of discrimination amongst samples within the same subset.

7.5 The Sourcing Algorithm

It is possible to explicitly describe each of the current defined hydration groups on the basis of the visual attributes defined above. Obviously the most basic discrimination made is based on transmitted colour. The defined hydration groups are both green in transmitted colour. Thus the sourcing protocol needs to only discriminate amongst the material that is green in transmitted light. The definitions of the hydration groups are as given in Table 7.1, with comparative attributes for the potentially confounding Waihi Source Group.

Table 7.1: Definition of the visual attributes for the Mayor Island and Kaeo hydration groups, and the potentially confounding Waihi source

Attribute	Hydration Groups		
	Mayor Island	Kaeo	Waihi
Transmitted Colour	green	green	green
Reflected Colour	black	black	olive-black
Lustre	vitreous	pitted	waxy-vitreous
Translucency	moderate-excellent	moderate-good	poor-moderate
Banding (external)	nil	nil	common
Banding (internal)	nil-present	nil-present	nil-present
Phenocrysts	rare	rare	rare
Spherulites	rare	nil	rare
micro crystal count	0.006 ± 0.005	0.036 ± 0.002	0.015 ± 0.005
microlite count	0.005 ± 0.005	0.007 ± 0.001	0.02 ± 0.008

As can be appreciated there is the potential for considerable confusion on the basis of macro-visual characteristics alone, however in combination with the micro-visual crystal count data each group is uniquely defined. On the basis of this, a sourcing algorithm is outlined in Figure 7.1.

While it is almost certain that this algorithm will exclude some valid members of each hydration group this is not of concern. The primary consideration is confidence that artefact association with either the Kaeo

or Mayor Island hydration groups under this protocol is valid. The tight defining criteria will ensure that this is the case. As future hydration groups are defined this protocol can be extended by defining protocols to discriminate each of the subgroups defined in Figure 7.1 as appropriate.

7.6 Protocol Evaluation

In order to evaluate the performance of this sourcing protocol two trials were run. In the first trial five sets of 20 flakes of random composition were generated and these were classified blind. In the second trial artefacts previously sourced by PIXE-PIGME (Neve *et al.* 1994) were again classified blind.

7.6.1 Source Sample Algorithm Test

In this test five sets of 20 samples each were generated from the reference collections. These samples were then associated with the subsets defined in Figure 7.1 under a blind experimental structure. The results of these experiments (Tables 7.2 & 7.3) show that the results of the sourcing algorithm consistently correspond to the true source distribution. In no cases is an invalid sample associated with either the Kaeo or Mayor Island Hydration Groups. While some valid members are excluded this is not of concern as long as sufficient samples can be identified for the purposes of dating.

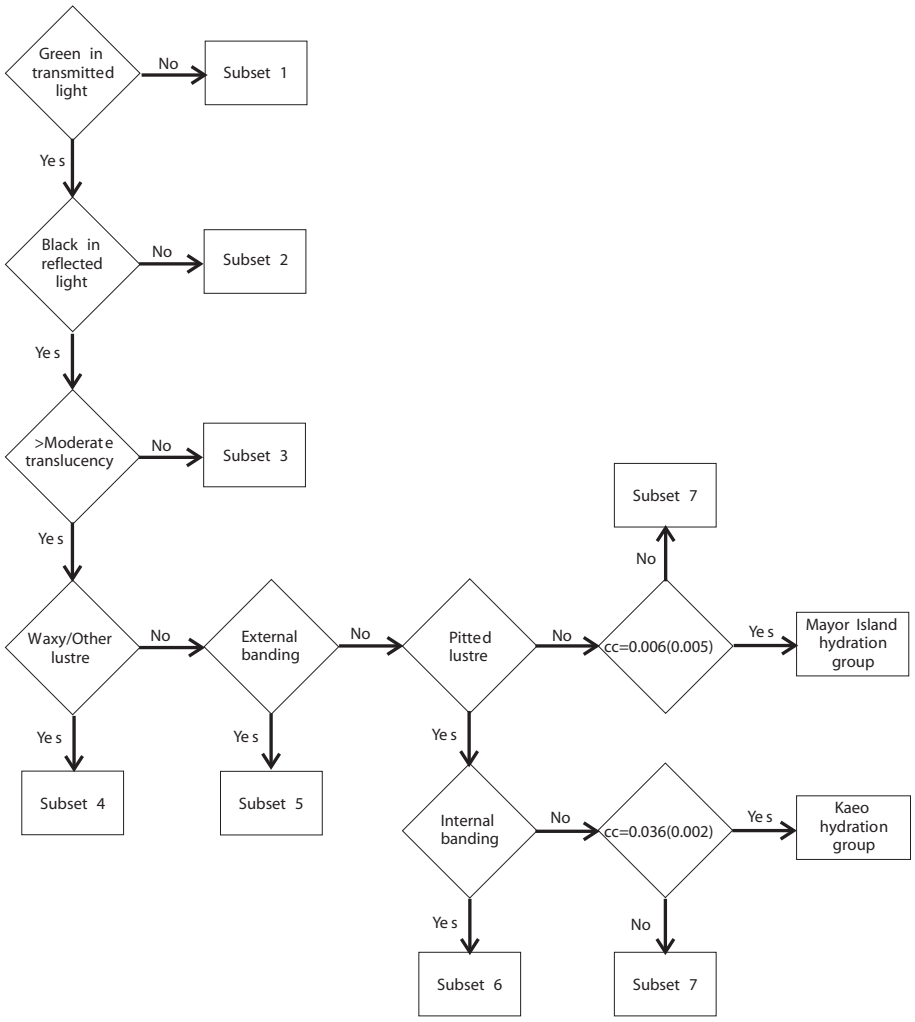

Figure 7.1: Flow chart for identification of artefacts belonging to Kaeo or Mayor Island hydration groups

Martin Jones 2002

Table 7.2: Single blind experimental structure testing sourcing algorithm

Sample	Experimental Runs				
	1	2	3	4	5
1	tr[†]	w	mi	mi	mi
2	k	tr	ta	mic	mi
3	mi	bl	mic	bl	mi
4	tr	ta	k	mi	bl
5	mi	c	w	bl	c
6	mi	mi	tr	mi	mi
7	bl	mi	mi	mi	mi
8	mi	k	ta	ta	mi
9	c	c	tr	mi	c
10	k	mic	ta	mi	k
11	bl	w	mi	bl	ta
12	bl	mi	mic	mi	mi
13	mi	w	bl	bl	bl
14	ta	ta	mi	mi	ta
15	mic	mic	tr	k	ta
16	k	bl	tr	mic	tr
17	mi	mi	mi	tr	mi
18	mi	mic	w	mi	bl
19	bl	bl	w	ta	mi
20	mi	mi	mi	c	mi

[†] bl = Ben Lomond
c = Cook's Beach
k = Kaeo
mi = Mayor Island Selvage
mic = Mayor Island Pyroclastic
ta = Te Ahumata
tr = Tairua
w = Waihi

Table 7.3: Results of sourcing the experimental structure outlined in Table 7.2

Sample	Experimental Runs				
	1	2	3	4	5
1	1	2	MHG	MHG	MHG
2	KHG	1	1	2	MHG
3	MHG	1	3	1	MHG
4	1	1	KHG	MHG	1
5	MHG	1	2	1	1
6	6	MHG	1	MHG	3
7	1	MHG	MHG	MHG	MHG
8	MHG	KHG	1	1	MHG
9	1	1	1	3	1
10	KHG	5	1	MHG	KHG
11	1	2	3	1	1
12	1	MHG	3	MHG	MHG
13	3	2	1	1	1
14	1	1	MHG	MHG	1
15	2	4	1	KHG	1
16	KHG	1	1	2	1
17	MHG	MHG	MHG	1	MHG
18	MHG	3	2	MHG	1
19	1	1	2	1	MHG
20	MHG	MHG	MHG	1	3

† Numbers stand for subset as defined in Figure 7.1

KHG = Kaeo Hydration Group

MHG = Mayor Island Hydration Group

7.6.2 PIXE Algorithm Comparison

Neve *et al.* (1994)obsidian artefacts from Opita (T13/324,788,789). On the basis of this analysis and a reference data base of source PIXE results they have produced, Neve *et al.* (1994) have provided provenance details for these 76 artefacts. Included amongst these artefacts are 34 sourced to Mayor Island and 20 to Waihi. Thus this collection represents a useful test case for the performance of the sourcing algorithm specified previously. This test was conducted by associating each of the artefacts with a subset defined in Figure 7.1. This was conducted as a single blind experiment. The comparative results are shown in Table 7.4 and it is apparent that the visual sourcing algorithm has produced results consistent with the analysis of Neve *et al.* (1994). No non-Mayor Island samples have been associated with the Mayor Island Hydration Group. Thus the procedure has been able to discriminate the potentially confounding Waihi samples. Of the 34 artefacts Neve *et al.* (1994) have sourced to Mayor Island, 27 have been associated with the Mayor Island Hydration Group. Thus some possibly valid members of the Mayor Island Hydration Group have been rejected. As outlined previously this is not a concern for the purposes of applied OHD.

Table 7.4: Comparison of PIXE provenance results (Neve *et al.* 1994) and subset classification according to the algorithm detailed in Figure 7.1

Sample Number (Neve *et al.* 1994)	Provenance (Neve *et al.* 1994)	Identified as MIHG
2	Mayor Island	
4	Waihi	
12	Mayor Island	✓
21	Waihi	

continued on the next page

Table 7.4: *continued*

Sample Number (Neve *et al.* 1994)	Provenance (Neve *et al.* 1994)	Identified as MIHG
38	Waihi	
44	Waihi	
46	Mayor Island	✓
47	Mayor Island	✓
66	Mayor Island	✓
70	Waihi	
77	Mayor Island	
87	Waihi	
98	Waihi	
103	Onemana	
116	Waihi	
117	Waihi	
119	Mayor Island	✓
124	Waihi	
130	Waihi	
146	Waihi	
287	Waihi	
322	Mayor Island	✓
337	Mayor Island	✓
338	Onemana	
339	Cooks Bay/Purangi	
378	Waihi	
395	Waihi	
411	Mayor Island	✓
416	Mayor Island	✓
417	Mayor Island	✓

continued on the next page

Table 7.4: *continued*

Sample Number (Neve *et al.* 1994)	Provenance (Neve *et al.* 1994)	Identified as MIHG
418	Mayor Island	
440	Waihi	
441	Mayor Island	✓
470	Waihi	
475	Onemana	
477	Waihi	
502	Mayor Island	✓
508	Mayor Island	✓
509	Mayor Island	✓
102e	Onemana	
106b	Cooks Bay/Purangi	
365a	Mayor Island	✓
365b	Mayor Island	✓
365c	Onemana	
366a	Waihi	
366b	Waihi	
367a	Waihi	
393a	Mayor Island	✓
394a	Waihi	
408c	Waihi	
414a	Onemana	
414b	Onemana	
414c	Mayor Island	
427a	Onemana	
446a	Mayor Island	✓
446b	Mayor Island	✓

continued on the next page

Table 7.4: *continued*

Sample Number (Neve *et al.* 1994)	Provenance (Neve *et al.* 1994)	Identified as MIHG
446c	Waihi	
446d	Mayor Island	✓
446e	Mayor Island	✓
446f	Waihi	
446g	Mayor Island	✓
452a	Onemana	
452b	Waihi	
471b	Mayor Island	✓
472a	Mayor Island	
472b	Mayor Island	✓
472c	Waihi	
472d	Onemana	
472e	Waihi	
472f	Mayor Island	✓
472g	Waihi	
472h	Mayor Island	
511a	Mayor Island	✓
511b	Mayor Island	✓
513a	Waihi	
51a	Mayor Island	

7.7 Conclusion

An important component of establishing rate controls for New Zealand obsidian is being able to identify artefacts that derive from the Kaeo hydration group or in particular the Mayor Island Hydration Group. This

allows the high precision primary hydration rate data presented in Chapter 6 to be used in both dating exercises and in developing hydration parameter estimates for further source groups through secondary methods. In this chapter we have seen that it is possible to confidently identify artefacts that are valid members of either the Kaeo or Mayor Island hydration groups on the basis of a simple, rapid and economical sourcing protocol based around identification of key visual attributes. This protocol does not currently provide similar control for any other groups. However further discrimination of the currently defined subsets could be made via the definition of further sample attributes as more hydration groups become defined.

The source identification protocol outlined in this chapter in conjunction with the hydration rate data presented in Chapter 6 allows glass specific hydration parameters to be established for artefacts that derive from the MIHG and KHG. Thus in order to fully specify the observation model $x(t,g,e)$ defined in Chapters 4 and 5 (§4.7 & §5.1) it only remains to define the environmental component e. As detailed previously (§4.7) this primarily involves defining the hydration temperature history for the artefact. Archaeological temperature regimes are considered in Chapters 8 – 12 that follow.

Chapter 8

Archaeological Soil Temperature Regimes

8.1 Introduction

While the hydration behaviour of an artefact is governed by constant factors such as glass chemistry (*infra vide*: Chapter 4), the actual rate of hydration at any given instant is a function of variable environmental factors. The most significant of these is the ambient temperature (*infra vide*:§4.7), and in order to make any attempt at OHD the influence of this environmental variable must be accounted for. In order to specify the influence of the ambient temperature regime upon obsidian hydration we simply need to make reference to the appropriate hydration model.

Under the hydration model outlined previously (Equation 4.3) the instantaneous rate of hydration is given as

$$k(t) = A \exp\left(\frac{-E}{RT(t)}\right) \tag{8.1}$$

A=pre-exponential component;E=gas activation energy;R=universal gas constant.

where $T(t)$ is a function that describes the ambient temperature T at any given time t. Thus the total extent of hydration (x^2) over any given interval $(t1, t2)$ is simply the integral of Equation 8.1 over this interval *i.e.*:

$$x^2_{(t_1,t_2)} = \int_{t_1}^{t_2} k(t)dt = A\int_{t_1}^{t_2} e^{\left(\frac{-E}{RT(t)}\right)}dt \tag{8.2}$$

As the ambient temperature function ($T(t)$) is variable, it is usual to estimate an "average" hydration temperature known as the effective hydration temperature (EHT). This figure represents a constant ambient temperature at which an identical hydration extent to that observed in the archaeological sample would have been generated over the hydration duration. Relating this to the relationships defined in Equation 8.2, the EHT can be defined as follows

$$(t_2 - t_1)\, e^{\left(\frac{-E}{R\times \mathrm{EHT}}\right)} = \int_{t_1}^{t_2} e^{\left(\frac{-E}{RT(t)}\right)}dt$$

$$EHT_{(t_1,t_2)} = \frac{-E}{R}\ln\left(\frac{\int_{t_1}^{t_2} e^{\left(\frac{-E}{RT(t)}\right)}dt}{t_2 - t_1}\right)^{-1} \tag{8.3}$$

Thus the EHT as defined in Equation 8.3 represents our understanding of the variable temperature regime that the artefact has been exposed to over the interval (t_1, t_2) (usually the entire hydration duration, *i.e* $t_1 = 0, t_2 = (present)$), the influence that this exerts upon the observed hydration extent, and hence the related OHD. It should be noted that the definition of EHT presented in Equation 8.3 is model specific in that it directly follows from the hydration model presented in Equation 8.1. Thus a different definition of EHT would be required for different hydration models.

In order to undertake any form of OHD we must be able to calculate or closely estimate the integral given in Equation 8.3. This requires an understanding of the variables and processes governing $T(t)$. The purpose of this chapter is to outline these with a view to providing a basis for evaluating and designing archaeological EHT estimation protocols (considered in the following Chapter). The intention is to present some theoretical baseline for identifying the processes and variables that may give rise to significant variations in EHT. However, in order for this discussion to be meaningful we need to have some idea of what constitutes suitable precision in terms of EHT estimation accuracy. On this basis it is possible to establish at what spatial and temporal scale this type of understanding is required. Following this discussion we will consider how archaeological EHT's may be estimated (Chapter 9) and then consider the specific case of EHT estimation in New Zealand (Chapters 10–12).

8.1.1 EHT and OHD Error

The significance of OHD error introduced by EHT estimation uncertainty can be calculated with reference to 4.17 as:

$$t_{apparent} = \frac{k_{true} t_{true}}{k_{apparent}} \tag{8.4}$$

For example, consider a typical Mayor Island obsidian[1] artefact (*infra vide*:§6.6) hydrating for 1000 years at an EHT of 17 ^{0}C. An estimated EHT of 17.5 ^{0}C corresponds to a calculated date of 940 years or a date error of around 6%. A more usual scenario is that the EHT would be estimated as a temperature range; for example 17 ± 0.4 ^{0}C. In the previous example this would correspond to a date range of 1051 years to 952 years or a date error of ≈ ±5%. The figures shown in 8.1 and Figures 8.2–8.2 illustrate the magnitude of errors introduced by EHT uncertainty in the range ± 10 ^{0}C over the temperature range 10-30 ^{0}C for typical samples of Mayor Island and Te Ahumata obsidian (*infra vide*:§3). Thus these figures are representative of the range of artefact geochemistry and archaeological environments likely to be experienced in New Zealand. As can be seen, very significant date errors arise from EHT uncertainty of only a few ^{0}C. It is clear that EHT's need to be calculated with errors of at most 2-3 ^{0}C, preferably much lower. While Bayesian modelling and date combination as outlined in Chapter 13 can significantly improve dating precision, EHT errors of any larger than 2-3 ^{0}C correspond to date errors that severely limit the utility of OHD as a practical archaeological tool.

Other than absolute dates we are also interested in absolute relativity (*infra vide*:§1.3.1). Absolute relativity ($\Delta_{(t1,t2)}$) is defined here as the absolute age difference between two events with true ages t_1 and t_2. In the case of two OHD assays $\Delta_{(t1,t2)}$ can be calculated as follows:

$$x_1^2 = k_1 t_1$$
$$x_2^2 = k_2 t_2$$
$$\frac{t_1}{t_2} = \left(\frac{k_2}{k_1}\right)\left(\frac{x_1^2}{x_2^2}\right)$$
$$t_1 = t_2\left(\frac{k_2}{k_1}\right)\left(\frac{x_1^2}{x_2^2}\right)$$
$$t_2 - t_1 = t_2\left(1 - \left(\frac{k_2}{k_1}\right)\left(\frac{x_1^2}{x_2^2}\right)\right)$$

[1] A=1.86×10^{10} μ^2 day^{-1} , E=86.7 kJ mol^{-1}

Table 8.1: Percentage Date Error in OHD assays arising from EHT estimation inaccuracy alone: Figures for typical Mayor Island † and Te Ahumata‡ samples

EHT Estimation	Mayor Island†			Te Ahumata‡		
Error	10 ^{0}C	20 ^{0}C	30 ^{0}C	10 ^{0}C	20 ^{0}C	30 ^{0}C
-10	285.1	251.2	223.3	270.1	238.5	212.3
-9	235.0	208.6	186.5	223.3	198.5	177.8
-8	191.8	171.3	154.1	182.7	163.4	147.2
-7	154.4	138.7	125.5	147.5	132.7	120.2
-6	122.0	110.3	100.3	116.8	105.7	96.2
-5	93.9	85.4	78.0	90.1	82.0	75.1
-4	69.5	63.6	58.4	66.9	61.2	56.3
-3	48.3	44.5	41.0	46.6	42.9	39.6
-2	30.0	27.7	25.7	29.0	26.8	24.8
-1	13.9	12.9	12.1	13.5	12.5	11.7
0	0.0	0.0	0.0	0.0	0.0	0.0
1	12.2	11.4	10.7	11.8	11.1	10.4
2	22.8	21.4	20.2	22.2	20.9	19.7
3	32.0	30.3	28.6	31.3	29.5	27.9
4	40.1	38.1	36.1	39.2	37.2	35.3
5	47.2	44.9	42.8	46.2	44.0	41.8
6	53.4	51.0	48.7	52.4	50.0	47.7
7	58.9	56.4	54.0	57.8	55.3	52.9
8	63.6	61.1	58.7	62.6	60.0	57.6
9	67.8	65.3	62.9	66.8	64.2	61.8
10	71.5	69.1	66.7	70.5	68.0	65.6

† $A = 1.86 \times 10^{10}\ \mu^2$ day^{-1} ; E = 86.7 kJ mol^{-1}

‡ $A = 1.124 \times 10^{10}\ \mu^2$ day^{-1} ; E = 84.2 kJ mol^{-1}

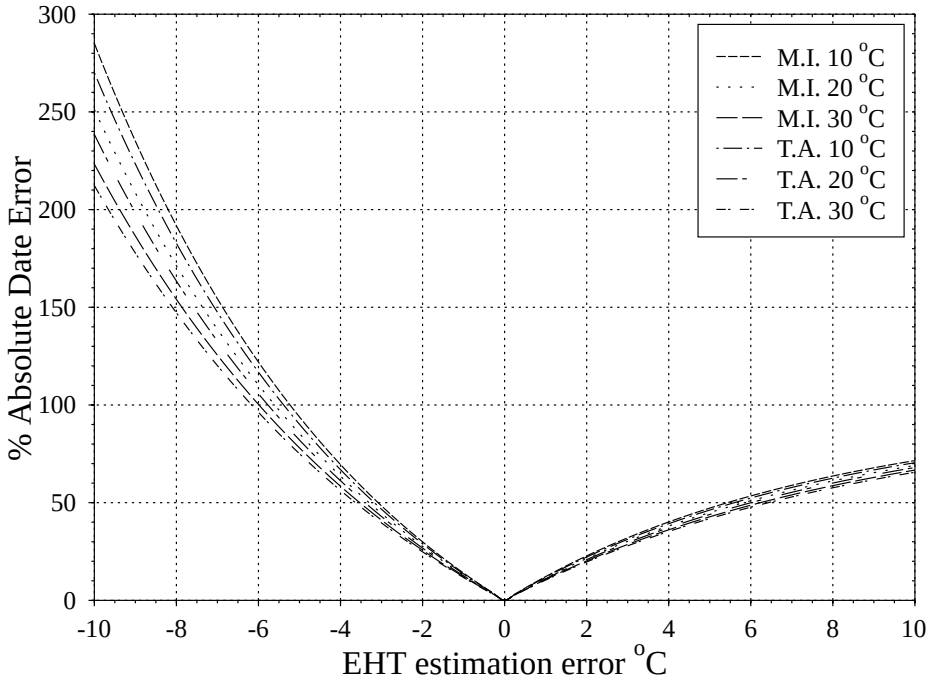

Figure 8.1: Percentage date error in OHD assays arising from EHT estimation inaccuracy alone: for the samples presented in 8.1

$$\Delta_{(t_1,t_2)} = t_2 \left(1 - \left(\frac{A_2 \exp\left(\frac{-E_2}{R \times EHT_2}\right)}{A_1 \exp\left(\frac{-E_1}{R \times EHT_1}\right)}\right)\right)\left(\frac{x_1^2}{x_2^2}\right) \tag{8.5}$$

As the calculations for $\Delta_{(t_1,t_2)}$ differ to those of absolute dating it is important to also assess the significance of EHT estimation error in terms of $\Delta_{(t_1,t_2)}$ estimation accuracy. For the case involving only two dates as defined in Equation 8.5 this can be simply calculated as

$$\frac{\Delta^{true}_{(t_1,t_2)} - \Delta^{estimated}_{(t_1,t_2)}}{\Delta^{true}_{(t_1,t_2)}} \tag{8.6}$$

In this case we are calculating an error term that is a function of a number of variables. Full consideration of this is problem specific, particularly when extended beyond the simple two date case above, and a general likelihood model needs to be developed to handle all problems

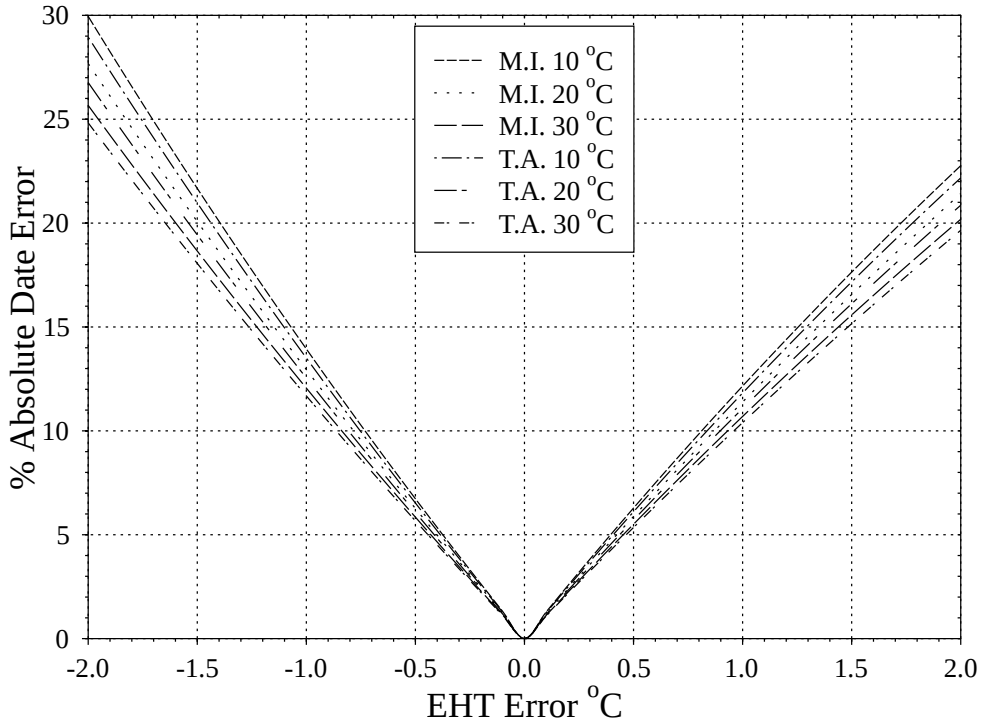

Figure 8.2: Percentage date error in OHD assays arising from EHT estimation inaccuracy in the range ± 2 ^{0}C for the samples presented in 8.1

(*supra vide*:§13). However the relationships defined above do allow us to set some baseline for the precision with which EHT needs to be estimated. It should be noted that in the calculation given in Equation 8.6 the magnitude of $\Delta_{(t_1,t_2)}$ error is a percentage of the age of one of the two dates (t_2). If this date is an OHD the $\Delta_{(t_1,t_2)}$ estimation error adds to the EHT estimation error already present in t_2. Thus in this case EHT estimation needs to be of higher precision than defined previously in the case of single absolute OHD determinations.

A simple example of the sensitivity of $\Delta_{(t_1,t_2)}$ error to Δ_{EHT} uncertainty can be given in the case that we are dealing with two artefacts with the

same geochemical properties. Here Equation 8.5 reduces to

$$\Delta_{t_1,t_2} = t_2 \left(1 - \exp\left(\frac{E}{R}\left(\frac{1}{t_2} - \frac{1}{t_2 + \Delta_{EHT}}\right)\right)\left(\frac{x_1^2}{x_2^2}\right)\right) \tag{8.7}$$

This is a very useful result as we can define the absolute age difference between two flaking events on the basis of the temperature difference Δ_{EHT} between the two locations given a reference temperature (t_2 in this case). This is a useful result as we may be able to define Δ_{EHT} with more precision than EHT. Thus it is useful to also consider the significance of Δ_{EHT} estimation error on Δ_{t_1,t_2}.

We can establish some general principals. The significance Δ_{EHT} estimation error to $\Delta_{(t_1,t_2)}$ is dependent upon the ratio $\left(\frac{x_1^2}{x_2^2}\right)$ with maximum sensitivity at $\left(\frac{x_1^2}{x_2^2}\right) = 1$ (see Table 8.2 and Table 8.3). Over the EHT range likely to be experienced in New Zealand the magnitude of $\Delta_{(t_1,t_2)}$ error as a result of Δ_{EHT} uncertainty is largely temperature independent (see Table 8.3 and Table 8.4). On this basis we can set a baseline for the Δ_{EHT} estimation required by setting $\left(\frac{x_1^2}{x_2^2}\right) = 1$ and $t_2 \in (10^0\text{C},30^0\text{C})$ in Equation 8.7. Examples of the magnitude of error that may be introduced are given in Figure 8.5 and Table 8.4 for a typical Mayor Island obsidian artefact. The Δ_{EHT} range over which errors have been calculated is representative of the magnitude likely to be experienced in New Zealand archaeological contexts (Jones *et al.* 1997*b*) and indicate that an error of $\gtrsim 0.2t_2$ arises from a Δ_{EHT} estimation error of $\pm 1 - 2\ ^0$C. From this we can see that in practice Δ_{EHT} estimation needs to be precise; ideally within the range (-1 ^{0}C,1^{0}C).

However, if the temperature history ($T(t)$) for the artefacts being analysed is essentially the same, the EHT estimation precision required is considerably reduced as outlined in the following 2 general scenarios.

1. The temperature history and geochemical parameters are essen-

Table 8.2: Absolute error in $\Delta_{(t_1,t_2)}$ as $\%t_2$ arising from Δ_{EHT} estimation inaccuracy alone following Equation 8.7 for $\Delta_{EHT} = 0.5$: Figures for a typical Mayor Island† sample

Δ_{EHT} estimation	$\left(\frac{x_1^2}{x_2^2}\right)$				
error	0.2	0.4	0.6	0.8	1
-5	9.3	18.5	27.8	37.0	46.3
-4.5	8.5	17.1	25.6	34.1	42.7
-4	7.8	15.6	23.3	31.1	38.9
-3.5	7.0	14.0	20.9	27.9	34.9
-3	6.1	12.3	18.4	24.6	30.7
-2.5	5.2	10.5	15.7	21.0	26.2
-2	4.3	8.6	12.9	17.2	21.5
-1.5	3.3	6.6	9.9	13.3	16.6
-1	2.3	4.5	6.8	9.1	11.3
-0.5	1.2	2.3	3.5	4.7	5.8
0	0.0	0.0	0.0	0.0	0.0
0.5	1.2	2.5	3.7	4.9	6.1
1	2.5	5.0	7.6	10.1	12.6
1.5	3.9	7.8	11.7	15.6	19.5
2	5.3	10.7	16.0	21.3	26.7
2.5	6.8	13.7	20.5	27.4	34.2
3	8.4	16.9	25.3	33.8	42.2
3.5	10.1	20.3	30.4	40.5	50.7
4	11.9	23.8	35.7	47.6	59.5
4.5	13.8	27.6	41.3	55.1	68.9
5	15.7	31.5	47.2	63.0	78.7

† $A = 1.86 \times 10^{10}\ \mu^2$ day^{-1} ; E = 86.7 kJ mol^{-1}

Table 8.3: Absolute error in $\Delta_{(t_1,t_2)}$ as $\%t_2$ arising from Δ_{EHT} estimation inaccuracy alone following Equation 8.7 for $\Delta_{EHT} = 0.5, \left(\frac{x_1^2}{x_2^2}\right) = 1$: Figures for a typical Mayor Island† sample

Δ_{EHT} estimation	T_2 ^{0}C				
error	10	15	20	25	30
-5	51.5	50.1	48.8	47.5	46.3
-4.5	47.7	46.4	45.1	43.9	42.7
-4	43.6	42.4	41.2	40.0	38.9
-3.5	39.3	38.1	37.0	35.9	34.9
-3	34.7	33.6	32.6	31.6	30.7
-2.5	29.7	28.8	27.9	27.1	26.2
-2	24.5	23.7	23.0	22.2	21.5
-1.5	18.9	18.3	17.7	17.1	16.6
-1	13.0	12.6	12.1	11.7	11.3
-0.5	6.7	6.5	6.2	6.0	5.8
0	0.0	0.0	0.0	0.0	0.0
0.5	7.1	6.9	6.6	6.4	6.1
1	14.7	14.1	13.6	13.1	12.6
1.5	22.8	21.9	21.0	20.2	19.5
2	31.3	30.0	28.8	27.7	26.7
2.5	40.4	38.7	37.1	35.6	34.2
3	50.1	47.9	45.9	44.0	42.2
3.5	60.3	57.6	55.2	52.8	50.7
4	71.2	68.0	64.9	62.2	59.5
4.5	82.7	78.9	75.3	72.0	68.9
5	95.0	90.4	86.2	82.4	78.7

† $A = 1.86 \times 10^{10}\ \mu^2$ day^{-1} ; E = 86.7 kJ mol^{-1}

Table 8.4: % Error in $\Delta_{(t_1,t_2)}$ arising from Δ_{EHT} estimation inaccuracy alone following Equation 8.7 for $\left(\frac{x_1^2}{x_2^2}\right) = 1$: Figures for a typical Mayor Island† sample

Δ_{EHT} estimation	Δ_{EHT} ^{0}C					
error	0	1	2	3	4	5
-5	43.8	48.8	54.4	60.5	67.2	74.7
-4.5	40.4	45.0	50.1	55.8	62.0	68.9
-4	36.9	41.1	45.7	50.8	56.5	62.7
-3.5	33.1	36.8	41.0	45.6	50.7	56.3
-3	29.1	32.4	36.0	40.1	44.5	49.4
-2.5	24.9	27.7	30.8	34.2	38.0	42.2
-2	20.4	22.7	25.3	28.1	31.2	34.6
-1.5	15.7	17.5	19.5	21.6	24.0	26.6
-1	10.8	12.0	13.3	14.8	16.4	18.2
-0.5	5.5	6.1	6.8	7.6	8.4	9.3
0	0.0	0.0	0.0	0.0	0.0	0.0
0.5	5.8	6.5	7.2	8.0	8.9	9.8
1	12.0	13.3	14.8	16.4	18.2	20.2
1.5	18.4	20.5	22.8	25.3	28.1	31.1
2	25.3	28.1	31.2	34.6	38.4	42.6
2.5	32.5	36.1	40.1	44.5	49.3	54.7
3	40.1	44.5	49.4	54.8	60.8	67.4
3.5	48.1	53.4	59.3	65.8	72.9	80.7
4	56.5	62.7	69.6	77.2	85.6	94.8
4.5	65.4	72.6	80.5	89.3	99.0	109.6
5	74.7	82.9	92.0	102.0	113.0	125.1

† $A = 1.86 \times 10^{10}\ \mu^2\ \text{day}^{-1}$; E = 86.7 kJ mol^{-1}

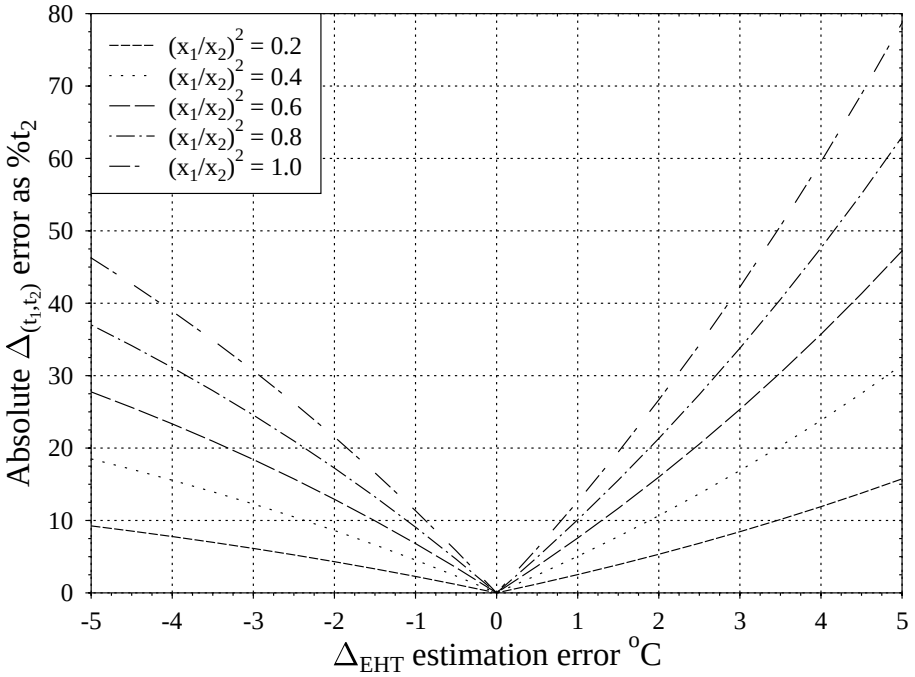

Figure 8.3: Absolute error in $\Delta_{(t_1,t_w)}$ as $\%t_2$ arising from Δ_{EHT} estimation inaccuracy for the sample presented in Table 8.2

tially identical for each artefact. Here Equation 8.5 reduces to

$$\Delta_{(t_1,t_2)} = t_2\left(1 - \left(\frac{x_1^2}{x_2^2}\right)\right) \tag{8.8}$$

as under this scenario $k_1 = k_2$. In this case there is no temperature dependence for the absolute age difference.

2. The temperature history is essentially identical for each artefact, however the geochemical parameters of each vary. Here Equation 8.5 reduces to

$$\Delta_{(t_1,t_2)} = t_2\left(1 - \left(\frac{A_1}{A_2}\exp\left(\frac{E_2 - E_1}{R \times \mathrm{EHT}}\right)\right)\left(\frac{x_1^2}{x_2^2}\right)\right) \tag{8.9}$$

As can be seen in the example calculations given in Table 8.5 and Figure 8.6 minimal $\Delta_{(t_1,t_2)}$ calculation errors arise due to EHT estimation error in this case. The figures presented in Table 8.5 and

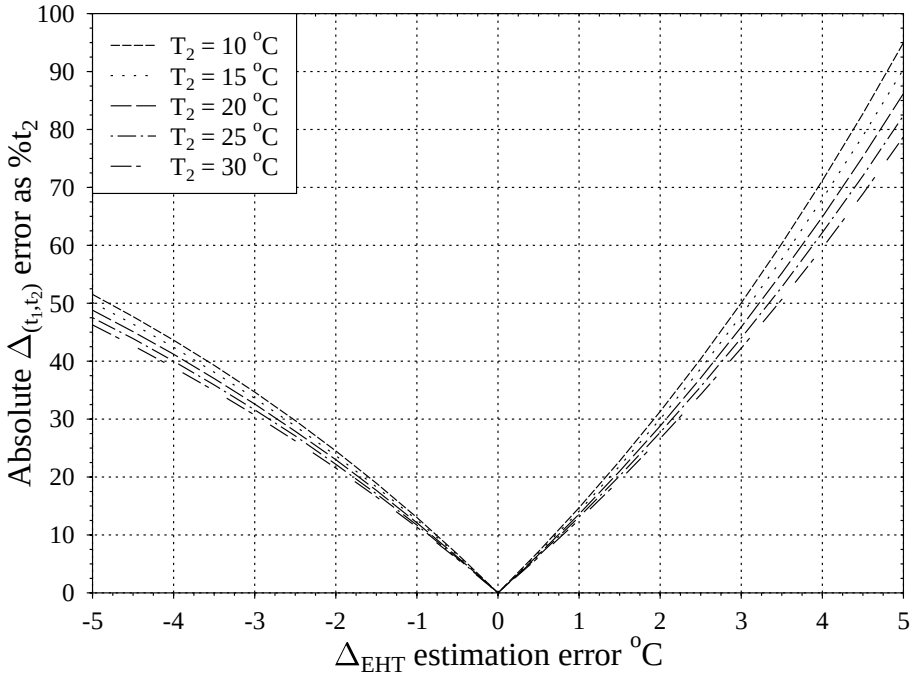

Figure 8.4: Absolute error in $\Delta_{(t_1,t_w)}$ as $\%t_2$ arising from Δ_{EHT} estimation inaccuracy for the sample presented in Table 8.3

Figure 8.6 represent the maximum likely to be observed in the New Zealand context in that they represent the maximum variation in geochemical hydration parameters likely for New Zealand obsidian (*infra vide*:§3) and the ratio $\left(\frac{x_1^2}{x_2^2}\right)$ is set as 1 which as illustrated earlier (Table 8.2) corresponds to the maximum sensitivity to EHT estimation error. On this basis we can establish that absolute EHT estimation errors of less than 10 ^{0}C will generally be sufficiently precise for this problem. However the error introduced by EHT estimation uncertainty will have to be included in the calculated date in this case in contrast to scenario 1 above.

The preceding consideration of EHT estimation inaccuracy and OHD error makes it clear that in the absence of high quality EHT estimates OHD

Table 8.5: Absolute error in $\Delta_{(t_1,t_2)}$ as $\%t_2$ arising from EHT estimation inaccuracy alone following Equation 8.9 for $\left(\frac{x_1^2}{x_2^2}\right) = 1$: Figures comparing typical Mayor Island† and Te Ahumata‡ samples

Δ_{EHT} estimation	T_2 ^{0}C		
error	10	20	30
-10	2.2	2.1	2.0
-9	2.0	1.9	1.8
-8	1.7	1.7	1.6
-7	1.5	1.5	1.4
-6	1.3	1.3	1.2
-5	1.1	1.0	1.0
-4	0.9	0.8	0.8
-3	0.6	0.6	0.6
-2	0.4	0.4	0.4
-1	0.2	0.2	0.2
0	0.0	0.0	0.0
1	0.2	0.2	0.2
2	0.4	0.4	0.4
3	0.6	0.6	0.6
4	0.9	0.8	0.8
5	1.1	1.0	1.0
6	1.3	1.2	1.2
7	1.5	1.4	1.4
8	1.7	1.6	1.6
9	1.9	1.8	1.8
10	2.1	2.0	2.0

† $A = 1.86 \times 10^{10}\ \mu^2$ day^{-1} ; E = 86.7 kJ mol^{-1}

‡ $A = 1.124 \times 10^{10}\ \mu^2$ day^{-1} ; E = 84.15 kJ mol^{-1}

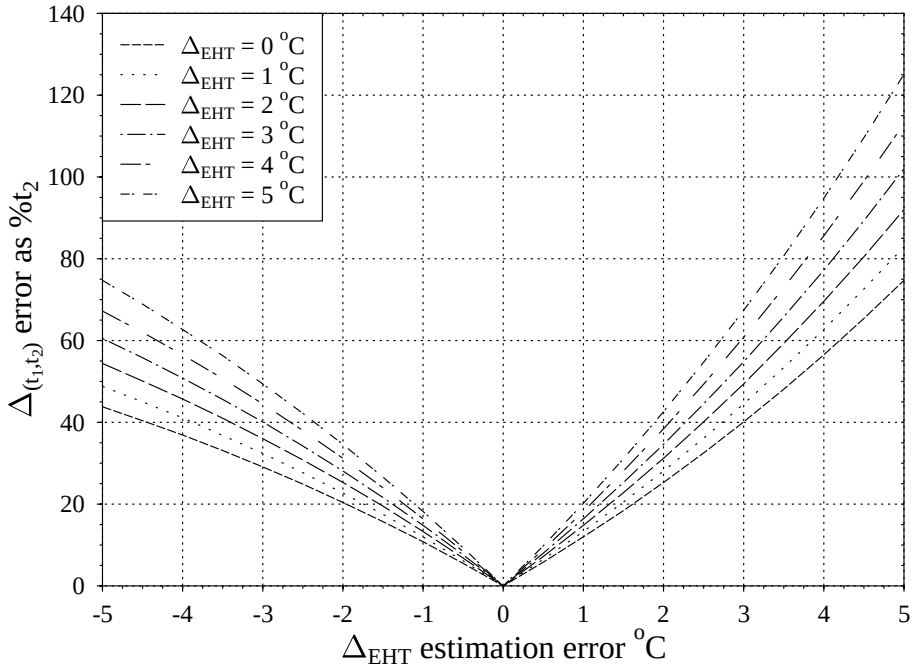

Figure 8.5: Percentage date error in OHD assays arising from EHT estimation inaccuracy alone for the sample presented in Table 8.4

is essentially useless as an archaeological tool. In practical terms this means that we need to be able to estimate both the absolute EHT and Δ_{EHT} to better than $\pm$ 2 ^{0}C. The exception to this conclusion is under the absolute relativity scenarios 1 & 2 given above. In this case the absolute date difference of two or more artefacts is effectively temperature independent. This is an extremely useful result as it means that OHD can address one of the primary weaknesses of ^{14}C dating (Chapter 1) even in the absence of specific high quality EHT data. In real world terms this means is that it is possible to take obsidian artefacts from a single hydration group within portions of a site that would have experienced a common temperature history and quantify the absolute time difference in the flaking event producing each artefact simply as a ratio of the squared rim thicknesses. This can be extended to more complex

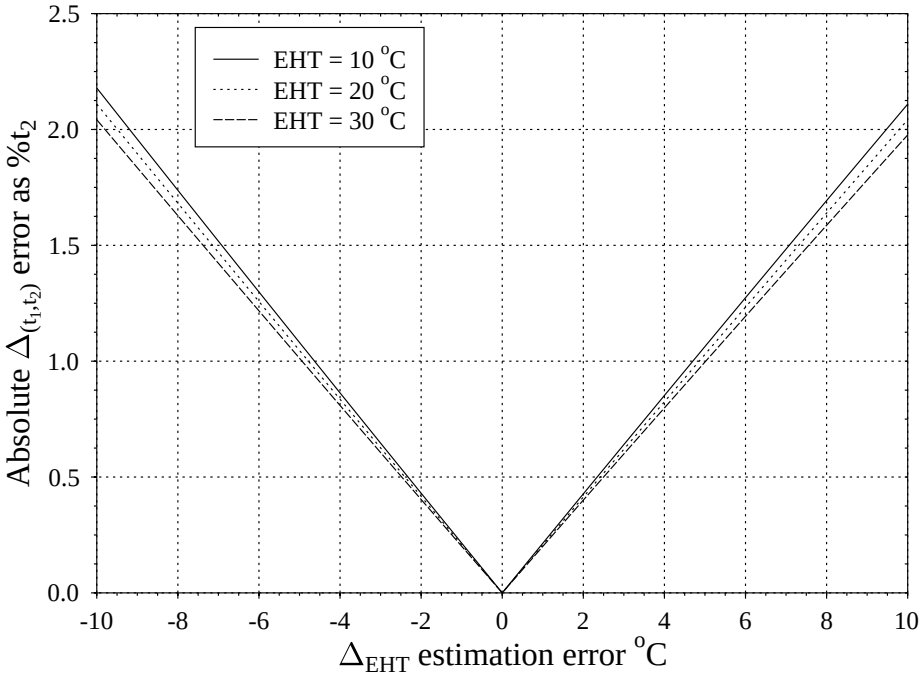

Figure 8.6: Absolute error in $\Delta_{(t_1,t_w)}$ as $\%t_2$ arising from Δ_{EHT} estimation inaccuracy for the sample presented in Table 8.5

forms via the Bayesian models outlined in Chapter 13, however the basic principal is clear. The result becomes even more useful when it is observed that the value for t_2 in Equation 8.8 can be generated via any other chronometric method. Thus the analysis can be rendered completely temperature independent. Other than with this unique case, EHT estimation inaccuracy will result in significant date errors in most applications of OHD. In light of this, it is critical that a properly considered quantification of EHT estimation uncertainty is incorporated into the observation model and likelihood for OHD (Chapter 13).

In addition to being able to generate high quality absolute EHT and Δ_{EHT} estimates we need a sound quantification of the associated uncertainty. Further, we need a method for incorporating these errors into the calculated OHD result. Without this there is no basis for generating a mean-

ingful distribution for any OHD assay.

In order to achieve this it is necessary to first outline all the variables that may give rise to significant variation in archaeological soil climate regimes and form an understanding of how $T(t)$ varies in response to these. In the following chapter the environmental variables and processes that govern EHT are outlined. On the basis of this discussion it will be possible to assess EHT estimation methods and identify the practical limits of OHD as a chronometric tool (§9).

8.1.2 Factors Governing the Soil Temperature Regime

As the EHT is a function of climatological variables it is useful to refer to the considerable volume of research available in this field (*e.g.*, Ayra 1988; Campbell 1977; 1985; Hanks and Ashcroft 1980; Monteith 1975; Monteith and Unsworth 1990; Oke 1987; Rosenberg *et al.* 1983; Stoutjesdijk and Barkman 1991) to establish a baseline for the study of $T(t)$.

Climate systems operate over all spatial resolutions and are typically studied at three general spatial scales Macro (>10 km), Meso (1-10km) and micro (1-10 m), with significant climatic variation operating at each of these scales (Monteith and Unsworth 1990). Of particular interest from this previous work is the wide variety of data that point to considerable variation in soil surface temperatures over small spatial scales (Chudnovskii 1962; Davidoff *et al.* 1986; Mahrer and Avissar 1985; Stoutjesdijk and Barkman 1991). For instance Stoutjesdijk (1977) reports a surface temperature range of 40 ^{0}C (-1 to 39 ^{0}C) over a transect with an associated 4 cm soil temperature range of 16.8 ^{0}C (1.4 to 18.2 ^{0}C) at midday in winter. While this will certainly be a short term manifestation there is evidence to suggest that these sorts of short term surface temperature fluctuations propagate to depths of at least 30 cm (Persaud and Chang 1984); this would certainly influence the EHT.

While there no soil climate research results suitable for directly determining sub surface EHT (as the researchers are predominantly interested in processes such as seed germination) the principal variables governing climatic systems have been established in previous research (See Monteith and Unsworth (1990) for an overview). This makes it possible to isolate a series of variables that are potentially significant in the explanation of variation in $T(t)$. This can be made easier by describing $T(t)$ as a function of two linked processes; the soil surface energy balance and the soil heat flux. The soil surface energy balance can be regarded as driving the soil heat flux (G). The soil heat flux in turn defines the temperature regime through the soil body and hence $T(t)$. Thus to understand the factors that govern $T(t)$ we need to understand what factors influence the soil surface energy balance and govern the flow of the soil heat flux. We can explicitly define the soil heat flux (G) as a function of the soil surface energy balance which allows us to isolate the critical environmental factors governing $T(t)$.

The energy balance at the soil surface is basically the difference between the amount of radiation energy absorbed and the amount of energy lost from the soil through its own blackbody radiation and the energy used in driving processes such as evaporation. This balance can be described by an energy budget equation;

$$G = R_n - H - L_e \tag{8.10}$$

Where: R_n is the net radiation flux at the soil surface

G is the soil heat flux

H is the sensible heat flux

L_e is the latent heat flux

With reference to Equation 8.10 it is apparent that in order to model archaeological EHT's we have to account for significant variations in the net radiation (*supra vide*:§8.2), sensible (*supra vide*:§8.3) and latent

(*supra vide*:§8.4) heat fluxes, as well as modelling the mechanism for soil heat transport (*supra vide*:§8.5).

8.2 Net Radiation Balance (R_n)

Ultimately all of the radiation received at the surface of the earth derives from the sun. The sun delivers a fairly constant stream of short-wave radiation to the top of the atmosphere known as the solar constant (I_0). As this incoming radiation travels through the atmosphere some of it is absorbed and converted into heat, which consequently gives rise to long-wave radiation fluxes. In addition to the short-wave and long-wave radiation received at the earth's surface, the surface itself emits long-wave radiation as a function of its temperature. The net radiation balance is the difference between the energy received from external sources and that lost through blackbody radiation, and can be summed up in the following relationship:

$$R_n = (1 - a)S_t + L_a - L_s \tag{8.11}$$

Where:
a=surface albedo
S_t=global short-wave
L_a=incoming long-wave
L_s=soil long-wave

While each of these components are part of the same process it is useful consider each separately, as even though the same factors influence each radiation type, the significance of each effect varies.

8.2.1 Short-wave Radiation (S_t)

The short-wave radiation reaching the earth's surface is made up of two components, diffuse (S_b) and direct (S_b). The direct radiation is that component of the solar ray that reaches the surface without being scattered or absorbed. The diffuse component results from scattering as the beam travels through the atmosphere, reflection from surrounding features and even multiple reflections between the surface and overhead clouds. In actual applications the distinction between diffuse and direct radiation is important as the directionality of the two components is different. To a large extent, diffuse radiation is isotropic in contrast to the direct beam. This means that the influence of a wide range of non-isotropic variables (*i.e.* aspect, vegetative cover) may vary for these two sources of short-wave radiation.

When the incident short-wave radiation (diffuse and direct) reaches the earth's surface, not all of it is absorbed, and some is reflected. The degree to which reflection takes place is mainly a function of the surface, though the angle of the incident ray also has an influence. The absorption characteristics of any particular surface is known as its albedo (a), which is a measure of the extent to which a surface will reflect incident radiation. An albedo of 1 means the surface is a perfect reflector, and of 0 means it is the perfect sink. In light of this the easiest way to represent the amount of short-wave radiation absorbed by any surface is $S_t(1-a)$ which is recognisable as the first term in Equation 8.11. Here S_t is a measure of the total amount of short-wave radiation incident on the surface in question, combining both direct and diffuse radiation sources, *i.e.*

$$S_t = S_b + S_d$$

To be able to calculate S_t it is important to be able to quantify and accurately estimate both the ratio of diffuse to direct solar radiation, and the influence of relief, environment, geography and climate on both of

these radiation components.

Direct Short-Wave Radiation (S_b)

The direct short-wave flux is the part of the solar ray incident on the upper atmosphere that reaches the earth's surface without being either scattered, absorbed or reflected. The ratio of direct to total varies depending on the atmospheric conditions, environment, geographic location and time of day. For instance in the shade, at dawn and dusk, as well as during overcast days, diffuse radiation accounts for all of the short-wave flux, whereas at solar noon on a clear day direct solar radiation may account for as much as 90% of the incoming flux. Micro-scale variations may occur due to processes such as shading or attributes such as orientation of the surface. Larger scale variations may be due to relief driven climatic process or shading from large geographic features (*e.g.* mountain ranges). As well, geographical position is important with diffuse radiation representing an increasing proportion of the total as latitude increases.

By developing geometric relationships between the sun and the earth in terms of geographic location, time of the day and time of the year many of the important aspects of both direct and diffuse short-wave fluxes can be resolved.

The solar flux at the top of the atmosphere over a surface normal to the incident ray is approximately 1373 Wm^{-2} (Hickey *et al.* 1982). This figure does vary with time, both seasonally as the distance between the earth and sun changes, and over longer time scales due to phenomena such as sun spot activity which seems to have an 11 year cycle (Rosenberg *et al.* 1983).

Using a corollary of Lambert's law known as the Law of Illumination the incident short-wave flux at the top of the atmosphere (S_i) can be

calculated as

$$S_i = I_o \left(\frac{dm}{d}\right)^2 \cos(\alpha) \tag{8.12}$$

Where dm/d is the ratio of the mean sun earth distance($dm = 1.5 \times 10^8 m$) to the actual sun earth distance (d), and α is the angle between the normal to the horizontal and the beam.

The ratio dm/d is a function of time and can be calculated to practically any degree of precision. An approximation is given by the following (Spitters *et al.* 1986):

$$\frac{dm}{d} = \sqrt{1 + 0.033 \cos\left(\frac{360 d_j}{365}\right)} \tag{8.13}$$

Where d_j is the Julian date (day of the year). More precise calculations are possible (*e.g.* Montenbruck and Pfleger 1991).

These relationships can be used to describe the maximum theoretical solar flux incident at the earth's surface. For any point on the earth's surface spherical trigonometry can be used to give a time dependent measure of α in terms of the surface of the earth. Known as the solar zenith angle (Z) this measure is given by the relationship

$$\cos(Z) = \sin(\phi)\sin(\delta) + \cos(\phi)\cos(\delta)\cos(\theta) = \sin(\beta) \tag{8.14}$$

Where δ is the solar declination; ϕ the latitude of the site; θ is the solar hour angle; and β is the solar altitude $= 90 - Z$. Thus S_i, varies as a function of latitude, solar declination (δ) and hour angle (θ). Both δ and θ are functions of time and can be calculated accordingly.

The solar declination is purely a function of the day of the year and as a first approximation can be calculated as:

$$\delta = -23.4 \cos[360(D + 10)/365] \tag{8.15}$$

Where D = the day of year. The hour angle is a function of the time of the day and can be calculated as

$$\theta = 15(12 - t) \tag{8.16}$$

where t=local apparent solar time.

These relationships make it possible to calculate the sun/earth angles over perfectly horizontal surfaces at any location and time, and consequently calculate S_i. As we will almost always have situations where the surface is not horizontal it is necessary to be able to calculate the effects due to aspect. Basically we want to know the angle of incidence between the normal to the slope and the solar beam and use this in a form of Lambert's Law of Illumination to calculate the non horizontal direct short-wave flux. If we introduce three new variables; the surface slope $\hat{\beta}$ measured from horizontal, the slope azimuth ($\hat{\psi}$) and solar azimuth (ψ). The angle of incidence between the solar beam and the normal to the slope (ρ) is given as

$$\cos(\rho) = \cos(\hat{\beta})\cos(Z) + \sin(\hat{\beta})\sin(Z)\cos(\psi - \hat{\psi}) \tag{8.17}$$

Where ψ can be calculated as

$$\begin{aligned} \psi &= (\sin(\delta)\cos(\phi) - \cos(\delta)\sin(\phi)\cos(\theta))/\sin(Z) && t < 12 \\ \psi &= 360 - (\sin(\delta)\cos(\phi) - \cos(\delta)\sin(\phi)\cos(\theta))/\sin(Z) && t > 12 \end{aligned} \tag{8.18}$$

and t is local apparent solar time. The maximum direct short-wave flux in terms of the horizontal flux (S_i) becomes

$$\hat{S_i} = \frac{S_i \cos(\rho)}{\sin(\beta)} \tag{8.19}$$

or in terms of the normal to the solar beam

$$\hat{Si} = I_o \left(\frac{dm}{d}\right)^2 \cos(\rho) \tag{8.20}$$

While these geometrical relationships allow us to calculate the theoretical maximum direct short-wave flux over any surface, we have to develop methods to account for atmospheric attenuation. The solar beam becomes depleted as it travels through the atmosphere. Many short wavelength, high energy, photons are absorbed in photochemical reactions high in the atmosphere, while others are absorbed in heating

molecules without chemical change. Gases such as CO_2, O_2, and H_2O absorb strongly at certain wavelengths resulting in corresponding depletions of the ray that reaches the earth (Monteith and Unsworth 1990).

While the processes of attenuation in a clear sky are fairly well understood, the situation becomes much more complex in the presence of turbidity and/or cloud cover (Liou 1992). Turbidity is basically any condition other than cloud cover that reduces atmospheric transparency to short-wave radiation. This arises from phenomena such as dust, smoke and volcanic activity. The effect of turbidity is to an extent dependent upon both the size of the particles and the wavelength of the light. This will determine whether Raleigh or Mie scattering is the predominant type, and also to what extent it will occur. The nature of any turbidity has implications for the directionality of the short-wave flux as the scattering geometry of Raleigh and Mie scattering differs resulting in different proportions of the scattered radiation being directed toward space and the earth respectively.

The effect of cloud cover has a significant impact on attenuation, and can be difficult to effectively quantify. The effect of cloud cover varies depending on its temperature, albedo, depth, altitude, type and the extent of cloud cover amongst other things. In addition there can be complicated reflection interactions between different clouds and cloud layers. As a result the processes governing attenuation through cloud cover are extremely difficult to accurately calculate, both due to the complex modelling, and to the difficulty of obtaining the required data.

As can be appreciated, a longer atmospheric path for the solar beam will result in greater exposure to the influences mentioned above, resulting in greater attenuation of the beam. A measure of the length of the atmospheric path (m,the optical air mass number) can be expressed as a ratio to the path length at the zenith normalised to a site elevation at

sea level as

$$m = \frac{p}{p_0} sec Z \tag{8.21}$$

Where the ratio p/p_0 is the ratio of site atmospheric pressure to sea level atmospheric pressure. The ratio p/p_0 can be estimated by

$$\frac{p}{p_o} = e^{-\frac{z}{z_h}}$$

z = altitude

z_h = scale height of the atmosphere $\approx$ 8km

This is acceptable for angles of Z less than 80^0. For $Z > 80^0$ it is necessary to account for effects such as refraction and a more appropriate formulation is given by Kasten (1965) as

$$m = \frac{p}{p_0} \times \frac{1}{sin\beta + 0.15(\beta + 3.885)^{-1.253}} \tag{8.22}$$

This dimensionless quantity can be used in conjunction with Beer's Law to describe the basic attenuation of a beam with initial density E_λ at a given wavelength (λ) as

$$\frac{\hat{E}_\lambda}{E_\lambda} = e^{-\psi_\lambda m} \tag{8.23}$$

where $\hat{E}_\lambda$ is the fraction reaching the earth and ψ_λ is the coefficient of absorption and scattering. At $m = 1$ the fraction of energy transmitted at wavelength λ is given by $e^{-\psi_\lambda}$. This is known as the spectral transmittance per unit air mass ($T(\lambda)$) and it follows that

$$\frac{\hat{E}_\lambda}{E_\lambda} = T(\lambda)^m \tag{8.24}$$

However, $T(\lambda)$ is difficult to calculate except for non turbid clear skies. As mentioned previously, turbidity and especially cloud cover complicate the calculation of this factor. A common simplification is to develop an approximation of Beer's law and apply it to all wavelengths. In

this approach a generalised atmospheric transmission coefficient for all wavelengths at any location is produced (ψ_a), and this is raised to m. This provides a good first order approximation of the attenuation of the beam due to atmospheric absorbtion across all wavelengths as

$$S_b = \hat{S}_i \psi_a^m \tag{8.25}$$

In general ψ_a ranges between 0.6 and 0.9 with 0.84 being a typical value (Campbell 1977).

A slightly more sophisticated treatment is offered through use of the Linke Turbidity Factor (T_L). T_L is based around comparing the actual atmospheric extinction co-efficient over the entire solar spectrum to the corresponding theoretical extinction coefficient for pure dry air. If a form of Equation 8.24 is integrated over the whole solar spectrum then a theoretical extinction coefficient for clear dry air can be calculated. This is given in terms of Beer's Law using a solar altitude/ air mass dependent function (the Rayleigh optical depth of pure dry atmosphere per unit air mass δ_R) and beam attenuation in clear dry air can be expressed as

$$e^{\delta_R m} \tag{8.26}$$

This provides a reference condition, and the real atmospheric situation can be modelled by defining a multiplying factor for δ_R to obtain a more realistic optical depth for the site. In this case the multiplying factor is the Linke Turbidity Factor which is dependant upon solar altitude β. Using this the direct shortwave beam can be modelled as

$$S_b = \hat{S}_i e^{-\delta_R m T_L(\beta)} \tag{8.27}$$

δ_R is a measure of pure Rayliegh scattering per unit airmass along a specified path length, and can be calculated as (Kasten 1980)

$$\delta_R = \frac{1}{0.9m + 9.4} \tag{8.28}$$

The Linke Turbidity Factor needs to be calculated from actual observed data as it typically varies through the year and over geographical locations. A method for calculating $T_L(\beta)$ with reference to a mean T_L standardised to $m = 2$ is given by

$$\begin{aligned} T_L(\beta) &= T_L - (0.85 - 2.25\sin(\beta) + 1.11\sin(\beta)^2) \quad \text{for} \quad T_L > 2.5 \\ T_L(\beta) &= T_L - \frac{(0.85 - 2.25\sin(\beta) + 1.11\sin(\beta)^2)(T_L - 1)}{1.5} \quad \text{for} \quad T_L < 2.5 \end{aligned} \tag{8.29}$$

This is strictly a first approximation, and more complex models that treat the attenuation of different wavelengths due to different atmospheric components can be developed. However, for the current purposes the relationships outlined in Equation 8.25 and Equation 8.27 are sufficient. The processes of beam attenuation in their entirety are complicated, with a multitude of interrelated processes in action. While the physics of many of the processes are well defined much of the data required as input parameters are sparse if in existence at all under the current type of application, thus there is no real benefit in pursuing a more complex model.

A common approach to the estimation of beam attenuation is to use geometric and predictable factors in combination with empirical derivations of turbidity. Fortunately for our purposes the whole question can be simplified as we are interested in long term climatic figures and it is not really necessary to be able to calculate time specific beam attenuation figures. As this is the case we can make use of normalised radiation readings from meteorological stations within the area of interest and use these to develop empirical measures of beam attenuation throughout the year. This sort of approach can take many forms. Either the data can be used to generate generalised long term weekly transmission coefficients to use in relationships such as outlined in Equation 8.25 and Equation 8.27, direct statistical models of the direct beam, or for use in a wide range of other empirical approaches (*e.g.* Ayra 1988; Campbell

1977; Monteith and Unsworth 1990; Oke 1987; Rosenberg *et al.* 1983; Stoutjesdijk and Barkman 1991).

Thus it is possible to specify models to describe the variation in direct short wave flux as a function of time, location, surface geometry and an empirical constant.

Diffuse Short-Wave Radiation

The diffuse component of the short-wave flux is an important part of the total, especially in higher latitudes. As mentioned previously there are many processes responsible for the production of diffuse radiation. On an uncovered surface diffuse radiation is primarily as a result of atmospheric scattering, though when cloud cover is present some of the radiation reflected off the surface may be reflected back by the cloud cover providing a source of reflected diffuse radiation. Under vegetation the diffuse component will also contain light reflected and scattered by the vegetation itself. For the purposes of describing $T(t)$ it is important to consider the ratio of diffuse to total short-wave radiation as this will vary with surface geometry.

There are two main scattering processes that take place in the atmosphere, Raleigh and Mie. Raleigh scattering is fairly uniform in all directions and takes place due to very small particles such as gas molecules in the atmosphere, where the diameter of the scatterer (d) is much smaller than the wavelength on the light. Named after the physicist who discovered this phenomenon, Raleigh scattering predicts that the effectiveness of molecular scattering is proportional to the inverse of the fourth power of the wavelength. This gives rise to the blue sky as the scattering of blue light (400 nm) exceeds that of red light (700 nm) by a factor of $\frac{7^4}{4^4}$ or about 9.

The conditions for Raleigh scattering are not met in the presence of

aerosols where the particles of dust, smoke, pollen etc are often of the same order of magnitude as the wavelength of the light. Theory developed by Mie predicts that the wavelength dependence of scattering due to aerosols of this size should be proportional to d/λ. However, as aerosols contain such a wide range of particle sizes the scattering is not strongly dependent on λ. With Mie scattering the direction of the scattering is predominantly forward, in the direction of the incident ray (Liou 1980), and is one of the main causes of the bright corona around the sun.

The intensity of the diffuse flux varies greatly though will rarely rise above 200 Wm^{-2}. The maximum diffuse intensity is typically observed during fractional cloud cover when the sky is half covered with clouds. The presence of incomplete cloud cover can produce areas of very high diffuse intensities as clouds are very efficient scatters of short-wave radiation. In some cases this can drive the actual incoming global short-wave flux above the solar constant, as the surface in question may be receiving unobstructed direct beam radiation while other parts of the sky may be acting as very intense centres of diffuse radiation (Stoutjesdijk and Barkman 1991). The ratio of diffuse radiation to the total short-wave varies in response to several factors. Obviously atmospheric conditions have an influence, and as cloud cover and turbidity increase so does the ratio of diffuse to total, with the ratio reaching unity under total cloud cover. This type of variation not only influences the absolute value of the diffuse flux, but also the angular distribution of diffuse intensity over the sky dome. The diffuse flux is rarely purely isotropic, but rather varies according to atmospheric conditions.

In clear skies the angular distribution of sunlight depends on the angle of the sun and cannot be described by any simple relationships. In general the sky around the sun and the horizon produces a more intense diffuse flux, and there is a sector in the sky about 90 degrees from the sun

that is relatively less intense (Monteith and Unsworth 1990). A heuristic method suggested by Monteith and Unsworth (1990) is that about 0.45 of the flux received at the surface could be considered as "localised in a large cone angle around the sun" and treated geometrically like the solar beam, with the balance (0.55) of the flux considered as relatively uniform over the hemisphere. As turbidity increases this basic pattern still holds, but the sky moves more towards an uniform intensity. At low sun angles the predominant flux of diffuse solar radiation comes from lower bands in the sky, and as the sun moves higher the upper bands contribute more until at 45 degrees the contribution from each band is approximately the same as from a uniformly overcast sky.

Some simplification of the angular distribution of the diffuse short-wave flux can be made by approximating the diffuse radiation as comprising two components. The intense corona around the sun is primarily due to the fact that Mie scattering by aerosols is primarily directed forward. A sensible approach is to calculate the component of the diffuse flux that originates in this circumsolar region and add this to the direct flux total to ease the calculations that require the directionality of the flux to be known. Temps and Coulson (1977) calculate that the circumsolar part equals $Cos^2(90-\beta)cos^3\beta$ times the remaining part of the diffuse flux under a clear sky. Klucher (1978) found that this factor needed to be multiplied by $1-(S_d/S_t)^2$ to interpolate to intermediate sky conditions. The fraction diffuse adjusted for circumsolar radiation therefore becomes

$$\frac{S'_d}{S_t} = \frac{S_d}{S_t} \times \frac{1}{1+\left[1-\left(\frac{S_d}{S_t}\right)^2\right] Cos^2(90-\beta)cos^3\beta} \tag{8.30}$$

and the remainder can be treated as isotropic. Thus in the case of a completely overcast sky this formulation treats the diffuse short-wave component as uniformly distributed over the sky dome, and this is known as a uniform overcast sky distribution. On heavily over cast days the average radiance is between two and three times greater at the zenith

than horizon, and this variation can be described by what is known as the standard overcast sky distribution (Monteith and Unsworth 1990)

$$R(Z) = \frac{R(0)(1 + bcosZ)}{1 + b} \tag{8.31}$$

Where R is the value of sky radiance at angle Z. In contrast a surface would receive a diffuse flux of πR if the whole sky where uniformly bright. The number $(1 + b)$ is the ratio of the radiance at the zenith to that at the horizon, and typically ranges from 2.1-2.4.

Thus it is possible to provide some basic descriptions of the angular distribution of diffuse short-wave flux. In practice the adoption of a model where the short wave diffuse flux is described as being comprised of isotropic and directional components such as outlined in Equation 8.33, is suitable for the purposes of estimating EHT's.

In addition to modelling the angular distribution of the diffuse short-wave flux, it is also necessary to be able to quantify the ratio of diffuse(S_d) to total (S_t) short-wave flux (*i.e.* S_d/S_t).

There are various approaches to the estimation of the Sd/St ratio. One of the most desirable would be some form of statistical model based on the results of an extensive network of stations measuring components of the radiation balance. If the effective atmospheric turbidity could be estimated allowing calculation of the direct short-wave flux via a relationship such as that presented in Equation 8.25, the effective diffuse flux could be estimated as

$$S_d = S_t - S_{dr} \tag{8.32}$$

Unfortunately in many locations only the global short-wave flux is measured, thus it may be necessary to adopt other approaches.

One approach that has received a fair amount of interest is the development of empirical relationships between atmospheric transmission and the diffuse component of the global flux (Spitters *et al.* 1986). In a review

of this approach Spitters *et al.* (1986) have shown that a wide range of locations followed the same relationship and that a formula could quite accurately predict the diffuse portion given the global flux. this is given as

$$\frac{S_d}{S_t} = 1 \quad for \quad \frac{S_t}{S_i} < 0.07$$

$$\frac{S_d}{S_t} = 1 - 2.3(\frac{S_t}{S_i} - 0.07)^2 \quad for \quad 0.07 \leqslant \frac{S_t}{S_i} < 0.35$$

$$\frac{S_d}{S_t} = 1.33 - 1.46\frac{S_t}{S_i} \quad for \quad 0.35 \leqslant \frac{S_t}{S_i} < 0.75 \tag{8.33}$$

$$\frac{S_d}{S_t} = 0.23 \quad for \quad 0.75 \leqslant \frac{S_t}{S_i} \tag{8.34}$$

Another approach is that suggested by Bristow and Campbell (1985). Here the diffuse transmissivity T_d is estimated from the following equation

$$T_d = T_t \left[1 - e^{0.6\left(\frac{(1-B/T_t)}{(B-0.4)}\right)} \right] \tag{8.35}$$

Where B is an empirical constant and approximates the maximum clear sky transmissivity, and T_t is the daily total transmittance (S_t/S_i). Thus

$$S_d = S_i \times T_d \tag{8.36}$$

and S_b can be calculated as the remainder. This approach has been shown to explain about 95 % of the variation in the diffuse component of the short-wave radiation.

Many empirical formulations could be developed, and to an extent the approach adopted depends upon the available data. Various examples have been published, for example the relationship

$$T_d = 1.2 - \frac{1.2}{T_t}$$

has been presented as appropriate for Canada. Similarly observations in the English midlands show that for $\beta > 30$ degrees the ratio S_d/S_t varies with turbidity according to the following relationship

$$\frac{S_d}{S_t} = 0.68\psi_a + 0.10 \tag{8.37}$$

though when $\beta < 30$ the ratio is a function of β and Equation 8.37 under estimates the ratio.

Another approach to estimating the diffuse shortwave flux is in association with the Linke Turbidity factor considered in the previous section. S_d is generated by the scattered component of the attenuated part of S_i. As we can calculate S_b we can calculate the attenuated portion of S_i and we simply need to be able to split this into absorbed and scattered components. The absorbed component of S_i can be calculated via a form of Equation 8.25

$$S_{\text{absorbed}} = S_i(1 - q_a^m)$$

where q_a is calculated as[2]

$$q_a = \left(\left(\sum_{i=0}^{5} a_i \beta^i\right)(0.506 - 0.010788 T_L(\beta))\right)^{-m} \tag{8.38}$$

Thus we can calculate the scattered component of S_i as

$$S_i q_a^m - S_b \tag{8.39}$$

Only a component will be directed towards the earth as some will be reflected back to space. As discussed earlier in this section the directionality of scattering varies, with Rayliegh scattering being fairly uniform and Mie being predominantly forward. On the basis of this we would expect that under pure Rayliegh conditions S_d would comprise half of the scattered component of S_i. However the presence of Mie scattering will mean that this factor is actually somewhere between 0.5 and 1 depending upon the (geographically and temporally dependant) atmospheric conditions. Thus if we can define the ratio (o) of the scattered component of S_i that is directed towards the earth then we can calculate s_d as

$$s_d = o(s_i q_a^m - s_d) \tag{8.40}$$

[2] $a_0 = 1.294, a_1 = 2.4417E-2, a_2 = -3.973E-4, a_3 = 3.8034E-6, a_4 = -2.2145E-8, a_5 = 5.8332E-11$

This requires that we can measure or estimate the appropriate local figures for T_L and o.

A final consideration with regards to the diffuse short-wave flux is a consideration of the flux intercepted by non-horizontal and/or partially shaded surfaces. The flux intercepted by any surface is simply the summation of the diffuse radiance over the visible sky dome. This exercise is simplified greatly by the treatment of the diffuse flux as consisting of an isotropic component (S'_d) and a directional component that can be added to the direct beam. In this case the directional component is dealt with as part of the direct flux, and the sky is treated as uniformly intense. Thus the isotropic diffuse flux simply becomes

$$\omega_s S'_d$$

where ω_s is the sky view, a dimensionless quantity varying between 0 and 1 that describes the ratio of visible sky area to total sky area. In the case that $\omega_s < 1$ there is the possibility that some short-wave radiation is reflected (S_r) from the obstructing object. If we assume that any such reflected radiation is isotropic then the atmospheric diffuse short-wave flux is augmented by this reflected radiation. Thus these sources of reflection need to be summed for all reflecting surfaces,*i.e.*

$$S_d = \omega_s S'_d + \sum_1^n \omega_i S_{r(i)}$$

Where ω_i[3] is the view figure for object i and $S_{r(i)}$ is the reflected flux from object i.

The basic view factors for some common surfaces can easily be calculated. For example, on a sloping surface the sky view factor is given by

$$\omega_s = \frac{(1 + \cos(\hat{\beta})}{2}$$

[3]Note: $\omega_s + \sum_1^n \omega_i$ must equal 1

the terrain view factor is obviously $1 - \omega_s$. Simplified relationships such as these can be outlined for valleys, basins and walls as follows (Oke 1987)

$$\begin{array}{lll} \text{Wall and Slope} & \phi_s = (1 + \cos(\hat{\beta}))/2 & \phi_t = (1 - \cos(\hat{\beta}))/2 \\ \text{Valley} & \phi_s = \cos(\hat{beta}) & \phi_t = 1 - \cos(\hat{\beta}) \end{array} \quad (8.41)$$

In many applications these simplified calculations will be sufficient. Full 3-D view factor models would need to be developed for specific cases. However these are very easy to calculate in most cases.

Summary

Many aspects of the global short-wave flux are readily predictable, predominantly on the basis of spherical geometry and some understanding of the local atmospheric transmissivity values. For the purposes of estimating EHT it is necessary to consider the ratio of diffuse to global short-wave as the directionality of these two components differ, and this may be of significance in some locations, particularly where there is significant shading and or differences in surface aspect. The particular methods adopted to estimate the short-wave components will largely depend upon the available data. There is little point in adopting a complex model for which no suitable data exist. Thus different models may be adopted for different locations. However it can be established that variation in Shortwave flux operates at a range of spatial scales. Micro-scale variation is governed by factors such as surface aspect $(\hat{\beta}, \hat{\psi})$, surface albedo (a) and object view parameters $(\omega_i, S_{r(i)})$. Macro-scale variation is governed by factors such as Latitude, Altitude, Atmospheric transmissivity (ψ_a), cloud cover and time.

8.2.2 Long-wave Radiation

The long-wave component of the net radiation balance derives from the energy emitted by objects as a function of their absolute temperature. Any object with a temperature above absolute zero emits radiation, though at any given temperature this radiative flux varies from object to object. The theoretical maximum flux at a given temperature for any wavelength ($E(\lambda)$)can be predicted using Planck's law

$$E(\lambda) = \frac{2\pi hc^2}{\lambda^5 \left[exp\left(\frac{hc}{\lambda kT}\right) - 1\right]} \tag{8.42}$$

Where
$E(\lambda)$ is in Wm^{-2}
k is the Boltzmann constant, 1.38×10^{-23} J^0K^{-1}
h is Planck's constant, 6.626×10^{-34} Js
T is the absolute temperature in ^0K

Any object that emits this maximum possible radiation at all wavelengths it is known as a "blackbody" or perfect radiator (Rosenberg *et al.* 1983). Real objects are rarely blackbodies and it is convenient to use two definitions introduced by Kirchoff to describe these objects. The absorptivity of a surface $\alpha(\lambda)$ is the fraction of the incident radiation absorbed at a specific wavelength lambda. The emissivity $\epsilon(\lambda)$ is defined as the ratio of the actual radiation emitted to the theoretical maximum flux. Kirchoff also demonstrated that for any surface $\alpha(\lambda)$ is equal to $\epsilon(\lambda)$. So for any object completely absorbing radiation at wavelength λ $\alpha(\lambda) = 1$, $\epsilon(\lambda) = 1$ and the emitted radiation is given by Planck's law. In the case of a blackbody $\epsilon(\lambda) = 1$ for all wavelengths.

The total theoretical flux F radiated a given temperature by a blackbody is the integral of Equation 8.42 (Planck's law) over all wavelengths, and can be calculated through the Stefan-Boltzman law

$$F = \sigma T^4 \tag{8.43}$$

Where σ is the Stefan-Boltzmann constant, 5.67×10^{-5} erg cm^{-2} sec^{-2} deg^{-4}.
This relationship can be modified to approximate non blackbody flux through the use of an all wavelength emissivity value (ϵ) giving

$$F = \epsilon \sigma T^4 \tag{8.44}$$

A surface will exchange Long-wave radiation with all objects within it's view plane. For a surface with a completely unobstructed sky view the only exchange taking place will be with the atmosphere. However, in other contexts exchange with additional objects will take place. The initial situation to consider is exchange of Long-wave radiation with the atmosphere.

Atmospheric Thermal Radiation

The atmospheric long-wave radiation flux is generated by the thermal emission of the various atmospheric components. This heat energy is mainly due to absorbed short-wave radiation, and as a result is highly dependent upon the atmospheric conditions. As was discussed in the previous section on short-wave radiation, different components of the atmosphere have different absorption properties, with clouds having the biggest effect on the variability of atmospheric thermal radiation. A clear atmosphere only absorbs in certain wavelengths, and as a result of Kirchoff's principle the emission spectra would be expected to closely follow the absorption spectra, which is indeed the case. In terms of estimation of the atmospheric radiation the biggest single factor contributing to variation is the cloud cover. Clouds emit almost as blackbodies in the long-wave spectra and as such have a significant impact. While general principals can be outlined with clear skies, it is probably of little use developing over-complex models for purely clear skies, as this condition is rarely met. In the type of long term climatic studies

we are considering cloudiness is a factor that will almost always have to be included. Having said this I will develop the argument for estimation of atmospheric thermal radiation by considering clear skies first before moving into the more complex situation incorporating clouds.

Clear Skies

In cloudless skies the primary source of atmospheric thermal radiation is the main emitting gasses H_2O and CO_2 (Monteith and Unsworth 1990). As would be expected the radiance of the atmosphere is the least at the zenith rising to a maximum on the horizon as a function of increasing path length of H_2O and CO_2. In general 50% of the radiant flux received at the surface from the atmosphere comes from gasses in the lowest 100 m and 90% from the lowest km(*ibid*). This most probably occurs due to variation in atmospheric pressure and concentrations of the main emitting gasses in the lower atmosphere.

The apparent atmospheric emissivity ϵ_a can be defined as the flux density of downward radiation at the measurement point divided by full radiation at the air temp T_a,*i.e.*

$$L_d = \epsilon_a \sigma T_a^4 \tag{8.45}$$

However in order to calculate L_d in this case we need to be able to estimate ϵ_a. Monteith and Unsworth (1990) suggest that the apparent emissivity at azimuth Z ($\epsilon_a(Z)$) can be taken as the flux density at Z divided by σT_a^4. On this basis it is possible to derive $\epsilon_a(Z)$ as a function of Z

$$\epsilon_a(Z) = a + b \ln(u \sec(Z)) \tag{8.46}$$

Here u is precipitable water (corrected for pressure dependence); a and b are constants depending on the vertical gradient of temperature and the distribution of aerosols.

In a study to determine the accuracy of these sorts of estimator Heitor *et al.* (1991) compared measured fluxes under a clear sky to fluxes calculated using radiosonde data and the numerical equation

$$L = -\sum_{1}^{\infty}(B_i + B_{i+1})[P(w_{i+1} - P(w_i)]/2 \tag{8.47}$$

Where B (Wm^{-2}) is the emittance of a black body at temperature T, $P(w)$ is the integral transmissivity function of the atmosphere for diffuse radiation (comprising the role of water vapour and carbon dioxide) and w_i (g cm^{-2}) is the effective water content between the earth's surface and level i. As can be seen this is a function of the H_2O and CO_2 levels throughout the atmosphere. Through comparison of the measured and computed fluxes Heitor *et al.* (1991) showed that this method explained 97% of the variation in L_d, which suggests that there are no other important infrared active components in a clear sky other than H_2O and CO_2. However it is very difficult to predict or measure appropriate values for a, b or u in Equation 8.46 and L_d is often estimated as a function of various meteorological variables at screen height. Many authors have presented formulas that do this. The simplest approaches that have been used offer estimates solely as a function of air temperature. Such the direct estimate of L_d originally proposed by Swinbank (1963)

$$L_d = a + b\sigma T_a^4 \tag{8.48}$$

Where c and d are empirical constants.

Other researchers have expressed the atmospheric emissivity as a function of air temperature at screen level. Many of these are based around the form suggest by Brunt (1934).

$$\epsilon_a = a + be^{1/2} \tag{8.49}$$

Where a and b are empirical constants.

In a comparison of the effectiveness of the various equations Heitor *et al.* (1991) showed that the use of Brunt's formula to give

$$L_d = (a + be^{0.5})\sigma T_a^4 \tag{8.50}$$

gave a standard deviation of 7 Wm^{-2} in comparison to the Swinbank-type formula which returned a 10 Wm^{-2} error.

More complex models can be developed, but these are to an extent spurious in the current discussion as the main uncertainty lies in cloudy conditions which prevail rather than the clear sky conditions the models above describe.

Cloudy Skies

Clouds dense enough to cast a shadow radiate as blackbodies at the temperature of their component water droplets. The presence of cloud increases the atmospheric radiation flux as the radiation from the carbon dioxide and water vapour in the lower atmosphere is augmented by the radiation from the clouds. The effect of clouds depend to a great extent on the type of cloud present. This is primarily due to the fact that different clouds exist at different heights and consequently have very different base temperatures.

As most of the radiation arises from the layer beneath the cloud cover the gaseous component of the downward flux can be treated as if the sky was cloudless with an apparent emissivity ϵ_a (Monteith and Unsworth 1990). From Kirchoff's principle the transmission of the radiation from beneath the cloud layer will be $1 - \epsilon_a$, and if the cloud base temperature is T_c the downward radiation from a cloudy sky will be

$$L_d = \epsilon_a \sigma T_a^4 + (1 - \epsilon_a)\sigma T_c^4 \tag{8.51}$$

or using a linear approximation

$$L_d = \sigma T_a^4 \left[1 - (1 - \epsilon_a)\frac{4\delta T}{T_a}\right] \tag{8.52}$$

Where $\delta T = Ta - Tc$
Thus the emissivity of an overcast sky ($\epsilon_a(1)$) can be calculated as

$$\epsilon_a(1) = \frac{L_d}{\sigma T_a^4} = 1 - (1 - \epsilon_a)\frac{4\delta T}{T_a} \tag{8.53}$$

and for a sky covered in a fraction c of cloud the emissivity ($\epsilon_a(c)$) can be interpolated as

$$\epsilon_a(c) = c\epsilon_a(1) + (1 - c)\epsilon_a \tag{8.54}$$

This can be used with meteorological data for a study region to provide statistical models for effective atmospheric emissivity that will incorporate the atmospheric structure of the area over time (Monteith and Unsworth 1990). Thus the atmospheric long-wave flux can be estimated on the basis of Equations 8.45–8.54. It should be noted that these relationships are empirical descriptions of the radiative flux at particular sites rather than direct functional relationships.

Heitor *et al.* (1991) offer a development upon this treatment. Under the assumption that there is a linear variation of atmospheric radiation with cloudiness and a single cloud layer they show that the atmospheric radiation flux can be described as

$$\begin{aligned} L_d &= \epsilon_a(1 + Kc)\sigma T_a^4 \\ K &= \tfrac{(1-\epsilon_a)\epsilon_c\Gamma}{\epsilon_0} \end{aligned} \tag{8.55}$$

Where Γ takes into consideration the difference between the cloud base temperature and air as being a function of the cloud base height given by

$$\Gamma = e^{-\gamma z}$$

Where z is the cloud base height and γ is related to the vertical lapse rate of temperature and typically $\gamma = 0.12\text{km}^{-1}$ (Martin and Berdahl 1984).

Using this approach Heitor *et al.* (1991) obtained estimates with a standard deviation of 30 Wm^{-2}, about 4 times larger than under a clear sky.

They found that by modifying the approach to discriminate between high cloud cover and low/medium cloud cover the model improved dramatically. In fitting the relationship

$$\epsilon = \epsilon_0(1 + K_x N_x + K_y N_y)$$

(x=low/medium cloud, y=high cloud) the correlation coefficient rose to 0.97. The application of this model again requires the development of empirical constants for each site.

Thus it is apparent that the atmospheric long-wave flux is essentially a function of cloudiness and atmospheric emissivity (i.e. H_2O and CO_2 levels) and that significant variation of these variables may influence the EHT. The atmospheric flux will not vary at the site level scale.

Net Long-wave Radiation Balance

Having defined the basic principles of atmospheric radiation it is possible to outline the net long-wave radiation balance (L_n). If exchange is solely between the ground surface and the atmosphere, then the incident short-wave flux (L_a in Equation 8.11) simply equals L_d. If the surface has an obstructed sky view then exchange will also take place between the surface and the obstructing objects. An approximation for the incoming flux can be generated by

$$L_a = \omega_s L_d + \sum \omega_i \epsilon_i \sigma T_i^4 \tag{8.56}$$

This takes into account the incident long-wave flux due to all objects with which a surface may undergo long-wave radiation exchange.

The outgoing Long-wave radiation flux is simply a function of the surface temperature and emittance and is calculated with reference to Equation 8.44. Thus the net long-wave radiation balance L_n can be expressed as

$$L_n = L_a - \epsilon \sigma T^4 \tag{8.57}$$

Where
ϵ = the surface emissivity
T = the surface temperature

Thus we can see that the net thermal radiation balance (L_n) at a particular location is influenced by both macro-scale variables (*e.g.* ϵ_a,T_a,ϵ_c,T_c,c,K) as well as micro-scale variables (ϵ,T,ω_s, ω_i, ϵ_i, T_i). Accordingly the significance of these in terms of estimating EHT's must be considered.

8.3 Sensible Heat Flux (H)

Sensible heat exchange occurs due to conduction and convection occurring between the atmosphere and the soil surface. This is known as sensible as it is the mechanism that gives rise to the heat exchange that we can feel or sense. Sensible heat flux occurs primarily through convection, which is a process that involves heat transport via turbulence. This is a mass atmospheric movement as opposed to the molecular exchange that occurs in conduction and consequently tends to be far more efficient. Thus H is to a large extent related to the prevailing turbulence conditions. This is influenced by a number of factors, however turbulence arises through two basic processes; buoyant forces arising from heat induced eddies, and from mechanical turbulence arising due to wind drag on a surface. In order to examine the sensible heat flux it is necessary to outline the factors that will govern both of these processes.It is useful to begin with a consideration of the basic properties of the boundary layer atmosphere interface.

At the immediate surface atmosphere interface there is a *laminar boundary layer*. This is a thin skin of air adhering to all surfaces within which the motion is laminar (Oke 1987). The thickness of this layer varies ac-

cording to factors such as windspeed (decreasing with increasing windspeed) but is of the order of several millimetres. As this layer is laminar no convection occurs and therefore all non-radiative heat transfer occurs through molecular diffusion. The flux of heat through this layer can be expressed as (Oke 1987):

$$H = -\rho c_p k_h \frac{\partial \bar{T}}{\partial z} \tag{8.58}$$

where

ρ = air density (kg m^{-3})

c_p = specific heat of air at constant pressure (J kg^{-1} K^{-1})

k_h = the molecular diffusion coefficient of heat in air (m^2 s^{-1})

$\partial \bar{T} / \partial z$ measures the rate of change in temperature with height

Values for k_h are very small (of the order 10^{-5} m^2 s^{-1}, Oke 1987) thus the laminar boundary layer provides a high degree of insulation between the surface and atmosphere. Accordingly the gradients of climatic properties are very steep through this layer. In the current context the laminar boundary layer does not have a significant influence on variation in EHT.

Immediately above the laminar surface layer is the roughness layer. In this layer irregular surface morphology arising due to features such as vegetation *etc.* known as *surface roughness elements* cause complex flows. The nature of these effects are obviously dependant upon the characteristics of the roughness elements. Above the surface layer is the turbulent surface layer and the two together are often treated as a combined zone known as the *surface boundary layer* or simply surface layer. This layer is 50-100m in thickness and heat exchange in this layer predominantly occurs through convection (Rosenberg *et al.* 1983). It is the factors governing this convective exchange in the surface boundary layer that need to be defined.

A number of approaches to modelling this exchange can be adopted.

However the study is complicated by the fact that H cannot be directly measured. Thus the description of H is typically made with reference to measurable variables. A standard method of describing and modelling H is via aerodynamically derived exchange relationships, usually related to momentum exchange flux. This approach is useful to consider here as it will allow us to outline the function of environmental variables that influence this flux and also allows us to model H on the basis of standard meteorological variables.

In order to model H, the flux of sensible heat in the surface layer can be regarded as analogous to molecular conduction. In this case H can be given by (Oke 1987):

$$H = -c_p \rho K_H \left(\frac{\partial \bar{T}}{\partial z} + \Gamma_d \right) \tag{8.59}$$

Here K_H is the turbulent exchange co-efficient ($m^2\ S^{-1}$) and we need to define the factors that will govern this critical variable. Given the fact that H is largely driven by mass atmospheric movement K_H is obviously related to the degree of turbulence of the surface layer and will be related to factors such as the wind speed and roughness characteristics of the surface. Considerable attention has been paid to the estimation of this measure and it is possible to outline some basic relationships to define the most significant variables.

One way of establishing the factors governing K_H is to relate H to momentum exchange processes in the surface boundary layer. This is useful as momentum exchange processes are typically easier to examine than H and it is possible to describe the transfer of momentum (and water vapour amongst other entities) by analogous equations[4] to Equation 8.59, each with it's own turbulent exchange coefficient (K_m & K_w

[4]For example the momentum exchange flux τ can be given as

$$\tau = \rho_a K_m \frac{\partial U}{\partial z}$$

respectively). If these exchange coefficients are assumed to be identical then knowledge of any one exchange coefficient allows the estimation of the other fluxes. This assumption known as the *Reynolds Analogy* is highly useful in that it allows us to estimate K_H (and hence H) on the basis of K_m.

K_m is related to the wind speed profile above the surface, and the drag of the surface. We can estimate K_m by developing an aerodynamic model of the momentum exchange flux τ. A standard formulation is

$$\tau = u_*^2 \rho_a \tag{8.60}$$

Where u_* is the friction velocity and can be given as

$$u_* = \frac{kU(z)}{\ln\left(\frac{z}{z_0}\right)} \tag{8.61}$$

$U(z)$ is the mean wind speed at elevation z

k is Von Karman's constant (≈ 0.41)

z_0 is the roughness factor

Over rough surfaces a zero plane displacement d is introduced and Equation 8.61 transforms into

$$u_* = \frac{kU(z)}{\ln\left(\frac{z-d}{z_0}\right)} \tag{8.62}$$

The roughness factor (Z_0) is a measure of the aerodynamic roughness of the surface over which the wind speed profile is measured. For vegetated surfaces this factor tends to be correlated with vegetation height (h) and empirical relationships have been produced to describe z_0 as a function of crop height. For example Szeicz *et al.* (1969) give

$$log_{10} z_0 = 0.997 log_{10} h - 0.833 \tag{8.63}$$

On the basis of these relationships it is possible to define a value for K_m and hence K_H. However these have been based around what is known as

the logarithmic law of windspeed profiles which is simply a re-arranged version of Equation 8.62

$$U(z) = \frac{u_*}{k} \ln\left(\frac{z-d}{z_0}\right) \tag{8.64}$$

This describes the wind speed profile ($U(z)$) in a neutral atmosphere over an open relatively smooth surface. However it has been shown this profile, and hence Reynolds analogy, is only applicable under conditions of atmospheric neutrality, a condition rarely achieved. Thus some form of correction for different conditions are required.

At this stage it is important to briefly consider atmospheric stability. If a dry pocket of air rises adiabatically it will expand as the pressure drops, and consequently it will cool. This rate of cooling is known as the *dry adiabatic lapse rate* (Γ_d) and has a value of around 9.8×10^{-3} ^{0}C m^{-1} (Oke 1987). The actual temperature lapse rate observed (the *environmental lapse rate ELR*) is a different quantity, and the atmospheric stability may be evaluated by comparing the ELR and Γ_d. Under the circumstance that the ELR is greater than Γ_d then displaced pockets of air will sink or rise depending on the direction of displacement. Under these circumstances the atmosphere is *unstable* and turbulence is promoted. In the opposite situation ($\Gamma_d > ELR$) the atmosphere is described as *stable* and turbulence is suppressed. This is as and displaced pocket of air will tend to return to its initial location. The final possibility is that $ELR = \Gamma_d$. Under this situation an atmosphere is described a *neutral* and any displace pocket will remain in its new location. Different zones of stability often occur in the atmosphere, and this structure can have a significant effect on the boundary layer temperature regime, as an upper stable layer will effectively trap heat in the lower layers. Atmospheric stability conditions influence H and accordingly are important components of any estimates.

The effects of atmospheric stability on the wind speed profile are usually expressed in terms of two non-dimensional parameters; the *Richardson*

Number (Ri) and the *Monin-Obukhov Parameter* (ζ).

The Richardson Number is essentially a description of the relative importance of buoyancy and mechanical forces and is given by

$$R_i = \frac{g((\partial \bar{T}/\partial z) + \Gamma_d)}{T(\partial U/\partial z)^2} \tag{8.65}$$

Where
g is gravity's acceleration

The Monin-Obukhov parameter (ζ) describes the ratio of buoyant production to mechanical production of turbulence and is given as

$$\zeta = \frac{kzgH}{\rho_a C_p T u_*^3} \tag{8.66}$$

and is considered the more precise indicator of thermal stability.

As a general guide ζ and Ri are related as follows

$$\begin{aligned} \zeta &= Ri, \quad for \quad Ri < 0 \\ \zeta &= \tfrac{Ri}{1-5Ri}, \quad for \quad 0 \leqslant Ri \leqslant 0.2 \end{aligned} \tag{8.67}$$

The influence of thermal stability effects is usually taken into account through dimensionless stability functions ϕ_m (dimensionless wind shear) and ϕ_h (dimensionless potential temperature gradient). These are expressed as functions of either R_i or ζ. For example (Ayra (1988) pp:162)

$$\phi_m = \begin{cases} (1-\gamma_1\zeta)^{-1/4} & for \zeta < 0 \\ 1+\beta\zeta, & for \zeta \geqslant 0 \end{cases} \tag{8.68}$$

$$\phi_h = \begin{cases} \alpha(1-\gamma_2\zeta)^{-1/2} & \text{for} \quad \zeta < 0 \\ \alpha+\beta\zeta, & \text{for} \quad \zeta \geqslant 0 \end{cases} \tag{8.69}$$

However given the inaccuracies in measuring the parameters associated with these constants, and the modelling approximations, a great deal of precision in estimating ϕ_m and ϕ_h is not warranted. For most practical

applications they can be given as (*ibid.*)

$$\begin{aligned} \phi_h &= \phi_m^2 = (1 - 15\zeta)^{-1/2} \quad \text{for} \quad \zeta < 0 \\ \phi_h &= \phi_m = 1 + 5\zeta \qquad\qquad \text{for} \quad \zeta \geqslant 0 \end{aligned} \tag{8.70}$$

On the basis of these stability correction factors empirical relationships have been developed to extend the Reynolds analogy into non-neutral atmospheric conditions. These allow the use of momentum exchange coefficients in the estimation of heat flux under non-neutral conditions (*e.g.* Dyer 1970; Pruitt *et al.* 1973; Webb 1970); For example

$$\begin{aligned} \frac{K_h}{K_m} \approx \frac{K_w}{K_m} &= 1 - 16Ri^{0.25} \quad \text{for} \quad \zeta < 0 \quad \text{(Dyer 1970)} \\ \frac{K_h}{K_m} \approx \frac{K_w}{K_m} &\approx 1 \qquad\qquad\quad \text{for} \quad \zeta \geqslant 0 \quad \text{(Webb 1970)} \end{aligned} \tag{8.71}$$

Using these types of relationships it is possible to give a general definition of K_m and thus re-write Equation 8.59 as

$$H = \rho_a C_p k^2 z^2 \left(\frac{\partial U}{\partial z}\right)\left(\frac{\partial \bar{T}}{\partial z} + \Gamma_d\right)\left(\frac{K_H}{K_m}\phi_m^{-2}\right) \tag{8.72}$$

While the relationship given in Equation 8.72 is useful in identifying critical factors that will govern H the required input variables cannot be realistically estimated in an archaeological context. Thus this does not represent a practical method for estimating variation in H for archaeological purposes. A simplification to Equation 8.72 can be made by deriving finite difference approximations to the gradients in the surface layer (Ayra 1988). For example

$$\frac{\partial U}{\partial \ln z} \simeq \frac{T_1 - T_2}{\ln\left(\frac{z_2}{z_1}\right)}$$

On this basis H can be given as

$$H = -\rho C_p \left[\frac{k^2 \Delta U \Delta T}{\phi_m \zeta \phi_h \zeta \left(\ln \frac{z_2}{z_1}\right)^2}\right] \tag{8.73}$$

If z_1 is the surface, than an identical formulation for H is given by the *resistance* approach (Monteith and Unsworth 1990; Rosenberg *et al.* 1983).

In this approach the flux of sensible heat is viewed as a process analogous to the flow of electrical current, and in an analogy to Ohm's law it is possible to write

$$H = \frac{\rho_a C_p (T_a - T_s)}{r_a} \tag{8.74}$$

where T_s and T_a are the surface and air temperatures respectively, and r_a is the boundary layer resistance to the flow of sensible heat. In order to apply this approach it is necessary to estimate r_a. Various approaches have been proposed to estimate r_a for different objects, primarily on the basis of wind tunnel experiments (*e.g.* Monteith and Unsworth 1990; Campbell 1977). However under the assumption that the logarithmic wind profile relationship is applicable, r_a can be generally estimated for surfaces as

$$r_a = \frac{[ln(z-d)/z_0]^2}{k^2 U(z)} \tag{8.75}$$

This can be modified to account for atmospheric stability in the same manner as Equation 8.73 giving r_a as (Campbell 1985)

$$r_a = \frac{[ln(z-d)/z_0]^2 + \ln(\phi_m \phi_h)}{k^2 U(z)} \tag{8.76}$$

Summary

As can be seen the same basic factors are taken into account in the estimates for H given in Equations 8.72–8.74. On the basis of this it is apparent that the sensible heat flux will be influenced by wind speed, atmospheric stability, differences between surface and air temperatures, the nature of the surface aerodynamic roughness, atmospheric pressure and humidity. The majority of these factors (wind speed, atmospheric stability, atmospheric pressure and humidity) will be relatively uniform over the intra-site scale. While factors such as surface wind speed will vary, the general wind speed profile will be similar. The relationships

discussed in this section provide a basis for assessing significant variations in EHT due to sensible heat flux.

8.4 Latent Heat Flux

The Latent Heat Flux (L_e) is a function of phase transformations of water, in particular the phase change between liquid and vapour. The latent heat of vaporisation of water (V_w) is approximately 2.48 MJ kg^{-1} at 20 ^{0}C thus the evaporation or transpiration of 1 kg of water requires this amount of energy with a concomitant release of 2.48 MJ kg^{-1} upon condensation; it i.e.

$$L_e = -V_w E$$

E = mass flux of water vapour

The latent heat flux can be large, and typically L_e represents the largest outgoing flux from the soil surface. Accordingly L_e and/or E need to be considered in modelling EHT at any level. L_e is comprises vaporisation through both direct evaporation and by transpiration of plants. As it is difficult to distinguish between the flux arising from each of these processes it is usual to refer to the combined vapour flux as evapotranspiration (E). Two aspects must be considered in modelling E. One is the phase transformation, and the other is the transport of water vapour to and from the exchange interface. In order to evaluate L_e it is necessary to consider both aspects of E.

As a basic formulation, the rate of evapotranspiration is a function of the vapour pressure gradient between the surface and the available energy to effect the phase transformation. Thus the mass flux of water vapour through the surface boundary layer(E) can be described in a similar fashion to Equation 8.59 as

$$E = -K_v \frac{\partial \bar{\rho}_v}{\partial z} \tag{8.77}$$

Where K_v is the turbulent transfer coefficient of water vapour

As the vast majority of the water vapour in the boundary layer derives from evapotranspiration, the vapour pressure gradient is essentially a function of the efficiency of vapour transport in the atmosphere. Thus L_e primarily depends upon the amount of available energy, the availability of water at the exchange surface and the efficiency of the vapour transport processes in action.

As discussed previously (*supra vide*:§8.3), turbulent transport is far more efficient than straight conduction. Thus a steeper vapour pressure gradient is maintained under turbulent conditions than under non-turbulent conditions. In a similar manner to the calculations of the sensible heat flux, it can be appreciated that the efficiency of turbulent exchange of water vapour in the atmosphere is related to factors such as atmospheric stability, wind speed and surface roughness characteristics. However, as mentioned previously E is not only governed by atmospheric transport efficiency but is also governed by the availability of water at the surface atmosphere interface and the need for sufficient energy to effect the phase transformations (for vaporisation at any rate). To a fairly large degree this aspect of E is governed by the surface conditions.

For a bare surface, evaporation proceeds as at a rate comparable to that of evaporation from free water so long as the surface is wet and the soil is not shaded by plants or mulches. Such evaporation is described as *first stage drying*. *Second stage drying* begins when the surface becomes visibly dry. During the first part of second stage drying soil evaporation rates are controlled by hydraulic properties, which determine the rate at which water will move through the soil and to the soil surface. This process tends to decrease approximately as the square root of the time elapsed and continues until adsorptive forces at the soil particle liquid interface exert control over the evaporation rate. At this point *third stage drying* begins. During this stage L_e accounts for less than 5% of

the surface energy balance. During second and third stage drying water transport within the soil body needs to be considered as the actual E becomes governed by this processes rather than other atmospheric factors as the surface dries (Campbell 1985).

The situation is a more complex for vegetated surfaces as E is a combination of transpiration and evaporation. However, it is possible to treat a vegetated surface as an effectively homogeneous surface with its own evapotranspiration characteristics. Plants move a large volume of water from the soil to atmosphere and are thus very active components of L_e. To an extent plants act as pumps, moving water from the soil to the air through the osmotic potential between the leaves and roots. The precise exchange characteristics vary from plant to plant and under different climatic conditions as factors such as the stomatal resistance to water vapour flow vary.

Due to the variations in surface conditions for which E needs to be calculated various "standardised" definitions of E have been employed and it is useful to consider two of these here as they are often used in models of E. A commonly used definition of E is E_0, the free water evaporation, which quantifies the magnitude of E over open water for any given climatic conditions. Another very common measure is E_p which defines the *potential evapotranspiration* rate. A definition of E_p is given in Rosenberg *et al.* (1983) pp: 211 as

> Potential evapotranspiration is the evaporation from an extended surface of a short green crop which fully shades the ground, exerts little or negligible resistance to the flow of water, and is always well supplied with water.

E_p is commonly used and, for example, is a reasonably widely recorded meteorological variable in New Zealand.

A number of approaches to estimating L_e due to combined evaporation

and transpiration have been proposed (see Rosenberg *et al.* (1983), Ayra (1988) or Monteith and Unsworth (1990) for an overview), some of which are more suitable for the current purposes than others. Pure empirical relationships that model L_e on the basis of a limited number of climatological variables, typically based on either air temperature or net solar radiation, have been formulated. While some of these relationships have proved to be of use in certain applications they tend to use wide scale climatological variables, and hence are not suitable for making inferences about variation in L_e at the intra-site scale. Further these empirical approaches are largely application specific and may not be of use in many archaeological contexts.

Other approaches are more useful for our current purpose of establishing the influence of environmental variables that will govern E. One of these is the use of mass transport models. This approach is based around the idea that evaporation can be predicted on the basis of vapour pressure and some form of wind function, after a relationship such as

$$E_o = C(e_o - e_a) \tag{8.78}$$

Where C is an empirically derived constant involving windiness, e_o and e_a are the vapour pressure at the surface and air respectively. This is known as a *Daltonian* type relationship, and several variations on this have been proposed. This type of approach has been shown to work well as long as the vegetation is not experiencing water stress and C has been locally determined. In an approach analogous to the resistance approach for estimating H (Equation 8.74) Monteith (1963) has proposed a resistance approach to calculate L_e. This is a Daltonian relationship where C is replaced by a term that includes both resistance to movement of water through the atmosphere (r_a) and canopy resistance to the release of water into the atmosphere (r_c). Under this scheme Equa-

tion 8.78 becomes

$$L_e = \frac{\rho_a C_p}{\gamma} \frac{e_a - e_{ss}}{r_a + r_c} \tag{8.79}$$

ρ_a = density of air (1.297 kg m^{-3} Table 8.6)

C_p = specific heat of air (1.01 J kg^{-1} k^{-1} Table 8.6)

γ = the psychometric constant

e_a = the vapour pressure of the air (kPa)

e_{ss} = the surface vapour saturation pressure (kPa)

Where the psychometric constant γ is given by

$$\gamma = \frac{PC_pM_a}{V_wM_w} \tag{8.80}$$

P = air pressure (kPa)

M_a = the molecular mass of air 0.02845 kg (Moeller *et al.* 1984)

e_{ss} can be calculated from the absolute temperature of the surface as (Rosenberg *et al.* 1983) pp. 170.

$$e_{ss} = 0.61078e^{\frac{17.269T}{T+247.5}} \tag{8.81}$$

T=temperature in ^{0}C

And e_a[5] can be calculated as (Rosenberg *et al.* 1983) pp. 170.

$$e_a = \frac{RHe_{ss}}{100} \tag{8.84}$$

RH = relative humidity

[5] e_a (and consequently RH) can be measured via wet and dry bulb temperatures according to the following equation (Rosenberg *et al.* 1983)

$$e_a = e_{ss} - AP(T - T_w) \tag{8.82}$$

where T and T_w are dry and wet bulb temperatures respectively (^{0}C), P is the air pressure and A is a constant of proportionality. A can be calculated as

$$A = 6.6 \times 10^{-4}(1 + 1.15 \times 10^{-3}T_w) \tag{8.83}$$

This type of model is applicable to micrometrological analyses of the type that need to be considered in the assessment of variables governing variation in EHT. Under the assumption that r_a as calculated in the estimation of H (*supra vide*:§8.3) is suitable in this case then the estimate for L_e given in Equation 8.79 can be used to outline the principle variables governing variation in L_e and the influence that these will exert (see Equation 8.93 for an estimate of r_c).

Another approach to estimating L_e is the *aerodynamic method*. This follows similar reasoning to that adopted in the modelling of H (*supra vide*:§8.3), in that E is predicted as a function of the gradients of specific humidity and the logarithmic wind profile. The original formulation was given by Thornwaite and Holzman (1942) as

$$E = \rho_a k^2 \frac{(h_2 - h_1)(U_2 - U_1)}{ln(z_2/z_1)^2} \tag{8.85}$$

h_1, h_2 = specific humidity at heights

U_1, U_2 = windspeed at z_1 and z_2

While having a sound theoretical basis this application requires a number of measurements to be made at and above the surface, and also as h_1 and h_2 are functions of L_e, Equation 8.85 tends to more descriptive rather than predictive regarding L_e. This means that it is not a particularly useful relationship in terms of defining factors that will influence the humidity profile and hence L_e.

Other common approaches to estimating L_e are based around combination formulas, which consider both the factors of energy supply and turbulent transport of water vapour away from the exchange interface. One of the most widely used methods for estimating L_e is based around a combination method originally proposed by Penman (1948). This approach was designed to estimate evaporation from open water surfaces and can be written as

$$E_o = \frac{sR_{no} + \gamma f(U)(e_s - e_a)}{s + \gamma} \tag{8.86}$$

s = the slope of the saturation vapour pressure curve at the wet mean bulb temperature of the air

R_{no} = the net radiation over open water

e_s = the vapour saturation pressure (mb)

U = the windrun in Km day^{-1} at z = 2m

Where s can be estimated as (Campbell 1985)

$$s = \exp(31.3716 - 6014.79/\Theta - 0.00792495\Theta)\left(\frac{V_w M_w}{R\Theta} - 1\right) \quad (8.87)$$

M_w is the molar mass of water (0.018 kg/mole)

R id the universal gas constant

And f(U) can be estimated via functions as

$$f(U) = 0.37(1 + U/160) \quad (8.88)$$

which acts as an appropriate generalised wind function (Stigter 1980).

An attractive feature of the Penman method is that other than R_{no} it only requires meteorological variables at one level as input variables. R_{no} can be estimated according to methods presented previously (*infra vide*:§8.2) Thus L_e can be estimated on the basis of standard screen measurements, or estimates of the same. In order to deal with vegetated surface E_p is related to E_o by

$$E_p = f_1 E_o \quad (8.89)$$

Where f_1 is an empirical factor with values of 0.8 in summer and 0.6 in winter. These figures are valid to within ±15% for all temperature climates (Monteith and Unsworth 1990). Under this model intra-site variation will relate solely to factors that influence the net radiation balance, as it is only R_{no} that will vary at the intra-site level. As a result the standard Penman estimate of L_e is not particularly suitable for estimating the significance of variation in archaeological EHT regimes.

A more appropriate form is given by the Penman-Monteith equation. The Penman-Monteith combination formula is of the form

$$L_e = -\frac{s(R_n + H - G) + \rho_a C_p (e_s - e_a)/r_a}{(s + \gamma)(r_a + r_c)/r_a} \quad (8.90)$$

and has been successfully used to estimate L_e (Calder 1977; Slabbers 1977). This relationship is useful in the archaeological context as it allows us to examine the influence of a number of variables governing L_e. Under the circumstances that E_p is known via some other model then E can be calculated on the basis of Equation 8.90 as (Campbell 1985)

$$E = E_p \left(\frac{s + \gamma_p^*}{s + \gamma^*} \right) \tag{8.91}$$

Here γ^* is the apparent psychrometer constant and is calculated from

$$\gamma^* = \frac{(r_a + r_c)K_w}{L} \approx \frac{(r_a + r_c)K_h}{L} \tag{8.92}$$

γ^* represents a value where r_c is a minimum. This is a useful relationship in that E_p or values from which E_p can readily be calculated are a reasonably widely measured meteorological variable, and this allows L_e to be estimated from this data.

Use of either form of Equation 8.90 requires that a measure for r_c can be calculated, as indeed does the resistance model given in Equation 8.79. Figures for r_c can be estimated according to various schemes (*e.g.* Black *et al.* 1970; Brun *et al.* 1973; Callander and Woodhead 1981; Norman 1982; Russell 1980; Singh and Szeicz 1980; Verma and Rosenberg 1977). An approach outlined by Campbell (1985) treats the canopy resistance as having the same water potential dependence as leaf stomatal resistance. Under this assumption he states that r_s can be reasonably well modelled by the relationship

$$r_s = r_s^o \left(1 + \left(\frac{\psi_L}{\psi_c} \right)^n \right) \tag{8.93}$$

r_s^o represents the stomatal resistance with no water stress

ψ_L represents the leaf water potential

ψ_c is a critical leaf water potential

n is an empirical constant which determines how steeply r_s increases with decreasing potential.

This allows us to make some assessment of the influence of different crop covers on L_e by varying the crop specific parameters for r_s^o, ψ_c & n.

Other approaches such as the *Bowen ratio*, resistance and *eddy correlation* methods have been developed (Ayra 1988; Monteith and Unsworth 1990; Rosenberg *et al.* 1983). However there is no real benefit in considering these the current purpose as they do not offer any other aspects on which variables might be most significant in governing L_e.

Summary

The latent heat flux is governed by the vapour pressure gradient between the exchange surface of the atmosphere and the availability of energy and water for the phase transformation. Thus the factors that influence L_e will relate to the efficiency of atmospheric transport (Surface roughness, wind speed, atmospheric stability), the availability of water which is a function of precipitation rates, soil moisture transport processes, type of vegetative cover and the availability of energy to effect phase transformations. Thus many of the variables that govern the sensible heat flux, and their functional relationships, are also of significance to L_e. However there are a number of additional factors that govern L_e which is clearly the most difficult component of the surface energy budget to calculate. In particular it would appear necessary to develop some understanding of the processes of water transport within the Soil-Plant-Atmosphere-Continuum (SPAC).

As L_e can account for a very significant component of the surface energy flux it would be expected that factors giving rise to significant uncertainty in L_e could translate to potentially significant EHT estimation uncertainty. In light of this it is important that variation of L_e at an intra-site level is considered in estimates of archaeological EHT regimes.

Martin Jones 2002

8.5 Soil Heat Flux

The transfer of the thermal heat flux G throughout the soil body is dependent upon the thermal properties of the soil body, and these can be described with reference to the concepts of mass density, specific heat, heat capacity and thermal conductivity.

The specific heat c ($\mathrm{Jkg^{-1}K^{-1}}$) of a material is defined as the amount of energy absorbed or released in heating the material 1 ^{0}C. The heat capacity or volumetric specific heat C_h ($\mathrm{Jm^{-3}K^{-1}}$) is simply the product of mass density ρ ($\mathrm{kgm^{-3}}$) and the specific heat (c).

While latent heat transfer occurs within the soil body, and can comprise a significant component of the soil heat flux under certain circumstances (Campbell 1985), soil heat flow primarily occurs through sensible heat transfer via conduction. As a result soil temperature regimes are commonly described in terms of the sensible component of the soil heat regime alone (*e.g.* Ayra 1988; Campbell 1985; Hanks and Ashcroft 1980; Monteith and Unsworth 1990; Richter 1987; 1990; Rosenberg *et al.* 1983). However a more complete treatment requires that the latent flux is also considered. In the following an outline of the sensible transfer process is considered and this is then generalised to allow incorporation of additional elements of the transfer process such as the latent heat flux.

For homogeneous material the sensible heat flux in any given direction is proportional to the temperature gradient in that direction. For example under steady state heat flow the flux in the z direction can be written as

$$G = -k\left(\frac{\partial T}{\partial z}\right) \tag{8.94}$$

where k is the thermal conductivity of the material ($\mathrm{Wm^{-1}K^{-1}}$). The flux in any other direction can be formulated in an identical fashion.

Equation 8.94 can be reworked to give a time dependent relationship for soil temperature by considering the energy balance for an infinitesimal

piece of soil (Volume = $\Delta x \Delta y \Delta z$). In the absence of transformation the difference between the quantity of heat entering and leaving the soil unit must be balanced by the quantity stored within the unit. As the heat content of any given soil unit (Q) is equal to the volume times the concentration (cn), the change in quantity in a unit over a small time step (Δt) can be given by

$$\frac{\Delta Q}{\Delta t} = \frac{\text{Volume} \times \Delta cn}{\Delta t} \tag{8.95}$$

At the same time we can establish that the change in energy quantity within the soil unit must be equal to the difference in heat flux into and out of the soil unit (ΔG)[6]. Here we must consider the flux divergence on all three principle axes , *i.e.*

$$\frac{\Delta Q}{\Delta t} = \Delta G_x \Delta y \Delta z + \Delta G_y \Delta x \Delta z + \Delta G_z \Delta x \Delta y \tag{8.96}$$

On the basis of Equations 8.95 and 8.96 we arrive at the following local balance equation

$$\frac{\Delta cn}{\Delta t} = \frac{\Delta G_x}{\Delta x} + \frac{\Delta G_y}{\Delta y} + \frac{\Delta G_z}{\Delta z} \tag{8.97}$$

And in the limit that $\Delta x, \Delta y, \Delta z$ and Δt tend to zero this becomes

$$\frac{\partial cn}{\partial t} = \frac{\partial G_x}{\partial x} + \frac{\partial G_y}{\partial y} + \frac{\partial G_z}{\partial z} \tag{8.98}$$

In the case of soil the concentration of heat (cn in Equation 8.98) is given by $C_h \times T$ and on this basis Equations 8.98 and 8.94 can be combined to obtain the time dependent differential equation

$$C_h \frac{\partial T}{\partial t} = \frac{\partial \left(k \frac{\partial T}{\partial x}\right)}{\partial x} + \frac{\partial \left(k \frac{\partial T}{\partial y}\right)}{\partial y} + \frac{\partial \left(k \frac{\partial T}{\partial z}\right)}{\partial z} \tag{8.99}$$

Thus the flux at any point in the soil body is dependent upon the temperature gradients at that point and the thermal characteristics of the soil at that location.

[6] this is only true in the absence of heat sources or heat sinks. In practice heat sources and sinks do need to be considered and can be included as additional flux elements as discussed later, see Equation 8.108

For a completely homogeneous soil Equation 8.99 can be simplified and the heat flux is described as

$$\frac{\partial T}{\partial t} = D_h \left(\frac{\partial^2 T}{\partial x^2} + \frac{\partial^2 T}{\partial y^2} + \frac{\partial^2 T}{\partial z^2} \right) \tag{8.100}$$

D_h is the thermal diffusivity $D_h = k/C_h \; ; m^2 s^{-1}$

Quite often Equations 8.98–8.100 are simplified to a 1 dimensional problem where heat flow is only considered on the z axis. The reduction of the problem to 1-D is done in the obvious way where the flux in two dimensions is assumed to be zero *i.e.*

$$\frac{\partial T}{\partial x} = \frac{\partial T}{\partial y} = 0$$

And for example Equation 8.100 reduces to

$$\frac{\partial T}{\partial t} = D_h \frac{\partial^2 T}{\partial z^2} \tag{8.101}$$

In order for any solution of Equations 8.94–8.101 to be used to generate soil temperature regimes we need to be able to describe the thermal parameters of the soil; that is the factors thermal conductivity, specific heat, volumetric specific heat and thermal diffusivity.

The specific heat of the soil can be calculated by defining the proportions of the soil made up of mineral (x_m), organic (x_o), clay (x_c), water (θ) and air (x_a). Such that $x_m + x_o + x_w + x_a = 1$ that is x_c is a component of x_m. As the approximate volumetric specific heats of these various components are known (Table 8.6) we can simply calculate the volumetric specific heat of the soil as

$$C_h = c_m x_m + c_w \theta + c_a x_a + c_o x_o \tag{8.102}$$

Calculation of k is more complex. However this can also be approximated from soil properties. Campbell (1985) gives the following equation for k

$$k = A + B\theta - (A - D)e^{-(c\theta)^4} \tag{8.103}$$

Table 8.6: Thermal properties soil components (after de Vries (1963) as reported in Campbell (1985); Monteith and Unsworth (1990))

	Density	Specific heat	Thermal conductivity	Heat capacity	Thermal diffusivity
	ρ	c	k	C_h	D_h
	Mgm^{-3}	$Jg^{-1}K^{-1}$	$Wm^{-1}K^{-1}$	$MJm^{-3}K^{-1}$	m^2s^{-1}
Material					
Quartz	2.66	0.8	8.8	2.13	4.18
Clay Minerals	2.65	0.9	2.92	2.39	1.22
Organic Matter	1.3	1.92	0.25	2.5	0.1
Water	1.00	4.18	0.57	4.18	0.14
Air (20 ^{0}C)	1.20×10^{-3}	1.01	0.025	0.0012	20.5
Ice	0.92	1.88	2.18	1.73	1.26

And he presents the following soil specific relationships for calculating the parameters $A \ldots D$

$$A = \frac{0.57 + 1.37x_q + 0.93x_{m-q}}{1 - 0.74x_q - 0.49x_{m-q}} - 0.28x_s(1 - x_s) \quad (8.104)$$

$$B = 2.8 * x_s \quad (8.105)$$

$$C = 1 + 2.6x_c^{-0.5} \quad (8.106)$$

$$D = 0.03 + 0.7x_s^2 \quad (8.107)$$

x_q is the volume fraction of quartz

$x_s = x_m + x_o$

8.5.1 Moisture Dependence of the Thermal Flux

While the relationships defined above allow us to model the basic thermal properties of soil, in order to properly model soil heat flow it is necessary to also consider the soil water regime. The reason for this de-

pendence is two-fold. At one level the thermal properties of the soil vary as a function of water content (*e.g.* Equation 8.103) and this influences the sensible heat flux in the soil. However, there is also a latent heat flux in the soil that arises from movement of water vapour within the soil. This movement is influenced by the soil temperature regime (*supra vide*:§8.6), which means that the latent component of k will be temperature dependent. Thus a linked soil temperature/soil moisture content model is required to give a reasonable approximation of the soil temperature regime. This involves modifying the flux dependent component of the continuity equation (Equation 8.98) to incorporate the moisture dependent thermal flux terms. Thus Equation 8.96 becomes

$$\frac{\Delta Q}{\Delta t} = (\Delta G_x + \sum \Delta F_{x_i})\Delta y \Delta z + (\Delta G_y + \sum \Delta F_{y_i})\Delta x \Delta z + (\Delta G_z + \sum \Delta F_{z_i})\Delta x \Delta y \tag{8.108}$$

where the $F_{.i}$[7] are additional flux terms that must be taken into account. In light of this the heatflow equation (Equation 8.99) becomes

$$C_h \frac{\partial T}{\partial t} = \frac{\partial \left(k \frac{\partial T}{\partial x}\right)}{\partial x} + \frac{\partial \left(k \frac{\partial T}{\partial y}\right)}{\partial y} + \frac{\partial \left(k \frac{\partial T}{\partial z}\right)}{\partial z} + \sum \frac{\partial F_{x_i}}{\partial x} + \sum \frac{\partial F_{y_i}}{\partial y} + \sum \frac{\partial F_{z_i}}{\partial z} \tag{8.109}$$

This is the relationship that must be solved in order to define the soil temperature regime and hence EHT in response to variations in the surface energy balance. There are no useful analytic solutions to this equation and numerical solutions must be conducted. However, under certain conditions it is possible to arrive at an analytic solution to Equation 8.101. While soils, particularly archaeological soils, are not homogeneous this solution allows some general observations about soil temperature regimes to be made.

[7] The definition of the $F_{.i}$ will be considered in the following sections where the soil moisture regime is discussed (*supra vide*:§8.6.2)

8.5.2 Analytic Solutions

It is possible to describe any series of values by a summed series of sine functions known as a *Fourier series* (Chatfield 1996). The cyclic nature of the annual and diurnal temperature regime in particular lends itself to this treatment, and it is possible to regard the temperature regime at any point in the soil as arising from the summation of a series of sine waves of different amplitude and frequency. These can be described as (Chudnovskii 1962)

$$T = \bar{T} + \sum A_i \sin(\omega\theta(t)) \tag{8.110}$$

A_i = the amplitude of wave i

ω = the frequency of wave $i = 2\pi/P$

P = period of the wave

θ = the phase angle of the wave.

This is useful because as any wave propagates through a medium such as the soil its amplitude decreases and it becomes phase lagged with respect to the surface wave, and it is possible to analytically calculate these changes. For the propagation of sinusoidal waves through homogeneous media the non-steady state heat equation for homogeneous media (Equation 8.100) can be solved under the boundary conditions that $z = 0, T = T(t)$ and $z \rightarrow \infty, T \rightarrow \bar{T}$. According to these conditions a propagating wave can be described as

$$T(z,t) = \bar{T} + \sum A_i e^{-z/d} \sin(\omega(t)\theta - z/d) \tag{8.111}$$

Where

z = depth

d = damping depth of the wave, and is given as

$$d = \sqrt{PD_h/\pi} \tag{8.112}$$

While this solution is at best a first approximation to the description of soil temperature regimes in response to fluctuations in the surface

temperature it does allow us to outline some basic parameters for modelling the soil temperature regime. The most critical observation is that the amplitude of any given wave decreases exponentially with depth *i.e.*

$$A(z) = A(0)\exp\left(-\frac{z}{\sqrt{PD_h/\pi}}\right) \tag{8.113}$$

This means that the difference in subsurface amplitudes amongst waves depends upon the surface amplitude, their period and depth of propagation; with higher frequency waves being damped more rapidly. For example consider a soil with a D_h of $0.25 \times 10^{-6}\mathrm{m}^2\mathrm{sec}^{-1}$. The amplitude damping with depth for waves of different frequency is shown in Figure 8.7. From this it is apparent that surface temperature fluctuations with a period of less than the half day are essentially insignificant factors in modelling soil temperatures except at very shallow depths ($\lessapprox 5cm$). This type of consideration provides some basis for understanding what sort of magnitude in surface temperature fluctuation we need to consider in order to accurately model EHT's.

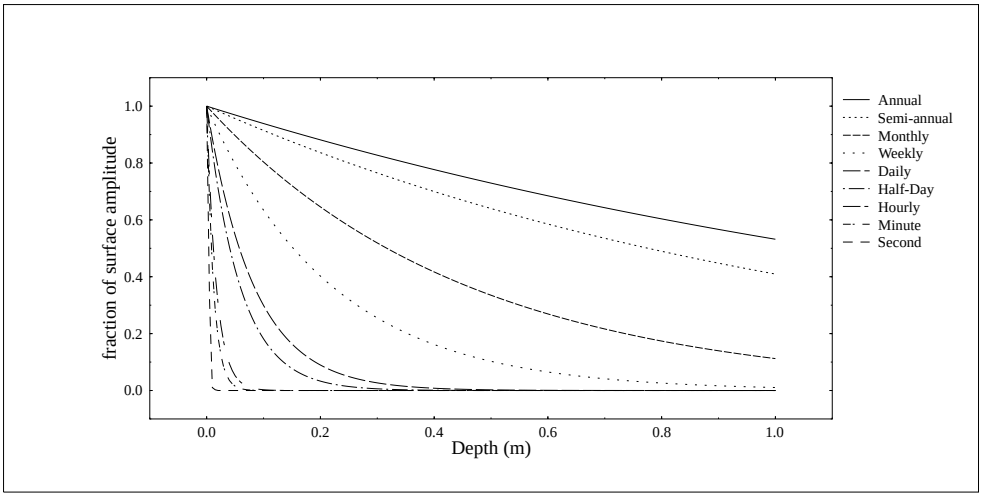

Figure 8.7: Damping of wave amplitude with depth for waves of different frequencies

Examples of this are given in Figures 8.8–8.9 which are graphics of hourly soil temperature data collected over the period 4/1/96 12:00 am to 10/1/96 12:00 am in Auckland. These data demonstrate that while significant short term fluctuations in the surface soil temperature occur (Figure 8.8) these do not propagate to significant short term soil temperature fluctuations even at very shallow depths (Figure 8.9). The data presented in these graphics have simply been chosen at random from a larger data-set (*supra vide*:§F). All the available data similarly illustrates this point.

A second observation that can be made from Equation 8.111 is that there is a phase lag as the waves propagate. This means that soil temperature maxima and minima are attained at different times at different depths. The result of this is that standard earth temperatures measured at meteorological stations are not suitable for directly estimating soil temperature regimes. This is because the temperature at all depths are measured at the same time. Thus the measurement may correspond to a maxima at one depth and a minima at another. In this case the recordings will systematically overestimate or underestimate the average temperature at each depth. The time lag of the temperature wave is given by

$$lag = \frac{zP}{2\pi d} \tag{8.114}$$

Thus for the soil in the previous example there would be about 12 hours lag between the 5cm and 30 cm diurnal wave. This means that as one attained maxima the other would be at a minimum. Again this phenomenon is illustrated in the data presented in Figures 8.8–8.9 where it is apparent that minima or maxima of the soil temperature waves are lagged with increasing depth relative to the surface wave. It will be readily appreciated that, if ignored, this phenomenon could give rise to quite misleading interpretations of meteorological soil temperature readings.

While this type of analysis can be used to produce some understanding of the characteristics of heat transfer through the soil it is not appropri-

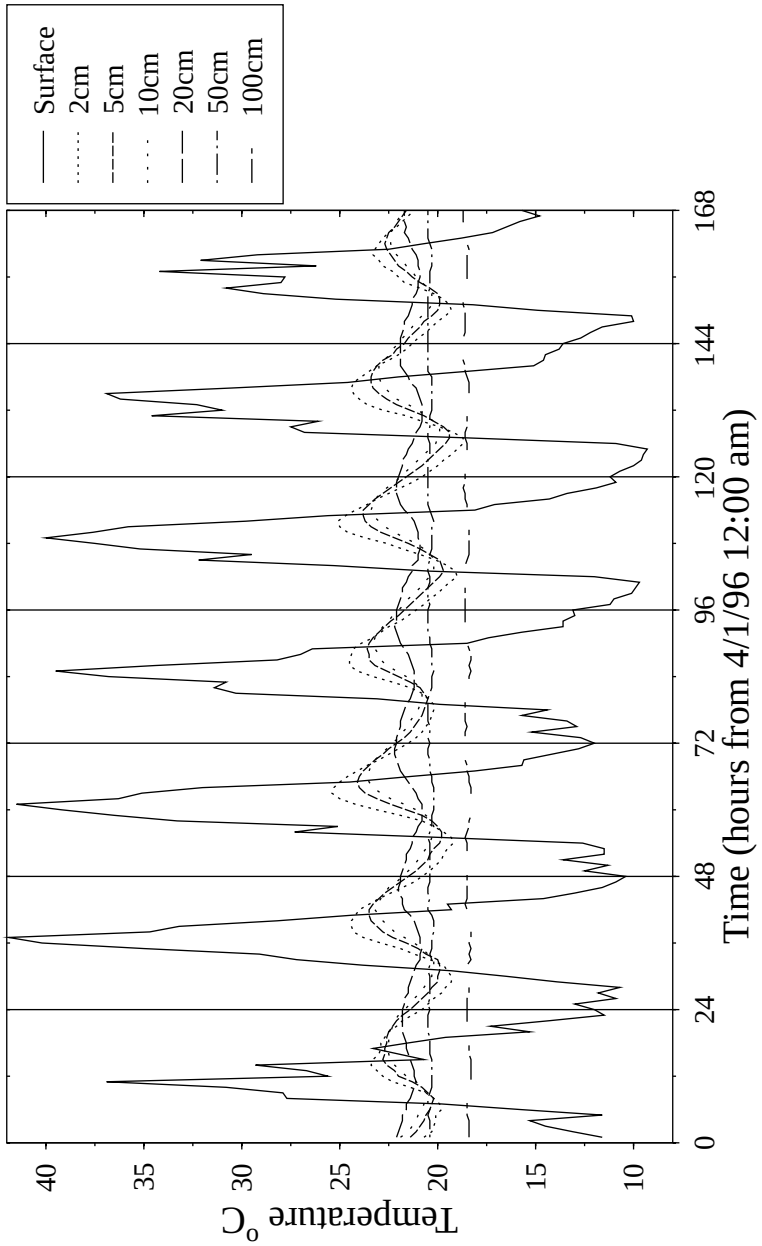

Figure 8.8: Hourly soil temperatures collected over the period 4/1/96 12:00am to 10/1/96 12:00am

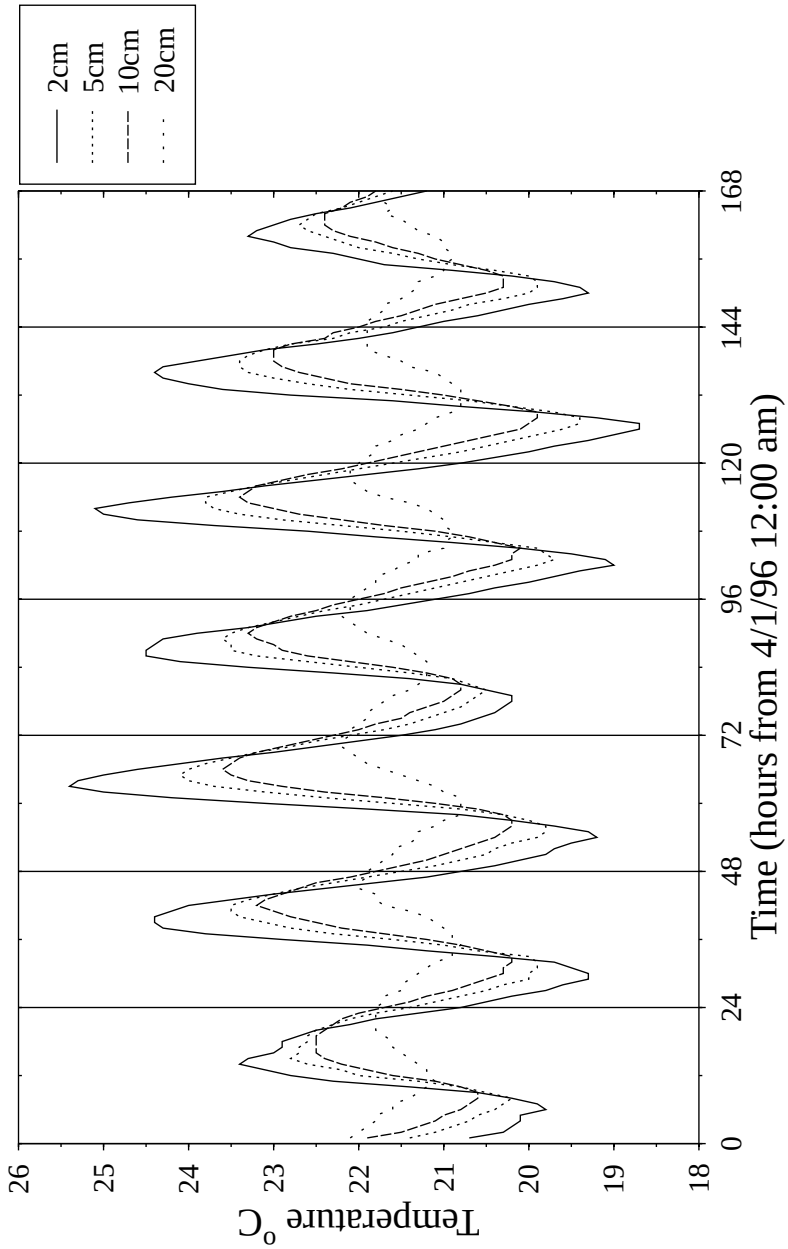

Figure 8.9: Hourly soil temperatures collected over the period 4/1/96 12:00am to 10/1/96 12:00am; graphing a subset of the data in Figure 8.8 representing the shallow sub-surface soil temperature regime

ate as a method for calculation of the actual soil temperature regime as most of the assumptions are unfounded. In particular, the soil body is not homogeneous and any method must be able to model heat transfer through an heterogeneous medium. This means solving the differential given in Equation 8.99. As there are no useful analytical solutions to this the solution is usually made via numerical methods.

8.6 Soil Water Transport

In an identical manner to the soil temperature regime, soils experience a varying soil moisture regime. To further the comparison we can describe this regime in terms of a governing surface balance as

$$N - A - I - E = 0 \tag{8.115}$$

N = precipitation

A = surface runoff

I = water infiltration into the soil

E = atmospheric flux as described earlier (*infra vide*:§8.4).

Here we are most interested in defining the distribution of I and on this basis the linked process of E. The Rainfall N is simply an environmental variable that can be modelled on the basis of meteorological data and we have already identified this variable as being a factor governing potentially significant variation in EHT.

The predominant soil moisture transport process within a soil is via the mass movement of liquid water, which is analogous to the transfer of sensible heat in the soil body. As discussed previously (*infra vide*:§8.5.1) there is also a vapour flux that needs to be considered as it is significant in some cases. In the following the broad principles of soil water distribution within the soil body will be considered and this will then be

generalised to incorporate vapour flow and define the elements of the thermal flux dependent upon vapour transport.

8.6.1 Water Transport in the Soil Body

Water flows within the soil matrix in response to gradients in soil water potential. This can be described by a relation known as Darcy's Law as

$$f_w = -k_w \frac{\partial \psi_h}{\partial z} \tag{8.116}$$

where f_w is the water flux density (kgm^{-2}s^{-1}), k_w is the hydraulic conductivity (kgsm^{-3}) and ψ_h is the soil water potential or hydraulic potential (Jkg^{-1}). On the basis of the continuity equation defined previously (Equation 8.98) we can derive a time dependent equation for the water content of the soil body as

$$\rho_w \frac{\partial \theta}{\partial t} = \frac{\partial \left(-k_w \frac{\partial \psi_h}{\partial x}\right)}{\partial x} + \frac{\partial \left(-k_w \frac{\partial \psi_h}{\partial y}\right)}{\partial y} + \frac{\partial \left(-k_w \frac{\partial \psi_h}{\partial z}\right)}{\partial z} \tag{8.117}$$

However, in order to consider a solution to this equation we need be able to eliminate either θ or ψ_h and estimate k_w. This requires a brief consideration of ψ_h, its relation to θ and k_w.

Water Potential

The water potential ψ_h is the potential energy per unit mass of water in the system (J kg^{-1})[8], compared to that of free water, and is analogous to the concept of heat. The actual hydraulic potential is the sum of a number of potentials (typically matric,osmotic, hydrostatic, pneumatic, overburden pressure and gravitation potentials (Campbell 1985; Richter

[8] potential can also be described as a measure of energy per unit volume in which case the units of potential are J m^{-3} which is dimensionally equivalent to Pascals or pressure

1987) however normally all potentials other than matric (ψ_m) and gravitational (ψ_g) are ignored (Richter 1987), and there is no need for more complexity than this in the current discussion. Thus ψ_h can be defined as

$$\psi_h = \psi_m + \psi_g$$

And we need to consider the matric and gravitational potentials in terms of solving Equation 8.117.

Matric Potential ψ_m

The matric potential ψ_m is one of the most important components of the water potential in soil and plant systems, and gives an expression for the adhesive strength between water and the soil. The formal definition of matric potential is

> ...the amount of utilisable work per unit volume which is needed to bring an infinitesimally small amount of water reversibly and isothermally from a free water surface to the liquid phase of a soil (Richter 1987)

Because energy is needed to get water out the matric energy content is $\leqslant 0$.

The matric potential depends upon water content (θ). This relationship is known as the soil moisture characteristic or moisture release curve, and is characteristic of the particular soil. These curves are described by the function

$$\psi_m(\theta) = \psi_e \left(\frac{\theta}{\theta_s}\right)^{-b} \tag{8.118}$$

where ψ_e and b are experimentally fitted variables. ψ_e is the air entry water potential, which is the potential at which the largest water filled

pores just drain and b is the slope of $\ln(\psi)$ vs $\ln(\theta)$. The relationship between water potential and water content is not unique. The moisture release curve depends upon the drying and wetting history; this is known as hysteresis. While it is possible to take hysteresis into account in describing soil moisture regimes (*e.g.* Mualem and Miller 1979; Gillham *et al.* 1979) it is common to ignore hysteresis in describing the moisture release curve and make the assumption that $\psi_m(\theta)$ is monotonic.

Approximations to the soil moisture release curve can be made on the basis of soil compositional properties (Campbell 1985; Richter 1987). Campbell (1985) gives the following relationships for a soil standardised to a bulk density (ρ_g) of 1.3 Mg M^{-3}

$$\psi_{es} = -0.5 d_g^{-0.5} \tag{8.119}$$

ψ_{es} denotes ψ_e at a standardised ρ_b of $1.3MgM-3$

d_g is the geometric particle diameter [9]

$$b = -2\psi_{es} + 0.2\sigma_g \tag{8.120}$$

σ_g is the geometric standard deviation [10]

In order to take account of variations in bulk density on soil moisture characteristics Campbell (1985) offers the following empirical relationship

$$\psi_e = \psi_{es} \left(\frac{\rho_b}{1.3} \right)^{0.67b} \tag{8.121}$$

Gravitational Potential ψ_g

The gravitational potential ψ_g arises from forces applied to the water as a result of being in a gravitational field. ψ_g represents the energy

[9] $d_g = \exp(a)$ where $a = \sum x_i \ln d_i$, x_i is the mass fraction of textural class i and d_i is the mean particle size of class i(three classes are considered sand,silt,clay).

[10] $\sigma_g = \exp(b)$ where $b = \sqrt{\sum x_i (\ln(d_i))^2 - a^2}$

content of given amount of water (as a mass or volume) relative to a given level h. This is usually taken to be either the water table or soil surface. ψ_z is given as

$$\psi_z = -g(z-h)$$

In flow problems we are most interested in the gradient of gravitational potential which is

$$\frac{d\psi_z}{dz} = -g$$

Hydraulic Conductivity

A final consideration in establishing the soil moisture properties necessary to offer solutions to Equation 8.116 is to describe the hydraulic conductivity k_w as a function of either θ or ψ. On the basis of the Hagen-Poiseuille equation for flux density of a fluid in a tube, the hydraulic conductivity of a soil can be approximated as (Campbell 1985)

$$k = \left(\frac{\sigma^2\theta_s^2}{2\rho_w\nu\psi_e^2(2b+1)2b+2)}\right)\left(\frac{\theta}{\theta}\right)^{2b+2} \quad (8.122)$$

On the basis of this relationship Campbell (1985) suggests that soil specific hydraulic conductivity for saturated soils (K_s) can be modelled on the basis of soil composition as

$$k_s = 4\times10^{-3}\left(\frac{1.3}{\rho_b}\right)^{1.3b} e^{-6.9x_c-3.7x_s} \quad (8.123)$$

Note: b is given in Equation 8.120

This can be extended into non-saturated soils by the relationship

$$k = k_s\left(\frac{\theta}{\theta_s}\right)^m \quad (8.124)$$

m = 2b+3

this can be re-written on the basis of Equation 8.118 as

$$k = k_s\left(\frac{\psi_e}{\psi}\right)^n \quad (8.125)$$

n=2+3/b

The Water Flow Equations

Having defined the necessary relationships between ψ_h, θ and k_w it is possible to re-work Equation 8.117 into a form suitable for solution and hence description of the soil moisture regime. This involves eliminating either ψ_h or θ from Equation 8.117. In order to do this it is necessary to define the specific water capacity.

The reciprocal of the moisture release curve $\psi_m(\theta)$ is known as the specific water capacity $C(\psi_m)$ and this defines the amount of storable water per incremental matric potential $d\psi_m$, dependent upon matric potential. The specific water capacity relates the matric potential and volumetric water content via the moisture release curve as

$$C(\psi_m) = \frac{d\theta}{d\psi_m} \tag{8.126}$$

This allows us to re-work Equation 8.117 using the chain rule to derive

$$\rho_w C(\psi_m)\frac{\partial \psi_m}{\partial t} = \frac{\partial\left(-k_w \frac{\partial \psi_h}{\partial x}\right)}{\partial x} + \frac{\partial\left(-k_w \frac{\partial \psi_h}{\partial y}\right)}{\partial y} + \frac{\partial\left(-k_w \frac{\partial \psi_h}{\partial z}\right)}{\partial z} \tag{8.127}$$

as ψ_g is only a factor on the z axis

$$\frac{\partial \psi_h}{\partial x} = \frac{\partial \psi_m}{\partial x}$$

and similarly for the y axis. However ψ_g needs to be considered in vertical flow thus

$$\frac{\partial \psi_h}{\partial z} = \frac{\partial \psi_m}{\partial z} + \frac{\partial \psi_g}{\partial z} = \frac{\partial \psi_m}{\partial z} - g$$

So we can write the soil water flow equation purely in terms of matric potential[11] as

$$\rho_w C(\psi_m)\frac{\partial \psi_m}{\partial t} = \frac{\partial\left(-k_w \frac{\partial \psi_m}{\partial x}\right)}{\partial x} + \frac{\partial\left(-k_w \frac{\partial \psi_m}{\partial y}\right)}{\partial y} + \frac{\partial\left(-k_w \frac{\partial \psi_m}{\partial z} - g\right)}{\partial z} \tag{8.129}$$

[11] this could also be re-worked purely in terms of volumetric water content on the basis of the soil water diffusivity D_w which is simply the product $k \times C(\psi_m)$ *i.e.*

$$D_w = k\frac{d\psi_m}{d\theta} \tag{8.128}$$

Solutions to this equation will describe water potential (and content) as a function of water flow. However, as for the heat transfer equations further flux terms need to be added to account for additional flux elements such as thermally induced water vapour flow and root uptake during evapotranspiration.

8.6.2 Water Vapour Flow Within the Soil Body

Vapour flow within the soil matrix arises through both diffusion and thermal induction. However, in the current context the consideration of vapour flux will include a discussion of both vapour movement within the soil matrix, and water uptake by roots as part of evapotranspiration. While root uptake is not strictly speaking a mechanism for vapour flow within the soil body it does act as a sink for water within the soil matrix and accordingly will be discussed here (*supra vide*:§8.6.2) following a discussion of vapour flow within the soil matrix.

Vapour Diffusion

The diffusion of water vapour through the soil can be described via Fick's Law

$$f_{v_z} = -D_v \frac{dc_v}{dz} \tag{8.130}$$

D_v is the vapour diffusivity in soil ($m^2 s^{-1}$)

c_v is the soil vapour concentration ($g m^{-3}$)

This allows the flux

$$k \frac{\partial \psi}{\partial z}$$

to be re-written as

$$D_w \frac{\partial \theta}{\partial z}$$

and the water flow equation to be modified accordingly

D_v can be calculated according to some form of the following equation

$$D_v = D_0 \varepsilon(\phi_g) \tag{8.131}$$

where a form suitable for water vapour in soil is given by (Campbell 1985)

$$D_v = D_0 0.66 \phi_g \tag{8.132}$$

ϕ_g = air filled porosity[12] D_0 for water vapour under standard conditions (NTP) is approximately 2.12×10^{-5} $m^2 s^{-1}$ and this can be extrapolated to non standard conditions via the following relationship

$$D_0 = D_0(NTP) \left(\frac{\theta}{\theta^0}\right)^n \left(\frac{P^0}{P}\right) \tag{8.133}$$

The vapour concentration c_v is given by

$$c_v = r_h c_v'$$

c_v' is the saturation vapour concentration at soil temperature[13]

r_h is the relative humidity

And r_h can be related to water potential and vapour pressure as follows

$$\psi_h = \frac{R\Theta}{M_w} \ln\left(\frac{p}{p_0}\right) = \frac{R\Theta}{M_w} \ln(r_h) \tag{8.135}$$

R = the universal gas constant

Θ = temperature in kelvin

M_w = molecular weight of water (0.018 kg mol^{-1})

p = the vapour pressure (Pa)

[12] for soil this can be given by saturated water content - actual water content *i.e.*

$$\phi_g = W_s - W$$

[13]

$$c_v' = \frac{e_{ss} M_w 1000}{RT} \tag{8.134}$$

(Rosenberg *et al.* 1983)

p_0 = the vapour pressure at saturation

Thus the relative humidity of the soil r_h is given by the ratio p/p_0, or from Equation 8.135

$$r_h = e^{\frac{0.018\psi_h}{R\Theta}} \tag{8.136}$$

From this the diffusive flux of water vapour can be written as

$$f_{v_z} = k_v \frac{d\psi_h}{dz} \tag{8.137}$$

where k_v is given by

$$k_v = \frac{0.018 D_v c'_v r_h}{R\Theta} \tag{8.138}$$

As the differential terms in calculating f_v are the same as those governing the flux of liquid water it is only necessary to add the terms k_w and k_v to account for combined liquid transport of vapour diffusion within the soil matrix.

This flux also needs inclusion within the heat flow calculations. When multiplied by the latent heat of vaporisation (V_w) the divergence of this flux can be included as one of the additional flux terms in Equation 8.109 (*i.e.* see Equation 8.148).

Thermally Induced Vapour Flow

Temperature gradients will also induce water vapour flow. As soil water temperature is increased, the pressure of both liquid and vapour increases. Thus water (both vapour and liquid) will tend to move toward colder soil. The influence of this on liquid flow is negligible (Campbell 1985). However it can be a significant component of vapour flow. Again Fick's Law (Equation 8.130) can be used to model this flux, except in this case r_h and c'_v vary with location. If the isothermal component of diffusion is described as given in Equation 8.137 then the thermally induced vapour flow can be given as

$$f_{vT} = -D_v r_h s \frac{dT}{dz} \tag{8.139}$$

s is the slope of the saturation vapour concentration function *i.e.* $s = \frac{dc'_v}{dT}$

The divergence of this flux can be incorporated within Equation 8.117 as an additional flux element (*i.e.* see Equation 8.147).

While this flux also influences the soil heat flux and can be explicitly included in the same manner as the diffusive vapour flux above, the thermal vapour flux is actually accounted for in the estimates of soil thermal conductivity given in Equation 8.103.

The Soil-Plant-Atmosphere-Continuum (SPAC)

Plants operate like pumps moving water from the soil to the atmosphere in response to differences in water potential in the soil, plant and air. This continuum is known as the SPAC and the movement of water through this system can be explained via the laws of thermodynamics. There is little point in presenting a detailed discussion of the SPAC here other than to outline the critical elements for the present discussion, more complete discussions of the SPAC can be found elsewhere (Rosenberg *et al.* 1983; Monteith and Unsworth 1990). The movement of water through the SPAC can be regarded as occurring along a gradient of decreasing water potential through the elements of the system; at a most basic level the soil, roots, xylem, leaves and air. The relevance of the SPAC is that the water flux E associated with L_e results in an uptake of water by roots which occur through the soil body. Thus E cannot be simply modelled as occurring from the soil surface and the distribution of $E(z)$ from throughout the soil body needs to be taken modelled and introduced as an additional flux element to Equation 8.117.

In some cases calculating $E(z)$ does not require any modelling of the SPAC at all. If we can calculate the latent heat flux L_e from the surface at any given time (*infra vide*:§8.4) we simply need some method for distributing the associated water uptake ($E = L_e/V_w$) from throughout the

soil profile. One simple method is on the basis of an idealised root density function (Richter 1987). Here we can assume a linear relationship between root density, soil hydraulic conductivity and uptake, and we can use this to calculate the uptake distribution with depth. We can define an idealised root density with depth ($rd(z)$) as (Richter 1987)

$$rd(z) = rd(o)e^{-\upsilon z} \tag{8.140}$$

Here $rd(0)$ is the theoretical surface root density and υ describes the gradient of root density against z. Campbell (1985) states that υ can be calculated as the reciprocal of the depth at which $rd(z)$ is 63% of $rd(0)$. However only the relative distribution of the root density in Equation 8.140 is important thus the absolute values for $rd(0)$ and υ are not important. On this basis the uptake of water via transpiration at any given depth $E(z)$ can be calculated as a fraction of the total transpiration as follows (Richter 1987; Syring 1990)

$$E(z) = E\frac{k(\psi)rd(z)}{\int_0^L k(\psi)rd(z)dz} \tag{8.141}$$

While this approach allows us to partition a calculated E as a distribution with depth, many methods for calculating L_e and E require an understanding upon the canopy resistance to water flow (*e.g.* r_c in Equation 8.90) which is typically a function of ψ_L and hence the entire SPAC. In order to take this into account we need to develop a basic model of water flow in the SPAC. We can model this flow via an electrical analogue using Ohm's law

$$\text{current} = \frac{\text{voltage}}{\text{resistance}}$$

Here we regard the difference in water potential ($\Delta\psi$) between two parts of the system as a driving force analogous to voltage working against the resistance of that part of the system, and E as analogous to electrical current. Under steady-state conditions the flow through each element is equal and the potential gradients and resistances can be related as

$$E = \frac{\psi_g - \psi_r}{r_g} = \frac{\psi_r - \psi_l}{r_r + r_x} = \frac{\psi_L - \psi_a}{r_s + r_a} \tag{8.142}$$

So, for example, we could use this analogy to give an estimate for ψ_L as

$$\psi_L = \psi_g - ER \tag{8.143}$$

where R is an overall combined resistance. However this relationship is not that useful as it stands because it gives us no way to calculate a figure for R and ψ_s which we know vary with z. This variation is principally a function of soil depth and rooting density, and it is possible to extend the simple series SPAC analog given in Equation 8.142 to describe the root system as a set of parallel resistors (Hillel 1980). Following this approach Campbell (1985) derives the following formulation for ψ_L

$$\psi_L = \frac{\sum\left[\frac{\psi_s(z)}{r_g(z)+r_r(z)}\right]}{\sum\left[\frac{1}{r_g(z)+r_r(z)}\right]} - E\left(\frac{1}{\sum\left[\frac{1}{r_g(z)+r_r(z)}\right]} + r_l\right) \tag{8.144}$$

It can be seen that this is simply Equation 8.143 with the term ψ_g replaced by a weighted mean soil potential and the term R replaced by the sum of two resistances, the weighted mean root soil resistance and the leaf resistance. Equation 8.144 can be re-arranged to give an uptake term for any given depth ($E(z)$) as

$$E(z) = \frac{\psi_g(z) - \psi_L - Er_l}{r_g(z) + r_r(z)} \tag{8.145}$$

Thus we can use either Equation 8.141 or Equation 8.145 to calculate the flux sink terms for inclusion in the over all soil water flow equations.

8.6.3 Soil Water and Heat Regime Formulas

At this stage it is possible to present a relationship describing the soil water regime including flux terms to take into account vapour flow and water sink via transpiration.

$$\rho_w C(\psi_m)\frac{\partial \psi_m}{\partial t} = \frac{\partial\left(-k_{(w+v)}\frac{\partial \psi_m}{\partial x}\right)}{\partial x} + \frac{\partial\left(-k_{(w+v)}\frac{\partial \psi_m}{\partial y}\right)}{\partial y} + \frac{\partial\left(-k_{(w+v)}\frac{\partial \psi_m}{\partial z} - g\right)}{\partial z} + \frac{-D_v r_h s\frac{\partial T}{\partial x}}{\partial x} + \frac{-D_v r_h s\frac{\partial T}{\partial y}}{\partial y} + \frac{-D_v r_h s\frac{\partial T}{\partial z}}{\partial z} + E(z) \tag{8.146}$$

$k_{(w+v)} = k_w$[14] $+ k_v$[15]

This can be reduced to a 1-D equation to deal with water flow on the vertical axis only as

$$\rho_w C(\psi_m)\frac{\partial \psi_m}{\partial t} = \frac{\partial\left(-k_{(w+v)}\frac{\partial \psi_m}{\partial z} - g\right)}{\partial z} + \frac{-D_v r_h s\frac{\partial T}{\partial z}}{\partial z} + E(z) \tag{8.147}$$

In a similar fashion we can explicitly define the additional flux elements in the soil heat flow equation (Equation 8.109) as follows

$$C_h\frac{\partial T}{\partial t} = \frac{\partial\left(k\frac{\partial T}{\partial x}\right)}{\partial x} + \frac{\partial\left(k\frac{\partial T}{\partial y}\right)}{\partial y} + \frac{\partial\left(k\frac{\partial T}{\partial z}\right)}{\partial z} + v_w\left(\frac{\partial\left(-k_v + \left(\frac{\partial \psi_m}{\partial x}\right)\right)}{\partial x} + \frac{\partial\left(-k_v\frac{\partial \psi_m}{\partial y}\right)}{\partial y} + \frac{\partial\left(-k_v\frac{\partial \psi_m}{\partial z} - g\right)}{\partial z}\right) \tag{8.148}$$

And again as a 1-dimensional problem treating heat flow on the vertical axis only Equation 8.148 reduces to

$$C_h\frac{\partial T}{\partial t} = \frac{\partial\left(k\frac{\partial T}{\partial z}\right)}{\partial z} + \frac{\partial\left(-k_v\frac{\partial \psi_m}{\partial z} - g\right)}{\partial z} \tag{8.149}$$

The solution to Equations 8.147–8.149 in response to the surface energy balance driven by the external processes described in §8.2–§8.4 would allow a description of soil heat and water regimes. By solving these equations we could study the influence of different environmental factors on the soil temperature regime and hence EHT. These need to be calculated numerically and in practice software needs to be written to make it possible to study the response of soil temperature regimes to fluctuations

[14] *e.g.*Equation 8.124
[15] *e.g.*Equation 8.138

in the various environmental parameters driving the surface energy balance. This type of analysis would make it possible to identify the critical variables that will govern EHT in different archaeological situations and makes it possible to give an approximate quantification of the uncertainty in EHT estimation that will arise from different estimation procedures. In a following chapter (§12) a software package to perform this analysis is described.

8.7 Conclusion

Small uncertainties in EHT estimation give rise to large errors in the associated OHD's. The significance of EHT estimation error for OHD varies, depending upon factors such as geochemistry, however rapidly rise to date error limits of over 100% within an EHT error of ± 6-8 ^{0}C. Certainly for most applications, EHT errors of greater than 2-3 ^{0}C will render OHD largely useless as a chronometric tool. Thus, typically, we require high precision EHT estimates in order to employ OHD; and essentially this comes down to how well we can define the time series $T(t)$ (Equation 8.1) and at what spatial resolution.

For the purposes of absolute relativity with OHD, however, there is not the same requirement for absolute precision in EHT estimates. Here it is only necessary to be able to define the relative difference in EHT (Δ_{EHT}) between two locations under study. However, this again requires an understanding of processes that give rise to significant micro-scale variations in EHT. Thus an understanding of micro-scale factors influencing $T(t)$ is fundamental to any application of OHD, or estimation of EHT, whether absolute or relative.

Thus for the purposes of OHD we have to account for systematic differences in $T(t)$ at differing temporal and spatial scales as required by the

particular problem at hand. As has been outlined through this chapter it is possible to define processes that will account for systematic spatial and temporal variation in $T(t)$. Only the most basic consideration has been given here, however, and it will be appreciated that modelling and accounting for $T(t)$ can be highly complex. This means that any practicable EHT estimates will have to work with approximations to $T(t)$. These approximations must be assessed in terms of how well they can take account of governing variables such as those outlined in this chapter. A number of different approaches have been, or could be, employed to undertake this type of analysis and it is critical to assess how well these estimates perform. Without this assessment it is impossible to quantify the OHD chronometric, *i.e.* OHD is not a viable chronometric tool. In the following chapter we consider how EHT estimates may be made and how well these could perform.

Chapter 9

Estimating Archaeological EHT for OHD

9.1 Introduction

The influence of EHT on OHD is significant[1], and without a suitable estimate of EHT, or Δ_{EHT}, OHD is not a viable dating method. Therefore EHT estimation methods are fundamental to any application of OHD. It is important that these estimates are accurate (as opposed to necessarily precise), and as no EHT estimate is infinitely precise an appropriate EHT estimate must quantify the associated uncertainty. In order for this to be possible an EHT estimation procedure must take into account all of the factors that will give rise to significant variations in the estimate (*e.g.* Chapter 8) and provide a realistic quantification of the uncertainty associated with these. In the following chapter methods that have been, or could be, used to estimate EHT are evaluated and an outline of what can be practically accomplished is presented. This evaluation is made with reference to the attributes of a suitable EHT estimate as defined below.

9.1.1 Suitable EHT estimates

An ideal approach to EHT estimation is to directly evaluate the integral given in Equation 8.3; Δ_{EHT} follows naturally. However, this requires that we know $T(t)$ over the entire hydration period, which is unlikely for most archaeological applications. This presents two general alternative options: one, we generate an estimate for the time series $T(t)$ over the hydration period and use this to evaluate the integral given in Equation 8.3 (*e.g.* Friedman (1976); *supra vide*:§9.2.1); two, we measure, or evaluate, some proxy reaction as an estimate (*e.g* Ambrose (1980; 1984); *supra vide*:§9.2.2). As outlined later both approaches are useful (*supra vide*:§9.3) and have been used previously in archaeological applications

[1] hereafter the use of the term significant in the context of EHT refers to the significance of an effect upon an OHD unless indicated otherwise

(*supra vide*:§9.2).

To an extent the option we employ depends upon the actual application. For example Δ_{EHT} estimation does not necessarily require a detailed understanding of the full time-series $T(t)$, and may be more amenable to estimation via modern proxy (*supra vide*:§9.3.1), while it is necessary to approximate the full time-series $T(t)$ in order to pursue absolute dating via OHD (*supra vide*:§9.3.2). What-ever approach is adopted, the estimate needs to be based around an understanding of the critical factors governing $T(t)$. This is required in order to quantify the precision and accuracy of the estimate, as any estimate must be evaluated in terms of how well it models the critical aspects of $T(t)$ for the particular application in question. To achieve this it is necessary to outline all the variables that may give rise to significant variation in archaeological soil climate regimes and form an understanding of how $T(t)$ varies in response to these (*e.g.* Chapter 8). However there are basic elements of sound EHT and Δ_{EHT} estimation procedures common to all applications, and these form the most basic definition of a suitable EHT estimate.

At the most fundamental level, suitable EHT estimates should take account of small scale temperature variation. Significant systematic variations in archaeological soil temperature regimes can occur over small spatial scales ($<$ 10m: Jones *et al.* 1997*b*; *infra vide*:Chapter 8), and this variation has implications for any application of OHD, relative or absolute. Thus if an EHT estimate cannot take small scale variation into account it is of no practical use for OHD.

In addition to modelling spatial variation in EHT at an appropriate resolution, suitable estimates should take temporal variation into account. This essentially means modelling long term climatic trends. Many EHT estimation methods are based around short term modern data and make the assumption that this is representative of the storage history of the artefact (*supra vide*:§9.2). This will rarely be the case and the long term

variation in soil climate needs to be taken into account. This aspect of EHT estimation is most critical for absolute dating applications as at a practical level it is only the spatial variation in EHT (*i.e.* Δ_{EHT}) that is necessary for relative dating applications. However it must be borne in mind that Δ_{EHT} will change through time in response to factors such as site taphonomy. Therefore the influence of these factors on Δ_{EHT} as a long term variable need to be considered.

A final property suitable EHT estimates should have is hydration model independence. This means that the estimation procedure should be able to provide an estimate for any hydration mechanism. This is important if different hydration models are applied, and ensures forward compatibility of EHT estimates. For example, estimates may be analogue dependant; some estimations are made by measuring the mean reaction rate of an analogous system (Ambrose 1980; Trembour *et al.* 1988). As the exponential temperature response of these systems will be different from that of obsidian the analogue rate cannot be used in its raw form as an EHT estimate for OHD. In a similar manner if a new hydration model with a different definition of EHT to that given in Equation 8.3 is developed then appropriate EHT estimates should be able to be adapted.

A number of approaches to estimating EHT have been used in previous applications of OHD and it is useful to review these and evaluate them in terms of the criteria outlined above. On the basis of this it is possible to establish how well current EHT estimation methods work, and what further developments would be of use.

9.2 Previous Archaeological Approaches to EHT Estimation

While EHT estimation procedures have advanced considerably beyond the initial designation of seven global climatic zones (Friedman and Smith 1960), very few of the approaches to EHT estimation that have been employed previously meet the requirements just outlined. For example archaeologists have tended to consider variation in EHT at macro and at best meso (Ambrose 1984; Friedman 1976; Leach and Hamel 1984) scales, with any consideration of micro scale variation reserved almost exclusively for the case of variation in EHT with depth (Ambrose 1984; Ridings 1991; Stevenson *et al.* 1989*a*). The EHT estimation procedures employed to date similarly fail to adequately deal with temporal variations in EHT and hydration model independence. Of greatest concern is the fact that almost no attempt has been made to quantify estimate uncertainty. In the following sections the approaches that have been used previously are reviewed. Here it is useful to consider the techniques within the two broad categories of $T(t)$ estimates and Analogue Models as the approaches within each category share common characteristics.

9.2.1 $T(t)$ Estimates

A number of EHT estimation procedures based around $T(t)$ approximates have been either proposed or employed. However, no formal definition of EHT such as that given in Equation 8.3 has been proposed thus there is no standard method of treating $T(t)$ approximates to produce an EHT estimate.

Typically the $T(t)$ estimates that have been employed involve the use of air temperature data in some form of empirical equation. A common approach to this is via a re-working of Lee's (1969; his equation (12) his p.

430) temperature integration equation (*e.g.* Michels *et al.* 1983; Ridings 1996; Stevenson *et al.* 1998). Here long term regional air temperature data are used to provide estimates of subsurface soil temperatures, *i.e.*:

$$T_e = \frac{T_a + 1.2316 + 0.1607R_T}{1.0645} \tag{9.1}$$

where
T_e=exponential mean temperature (used as an estimate of EHT)
T_a=arithmetic mean temperature
R_T= annual temperature range, monthly maximum minus monthly minimum.

Unfortunately Lee's formula is designed to model the rate of sucrose inversion at screen air temperature. Thus there are two clear problems with using this type of approach to directly estimate an archaeological EHT. Firstly the estimate produces an exponential mean temperature for sucrose inversion not obsidian hydration thus cannot produce an EHT; there is clear hydration model dependence. Secondly, the soil temperature regime differs from that of the air. While the two are correlated the differences between them renders an air temperature EHT completely inappropriate for the purposes of estimating soil temperature EHT. Ridings (1996) also draws this conclusion except with reference to experimental data.

Some of these problems have been discussed by Stevenson *et al.* (1989*a*) who point out that this estimate does not allow for changes in temperature with depth. To address this Stevenson *et al.* (1989*a*) proposed a model that accounted for variation in EHT with depth. Their model is essentially a simplified form of the analytic solution to the Fourier-Biot heat flow equation. The idea is to use this analytical solution to calculate the amplitude damping of the air temperature wave with depth so that the variable R_T in Equation 9.1 can be varied with depth, essentially providing some depth dependence to Equation 9.1. However, there are problems with this approach. Firstly, as discussed previously, the

analytic solution to the Fourier-Biot heat flow equation is not suitable for making this type of calculation (*infra vide*:§8.5.2). Secondly in order to use this estimation procedure we have to assume that the soil surface temperature wave is exactly the same as the screen air temperature wave. This is incorrect. Thirdly, the estimate still suffers from hydration model dependence. Finally, there is no way of accounting for spatial variation beyond approximating differences with depth. Thus this EHT estimation approach is clearly unsuitable for providing EHTs of the necessary accuracy.

One $T(t)$ estimation procedure used previously that comes close to meeting the requirements for a suitable EHT estimate is that described by Friedman (1976). He proposed that hourly soil temperatures should be measured for a period of at least 24 h and the hydration rate, averaged over this period, used as an EHT estimate. In practice this approach is evaluating the integral given in Equation 8.3 over a different time interval than that for which the EHT is required. However, this is a fundamentally sound approach if it can be established that the time interval over which the integral is evaluated is a suitable estimator for $T(t)$ over the interval for which the EHT is required. This method is limited in terms of accuracy and spatial resolution unless a large-scale monitoring programme measuring temperatures at many locations within a site over a long-term period (at least 12 months, covering the annual temperature cycle) is carried out. However this approach could be applied in a way that was directly suitable for Δ_{EHT} estimation and if long term soil temperature estimates could be taken into account this approach could be used to estimate EHT.

9.2.2 Analogue Estimates

One of the most common approaches to estimating an EHT involves the use of analogues to the obsidian hydration reaction (*e.g.* Ambrose 1984; Jones *et al.* 1997*b*; Trembour *et al.* 1988). In this approach hydration cells are placed in locations for which an EHT estimate is required and the extent of the analogue hydration reaction is measured over a short time scale (months to a few years). This type of study can either consist of large-scale regional studies (*e.g.* Leach and Hamel 1984; Jones *et al.* 1995; 1997*b*), or smaller scale approaches where cells are placed in a few sites of interest. Invariably the effort is directed at providing a "temperature" for any given site, ignoring intra-site variation. However, it is possible to design a survey making use of hydration cells to account for variation introduced by any number of variables.

There are two major drawbacks to this type of survey. The first is that the measured hydration reaction has a different temperature response that the obsidian hydration reaction, so does not directly estimate the EHT as defined in Equation 8.3. The second is that the results will not account for long term climatic trends. In practice, temperature cells are of most use in establishing Δ_{EHT} and as tests of $T(t)$ estimation models *supra vide*:§9.3.1. However the principal use of these devices has been to estimate EHTs for either OHD or AAR, a purpose for which they are not directly suitable. While useful data can be provided by hydration analogues it is necessary that some method of taking account of hydration model dependence is used in the analysis of their results. Further some other approach needs to be used to take account of long term variation in the soil climate.

Related to the use of hydration analogues is the derivation of an EHT through cross dating of an obsidian artefact. A local EHT can be calculated by measuring the hydration extent on a sample of known age. In this case an obsidian artefact acts as a long-term hydration cell and

the results are directly comparable to those of analogue cells. Except that in this case the observed hydration model matches that of obsidian. While the focus of this type of measurement is again typically directed at providing a "temperature" for any given site the nature of the results differ to those of analogue cells. Cross dated EHT measurements do take account of long term temperature variation for the samples in question and do provide an EHT directly applicable to OHD. However, unlike the analogue cells, it is not practical to conduct an extensive Δ_{EHT} survey through cross dating as this would tend to render OHD redundant. A further consideration is the manner in which the EHT is actually calculated. The calibrated primary date will typically have a complex distribution as will the hydration parameters of the artefact under analysis. In light of this it is important that the distribution of the EHT estimate arising from a cross-dated sample is properly calculated. However, no sound method has been proposed to make this calculation and any meaningful application of cross-dated EHT estimates requires a sound consideration of this calculation. This problem is considered further in §13.2.1 & §13.5.

It will be apparent that a combination of analogue cell data and cross dating data could allow the production of EHT estimates for any surveyed location. While this would limit OHD assays to measured locations the results would meet the criteria for suitable EHT estimates given a suitably designed experimental programme.

9.2.3 Summary

Both $T(t)$ and analogue approaches have been used to provide estimates for EHT. While the typical application of these approaches does not meet the criteria for suitable EHT estimation procedures, suitable estimates for Δ_{EHT} and EHT could be generated for some applications given a properly designed survey. However, no sound quantification of the un-

certainty associated with any of these estimates has been carried out. A further limitation to the types of approaches that have been used to-date is that the associated Δ_{EHT} estimates (where they are calculated at all) are limited to locations for which modern data have been measured. There is no method to extrapolate the estimates to produce sound Δ_{EHT} nor EHT estimates for locations at which base survey data have not been measured.

Thus the standard EHT estimation procedures that have been used for OHD are largely unsuitable and refinements to EHT estimation are required.

9.3 EHT Estimation

As can be appreciated in light of the preceding discussion none of the EHT estimation techniques in mainstream use fully meet the requirements of an ideal EHT estimation approach. It is apparent that most approaches have a limited capacity to incorporate intra-site variation, that long term climatic trends are rarely considered, and in some cases the calculated temperature does not estimate an EHT relating to the obsidian hydration reaction. In order to produce appropriate estimates it is necessary to develop an estimation protocol that considers the fundamental factors governing variation in EHT spatially and temporally. At the most basic level this requires an estimation of Δ_{EHT}. By itself this will meet the requirements for absolute relative dating via OHD (*infra vide*:§8.1.1), and can be extended to take account of temporal variation and model EHT for the purposes of absolute dating via OHD. To reflect this a useful re-formulation of EHT is

$$EHT = \bar{T} + \Delta_{EHT} \tag{9.2}$$

Where $\bar{T}$ is a reference EHT for the Δ_{EHT} values. This describes the two fundamental elements that need to be defined in order to produce a sound EHT estimate. However, as outlined previously, OHD can be usefully applied in the case that $\bar{T}$ in Equation 9.2 above is not known. Thus while both $\bar{T}$ and Δ_{EHT} are necessary for absolute dating via OHD, absolute relative dating can be performed on the basis of Δ_{EHT} estimates alone. In the following we will first consider a general approach to estimating Δ_{EHT} and then consider the extension of these estimates into absolute EHT estimates.

9.3.1 Δ_{EHT}

It is possible to use either analogue or $T(t)$ approximates to estimate Δ_{EHT}. Thus in terms of the methods discussed previously either an appropriately designed analogue cell experiment or environmental temperature logging experiment would be suitable. Strictly speaking $T(t)$ measurement is preferable in that there is less hydration model dependence. However as we are referring to Δ_{EHT} the differences in absolute value of the hydration reaction between obsidian and an analogue are less significant, with Δ_{EHT} in the analogue being of a similar value to Δ_{EHT} in obsidian hydration. Thus it is possible to conduct an analogue experiment that exhibits little in the way of model dependent problems. In light of this there is no real reason to favour one approach over another.

There are big differences in the practical implementation of the two approaches however. While it might be possible to conduct a real time temperature logging exercise over a limited area, the cost and logistics effectively rule out this type of monitoring over large areas. In comparison, analogue cells are cheaper, more compact and generally more robust. This makes it practical to conduct a much more extensive experimental program with analogue cells than might be possible with a

real time temperature logging approach. To an extent the approach employed would depend upon the actual application, and in some cases it may be that a combination of the two approaches would be the most effective. For example, the measurement characteristics of the analogue reaction could be tested in a field trial at a small number of locations against real-time data to establish the effective performance and uncertainty of the measured data in terms of modelling EHT.

The primary limitation to precision and accuracy with this type of approach is that it is only possible to provide estimates for the exact locations monitored. There is no natural way to provide suitable estimates for non-monitored locations without employing some form of predictive model regarding the spatial variation in EHT. This limitation applies equally to the influence of factors such as site formation processes upon Δ_{EHT}.

A general estimation approach that could explicitly take account of spatial variations in soil climates is through the use of numerical models. As numerical models can directly describe spatial and temporal variation in the soil climate these avoid some of the problems inherent in direct measurement of Δ_{EHT}. A model of systematic variations in $T(t)$ over the area of interest could generate an approximation for $T(t)$ for any location. This would allow the influence of factors such as site formation processes to be taken into account. Thus numerical models can estimate a modern EHT at any given location via Equation 4.17 and hence Δ_{EHT}. However, numerical models require a variety of site related input data and, depending on the modelling approach taken, many parameters may need to be calibrated for the location in question. So in order to be able to employ numerical models it is necessary to be able to provide appropriate input data — which may not exist. An additional complication with numerical models is that in the absence of comparative soil temperature data it would be difficult to establish the uncertainty asso-

ciated with any of the estimates produced through the model.

The limitations of both general estimation approaches could be ameliorated through a combined numeric EHT model and experimental soil temperature monitoring program. In a combined approach the measured data would both act as a control for the accuracy and precision of the numerical estimates and provide background data for calibration of any necessary model parameters. The numerical model would in turn allow an estimate of Δ_{EHT} with a quantifiable uncertainty to be produced for any location within the study area. Thus in effect the numerical model serves to interpolate results between measurement locations. An added benefit of this approach is that the numerical model could be used to aid in designing the monitoring program, ensuring that the critical systematic spatial variations within the study area were taken into account. Limited field trials of this type of approach have been described by Jones *et al.* (1998) and Ridings (1996), both of whom report some promise for the general approach.

Thus suitable Δ_{EHT} estimates could be produced via a combination of modern data measurements and a numerical model of significant systematic variations in Δ_{EHT} within the area of interest. In order to employ this approach we have to be able to make the modern measurements, develop a numeric model and correctly calculate the estimation error. As discussed previously a number of approaches to making the modern measurements exist, and the main areas requiring development are the modelling and error treatment. A comparison of the predicted and measured Δ_{EHT} results would allow a quantification of the simulation accuracy and would serve as a quantification of Δ_{EHT} (and possibly EHT also) error arising from prediction via the simulation. It would also allow a more realistic quantification of Δ_{EHT} as might be influenced by temporal factors such as site formation processes.

9.3.2 EHT

The situation becomes more complex when an absolute EHT estimate is required. It is now necessary to take account of temporal variation in the soil climate. Additionally the absolute soil temperature becomes an issue. Thus factors such as differences between analogue and obsidian hydration need to be addressed.

Most of the complexity in estimating an EHT is due to the fact that the primary data for the estimate are modern measurements. This means that measures of long term variation in soil climate need to be incorporated with the modern data to produce a suitable estimate. Without this we make the assumption that the period over which the modern data was collected is representative of the total period for which an EHT is required. This assumption will very rarely be valid, and the older the samples the less likely this is to be correct. However in spite of this, none of the EHT estimation procedures in mainstream use can do anything other than assume that the soil climate has been constant throughout the hydration history of the artefact under analysis (*infra vide*:§9.2.3). As small variations in temperature can have a very significant influence on the date this is clearly problematic. It is important that long term variations can be quantified and the associated uncertainty incorporated into the overall EHT estimation uncertainty. There are two feasible approaches to this problem; 1) using long term calibration samples, 2) modelling $T(t)$ over the entire hydration period.

Long term calibration samples essentially consist of cross-dated samples of obsidian. As discussed previously it is possible to treat obsidian samples as long term EHT monitoring experiments in a similar fashion to the use of analogue temperature cells. If we can cross date a sample of obsidian via a technique such as ^{14}C dating then an EHT can be

calculated from the measured hydration extent as

$$EHT = \frac{-E}{\ln\left(\frac{x^2}{At}\right) R} \tag{9.3}$$

In combination with Δ_{EHT} estimates we could use the EHT estimate given in Equation 9.3 to provide approximate estimates of EHT for all locations at which a Δ_{EHT} related to the cross-dated sample was available. However the terms E, A, x^2 and t in Equation 9.3 all represent probability distributions. Thus a general method for calculating the arising EHT distribution needs to be outlined (*supra vide*:§13) and the precision of the resulting OHD's would always be limited to the precision of the original primary cross-date. While high precision cross-dates could be provided, especially via Bayesian date combination (*e.g.* Nicholls and Jones 2001) an extensive cross dating program would tend to make OHD redundant, particularly as an absolute technique. In practice this type of data would be most suited to providing a site specific $\bar{T}$ which could be used in conjunction with Δ_{EHT} estimates to provide EHT control for a number of locations via Equation 9.2.

A second general approach is to model $T(t)$ over the entire hydration period. Essentially this means using the type of numerical model described previously for the estimation of Δ_{EHT} extended to take account of long term variation in the model variables. However, at best only limited data on the long term variation in climatic variables is likely to be available. In the case that suitable long term data can be used as input to a numeric model for EHT then it might be possible to attempt to estimate $T(t)$ over the entire hydration period. However in a similar fashion to the application of numerical models to Δ_{EHT} it is difficult to quantify the accuracy or precision of numerical estimates without reference soil temperature data.

Thus in conjunction with suitable Δ_{EHT} estimates it can be seen that suitable EHT estimates could be developed. However the absolute EHT

data will need to take account of a wide range of sources of uncertainty. Given this it is very likely that general EHT estimates will have wide distributions that will give rise to low precision event dates.

9.3.3 Summary

From the discussion in the preceding two sections it should be clear that data from a combination of techniques is the most sound general approach to producing useful EHT measurements. At the most basic level a reference data set of modern temperature data is required to model Δ_{EHT}, and where necessary some form of numerical modelling approach is required to interpolate estimates between measurement locations. Here the modern data serve to calibrate numerical models of the soil climate at the site of interest and quantify the accuracy and precision of the numerical estimates. In order to make EHT estimates additional data, relating to long term climate variation, is required. Thus while isolated estimation approaches will suffice in some situations (for example the use of analogue monitoring experiments to quantify Δ_{EHT} for a limited number of precisely monitored locations), in general using a combination of data types will allow an appropriate estimate to be produced.

While several different approaches that can be used to measure modern reference data exist, suitable numerical modelling approaches need to be developed, correct procedures for the estimation of cross-dated EHT measurement need to be defined and methods for quantifying the uncertainty associated with the final EHT estimate need to be outlined. In the remainder of this chapter we will look at how appropriate numerical models might be developed. Cross-dated estimates and error treatment are considered later (Chapter 13).

9.4 Numerical Models for EHT

Numerical models of EHT response to variations in governing meteorological variables are central to combined Δ_{EHT} and EHT estimates. These models represent the state of understanding regarding the relationship between EHT and meteorological variables at the study location, and form the basis for EHT estimates and their associated uncertainties. Thus the design and function of numerical models needs to be carefully considered.

Any numerical model only needs to be sufficiently complex to describe the soil temperature regime in response to environmental variables which will vary significantly over the study area. So while it is possible to produce a model that involves a highly complex simulation of the soil environment, this may not be necessary in some circumstances. For example EHT estimates may only be required for a small number of locations where a simple empirical model describing the relationship between $T(t)$ and the environment can be defined.

Regardless of model design it is necessary to be able to provide input data. In the case of Δ_{EHT} this is relatively straight forward, we can make use of modern data. The situation is more difficult for an EHT as it is necessary to reconstruct the series $T(t)$ over the entire hydration period. In spite of the fact that the temporal variation of some climatic variables can be quantified this is clearly a very difficult if not impossible exercise. However the problem is simplified a little as it is only necessary to approximate the distribution of T within the series $T(t)$.

9.4.1 Distribution Integrals

Our interest is not in being able to precisely estimate the temperature at any given point in time in the past, rather to accurately estimate the

integral of a temperature series. This results in a simplification of the problem because we only need to know the distribution of T in $T(t)$ rather than the exact series. This can be simply demonstrated as follows. If we approximate $T(t)$ as being a series of n piecewise constant temperature values (T_i) each of a uniform time span Δ_t, then the time series $T(t)$ can be represented by a histogram of each value T_i over bins of size Δ_t. The integral of this approximation is simply the sum of the histogram values (T_i) multiplied by the time interval Δ_t. As the time span becomes divided into finer intervals the number of histogram bins increases and the sum described above becomes closer to the value of the integral in Equation 8.3. The key point here is that we need to know the sum of the bin values $\sum_{i=1}^{n} T_i$ in order to evaluate the integral, we do not need to know the order in which individual bins T_i occur. This means that if we know the frequency with which each discrete temperature value occurs as a bin ($f(T)$) within the integration region we can evaluate the sum as $\Delta_t \sum_{-\infty}^{\infty} Tf(t)$. This frequency normalised to 1 is known as the distribution of the value over the interval, and given the distribution $D(T)$ we can integrate the temperature series as

$$\int_{-\infty}^{\infty} TD(T)dt \tag{9.4}$$

Thus we only need to be able to describe the distribution of T over the hydration period in order to evaluate the associated EHT.

A simple case example of this can based around data from an experimental climate monitoring station. Amongst other variables, soil temperatures were monitored at surface, two cm, five cm, ten cm, twenty cm and fifty cm depth at Kumeu over a five month period (*supra vide*:§11.2 for full experimental structure). Over the same period Zeolite temperature cell pairs were buried at the precise monitoring location at soil surface, 10, 20, 30 and 50 cm depths This data set represents a useful case study of the approach outlined above. We can directly evaluate an integral of the form given in Equation 8.3 using the parameters of the

zeolite temperature cells to determine the degree to which the integral predicts the measured hydration response of these devices and compare this to the same integral using $D(T)$.

If we model the temperature as piece wise constant over any given hour unit the integral following Equation 8.3 using $T(t)$ can be evaluated as

$$EHT = \frac{\frac{A}{\ln\left(\frac{\sum_{t_1=0}^{t_2=4080} \exp\frac{A}{data[x]+273.16}+B}{t_2-t_1}\right)}-B}{4080} \tag{9.5}$$

where $data[x]$ corresponds to reading number x in the data series for the particular climatological variable under consideration. Following this the EHT for the soil temperatures at depths 0,10,20, 40 cm are given in Table 9.1 along with the measure EHT.

$D(T)$ is the distribution of $data[x]$. Here $D(T)$ can be approximated by a discrete histogram of the $data[x]$ values with histogram bins of 0.1 ^{0}C. The frequency of each bin value $bin[x]$ is given by $hist[x]$. Accordingly the integral following Equation 8.3 using $D(T)$ can be evaluated as

$$EHT = \frac{\frac{A}{\ln\left(\frac{\sum_{x=1}^{x=n_{bins}} hist[x]\exp\frac{A}{bin[x]+273.16}+B}{t_2-t_1}\right)}-B}{4080} \tag{9.6}$$

Two obvious conclusions can be drawn from the results which are given in Equation 9.1. Firstly, there is no difference between the integrated EHT estimates via the distribution (Equation 9.6) versus the actual temperature series (Equation 9.5). This is exactly what we would expect as both calculations are identical, simply appearing in a different form. The second observation is that the calculated and measured EHT values are on close agreement within ± 0.2 ^{0}C. Obviously as the resolution of $T(t)$ and $D(T)$ increases, the more accurate the estimate will become, and the closer the measured and calculated EHT values will become. This simple example illustrates the fact that if we can approximate a distribution

Table 9.1: Comparative Kumeu results

depth	Measured EHT	Integral after Equation 9.5	Integral after Equation 9.6
2cm	23.55	23.79	23.79
10cm	22.11	22.3	22.3
20cm	21.36	21.45	21.45
50cm	20.45	20.28	20.28

for T over the period of interest we can evaluate the integral given in Equation 8.3 and hence estimate EHT.

One of the primary reasons that this result is useful is that it is possible to combine distributions. For example we can describe a temperature series as comprising systematic and stochastic components and combine the distributions of each of these components to define an overall distribution $D(T)$. This is useful as it is possible to model the systematic distribution of $T(t)$ and combine this with an estimated stochastic distribution to approximate the over all distribution for the temperature series $D(T)$. A systematic model for soil temperature regimes can be based around theory such as that presented in Chapter 8 and is more easily defined than the total series $T(t)$. The stochastic component of meteorological variables can be defined on the basis of modern data. Thus if we can define the systematic components of the soil temperature regime spatially and temporally and estimate the stochastic component associated with these variables we can estimate $D(T)$ and hence the EHT. This means that for approximating $T(t)$ we only need to be able to describe the long term systematic distribution of meteorological variables along with an estimate of the stochastic distribution. This concept is explored further in Chapter 11.

9.4.2 Summary

Numerical models for $T(t)$ are central to providing sound Δ_{EHT} and EHT estimates. These models can be of any form that describes the relationship between key environmental variables and the soil temperature regime in the study area. The main difficulty with numerical models is providing suitable input data. In the case of Δ_{EHT} it is possible to use modern data, however long term variation needs to be taken into account for EHT estimates. This process is simplified by the fact that it is possible to work with the temperature distribution $D(T)$ rather than the temperature series $T(t)$. This means that it is only necessary to directly model the systematic component of $T(t)$ from which a first approximation $D'(T)$ can be calculated. An estimated stochastic component for $T(t)$ can be combined with $D'(T)$ to produce an approximation to $D(T)$. The EHT can be directly calculated from $D(T)$.

9.5 Conclusion

The influence of EHT on OHD is significant, and without a suitable estimate of EHT, or Δ_{EHT}, OHD is not a viable dating method. Therefore EHT estimation methods are fundamental to any application of OHD and it is important that these estimates and their associated uncertainties are accurate. In order for this to be possible an EHT estimation procedure must take into account all of the factors that will give rise to significant variations in the estimate and provide a realistic quantification of the uncertainty associated with these. In practice this can be accomplished by either approximating the time series $T(t)$ over the hydration period and evaluating the integral given in Equation 8.3 or by measuring some proxy reaction as an estimate.

While both of these approaches can be used to provide useful estimates

it is important that the manner in which they are applied relates to the hydration of the actual artefact under question, and accurately quantifies the uncertainty associated with the estimate. In order to do this suitable estimation procedures will:

1. Take account of significant systematic small scale variation in soil temperatures
2. Take account of long term variation in the soil climate
3. Be independent of any particular hydration model
4. Quantify the uncertainty associated with the estimate

Unfortunately archaeological EHT estimation approaches used to-date largely fail to meet these criteria. Almost all published applications have focussed on EHT estimates for the purpose of absolute assays via OHD, and in almost all cases the focus has been upon measuring very short-term modern data as an approximation for the series $T(t)$. Often there is little or no attempt to take account of micro-scale variation. An additional failing is that there has almost invariably been no consideration of the uncertainty associated with the EHT estimates that have been produced. Further problems in most EHT estimates lie in the manner in which the estimates have been produced. Either the modern data derive from hydration analogues where the measured EHT is not directly suitable for OHD, or the modern data are used to approximate $T(t)$ with a poorly considered EHT definition. In short many of the problems in previously applied EHT estimation approaches arise from the manner of application and analysis rather than the actual techniques that have been used.

It is possible to apply estimation approaches that have been used previously to provide suitable EHT and Δ_{EHT} estimation controls. Given a properly designed experimental structure the modern EHT or Δ_{EHT} can

be directly measured at specific locations of interest, and in some cases this will enable OHD analyses to be conducted — especially in the case of Δ_{EHT} measurements for the purpose of absolute relativity assays. However, in many cases modern measurements alone will be insufficient. It is often the case that long-term climate variations make modern measurements unsuitable for direct estimation of EHT throughout the hydration history of an artefact. Additionally, it will often be the case that artefacts do not derive from an exact location where modern temperature data have been collected. Under these circumstances the influence of long-term climate variations and the nature of micro-scale variation in the soil climate need to be taken into account, and the uncertainty of the resulting EHT estimate needs to be properly developed.

The actual approach adopted will be problem specific. However, in general, sound EHT estimates require the combination of several data types, and in many cases will involve some form of numerical modelling. In almost all cases some form of modern soil temperature data will be required, and for the purposes of general Δ_{EHT} estimation a numerical procedure to extrapolate these results to non-monitored locations is required. To extend Δ_{EHT} estimates to actual EHT estimates it is necessary to take account of long-term temperature variations. This requires either cross-dated data or data on long-term local climate variation; individually or in combination. None of the components of this type of combined approach are novel. Cross-dated EHT estimates, Analogue estimates, $T(t)$ integration and numerical modelling have all been applied previously. What needs to be advanced is the manner in which the data types are integrated and the methods for calculating the arising EHT estimate and its associated uncertainty.

In the following four chapters we will further examine EHT estimates via a case study of providing control for EHT in New Zealand. Here the general issues discussed in this chapter will be considered and some

approaches to providing suitable EHT control will outlined. Initially we will describe an analogue cell survey (Chapter 10). This survey provides baseline data for estimating Δ_{EHT} at the particular locations surveyed, and by itself this allows absolute relative dating assays for some locations. This data also acts as reference for evaluating numerical models that are developed in the two following sections. Following Chapter 10 we will consider an approach to developing numerical models for $D(T)$ based around historical meteorological data (Chapter 11). This provides a general model for $\bar{T}$ in New Zealand. Following this we will look at a simulation based approach to approximating $T(t)$ which allows us to model intra-site Δ_{EHT} and hence conduct absolute relativity essays for a given location, or to extrapolate EHT values to locations other than those for which a specific value exists (Chapter 12). Finally models to calculate the distribution of cross-dated EHT values and to incorporate EHT uncertainty into the OHD process will be considered as part of Chapter 13.

Chapter 10

An Analogue EHT Cell Survey of New Zealand

10.1 Introduction

As discussed in the preceding chapter analogue hydration cell data can be a key element of useful EHT estimation programmes. While this data cannot be used to directly estimate EHT's for OHD the data can be used to provide estimates of Δ_{EHT} between critical locations, and perhaps most importantly act as controls for the precision and accuracy of any EHT estimation protocol actually employed.

A further use of these analogue cells is in exploring the influence of soil humidity on hydration reactions. As discussed previously it is unclear what influence fluctuating environmental rH may have on the hydration rate of obsidian (*infra vide*:§4.4.3). Accordingly it is best that OHD is conducted on samples for which the soil rH has been at 100 %. Analogue cells can be used to monitor the relative humidity of soil (§10.4), and this can be used to identify locations and conditions where soil rH may fall below 100 %

In this chapter the results and design of an analogue soil temperature and humidity monitoring programme are presented and discussed. The intention of this program has been to

1. provide controls for EHT estimates in New Zealand (§10.3)

2. Explore the nature of soil rH in New Zealand (§10.4)

However a necessary first element that must be considered is the performance parameters of the analogue cells themselves. In the current exercise the zeolite analogue cells (Ambrose 1980; 1984) supplied by Wal Ambrose were used.

10.2 Temperature Cell Monitoring Programme

In order to make use of analogue cell hydration data it is necessary to establish the performance parameters of the hydration cells used. That is identify the precision and accuracy of the cell data. Further, the cells operate via absorbtion of water and this absorbtion function can only remain constant for a finite extent (i.e. a limited range of weight gain). It is necessary to establish that the absorbtion function is constant over the extent of weight gain for which the cells have been employed in the current experimental program. A final point that needs to be explored is the use of analogue cells as measures of the soil rH. It needs to be established that the cells do indeed perform in this capacity, and at what precision the returned data may be interpreted. These issues were explored through two laboratory based experimental hydration programs.

10.2.1 Cell Temperature Precision

Cell temperature precision was tested by conducting two controlled temperature experiments. In each experiment a number of cells where held at an identical temperature over a fixed period of time. As the temperature was held constant over the duration of the experiment the calculated EHT returned by these cells should be the same as the measured experimental temperature, and the cells should each return an identical result. Thus this experiment allows us to measure both the precision and accuracy of the hydration cells used in this monitoring program. This experimental was conducted at two temperatures; 10 ^{0}C and 30 ^{0}C. These were chosen as they bracket the general range of EHT's expected to be observed throughout the full survey program.

As an extra factor, in the 30 ^{0}C experiment cells with different quantities of prior weight gain were included. Thus current weight gain can be

included as a covariant variable to enable an assessment of how the precision and accuracy may vary as a function of cell weight gain. The results are given below in Table 10.1.

Table 10.1: Experimental cell hydration results

Experimental Temperature	Measured EHT (^{0}C)	EHT error (^{0}C)	Experiment Duration	Total weight gain	Experimental weight gain
10	10.017	-0.017	370	0.576	0.576
10	9.974	0.026	370	0.575	0.575
10	9.797	0.203	370	0.568	0.568
10	9.989	0.011	370	0.575	0.575
30	29.991	0.009	14.917	0.456	0.075
30	30.540	-0.540	14.917	0.506	0.078
30	29.401	0.599	14.917	0.527	0.073
30	30.231	-0.231	14.917	0.436	0.076
30	29.991	0.009	14.917	0.450	0.075
30	33.006	-3.006	14.917	0.561	0.089
30	30.891	-0.891	14.917	0.610	0.079
30	29.126	0.874	14.917	0.575	0.072
30	34.600	-4.600	14.917	1.068	0.096
30	29.674	0.326	14.917	0.971	0.074
30	29.991	0.009	14.917	0.426	0.075
30	10.731	19.269	14.917	1.533	0.024
30	30.517	-0.517	14.917	0.410	0.077
30	1.758	28.242	14.917	1.429	0.014
30	29.991	0.009	14.917	0.965	0.075
30	11.753	18.247	14.917	1.510	0.026
30	30.446	-0.446	14.917	0.756	0.077
30	29.821	0.179	14.917	0.769	0.075
30	29.942	0.058	14.917	0.789	0.075
30	3.131	26.869	14.917	1.505	0.015
30	29.501	0.499	14.917	1.220	0.073
30	30.015	-0.015	14.917	0.646	0.075
30	30.087	-0.087	14.917	0.660	0.076
30	30.063	-0.063	14.917	0.672	0.075
30	29.845	0.155	14.917	0.616	0.075
30	5.847	24.153	14.917	1.462	0.018
30	30.231	-0.231	14.917	0.668	0.076
30	30.279	-0.279	14.917	0.768	0.076
30	30.255	-0.255	14.917	0.675	0.076
30	29.575	0.425	14.917	1.226	0.074
30	5.497	24.503	14.917	1.517	0.017
30	29.575	0.425	14.917	1.010	0.073
30	24.560	5.440	14.917	1.358	0.056
30	24.780	5.220	14.917	1.416	0.056

continued on the next page

Table 10.1: *continued*

Experimental Temperature	Measured EHT (^{0}C)	EHT error (^{0}C)	Experiment Duration	Total weight gain	Experimental weight gain
30	29.967	0.033	14.917	0.996	0.075
30	29.967	0.033	14.917	1.038	0.075

Several clear results arise from this experiment. The first point relates to cell performance as a function of weight gain. As illustrated in Figure 10.1 the cell absorbtion function ceases to be constant following a total weight gain of around 1.3g. The exact change point is unclear, however on the basis of the current results we would expect all EHT's relating to a weight gain of less than 1.3 g to relate to a constant absorbtion function. On this basis the following environmental temperature and monitoring duration limits can be established to define appropriate experimental parameters (Table 10.2).

Table 10.2: Constant cell hydration duration at different EHT's

EHT (^{0}C)	Max Duration (days)
0	1605
2.5	1357
5	1151
7.5	979
10	836
12.5	715
15	613
17.5	527
20	455
22.5	393
25	341
27.5	296
30	258

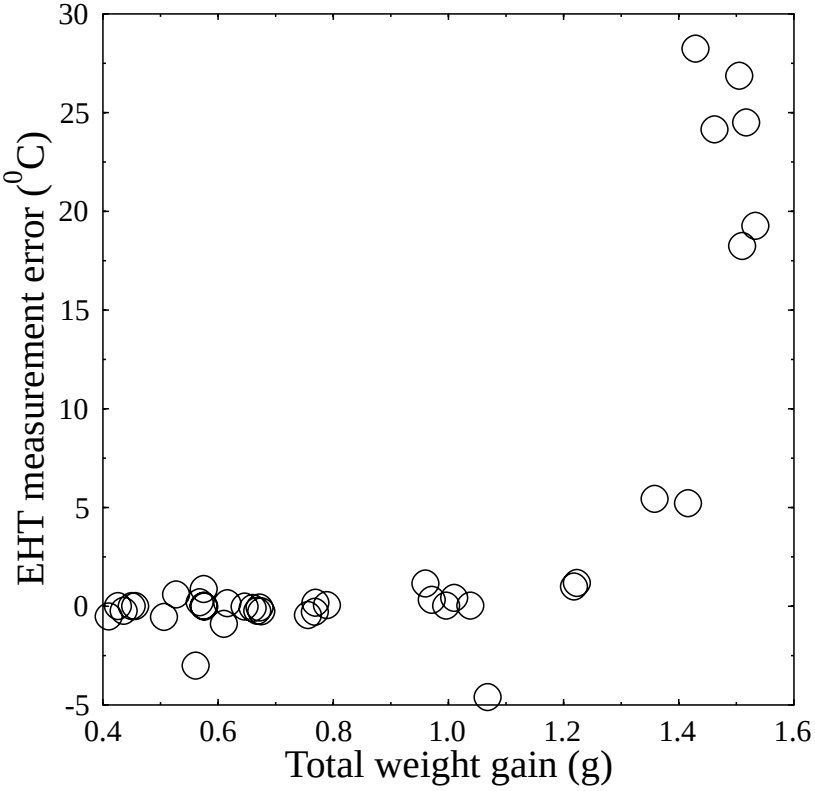

Figure 10.1: Plot of EHT error versus total weight gain for the experimentally hydrated temperature cells

We can use a subset of the experimental results that relate to a total weight gain of less than 1.3 g to define the precision and accuracy of the temperature cells. In theory the EHT measurement error should be a normally distributed random scatter around 0. However, there are two clear outliers in this dataset comprising around 5% of the cases (Figure 10.2). If these are removed then the remaining data is scattered normally about zero[1] as would be expected.

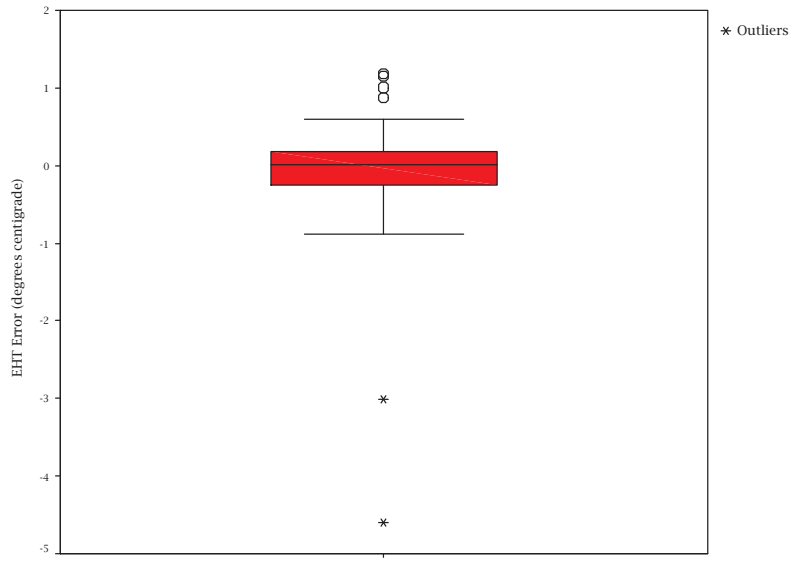

Figure 10.2: Box plot of EHT error for the experimentally hydrated temperature cells

The mean of this data set is 0.091 ^{0}C with a standard deviation of 0.36 ^{0}C (Table 10.3). Thus the accuracy of the cell results is of the order of 1 tenth of a degree with a precision of around half a degree.

[1]The Komologrov Smirnov test statistic is not significant (Table 10.3)

Table 10.3: One-Sample Kolmogorov-Smirnov Test statistics for EHT measurement error against a normal distribution

N		30
Normal Parameters[a,b]	Mean	0.0103
	Std. Deviation	0.3598
Most Extreme Differences	Absolute	0.1477
	Positive	0.1477
	Negative	-0.1368
Kolmogorov-Smirnov Z		0.8088
Asymp. Sig. (2-tailed)		0.5299

[a] Test distribution is Normal.

[b] Calculated from data.

10.2.2 Cell Humidity Performance

The assumption underlying the use of hydration cells as a measure of soil humidity is that a cell in a soil of 100 % rH will experience the same weight gain as a cell in a complete water jacket, where both cells are exposed to the same temperature regime over the same period of time. In order to test this assumption a simple experiment consisting of 4 cell pairs was conducted in a closed soil system maintained at an rH of 100%. Each pair consisted of a cell in a water jacket and a cell placed directly in the soil matrix. If the assumption regarding the use of these cells as humidity controls is correct then all eight cells should experience the same weight gain. The results of this experiment are given in Table 10.4 and show that the assumption is correct; for soils of 100% rH weight gain will be the same for cells in a water jacket and those directly exposed to the soil matrix. The mean within cell pair EHT difference for this dataset is -0.1 ^{0}C with a standard deviation of 0.9 ^{0}C. Thus we cannot reject the null-hypothesis that the measured EHT will be the same for cells maintained in a complete water jacket and those placed in a soil with an rH of 100%. While this result does not allow us to directly measure the

mean humidity of a soil, it does mean that we can use the cells to identify locations where the soil humidity falls below 100 %rH. This is useful as it allows us to establish whether the fundamental assumption that obsidian hydration proceeds in an environment of 100 %rH is violated for any given location.

Table 10.4: Results of the humidity cell performance experiment

Pair	duration	wet EHT	dry EHT	difference
1	300	19.196	19.270	-0.074
2	300	18.716	19.717	-1.002
3	300	19.171	19.586	-0.415
4	300	19.858	18.783	1.075

10.2.3 Conclusion

The two experiments described above allow us to set performance parameters for the humidity cells. The measurement accuracy should be in the order of 0.01 ^{0}C with a precision of around 0.36 ^{0}C. This means that we would expect an apparent $\Delta_{EHT} \sim N(0, 0.36^2)$ to arise from inherent cell performance variations alone. Additionally, outliers are likely. On the basis of the results reported here we would expect around 5% of cells to return spurious readings. This conclusion is supported by data from Leach and Hamel (1984) who also identify the presence of outliers with these types of cell, reporting the incidence of 7 clear outliers out of 88 results ($\approx$ 8 %).

The humidity cell performance experiment has shown that it is possible to use humidity cell pairs to monitor soil humidity and identify where rH falls below 100%. We would expect the measured difference in EHT within each cell pair to exhibit the same level of variance as that for individual cells. That is the within cell comparison would be expected to

have an accuracy of around 0.01 ^{0}C and a standard deviation of around 0.36 ^{0}C.

10.3 Temperature Cell Survey

An analogue temperature cell survey of New Zealand was conducted in order to identify the spatial scale at which EHT estimates for New Zealand need to operate, and to provide a control data set for EHT estimation protocols. On the basis of theory outlined earlier (*infra vide*:§8) it was to be expected that significant micro-scale variations in EHT would occur. In light of this the experimental design is based around two components; macro-scale and micro-scale variation in EHT.

10.3.1 Macro-Scale Survey

The Macro-scale data has been collected for flat, grass covered, locations at 20-30cm depth. This means that confounding micro-scale variables such as surface topography, burial depth and nature of the soil surface are largely held constant. Thus this component of the survey will monitor the extent of Δ_{EHT} over New Zealand as a whole.

While it was important to consider Δ_{EHT} over the geographical extent of New Zealand, a survey of the entire New Zealand landmass was too large an exercise for the current program. Thus two survey areas were identified, the upper North Island and the East coast of the South Island (Figure 10.3). These two areas allow the geographical extent of New Zealand to be surveyed and also represent those areas in which the application of OHD is of most personal interest.

Temperatures were recorded for 77 locations (Figure 10.3; Table 10.5) during the course of this survey. These locations were largely selected

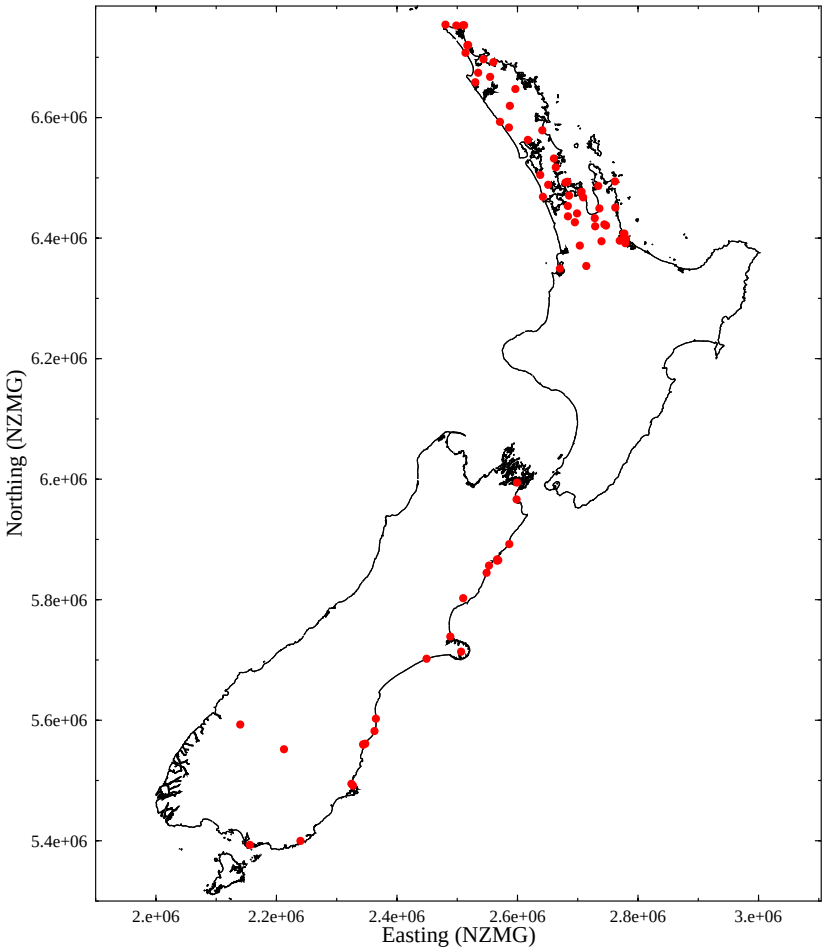

Figure 10.3: Location of the macroregional survey sites

to provide a suitable spatial coverage over the extent of each survey area. However, in 30 cases the locations monitored are adjacent to identified archaeological sites. These data will act as a control for EHT estimates at those sites.

Table 10.5: Macro-regional cell survey results

Location	Depth (cm)	Temperature ^{0}C	Easting NZMG[2]	Northing NZMG	Altitude m
Warkworth	30	17.5	2660450	6531950	20
Waikuku	30	17.9	2511400	6753100	5
Spirits Bay	30	17.8	2498450	6752605	5
Hihi	30	17.9	2559950	6691745	20
Karikari	30	19.1	2543600	6696655	20
Kaitia	30	18.7	2534726.17	6674248.49	12.76
Herekino	30	17.1	2529925	6658500	60
Haratua's pa	30	17.7	2596500	6647285	120
Waipu	30	16.9	2641180	6578700	10
Twin Bridges	20	17.2	2587350	6619355	40
Omamari	30	17.7	2570910	6592795	10
Dargaville	30	16.9	2585776.57	6583387.72	55.04
Gate Memorial	30	16.3	2617225	6562880	40
Mangamuka	30	14.8	2554550	6667400	80
90 mile Beach	30	19.8	2413705	6707320	4
Rawara beach	30	19.5	2518075	6720450	8
Rawara road	30	18.0	2516800	6719555	30
Cape Reinga	30	18.9	2480465.31	6754054.04	14.52
North Cape	10	18.2	2509350	6753000	5
Avoca	10	14.2	2568100	5865300	3
Awamoa	20	10.9	2347400	5560900	2
Tramvalley Road	30	15.9	2347400	5560900	2
Karekare	30	18.6	2642200	6468410	40
Taupaki	30	18.2	2650930	6488320	30
Parakai	30	17.5	2637700	6504690	3
Wenderholm	30	18.4	2663500	6517300	4
spring road	30	15.8	2695215	6426150	30
Horatu	30	16.7	2703430	6387465	20
Te Awamutu	30	17.2	2714195	6353595	55
Kawhia	30	18.0	2670445	2349230	6
Tuakau	30	16.0	2683700	6436000	40
Whitford	30	15.8	2685560	6470410	20
Orere Pt	30	16.7	2708920	6467500	30
Mangatawhiri	20	16.0	2698795	6440850	20
Drury	30	16.2	2683515	6453160	15

continued on the next page

[2]NZMG = New Zealand Map Grid reference

Table 10.5: *continued*

Location	Depth (cm)	Temperature ^{0}C	Easting NZMG	Northing NZMG	Altitude m
Clarence	30	13.7	2586400	5892100	10
Pouarua Rd	30	15.7	2728200	6432930	6
matakana south end	30	15.2	2779010	6391400	2
Matahue	30	16.1	2769650	6395550	15
Oputere	30	14.3	2762265	6450535	140
30 cm open	30	17.9	2761760	6493995	6
Patetonga	30	17.1	2728875	6419450	11
Coromandel	30	17.1	2734000	6486450	5
Thames	30	16.7	2735880	6449065	12
H26 H27 Jnc	30	16.3	2739400	6394625	28
Paeroa A	30	15.9	2746953	6420700	10
Paeroa B	30	15.1	2744150	6422600	8
Matakana	30	16.5	2777300	6407350	6
Matakana	30	13.7	2776200	6406700	6
Matakana	30	14.6	2776220	6406690	6
Matakana	30	15.5	2779900	6498600	15
Dart River	20	10.0	2139900	5592700	440
Glen Glynk	20	15.3	2509900	5802400	560
Hawksburn	20	12.0	2212500	5551700	560
Karaka Pa	30	15.2	2599200	5994200	21
Lagoon flat	20	14.9	2548700	5844500	10
long Beach	20	12.0	2326900	5491400	4
Mapoutahi pa	20	10.6	2324400	5494300	16
Station Bay	20	18.6	2682900	6493300	25
Sunde	20	19.5	2679700	6492200	3
Omihi	20	17.0	2552700	5856500	5
Ototara	30	11.5	2344200	5559300	40
Papatowai	10	10.1	2239800	5399600	3
Ponui	20	21.1	2705300	6476200	2
Ponui	20	21.5	2705300	6475500	15
Ponui	20	18.3	2705300	6475500	15
Ponui	20	17.3	2706380	6476710	30
Rakaia	20	12.3	2449100	5701900	3
Redcliffs flats	20	13.8	2488500	5738700	3
South Bay	10	14.5	2566200	5864600	4
Tai Rua	20	11.8	2344000	5559900	5
Takahanga	30	13.8	2566200	5866800	4
Takamatua	20	17.2	2506400	5713600	3
Tiwai Point	30	10.0	2155996	5392997	27.69041096
Waihao	20	17.1	2365000	5602400	3
Wairau Bar	10	13.5	2598500	5966300	4
Waitaki	20	11.5	2362700	5581900	4

The results from this component of the survey are entirely as expected. The range in measured EHT's is 11.5 ^{0}C ranging from a maximum of 21.5[3] ^{0}C to a minimum of 10 ^{0}C. Unsurprisingly, EHT has to be estimated with a better precision than simply estimating an EHT for New Zealand. Further, as expected, there is no simple relationship between latitude, longitude, altitude and the measured EHT (e.g. Figure 10.4). If we apply a simple linear model that regresses measured EHT against the predictors of latitude, longitude and altitude a statistically significant relationship between latitude and EHT is returned (at $\alpha = 0.05$). However this model only explains around 63 % of the variation in EHT throughout the survey (Table 10.6). Use of this type of model will only provide EHT predictions to a precision of around $\pm$ 4 ^{0}C at 1σ (see Residual Statistics in Table 10.6), nowhere near the required estimation precision. As would be expected on the basis of the theory outlined earlier (Chapter 8) the relationships between meteorological variables, environmental conditions and the measured EHT will be more complex than a simple additive model of the type considered here.

While this component of the experimental survey program has allowed a quantification of the extent of temperature variation throughout New Zealand as a whole and acts as a basic control data set for EHT estimates in certain locations it does not give any real information regarding the nature, spatial scale and extent of micro-scale variation.

10.3.2 Micro-Scale Survey

The microscale component of the survey program was designed to identify the extent to which significant micro-scale variation in EHT might occur, and to provide a control data set with which it is possible to as-

[3] Thus as the maximum survey period is 370 days these results are all fall within the maximum monitoring envelope for these cells (Table 10.2)

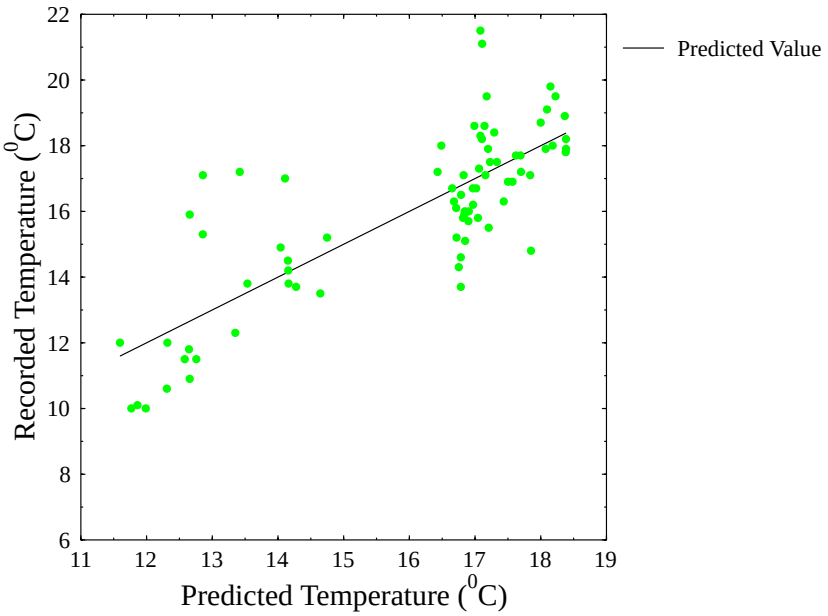

Figure 10.4: Relationship between predicted and measured data for the Macro-regional cell survey using a linear regression on latitude, longitude and altitude

Table 10.6: Model summary statistics for macroregional data model

Model Summary

Model	R	R Square	Adjusted R Square	Std. Error of the Estimate
1	.793	.629	.614	1.6115

a (Constant), ALT, LONG, LAT

b Dependent Variable: EHT

ANOVA

Model		Sum of Squares	df	Mean Square	F	Sig.
1	Regression	321.284	3	107.095	41.239	.000
	Residual	189.576	73	2.597		
	Total	510.859	76			

a Predictors: (Constant), ALT, LONG, LAT

b Dependent Variable: EHT

Coefficients

	Unstandardised Coefficients		Standardised Coefficients	t	Sig.
	B	Std. Error	Beta		
(Constant)	-14.417	3.405		-4.235	.000
ALT	2.119E-07	.000	.013	.131	.897
LAT	4.780E-06	.000	.766	8.013	.000
LONG	-1.773E-03	.002	-.069	-.917	.362

a Dependent Variable: EHT

Residual Statistics

N	77
Range	7.502122306
Minimum	-3.08332501
Maximum	4.418797296
Mean	1.39819E-15
Std. Deviation	1.57937298

sess EHT estimation protocols. This component of the survey is made up of two separate parts. In the first part micro-scale measurements were made at 20 of the macroscale survey locations (Figure 10.5). The intention of this was to establish the degree of Δ_{EHT} that may occur and establish how this might vary through the survey areas. The second part of the micro-scale survey program comprised 12 locations at which intensive micro-scale experiments were conducted (Figure 10.8). These experiments were designed to provide data with which it is possible to quantify the influence of different microscale variables, and which serve to act as controls for EHT estimation protocols.

Site Survey

Micro-scale Δ_{EHT} data were collected at 20 of the macro-scale locations (Table 10.5; Table 10.7). This data was collected to allow an assessment of the degree and significance of Δ_{EHT} within archaeological sites and to establish how this may vary through the survey areas. A summary of part of these results is reported in Jones *et al.* (1997*b*).

Table 10.7: Micro-regional site survey results

Location	Depth (cm)	EHT (^{0}C)	Easting (NZMG)	Northing (NZMG)	Altitude (m)
90 mile Beach	30	19.8	2413705	6707320	4
90 mile Beach	30	20.2	2413705	6707320	4
Clarence	20	14.3	2586400	5892100	10
Clarence	15	14.0	2586400	5892100	10
Clarence	20	14.0	2586400	5892100	10
Clarence	30	13.7	2586400	5892100	10
Dart	20	10.0	2139900	5592700	440
Dart	20	16.6	2139900	5592700	440
Haratua's Pa	10	17.9	2596500	6647285	120
Haratua's Pa	30	17.7	2596500	6647285	120
Haratua's Pa	30	17.7	2596500	6647285	120
Haratua's Pa	30	18.1	2596500	6647285	120
Haratua's Pa	30	17.9	2596500	6647285	120
Haratua's Pa	30	17.1	2596500	6647285	120
Haratua's Pa	30	15.5	2596500	6647285	120

continued on the next page

Table 10.7: *continued*

Location	Depth (cm)	EHT (^{0}C)	Easting (NZMG)	Northing (NZMG)	Altitude (m)
Haratua's Pa	30	17.4	2596500	6647285	120
Hawksburn	20	11.8	2212500	5551700	560
Hawksburn	20	10.5	2212500	5551700	560
Hawksburn	20	12.1	2212500	5551700	560
Hawksburn	20	12.0	2212500	5551700	560
Karaka Pa	30	15.2	2599200	5994200	21
Karaka Pa	20	14.7	2599200	5994200	21
long Beach	10	12.0	2326900	5491400	4
long Beach	20	11.5	2326900	5491400	4
long Beach	20	12.0	2326900	5491400	4
long Beach	20	12.3	2326900	5491400	4
Mapoutahi pa	10	10.8	2324400	5494300	16
Mapoutahi pa	20	10.6	2324400	5494300	16
Matakana	30	13.7	2776200	6406700	6
Matakana	30	14.6	2776220	6406690	6
Matakana	10	15.7	2779900	6498600	15
Matakana	30	15.5	2779900	6498600	15
Matakana	60	15.0	2779900	6498600	15
Matakana	30	15.7	2779900	6498600	15
Matakana	30	15.5	2779900	6498600	15
Matakana	30	13.3	2779900	6498600	15
Motutapu	20	18.6	2682900	6493300	25
Motutapu	20	18.4	2682900	6493300	25
Opito	10	17.6	2761760	6493995	6
Opito	30	17.9	2761760	6493995	6
Opito	60	17.1	2761760	6493995	6
Opito	30	15.4	2761760	6493785	6
Opito	30	14.9	2762210	6494145	80
Opito	30	15.3	2762210	6494145	80
Opito	30	14.9	2762210	6494145	80
Ototara	30	11.5	2344200	5559300	40
Ototara	20	11.6	2344200	5559300	40
Paeroa	30	16.3	2746950	6420700	10
Paeroa	30	15.9	2746953	6420700	10
Paeroa	10	17.0	2744150	6422600	8
Paeroa	30	15.1	2744150	6422600	8
Paeroa	60	15.2	2744150	6422600	8
Paeroa	30	13.9	2744180	6422350	8
Paeroa	30	14.2	2744050	6422415	8
Ponui	20	21.5	2705300	6475500	15
Ponui	20	21.1	2705300	6476200	2
Ponui	20	18.3	2705300	6475500	15
Rawara	30	19.5	2518075	6720450	8

continued on the next page

Table 10.7: *continued*

Location	Depth (cm)	EHT (^{0}C)	Easting (NZMG)	Northing (NZMG)	Altitude (m)
Rawara	30	18.0	2516800	6719555	30
Redcliffs	surface	14.4	2488400	5738800	5
Redcliffs	20	13.8	2488500	5738700	3
Shag Mouth	20	13.0	2339100	5522900	4
Shag Mouth	30	12.9	2339100	5522900	4
Shag Mouth	20	13.4	2339100	5522900	4
South Bay	10	14.5	2566200	5864600	4
South Bay	10	15.2	2566200	5864600	4
Tai Rua	20	10.5	2344000	5559900	5
Tai Rua	20	11.8	2344000	5559900	5
Tai Rua	10	11.6	2344000	5559900	5
Takahanga	20	14.6	2566200	5866800	4
Takahanga	30	13.8	2566200	5866800	4
Wairau Bar	10	13.5	2598500	5966300	4
Wairau Bar	10	13.4	2598500	5966300	4
Wairau Bar	10	13.8	2598500	5966300	4

On the basis of this data we can assess the implications of assuming that intra-site Δ_{EHT} is 0 ^{0}C (i.e. modelling EHT by each single value for a given site). One way of doing this is to model the EHT using a GLM with site location as a factor[4]. For the data set given in Table 10.7 this model provides a good fit, explaining around 94 % of the observed variance in EHT (Table 10.8; Figure 10.6). However if we look at the model residuals it is apparent that significant EHT estimation error will arise through this practice. Significant Δ_{EHT} occurs within the monitored sites, with an average Δ_{EHT} of 1 ^{0}C and a maximum of 3 ^{0}C for the locations within this survey (Table 10.9; Table 10.10). This observed Δ_{EHT} is a function of both true intra-site Δ_{EHT} and apparent Δ_{EHT} due to inherent variation in cell performance, and it is important to determine the extent to which the observed variation in intrasite EHT actually arises from microscale Δ_{EHT}. We can assess this by testing whether the observed variance in intrasite EHT is significantly different from the expected value of 0.36

[4]in the model used here Altitude and Northing are included as covariates. This still has the effect of predicting a single EHT for each location

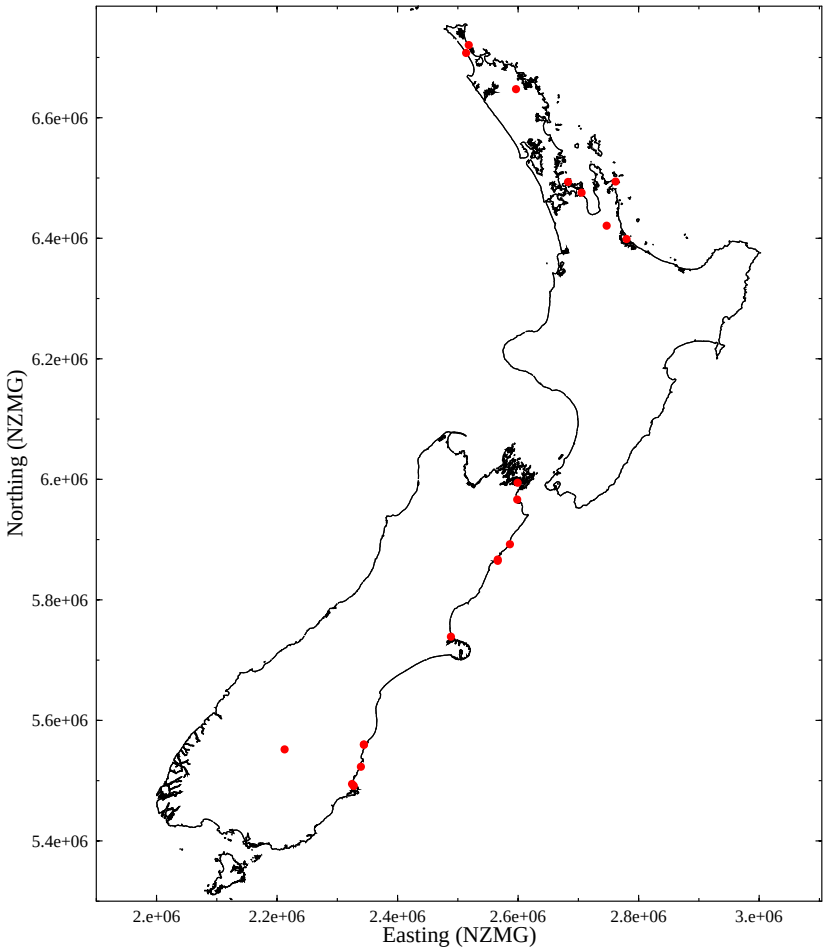

Figure 10.5: Relationship between predicted and measured data for the macro-regional cell survey

(§10.2.1) using the statistic

$$V = \frac{\sum(X_i - \bar{X})}{\sigma^2_{\text{cell}}} \tag{10.1}$$

tested against a $\chi^2_{1-\alpha}(n-1)$ distribution (Mood *et al.* 1974pp. 431). This tests the null hypothesis $\mathcal{H}_0 : \sigma^2_{diff} \leqslant \sigma^2_{\text{cell}}$ versus $\mathcal{H}_1 : \sigma^2_{diff} > \sigma^2_{\text{cell}}$. Values for V are given in Table 10.9 and five of these comparisons are significant at $\alpha = 0.05$.

Further there is a significant relationship between the observed range in Δ_{EHT} and the number of data points measured, with the magnitude of Δ_{EHT} tending to increase as the number of measurement points rise (Figure 10.7; Table 10.10). This indicates that greater intra-site Δ_{EHT} is becoming incorporated within the survey as the number of locations monitored at each site increase. This demonstrates that EHT measurements cannot be simply applied to adjacent non-monitored locations without the potential for significant error in EHT estimation. Thus we can conclude that significant real microscale Δ_{EHT} occurs on the basis of these data.

Interestingly, the observed magnitude in Δ_{EHT} is not significantly correlated with either the mean EHT nor latitude for the monitored locations. This indicates that the magnitude of Δ_{EHT} observed here is representative for the whole of New Zealand, and that Δ_{EHT} will need to be considered for any location for which OHD is to be performed. On the basis of this result it became apparent that further micro-scale analogue EHT controls would be valuable in order to assess the performance of EHT estimates.

Experimental Survey

As an extension to the micro-scale site survey described above a second set of experimental data was collected. In this survey intensive mi-

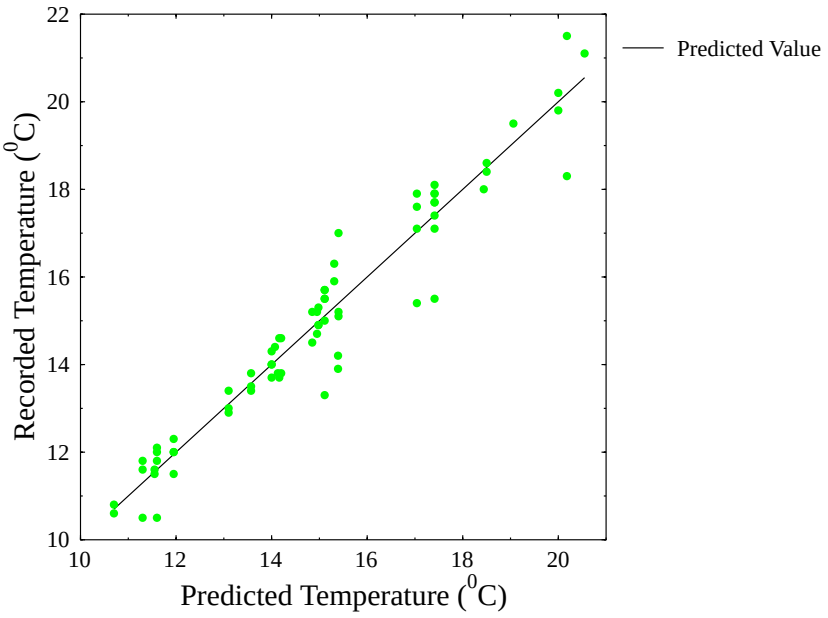

Figure 10.6: Relationship between predicted and measured data for the micro-regional site survey

Table 10.8: Anova for the no Δ_{EHT} model applied to the micro-scale site survey (§10.3.2)

Source	Type III Sum of Squares	df	Mean Square	F	Sig.	Eta Squared
Corrected Model	462.17	21	22.01	35.00	0	0.94
Intercept	1.38	1	1.38	2.20	0.14	0.04
LONG	2.17	1	2.169	3.45	0.07	0.06
ALT	7.63	1	7.63	12.14	0.00	0.20
LOCATION	116.67	19	6.14	9.76	0.00	0.79
Error	31.44	50	0.63			
Total	16669.62	72				
Corrected Total	493.61	71				

a R Squared = .936 (Adjusted R Squared = .910)

Table 10.9: Residual statistics for the no Δ_{EHT} model applied to the micro-scale site survey (§10.3.2)

LOCATION	Mean Temp	N	Residuals				V
			Minimum	Maximum	Range	Std. Deviation	
90 mile Beach	20	2	-0.2	0.2	0.4	0.28	0.33
Clarence	14	4	-0.3	0.3	0.6	0.24	0.72
Haratua's Pa	17.4	8	-1.91	0.69	2.6	0.83	20.08†
Hawksburn	11.6	4	-1.1	0.5	1.6	0.74	6.84
Karaka Pa	15	2	-0.25	0.25	0.5	0.35	0.51
long Beach	12	4	-0.45	0.35	0.8	0.33	1.36
Mapoutahi pa	10.7	2	-0.1	0.1	0.2	0.14	0.08
Matakana	14.9	8	-1.81	0.59	2.4	0.82	19.60†
Motutapu	18.5	2	-0.1	0.1	0.2	0.14	0.08
Opito	16.2	7	-1.64	0.86	2.5	0.8	15.99†
Ototara	11.6	2	-0.05	0.05	0.1	0.07	0.02
Paeroa	15.4	7	-1.49	1.6	3.1	1.13	31.91†
Ponui	20.3	3	-1.88	1.32	3.2	1.67	23.23†
Rawara	18.8	2	-0.44	0.44	0.87	0.62	1.60
Redcliffs	14.1	2	-0.33	0.33	0.65	0.46	0.88
Shag Mouth	13.1	3	-0.2	0.3	0.5	0.26	0.56
South Bay	14.9	2	-0.35	0.35	0.7	0.49	1.00
Tai Rua	11.3	3	-0.8	0.5	1.3	0.7	4.08
Takahanga	14.2	2	-0.4	0.4	0.8	0.57	1.35
Wairau Bar	13.6	3	-0.17	0.23	0.4	0.21	0.37

$^{\dagger}V$ significant at $\alpha = 0.05$

Table 10.10: Δ_{EHT} Range statistics for the micro-scale site survey (§10.3.2)

Δ_{EHT} Range Statistics

N	20
Range	3.1
Minimum	0.1
Maximum	3.2
Mean	1.171060959
Std. Deviation	1.01665503

Correlation between Δ_{EHT} Range and Mean EHT

	Correlation Coefficient	Sig. (2-tailed)	N
Kendall's tau$_b$	0.540	0.002	20
Spearman's rho	0.676	0.001	20
Pearson Correlation	0.773	0.000	20

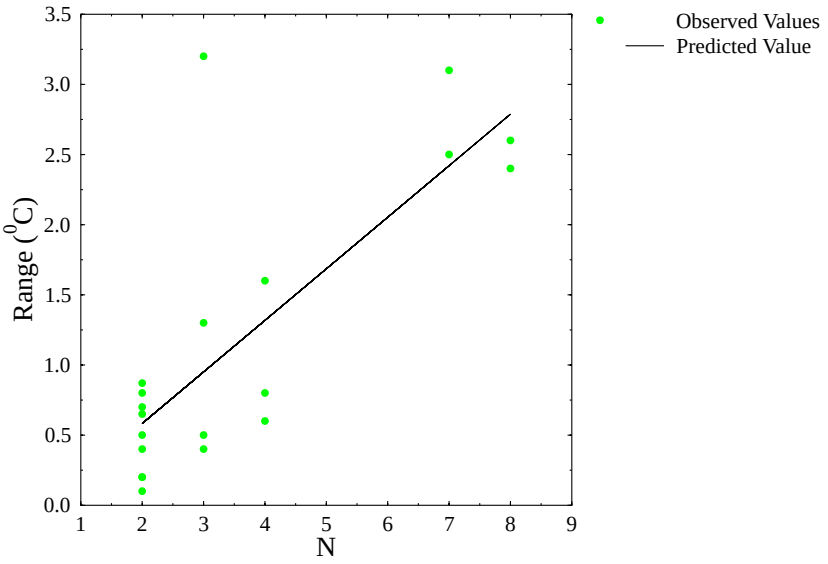

Figure 10.7: Relationship between Δ_{EHT} range and number of measured data for the micro-regional site survey

croscale monitoring of EHT was conducted at 12 locations (Figure 10.8). The intention of this programme was to provide a set of data for which precise topographic, locational, surface cover and soil conductivity data were available. Thus this data set allows an exploration of how well microscale Δ_{EHT} can be modelled via the type of simulation approaches described later (Chapter 9) and acts as a control allowing quantification of accuracy and precision for both EHT and Δ_{EHT} estimates. These results are considered in more detail in the following chapter where these data are used as controls for microscale EHT estimates (Chapter 11).

Table 10.11: Micro-regional experimental survey results

Location	Depth (cm)	Surface Description	matrix	Temperature (^{0}C)	Easting (NZMG)	Northing (NZMG)	Altitude (m)
Bethells	10	bare sand	sand	20.11	2639450	6477800	6
Bethells	20	bare sand	sand	19.62	2639450	6477800	6
Bethells	30	bare sand	sand	17.39	2639450	6477800	6
Bethells	20	bare sand	sand	19.45	2639450	6477800	6

continued on the next page

Table 10.11: *continued*

Location	Depth (cm)	Surface Description	matrix	Temperature (^{0}C)	Easting (NZMG)	Northing (NZMG)	Altitude (m)
Bethells	20	bare sand	sand	19.80	2639450	6477800	6
Bethells	20	bare sand	sand	19.24	2639450	6477800	6
Bethells	20	bare sand	sand	19.14	2639450	6477800	6
Hot Water Beach	10	bare sand	sand	20.15	2654617	6482471	25
Hot Water Beach	20	bare sand	sand	19.40	2654617	6482471	25
Hot Water Beach	30	bare sand	sand	17.02	2654617	6482471	25
Hot Water Beach	40	bare sand	sand	19.23	2654617	6482471	25
Hot Water Beach	30	bare sand	sand	19.07	2654617	6482471	25
Hot Water Beach	30	bare sand	sand	19.09	2654617	6482471	25
Hot Water Beach	30	bare sand	sand	19.51	2654617	6482471	25
Hot Water Beach	30	bare sand	sand	19.10	2654617	6482471	25
Leigh	10	short grass	soil	17.83	2672286	6546830	24
Leigh	20	short grass	soil	17.03	2672286	6546830	24
Leigh	40	short grass	soil	17.14	2672286	6546830	24
Leigh	30	short grass	soil	20.20	2672286	6546830	24
Pakiri	10	sand	sand	17.97	2665350	6549580	6
Pakiri	20	sand	sand	17.40	2665350	6549580	6
Pakiri	30	sand	sand	17.01	2665350	6549580	6
Pakiri	10	sand	sand	15.74	2665350	6549580	6
Pakiri	20	sand	sand	15.31	2665350	6549580	6
Pakiri	30	sand	sand	15.55	2665350	6549580	6
Pakiri	10	sand	sand	16.46	2665350	6549580	6
Pakiri	20	sand	sand	15.82	2665350	6549580	6
Pakiri	30	sand	sand	15.84	2665350	6549580	6
Pakiri	10	sand	sand	17.32	2665350	6549580	6
Pakiri	20	sand	sand	16.77	2665350	6549580	6
Pakiri	30	sand	sand	16.90	2665350	6549580	6
Pakiri	10	sand	sand	17.20	2665350	6549580	6
Pakiri	20	sand	sand	16.75	2665350	6549580	6
Pakiri	30	sand	sand	16.28	2665350	6549580	6
pukekohe	10	bare ground	soil	18.03	2674563	6443219	12
pukekohe	20	short grass	soil	17.28	2674563	6443219	12
pukekohe	30	short grass	soil	17.44	2674563	6443219	12
pukekohe	40	short grass	soil	17.33	2674563	6443219	12
Tapharanui	10	sand	sand	18.24	2675620	6535000	11
Tapharanui	20	sand	sand	13.43	2675620	6535000	11
Tapharanui	30	sand	sand	17.62	2675620	6535000	11
Tapharanui	40	sand	sand	17.20	2675620	6535000	11
Tapharanui	30	sand	sand	17.73	2675620	6535000	11
Tapharanui	30	short grass	sandy soil	16.86	2675620	6535000	11
Tapharanui	10	short grass	sandy soil	17.84	2675620	6535000	11
Tapharanui	20	short grass	sandy soil	17.06	2675620	6535000	11
Tapharanui	30	short grass	sandy soil	16.89	2675620	6535000	11

continued on the next page

Table 10.11: *continued*

Location	Depth (cm)	Surface Description	matrix	Temperature (^{0}C)	Easting (NZMG)	Northing (NZMG)	Altitude (m)
Tapharanui	30	short grass	sandy soil	17.17	2675620	6535000	11
Tramvalley road	20	short grass	compost	16.59	2650200	6479900	50
Tramvalley road	20	short grass	iron sand	16.17	2650200	6479900	50
Tramvalley road	20	short grass	clay soil	16.28	2650200	6479900	50
Tramvalley road	20	short grass	silica sand	16.50	2650200	6479900	50
Tramvalley road	20	short grass	shell	15.88	2650200	6479900	50

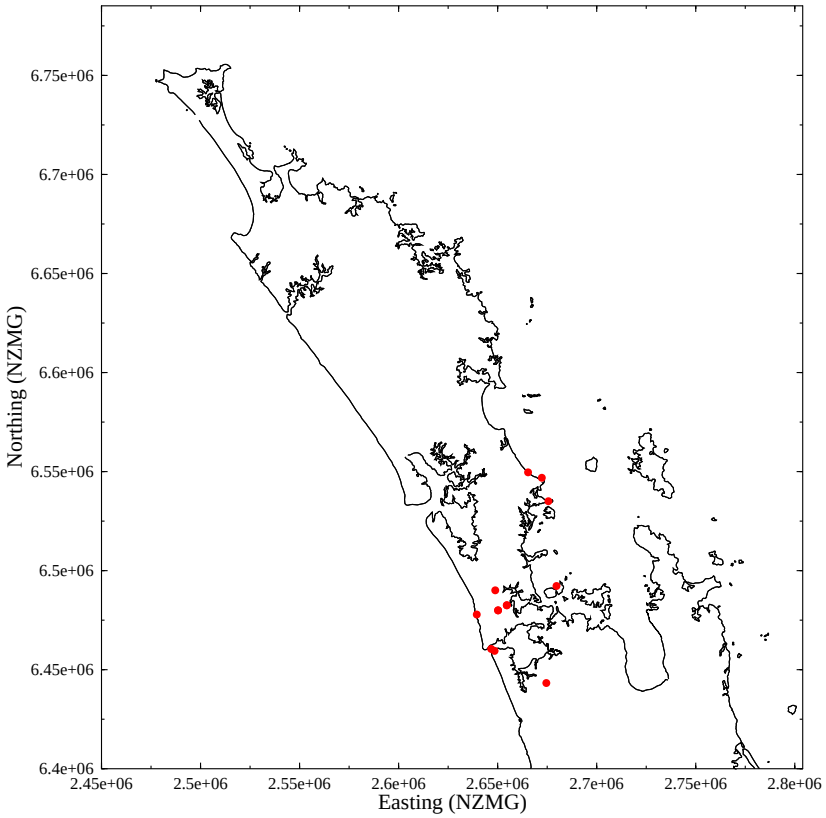

Figure 10.8: Locations of the microexperimental sites

10.3.3 Meteorological Data Controls

As long term meteorological data will be used as a basis for actual EHT estimates (*supra vide*:§11) 9 of monitoring locations were at meteorological stations (Table 10.3.3; Figure 10.9). These data provide controls for specific meteorological data sets and will allow an assessment of how precisely meteorological data can be used to model Δ_{EHT} and EHT (*supra vide*:§11). The meteorological data for the period of the cell surveys has been obtained for each location and this is used in the following chapter as part of an assessment of meteorological models for EHT estimation.

Table 10.12: Location of the meteorological cell sites

Location	Map	Easting	Northing	Altitude
Kaitia	O04	2534726.17	6674248.49	12.76
Dargaville	P07	2585776.57	6583387.72	55.04
Cape Reinga	M02	2480465.31	6754054.04	14.52
Henderson	R11	2654616.72	6482471.05	25.35
kumeu met	Q11	2648777.61	6490016.36	11.84
Leigh	R07	2672286.27	6546829.84	31.44
Manukau	Q12	2646725.73	6460417.47	62.21
pukekohe	R12	2674562.92	6443219.32	11.92
Tiwai Point	E47	2155996	5392997	27.69

10.4 Humidity Cell Survey

The significance of soil humidity (rH) to OHD is not clear (*supra vide*:§4.7). However this variable may influence OHD and it is important to develop some understanding about how archaeological soil humidity may vary. In the first instance it is useful to assess the magnitude of variation in soil humidity regimes and establish to what extent deviation from an

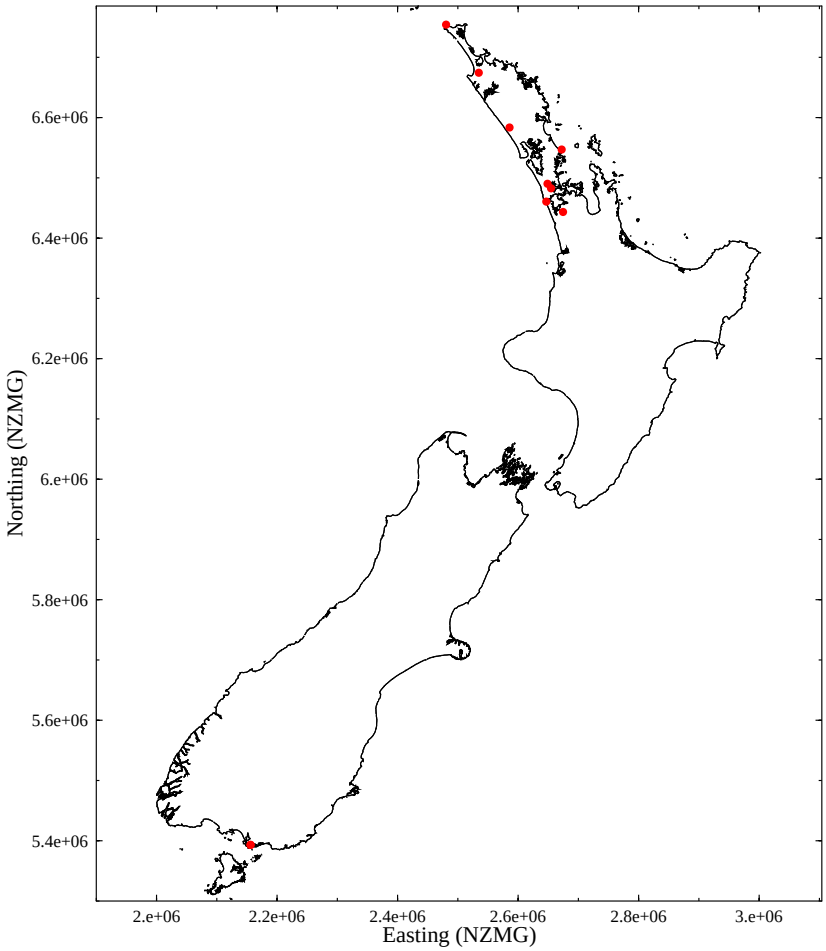

Figure 10.9: Locations of the meteorological monitoring sites

effective rH of 100% may occur. It may well be the case that short term fluctuations in rH are insignificant as the hydration reaction is slow. For example, hydration in an environment that periodically attains an rH of 100% may proceed identically to that in an environment that is constantly at an rH of 100 %. In light of this it is useful to talk in terms of effective relative humidity (ERH) which quantifies a constant ambient humidity at which an identical hydration rate to that observed in the archaeological sample occurs. In order to explore this issue, humidity surveys were conducted as part of the experimental soil climate surveys described in above. As outlined previously it is possible to make use of zeolite cells to identify locations where the ERH falls below 100% (§10.2.2).

The ERH survey comprised two general components. In an initial exercise ERH measurement experiments were conducted at 12 locations in the general Auckland area (§10.4.1; Figure 10.10; Table 10.13; Figure 10.13; Table 10.15). The intention of this exercise was to identify whether ERH deviated from 100 % in the monitored locations, and under what conditions. The second component of the ERH survey was to monitor ERH at 9 locations throughout the broader survey region to test the conclusions drawn through the initial experimental program (§10.4.2; Table 10.20). Thus the second component acts as a field trial of the experimental conclusions drawn in the first component of the survey.

In the following section data analyses of the ERH monitoring program are conducted following a simple model. If the ERH is 100 % the measured EHT for each cell in the humidity pair will be the same (within the limits of measurement precision). The identification of deviation from 100 % ERH is simple. If a linear regression is carried out using the EHT for the cell in a water jacket (Variable Jartemp) as a predictor for the EHT measured by the soil cell (Variable Celltemp) the coefficient should equal 1 and the intercept should not be significant. If the regression co-

efficient for Jartemp is significantly different from 1 or the intercept is significant then we can reject the null-hypothesis that ERH = 100 %. This simple test is applied to all of the following data.

As the measured EHT is a value calculated according to cell weight gain it may seem more sensible to use cell weight gain as the comparative variable. However the absorbtion characteristics of each cell may vary slightly, and the absolute hydration time will vary between the different humidity pairs. The measured EHT represents a normalised value that takes into account total hydration time and variation in cell absorbtion characteristics. Thus the measured EHT is the most appropriate comparative variable.

10.4.1 Experimental Survey

On the basis of theory outlined previously it would be expected that for most vegetated soils the ERH will be close to 100 % (§8.6), however the situation for surface samples is less clear. Thus in the experimental ERH monitoring program a distinction was drawn between surface and subsurface locations, as it would be expected that a difference in ERH may occur between these. The results of the surface and subsurface monitoring program will allow some assessment of the conditions under which it is appropriate to assume that ERH is 100 %.

Surface Humidity

The surface ERH survey consists of five humidity cell comparisons made inside standard meteorological screens at four locations and 12 comparisons on the soil surface under differing vegetation conditions (Figure 10.10; Table 10.13). The regression of Celltemp on Jartemp shows that the ERH is significantly different from 100 % for these data, this

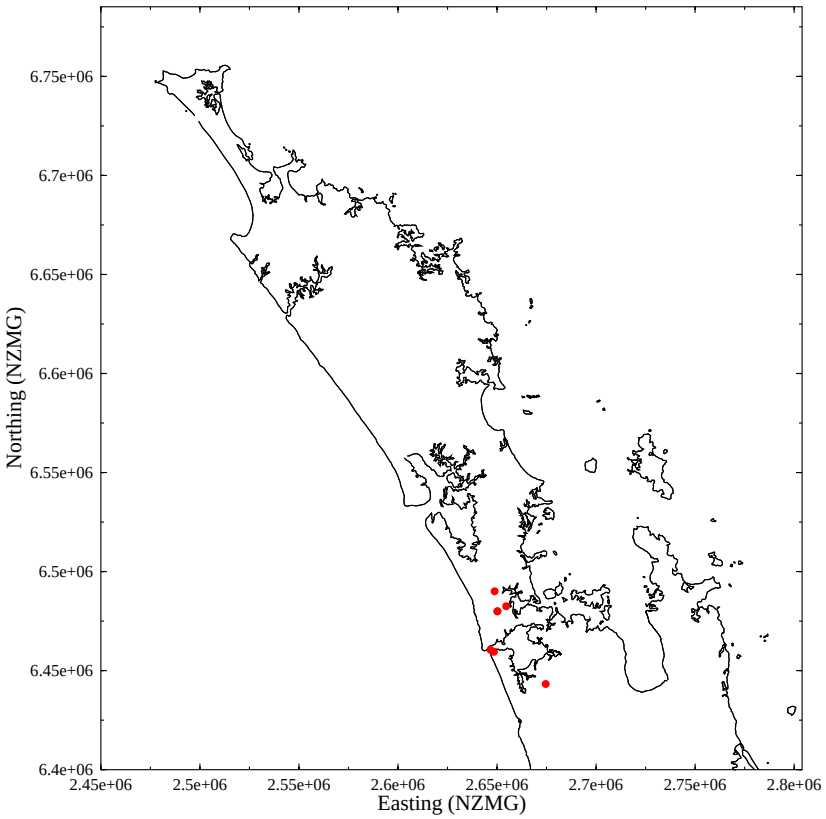

Figure 10.10: Locations of the surface humidity monitoring sites

is immediately apparent from Figure 10.11. However, as shown in Figure 10.11, the comparisons from vegetated surfaces do appear to indicate a 100 % ERH environment.

Table 10.13: Auckland region humidity survey: surface results

Location	Depth	surface	matrix	JarTemp	celltemp	tdiff
Henderson	in screen	short grass	brown organic soil	18.09	13.46	-4.64
kumeu met	in screen	0	brown organic soil	17.61	13.22	-4.39
kumeu met	in screen	0	brown organic soil	17.40	13.19	-4.21
kumeu met	surface	vshort grass	brown organic soil	21.66	21.07	-0.59
kumeu met	surface	vshort grass	brown organic soil	21.44	20.90	-0.54
Manuakau 2	surface	bracken	light brown sandy soil	15.58	14.90	-0.68
Manukau	in screen	0	light brown sandy soil	16.87	13.84	-3.03
pukekohe	in screen	0	brown organic soil	17.36	12.85	-4.51
pukekohe	surface	bare ground	brown organic soil	19.12	13.18	-5.94
tvr	surface	bare soil	brown clay and organics	25.15	15.97	-9.18
tvr	surface	short grass	brown clay and organics	19.16	18.98	-0.20
tvr	surface	short grass	brown clay and organics	18.57	18.40	-0.17
tvr	surface	long grass	brown clay and organics	16.45	16.32	-0.13
tvr	surface	short grass	brown clay and organics	19.16	19.03	-0.13
tvr	surface	long grass	brown clay and organics	16.24	16.32	0.08
tvr	surface	long grass	brown clay and organics	16.31	16.45	0.13
tvr	surface	bare soil	brown clay and organics	17.94	15.57	-2.37

If a subset of the surface data corresponding to vegetated surface conditions is analysed the results indicate that these locations may correspond to a condition of 100 % ERH (Figure 10.12; Table 10.4.1). While there is no reason to adopt a null-hypothesis that the ERH will be 100 % in this case we cannot reject the possibility that the surface ERH was 100 % for the locations monitored.

Table 10.14: Regression coefficients for surface humidity pairs

Coefficients

Unstandardised Coefficients		Standardised Coefficients	t	Sig.	
	B	Std. Error	Beta		
(Constant)	.795	.801		.993	.354
JARTEMP	.943	.043	.993	21.688	.000

a Dependent Variable: CELLTEMP

This experiment shows that ERH in the air and on bare surfaces can fall

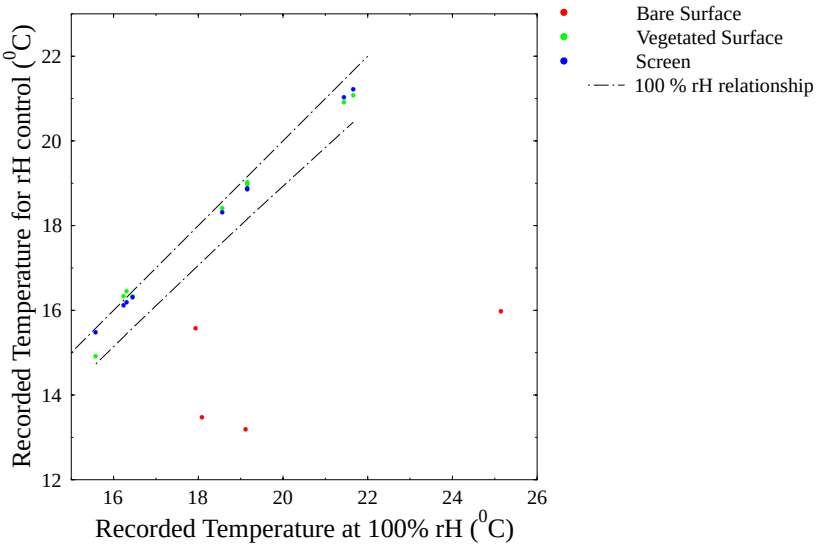

Figure 10.11: Humidity cell data for the surface monitoring experiments

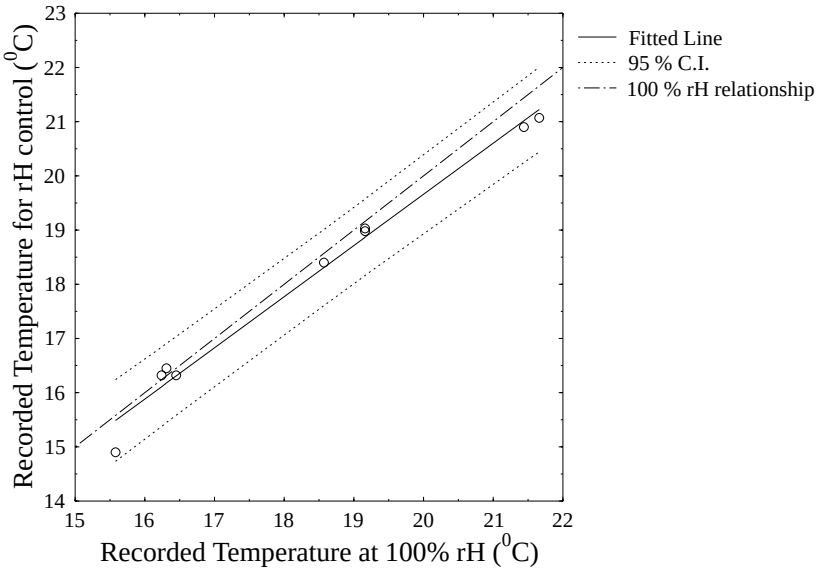

Figure 10.12: Humidity cell data for vegetated surfaces only

well below 100 %. This is both under the condition where the cell is only exposed to the air such as in the meteorological screens and under conditions of periodic wetting.

In contrast surface ERH measurements made for vegetated surfaces indicates that the ERH may be close to 100 %. The grass cover surface comparative measurements were made in very close proximity ($< 5m$) to the bare surface comparisons. Thus it is valid to make the observation that the humidity cell differences are of a significantly smaller magnitude under both short and long grass cover than on bare soil. This suggests that ERH will be higher for vegetated surfaces than for bare surfaces.

The results from this set of measurements suggest that soil surface ERH falls below 100 % in many conditions. It is apparent that the ERH is influenced by the nature of vegetative cover, with some degree of vegetative cover tending to raise ERH in comparison to bare surfaces. It is possible that in some environments ERH may reach 100 % under certain vegetative covers.

Subsurface ERH

Subsurface ERH was examined at ten locations, and in total 63 comparisons have been made at depths ranging from 10 to 40 cm (Table 10.15; Figure 10.13).

Table 10.15: Auckland region humidity survey: sub-surface results

Location	Depth (cm)	surface	matrix	JarTemp (^{0}C)	celltemp (^{0}C)	tdiff (^{0}C)
beth	20	bare sand	sand	19.45	19.55	0.10
beth	20	bare sand	sand	19.14	18.42	-0.72
beth	20	bare sand	sand	19.24	19.18	-0.06
beth	20	bare sand	sand	19.62	19.75	0.13
beth	20	bare sand	sand	19.80	19.14	-0.65
beth	30	bare sand	sand	17.39	17.94	0.54
hwb	10	bare sand	sand	20.15	23.14	2.99

continued on the next page

Table 10.15: *continued*

Location	Depth (cm)	surface	matrix	JarTemp (^{0}C)	celltemp (^{0}C)	tdiff (^{0}C)
hwb	20	bare sand	sand	19.40	19.57	0.17
hwb	30	short shrub	sand	15.90	15.74	-0.16
hwb	30	bare sand	sand	17.02	11.47	-5.55
hwb	30	bare sand	sand	19.07	18.99	-0.08
hwb	30	bare sand	sand	19.09	18.68	-0.40
hwb	30	bare sand	sand	19.10	18.55	-0.55
hwb	30	bare sand	sand	19.51	18.97	-0.54
hwb	30	bare sand	sand	18.60	13.86	-4.74
hwb	40	bare sand	sand	19.23	19.17	-0.06
kumeu met	10	short grass	brown organic soil	21.11	25.51	4.40
kumeu met	20	short grass	brown organic soil	21.00	21.73	0.74
kumeu met	30	short grass	brown organic soil	20.48	21.71	1.23
kumeu met	40	short grass	brown organic soil	20.15	20.76	0.61
Leigh	20	short grass	brown organic soil	17.83	16.51	-1.33
Leigh	30	short grass	brown organic soil	20.20	18.71	-1.49
Leigh	40	short grass	brown organic soil	17.14	17.26	0.12
Manuakau 2	10	short grass	light brown sandy soil	17.80	17.87	0.07
Manuakau 2	20	short grass	light brown sandy soil	19.10	17.77	-1.33
mh	10	short grass	rich volcanic soil	16.53	16.65	0.12
mh	10	short grass	rich volcanic soil	16.01	16.18	0.18
mh	10	short grass	rich volcanic soil	16.98	17.25	0.27
mh	10	short grass	rich volcanic soil	14.74	15.57	0.83
mh	20	short grass	rich volcanic soil	16.62	16.45	-0.17
mh	20	short grass	rich volcanic soil	17.10	16.96	-0.14
mh	20	short grass	rich volcanic soil	15.93	16.99	1.06
mh	20	short grass	rich volcanic soil	14.68	15.99	1.31

continued on the next page

Table 10.15: *continued*

Location	Depth (cm)	surface	matrix	JarTemp (^{0}C)	celltemp (^{0}C)	tdiff (^{0}C)
pak	10	sand	sand	15.74	14.09	-1.65
pak	10	sand	sand	17.32	16.84	-0.48
pak	10	sand	sand	17.20	16.75	-0.45
pak	10	sand	sand	16.46	16.10	-0.36
pak	10	sand	sand	17.97	18.17	0.21
pak	20	sand	sand	17.40	16.75	-0.65
pak	20	sand	sand	16.75	16.59	-0.16
pak	20	sand	sand	15.31	15.23	-0.08
pak	20	sand	sand	15.82	16.01	0.19
pak	20	sand	sand	16.77	17.87	1.11
pak	30	sand	sand	15.55	15.33	-0.22
pak	30	sand	sand	15.84	15.84	0.00
pak	30	sand	sand	16.28	16.29	0.02
pak	30	sand	sand	16.90	16.94	0.04
pak	30	sand	sand	17.01	17.66	0.65
pukekohe	20	short grass	brown organic soil	17.28	20.04	2.76
pukekohe	30	short grass	brown organic soil	17.44	16.20	-1.24
taph	10	short grass	sandy soil	17.84	17.21	-0.63
taph	10	sand	sand	18.24	17.99	-0.25
taph	20	short grass	sandy soil	17.06	17.70	0.64
taph	30	short grass	sandy soil	16.86	15.60	-1.25
taph	30	short grass	sandy soil	17.17	17.28	0.11
taph	30	sand	sand	17.73	17.95	0.22
taph	40	sand	sand	17.20	17.50	0.30
tvr	20	short grass	clay organic soil	16.28	16.06	-0.22
tvr	20	short grass	silica sand	16.50	16.56	0.06
tvr	20	short grass	compost	16.59	16.85	0.27
tvr	20	short grass	iron sand	16.17	16.97	0.80
tvr	20	short grass	shell	15.88	17.35	1.47

Analysis of this data indicates that the results are consistent with hydration at 100 % ERH. However five outliers are identified are should be removed from the analysis. The outliers are indicated in Figure 10.14 and were identified on the basis of the outlier statistics presented in Table 10.16. With these outliers removed a regression of Jartemp on Celltemp indicates that the measured results are entirely consistent with an ERH of 100 % in the locations monitored (Figure 10.15; Table 10.4.1). The

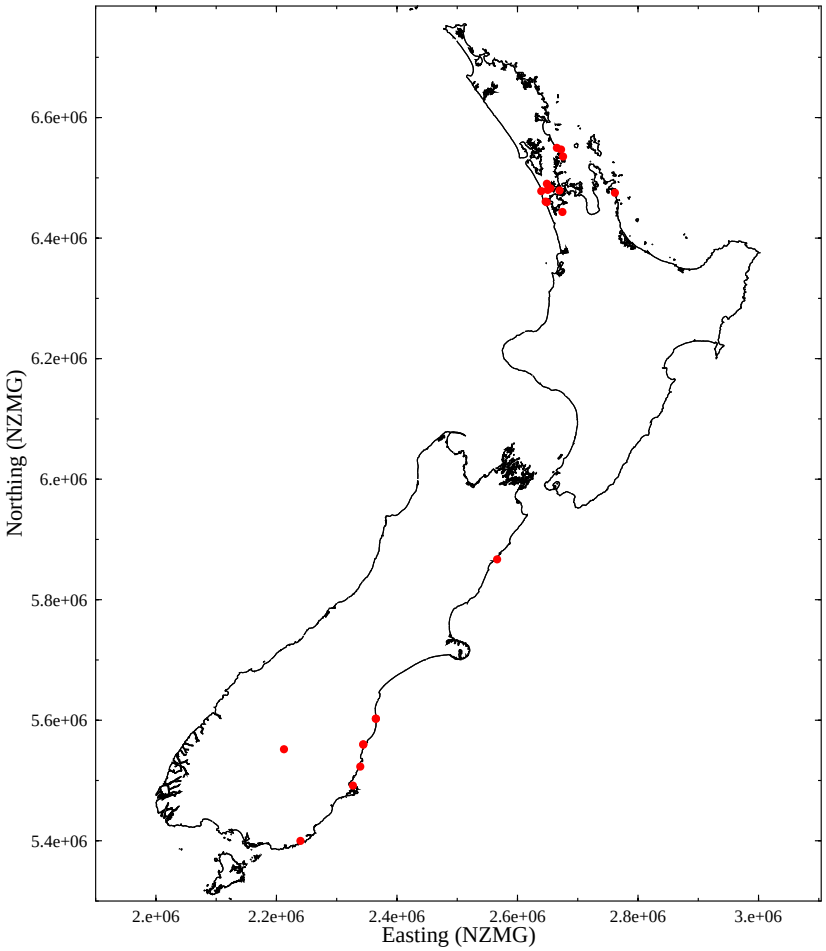

Figure 10.13: subsurface humidity monitoring sites

coefficient for Celltemp is not significantly different from 1 at $\alpha = 0.05$ and the intercept is not significant at $\alpha = 0.05$. Analysis of the residuals from this regression shows no problems with the applied model. There is no apparent structure in the Plot of Residuals versus Predicted values (Figure 10.16) and a one-sample Kolmogorov-Smirnov test does not reject the idea that the residuals are normally distributed (Table 10.18).

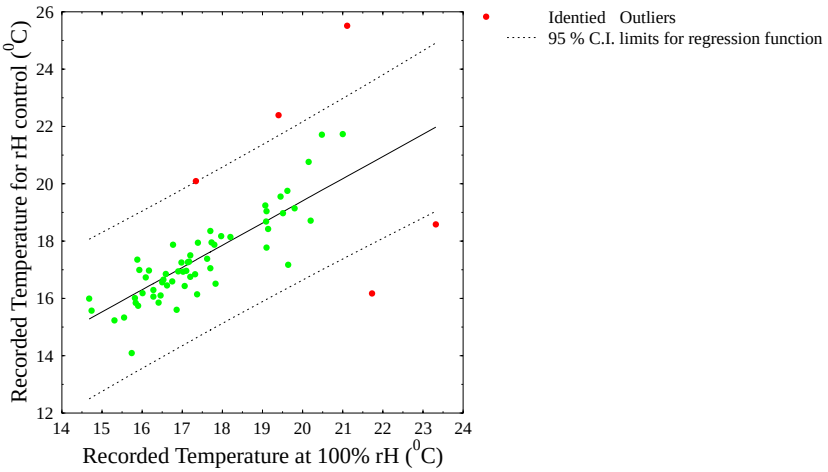

Figure 10.14: Humidity cell data for the surface monitoring experiments

This result appears to be independent of factors such as the presence or absence of surface vegetation or burial depth. This can be seen by conducting a univariate GLM where Celltemp is predicted on the basis of Jartemp and Depth as covariates and surface vegetation type as a factor[5]. In this analysis all variables except for Jartemp are not significant (Table 10.19), and this is graphically illustrated in Figures 10.17–10.19. Thus we would conclude that subsurface ERH does not significantly deviate from an ERH of 100 % in the monitored locations independent of burial depth and surface vegetation characteristics.

[5] factor levels being unvegetated and vegetated

Table 10.16: Statistics to identify outliers in humidity cell EHT differences (Tdiff)

	Percentiles						
	5	10	25	50	75	90	95
Weighted Average	-2.31	-1.33	-0.48	0.02	0.30	1.18	2.50
Tukey's Hinges			-0.46	0.02	0.29		

		Value
Highest	1	4.402167775
	2	2.988238171
	3	2.755446908
	4	1.471563864
	5	1.314549309
Lowest	1	-5.554349742
	2	-4.739252526
	3	-2.470084048
	4	-1.649309937
	5	-1.490658694

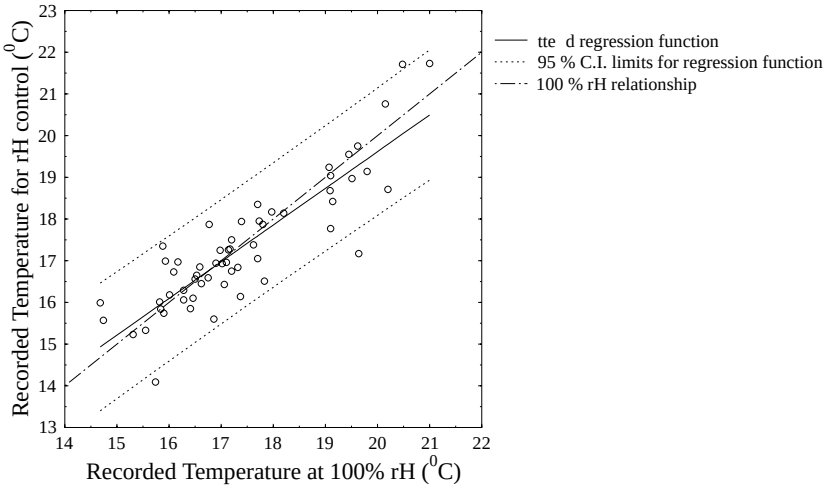

Figure 10.15: Humidity cell data for the subsurface monitoring experiments

Table 10.17: Model summary statistics for subsurface experimental humidity data analysis

Model Summary

Model	R	R Square	Adjusted R Square	Std. Error of the Estimate
1	.876	.767	.763	.7376

a Predictors: (Constant), JARTEMP

b Dependent Variable: CELLTEMP

ANOVA

Model		Sum of Squares	df	Mean Square	F	Sig.
1	Regression	100.326	1	100.326	184.412	.000
	Residual	30.466	56	.544		
	Total	130.791	57			

a Predictors: (Constant), JARTEMP

b Dependent Variable: CELLTEMP

Coefficients

Model		Unstandardised Coefficients		Standardised Coefficients	t	Sig.
		B	Std. Error	Beta		
1	(Constant)	2.015	1.132		1.780	.080
	JARTEMP	.880	.065	.876	13.580	.000

a Dependent Variable: CELLTEMP

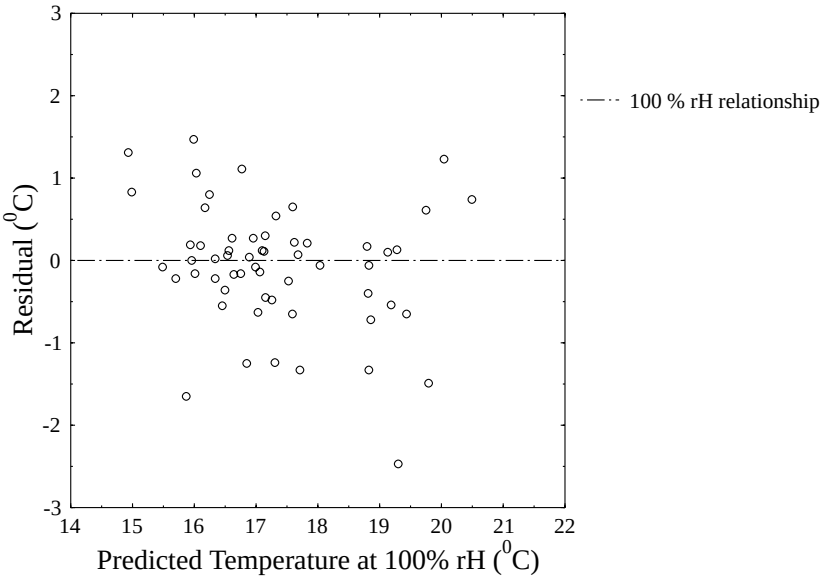

Figure 10.16: Residuals vs predicted values for the model fitted to the subsurface humidity data

Table 10.18: One-Sample Kolmogorov-Smirnov Test statistics for the normality of the subsurface model residuals

		TDIFF
N		58
Normal Parameters	Mean	-0.072953545
	Std. Deviation	0.753132701
Most Extreme Differences	Absolute	0.114651866
	Positive	0.10144674
	Negative	-0.114651866
Kolmogorov-Smirnov Z		0.873162627
Asymp. Sig. (2-tailed)		0.430831611

a Test distribution is Normal.
b Calculated from data.

Table 10.19: Summary effects for GLM of subsurface Celltemp predicted by Jartemp, Burial depth and Surface vegetation type

Tests of Between-Subjects Effects

Dependent Variable: CELLTEMP

Source		Type III Sum of Squares	df	Mean Square	F	Sig.
Intercept	Hypothesis	1.41	1	1.41	2.55	0.12
	Error	30.27	55	0.55		
JARTEMP	Hypothesis	92.78	1	93	167.35	0
	Error	29.94	54	0.55		
DEPTH	Hypothesis	0.00	1	0.00	0.00	0.97
	Error	29.94	54	0.55		
VEG	Hypothesis	0.53	1	0.53	0.95	0.33
	Error	29.94	54	0.55		

a 7.303E-03 MS(VEG) + .993 MS(Error)
b MS(Error)

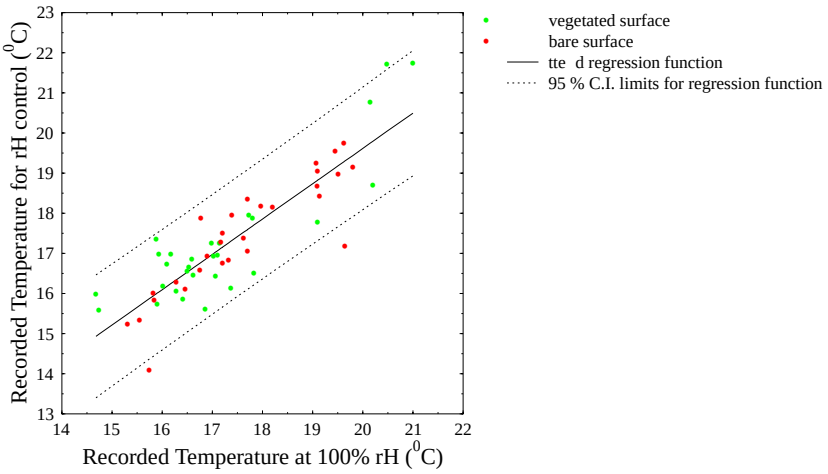

Figure 10.17: Humidity cell data for the subsurface monitoring experiments, coded by surface vegetation cover

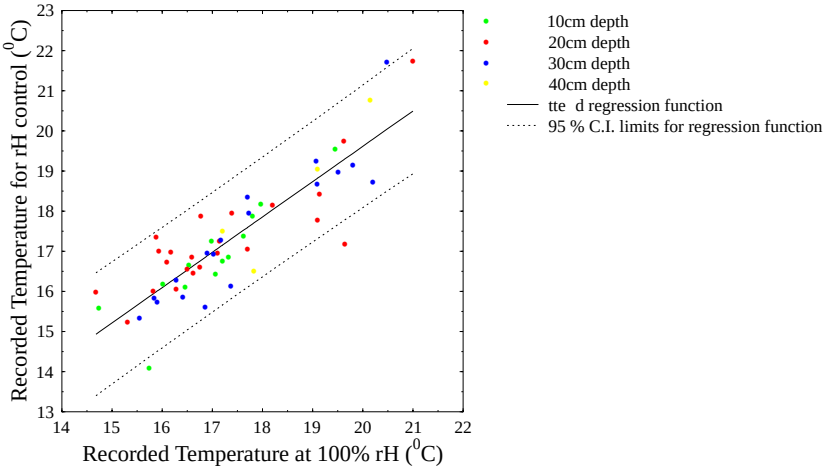

Figure 10.18: Humidity cell data for the subsurface monitoring experiments, coded by depth

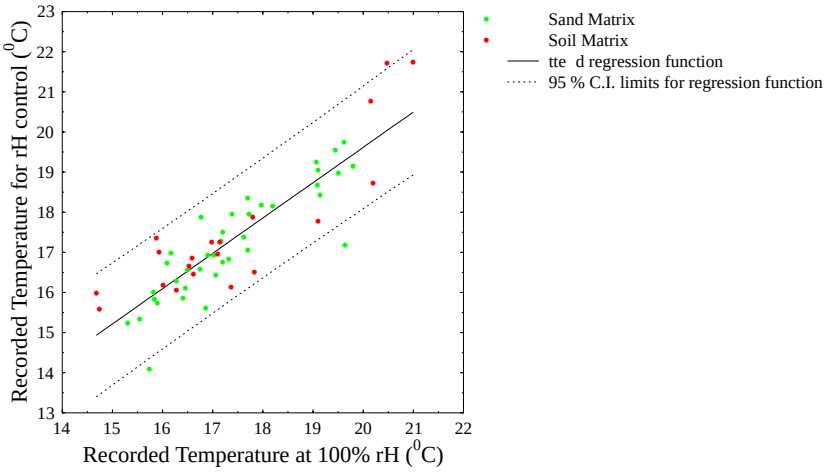

Figure 10.19: Humidity cell data for the subsurface monitoring experiments, coded by matrix type

In summary, the results of these experimental humidity comparisons suggest that

1. Surface ERH tends to vary significantly, and in general falls below 100 %.
2. Subsurface ERH tends to be constant at 100 %.

While these results will require further checks the broad conclusion is that ERH can be largely ignored as a significant variable for samples that have experienced a subsurface storage history. In the following section the results of a field trial of this conclusion are presented.

10.4.2 Site Survey

As a test of the results derived from the experimental humidity program presented in the preceding section 15 ERH comparisons were made at 9 archaeological sites (Table 10.20). Again outliers are identified in this data set (Figure 10.20; Table 10.21), and when three clear outliers are removed the remaining 12 data points are entirely consistent with an ERH of 100 %. A linear regression of Celltemp vs Jartemp returns a coefficient for Jartemp that is not significantly different from 1 at α = 0.05 and the intercept is not significant (Figure 10.21; Table 10.22) . Thus we cannot reject that null hypothesis that Celltemp = Jartemp.

The residuals from this model do not indicate any problems with model fit. There is no apparent structure in the Plot of Residuals versus Predicted values and a one-sample Kolmogorov-Smirnov test does not reject the idea that the residuals are normally distributed (Table 10.4.2). Thus the site survey data supports the conclusions drawn from the subsurface ERH monitoring experiments, and on the basis of the data presented here it can be concluded that subsurface ERH is unlikely to significantly deviate from 100 % in New Zealand.

Table 10.20: Auckland region humidity survey: surface results

Location	Depth	surface	JarTemp	celltemp	tdiff
Hawksburn	20	short grass	10.50	10.20	-0.31
Hawksburn	20	short grass	12.05	11.59	-0.46
long Beach	20	short grass	12.05	11.92	-0.13
long Beach	20	short grass	12.35	12.83	0.48
Ototara	20	short grass	11.64	11.75	0.11
Ototara	30	short grass	11.47	11.29	-0.18
Papatowai	10	sand	13.092	9.18	-3.91
Papatowai	10	sand	10.14	13.88	3.74
Shag Mouth	20	sand	13.42	12.88	-0.54
Shag Mouth	30	sand	12.90	12.83	-0.07
Tai Rua	10	short grass	11.64	11.19	-0.45
Takahanga	20	short grass	14.64	13.87	-0.78
Takahanga	30	short grass	13.84	13.82	-0.02
Takamatua	20	short grass	17.17	16.98	-0.18
Waihao	20	short grass	17.08	13.52	-3.56

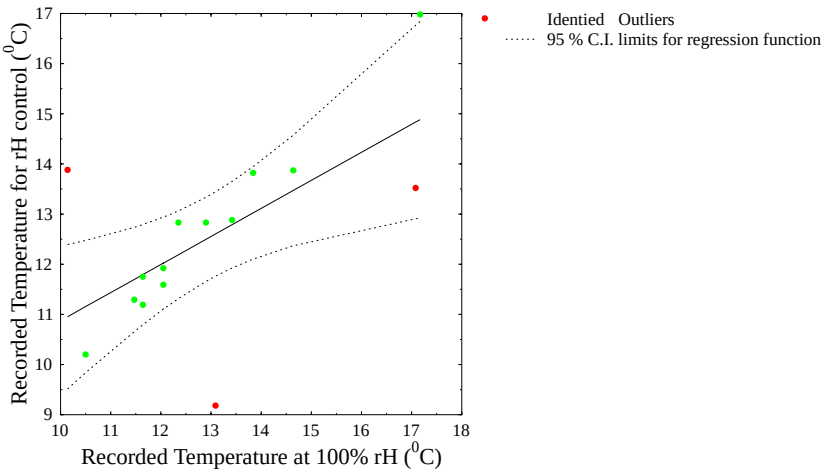

Figure 10.20: Humidity cell data for the surface monitoring experiments

Table 10.21: Outlier statistics for the humidity site survey results

		Percentiles						
		5	10	25	50	75	90	95
Weighted Average(Definition 1)	TDIFF	-3.9134	-3.7041	-.5431	-.1821	-1.7869E-02	1.7843	.
Tukey's Hinges	TDIFF			-.5016	-.1821	-4.4449E-02		

		Value
Highest	1	3.74
	2	.48
	3	.11
	4	-.02
	5	-.07
Lowest	1	-3.91
	2	-3.56
	3	-.78
	4	-.54
	5	-.46

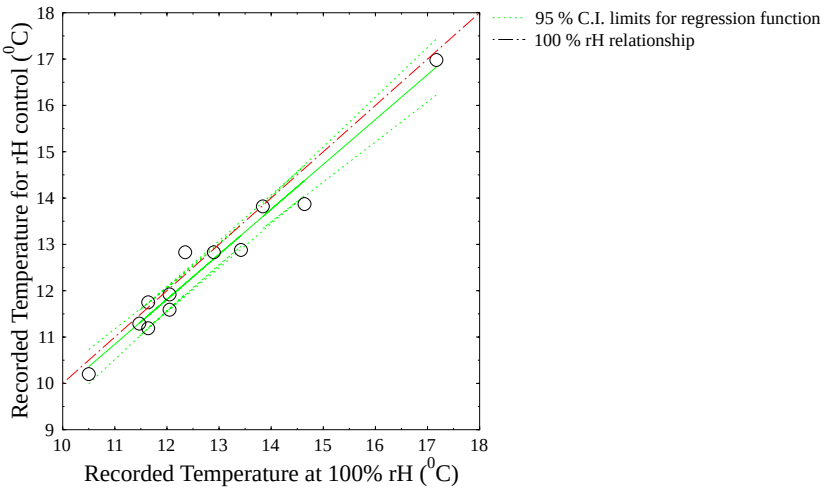

Figure 10.21: Humidity cell data for the subsurface monitoring experiments

Table 10.22: Model summary statistics for site humidity data model

Model Summary

Model	R	R Square	Adjusted R Square	Std. Error of the Estimate
1	.983	.966	.962	.3428

a Predictors: (Constant), JARTEMP
b Dependent Variable: CELLTEMP

ANOVA

Model		Sum of Squares	df	Mean Square	F	Sig.
1	Regression	33.000	1	33.000	280.754	.000
	Residual	1.175	10	.118		
	Total	34.175	11			

a Predictors: (Constant), JARTEMP
b Dependent Variable: CELLTEMP

Coefficients

		Unstandardised Coefficients		Standardised Coefficients	t	Sig.
Model		B	Std. Error	Beta		
1	(Constant)	.162	.749		.216	.833
	JARTEMP	.971	.058	.983	16.756	.000

a Dependent Variable: CELLTEMP

Table 10.23: One-Sample Kolmogorov-Smirnov Test statistics for the normality of the site humidity survey model residuals

		TDIFF
N		58
Normal Parameters	Mean	-.2100
	Std. Deviation	.3310
Most Extreme Differences	Absolute	.117
	Positive	.114
	Negative	-.117
Kolmogorov-Smirnov Z		.405
Asymp. Sig. (2-tailed)		.997
a	Test distribution is Normal.	
b	Calculated from data.	

10.5 Conclusion

The survey results presented in this chapter make a useful contribution to our understanding of archaeological soil EHT, Δ_{EHT} and ERH regimes. In addition to providing a reference modern data set for the numerical modelling approaches developed in the following chapters they shed light upon some aspects of the theoretically motivated discussion on soil climate models presented earlier (Chapter 8). Specifically, the humidity results support the notion that under most circumstances the ERH will be at 100 % for subsurface environments (*infra vide*:§8.6) and the EHT results support the conclusions drawn regarding the use of analogue cell surveys as an EHT estimation method for OHD (*infra vide*:§9.2.2). While the ERH results suggest that we can largely ignore ERH as a factor in OHD (for New zealand at least) EHT and Δ_{EHT} are identified as being highly significant and of prime importance to any application of OHD. Significant EHT estimation errors will arise from assuming that Δ_{EHT} = 0 at an intra-site spatial scale, and in the absence of high precision estimates of micro-scale Δ_{EHT} OHD cannot be usefully conducted. Routine EHT estimation errors in excess of 4 ^{0}C could be expected which could correspond to date errors in excess of 1000 %.

In addition to these general observations the survey data allow us to evaluate the utility of analogue cell survey data as the sole component of an EHT estimation programme. Ignoring the fact that the cell exponential temperature response (and hence the measured EHT) differs from that of obsidian, these results show that measured EHT's cannot be simplistically applied to other locations without incurring potentially significant errors. This finding supports the conclusion drawn earlier that analogue cell data alone cannot be used to provide EHT estimates, and that the practice of measuring a single EHT value for any given site is prone to significant error. Significant and predictable Δ_{EHT} occurs at an intra-site level, and accordingly a single measurement cannot be

meaningfully used to infer EHT for any region as a whole. Additionally, there is an inherent variability in the cells performance. Thus the temperature at any given point cannot be monitored to absolute precision. In combination this means that the reported EHT for any given site could vary considerably due to intra-site Δ_{EHT}, differences in the precise monitoring location and the inherent variability of cell function. Thus the practice of reporting a single EHT value — especially with no error — for a site is invalid and will give rise to significant dating errors. An example of this can be given by a comparison of some of the results reported by Leach and Hamel (1984) and those presented here.

Leach and Hamel (1984) conducted an analogue cell survey of a number of archaeological sites using the same type of analogue cells used in the survey discussed here. Eight of their locations correspond to locations monitored in this survey. The comparative results between the two surveys are given in Table 10.24. As can be seen there are some large differences between the two sets of results with a maximum difference of 2.9 ^{0}C. The average difference between the two sets of results is -0.14 ^{0}C with a standard deviation of 1.56 ^{0}C. This is substantial and

Table 10.24: Comparative analogue cell EHT measurement between Leach and Hamel (1984) and the current survey

Location	Leach and Hamel (1984)		Current Survey		diff
	EHT	depth	EHT	depth	
Clarence	16.6	22	13.7	30	-2.9
station bay	17.3	30	18.6	20	1.3
Kauri point swamp	17.5	60	17.1	40	-0.4
long beach	12.8	42	12	20	-0.8
hotwater beach	17.4	35	19.5	30	2.1
shag river	12.5	18	13.2	20	0.7
papatowai	10	23	10.1	10	0.1
tiwai point	11.2	30	10	30	-1.2

it is useful to establish whether there is a significant difference between the variance observed in this comparison and that expected due to inherent cell variance ($\sigma_{\text{cell}} = 0.49$; §10.2.1). We can assess the difference in variance by testing the statistic

$$V = \frac{\sum(X_i - \bar{X})}{\sigma^2_{\text{cell}}}$$

against a $\chi^2_{1-\alpha}(n-1)$ distribution (Mood *et al.* 1974pp. 431). This tests the null hypothesis $\mathcal{H}_0 : \sigma^2_{diff} \leqslant \sigma^2_{\text{cell}}$ versus $\mathcal{H}_1 : \sigma^2_{diff} > \sigma^2_{\text{cell}}$. In this case $V = 71.22$ which is significant at $\alpha = 0.05$ ($\chi^2_{1-0.05}(7) = 14.1$). Thus we would conclude that the observed differences between these results are greater than would arise due to the inherent variance in cell measurement results. This serves to illustrate both the magnitude of microscale Δ_{EHT} that may be observed within archaeological sites and the problems of using analogue results to try and estimate a single site specific EHT. Clearly it is not feasible to simply use measured EHT results such as those presented here or by Leach and Hamel (1984) to estimate EHT's in archaeological sites. Even if the EHT's returned by analogue cells were the same as that for obsidian we would still have to monitor each specific location for which OHD was to be employed.

Thus the survey results presented here cannot be used to directly estimate EHT and Δ_{EHT} for New Zealand. However, they do provide a primary reference set of modern data for the development of further Δ_{EHT} and EHT estimates in New Zealand — a central component of all suitable EHT estimates (*infra vide*:§9.5). In order to develop EHT estimation procedures further we must incorporate some form of procedure to extrapolate the measured cell data to non-monitored locations. As outlined earlier one approach to doing this is through the use of numerical soil temperature models that can take account of micro-scale Δ_{EHT}. The development of such models is discussed in the following chapters.

Chapter 11

A Simple Numerical Model for EHT Estimation in New Zealand

11.1 Introduction

In this chapter long-term soil temperature data from meteorological stations throughout New Zealand is used to estimate archaeological EHT's by approximating the distribution of the temperature series $T(x)$ (*infra vide*:§9.4.1) and directly evaluating the integral given in Equation 8.3. This is an exercise in the use of long-term meteorological data to estimate absolute EHT's. However, through the sole use of meteorological soil temperature data we have no facility for estimating Δ_{EHT}. Thus this approach is not an ideal EHT estimation procedure in itself (*infra vide*:§9). However, the analysis is a useful exercise and the method for analysing meteorological data presented in this chapter can be applied in more detailed numerical estimation approaches such as that presented in the next chapter. Additionally, the analysis presented here allows us to establish the magnitude of precision in EHT estimation that could realistically be expected to derive from models of meteorological data. This is useful as meteorological data are used to try and estimate EHT's for the purpose of OHD (e.g., Stevenson *et al.* 1989*a*; §9.2). Finally the model developed here provides a first approximation for $\bar{T}$ estimates in New Zealand, a central component of appropriate EHT estimation procedures (*infra vide*:§9.3.3).

The primary data-base used for this exercise has been extracted from the full New Zealand climate data-base to provide monthly average soil temperatures from 108 stations throughout New Zealand (§F, 11.2). In order to make use of this meteorological data-base we need to be able to parameterise the data. That is to produce a model that describes the fundamental data structure. If we have such a model then it is possible to predict how the model parameters observed over a fixed time period at the 108 measurement locations may vary over longer time-periods and at different geographical locations. On this basis we can generate soil temperature distributions for differing time-periods and at different

locations to those monitored historically. Hence we can calculate an estimated EHT according to Equation 8.3 following the approach outlined in §9.4.1.

Thus this chapter develops a spatial model for soil temperature distributions throughout New Zealand and demonstrates how these models can be used to predict an EHT. While the results are empirical and limited exclusively to New Zealand the general modelling approach will be applicable anywhere.

11.2 The Meteorological Database

The meteorological data-base used in this chapter, and elsewhere throughout this thesis, primarily derives from the full New Zealand climate database maintained by the National Institute for Water and Atmospheric Research (NIWA). Other than the NIWA data, some of the hourly data was provided by HORTRESEARCH (Mt Albert) as discussed below. The data-base comprises three different data types: Monthly averages; daily readings; and hourly readings.

The majority of the data are monthly means for the variables given in Table 11.1.

Table 11.1: Meteorological Variables included in the long-term data-set

Variable	ID	Description
Air Max	mairmax	mean daily maximum temperature for the month
Air Min	mainmin	mean daily minimum temperature for the month
Grass Min	mgrassmin	mean daily grass minimum temperature for the month
Extreme Air Max	xairmax	maximum daily air maximum temperature for the month
Extreme Air Min	xairmin	minimum daily air minimum temperature for the month
Extreme Grass Min	xgrassmin	minimum daily grass minimum temperature for the month

continued on the next page

Table 11.1: *continued*

Variable	ID	Description
Min Air Max	lairmax	minimum daily air maximum temperature for the month
Max Air Min	lairmin	maximum daily air minimum temperature for the month
5cm Soil Temperature	fivecm	mean daily five cm soil temperature for the month
10cm Soil Temperature	tencm	mean daily ten cm soil temperature for the month
20cm Soil Temperature	twentcm	mean daily twenty cm soil temperature for the month
30cm Soil Temperature	thirtcm	mean daily thirty cm soil temperature for the month
50cm Soil Temperature	fiftcm	mean daily fifty cm soil temperature for the month
100cm Soil Temperature	onecm	mean daily one hundred cm soil temperature for the month
Rain total	raintot	total monthly rainfal in mm
Global Radiation	meanglob	mean monthly global radiation in MJ M^{-2}
Total Sun	totsun	Total sunshine hours for the month
Max Wind Run	mwindrun	maximum daily wind run in kilometres
Wind Run	windrun	
VPRESS	vpress	mean monthly atmospheric pressure in MB
Mean Rh	meanrh	mean daily Rh for the month
Sunken Pan Evaporation	tspevap	total sunken pan evapouration for the month in mm
Penman	penman	calculated mean monthly penman value

These data have been collated (where available) for 197 locations throughout New Zealand (Figure 11.1, Table F.3), with the major concentration on the study area(s) defined in §10. Full details of the monitored locations are given in Table F.3 and the variables monitored at each location are presented in Table F.4. In some locations these data span back to 1862, thus these data allow us to develop meteorological models informed by long-term data over a wide, relatively densely sampled, spatial area.

To complement these long-term data, daily data have been collated from a sub-set of the stations included in the long-term data set. These provide a reference-set for establishing any model components that need

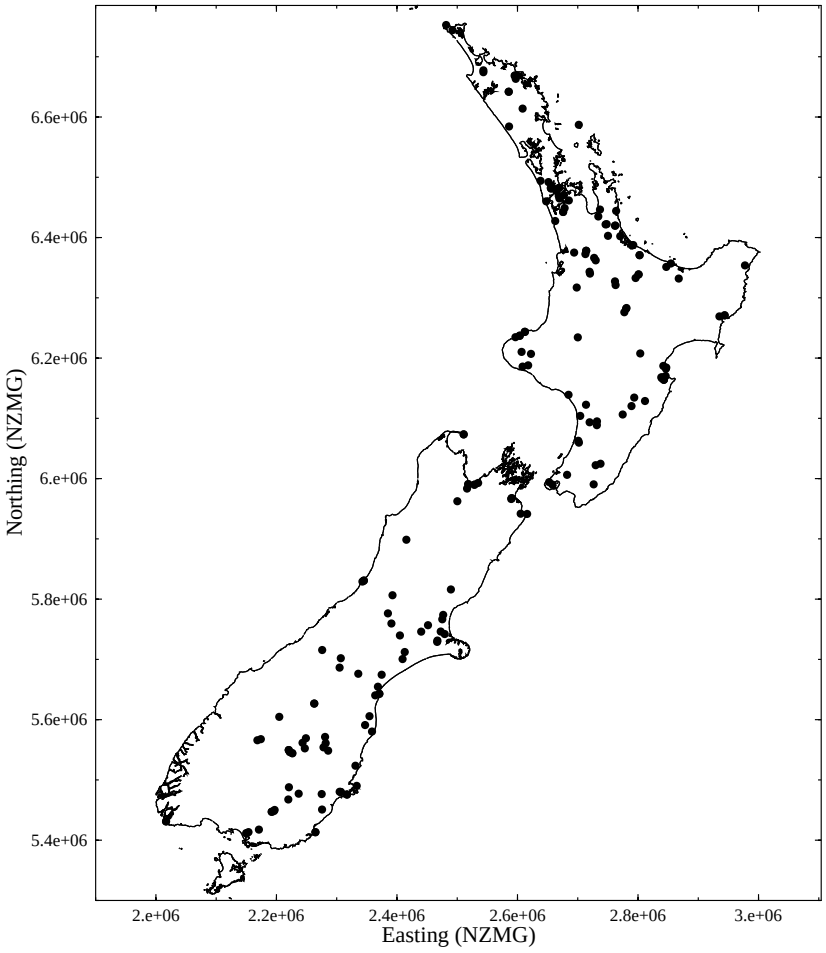

Figure 11.1: Location of sites from which long-term meteorological data have been obtained

to be added to the monthly data to take account of the data simplifications introduced through using monthly averages. In total 12 stations (Figure 11.2) are included in this data-set. Their details are presented in Table F.1 and the monitored variables are indicated in Table F.2.

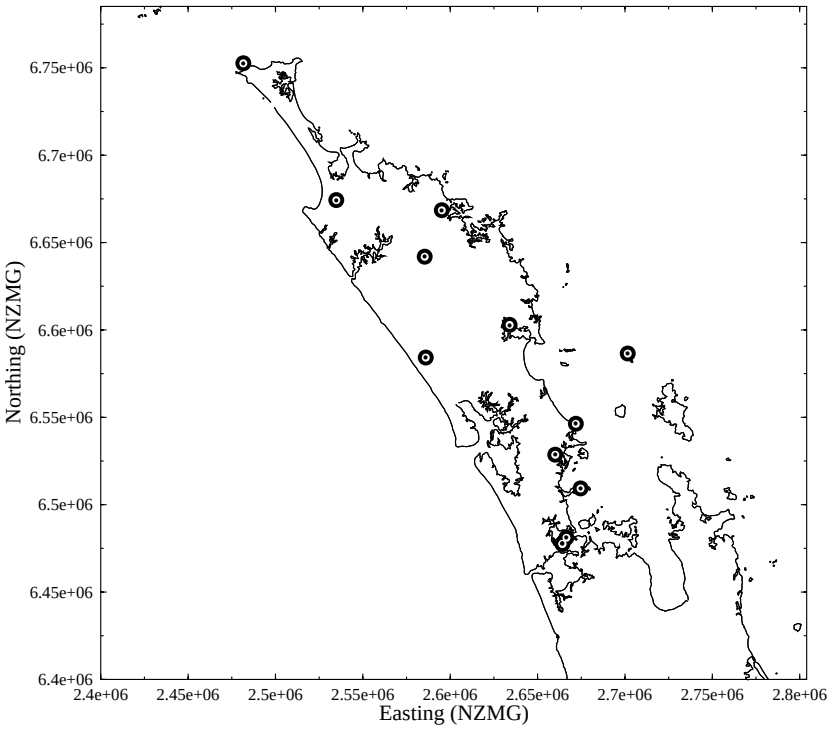

Figure 11.2: Location of sites from which daily meteorological data have been obtained

While the majority of the meteorological models will derive from the monthly and daily data, two, hourly, data-sets have also been collated. These comprise a single location for which hourly data for a range of meteorological variables (Tables 11.2)have been collected over a six month period, and hourly radiation data for two locations over a sixteen month period.

The hourly meteorological data was provided by Warwick Henshaw of HORTRESEARCH (Mt Albert), and comprises hourly readings of the variables given in Table 11.2 over the period 11/10/1995 – 28/3/1996 :

Table 11.2: Meteorological variables included in the hourly data-set

Variable	Code
Dry bulb air temperature	DB
Wet bulb air temperature	WB
Daily grass minimum temperature	Grass
Daily rainfall in 0.1mm	Rain
two cm soil temperature	2cm
five cm soil temperture	5cm
ten cm soil temperature	10cm
twenty cm soil temperature	20cm
fifty cm soil temperature	50cm
one hundred cm soil temperature	100cm

This data was obtained as a test set to compare the nature of variation at an hourly level to that which is modelled on the basis of daily or monthly data, and also as an experimental data set for EHT estimation and analogue cell temperature comparisons (as outlined in §9.4.1 & §10).

The hourly radiation data comprises hourly data for direct radiation, diffuse radiation and total global radiation from the A53125 and E04991 meteorological stations over the interval 1/1/1991 – 20/3/1992. The purpose of this data is to allow an evaluation of estimates for S_t (*infra vide*:§8.2). This is necessary for the numerical model that will be explored in the next chapter.

11.3 Analytic Structure

In the following section we will develop an approach to modelling the available meteorological data. For simplicity, in this exercise we will work with a single data series; the mean monthly 30cm soil temperature series from the Owairaka Meteorological station, Auckland (Station

A64971) over the period January 1949-January 1998 (Figure 11.3). The basic structure of the A64971 30cm temperature series is identical to all of the seasonal temperature series we need to work with so acts as a test data-set where the basic modelling approach can be developed and illustrated before being applied in a spatial context.

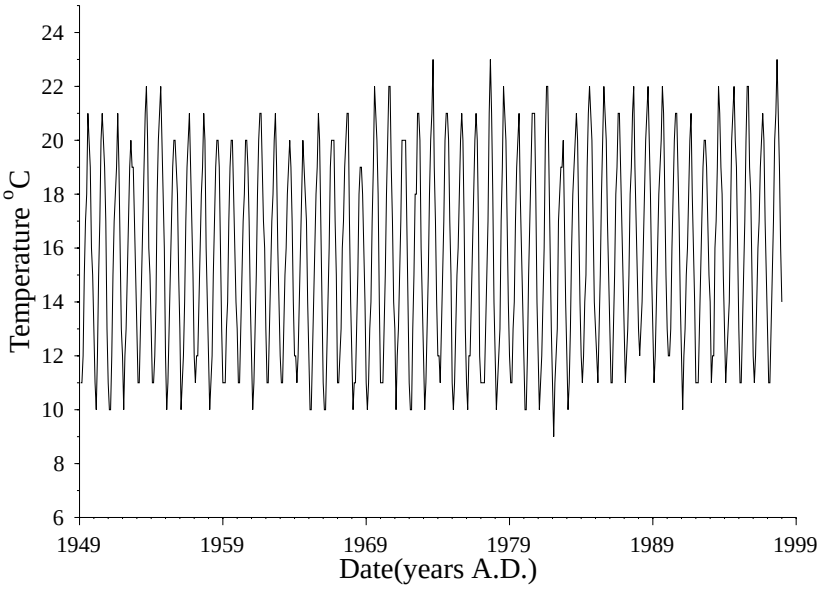

Figure 11.3: Average monthly 30 cm soil temperature for station A64971 (Owairaka, Auckland), 1949-1999

The basic data-series given in Figure 11.3 is an approximation of the function $T(x)$ that is required for calculation of an EHT after Equation 8.3. In order for us to make any use of this type of data series — beyond simply using it as an estimate of $T(x)$ and evaluating the EHT for that particular location and time period — we must be able to construct a model that describes the data and can be used to estimate an equivalent data series at other locations for which monitored data are not available. This means that we must be able to define the data series in terms of some set of parameters. When we introduce the spatial model in the following section it is the spatial distribution of these pa-

rameters that we will model. Thus by defining a model and the spatial distribution of the model parameters we can estimate a data-series for any given spatial location. In the current section we will consider how we can most simply model the type of data series given in Figure 11.3.

As an important component of any model that is useful for our purpose is the long-term temperature fluctuation, it is useful to break the temperature series ($T(x)$) into two components: one that describes the fluctuations in annual mean temperature (T_{trend} the trend component); and a component that describes the structure of the stationary temperature series (T_{stat} the stationary component) that arises through removal of the long-term trend from $T(x)$. That is:

$$T(x) = T_{trend}(x) + T_{stat}(x) \tag{11.1}$$

Thus we model the long-term temperature series as corresponding to the summation of a stationary series and a long-term temperature trend. In this manner we can model any long-term trend (T_{trend}) in order to reflect current understanding about palaeo-temperature fluctuations, while making use of historical data to provide a structure for the stationary series (T_{stat}).

This model structure reflects the most obvious features in the A64971 30cm soil temperature series shown in Figure 11.3: the regular seasonal temperature cycle; and what appear to be variations in the average temperature through time with a general trend for an increasing average temperature in the decade 1988-1998. In addition, the model structure given in Equation 11.1 reflects standard approaches to time-series analysis. Technically a series with an underlying trend – such as that graphed in Figure 11.3 – is known as a non-stationary time-series. In order to use many of the standard statistical tools that have been developed for time-series analysis it is necessary to remove such long-term trends and produce a stationary series (Chatfield 1996). Thus using the type of structure defined in Equation 11.1 allows us to describe the series in a

suitable manner for our purposes, to use standard time-series analysis techniques on the $T_{stat}(x)$ data component (and also on the $T_{trend}(x)$ component to as we shall see), and reflects the gross structure of the data-sets we are working with. Thus if we can develop a model to describe the $T_{stat}(x)$ and $T_{trend}(x)$ components we can calculate an EHT that takes into account any degree of long-term temperature trend that we desire while taking into account the structure of historical data.

In the following two sections we consider models for $T_{stat}(x)$ and $T_{trend}(x)$. However, first we have to be able to extract the two components $T_{trend}(x)$ and $T_{stat}(x)$ from the data-series $T(x)$. In order to do this a simple scheme that is commonly used for monthly time-series data is to calculate $T_{trend}(x)$ as (Chatfield 1996):

$$T_{trend}(x) = \frac{\frac{1}{2}T(x-6) + T(x-5) + \cdots + T(x+5) + \frac{1}{2}T(x+6)}{12} \quad (11.2)$$

which is essentially a 12 month moving average. The $T_{stat}(x)$ component is then simply the difference between $T(x)$ and $T_{trend}(x)$. This break down is given in Figure 11.4 which graphs $T(x)$ broken into the components $T_{stat}(x)$ and $T_{trend}(x)$ following Equation 11.2

11.3.1 Modelling the Stationary Series $T_{stat}(x)$

The de-trended, or stationary, mean monthly 30cm soil temperature series for station A64971 is plotted in Figure 11.5. It is clear that the predominant structure of this data-series is the regular seasonal trend occurring over the 12 months of the year. This is reflected in the ACF plot (Figure 11.6) which is dominated by a clear cyclical correlation at a period of 12, as expected.

The series given in Figure 11.5 can be generated by the sum of a regular deterministic function ($T_{det}(x)$) and a (probably temporally correlated)

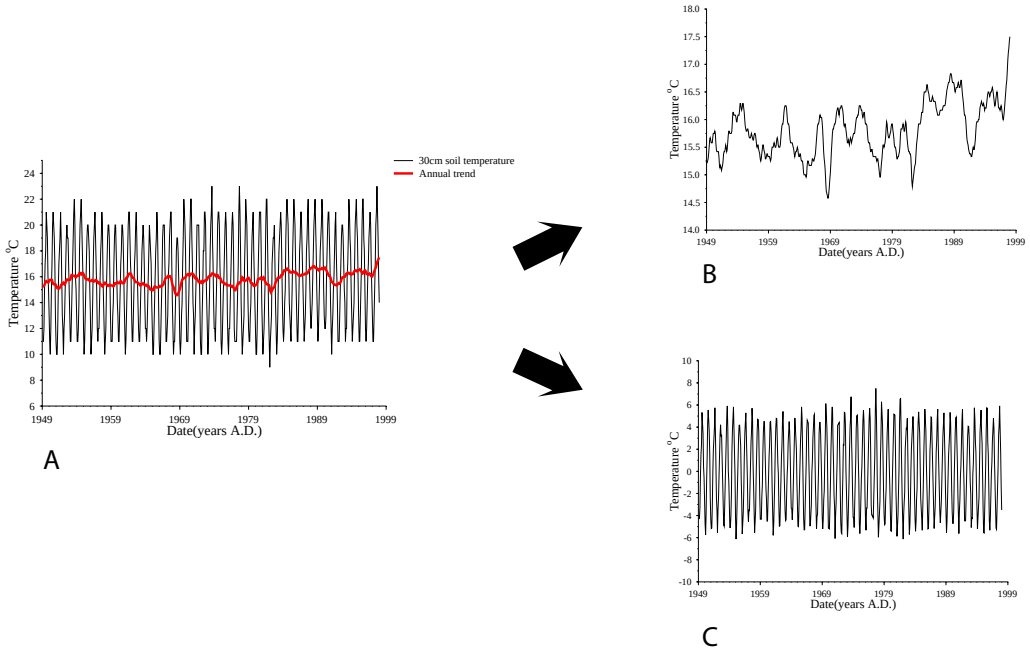

Figure 11.4: Break down of the 30cm monthly soil temperature series for A64971 into trend and stationary components. **A** The observed temperature series ($T(x)$) with the annual trend series ($T_{trend}(x)$) after Equation 11.2 overlayed; **B** The Annual trend component ($T_{trend}(x)$) after Equation 11.2; **C** The stationary series

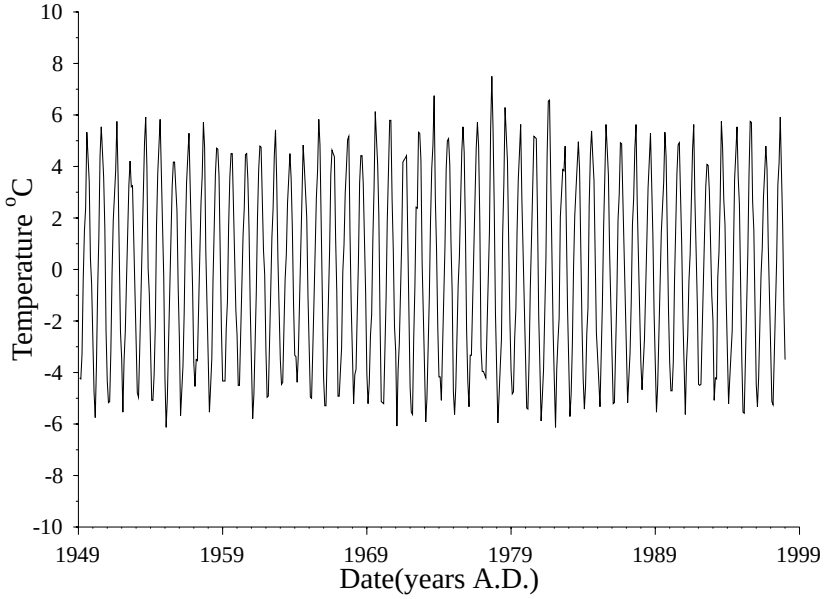

Figure 11.5: De-trended 30cm soil temperature series

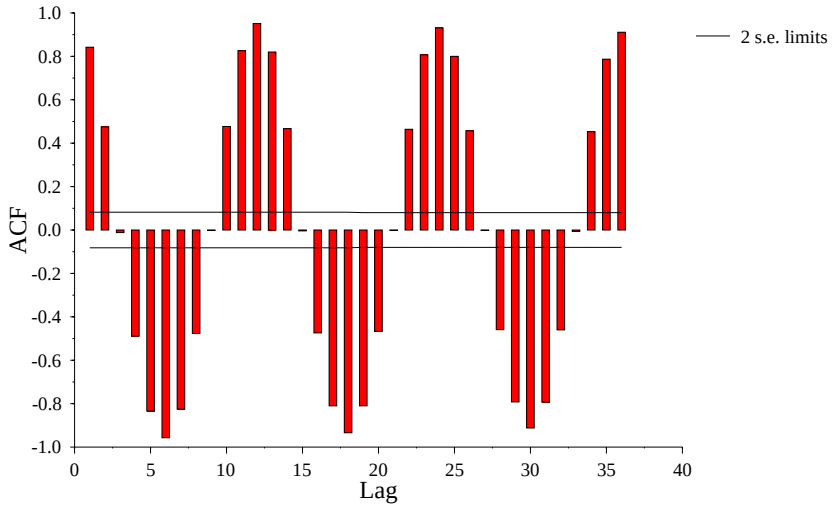

Figure 11.6: ACF plot for the de-trended 30cm data series

stochastic noise ε_t, e.g.

$$T_{stat}(x) = T_{det}(x) + \varepsilon_t \tag{11.3}$$

So we can regard the series as comprising deviations from idealised seasonal cycle that give rise to periods of warmer than expected or cooler than expected temperatures. This is useful as the underlying deterministic seasonal cycle can be closely approximated by sine waves through spectral decomposition. In order to do this it is simply necessary to solve for a_i & b_i in

$$T_{det}(x) = \frac{1}{2} + \sum_{j=1}^{m} (a_j cos\alpha_j x + b_j sin\alpha_j x) \tag{11.4}$$

where

$$\begin{aligned} &a_0 = \bar{y}, \\ &na_j = 2\sum I_i cos\alpha_j x, \quad j = 1, \ldots, m; \\ &nb_j = 2\sum I - isin\alpha_j x, \quad j = 1, \ldots, m. \end{aligned} \tag{11.5}$$

which corresponds to a weighted average of sin waves for the $n = 2m+1$ data values. In the current analysis we will only use the first two wave frequencies as the seasonal trend is very nearly sinusoidal. So to fit the deterministic function we simply regress the stationary data series on the variables

$$\begin{aligned} sm &= \sin(2\pi month/12) \\ cm &= \cos(2\pi month/12) \\ sm2 &= \sin(4\pi month/12) \\ cm2 &= \cos(4\pi month/12) \end{aligned} \tag{11.6}$$

As the analysed series is stationary there should be no constant term (i.e., $a_0 = 0$) thus the regression is carried out through the origin. The regression statistics for this regression are given in Table 11.3 and show that this model is a good fit, explaining around 97% of the observed variation in the data. The stochastic component of this stationary data series (ε_t) is simply the residual component of the regression model.

Thus following the statistics given in Table 11.3 we can describe $T_{det}(x)$ as

$$T_{det}(x) := 3.458 * \sin\left(\frac{2*\pi*x}{12}\right) + 3.575 * \cos\left(\frac{2*\pi*x}{12}\right) - 0.281 * \cos\left(\frac{4*\pi*x}{12}\right) \quad (11.7)$$

This break down is plotted in Figure 11.7.

Table 11.3: Regression statistics for fitting the determinant function to the stationary 30cm data

Model Summary

R	R Square	Adjusted R Square	Std. Error of the Estimate
0.983	0.967	0.967	0.6543

ANOVA

	Sum of Squares	df	Mean Square	F	Sig.
Regression	7296.358	3	2432.119	5680.278	.000
Residual	250.479	585	0.428		
Total	7546.837	588			

Coefficients

	Unstandardized Coefficients		Standardized Coefficients	t	Sig.
	B	Std. Error	Beta		
SM	3.458	0.038	0.682	90.603	.000
CM	3.575	0.038	0.706	93.688	.000
CM2	-.281	0.038	-0.056	-7.374	.000

Residuals Statistics

	Minimum	Maximum	Mean	Std. Deviation	N
Predicted Value	-4.9659	4.9228	-7.7785E-10	3.5256	588
Residual	-1.8356	2.5772	1.701E-03	0.6532	588
Std. Predicted Value	-1.409	1.396	.000	1.000	588
Std. Residual	-2.805	3.939	.003	.998	588

While we now have a model for one component of $T_{stat}(x)$ it is also necessary to consider the structure of ε_t. We would expect some form of temporal correlation within the series ε_t (Figure 11.7C). For example, months that are warmer than average would be expected the be followed by months where the temperature also tends to be above the mean. This expectation is borne out in the ACF plot of ε_t which shows significant autocorrelations. The general autocorrelation structure we expect for the series ε_t is that the current value ε_t is a function of the immediately preceding values plus some error term. A number of models exist in the

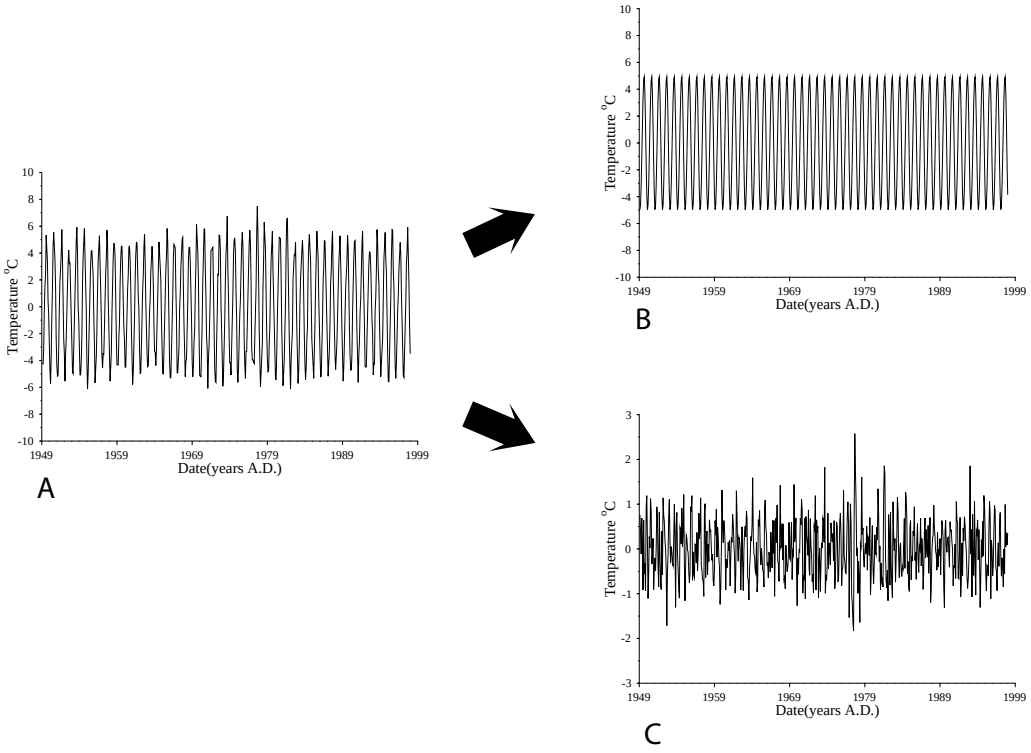

Figure 11.7: Break down of $T_{stat}(x)$ into deterministic ($T_{stat}(x)$) and stochastic (ε_t) components. **A** The stationary temperature series $T_{stat}(x)$; **B** The deterministic temperature function $T_{det}(x)$ after Equation 11.7; **C** The stochastic component ε_t

Figure 11.8: ACF plot for the stochastic component of the de-trended monthly data

literature to describe models such as this, mostly based around some form of Box-Jenkins or ARIMA model (Chatfield 1996). Clearly the type of model just described is some form of autoregressive model and we might like to model ε_t as an ARIMA(n,0,0) series. This model does fit, however a little EDA has indicated that in this case an ARMA(2,1) model is an appropriate simple model to describe ε_t. The model fit statistics are given in Table 11.4 and as can be seen the parameters for this model are statistically significant. Following this analysis we can describe ε_t as

$$\varepsilon_t := 1.0458 * \varepsilon_{t-1} - 0.4169 * \varepsilon_{t-2} + 0.9956 * \epsilon_t + \epsilon_t \qquad (11.8)$$

Here $\epsilon_t \sim N(0, 0.55)$ and can be treated as a purely random process with no correlation as indicated by an ACF plot (Figure 11.9). The break down of ε_t following Equation 11.8 is plotted in Figure 11.10.

Thus we can model the stationary component of the A64971 monthly

Table 11.4: Model fit statistics for the ARMA(2,1) model applied to ε_t

Analysis of Variance

	DF	Adj. Sum of Squares	Residual Variance
Residuals	585	178.84181	.30368081

Variables in the Model

	B	SEB	T-RATIO	APPROX. PROB.
AR1	1.0457874	0.03812172	27.432853	.0000000
AR2	-.4168574	0.03776845	-11.037184	.0000000
MA1	.9955996	0.02995461	33.236943	.0000000

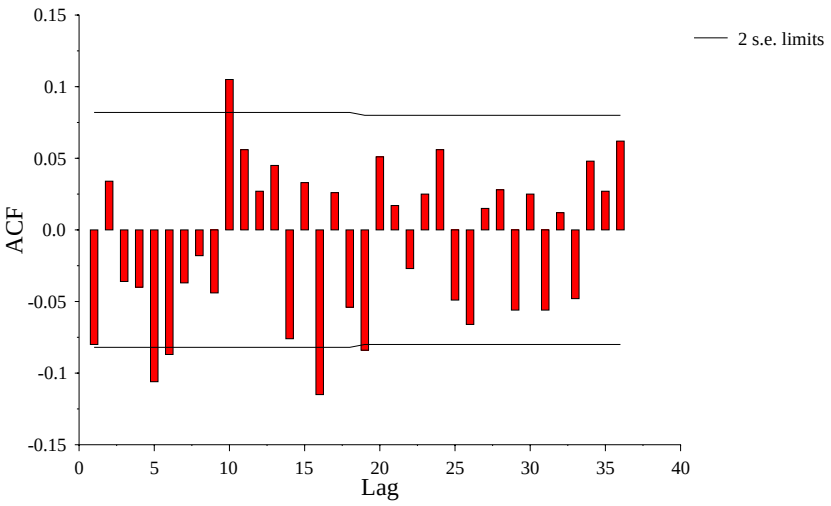

Figure 11.9: ACF plot for the residuals from the model fitted to the stochastic component of the de-trended monthly data

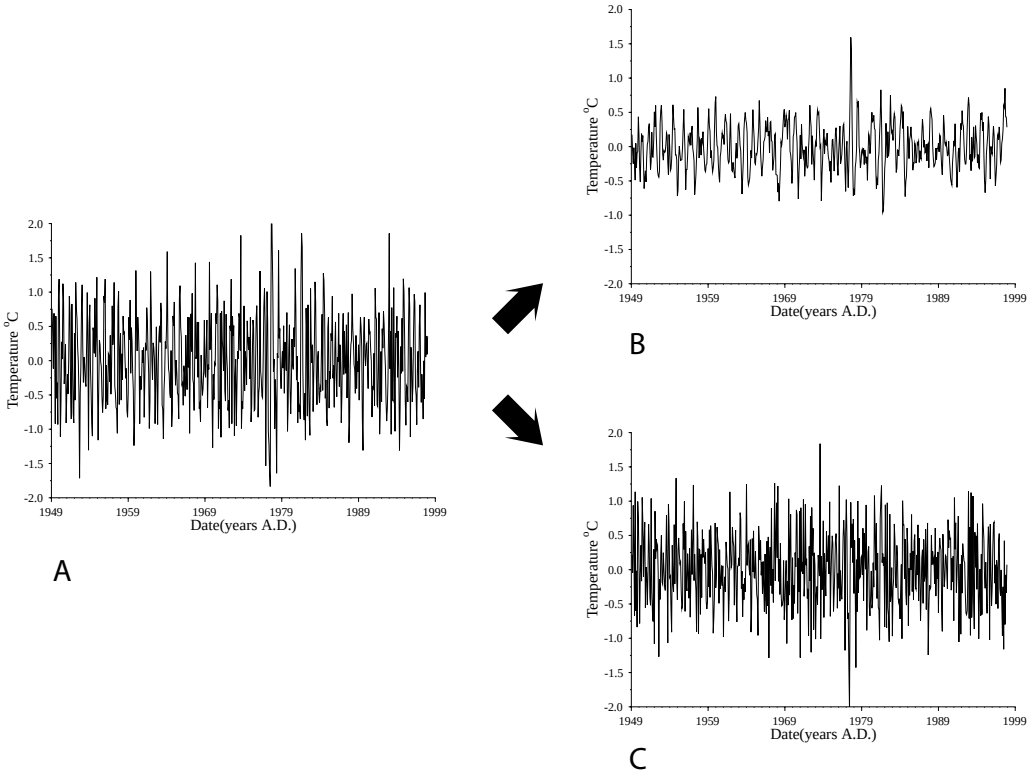

Figure 11.10: Break down of ε_t into ARMA and purely random components. **A** The series ε_t; **B** The predicted ARMA model after Equation 11.8; **C** The purely random component ϵ_t

30cm temperature series as follows

$$\begin{aligned} T_{stat}(x) = \; & 3.458 * \sin\left(\tfrac{2*\pi*x}{12}\right) + 3.575 * \cos\left(\tfrac{2*\pi*x}{12}\right) \\ & + \cos\left(\tfrac{4*\pi*x}{12}\right) + 1.0458 * \varepsilon_{t-1} - 0.4169 * \varepsilon_{t-2} \\ & + 0.9956 * \epsilon_t + \epsilon_t \end{aligned} \tag{11.9}$$

A fairly simple break-down of the temperature series that is of the form

$$T_{stat}(x) = \text{deterministic model} + \text{ARIMA model} + \text{Random Error}$$

While this model will not allow us to generate the exact series that has been observed, we can use this model to generate time series that have the same structure as that observed. This means that aspects such as the distribution of the time series will be the same for both modelled and observed time series, and that either time series would be appropriate for predicting an EHT following Equation 8.3. We can apply this structure to any series we wish to model thus it is possible to use an identical parameterisation of the station data series from a number of locations throughout New Zealand.

11.3.2 Modelling the Trend Series $T_{trend}(x)$

In modelling $T_{trend}(x)$ we can adopt a similar approach to that already used for $T_{stat}(x)$.

We would expect that there may be some form of steady long-term trend function ($F_{trend}(x)$) in the observed data, about which there will be some form of stochastic variation (ε_x^T). So again we wish to model the series as the sum of a deterministic and stochastic series, e.g.

$$T_{trend}(x) = F_{trend}(x) + \varepsilon_x^T \tag{11.10}$$

This has the effect that the stochastic component is now stationary as the trend has been removed and we can again use some form of ARIMA

model to describe the stochastic function in the same way as the T_{stat} series.

In the current analysis a simple polynomial regression was carried out on $T_{trend}(x)$ to fit the annual trend function shown in Figure 11.11 with the corresponding annual stochastic function given in Figure 11.13A. The model statistics for this regression analysis are given in Table 11.5. Following this we can model the central trend function as

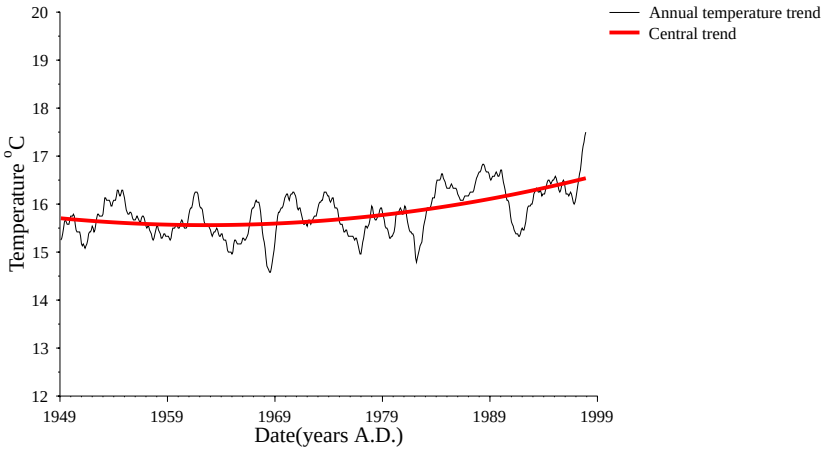

Figure 11.11: Central trend for the annual trend series

$$F_{trend}(x) = 15.719 - 1.847E - 03x + 5.4345E - 06x^2 \qquad (11.11)$$

The ACF plot for the Annual Stochastic function shows that — as we would expect — there are autocorrelations in the deviations from the central trend. Thus warmer than average deviations are followed by deviations that also tend to be warmer than average. Similarly to the stochastic component of the $T_{stat}(x)$ series we would expect that this data series would follow some form of autoregressive model. From the ACF plot (Figure 11.12) we can see that there are significant autocorrelations to a high number of lags. This is to be expected as we would expect warm years to follow warm years, thus affecting 12 terms of the

Table 11.5: Regression statistics for the polynomial model fitted to $T_{trend}(x)$

Model Summary

R	R Square	Adjusted R Square	Std. Error of the Estimate
0.582	0.338	0.336	0.3907

ANOVA

	Sum of Squares	df	Mean Square	F	Sig.
Regression	45.665	2	22.832	149.571	.000
Residual	89.301	585	0.153		
Total	134.966	587			

Coefficients

	Unstandardized Coefficients		Standardized Coefficients	t	Sig.
	B	Std. Error	Beta		
(Constant)	15.719	0.051	311	.201	.000
MONTH2	-1.847E-03	.000	-.654	-4.765	.000
MONTH22	5.435E-06	.000	1.194	8.692	.000

Residuals Statistics

	Minimum	Maximum	Mean	Std. Deviation	N
Predicted Value	15.5620	16.5394	15.8112	0.2789	588
Residual	-1.0707	.9606	3.094E-15	0.3900	588
Std. Predicted Value	-.894	2.611	0.000	1.000	588
Std. Residual	-2.740	2.459	0.000	0.998	588

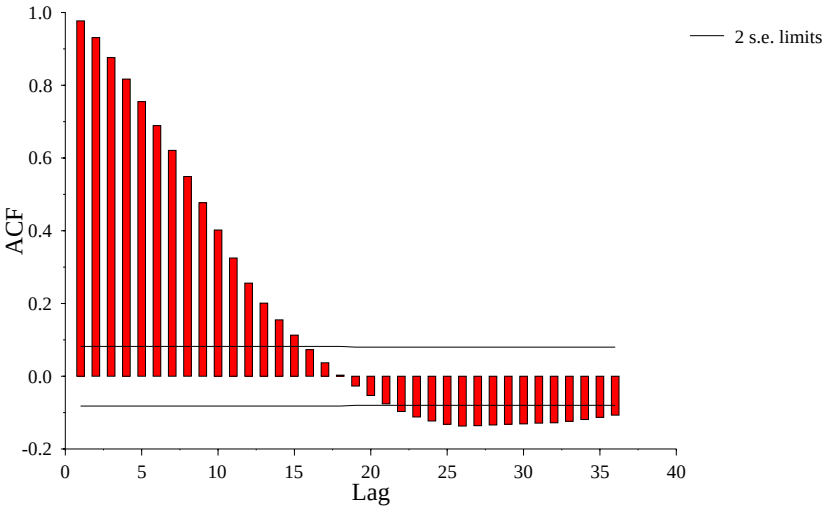

Figure 11.12: ACF plot for the de-trended annual trend series

data series (there being 12 months per year). For this example we will fit an AR(24) model to the data, which essentially says that the deviations are influenced by the deviations for the previous 2 years. This model explains much of the structure in ε_x^T as can be seen by the model fit statistics given in Table 11.6 and the break down plotted in Figure 11.13 From this analysis we can model ε_x^T as

Table 11.6: AR(24) model statistics for the series ε_x^T

Number of residuals	588
Standard error	.03368575
Log likelihood	1164.9701
AIC	-2281.9403
SBC	-2176.8988

Analysis of Variance

	DF	Adj. Sum of Squares	Residual Variance
Residuals	564	.65454410	.00113473

	B	SEB	T-RATIO	APPROX. PROB.
AR1	2.2833639	.04065201	56.168539	.00000000
AR2	-2.4149043	.10197368	-23.681644	.00000000
AR3	2.0806849	.14255036	14.596139	.00000000
AR4	-1.7254845	.16608550	-10.389134	.00000000
AR5	1.4871878	.17920728	8.298702	.00000000
AR6	-1.3134814	.18658585	-7.039555	.00000000
AR7	1.1142162	.19042480	5.851214	.00000000
AR8	-.9072856	.19113813	-4.746754	.00000262
AR9	.6597373	.18943078	3.482735	.00053480
AR10	-.3040653	.18455904	-1.647523	.10000752
AR11	.0040425	.17518640	.023076	.98159812
AR12	-.5553752	.16582881	-3.349088	.00086491
AR13	1.3437534	.16517093	8.135532	.00000000
AR14	-1.4606831	.17309634	-8.438556	.00000000
AR15	1.2833530	.18190557	7.055051	.00000000
AR16	-1.1200692	.18693785	-5.991666	.00000000
AR17	1.0485453	.18878804	5.554087	.00000004
AR18	-.9635360	.18846367	-5.112582	.00000044
AR19	.7816991	.18551216	4.213735	.00002924
AR20	-.4892878	.17904374	-2.732784	.00647713
AR21	.1898036	.16679059	1.137975	.25561399
AR22	.0939302	.14427287	.651059	.51527331
AR23	-.3491163	.10393244	-3.359070	.00083486
AR24	.2149678	.04160103	5.167369	.00000033

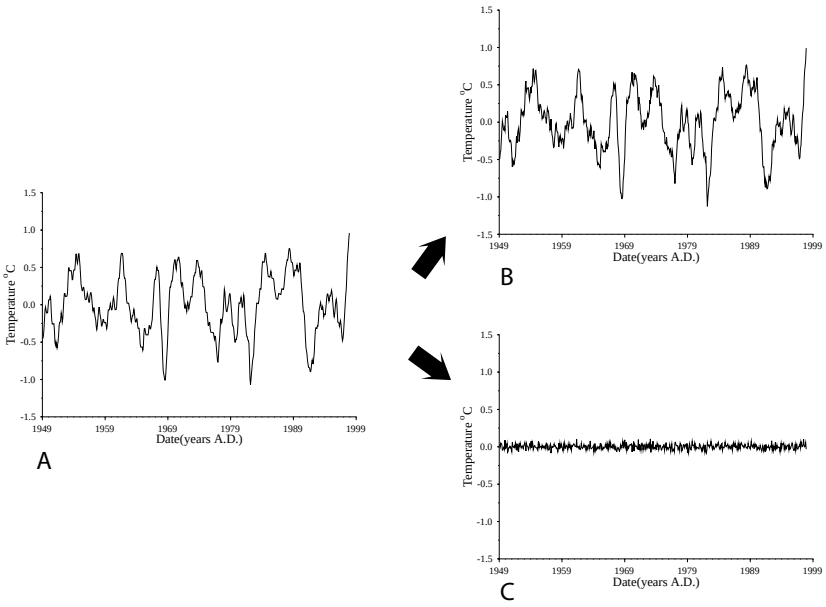

Figure 11.13: Break down of ε_x^T into AR and purely random components. **A** The series ε_x^T; **B** The predicted AR model after Equation 11.12; **C** The purely random component ϵ_x^T

$$\begin{aligned}\varepsilon_x^T = \; & 2.2833639x_{t-1} - 2.4149043x_{t-2} + 2.0806849x_{t-3} \\ & -1.7254845x_{t-4} + 1.4871878x_{t-5} - 1.3134814x_{t-6} \\ & +1.1142162x_{t-7} - 0.9072856x_{t-8} + 0.6597373x_{t-9} \\ & -0.3040653x_{t-10} + 0.0040425x_{t-11} - 0.5553752x_{t-12} \\ & +1.3437534x_{t-13} - 1.4606831x_{t-14} + 1.283353x_{t-15} \\ & -1.1200692x_{t-16} + 1.0485453x_{t-17} - 0.963536x_{t-18} \\ & +0.7816991x_{t-19} - 0.4892878x_{t-20} + 0.1898036x_{t-21} \\ & +0.0939302x_{t-22} - 0.3491163x_{t-23} + 0.2149678x_{t-24} \\ & +\epsilon_t^T\end{aligned} \tag{11.12}$$

Here $\epsilon_x^T \sim N(0, 0.034)$ and can be treated as a purely random process with no correlation as indicated by an ACF plot (Figure 11.14). Thus

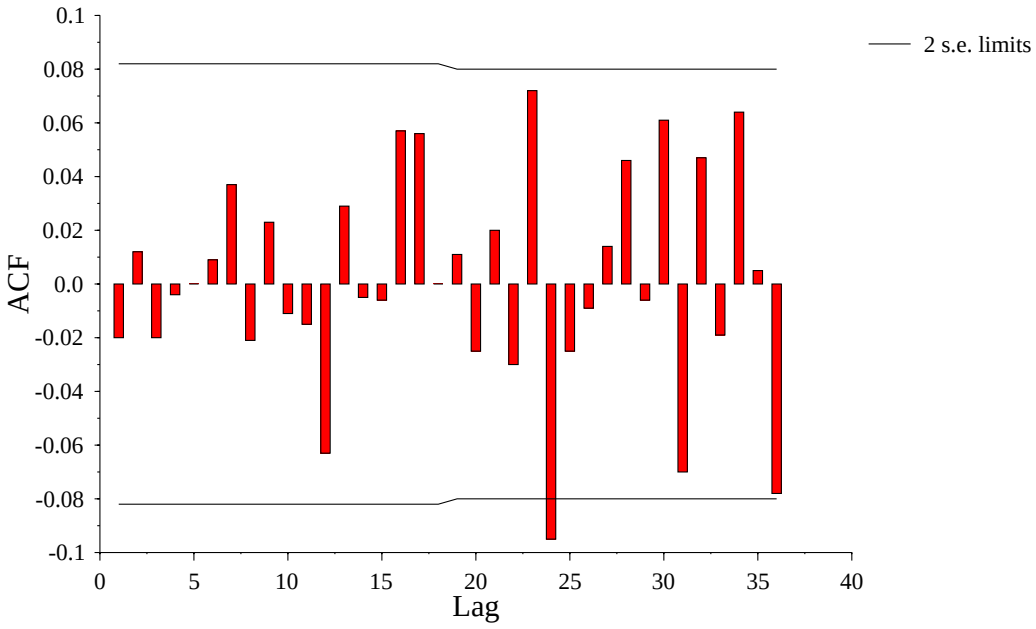

Figure 11.14: ACF plot for the residuals from the stochastic model fitted to the annual trend data

we can parameterise the series $T_{trend}(x)$ as being the sum of Equations 11.11 and 11.12 as described in Equation 11.10. Again as was outlined for Equation 11.9 describing the series $T_{stat}(x)$, the function

given in Equation 11.10 does not allow us to predict the actual observed series, but rather a series that has the same structure as that observed. This is all that we need, and Equation 11.10 provides a structure suitable for the purposes of developing a spatial model to predict EHT. In order to predict a full temperature series we simply need to produce a combined model that sums the $T_{stat}(x)$ and $T_{trend}(x)$ series.

11.3.3 The Combined Model

While we can parameterise $T(x)$ via a simple summation of $T_{stat}(x)$ and $T_{trend}(x)$ as described in Equations 11.9, 11.11 and 11.12 we can make some significant simplifications to this combined model. For example, as the two error terms ϵ_x^S and ϵ_x^T are independent normally distributed variables we can combine these to produce a single error term ϵ_x distributed as the sum of the two normal distributions. This combined error series ϵ_x is plotted in Figure 11.15. However, we can take the simplification beyond this as the stochastic series defined in Equations 11.8 and 11.12 are also normally distributed (Chatfield 1996). For the purposes of the current model we are only interested in the distribution of the series $T(x)$ rather than being able to construct an actual time-series (*infra vide*:§9.4.1), thus we do not need to describe the autocorrelation structure in the stochastic components of $T_{trend}(x)$ and $T_{stat}(x)$ and can treat these as purely independent normal distributions. This means that we can sum all of these stochastic components to produce a single normal distribution and break down $T(x)$ as

$$T(x) = \text{deterministic function} + \epsilon \tag{11.13}$$

where $\epsilon \sim N(0, \sigma_\epsilon^2)$ is the stochastic component. To date we have described the deterministic component as the sum of a long-term trend function and a standard monthly cycle, i.e.

$$\text{deterministic function} = F_{Trend}(x) + F_{month}(x) \tag{11.14}$$

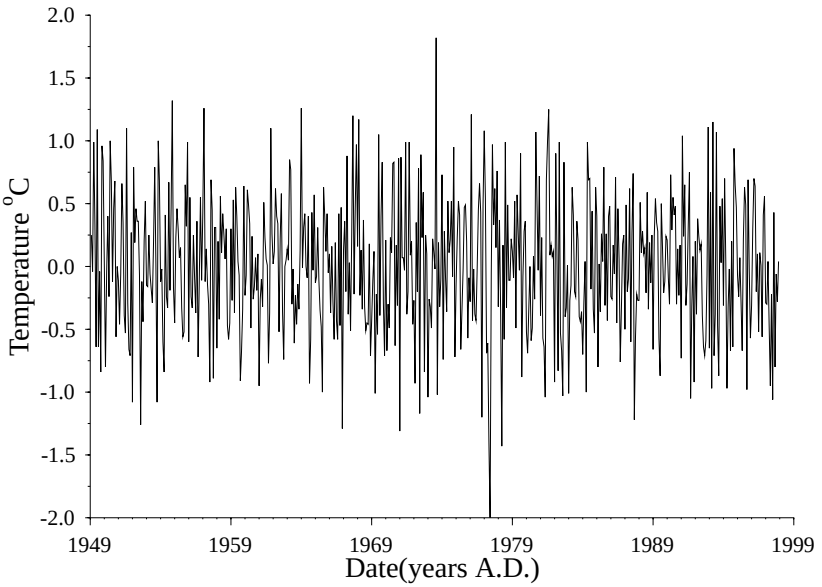

Figure 11.15: Combined noise terms from the annual trend series and the monthly series

However, any other structure could be applied.

As an example of this breakdown, the combined stochastic component of $T(x)$ for the A64971 monthly 30cm temperature series is plotted in Figure 11.16. In this example $\sigma_\epsilon^2 = 0.77$ and the distribution of ϵ (Figure 11.17) can be treated as normal on the basis of a 1-sample Kolmogorov-Smirnov test for normality of the stochastic data from the 30cm soil temperature data. This result is in accordance with the discussion that has been developed to this point, and illustrates that for the purposes of estimating EHT values the distribution for T given in Equation 11.13 is suitable. Thus the model of soil temperature series for the purposes of predicting EHT values can be very simple, only requiring the parameters to describe the two components given in Equation 11.13. As an example these two components are plotted in Figure 11.18 which breaks $T(x)$ for the A64971 monthly mean 30cm soil temperature data down into the stochastic and deterministic components.

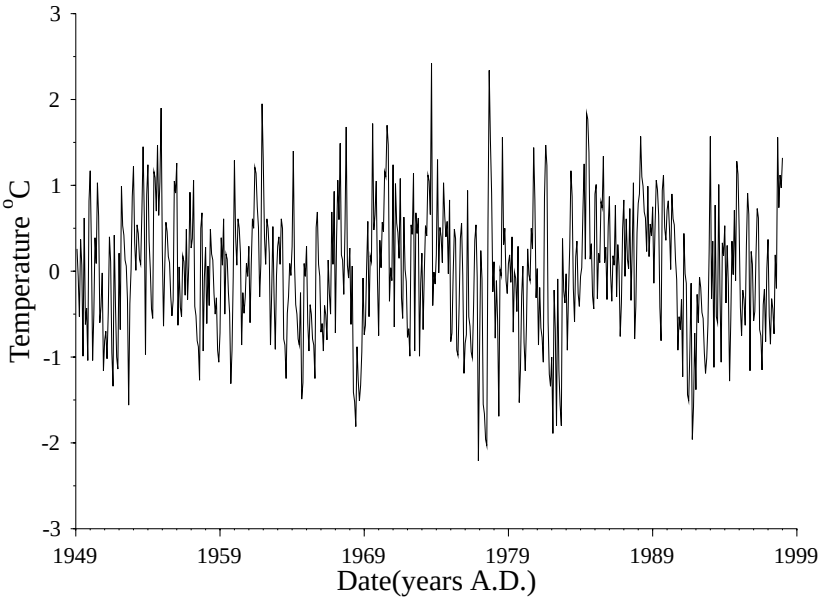

Figure 11.16: Full stochastic component of the 30cm monthly soil temperature data

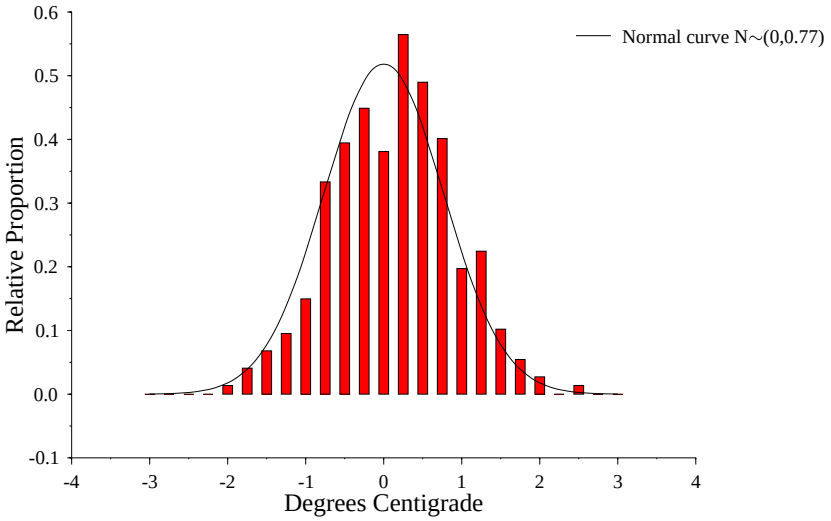

Figure 11.17: Histogram of the stochastic data from the 30cm monthly soil temperature data

Table 11.7: 1-sample Kolmogorov-Smirnov test for normality of the stochastic data from the 30cm soil temperature data

N		588
Normal Parameters[a,b]	Mean	0.001700681
	Std. Deviation	0.770789504
Most Extreme Differences	Absolute	0.025209757
	Positive	0.01707023
	Negative	-0.025209757
Kolmogorov-Smirnov Z		0.611304104
Asymp. Sig. (2-tailed)		0.848970354

[a]Test distribution is Normal.

[b]Calculated from data.

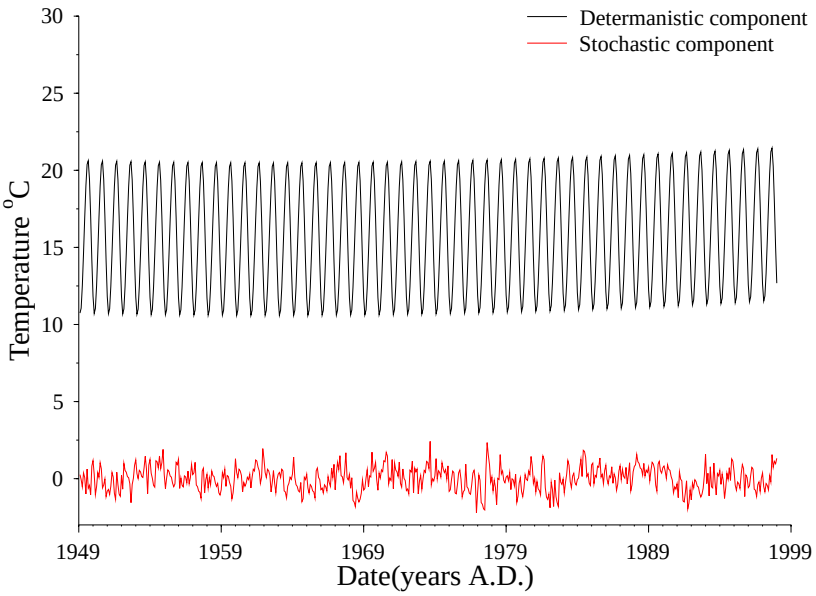

Figure 11.18: Break down of $T(x)$ (Figure 11.3) into deterministic and stochastic components

11.3.4 Discussion

In this section we have established that it is possible to use standard time-series analysis techniques to provide fairly simple models that describe the structure of meteorological data. Specifically in this example the average monthly 30cm soil temperature series at station A64971 (Owairaka, Auckland) over the period January 1949 to January 1998. While these models cannot be used to predict the exact time-series that has been observed they can be used to generate time-series that exhibit the same data structure to that observed. Thus these models will be suitable for providing the series $T(x)$ required for estimating EHT after Equation 8.3. The general structure for these models is to break the time series down into three components: 1) a deterministic component which describes regular seasonal patterns and can be used to model factors such as long term temperature changes 2) a stochastic model component which describes the general autocorrelation of deviations from the deterministic model 3) a pure random component which is an independent error term describing the noise in the observation process. We can formulate this as

$$T(x) = f_d(x) + f_s(x) + \epsilon \tag{11.15}$$

where $f_d(x)$ is the deterministic model, $f_s(x)$ is the stochastic model and ϵ is the random noise.

While it is necessary to be able to generate realistic time-series data as input to simulation programmes such as **RADLAB** (*supra vide*:§12.2) the EHT can be calculated directly from the distribution of a meteorological variable rather than requiring its series (*infra vide*:§9.4.1). In this case it is possible to simplify Equation 11.15. This simplification arises from the fact that both $f_s(x)$ and ϵ are normally distributed variables and can thus be combined to generate a single general normally distributed error

term ($\tilde{\epsilon}$),i.e.,

$$\begin{aligned} &\epsilon \sim N\left(0, \sigma_{\epsilon}^2\right) \\ &f_s \sim N\left(0, \sigma_{f_s}^2\right) \\ &\tilde{\epsilon} \sim N\left(0, \sigma_{\tilde{\epsilon}}^2\right) \\ &\text{where} \\ &\sigma_{\tilde{\epsilon}}^2 = \sigma_{f_s}^2 + \sigma_{\epsilon}^2 \end{aligned} \tag{11.16}$$

This reduces Equation 11.15 to

$$T(x) = f_d(x) + \tilde{\epsilon} \tag{11.17}$$

Thus the 30cm soil temperature series plotted in Figure 11.3 can be broken down into the two components given in Figure 11.18.

Therefore, in order to produce a predictive model for EHT using long-term recorded soil temperature data we simply need to be able to produce a spatially indexed model that allows us to predict the parameters of $f_d(x)$ and $\tilde{\epsilon}$. This is considered in the following section.

11.4 Spatial Model

To develop a spatial model for predicting EHT we simply need to be able to predict parameter values for Equation 11.17 on the basis of spatial location. Obviously the precise details of any spatial model will depend upon the exact model for $f_d(x)$. For the current exercise we will adopt the same model structure for $F_d(x)$ that was applied to the 30cm soil temperature series for station A64971 in the previous section. That is we will model $f_d(x)$ as being made up of a long-term trend component ($T_{trend}(x)$) and a deterministic monthly cycle ($T_{stat}(x)$) as given in Equation 11.14. We will use functions of the spatial variables latitude, Longitude and altitude to provide the spatial index. Thus for a spatial model Equation 11.17 becomes:

$$T(x, lat, long, alt) = f_d(x, lat, long, alt) + \tilde{\epsilon} \tag{11.18}$$

Here we will break the deterministic function ($f_d(x, lat, long, alt)$) into spatially indexed trend and monthly functions after Equation 11.14 giving

$$\begin{aligned} T(x, lat, long, alt) &= F_{trend}(x, lat, long, alt) \\ &\quad + F_{month}(x, lat, long, alt) + \tilde{\epsilon} \end{aligned} \tag{11.19}$$

To model the long-term trend function ($F_{trend}(x, lat, long, alt)$) we will use a five term polynomial incorporating the following variables:

Variable	Code
$year(x)$	$year$
$year(x)^2$	$year2$
$year(x)^3$	$year3$
$year(x)^4$	$year4$

Thus $F_{trend}(x, lat, long, alt)$ is modelled as:

$$\begin{aligned} F_{trend}(x, lat, long, alt) = \; & \beta_0^T(lat, long, alt) + \beta_1^T * year \\ & + \beta_2^T * year2 + \beta_3^T * year3 \\ & + \beta_4^T * year4 \end{aligned} \tag{11.20}$$

Hear $\beta_0^T(lat, long, alt)$ relates to the mean temperature value at any given location, which would be expected to vary spatially. The terms β_1^T–β_4^T relate to the long-term trend. This is regarded as being global, thus will not vary spatially. Therefore for the long-term trend component we only need to model the spatial variation in parameter value for $\beta_0^T(lat, long, alt)$.

To model the deterministic monthly cycle function ($F_{month}(x, lat, long, alt)$) we will use the first two terms of the sine wave series given in Equation 11.4. This requires the following variables:

Table 11.8: Meteorological variables included in the long-term data-set

Variable	Code
$\sin\left(\frac{2\pi month(x)}{12}\right)$	sm
$\cos\left(\frac{2\pi month(x)}{12}\right)$	cm
$\sin\left(\frac{4\pi month(x)}{12}\right)$	$sm2$
$\cos\left(\frac{4\pi month(x)}{12}\right)$	$cm2$

And $F_{month}(x, lat, long, alt)$ is modelled as:

$$\begin{aligned} F_{month}(x, lat, long, alt) = \; & \beta_1^S(lat, long, alt) * sm \\ & + \beta_2^S(lat, long, alt) * cm \\ & + \beta_3^S(lat, long, alt) * sm2 \\ & + \beta_4^S(lat, long, alt) * cm2 \end{aligned} \tag{11.21}$$

This follows the monthly model applied to the A64971 30cm soil temperature in the previous section. We would expect that the amplitude and phase of this deterministic monthly cycle would vary spatially. Thus the values of all four parameters for this function ($\beta_1^S(lat, long, alt)$ – $\beta_4^S(lat, long, alt)$) would be expected to vary spatially.

11.4.1 Spatial Variables

To model the spatial variation a simple trend surface will be used, based around the longitude, latitude and altitude of the geographical position. We will use a cubic model for these three variables and additionally on the basis of the theory outlined earlier (*infra vide*:§8) we would expect the surface energy balance to vary approximately according to the sin of latitude (to incorporate variation in the phase of the sine wave we introduce both the sin and cos of latitude as variables) and the variables $\sqrt{altitude}$ & $\exp(altitude)$. Thus we define the following variables to

describe a basic trend surface for New Zealand.

Table 11.9: Meteorological variables included in the long-term data-set

Variable	Code
$latitude$	lat
$latitude^2$	$lat2$
$latitude^3$	$lat3$
$\cos(2\pi latitude/90)$	$clat$
$\sin(2\pi latitude/90)$	$slat$
$longtitude$	$long$
$lontitude^2$	$long2$
$longtitude^3$	$long3$
$altitude$	$altitude$
$altitude^2$	$alt2$
$altitude^3$	$alt3$
$\sqrt{altitude}$	$alt12$
$\exp altitude$	$expalt$

We will add additional structure to this surface by including 2-way interactions of the cubic terms for latitude and longitude. On the basis of the theory outlined earlier we might expect that the effects of altitude may vary with latitude so the interactions of the latitude and longitude variables are included. Any interactions between longitude and altitude are likely to be influenced by the latitude so the 3-way interactions between altitude, latitude and longitude are also included along with a term for the interaction between longitude and altitude.

Table 11.10: Meteorological variables included in the long-term data-set

Variable	Code
$latitude * longitude$	$latlong$
$latitude * longitude^2$	$latlong2$
$latitude * longitude^3$	$latlong3$
$latitude^2 * longitude$	$lat2long$
$latitude^2 * longitude^2$	$lat2lon2$
$latitude^2 * longitude^3$	$lat2lon3$
$latitude^3 * longitude$	$lat3long$
$latitude^3 * longitude^2$	$lat3lon2$
$latitude^3 * longitude^3$	$lat3lon3$
$altitude * longitude$	$altlong$
$altitude * latitude$	$altlat$
$altitude * latitude^2$	$altlat2$
$altitude * latitude^3$	$altlat3$
$altitude * slat$	$altslat$
$altitude^2 * slat$	$alt2slat$
$altitude^3 * slat$	$alt3slat$
$altitude * latitude * longitude$	$altlatlo$
$altitude^2 * latitude * longitude$	$alt2ll$
$altitude^3 * latitude * longitude$	$alt3ll$

The variables outlined in Tables 11.9 & 11.10 above provide a basic spatial index and we model $\beta_0^T(lat, long, alt)$ as,

$$\begin{aligned}\beta_0^T(lat, long, alt) = \\ &\beta_1 lat + \beta_2 lat2 + \beta_3 lat3 + \beta_4 clat + \beta_5 slat \\ &+\beta_6 long + \beta_7 long2 + \beta_8 long3 + \beta_9 alt + \beta_{10} alt2 \\ &+\beta_{11} alt3 + \beta_{12} alt12 + \beta_{13} expalt + \beta_{14} latlong\end{aligned}$$

$$
\begin{aligned}
&+\beta_{15} latlong2 + \beta_{16} latlong3 + \beta_{17} lat2long + \beta_{18} lat2lon2 + \\
&\beta_{19} lat2lon3 + \beta_{20} lat3long + \beta_{21} lat3lon2 + \beta_{22} lat3lon3 \\
&+\beta_{23} altlong + \beta_{24} altlat + \beta_{25} altlat2 + \beta_{26} altlat3 \\
&+\beta_{27} altslat + \beta_{28} alt2slat + \beta_{29} alt3slat \\
&+\beta_{30} altlatlo + \beta_{31} alt2ll + \beta_{32} alt3ll
\end{aligned} \tag{11.22}
$$

In order to model the spatial variation of the parameters $\beta_1^S(lat, long, alt)$ – $\beta_4^S(lat, long, alt)$ we cross the effects defined in Table 11.8 with many of the spatial variables defined in Tables 11.9 & 11.10. A full spatial model will only be applied to the first term of the sine series with the second term simply being crossed with latitude and altitude. This generates the following set of variables

Variable	Code
$latitude * sm$	$latsm$
$latitude * sm2$	$latsm2$
$latitude * cm$	$latcm$
$latitude * cm2$	$latcm2$
$latitude^2 * sm$	$smlat2$
$latitude^3 * sm$	$smlat3$
$latitude^2 * cm$	$cmlat2$
$latitude^3 * cm$	$cmlat3$
$cm * slat$	$cmslat$
$cm * clat$	$cmclat$
$sm * clat$	$smclat$
$sm * slat$	$smslat$
$longtitude * sm$	$longsm$
$longtitude * sm2$	$longsm2$
$longtitude * cm$	$longcm$
$longtitude * cm2$	$longcm2$
$longtitude^2 * sm$	$smlon2$

continued on the next page

Table 11.11: *continued*

Variable	Code
$longtitude^3 * sm$	$smlon3$
$longtitude^2 * cm$	$cmlon2$
$longtitude^3 * cm$	$cmlon3$
$sm * latitude * longtitude$	$smlatlon$
$cm * latitude * longtitude$	$cmlatlon$
$cm * latitude^2 * longtitude^2$	$cml2l2$
$sm * latitude^2 * longtitude^2$	$sml2l2$
$sm * altitude$	$smalt$
$sm * altitude^2$	$smalt2$
$sm * altitude^3$	$smalt3$
$cm * altitude$	$cmalt$
$cm * altitude^2$	$cmalt2$
$cm * altitude^3$	$cmalt3$
$cm * altitude * longtitude$	$cmaltlon$
$sm * altitude * longtitude$	$smaltlon$
$sm * altitude * latitude$	$smaltlat$
$cm * altitude * latitude$	$cmaltlat$
$cm * altitude * latitude^2$	$cmaltlt2$
$sm * altitude * latitude^2$	$smaltlt2$
$sm * altitude * slat$	$smaltslt$
$cm * altitude * slat$	$cmaltslt$
$cm * altitude * latitude * longtitude$	$cmalll$
$sm * altitude * latitude * longtitude$	$smalll$
$sm * altitude^2 * latitude * longtitude$	$sma2ll$
$cm * altitude^2 * latitude * longtitude$	$cma2ll$
$cm * altitude^3 * latitude * longtitude$	$cma3ll$
$sm * altitude^3 * latitude * longtitude$	$sma3ll$

Following this we model $\beta_1^S(lat, long, alt)$ and $\beta_2^S(lat, long, alt)$ as

$$\begin{aligned}\beta_{1(or2)}^S(lat, long, alt) = \\ &\beta_0 + \beta_1 lat + \beta_2 lat2 + \beta_3 lat3 + \beta_4 clat + \beta_5 slat \\ &+\beta_6 long + \beta_7 lon2 + \beta_8 lon3 + \beta_9 latlon + \beta_{10} l2l2 \\ &+\beta_{11} alt + \beta_{12} alt2 + \beta_{13} alt3 + \beta_{14} altlon + \beta_{15} altlat \\ &+\beta_{16} altlt2 + \beta_{17} altslt + \beta_{18} alll + \beta_{19} a2ll + \beta_{20} a3ll \end{aligned} \quad (11.23)$$

And $\beta_3^S(lat, long, alt)$ and $\beta_4^S(lat, long, alt)$ as

$$\beta_{3(or4)}^S(lat, long, alt) = \beta_0 + \beta_1 lat + \beta_2 long \quad (11.24)$$

By substituting the functions defined for $\beta_0^T(lat, long, alt)$ & $\beta_1^S(lat, long, alt)$–$\beta_4^S(lat, long, alt)$ in Equations 11.22, 11.23 and 11.24 into Equation 11.19 we have a fully defined spatial model for $T(x, lat, long, alt)$.

11.4.2 Fitted Model

In order to establish the parameter values for the full spatially indexed model it is a simple matter of fitting Equation 11.19 to the data via a linear regression. The predicted component of the regression model corresponds to f_d and the residuals correspond to $\tilde{\epsilon}$. In practice not all of the model variables may be significant, so the model fit is probably best carried out through a stepwise regression.

The available data-set contains soil temperature readings from 5cm, 10cm, 20cm, 30cm, 50cm and 100cm depths, and an analysis has been carried out to establish the parameter values for Equation 11.19 at all of these depths. From this we can predict a distribution for $T(x)$ at any given location (indexed by longitude, latitude and altitude) in New Zealand. In the following section the model fit for the 30cm data will be presented as an example of the analysis and summary results of model fitting for all depths is then presented.

The locations for which 30cm mean monthly soil temperature data have been collated are plotted in Figure 11.19. Equation 11.19 was fitted to

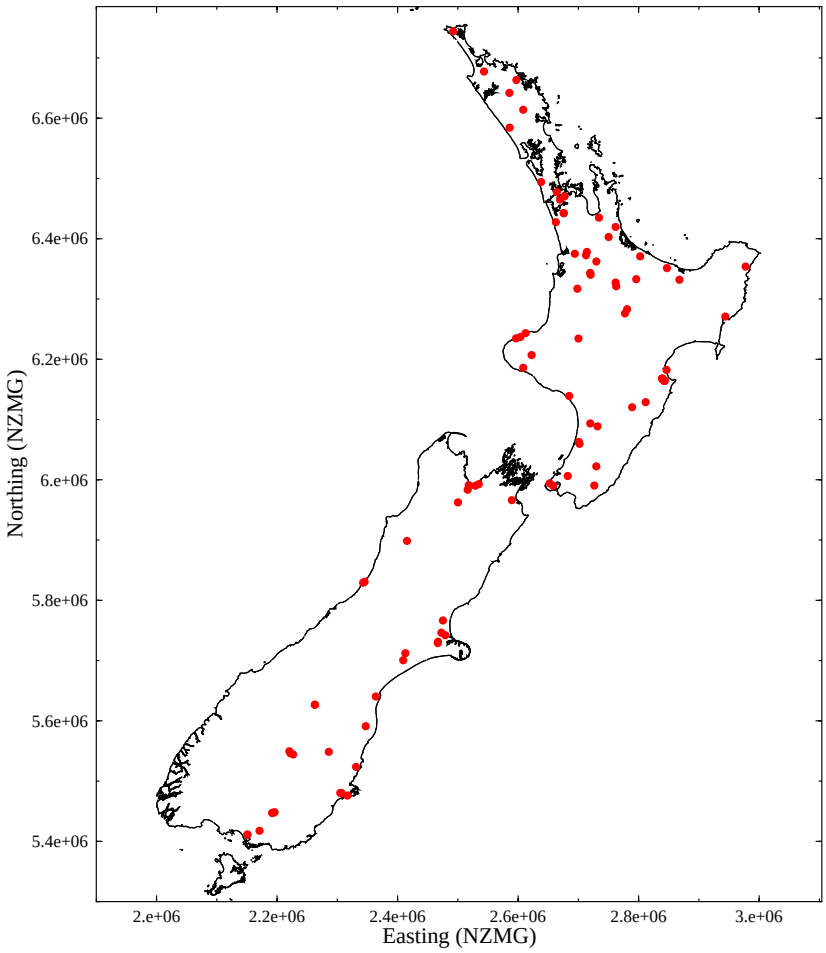

Figure 11.19: Locations for which 30cm mean monthly soil temperature data have been collated

the data from these locations via a stepwise regression and the model fit statistics are presented in Table 11.12. These show that the fitted model is significant (Pval. = 0.00) and explains around 95 % of the variation in the data. That is f_d explains around 95 % of $T(x)$ with $\tilde{\epsilon}$ explaining the remaining 5 % of $T(x)$. From the model coefficients given in Table F.5 we

Table 11.12: Regression statistics for the fit of Equation 11.19 to the mean monthly 30cm soil temperature data

ANOVA	Sum of Squares	df	Mean Square	F	Sig.
Regression	727817.4331	22	33082.61059	28745.53573	0
Residual	39002.11152	33889	1.150878206		
Total	766819.5446	33911			

R	R Square	Adjusted R Square	Std. Error of the Estimate
0.974237047	0.949137823	0.949104804	1.072789917

can model the distribution for 30 cm soil temperatures in New Zealand as

$$\begin{aligned} T(x) = \; & -6.29E+00(Constant) + 2.94E-02ALT12 - 2.54E-05ALT2SLAT \\ & -5.20E-06ALTLATLO - 2.63E-04ALTLONG + 1.66E+00CM \\ & +8.49E-11CMA3LL + 6.41E-03CMALT + 6.36E-07CMALT3 \\ & +3.42E-02CMALTSLT - 2.67E+00CMCLAT + 1.52E-07CML2L2 \\ & -4.19E-03CMLAT2 + 9.03E-03LATCM2 - 3.85E-01LATITUDE \\ & -1.51E+01SLAT + 2.01E+00SM + 2.95E-11SMA3LL \\ & +2.23E-07SMALT3 + 1.17E-06SMALTLT2 + 1.06E-02SMALTSLT \\ & -3.15E+00SMCLAT + 1.85E-05SMLAT3 + \tilde{\epsilon} \end{aligned} \tag{11.25}$$

Where $\tilde{\epsilon} \sim N(0, 1.07)$ (from Table 11.13).

At this stage it is useful to clarify the meaning of $\tilde{\epsilon}$ actually means. Clearly the magnitude of variation for $\tilde{\epsilon}$ is greater than that for the variation at any given location (See the Deviations given in Table 11.13), so there is some form of variance inflation that has taken place. Also we have no spatial model for $\tilde{\epsilon}$ so we are stating that $\tilde{\epsilon}$ is identical for all locations, is this valid?

Table 11.13: Residual stats for 30cm soil temperatures fitted model

STATION	Mean	Std. Deviation	Median	Range	Minimum	Maximum	N
A42581	0.34	0.97	0.43	5.39	-2.34	3.05	458
A53021	-0.50	0.71	-0.56	4.09	-2.65	1.44	285
A53291	-0.10	0.91	-0.08	6.35	-3.70	2.65	323
A53482	-0.25	1.08	-0.39	5.65	-2.45	3.20	158
A53982	-0.80	0.88	-0.75	5.58	-3.33	2.25	534
A54601	-0.17	0.91	-0.33	5.62	-2.33	3.29	121
A64741	0.39	0.89	0.32	5.01	-2.10	2.90	549
A64971	0.11	0.92	0.18	6.19	-2.43	3.75	593

continued on the next page

Table 11.13: *continued*

STATION	Mean	Std. Deviation	Median	Range	Minimum	Maximum	N
B75252	0.07	0.81	0.08	3.92	-1.80	2.12	100
B75381	-0.43	0.90	-0.37	5.07	-2.91	2.16	398
B75571	1.69	0.85	1.70	5.05	-0.76	4.30	664
B76835	0.44	0.93	0.34	5.04	-2.02	3.02	199
B76984	0.02	0.83	-0.01	4.06	-2.32	1.75	162
B85284	-1.29	0.57	-1.39	1.97	-2.29	-0.32	16
B85285	-0.61	1.12	-0.51	5.37	-3.31	2.06	255
B86124	0.99	0.96	1.08	4.99	-1.28	3.72	366
B86602	0.08	0.94	0.03	5.65	-2.63	3.03	529
B86612	0.02	0.90	-0.07	5.01	-2.44	2.57	303
B87103	-0.16	0.92	-0.12	4.53	-2.24	2.29	357
C64981	-0.38	0.84	-0.19	4.56	-2.75	1.81	415
C74082	0.01	0.87	0.14	4.87	-2.98	1.89	316
C74282	-0.10	0.76	-0.11	4.24	-2.21	2.03	217
C74283	0.34	0.99	0.42	4.03	-1.56	2.47	106
C74371	0.42	0.88	0.50	5.45	-2.95	2.50	647
C75731	-0.71	0.82	-0.65	5.20	-3.65	1.55	607
C75801	-0.01	0.75	-0.04	5.24	-2.76	2.48	427
C75831	-0.23	0.85	-0.17	5.53	-3.17	2.36	454
C75953	-0.25	0.95	-0.14	5.89	-3.04	2.85	180
C85132	0.05	1.25	0.01	6.69	-3.24	3.45	260
C85141	-0.47	0.84	-0.34	4.57	-2.54	2.03	232
C85314	0.22	0.83	0.22	5.03	-2.24	2.79	444
C94002	1.02	0.89	1.17	5.15	-1.94	3.21	216
C94003	0.13	0.88	-0.11	3.13	-0.93	2.20	14
C94011	-0.38	1.15	-0.38	7.52	-4.37	3.15	574
C95022	0.07	1.00	0.13	4.73	-2.23	2.50	90
D05964	-0.07	0.87	0.06	5.22	-2.81	2.41	576
D06022	0.22	0.83	0.33	4.59	-2.18	2.40	436
D06051	-0.18	0.88	-0.31	5.05	-2.94	2.11	594
D15253	-0.07	0.91	-0.15	4.90	-2.80	2.09	80
D78931	0.22	1.07	0.12	5.92	-2.34	3.57	434
D87692	-0.42	0.96	-0.49	7.00	-3.02	3.98	668
D96591	0.46	0.87	0.44	5.72	-2.26	3.46	766
D96680	0.14	1.04	-0.05	4.53	-1.58	2.95	99
D96681	-0.02	1.26	-0.06	9.08	-3.14	5.94	464
D96688	-0.02	1.13	-0.07	6.00	-2.48	3.52	192
D96689	-0.38	0.90	-0.42	5.62	-3.12	2.49	394
D9668A	-0.21	1.14	-0.42	5.02	-2.14	2.88	85
D9668B	-0.71	1.04	-0.87	5.01	-3.43	1.58	89
E05343	-0.16	1.03	-0.17	5.26	-3.02	2.24	249
E05363	-0.35	1.11	-0.37	6.39	-3.80	2.59	840
E05620	-0.07	1.24	-0.11	4.94	-2.47	2.47	19
E05622	0.38	0.95	0.50	6.68	-3.15	3.53	502
E14272	0.21	0.94	0.31	5.91	-2.61	3.31	852
E14273	-0.51	1.38	-0.48	7.10	-4.01	3.09	244
E15102	-0.17	1.01	-0.07	6.18	-3.24	2.94	709
E94333	-0.38	0.97	-0.30	6.25	-3.46	2.79	451
E94512	-0.41	0.92	-0.31	6.00	-3.36	2.64	371
E95902	-0.05	0.98	-0.03	6.04	-3.17	2.86	702
F20791	-0.24	0.89	-0.30	4.88	-2.98	1.90	236
F20793	0.07	0.91	0.10	6.00	-3.29	2.71	422
F21182	0.09	0.91	0.04	5.42	-2.99	2.43	423
G12581	-0.29	0.97	-0.36	5.44	-2.99	2.44	363
G13211	-0.02	0.98	0.00	6.53	-3.00	3.53	779
G13212	0.70	0.82	0.82	3.29	-0.60	2.70	26
G13222	-0.27	0.84	-0.22	5.00	-3.02	1.98	529
G13231	-0.02	0.91	-0.01	6.17	-2.65	3.52	372
G13301	0.41	1.06	0.38	6.31	-1.92	4.40	310
G13592	-0.01	0.93	0.00	5.39	-2.34	3.05	451
H31883	-0.20	0.87	-0.27	5.28	-2.72	2.56	555

continued on the next page

Table 11.13: *continued*

STATION	Mean	Std. Deviation	Median	Range	Minimum	Maximum	N
H31971	0.14	1.06	0.18	6.83	-2.55	4.28	627
H32352	0.37	1.03	0.35	6.12	-2.10	4.02	400
H32451	-0.02	1.01	-0.05	5.84	-2.74	3.11	426
H32561	0.47	1.42	0.34	8.07	-2.72	5.34	747
H32641	-0.30	0.97	-0.54	6.38	-3.30	3.09	527
H32642	-0.53	0.95	-0.56	6.00	-2.82	3.18	136
H40892	0.06	0.74	0.11	4.42	-2.20	2.21	270
H41411	-0.21	0.92	-0.12	6.00	-3.45	2.55	416
I49591	0.33	1.15	0.33	7.84	-3.66	4.18	433
I49592	0.10	0.88	0.18	4.13	-1.81	2.33	100
I50212	-0.29	1.14	-0.22	6.47	-3.39	3.08	437
I50471	-0.18	0.81	-0.35	4.51	-2.47	2.04	358
I50831	-0.29	0.89	-0.24	6.24	-3.93	2.31	387
I50835	-0.19	0.92	-0.18	4.24	-2.40	1.83	116
I50836	-0.60	1.16	-0.38	5.38	-3.41	1.97	94
I50951	0.50	0.79	0.61	4.86	-1.76	3.10	156
I59232	-0.17	1.36	-0.18	6.59	-3.47	3.12	432
I59234	0.59	1.37	0.66	7.86	-2.63	5.23	572
I59239	1.19	2.22	0.55	9.40	-3.31	6.09	30
I68182	-1.05	1.55	-0.95	9.00	-6.99	2.01	131
I68191	-0.02	1.05	0.09	6.43	-3.41	3.02	341
I68192	-0.16	1.22	0.01	5.60	-3.41	2.19	184
I68362	0.56	0.89	0.71	5.61	-2.89	2.71	166
I68433	0.03	0.95	-0.09	5.41	-2.50	2.91	575
Total	0.00	1.07	0.00	13.08	-6.99	6.09	33912

The observed variance inflation is due to stochastic elements associated with the spatial model that were not considered in the initial discussion of the single A64971 temperature series given in §11.3. For example, consider the mean of the residuals by location given in Table 11.13. The mean values for the residuals by location vary significantly from zero. This is to be expected, as the spatial model used is too simple to fit the real spatial structure. This means that the true constant value will either be under or overestimated by the model, thus we would expect the true mean to be randomly offset from the modelled mean. An additional source of variation will be due to variation in the soil thermal properties. The model that has been applied assumes that the soil thermal properties are the same at all locations. In reality there will be a random spatial variation due to this variable. Both of these variance terms will be incorporated within $\tilde{\epsilon}$. Hence $\tilde{\epsilon}$ takes into account spatial variation due to lack of model fit and variation in soil thermal properties, as well as the other stochastic elements discussed previously (§11.3). As we would expect these extra stochastic elements to be spatially random it is suitable to

model them in this manner.

There is no spatial structure to the magnitude of variation for the model residuals given in Table 11.13. Thus even though the magnitude of variation does differ between locations we have no method for establishing the correct magnitude of variation for any given location. This extra element of uncertainty is accounted for in the full $\tilde{\epsilon}$. So we can see that $\tilde{\epsilon}$ derived from the full spatial model acts as we originally intended, representing the random error terms of the estimate for $T(x)$. The only structure we would expect to see in $\tilde{\epsilon}$ is that its value should decrease with depth. This is because we would expect the effects of random climatic events to be less apparent at greater soil depths. This pattern is apparent in the calculated $\tilde{\epsilon}$ values given in Table 11.14 where there is a monotonic decrease in $\tilde{\epsilon}$ values with depth.

In a similar fashion to the analysis of the 30cm soil temperature data that has been considered here we can define the parameters for f_d and $\tilde{\epsilon}$ for soil temperatures at the depths 5cm, 10cm, 20cm, 30cm, 50cm and 100cm. These are presented in Tables F.5 and 11.14, and provide models by which we can estimate absolute EHT values for New Zealand. This calculation is considered in the next section.

Table 11.14: Calculated $\tilde{\epsilon}$ values for Equation 11.19 at different soil depths in New Zealand.

	mean	var	
	std	av	std
5cm	0.381	1.233	0.225
10cm	0.400	1.130	0.188
20cm	0.383	1.021	0.193
30cm	0.444	0.984	0.207
50cm	0.355	0.954	0.202
100cm	0.406	0.846	0.217

11.5 EHT Calculation

Having quantified the parameters for f_d and $\tilde{\epsilon}$ we now need to outline precisely how an EHT may be calculated from the details presented in Tables F.5 and 11.14. Essentially we need to evaluate the integral given in Equation 8.3. While it may be possible to perform this analysis analytically for some models of $T(x)$ the most general scheme is to use some form of numerical integration. Here we will use Monte Carlo integration (see Press *et al.* 1992: 304, for a discussion of this method) as this is easy to implement for the current problem. The general approach to Monte Carlo integration is straightforward. Suppose that we pick N random points, uniformly distributed in a space V; $x_1, \ldots, x_N$ say. Then Monte Carlo integration estimates the integral of the function f over V as

$$\int f dV \approx \frac{V}{N} \sum_{i=1}^{N} f(x_i) \pm V \sqrt{\frac{\sum_{i=1}^{N} f^2(x_i)}{N^2} - \frac{\left(\sum_{i=1}^{N} f(x_i)\right)^2}{N^3}} \qquad (11.26)$$

where the associated error term decreases to insignificance as N gets large.

In terms of the integral from Equation 8.3 the Monte Carlo approximation is

$$\int_{t_1}^{t_2} e^{\frac{-E}{RT(x)}} \approx \frac{t_2 - t_1}{N} \sum_{i=1}^{N} e^{\frac{-E}{Rx_i}} \qquad (11.27)$$

where the x_i are uniformly randomly sampled from within the distribution of $T(x)$ over the interval (t_1, t_2).

The only complication in this calculation is generating suitable samples x_i from within the distribution of $T(x)$. In practice the process is simple. We randomly generate a temperature according to our predictive model. So for the 30 cm model given in Equation 11.25, for example, we would randomly generate a value for month in the interval [0,12] and randomly generate a value for $\tilde{\epsilon}$. From these values we would predict

a soil temperature. As this process repeats we generate a random sample of soil temperatures from $T(x)$ such as that given in Figure 11.20. For each value in this series we calculate an exponential temperature response giving rise to a series such as that given in Figure 11.21. The full

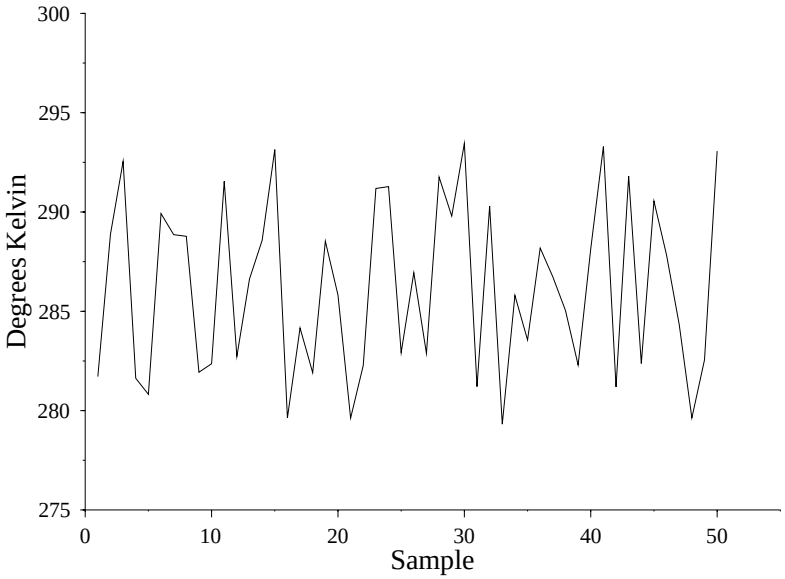

Figure 11.20: Example random temperature series

temperature series that we generate (such as that given in Figure 11.22) has the same distribution as $T(x)$ and thus represent suitable x_i for the purposes of evaluating Equation 11.27.

Through sampling $T(x)$ in this manner we can substitute Equation 11.27 into Equation 8.3 and calculate the EHT as

$$EHT_{(t_1,t_2)} = \frac{-E}{R} \ln \left(\frac{1}{N} \sum_{i=1}^{N} e^{\frac{-E}{RX_i}} \right)^{-1} \tag{11.28}$$

This value has an error term associated with it as defined in Equation 11.26 and that error is not necessarily Gaussian. It would simplify matters if we could ensure that the sample size N is large enough that we can ignore the error term as being insignificant. However, we do not want to

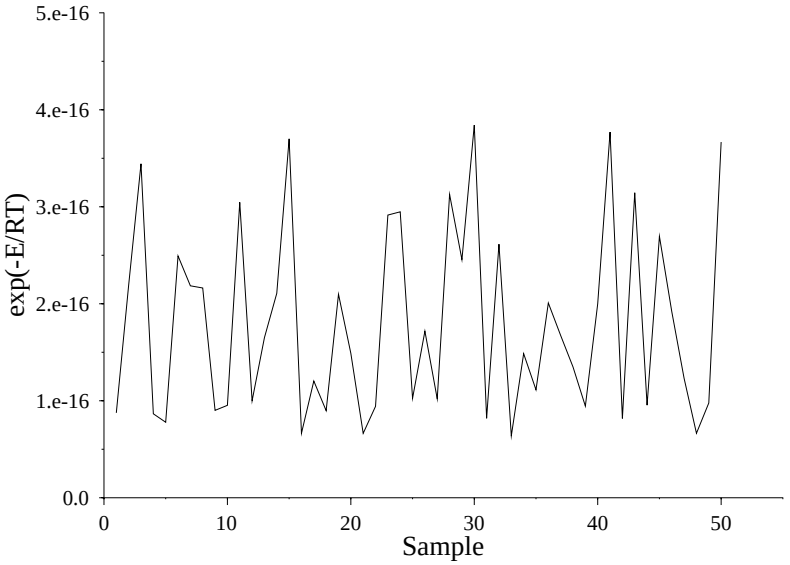

Figure 11.21: Example random exponential temperature series

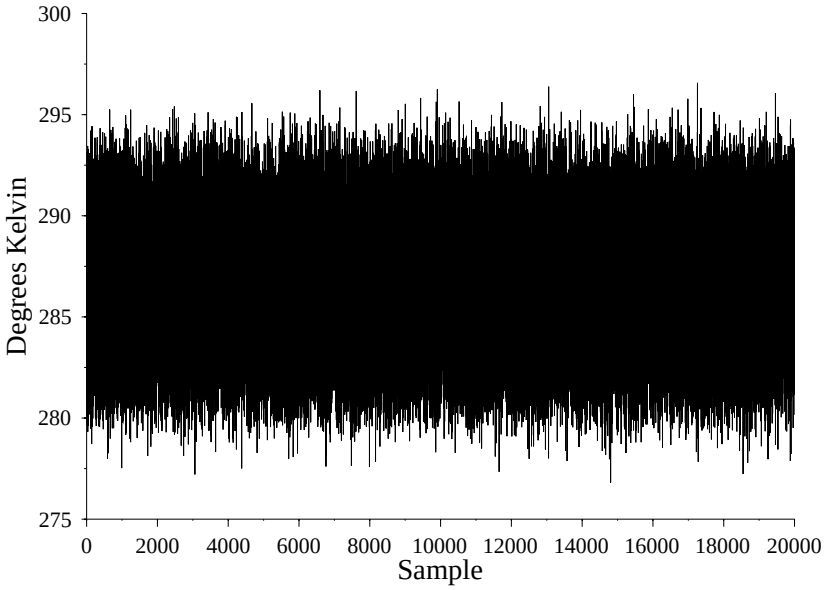

Figure 11.22: Full temperature series with $N = 20000$

set N at too great a figure as this will incur significant computing-time costs. We can evaluate a suitable N through re-arranging Equation 11.26 where the percentage error (at 1σ) of the integral estimate is given by

$$\frac{\frac{1}{N}\sum_{i=1}^{N} f(x_i)}{\sqrt{\frac{\sum_{i=1}^{N} f^2(x_i)}{N^2} - \frac{\left(\sum_{i=1}^{N} f(x_i)\right)^2}{N^3}}} \tag{11.29}$$

Examples of the error magnitude associated with the integral at different sample sizes are given in Table 11.15. From this we can see that for sample sizes $N \geq 10000$ the integral error is largely insignificant. To be conservative we will use a sample size of $N = 50000$ as suitably large to allow us to ignore the integration error. Thus we can calculate an EHT for the model specified in Equation 11.25 after Equation 11.28 using a sample size of $N = 50000$.

Table 11.15: Percentage integration error at 1σ for different sample sizes. Calculation carried out after Equation 11.29 and an example gas activation energy (E) of 86000

N	% integration error at 1σ
10	16.4
100	5.1
1000	1.6
10000	0.5
50000	0.2

However, the EHT estimate calculated through Equation 11.28 is not the end of the story as there is uncertainty associated with the model parameters for the integrated temperature function (see the parameter errors in Table F.5). This means that there is actually a distribution of EHT values that arise from the model given in Equation 11.25. The EHT value calculated through Equation 11.28 is simply a sample from this distribution that depends upon the precise parameter values used in the model.

Our real interest is in reconstructing this distribution. To do this we generate a series of parameter value sets for Equation 11.25 and calculate an EHT value for each of these following Equation 11.28. If the parameter value sets have the same distribution as the model parameters then the distribution of the calculated EHT values will have the correct distribution. As the errors associated with the model parameters values are (assumed to be) Gaussian, we simply need to randomly sample a Gaussian variable for each model parameter (using the appropriate mean and standard deviation given in Table F.5) to generate each parameter value set.

Thus the process is to randomly generate a parameter value set for the model given in Equation 11.25 and then calculate an EHT value after Equation 11.28. As this process repeats we generate a series of EHT values in the same manner as we generated the temperature series previously (an example is given in Figure 11.23). If we sample a large number of these values, such as the plot given in Figure 11.24 the distribution of the series will tend to the same distribution as the EHT calculated by the parameters given in Table F.5. As an example the EHT at 30cm depth for station A64971 following the analysis presented in this section is plotted in Figure 11.25.

11.5.1 Discussion

In this section we have established a simple method for calculating a distribution for an EHT at a range of soil depths on the basis of long-term meteorological data. We have established that we can use a fairly simple Monte Carlo integration scheme to generate EHT estimates for any given model of $T(x)$ and that we can sample from within the model parameter distributions to produce a distribution for the calculated EHT value that reflects the uncertainty in model parameters.

Martin Jones 2002

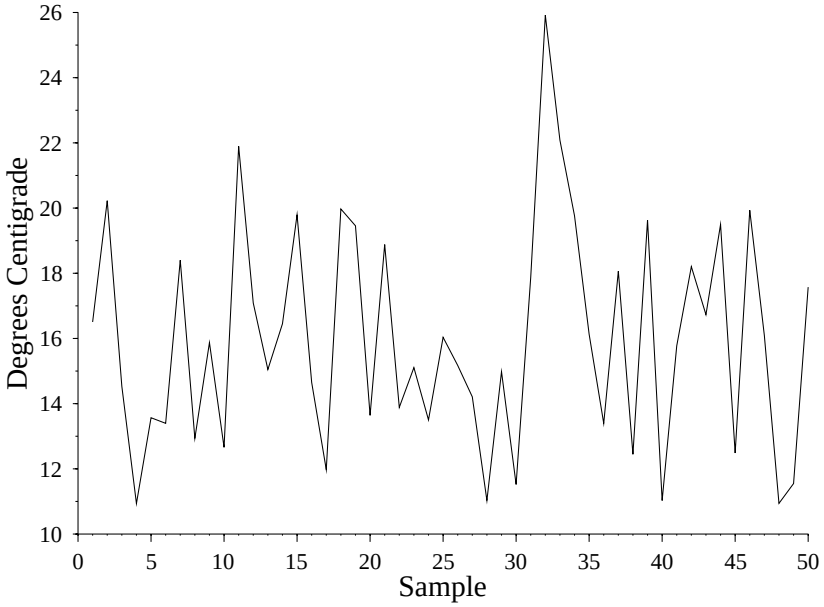

Figure 11.23: Example of a random sample of EHT values

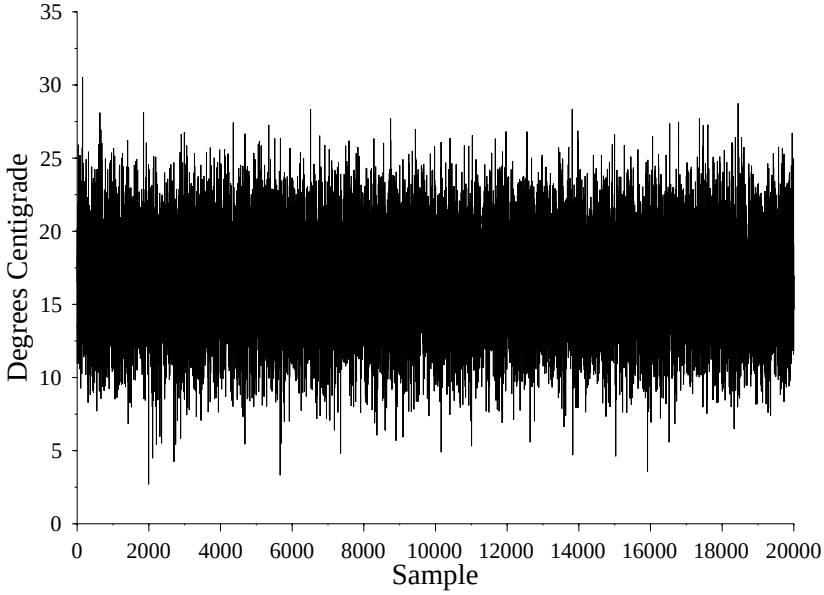

Figure 11.24: A full random EHT sample with $N = 20000$

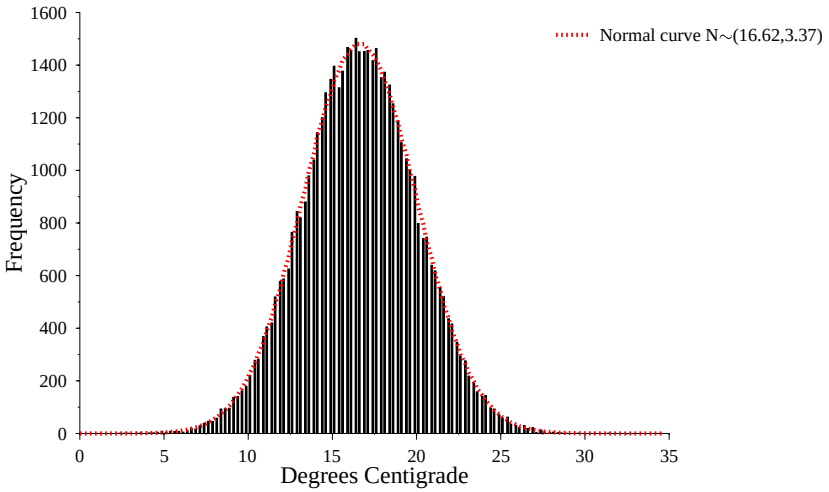

Figure 11.25: Distribution of the sampled EHT values

However, the model that we have used to this point is based exclusively around mean monthly data. Before we employ this EHT estimation approach in real-world applications it is useful to establish whether there are other significant components of $f_d(x)$ or $\tilde{\epsilon}$ that need to be incorporated to take into account daily and hourly temperature variation. This is considered in the following section.

11.6 Additional Model Components

The fact that the estimated EHT values produced through this approach are based around monthly average data needs to be addressed. Clearly there will be other stochastic and deterministic components of the real soil temperature series that operate at daily and hourly frequencies; the daily temperature cycle for example. We need to consider whether it is necessary to take these components into account. This needs to be addressed at the level of establishing whether there will be a significant difference in the calculated EHT distribution.

11.6.1 $\tilde{\epsilon}$ Terms

We would expect that variation occurring at shorter than monthly periods may be a significant source of variation within the soil temperature regime. As the EHT is a mean *exponential* response it is possible that such extra sources of variation may have a significant influence on the calculated EHT. Thus we need to consider the possibility of adding extra terms to $\tilde{\epsilon}$ in order to take these into account. On the basis of the analytic solution to propagation of the soil temperature wave (§8.5.2) we would expect little influence from variation at less than daily periods (see Figure 8.7). Therefore we will make use of the available daily data to make a comparison between the mean monthly and mean daily data to determine if there is a significant variance component that needs to be added to $\tilde{\epsilon}$ arising from temperature variation occurring at shorter than monthly periods.

In order to explore and illustrate this issue we again return to the 30 cm soil temperature series for station A64971. The daily 30cm soil temperature data for the period to is plotted in Figure 11.26. If we fit the same annual temperature function to this data that was calculated for the average monthly data (e.g., Figure 11.27) then the residual standard deviation will arise from the stochastic components considered previously plus that arising from a daily stochastic component. The residual standard deviation for the daily data is 0.85 and can be treated as Normally distributed (1 sample Komologrov-Smirnov z=1.029, pval = 0.24). In contrast the residual standard deviation for the monthly data is 0.49. Thus for this site we would estimate that the standard deviation of the daily stochastic component would equal

$$\sqrt{0.85^2 - 0.49^2} = 0.69$$

Thus this almost doubles the variance of $\tilde{\epsilon}$. In reality the addition of this component only makes a small difference to the total variance of

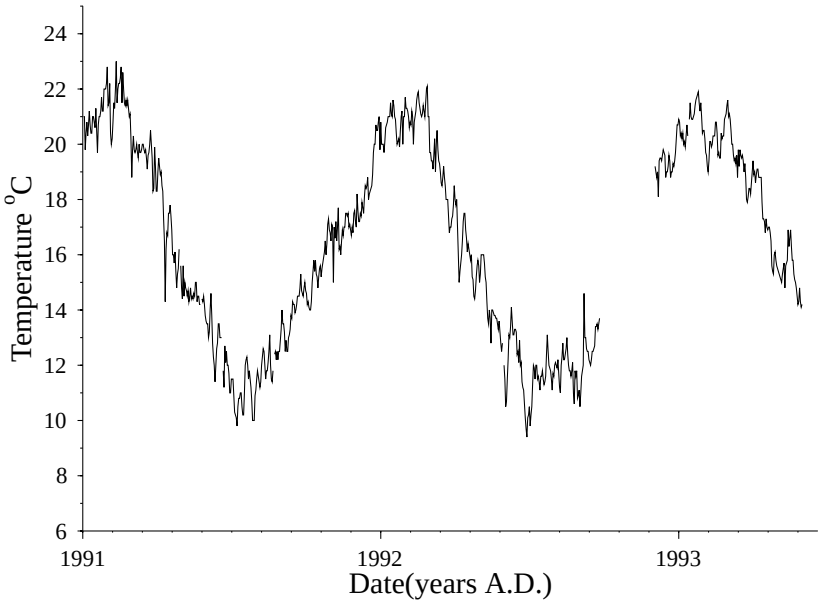

Figure 11.26: Daily 30cm soil temperature data from station A64971 for the period 1/1/1991–31/12/1993

the temperature series (≈ 1%) and we would not expect a large influence on the calculated EHT through addition of a daily stochastic component. However it is useful to address this component as the extra variance will result in a (marginally) higher EHT than might be otherwise calculated. We can calculate the additional variance component required to take account of the daily variation component of $\tilde{\epsilon}$ in a similar manner to that just outlined for A64971. By fitting the monthly model to the daily data we can estimate the variance inflation due to the daily stochastic component by comparing the residual variance observed for the monthly data to that of the daily data. The results of this comparison are presented in Table 11.16 and show that the influence of the daily stochastic component decreases with depth. In fact the decrease observed in the example presented here is approximately an inverse exponential relationship (Figure 11.28) as we would expect from the analytic solution to the propagation of the soil temperature wave given in §8.5.2. Thus the

observed effect matches that which we would predict theoretically. The question is how do we take this variance into account. Following approach that has already been outlined for the calculation of $\tilde{\epsilon}$ (§11.4.2) we could use the daily variance values given in Table 11.16 as empirical values. Another approach would be to predict the variance from the surface variance through an inverse exponential function such as that given in Equation 8.113. However this would require some empirical estimation of the surface variance so would offer no better solution given the data we have available. Thus to incorporate short-term temperature variation into $\tilde{\epsilon}$ for the purposes of calculating an EHT we will simply incorporate a normally distributed variable into $\tilde{\epsilon}$ with a mean of 0 and the appropriate standard deviation from Table 11.16.

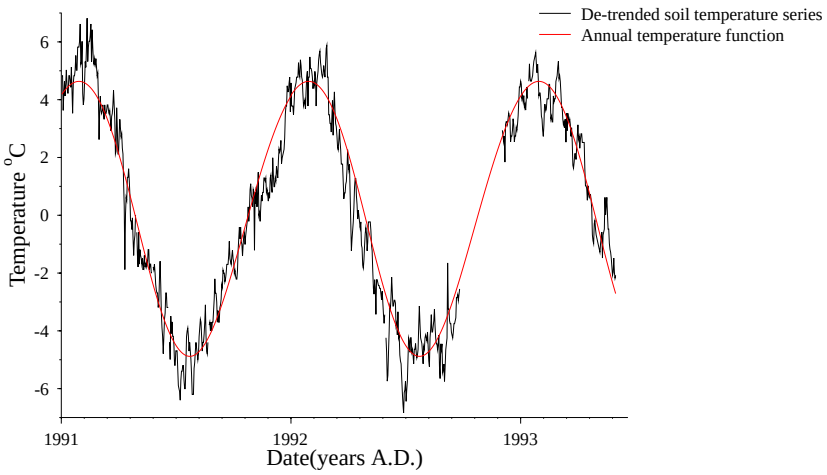

Figure 11.27: Daily 30cm soil temperature data from station A64971 for the period 1/1/1991–31/12/1993 overlayed with the annual temperature function calculated from monthly average data

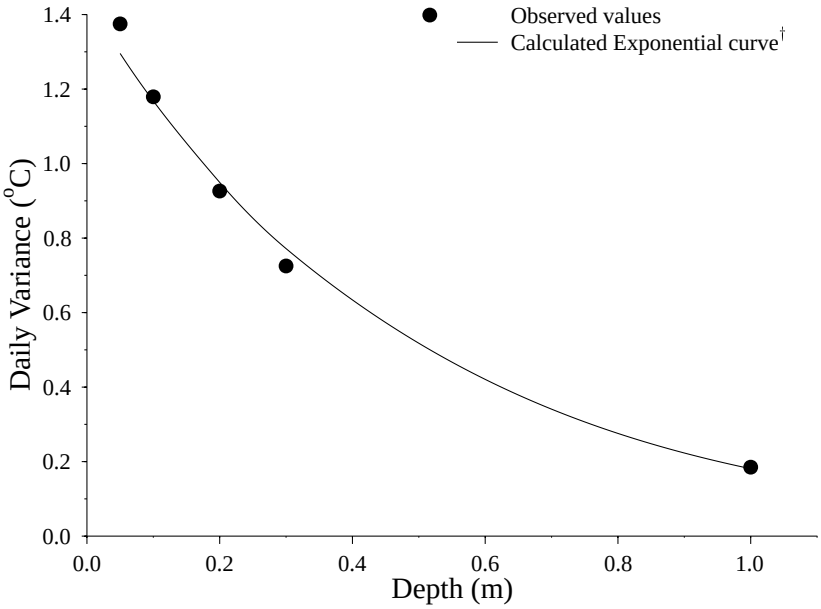

Figure 11.28: Plot of the observed daily variance component of $\tilde{\epsilon}$ against depth.

† calculated as $y = 1.4371e^{-2.0723x}$ for interpretation of this equation see Equation 8.113, $R^2 = 0.9967$

Table 11.16: Comparison between the magnitude of $\tilde{\epsilon}$ using mean monthly and daily data.

Depth	$\sigma^{\flat}$	$\sigma^{\natural}$	$\sigma^{\sharp}$
5	0.744083477	1.562971739	1.374489154
10	0.658043509	1.35	1.178761528
20	0.567732993	1.086011194	0.925796717
30	0.598567118	0.939900929	0.724659342
100	0.332661859	0.3804478	0.184598527

$^{\flat}$ Mean Monthly Data

$^{\natural}$ Daily Data

$^{\sharp}$ Extra variance component for $\tilde{\epsilon}$ calculated from monthly data to take into account the daily variance.

11.6.2 Terms for $f_d(x)$

The function $f_d(x)$ describes the regular deterministic component of the temperature series $T(x)$. Currently we simply model this as comprising the regular seasonal cycle over the twelve months of the year. There are two other deterministic function components we might like to consider; 1) the daily cycle 2) measurement bias. These are considered in the following two sub-sections

The Daily Cycle

In addition to the regular seasonal cycle there is the regular diurnal cycle that we may wish to incorporate within our model. While we know that there is definitely a diurnal cycle, there is a question as to whether it's inclusion in $f_d(x)$ will have a significant effect within the type of model we are currently considering. That is will a diurnal component appreciably alter the modelled distribution of $T(x)$?

We test this through an analysis of the hourly Kumeu data set described

in §11.2. We can compare the residuals from models fitted to this data that do and do not include a component for the diurnal cycle. Of additional interest is a comparison between the residual from the hourly and daily readings for the same data set. In this manner we can further evaluate the discussion regarding short-term variance components for $\tilde{\epsilon}$.

The results of this comparison are summarised in Table 11.17 and Figure 11.29. From this we can see that for depths greater than ≈20cm the addition of a deterministic diurnal component is not significant. Further, for the same depths the daily data gives a reasonable approximation of $\tilde{\epsilon}$ supporting the conclusions drawn in §11.6.1 above. Thus for depths ≳

Table 11.17: Comparison between the magnitude of $\tilde{\epsilon}$ using mean daily and hourly data.

Depth	$\sigma^{\flat}$	$\sigma^{\natural}$	$\sigma^{\sharp}$
2	1.24815281	2.111060029	1.000757839
5	1.04585693	1.609778748	0.892916599
10	0.944189864	1.350803885	0.831262704
20	0.646630914	0.733857759	0.618385638
50	0.288912983	0.293065948	0.283068677
100	0.141729293	0.151082066	0.127212019

$^{\flat}$ hourly data with a diurnal component

$^{\natural}$ hourly data with no diurnal component

$^{\sharp}$ daily data

20cm, the hourly readings modelled with a diurnal component (as given in Figure 11.30) are suitably well approximated by the daily data and the standard monthly model (as given in Figure 11.31) for the Kumeu data. Again this result follows from the theory presented in §8.5.2, which predicts that variations occurring at a period of less than 24 hours are unlikely to give rise to significant temperature variations in the soil body at depths of greater than 20-30 cm (within the range of thermal param-

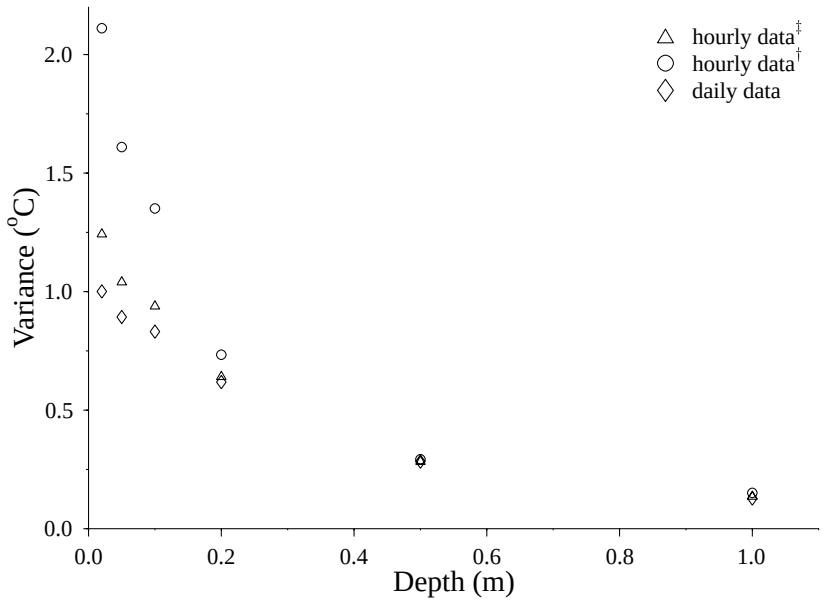

Figure 11.29: Plot of the residuals against depth from fitting a deterministic model based around a simply monthly cycle to the Kumeu soil temperature data presented in §11.2

‡ hourly data with a diurnal component in $f_d(x)$

† hourly data with no diurnal component in $f_d(x)$

eters expected for normal soils). Thus the difficulty arises in modelling

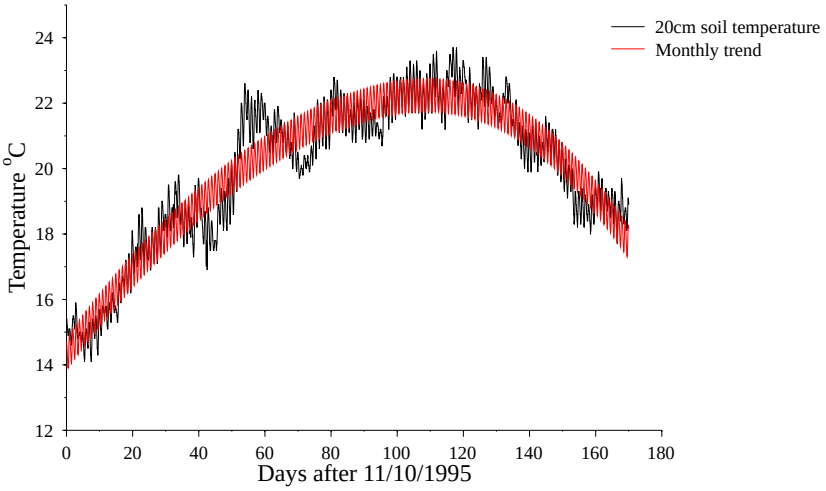

Figure 11.30: hourly soil temperature data from Kumeu at 20cm depth with fitted deterministic model

soil temperatures at shallow depths (i.e., $\lesssim$ 20cm). Clearly the diurnal cycle has an influence at these depths, and short term climatic fluctuations will propagate to these shallow depths. If terms are not included in the model to take these effects into account the calculated EHT will systematically under-estimate the true EHT. Several approaches can be taken to treating this problem:

- we could simply choose not to predict EHT's for depths of less than 20cm. This is probably the simplest solution as a proper treatment of the soil temperature regime needs to be more sophisticated than the current type of modelling approach can realistically deal with. A more detailed treatment can be undertaken through the simulation approach discussed in §12.2 and this is considered again in the following chapter.
- we could include a diurnal component within the model. This can be approximated by damping the diurnal air-temperature cycle af-

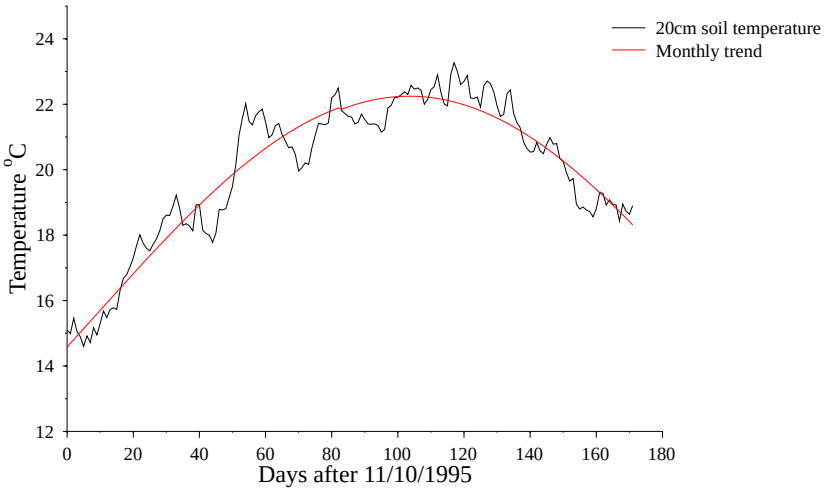

Figure 11.31: Daily soil temperature data from Kumeu at 20cm depth with fitted monthly deterministic model

ter Equation 8.113. However this requires that we can estimate both the diurnal air-wave function and the soil thermal properties for that location.

- we could simply add an empirical error term to take into account the additional variance at shallow depths. In effect this is an extra term for $\tilde{\epsilon}$ in the same manner as discussed previously (§11.3.3,§11.4.2 & §11.6.1).

Here we will add a variance component to $\tilde{\epsilon}$ for EHT estimates at five and ten cm depths. This will be estimated from the residual statistics given in Table 11.17 for the hourly data with no diurnal component compared to the statistics from the analysis of the daily data. Thus we have an extra $\tilde{\epsilon}$ component for the five cm and ten cm model as given in Table 11.18.

Table 11.18: Extra $\tilde{\epsilon}$ components to take account of short term temperature fluctuations at shallow depths

Depth	short-term $\tilde{\epsilon}$ component
5cm	$\sigma = \sqrt{1.6^2 - 0.9^2} = 1.3$
10cm	$\sigma = \sqrt{1.4^2 - 0.8^2} = 1.1$

Measurement Bias

A final consideration regarding the model for $f_d(x)$ is the measurement bias of the recorded meteorological data. The standard meteorological soil temperature data readings contained within the data base that has been considered here (§11.2) are made at 0900 hours. However, it will be appreciated that at this time the diurnal soil temperature wave is unlikely to approximate the mean daily temperature. In fact due to the retarded phase of the propagating air temperature wave (§8.5.2) we would expect that soil temperature readings made at 0900 hours would systematically under-estimate the mean daily soil temperature. This is illustrated in Figures 11.32 & 11.33 which present a simulated diurnal wave for the arbitrary date of 26/3/94. From this simulated data we can see that measurement bias in the order of magnitude of 1-2 ^{0}C may be expected. Clearly the magnitude of the bias will depend upon the amplitude of the diurnal wave, measurement depth and the local soil properties. However we would expect that there will be a general trend for the $f_d(x)$ model presented so far to systematically under-estimate the soil temperature regime. This is confirmed through measured data for the same period presented in Figures 11.34 & 11.35, which again shows that significant measurement bias may be present in the database. There are a number of approaches that we could adopt in order to account for this bias. For the purpose of the current exercise we will estimate an empirical adjustment term for $f_d(x)$ on the basis of recorded temperature cell data. This is considered in §11.8 below.

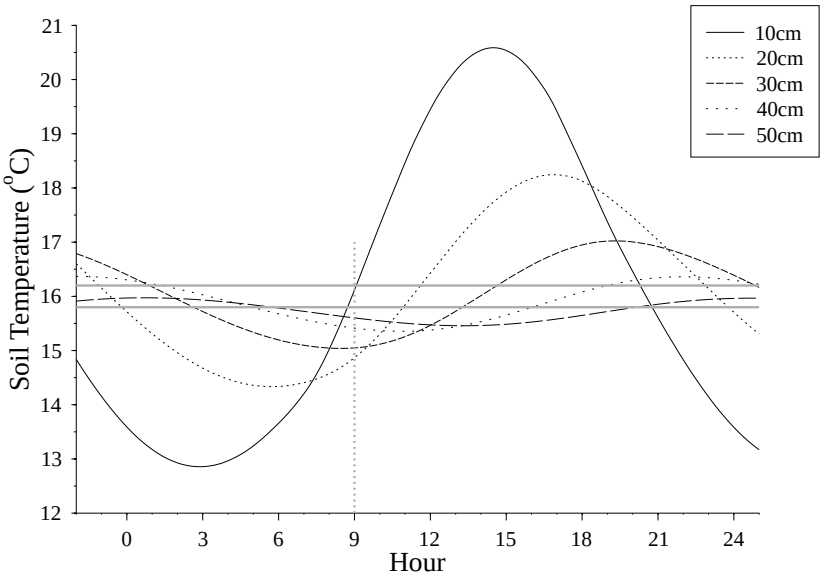

Figure 11.32: Simulated diurnal soil temperature wave for 23/6/1996 using default RADLAB settings

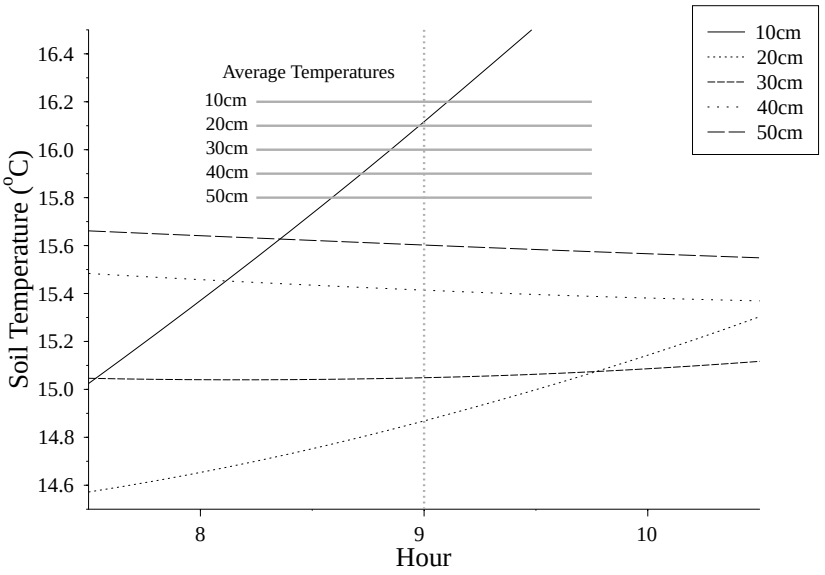

Figure 11.33: enlargement of Figure 11.32 over the standard recording period of 0900 hours

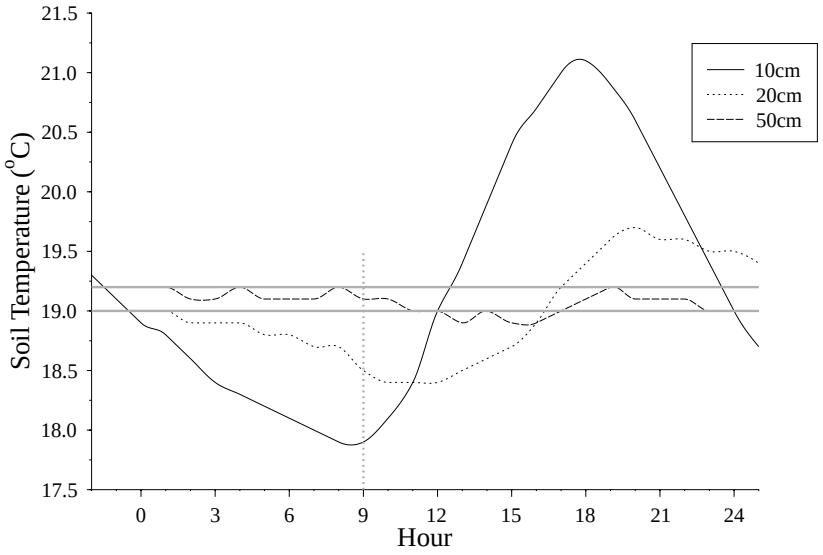

Figure 11.34: Diurnal soil temperature wave for 23/6/1996 from Kumeu hourly data (*infra vide*:§11.2)

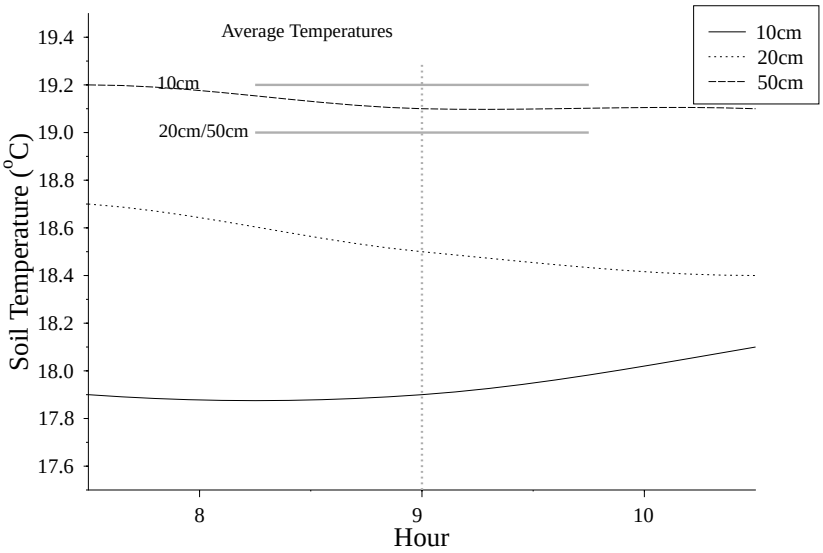

Figure 11.35: Enlargement of Figure 11.34 over the standard recording period of 0900 hours

11.6.3 Summary

Following the discussion in §11.6.1 and §11.6.2 above we can model the distribution for $T(x)$ in New Zealand through the two components $f_d(x)$ and $\tilde{\epsilon}$ after Equation 11.17 where $f_d(x)$ is defined in §11.4.2 and $\tilde{\epsilon}$ is given in Table 11.19 following the figures given in Tables 11.14, 11.16 & 11.18.

Table 11.19: Empirical values for $\tilde{\epsilon}$

Depth	$\tilde{\epsilon}$	
	Mean	σ
5cm	$\sqrt{1.2^2 + 1.3^2 + 1.3^2} = 2.2$	$\sqrt{0.2^2 + 0.4^2} = 0.4$
10cm	$\sqrt{1.1^2 + 1.1^2 + 1.2^2} = 2.0$	$\sqrt{0.2^2 + 0.4^2} = 0.4$
20cm	$\sqrt{1 + 0.9^2} = 1.3$	$\sqrt{0.2^2 + 0.4^2} = 0.4$
30cm	$\sqrt{1 + 0.7^2} = 1.2$	$\sqrt{0.2^2 + 0.4^2} = 0.4$
50cm†	$\sqrt{1 + 0.5^2} = 1.1$	$\sqrt{0.2^2 + 0.4^2} = 0.4$
100cm	$\sqrt{0.8^2 + 0.2^2} = 0.8$	$\sqrt{0.2^2 + 0.4^2} = 0.4$

† The daily error component for $\tilde{\epsilon}$ at 50cm depth is calculated from the function in Figure 11.28.

In the following section code to compute EHT estimates following this model is presented.

11.7 RADLAB Routine

Code to implement calculation of EHT's following the analysis presented in the preceding chapters has been implemented within the **RADLAB** toolkit (*supra vide*:§12.2) through the unit `empirical`. This is selected as a tab within the main **RADLAB** interface (Figure 11.36) where the basic locational parameters can be set.

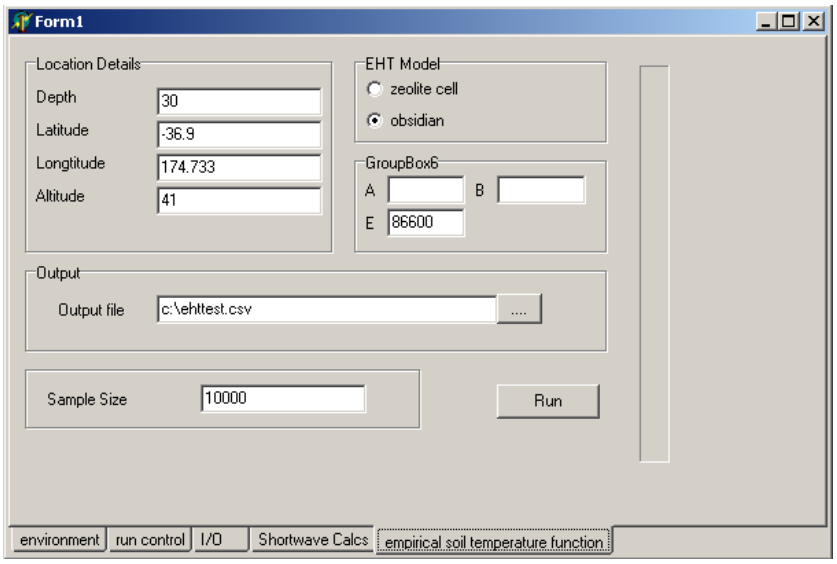

Figure 11.36: **RADLAB** interface to the unit `empirical`

```
 1: unit empirical;
 2:
 3: interface
 4:
 5:  uses sysutils, histutils, math;
 6:
 7:
 8: function initialise : boolean;
 9: procedure run;
10: function EHT : double;
11: function get_temp : double;
12: procedure set_coeffs;
13: procedure random_coeffs;
14: procedure set_det;
15: procedure output_hist;
16: var
17:
18: data : array[1..50000] of double;
19: altitude : single;
20: longtitude : single;
21: latitude : single;
22: depth : single;
23: sample_size : integer;
24: obsidian : boolean;
25: E : single;
```

```
26: A : single;
27: B : single;
28: f_count : integer;
29: out_file : string;
30: output : textfile;
31: ehthist : thist;
32: constant,
33: ALT12   ,
34: ALT2    ,
35: ALT2SLAT    ,
36: ALT3LL  ,
37: ALT3SLAT    ,
38: ALTLAT  ,
39: ALTLATLO    ,
40: ALTLONG ,
41: ALTSLAT ,
42: LAT2LON3    ,
43: LAT3    ,
44: LONG3   ,
45: LAT3LON3    ,
46: LAT3LONG    ,
47: LATLONG ,
48: SLAT    ,
49: CM  ,
50: CM2 ,
51: CMA2LL  ,
52: CMA3LL  ,
53: CMALT   ,
54: CMALT2  ,
55: CMALT3  ,
56: CMALTLON    ,
57: CMALTLT2    ,
58: CMALTSLT    ,
59: CMCLAT  ,
60: CML2L2  ,
61: CMLAT2  ,
62: CMLAT3  ,
63: CMLON3  ,
64: CMSLAT  ,
65: LATCM   ,
66: LATCM2  ,
67: LATSM   ,
68: LATSM2  ,
69: LONGSM  ,
70: LONGSM2 ,
71: SM  ,
72: SM2 ,
```

```
 73: SMA2LL  ,
 74: SMA3LL  ,
 75: SMALLL  ,
 76: SMALT   ,
 77: SMALT3  ,
 78: SMALTLON    ,
 79: SMALTLT2    ,
 80: SMALTSLT    ,
 81: SMCLAT  ,
 82: SML2L2  ,
 83: SMLAT3  ,
 84: SMLON2  ,
 85: SMLON3  ,
 86:         clat : single;
 87: var_val : single;
 88: loc_val : single;
 89:         b0,
 90:         b2,
 91:         b3,
 92:         b4,
 93:         b5,
 94:         b6,
 95:         b7,
 96:         b8,
 97:         b9,
 98:         b10,
 99:         b11,
100:         b12,
101:         b13,
102:         b14,
103:         b15,
104:         b16,
105:         b17,
106:         b18,
107:         b19,
108:         b20,
109:         b21,
110:         b22,
111:         b23,
112:         b24,
113:         b25,
114:         b26,
115:         b27,
116:         b28,
117:         b29,
118:         b30,
119:         b31 : single;
```

```
120:
121:
122: implementation
123: uses main;
124:
125: function initialise : boolean;
126: var
127:         x : integer;
128: begin
129: result := true;
130: try
131: assignfile(output,out_file);
132: rewrite(output);
133: ehthist := thist.create;
134: //set histogram parameters here
135: setlength(ehthist.bin,161);
136: ehthist.n_bins := 160;
137: ehthist.bin_width := 0.25;
138: ehthist.hist_start := -5;
139: for x := 1 to 160 do ehthist.bin[x] := 0;
140: for x := 1 to 50000 do
141:         begin
142:         data[x] := -100;
143:         end;
144: except
145: result := false;
146: closefile(output);
147: end;
148: end;
149:
```

The procedure **run** coded in lines 150-168 is the main calculation routine for the unit **empirical** and follows the discussion of EHT calculation given in §11.5. An estimated EHT distribution is calculated by collection of **sample_size** EHT estimates through a simple loop. At each iteration of the loop an EHT estimate is calculated through a call to the function **EHT** discussed below (coded in lines 170-198). Prior to each call to **EHT** a new state for the model parameter values are randomly selected through a call to the procedure **set_det** (in line 160).

```
150: procedure run;
151: var
```

```
152:         x : integer;
153: begin
154: if initialise then
155:         begin
156:         f_count := 0;
157:         set_coeffs;
158:         for x := 1 to sample_size do
159:                 begin
160:                 set_det;
161:                 data[x] := EHT;
162:                 ehthist.add(data[x]);
163:                 form1.progressbar3.Position := x;
164:                 end;
165:         output_hist;
166:         closefile(output);
167:         end;
168: end;
169:
```

The function **EHT** coded in lines 170-198 below calculates an EHT estimate using the monte carlo integration approach discussed in §11.5. As established in that discussion, 50,000 random samples are used for the integration which is based around generating a uniformly random temperature from within the temperature distribution at the particular location. At each sample step this variable is calculated through a call to the function **get_temp**. Prior to calling **get_temp** a random state for the new temperature value is selected by calling the procedure **random_coeffs**. Two different exponential temperature functions are coded depending upon whether the exponential temperature response of a zeolite cell or that of OHD is being modelled.

```
170: function EHT : double;
171: var
172:         x : integer;
173:         T : double;
174:         int_count : integer;
175: begin
176: inc(f_count);
177: result := 0;
178: int_count := 0;
179: for x := 1 to 50000 do
```

```
180:         begin
181:         random_coeffs;
182:         inc(int_count);
183:         T := get_temp + 273.15;
184:         if obsidian then
185:                 result := result + exp(-1*E/(8.314*T))
186:         else
187:                 result := result + exp((A/T)+B);
188:         if int_count = 1000 then
189:                 begin
190:                 int_count := 0;
191:                 end;
192:         end;
193: if obsidian then
194:         result := -1*E/(8.314*ln(result/50000)) -273.15
195: else
196:         result := A/(ln(result/50000)-B) -273.15;
197:
198: end;
199:
```

The function **get_temp** coded in lines 200–363 below simply calculates the temperature at a given spatial location according to the fitted models presented in Tables F.5 and 11.14 (as discussed in §11.4) and the coefficient values set through the calls to the procedures **random_coeffs** and **set_det** (from the functions **EHT** and **run** respectively). As a first step the depth dependent deterministic component of the model is calculated (lines 203–363) Following this the stochastic component is calculated (line 364–366).

```
200: function get_temp : double;
201: begin
202: // deterministic component first
203: if depth = 5 then
204:         begin
205:         result :=       b0  +
206:                         b2*ALT12   +
207:                         b3*ALT2    +
208:                         b4*ALT2SLAT    +
209:                         b5*ALTLATLO    +
210:                         b6*ALTSLAT +
211:                         b7*CM2 +
```

```
212:                          b8*CMA2LL  +
213:                          b9*CMALT3  +
214:                          b10*CMALTLT2    +
215:                          b11*CMALTSLT    +
216:                          b12*CMCLAT  +
217:                          b13*LAT2LON3    +
218:                          b14*LATCM   +
219:                          b15*LATLONG +
220:                          b16*LATSM2  +
221:                          b17*SMALT   +
222:                          b18*SMLON2;
223:          end
224: else if depth = 10 then
225:          begin
226:          result :=
227:          b0+
228:          b2*ALT12   +
229:          b3*ALT2    +
230:          b4*ALT3LL  +
231:          b5*ALTITUDE    +
232:          b6*ALTLONG +
233:          b7*CM2 +
234:          b8*CMA2LL  +
235:          b9*CMA3LL  +
236:          b10*CMALT   +
237:          b11*CMALTLON    +
238:          b12*CMCLAT  +
239:          b13*CML2L2  +
240:          b14*CMLON3  +
241:          b15*LATCM   +
242:          b16*LATITUDE    +
243:          b17*LONGSM  +
244:          b18*LONGSM2 +
245:          b19*SLAT    +
246:          b20*SM2 +
247:          b21*SMA2LL  +
248:          b22*SMA3LL;
249:          end
250: else if depth = 20 then
251:          begin
252:          result :=
253:          b0+
254:          b2*ALT12   +
255:          b3*ALT2SLAT    +
256:          b4*ALT3LL  +
257:          b5*ALTLAT  +
258:          b6*ALTLONG +
```

```
259:         b7*CMA2LL  +
260:         b8*CMA3LL  +
261:         b9*CMALT   +
262:         b10*CMALT3  +
263:         b11*CMALTSLT    +
264:         b12*CMCLAT  +
265:         b13*CMLON3  +
266:         b14*CMSLAT  +
267:         b15*LAT3LONG    +
268:         b16*LATCM   +
269:         b17*LATCM2  +
270:         b18*LATITUDE    +
271:         b19*LONGSM  +
272:         b20*LONGSM2 +
273:         b21*SLAT    +
274:         b22*SM  +
275:         b23*SM2 +
276:         b24*SMA2LL  +
277:         b25*SMA3LL  +
278:         b26*SMALT  +
279:         b27*SMALT3   +
280:         b28*SMALTSLT;
281:         end
282: else if depth = 30 then
283:         begin
284:         result :=
285:         b0+
286:         b2*ALT12   +
287:         b3*ALT2SLAT    +
288:         b4*ALTLATLO    +
289:         b5*ALTLONG +
290:         b6*CM  +
291:         b7*CMA3LL  +
292:         b8*CMALT   +
293:         b9*CMALT3  +
294:         b10*CMALTSLT    +
295:         b11*CMCLAT  +
296:         b12*CML2L2  +
297:         b13*CMLAT2  +
298:         b14*LATCM2  +
299:         b15*LATITUDE    +
300:         b16*SLAT    +
301:         b17*SM  +
302:         b18*SMA3LL  +
303:         b19*SMALT3  +
304:         b20*SMALTLT2    +
305:         b21*SMALTSLT    +
```

```
306:         b22*SMCLAT  +
307:         b23*SMLAT3;
308:         end
309: else if depth = 50 then
310:         begin
311:         result :=
312:         b0+
313:         b2*ALT12   +
314:         b3*ALT2SLAT    +
315:         b4*ALT3SLAT    +
316:         b5*ALTSLAT +
317:         b6*CMA2LL  +
318:         b7*CMCLAT  +
319:         b8*CML2L2  +
320:         b9*CMLAT2  +
321:         b10*LAT3    +
322:         b11*LATCM2  +
323:         b12*SLAT    +
324:         b13*SMALLL  +
325:         b14*SMALTLON    +
326:         b15*SMCLAT  +
327:         b16*SMLON3;
328:         end
329: else if depth = 100 then
330:         begin
331:         result :=
332:         b0+
333:         b2*ALT12   +
334:         b3*ALT2    +
335:         b4*ALT3LL  +
336:         b5*ALT3SLAT    +
337:         b6*ALTLONG +
338:         b7*ALTSLAT +
339:         b8*CMA2LL  +
340:         b9*CMA3LL  +
341:         b10*CMALT   +
342:         b11*CMALT2  +
343:         b12*CMALTSLT    +
344:         b13*CMCLAT  +
345:         b14*CMLAT3  +
346:         b15*CMLON3  +
347:         b16*CMSLAT  +
348:         b17*LAT3    +
349:         b18*LAT3LON3    +
350:         b19*LATCM2  +
351:         b20*LATLONG +
352:         b21*LATSM   +
```

```
353:         b22*LATSM2  +
354:         b23*LONG3   +
355:         b24*LONGSM2 +
356:         b25*SMA2LL  +
357:         b26*SMA3LL  +
358:         b27*SMALT3  +
359:         b28*SMALTLT2    +
360:         b29*SMALTSLT    +
361:         b30*SMCLAT  +
362:         b31*SML2L2;
363:         end;
364: result := result + loc_val;
365: //variance component next
366: result := result + randg(0,var_val);
367: end;
368:
369: procedure set_coeffs;
370: begin
371: ALT12 := sqrt(altitude);
372: ALT2 := altitude*altitude;
373: slat := sin(latitude*2*3.141592653/90);
374: clat := cos(2*3.141592653*latitude/90);
375: alt2slat := alt2*slat;
376: latlong := latitude* longtitude;
377: alt3ll := altitude*altitude*altitude*latlong;
378: alt3slat := altitude*altitude*altitude*slat;
379: altlat := altitude*latitude;
380: altlatlo := altlat*longtitude;
381: altlong := altitude*longtitude;
382: altslat := altitude*slat;
383: long3 := longtitude*longtitude*longtitude;
384: lat3 := latitude*latitude*latitude;
385: lat2lon3 := latitude*latitude*long3;
386: lat3lon3 := lat3*long3;
387: lat3long := lat3*longtitude;
388: random_coeffs;
389: end;
390:
391: procedure random_coeffs;
392: var
393:         month : single;
394: begin
395: month := random*12;
396: cm := cos(2*3.141592653*month/12);
397: cm2 := cos(4*3.141592653*month/12);
398: sm := sin(2*3.141592653*month/12);
399: sm2 := sin(4*3.141592653*month/12);
```

```
400: cma2ll := cm*alt2*latlong;
401: cmalt := cm*altitude;
402: cmalt3 := cmalt*alt2;
403: cmaltlon := cm*altlong;
404: cmaltlt2 := cm*altlat*latitude;
405: cmaltslt := cmalt*slat;
406: cmclat := cm*clat;
407: //cm2l2 := cm*latitude*latitude;
408: cmlat3 := cm*lat3;
409: cmlon3 := cm*long3;
410: cmslat := cm*slat;
411: latcm := latitude*cm;
412: latcm2 := latitude*cm2;
413: latsm := latitude*sm;
414: latsm2 := latitude*sm2;
415: longsm := longtitude*sm;
416: longsm2 := longtitude*sm2;
417: smalll := sm*altlatlo;
418: sma2ll := smalll*altitude;
419: sma3ll := sma2ll*altitude;
420: smalt := sm*altitude;
421: smalt3 := sm*alt2*altitude;
422: smaltlon := sm*altlong;
423: smaltlt2 := sm*altlat*latitude;
424: smaltslt := sm*altslat;
425: smclat := sm*clat;
426: sml2l2 := sm*latlong*latlong;
427: smlat3 := sm*lat3;
428: smlon2 := sm*longtitude*longtitude;
429: smlon3 := sm*long3;
430: CMA3LL := cm*alt3ll;
431: CMALT2 := cm*alt2;
432: CML2L2 := cm*latlong*latlong;
433: CMLAT2 := cm*latitude*latitude;
434: end;
435:
```

In the procedure **set_det** coded in lines 436–601 below a new state for the deterministic model parameter values is set. This is simply set by selecting a random state for each parameter value from within the calculated distribution for each parameter as given in Table F.5.

```
436: procedure set_det;
437: begin
438: if depth = 5 then
```

```
439:         begin
440:         b0:=randg(6.80E+01,4.15E+00);//(Constant);
441:         b2:=randg(-1.82E-01,8.05E-02);//ALT12
442:         b3:=randg(-3.57E-04,4.85E-05);//ALT2
443:         b4:=randg(-7.12E-04,9.16E-05);//ALT2SLAT
444:         b5:=randg(-7.35E-06,1.54E-06);//ALTLATLO
445:         b6:=randg(7.46E-02,9.14E-03);//ALTSLAT
446:         b7:=randg(-3.04E-01,3.48E-02);//CM2
447:         b8:=randg(1.73E-08,3.31E-09);//CMA2LL
448:         b9:=randg(2.59E-07,4.33E-08);//CMALT3
449:         b10:=randg(1.11E-05,1.70E-06);//CMALTLT2
450:         b11:=randg(2.67E-02,4.12E-03);//CMALTSLT
451:         b12:=randg(-3.35E+01,1.76E+00);//CMCLAT
452:         b13:=randg(3.36E-09,5.22E-10);//LAT3LON3
453:         b14:=randg(6.17E-01,4.06E-02);//LATCM
454:         b15:=randg(1.21E-02,1.22E-03);//LATLONG
455:         b16:=randg(2.21E-03,8.69E-04);//LATSM2
456:         b17:=randg(-7.73E-04,3.18E-04);//SMALT
457:         b18:=randg(1.06E-04,1.42E-06);//SMLON2
458:         var_val := randg(2.2,0.225);
459:         end
460: else if depth = 10 then
461:         begin
462:         b0:=randg(-1.07E+01,3.46E+00);//(Constant)
463:         b2:=randg(3.24E-02,1.36E-02);//ALT12
464:         b3:=randg(-2.68E-05,3.99E-06);//ALT2
465:         b4:=randg(-6.76E-12,6.82E-13);//ALT3LL
466:         b5:=randg(-1.77E-02,5.00E-03);//ALTITUDE
467:         b6:=randg(8.42E-05,3.09E-05);//ALTLONG
468:         b7:=randg(-2.80E-01,9.42E-03);//CM2
469:         b8:=randg(1.76E-09,4.86E-10);//CMA2LL
470:         b9:=randg(-4.46E-12,7.80E-13);//CMA3LL
471:         b10:=randg(7.47E-02,5.97E-03);//CMALT
472:         b11:=randg(-4.28E-04,3.44E-05);//CMALTLON
473:         b12:=randg(-8.51E+00,6.20E-01);//CMCLAT
474:         b13:=randg(1.54E-07,9.33E-09);//CML2L2
475:         b14:=randg(6.99E-07,5.44E-08);//CMLON3
476:         b15:=randg(3.48E-01,1.52E-02);//LATCM
477:         b16:=randg(-4.45E-01,7.68E-02);//LATITUDE
478:         b17:=randg(1.92E-02,6.74E-05);//LONGSM
479:         b18:=randg(2.13E-02,3.83E-03);//LONGSM2
480:         b19:=randg(-1.52E+01,1.16E+00);//SLAT
481:         b20:=randg(-3.68E+00,6.66E-01);//SM2
482:         b21:=randg(5.61E-10,1.37E-10);//SMA2LL
483:         b22:=randg(-1.78E-12,3.17E-13);//SMA3LL
484:         var_val := randg(2,0.188);
485:         end
```

```
486: else if depth = 20 then
487:          begin
488:          b0:=randg(-4.07E+01,3.52E+00);//(Constant)
489:          b2:=randg(6.59E-02,7.48E-03);//ALT12
490:          b3:=randg(1.64E-05,2.30E-06);//ALT2SLAT
491:          b4:=randg(-1.89E-12,1.62E-13);//ALT3LL
492:          b5:=randg(3.65E-04,5.33E-05);//ALTLAT
493:          b6:=randg(4.21E-05,1.38E-05);//ALTLONG
494:          b7:=randg(3.87E-09,4.53E-10);//CMA2LL
495:          b8:=randg(5.72E-11,3.02E-12);//CMA3LL
496:          b9:=randg(7.32E-03,5.98E-04);//CMALT
497:          b10:=randg(4.81E-07,2.28E-08);//CMALT3
498:          b11:=randg(2.29E-02,1.02E-03);//CMALTSLT
499:          b12:=randg(-7.07E+00,5.52E-01);//CMCLAT
500:          b13:=randg(1.04E-06,9.13E-08);//CMLON3
501:          b14:=randg(2.03E+00,2.23E-01);//CMSLAT
502:          b15:=randg(-3.98E-07,8.46E-08);//LAT3LON3
503:          b16:=randg(1.62E-01,1.02E-02);//LATCM
504:          b17:=randg(8.83E-03,2.11E-04);//LATCM2
505:          b18:=randg(-9.96E-01,6.77E-02);//LATITUDE
506:          b19:=randg(4.55E-02,4.76E-03);//LONGSM
507:          b20:=randg(2.59E-02,3.51E-03);//LONGSM2
508:          b21:=randg(-2.85E+01,1.60E+00);//SLAT
509:          b22:=randg(-4.37E+00,8.30E-01);//SM
510:          b23:=randg(-4.45E+00,6.10E-01);//SM2
511:          b24:=randg(2.13E-09,4.48E-10);//SMA2LL
512:          b25:=randg(1.52E-11,2.59E-12);//SMA3LL
513:          b26:=randg(3.45E-03,5.93E-04);//SMALLL
514:          b27:=randg(1.42E-07,2.02E-08);//SMALT
515:          b28:=randg(6.74E-03,8.40E-04);//SMALTSLT
516:          var_val := randg(1.3,0.193);
517:         end
518: else if depth = 30 then
519:          begin
520:          b0:=randg(-6.29E+00,2.57E+00);//(Constant)
521:          b2:=randg(2.94E-02,5.25E-03);//ALT12
522:          b3:=randg(-2.54E-05,2.23E-06);//ALT2SLAT
523:          b4:=randg(-5.20E-06,3.30E-07);//ALTLATLO
524:          b5:=randg(-2.63E-04,1.56E-05);//ALTLONG
525:          b6:=randg(1.66E+00,2.61E-01);//CM
526:          b7:=randg(8.49E-11,2.87E-12);//CMA3LL
527:          b8:=randg(6.41E-03,3.07E-04);//CMALT
528:          b9:=randg(6.36E-07,2.12E-08);//CMALT3
529:          b10:=randg(3.42E-02,1.02E-03);//CMALTSLT
530:          b11:=randg(-2.67E+00,5.78E-01);//CMCLAT
531:          b12:=randg(1.52E-07,1.52E-08);//CML2L2
532:          b13:=randg(-4.19E-03,3.03E-04);//CMLAT2
```

```
533:         b14:=randg(9.03E-03,2.03E-04);//LATCM2
534:         b15:=randg(-3.85E-01,5.71E-02);//LATITUDE
535:         b16:=randg(-1.51E+01,8.61E-01);//SLAT
536:         b17:=randg(2.01E+00,2.32E-01);//SM
537:         b18:=randg(2.95E-11,2.86E-12);//SMA3LL
538:         b19:=randg(2.23E-07,2.11E-08);//SMALT3
539:         b20:=randg(1.17E-06,1.49E-07);//SMALTLT2
540:         b21:=randg(1.06E-02,8.68E-04);//SMALTSLT
541:         b22:=randg(-3.15E+00,3.20E-01);//SMCLAT
542:         b23:=randg(1.85E-05,1.45E-06);//SMLAT3
543:         var_val := randg(1.2,0.207);
544:         end
545: else if depth = 50 then
546:         begin
547:         b0:=randg(-4.59E+01,7.02E+00);//(Constant)
548:         b2:=randg(-8.34E-02,9.11E-03);//ALT12
549:         b3:=randg(4.63E-04,5.03E-05);//ALT2SLAT
550:         b4:=randg(-1.01E-06,1.02E-07);//ALT3SLAT
551:         b5:=randg(-3.54E-02,8.08E-03);//ALTSLAT
552:         b6:=randg(-1.54E-09,9.66E-11);//CMA2LL
553:         b7:=randg(8.58E+00,1.19E+00);//CMCLAT
554:         b8:=randg(8.09E-07,8.12E-08);//CML2L2
555:         b9:=randg(-1.75E-02,1.84E-03);//CMLAT2
556:         b10:=randg(-6.27E-04,7.63E-05);//LAT3
557:         b11:=randg(6.69E-03,1.08E-03);//LATCM2
558:         b12:=randg(-5.87E+01,6.13E+00);//SLAT
559:         b13:=randg(-5.08E-06,7.96E-07);//SMALLL
560:         b14:=randg(-2.02E-04,3.44E-05);//SMALTLON
561:         b15:=randg(3.41E+00,8.66E-01);//SMCLAT
562:         b16:=randg(1.26E-06,1.58E-07);//SMLON3
563:         var_val := randg(1.1,0.202);
564:         end
565: else if depth = 100 then
566:         begin
567:         b0:=randg(6.32E+01,3.36E+00);//(Constant)
568:         b2:=randg(-2.19E-01,1.70E-02);//ALT12
569:         b3:=randg(-7.67E-05,6.63E-06);//ALT2
570:         b4:=randg(-1.13E-11,1.10E-12);//ALT3LL
571:         b5:=randg(-8.68E-08,6.64E-09);//ALT3SLAT
572:         b6:=randg(1.38E-04,1.19E-05);//ALTLONG
573:         b7:=randg(1.70E-02,8.73E-04);//ALTSLAT
574:         b8:=randg(5.77E-08,2.31E-09);//CMA2LL
575:         b9:=randg(-3.76E-12,1.03E-12);//CMA3LL
576:         b10:=randg(1.21E-02,7.49E-04);//CMALT
577:         b11:=randg(4.11E-04,1.49E-05);//CMALT2
578:         b12:=randg(5.85E-02,1.49E-03);//CMALTSLT
579:         b13:=randg(-7.70E+00,5.55E-01);//CMCLAT
```

```
580:         b14:=randg(3.57E-05,4.12E-06);//CMLAT3
581:         b15:=randg(-3.14E-07,1.06E-07);//CMLON3
582:         b16:=randg(9.08E-01,3.76E-01);//CMSLAT
583:         b17:=randg(4.17E-04,2.16E-05);//LAT3
584:         b18:=randg(-8.50E-11,6.83E-12);//LAT3LON3
585:         b19:=randg(5.46E-03,2.21E-04);//LATCM2
586:         b20:=randg(4.12E-03,4.95E-04);//LATLONG
587:         b21:=randg(-6.81E-02,1.42E-02);//LATSM
588:         b22:=randg(1.56E-02,2.88E-03);//LATSM2
589:         b23:=randg(-4.06E-06,2.86E-07);//LONG3
590:         b24:=randg(2.64E-03,6.75E-04);//LONGSM2
591:         b25:=randg(1.95E-09,6.21E-10);//SMA2LL
592:         b26:=randg(6.66E-11,3.43E-12);//SMA3LL
593:         b27:=randg(5.20E-07,2.58E-08);//SMALT3
594:         b28:=randg(3.01E-06,3.28E-07);//SMALTLT2
595:         b29:=randg(2.15E-02,9.71E-04);//SMALTSLT
596:         b30:=randg(-6.23E+00,4.53E-01);//SMCLAT
597:         b31:=randg(-9.75E-08,6.03E-09);//SML2L2
598:         var_val := randg(0.8,0.217);
599:         end;
600: loc_val := randg(0,0.4);
601: end;
602:
```

The procedure **output_hist** coded in lines 603–647 outputs the calculated distribution for the EHT at the particular location.

```
603: procedure output_hist;
604: var
605:         x, y, z : integer;
606:         mean, stdev : single;
607: begin
608: for x := 1 to sample_size do
609:         begin
610:         mean := mean + data[x];
611:         writeln(output,data[x]);
612:         end;
613: mean := mean/sample_size;
614: for x := 1 to sample_size do
615:         begin
616:         stdev := stdev + ((data[x]-mean)*(data[x] -mean));
617:         end;
618: stdev := sqrt(stdev/(sample_size-1));
619: for x := 1 to ehthist.n_bins-1 do
620:         begin
621:         writeln(output,(x-1)*0.25 -4.875,',',ehthist.bin[x]);
```

```
622:         end;
623: writeln(output);
624: writeln(output,'Mean, ',mean,',Standard deviation,',stdev);
625: write(output, ',68% HPD');
626: ehthist.hpd(0.68);
627: for y := 1 to 3 do
628:         begin
629:         if y > 1 then write(output, ' ,  ');
630:         for z := 1 to ehthist.ci_count do
631:                 begin
632:                 write(output,',',ehthist.hpds[y,z]);
633:                 end;
634:         writeln(output);
635:         end;
636: write(output, ',95% HPD');
637: ehthist.hpd(0.95);
638: for y := 1 to 3 do
639:         begin
640:         if y > 1 then write(output, ',');
641:         for z := 1 to ehthist.ci_count do
642:                 begin
643:                 write(output,',',ehthist.hpds[y,z]);
644:                 end;
645:         writeln(output);
646:         end;
647: end;
648:
649: end.
```

11.8 Model Evaluation

An evaluation of the EHT estimates made via the empirical model implemented in the code just described can be made by comparing simulated EHT's and those recorded through the cell survey programme described previously (Chapter 10). There are two parts to this comparison :

- establishing an empirical adjustment to take account of any measurement bias as discussed previously (*infra vide*:§11.6.2)
- evaluating the performance of the simulation results, both in terms

of precision and suitability of the error calculations.

A comparison of recorded zeolite cell EHT's and simulated EHT values from the same locations are presented in Table 11.20 below. From these results it is immediately apparent that the simulated results systematically underestimate the recorded EHT values. A summary of this comparison is presented in Table 11.21 and from this we can see that the estimation bias is dependant upon measurement depth and is highly significant — amounting to a bias of up to 2.4 ^{0}C (See **total** stats in Table 11.21). This follows the expected pattern as discussed in §11.6.2.

Table 11.20: Comparison between recorded and simulated EHT results

Location	Depth	Recorded Cell EHT	altitude	longtitude	latitude	simulated results		Group
						Mean	SD	
North Cape	10	18.2	5	172.98	-34.43	15.3	4.5	1
Papatowai	10	10.1	3	169.48	-46.56	9.2	5.0	1
South Bay	10	14.5	4	173.68	-42.43	11.7	4.8	1
Avoca	10	14.2	3	173.71	-42.42	11.6	4.7	2
Wairau Bar	10	13.5	4	174.06	-41.51	12.2	4.7	2
Awamoa	20	10.9	2	170.93	-45.14	10.9	4.7	1
Dart River	20	10	440	168.32	-44.78	9.8	5.1	1
Hawksburn	20	12	560	169.21	-45.18	11.0	5.4	1
long Beach	20	12	4	170.65	-45.76	10.6	4.9	1
Station Bay	20	18.6	25	174.93	-36.75	15.7	4.4	1
Omihi	20	17	5	173.52	-42.50	12.5	4.6	1
Ponui	20	21.5	15	175.19	-36.90	15.4	4.5	1
Ponui	20	17.3	30	175.20	-36.89	15.6	4.5	1
Redcliffs flats	20	13.8	3	172.73	-43.56	11.9	4.8	1
Takamatua	20	17.2	3	172.95	-43.79	11.9	4.8	1
Waitaki	20	11.5	4	171.13	-44.96	11.0	4.9	1
Twin Bridges	20	17.2	40	173.85	-35.63	15.8	4.5	2
Mangatawhiri	20	16	20	175.12	-37.22	15.4	4.5	2
Glen Glynk	20	15.3	560	173.00	-42.99	12.1	5.3	2
Lagoon flat	20	14.9	10	173.47	-42.61	12.5	4.7	2
Mapoutahi pa	20	10.6	16	170.62	-45.74	10.6	4.9	2
Sunde	20	19.5	3	174.90	-36.76	15.5	4.5	2
Ponui	20	21.1	2	175.19	-36.90	15.3	4.4	2
Ponui	20	18.3	15	175.19	-36.90	15.5	4.5	2
Rakaia	20	12.3	3	172.24	-43.89	11.8	4.7	2
Tai Rua	20	11.8	5	170.89	-45.15	10.9	4.9	2
Waihao	20	17.1	3	171.17	-44.77	11.1	4.7	2

continued on the next page

Table 11.20: *continued*

Location	Depth	Recorded Cell EHT	altitude	longtitude	latitude	simulated results		Group
						Mean	SD	
Waikuku	30	17.9	5	173.00	-34.43	17.5	3.3	1
Hihi	30	17.9	20	173.54	-34.98	17.1	3.3	1
Kaitia	30	18.7	12.76	173.26	-35.14	17.3	3.3	1
Haratua's pa	30	17.7	120	173.94	-35.37	15.8	3.3	1
Omamari	30	17.7	10	173.67	-35.87	17.0	3.3	1
Gate Memorial	30	16.3	40	174.18	-36.13	16.5	3.3	1
90 mile Beach	30	19.8	4	171.94	-34.84	17.4	3.3	1
Rawara road	30	18	30	173.06	-34.73	17.1	3.3	1
Tramvalley Road	30	15.9	2	170.93	-45.14	11.5	3.6	1
Taupaki	30	18.2	30	174.57	-36.80	16.3	3.4	1
Wenderholm	30	18.4	4	174.71	-36.53	16.7	3.3	1
Horatu	30	16.7	20	175.19	-37.70	16.0	3.4	1
Kawhia	30	18	6	178.88	-65.39			1
Whitford	30	15.8	20	174.97	-36.95	16.4	3.4	1
Drury	30	16.2	15	174.95	-37.11	16.3	3.3	1
Pouarua Rd	30	15.7	6	175.46	-37.28	16.3	3.4	1
Matahue	30	16.1	15	175.94	-37.61	16.2	3.4	1
30 cm open	30	17.9	6	175.81	-36.72	16.6	3.4	1
Coromandel	30	17.1	5	175.51	-36.80	16.6	3.4	1
H26 H27 Jnc	30	16.3	28	175.60	-37.62	16.0	3.4	1
Paeroa B	30	15.1	8	175.64	-37.37	16.3	3.3	1
Matakana	30	13.7	6	176.01	-37.50	16.2	3.4	1
Matakana	30	15.5	15	176.01	-36.67	16.6	3.4	1
Ototara	30	11.5	40	170.89	-45.16	11.5	3.7	1
Tiwai Point	30	10	27.7	168.38	-46.58	10.7	3.7	1
Warkworth	30	17.5	20	174.67	-36.40	16.6	3.4	2
Spirits Bay	30	17.8	5	172.86	-34.43	17.5	3.3	2
Karikari	30	19.1	20	173.36	-34.93	17.2	3.3	2
Herekino	30	17.1	60	173.21	-35.28	16.6	3.3	2
Waipu	30	16.9	10	174.45	-35.99	16.8	3.3	2
Dargaville	30	16.9	55.04	173.83	-35.95	16.4	3.4	2
Mangamuka	30	14.8	80	173.48	-35.20	16.4	3.3	2
Rawara beach	30	19.5	8	173.08	-34.72	17.4	3.3	2
Cape Reinga	30	18.9	14.52	172.67	-34.42	17.4	3.3	2
Karekare	30	18.6	40	174.48	-36.98	16.1	3.3	2
Parakai	30	17.5	3	174.42	-36.65	16.7	3.4	2
spring road	30	15.8	30	175.09	-37.35	16.0	3.4	2
Te Awamutu	30	17.2	55	175.32	-38.00	15.5	3.4	2
Tuakau	30	16	40	174.95	-37.26	16.0	3.3	2
Orere Pt	30	16.7	30	175.23	-36.97	16.2	3.4	2
Clarence	30	13.7	10	173.92	-42.18	13.4	3.6	2

continued on the next page

Table 11.20: *continued*

Location	Depth	Recorded Cell EHT	altitude	longtitude	latitude	simulated results		Group
						Mean	SD	
matakana south end	30	15.2	2	176.05	-37.64	16.2	3.5	2
Oputere	30	14.3	140	175.83	-37.11	15.1	3.5	2
Patetonga	30	17.1	11	175.47	-37.40	16.2	3.4	2
Thames	30	16.7	12	175.54	-37.13	16.4	3.3	2
Paeroa A	30	15.9	10	175.67	-37.39	16.3	3.3	2
Matakana	30	16.5	6	176.02	-37.50	16.2	3.4	2
Matakana	30	14.6	6	176.01	-37.50	16.2	3.4	2
Karaka Pa	30	15.2	21	174.06	-41.26	14.0	3.5	2
Takahanga	30	13.8	4	173.68	-42.41	13.3	3.6	2

We can use the comparative results given in Table 11.20 to derive an empirical adjustment for the observed measurement bias. However, this means that we cannot then use the comparative results upon which the adjustment is based as part of an assessment of the simulation performance. Thus for the purposes of an assessment exercise the comparative results from Table 11.20 have been randomly grouped into two sets. For the purpose of the assessment exercise we will calculate the bias adjustment using a control group (Code label 1 in Table 11.20; adjustment values given in **control** group of Table 11.21) and perform the comparison between measured and simulated EHT values using an adjusted test group (Code label 2 in Table 11.20; summary statistics for the mean difference between estimated and measured EHT given in **test** group of Table 11.21).

The values of the adjusted test set (Table 11.21; **test** group) indicate that the simulated results adjusted for measurement bias return reasonable results. The mean difference between the simulated values and the actual recorded cell EHT's is not statistically different from 0 for any of the depths. Thus the central tendency of the simulated results are appropriate. Accordingly we will use the mean deviation values for the total comparison – given in Table 11.21 **total** group – as empirical values to

Table 11.21: Statistics for difference between estimated and recorded cell EHT values by depth

Set	depth	mean	stdev	se
control	10	2.210466003	1.108925358	0.640238354
	20	2.317513969	2.233383265	0.673390391
	30	0.510471129	1.401726489	0.280345298
test	10	-0.244717598	0.938270579	0.663457489
	20	0.194273931	2.085889513	0.628919352
	30	-0.067298339	1.050176317	0.210035263
total	10	2.112578964	0.923532162	0.413016139
	20	2.414650934	2.05251899	0.437598519
	30	0.476135242	1.222323603	0.174617658

account for the observation bias present in $f_d(x)$.

In contrast to the central tendency, the calculated values for the variance associated with the EHT estimates do not seem to be entirely suitable. The observed variance for the mean difference between the simulated values and the actual recorded cell EHT's is smaller than the variance statistics calculated for the simulated values. For example only 1 of the 77 adjusted comparative values fall outside the calculated 1σ range and none fall outside of the calculated 2σ range: This compares to expected counts of 26 and 4 respectively. Thus the standard deviation of the EHT estimate calculated through the simulation appears to overestimate the true variance. Again we can use the comparative results given in Table 11.20 to calculate an empirical measure for the variance of the simulated estimates for locations from within archaeological sites. The overall standard deviation of the difference between estimated and observed EHT values for the 76 comparative samples considered here is $\approx 1.5^0$C and on the basis of a Kolmogorov-Smirnov test may be regarded as normally distributed (Table 11.22). Thus we would conclude that the simulation results adjusted for measurement bias will return an EHT for a standard short grass covered flat un-obstructed surface as a normally distributed variable with a standard deviation in the order 1.5 ^{0}C.

Table 11.22: Kolmogorov-Smirnov test for normality of the distribution of difference between estimated and observed EHT values in the test set presented in Table 11.20

N		31
Normal Parameters	Mean	0.028470971
	Std. Deviation	1.242952824
Most Extreme Differences	Absolute	0.109303251
	Positive	0.109303251
	Negative	-0.095070325
Kolmogorov-Smirnov Z		0.608574748
Asymp. Sig. (2-tailed)		0.852729321

We can test this conclusion by considering a completely separate set of data and performing the same comparative exercise. A simulation exercise was conducted for the 33 locations given in Table11.23 below using the empirical simulation figures derived in the preceding discussion. As can be seen the results suggest that the estimation approach is suitable. The mean difference between estimated and observed cell EHT for this test set is 0.03 ^{0}C with a standard error of 0.22 ^{0}C. Clearly there is no significant deviation from zero for the central tendency of this statistic. This indicates that the bias adjustment is suitable. Further the standard deviation for the difference statistic is 1.24 ^{0}C which is in agreement with the conclusion drawn above that the simulated results over estimate the true error. This figure is in accordance with the empirical estimate of 1.5 ^{0}C as being an appropriate measure of the deviation by estimates.

11.9 Conclusion

In this chapter we have used long-term soil temperature data from meteorological stations throughout New Zealand to estimate archaeological EHT's by approximating the distribution of the temperature series $T(x)$ (*infra vide*:§9.4.1) and directly evaluating the integral given in Equation 8.3. The estimate developed in this chapter is not a fully suit-

Table 11.23: Comparison between recorded and simulated EHT values

Location	Depth	longtitude	latitude	Altitude	eht	mean	stdev	estimation error
A17a	10	173.94	-35.37	120	17.87	16.84	4.59	1.03
B2	10	170.93	-45.14	2	15.98	12.03	4.89	3.95
D17a	10	175.81	-36.72	6	17.58	16.67	4.56	0.91
D6a	10	175.64	-37.37	8	17.00	16.33	4.55	0.67
kpp	10	175.97	-37.52	7	18.01	16.26	4.56	1.75
long Beach	10	170.65	-45.76	4	11.96	11.70	4.99	0.26
Mapoutahi pa	10	170.62	-45.74	16	10.77	11.69	4.90	-0.92
mh	10	174.79	-36.88	140	15.52	16.15	4.73	-0.63
mh	10	174.79	-36.88	140	16.22	16.03	4.61	0.18
Tai Rua	10	170.89	-45.15	5	11.64	12.01	4.91	-0.37
Clarence	20	173.92	-42.18	10	14.33	15.19	4.62	-0.86
Clarence	20	173.92	-42.18	10	13.97	15.25	4.74	-1.28
Karaka Pa	20	174.06	-41.26	21	14.67	15.76	4.72	-1.09
kps	20	175.97	-37.51	5	19.86	17.81	4.53	2.05
mot(stat/pa)	20	174.93	-36.75	25	18.58	17.86	4.41	0.72
mot(stat/pa)	20	174.93	-36.75	25	18.39	17.92	4.55	0.47
mot(sunde)	20	174.90	-36.76	3	19.52	17.84	4.53	1.69
Ototara	20	170.89	-45.16	40	11.64	13.21	4.77	-1.57
Shag Mouth	20	170.82	-45.48	4	13.01	13.13	4.91	-0.12
Takahanga	20	173.68	-42.41	4	14.64	15.03	4.67	-0.39
tvr	20	174.57	-36.87	50	16.59	17.81	4.53	-1.22
A25	30	173.85	-35.63	40	17.18	17.13	3.35	0.05
D1	30	175.46	-37.28	6	15.72	16.77	3.36	-1.05
D19	30	175.44	-36.68	5	16.21	17.02	3.46	-0.82
D2	30	175.47	-37.40	11	17.09	16.77	3.42	0.32
D20	30	175.51	-36.80	5	17.07	17.11	3.43	-0.04
D5a	30	175.67	-37.39	10	16.25	16.76	3.36	-0.51
D6b	30	175.64	-37.37	8	15.15	16.74	3.38	-1.60
D9d	30	176.01	-36.67	15	15.68	17.07	3.35	-1.39
hwb	30	175.82	-36.89	10	16.41	16.94	3.31	-0.53
Shag Mouth	30	170.82	-45.48	4	12.90	11.68	3.67	1.22

able EHT estimate as it cannot account for intra-site Δ_{EHT}. However, the model does allow an EHT estimate to be produced for an abstract meteorological station at any given location in New Zealand. In itself this is of limited value to applied OHD, but it does act as a first approximation to $\bar{T}$ in New Zealand. Thus the estimation model proposed here can act as a component of a suitable EHT estimate when used in conjunction with Δ_{EHT} estimates (*infra vide*:§9.3.3).

While the model presented here has significant limitations the general approach is useful, in particular it can:

- model long term temperature fluctuations. In the model developed throughout this chapter long-term temperature trends have been modelled as a stochastic process. However $f_d(x)$ and $\tilde{\epsilon}$ can be modified to accommodate any particular model that may be desired.

- produce EHT results that are exponential temperature response model independent. Two exponential temperature response functions are coded in the **RADLAB** unit **empirical** discussed above (§11.7). In a similar fashion any other exponential temperature response function can be modelled. In this manner the estimated EHT is actually relevant to the particular process under study. That this is a significant advance can be seen in Table 11.24 which gives the estimated 30cm EHT values for five locations throughout the latitude range of New Zealand using an arithmetic mean EHT, an exponential mean for zeolite cells and an exponential mean for the hydration of a typical Mayor Island obsidian (§6). As can be seen there are highly significant differences in these values. In spite of this fact arithmetic mean data estimates on meteorological data and unmodified cell data have been routinely used to estimate EHTS for obsidian hydration (§9.2).

- Produce a measure of the uncertainty associated with the EHT estimate. In typical applications of EHT estimates they are assumed to have no associated uncertainty. This is clearly incorrect.

Table 11.24: Comparison of simulated mean temperature, zeolite cell EHT and obsidian EHT for five locations from New Zealand

Depth	Longtitude	Latitude	Altitude	Arithmetic mean	Cell EHT	Obsidian EHT†
30	172.00	-46.00	10	10.91	11.49	12.04
30	173.00	-43.25	10	12.73	13.31	13.93
30	174.00	-40.50	10	14.44	15.00	15.62
30	176.00	-37.75	10	16.12	16.64	17.20
30	173.00	-35.00	10	17.33	17.76	18.25

†

E=86600

And given suitable data the model could be extended to take account of intra-site Δ_{EHT}. Thus this represents a significant advance in the manner in which meteorological data are used to model EHT.

The analysis presented through this chapter also allows us to establish the magnitude of precision in EHT estimation that could realistically be expected to derive from models of meteorological data. The current analysis suggests that the EHT estimates for New Zealand can be regarded as normally distributed with a standard deviation in the order of magnitude of 1.5 ^{0}C. This figure derives from a relatively spatially dense set of monitoring locations and from a far more complex modelling approach than that typically applied to predicting EHT's from meteorological data (*e.g.* Stevenson and Scheetz 1989*a*). Thus the magnitude of uncertainty observed here should be regarded as on the low end of the spectrum. EHT uncertainty at this level of magnitude cannot be ignored in the dating process and to do so renders the whole exercise meaningless. This has significant implications for many of the OHD applications that have been conducted to date.

While the model generated through this chapter does provide base-line EHT estimates for OHD in New Zealand, model limitations mean that the

estimates will not be of use in most situations. A particular limitation is the lack of an ability to make Δ_{EHT} estimates. Thus the model presented here can only really act as a component of an EHT estimation procedure, providing estimates for $\bar{T}$. Δ_{EHT} estimates are required in conjunction with this value to fully define an EHT (*infra vide*:§9.3.3). In the following chapter we will build upon the concepts presented in this chapter and develop a modelling approach directed at estimating Δ_{EHT}.

Chapter 12

A Numerical Model for Δ_{EHT} Estimation

12.1 Introduction

In this chapter software (**RADLAB**) to simulate $T(t)$ on the basis of the theory outlined in Chapter 8 is described. Through the use of this software it is possible to produce an estimate of $D(T)$ and hence estimate Δ_{EHT} and EHT. Here the primary focus is on modelling intra-site Δ_{EHT}— a key component of general EHT estimation procedures (*infra vide*:§9.3.3). However the software presented here forms the basis from which are range of different, problem specific, applications can be developed.

In order to estimate $D(T)$ through **RADLAB** , models of the governing climatic variables are used to simulate the soil temperature regime. These models are basically an implementation of the theory outlined in Chapter 8, and thus the software provides a very general toolkit for soil climate analysis. Modelling EHT in this manner requires valid input data for the site in question in order to model the systematic and stochastic components of the governing meteorological variables. The collection and generation of such input data is site specific. The New Zealand case is considered this chapter, where key controlling environmental variables are modelled following the general approach outlined in Chapter 11. The resulting Δ_{EHT} estimates can then be evaluated against the modern measurements presented in Chapter 10.

Thus this chapter presents simulation software that can be adapted to provide Δ_{EHT} control for any required location plus a New Zealand specific implementation, hence enabling the application of OHD in New Zealand. In the following section the **RADLAB** software is presented. Following this New Zealand specific input data are described. The simulated estimates are then evaluated against experimental data collected as part of the analogue cell survey presented in Chapter 10 (*infra vide*:§34).

12.2 RadLab

Radlab is a collection of PASCAL routines that allow simulation of soil moisture and temperature regimes in response to a given set of environmental variables. Thus at the level presented here Radlab represents a programmers toolbox. A solution to each of the mechanisms that govern the surface energy balance — as outlined in Sections 8.2–8.4 — is implemented. Solutions to the resulting soil climate are also implemented as described in the following sections. Thus Radlab comprises an experimental tool with which it is possible to simulate the soil climate under differing environmental conditions. This in turn allows us to explore the nature and spatial scale of significant variations in EHT within a study area.

Radlab comprises eight Pascal units - environment.pas §12.2.1; flux.pas §12.2.4; latent.pas §12.2.5; longwave.pas §12.2.5; sensible.pas §12.2.5; shortwaverad.pas §12.2.5; temperature_regime.pas §12.2.2; water_regime.pas - which are detailed in the following sections. The general operation of the toolkit is based around the variables defined in the `environment.pas` unit. The source code for Radlab can be found on the companion CD in addition to an installation package for a compiled binary with GUI (*supra vide*:§12.2.6).

12.2.1 environment.pas

The driving environmental variables (*e.g.* air temperature, windspeed *etc.*) are set in this unit and calls are then made to analysis procedures (*e.g.* the `soil_temps` procedure §12.2.2) which update the status of the environmental variables - atmospheric and soil - allowing any of these to be read directly from `environment.pas`. Thus the programming interface to this toolkit is principally via the `environment.pas` unit, the

analytic implementation is contained in the other 8 units. A simple GUI to Radlab is provided through the biolab project as discussed in §12.2.6. However this does not encompass the full functionality of the toolbox, and typically any application of `Radlab` will require some problem specific coding.

```
  1: unit environment;
  2:
  3: interface
  4:
  5: uses main,Windows, Messages, SysUtils, Classes, Graphics, Control ↩
⇒    s, Forms, Dialogs,
  6:   StdCtrls;
  7:
  8: const
  9:         vw = 2480000;
 10:         mw = 0.018;
 11:         ma = 0.02845;
 12:         rho_a = 1.2716;
 13:         cp = 1010;
 14:         R = 8.3143;
 15:         gr = 9.8;
 16:
 17: procedure initialise_variables;
 18: function air_temp : double;
 19: function wet_bulb_temp : double;
 20: function wind_speed : double;
 21: function cloudiness : double;
 22: function air_humidity : double;
 23: function local_time : double;
 24: function air_pressure : double;
 25: function air_vapour_pressure : double;
 26: function surface_vapour_pressure : double;
 27: function saturated_air_vapour_pressure : double;
 28: function rainfall : double;
 29:
 30:(***the global environmental variables for the entire toolbox are defined here***);
 31: var
 32: (***for shortwave radiation***)
 33: altitude,ut, surround_albedo, albedo : double;
 34: latitude, longtitude, secs : double;
 35: mins, hours, days,months, years : integer;
 36: surface_slope, surface_azimuth, linket : double;
 37: (***for longwave radiation***)
 38: es,ea,ld_k :double ;
```

```
39: (***for sensible flux***)
40: air_height, surface_temp : double;
41: ra,displacement, roughness_factor, veg_height : double;
42: ***for latent flux***
43: Rn,PL,PB,RL,RB, typical_pl : double;
44: rw : double;
45: rs0,pc, leaf_n, Le : double;
46: r1, rd0, rdv : double;
47: ***for soil flux***
48: ground_flux, typical_ground_flux : double;
49:
50:
51: implementation
52:
```

The environmental variables used by Radlab are initialised in the following procedure. In order to modify the behaviour of different aspects of the environment the appropriate variable parameters can be programmed here.

```
53: procedure initialise_variables;
54: begin
55: with form1 do
56: begin
57: //************short wave************
58: latitude := strtofloat(edit1.text);
59: longtitude := strtofloat(edit5.text);
60: secs := strtofloat(edit23.text);
61: mins := strtoint(edit18.text);
62: hours := strtoint(edit12.text);
63: days := strtoint(edit11.text);
64: months := strtoint(edit10.text);
65: years :=  strtoint(edit9.text);
66: surface_slope := strtofloat(edit24.text);
67: surface_azimuth := strtofloat(edit25.Text);
68: altitude := strtofloat(edit17.text);
69: Linket := strtofloat(edit19.text);
70: albedo := strtofloat(edit21.text);
71: surround_albedo := strtofloat(edit22.text);
72: //************long wave**************
73: es := 0.9;
74: ea := 0.9;
75: ld_k := 1;
76: //***********sensible*****************
```

```
 77: air_height := 1.5;
 78: displacement := 0.1;
 79: roughness_factor := 0.75;
 80: veg_height := 0.1;
 81: //soil properties
 82: wv := 0;
 83: bd := 1.3;
 84: mc := 0.12;
 85: P := -1300; //initial potential
 86: ks := 0.001; //saturated conductivity
 87: pe := -0.5/sqrt(0.1);//air entry potential
 88: soil_b := -2*pe + 0.2*5;//soil b value
 89: ws := 1 - bd/2.6;
 90: et := 300; //total evap in mm/day
 91: ep := et/86400;
 92: b1 := 1/soil_b;
 93: n := 2 + 3/soil_b;
 94: n1 := 1-n;
 95: wd := 1000;
 96: dv := 0.000024;
 97: vp := 0.017;
 98: //set root resistances etc
 99: rw := 2.5E10;
100: rs0 := 20;
101: pc := -1500;
102: RL := 2000000;
103: leaf_n := 10;
104: r1 := 0.001;
105: rd0 := 50000;
106: rdv := 50;
107:
pl := -1000;
108: end;
109: end;
110:
```

The functions given in lines 111-189 following, are highly simplified and arbitrary models of dynamic environmental variables. In practice these functions will need to be re-written for different problems. In a similar fashion to this, functions for all of the environmental variables defined above could be re-implemented as functions. A more realistic implementation of this aspect of the `environment.pas` unit requires a thorough examination of the specific problem. The New Zealand case is

discussed later (*supra vide*:§12.3).

```
111: function air_temp : double;
112: begin
113: result := 15 + 5*sin(2*pi*(local_time-6)/24);
114: end;
115:
116: function wind_speed : double;
117: begin
118: result := 10;
119: end;
120:
121: function cloudiness : double;
122: begin
123: result := 0;
124: end;
125:
126: function air_humidity : double;
127: begin
128: result := air_vapour_pressure/saturated_air_vapour_pressure;
129: end;
130:
131: function local_time : double;
132: var
133:         sign : integer;
134: begin
135: if ((hours<0) or (mins<0) or (secs<0)) then sign := -1 else sign ↩
⇒    := 1;
136: result := sign*(abs(hours) + abs(mins)/60 + abs(secs)/3600);
137: end;
138:
139: function
wet_bulb_temp : double;
140: begin
141: result := air_temp-10;
142: end;
143:
144:
145: function air_pressure : double;
146:
begin
147: result := 100;
148: end;
149:
150: function air_vapour_pressure : double;
151: var
152:         temp,temp2,p0: double;
```

```
153: begin
154: temp := air_temp;
155: temp2 := wet_bulb_temp;
156: p0 := saturated_air_vapour_pressure;
157:
result := p0 - air_pressure*(6.6e-4*(1+1.15e-3*temp2))*(air_temp-↩
⇛    wet_bulb_temp);
158: end;
159:
160: function surface_vapour_pressure : double;
161: var
162:         temp : double;
163: begin
164: temp := surface_temp;
165:        result:= 0.61087*exp(17.269*temp/(temp + 237.3))
166:
167: end;
168:
169: function saturated_air_vapour_pressure : double;
170: var
171:         temp : double;
172: begin
173: temp := air_temp;
174: result := 0.61087*exp(17.269*temp/(temp + 237.3));
175: end;
176:
177: function rainfall : double;
178: begin
179: //return a flux in kg m2 s
180: //1mm of rain per m2 = 10 kg
181: //for the time being assume a rainfall of 5mm hr as a rainfall ev↩
⇛    ent
182: //ie a flux of 50/3600
183: if (days = 4) and (hours >10) and (hours < 1500) then
184: result := 50/3600
185: else
186: result := 0;
187: end;
188:
189: end.
```

12.2.2 The Soil Climate: `temperature_regime.pas`

This unit is the main analytic component of `Radlab`. The simulated timeseries is controlled through this unit with the other analytic units being called as appropriate and the environmental variables within `environment.pas` being updated in response to the updated time steps set from within `temperature_regime.pas`. Within this unit we seek to simulate a time series of soil temperature and water content values in response to the governing environmental processes. This entails calculating a new set of values for the soil climate at each time step in response to the prevailing atmospheric climate. Thus this is a boundary value problem with the governing boundary value being G (or E in the case of soil moisture regimes).

The program structure is very simple. A loop within the procedure `soil_temps` described below (§12.2.2) steps the simulation in uniform time intervals over the entire analysis period. Within this loop the state of the atmospheric and soil climates are simulated at each time step, generating a timeseries for each climatic variable. This proceeds by generating a new state for the soil temperature regime which requires an iterative solution of the soil surface energy balance. This is solved via the routine `g_flux` (§12.2.3). All calls to the routines defining the surface energy flux's R,H and LE are made from within the program flow of `g_flux`. Once a new state for the soil temperature regime has been established the soil water regime is calculated via the routine `water_flow`. These three key routines are described in more detail below.

```
  1: unit temperature_regime;
  2:
  3: interface
  4:
  5: uses
  6:         math, environment, flux, latent, sensible ,longwave,short↩
⇛    waverad;
  7:
```

```
 8: const
 9:         pi = 3.141592653;
10:
11: procedure soil_temps;
12: procedure set_arrays;
13: procedure water_flow;
14: procedure evapotranspiration;
15: procedure plant_uptake;
16: procedure water_res;
17: procedure g_flux(x1, x2, tol : double);
18: function fx(gf : double):double;
19:
20: var
21:         temps,new_temps,a,b,c,d,k,cp : array of double;
22:         rs,rd,rr,bz,dpw,jv,dj,humidity,new_water,water,potential,↩
⇛    aw,bw,cw,dw,kw,cpw,fw,ez,v : array of double;
23:         temp_d : array of double;
24:         depth,dz,dt,f,g : single;
25:         run_time, time : single;
26:         m : integer;
27:         tp,ks : double;
28:
29:
30:
31: implementation
32:
33: uses
34:         sample;
35:
```

The soil_temps Procedure

As described above the `soil_temps` procedure, contained in lines of code 36-109 below, controls the simulation. This routine controls the simulation time and the environmental variables are updated in `environment.pas` in response to the time.

```
36: procedure soil_temps;
37: var
38:         x, burn, its : integer;
39:         f1 : textfile;
40:         delta_new_temps : double;
41:
```

```
42: begin
43: ssignfile(f1,'d:\temp_dt.csv');
44: rewrite(f1);
45: set_arrays;
46: setlength(temp_d,m+2);
47: //initialise_flux;
48: run_time := 24; //in the end set run_time to some form of UT
49:                       //calc run time from start and end dates
50: f := 0.5;
51: g := 1 - f;
52: for burn := 1 to 10 do
53: begin
54: time := 0;
55: hours := 0;
56: mins := 0;
```

The simulation time is controlled in the following section of code (lines 57-72 below).

```
57: while time < run_time do
58:         begin
59:         //increment time
60:         inc(mins);
61:         if mins >= 60 then
62:                 begin
63:                 inc(hours);
64:                 mins := 0;
65:                 time := time + 1;
66:                 end;
67:
68:         if hours >= 24 then
69:                 begin
70:                 inc(days);
71:                 hours := 0;
72:                 end;
73:         // calc surface flux
74:         //mock with an aritemp model first off
75:         //new_temps[0] := 15 + 5*sin(2*pi*(time-6)/24);
76:         //calculate soil temperatures
```

A numerical solution to 1-D soil heat flow after Equation 8.149 can be developed by considering the flux conservation equation (Equation 8.97)

for a thin slice of soil in a vertical column. From this the following relationship follows:

$$\frac{\text{volume} \times \Delta\text{heat capacity}}{\Delta T} = \Delta G \tag{12.1}$$

We can expand this to give the following

$$\begin{aligned} &\frac{\Delta z C_h (T_i^{j+1} - T_i^j)}{\Delta t} = k_i(\bar{T}_{i+1} - \bar{T}) - k_{i-1}(\bar{T}_i - \bar{T}_{i-1}) \\ &+ k_{v_i}(\bar{\psi}_{m_{i+1}} - \bar{\psi}_m) - k_{v_{i-1}}(\bar{\psi}_{m_i} - \bar{\psi}_{m_{i-1}}) \end{aligned} \tag{12.2}$$

Here the k_i describe the thermal conductance between the centroids of elements i and $i+1$. Similarly the K_{v_i} describe the vapour conductances. The only wrinkle here is that the flux divergence (ΔG) is described in terms of mean temperatures ($\bar{T}$) and potentials ($\bar{\psi}_m$) over the time interval Δt. The question is what are the appropriate mean temperature values to use? The two extremes are to estimate the mean as either the initial value (*i.e.* T_i^j or ψ_i^j) or the final value (*i.e.* T_i^{j+1} or ψ_i^{j+1}); known as explicit (forward) and implicit (backward) differencing schemes respectively. As discussed elsewhere (§C.2) the different schemes have differing properties with respect to accuracy and stability of the estimate in terms of the stepsize in time and space. While either scheme can be used to give stable and accurate answers this does require attention to ensure that suitable step sizes are used. A more robust approach which is largely stable and accurate is to take the arithmetical average of the two values (Press *et al.* 1992). This is known as the Crank-Nicholson or time-centered scheme. This is the approach that will be adopted here for the values $\bar{T}$. Thus

$$\bar{T}_{\cdot} = \frac{T^j + T^{j+1}}{2}$$

In the case of the $\bar{\psi_m}$ we will use an explicit forward difference scheme. This is as the values for ψ_m will not be expected to vary greatly over the interval Δt, this component of the flux divergence is not highly significant, and treating the vapour component in this manner avoids a computationally costly step of rendering the solution of the $T_{\cdot}^{j+1}$ non-linear.

We can re-work Equation 12.2 to isolate the required new temperature values T^{j+1} as

$$\begin{aligned} &T_i^{j+1}\left(\tfrac{(k_{i-1}+k_i)}{2}+\tfrac{\Delta z C_h}{\Delta t}\right)-T_{i-1}^{j+1}\tfrac{k_{i-1}}{2}-T_{i+1}^{j+1}\tfrac{k_{i+1}}{2}= \\ &T_i^{j}\left(\tfrac{C_h\Delta z}{\Delta t}-\tfrac{(k_{i-1}+k_i)}{2}\right)+T_{i-1}^{j}\tfrac{k_{i-1}}{2}+T_{i+1}^{j}\tfrac{k_i}{2} \\ &+\psi_{m_{i+1}}^{j}k_{v_i}+\psi_{m_{i-1}}^{j}k_{v_{i-1}}+\psi_{m_i}^{j}(k_{v_i}+k_{v_{i-1}}) \end{aligned} \tag{12.3}$$

Thus if we divide the soil column under study into m slices we can simultaneously evaluate the relationship given in Equation 12.2 for m equations ($i \in (1..m)$) to provide a solution for the new soil temperatures $T_{\cdot}^{j+1}$. Given boundary conditions this is straightforward. Equation 12.2 can be reworked to derive a tridiagonal set of simultaneous equations as:

$$\begin{bmatrix} B(1) & C(1) & 0 & 0 & \cdots & 0 \\ A(2) & B(2) & C(2) & 0 & \cdots & 0 \\ 0 & A(3) & B(3) & C(3) & \cdots & 0 \\ \vdots & \vdots & \vdots & \vdots & \ddots & C(m-1) \\ 0 & 0 & 0 & 0\cdots & A(m) & B(m) \end{bmatrix} \begin{bmatrix} TN(1) \\ TN(2) \\ TN(3) \\ \vdots \\ TN(m) \end{bmatrix} = \begin{bmatrix} D(1) \\ D(2) \\ D(3) \\ \vdots \\ D(m) \end{bmatrix} \tag{12.4}$$

where

$A[i+1] = C[i] = 0.5k_i$

$B[i] = 0.5(k_i + k_{i-1}) + \frac{C_h\Delta z}{\Delta t}$

and

$D(i)$ = the entire right hand side of Equation 12.3

These values are calculated in the following lines of code.

```
 77:         for x := 1 to m do
 78:                 begin
 79:                 c[x] := -k[x]*f;
 80:                 a[x+1]:=c[x];
 81:                 b[x] := f*(k[x] + k[x-1]) + cp[x];
 82:                 d[x] := g*k[x-1]*temps[x-1] + (cp[x]-g*(k[x]+k[x-↩
⇒    1]))*temps[x] + g*k[x]*temps[x+1];
 83:                 end;
```

A set of equations in this form can be efficiently solved using the Thomas algorithm.

The final point that needs to be dealt with here are the boundary conditions. These influence the flux divergence values $D(1)$ and $D(m)$. At the base of the soil column a boundary temperature needs to be specified. That is T_{m+1}^{j+1}. Here the value $k_m T_{m+1}^{j+1}$ needs to be added to the value for $D(m)$ calculated under the scheme above. This is implemented in line 87 below. The upper boundary condition is simply derived by adding G to the value calculated for $D(1)$ under the scheme above. However this value must be calculated iteratively as the relationship is non-linear. In light of this a separate routine is required to solve the problem of the upper boundary conditions and we will return to the problem of calculating G below (§12.2.3). As the upper flux condition only influences the value of $D[i]$ a partial implementation of the Thomas algorithm can be implemented here leaving only the parts that involve $D[i]$ to be computed as part of the boundary flux routine.

```
 84:         a[1] := 0;
 85:         water_res; (******surface water uptake routine****)
 86:         (************set lower boundary condition and non-d part ↩
⇒    of solution****************)
 87:         d[m] := d[m] + k[m]*f*new_temps[m+1];
 88:         //populate temp_d
 89:         for x := 0 to m do temp_d[x] := d[x];
 90:         for x := 1 to m-1 do
 91:                 begin
 92:                 c[x] := c[x]/b[x];
 93:                 b[x+1] := b[x+1] - a[x+1]*c[x];
 94:                 end;
 95:         (************set upper boundary condition***************↩
⇒    )
```

This line calls the routine to calculate the new upper boundary conditions for the soil.

```
 96:         g_flux(-1000,1000,1);
```

Following the establishment of the new soil temperature values and the surface water flux the soil water flux is updated to establish new values for the soil moisture content. This is performed in the routine `water_flow` called in line 97 below.

Thus line 110 below marks the end of the routine that controls the simulation.

```
 97:         water_flow;
 98:
 99:         for x := 1 to m do temps[x] := new_temps[x];
100:         old_surface_temperature_flux :=
new_surface_temperature_f↩
⇒    lux;
101:         //output trace
102:         end;
103: end;
104: writeln(f1);
105: writeln(f1);
106: writeln(f1,k[0],',',k[5],',',k[10],',',k[20]);
107: writeln(f1,cp[0],',',cp[5],',',cp[10],',',cp[20]);
108: closefile(f1);
109: end;
110:
```

The Following procedure initialises the soil property variable arrays necessary for the simulation. The values given here follow the formulations presented in §8.5 & 8.6.

```
111: procedure set_arrays;
112: var
113:         x,n_elements : integer;
114:         c1,c2,c3,c4 : single;
115: begin
116:
117: //temp stuff first
118:
119: //set array dimensions 120: depth := 1;
121: dz := 0.01; //z in m
122: dt := 1;   //t in seconds
123: m := ceil(depth/dz);
124: n_elements := m + 2;
```

```
125: setlength(temps,n_elements);
126: setlength(new_temps,n_elements);
127: setlength(a,n_elements);
128: setlength(b,n_elements);
129: setlength(c,n_elements);
130: setlength(d,n_elements);
131: setlength(k,n_elements);
132: setlength(cp,n_elements);
133: //initialise the arrays
134:
135: //1: temps
136: for x := 1 to m+1 do
137:         begin
138:         temps[x] := 15;
139:         new_temps[x] := temps[x];
140:         end;
141: temps[0] := 0;
142: new_temps[0] := 0;
143: //2: cp
144:
145: for x := 1 to m do
146:         begin
147:         cp[x] := ((2400000*bd/2.65)+(4180000*wv))*dz/(2*dt);
148:         end;
149: cp[1] := cp[1]/2;
150: //3: k
151: c1 := 0.65 - 0.78*bd + 0.6*bd*bd;
152: c2 := 1.06*bd;
153: c3 := 1 + 2.6/sqrt(mc);
154: c4 := 0.3 + 0.1*bd*bd;
155: for x := 1 to m do
156:         begin
157:         k[x] := (c1 + c2*wv - ((c1-c4)*exp(power(-c3*wv,4))))/dz;
158:         end;
159: k[0] := 0;
160:
161: //water stuff second
162:
163: //1: the arrays
164:
165: setlength(jv,n_elements);
166: setlength(dj,n_elements);
167: setlength(humidity,n_elements);
168: setlength(new_water,n_elements);
169: setlength(water,n_elements);
170: setlength(potential,n_elements);
171: setlength(aw,n_elements);
```

```
172: setlength(aw,n_elements);
173: setlength(bw,n_elements);
174: setlength(cw,n_elements);
175: setlength(dw,n_elements);
176: setlength(kw,n_elements);
177: setlength(cpw,n_elements);
178: setlength(ez,n_elements);
179: setlength(fw,n_elements);
180: setlength(v,n_elements);
181: setlength(dpw,n_elements);
182: setlength(rd,n_elements);
183: setlength(rr,n_elements);
184: setlength(bz,n_elements);
185: setlength(rs,n_elements);
186:
187: for x := 1 to m do
188:         begin
189:         potential[x] := p;
190:         water[x] := ws*power((pe/potential[x]),b1);
191:         new_water[x] := water[x];
192:         humidity[x] := exp(mw*potential[x]/(8.314*(273.15+15)));
193:         kw[x] := ks*power((pe/potential[x]),n);
194:         v[x] := wd*dz;
195:         end;
196: potential[m+1] := potential[m];
197: potential[0] := potential[1];
198: humidity[m+1] := humidity[m];
199: kw[m+1] := ks*power((pe/potential[m+1]),n);
200: kw[0] := 0;
201: for x := 1 to m do
202:         begin
203:         rd[x] := rd0*exp(-dz*x*rdv);
204:         if rd[x] > 0 then
205:                 begin
206:                 rr[x] := rw/(rd[x]*dz);
207:                 bz[x] :=(1-n)*ln(pi*r1*r1*rd[x])/(pi*rd[x]*dz);
208:                 end
209:         else
210:                 begin
211:                 rr[x] := 1E20;
212:                 bz[x] := 0;
213:                 end;
214:         end;
215:
216: end;
217:
```

12.2.3 The Soil Moisture Regime

In a manner similar to that just described for the soil temperature regime, a solution to the 1-D soil moisture regime (Equation 8.147) can be obtained by solving a series of simultaneous equations. However in this case the solution is complicated by the fact that the relationship between water potential and conductivity are such that Equation 8.147 is highly non-linear. Thus solution of the soil water regime is slightly more complex than that for soil temperature. Again a system of simultaneous equations can be defined in order to solve for the new water content at the end of each time step. However in this case it is a system of non-linear equations that needs to be solved. This can be likened to a circular problem in that the solution of the problem depends upon its own value. As will be appreciated this complicates arriving at a solution and generally requires an iterative solution. A common approach to solving this type of problem is via the Newton-Raphson method. For a single function ($f(x)$ say) the roots correspond to

$$f(x) = 0$$

For some guess at a root x^0 $f(x^0)$ will have some value which will not usually be zero. According to the Newton-Raphson method the difference between x^0 and a true root of $f(x)$ can be approximated as

$$\frac{\partial f(x^0)}{\partial x}(x^0 - x^1) = F^0$$

Here x^1 is the only unknown and can easily be calculated, so generating the next estimate of a root for $f(x)$. This process can be iterated until the value $f(x^i)$ is sufficiently small to act as an appropriate approximation of the root for $f(x)$. In practice there are problems with this approach as it does not necessarily converge to a root. However given a reasonable initial estimate for x^0, and a suitable problem, this approach should work. A good discussion of the merits of Newton-

Raphson method and approaches to making it more robust is given in Press *et al.* (1992: p. 362).

For simultaneous equations the process is almost identical. However now the values x^i become vectors. Here the root is found by iteratively solving the system of equations

$$\begin{bmatrix} \partial f_1(\bar{x})\partial x_1 & \partial f_1(\bar{x})\partial x_2 & \cdots & \partial f_1(\bar{x})\partial x_m \\ \partial f_2(\bar{x})\partial x_1 & \partial f_2(\bar{x})\partial x_2 & \cdots & \partial f_2(\bar{x})\partial x_m \\ \vdots & \vdots & \ddots & \vdots \\ \partial f_m(\bar{x})\partial x_1 & \partial f_m(\bar{x})\partial x_2 & \cdots & \partial f_m(\bar{x})\partial x_m \end{bmatrix} \begin{bmatrix} x_1^i - x_1^{i+1} \\ x_2^i - x_2^{i+1} \\ \vdots \\ x_m^i - x_m^{i+1} \end{bmatrix} = \begin{bmatrix} f_1(\bar{x}) \\ f_2(\bar{x}) \\ \vdots \\ f_m(\bar{x}) \end{bmatrix} \tag{12.5}$$

It is possible to work the jacobian in Equation 12.5 into tridiagonal form so that the solution can be calculated via the Thomas algorithm as for the Soil temperature regimes.

```
218: procedure water_flow;
219: const
220:         r = 8.314;
221: var
222:         se : single;
223:         x : integer;
224:         kv : double;
225: begin
226: se := 10;
227: //ks := 5;
228: //evapotranspiration;
229: plant_uptake;
230: while se > 0.00001 do
231: begin
232: se := 0;
233: for x := 1 to m do
234:         begin
235:         kw[x] := ks*power(pe/potential[x],n);
236:         end;
237: //calc a more sensible statement here, that allows irrigation or ↩
⇒    rainfall
238: //jv[0] := E*0.1;
239: //dj[0] := E*0.1;
240: jv[x] := 0;
241: dj[x] := 0;
```

An appropriate formulation is given in Campbell (1985) pp. 84. Following him we can write F_i^i for the soil water regime as

$$F_i^i = \frac{2kw_i\psi_{m_i} - kw_{i-1}\psi_{m_{i-1}} - kw_{i+1}\psi_{m_{i+1}}}{(1-n)\Delta z} + g(kw_{i-1} - kw_i) + \frac{\rho_w(\theta_i^{j+1} - \theta_i^j)\Delta z}{\Delta t} \tag{12.6}$$

From this we derive the following differentials

$$\begin{aligned}
\frac{\partial F_i}{\partial \psi_{m_i}} &= \frac{kw_i}{\Delta z} + \frac{\rho_w \Delta z \theta_i}{b\psi_{m_i}\Delta t} - \frac{ngk_i}{\psi_{m_i}} \\
\frac{\partial F_i}{\partial \psi_{m_{i-1}}} &= \frac{-kw_{i-1}}{\Delta z} + \frac{ngk_{i-1}}{\psi_{m_{i-1}}} \\
\frac{\partial F_i}{\partial \psi_{m_{i+1}}} &= \frac{-kw_{i+1}}{\Delta z}
\end{aligned} \tag{12.7}$$

with all other differentials equal to zero. These values are calculated in lines 244-256 below

```
242: for x := 1 to m-1 do
243:         begin
244:         kv := 0.66*dv*vp*(ws-(new_water[x]+ new_water[x+1])/2)/dz↩
⇒    ;
245:         jv[x] := kv*(humidity[x+1]-humidity[x]);
246:         dj[x] := mw*humidity[x]*kv/(8.314*(273.15+temps[x]));
247:         dj[x] := 0;
248:         jv[x] := 0;
249:         cpw[x] := -v[x]*new_water[x]/(soil_b*potential[x]*dt);
250:         aw[x] := -kw[x-1]/dz + gr*n*kw[x-1]/potential[x-1];
251:         cw[x] := -kw[x+1]/dz;
252:         bw[x] := 2*kw[x]/dz + cpw[x] - gr*n*kw[x]/potential[x]+ d↩
⇒    j[x-1] + dj[x];
253:         fw[x] := (2*potential[x]*kw[x]-potential[x-1]*kw[x-1] - p↩
⇒    otential[x+1]*kw[x+1])/(dz*n1);
254: fw[x] := fw[x] + v[x]*(new_water[x]-water[x])/dt - gr*(kw↩
⇒    [x-1]-kw[x]) + jv[x-1] -jv[x] + ez[x];
255:         se := se + abs(fw[x]);
256: end;
```

Thus the Jacobian is tridiagonal and we can calculate a solution using the Thomas algorithm as for the soil temperature regime.

```
257: jv[m] := 0;
258: dj[m] := mw*humidity[m]*kv/(8.314*(273.15+temps[m]));
259: cpw[m] := -v[m]*new_water[m]/(soil_b*potential[m]*dt);
260: aw[m] := -kw[m-1]/dz + gr*n*kw[m-1]/potential[m-1];
```

```
261: cw[m] := 0;
262: bw[m] := kw[m]/dz + cpw[m] - gr*n*kw[m]/potential[m] + dj[m-1];
263: fw[m] := ((potential[m]*kw[m]-potential[m-1]*kw[m-1])/dz )/n1;
264: fw[m] := fw[m] + v[m]*(new_water[m]-water[m])/dt - gr*(kw[m-1]-kw↩
⇛    [m]) + jv[m-1] + ez[m];
```

It is simply necessary to iterate the solution to Equation 12.5 using the calculation for F_i given in Equation 12.6 and the derivatives in Equation 12.7 until the value for F_i are sufficiently small. F_i is calculated in line 265: below and is tested at the start of the iteration loop at line 230: above. It is easy to incorporate the boundary values for the soil moisture regime into the calculations given above. The term $E(z)$ used above directly deals with water loss to the atmosphere and arises from the flux LE which is dealt with below. For infiltration of moisture into the soil (*i.e.* dew and rainfall) the flux is simply added to the value for F[1] given above. Here the lower boundary condition will be set to some constant potential.

```
265: se := se + abs(fw[m]);
266: //fw[1] := 0;
267: //cw[1] := 0;
268: for x := 1 to m-1 do
269:         begin
270:         if bw[x] > 0 then cw[x] := cw[x]/bw[x];
271:         if bw[x] > 0 then fw[x] := fw[x]/bw[x];
272:         bw[x+1] := bw[x+1] - aw[x+1]*cw[x];
273:         fw[x+1] := fw[x+1] - aw[x+1]*fw[x];
274:         end;
275: dpw[m] := fw[m]/bw[m];
276: potential[m] := potential[m]-dpw[m];
277: if potential[m] > pe then potential[m] := pe;
278: for x := m-1 downto 1 do
279: begin
280:         dpw[x] := fw[x] - cw[x]*dpw[x+1];
281:         potential[x] := potential[x]-dpw[x];
282:         if potential[x]>pe then potential[x] := (potential[x]+dpw↩
⇛    [x]+pe)/2;
283:         end; 284: for x := 1 to m do
285:         begin
286:         new_water[x] := ws*power((pe/potential[x]),b1);
287:         humidity[x] := exp((mw*potential[x])/(8.314*(273.15+temps↩
```

```
⇒    [x])));
288:         end;
289: end;
290:
291: //sw := 0;
292: for x := 1 to m do
293:         begin
294:         //sw := sw + v[x]*(new_water[x]-water[x]);
295:         water[x] := new_water[x];
296:         end;
297: end;
298:
```

The following routine is a simply a piece of test code. This routine is not actually used.

```
299: procedure evapotranspiration;
300: var
301:         x : integer;
302:         e0 : double;
303: begin
304: e0 := 2.3*et*(0.5 + power(sin(0.0175*7.5*local_time),4))/86400;
305: //e0 := 1;
306: ep := 0.1*e0;
307: tp := e0 - ep;
308: end;
309:
```

The routine below is used to calculate the root moisture uptake at depth `x` given a known boundary moisture flux and the current soil moisture environment. The calculation used here follows that given in Equation 8.145, and populates the arrays values for `ez[i]` used in the water potential calculations at line 254 above.

```
310: procedure plant_uptake;
311: var
312:         x : integer;
313:         tr : double;
314: begin
315: tr := E;
316: if E >0 then
317: for x := 1 to m do
```

```
318:         begin
319:         ez[x] := (potential[x] - pl - rl*tr)/(rr[x] + rs[x]);
320:         end
321: else
322:         begin
323:         for x := 1 to m do
324:                 begin
325:                 ez[x] := 0;
326:                 end;
327:         ez[1] := e;
328:         end;
329: ez[1] := ez[1] - rainfall;
330: end;
331:
```

The procedure `water_res` given below calculates the SPAC water resistances necessary to perform the uptake calculation given above.

```
332: procedure water_res;
333: var
334:         x : integer;
335: begin
336: pb := 0;
337: rb := 0;
338: for x := 1 to m do
339:         begin
340:         rs[x] := bz[x]/kw[x];
341:         pb := pb + potential[x]/(rr[x] + rs[x]);
342:         rb := rb+1/(rs[x] + rr[x]);
343:         end;
344: pb := pb/rb;
345: rb := 1/rb;
346: end;
347:
```

The Surface Energy Balance

As has been outlined previously we can regard the soil surface energy (and moisture) balance as in some sense driving the soil climate. This balance defines the upper boundary conditions for the soil temperature and moisture regime calculations just presented. Thus we need some

method of calculating the surface balance in response to the prevailing climatic conditions. In practice this must be calculated via some form of numerical solution to the equation

$$R - H - LE - G = 0$$

Here we need to estimate a new value for G on the basis of;

1. the previous values for G,R,H and LE
2. the new values for R,H and LE we calculate on the basis of known environmental conditions.

This is complicated a little by the fact that the updated values for R,H and LE depend upon the new value for G and that G also depends upon the new soil temperature and moisture regimes at each time step. Clearly this is a non-linear relationship. One feature of this is that by solving the energy balance at each time step we must arrive at the new soil climate state.

A number of methods exist for solving this type of problem. Probably the most well known methods are based around using the first derivative of the governing function; such as the Newton-Raphson method. However in the current case we do not want to work with the derivatives as this requires that we either

1. calculate the derivative analytically which is difficult and means that if we ever change the manner in which R,H or LE are calculated we need to re-work the solution. This makes the code less flexible and usable
2. calculate the derivative numerically which requires a large amount of computation and significantly slows down the calculation.

A stable, rapid, non-derivative based solution is given by Brent's algorithm. Basically this method is based around making systematically directed guesses at G for the new timestep and then assessing how well this guess acts as a solution. Thus for each guess G' we will arrive at the following

$$R - H - LE - G' = x' \tag{12.8}$$

Brent's algorithm ensures that each successive guess G' improves the estimate (*i.e.* $\lim_{i \to \infty} x' = 0$). Thus we simply have to perform this estimation iteration a sufficient number of times until x' is suitably small. A detailed description of Brent's Algorithm is given in Press *et al.* (1992: p. 359).

As a general algorithm the approach to updating the soil climate is as follows:

1. estimate G'
2. calculate the new soil temperatures on this basis
3. calculate the new fluxes R, H and LE on the basis of the newly updated soil surface temperature and the new state of the atmospheric climate
4. assess the surface energy balance if x' is not sufficiently close to zero calculate an improved G' goto 2:
5. calculate the water regime

The code below is a direct implementation of Brent's Algorithm as given in Press *et al.* (1992). Here the function `fx()` evaluates x' for any given argument G'. Thus the critical variations in surface flux are controlled from with in the function `fx()` discussed below (lines 442-463).

```
348: procedure g_flux(x1, x2, tol : double);
```

```
349: label gotroot;
350: const
351:         itmax = 100;
352:         eps = 3e-8;
353: var
354:         a,b,c,d,e : double;
355:         min1,min2,min : double;
356:         fa,fb,fc,p,q,r : double;
357:         s, tol1,xm : double;
358:         iter : integer;
359: begin
360: a := x1;
361: b := x2;
362: fa := fx(a);
363: fb := fx(b);
364: if fa*fb >= 0 then
365:         begin
366: //increase limits until there is a bracket
367:         end;
368: fc:=fb;
369: for iter := 1 to ITMAX do
370:         begin
371:         if fb*fc > 0 then
372:                 begin
373:                 c:=a;
374:                 fc:=fa;
375:                 d:=b-a;
376:                 e := d;
377:                 end;
378:         if abs(fc) < abs(fb) then
379:                 begin
380:                 a:=b;
381:                 b:=c;
382:                 c:=a;
383:                 fa:=fb;
384:                 fb:=fc;
385:                 fc:=fa;
386:                 end;
387:         tol1:=2.0*eps*abs(b)+0.5*tol;
388:         xm:=0.5*(c-b);
389:         if (abs(xm) <= tol1) or (fb = 0.0) then
390:                 begin
391:                 goto gotroot;
392:                 end;
393:         if (abs(e) >= tol1) and (abs(fa) > abs(fb)) then
394:                 begin
395:                 s:=fb/fa;
```

```
396:                 if (a = c) then
397:                         begin
398:                         p:=2.0*xm*s;
399:                         q:=1.0-s;
400:                         end
401:                 else
402:                         begin
403:                         q:=fa/fc;
404:                         r:=fb/fc;
405:                         p:=s*(2.0*xm*q*(q-r)-(b-a)*(r-1.0));
406:                         q:=(q-1.0)*(r-1.0)*(s-1.0);
407:                         end;
408:                 if (p > 0.0) then q := -q;
409:                 p:=abs(p);
410:                 min1:=3.0*xm*q-abs(tol1*q);
411:                 min2:=abs(e*q);
412:                 if min1 < min2 then min := min1 else min := min2;
413:                 if 2.0*p < min then
414:                         begin
415:                         e:=d;
416:                         d:=p/q;
417:                         end
418:                 else
419:                         begin
420:                         d:=xm;
421:                         e:=d;
422:                         end
423:                 end
424:         else
425:                 begin
426:                 d:=xm;
427:                 e:=d;
428:                 end;
429:         a:=b;
430:         fa:=fb;
431:         if abs(d) > tol1 then b := b+d
432:         else
433:                 begin
434:                 if xm >= 0 then b := b+abs(tol1)
435:                 else b := b-abs(tol1);
436:                 end;
437:         fb:=fx(b);
438:         end;
439: gotroot:
440: end;
441:
```

The argument to `fx()` given below is an estimate G', and the function returns the difference between this estimate and the calculated G. The first part of this procedure is to update the soil temperature regime to calculate a new soil surface temperature for the purpose of updating the surface fluxes dependent upon surface temperature. Here we simply complete the final part of the Thomas algorithm begun above assuming that G' is correct. A dummy array is used (`new_temps[]`) to ensure that we do not need to re-compute the initial part of the Thomas algorithm at each iteration of Brent's algorithm.

```
442: function fx(gf : double) : double;
443: var
444:         x :  integer;
445: begin
446: //calc the surface energy balance if the ground_flux is x
447: //1: calc the new surface temp
448: for x := 0 to m do d[x] := temp_d[x];
449: d[1] := d[1] + g*old_surface_temperature_flux + f*gf;
450: for x := 1 to m-1 do
451:         begin
452:         d[x] := d[x]/b[x];
453:         d[x+1] := d[x+1] - a[x+1]*d[x];
454:         end;
455:         new_temps[m] := d[m]/b[m];
456: for x := m-1 downto 1 do
457:         begin
458:         new_temps[x] := d[x] - c[x]*new_temps[x+1];
459:         end;
460: surface_temp := new_temps[1];
```

This solution leads to a new surface temperature and on this basis it is possible to update the surface temperature dependent surface fluxes. This is computed via the procedure `surface_flux` called in line 461 below.

```
461: surface_flux;
462: result := new_surface_temperature_flux - gf;
463: end;
464:
465: end.
```

12.2.4 Flux.pas

The surface flux calculations are controlled from within this unit, however only four of the procedures contained in this unit are currently used. No actual surface flux calculations are made within this unit, calls are simply made to the relevant analytic units (*i.e.* `latent.pas` §12.2.5, `longwave.pas` §12.2.5, `sensible.pas` §12.2.5 & `shortwaverad.pas` §12.2.5).

The principal routine contained within `flux.pas` is the procedure `surface_flux` required to implement the `g_flux` routine as described above (§12.2.3). This is coded in lines 71-88 below (on page 631). The majority of the routines in this unit provide an alternative to the g_flux routine described above, and are a direct implementation of a general solution to non-linear systems of equations given by Press *et al.* (1992) pp. 385-389. This approach is less efficient than that contained in `g_flux`, however, and is not currently used. It is still possible to call this code if required.

```
 1: unit flux;
 2:
 3: interface
 4:
 5: uses
 6:         math,environment,longwave,shortwaverad,sensible,latent;
 7:
 8: const
 9:         MAXITS = 200;
10:         TOLF = 1.0e-4;
11:         TOLMIN = 1.0e-6;
12:         TOLX = 1.0e-7;
13:         STPMX = 100.0;
14:         eps = 1.0e-4;
15:         TINY = 1.0e-20;
16:         ALF = 1.0e-4;
17:
18:
19: procedure initialise_flux;
20: procedure surface_flux;
21: procedure newt;
22: function fmin : double;
23: procedure fdjac;
```

```
24: procedure ludcmp;//(fjac,n,indx,&d);
25: procedure lubksb;//(fjac,n,indx,p);
26: procedure lnsrch;//(n,xold,fold,g,p,x,&f,stpmax,check,fmin);
27: procedure calc_fvec(var f : array of double);
28: procedure water_flux(x1,x2:double);
29: procedure funcd(x1 : double; var f,df : double);
30:
31:
32:
33: var
34:         fold,f,stpmax,old_surface_temperature_flux, new_surface_t↩
⇒    emperature_flux : double;
35:         indx : array of integer;
36:         fvec,g,p,xold,x : array of double;
37:         fjac : array of array of double;
38:         nn : integer;
39:         check : boolean;
40:         typical_f1,typical_f2 : double;
41:
42: implementation
43:
```

The following routine (lines 45-69) simply initialises the arrays and initial values required by the flux unit. The values of the variables initialised here are not critical.

```
44:
45: procedure initialise_flux;
46: var
47:         i,n : integer;
48: begin
49:     n := 1;
50:     setlength(x,n+1);
51:     setlength(indx,n+1);
52:     setlength(fjac,n+1);
53:     for i := 1 to n do
54:         begin
55:         setlength(fjac[i],n+1);
56:         end;
57:     setlength(g,n+1);
58:     setlength(p,n+1);
59:     setlength(xold,n+1);
60:     setlength(fvec,n+1);
61:     nn:=n;
62:    typical_ground_flux := 20;
```

```
 63:    typical_pl := -10;
 64:    ground_flux := typical_ground_flux;
 65:    pl := typical_pl;
 66:    //typical_f1 := ((total_shortwave + net_longwave) - ground_flu↩
⇛    x - H - E);
 67:    typical_f1 := (PB-PL-E*(RL+RB));
 68:
 69: end;
 70:
```

The surface_flux procedure coded below (lines 71-88) is the principal procedure in the Flux.pas unit. This operates by calling the shortwave, longwave and sensible flux units to establish new values for these surface fluxes. The procedure is simple. A new candidate surface temperature has been calculated on the basis of an estimated G' in the routine g_flux (§12.2.3) and this has been set in the environment.pas unit (§12.2.1) via the variable surface_temp. The routines shortwave_rad (§12.2.5 on page 657), longwave_rad (§12.2.5 on page 642) and sensible_flux (§12.2.5 on page 660) are called to update the appropriate environmental variables in light of the new time step and the new soil temperature. Following this, a new latent heat flux is calculated via the water_flux routine described below (on page 639). Thus at this stage updated estimates are available for R, H & LE and it is possible to calculate the ground flux G implied by these. This calculated value and the estimated G' are compared in the routine g_flux (§12.2.3). If they are not sufficiently close, a new, more accurate, estimate for G' is calculated and the surface_flux routine coded below is called again.

```
 71: procedure surface_flux;
 72: begin
 73: shortwave_rad;
 74: long_wave;
 75: sensible_flux;
 76: Rn := total_shortwave + net_longwave;
 77: //rtsafe for E here
 78: ground_flux := new_surface_temperature_flux;
 79: water_flux(-10,-5000.0);
 80: //x[1] := ground_flux/typical_ground_flux;
```

```
 81: //x[1] := pl/typical_pl;
 82: //newt;
 83: //ground_flux := x[1]*typical_ground_flux;
 84: //pl := x[1]*typical_pl;
 85: //Le := -Vw*E;
 86: new_surface_temperature_flux := Rn+H+le;
 87: //ground_flux := new_surface_temperature_flux;
 88: end;
 89:
```

The set of routines from line 90-387 below are an implementation of a general solution to non-linear systems of equation given by Press *et al.* (1992: pp. 385-389). While these routines will generate the required solution, the approach adopted in the `g_flux` routine (§12.2.3) is simpler and more efficient for the particular problem at hand. These routines were implemented as part of the development process to check the results produced by the `g_flux` routine. Thus the routines in lines 90-387 below are not implemented within the general climate solutions. However they could easily be re-introduced if required.

```
 90: procedure newt;
 91: var
 92: i,its,j : integer;
 93: d,den, sum, temp, test : double;
 94: #define FREERETURN  free_vector(fvec,1,n);free_vector(xold,1,n);↩
⇒      95:     free_vector(p,1,n);free_vector(g,1,n);free_matrix(fjac,1,n,1,↩
⇒    n);  96:     free_ivector(indx,1,n);return;
 97:
 98: //void newt(float x[], int n, int *check,
 99: //    void ( *vecfunc)(int, float [], float []))
100: begin
101:     f:=fmin;
102:     test:=0.0;
103:         for i:=1 to nn do if (abs(fvec[i]) > test) then test :=a↩
⇒    bs(fvec[i]);
104:     if (test< 0.01*TOLF) then
105:         begin
106:         check := false;
107:         //FREERETURN;
108:         end;
109:     sum := 0;
110:     for i:=1 to nn do sum := sum + sqr(x[i]);
```

```
111:     stpmax:=STPMX*max(sqrt(sum),nn);
112: its := 0;
113: check := true;
114: while (check = true) and (its < MAXITS) do
115: begin
116:         inc(its);
117:         fdjac;//(n,x,fvec,fjac,vecfunc);
118:         for i:=1 to nn do
119:             begin
120:             sum := 0;
121:             for j:=1 to nn do sum := sum + fjac[j][i]*fvec[j];
122:             g[i]:=sum;
123:             end;
124:         for i:=1 to nn do xold[i]:=x[i];
125:         fold:=f;
126:         for i:=1 to nn do p[i] := -fvec[i];
127:         ludcmp;//(fjac,n,indx,&d);
128:         lubksb;//(fjac,n,indx,p);
129:         lnsrch;//(n,xold,fold,g,p,x,&f,stpmax,check,fmin);
130:         test:=0.0;
131:         for i:=1 to nn do if (abs(fvec[i]) > test) then test:=abs↩
⇛    (fvec[i]);
132:         if (test < TOLF) then
133:                 begin
134:                 check := false;
135: //FREERETURN
136:                 end;
137:         if (check) then
138:             begin
139:             test:=0.0;
140:             den:=max(f,0.5*nn);
141:             for i:=1 to nn do
142:                 begin
143:                 temp:=abs(g[i])*max(abs(x[i]),1)/den;
144:                 if temp > test then test:=temp;
145:                 end;
146:             if test < tolmin then
147:                 begin
148:                 check:=false;
149:                  //FREERETURN
150:                 end;
151:             end;
152:         test:=0.0;
153:         for i:=1 to nn do
154:             begin
155:             temp:=(abs(x[i]-xold[i]))/MAX(abs(x[i]),1.0);
156:             if (temp > test) then test :=temp;
```

```
157:             end;
158:         if (test < TOLX) then check := false;
159:     end;
160: if check = true then
161:         begin
162: //nrerror(''MAXITS exceeded in newt'');
163:         end;
164: end;
165:
166: function fmin : double;
167: var
168:         i : integer;
169:         sum : double;
170: begin
171:
172: extern int nn;
173: extern float *fvec;
174: extern void ( *nrfuncv)(int n, float v[], float f[]);
175:
176:     calc_fvec(fvec);
177:     sum := 0;
178:     for i:=1 to nn do sum := sum + sqr(fvec[i]);
179:     result := 0.5*sum;
180: end;
181:
182: procedure fdjac;
183: var
184: i, j : integer;
185: h,temp : double;
186: f : array of double;
187: begin
188:
189: //void fdjac(int n, float x[], float fvec[], float **df,
190: //    void ( *vecfunc)(int, float [], float []))
191:
192: setlength(f,nn+1);
193: for j:=1 to nn do
194:         begin
195:         temp:=x[j];
196:         h:=eps*abs(temp);
197:         if (h = 0.0) then h:=eps;
198:         x[j]:=temp+h;
199:         h:=x[j]-temp;
200:         calc_fvec(f);
201:         x[j]:=temp;
202: for i:=1 to nn do fjac[i][j]:=(f[i]-fvec[i])/h;
203:         end;
```

```
204:     f:=nil;
205: end;
206:
207: procedure ludcmp;//(fjac,n,indx,&d);
208: var
209: i,imax,j,k : integer;
210: big,dum,sum,temp : double;
211: vv : array of double;
212: begin
213: //void ludcmp(float **a, int n, int *indx, float *d)
214: setlength(vv,nn+1);
215:     //d:=1.0;
216:     for i:=1 to nn do
217:         begin
218:         big := 0.0;
219:     for j:=1 to nn do
220:             begin
221:             temp := abs(fjac[i][j]);
222:             if (temp > big) then big:=temp;
223:             end;
224:         if (big = 0.0) then
225:                 begin
226: //nrerror(‘‘Singular matrix in routine ludcmp’’);
227:                 end
228:        else
229:                 vv[i]:=1.0/big;
230:         end;
231:     for j:=1 to nn do
232:         begin
233:         for i:=1 to j do
234:           begin
235:             sum:=fjac[i][j];
236:             for k:=1 to i do sum := sum - fjac[i][k]*fjac[k][j];
237:               fjac[i][j]:=sum;
238:             end;
239:         big:=0.0;
240:         for i:=j to nn do
241:             begin
242:             sum:=fjac[i][j];
243:             for k:=1 to j do
244:                 sum := sum - fjac[i][k]*fjac[k][j];
245:             fjac[i][j]:=sum;
246:             dum := vv[i]*abs(sum);
247:             if ( dum >= big) then
248:                 begin
249:                 big:=dum;
250:                 imax:=i;
```

```
251:                 end;
252:             end;
253:         if (j <> imax) then
254:             begin
255:             for k :=1 to nn do
256:                 begin
257:                 dum:=fjac[imax][k];
258:                 fjac[imax][k]:= fjac[j][k];
259:                 fjac[j][k] := dum;
260:                 end;
261:             //*d = -( *d);
262:             vv[imax]:=vv[j];
263:             end;
264:         indx[j]:=imax;
265:         if (fjac[j][j] = 0.0) then fjac[j][j]:=TINY;
266:         if (j <> nn) then
267:             begin
268:             dum:=1.0/(fjac[j][j]);
269:             for i:=j+1 to nn do fjac[i][j] := fjac[i][j]*dum;
270:             end;
271:         end;
272:     vv := nil;
273:
274: end;
275:
276: procedure lubksb;//(fjac,n,indx,p);
277: var
278:     i,ii,ip,j : integer;
279:     sum : double;
280:
281:begin
282: ii := 0;
283: //void lubksb(float **a, int n, int *indx, float b[])
284:     for i :=1 to nn do
285:         begin
286:         ip:=indx[i];
287:         sum:=p[ip];
288:         p[ip]:=p[i];
289:         if (ii <> 0) then
290:             for j:=ii to i-1 do sum := sum-fjac[i][j]*p[j]
291:         else if (sum <> 0) then ii:=i;
292:         p[i]:=sum;
293:         end;
294:     for i := nn downto 1 do
295:         begin
296:         sum:=p[i];
297:         for j:=i+1 to nn do sum := sum-fjac[i][j]*p[j];
```

```
298:         p[i]:=sum/fjac[i][i];
299:         end;
300: end;
301:
302: procedure lnsrch;//(n,xold,fold,g,p,x,&f,stpmax,check,fmin);
303: var
304:     i : integer;
305:     a,alam,alam2,alamin,b,disc,f2,fold2,rhs1,rhs2,slope,sum,temp,↩
⇛    test,tmplam,temp2 : double;
306:     fail : boolean;
307: begin
308:
309: //void lnsrch(int n, float xold[],float fold, float g[], float p↩ ⇛  [], float x[],
310: //    float *f, float stpmax, int *check,float (*func)(float [])↩ ⇛    )
311:
312:
313:     check:=false;
314:     sum := 0;
315:     for i:=1 to nn do sum := sum + p[i]*p[i];
316:     sum:=sqrt(sum);
317:     if (sum > stpmax) then
318:         for i:=1 to nn do p[i] := p[i]*stpmax/sum;
319:     slope := 0;
320:     for i := 1 to nn do
321:         slope := slope+g[i]*p[i];
322:     test:=0;
323:     for i:=1 to nn do
324:         begin
325:         temp:=abs(p[i])/MAX(abs(xold[i]),1.0);
326:         if (temp > test) then test:=temp;
327:         end;
328:     alamin:=TOLX/test;
329:     alam:=1.0;
330:     fail := true;
331:     while fail do
332:         begin
333:         temp2 := ALF*alam*slope;
334:         for i:=1 to nn do x[i]:=xold[i]+alam*p[i];
335:         f := fmin;
336:         if(alam < alamin) then
337:             begin
338:             for i:=1 to nn do x[i]:=xold[i];
339:             check := true;
340:             fail := false;
341:             //return;
342:             end
343:         else if (f <= fold+ALF*alam*slope) then
```

```
344:             begin
345:             fail := false;
346:             //return;
347:             end
348:         else
349:             begin
350:             if(alam = 1.0) then
351:                 tmplam := -slope/(2.0*(f-fold-slope))
352:             else
353:                 begin
354:                 rhs1 := f-fold-alam*slope;
355:                 rhs2:=f2-fold2-alam2*slope;
356:                 a:=(rhs1/(alam*alam)-rhs2/(alam2*alam2))/(alam-al↩
⇒    am2);
357:                 b:=(-alam2*rhs1/(alam*alam)+alam*rhs2/(alam2*alam↩
⇒    2))/(alam-alam2);
358:                 if (a = 0.0) then tmplam := tmplam - slope/(2.0*b↩
⇒    )
359:                 else
360:                     begin
361:                     disc:=b*b-3.0*a*slope;
362:                     if (disc<0.0) then
363:                         begin
364://nrerror(‘‘Roundoff problem in lnsrch.’’)↩
⇒    ;
365:                         end
366:                     else tmplam:=(-b+sqrt(disc))/(3.0*a);
367:                     end;
368:                 if (tmplam>0.5*alam) then tmplam:=0.5*alam;
369:                 end;
370:             end;
371:         alam2:=alam;
372:         f2 := f;
373:         fold2:=fold;
374:         alam:=MAX(tmplam,0.1*alam);
375:         end;
376: end;
377:
378: procedure calc_fvec(var f : array of double);
379: var
380:         i : integer;
381:         //G : double;
382: begin
383: //ground_flux := x[1]*typical_ground_flux;
384: PL := x[1]*typical_pl;
385: //f[1] := ((total_shortwave + net_longwave) - ground_flux - H - L↩
⇒  e)/typical_f1;
```

```
386: f[1] := (PB-PL-E*(RL+RB))/typical_f1;
387:end;
388:
```

The procedure `water_flux` coded below (lines 389-441) solves the non-linear relationship between leaf potential and water flux (Equation 8.144). The solution is calculated here by an implementation of Ridder's method as presented in Press *et al.* (1992: pp.358-359). This is basically an improved method of bisection that makes use of the first derivative of the function being evaluated. Unlike the soil temperature case it is easy to calculate the derivative here (this is calculated in a call to the function `d_e` on line 454 below) and consequently it is sensible to use this as it will produce a more efficient solution. As mentioned previously the Newton-Raphson method is not globally convergent. That is the method may not arrive at a solution no matter how many iterations are performed. In contrast, Ridder's method is globally convergent which is why it is used here. The arguments to `water_flux` (x1 and x2) are bounds on the true value for leaf potential (the variable `PL`).

```
389: procedure water_flux(x1,x2:double);
390: label got_root,no_bounds;
391: var
392: f,df,dx,dxold,fh,fl,temp,xh,xl,rts : double;
393:         j : integer;
394: begin
395:     funcd(x1,fl,df);
396:     if fl >= 0 then goto no_bounds;
397:     funcd(x2,fh,df);
398:     if fl*fh >= 0 then goto no_bounds;
399:     if fl < 0.0 then
400:         begin
401:         xl:=x1;
402:         xh:=x2;
403:         end
404:     else
405:         begin
406:         xh:=x1;
407:         xl:=x2;
408:         end;
```

```
409:     rts:=0.5*(x1+x2);
410:     dxold:=abs(x2-x1);
411:     dx:=dxold;
412:     funcd(rts,f,df);
413:     for j:= 1 to MAXITS do
414:         begin
415:         if (((rts-xh)*df-f)*((rts-xl)*df-f) >= 0.0) or (abs(2.0*f↩
⇒    ) > abs(dxold*df)) then
416:                 begin
417:                 dxold:=dx;
418:                 dx:=0.5*(xh-xl);
419:                 rts:=xl+dx;
420:                 if xl = rts then goto got_root;
421:                 end
422:         else
423:                 begin
424:                 dxold:=dx;
425:                 dx:=f/df;
426:                 temp:=rts;
427:
428:                 rts := rts - dx;
429:                 if temp = rts then goto got_root;
430:                 end;
431:         if (abs(dx) < 0.5) then goto got_root;
432:         funcd(rts,f,df);
433:         if f < 0.0 then xl:=rts
434:         else xh:=rts;
435:         end;
436: //root finding fails need to catch it here
437: pl := 0;
438: got_root:
439:         pl := rts;
440: no_bounds:
441: end;
442:
```

The procedure `funcd` coded below is part of the Ridders algorithm described above. This essentially evaluates the value of the function for which a solution is required at the value $PL = x1$ (f) and also returns the value of the derivative at this point (df). The new value for the latent flux (LE) is set via a call to the function `E` (§12.2.5 on page 662) in line 448 below. In addition to updating LE in the `environment.pas` unit (§12.2.1) `E` returns the required value for E (the return variable `f` in this

code). The derivative of the function is calculated in line 454 via a call to the function d_e (§12.2.5 on page 663).

```
443: procedure funcd(x1 : double; var f,df : double);
444: var
445:         temp : double;
446: begin
447: pl := x1;
448: temp := E;
449: if temp <= 0 then f := 0
450: else
451:         begin
452:         temp := PB-pl-E*(RL+RL);
453:         f := temp;
454:         df := d_e;
455:         end;
456: end;
457:
458: end.
```

12.2.5 *R*

The calculation of *R* as implemented in Radlab is straight forward and directly follows from the theory outlined in §8.2. The calculations for *R* are given in the units `Longwaverad.pas` (§12.2.5) and `shortwaverad.pas` (§12.2.5).

longwave.pas

This unit implements some of the calculations outlined in §8.2.2 and allows the net longwave component of *R* to be calculated.`Long_wave` is the main function called externally to this unit, and this routine will return the net atmospheric surface longwave flux based on the prevailing environmental conditions. This is calculated from the balance of surface flux ld and atmospheric flux lu — returned by the procedures

surface_longwave and atmospheric_longwave respectively — as defined in Equation 8.44.

```
 1: unit longwave;
 2:
 3: interface
 4:
 5: uses
 6:         math,environment;
 7:
 8: const
 9:         sigma = 0.000000567;
10:
11: procedure long_wave;
12: procedure atmospheric_longwave;
13: procedure surface_longwave;
14: function brunt(a,b : double) : double;
15:
16: var
17:         ld,lu,net_longwave : double;
18:
19: implementation
20: procedure long_wave;
21: begin
22: atmospheric_longwave;
23: surface_longwave;
24: net_longwave := ld-lu;
25: end;
26:
27: procedure atmospheric_longwave;
28: begin
29: ld := ea*(1+ld_k*cloudiness)*sigma*intpower((air_temp + 273.15),4)↩ ⇛    ;
30: end;
```

The atmospheric longwave calculated in the routine above is a direct implementation of Equation 8.55. This relies upon atmospheric variables defined in the environment.pas unit (§12.2.1). The surface longwave flux calculated below is a direct implementation of Equation 8.57

```
31: procedure surface_longwave;
32: begin
33: lu := es*sigma*intpower((surface_temp+273.15),4);
34: end;
35:
```

The function brunt below is a direct implementation of Equation 8.49, however is not currently used.

```
36:
37: function brunt(a,b : double) : double;
38: begin
39: result := a + b*exp(0.5);
40: end;
41:
42: end.
```

shortwave.pas

This unit calculates the surface shortwave flux, taking account of reflected shortwave flux and the direct and diffuse beam components. The principal routine called from outside of this unit is the procedure `shortwave_rad`. Currently this is called from within the routine `surface_flux` in the `flux.pas` unit (§12.2.4 on page 631). `shortwave_rad` calls the necessary routines to calculate the various components of the shortwave flux, and parameters describing sun-earth geometry, and then updates the appropriate variables within the `environment.pas` unit (12.2.1).

```
 1: unit shortwaverad;
 2:
 3: interface
 4:
 5: uses
 6:         math;
 7:
 8: const
 9:         rad =3.141592653/180;
10:         io = 1373;
11:
```

The majority of the code in this unit relates to calculating the precise location of the sun at any given point time. Obviously this is a central component of being able to predict the shortwave flux, and the predictive

approach implemented here is far more advanced than that presented in the discussion given in §8.2.1. The functions and procedures defined on lines 12-31 below all relate to this calculation and are all derived from functions of the same name and purpose given by Montenbruck and Pfleger (1991).

```
 12: procedure sun_coords;
 13: //function sun_earth_distance(local_time:double):double;
 14: //procedure sun(mjd:double;var declination,right_ascention:double↩
⇛    );
 15: //function solar_altitude(local_time,latitude : double):double;
 16: //function solar_azimuth(local_time,latitude,longtitude : double)↩
⇛    :double;
 17: function local_mean_sidereal_time(mjd:double):double;
 18: //function hour_angle(local_time,longtitude,right_ascention: doub↩
⇛    le):double;
 19: function mjd :double;
 20: function jd :double;
 21: function jd2000 :double;
 22: procedure ddd(d,m:integer;s:double;var dd : double);
 23: procedure dms(dd:double;var d,m : integer ; var s : double);
 24: function local_apparent_solar_time(hourangle : double):double;
 25: function time_correction(local_time:double):double;
 26: procedure equhor(dec,ha,lat : double; var alt,az : double);
 27: procedure polar(x,y,z : double; var r, theta, phi : double);
 28: function atn2(y,x : double):double;
 29: procedure sun200(t : double; var l,b,r : double);
 30: procedure cart(r,theta,phi : double;var x,y,z : double);
 31: procedure eclequ(t : double;var x,y,z : double);
```

The remainder of the procedures and functions defined in this unit relate to calculating the various components of the net shortwave flux on the basis of defined environmental variables and the calculated position of the sun. These are defined below.

```
 32: function m_beam : double;
 33: function m : double;
 34: function transmitted_beam : double;
 35: function diffuse_shortwave(st : double) : double;
 36: procedure calc_diffuse1 ;
 37: procedure calc_diffuse2 ;
 38: procedure shortwave_rad ;
```

```
 39: function attenuated_beam(slope : double) : double ;
 40: function linke_turb : double;
 41: function skyview : double;
 42:
 43: var
 44:
 45:         solar_altitude, solar_azimuth, R : double;
 46:         declination, ra, ha, hr : double;
 47:         total_shortwave,max_beam, trans_beam, horz_direct_beam,di↩
⇛    rect_beam, diffuse_beam, horz_diffuse_beam :
double↩ ⇛    ;
 48: implementation
 49:
 50: uses environment;
 51:
```

The procedure sun_coords coded below is the principal routine used to calculate the precise position of the sun. This routine makes the necessary calls to calculate the suns position and then convert this location into units suitable for shortwave flux calculations. This is primarily accomplished by a call to the routine sun2000. The remaining calls deal with conversion of time and location units. While sun_coords is not contained in Montenbruck and Pfleger (1991), they should be consulted for precise details of the routines called.

```
 52: procedure sun_coords;
 53: var
 54:         lmst,j2000 : double ;
 55:         A,ls,bs,rs,xs,ys,zs,tz : double;
 56:         mojd : double;
 57: begin
 58: ddd(hours,mins,secs,hr);
 59: tz := int(-longtitude/15);
 60: ut := hr - tz;
 61: j2000 := jd2000;
 62: mojd := mjd;
 63: sun200(j2000,ls,bs,rs);
 64: cart(rs,bs,ls,xs,ys,zs);
 65: eclequ(j2000,xs,ys,zs);
 66: polar(xs,ys,zs,R,declination,ra);
 67: declination := declination*-1;
 68: ra := 24*(ra/360);
```

```
 69: lmst := local_mean_sidereal_time(mojd);
 70: ha := (15*(lmst-ra));
 71: //ha := 360*frac(ha/360);
 72: //if ha < 360 then ha := 360*frac(ha/360)-360
 73: //else ha := 360*frac(ha/360);
 74: equhor(declination,ha,latitude,solar_altitude,solar_azimuth);
 75: end;
 76:
 77:
 78: {
```

The code down to line 129 was implemented for testing purposes only, and is actually commented out.

```
 79: procedure sun(mjd:double;var declination,right_ascention:double);
 80: var
 81:         M : double;
 82:         dl : double;
 83:         l : double;
 84:         sl : double;
 85:         x,y,z : double;
 86:         rho : double;
 87:         julian2000 : double;
 88: begin
 89: julian2000 := (mjd-51544.5)/36525;
 90: M := 6.283185307*frac(0.993133+99.997361*julian2000);
 91: dl := 6893.0*sin(M)+72*sin(2*M);
 92: l := 2*3.141592653*frac(0.7859453 + (m/(2*3.141592653)) + ((6191.↩
⇛    2*julian2000)+DL)/1296E3);
 93: sl := sin(l);
 94: x := cos(l);
 95: y:=0.91748*sl;
 96: z:=0.39778*sl;
 97: rho:=sqrt(1-(z*z));
 98: declination := (180/3.141592653)*arctan(z/rho);
 99: right_ascention := (48/(2*3.141592653))*arctan(y/(x+rho));
100: if right_ascention < 0 then right_ascention := right_ascention + ↩ ⇛  24;
101: end;
102:
103: function solar_altitude(local_time,latitude : double):double;
104: var
105:         dec,ra,ha : double;
106:         sinb : double;
107: begin
108:
```

```
109: declination(local_time,dec,ra);
110: ha := hour_angle(local_time,latitude,ra)*15;
111: sinb := sin(latitude*(3.141592653/180))*sin(dec*(3.141592653/180)↩
⇛    );
112: sinb := sinb + cos(latitude*(3.141592653/180))*cos(dec*(3.1415926↩
⇛    53/180))*cos(ha*3.141592653/180);
113: result := 180*arcsin(sinb)/3.141592653;
114: end;
115:
116: function solar_azimuth(local_time,latitude,longtitude : double):d↩ ⇛    ouble;
117: var
118:         dec,ra : double;
119:         t : double;
120:         azimuth : double;
121: begin
122: declination(local_time,dec,ra);
123: t := local_apparent_solar_time(hour_angle(local_time,longtitude,r↩
⇛    a));
124: azimuth := sin(dec*(3.141592653/180))*cos(latitude*(3.141592653/1↩
⇛    80));
125: azimuth := azimuth - (cos(dec*(3.141592653/180))*sin(latitude*(3.↩
⇛
141592653/180))*cos(hour_angle(local_time,latitude,↩
⇛    ra)*(3.141592653/180)));
126: if t > 12 then azimuth := 360-azimuth;
127: result := azimuth;
128: end;
129:
130:
131: function local_mean_sidereal_time(mjd:double):double;
132: var
133:         mjdo,gmst,lmst,t : double;
134: begin
135: mjdo := int(mjd);
136: t := (mjdo-51544.5)/36525;
137: gmst := 6.697374558 + 1.0027379093*ut + (8640184.812866 + (0.0931↩
⇛    04 - 0.0000062*t)*t)*t/3600;
138: lmst := 24*frac((gmst-longtitude/15)/24);
139: result :=lmst;
140: end;
141:
142: function mjd:double;
143: var
144:         a : double;
145:         b : integer;
146: begin
147: a := 10000*years+100*months+days;
```

```
148: if (months<=2) then
149:         begin
150:         months := months+12;
151:         years := years-1;
152:         end;
153: if (a<=15821004.1) then
154:         b := -2+trunc((years+4716)/4)-1179
155: else
156:         b := trunc(years/400)-trunc(years/100)+trunc(years/4);
157: a := 365*years -679004;
158: result := a+b+trunc(30.6001*(months+1))+days+hr/24;
159: end;
160:
161: function jd:double;
162: begin
163: result := mjd+2400000.5;
164: end;
165:
166: function jd2000:double;
167: begin
168: result := (jd-2451545)/36525;
169: end;
170:
171: procedure ddd(d,m:integer;s:double;var dd : double);
172: var sign : double;
173: begin
174: if ((d<0) or (m<0) or (s<0)) then sign := -1 else sign := 1;
175: dd := sign*(abs(d)+abs(m)/60 + abs(s)/3600);
176: end;
177:
178: procedure dms(dd:double;var d,m : integer ; var s : double);
179: var d1 : real;
180: begin
181: d1 := abs(dd);
182: d:=trunc(d1);
183: d1 := (d1-d)*60;
184: m :=trunc(d1);
185: s := (d1-m)*60;
186: if (dd<0) then
187:         begin
188:         if (d<>0) then d:=-d
189:         else if (m<>0) then m := -m
190:         else s:= -s;
191:         end;
192: end;
193:
194:
```

```
195: function local_apparent_solar_time(hourangle : double):double;
196: begin
197: result := 12-hourangle;
198: end;
199:
200: function time_correction(local_time:double):double;
201: begin
202: result := local_apparent_solar_time(ha)-(local_time -(longtitude↩ ⇛    /15));
203: end;
204:
205:
206: procedure equhor(dec,ha,lat : double; var alt,az : double);
207: var
208: coslat,sinlat,cosdec,sindec,cosha,sinha : double;
209: x,y,z,dummy : double;
210: begin
211: coslat := cos(lat*3.141592653/180);
212: sinlat := sin(lat*3.141592653/180);
213: cosdec := cos(dec*3.141592653/180);
214: sindec := sin(dec*3.141592653/180);
215: cosha := cos(3.141592653*ha/180);
216: sinha := sin(3.141592653*ha/180);
217: x := cosdec*sinlat*cosha - sindec*coslat;
218: y := cosdec*sinha;
219: z := cosdec*coslat*cosha + sindec*sinlat;
220: polar(x,y,z,dummy,alt,az);
221: end;
222:
223: procedure polar(x,y,z : double; var r, theta, phi : double);
224: var
225:         rho : double;
226: begin
227: rho := x*x + y*y;
228: r := sqrt(rho + z*z);
229: phi := atn2(y,x);
230: if phi < 0 then phi := phi + 360;
231: rho := sqrt(rho);
232: theta := atn2(z,rho);
233: end;
234:
235: function atn2(y,x : double):double;
236: const rad = 3.141592653/180;
237: var ax,ay,phi : double;
238: begin
239: if (x=0) or (y=0) then
240:         result := 0
241: else
```

```
242:         begin
243:         ax := abs(x);
244:         ay := abs(y);
245:         if (ax>ay) then phi := arctan(ay/ax)/rad
246:         else phi := 90-arctan(ax/ay)/rad;
247:         if (x<0) then phi:= 180-phi;
248:         if (y < 0) then phi := -phi;
249:         result := phi;
250:         end;
251:
252:
253: end;
254:
255: procedure sun200(t : double; var l,b,r : double);
256: const
257:         p2 = 2*3.141592653;
258: var
259:         c3,s3 : array[-1..7] of double;
260:         c,s : array[-8..0] of double;
261:         m2,m3,m4,m5,m6 : double;
262:         d,a,uu : double;
263:         u,v,dl,dr,db : double;
264:         i : integer;
265: procedure addthe(c1,s1,c2,s2 : double; var c,s:double);
266: begin
267: c:=c1*c2-s1*s2;
268: s:= s1*c2+c1*s2;
269: end;
270:
271: procedure term(i1,i,it : integer;dlc,dls,drc,drs,dbc,dbs:double);
272: begin
273: if it = 0 then addthe(c3[i1],s3[i1],c[i],s[i],u,v)
274: else
275: begin
276:         u := u*t;
277:         v := v*t;
278: end;
279: dl := dl+dlc*u+dls*v;
280: dr:=dr+drc*u+drs*v;
281: db := db+dbc*u+dbs*v;
282: end;
283:
284: procedure pertven;
285: var i : integer;
286: begin
287: c[0] := 1;
288: s[0] := 1;
```

```
289: c[-1] := cos(m2);
290: s[-1] := sin(m2);
291: for i := -1 downto -5 do addthe(c[i],s[i],c[-1],s[-1],c[i-1],s[i-↩
⇒    1]);
292: term(1,0,0,-0.22,6892.76,-16707.37,-0.54,0,0);
293: term(1,0,1,-0.06,-17.35,42.04,-0.15,0,0);
294: term(1,0,2,-0.01,-0.05,0.13,-0.02,0,0);
295: term(2,0,0,0,71.98,-139.57,0,0,0);
296: term(2,0,1,0,-0.36,0.7,0,0,0);
297: term(3,0,0,0,1.04,-1.75,0,0,0);
298: term(0,-1,0,0.03,-0.07,-0.16,-0.07,0.02,-0.02);
299: term(1,-1,0,2.35,-4.23,-4.75,-2.64,0,0);
300: term(1,-2,0,-0.1,0.06,0.12,0.2,0.02,0);
301: term(2,-1,0,-0.06,-0.03,0.2,-0.01,0.01,-0.09);
302: term(2,-2,0,-4.7,2.9,8.28,13.42,0.01,-0.01);
303: term(3,-2,0,1.8,-1.74,-1.44,-1.57,0.04,-0.06);
304: term(3,-3,0,-0.67,0.03,0.11,2.43,0.01,0);
305: term(4,-2,0,0.03,-0.03,0.1,0.09,0.01,-0.01);
306: term(4,-3,0,1.51,-0.4,-0.88,-3.36,0.18,-0.01);
307: term(4,-4,0,-0.19,-0.09,-0.38,0.77,0,0);
308: term(5,-3,0,0.76,-0.68,0.3,0.37,0.01,0);
309: term(5,-4,0,-0.14,-0.04,-0.11,0.43,-0.03,0);
310: term(5,-5,0,-0.05,-0.07,-0.31,0.21,0,0);
311: term(6,-4,0,0.15,-0.04,-0.06,-0.21,0.01,0);
312: term(6,-5,0,-0.03,-0.03,-0.09,0.09,-0.01,0);
313: term(6,-6,0,0,-0.04,-0.18,0.02,0,0);
314: term(7,-5,0,-0.12,-0.03,-0.08,0.31,-0.02,-0.01);
315: end;
316:
317: procedure pertmar;
318: var
319:         i : integer;
320: begin 321: c[-1] := cos(m4);
322: s[-1] := -sin(m4);
323: for i := -1 downto -7 do addthe(c[i],s[i],c[-1],s[-1],c[i-1],s[i-↩
⇒    1]);
324: term(1,-1,0,-0.22,0.17,-0.21,-0.27,0,0);
325: term(1,-2,0,-1.66,0.62,0.16,0.28,0,0);
326: term(2,-2,0,1.96,0.57,-1.32,4.55,0,0.01);
327: term(2,-3,0,0.4,0.15,-0.17,0.46,0,0);
328: term(2,-4,0,0.53,0.26,0.09,-0.22,0,0);
329: term(3,-3,0,0.05,0.12,-0.35,0.15,0,0);
330: term(3,-4,0,-0.13,-0.48,1.06,-0.29,0.01,0);
331: term(3,-5,0,-0.04,-0.2,0.2,-0.04,0,0);
332: term(4,-4,0,0,-0.03,0.1,0.04,0,0);
333: term(4,-5,0,0.05,-0.07,0.2,0.14,0,0);
334: term(4,-6,0,-0.1,0.11,-0.23,-0.22,0,0);
```

```
335: term(5,-7,0,-0.05,0,0.01,-0.14,0,0);
336: term(5,-8,0,0.05,0.01,-0.02,0.1,0,0);
337: end;
338:
339: procedure pertjup;
340: var i : integer;
341: begin
342: c[-1] := cos(m5);
343: s[-1]:= -sin(m5);
344: for i := -1 downto -3 do addthe(c[i],s[i],c[-1],s[-1],c[i-1],s[i-↩
⇒    1]);
345: term(-1,-1,0,0.01,0.07,0.18,-0.02,0,-0.02);
346: term(0,-1,0,-0.031,2.58,0.52,0.34,0.02,0);
347: term(1,-1,0,-7.21,-0.06,0.13,-16.27,0,-0.02);
348: term(1,-2,0,-0.54,-1.52,3.09,-1.12,0.01,-0.17);
349: term(1,-3,0,-0.03,-0.21,0.38,-0.06,0,-0.02);
350: term(2,-1,0,-0.16,0.05,-0.18,-0.31,0.01,0);
351: term(2,-2,0,0.14,-2.73,9.23,0.48,0,0);
352: term(2,-3,0,0.07,-0.55,1.83,0.25,0.01,0);
353: term(2,-4,0,0.02,-0.08,0.25,0.06,0,0);
354: term(3,-2,0,0.01,-0.07,0.16,0.04,0,0);
355: term(3,-3,0,-0.16,-0.03,0.08,-0.64,0,0);
356: term(3,-4,0,-0.04,-0.01,0.03,-0.17,0,0);
357: end;
358:
359: procedure pertsat;
360: begin
361: c[-1] := cos(m6);
362: s[-1] := -sin(m6);
363: addthe(c[-1],s[-1],c[-1],s[-1],c[-2],s[-2]);
364: term(0,-1,0,0,0.32,0.01,0,0,0);
365: term(1,-1,0,-0.08,-0.41,0.97,-0.18,0,-0.01);
366: term(1,-2,0,0.04,0.1,-0.23,0.1,0,0);
367: term(2,-2,0,0.04,0.1,-0.35,0.13,0,0);
368: end;
369:
370: procedure pertmoo;
371: begin
372: dl := dl + 6.45*sin(d) - 0.42*sin(d-a) + 0.18*sin(d+a) + 0.17*sin↩
⇒    (d-m3) - 0.06*sin(d+m3);
373: dr := dr + 30.76*cos(d) - 3.06*cos(d-a) + 0.85*cos(d+a) -0.58*cos↩
⇒    (d+m3) + 0.57*cos(d-m3);
374: db := db + 0.567*sin(uu);
375: end;
376:
377: begin
378: dl := 0;
```

```
379: dr := 0;
380: db := 0;
381: m2 := p2*frac(0.1387306+162.5485917*t);
382: m3 := p2*frac(0.9931266+99.9973604*t);
383: m4 := p2*frac(0.054325+53.1666028*t);
384: m5 := p2*frac(0.055175+8.4293972*t);
385: m6 := p2*frac(0.88165+3.3938722*t);
386: d :=  p2*frac(0.8274+1236.8531*t);
387: a := p2*frac(0.3749+1325.5524*t);
388: uu := p2*frac(0.2591+1342.2278*t);
389: c3[0] := 1;
390: s3[0] :=0;
391: c3[1] := cos(m3);
392: s3[1] := sin(m3);
393: c3[-1] := c3[1];
394: s3[-1] := s3[1];
395: for i := 2 to 7 do addthe(c3[i-1],s3[i-1],c3[1],s3[1],c3[i],s3[i]↩
⇒    );
396: pertven;
397: pertmar;
398: pertjup;
399: pertsat;
400: pertmoo;
401: dl := dl + 6.4*sin(p2*(0.6983+0.0561*t))+1.87*sin(p2*(0.5764+0.41↩
⇒  74*t))+0.27*sin(p2*(0.4189+0.3306*t))+0.2*sin(p2*(0↩
⇒    .3581+2.4814*t));
402: l := 360*frac(0.7859453 + (m3/p2) + ((6191.2+1.1*t)*t+dl)/1296000↩
⇒    );
403: R := 1.0001398 - 0.0000007*t + dr*0.000001;
404: b := db/3600;
405: end;
406:
407: procedure cart(r,theta,phi : double;var x,y,z : double);
408: var rcst : double;
409: begin
410: rcst := r*cos(2*3.141592653*theta/360);
411: x := rcst*cos(2*3.141592653*phi/360);
412: y := rcst*sin(2*3.141592653*phi/360);
413: z := r*sin(2*3.141592653*theta/360);
414: end;
415:
416: procedure eclequ(t : double;var x,y,z : double);
417: var eps,c,s,v : real;
418: begin
419: eps := 23.43292111-(46.8150+(0.00059-0.001813*t)*t)*t/3600;
420: c := cos(2*3.141592653*eps/360);
421: s := sin(2*3.141592653*eps/360);
```

```
422: v := c*y + s*z;
423: z := -s*y + c*z;
424: y := v;
425: end;
426:
```

The function m_beam coded in lines 427-433 below is a direct implementation of Equation 8.12 and calculates the maximum normal shortwave flux given the sun-earth geometry defined in the environment.pas unit (§12.2.1). This is called through the shortwave_rad routine described below.

```
427: function m_beam : double;
428: begin
429: if solar_altitude > 0 then
430: result := io*(1/(R*R))*sin(solar_altitude*rad)
431: else
432: result := 0;
433: end;
434:
```

The function m coded in lines 435-441 below is an implementation of Equation 8.22 used in various derivations of Beer's law as described in §8.2.1.

```
435: function m : double;
436: begin
437: if solar_altitude > 0 then
438: result := exp(-altitude/8000)/(sin(rad*solar_altitude) + 0.15*pow↩
⇒    er((solar_altitude +3.885),-1.253))
439: else
440: result := 0;
441: end;
442:
```

The function transmitted_beam coded in lines 443-449 below is an implementation of Equation 8.25 which calculates the total atmospheric shortwave transmittance via a generalised form of Beer's law. This function calls the function m described immediately above.

```
443: function transmitted_beam : double;
444: begin 445: if solar_altitude > 0 then
446: result := max_beam*power(0.9,m)
447: else
448: result := 0;
449: end;
450:
```

The function diffuse_shortwave coded in lines 451-476 below is an implementation of a method for calculating the diffuse shortwave component of the shortwave flux. This implementation follows the calculation given in Equation 8.33. This particular method is not used to calculate the shortwave flux in the routine shortwave_rad. However this routine could be called in place of the routine currently used (calc_diffuse2).

```
451: function diffuse_shortwave(st : double) : double;
452: var
453:         ratio : double;
454: begin
455: if max_beam > 0 then
456: begin
457: ratio := st/max_beam;
458: if ratio < 0.07 then
459:         begin
460:         result := 1;
461:         end
462: else if (0.7 <= ratio) and (ratio < 0.35) then
463:         begin
464:         result := 1-2.3*sqr(ratio-0.07);
465:         end
466: else if (0.35 <= ratio) and (ratio < 0.75) then
467:         begin
468:         result := 1.33 -1.46*ratio;
469:         end
470: else
471:         begin
472:         result := 0.23;
473:         end;
474: end
475: else result := 0;
476: end;
477:
```

The function calc_diffuse1 coded in lines 478-509 below is another implementation of a method for calculating the diffuse shortwave component of the shortwave flux. This particular method is not used to calculate the shortwave flux in the routine shortwave_rad. This routine is principally experimental and was designed for code checking purposes.

```
478: procedure calc_diffuse1 ;
479: var
480:         st, lower,upper : double;
481:         comp1,comp2 : double;
482: begin
483: if (max_beam > 0) and (direct_beam > 0) then
484: begin
485: lower := direct_beam;
486: upper := max_beam;
487: st := max_beam;
488: comp1 := diffuse_shortwave(st);
489: comp2 := (1-(st/direct_beam));
490: if comp1 > comp2 then
491:         begin
492:         // have a prob in that st > si
493:         diffuse_beam := max_beam-direct_beam;
494:         end 4
95: else
496:         begin
497:         while upper- lower > 0.001 do
498:         begin
499:         st := (upper + lower)/2;
500:         comp1 := diffuse_shortwave(st);
501:         comp2 := (1-(st/direct_beam));
502:         if comp1 < comp2 then lower := st
503:         else upper := st;
504:         end;
505:         diffuse_beam := upper*diffuse_shortwave(upper);
506:         end;
507: end
508: else diffuse_beam := 0;
509: end;
510:
```

The procedure calc_diffuse2 coded in lines 511-515 below implements the actual routine used to calculate the diffuse shortwave flux component. The horizontal diffuse beam is calculated following Equation 8.40.

The actual diffuse component is then corrected for surface slope by taking into account the sky view and the reflectance of the surrounding surface. Here it is assumed that the surrounding surface is a plane. More complex surface morphologies could be modelled at this point.

```
511: procedure calc_diffuse2;
512: begin
513: horz_diffuse_beam := 0.6*(trans_beam-horz_direct_beam);
514: diffuse_beam := skyview*horz_diffuse_beam + (1-skyview)*surround_↩
⇒    albedo*(horz_direct_beam+horz_diffuse_beam);
515: end;
516:
```

As outlined above, the procedure `shortwave_rad` coded in lines 517-526 below is the principal routine called externally to the unit `shortwave.pas`. This unit operates by establishing the correct position of the sun for the current time (via `sun_coords`) and then updates the shortwave variables defined in the `environement.pas` unit (lines 520-523,545 below) via functions defined within the current code unit.

```
517: procedure shortwave_rad;
518: begin
519: sun_coords;
520: max_beam := m_beam;
521: trans_beam := transmitted_beam;
522: horz_direct_beam := attenuated_beam(0);
523: direct_beam := attenuated_beam(1);
524: calc_diffuse2;
525: total_shortwave := (1-albedo)*(direct_beam+diffuse_beam);
526: end;
527:
```

The function `attenuated_beam` coded in lines 528-543 below calculates the direct shortwave flux, either normal to a horizontal surface or on the actual surface depending on the value of the argument `slope`. In this context `slope` is a Boolean variable that toggles using local slope information if slope is true (`slope` = 1). The calculations of the horizontal attenuated beam follow the calculations given in Equation 8.27 along with the geometric discussion given in §8.2.1.

```
528: function attenuated_beam(slope :double) : double ;
529: var
530:  airmass : double;
531: begin
532: airmass := m;
533: if solar_altitude > 0 then
534: result := sqr(1/R)*io*exp(-linke_turb*airmass*(1/(0.9*airmass + 9↩
⇒    .4)))*sin(solar_altitude*rad)
535: else
536: result := 0;
537: if result > trans_beam then result := trans_beam;
538: if slope <> 0 then
539:         begin
540:         result := result*(cos(surface_slope*rad)*sin(solar_altitu↩
⇒    de*rad) + sin(surface_slope*rad)*cos(solar_altitude↩
⇒  )*cos((solar_azimuth-surface_azimuth)*rad))/sin(sol↩
⇒    ar_altitude*rad);
541:         if result < 0 then result := 0;
542:         end;
543: end;
544:
```

The function `linke_turb` below calculates the Linke turbidity value as given in Equation 8.29 and discussed in the associated text. This value is used in the calculation of the attenuated direct shortwave flux described in the routine immediately above.

```
545: function linke_turb : double;
546: begin
547: if linket > 2.5 then
548: result := linket - (0.85 - 2.25*sin(solar_altitude*rad) + 1.11*sq↩
⇒    r(sin(solar_altitude*rad)))
549: else
550: result := linket - (0.85 - 2.25*sin(solar_altitude*rad) + 1.11*sq↩
⇒    r(sin(solar_altitude*rad)))*(linket-1)/1.5;
551: end;
552:
```

The function `skyview` given below is a simple function to calculate the effective fraction of sky visible at a point of sloping earth. The calculation here assumes that the surface morphology can be approximated by a point at the intersection of two planes. Much more sophisticated surface models could be implemented here.

```
553: function skyview : double;
554: begin
555: result := (1 + cos(surface_slope*rad))/2;
556: end;
557:
558: end.
```

H: sensible.pas

Sensible.pas is a short code unit that implements a solution to the surface sensible flux H following the discussion given in §8.3. There are three routines in this unit and only the procedure sensible_flux is designed to be called externally. The solution derived here is via a simple resistance model using an aerodynamic estimate of boundary layer resistance to heat flow (§8.3). sensible_flux first calculates the surface roughness (Z_o)via a call to the procedure roughness. The boundary layer resistance to the flow of sensible heat (ra) is then calculated via a call to the function kh and the sensible heat flux is then calculated on line 29 below following Equation 8.74.

```
 1: unit sensible;
 2:
 3: interface
 4:
 5: uses
 6:         math,environment;
 7:
 8: const
 9:         k = 0.41;
10:         gravity = 9.8;
11:         ch = 1200;
12:
13: procedure sensible_flux;
14: function Kh : double;
15: procedure roughness;
16:
17: var
18:         H : double;
19:
20: implementation
```

```
21:
22: procedure sensible_flux;
23: var
24:         temp : double;
25: begin
26: roughness;
27: temp := kh;
28: if temp > 0 then ra := 1/temp;
29: H := ch*temp*(air_temp - surface_temp);
30: end;
```

The function Kh coded in lines 32-57 below calculates the boundary layer resistance to the flow of sensible heat following Equation 8.76 using estimates of the atmospheric stability parameters ϕ_m and ϕ_h given in Equation 8.70. The general form of the code follows that given by Campbell (1985: p. 140) for a similar calculation.

```
31:
32: function Kh : double;
33: var
34:         x : integer;
35:         ustar, phih, phim, zeta : double;
36: begin
37: ustar := 0;
38: phih := 1;
39: phim := 1;
40: zeta := 0;
41: for x := 1 to 10 do
42:         begin
43:         ustar := wind_speed*k/(ln((air_height-displacement)/roughn↩
⇒   ess_factor) + ln(phim));
44:         result := k*ustar/(ln((air_height-displacement)/roughness_↩
⇒   factor) + ln(phih));
45:         zeta := -k*air_height*gravity*result*(air_temp-surface_tem↩
⇒   p)/((air_temp+273.15)*ustar*ustar*ustar);
46:         if zeta >= 0 then
47:                 begin
48:                 phim := 1 + 5*zeta;
49:                 phih := phim;
50:                 end
51:         else
52:                 begin
53:                 phim := power((1-15*zeta),-0.25);
54:                 phih := phim*phim;
```

```
55:                 end;
56:         end;
57: end;
58:
```

The procedure `roughness` coded below calculates a surface roughness factor (Z_0) following Equation 8.63 on the basis of variables defined in the `environment.pas` unit (§12.2.1)

```
59: procedure roughness;
60: var
61: lf : double;
62: begin
63: lf := 0.997*log10(veg_height) -0.833;
64: roughness_factor := power(10,lf);
65: end;
66:
67: end.
```

LE: `latent.pas`

`Latent.pas` implements the code necessary to provide estimates of the surface latent heat flux. There are five functions defined within this unit only two of which (`E` and `d_e` called from `funcd` in `flux.pas` §12.2.4 on page 641) are called externally to `latent.pas`. The principal function of this unit is `E` coded in lines 20-45 below. This function returns an estimate for E following the discussion presented in §8.4 on the basis of variables defined in the `environment.pas` unit (§12.2.1).

```
 1: unit latent;
 2:
 3: interface
 4:
 5: uses
 6:         math, environment,sensible;
 7:
 8: //const
 9:
10: function E : double;
```

```
11: function d_e : double;
12: function s : double;
13: function rc : double;
14: function psycho : double;
15:
16: //var
17:
18: implementation
19:
```

The solution to E implemented in the function `E` below follows Equation 8.79. This is a modified Daltonian relationship which we can use here as we are able to define all of the relevant environmental variables within the simulation. This differs from an experimental field setting where many of these variables could not be measured and it would be more common to use some form of aerodynamic model. The use of this model requires that the atmospheric and canopy resistances to evapotranspiration can be calculated. Following the Reynolds analogy we can simply use the value calculated for ra in the `sensible.pas` unit described above to estimate the atmospheric resistance. The canopy resistance is calculated in the function `rc` described below.

```
20: function E : double;
21: var
22: denom,temp1,temp2,temp3, temp4, temp5, temp6 : double;
23:         error : boolean;
24: begin
25: denom := 0;
26: temp1 := ra;
27: temp2 := rc;
28: temp3 := temp1+temp2;
29: temp5 := air_vapour_pressure;
30: temp6 := surface_vapour_pressure;
31: temp4 := temp5-temp6;
32: error := false;
33:         le := vw*rho_a*Mw*temp4;
34:         denom := Ma*air_pressure*temp3;
35: if denom <> 0 then
36:         begin
37:         le := le/denom;
38:         end
```

```
39: else error := true;
40: if error then
41:         begin
42:         end
43: else
44:         result := -le/vw;
45: end;
46:
```

The function d_e coded in lines 47-55 below returns the first derivative of the function above (E). This is simply an analytic calculation of the derivative which is a straight forward calculation. If the calculation for *E* given above were to be changed then this derivative would need to be re-calculated.

```
47: function d_e : double;
48: var
49:         top,denom : double;
50: begin
51: top := -1*rho_a*Mw*(air_vapour_pressure - surface_vapour_pressure)↩
⇒  *rs0*leaf_n*power((pl/pc),leaf_n);
52: denom := air_pressure*(ra+rc)*(ra+rc)*Ma*Pl;
53: //denom := air_pressure*(20+rc)*(20+rc)*Ma*Pl;
54: if denom <> 0 then result := top/denom;
55: end;
56:
```

The function s coded in lines 57-65 below calculates the slope of the saturation vapour pressure curve at the mean wet bulb air temperature. This follows Equation 8.87. However this function is not used, as the method for estimating *E* currently implemented does not require this value in contrast to other calculations such as those given in Equation 8.86 or Equation 8.90.

```
57: function s : double;
58: var
59:         temp,temp2 : double;
60: begin
61: temp2 := wet_bulb_temp + 273.15;
62: temp := 31.3716 - (6014.79/temp2) - (0.00792495*temp2);
```

```
63: temp := exp(temp);
64: result := temp*((vw*mw/(temp2*8.314))-1);
65: end;
66:
```

The function `rc` coded in lines 67-70 below calculates an estimate of the canopy resistance rc following an approximation given in Equation 8.93 and discussed in the associated text. The value here is dependent upon parameters describing the canopy defined in `environment.pas` (§12.2.1).

```
67: function rc : double;
68: begin
69: result := rs0*(1+ power((pl/pc),leaf_n));
70: end;
71:
```

The function `psycho` coded in lines 72-79 below returns an estimate of the psychometric constant after Equation 8.80. The input variable for this calculation are defined in the unit `environment.pas` (§12.2.1).

```
72: function psycho : double;
73: var
74:         temp : double;
75: begin
76: temp := vw*mw;
77: if temp <> 0 then
78: result := air_pressure*cp*ma/temp;
79: end;
80:
81:
82: end.
```

12.2.6 Interface and use of Radlab

The primary interface to **RADLAB** is programmatic. It is intended that problem specific applications are written to make use of the **RADLAB** toolkit. The programmatic interface to **Radlab** is simple. The basic process is to initialise the variables in `environment.pas` (*infra vide*:§12.2.1)

and then call the `soil_temps` procedure (*infra vide*:§12.2.2). So a basic code fragment would be:

```
 1: unit interface;
 2:
 3: interface
 4:
 5: uses
 6: shortwaverad,temperature_regime,environment,sample;
 7: procedure run;
 8: implementation
 9: procedure run;
10: begin
11:
********variable initialisation here ***********************

12: temperature_regime.soil_temps;
13: end;
14: end.
```

Thus the interface can be very simple. The major effort required for a new application is 1) the initialisation of the environmental variables 2) writing appropriate code for the environmental variables defined in `environment.pas`. Typically both will be required for each application and for a useful simulation it is important that the input at this point is of high quality. Calibration and testing of this software for New Zealand is undertaken in the remainder of this chapter.

An example application that provides a GUI interface to **RADLAB** is available on the companion CD. This is available as the Delphi project **biolab** in /software/radlab and an installation package for the compiled application is available in the /software/radlab/installation directory of the companion CD. This project both demonstrates the development of applications that make use of the **RADLAB** toolkit and produces an application which provides access to most of the functionality of Radlab. The GUI consists of a single window with five main pages providing an interface to environmental variables, simulation run control, simulation

I/O, an empirical EHT function (*infra vide*:§11.7), and EHT estimation control respectively (Figure 12.1).

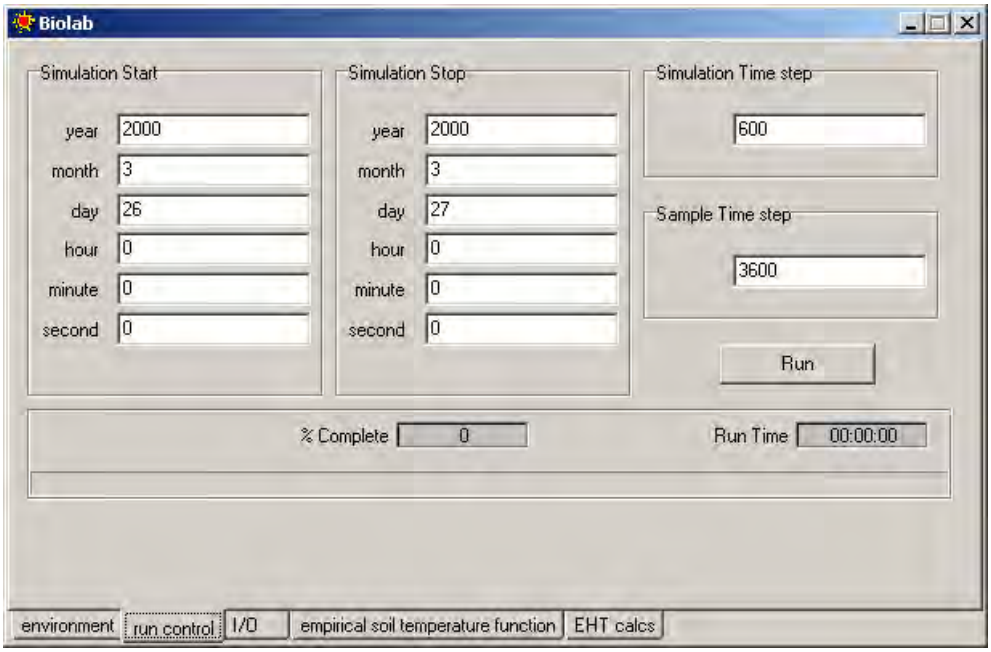

Figure 12.1: The biolab GUI to **RADLAB**

All of the environmental variables discussed in the earlier parts of this chapter can be defined through the interface in the environment page. This page is itself broken down into seven sub-pages; defining the variables for soil, surface, location, climate, radiation and plant factors respectively. All of these are self explanatory and do not require further discussion with the exception of the soil variables. These variables are input via a spreadsheet. The method of use is to input the thickness and parameters for each successive strata into this sheet. So if there were only a single homogenous soil layer, only 1 line of the spreadsheet should be used. The total depth of the simulation is calculated from the sum of the individual soil strata.

The Run control page is used to define the period over which the simulation will take place, and the size of the simulation and sampling

timesteps. It is simply a matter of setting the start and end dates of the simulation and setting the two relevant time steps (an integer value in seconds). Again the default settings are valid and will allow a simulation to be run. It should be noted that the simulation can be slow so initial experimental simulations should be over a short time period such as a few days in order to explore the speed of the simulation.

The simulation I/O page is essentially an interface to the `sampling.pas` unit. This interface is primitive and modifications are most easily achieved through direct coding of the sampling.pas unit. However the GUI I/O interface allows the basic soil climate data necessary for EHT simulation to be output. The I/O page is divided into three sub-pages dealing with soil temperature, soil moisture and the surface flux variables. In each of these pages it is possible to switch the output stream for each of these variable sets on or off, select the output file and choose the exact variables to be sampled. In the case of soil temperature and moisture the exact variables to be sampled are identified by choosing the depth at which to start monitoring the temperature (moisture) variables, the depth at which to stop sampling the variables and the depth interval at which to monitor the simulation. These parameters are all integers and represent the depth in millimetres. So for example, to measure the soil temperature at 5 cm intervals from 20 to 50 cm depth the sample start depth would be set to 200 the sample end depth to 500 and the sample interval to 50.

The empirical soil temperature function page is simply an interface to the empirical soil temperature function defined in Chapter 11 (*infra vide*:§11.7).

The final page is the EHT calc page. This page is essentially an interface to a Δ_{EHT} estimation routine following the code outlined in §12.4. This interface allows identification of the exponential temperature response function to be modelled and the entire simulation is run from

this interface. Other than the variables which are input through the location file (soil bulk density, soil quartz fraction, soil mineral fraction, soil clay fraction, surface slope, surface aspect, surface albedo, surrounding albedo, vegetation height and leaf area index) the simulation proceeds according to the parameters defined in the control pages of the GUI.

The **biolab** project can act as a template for the development of problem specific applications. Many simulations can be run and controlled via this interface and the primary effort required for new applications is to code appropriate functions for the environmental variables in environment.pas.

Examples of simulation output from **Radlab** follow. These were produced through the **biolab** GUI interface with the only change to the default variables being setting the LAI to 0. For the examples presented here the simulation was run from January 1 2000 0:00 hrs to February 1 2000 0:00 hrs. The simulated time step was 60 seconds and the sampling time step was 10 minutes (600 seconds). The environmental functions used for this simulation are as described previously (*infra vide*:§12.2.1) and accordingly the intention is not to simulate any real world location rather to demonstrate the type of output that might be produced.

The controlling surface fluxes that drive the surface energy balance govern the simulation and can be output through the flux I/O options. Examples of the simulated surface flux values are given in Figure 12.2 for a 48 hour period. This data is easily interpreted. Positive values indicate a net flow into the soil surface, negative values indicate flow out of the soil surface. This aspect of the simulation is useful for determining the components of the surface energy balance that are having the greatest influence over the soil flux. As the spatial variability of each of these flux's will differ at any given study site these values are useful for identifying where significant systematic variations might occur within

the study area.

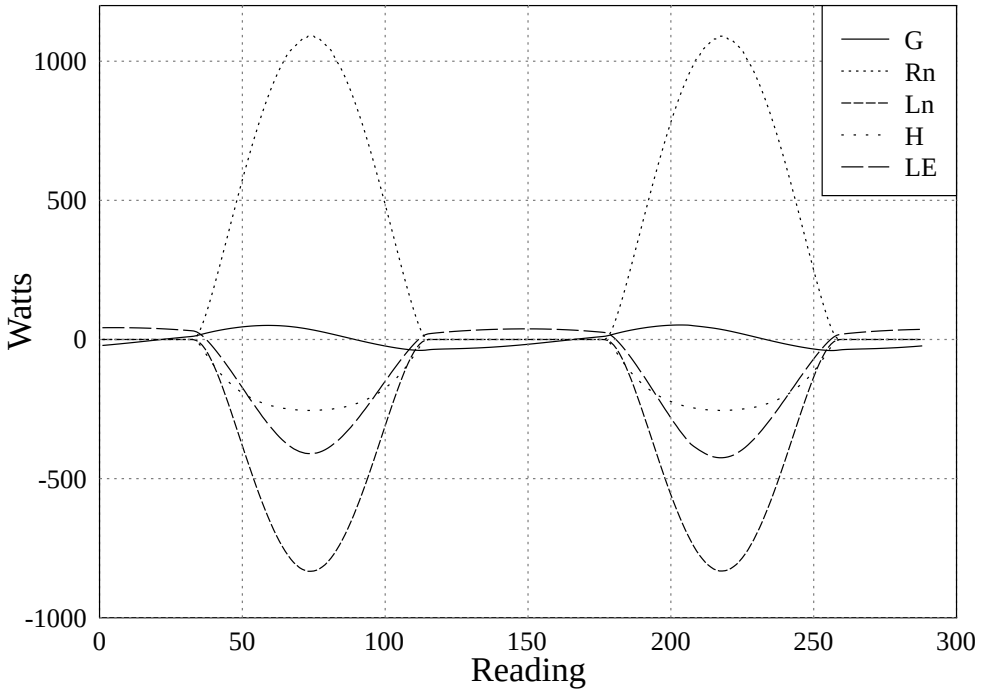

Figure 12.2: Surface flux variables simulated in Radlab for the period 10th January 0:00 hrs - 11th Jan 24:00 hrs sampled at 10 minute intervals

Simulated soil temperature and water values are the primary output of the **Radlab** simulations. Examples of simulated temperature data are given in Figures 12.3–12.4. This data can either be represented as temperature series data for any number of different depths as shown in Figure 12.3 or can be used to provide depth profiles as shown in Figure 12.4. It is this data that is used to approximate $T(t)$ or $D(T)$ and hence the EHT. Similar data can be produced for soil water content, providing values for variables such as soil humidity.

A simple test of the simulated estimates given in these simple examples can be made with reference to the analytic solution to soil heat flow

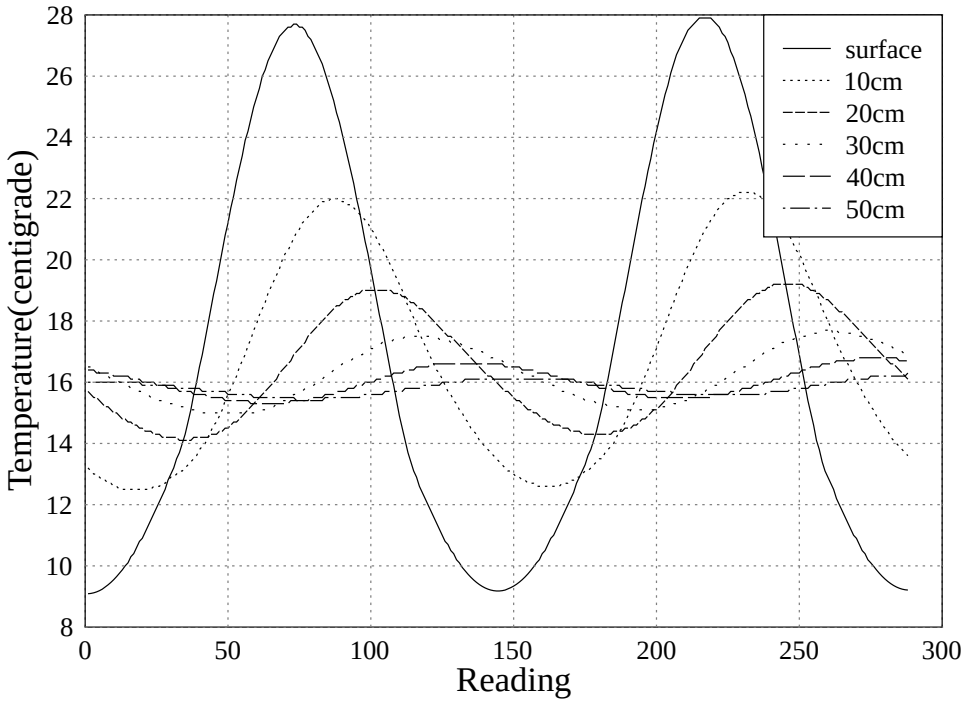

Figure 12.3: Soil temperature variables simulated in Radlab for the period 10th January 0:00 hrs - 11th Jan 24:00 hrs sampled at 10 minute intervals

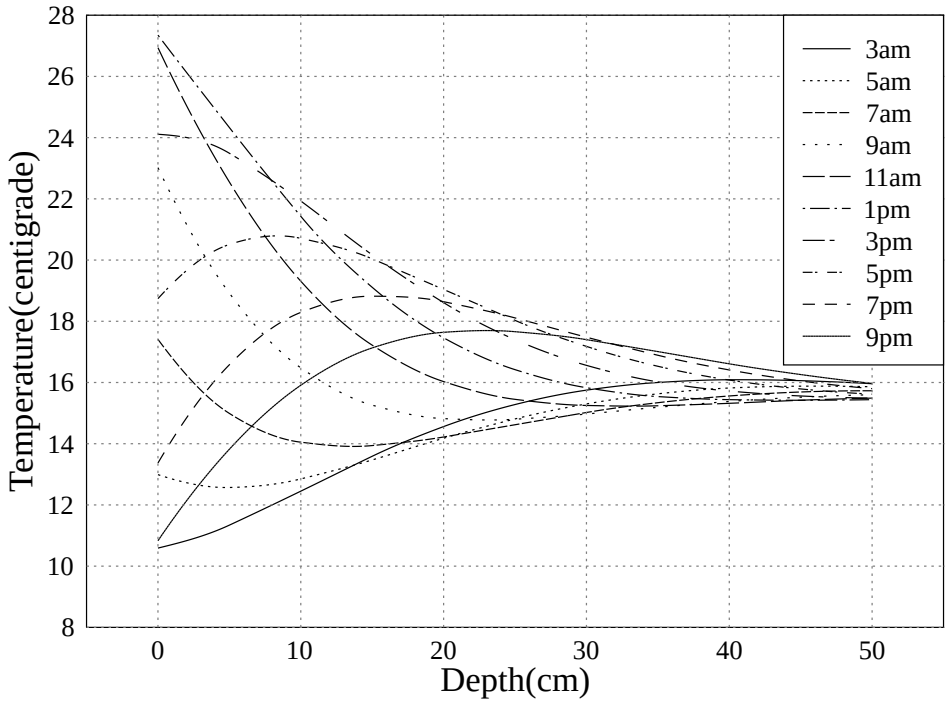

Figure 12.4: Soil temperature profiles simulated in Radlab for the 10th January

(Equation 8.111). As the underlying assumptions for the analytic temperature solution are essentially met in this example, the simulation and analytic results should be similar. We can calculate the damping depth parameter d of the analytic solution (Equation 8.112) and compare this to an experimental value for d from the simulation. An experimental value can be calculated by reworking Equation 8.113 as

$$d = -\ln\left(\frac{\text{Amplitude}(0)}{\text{Amplitude}(z)}\right) \tag{12.9}$$

Where Amplitude(z) is the amplitude of the simulated temperature wave at depth z. However a primary assumption underlying the analytic solution is violated by the simulation. This is the fact that the thermal diffusivity of the soil will vary with depth in the simulation - exactly as we would want - however the analytic solution assumes that the thermal diffusivity will be constant. Therefore we have to use an averaged measure of the thermal diffusivity for the analytic solution and we would expect to see a systematic deviation from the analytic solution with depth as the actual thermal diffusivity varies with depth (Figure 12.5). In the example used here the average thermal diffusivity is 0.00889 and the analytic and simulated d values given in Table 12.2.6 show exactly the expected pattern. This indicates that the simulation is giving sensible results, given the environment defined in `environment.pas`(*infra vide*:§12.2.1).

Thus **Radlab** can be use to simulate soil climate data given driving environmental variables. In order to use this software in an actual application it is necessary to develop and code realistic functions for the driving environmental variables for the locations of interest and then to test the numerical estimates produced. This is considered for New Zealand in the remainder of this chapter.

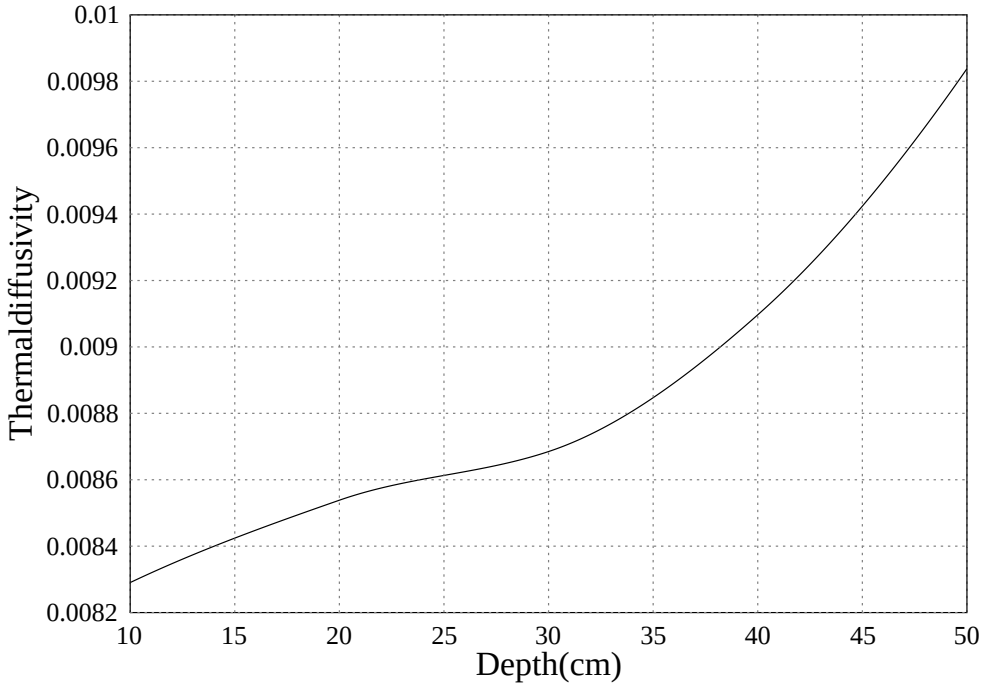

Figure 12.5: Simulated soil thermal diffusivity versus depth for the 10th January

Table 12.1: Comparative d results for the simulated soil

Depth	Amplitude	Analytic d	Experimental d
0	18.81	0	0
10	9.71	-0.660192189	-0.661232361
20	5.01	-1.320384378	-1.322952728
30	2.6	-1.980576568	-1.978877198
40	1.34	-2.640768757	-2.641719029
50	0.7	-3.300960946	-3.291063587

12.3 Environmental Variable Models for New Zealand

In order to apply the **RADLAB** toolkit for Δ_{EHT} or EHT estimation suitable input data are required. This largely involves defining suitable functions for the environmental variables coded in the `env.pas` unit (*infra vide*:§12.2.1). In this section we will describe New Zealand specific models for the key environmental variables of air temperature (*supra vide*:§12.3.2), air humidity (*supra vide*:§G.1), wind speed (*supra vide*:§G.2), rainfall (*supra vide*:§G.3), cloudiness (*supra vide*:§G.4), and Linke t (*supra vide*:§G.5). The focus of this analysis is on enabling the estimation of intra-site Δ_{EHT} for New Zealand. However, as the development of these models will be based around analysis of the meteorological database presented earlier (*infra vide*:§11.2) the variables cannot be modelled at a micro-meteorological scale. This requires an assumption that the only significant micro-meteorological variation at an intra-site scale will be due to differences in the surface radiation budget arising from variation in surface slope and aspect. While this is incorrect, it should allow valid Δ_{EHT} estimates from within areas where this assumption is valid. As we are not trying to estimate absolute EHT values we only need to develop approximating functions for the variables listed above that will allow estimation of the relative temperature regime from within sites. Accordingly the models developed here are simple. Far more sophisticated models could be developed given suitable data. However, given the limitations of the current database there is little point in pursuing more complex models. Thus the models developed and presented here are general first approximations that serve to illustrate the use of **RADLAB** , and provide a method for Δ_{EHT} estimation in limited New Zealand contexts. The conditions under which the type of models developed here can act as useful Δ_{EHT} estimates are considered later (*supra vide*:§12.5).

12.3.1 Model Structure

The modelling approach that we will use here is essentially the same as that applied to the soil temperature data in Chapter 11. The general approach is to break the available data into stationary and long-term trend series as discussed in §11.3, which have been normalised to take into account spatial variation. We then model the deterministic and stochastic components of the long-term trend, seasonal and spatial elements of the data.

The initial break down of the data is performed through the seasonal moving average given in Equation 11.2 which splits the data into a normalised stationary seasonal series and series containing a spatially indexed long-term trend. This long-term data is further split into two sets; the location mean is calculated for each station and removed from the long-term trend data. Thus ultimately the data set is split into three parts – seasonal, long-term-trend and spatial – and each of these is analysed in a separate sub-section to produce a model of the form

$$\text{data series} = \text{deterministic component} + \text{stochastic component} \quad (12.10)$$

for each element. Thus we are modelling each environmental variable considered here as comprising six additive terms:

$$\begin{aligned} \text{data} \quad &= \text{long} - \text{term}_{\text{det}} + \text{long} - \text{term}_{\text{stoch}} \\ &+ \text{spatial}_{\text{det}} + \text{spatial}_{\text{stoch}} \\ &+ \text{seasonal}_{\text{det}} + \text{seasonal}_{\text{stoch}} \end{aligned} \quad (12.11)$$

where the subscripts det and stoch refer to the deterministic and stochastic components respectively

The seasonal deterministic model is in each case modelled by the first two terms of the harmonic series given in Equation 11.4. To allow for spatial differences in the seasonal series this term is crossed with a fully crossed fourth order spatial polynomial model using the variables longitude, latitude and altitude. The spatial component is modelled by a

fully crossed fourth order polynomial on the variables longitude, latitude and altitude. Here the variable codes are the same as those defined in §11.4. The long-term deterministic model is modelled by a fourth order polynomial model of year. This assumes that long-term effects are global.

The stochastic model for seasonal and long-term components is the same. These components will be modelled as autoregressive processes. That is we will assume that the deviation of the observed value from the underlying trend is a random value that is correlated with the deviation of the proceeding x values plus a purely random variable. In each case the number of proceeding values that are significant (the lag) may vary. The deviation of the observed spatial means from the model will be assumed to be a purely random normal variable.

The modelling approach is illustrated for the Air temperature variable in the following section, and the analysis of the remaining variables is presented in Appendix G.

12.3.2 Air Temperature

The environmental air temperature variable will have a significant influence upon the modelled soil temperature climates through the **RADLAB** simulation. This is because the air temperature is a key variable in most of the surface energy exchange models. Accordingly it is important that we can provide a model that produces suitable air temperature sequences for New Zealand.

The purpose of this section is to outline a model that enables us to produce a spatially indexed air temperature time series for locations throughout New Zealand. As discussed previously with the models for soil temperature data (*infra vide*:§11) we are not trying to reconstruct

the actual temperature series for any given time and location, rather trying to develop a time series that has a similar structure to that which is likely to have been experienced in the particular location.

In addition to developing a model for New Zealand air temperature that is suitable for use with **RADLAB** we will use this section to illustrate general modelling approach discussed above.

For the purposes of modelling the air temperature we need to be able to predict a daily temperature wave. To achieve this we will use the monthly mean air maximum ($MAIRMAX$) and monthly mean air minimum ($MAIRMIN$) temperature data — these data values give the mean daily air maximum temperature and the mean daily minimum air temperature respectively. From these we will produce a model for the air maximum ($MAIRMAX(t)$) and air minimum ($MAIRMIN(t)$) for any given instant in time t. From this we can model the daily air temperature as a sine wave that has an amplitude of

$$MAIRMAX(t) - MAIRMIN(t)$$

and a mean of

$$\frac{MAIRMAX(t) + MAIRMIN(t)}{2}$$

In the meteorological database described previously we have air temperature data from 158 stations (*infra vide*:§11.2; Table F.4). Thus what we need to do is produce a model that allows us to describe the structure of this data set. That is to describe the spatial, seasonal and long-term variation of the available air temperature data. As described above we will adopt the procedure outlined in §11.3 for the soil temperature data. So we will use a general model that is of the form

observed data = deterministic component + stochastic component

where each of the deterministic and stochastic components have additive terms for the spatial, long-term and seasonal elements of the model.

In order to conduct this analysis we will first split the data into stationary and trend parts following Equation 11.2 as described in §11.3. Following this we will derive the deterministic and stochastic components of spatial and long term elements from the trend data, and the deterministic and stochastic components of the seasonal element from the stationary data. In the following three sections we will generate models for the seasonal, spatial and trend components.

Deterministic Seasonal Model for *MAIRMAX* and *MAIRMIN*

The stationary seasonal data for *MAIRMAX* an *MAIRMIN* were extracted using the seasonal average given in Equation 11.2. The seasonal series for *MAIRMAX* was then modelled using a spatially indexed harmonic series as discussed above (§12.3.1). The regression has been conducted with no constant as we have defined the constant to be equal to zero through the normalisation procedure which produced the stationary series. The seasonal component for *MAIRMIN* was calculated by modelling the difference between *MARIMAX* and *MAIRMIN* as a spatially indexed harmonic series. This approach allows us to take into account the expected correlation between *MARIMIN* and *MAIRMAX* values. Summaries of the fitted models for *MAIRMAX* and *MAIRMIN* are given in Tables 12.2 and 12.3.

Following these analyses we can model the deterministic seasonal component of *MAIRMAX* as

$$
\begin{aligned}
MAIRMAX_{detseasonal} :=& \\
&-2.254E-07CML2L2 - 0.6610CM2 - 1.065E-06CMALTL3 \\
&-1.657E-04SMALTLAT - 1.060E-20CMA2L4L4 \\
&+9.522E-12CMAL3L2 + 2.063E-15CMA2L2L3 \\
&+0.0960SM2 - 6.167E-06SMALT2 \\
&+1.713E-18CMALT4L4 - 3.968E-13SMALT3L3 \\
&+7.546E-12CML4L2 - 1.583E-21SMA3L4L3
\end{aligned}
$$

Table 12.2: Fitted model for the deterministic seasonal component of *MAIRMAX*

Model Summary

R	R Square	Adjusted R Square	Std. Error of the Estimate
0.9439	0.8910	0.8909	1.3374

ANOVA

	Sum of Squares	df	Mean Square	F	Sig.
Regression	858603.9364	18	47700.2187	26668.1882	0
Residual	105090.7032	58754	1.7887		
Total	963694.6396	58772			

Coefficients

	Unstandardized Coefficients		Standardized Coefficients	t	Sig.
	B	Std. Error	Beta		
CML2L2	-2.254E-07	1.423E-08	-2.0340	-15.8334	0.0000
CM2	-0.6610	0.0078	-0.1154	-84.7337	0.0000
CMALTL3	-1.065E-06	4.440E-08	-3.2607	-23.9907	0.0000
SMALTLAT	-1.657E-04	2.491E-05	-0.2710	-6.6535	0.0000
CMA2L4L4	-1.060E-20	5.262E-22	-0.7031	-20.1419	0.0000
CML2L4	9.522E-12	4.125E-13	2.5666	23.0865	0.0000
CMAL3L2	3.249E-11	1.499E-12	2.9139	21.6699	0.0000
CMA2L2L3	2.063E-15	1.726E-16	0.4278	11.9581	0.0000
SM2	0.0960	0.0078	0.0168	12.3040	0.0000
SMALT2	-6.167E-06	9.867E-07	-0.1373	-6.2505	0.0000
CMALT4L4	1.713E-18	2.207E-19	0.0710	7.7585	0.0000
SMALT3L3	-3.968E-13	9.659E-14	-0.5019	-4.1083	0.0000
CML4L2	7.546E-12	1.265E-12	0.1223	5.9660	0.0000
SMA3L4L3	-1.583E-21	4.277E-22	-0.4333	-3.7018	0.0002
SMALT	-3.858E-03	0.0011	-0.1475	-3.4480	0.0006
SML4L4	-1.057E-15	3.914E-17	-0.5069	-27.0017	0.0000
SMLATLON	-0.0005	4.178E-05	-0.6056	-11.6070	0.0000
SML2L4	1.433E-12	2.467E-13	0.3855	5.8082	0.0000

Residuals Statistics

	Minimum	Maximum	Mean	Std. Deviation	N
Predicted Value	-7.4027	6.9081	-0.0006	3.8222	58772
Residual	-7.4068	11.8832	0.1042	1.3331	58772

Table 12.3: Fitted model for the deterministic seasonal component of *MAIRMIN*

Model Summary

R	R Square	Adjusted R Square	Std. Error of the Estimate
0.5035	0.2535	0.2532	1.3061

ANOVA

	Sum of Squares	df	Mean Square	F	Sig.
Regression	32726.2449	24	1363.5935	799.3493	0.0000
Residual	96349.7818	56481	1.7059		
Total	129076.0267	56505			

Coefficients

	Unstandardized Coefficients		Standardized Coefficients	t	Sig.
	B	Std. Error	Beta		
(Constant)	0.1945	0.0234		8.2957	0.0000
CMAL4L4	-1.449E-17	1.065E-18	-4.3905	-13.6113	0.0000
SMLON4	5.554E-09	6.444E-10	2.3468	8.6200	0.0000
CMLAT4	-1.764E-07	5.877E-08	-0.2592	-3.0023	0.0027
CM2	-1.998E-01	8.526E-03	-0.0935	-23.4312	0.0000
CMALT2L4	-1.680E-11	1.017E-12	-3.4572	-16.5225	0.0000
SMALT	-2.321E-02	2.816E-03	-2.3583	-8.2427	0.0000
SMLL4	1.238E-10	1.659E-11	2.1485	7.4630	0.0000
CMALT3L4	3.081E-14	2.341E-15	4.4749	13.1603	0.0000
CMALTL4	1.402E-08	7.898E-10	4.9642	17.7574	0.0000
SMALL2	-2.142E-08	2.322E-09	-2.7420	-9.2245	0.0000
SMA2L3L4	3.828E-19	7.848E-20	1.5492	4.8785	0.0000
MONTH	-2.540E-02	3.506E-03	-0.0580	-7.2445	0.0000
CMALT	8.682E-03	6.837E-04	0.8851	12.6974	0.0000
SMALT3L4	1.742E-15	3.132E-16	0.2518	5.5630	0.0000
CMALT4L4	-3.214E-17	2.867E-18	-3.5341	-11.2102	0.0000
CMA4L4L4	3.654E-26	3.256E-27	3.4861	11.2219	0.0000
SM2	-4.013E-02	9.866E-03	-0.0188	-4.0675	0.0000
CMALT4L3	7.931E-16	1.190E-16	2.0425	6.6666	0.0000
CML4L4	1.402E-15	1.412E-16	1.8065	9.9291	0.0000
CMLAT3	4.324E-05	4.535E-06	1.4859	9.5359	0.0000
SMALT2L2	8.030E-09	2.784E-09	0.8756	2.8844	0.0039
SMLAT4	4.440E-07	1.506E-07	0.6510	2.9481	0.0032
SMALT2	3.229E-06	1.235E-06	0.1911	2.6155	0.0089
SMLAT2	-9.677E-04	4.421E-04	-0.7839	-2.1890	0.0286

Residuals Statistics

	Minimum	Maximum	Mean	Std. Deviation	N
Predicted Value	-2.4979	2.4144	0.0282	0.7610	56506
Residual	-9.1347	11.6690	0.0000	1.3058	56506

$$
\begin{aligned}
&-3.858E-03SMALT - 1.057E-15SML4L4 \\
&-0.0005SMLATLON + 1.433E-12SML2L4
\end{aligned} \tag{12.12}
$$

and $MAIRMIN$ as

$$
\begin{aligned}
MAIRMIN_{detseasonal} &:= MAIRMAX \\
&-0.1945 + 1.449E-17CMAL4L4 - 5.554E-09SMLON4 \\
&+1.764E-07CMLAT4 + 1.998E-01CM2 + 1.680E-11CMALT2L4 \\
&+2.321E-02SMALT - 1.238E-10SMLL4 - 3.081E-14CMALT3L4 \\
&-1.402E-08CMALTL4 + 2.142E-08SMALL2 - 3.828E-19SMA2L3L4 \\
&+2.540E-02MONTH - 8.682E-03CMALT - 1.742E-15SMALT3L4 \\
&+3.214E-17CMALT4L4 - 3.654E-26CMA4L4L4 + 4.013E-02SM2 \\
&-7.931E-16CMALT4L3 - 1.402E-15CML4L4 - 4.324E-05CMLAT3 \\
&-8.030E-09SMALT2L2 - 4.440E-07SMLAT4 - 3.229E-06SMALT2 \\
&+9.677E-04SMLAT2
\end{aligned} \tag{12.13}
$$

Stochastic Seasonal Component

The stochastic element of the seasonal component describes the residuals of the deterministic model given above. In modelling the residuals we assume that there is correlation between successive residuals; i.e. colder than usual air temperatures are most likely to be proceeded by colder temperatures. We will also assume that there is a correlation between the residuals for daily air maximum temperature and daily air minimum temperature; i.e. on a day where the maximum air temperature is colder than usual we might expect the daily air minimum temperature to also fall below that expected. In order to model these correlations we will use an ARIMA(1,0,0) model to describe the airmax residuals and we will make a correlation between the air maximum and air minimum temperature. That is we will model the air maximum residuals as

$$
r_{airmax}(x) := \beta_{dsairmax} r_{airmax}(x-1) + z^{dsairmax} \tag{12.14}
$$

where $z^{dsairmax} \sim N(0, \sigma_z^{dsairmax})$

and the air minimum residuals as

$$r_{airmin}(x) := \beta_{dsairmin} r_{airmax} + z^{dsairmin} \tag{12.15}$$

where $z^{dsairmin} \sim N(0, \sigma_z^{dsairmin})$

Thus we simply need to establish the parameters $\beta_{dsairmax}$, $\beta_{dsairmin}$, $\sigma_z^{dsairmax}$ and $\sigma_z^{dsairmin}$. These were fitted through an ARIMA(1,0,0) analysis on the residuals for $MAIRMAX$ (Table 12.4) and by regressing the residuals for $MAIRMIN$ on the residuals for $MAIRMAX$ (Table 12.5). From these we have the following values

Parameter	Value
$\beta_{dsairmax}$	0.18980394
$\beta_{dsairmin}$	0.554
$\sigma_z^{dsairmax}$	1.3209434
$\sigma_z^{dsairmin}$	1.0858

Table 12.4: ARIMA(1,0,0) model for $MAIRMAX$

Analysis of Variance

	DF	Adj. Sum of Squares	Residual Variance
Residuals	58771	102487.48	1.7431216

Coefficients

	B	SEB	T-RATIO	APPROX. PROB.
AR1	.18980394	.00442951	42.849837	.0000

Residual Statistics

	N	Minimum	Maximum	Mean	Std. Deviation
Residual	58772	-7.25208	11.88319	9.440978E-02	1.3209434

Having defined a model for the deterministic and stochastic components of the seasonal element from the stationary part of the air temperature we will now consider the spatial and long-term elements of the trend data part.

Table 12.5: Summary of the regression of AIRMIN residuals on AIRMAX residuals

Model Summary

R	R Square	Adjusted R Square	Std. Error of the Estimate
0.5544	0.3073	0.3073	1.0868

ANOVA

	Sum of Squares	df	Mean Square	F	Sig.
Regression	29608.8800	1	29608.8800	25067.8327	0.0000
Residual	66740.9018	56505	1.1812		
Total	96349.7818	56506			

Coefficients

	Unstandardized Coefficients		Standardized Coefficients	t	Sig.
	B	Std. Error	Beta		
RMAIRMAX	0.5540	0.0035	0.5544	158.3282	0.0000

Residuals Statistics

	Minimum	Maximum	Mean	Std. Deviation	N
Predicted Value	-4.0175	6.5831	0.0478	0.7223	56506
Residual	-9.5878	6.3268	-0.0478	1.0858	56506

Spatial Model for Mean Air Maximum and Mean Air Minimum in New Zealand

The spatial model describes the variation in mean variable value throughout New Zealand. Here the model will describe the spatial variation in mean air maximum ($MAIRMAX$) and mean air minimum ($MAIRMIN$). In order to fit this model the mean trend values for each location were extracted from the trend data, thus normalising the trend data to zero for each location. Following this the mean location values where then regressed against fully crossed fourth order spatial polynomial model of longitude, latitude and altitude, using a stepwise regression (The variable codes follow those given in §11.4). This develops a spatial model for the mean variable value. Summaries of this analysis for locational mean $MAIRMAX$ and $MAIRMIN$ values are presented in Tables 12.6 and 12.7 with summary residual statistics in Table 12.8.

Following these analyses we can describe the location mean values for $MAIRMAX$ as:

Table 12.6: Regression model summary for the mean air maximum spatial model fit

Model Summary

Model	R	R Square	Adjusted R Square	Std. Error of the Estimate
1	0.9020	0.8135	0.7953	0.8364

ANOVA

Model		Sum of Squares	df	Mean Square	F	Sig.
1	Regression	436.3629	14	31.1688	44.5588	5.172E-45
	Residual	100.0281	143	0.6995		
	Total	536.3909	157			

Coefficients

		Unstandardized		Standardized	t	Sig.
Model		B	Std. Error	Beta		
1	(Constant)	15.4928	3.9323		3.9399	0.0001
	ALTITUDE	-0.0054	0.0345	-0.5347	-0.1570	0.8755
	LONG	0.0123	0.0230	0.0848	0.5379	0.5915
	LAT5	0.0000	0.0000	1.8732	2.0035	0.0470
	LONG5	2.580E-10	8.109E-11	1.6882	3.1810	0.0018
	ALT2	3.679E-05	4.033E-05	2.6070	0.9123	0.3631
	LATLONG5	8.298E-12	3.194E-12	1.3742	2.5983	0.0103
	LAT4LON5	4.499E-17	2.263E-17	2.7823	1.9881	0.0487
	ALTLON5	-5.385E-14	1.658E-13	-0.8195	-0.3248	0.7458
	ALTLAT5	-1.022E-10	7.026E-11	-1.4833	-1.4545	0.1480
	ALT3LON5	-2.063E-19	3.581E-19	-1.9143	-0.5760	0.5655
	ALT3LAT5	2.388E-17	3.468E-16	0.1686	0.0689	0.9452
	ALT5LON5	-1.793E-26	3.094E-25	-0.1350	-0.0580	0.9539
	ALT2L5L5	1.560E-24	1.625E-24	2.2089	0.9600	0.3387
	ALT5L5L5	-1.796E-33	2.406E-33	-1.4060	-0.7463	0.4567

Table 12.7: Regression model summary for the mean air minimum spatial model fit

Model Summary

Model	R	R Square	Adjusted R Square	Std. Error of the Estimate
1	0.9056	0.8202	0.8025	1.0466

ANOVA

Model		Sum of Squares	df	Mean Square	F	Sig.
	Regression	714.3268	14	51.0233	46.5800	4.067E-46
	Residual	156.6411	143	1.0954		
	Total	870.9680	157			

Coefficients

		Unstandardized		Standardized	t	Sig.
Model		B	Std. Error	Beta		
1	(Constant)	20.6812	4.9208		4.2028	0.0000
	ALTITUDE	-0.0007	0.0431	-0.0552	-0.0165	0.9868
	LONG	-0.0093	0.0287	-0.0501	-0.3237	0.7467
	LAT5	1.657E-09	4.359E-08	0.0349	0.0380	0.9697
	LONG5	-5.872E-11	1.015E-10	-0.3016	-0.5786	0.5638
	ALT2	-2.830E-05	5.046E-05	-1.5740	-0.5609	0.5757
	LATLONG5	-9.452E-13	3.996E-12	-0.1228	-0.2365	0.8134
	LAT4LON5	-1.799E-17	2.832E-17	-0.8729	-0.6351	0.5264
	ALTLON5	4.550E-14	2.075E-13	0.5434	0.2193	0.8267
	ALTLAT5	7.384E-11	8.793E-11	0.8411	0.8398	0.4024
	ALT3LON5	-4.814E-20	4.481E-19	-0.3506	-0.1074	0.9146
	ALT3LAT5	-2.256E-16	4.340E-16	-1.2505	-0.5200	0.6039
	ALT5LON5	1.900E-25	3.872E-25	1.1229	0.4909	0.6243
	ALT2L5L5	-6.214E-25	2.034E-24	-0.6904	-0.3055	0.7604
	ALT5L5L5	1.903E-33	3.011E-33	1.1692	0.6319	0.5284

Table 12.8: Residual statistics for the spatial regression models fitted to the air temperature data

Measure	N	Min	Max	Mean	σ
rmairmin	158	-3.53	3.13	9.31E-15	1.00
rmairmax	158	-4.85	1.81	-3.38E-14	0.80

$$
\begin{aligned}
MAIRMAX_{spatial}(latitude, longtitude, altitude) := \\
&15.4928 - 0.0054ALTITUDE + 0.0123LONG + 2.580E - 10LONG5 \\
&+3.679E - 05ALT2 + 8.298E - 12LATLONG5 \\
&+4.499E - 17LAT4LON5 - 5.385E - 14ALTLON5 \\
&-1.022E - 10ALTLAT5 - 2.063E - 19ALT3LON5 \\
&+2.388E - 17ALT3LAT5 - 1.793E - 26ALT5LON5 \\
&+1.560E - 24ALT2L5L5 - 1.796E - 33ALT5L5L5 + z^{spairmax}
\end{aligned} \tag{12.16}
$$

where $z^{spairmax} = 0.80$

and $MAIRMIN$ as:

$$
\begin{aligned}
MAIRMIN_{spatial}(latitude, longtitude, altitude) := \\
&20.6812 - 0.0007ALTITUDE - 0.0093LONG + 1.657E - 09LAT5 \\
&-5.872E - 11LONG5 - 2.830E - 05ALT2 - 9.452E - 13LATLONG5 \\
&-1.799E - 17LAT4LON5 + 4.550E - 14ALTLON5 \\
&+7.384E - 11ALTLAT5 - 4.814E - 20ALT3LON5 \\
&-2.256E - 16ALT3LAT5 + 1.900E - 25ALT5LON5 \\
&-6.214E - 25ALT2L5L5 + 1.903E - 33ALT5L5L5 + z^{spairmin}
\end{aligned} \tag{12.17}
$$

where $z^{spairmin} = 1.00$

Long-Term Trend

The final model element is the long-term trend. This is analysed using the normalised trend data produced through the spatial analysis conducted above. As a first step in modelling the long term trend for the $MAIRMAX$ and $MAIRMIN$ data any apparent long term trend over the duration of the recording period was removed. This was achieved by regressing the data against a cubic model of year. This model treats any apparent long-term trend as an additive effect that is global to New Zealand as a whole. A summary of this analysis for $MAIRMAX$ and $MAIRMIN$ is given in Figures 12.6 and 12.6 respectively.

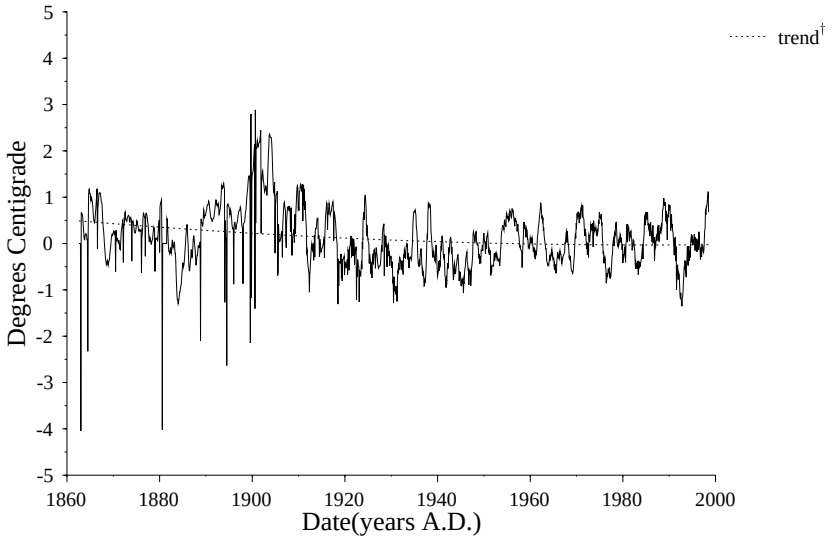

Figure 12.6: Long-term trend for mean air maximum temperature

† $x = 93.094 - 7.037E-02X + 5.953E-09x^3$ $R^2 = 0.058$ Sig. = 0

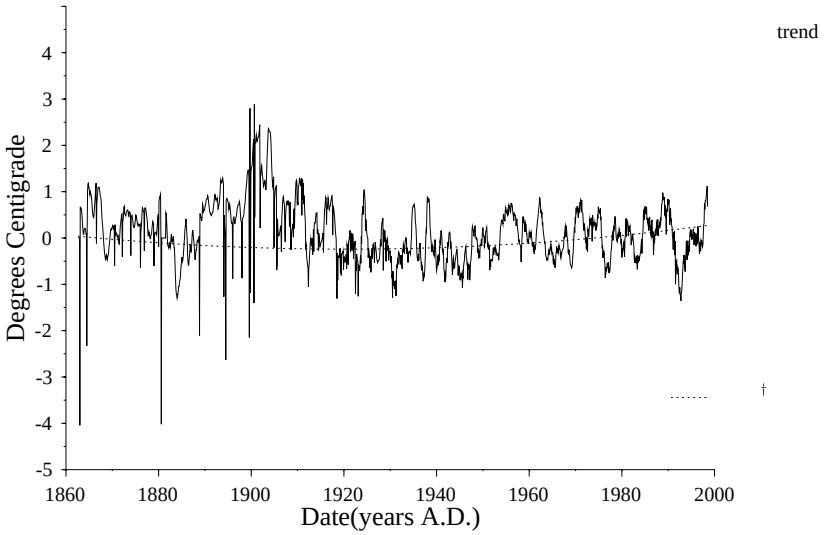

Figure 12.7: Long-term trend for mean air minimum temperature

† $x = 205.109 - .160X + 1.449E-08x^3$ $R^2 = 0.058$ Sig. = 0

We would expect the long-term trend for $MAIRMAX$ and $MAIRMIN$ to be correlated. For example low air maximums may tend to be correlated with low air minimums. Thus for the purposes of modelling long-term trends in air temperature we will model the long-term trend structure in $MARIMAX$ and then model the trend in $MARIMIN$ as a function of the $MAIRMAX$.

In this analysis we are most interested in the residuals from the regression models as it is the stochastic structure of these residuals that define the nature of the long-term stochastic behaviour of the simulation model. Summary residual statistics are presented in Table 12.9, and one approach would be to treat the residuals as completely independent normal variables. However, we would expect that there would be correlation

Table 12.9: mean standard deviation values from annual trend for the analysis variables

Variable	σ
Monthly Rain Total	20.543
Mean monthly Air Maximum	0.936
Mean monthly Air Minimum	0.811
monthly sun total	4.934
monthly windrun	5.045
monthly mean relative humidity	2.822

between successive residuals. For example we would expect that cooler than average temperatures would tend to follow temperatures that were also cooler than average. As we wish to model any such stochastic structure that may exist in the residuals we have conducted an ARIMA(lag,0,0) analysis on the residuals. This models the residuals as

$$res(x) := \beta_1 res(x-1) + \beta_2 res(x-2) \ldots + \beta_{lag} res(x-lag) + z$$

where $z \sim N(0, \sigma_z)$.

Thus we need to be able to establish the appropriate lag value and then establish the values for the parameters $\beta_1 \ldots \beta_{lag}$ and σ_z. The appropri-

ate *lag* values for the long-term variable trends analysed in this chapter were established by looking at the cut off values in the associated partial ACF plots and are given in Table 12.10. From this we can see that a lag of 3 is suitable for *MARIMAX*. Accordingly an ARIMA(3,0,0) model was fitted to the long-term trend residuals for *MAIRMAX*. The fitted parameter values for these are given in Tables 12.11 and 12.12. As an example, a set of residuals for *MAIRMAX* and the fitted stochastic model are plotted in Figure 12.8. As can be seen significant autocorrelation structure in the residuals is explained by the fitted model. This is identical to the process applied to the soil temperature series data as illustrated in Figures 11.4, 11.7 and 11.10.

Table 12.10: Significant autoregressive lags for annual trend data

Variable	Lag p
Monthly Rain Total	4
Mean monthly Air Maximum	3
monthly windrun	1
cloudiness	0
monthly mean relative humidity	3

Table 12.11: Fitted parameters for the air temperature stochastic models

		B	SEB	T-RATIO	PROB
RMAIRMAX	AR1	0.42305133	0.02558285	16.536523	0
	AR2	0.25436709	0.02711212	9.382045	0
	AR3	0.21717532	0.02554681	8.501074	0

For the purposes of the **RADLAB** simulation we will not use the fitted long-term trend equations given in Figures 12.7 and 12.6 as we can-

Table 12.12: Summary residual statistics for the long-term stochastic models fitted to the environmental variables

	N	Minimum	Maximum	Mean		Std. Deviation
	Statistic	Statistic	Statistic	Statistic	Std. Error	Statistic
MAIRMAX	1616	-4.5293	3.7511	0.0006	0.0094	0.3775
RH	1122	-14.4624	7.9659	-0.0288	0.0423	1.4174
RAINTOT	1632	-13.0168	28.8466	-0.0019	0.0630	2.5437
WINDRUN	1418	-137.3723	150.4267	-0.0319	0.2511	9.4561

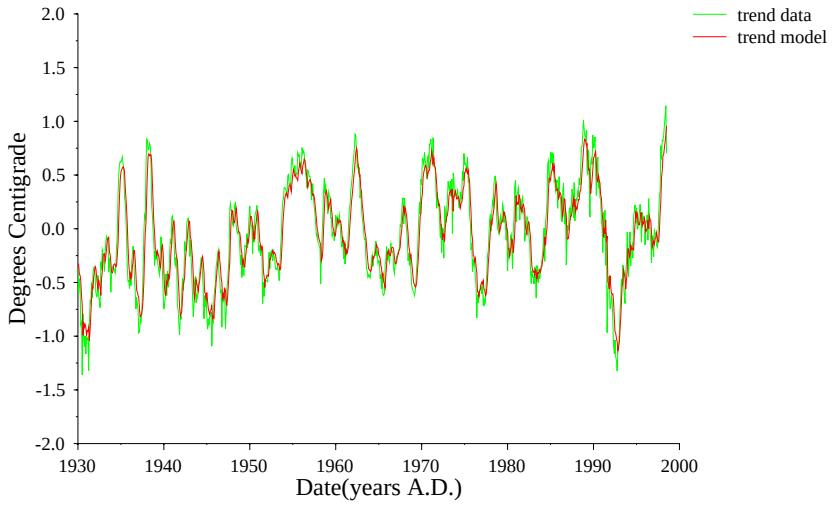

Figure 12.8: Trend data and fitted stochastic model for the monthly mean air maximum temperature

not extrapolate these trends beyond the recording period. The model applied will be that there has been no long-term trend other than the variations observed as a function of long-term stochastic variation such as that illustrated in Figure 12.8. Thus we model the long-term trend component of $MAIRMAX$ as:

$$MAIRMAX_{trend}(x) := 0.42305133(x-1) + 0.25436709(x-2) + 0.21717532(x-3) + z \quad (12.18)$$

where $z \sim N(0, 0.38)$

As discussed above we will model the stochastic structure of the long-term trend in $MARIMIN$ as a function of the stochastic structure in $MARIMAX$. In effect this amounts to regressing the normalised trend data for $MAIRMIN$ against the normalised trend data for $MAIRMAX$. A summary of this analysis is presented in Table 12.13

Following this analysis we can model the long-term trend component of $MARIMIN$ as

$$MAIRMIN_{trend}(x) := 0.3308 * MAIRMAX + z \quad (12.19)$$

Table 12.13: Fitted model for the deterministic seasonal component of *MAIRMAX*

Model Summary

R	R Square	Adjusted R Square	Std. Error of the Estimate
0.3844	0.1478	0.1473	0.5137

ANOVA

	Sum of Squares	df	Mean Square	F	Sig.
Regression	73.1360	1	73.1360	277.1246	0.0000
Residual	421.7283	1598	0.2639		
Total	494.8643	1599			

Coefficients

	Unstandardized Coefficients		Standardized Coefficients	t	Sig.
	B	Std. Error	Beta		
MAIRMAX	0.3308	0.0199	0.3844	16.6471	0.0000

Residuals Statistics

	Minimum	Maximum	Mean	Std. Deviation	N
Predicted Value	-1.3293	0.9544	0.0412	0.2099	1599
Residual	-3.2539	0.8931	-0.1436	0.4932	1599

where $z \sim N(0, 0.4932)$

Air Temperature Model

As discussed above, in order to predict the short term air temperature the diurnal cycle will be approximated with a sine wave that oscillates between the air maximum temperature and air minimum temperature for any given day as estimated through the models defined above. This will be offset such that the minimum air temperature is attained at 6am (approximate average pre-dawn minimum);ie a phase offset of $\pi/2$. Thus we model the diurnal air temperature as

$$\begin{aligned} temp(t) &:= \bar{T} + \alpha \sin\left(\frac{t*2\pi}{24} - \frac{\pi}{2}\right) \\ \bar{T} &:= \frac{MAIRMAX(t)+MAIRMIN(t)}{2} \\ \alpha &:= MAIRMAX(t) - MAIRMIN(t) \end{aligned} \tag{12.20}$$

where t is the instant in time and $MAIRMAX$ ($MAIRMIN$) is given by the summation of Equations 12.16, 12.18, 12.12 and 12.14 (12.17, 12.19, 12.13 and 12.15) after Equation 12.11.

Martin Jones 2002

12.3.3 Summary

In this section a simple model for describing the structure of key long-term meteorological variables for **RADLAB** simulations in New Zealand has been outlined. The general model approach is to describe the observed long-term data as comprising three additive elements; spatial, long-term and seasonal. Each of these in turn comprising a deterministic and stochastic component (*e.g.* 12.11). This follows the model structure described in Chapter 11 (*infra vide*:§11.3). Models have been developed for the key environmental variables of air temperature (*supra vide*:§12.3.2), air humidity (*supra vide*:§G.1), wind speed (*supra vide*:§G.2), rainfall (*supra vide*:§G.3), cloudiness (*supra vide*:§G.4), and Linke t (*supra vide*:§G.5), based around analysis of the meteorological database presented earlier (*infra vide*:§11.2). The air temperature analysis has been presented in this section to illustrate the method, while the remaining analyses are presented in Appendix G. A code implementation of these models that integrates into **RADLAB** is outlined in Appendix G (*supra vide*:§G.6).

The models defined here provide New Zealand specific estimates of the environmental variables required for soil temperature regime simulations through **RADLAB** . These models are simplistic and are only intended to generate series data that have similar properties to that which is observed rather than to provide an explicit predictive model for any given meteorological variable. Further, due to the spatial scale of the data upon which the meteorological models have been based the models cannot describe micro-meteorological variation. This limits the general applicability of the associated Δ_{EHT} estimates to locations in which the only variations in surface energy budget arise due to variations in the net radiation budget through differences in surface slope and aspect. However, this may be sufficient for many OHD applications. We can test the suitability of these models by comparing Δ_{EHT} values simulated through

RADLAB to those actually observed. In the following section an approach to simulating Δ_{EHT} through **RADLAB** is discussed, and following this we will compare a series of simulated and measured Δ_{EHT} values for the experimental micro-scale analogue cell survey described in Chapter 10 (*infra vide*:§34).

12.4 Δ_{EHT} Simulation

In order to simulate an EHT through the **RADLAB** simulation we perform precisely the same calculation as previously described for the empirical soil temperature model (§11.5). Thus, we initially simulate a series of soil temperature data through **RADLAB** , such as that illustrated in Figure 12.3, and this data is then used as input into Equation 11.27 from which we can calculate an EHT estimate.

In order to calculate Δ_{EHT} values we simply calculate the soil temperature series at each location to be compared and calculate the difference in EHT between the two locations in response to the same environmental conditions. Again following the procedure outlined in Chapter 11, by varying the driving environmental conditions through sampling from within the state space of the parameter values for the governing climatic models we can generate a series of Δ_{EHT} values and hence generate a distribution for Δ_{EHT} from the locations under consideration.

The following code example illustrates the general process and also serves to demonstrate the manner in which the **RADLAB** toolkit may be used. The procedure calc_eht coded below is designed to be compiled with the **RADLAB** toolkit as part of a GUI interface. The procedure is designed to read a file containing a description of a series of locations for which Δ_{EHT} values are required. In this example each location has a unique value for surface slope, surface aspect, leaf area index and soil

thermal diffusivity. The file input is handled in lines 19-45 below.

```
 1: procedure calc_eht;
 2: var
 3:         f1 : textfile;
 4:         seed : longint;
 5:         total_sample_count, number_locs, col, x, sample_count, xx↩
⇒    , y, yy, zz : integer;
 6:         s1,s2, title_string : string;
 7:         job : array[1..100,1..6] of string;
 8:         eht_run : array[1..10,1..10,1..10] of single;
 9:         de, de_std, dummy : double;
10: begin
11: //********set io parameters
12: sample_temp := false;
13: sample_water := false;
14: sample_flux := false;
15: calc_eht :=true;
16:        temp_sample_start_depth := strtoint(numio18.text);
17:         temp_sample_interval := strtoint(numio19.text) ;
18:         temp_sample_count := 1 + ((strtoint(numio20.text) - temp_↩
⇒    sample_start_depth) div temp_sample_interval);
19: assignfile(f1,edit40.text);
20: reset(f1);
21: number_locs := 0;
22: while not eof(f1) do
23:         begin
24:         readln(f1,s1);
25:         inc(number_locs);
26:         s2 := '';
27:         col := 1;
28:         for x := 1 to length(s1) do
29:                 begin
30:                 if s1[x] = ',' then
31:                         begin
32:                         trim(s2);
33:                         job[number_locs,col] := s2;
34:                         s2 := '';
35:                         inc(col);
36:                         end
37:                 else
38:                         begin
39:                         s2 := s2 + s1[x];
40:                         end;
41:                 end;
42:         trim(s2);
43:         job[number_locs,col] := s2;
```

```
44:         end;
45: closefile(f1);
46: assignfile(temperature_regime.eht_out,'c:\eht_out.csv');
47: rewrite(temperature_regime.eht_out);
48: for xx := 1 to temp_sample_count do
49:         begin
50:         for x := 1 to number_locs do
51:                 begin
52:                 write(eht_out,',',job[x,1] + '-' + inttostr(xx));
53:                 end;
54:         end;
55: writeln(eht_out);
56: total_sample_count := strtoint(edit41.text);
```

The actual simulation is controlled in lines 57-142 below. An outer loop repeats the Δ_{EHT} simulation to collect the required number of Δ_{EHT} samples. The number of samples required is set by the value of the total_sample_count variable. At the start of each sampling loop a new state for the parameters of the controlling environmental variables are set through the calls in lines 60-64. These parameter values are then used for calculating the EHT at each of the locations identified in the input file described above.

```
57: for sample_count := 1 to total_sample_count do
58: begin
59: title_string := 'Run ' + inttostr(sample_count);
60: set_air_temp_params;
61: set_rh_params;
62: set_ws_params;
63: set_rf_params;
64: set_cloud_params;
65: seed := floor(random*2147483647);
66: for x := 1 to number_locs do
67: begin
68: form1.Caption := title_string + ' sample ' + inttostr(x);
69: randseed := seed;
70: calc_eht := true;
71:         if radiogroup2.ItemIndex =1 then
72:                 begin
73:                 temperature_regime.obsidian := true;
74:                 temperature_regime.E_eht := strtofloat(numio35.te↩
⇛    xt);
```

```
 75:                 end
 76:         else
 77:                 begin
 78:                 temperature_regime.obsidian := false;
 79:                 temperature_regime.A_eht := strtofloat(numio32.te↩
⇒    xt);
 80:                 temperature_regime.B_eht := strtofloat(numio34.te↩
⇒    xt);
 81:                 end;
 82: numlab1.Value := 0;
 83: timer1.Enabled := true;
 84: start_time := encodedate(strtoint(edit31.text),strtoint(edit10.te↩
⇒    xt),strtoint(edit11.text));
 85: start_time := start_time + encodetime(strtoint(edit12.text),strto↩
⇒    int(edit18.text),strtoint(edit23.text),0);
 86: end_time := encodedate(strtoint(edit9.text),strtoint(edit26.text)↩
⇒    ,strtoint(edit27.text));
 87: end_time := end_time + encodetime(strtoint(edit28.text),strtoint(↩
⇒    edit29.text),strtoint(edit30.text),0);
 88: run_time := trunc((end_time - start_time)*86400);
 89: time_step := strtoint(numio1.text);
 90: sample_step := strtoint(numio2.text) div time_step;
 91: if sample_step < 1 then sample_step := 1;
 92: years := 2000;
 93: dt := time_step;   //t in seconds
 94: initialise_variables;
 95: //********location****************
 96: latitude := strtofloat(job[x,2]);
 97: longtitude := strtofloat(job[x,3]);
 98: altitude := strtofloat(job[x,4]);
 99: surface_slope := strtofloat(job[x,5]);
100: surface_azimuth := strtofloat(job[x,6]);
101: if checkbox1.checked then
102:         begin
103:
104:         assignfile(temp_output,edit33.Text);
105:
106:         end
107: else
108:         begin
109:         sample_temp := false;
110:         end;
111: if checkbox2.checked then
112:         begin
113:         sample_water := true;
114:         assignfile(water_output,edit34.text);
115:         water_sample_start_depth := strtoint(numio21.text);
```

```
116:         water_sample_interval := strtoint(numio22.text);
117:         water_sample_count := 1 + ((strtoint(numio23.text) - wate↩
⇒    r_sample_start_depth) div water_sample_interval);
118:         end
119: else
120:         begin
121:         sample_water := false;
122:         end;
123: if checkbox3.checked then
124:         begin
125:         sample_flux := true;
126:         assignfile(flux_output,edit35.text);
127:         end
128: else
129:         begin
130:         sample_flux := false;
131:         end;
132: start_io;
133: writeln(temperature_regime.eht_out,job[x,1]);
```

The actual simulation is performed through calling the soil_temps procedure (*infra vide*:§12.2.2) in line 134 below. This calculates an EHT value for the current location which is then stored in the EHT_run array in lines 136–139.

```
134: temperature_regime.soil_temps;
135: //end_io;
136: for xx := 1 to temp_sample_count do
137:         begin
138:         EHT_run[x,xx,sample_count] := eht_array[xx,2];
139:         end;
140: timer1.enabled := false;
141: end;
142: end;
143: form1.caption := 'Analysing data';
144: //xxxxxxxxxxx output the delta eht here xxxxxxxxxxxxxxx
```

The Δ_{EHT} calculation is coded in lines 145–180 below. Here the mean difference and variance of difference in EHT value between each location is calculated. This is our Δ_{EHT} estimate. This estimate is then output as an upper triangular array such as the example given in Table 12.14.

Thus this gives a simulated Δ_{EHT} estimate for the locations given in the input file.

```
145: for xx := 1 to temp_sample_count do
146:         begin
147:         for x := 1 to number_locs do
148:                 begin
149:                 write(eht_out,job[x,1] + '-' + inttostr(xx));
150:                 for  yy := 1 to temp_sample_count do
151:                         begin
152:                         for y := 1 to number_locs do
153:                                 begin
154:                                 if (yy < xx) or ((yy = xx) and (y↩
⇛     <= x)) then
155:                                         begin
156:                                         write(eht_out,',');
157:                                         end
158:                                 else
159:                                         begin
160:                                         de := 0;
161:                                         de_std := 0;
162:                                         for zz := 1 to total_samp↩
⇛    le_count do
163:                                                 begin
164:                                                 dummy := eht_run[↩
⇛    x,xx,zz] - eht_run[y,yy,zz];
165:                                                 de := de + dummy;
166:                                                 de_std := de_std ↩
⇛    + sqr(dummy);
167:                                                 end;
168:                                         de := de/total_sample_cou↩
⇛    nt;
169:                                         try
170:                                         de_std := 0;//sqrt((de_st↩
⇛    d - sqr(de))/total_sample_count-1);
171:                                         except
172:                                         de_std := 0;
173:                                         end;
174:                                         write(eht_out,',',de);
175:                                         end;
176:                                 end;
177:                         end;
178:                 writeln(eht_out);
179:                 end;
180:         end;
181: form1.caption := '';
182: closefile(temperature_regime.eht_out);
```

```
183: end;
184:
```

Table 12.14: Example simulated Δ_{EHT} output following the function coded in §12.4. The reported values are the simulated Δ_{EHT} results between each location in ^{0}C

	beth1-1	beth2-1	beth3-1	beth4-1	beth5-1
beth1-1		0.24	-0.03	0.28	-0.01
beth2-1			-0.27	0.03	-0.25
beth3-1				0.30	0.02
beth4-1					-0.28
beth5-1					

Thus by using a controlling procedure such as that described above we can generate Δ_{EHT} estimates such as those given in Table 12.14 for any set of locations we desire. In the following section simulated and measured Δ_{EHT} values are compared and the general applicability of the models presented here are evaluated.

12.5 Δ_{EHT} Model Evaluation

In order to evaluate **RADLAB** simulations of Δ_{EHT} values we can make use of the micro-scale cell survey experiments described in Chapter 10 (*infra vide*:§10.3.2; Table 10.11). The Δ_{EHT} values for these locations can be simulated through **RADLAB** and compared to those actually observed. As we can implement a model to directly calculate the cell specific Δ_{EHT} there will be no problems arising due to differences in observed and modelled temperature response functions. Thus the comparison will be a direct assessment of the **RADLAB** Δ_{EHT} simulation approach as discussed above (*infra vide*:§12.4). In total 50 observed and simulated Δ_{EHT} values have been compared at seven general locations.

As previously discussed the spatial variation of these estimates is limited to the micro-scale response of the governing environmental variables. In the current case the governing environmental variables are not modelled at a micro-meteorological level. This means that the simulated Δ_{EHT} values will only vary in response to immediate surface geometry, burial depth and matrix composition. In reality we would expect that other driving environmental variables would also vary at an intra-site scale. Thus we would expect that there may be problems with the simulated Δ_{EHT} values where the analysis locations do not comprise uniform micro-climates. In light of this we would expect that the validity of the simulated Δ_{EHT} estimates will vary depending upon the nature of the problem, specifically the extent of spatial variation within the analysis area. Accordingly the following evaluation exercise will be broken into two sections; variation in Δ_{EHT} as a function of depth, and spatial variation in Δ_{EHT}. This is because we would expect that the approximating assumptions of the current models would be more suitable to the case of Δ_{EHT} variation with depth than that of general spatial variation in Δ_{EHT}.

In the following two sections the reported results are assumed to be normally distributed with a standard deviation of 0.1 ^{0}C. While a direct standard deviation can be calculated through the Δ_{EHT} simulation, the simulations are computationally intensive and involve significant amounts of time. The results presented here only represent a sample of 10 Δ_{EHT} estimates per result. This alone requires 30 days to run on a fast computer. Thus the routine calculation of statistics arising from hundreds of samples is not computationally plausible in a short period of time. Accordingly an effort has been made to generate an approximate figure for the uncertainty associated with the Δ_{EHT} estimates arising from simulations through **RADLAB** using the models developed in this chapter. This figure has been derived from generating a series of 500 Δ_{EHT} estimates from 4 different locations. The standard deviation from these runs was 0.1^0C. This figure is consistent with the results from the Δ_{EHT} simula-

tions considered here and the comparisons in the following sections can be used to test the suitability of this variance estimate.

12.5.1 Δ_{EHT} as a Function of Burial Depth

Variation in Δ_{EHT} as a function of depth has been measured at 11 locations within six general sites (*infra vide*:§34; Table 10.11). Δ_{EHT} estimates have been simulated for each of these locations and a summary of the comparisons between the observed and measured results is presented in Table 12.15. Tables of the simulated Δ_{EHT} values and contrasts between simulated and observed values are given in Appendix G (*supra vide*:§G.7). The influence of clear outliers have been removed from all reported results.

These contrasts show that the simulated Δ_{EHT} values approximate those observed within the measurement limits of the analogue cells. The overall mean for the contrasts is -0.069 ^{0}C with a standard deviation of 0.26 ^{0}C. Thus the mean is not statistically different from zero and there is no indication of a bias in the contrasts. On the basis of the test statistic V (Equation 10.1 described in §10.3.2) we cannot reject the null hypothesis that the overall variability is solely due to variation in the analogue cell function. Further, in no individual case is the variation of the contrast greater that that which would be expected due to the inherent variability of the cell measurement devices. Thus the conclusion is that the environmental models presented in this chapter can be used in conjunction with **RADLAB** to approximate variation in Δ_{EHT} with depth.

We can also use these contrasts to assess the suitability of the variance estimation associated with the Δ_{EHT} estimates. The overall σ of 0.26 ^{0}C given in Table 12.15 is a function of both the variability in the simulated Δ_{EHT} estimates and the analogue temperature cell function. As discussed above the Δ_{EHT} estimates are assumed to have a normally dis-

Table 12.15: Summary of contrasts between observed and measured Δ_{EHT} values for the variation in Δ_{EHT} as a function of burial depth experiments

Location	$N^{\ddagger}$	Mean	σ	V
beth	3	-0.30	0.23	1.17
hwb	3	-0.12	0.07	0.11
leigh	3	0.05	0.22	1.07
Pakiri 1	3	-0.13	0.16	0.56
Pakiri 2	3	0.32	0.18	0.71
Pakiri 3	3	0.08	0.10	0.21
Pakiri 4	3	0.23	0.14	0.45
Pakiri 5	3	-0.11	0.26	1.46
Pukekohe	6	0.09	0.16	1.47
Tapharanui 1	3	-0.18	0.29	1.89
Tapharanui 2	3	-0.16	0.10	0.21
total	36	-0.07	0.26	21.67

‡ here N refers to the number of contrasts rather than the number of individual measurements.

tributed uncertainty with $\sigma = 0.1\ ^0$C. In this case the observed variance in the temperature cell function is given by

$$\sigma^2_{cell} = 0.26^2 - 0.1^2 = 0.0576 \tag{12.21}$$

with a corresponding standard deviation of 0.24 ^{0}C. Thus we do not see any inflation in the apparent cell variance beyond that established for the experimental controls in §10.2.1. Thus the results are in accordance with an estimated σ for the Δ_{EHT} simulation results of 0.1 ^{0}C.

12.5.2 Spatial Variation in Δ_{EHT}

Spatial variation in Δ_{EHT} has been measured at 39 locations within five general sites (*infra vide*:§34; Table 10.11). Δ_{EHT} estimates have been simulated for each of these locations and a summary of the comparisons between the observed and measured results is presented in Table 12.16. Tables of the simulated Δ_{EHT} values and contrasts between simulated and observed values are given in Appendix G (*supra vide*:§G.7). The influence of clear outliers have been removed from all reported results.

It is immediately apparent from Table 12.16 that the spatial contrasts are more variable than those for the variation in Δ_{EHT} with depth. In this case the mean contrast value is 0.211 ^{0}C with a standard deviation of 1.04 ^{0}C. Clearly variation of this magnitude is much larger than would be expected due to variation in analogue cell function alone. This is illustrated by the magnitude of the test statistic V which is significant at $\alpha = 0.05$ for the overall contrast variability. Thus we can reject the null hypothesis that the magnitude of the observed variation is solely due to variability in function of the analogue cells. This indicates that there are problems with the Δ_{EHT} estimates in that they do not suitably estimate the observed spatial variation in Δ_{EHT}. This almost certainly arises due to the fact that the governing environmental variables vary over the survey areas, violating the model assumptions that the only variables

Table 12.16: Summary of contrasts between observed and measured Δ_{EHT} values for the spatial variation in Δ_{EHT} experiments

Location	$N^{\ddagger}$	Mean	σ	V
Bethells	10	-0.14	0.23	5.15
Hot Water Beach	6	0.00	0.47	$12.18^{\dagger}$
Pakiri	105	0.29	1.19	$1629.24^{\dagger}$
Tapharanui	28	-0.23	0.64	$122.78^{\dagger}$
Tapharanui loc1	3	0.43	0.42	3.93
Tapharanui loc2	10	0.21	0.32	9.94
Tram Valley Road	10	-0.21	0.34	11.86
total	172	0.211	1.04	$2056.41^{\dagger}$

‡ here N refers to the number of contrasts rather than the number of individual measurements.

$^{\dagger}V$ significant at $\alpha = 0.05$

varying at an intra-site scale are surface slope, surface aspect and matrix composition. However, some of these results do derive from locations in which we may expect the model assumptions to be valid. In particular at the Bethells and Tramvalley road locations, where the cells were placed within 3 metres of one another. At Bethells the matrix was constant between locations, whereas the five Tramvalley Road locations were artificial plots which were filled with a differing matrix composition to test the sensitivity of both observed and simulated Δ_{EHT} to matrix composition. Thus we would expect that in both of these cases micro-scale variations would be limited to immediate surface morphology and matrix composition. Additionally, we can split the Tapharanui results into two sets, coded loc1 and loc2 in Table 12.16. The loc2 location corresponds to cells placed within 4 metres of one another. The only variation being due to surface slope and aspect with surface cover and matrix composition remaining constant. Thus at this location the model assumptions

should also be valid. In these three locations (Bethells, Tapharanui loc2 and Tramvalley road) the contrast variation is no greater than that which would be expected due to variation in measured cell response (the test statistic V is not significant for these locations). The locations for which measurements are made over a wider spatial scale (Hot Water Beach, Pakiri, Tapharanui) exhibit a much greater contrast variance which is significantly larger than what we would expect to observe due to variation in analogue cell function alone. In all of these cases there is considerable scope for differing micro-climates due to factors such as differential shelter from the wind (which will influence sensible and latent heat fluxes) differing hydrology which will influence soil water content (affecting the latent heat flux) and the arising variations in air temperature. No factors such as these can be taken into account under the models defined in this chapter.

The conclusion from this comparison is that — as expected — governing environmental variables need to be modelled at a micro-scale level to enable general estimation of spatial variation in Δ_{EHT}, and accordingly the models developed to-date cannot be used as a general Δ_{EHT} estimation procedure for New Zealand. However, we can also conclude that the current models will allow valid Δ_{EHT} estimates to be produced for spatially limited locations over which it is valid to assume that the governing meteorological variables do not vary.

12.5.3 Discussion

These results are very interesting. A direct comparison between the simulated and observed results indicates that the simulated Δ_{EHT} values are in general poor estimates of those actually observed. The conclusion is that this arises due to violated model assumptions. However, the results have also shown that the simulated Δ_{EHT} results are good estimators

under conditions where the model assumptions are valid, generating normally distributed estimates with a standard deviation of around 0.1 ^{0}C. This means that the simulated Δ_{EHT} values can give useful approximations to variations in Δ_{EHT} with depth, can take account of varying matrix composition and can provide useful estimates for spatial variation in Δ_{EHT} over scales where the governing factors of air-temperature, wind-speed and soil hydrology, in particular, are uniform. While this limits the applicability of the current numerical model this is still a useful result for OHD in New Zealand. Archaeological excavations in New Zealand are typically of limited areal extent. Thus, in many cases, the model presented here could be expected to provide Δ_{EHT} control from within excavation units. However, the model could not be expected to provide valid estimations for Δ_{EHT} from between excavation units and other approaches would have to be adopted. This could either involve the development of more sophisticated location specific micro-climatic models for Δ_{EHT} simulations, the use of medium term modern data measurements to directly measure Δ_{EHT} or the use of cross-dated samples.

12.6 Conclusion

In this chapter software (**RADLAB**) to simulate $T(t)$ on the basis of the theory outlined in Chapter 8 has been presented (*infra vide*:§12.2) and some basic, New Zealand specific, models of governing environmental variables have been defined (*infra vide*:§12.3). Through the use of this approach it has proved possible to estimate Δ_{EHT} values for spatially limited areas within which governing environmental variables, other than immediate surface morphology and matrix composition, are uniform (*infra vide*:§12.5). While this is highly limited it does allow for Δ_{EHT} control from within the spatially limited units that are typical of archaeological excavation in New Zealand. In conjunction with $\bar{T}$ estimates (*i.e.* Chap-

ter 11) this allows for EHT estimation within some New Zealand archaeological contexts. Additionally this scheme provides suitable Δ_{EHT} data for the application of OHD chronometric data in conjunction with absolute dating assays. The specific case of the OHD chronometric in conjunction with the radiocarbon chronometric is considered in the next chapter. Here the long term EHT control is provided through a combination of cross-dating and Δ_{EHT} simulation data, one of the schemes outlined earlier (*infra vide*:§9.3.3).

In addition to the particular outcome of providing Δ_{EHT} control for New Zealand archaeological contexts, the application presented in this chapter illustrates the development and use of the **RADLAB** toolkit. It should be clear that this software provides the basis for developing further soil simulation programmes that may involve far more sophisticated environmental models. The environmental variable models that have been developed in this chapter are of a simple form, limited by the nature of the available meteorological database. More complex models could be developed given suitable micro-meteorological data. Thus in a general sense the simulation approach presented here has demonstrated the development, implementation and evaluation of a numerical scheme for the purposes of Δ_{EHT} estimation — a key component of general EHT estimation procedures (*infra vide*:§9.3.3). This software forms the basis from which a range of different, problem specific, applications can be developed, and represents a significant advance upon the standard approaches for estimating Δ_{EHT}.

At this stage we have explored a range of approaches to providing archaeological Δ_{EHT} and EHT estimates. In addition to the very limited numerical EHT estimate developed in Chapter 11 it has proven possible to produce Δ_{EHT} estimates via analogue cell survey as outlined in Chapter 10 and through numerical simulation as described in this chapter. These two techniques are complementary, cell surveys being able

to provide Δ_{EHT} estimates over large spatial scales while the Δ_{EHT} simulations presented here are more suited to providing fine grained Δ_{EHT} estimates from within spatially discrete regions. A combination of the two approaches should allow accurate Δ_{EHT} estimation over any spatial scale. The extensive cell survey data presented in Chapter 10 in conjunction with the **RADLAB** simulation presented here will allow this combined analysis for a number of archaeological sites within New Zealand. Together with $\bar{T}$ estimates derived from the empirical model presented in Chapter 11, or through cross-dated controls as discussed in the following chapter, this enables EHT estimates to be produced for some New Zealand archaeological contexts. Thus we can now specify a complete set of priors and an observation model for the OHD chronometric, allowing us to employ OHD within a Bayesian analysis for the purpose of chronology building (*infra vide*:§1.4). This is considered in the following chapter where a framework for the analysis of the OHD chronometric is outlined.

Chapter 13

OHD as a Chronometric

13.1 Introduction

In the preceding 12 chapters we have considered the obsidian hydration reaction, identified a model to describe the temporal dependance of this reaction (Chapter 4), defined the governing parameters (Chapters 5,6 and 8) and proposed a method for measuring the OHD chronometric (Chapter 2). In this chapter we will bring these models together within the chronology building framework discussed in Chapter 1 (*infra vide*:§1.2) to enable the OHD chronometric as a chronology building tool.

Initially we will consider analysis of the OHD chronometric as an independent dating system. This defines the method by which absolute obsidian hydration dates can be "calibrated" in a manner directly analogous to radiocarbon calibration. Following this we will explore the combination of multiple chronometric data types. In particular we will look at the combination of radiocarbon and OHD chronometric data. This both implements a particularly useful analysis (*infra vide*:§1.4) and acts as a demonstration of how different chronometric data types can be combined. Finally, software to implement the analysis is presented and the chronology building exercise is illustrated through archaeological case studies.

13.2 Bayesian Analysis of the OHD Chronometric

Here we set up the OHD chronometric within the chronology building framework outlined in Chapter 1 (*infra vide*:§1.2). This amounts to specifying posterior temporal distributions for the parameters ψ, ϕ and θ (the process parameters, context dates and event dates respectively) on the basis of the measured chronometric data (x for OHD). In

the case of OHD we need to accommodate uncertainty in the parameter values $A, E, \bar{T}$ andΔ_T which define the Arrhenius rate relationship given in Equation 4.23 following the EHT parameterisation given in Equation 9.2. Thus we wish to define the posterior density for the unknown parameter values $\psi, \phi, \theta, A, E, \bar{T}$ and Δ_T given x, a single rim thickness measurement. The posterior probability density $h(v|x)$ for the vector $v = (\psi, \phi, \theta, A, E, \bar{T}, \Delta_T)$ of unknown parameters of interest, given data x, is expressed in terms of a likelihood ℓ and a prior probability density f as

$$h(v|x) \propto \ell(x|v) f(v) \tag{13.1}$$

If we can define the likelihood and prior terms in Equation 13.1 above then we can implement Bayesian calibration of the OHD chronometric.

In the next two sections we will define the likelihood

$$\ell(x|v)$$

and the prior

$$f(v)$$

Following this we will consider an extension of the posterior given in Equation 13.1 above to allow the combination of multiple data types — in this case, the OHD and radiocarbon chronometrics.

13.2.1 The OHD Likelihood

In a likelihood we specify the probability, or probability density, of observing the data given a particular state of the governing variables in the observation model. Following the hydration model of Chapter 4 (*infra vide*:§4.7), the relationship between measured hydration extent (x) and the parameters governing obsidian hydration is

$$\begin{aligned} x &= \mu_x + \epsilon \\ \mu_x &= \sqrt{\theta A e^{-\frac{E}{R(\bar{T}+\Delta_T)}}} \end{aligned} \tag{13.2}$$

Where ϵ is an additive noise term.

For normally distributed hydration rim measurement such as those produced through the intensity reconstruction measurements discussed previously (*infra vide*:§2.6.4)

$$\epsilon \sim N(0, \sigma_x^2)$$

It follows that the likelihood of observing this data is

$$\ell(x|v) = \frac{1}{\sigma_X\sqrt{2\pi}} e^{(-(x-\mu_x)^2/2\sigma_x^2)} \tag{13.3}$$

The likelihood for data with different distributions can be calculated in a similar fashion. For example the OHD chronometric data deriving from the Simple Pixel Count method (*infra vide*:§2.6.4) are uniformly distributed. If the data is $x \pm b$ then the likelihood is

$$\ell(x|v) = \frac{1}{2b} I_{[x-b,x+b]}(\mu_x) \tag{13.4}$$

Where $I_{[x-b,x+b]}(\mu_x)$ is an indicator function such that $I_{[x-b,x+b]}(\mu_x) = 1$ where $x - b < \mu_x < x + b$ and 0 otherwise.

It simply remains to define the prior term $f(v)$. Priors for $A, E, \bar{T}$ and Δ_T are determined from measured data. Priors for θ, ϕ and ψ are problem dependent. Following this $f(v)$ can be usefully broken down into two independent terms

$$f(v) \propto f(\theta, \phi, \psi) f(A, E, \bar{T}, \Delta_T)$$

and we will consider each of these separately.

13.2.2 The $f(A, E, \bar{T}, \Delta_T)$ Prior Term

The dependency relationships of this density break down as

$$f(A, E, \bar{T}, \Delta_T) \propto f_A(A) f_E(E) f_{\bar{T}}(\bar{T}) f_\Delta(\Delta_T)$$

Thus we simply need to be able to define prior distributions for the four terms $f_A(A), f_E(E)f_{\bar{T}}(\bar{T})$ and $f_\Delta(\Delta_T)$

Estimates $\mu_A, \mu_E, \mu_{\bar{T}}$ and μ_{Δ_T} of $A, E, \bar{T}$ and Δ_T are given in Table 6.7, Table 6.6, Chapter 11 and Chapter 12 respectively, along with standard errors $\sigma_A, \sigma_E, \sigma_T$ and σ_Δ. Our priors are therefore

$$\begin{aligned} f_A(A) &= \frac{1}{\sigma_A\sqrt{2\pi}} e^{-\frac{(A-\mu_A)^2}{\sigma_A^2}} \\ f_E(E) &= \frac{1}{\sigma_E\sqrt{2\pi}} e^{-\frac{(E-\mu_E)^2}{\sigma_E^2}} \\ f_{\bar{T}}(\bar{T}) &= \frac{1}{\sigma_T\sqrt{2\pi}} e^{-\frac{(T-\mu_T)^2}{\sigma_T^2}} \\ f_\Delta(\Delta_T) &= \frac{1}{\sigma_\Delta\sqrt{2\pi}} e^{-\frac{(\Delta_T-\mu_\Delta)^2}{\sigma_\Delta^2}} \end{aligned} \tag{13.5}$$

In the case that the prior density for any of these terms is unknown the prior can be represented by $f \propto 1$. That is, the density is a constant, and any value is equally likely *a priori*. So, for example, in the case that we do not have a valid estimate of the distribution for $f_{\bar{T}}(\bar{T})$ (a highly probable scenario) we would use the density

$$f_{\bar{T}}(\bar{T}) \propto 1$$

The other densities can be treated in a similar manner. However, this is only possible when calibrating OHD in conjunction with other chronometric data. In the absence of other chronometric data this will lead to an invalid (improper) posterior.

Having dealt with scalar $A, E, \bar{T}$ and Δ_T the case of multiple chronometrics is as follows. Suppose N observations $x = (x_1 \ldots x_N)$ are made in all. It will often be the case that observations are correlated. Some or all of x, E, A and Δ_T may be identical from one measurement to another. For example measurements may relate to obsidian deriving from the same hydration group in which case A and E are correlated, and by definition we only require a single variable $\bar{T}$. The parameter sets are thus $\theta = (\theta_1 \ldots \theta_{N_\Theta})$, $A = (A_1 \ldots A_{N_A})$, $E = (E_1 \ldots E_{N_E})$ and

$\Delta_T = (\Delta_{T,1} \ldots \Delta_{T,N_\Delta})$. The prior density is simply a product of the independent terms

$$f(A, E, \bar{T}, \Delta_T) \propto f_{\bar{T}}\bar{T} \prod_{i=1}^{N_A} f_{A_i}(A_i) \prod_{r=1}^{N_E} f_{E_r}(E_r) \prod_{j=1}^{N_T} f_{\Delta_j}(\Delta_T, j) \tag{13.6}$$

The likelihood can be extended in a similar fashion. For measurement k let $n = \upsilon_\Theta(k)$ give the index of the associated age parameter θ_n. Let υ_E, υ_T, υ_A be the corresponding index mappings for the $E-$, Δ_T- and $A-$parameters. The joint likelihood for multiple chronometrics is

$$\ell(x|\theta, A, E, T) \propto \prod_{k=1}^{N} \ell(x_k|\theta_{\upsilon_\Theta(k)}, A_{\upsilon_A(k)}, E_{\upsilon_E(k)}, \bar{T}, \Delta_{T\upsilon_T(k)}) \tag{13.7}$$

The likelihood and prior given in Equations 13.7 and 13.6 above describe the general case for OHD chronometric data.

13.2.3 Prior for $f(\theta, \phi, \psi)$

With OHD we can make the assumption that the event and context are isochronous as we directly date a cultural event. In this case $\phi = \theta$ thus the density $f(\theta, \phi, \psi)$ can be reduced to $f(\theta, \psi)$. The models used at this stage are independent of chronometric data type and it is possible to employ modelling approaches that have been developed for any chronometric data. In practice the $f(\theta, \psi)$ model may need to change depending upon the specific dating question. Here we will adopt the phase model for $f(\theta, \psi)$ defined by Nicholls and Jones (2001).

For further discussion of this model it is necessary to define the following notation. Dates are regarded as arising from a single series of M abutting phases. N_m age determinations are gathered from phase m, making $K \equiv \sum N_m$ dates in all. For $n \in \{1, 2 \ldots N_m\}$ let $x_{m,n}$ denote the value of the n'th chronometric measured in the m'th phase. For all

quantities $X_{m,n}$ let X denote the corresponding vector in the natural ordering, so that $x \equiv (x_{1,1},...,x_{M,NM})$, etc. Let $\theta_{m,n}$ be an event date for specimen (m,n), with units calendar years AD, and assumed to equal the context date associated with the (m,n)'th specimen. For $m \in \{0,1...M\}$ let ψ_m denote the boundary date at the lower boundary of phase m. We have a total $K+M+1$ unknown parameters: the $M+1$ layer boundary dates $\psi_0...\psi_M$, and the K unknown object dates, $\theta_{1,1}...\theta_{M,NM}$. Let P and A, $P \leq A$ be given termini, setting lower and upper bounds on the dates. Possible parameter sets (ψ,θ) take some value in a parameter space Ω. This space is simply the set of all states (ψ,θ) satisfying prior constraints such as super-position, e.g.

$$\Omega \equiv \{(\psi,\theta); P \leq \psi_M \leq \theta_{M,.} \leq \psi_{M-1} \leq \ldots \leq \psi_1 \leq \theta_{1,.} \leq \psi_0 \leq A\} \quad (13.8)$$

Nicholls and Jones (2001) break the prior $f(\psi,\theta)$ into two pieces

$$f(\psi,\theta) = f_{\Theta|\Psi}(\theta|\psi) f_{\Psi}(\psi) \quad (13.9)$$

modelling the event-context dates θ conditional upon the layer boundary dates ψ. Following this the prior $f_{\Theta|\Psi}(\theta|\psi)$ can be defined as

$$f_{\Theta|\Psi}(\theta|\psi) = \prod_{m=1}^{M} \frac{1}{(\psi_{m-1}-\psi_m)^{n_m}} \quad (13.10)$$

for (ψ,θ) restricted to Ω.

The density $f_{\Psi}(\psi)$ can take on any form. A standard approach has been to model this as a constant (*e.g.* Buck *et al.* 1991; 1996; Christen 1994*a*); *i.e.*

$$f_{\Psi}(\psi) \propto 1$$

However (Nicholls and Jones 2001) have shown that this weights the prior in favour of more widely spread sets of dates, and this can bias the whole analysis. They propose the following prior

$$f_{\Psi}(\psi) = \frac{1}{(R-\psi_0-\psi_M)} \frac{1}{(\psi_0-\psi_M)^{M-1}} \quad (13.11)$$

as being a more suitable "non-informative" prior for $f_\Psi(\psi)$.

Following the non-informative prior given by Nicholls and Jones (2001) the prior $f(\theta, \psi)$ is specified by the product of Equations 13.6 and 13.11; *i.e.*

$$f(\theta, \psi) \propto \frac{1}{(R - \psi_0 - \psi_M)} \frac{1}{(\psi_0 - \psi_M)^{M-1}} \prod_{m=1}^{M} \frac{1}{(\psi_{m-1} - \psi_m)^{n_m}} \quad (13.12)$$

Thus we can fully specify the OHD posterior given in Equation 13.1 as a product of Equations 13.7, 13.6 and 13.12.

The calibration of scalar OHD data in an analogous to manner to that of standard radiocarbon calibration is a special case of this posterior. In this case we are not interested in the chronology building terms ψ and ϕ and are simply interested in the temporal distribution of the flaking event θ_i. Thus the posterior of interest is

$$h(\theta, A, E, \bar{T}, \Delta_T | x) \propto \ell(x | \theta, A, E, \bar{T}, \Delta_T) f(\theta, A, E, \bar{T}, \Delta_T) \quad (13.13)$$

If the prior density for θ is constant, the prior term $f(\theta, A, E, \bar{T}, \Delta_T)$ is proportional to the prior given in Equation 13.6 with $N = 1$. Thus we can perform calibration of individual OHD chronometric data in an analogous fashion to radiocarbon calibration through the posterior given in Equation 13.13 above.

While the posteriors defined in Equations 13.1 and 13.13 allow us to define posterior distributions for parameters of interest on the basis of the OHD chronometric, as stated at the outset one of our primary interests is in combining different chronometric data types — specifically radiocarbon and OHD — to leverage the power of different techniques. This is considered in the following section.

13.2.4 Date Combination

Here we will consider the combination of OHD chronometric data x and radiocarbon chronometric data y. In this case we want to resolve the posterior $h(v|x,y)$ given as

$$h(v|x,y) \propto \ell(x,y|v)f(v) \tag{13.14}$$

The likelihood can be broken up as

$$\ell(x,y|v) \propto \ell(x|\theta,A,E,\bar{T},\Delta_T)\ell(y|\theta)$$

which is simply a product of the OHD likelihood given above and the standard radiocarbon likelihood (*e.g.* Buck *et al.* 1991; 1996; Christen 1994*a*).

The posterior density $f(v)$ can be broken into the two terms $f(\psi,\phi,\theta)$ and $f(A,E,\bar{T},\Delta_T)$ used previously. In this case the density $f(A,E,\bar{T},\Delta_T)$ remains exactly as specified in Equation 13.6. In the case that we assume the event context relationship for the radiocarbon chronometric is isochronous then the density $f(\psi,\phi,\theta)$ remains as given in Equation 13.6. However we need to extend the notation given in §13.2.3 slightly. There are now N_m^y radiocarbon determinations gathered from phase m and N_m^x OHD determinations gathered from phase m making $N_m \equiv N_m^y + N_m^x$ chronometric data gathered from phase m in total. All other terms remain the same and the prior is as specified in Equation 13.12. Thus the posterior density given in Equation 13.14 above is a relatively simple extension of the CRA posterior given by Nicholls and Jones (2001).

13.2.5 Summary

It is relatively straightforward to specify a posterior for the OHD chronometric, and for a combination of OHD and CRA chronometrics, as a prod-

uct of likelihood and prior terms (§13.2,§13.2.4). The OHD likelihood follows from the data observation model, and the normal and uniform cases are treated above (§13.2.1). The likelihood for different observation models and/or data distributions would follow the approach given in §13.2.1. The prior densities are also easy to specify. The prior density can be broken down into two components one ($f(A, E, \bar{T}, \Delta_T)$) which relates to OHD specific parameters and the other ($f(\psi, \phi, \theta)$) which relates to the chronology building parameters outlined in Chapter 1 (*infra vide*:§1.2). We can use generic priors that are independent of chronometric data type for $f(\psi, \phi, \theta)$, and here we have used the non-informative prior developed by Nicholls and Jones (2001). The OHD specific prior simply reflects the current understanding of the reaction controlling parameters $A, E, \bar{T}$ and Δ_T.

The combined OHD and CRA posterior is simply the product of the likelihood terms for the two chronometric data types and the OHD prior with some small extensions (§13.2.4). This is a useful result as it enables OHD to be employed in a capacity of providing information on the absolute time difference between two different events, without having to specify a prior for $\bar{T}$ (*i.e.* we don't need to know the EHT). Here we recall the formulations for the absolute relative time difference of two flaking events given in §8.1.1. These show that the difference in age between two flaking events is proportional to the ratio of squared rim thicknesses. We can exploit this fact where the age (and possibly the hydration parameters) of one of the samples can be established. The posterior given in Equation 13.14 allows us to establish this control with reference to the CRA data. Thus we leverage the benefits of both techniques CRA to provide absolute temporal information and OHD to provide absolute relative temporal information.

The definition of the posteriors given in Equations 13.1, 13.13 and 13.14 allow us to generate posterior distributions for process parameters (ψ),

event(s) (θ), glass hydration parameters (A & E) and the palaeo-temperature history (T). In addition it is possible to generate the posterior distribution of statistics of these parameters. So, for example, the absolute relative difference between two flaking events, θ_1 and θ_2 say, given by

$$\Delta(\theta_1, \theta_2) = \theta_1 - \theta_2$$

can be derived from the posteriors defined above. The same is possible for any statistic of the variables defined in the posterior. However, the posterior defined in Equation 13.1 or Equation 13.14 is a complex multi-dimensional distribution and in order to consider the distribution of some meaningful statistic of direct interest we need to integrate out the "marginal distribution" for this statistic. That is we need to integrate out all of the variables in the posterior other than the one of interest. This is complex, and it is usually necessary to carry out the integration numerically, using a computer, as the integrals involved cannot usually be done by hand. Typically this type of analysis is conducted through some form of sample based integration process (*e.g.* Nicholls and Jones 2001), and requires specialised software. Thus in order to actually make use of the posteriors defined in Equations 13.1 and 13.13 we need to have a system that can integrate the required marginal posterior distributions out of the full posterior. An extension of the Date Lab software package (Jones and Nicholls submitted; 2002; Nicholls and Jones 2001) designed to perform this analysis is described in the next section.

13.3 The OHD Chronometric in Date Lab

Date Lab is a software system that has been developed to implement Bayesian analyses of archaeological chronometric data (Jones and Nicholls submitted; 2002; Nicholls and Jones 2001). The initial version of Date Lab (version 1.0) has only implemented the analysis of radiocarbon chronometric data. Here an extension of Date Lab to allow analysis of OHD

chronometric data (version 1.1) is described. General operation of the Date Lab package is detailed elsewhere and only those features specific to the OHD chronometric will be discussed here. The features discussed below assume the details presented in the Date Lab 1.0 manual.

13.3.1 Interface

The primary OHD specific interface element is an additional data-sheet section allowing input of OHD specific data (Figure 13.1). This allows input of the data required for calculation of the likelihood and priors outlined in §13.2.1 and §13.2.2. Three data elements are input through this interface; OHD chronometric data, Hydration group data, and Temperature data.

The OHD chronometric data are entered into the OHD data sheet. The specific entries are

1. **Date:** The identifying label of the chronometric is input into this column.

2. **OHD:** The mean OHD measurement is input into this column. Currently two measurement distributions are supported, normal and uniform. The OHD measurement corresponds to the mean of the measurement distribution. The values input here in conjunction with the column 3 error terms define the OHD chronometric data x_i used in the likelihoods given in Equations 13.3 and 13.4.

3. **Error:** This term describes the distribution of the measurement. If the measurement data is normal then the standard deviation of the measurement is entered here. Alternatively, if the data is uniform the value entered here is half the span of the distribution.

4. **Model:** The distribution model for the OHD data is identified in this

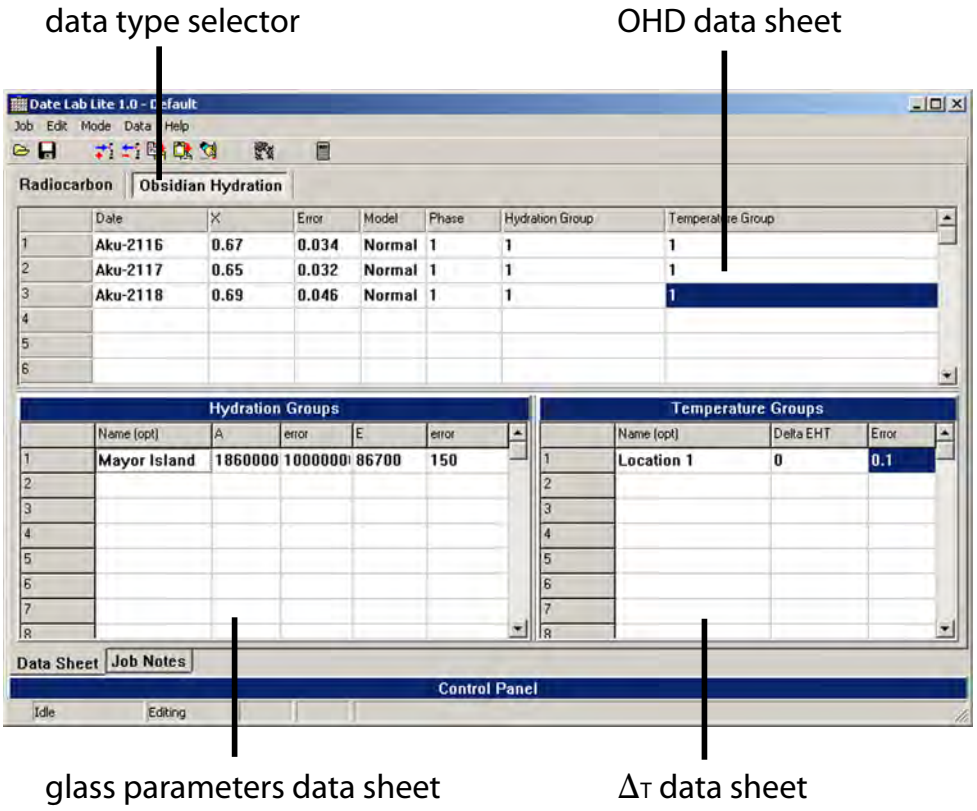

Figure 13.1: OHD data interface for Date Lab 1.1

column via a drop down combo box. This identifies the particular likelihood that is associated with the specific OHD chronometric. Currently Normal and uniform measurement data are supported as defined in the likelihoods given in Equations 13.3 and 13.4 respectively. Different data entries can have different distribution models.

5. **Phase:** This identifies the phase (m defined in §13.2.4) association for the chronometric data entry. This corresponds to the phase entry in the radiocarbon data sheet.

6. **Hydration Group:** This defines the mapping v_A and v_E used in Equation 13.7. As different chronometric data may be associated with the same glass parameters the glass hydration parameters are entered in a separate sheet and the value input into this column identifies the appropriate entry within the glass parameters data sheet. So to associated the OHD data with the first entry in the glass parameters sheet the value "1" would be input here. Similarly the value"2" would identify the second entry in the glass parameters sheet and so on.

7. **Temperature Group:** This acts in an identical manner the **Hydration Group** column just described. The value input here defines the mapping v_Δ used in Equation 13.7. As different chronometric data may be associated with the same Δ_{EHT} variable the Δ_{EHT} variables are entered in a separate sheet and the value input into this column identifies the appropriate entry within the Δ_T data sheet. So to associated the OHD data with the first entry in the Δ_T data sheet the value "1" would be input here. Similarly the value"2" would identify the second entry in the Δ_T data sheet and so on.

The Hydration group parameters are entered into glass parameters data sheet. These are the specific groups of glass hydration parameters as-

sociated with the OHD data defined in the OHD data sheet described above, and correspond to the elements of the vectors $A = (A_1 \ldots A_{N_A})$, $E = (E_1 \ldots E_{N_E})$ used for the OHD likelihood as defined in Equation 13.7. In the current implementation it is assumed that the estimates for A and E are normally distributed. Thus the mean and standard deviation of the A and E estimates are input into this sheet. If the glass specific hydration parameters are unknown for any given hydration group the entries are simply left blank. This allows estimates of these variables to be calculated through cross-dating as discussed in Chapter 9 (*infra vide*:§9.3.2) and as will be demonstrated later in this chapter (*supra vide*:§13.4.5).

1. **Name (opt):** This is an optional identifier for the particular set of hydration data. For example, the hydration parameters for the Mayor Island hydration group (*infra vide*:§6.6), which are loaded by default into entry 1, are identified by the name "Mayor Island".

2. **A:** The mean value for the pre-exponential component of the hydration rate (A in Equation 4.23) is input here. The units are days μm^{-2}. If this value is not known, leave the entry blank.

3. **A error:** This is the standard deviation of the A estimate. If this value is not known, leave the entry blank.

4. **E:** The mean value for the glass specific gas activation energy (E in Equation 4.23) is input here. The units are $Jmol^{-1}$. If this value is not known, leave the entry blank.

5. **E error:** This is the standard deviation of the E estimate. If this value is not known, leave the entry blank.

The final data entry elements for OHD during editing mode are the temperature groups. These are entered into the Δ_T data sheet. These are the specific Δ_T variables associated with the OHD data entered into the

OHD data sheet described above, and correspond to the elements of the vector $\Delta_T = (\Delta_{T1} \ldots \Delta_{TN_\Delta})$ used for the OHD likelihood as defined in Equation 13.7. In the current implementation it is assumed that the Δ_T estimates are normally distributed. Thus the mean and standard deviation of the Δ_T variables are input into this sheet.

1. **Name (opt):** This is an optional identifier for the particular Δ_T variable.
2. **Delta EHT:** The mean of the Δ_T variable is entered here.
3. **Error:** The standard deviation of the Δ_T variable is entered here.

In addition to the data input elements described above, the control panel accessible during analysis mode also differs between versions 1.0 and 1.1 of Date Lab. However, there is only one change. An Obsidian Hydration page has been added to the control panel (Figure 13.2). The $\bar{T}$ variable is defined here. It is assumed that $\bar{T}$ is normally distributed. In this case the mean and standard deviation are entered into the Mean EHT and EHT error controls respectively. In the (probably quit common) circumstance that and EHT estimate is not known these values are left blank. This allows absolute relativity dating analyses to be conducted, and additionally $\bar{T}$ is estimated as part of the posterior allowing palaeotemperature analyses to be conducted (*supra vide*:§13.4, §13.5, §13.6).

Other than these settings the use of Date Lab is exactly as described for version 1.0.

Thus the Date Lab 1.1 interface allows us to input the sets of chronometric data and prior parameters required to define the posterior distributions given in Equations 13.1, 13.13 & 13.14. However, this alone is not particularly useful. As described in §13.2.5 we need to be able to calculate marginal posterior distributions from the full posterior defined on the basis of the data input through the Date Lab interface.

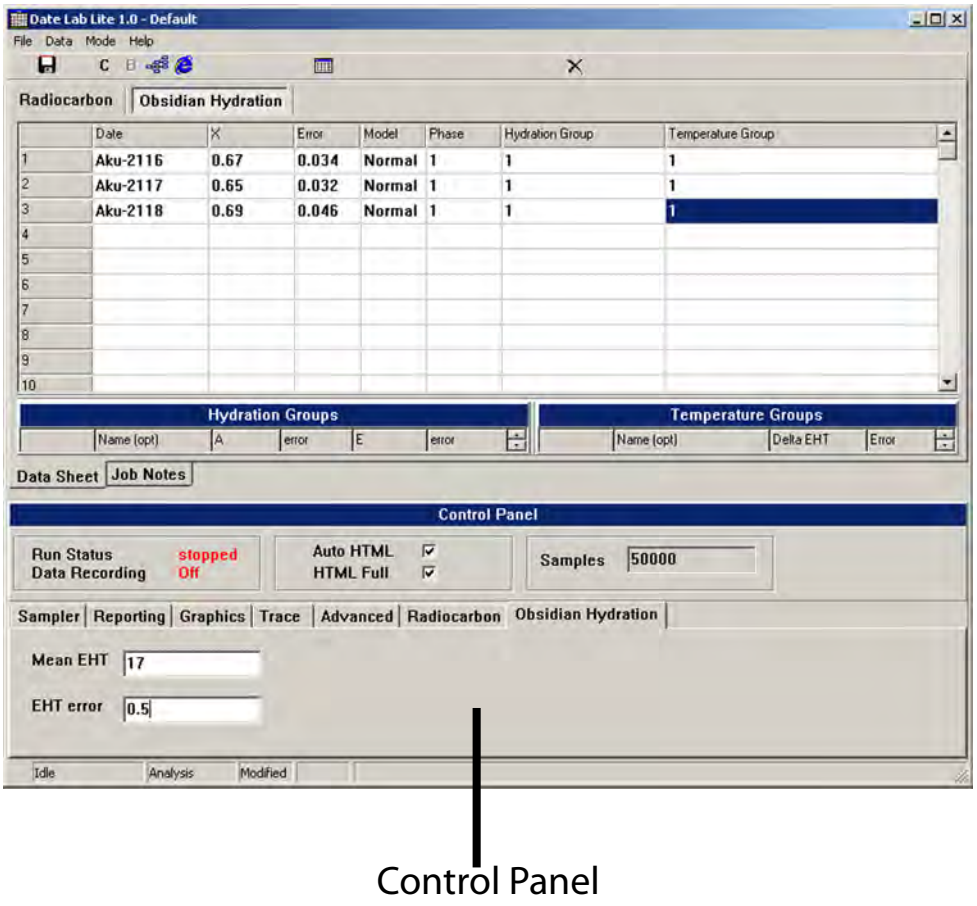

Figure 13.2: OHD control panel element for Date Lab 1.1

13.3.2 Analysis

The primary analysis function of Date Lab 1.1 is to integrate marginal values from the posteriors defined in Equations 13.1, 13.13 and 13.14. A sample based integration scheme is used to perform this analysis. Sample based inference allows us to form summarising statements from the posterior density in a straightforward manner. The probability assertion X is the case, given the data and prior knowledge represented in the posterior, is simply estimated by sampling parameter sets from the posterior distribution (in this case sets of $\psi, \theta, A, E, \bar{T}, \Delta_T$). These samples can then be used to empirically describe the posterior distribution(s) of interest. The problem then is to generate suitable samples from the posterior. In general this is achieved through using Markov chain Monte Carlo (MCMC) algorithms, which employ Gibbs sampling (e.g. Christen 1994*a*) or some more general Metropolis-Hastings algorithm (e.g. Nicholls and Jones 2001). Other sampling schemes such as rejection sampling (e.g. Nicholls and Jones 2001), or direct numerical integration could also be employed. Date Lab 1.0 implements the sampling scheme described by Nicholls and Jones (2001) for radiocarbon chronometric data. In Date Lab 1.1 this is extended to account for the different posteriors defined here (*i.e.* Equation 13.14). Further, as no definition of the OHD likelihood is used in Date Lab 1.0 a scheme has been implemented to calculate the calibrated likelihood given in Equation 13.13in Date Lab 1.1.

For the integration of the posteriors defined in Equations 13.1, 13.13 and 13.14 we use two different schemes. We analyse the simple "calibration" of OHD data (i.e. calculate the marginal posterior distribution for θ associated with single OHD determinations) as defined in Equation 13.13 via a simple monte carlo integration. For the more complex integration required with the posteriors defined in Equations 13.1 and 13.14 we use a modification of the Metropolis-Hastings MCMC algorithm defined by (Nicholls and Jones 2001) and implemented in Date Lab 1.0.

With simple monte carlo integration we simply generate N variates $(X_i, i = 1, 2, \ldots, N)$ uniformly distributed over the region of integration (a, b). We then evaluate $f(X_i), i = 1, 2, \ldots, N$, and estimate the integral I as

$$I \propto \frac{\sum_{i=1}^{N} f(X_i)}{N}$$

For the purposes of analysing the posterior given in Equation 13.13 we want to integrate out the parameters A, E, T to generate the density $h(\theta|x)$. To do this we simply need to calculate $I \equiv h(\theta, A, E, T|x)$ over the region of support for A, E and T for each potential value θ. Thus a simple algorithm for calculating $h(\theta|x)$ over the interval $[A, P]$ is to perform the following for each year in the interval $[A, P]$

1. generate N random sets $(E_i, A_i, T_i), i = 1, 2, \ldots, N$ uniformly at random from with their respective regions of support.
2. calculate $h(\theta|x) \propto \sum_{i=1}^{N} h(\theta, A, E, T|x)/N$

The region of support for A, E and T is defined to be the 99.9% HPD[1] of the respective distribution (*i.e.* 4σ for in the case of normal variables). This analysis is employed to calculate the basic calibrated OHD distributions produced through Date Lab. The size of the integration sample N is set through the **sample size for OHD likelihood** control on the **obsidian hydration** page of the Date Lab control panel. By default this is 1000.

To perform the more complex integrations required for analysis of the posteriors defined in Equations 13.1 and 13.14 Date Lab 1.1 employs an extension of the Metropolis Hastings MCMC algorithm given by Nicholls and Jones (2001) and implemented in Date Lab 1.0. That sampling

[1] HPD stand for Highest Posterior Density. This is analogous to a confidence interval and defines the most constrained region of support in the posterior summing to the particular HPD value. Thus the 68% HPD defines the most tightly constrained region over which the integral of the posterior density is equal to 0.68

scheme is designed to sample from the posterior $h(\psi, \theta|\mathcal{Y})$ thus we need to extend the sampler to account for the full posterior defined in Equation 13.14. However as described above (*infra vide*:§13.2.4) this is a relatively simple extension of the posterior sampled by Nicholls and Jones (2001), only really requiring the prior term $f(A, E, \bar{T}, \Delta_T)$ to be taken into account in addition to the modified definition of Nm in Equation 13.12. This can be accomplished through the definition of four new sampler up-dates in addition to those given by Nicholls and Jones (2001). Details of this sampling routine are given in Appendix H.

13.3.3 Output

The general output from a Date Lab analysis is a series of samples from the posterior distributions of interest, this is known as the trace. The samples for individual variables describe the marginal posterior distributions for these variables. Thus the chronological arguments we seek to advance are based around analyses of the trace. The type of analysis conducted can vary from forming simple summarising statements regarding the distribution of marginal posteriors through to more complex functions of posterior variables. Both of these processes are discussed in the Case studies that follow.

Some basic graphical summaries of the trace are presented by default through the Date Lab analysis. So for example the posterior distributions for the θ variables and the span statistic are plotted. This is described in detail by Jones and Nicholls (2002). In addition to these summaries the raw MCMC trace can be also be saved. This can be directly analysed, which is the most appropriate approach for complex functions of the posterior variables. We will visit this further when we examine the use of OHD chronometric data for palaeo-temperature estimates (*supra vide*:§13.4,§13.5,§13.6) and estimating glass hydration parameters via

cross-dating (*supra vide*:§13.4).

Under Date Lab 1.1 six trace files are recorded; deltar.csv, glass_samp.csv, phi_samp.csv, psi_samp.csv, temperature_samp.csv and theta_samp.csv. The two new output files under Date Lab 1.1 are glass_samp.csv and temperature_samp.csv. These record the trace for the E & A variables and the $\bar{T}$ & Δ_T variables respectively.

13.3.4 Summary

The extension of Date Lab described here allows the input of chronometric and prior data that define the posteriors given in Equations 13.1, 13.13 and 13.14. The primary function of Date Lab is to output samples of marginal posteriors from these distributions. Through analysis of these samples we are able to make statements regarding functions of the chronology building elements defined in §1.2. Thus Date Lab is an implementation of the chronology building framework defined in §1.2 that allows the use of the OHD chronometric as a chronology building tool; both independently and in conjunction with radiocarbon chronometric data. In the following sections four case studies are presented to illustrate the use of OHD chronometric data as a chronology building tool within the framework defined in this thesis and implemented in the Date Lab 1.1 package described here.

13.4 Tiritiri Matangi R9/779

The R9/779 case study is presented here to demonstrate the use of OHD as a chronology building tool, and to provide an assessment of the performance and utility of the OHD chronometric. In light of this, the archaeological record and case study as presented here is a simplification

purely for the current purposes. A fuller description of the chronology of the site is under preparation in collaboration with Robert Brassey who undertook the excavation.

The site R9/779, generally known as the Tiri wharf site, is a stratified occupation site located at Wharf Bay on Tiritiri Matangi Island in the Hauraki Gulf, Auckland. The excavated stratigraphy was relatively simple, with three phases of pre-European occupation represented. A basal layer we will designated Layer 4 was overlain by a clay fill deposit (here designated as Layer 3). Above this two occupation layers (Layers 1 and 2) are capped by a European period (1953) cut and fill deposit. Both radiocarbon and OHD chronometric data have been obtained for samples deriving from throughout this sequence (Table 13.1).

The chronological question that we consider here is the absolute date at which the R9/779 formation processes occurred and also the time span over which the activity represented by R9/779 has taken place. Thus we wish to address questions of both absolute and relative timing. As both OHD and radiocarbon chronometric data are available we can use this analysis to compare the performance of OHD and radiocarbon as chronology building tools.

13.4.1 Chronometric Analysis

Two types of chronometric data have been collected from archaeological contexts within the R9/779 archaeological record. Five radiocarbon determinations and seven OHD determinations. These are reported in Table 13.1. In a real-world analysis our sole interest would be in defining the temporal parameters for the cultural processes represented by R9/779, and perhaps recovering some cross-dated information. However, in the current analysis the primary goal is to illustrate the use of OHD as a chronometry building tool and to make an assessment of the

general utility of OHD as a chronometric. Accordingly, we will analyse the available chronometric data in four separate stages to allow a more general exploration of the chronology building exercise. Initially, we will perform a Bayesian calibration of the Radiocarbon data alone (*supra vide*:§13.4.2). This sets a reference base-line against which we can compare the OHD chronometric data. Following the radiocarbon analysis we will perform a Bayesian calibration of the OHD chronometric data alone (*supra vide*:§13.4.3). We will then perform a combined calibration analysis of the two chronometric data types where OHD acts in a capacity of providing absolute relative dates (*supra vide*:§13.4.4). Finally, we will conduct an analysis of the full chronometric data set where we will recover posterior data on glass hydration parameters through cross-dating (*supra vide*:§13.4.5).

The Chronometric Data

Charcoal samples obtained from firescoops in Layers 1,2, and 4 were submitted for dating at the University of Waikato Radiocarbon Laboratory. All samples submitted were of charcoal identified as being of short-lived shrub species. In addition to the charcoal samples, a sample of dog cockle (*Glycymeris laticostata*) from Layer 7 was submitted for radiocarbon dating. It is reasonable to assume that $\psi \equiv \theta$ for these samples.

Obsidian samples were collected for all potentially dateable obsidian artefacts in accordance with the protocol outlined by Jones *et al.* (1997*a*). Six obsidian artefacts, all originally derived from a Mayor Island source were subsequently selected for dating. Additionally, a single artefact from an unknown hydration group has been included in the analysis to illustrate the use of cross-dating controls to generate estimates of glass specific hydration parameters as discussed in Chapter 6 (*infra vide*:§6.1.2).

Table 13.1: Tiritiri Matangi dating results

OHD Results

Sample	Source	Context	Rim (Fm)	Error (2s)	m	n	i
Aku/500	MI	Layer 4	0.998	0.023	4	4	1
Aku/494	MI	Layer 3	1.020	0.075	3	1	2
Aku/502	MI	Layer 2	0.950	0.030	2	1	3
Aku/503	MI	Layer 2	0.964	0.026	2	2	4
Aku/505	MI	Layer 2	0.930	0.030	2	3	5
Aku/506	MI	Layer 2	0.935	0.018	2	4	6
Aku/501	Unknown	Layer 2	2.01	0.078	2	5	7

Radiocarbon Results

Sample	Material	Context	CRA (B.P.)	error	m	n	i
Wk-5802	Shell (Glycimeris laticostata)	L7a	870	50	4	1	1
Wk-5867	Charcoal	F2, L7a	440	40	4	2	2
Wk-5803	Charcoal	F3, L5	390	50	2	1	3
Wk-5869	Charcoal	F6, L5	450	40	2	2	4
Wk-5868	Charcoal	F22, L3	390	40	1	1	5

Model Structure

In the current analysis we will seek to model temporal bounds for the strata observed in the R9/779 archaeological record, and additionally to model the duration of time over which activity represented by the R9/779 archaeological record took place. Thus our chronology is a temporal description of the processes that have given rise to the observed archaeological record. Our chronometry is the $K = 12$ chronometric determinations given in Table 13.1. Following the notation outlined for the chronology building framework discussed previously (*infra vide*:§1.2), we define the following temporal parameters for the R9/779 formation process:

ψ_4	the date at which the Layer 4 record began to be formed
ψ_3	the date of the Layer 3-4 interface
ψ_2	the date of the Layer 2-3 interface
ψ_1	the date of the Layer 2-1 interface
ψ_0	the date at which Layer 1 ceased to be formed

Accordingly the state space (Ω) is

$$\begin{aligned} \Omega &\equiv \{(\psi, \theta); \\ TPQ \leq \psi_4 \leq \theta_{4,.} \leq \ldots \leq \theta_1, . \leq \\ \psi_0 \leq TAQ \end{aligned} \tag{13.15}$$

Where in this case the TAQ and TPQ are conservative bounds that we will set at 1900 and 800 A.D. respectively (see Nicholls and Jones 2001 for further discussion on setting bounds).

Our primary archaeological interest here is the posterior distribution of the parameters ψ_4 — ψ_0 as well as the span statistic $R = \psi_4 - \psi_0$. These parameters define a chronology for processes associated with the formation of the observed archaeological record. However, for the current exercise we will define a new span statistic, $R1 = \psi_4 - \psi_1$. OHD chronometric data are limited to layers 2–4 thus the span statistic $R1$ relates to the phases of activity associated with these data. The use of the $R1$ statistic allows a direct comparison in posterior span between the OHD and CRA chronometric data; one of the primary purposes of the analysis presented here.

As discussed above we will recover the posterior distributions for $\psi_0, \ldots, \psi_4$ and $R1$ under four different analyses using different subsets of the chronometric data presented in Table 13.1. We will begin with an analysis of the CRA data as a sole chronometric data type.

13.4.2 Analysis of the Radiocarbon Results

As a preliminary step in the current exercise we will analyse the radiocarbon chronometric data alone. This allows us to define temporal distributions for the ψ parameters and the span statistic R as a comparative test for those produced through analysis of the OHD chronometric data. We will also take the opportunity to introduce the various analysis steps and output from this type of analysis.

To perform the analysis we need to calculate the marginal posterior distributions for $\psi_0, \ldots, \psi_m$ and $R1$ from the posterior defined in Equation 13.14 with $N_m^x = 0, m = 1, \ldots, 4$. This is precisely the calibration scheme given by Nicholls and Jones (2001). In order to run this analysis the radiocarbon chronometric data are entered into Date Lab as described by Jones and Nicholls (2002) and a Metropolis-Hastings sampler was run with a sample size of 20000, a Burn of 20000, and a sample step of 100. This analysis is saved as the **tiri1.dla** file and is installed in the **jobs** subdirectory when Date Lab 1.1 is installed. From this analysis a default analysis report is produced (a copy of this report can be found on the companion C.D. as the tiri1 analysis in the **PHD.html** document).

One of the outputs is a graphic of the calibrated likelihoods for the analysed chronometric data. For the radiocarbon data considered in this particular analysis these plots correspond to the standard calibrated distributions as would be produced through Calib (Stuiver and Reimer 1993) or some other such programme. This plot is given for the current analysis data in Figures 13.3 & 13.4. These are presented to demonstrate the two general graphical formats produced. In Figure 13.3 a combined histogram plot of the calibrated radiocarbon data is presented. This is a fairly standard representation for calibrated distributions. In Figure 13.4 an alternative plot format is presented. In this format the solid box represents the 68% HPD region for distribution and the line represents the 95% HPD for the distribution. In general this style of plot is more suited to summarising the relative regions of support for multiple distributions, and thus will be used through the remainder of the examples presented here. However both formats are presented by default. Additionally, multiple graphical formats can be output. It is possible to automatically generate GIF, EMF, WMF and EPS versions of each graphic, and in addition TIFF, JPEG and BMP versions can also be produced. This is described in Jones and Nicholls (2002). The EPS versions of the graphic are used in this thesis.

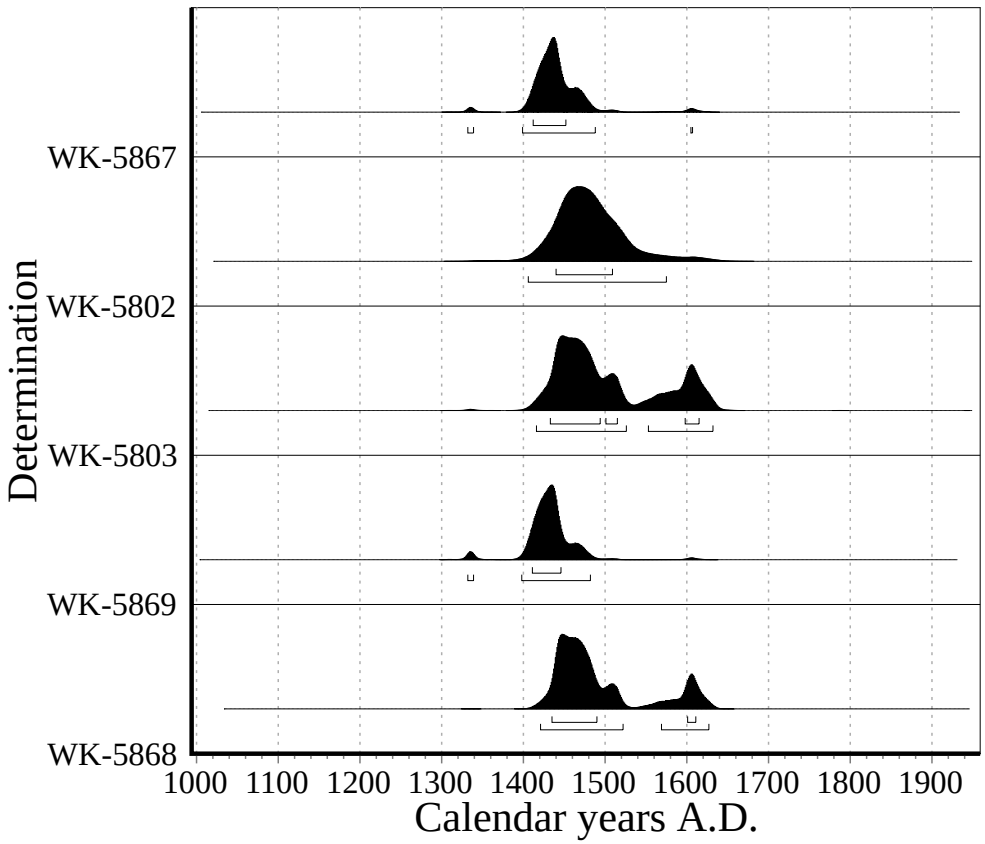

Figure 13.3: Posterior distribution of calibrated CRA chronometrics given in Table 13.1

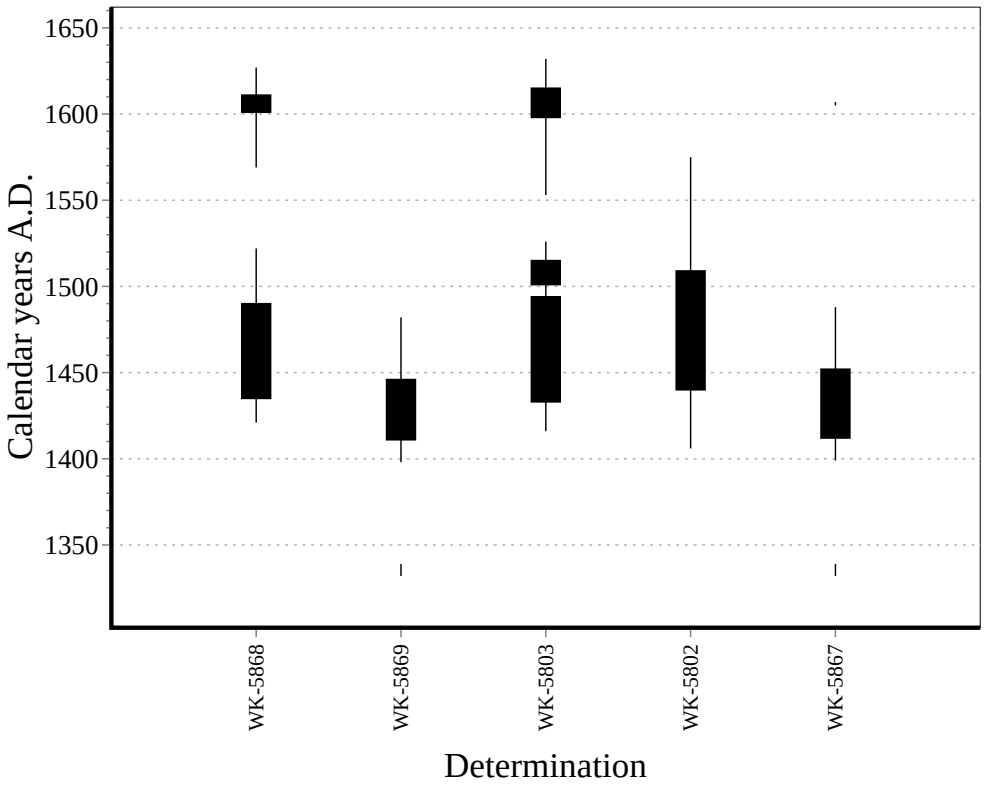

Figure 13.4: Posterior distribution of calibrated CRA chronometrics given in Table 13.1: solid bars represent the 68 % HPD, lines represent the 95 % HPD

In addition to the calibrated likelihood distributions, graphical summaries of some of the marginal posterior distributions are also produced by default through a Date Lab analysis. For example Figure 13.5 is a standard output graphic. This plots the calibrated distribution for θ (i.e. Figures 13.3 & 13.4) against the marginal posterior distributions for the θ variables. In this graphic the clear boxes represent the posterior distributions and the solid boxes represent the calibrated likelihoods. Additional to summaries of the θ variables some statistics of the ψ variables are also summarised. For example, the span statistic $R = \psi_m - \psi_0$ as plotted in Figure 13.6 is output as standard. Thus many of the standard questions regarding chronology building from a chronometric dataset are addressed in the Date Lab output report.

In addition to the standard output it is often useful to directly analyse the trace. This allows us to make statements regarding functions of the posterior variables that are not presented by default. For example in the current analysis we are interested in the distribution of all of the ψ variables, which is not a default plot, and we are also interested in the span statistic $R1 = \psi_m - \psi_1$, which differs from the standard R statistic plotted in Date Lab. Thus we need to directly analyse the output trace. In this case we will be analysing the trace file **psi_samp.csv**. These data are plotted in Figure 13.7 and can be directly analysed via any standard data analysis technique. For example the graphs in Figure 13.8 are histograms produced directly from the trace graphed in Figure 13.7.

The distributions given in Figure 13.8 define the chronology we seek to describe. As can be seen the temporal distribution of these variables is tightly constrained by the available CRA chronometric data. The analysis of the radiocarbon data suggests that the activity generating the visible archaeological record has taken place over a very brief period of time (less than 90 years at a 95% HPD; Table 13.4.6) in the 15th century. Thus the chronology is simple and brief.

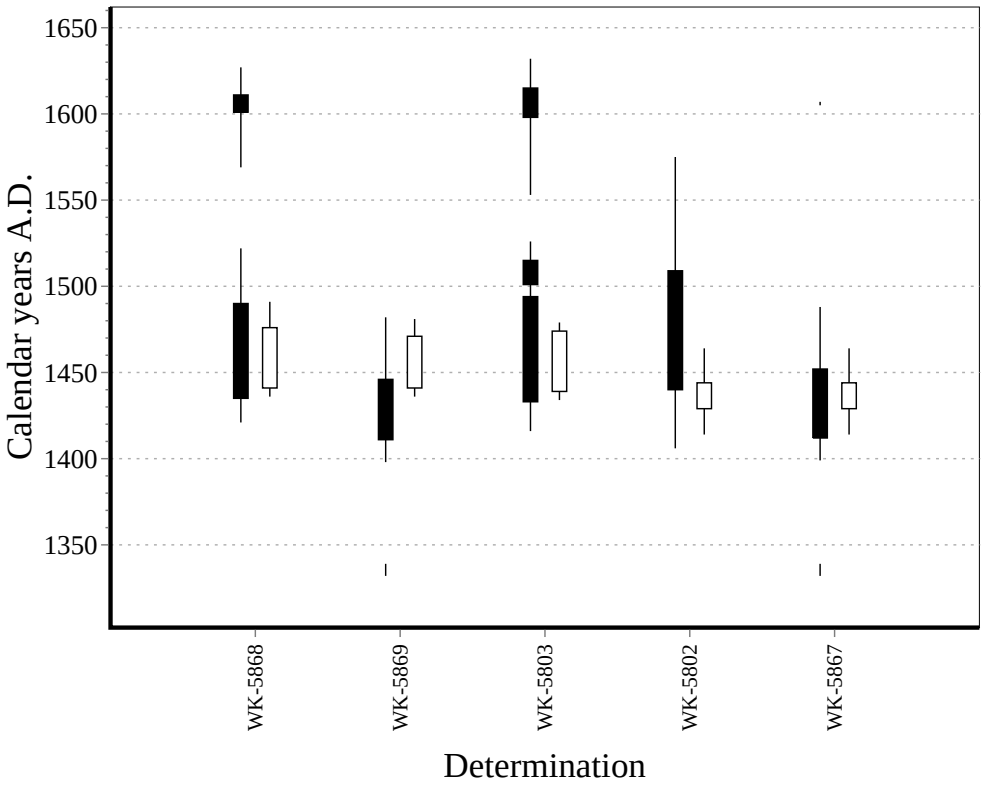

Figure 13.5: Posterior distribution of calibrated CRA chronometrics given in Table 13.1: clear bars represent the posterior distribution

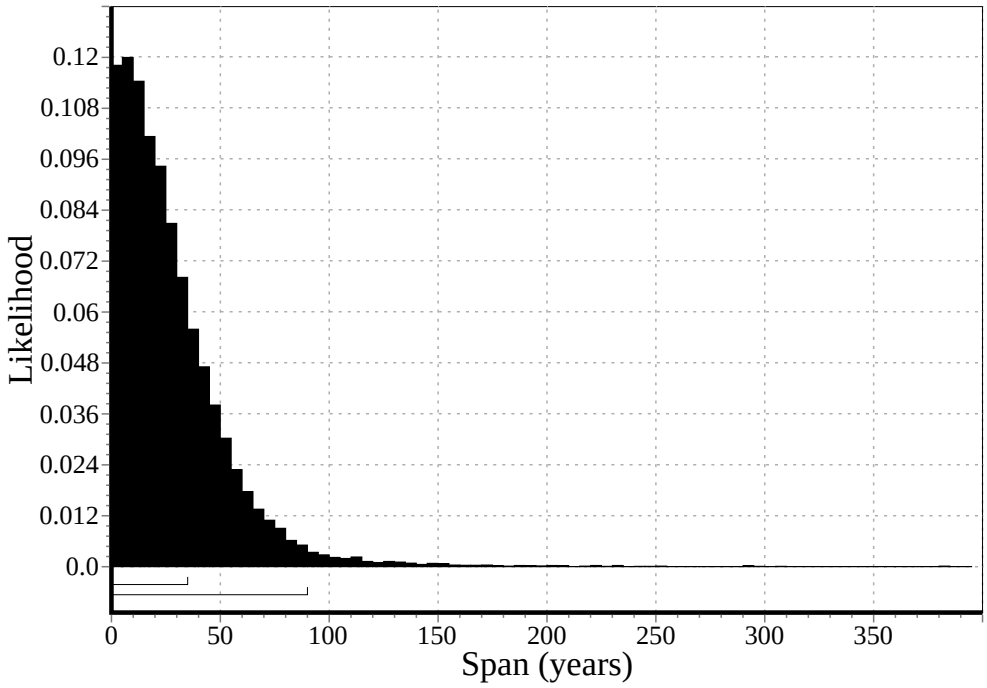

Figure 13.6: Posterior distribution of $R1$ following analysis of the R9/779 CRA as the sole chronometric data type

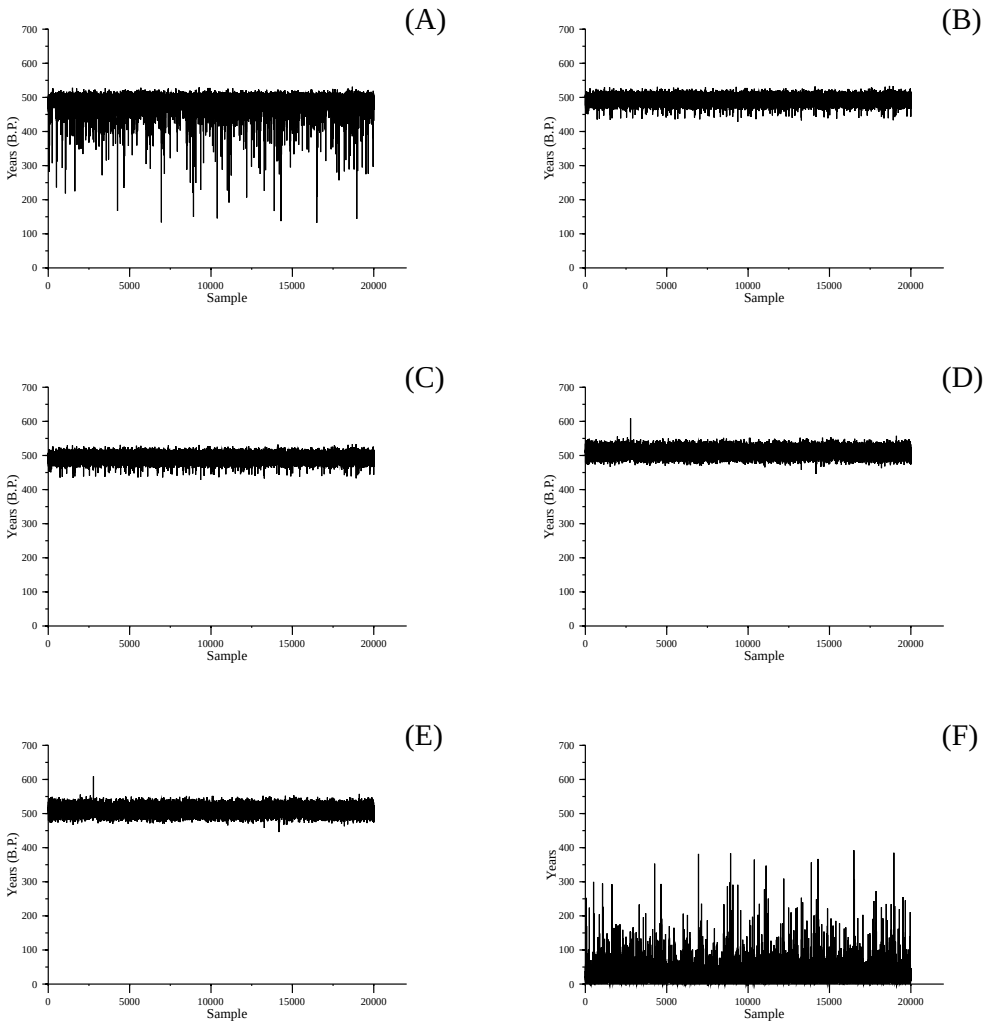

Figure 13.7: Plots of the trace from analysis of the R9/779 CRA data: (A) ψ_0 ;(B) ψ_1 ;(C) ψ_2 ;(D) ψ_3 ;(E) ψ_4 ;(F) $R1 \equiv \psi_1 - \psi_4$

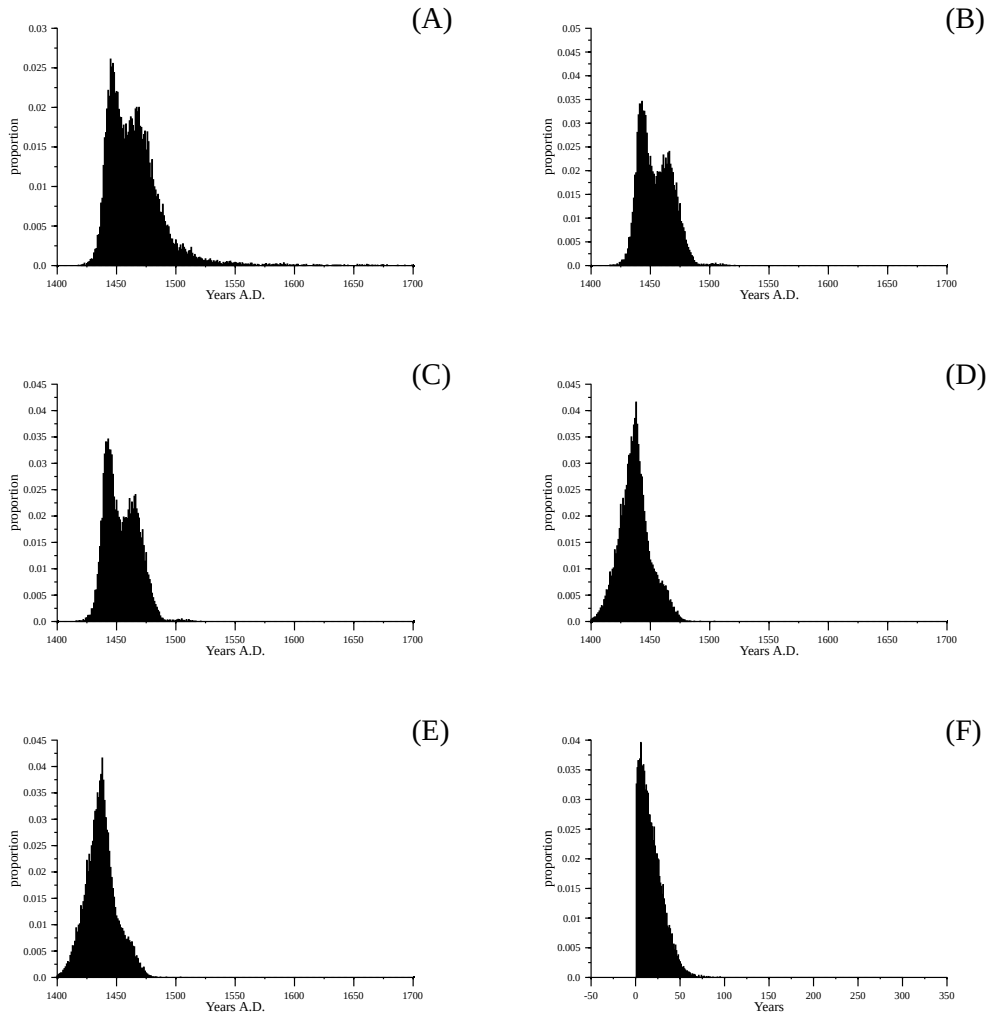

Figure 13.8: Posterior distribution of temporal parameters for the R9/779 archaeological record following analysis of the CRA data alone: (A) ψ_0 ;(B) ψ_1 ;(C) ψ_2 ;(D) ψ_3 ;(E) ψ_4 ;(F) $R1 \equiv \psi_1 - \psi_4$

This provides a useful test case for the OHD chronometric data. Firstly, we can determine how closely the chronology defined by the OHD chronometric data matches that given above. Secondly, we can determine how much influence the combined calibration has on the interpreted chronology. Finally, given the precision of the temporal parameters recovered through the analysis presented here the R7/779 chronometric data set represents a good example for generating cross-dated data such as the palaeo-temperature estimates (*infra vide*:§9.3.2) and glass hydration parameter estimates (*infra vide*:§6.1.2) discussed previously.

13.4.3 OHD as a Sole Chronometric Data Type

Analysis of the first six OHD chronometric determinations given in Table 13.1 was conducted through integrating the marginal distributions from the posterior density defined in Equation 13.1. Here the likelihood follows Equation 13.7 and we have correlated glass hydration parameter values and temperature values. In this particular analysis all of the glass derives from the Mayor Island Hydration Group thus we will assume that the unknown Glass specific hydration parameters are the same for all of the analysed artefacts. In this case $N_A = 1$ and $N_E = 1$. Thus the parameter sets are $A_1 \sim N(1.86E + 10, (1E + 9)^2)$ (Table 6.7) and $E_1 \sim N(86700, 150^2)$ (Table 6.6) with the mappings $\upsilon_A(i) = 1$ and $\upsilon_E(i) = 1$. The temperature estimates used here follow the models outlined in Chapters 11 and 12. $\bar{T}$ is estimated as $\sim N(17.5, 2.25)$ ^{0}C at 30cm following the empirical model given in Chapter 11. We will model Δ_{EHT} as being constant within any given strata, but as varying between the strata. As we have OHD determinations on artefacts from three different strata $N_\Delta = 3$. We will model Δ_{EHT} using the Radlab simulation package described in Chapter 12 and we can calculate the Δ_{EHT} values for the different contexts as -0.1,-0.2 and -0.25 ^{0}C for samples deriving from layers 2,3 and 4 respectively. in this case the mapping υ_T is given

as

$$v_T(i) = \begin{cases} 1 & i > 2 \\ 2 & i = 2 \\ 3 & i = 1 \end{cases}$$

Following these definitions we can calculate a calibrated likelihood for the individual OHD chronometric data via the posterior density defined in Equation 13.13. This is presented in Figure 13.9 and is directly analogous to standard radiocarbon calibration. In itself this plot is a significant development as it is the first presentation of a properly calibrated OHD. However, the results are not very precise. The calibrated radiocarbon and OHD distributions are plotted together in Figure 13.9 to ease comparison of the distributions. As can be seen the calibrated OHD likelihoods are much less precise than those for radiocarbon. This is as expected and reflects a greater degree of uncertainty with the OHD chronometric in comparison to the CRA. However, the calibrated distributions do cover the period over which the radiocarbon determinations lie. The fact that the 95% HPD of the calibrated distribution for the OHD determinations spans some 500-600 years suggests that the use of OHD as a method for dating independent flaking events is unlikely to provide sufficient resolution to be useful in addressing chronological questions at the resolution required for short pre-historic sequences such as that of New Zealand.

Analysis of the full posterior given in Equation 13.1 was run through Date Lab 1.1 using a Metropolis-Hastings sampler to collect 20000 samples at a sample interval of 100 following a burn of 20000 samples. To run this analysis the OHD data given in Table 13.1 are entered into the OHD data sheet described above (*infra vide*:§13.3.1). Here the models are all normal, the phase associations are given in Table 13.1 and the hydration and temperature group associations follow the mappings $v_E(i)$ & $v_T(i)$ defined above. The Hydration parameters for A_1 and E_1 are entered into the glass parameters data sheet, and the Δ_{EHT} estimates are

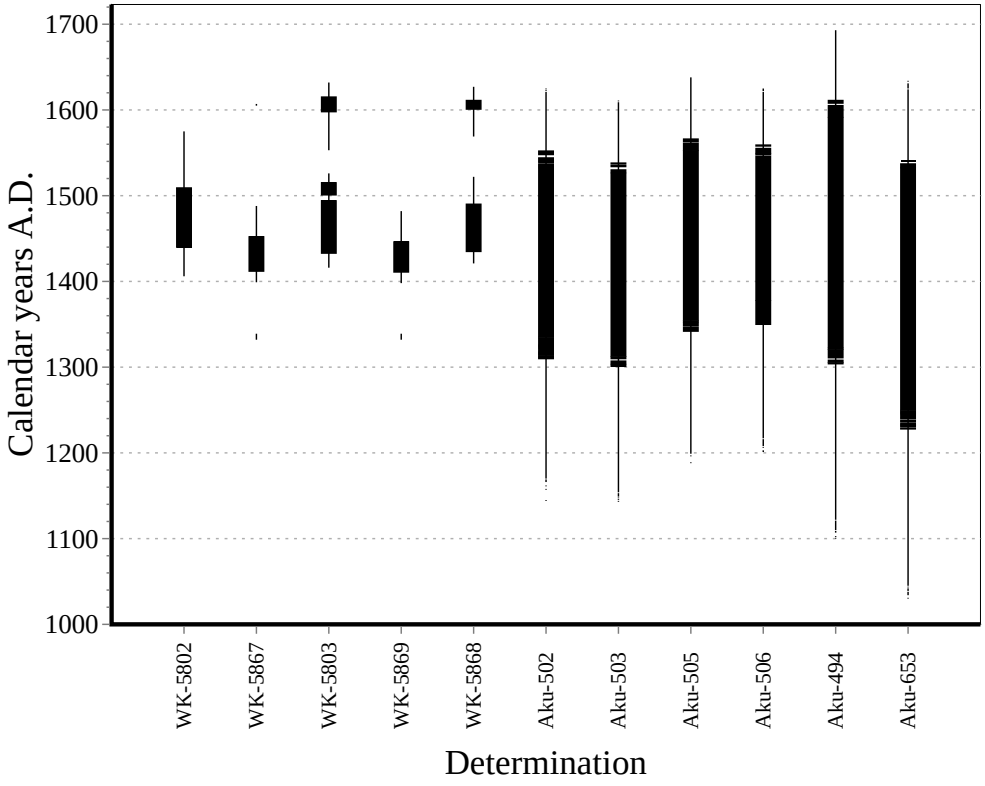

Figure 13.9: Calibrated distributions for the chronometrics given in Table 13.1

entered into the Δ_T data sheet (Figure 13.1). The prior for $\bar{T}$ is specified in the Obsidian Hydration tab of the Date Lab control panel (Figure 13.2). This analysis data-set can be loaded into Date Lab via the **tiri2.dla** file which will be place in the jobs subdirectory after installation of the Date Lab 1.1 package, and the full Date Lab analysis report can be as the **tiri2** link in the PHD.html document on the companion CD.

The posterior θ distributions are plotted in Figure 13.10. As can be seen there is an increase in precision for these, however the regions of support are still broad, covering several centuries. This is reflected in

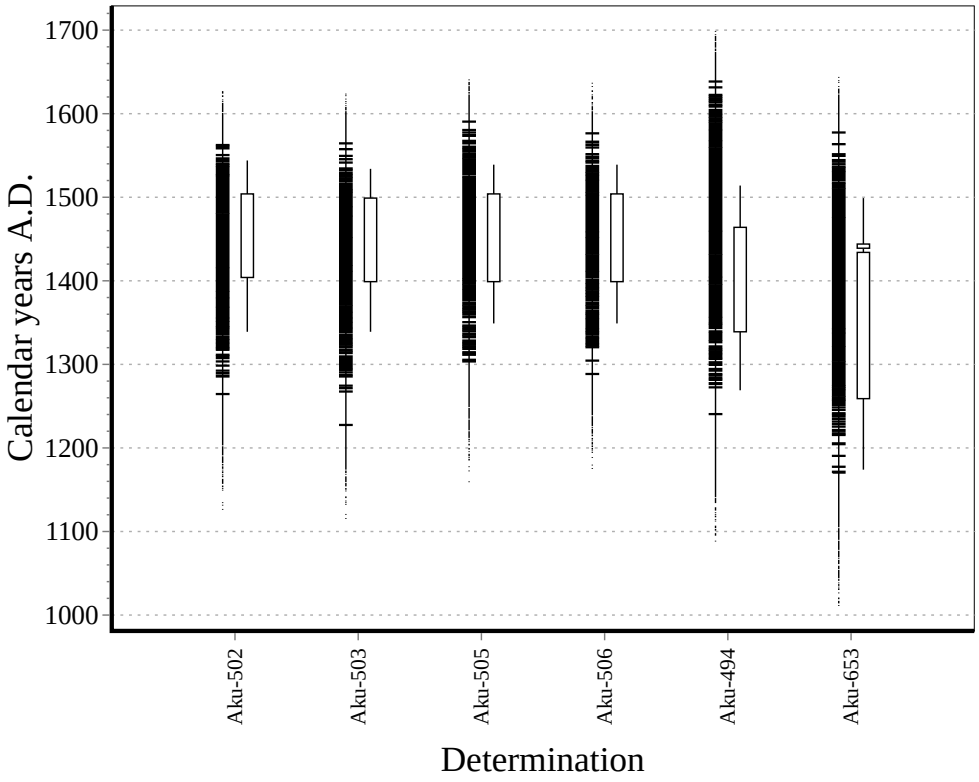

Figure 13.10: Posterior distribution of calibrated OHD chronometrics given in Table 13.1

the posterior distributions for the chronology parameters $\psi_1, \ldots, \psi_4$ & $R1$. The distribution of these parameters is given in Figure 13.11 which

has been directly calculated from the trace file **psi_samp.csv** as discussed previously for the radiocarbon results. These distributions are less precise than those derived through analysis of the radiocarbon results. From the OHD analysis we would interpret that the occupation has taken place over anything from 0-490 years over the 11th-17th centuries. Thus these results do not contradict those generated through the radiocarbon analysis, but do not really provide any useful information. The results have basically suggested that the activity represented by the R9/779 archaeological record has taken place some time during New Zealand's prehistoric sequence.

The lack of resolution provided via the analysis of the OHD results is due to the fact that the state of the variables governing the hydration reaction are imprecisely known, and that the actual measurements have a relatively large associated uncertainty. However, some improvement upon this can be made through a combined radiocarbon and OHD analysis where OHD acts in the capacity of providing absolute relative determinations.

13.4.4 Combined Analysis of the CRA and OHD Chronometric Data

In this analysis we use a subset of the radiocarbon data and the full OHD data-set to demonstrate one of the most practical uses of combined OHD and radiocarbon analysis; the use of OHD as a measure of absolute relativity in conjunction with radiocarbon to provide absolute temporal control. Here we will only use the two Layer 4 radiocarbon determinations (Wk-5802, Wk-5867). The OHD determinations will then serve to provide a measure of the absolute time difference between that strata and those from which other OHD data derive. In this case we do not have to make any EHT estimations. This recalls the results discussed in §8.1.1 and

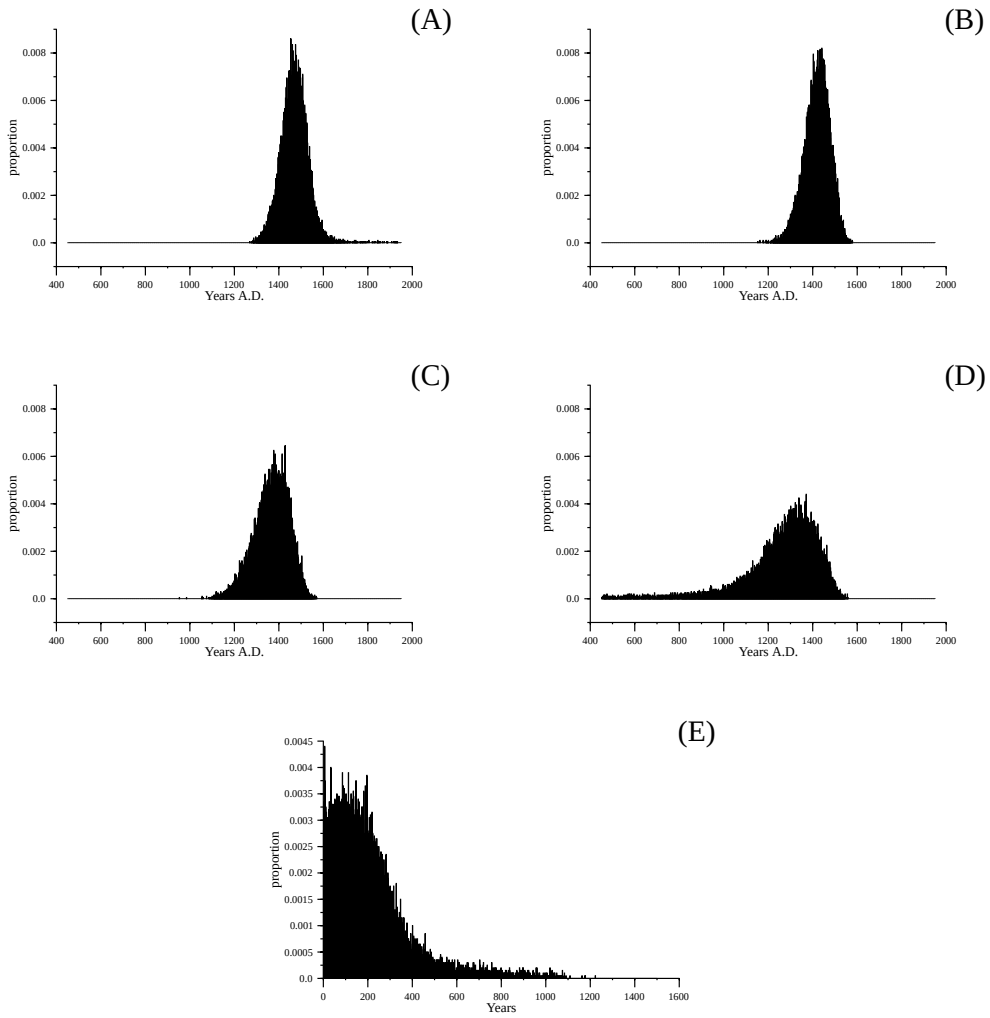

Figure 13.11: Posterior distribution of temporal parameters $\psi_1, \ldots, \psi_4$ & $R1$ under analysis of the R9/779 OHD data in isolation: (A) ψ_1 ;(B) ψ_2 ;(C) ψ_3 ;(D) ψ_4 ;(E) $R1 \equiv \psi_4 - \psi_1$

summarised in Equations 8.7 and 8.8 which basically show that the relative time difference between two flaking events is proportional to the ratio of the squared rim thicknesses. Further, if the artefacts have the same glass specific hydration properties this result is independent of those estimates, and finally the results only rely upon Δ_{EHT} rather than EHT estimates. Thus for this analysis we will generate marginal posteriors from the density given in Equation 13.14 where the OHD specific priors are as specified in §13.4.3 above with the exception that $\bar{T}$ is not specified, (*i.e.* $F_{\bar{T}}(\bar{T}) \propto 1$).

This analysis was run using the Metropolis-Hastings sampler to collect 20000 samples at a sample step of 100 following a burn of 20000 samples. To run this analysis the two radiocarbon chronometric data are entered as described by Jones and Nicholls (2002) and the OHD data given in Table 13.1 are entered into the OHD data sheet described above (*infra vide*:§13.3.1). Here the models are all normal, the phase associations are given in Table 13.1 and the hydration and temperature group associations follow the mappings $\upsilon_E(i)$ & $\upsilon_T(i)$ defined in §13.4.3. The Hydration parameters for A_1 and E_1 are entered into the glass parameters data sheet, and the Δ_{EHT} estimates are entered into the Δ_T data sheet (Figure 13.1). In this case we do not need to set a prior for $\bar{T}$ hence the settings for $\bar{T}$ in the Obsidian Hydration tab of the Date Lab control panel (Figure 13.2) are left blank. This analysis data-set can be loaded into date lab via the **tiri3.dla** file which will be place in the jobs subdirectory after installation of the Date Lab 1.1 package, and the full Date Lab analysis report can be as the **tiri3** link in the **PHD.html** document on the companion CD.

The results from this analysis are given in Figure 13.12 and show that a more precise posterior distribution has been generated than for an analysis using OHD data alone. In this case the results suggest that the processes generating the analysed component of the R9/779 archaeolog-

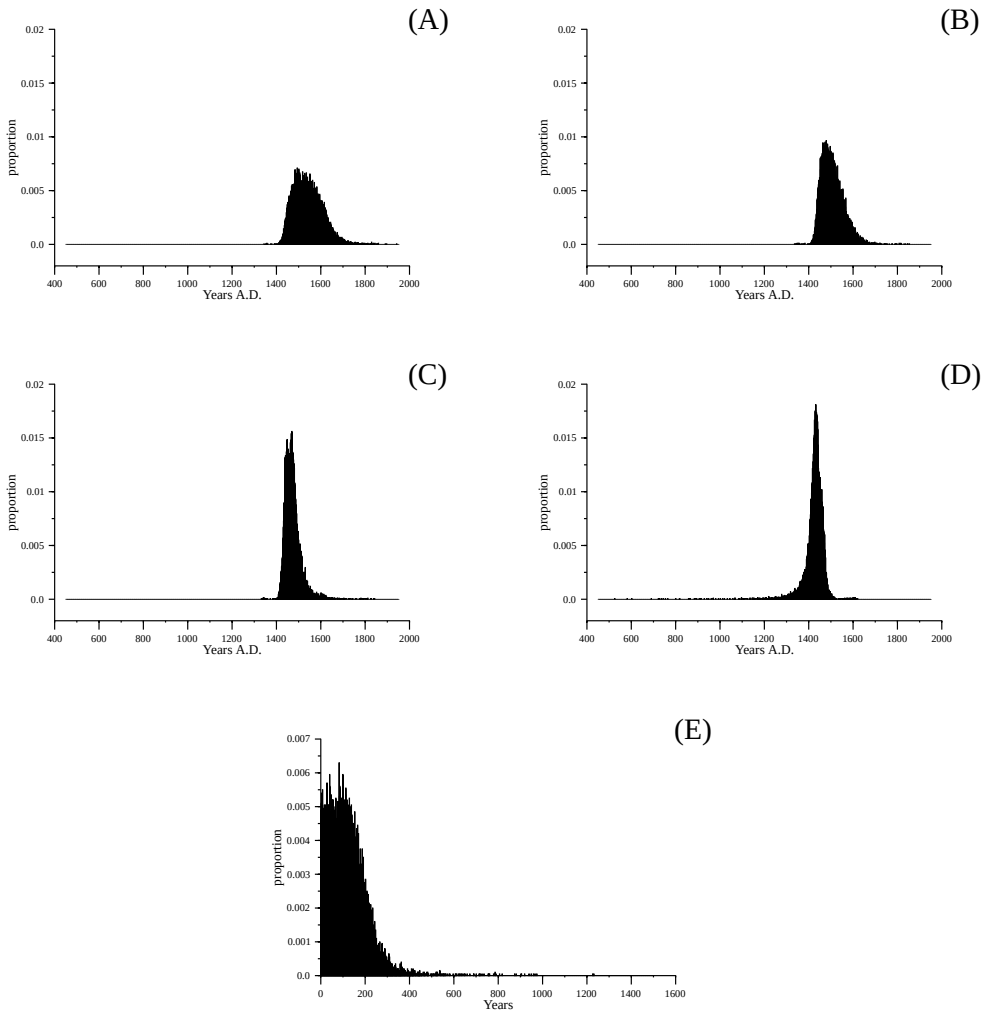

Figure 13.12: Posterior distribution of calibrated CRA chronometrics given in Table 13.1

ical record have taken place over 0-250 years in the 15th-16th centuries. This is 2-3 times more precise that the analysis conducted through using the OHD data alone. The increase in precision arises from the fact that the uncertainty in the hydration rate governing parameters of A,E or EHT are minimised as OHD is acting in the capacity of absolute relativity. The primary uncertainty in the system is due to a combination of the uncertainty associated with the hydration thickness measurements and the calibrated radiocarbon distributions.

This is an important result. It shows that OHD can generate posterior temporal parameters for processes at a resolution that provides useful chronological information in pre-historic sequences as short as that seen in New Zealand. Further, we do not need to employ poorly developed estimates for EHT or glass specific hydration parameters. While the results of the analysis presented here are less precise than the equivalent analysis conducted with radiocarbon data, a similar analysis could provide useful information in circumstances where suitable samples for radiocarbon dating where unavailable, and could also act as an independent check of radiocarbon chronologies. If more precise hydration rim measurements could be developed than those employed here this would constitute a particularly powerful form of chronological enquiry.

In practice, the available chronometric data for the R9/779 site is most suited to an analysis of the full chronometric data-set. In this analysis the OHD data would serve as a check on the radiocarbon results, and the posterior distributions of the parameters A, E & $\bar{T}$ would allow the development of palaeo-temperature estimates for this location (i.e. *infra vide*:§9.3.2) and the generation of cross-dated glass specific hydration parameter estimates (*infra vide*:§6.1.2). We will consider this analysis in the following section.

13.4.5 Cross-Dating Estimates

Here we run an analysis of the full chronometric data-set given in Table 13.1 including the seventh OHD determination (AKU-501). This determination was made on a sample of obsidian that does not derive from the Mayor Island Hydration Group. In this case we do not know the glass specific hydration parameters however we can use the current analysis to generate posterior distributions for these unknown values.

In the current analysis the OHD specific priors differ to those used previously. Here $N_A = 2$ and $N_E = 2$. Thus the parameter sets are $A = (A_1, A_2)$ and $E = (E_1, E_2)$. A_1 and E_1 are associated with the Mayor Island Hydration Group and hence $A_1 \sim N(1.86E + 10, (1E + 9)^2)$ (Table 6.7) and $E_1 \sim N(86700, 150^2)$ (Table 6.6). The parameters A_2 and E_2 are unknown. Hence $f_{A_2}(A_2) \propto 1$ and $f_{E_2}(E_2) \propto 1$. The mappings $v_A(i)$ and $v_E(i)$ are given as

$$v_A(i) = v_E(i) = \begin{cases} 1 & i < 7 \\ 2 & i = 7 \end{cases}$$

Other than this the temperature estimates are as given in §13.4.4 above.

The marginal posteriors were integrated out of the full posterior given in Equation 13.14 via a Metropolis-Hastings analysis run through Date Lab using the sampler settings described above. To run this analysis the radiocarbon chronometric data were entered as described by Jones and Nicholls (2002) and the OHD data given in Table 13.1 were entered into the OHD data sheet described above (*infra vide*:§13.3.1). Here the models are all normal, the phase associations are given in Table 13.1 and the hydration and temperature group associations follow the mappings $v_E(i)$ & $v_T(i)$ defined in this section. The Hydration parameters for A_1 and E_1 are entered into the glass parameters data sheet. However as the values for A_2 & E_2 are unknown these values are left blank in the glass parameters data sheet. The Δ_{EHT} estimates are entered into the

Δ_T data sheet (Figure 13.1). In this case we do not need to set a prior for $\bar{T}$ hence the settings for $\bar{T}$ in Obsidian Hydration tab of the Date Lab control panel (Figure 13.2) are left blank. This analysis data-set can be loaded into date lab via the **tiri4.dla** file which will be place in the jobs subdirectory after installation of the Date Lab 1.1 package, and the full Date Lab analysis report can be as the **tiri4** link in the **PHD.html** document on the companion CD.

The posterior distributions for $\psi_1, \ldots, \psi_4$ and $R1$ are not plotted, however they are much the same as for the analysis on the radiocarbon data alone as presented in §13.4.2 (*e.g.* Table 13.4.6). This is to be expected as the results from the radiocarbon analysis (*infra vide*:§13.4.2 and the OHD analysis (§13.4.3;§13.4.4) are consistent. The true utility of the analysis run here is in recovering the posterior distributions of the variables A_i, E_i and $\bar{T}$. These are plotted in Figure 13.13. As can be seen we have been able to recover posterior distributions for all of these variables. The posterior distributions for the Mayor Island Hydration group parameters are more precise than the prior specification, with $A_1 \sim N(1.80E + 10, 1.46E + 15)$ and $E_1 \sim N(86600.2, 3236.3)$ in the posterior. These distributions have 3 and 30 times the precision of the estimates given in Tables 6.6 and 6.7 respectively. Additionally, we have been able to recover glass specific hydration parameters for AKU-501 which derives from an unknown hydration group. In this case the distribution for E_2 is normally distributed as $\sim N(85091.2, 92354.1)$. However the posterior distribution for A_2 is a complex multi-modal distribution. This is to be expected as A needs to be defined at at least two different temperatures. Thus we would need to repeat this type of cross-dating exercise in another context where the EHT differed in order to generate a more meaningful posterior for A_2. However, this is a useful analysis and it illustrates an implementation of the approach to providing glass specific hydration parameters via cross-dating samples with known hydration behaviour and those with unknown hydration be-

haviour as outlined in Chapter 6 (*infra vide*:§6.1.2).

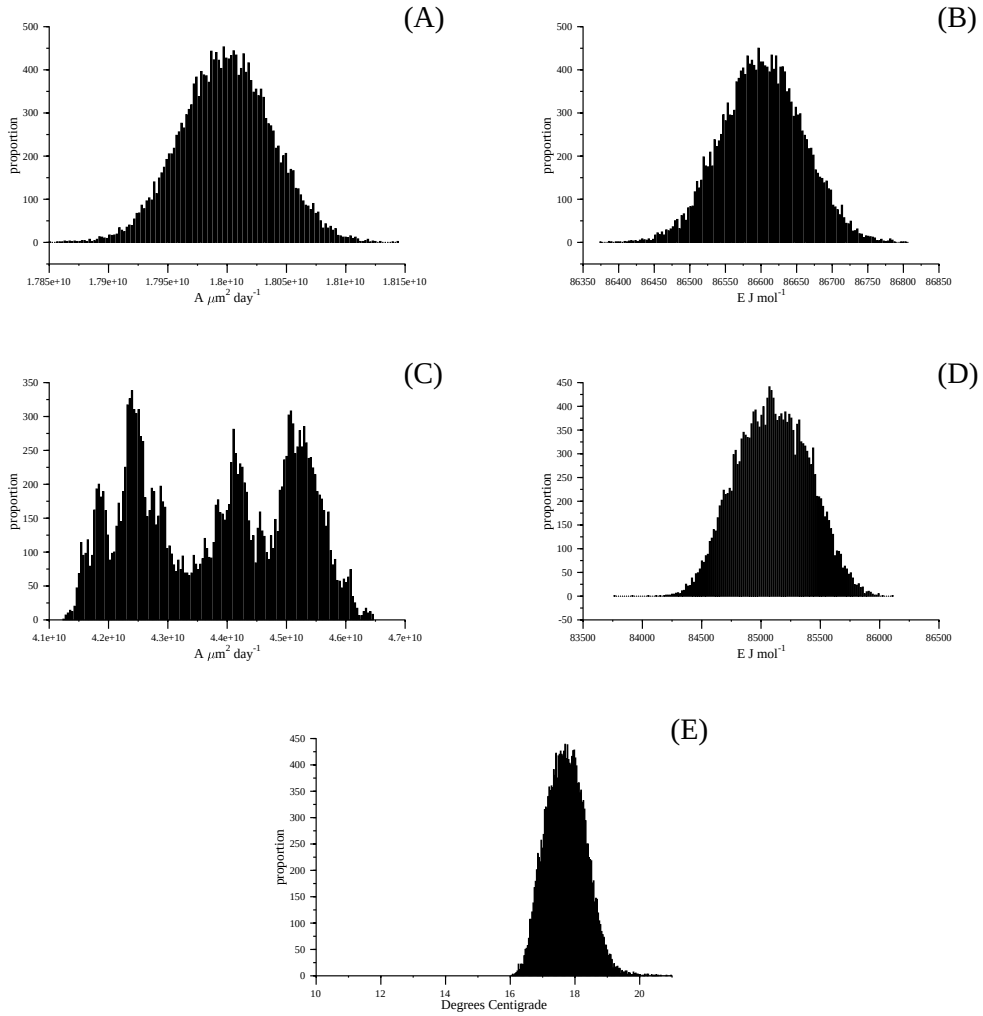

Figure 13.13: Posterior distribution of cross dated hydration parameters: (A) A_1 (B) E_1 (C) A_2 (D) E_2 (E) $\bar{T}$

Another outcome of this analysis is the recovery of a posterior distribution for the unknown $\bar{T}$ variable. The posterior for $\bar{T}$ is distributed as $\sim N(18.5, 2.0)$. This is interesting for two reasons. Firstly it illustrates the use of OHD chronometric data to derive palaeo-temperature determinations — this is a highly useful outcome in its own right. Secondly, we can use the posterior $\bar{T}$ estimate as a comparison for the output of the

empirical temperature estimate outlined in Chapter 11. The estimate derived through that model was $\sim N(17.5, 2.25)$. Thus the recovered value for $\bar{T}$ is consistent with the model proposed in Chapter 11.

13.4.6 Conclusion

In the case study presented here we have considered a simplified analysis of the R9/779 archaeological record. The purpose of this has been to demonstrate the use of OHD as a chronology building tool, and to perform an assessment of the utility of OHD. Through this study we have used the OHD chronometric in three different capacities — as a stand alone dating system, as part of a combined analysis with radiocarbon data, and as a system to recover cross-dated posterior distributions for palaeo-temperatures and glass hydration parameters. These serve to demonstrate the range of basic analyses that may be conducted with OHD chronometric data, and — not insignificantly — are the first instances of properly calibrated OHD determinations (and to my knowledge one of the first properly defined calibrations of a non-radiocarbon chronometric).

The basic conclusion that can be drawn is that the OHD chronometric is in general a less precise chronology building tool than the CRA. This is particularly the case where OHD acts in a capacity as a stand alone dating system. This can be demonstrated with reference to the posterior distribution for the statistic $R1$. The 68% and 95% HPD's for $R1$ under the four different analyses are given in Table 13.4.6 below. As can be seen there is a significant range in the precision of the reported statistic, with the analysis of OHD data in isolation returning a distribution spanning almost 5 times that of the equivalent analysis using the CRA chronometric. This is simply too imprecise to be of any practical use in a short pre-historic sequence such as that represented by New Zealand's

Table 13.2: Comparison of R statistic for R9/779 calculated under the different analyses presented in §13.4

Analysis	68% HPD	95 % HPD
1	0–35	0–90
2	0-240	0–485
3	0–130	0–250
4	0–50	0–100

archaeological record. This is an interesting results in itself as it suggests that analyses that do not fully factor the influence of uncertainty in glass hydration parameters and temperature estimates will produce spuriously precise dates.

In contrast, the other two analyses using OHD have returned useful data. Acting in the capacity of providing absolute relative dates in conjunction with a primary absolute dating system (radiocarbon in this case) OHD data has been shown to be provide usefully precise chronological information – albeit still less precise than the equivalent CRA results. Additionally it has proved possible to recover useful cross-dated hydration controls.

In reality the precision of optical hydration rim measurements as employed in this thesis are too imprecise to enable OHD to act as a high resolution chronological tool. However, the results have shown that we can use OHD to resolve chronological questions in the order of one to two centuries. This is both useful as a check of contentious chronologies developed via other types of chronometric data, and in situations where other chronometric data may not be available. Additionally the use of OHD to provide cross-dated palaeo-temperature estimates may be very useful in some applications. In the following sections we will consider three further case studies that illustrate some applications in which OHD may be a useful tool given current limitations in the mea-

surement resolution of the basic chronometric data.

13.5 Tairua T11/62 (N44/2)

In this example we will undertake a combined analysis of the CRA and OHD data for the T11/62 archaeological site. The purpose of this analysis is to demonstrate the use of OHD in a context where the CRA results may be erroneous, and to further demonstrate OHD as a tool to recover palaeo-temperature data.

Tairua (T11/62) is one of a series of sites located on a sand tombolo running approximately 1.5 km between Paku island and the mainland in Tairua Harbour. The T11/62 deposit appears to correspond to a short term camp spread over an area of approximately 600 m^2 (Green 1967; Smart and Green 1962). There are two main cultural deposits, an upper layer of dense midden and flaking debris (Bed 6) is separated by sterile sand from a lower layer (Bed 2) containing an apparent archaic camp. The excavations ($\approx$ 125 m^2 in extent) revealed a distinct spatial pattern in Bed 2 deposits with an area of midden and debitage being distinct from an oven area and a further area of firescoops and postholes.

13.5.1 Chronometric Analysis

A short occupation is implied by the Bed 2 deposit (Green 1967; Smart and Green 1962). The deposits are not widely spread and do not occur to a great depth (generally less than 20 cm). Similarly, the volume of faunal and artefactual material in this deposit does not argue for a long occupation. Thus the deposit almost certainly corresponds to a single short-term camp (Green pers. comms). This is a useful case study where we have an independent assessment of the span of activity represented

by an archaeological record. Here we can compare the performance of the CRA and OHD chronometrics against an independent measure. As obsidian is only available from the Bed 2 deposit we will treat the current example as if the T11/62 archaeological record consisted of a single cultural horizon. We can then asses how well the available chronometric data recovers the independent assessment that the chronology is very brief.

Chronometric Data

Seven radiocarbon dates have been obtained from this site (Green 1967; Rowland 1976; Schmidt and Higham 1997). Two of these (NZ 594, NZ 595) are on charcoal samples extracted from the same oven in Bed 2. The two samples were extracted 5 years apart and have returned quite different results. Initially, Green (1967) believed that the younger date (NZ 595) had been contaminated as the dated sample had been extracted five years after the original (NZ 594) sample. Subsequent to the submission of these two dates the remaining charcoal samples were analysed and it became apparent that a component of charcoal from this site consisted of samples of old wood, possibly drift wood, indicated by worm holed or pocket rotted Kauri and Kahikatea (Green pers comm.) Additionally, long lived species were predominant in the sample. Though a proportion was of sound[2] relatively small diameter Rimu. It is apparent that the difference observed between the two dates could easily have arisen as a function of sample composition and would be an obvious instance of the context and event dates being non-isochronous. In light of both of these points the younger date is preferred. This conclusion is supported by the five radiocarbon determinations on marine mollusc shell (MMS) that have been obtained for this site. MMS samples from the upper (Bed 6) and lower (Bed 2) cultural layers have been dated, and the

[2] implying a recent death

MMS dates for Bed 2 (NZ 1875,Wk 5444,Wk 5445) closely correspond to the younger terrestrial ^{14}C date (NZ 595). Thus we will not include NZ 594 in the current analysis example.

In addition to the CRA chronometrics reported in Table 13.3 OHD determinations have been made on eight obsidian artefacts from the Bed 2 deposit. These all derive from the Mayor Island Hydration group.

Table 13.3: T11/62 chronometric data

OHD Results

Date	CRA	Material	Layer
NZ 594	885 ± 52	Charcoal	Bed 2
NZ 595	449 ± 44	Charcoal	Bed 2
NZ 1875	885 ± 58	Marine Mollusc Shell	Bed 2
Wk 5444	1000 ± 50	Marine Mollusc Shell	Bed 2
Wk 5445	1090 ± 50	Marine Mollusc Shell	Bed 2
NZ 1876	566 ± 57	Marine Mollusc Shell	Bed 6
Wk 5446	570 ± 40	Marine Mollusc Shell	Bed 6

OHD Results

Sample	Source	Rim (Fm)	Error (2s)	Layer
ohd1	Mayor Island	0.964	0.032	Bed 2
ohd2	Mayor Island	0.944	0.051	Bed 2
ohd3	Mayor Island	0.994	0.036	Bed 2
ohd4	Mayor Island	0.953	0.022	Bed 2
ohd5	Mayor Island	0.949	0.021	Bed 2
ohd6	Mayor Island	0.960	0.045	Bed 2
ohd7	Mayor Island	1.069	0.084	Bed 2
ohd8	Mayor Island	0.923	0.124	Bed 2

Model Structure

In the current analysis we will seek to model temporal bounds for the activity represented by the Bed 2 deposit in the T11/62 archaeological record — when this activity began, when it ceased and over what period of time it took place. Thus our chronology is a description of the timing of processes that have given rise to the observed T11/62 archaeological record. Our chronometry is the $K = 12$ valid Bed 2 chronometric determinations given in Table 13.3. Following the notation outlined for the chronology building framework defined previously (*infra vide*:§1.2), we define the following temporal parameters for the T11/62 formation process:

ψ_1	the date at which the Bed 2 record began to be formed
ψ_0	the date at which Bed 2 record ceased to be formed

Accordingly the state space (Ω) is

$$\Omega \equiv \{(\psi, \theta); TPQ \leq \psi_1 \leq \theta_{\cdot} \leq \psi_0 \leq TAQ\} \tag{13.16}$$

Where in this case the TAQ and TPQ are conservative bounds that we will set at 1850 and 450 A.D. respectively (see Nicholls and Jones 2001 for further discussion on setting bounds).

As discussed above our interest in this example is to recover the posterior distribution of the parameters ψ_1 & ψ_0 as well as the span statistic $R = \psi_0 - \psi_1$. We can then asses the posterior for R against the prior contention that R is brief, almost certainly less than one year. Here we again conduct the analysis in two stages, to allow us to asses the utility of OHD as a chronology building tool in comparison to the sole use of CRA data.

13.5.2 Results

Initially we will look at the CRA chronometric data in isolation (Analysis 1). To perform this analysis we need to calculate the marginal posterior distributions for ψ_0, ψ_1 and R from the posterior defined in Equation 13.14 with $N_1^x = 0$ (*i.e.* the radiocarbon calibration scheme given by Nicholls and Jones (2001)). Here the INTERCAL 98 radiocarbon calibration data (Stuiver *et al.* 1998) were used with ΔR set at -25±15 radiocarbon years (Higham and Hogg 1995) for the marine samples and ΔR set at 27±5 for the terrestrial sample (McCormac *et al.* 1998) using correlated reservoir offsets as described by Jones and Nicholls (2001). In order to run this analysis the radiocarbon chronometric data are entered into Date Lab as described by Jones and Nicholls (2002) and a Metropolis-Hastings sampler was run with a sample size of 20000, a Burn of 20000, and a sample step of 100.

The posterior distributions for ψ_0, ψ_1 & R are given in Figure 13.14. As can be seen the recovered span statistic is broad, spanning over 800 years for the 95% HPD and with the strongest support falling in the region 100-300 years. While this is consistent with a span of less than 1 year the overwhelming impression is that the span of occupation is long, and further more the results are imprecise. This primarily comes about as the observed radiocarbon dates favour a distribution in time that implies a low intensity process in the poisson model underlying the prior for $f(\psi, \theta)$ used here (Nicholls and Jones 2001). In part this may be due to the fact that the dated species of Marine Mollusc differ. The three Bed 2 MMS samples all comprise different species (NZ 1875 *Cellana denticulata*; Wk 5444 *Austrovenus stutchburyi*; Wk 5445 *Lunella smaradaga*) that occupy different estuarine locations and hence may relate to different carbon reservoirs (Schmidt and Higham 1997). In the case that this is true we would not know the correct reservoir offsets to apply to these data. The second analysis reflects this possibility.

In the second analysis (Analysis 2) we use the OHD chronometric data in a capacity of providing absolute relative temporal information, with the single terrestrial CRA (NZ 595) providing absolute temporal control. This is essentially the same analysis that was conducted for the R9/779 site in §13.4.4. However, in this case we make the statement that *a priori* we do not know the correct reservoir offsets to apply to the MMS samples. Thus in this case we will model the reservoir offsets as being un-correlated and *a priori* uniform on the interval $[-\infty, \infty]$. Under this analysis we will be able to recover posterior distributions for the reservoir offsets of the MMS samples and a palaeo-temperature estimate for this site in addition to distributions for the parameters ψ_0, ψ_1 and R.

Here the OHD likelihood follows Equation 13.7 and we have correlated glass hydration parameter values and temperature values. In this particular analysis all of the glass derives from the Mayor Island Hydration Group thus we will assume that the glass specific hydration parameters are the same for all of the analysed artefacts. In this case $N_A = 1$ and $N_E = 1$. Thus the parameter sets are $A_1 \sim N(1.86E + 10, (1E + 9)^2)$ (Table 6.7) and $E_1 \sim N(86700, 150^2)$ (Table 6.6) with the mappings $v_A(i) = 1$ and $v_E(i) = 1$. $\bar{T}$ is modelled as unknown *a priori* (*i.e.* $f_{\bar{T}}(\bar{T}) \propto 1$), and we will assume the same Δ_{EHT} for all samples as they derive from close spatial proximity. We will model Δ_{EHT} relative to a $\bar{T}$ at 30 cm depth so that we can compare the posterior $\bar{T}$ and the 30cm EHT estimate derived from the empirical model presented in Chapter 11. Thus here $\Delta_T \sim N(-0.3, 0.1^2)$. In this case the mapping $v_T(i) = 1$.

To run this analysis the four radiocarbon chronometric data are entered into Date Lab as described by Jones and Nicholls (2002). The reservoir offsets are set on the radiocarbon tab of the Date Lab control panel. In this case the **Independent Sampled** reservoir offsets option is selected, and the **infinity** check box is selected for the marine reservoir offset. This identifies that the reservoir offset for marine samples is *a prior*

uniform on the interval $[-\infty, \infty]$. The OHD data given in Table 13.1 are entered into the OHD data sheet described above (*infra vide*:§13.3.1). Here the models are all normal and $m = 1$, $N_A = 1$, $N_E = 1$, $N_T = 1$ (*i.e.* $\nu_A(i) = 1, \nu_E(i) = 1, \nu_T(i) = 1$). Thus phase, hydration and temperature group associations are constant for all of the OHD data following the appropriate mappings. The Hydration parameters for A_1 and E_1 are entered into the glass parameters data sheet, and the Δ_{EHT} estimates are entered into the Δ_T data sheet (Figure 13.1). In this case we do not need to set a prior for $\bar{T}$ hence the settings for $\bar{T}$ in Obsidian Hydration tab of the Date Lab control panel (Figure 13.2) are left blank.

The posterior distributions for ψ_0, ψ_1 and R under Analysis 2 are presented in Figure 13.14. The distribution of these temporal parameters differs substantially to that recovered from Analysis 1 (see Table 13.5.2). In this case the distributions are more in line with our prior expectations, and more precise.

Table 13.4: Comparison of the posterior temporal parameters for T11/62 Bed 2 activity Analysis 1 and Analysis 2

Parameter	Analysis 1		Analysis 2	
	68 % HPD	95% HPD	68 % HPD	95% HPD
R	45-360	0-810	0–135	0–360
ψ_0	1420–1570	1405-1775	1415–1500	1395-1585
ψ_1	1225–1400	905–1435	1350–1450	1140–1500

In addition to posteriors for the parameters ψ_0, ψ_1 & R, under Analysis 2 we are able to recover posterior information on (amongst other variables) the EHT for this record and the reservoir offsets for the individual MMS samples.

The posterior distribution for EHT from this site is distributed as $\sim N(17.4, 1.12^2)$. As mentioned previously this is useful information in terms of palaeo-environmental reconstruction. In the current case this

Figure 13.14: Posterior temporal parameters for T11/62 Bed 2 activity Analysis 1 and Analysis 2

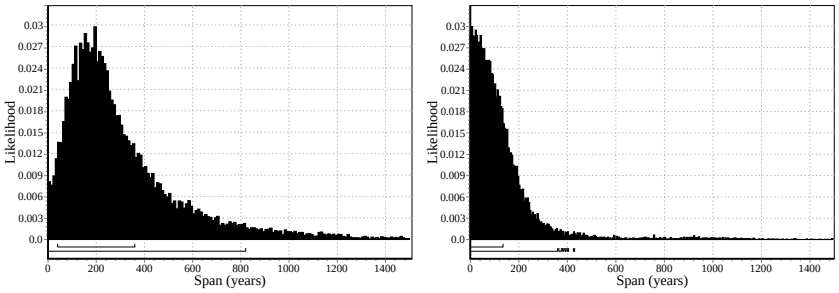

(a) Span Analysis 1

(b) Span Analysis 2

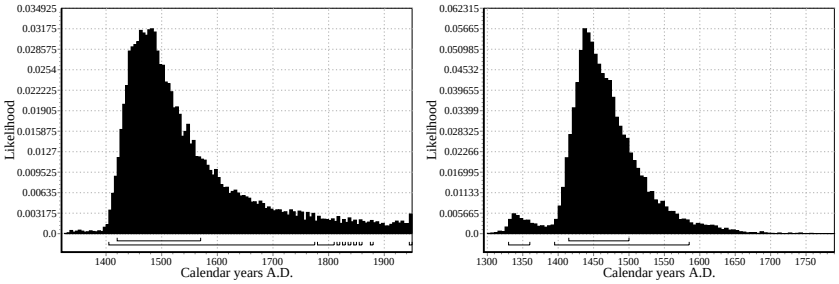

(c) ψ_0 Analysis 1

(d) ψ_0 Analysis 2

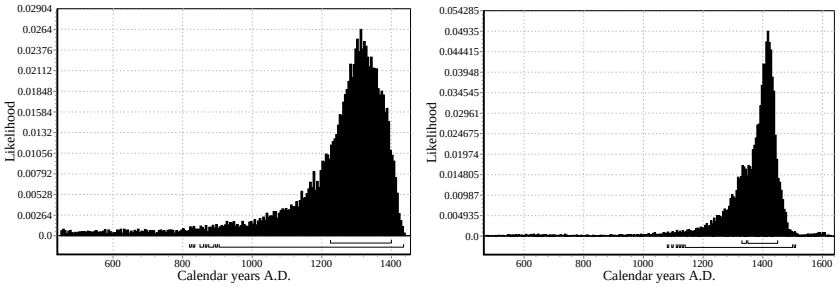

(e) ψ_1 Analysis 1

(f) ψ_1 Analysis 2

is also another opportunity to test the empirical EHT model presented in Chapter 11. Under that model the predicted EHT for Tairua at 30 cm depth is 17.3±1.5 ^{0}C. Thus in this case the observed and modelled EHT results are consistent. We can use this recovered temperature estimate to calculate calibrated likelihood distributions for the T11/62 OHD chronometrics. These are plotted in Figure 13.15 along with the calibrated CRA data. As can be seen the calibrated OHD data are again very broad with the 95 % HPD spanning 600-800 years, inspite of the fact that we are able to use a valid and relatively precise EHT estimate. This supports the observation made in §13.4 that in general the OHD chronometric is insufficiently precise to act as an absolute dating tool.

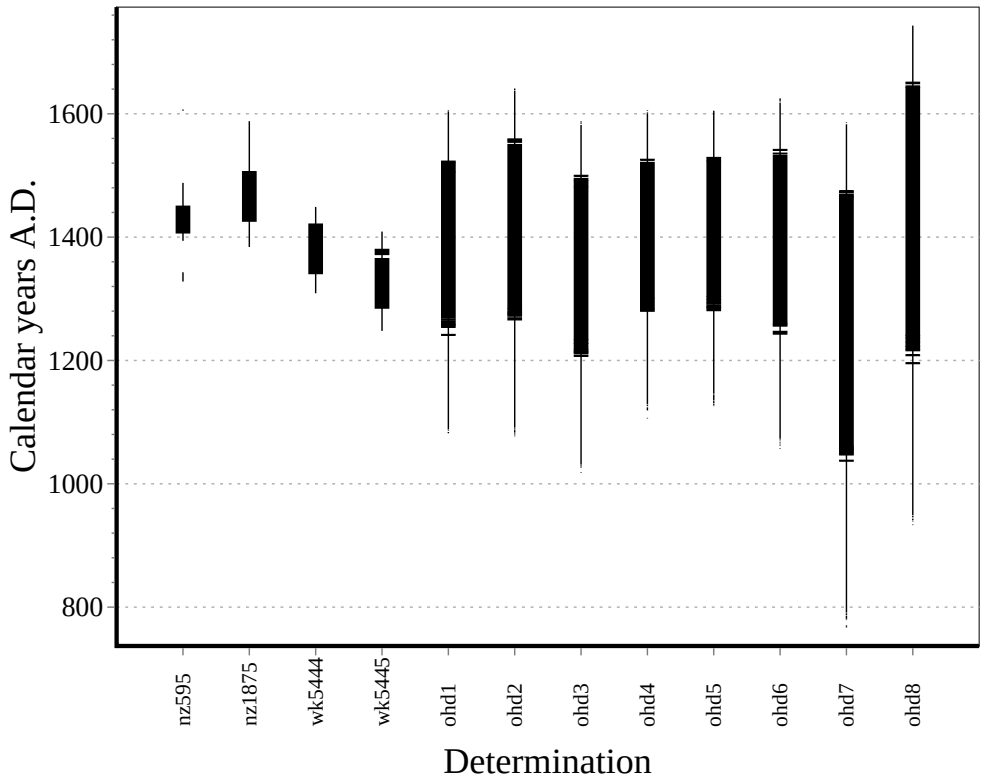

Figure 13.15: Calibrated CRA and OHD chronometrics given in Table 13.3

The posterior distributions for the reservoir corrections to be applied to the MMS samples are not significantly different as the distributions are broad however the central tendencies differ (Table 13.5.2).

Table 13.5: Posterior ΔR statistics for the T11/62 Marine samples

Sample	posterior ΔR	$\sigma_{\Delta R}$
Wk 5444	-7.30E+01	113
Wk 5445	-1.46E+02	143
NZ 1875	+58	152

13.5.3 Conclusion

In this example we have considered a simplified chronology for the T11/62 archaeological record. We can state *a priori* that the span of activity represented by the T11/632 Bed 2 deposit is brief, thus we have conducted a chronology building exercise using the available chronometric data to establish how well this prior expectation is recovered. This is purely a test case as in a real analysis we would make use of this prior information by constraining the state space.

In this analysis the use of OHD chronometric data has enabled a more precise posterior chronology — and one that is more in line with our prior expectations — to be constructed than has been possible through using CRA data alone. In part this may have arisen through the fact that the three dated marine mollusc shell samples comprise different species and thus may derive from different carbon reservoirs. To reflect this possibility the use of OHD data has allowed us to recover posterior data on the appropriate marine reservoir ΔR offsets for these three MMS samples. While these posterior distributions are not significantly different the central tendency of the distributions differ substantially (Table 13.5.2).

Martin Jones 2002

The conclusion from this exercise is that OHD chronometric data can give rise to useful chronological information in circumstances where the radiocarbon chronometry may be problematic. Further, the ability to recover cross-dated posterior information through combined calibration of multiple chronometric data types has been illustrated. In this case posterior information relating to both CRA and OHD chronometric data has been recovered. In the next case study we will consider a very similar problem but in a different environmental setting.

13.6 Hawksburn G42/13 (S133/5)

In this case study we will again use a combination of OHD and CRA chronometric data. Here the OHD chronometric data will be used to provide absolute relative data and also to provide palaeo-temperature data in a cross-dating exercise. This is a very similar case study to that considered for Tairua (*infra vide*:§13.5) however in this case the site is far inland (for New Zealand) and would be expected to be very much colder (The empirical model presented in Chapter 11 predicts a 30 cm EHT of 10.4 ^{0}C at Hawksburn as opposed to 17.3 ^{0}C for Tairua). Thus the study will allow us to establish how OHD performs for a similar problem but under substantially different environmental conditions.

Hawksburn (G42/13) lies in inland central Otago and appears to be a specialised moa hunting camp (Anderson 1979; 1982). Archaeological investigations at G42/13 have revealed a stratigraphically simple site containing a single cultural deposit with some lensing and inclusions (Anderson 1979). A number of different areas in the site have been investigated, and it is apparent that the spatial structure is more complex than the apparent stratigraphy. This spatial structure may be associated with what Anderson (1982) interprets as a dual moa butchery process: One being the immediate consumption of moa; the other being the

preservation of moa.

13.6.1 Chronometric Analysis

One of the prime archaeological questions to be addressed in the case of Hawksburn is how long the site has been occupied, as well as when this occupation may have taken place. Here we will compare the use CRA alone and a combination of CRA and OHD chronometrics.

Chronometric Data

In total 14 ^{14}C dates have been obtained for this site (Table 13.6). Four (NZ 59-62) were obtained by Lockerbie (Hamel 1978; Lockerbie 1959; 1955). Two of these (NZ 59, NZ 60) were on bone carbonate and will be excluded from the following analysis (Anderson 1991). The other two Lockerbie dates (NZ 61 & NZ 62) are on charcoal of unknown species composition. In light of this it is possible that these determinations incorporate significant inbuilt age.

Ten further dates on material from G42/13 were obtained by Anderson (1981). Nine of these (NZ 5044-5052) were on charcoal composed mainly of short lived species. These dates should exhibit little inbuilt age and thus closely approximate the actual context dates. The date NZ 5053 on burnt soil is more difficult to assess, Anderson (1981) states the sample:

> ...contained no identifiable charcoal. It was of a sample of burnt soil containing finely comminuted carbonaceous material from a stone hearth.

The assumption here is that the dated material relates to the material burnt in the hearth. As there is no identifiable dated component in this

Table 13.6: Hawksburn CRA data

Date	CRA	Provenance
NZ 61	590 ± 50	bottom layer
NZ 62	593 ± 65	occupation layer
NZ 5044	692 ± 33	HB/H/14 spit II
NZ 5045	709 ± 33	HB/H/8 spit III
NZ 5046	714 ± 33	HB/I/23 Spit II
NZ 5047	611 ± 33	HB/M/6 spit II
NZ 5048	691 ± 33	HB/FB/8 spit II
NZ 5049	652 ± 33	HB/L/5 layer 3
NZ 5050	720 ± 33	HB/M/14 spit IV
NZ 5051	668 ± 33	HB/FA/15 spit III
NZ 5052	663 ± 28	HB/L/10 layer 3
NZ 5053	592 ± 33	HB/E/2 layer 1

sample it is very difficult to confidently associate the dated sample with any distinct event. Consequently this result is excluded from the analysis to follow.

In total 20 OHD measurements have been made on obsidian artefacts from throughout G41/13 (Table 13.7). The dated artefacts all derive from the Mayor Island hydration Group.

Chronometric Model

The dates for G42/13 come from a single layer sampled from throughout the approximate spatial extent of the site. Thus must be modelled as relating to a single phase of activity of unknown duration. The observations made by Lockerbie (1959) are relevant in this case, he notes that the site may have been built up over a considerable period of time

Table 13.7: Hawksburn OHD chronometrics

lab	Location	measured	error
AKU-737	HB/C/11, SURFACE + SPIT 1	0.674	0.066
AKU-738	HB/L/22, SPIT 1	0.624	0.041
AKU-739	HB/C/2, SPIT 1	0.671	0.036
AKU-740	HB/D/2, SURFACE + SPIT 1	0.7	0.042
AKU-741	HB/D/4, SURFACE + SPIT1	0.629	0.057
AKU-742	HB/D/1, SPIT 1	0.668	0.032
AKU-743	HB/D/15, SPIT 1	0.631	0.031
AKU-744	HB/D/1, SPIT 1	0.637	0.042
AKU-745	HB/D/1, SPIT 1	0.634	0.031
AKU-746	HB/S/24, SURFACE	0.674	0.036
AKU-747	HB/D/7, SPIT 1	0.626	0.021
AKU-748	HB/U/14, SPIT 1	0.696	0.057
AKU-749	HB/D/2, SURFACE + SPIT 1	0.634	0.038
AKU-750	HB/D/2, SURFACE + SPIT 1	0.69	0.042
AKU-751	HB/D/2, SURFACE + SPIT 1	0.706	0.051
AKU-752	HB/D/2, SURFACE + SPIT 1	0.708	0.038
AKU-753	HB/D/2, SURFACE + SPIT 1	0.669	0.042
AKU-754	HB/D/2, SURFACE + SPIT 1	0.69	0.042
AKU-755	AL 668	0.666	0.046
AKU-756	AL 703	0.677	0.033

and that what appears to be a single strata may exhibit considerable horizontal stratigraphy, *i.e.*

> "Refuse deposited by the moa-hunter on one visit could lie side by side with material from a much earlier visit" (Lockerbie 1959, p86)

This would be particularly difficult to detect structurally given the very slow soil deposition rates in this area. As the available dates will sample any apparent horizontal stratigraphy in this site we can treat the dates as estimates of events falling from within an occupation phase of unknown duration. Thus we define the following parameters of interest

ψ_1	the date at which activity began at G42/13
ψ_0	the date at which activity ceased at G42/13
$R \equiv \psi_0 - \psi_1$	the duration of activity at G42/13

Following this the state space (Ω) can be given as

$$\Omega \equiv \{(\psi, \theta); TPQ \leq \psi_1 \leq \theta \leq\leq \psi_0 \leq TAQ\} \tag{13.17}$$

Where in this case the TAQ and TPQ are conservative bounds that we will set at 1950 and 450 A.D. respectively.

The span of activity R is of particular interest in this case as the duration of this type of activity has significant implications for our understanding of the rate at which moa where exterminated and the rate at which New Zealand was settled.

13.6.2 Results

The Calibrated CRA determinations (Figure 13.16) do not provide a clear picture of what duration may be represented by the G41/13 archaeological record. At this period in time there are multiple intercepts for the calibration curve (Figure 13.17) which give rise to widely disbursed multi-modal distributions for the calibrated CRA's. This suggests the possibility of a relatively long-term occupation (centuries) to a short-term occupation located anywhere from the thirteenth to early fifteen centuries.

We can perform a Bayesian calibration analysis of the CRA data through Date Lab (*e.g.* §13.4.2; §13.5 Analysis 1) to generate a posterior for ψ_0, ψ_1 and R. To perform this analysis we calculate the marginal posterior distributions for ψ_0, ψ_1 and R from the posterior defined in Equation 13.14 with $N_1^x = 0$ (*i.e.* the radiocarbon calibration scheme given by Nicholls and Jones (2001)). Here the INTERCAL 98 radiocarbon calibration data (Stuiver *et al.* 1998) were used with ΔR set at 27±5 (McCormac *et al.* 1998) using correlated reservoir offsets as described by Jones and Nicholls (2001). This analysis returns a short posterior distribution for R with correspondingly tight posterior distributions for ψ_0 and ψ_1 (Fig-

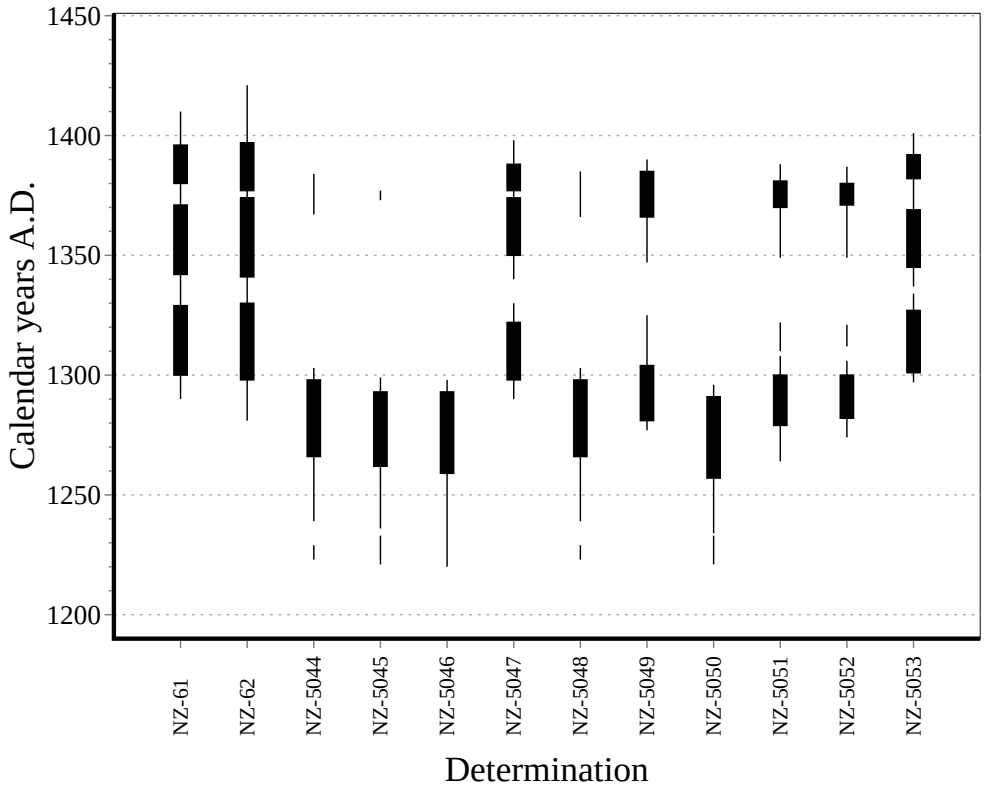

Figure 13.16: Calibrated distributions for the Hawksburn CRA data (Table 13.6

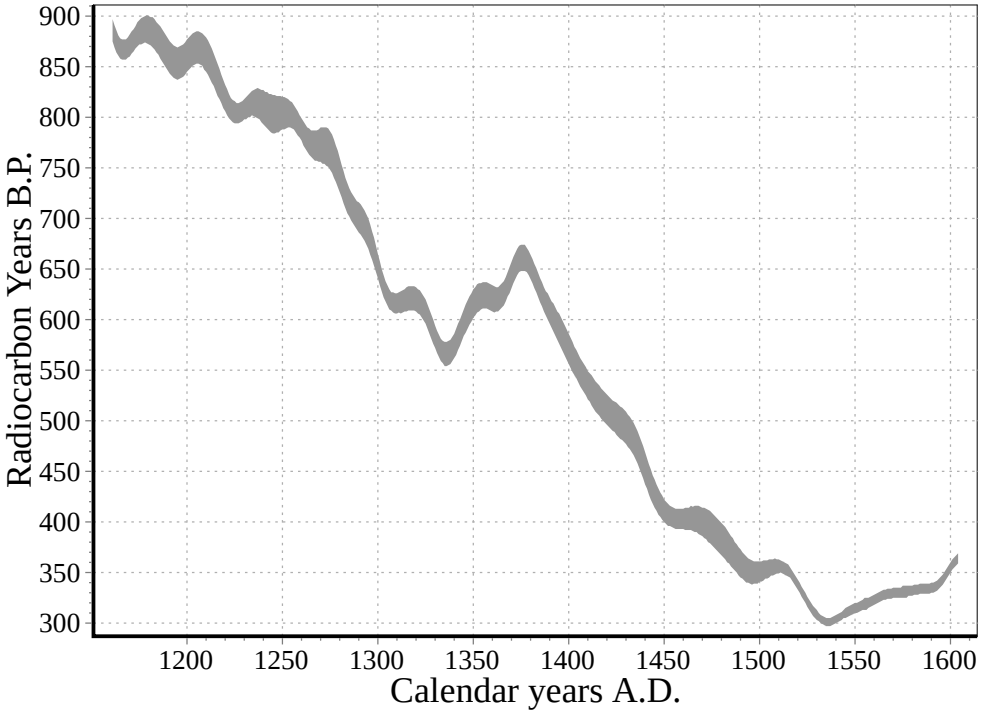

Figure 13.17: Calibration curve during the period over which Hawksburn was occupied

ure 13.18). However, in this case we must be conscious of the fact that a small change in the terrestrial reservoir offset would shift the analysis into a zone where there are significant perturbations in the calibration data (e.g. Figure 13.17). This would potentially give rise to a higher value for R. Thus in this case it is useful to run a comparative analysis using OHD data to check for consistency in the recovered chronological parameters ψ_0, ψ_1 and R. In this analysis we use OHD in the capacity of providing absolute relative chronometric data, and we randomly select two of the CRA determinations to provide absolute temporal control (NZ 5045 and NZ 5051). This analysis is largely identical to that conducted in §13.4.4 and §13.5 Analysis 2.

Here the OHD likelihood follows Equation 13.7 and we have correlated glass hydration parameter values. In this particular analysis all of the glass derives from the Mayor Island Hydration Group thus we will assume that the Glass specific hydration parameters are the same for all of the analysed artefacts. In this case $N_A = 1$ and $N_E = 1$. Thus the parameter sets are $A_1 \sim N(1.86E + 10, (1E + 9)^2)$ (Table 6.7) and $E_1 \sim N(86700, 150^2)$ (Table 6.6) with the mappings $v_A(i) = 1$ and $v_E(i) = 1$. $\bar{T}$ is modelled as unknown *a priori* (*i.e.* $f_{\bar{T}}(\bar{T}) \propto 1$). However in this case we will not assume that Δ_{EHT} is the same for all of the samples as they come from a wide spatial distribution. Therefore we cannot assume that Δ_{EHT} is correlated for the dated samples and we will use an independent Δ_T estimate for each OHD chronometric (*i.e.* $N_T = 20$). We can generate an estimate for Δ_{EHT} through the **RADLAB** simulation described earlier (§12), and in the case of Hawksburn we have an experimental control set of analogue cells through which we can asses the Δ_{EHT} estimates. The **RADLAB** simulation estimates that Δ_{EHT} values will vary by up to 0.2 ^{0}C. This is consistent with the measured cell values for the Hawksburn control set (Table 13.8). To accommodate this variation we will model each Δ_T variable as being normally distributed with $\sigma = 0.1$ ^{0}C (Thus the Δ_{EHT} range of 0.2 ^{0}C corresponds to 2σ). We will model the mean Δ_{EHT}

Table 13.8: Comparative Δ_{EHT} values for Hawksburn

	Depth	slope	azimuth	Δ_{EHT}
Hawksburn	20	0	0	0
Hawksburn	20	18	0	0.3
Hawksburn	20	18	45	0.2

relative to a $\bar{T}$ at 30 cm depth so that we can compare the posterior $\bar{T}$ and the 30cm EHT estimate derived from the empirical model presented in Chapter 11. Thus here $\Delta_T \sim N(0.2, 0.1^2)$. In this case the mapping $v_T(i) = i$.

The results from this analysis are very similar to those returned under the CRA analysis, simply being slightly less precise (Figure 13.18). Thus the OHD results support those derived from the CRA data, and we can conclude that the chronometric data are consistent with a brief phase of activity associated with the G42/13 archaeological record.

As a final aspect of this case study we will run the complete chronometric data set in a combined calibration analysis to recover the posterior $\bar{T}$ variable via cross-dating. This is identical to the analysis conducted for the R9/119 chronometric data set as presented in §13.4.5.

This is simply a repeat of the analysis just described except in this case the full CRA chronometric dataset is used. The posterior $\bar{T}$ recovered from this analysis is distributed as $N(9.38, 0.5^2)$. Again this is consistent with the empirical estimate of $10.4 \pm 1.5\ ^0$C generated through the model presented in Chapter 11.

13.6.3 Conclusion

The analysis presented here is largely the same as that presented for the T11/62 record in §13.5. The primary chronological question posed in this analysis is "when did the activity represented by the G42/13 archaeological record take place, and over what period of time?". Analysis

Figure 13.18: Posterior temporal parameters for G42/13: Analysis 1 and Analysis 2

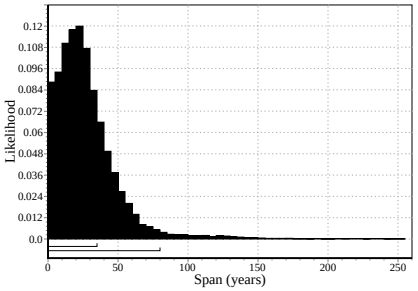

(a) Span Analysis 1

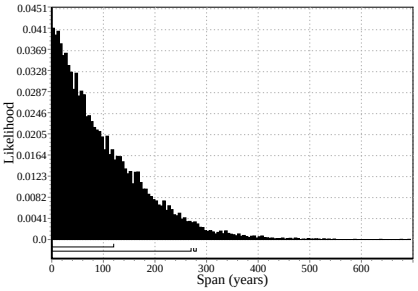

(b) Span Analysis 2

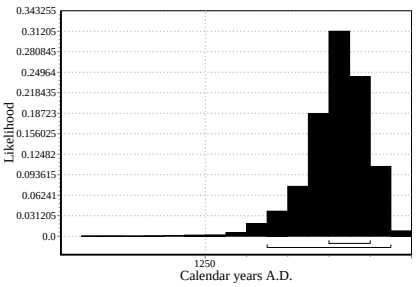

(c) ψ_0 Analysis 1

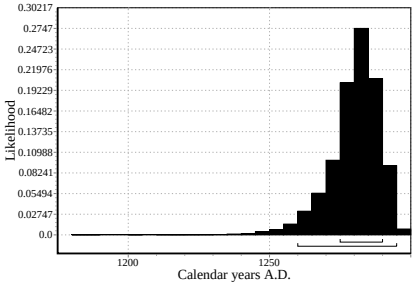

(d) ψ_0 Analysis 2

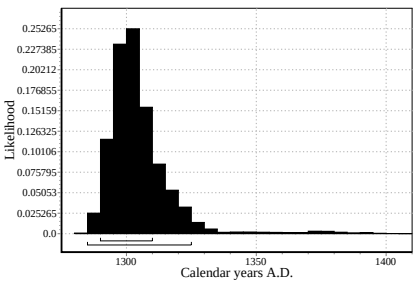

(e) ψ_1 Analysis 1

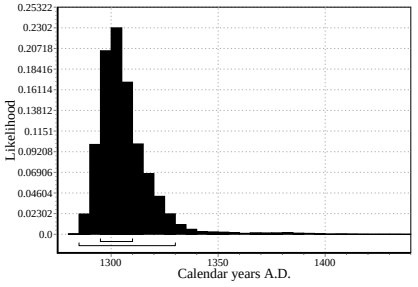

(f) ψ_1 Analysis 2

of the radiocarbon data suggests that the activity represented by the G42/13 record is brief (less than 80 years at a 95% HPD) and takes place in the interval 1250-1350 AD. This is an important result in terms of arguments relating to the initial human settlement of New Zealand. As this result could be influenced by perturbations in the radiocarbon calibration curve given minor changes in the applied reservoir correction, this result has been checked via a combined CRA and OHD calibration. The results from this analysis are consistent with the those derived from the CRA data alone. Thus we would concluded that the G42/13 record has arisen from a brief period of activity in the period 1250-1350 AD.

This analysis illustrates the use of OHD chronometric data to corroborate chronologies derived from CRA chronometric data. Additionally a palaeo temperature estimate has been recovered for this site. In the current example this posterior estimate acts as a test of the empirical EHT model presented in Chapter 11. The posterior estimate for $\bar{T}$ of 9.4 $\pm$ 0.5 ^{0}C is consistent with the modelled estimate of 10.4 $\pm$ 1.5 ^{0}C.

We will now consider one last case-study to explore the use of OHD chronometric data to explore chronological questions within the past 250 years.

13.7 Papahinau R11/229

Papahinau is a proto-historic site in Auckland, New Zealand that dates from the late eighteenth century to the mid-nineteenth century. This is established on the basis of historical records and the artefacts present (Foster and Sewell 1996). There are two general cultural horizons present, designated Layer 4 and Layer 2. The interpretation is that Layer 4 is a short term prehistoric midden and that the majority of the Layer 2 record belongs to the post-European contact period and relates to a

recorded settlement between 1835 and 1863. However, some features consistent with pre-European activity have been identified in the Layer 2 record, and Foster and Sewell (1996) believe these may indicate settlement occurred earlier than 1835. Thus we will perform an analysis of OHD dates to try and establish when the activity represented by the R11/229 Layer 2 deposit began. Our interest is trying to determine whether this began prior to 1835 or not.

In addition to the general chronological question we address here the analysis of OHD measurements from this site is interesting in a New Zealand context as a substantial part of New Zealand's archaeological record dates to within the past 250 years — a period over which radiocarbon dating is of very limited applicability. Therefore if OHD proves viable over this period then this is a significant development for the study of the recent period of New Zealand's archaeological record.

13.7.1 Chronometric Analysis

In this example we are interested in establishing the duration of activity represented by the proto-historic phase of activity at R11/229. We know *a priori* that this phase of activity ended in 1867. Thus the question is how long prior to 1867 did the activity associated with the R11/229 Layer 2 deposit start. Thus we are only really interested in a single posterior statistic, the span $R = \psi_1 - \psi_0$. This is because as ψ_0 is defined *a priori* ψ_1 is defined by R (and vice versa). Thus recovery of R will allow an assessment of whether the identified R11/229 settlement represented in Layer 2 began prior to 1835.

Martin Jones 2002

Chronometric Data

Three radiocarbon determinations have been made on marine mollusc shell from this site (Table 13.9). In addition, hydration measurements have been made on 38 obsidian artefacts from the Papahinau site (Table 13.9). These are also reported by Jones *et al.* (1998) who present a limited analysis of the results.

Chronometric Model

There are two general phases of cultural activity represented by the R11/229 archaeological record, thus we defined the following parameters:

ψ_2	the date of the Layer 3-2 interface
ψ_1	the date of the Layer 2-1 interface
ψ_0	the date at which Layer 1 ceased to be formed

Accordingly the state space (Ω) is

$$\Omega \equiv \{(\psi, \theta); TPQ \leq \psi_2 \leq \theta_{2,.} \leq \psi_1 \leq \theta_1, . \leq psi_0 = TAQ \qquad (13.18)$$

Here ψ_0 is known to be equalto a TAQ of 1863 (Foster and Sewell 1996). We do not have similar data for the TPQ so this is set to a conservative bound of 800 A.D.

13.7.2 Results

A Bayesian analysis of the radiocarbon data following Nicholls and Jones (2001) does not return any useful information regarding the distribution of ψ_1 and R (Figure 13.19(g)). The chronometric data simply fails to provide suitable temporal discrimination for this problem. In contrast the OHD chronometric data provide a more useful analysis.

Table 13.9: Chronometric data for the Papahinau site

CRA data

Date	CRA	Material	Layer
Wk 3315	490 ± 50	Marine Mollusc Shell	Layer 2
Wk 3316	750 ± 50	Marine Mollusc Shell	Layer 4
Wk 3317	520 ± 50	Marine Mollusc Shell	Layer 2

OHD data

Lab Number	Measured		calibrated	
	Rim	error	μ	σ
950	0.6	0.052	102	39
951	0.7875	0.061	176	55
952	0.7125	0.064	118	42
953	0.6	0.051	101	38
955	0.825	0.026	193	38
957	0.6	0.120	102	59
960	0.675	0.036	129	36
962	0.6	0.053	102	39
963	0.75	0.014	160	25
965	0.75	0.044	160	45
967	0.75	0.034	154	38
968	0.75	0.063	156	52
969	0.75	0.056	158	50
970	0.798	0.050	182	51
972	0.6	0.093	103	52
974	0.675	0.087	130	57
976	0.675	0.041	130	39
977	0.5625	0.078	90	45
978	0.7875	0.043	171	45
979	0.675	0.036	129	36
980	0.675	0.082	129	55
981	0.6	0.070	102	45
982	0.5625	0.063	88	39
984	0.525	0.055	79	35
985	0.9	0.068	231	67
986	0.525	0.046	78	32
987	0.675	0.055	124	43

Here we integrate the marginal posterior distribution for ψ_1 from the posterior given in Equation 13.14 defined by the full chronometric data set given in Table 13.9. We use the standard radiocarbon likelihood as defined by Nicholls and Jones (2001) using the INTERCAL98 marine calibration data (Stuiver *et al.* 1998) with a correlated reservoir offset (Jones and Nicholls 2001) of -27±15 (McCormac *et al.* 1998).

The OHD likelihood follows Equation 13.7 with $N_A = N_E = 1$. Thus the parameter sets $A_1 \sim N(1.86E + 10, (1E + 9)^2)$ (Table 6.7) and $E_1 \sim N(86700, 150^2)$ (Table 6.6), and the mapping $v_A(i) = 1$. Using the temperature model developed in Chapter 11 we would estimate that $\bar{T} \sim N(17.5, 1.5^2)$ ^{0}C at 30 cm depth. In this case the model should be a reasonable approximation, as the data upon which the EHT estimate is based covers the approximate time period for which the EHT estimate is required. As these samples are extracted from the same horizon but at depths ranging from ≈ 10-20 cm we would cannot use a correlated Δ_T variable for all of the measurements and we will use a separate Δ_T variable for each measurement. Using the numerical simulation presented in Chapter 12 we would estimate that the artefact specific Δ_{EHT} will be in the region + 0.5-0.9 ^{0}C relative to the 30 cm EHT estimate given above. To approximate this distribution we will use an independent Δ_T variable distributed as $N(0.7, 0.15^2)$ for each measurement. Thus here $\Delta_{T,i} \sim N(-0.3, 0.1^2), i = 1, \ldots, 35$ and the mapping $v_T(i) = i$.

The posterior distribution for $R = \psi_1 - \psi_0$ is given in Figure 13.19(h). As can be seen the posterior for R recovered from the combined CRA-OHD analysis is more informative than that produced through analysis of the CRA data alone. The 95% HPD for R is 185-310 years in contrast to 0-270 under analysis of the CRA data alone.

Also of interest in this analysis is a comparison of the calibrated likelihood distributions for the CRA and OHD data. These are plotted in Figures 13.20 and 13.21. As can be seen the OHD distributions are again

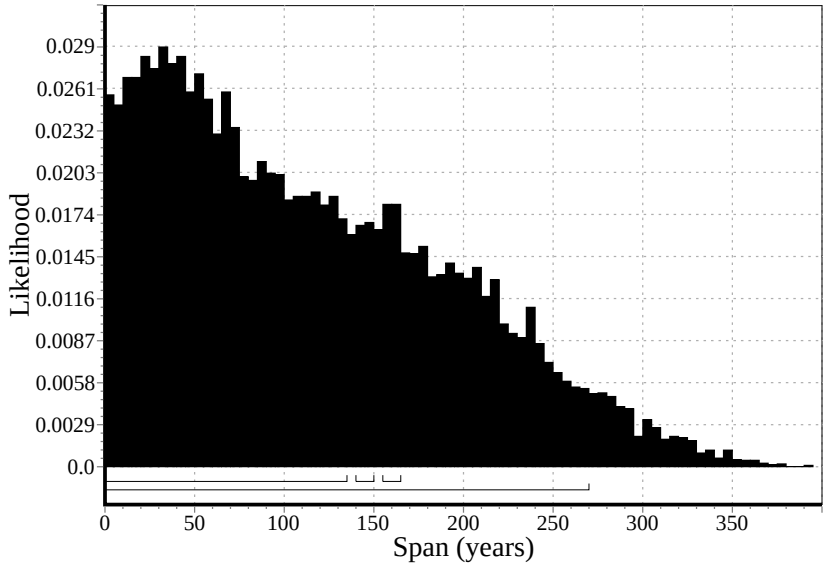

(g) Span under Analysis 1

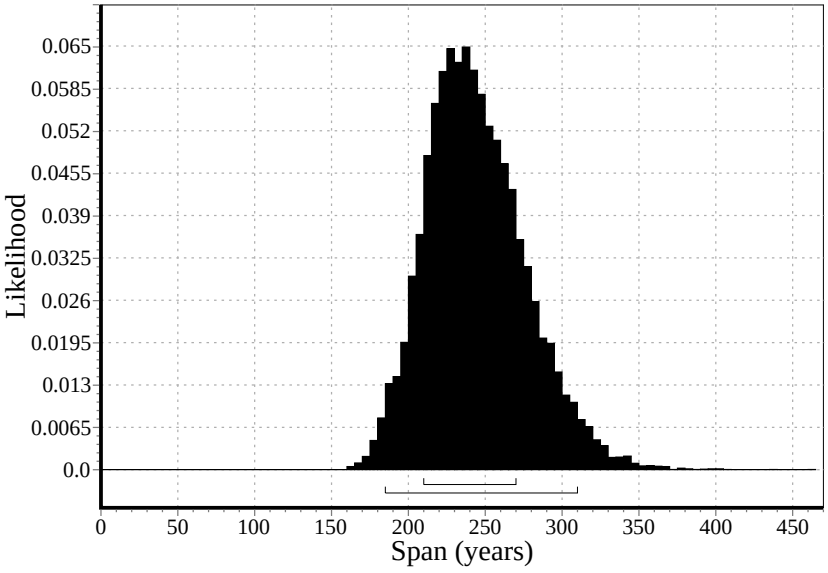

(h) Span under Analysis 2

Figure 13.19: Comparison between the posterior span for the duration of activity represented by R11/229 Layer 2 following analysis of the CRA data alone (Analysis 1) and a combined analysis of the CRA and OHD data (Analysis 2)
Martin Jones 2002

extremely broad spanning almost the entire prehistoric sequence for New Zealand. This further supports the conclusion drawn in §13.4 & §13.5 that individually calibrated OHD determinations are too imprecise to be of any real use in providing chronological control independent of correlated chronometric data.

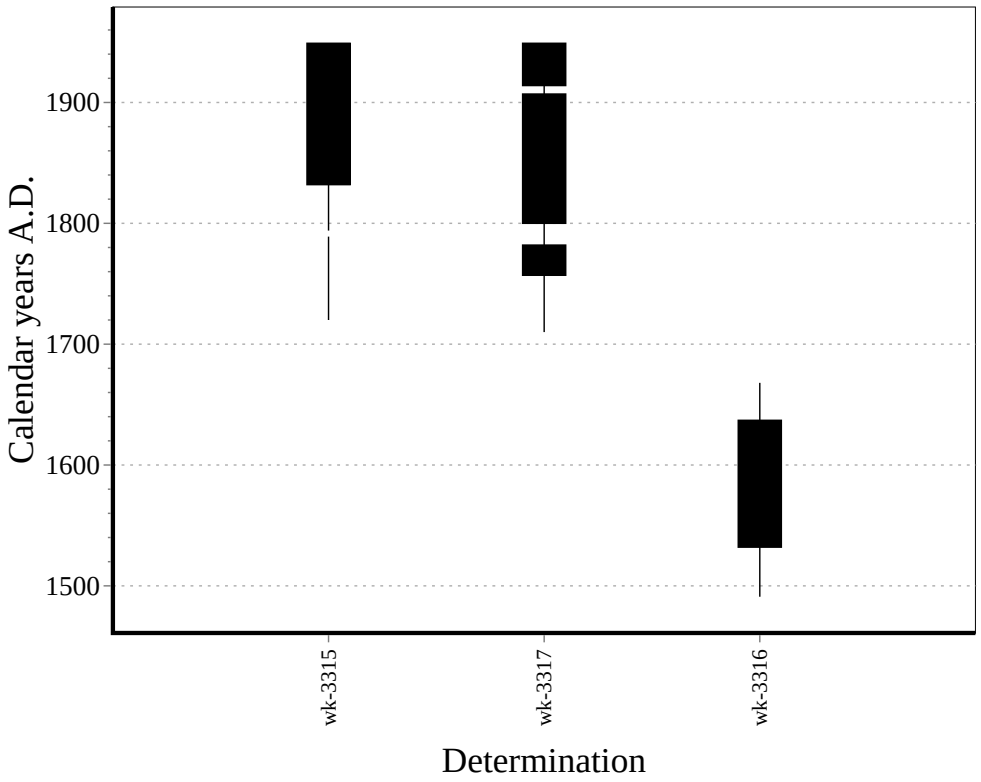

Figure 13.20: Calibrated likelihood distributions for the R11/229 CRA data

13.7.3 Discussion

In this example we have used a combined analysis of OHD and CRA chronometric data to resolve a chronological question regarding cultural activity in the past 250 years. The data supports the notion that the ac-

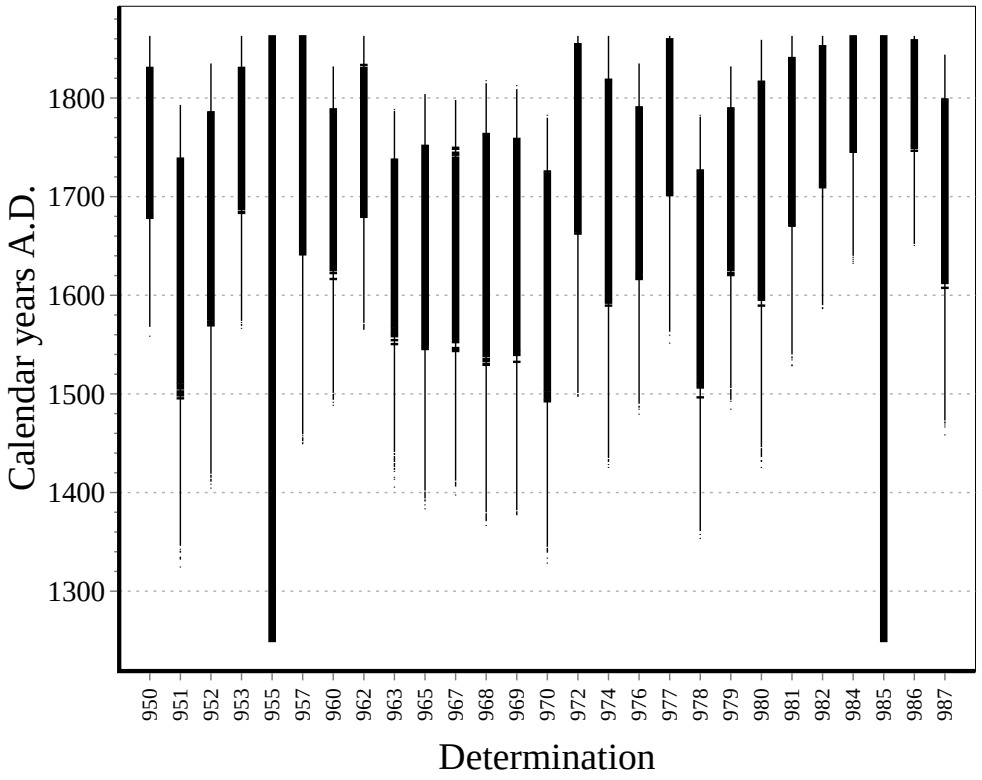

Figure 13.21: Calibrated likelihood distributions for the R11/229 OHD data

tivity represented by the R11/229 Layer 2 record pre-dates 1835. Resolution of this problem was not possible using the available CRA data, thus in this case OHD chronometric data has proved to be a useful chronology building tool. However, in spite of this, the calibrated distributions of individual OHD data are orders of magnitude less precise than the equivalent CRA. Thus calibrated OHD distributions are too imprecise to provide useful absolute dating assays in this time period. This repeats the results observed for archaeological records of greater antiquity at Tairua (*infra vide*:§13.5) and Tiritiri Matangi (*infra vide*:§13.4). In this case the conclusion is interesting as the results have been previously published by Jones *et al.* (1998) who report the OHD determinations after the standard practice of only accounting for uncertainty in the actual hydration rim measurement. The errors reported by Jones *et al.* (1998) are significantly smaller than those given here.

13.8 Summary

This chapter brings the models of obsidian hydration and approaches to measuring hydration extent discussed in the preceding 12 chapters together within a consistent interpretive framework. This realises a primary research objective as outlined in Chapter 1. The interpretive framework presented in this chapter (*infra vide*:§13.2) allows us to calibrate the measured OHD chronometric data to standard calendar years via a sound statistical method. This is directly analogous to radiocarbon calibration and is completely novel for OHD. More importantly, however, this framework defines an approach to building chronology from the OHD chronometric, both as a stand-alone method and in combination with CRA data. Again this is a novel result, and at a general level demonstrates the use of chronometric data combination within a Bayesian framework. While different observation models and measure-

ment distributions may be developed in future OHD research the interpretive framework presented in this chapter defines the template for employing the OHD chronometric as a chronology building tool.

The analysis presented in this chapter is complex and requires specialised software. A suitable software package for the calibration of OHD chronometric data based around an extension of the Date Lab package has been presented (*infra vide*:§13.3). This software represents a very real advance in OHD analysis as it makes a sound calibration approach for OHD chronometric data widely available. The use of OHD as a chronology building tool has been demonstrated through four case studies that have been used to illustrate analysis of the posteriors defined in §13.2 through the Date Lab 1.1 package, and perform a general assessment of the utility of OHD as a chronometric.

The primary conclusion drawn from these assessments is that OHD cannot provide useful absolute dating assays in a prehistoric sequence as brief as that seen in New Zealand. Examples of calibrated distributions are given in §13.4,§13.5 and §13.7. The analysed artefacts derive from throughout New Zealand's prehistoric sequence and in all cases the calibrated distributions span a substantial part of New Zealand's prehistory. This lack of precision is interesting, and suggests that many of the previously reported OHD assays are spuriously precise by many orders of magnitude. This is especially so in light of the fact that the glass hydration parameters and the EHT models employed in this analysis are more precise than many of those which should have been used in previously reported OHD assays.

While OHD cannot provide useful absolute data, OHD determinations have proven to provide useful chronological data regarding the absolute relative timing of events and in recovering cross-dated hydration parameters. Acting in this capacity the uncertainty associated with absolute EHT estimates are largely removed from the calibration process. This is

very useful result as it means that OHD as a chronometric tool does not require the use of poorly formulated and implausibly precise estimates of hydration parameters. In practice this largely limits the use of OHD to that of a supplementary dating technique. However this is not necessarily a drawback but rather an opportunity to enhance the current ability to resolve chronological issues via other dating approaches — primarily radiocarbon. The use of OHD in combination with a primary absolute technique also offers the opportunity to recover cross-dated hydration parameters. In terms of the hydration model employed in this thesis this means recovering data on the EHT and glass parameters A and E. The most generally useful outcome of cross-dating is the ability to recover palaeo-temperature data through the posterior EHT. This offers the very real possibility of building fine grained palaeo-temperature histories through fine grained Bayesian analyses of multiple chronometric data types.

Chapter 14

Discussion

As outlined in Chapter 1 there are two main goals in this thesis. At a general level this thesis presents a case study in chronology building. OHD chronometric data are used to demonstrate the development of chronology from chronometry. A second goal is to develop and assess OHD as a useful chronology building tool— specifically for archaeological research in New Zealand. Both of these goals have been met with some degree of success. While no definitive nor final solutions have been proposed some foundations have been laid that enable certain analyses to be conducted now, and will hopefully help future developments of this type of research.

In terms of presenting a general case study in building chronologies from chronometries the intention in this thesis has been to consider the fundamental models and assumptions giving rise to a chronometric data determination — OHD chronometric data in this case — and then look at how this underlying framework can be related to questions of chronology. Thus we have looked at how the raw chronometric data are measured (Chapter 2), defined an observation model for this determination (Chapter 4) and established some measures for the parameters of this model (Chapters 6,10,11 and 12). Finally, the chronometric, observation model and estimates for the model parameters have been brought together in an inferential framework that allows certain chronological questions to be addressed (Chapter 13). In particular, a fairly general framework has been specified that allows OHD to be used in many chronology building applications either as a stand alone tool, or in conjunction with radiocarbon chronometric data. In the case of OHD this is completely novel and is also largely unique as a formal definition of calibrating multiple chronometric data types. As a general outline this case study applies to chronology building for all chronometric data types. The specifics of observation model form etc. will vary, but the general issues remain the same. Thus the development of OHD as a chronology building tool presented through this thesis acts as a general

template for the consideration of any data type as a chronological tool.

In terms of developing and assessing OHD as a chronology building tool, with a specific focus on application in New Zealand the research has generated several useful outcomes:

- A method to measure hydration rim thicknesses through digital image analysis has been outlined. This is an extension of the measurement process outlined by Ambrose (1993) that allows more general measurement distributions to be calculated. A software package to implement this measurement approach has been written and is presented in Chapter 2. This is a useful contribution to the general discipline. A more sophisticated treatment of the type of analysis proposed could (and probably should) be undertaken. However, the system can generate useful hydration rim measurements and provides an outline of how a more sophisticated approach might be developed. Further, a body of source code that can serve as the basis for further experimentation and development has been produced. Unfortunately the realised measurement precision through this system is insufficient to enable fine grained chronological analysis via OHD (*infra vide*:§13.4.6). And in reality, no matter how sophisticated a development of this approach is undertaken, it is unlikely that optical measurement systems will ever be able to produce sufficiently precise measurements to enable fine grained chronological control via OHD. However, the measurements produced through the system outlined in Chapter 2 are sufficiently precise to provide useful chronological control under some circumstances (*infra vide*:§13.8).

- An observation model for the hydration of New Zealand obsidian has been outlined, and high precision estimates of glass specific hydration parameters for Mayor Island obsidian have been generated (*infra vide*:§6.6). As Mayor Island obsidian is all but ubiqui-

tous in New Zealand's archaeological sites this allows a fairly general application of OHD analysis in New Zealand. Additionally this allows the development of high precision glass specific hydration parameters via cross-dated controls. This outcome is New Zealand specific. However some of the approaches to providing control over glass specific hydration parameters — such as the development of secondary hydration parameters from a primary reference set (*infra vide*:§6.1.2,§13.4.5) — may be usefully applied elsewhere.

- An approach to providing temperature control for archaeological contexts has been outlined (Chapters 8–12). Following this, New Zealand specific EHT and Δ_{EHT} estimation models have been developed. While these are New Zealand specific, the general approach used may be applicable elsewhere. Particularly the concept of Δ_{EHT}, where the simulation software presented in Chapter 12 represents a useful experimental toolkit for Δ_{EHT} modelling in any location. As outlined here precise EHT control is very difficult, however useful Δ_{EHT} estimates are more readily modelled. This enables some useful chronological applications for OHD without requiring that uncertain and/or implausibly precise EHT estimates are adopted.

- Finally, a Bayesian calibration framework for OHD, with a software implementation, has been developed. This allows straightforward Bayesian calibration analyses of OHD chronometric data to be conducted, in a very similar manner to which radiocarbon data are routinely analysed through systems such as Calib or Oxcal. This is completely novel for OHD and is a particularly useful development, not limited to application in New Zealand.

On the basis of these development it has been possible to asses OHD as a chronology building tool, both in New Zealand specifically and more generally.

The first observation that needs to be made is that OHD is of limited use as an absolute dating tool. If OHD chronometric data are calibrated in a sound statistical fashion that takes account of all sources of uncertainty the distributions are very broad, typically spanning many centuries in the examples presented in Chapter 13. Given that these distributions derive from samples where a high degree of effort has been made to ensure suitable hydration rate parameter estimates have been used the hydration rate uncertainty will be lower than for many published OHD applications. This suggests that most of the OHD assays that have been produced to date are spuriously precise. This problem arises as uncertainty in glass hydration parameters and particularly EHT give rise to highly uncertain hydration rate estimates. However, standard practice appears to be only to take uncertainty in hydration rim measurements into account when reporting OHD results. Given the fact that uncertainty in EHT estimates in particular can give rise to significant uncertainty in hydration rates this uncertainty must be factored into the reported results. The reason that this has not been routine is probably due to the fact that previously no clear method by which this type of analysis might be undertaken had been proposed.

In spite of this, however, OHD data can provide useful chronological information. While OHD is only capable of very coarse absolute chronological control, in some circumstances it can act as a powerful method of measuring the absolute age difference of flaking events. As discussed through this thesis this comes about because where the hydration rates of two flakes are the same then — even if we do not know what these rates are — the age difference between two flaking events is proportional to the ratio of the squared rim thicknesses (*infra vide*:§8.1.1, Equation 8.8). This result is independent of EHT and glass hydration parameters thus the only uncertainty arises through the rim measurement process. This result can be extended to situations where the only variation in hydration rate is due to Δ_{EHT} with minimal increase in uncer-

tainty where EHT control is provided through cross-dating via a primary technique. Under these scenarios OHD can provide useful chronometric data.

In addition to providing direct chronometric data, we can recover the effective hydration rate for obsidian artefacts through the cross-dating of samples for which OHD assays have been made. This enables us to recover palaeo-temperature data and data on glass specific hydration parameters (*infra vide*:§6.1.2, §9.3.2, §13.8).

Thus we would conclude that:

1. OHD does not represent a viable absolute dating method in most circumstances.
2. OHD can provide useful data regarding the relative timing of events when used in conjunction with other chronometric data.
3. OHD can be used to recover data on palaeo-temperatures and glass hydration parameters through cross-dating.

OHD, therefore, does not represent a "magic bullet" for chronological research in New Zealand (nor elsewhere), but does provide a tool that can in some circumstances usefully augment other chronometric data. However, significant advances in the utility of OHD would be brought about by increasing the precision of hydration measurements. This would enable high resolution absolute relativity via OHD. In reality this is unlikely to be accomplished through optical measurement approaches. Thus the use of OHD as a high resolution chronological tool requires the development of suitably high precision measurements.

To conclude, the research presented in this thesis provides a general overview of building chronologies from chronometric data with a particular focus on the use of combined analyses of multiple chronometric data types. The specific case of combined OHD and CRA calibrations has

been considered in detail and a sound inferential framework to treat this problem has been outlined. Further, a software implementation of this inferential framework enables the routine use of OHD and CRA chronometric data in chronology building exercises. This is a significant and novel development. However, much of the research presented in this thesis is by nature preliminary, and it is hoped that this may help provide the basis for more sophisticated developments in the future.

Bibliography

Aertsens, M. (1997). Modelling glass dissolution in clay with analytic and stochastic methods. In W. J. Gray and I. A. Triay (Eds.), *Scientific Basis for Nuclear Waste Management XX*, pp. 197–204. MRS Symposium Proceedings 465, Materials Research Society, Pittsburgh.

Ambrose, W. R. (1976). Intrinsic Hydration Rate Dating of Obsidian. In R.E.Taylor (Ed.), *Advances in Obsidian Glass Studies*, pp. 81–105. Noyes Press, New Jersey.

Ambrose, W. R. (1980). Monitoring Long-Term Temperature and Humidity. *Institute for the Conservation of Cultural Material Bulletin*, 6(1):36–42.

Ambrose, W. R. (1984). Soil Temperature Monitoring at Lake Mungo; Implications for Racemisation Dating. *Australian Archaeology*, 19:64–74.

Ambrose, W. R. (1993). Obsidian Hydration Dating. In B.L.Frankhauser and J.R.Bird (Eds.), *Archaeometry: Current Australasian Research*, pp. 79–84. Australian National University, Canberra, Australia.

Ambrose, W. R. (1994). Obsidian Hydration Dating of a Pleistocene Age Site from the Manus Islands, Papua New Guinea. *Quaternary Geochronology (Quaternary Science Reviews)*, 13:137–142.

Ambrose, W. R. (2001). Obsidian Hydration Dating. In D. R. Brothwell and

A. M. Pollard (Eds.), *Handbook of Archaeological Sciences*, pp. 81–92. John Wiley & Sons, Ltd.

Anderson, A. (1979). Excavations at the Hawksburn Moa-Hunting Site: An Interim Report. *NZAANL*, 22:48–59.

Anderson, A. (1981). Radiocarbon Dates for Archaic Sites at Purakanui and Hawksburn, Otago. *NZAANL*, 24:63–64.

Anderson, A. (1982). A Review of Economic Patterns During the Archaic Phase in Southern New Zealand. *NZJA*, 4:45–75.

Anderson, A. (1991). The Chronology of Colonisation in New Zealand. *Antiquity*, 65:767–795.

Anderson, A. and McFadgen, B. (1990). Prehistoric Two-Way Voyaging Between New Zealand and East Polynesia: Mayor Island Obsidian on Raoul Island and Possible Raoul Island Obsidian in New Zealand. *Archaeology in Oceania*, 25:37–42.

Anderson, A., Smith, I., and Higham, T. (1996). Radiocarbon Chronology. In A. Anderson, B. Allingham, and I. Smith (Eds.), *Shag River Mouth, the Archaeology of an Early Southern Maori Village*, pp. 60–69. ANH Publications, Research School of Pacific and Asian Studies, The Australian National University.

Anovitz, L., Elam, J., Riciputi, L., and Cole, T. (1999). The Failure of Obsidian Hydration Dating: Sources, Implications, and New Directions. *Journal of Archaeological Science*.

Armitage, G., Reeves, R., and Bellwood, P. (1972). Source Identification of Archaeological Obsidians in New Zealand. *New Zealand Journal of Science*, 15:408–420.

Ayra, S. (1988). *Introduction to Micrometeorology*. Academic Press, London.

Bates, J. K., Abrajano, T. A., Ebert, W. L., Mazer, J. J., and Gerding., T. J. (1988). Experimental Hydration Studies OfNatural and Synthetic Glasses. *Materials Research Society Symposium Proceedings*, 123:237–244.

Bell, J. and Clark, E. (1909). The Geology of the Whangaroa Subdivision, Hokianga Division. Technical Report 8, New Zealand Geological Survey Bulletin.

Bird, J., Duerden, P., Ambrose, W., and Leach, B. (1981). Pacific Obsidian Catalogue. In B. Leach and J. Davidson (Eds.), *Archaeological Studies of Pacific Stone Resources*, volume 104, pp. 31–43. B.A.R. International Series104.

Black, T., Tanner, C., and Gardener, W. (1970). Evapotranspiration from a Snap Bean Crop. *Agron. Journal*, 62:66–69.

Bollong, C. (1983). *Automted Isoprobe Analysis of New Zealand and Oceanic Volcanic Glass*. Master's thesis, Department of Anthropology, University of Otago.

Brassey, R. (1985). *An Analysis Of some Lithic Artefact Assemblages from Pouerua, Northland*. Master's thesis, University of Auckland.

Brassey, R. and Seelenfreund, A. (1984). Sources of Obsidian Artefacts from Pourerua, Bay of Islands. *New Zealand Archaeological Association Newsletter*, 27:39–42.

Bristow, K. and Campbell, G. (1985). An Equation for Separating Daily Solar Irradiation Into Direct and Diffuse Components. *Agricultural and Forest Meteorology*, 35:123–131.

Brothers, R. (1957). The Volcanic Domes at Mayor Island, New Zealand. *Transactions of the Royal Society of New Zealand*, 84:549–560.

Brun, L., Kanemasu, E., and Powers, W. (1973). Estimating Transpiration Resistance. *Agron. Journal*, 65:326–328.

Brunt, D. (1934). *Physical and Dynamical Meteorology*. Cambridge University Press, London.

Buck, C., Cavanagh, W., and C.D.Litton (1996). *Bayesian Approach to Interpreting Archaeological Data*. Wiley, Chichester.

Buck, C., Kenworthy, J., C.D.Litton, and Smith, A. (1991). Combining archaeological and radiocarbon information: a Bayesian approach to calibration. *Antiquity*, 65:808–821.

Buck, C., Litton, C., and Smith, A. (1992). Calibration of Radiocarbon Results Pertaining to Related Archaeological Events. *Journal of Archaeological Science*, 19:497–512.

Buck, C. E., Christen, J. A., Kenworthy, J. B., and Litton, C. D. (1994). Estimating the Duration of Archaeological Activity Using 14C Determinations. *Oxford Journal of Archaeology*, 13:229–240.

Buck, M. (1985). An Assessnment of Volcanic Risk on and from Mayor Island, New Zealand. *New Zealand Journal of Geology and Geophysics*, 28:283–298.

Buck, M., Briggs, R., and Nelson, C. (1981*a*). Pyroclastic Deposits and Volcanic History of Mayor Island. *New Zealand Journal of Geology and Geophysics*, 24:449–467.

Buck, M., Briggs, R., and Nelson, C. S. (1981*b*). Pyroclastic Deposits and Volcanic History of Mayor Island. *New Zealand Journal of Geology and Geophysics*, 24:449–467.

Calder, I. (1977). A Model of Transpiration and Interception Loss from Spruce Forest in Plynlimon, Central Wales. *Journal of Hydrology*, 33:33–47.

Callander, B. and Woodhead, T. (1981). Canopy Resistance of Estate Tea in Kenya. *Agricultural meteorology*, 23:151–167.

Campbell, G. (1977). *An Introduction Into Environmental Biophysics*. Springer-Verlag, New York.

Campbell, G. (1985). *Soil Physics with Basic: Transport Models for Soil-Plant Systems*. Elsevier, Oxford.

Challis, G. (1978*a*). Paleocene-Eocene. In R. Suggate (Ed.), *The Geology of New Zealand*, chapter The Late Mobile Phase: Igneous Activity, pp. 632–636. E. C. Keating Government Printer, Wellington, New Zealand.

Challis, G. (1978*b*). Upper Quaternary. In R. Suggate (Ed.), *The Geology of New Zealand*, chapter The Late Mobile Phase: Igneous Activity, pp. 651–663. E. C. Keating Government Printer, Wellington, New Zealand.

Charles, R. (1958). Static Fatigue of Glass I. *Journal of Applied Physics*, 29:1549–1553.

Chatfield, C. (1996). *The analysis of time series : an introduction*. Chapman & Hall, London, 5th edition.

Christen, J. (1994*a*). *Bayesian Interpretation of Radiocarbon Results*. Ph.D. thesis, University of Nottingham.

Christen, J. (1994*b*). Summarizing a Set of Radiocarbon Determinations: a Robust Approach. *Applied Statistics*, 43:489–503.

Christen, J. A. and Buck, C. E. (1998). Sample Selection in Radiocarbon Dating. *Applied Statistics*, 47:543–557.

Christen, J. A., Clymo, R. S., and Litton, C. D. (1995). A Bayesian Approach to the Use of 14C Dates in the Estimation of the Age of Peat. *Radiocarbon*, 37:431–442.

Christen, J. A. and Litton, C. D. (1995). A Bayesian Approach to Wiggle-Matching. *Journal of Archaeological Science*, 22:719–725.

Chudnovskii, A. (1962). *Heat Transfer in the Soil*. Israel Program for Scientific Translations, Jerusalem. Translated from Russian.

Clark, D. (1984). Effects of Flow on Corrosion and Surface Film Formation on an Alkali Borosilicate Glass.

Clark, J. T., Sheppard, P., and Jones, M. (1998). Late Ceramics in Samoa: A Test Using Hydration Rim Measurements. *Current Anthropology*, 38(5):898–904.

Coote, G. and Nistor, P. (1982). Depth Profiles of Sodium in Obsidian by the Resonant Nuclear Reaction Method: A Potential Dating Technique. In W. Ambrose and P. Duerden (Eds.), *Archaeometry: An Australasian Perspective*, pp. 243–250. Australian National University, Canberra, Australia.

Crank, J. (1975). *The Mathematics of Diffusion*. Oxford University Press, London, second edition.

Davidoff, B., Lewis, J., and Selim, H. (1986). Variability of Soil temperature with depth along a transect. *Soil Science*, 142:114–124.

Davidson, J. (1981). The Prehistoric Exploitation of Stone Resources in Northern New Zealand. In B. Leach and J. Davidson (Eds.), *Archaeological Studies of Pacific Stone Resources*, pp. 107–119. B.A.R. International Series 104.

de Vries, D. (1963). Thermal Properties of Soils. In W. Van Wijlk (Ed.), *Physics of the Plant Environment*, pp. 210–235. North-Holland Publishing Company, Amsterdam.

Doremus, R. H. (1994). *Glass Science*. Wiley, New York.

Doremus, R. H. (1995). Diffusion of water in silica glass. *Journal of Materials Research*, 10:2379–2389.

Duerden, P., Clayton, E., Bird, J., Ambrose, W., and Leach, B. (1987). Obsidian Composition Catalogue. In W. Ambrose and J. Mummery (Eds.), *Archaeometry: Further Australasian Studies*. Australian National University, Canberra, Australia.

Duerden, P., Cohen, D., and Ambrose., W. (1982). The Measurement of Hydration Profiles in Obsidian. In W. Ambrose and P. Duerden (Eds.), *Archaeometry: An Australasian Perspective*, pp. 236–242. Australian National University, Canberra, Australia.

Dyer, B., A.J.and Hicks (1970). Flux-Gradient Relationships in the Constant Flux Layer. *Quarterly Journal of the Royal Meteorological Society*, 96:715–721.

Ericson, J. (1989). Toward Flow-Specific Obsidian Hydration Rates: Coso Volcanic Field, Inyo County, California. In R. Hughes (Ed.), *Current Directions in California Obsidian Studies*, pp. 13–22. Contributions of California Archaeological Research Facility No. 48, Berkeley, California.

Ericson, J., Mackenzie, J., and Berger, R. (1976). Physics and Chemistry of the Hydration Process in Obsidians I: Theoretical Implications. In R. Taylor (Ed.), *Advances in Obsidian Glass Studies*, pp. 25–45. Noyes Press, Park Ridge,New Jersey.

Ericson, J., Makishima, A., Mackenzie, J., and Berger, R. (1975). Chemical and Physical Properties of Obsidian: A Naturally Occurring Glass. *Journal of Non-Crystalline Solids*, 17:129–142.

Ericson, J. E. (1988). Obsidian Hydration Rate Development. *Materials Research Society Symposium Proceedings*, 123:215–224.

Ewart, A., Taylor, S. R., and Capp, A. C. (1968). Geochemistry of the Pantellerites of Mayor Island, New Zealand. *Contr. Mineralogy and Petrology*, 17:116–140.

Ferrar, H. (1925). The Geology of the Whangerei-Bay of Islands Subdivision, Kaipara Division. Technical Report 27, New Zealand Geological Survey Bulletin.

Findlow, F. J. and DeAtley, S. (1976). Photographic Measurement in Obsidian Hydration Dating. In R. Taylor (Ed.), *Advances in Obsidian Glass Studies*, pp. 165–172. Noyes Press, Park Ridge, New Jersey.

Foster, R. and Sewell, B. (1996). *Papāhīnu. The archaeology of an early 19th century maori settlement on the bank of the Pukaki Creek, Manukau City*. Auckland Conservancy Historic Resource Series No. 12, Department of Conservation.

Fowles, G. (1968). *Introduction to Modern Optics*. Holt, Rinehart and Winston, INC., New York.

Fox, A. (1982). Obsidian from Excavations in Auckland and Hawkes Bay. *New Zealand Archaeological Association Newsletter*, 25(3):208–9.

Fraser, C. and Adams, J. (1907). The Geology of the Coromandel Subdivision, Hauraki, Auckland. Technical Report 4, Bulletin of the New Zealand Geological Survey.

Fredricksen, C. (1991). Description of a Lithic Assemblage from Motukorea (Browns Island). *New Zealand Archaeological Association Newsletter*, 34(2):91–104.

Friedman, I. (1976). Calculation of Obsidian Hydration Rates from Temperature Measurements. In R. Taylor (Ed.), *Advances in Obsidian Glass Studies*, pp. 173–181. Noyes Press, New Jersey.

Friedman, I. and Evans, C. (1968). Obsidian Dating Revisited. *Science*, 162:813–814.

Friedman, I. and Long, W. (1976). Hydration Rate of Obsidian. *Science*, 159:347–352.

Friedman, I. and Obradovich, J. (1981). Obsidian Hydration Dating of Volcanic Events. *Quaternary Research*, 16:37–47.

Friedman, I. and Smith, R. (1960). A New Dating Method Using Obsidian: Part I, the Development of the Method. *American Antiquity*, 25:476–493.

Friedman, I., Trembour, F., and Smith, F. (1994). Is obsidian hydration dating affected by relative humidity. *Quaternary Research*, 41:185–190.

Gillham, R., Klute, A., and Heermann, D. (1979). Measurement and Numerical Simulation of Hysteric Flow in a Heteregeneous Porous Medium. *Soil Science Society of America Jounal*, 43:1061–1067.

Gold-Smith, E. (1884). Description of Mayor Island. Read before the Auckland Institute, 11th August, 1884.

Green, R. (1962). Obsidian: Its Application to New Zealand Archaeology. *New Zealand Archaeology Association Newsletter*, 5:8–16.

Green, R. (1964). Sources, Ages and Exploitation of New Zealand Obsidian: An Interim Report. *New Zealand Archaeological Association Newsletter.*, 7(3):134–143.

Green, R. (1967). Sources of New Zealand's East Polynesian Culture: The Evidence of a Pearl Shell Lure Shank. *Archaeology and Physical Anthropology in Oceania*, 2:81–90.

Green, R., Brooks, R., and Reeves, R. (1967). Characterization of New Zealand Obsidians by Emission Spectroscopy. *New Zealand Journal of Science*, 10:975–82.

Häder, D.-P. (Ed.) (1992). *Image analysis in biology*. CRC Press, Boca Raton, Fla.

Haller, W. (1963). Concentration-Dependent Diffusion Coefficient of Water in Glass. *Physics and Chemistry of Glasses*, 4(6):217–220.

Hamel, G. (1978). Hawksburn Revisited: An Ecological Assesment. *New Zealand Archaeological Association News Letter*, 21(4):116–128.

Hanks, R. and Ashcroft, G. (1980). *Applied Soil Physics*. Springer-Verlag, Berlin, New York.

Harsant, W. (1985). The Hahei (N44/97) Assemblage of Archaic Artefacts. *New Zealand Journal of Archaeology*, 7:5–37.

Healy, J. (1962). Structure and Volcanism in the Taupo Volcanic Zone, New Zealand. *American Geophysical Union Monographs*, 6:151–7.

Heitor, A., Biga, A., and Rosa, R. (1991). Thermal Radiation Components of the Energy Balance at the Ground. *Agricultural and Forest Meteorology*, 54:29–48.

Henderson, J. and Bartrum, J. (1913). The Geology of the Aroha Subdivision, Hauraki, Auckland. Technical Report 16, New Zealand Geological Survey Bulletin.

Hickey, J., Alton, B., Griffen, F., Jacobowitz, H., Pelegrino, P., Maschhoff, R., Smith, E., and von der Harr, T. (1982). Extraterrestrial solar irradiance variability. Two and one-half years of measurements from Numbus 7.

Higham, T., Anderson, A., and Jacomb, C. (1999). Dating the first New Zealanders: the chronology of Wairau Bar. *Antiquity*, 73:420–27.

Higham, T. and Hogg, A. (1995). Radiocarbon Dating of Prehistoric Shell from New Zealand and Calculation of the ΔR Value Using Fish Otoliths. *Radiocarbon*, 37(2):409–416.

Hillel, D. (1980). *Applications of Soil Physics*. Academic Press, New York.

Holroyd, S. (1993). *Obsidian Sources of the North Island: Location and Identifying Characteristics*. Research essay, on file Department of Anthropology, Unversity of Auckland.

Houghton, B., Weaver, S., Wilson, C., and Lanphere, M. (1992). Evolution of a Quaternary Peralkaline Volcano: Mayor Island, New Zealand. *Journal of Volcanology and Geothermal Research*, 51:217–236.

Inoué, S. (1986). *Video Microscopy*. Plenum Press, New York.

Jantzen, C. (1988). Prediction of Glass Durability as a Function of Environmental Conditions. *Materials Research Society Symposium Proceedings*, 125:143–159.

Jones, M. and Nicholls, G. (2002). *Date Lab 1.0*. Centre for Archaeological Research, http:
www.car.auckland.ac.nz.

Jones, M., Sheppard, P., and Sutton, D. (1997*a*). Sample Collecting & Submission for Obsidian Hydration Dating. *Archaeology in New Zealand*, 40(2):136–142.

Jones, M., Sheppard, P., and Sutton, D. (1997*b*). Soil Temperature and Obsidian Hydration Dating: A Clarification of Variables Affecting Accuracy. *Journal of Archaeological Science*, 24(6):505–516.

Jones, M., Sheppard, P., and Sutton, D. (1998). Recent Developments in Obsidian Hydration Dating. *Records of the Australian Museum*, 50:235–240.

Jones, M., Sutton, D., Jones, G., and McLeod, C. (1995). Measuring Soil Temperatures for Obsidian Hydration Dating in Northern New Zealand. *AINZ*, 38:9–16.

Jones, M. D. (2001). Lies, Damn Lies and Statistics. In M. Jones and P. Sheppard (Eds.), *Australasian Connections and New Directions: Proceedings of the 7^{th} Australasian Archaeometry Conference*, pp. 171–180. Research in Anthropology & Linguistics, Department of Anthropology, The University of Auckland.

Jones, M. D. and Nicholls, G. K. (2001). Reservoir offset models for radiocarbon dating. *Radiocarbon*, 43:119–124.

Jones, M. D. and Nicholls, G. K. (submitted). New Radiocarbon Calibration Software. *Radiocarbon*.

Kasten, F. (1965). A New Table and Approximation Formula for the Relative Optical Air Mass. *Arch. Met. Geoph. Bibl., B*, 14:206–223.

Kasten, F. (1980). A Simple Parametrisation of the Pyrheliometric Formula for Determining the Linke Turbidity Factor. *Meteorologische Rundshau*, 33:124–127.

Katsui, Y. and Kondo, Y. (1976). Variation in obsidian hydration rates for Hokkaido, northern Japan. In R. E. Taylor (Ed.), *Advances in Obsidian Glass Studies: Archaeological and Geochemical Perspectives*, pp. 120–140. Noyes Press, New Jersey.

Kear, D. (1960). Sheet 4 - Hamilton (1st Ed). In *Geological Map of New Zeland, 1:250,000*. DSIR.

Kear, D. and Thompson, B. N. (1964). Volcanic Risk in Northland. *New Zealand Journal of Geology and Geophysics*, 7:97–93.

Kimberlin, J. (1976). Obsidian Hydration Rate Determination on Chemically Characterized Samples. In R. Taylor (Ed.), *Advances in Obsidian Glass Studies*, pp. 63–80. Noyes Press, Park Ridge, New Jersey.

Klein, M. (1970). *Optics*. Wiley, New York.

Klucher, T. (1978). Evaluation of Models to Predict Insolation on Tilted Surfaces. N.A.S.A TM-78842.

Kondo, Y. and Matsui, S. (1992). Application of Obsidian Hydration Dating with the Hitachi Model U-6000 Microscopic Fourier-Transformed Spectrophotometer-Dating of Stone Implements by Using a New Non Destructive Analysis. *Hitachi Scientific Instrument News*, 35.

Lanford, W. (1978). 15N Hydrogen Profiling: Scientific Applications. *Nuclear Instruments and Methods*, 149(1-2):1–8.

Laursen, T. and Lanford., W. (1978). Hydration of Obsidian. *Nature*, 276(5684):153–156.

Leach, B. (1973). Obsidian in the Chatham Islands. *New Zealand Archaeological Association Newsletter*, 16(3):104–6.

Leach, B. (1977). A Rapid Method of Sourcing New Zealand Lithic Material Using a Low Power XRF Analyser. *Oceanic Prehistory Records*, 3.

Leach, B. (1983). A Transportable Instrument for Dating Obsidian by Argon Induced Luminescence Analysis (Abstract). *Pacific Science Congress Abstracts*, p. 142.

Leach, B. (1996). New Zealand and Oceanic Obsidians: An Archaeological Perspective Using Neutron Activation Analysis. *Journal of The Royal Society of New Zealand*, 26(1):79–105.

Leach, B., Anderson, A., Sutton, D., Bird, R., Duerden, P., and Clayton, E. (1986*a*). The Origin of Prehistoric Obsidian Artefacts from the Chatam

and Kermadec Islands. *New Zealand Journal of Archaeology*, 8:143–170.

Leach, B., Anderson, A., Sutton, D., Bird, R., Duerdon, P., and Clayton, E. (1986*b*). The Origin of Prehistoric Obsidian Artefacts from the Chatham and Kermadec Islands. *New Zealand Journal of Archaeology*, 8:143–170.

Leach, B. and de Souza, P. (1979). The Changing Proportions of Mayor Island Obsidian in New Zealand Prehistory. *New Zealand Journal of Archaeology.*, 1:29–51.

Leach, B. and Hamel, J. (1984). The Influence of Archaeological Soil Temperatures on Obsidian Dating in New Zealand. *New Zealand Journal of Science*, 27:399–408.

Leach, B. and Manly, B. (1982). Minimum Mahalanobis Distance Functions and Lithic Source Characterisation by Multi-Element Analysis. *New Zealand Journal of Archaeology*, 4:77–109.

Leach, B. and Warren, S. (1981). Neutron Activation Analysis of New Zealand and Pacific Obsidians: Towards a Simple Screening Technique. In B. Leach and J. Davidson (Eds.), *Archaeological Studies of Pacific Stone Resources*, pp. 151–66. B.A.R International Series 104.

Leach, B., Warren, S., and Fankhauser, B. (1978*a*). Obsidian from the Far North of New Zealand: A Method of Sourcing Based on Natural Radioactive Emission. *New Zealand Journal of Science*, 21:123–128.

Leach, B., Warren, S., and Fankhouser, B. (1978*b*). Obsidian from the Far North of New Zealand: A Method of Sourcing Based on Natural Radioactive Emission. *New Zealand Journal of Science*, 21:123–8.

Leach, B. F. and Naylor, H. (1981). Dating New Zealand Obsidians by Nuclear Resonant Reactions. *New Zealand Journal of Archaeology*, 3:33–39.

Lee, R. (1969). Chemical temperature integration. *Journal of Applied Meteorology*, 8:423–430.

Lee, R., Leich, D., Tombrello, T., Ericson, J., and Friedman., I. (1974). Obsidian Hydration Profile Measurements Using a Nuclear Reaction Technique. *Nature*, 250(5461):44–47.

Liggett, K. and Gregg, D. (1965). Geology of Banks Peninsula. In *New Zealand Volcanology. South Island*, pp. 9–23. New Zealand Department of Scientific and Industrial Research Information Series 51.

Liou, K. (1980). *An Introduction to Atmospheric Radiation*. Academic Press, New York.

Liou, K. (1992). *Radiation and Cloud Processes in the Atmosphere: Theory, Observations and Modelling*. Oxford University Press, New York.

Lipson, S., Lipson, H., and Tannhauser, D. (1995). *Optical Physics*. Cambridge University Press., 3rd edition.

Litton, C. and Buck, C. (1996). *Markov Chain Monte Carlo in Practice*, chapter 25, pp. 466–486. Chapman and Hall.

Litton, C. D. and Leese, M. N. (1991). Some Statistical Problems Arising in Radiocarbon Calibration. In K. Lockyear and S. P. Q. Rahtz (Eds.), *Computer Applications and Quantitative Methods in Archaeology 1990*, pp. 101–109. Tempus Reparatum, Oxford.

Lockerbie, L. (1955). Otago Museum Expedition to Hawksburn, Central Otago. *JPS*, 64:351–352.

Lockerbie, L. (1959). From Moa-Hunter to Classic Maori in Southern New Zealand. In J. Freeman and W. Geddes (Eds.), *Anthropology in the South Seas*, pp. 75–110. Thomas Avery and Sons ltd, New Plymouth.

Lokken, R. and Strachan, D. (1984). Long-Term Leaching of Two Simulated Waste Glasses. *Advances in Ceramics*, 8:39–48.

Lowe, J. (1977). *A New Method of Obsidian Hydration Shell Measurement*. Master's thesis, University of Waikato.

Mahrer, Y. and Avissar, R. (1985). A Numerical Study of the Effects of Soil Surface Shape Upon the Soil Temperature and Moisture Regimes. *Soil Science*, 139:6.

Martin, M. and Berdahl, P. (1984). Characteristics of infrared sky radiation in the United States. *Solar Energy*, 33:321–336.

Mazer, J., Stevenson, W., Ebert, W., and Bates, J. (1991). The Experimental Hydration of Obsidian as a Function of Relative Humidity and Temperature. *American Antiquity*, 56:504–513.

Mazer, J. J., Bates, J. K., Stevenson, C. M., and Bradley, C. R. (1992). Obsidians and tektites: natural analogues for water diffusion in nuclear waste glasses. In A. Anderson, B. Allingham, and I. Smith (Eds.), *Scientific Basis for Nuclear Waste Management*, pp. 513–520. Material Research Society Proceedings 257, Materials Research Society, Pittsburgh.

McCormac, F., Hogg, A., Higham, T., Baillie, M., Palmer, J., Xiong, L., Pilcher, J., Brown, D., and Hoper, S. (1998). Variations of Radiocarbon in Tree-Rings: Southern Hemisphere Offset Preliminary Results. *Radiocarbon*, 40(3):1153.

McGrail, B., Pederson, L., Strachan, D., Ewing, R., and Cordell, L. (1988). Obsidian Hydration Dating-Field, Laboratory, and Modelling Results. *Materials Research Society Symposium Proceedings*, 123:263–269.

McPherson, D., Pye, L., Fréchette, V., and Tong, S. (1984). Microstructure of Natural Glasses. *Journal of Non-Crystalline Solids*, 67:61–79.

Meighan, C. (1988). Progress in obsidian dating studies. In C. Meighan and J. Scalise (Eds.), *Obsidian Dates IV*, pp. 3–9. Monograph 29, Institute of Archaeology, University of California, Los Angeles.

Meighan, C. and Scalise, J. (Eds.) (1988). Monograph 29, Institute of Archaeology, University of California, Los Angeles.

Meighan, C. W. (1983). Obsidian Dating in California. *American Antiquity*, 48:600–609.

Meighan, C. W., Foote, L. J., and Aiello, P. V. (1968). Obsidian Dating Revisited. *Science*, 162:813–814.

Michels, J., Tsong, I., and Smith, G. (1983). Experimentally Derived Hydration Rates in Obsidian Dating. *Archaeometry*, 25:107–117.

Michels, J. W. (1971). The colonial obsidian industry of the Valley of Mexico. In R. H. Brill (Ed.), *Science and Archaeology*, pp. 251–271. MIT Press, Cambridge, Massachusets.

Moeller, T., Bailar, J., Kleinberg, J., Guss, C., Castellion, M., and Metz, C. (1984). *Chemistry with Inorganic Qualitative Analysis*. Academic Press, Orlando, London, Toronto, 2nd edition.

Monteith, J. (1963). Gas Exchange in Plant Communities. In L. Evans (Ed.), *Evironmental Control of Plant Growth*, pp. 95–112. Academic Press, New York.

Monteith, J. (1975). *Principles of Environmental Physics*. Edward Arnold, London, first edition.

Monteith, J. and Unsworth, M. (1990). *Principles of Environmental Physics*. Edward Arnold, London.

Montenbruck, O. and Pfleger, T. (1991). *Astronomy on the Personal Computer*. Springer-Verlag, Berlin.

Mood, M., Graybill, F., and Boes, D. (1974). *Introduction to the Theory of Statistics*. McGraw-Hill, London.

Moore, P. (1982). Obsidian Deposits at Huruiki Northland. *New Zealand Archaeology Association Newsletter*, 25.

Moore, P. (1983). Geology and Geochemistry of Obsidian Deposits in the Cooks Beach Hahei Area, Coromandel Peninsula: A Contribution to Archaeological Sourcing Studies. *New Zealand Journal of Science*, 26:523–33.

Moore, P. (1985). Archaeological Sites and Obsidian Depositson the Mokohinau Islands, Hauraki Gulf. *Tane*, 31:75–84.

Moore, P. (1985-6). Archaeological Sites and Obsidian Deposits on the Mokohinau Islands, Hauraki Gulf. *Tane*, 31:75–54.

Moore, P. (1988). Physical Characteristics of New Zealand Obsidians and their Use in Archaeological Sourcing Studies. Unpublished Manuscript. New Zealand Geological Survey, Lower Hutt.

Moore, P. (n.d.). Physical Characteristicsof New Zealand Obsidians and their Use in Archaeological Sourcing Studies. unpublished manuscript.

Moore, P. and Coster, J. (1984*a*). Obsidian Deposits in the Woody Hill Area, Near Tairua, Coromandel Peninsular. *New Zealand Archaeological Association Newsletter*, 27:144–55.

Moore, P. and Coster, J. (1984*b*). Obsidian Deposits in the Woody Hill Area, Near Tairua, Coromandel Peninsula. *New Zealand Archaeological Association Newsletter.*, 27(3):144–155.

Moore, P. and Coster, J. (1989*a*). Waihi Obsidian. *New Zeland Archaeology Association Newsletter*, 32:26–30.

Moore, P. and Coster, J. (1989*b*). Waihi Obsidian. *New Zealand Archaeological Association Newsletter*, 32(1):26–30.

Morgan, P. G. (1927). *Minerals and Mineral Substances of New Zealand*. New Zealand Geological Survey Bulletin 32.

Mualem, Y. and Miller, E. (1979). A Hysteresis Model Based on an Explicit Domain Dependence Function. *Soil science society of America Journal*, 43:1067–1073.

Naylor, J. C. and Smith, A. F. M. (1988). An Archaeological Inference Problem. *Journal of the American Statistical Association*, 83:588–595.

Nesse, W. D. (1991). *Introduction To Optical Mineralogy*. Oxford University Press, Oxford, second edition.

Neve, S. and Barker, P. (1997). Hydration Depth Profiling of obsidian surfaces usinf ^{7}Li ions. In *Proceedings of the fourteenth International Conference on the Application of Accelerators in Research and Industry*. AIP, Vol. CP391, Denton, Texas, U.S.A.

Neve, S., Barker, P., Holroyd, S., and Sheppard, P. (1994). Obsidian Sourcing by PIXE Analysis at AURA2. *New Zealand Journal of Archaeology*, 16:93–121.

Newman, S., Stopler, E., and Epstein, S. (1986). Measurement of Water in Rhyolitic Glasses: Calibration of an Infrared Spectroscopic Technique. *American Mineralogist*, 71:1527–1541.

Nicholls, G. and Jones, M. (1998). Radiocarbon dating with temporal order constraints. Technical report, Mathematics Department, Auckland University, New Zealand. No. 407 `http://www.math.auckland.ac.nz/~nicholls`.

Nicholls, G. K. and Jones, M. D. (2001). Radiocarbon Dating with Temporal Order Constraints. *International Journal of Applied Statistics*.

Norman, J. (1982). Simulation of Microclimate. In J. Hatfield and I. Thomason (Eds.), *Biometeorlogy in Integrated Pest Management*, pp. 62–99. Academic press, New York.

Oke, T. (1987). *Boundary Layer Climates*. Methuen, London.

Okuno, M., Iwatsuki, H., and Matsumoto, T. (1996). Structural Analysis of an Obsidian by X-Ray Diffraction Method. *European Journal of Mineralogy*, 8:1257–1264.

Paul, A. (1990). *Chemistry of glasses*. Chapman and Hall, London.

Penman, H. (1948). Natural Evaporation from Open Water, Bare Soil and Grass. *Proceedings of the Royal society of London A*, 194:120–145.

Persaud, N. and Chang, C. (1984). Analysis of the Stochastic Component in Observed Soil Profile Temperature. *Soil Science*, 138:326–334.

Pluta, M. (1988). *Advanced Light Microscopy*, volume 1,2,3. Elsevier, Amsterdam.

Porai-Koshits, E. (1990). Genesis of Concepts on Structure of Inorganic Glasses. *Journal of Non-Crystalline Solids*, 123:1–13.

Pos, H. (1961). Tuhua or Mayor Island: Its Importance to Maori History. *New Zealand Archaeological Association Newsletter*, 4(2):46–48.

Pos, H. (1965). Site Survey of Tahua or Mayor Island. *New Zealand Archaeological Association Newsletter*, 8(3):104–9.

Press, W., Flannery, B., Teukolsky, S., and Vetterling, W. (1992). *Numerical Recipes in Pascal: The Art of Scientific Computing*. Cambridge University Press, Cambridge.

Pruitt, W., Morgan, D., and Lourence, F. (1973). Momentum and Mass Transfer in the Surface Boundary Layer. *Quarterly Journal of the Royal Meteorological Society*, 99:370–386.

Reeves, R. and Armitage, G. (1973*a*). Density Measurements and Chemical Analysis in the Identification of New Zealand Archaeological Obsidians. *New Zealand Journal of Science*, 16:561–572.

Reeves, R. and Armitage, G. (1973*b*). Density Measurements and Chemical Analysis in the Identification of New Zealand Archaeological Obsidians. *New Zealand Journal of Science*, 16:561–572.

Renfrew, C. (1973). *Before Civilization*. Penguin Books Ltd., Harmondsworth, England.

Richter, J. (1987). *The Soil as a Reactor*. Catena, Cremlingen, Germany.

Richter, J. (Ed.) (1990). *Models for Processes in the Soil*. Catena Verlag, Cremlingen, Germany.

Ridings, R. (1991). Obsidian Hydration Dating: The Effects of Mean Exponential Ground Temperature and Depth of Artifact Recovery. *Journal of Field Archaeology*, 18:77–85.

Ridings, R. (1996). Where in the world does obsidian hydration dating work? *American Antiquity*, 61:136–148.

Rosenberg, N., Blad, B., and Verma, S. (1983). *Microclimate the Biological Environment*. Wiley and Sons, New York, second edition.

Rowland, M. (1976). *Cellana denticulata* in Middens on the Coromandel Coast, N.Z., - Possibilities for a Temporal Horizon. *JPS*, 6:1–15.

Ruddock, R. (1988). Source Determination of Obsidian from the Westfield (R11/898) Site Using Geochemical Analysis. *Records of the Auckland Institute and Museum*, 25:49–56.

Russell, G. (1980). Crop Evaporation, Surface Resistance and Soil Water Status. *Agricultural meteorology*, 21:213–226.

Ryan, M. and Brown, I. (1985). Electrical Conduction in New Zealand Obsidian. *Journal of Non-Crystalline Solids*, 70(1):157–175.

Scheetz, B. and Stevenson, C. (1988). The Role of Resolution and Sample Preparation in Hydration Rim Measurement: Implications for Experimentally Determined Hydration Rates. *American Antiquity*, 53(1):110–117.

Schiffman, H. (1990). *Sensation and Perception: An Integrated Approach*. Wiley, New York, 3rd edition.

Schmidt, M. and Higham, T. (1997). Sources of New Zealand's East Polynesian Culture Revisited: The Radiocarbon chronology of the Tairua Archaeological Site. *Journal of the Polynesian Society*.

Schofield, J. (1967). Sheet 3-Auckland (1st Ed). In *Geological Map of New Zealand, 1:250,000*. DSIR.

Seelenfreund, A. (1983). Site Survey on Mayor Island. *New Zealand Archaeological Association Newsletter*, 26(1):51–8.

Seelenfreund, A. (1985). *The Prehistoric Exploitation of Mayor Island in New Zealand Prehistory*. Unpublished m.a. thesis, Department of Anthropology, Unversity of Otago.

Seelenfreund, A. and Bollong, C. (1990). The Sourcing of New Zealand Archaeological Obsidian Artefacts Using Energy Dispersive XRF Sprectroscopy. *Saying So Doesn't Make it So: Essays in Honour of B. Foss Leach, Sutton, D.G. (ed.) New Zealand Archaeological Association Monograph*, 17:168–189.

Seelenfreund-Hirsch, A. (1985). *The Exploitation of Mayor Island Obsidian in the Prehistory of New Zealand*. Ph.D. thesis, Otago University.

Singh, B. and Szeicz, G. (1980). Predicting the Canopy Resistance of Mixed Hardwood Forest. *Agricultural Meterology*, 21:49–58.

Slabbers, P. (1977). Surface Roughness of Crops and Potential Evapotranspiration. *Journal of Hydrology*, 34:181–191.

Smart, C. and Green, R. (1962). A Stratified Dune Site at Tairua, Coromandel. *Dominion Museum Records in Ethnology*, 1(7):243–266.

Smith, I., Ward, G., and Ambrose, W. (1977). Geographic Distribution and the Characterization of Volcanic Glasses in Oceania. *Archaeology and Physical Anthropology in Oceania.*, XII, No. 3:173–201.

Spencer, M. (1982). *Fundamentals of Light Microscopy*. Cambridge University Press, Cambridge.

Spitters, C., Toussaint, H., and Goudriaan, J. (1986). Seperating the Diffuse and Direct Component of Global Radiation and its Implications for Modelling Canopy Photosynthesis. *Agricultural and Forest Meteorology*, 38:217–229.

Spring-Rice, W. (1962). Great Barrier Island. *New Zealand Archaeological Association Newsletter*, 5(1):92–96.

Spring-Rice, W. (1963). Haratonga - Great Barrier Island. *New Zealand Archaeological Association Newsletter*, 6(1):25–27.

Spring-Rice, W. (1980). Fanal Island (Motukino) Archaeological Survey and Historical Account. *Tane*, 26:99–105.

Stevenson, C., Carpenter, J., and Scheetz, B. (1989*a*). Obsidian Dating: Recent Advances in the Experimental Determination and Application of Hydration Rates. *Archaeometry*, 31:193–206.

Stevenson, C., Freeborn, W., and Scheetz, B. (1987). Obsidian Hydration Dating: An Improved Optical Technique for Measuring the Width of the Hydration Rim. *Archaeometry*, 29(1):120–123.

Stevenson, C., Knaus, E., Mazer, J., and Bates, J. (1993). Homogeneity of Water Content in Obsidian from the Coso Volcanic Field: Implications for Obsidian Hydration Dating. *Geoarchaeology*, 8:371–384.

Stevenson, C., Mazer, J., and Scheetz, B. (1998). Laboratory obsidian hydration rates. In M. S. Shackley (Ed.), *Archaeological Obsidian Studies: Method and Theory*, pp. 181–204. Plenum Press, New York.

Stevenson, C. and Scheetz, B. (1989*a*). Induced Hydration Rate Development of Obsidians from the Coso Volcanic field: A Comparison of Experimental Procedures. In R. Hughes (Ed.), *Current Directions in California Obsidian Studies*, pp. 23–30. Contributions of the University of California Archaeology Research Facility No. 48, Berkeley, California.

Stevenson, C. and Scheetz, B. (1989*b*). Rate development of Obsidians from the Coso Volcanic Field: A Comparison of Experimental Procedures. In R. Hughes (Ed.), *Current Directions in California Obsidian Studies*, pp. 23–30. Contributions of the University of California Archaeological Research Facility No. 48, Berkeley, California.

Stevenson, C., Scheetz, B., and Dinsmore, D. (1989*b*). An inter-laboratory comparison of hydration rim measurement. *IAOS Bulletin*, 1:7–13.

Stevenson, C., Sheppard, P., Sutton, D., and Ambrose, W. (1995). Advances in the Hydration Dating of New Zealand Obsidian. *Journal of Archaeological Science*, 23:233–242.

Stigter, C. (1980). Assesment of the Quality of Generalized Wind Functions in Penman's Equations. *Journal of Hydrology*, 45:321–331.

Stoutjesdijk, P. (1977). High Surface Temperatures of Trees and Pine Litter in the Winter and their Biological Importance. *International Journal of Biometeorology*, 21:325–331.

Stoutjesdijk, P. and Barkman, J. (1991). *Microclimate, Vegetation and Fauna*. Opulus Press, Knivsta.

Strachan, D. (1984). Effects of flow rate on the leaching of nuclear waste glass. *Advances in Ceramics*, 8:12–18.

Stuiver, M. and Reimer, P. (1993). Extended 14C database and revised CALIB radiocarbon calibration program. *Radiocarbon*, 35:215–230.

Stuiver, M., Reimer, P., Bard, E., Beck, J., Burr, G., Hughen, K., Kromer, B., McCormac, F., Plicht, J., and Spurk., M. (1998). INTERCAL98 Radiocarbon Age Calibration, 24,000-0 Cal BP. *Radiocarbon*, 40:1041–1083.

Sullivan, T. and Machiels, A. (1984). Growth of Hydrated Gel Layers in Nuclear Waste Glasses. *Advances in Ceramics*, 8:519–527.

Swets, D., Lee, R., and Frank, R. (1961). Diffusion Coefficients of Helium in Fused Quartz. *J. Chem. Phys.*, 34:17.

Swinbank, W. (1963). Long-wave radiation from clear skies. *Quarterly Journal of the Royal Meteorological Society*, 89:339–348.

Syring, K. (1990). A Simple Water Regime Model. In J. Richter (Ed.), *Models for Processes in the Soil*, pp. 65–71. Catena Verlag, Cremlingen, Germany.

Szeicz, G., Endrodi, G., and Tajchman, S. (1969). Aerodynamic and Surface Factors in Evaporation. *Water Resour. Res.*, 5:380–394.

Temps, R. and Coulson, K. (1977). Solar Radiation Incident Upon Slopes of Different Orientations. *Solar Energy*, 18:179–184.

Thompson, B. (1960). Sheet 2B - Barrier (1st Ed). In *Geological Map of New Zeland, 1:250,000*. DSIR.

Thompson, B. (1961). Sheet 2A - Whangerei (1st Ed). In *Geological Map of New Zealand: 1:250,000*. DSIR.

Thornton, J. (1985). *Field Guide to New Zealand Geology*. Reed Methuen, Auckland, New Zealand.

Thornwaite, C. and Holzman, B. (1942). Measurement of Evaporation from Land and Water Surface. *USDA Technical Bulletin*, 817:1–75.

Thorseth, I., Furness, H., and Heldal, M. (1992). *Geochimica et Cosmochimica Acta*, 56:845–850.

Tremaine, K. and Fredrickson, D. (1988). Induced Obsidian Hydration Experiments: An Investigation in Relative Dating. *Materials Research Society Symposium Proceedings*, 123:271–278.

Trembour, F., Smith, F., and Friedman, I. (1988). Diffusion Cells for Integrating Temperature and Humidity over Long Periods of Time. *Materials Research Society Symposium Proceedings*, 123:245–251.

Tsong, I., Houser, C., and Tong., S. (1980). Depth Profiles of Interdiffusing Species in Hydrated Glasses. *Physics and Chemistry of Glasses*, 21(5):197–198.

Tsong, I., Houser, C., Yusuf, N., Messier, R., White, W., and Michels., J. (1978). Obsidian Hydration Profiles Measured BySputter-Induced Optical Emission. *Science*, 201:339–341.

Tsong, I., Smith, G., Michels, J., Wintenberg, A., Miller, P., and Moak., C. (1981). Dating of Obsidian Artifacts by Depth-Profiling Of Artificially-Hydrated Surface Layers. *Nuclear Instruments and Methods*, (191):403–407.

Verma, S. and Rosenberg, N. (1977). The Brown-Rosenberg Resistance Model of Crop Evapotranspiration Modified Tests in an Inrrigated Sorghum Field. *Agron. Journal*, 69:332–335.

Ward, G. (1972). *Obsidian & New Zealand Archaeology*. Master's thesis, University of Otago.

Ward, G. (1973). Obsidian Source Locations in the North Island of New Zealand. *New Zealand Archaeological Association Newsletter*, 16(2):85–103.

Ward, G. (1974*a*). A Paradigm for Sourcing New Zealand Archaeological Obsidian. *Journal of the Royal Society of New Zealand*, 4:47–62.

Ward, G. (1974*b*). A Paradigm for Sourcing New Zealand Archaeological Obsidians. *Journal of the Royal Society of New Zealand.*, Vol. 4:47–62.

Ward, G. (1974*c*). A Systematic Approach to the Definition of Sources of Raw Material. *Archaeometry*, 16(1):41–53.

Warren, B. (1937). X-Ray Determination of Thestructure of Liquids and Glass. *Journal of Applied Physics*, 8:645–654.

Warren, B. and Biscoe, J. (1938). Fourier Analysis of X-Ray Patterns of Soda-Silica Glass. *Journal of the American Ceramic Society*, 21:259–265.

Watters, W. (1978*a*). Lower Quaternary. In R. Suggate (Ed.), *The Geology of New Zealand*, chapter The Late Mobile Phase: Igneous Activity, pp. 647–651. E.C. Keating Government Printer, Wellington, New Zealand.

Watters, W. (1978*b*). Miocene. In R. Suggate (Ed.), *The Geology of New Zealand*, chapter The Late Mobile Phase: Igneous Activity, pp. 637–644. E.C. Keating Government Printer, Wellington, New Zealand.

Webb, E. (1970). Profile Relationships: The Log-Linear Range, and Extension to Strong Stability. *Quarterly Journal Ofthe Royal Meteorological Society*, 96:67–90.

Webster, D., Freter, A., and Rue, D. (1993). The obsidian dating project at Copán: a regional approach and why it works. *Latin American Antiquity*, 4:303–324.

Weiss, D. G. and GaGlfe, G. (1986). Video-Microscopic Techniques to study the Living Cytoplasm. In D. Häder (Ed.), *Image Analysis in Biology*, pp. 135–158. CRC Press, London.

White, W. (1988). Glass hydartion mechanisms with application to obsidian hydration dating. In E. Sayre, P. Vandiver, J. Druzik, and C. Stecenson (Eds.), *Materials Issues in Art and Archaeology*, pp. 225–236. MRS Symposium Proceedings 123, Materials Research Society, Pittsburgh.

White, W. B. and Minser, D. (1984). Raman Spectra and Structure of Natural Glasses. *Journal of Non-Crystalline Solids*, 67:45–59.

Wilson, G. (1988). Obsidian Quarry Identification under the Microscope. *International Association for Obsidian Studies Bulletin*, 22:14–15.

Zacharisen, W. (1932). The atomic arrangement in glass. *Journal of the American Chemical Society*, 54:3841–3851.

Zeidler, J. A., Buck, C. E., and Litton, C. D. (1998). The Integration of Archaeological Phase Information and Radiocarbon Results from the Jama River Valley, Ecuador: A Bayesian Approach. *Latin American Antiquity*, 9:135–159.

Appendix A

Rim Buster Code

A.1 Introduction to Rim Buster

This section is intended to be a brief introductory tutorial to Rim Buster. If Rim buster has not already been installed install this application by running setup.exe found in the /software/rim buster/installation directory on the companion CD.

During installation two example images — test.bmp and test background.bmp — have been installed in the images subdirectory under the main installation directory. We will use these two images to demonstrate the basic functionality of Rim Buster.

1. First run Rim Buster.

2. Then open the **test.bmp** image. Use the **`File | Open`** menu item. This will open the **test** image into its own image window. You will notice that a number of image artefacts are present in this image. We can clean these by performing a background subtraction as described in §2.6.3.

3. To perform a background removal use the **`tools | remove background`** menu item. This will open a dialog window through which you can select the appropriate background image. In this case choose the **test background.bmp** file. Once this selection is made you will return to the test image window where you will notice that most of the original image artefacts have been removed. We can now select an analysis region.

4. Marquee an area of the rim image to select an analysis region for rim measurement using the left mouse button. To select a different region simply right click the image. The marquee box will disappear and you can now select a new analysis region.

5. Once a suitable analysis region has been selected click on **tools | bust rims** menu item. This will produce a plot of the pixel intensity across the analysis region and paste the analysis data into the datasheet. We can now begin to perform some image analyses.

6. Initially identify the two pixel minim. Use the left mouse button to click on the left pixel minima on the data plot. As you do this the pixel location will be recorded in the data sheet and on the status bar at the bottom of the data plot window. Use the right mouse button to choose the right pixel minima. Again the pixel location is recorded and this time the simple pixel count value is also calculated (Coded by the label SPP). We can now begin an intensity reconstruction measurement.

7. Initially try fitting an example curve to the data to check the suitability of the approximating curve function. Use the **Rim Measurement | fit curve menu** item. This will fit the approximating functions over the analysis zone surrounding each minima and report the associated R^2 statistics in the Plot area status bar. Different approximating functions can be chosen through selecting the appropriate model under the **Rim Measurement** menu. Try the other models and re-run the curve fit to see what effect this has on the goodness of fit. Once suitable analysis zones have been identified we can run the measurement analysis.

8. To run an analysis simply select the **Rim Measurement | Run analysis** menu item. The analysis will now run over 5-10 seconds depending on the speed of your computer. Once the analysis has completed the distribution of the location of each minima is plotted in the data plot region and recorded in the datasheet. The rim thickness measurement is also recorded in columns 1 and 2 of the data sheet in the row titled 'RUN'. The values should be in the region $0.85 \pm 0.1\mu$m. However this could vary substantially

depending upon the image analysis region that has been selected. This analysis can be re-run for a different approximating function simply by choosing a different approximating function under the **Rim Measurement** menu and re-running **Rim Measurement | Run analysis**.

9. This basic process can be repeated any number of times to select different portions of the image for measurement analysis. Usually image analysis locations would be selected through repeating steps 4–6 before running the analysis. Try this by repeating steps 4–6 for several different locations on the test image. Now re-run **Rim Measurement | Run analysis**. This time an analysis will be performed for all of the entries in the datasheet. In order to plot different datasets simply click in the leftmost column of the datasheet on one of the two rows corresponding to a particular dataset. As different datasets are selected in this manner they will be plotted in the dataplot region and the image analysis zone will be indicated on the rim image. This enables an assessment of the degree of variation in rim thickness throughout the image to be made.

The processes detailed above can be repeated for any number of images and forms a basic introduction to the use of Rim Buster.

A.2 Code Units

The Rim Buster application principally comprises three pascal units; Main.pas, Graph.pas and image.pas. The Image Lab framework is defined in Main.pas and the rim buster window is defined in graph.pas. The individual image windows are defined in image.pas.

A.2.1 Main.pas

```
  1: unit Main;
  2:
  3: interface
  4:
  5: uses
  6:   SysUtils, Windows, Messages, Classes, Graphics, Controls,
  7:   Forms, Dialogs, StdCtrls, Buttons, ExtCtrls, Menus, image,ComCt↩
⇛    rls;
  8:
  9: type
 10:   Tframeform = class(TForm)
 11:     MainMenu: TMainMenu;
 12:     FileOpenItem: TMenuItem;
 13:     WindowTileItem: TMenuItem;
 14:     WindowCascadeItem: TMenuItem;
 15:     WindowArrangeItem: TMenuItem;
 16:     StatusLine: TStatusBar;
 17:     OpenDialog: TOpenDialog;
 18:     SaveDialog: TSaveDialog;
 19:     PrintDialog: TPrintDialog;
 20:     PrintSetupDialog: TPrinterSetupDialog;
 21:     split1: TMenuItem;
 22:     overlayimages1: TMenuItem;
 23:     tileimages1: TMenuItem;
 24:     Use1: TMenuItem;   &Contents
 25:     procedure FormCreate(Sender: TObject);
 26:     procedure ShowHint(Sender: TObject);
 27:     procedure FileOpen(Sender: TObject);
 28:     procedure FileExit(Sender: TObject);
 29:     procedure WindowTile(Sender: TObject);
 30:     procedure WindowCascade(Sender: TObject);
 31:     procedure WindowArrange(Sender: TObject);
 32:     procedure split1Click(Sender: TObject);
 33:     procedure overlayimages1Click(Sender: TObject);
 34:     procedure tileimages1Click(Sender: TObject);
 35:     procedure Use1Click(Sender: TObject);
 36:
 37:   private
 38:     PathName: string;
 39:   public
 40:      inside_width, inside_height : integer;
 41:   end;
 42:
 43: var
 44:   frameform: Tframeform;
```

```
 45:   image_list : array[1..25] of pointer;
 46:   image_count : integer;
 47:
 48: implementation
 49:
 50: uses  Graph;
 51: $R *.DFM
 52:
 53: procedure Tframeform.FormCreate(Sender: TObject);
 54: var
 55:         x : integer;
 56: begin
 57:   application.Icon := frameform.Icon;
 58:   Application.OnHint := ShowHint;
 59:   image_count := 0;
 60:   inside_width := frameform.clientwidth;
 61:   inside_height := frameform.ClientHeight;
 62: end;
 63:
 64: procedure Tframeform.ShowHint(Sender: TObject);
 65: begin
 66:   StatusLine.SimpleText := Application.Hint;
 67: end;
 68:
 69:
 70: procedure Tframeform.FileOpen(Sender: TObject);
 71: begin
 72:   if OpenDialog.Execute then
 73:         begin
 74:           //  with TimageForm.Create(Self) do
 75:          // Open(OpenDialog.FileName);
 76:         inc(image_count);
 77:         image_list[image_count] :=  TimageForm.Create(Self);
 78:         timageform(image_list[image_count]).Open(OpenDialog.FileN↩
⇒    ame);
 79:         timageform(image_list[image_count]).count_index := image_↩
⇒    count;
 80:         tileimages1Click(Self);
 81:   end;
 82: end;
 83:
 84:
 85: procedure Tframeform.FileExit(Sender: TObject);
 86: begin
 87:   Close;
 88: end;
 89:
```

```
 90:
 91: procedure Tframeform.WindowTile(Sender: TObject);
 92: begin
 93:   Tile;
 94: end;
 95:
 96: procedure Tframeform.WindowCascade(Sender: TObject);
 97: begin
 98:   Cascade;
 99: end;
100:
101: procedure Tframeform.WindowArrange(Sender: TObject);
102: begin
103:   ArrangeIcons;
104: end;
105:
106: procedure Tframeform.split1Click(Sender: TObject);
107: begin
108: histfrm.Top := 0;
109: histfrm.Left := 0;
110: histfrm.Width := frameform.inside_width div 2;
111: histfrm.Height := frameform.inside_height-statusline.height -4;
112: end;
113:
114: procedure Tframeform.overlayimages1Click(Sender: TObject);
115: var
116:         x : integer;
117: begin
118: split1Click(self);
119: for x := 1 to image_count do
120:         begin
121:         timageform(image_list[x]).height := histfrm.height;
122:         timageform(image_list[x]).width := histfrm.Width -5;
123:         timageform(image_list[x]).left := histfrm.width;
124:         timageform(image_list[x]).top := 0;
125:         end;
126: end;
127:
128: procedure Tframeform.tileimages1Click(Sender: TObject);
129: var
130:         x : integer;
131:          dummy : timageform;
132:          height : integer;
133:          width : integer;
134: begin
135: split1Click(self);
136: if image_count =1 then overlayimages1Click(self)
```

```
137: else if image_count = 2 then
138:         begin
139:         height := histfrm.Height div 2;
140:         width := histfrm.Width - 4;
141:         for x := 1 to image_count do
142:                 begin
143:                 timageform(image_list[x]).height := height;
144:                 timageform(image_list[x]).width := width;
145:                 timageform(image_list[x]).left := histfrm.width;
146:                 timageform(image_list[x]).top := 0 + (x-1)*height↩
⇛    ;
147:                 end;
148:         end
149: else if (image_count > 2) and (image_count <5) then
150:         begin
151:         height := histfrm.Height div 2;
152:         width := (histfrm.Width - 4)  div 2;
153:         for x := 1 to image_count do
154:                 begin
155:                 timageform(image_list[x]).height := height;
156:                 timageform(image_list[x]).width := width;
157:                 if x < 3 then timageform(image_list[x]).left := h↩
⇛    istfrm.width
158:                 else timageform(image_list[x]).left := histfrm.wi↩
⇛    dth + width;
159:                 if (x = 1) or (x=3) then timageform(image_list[x]↩
⇛    ).top := 0
160:                 else timageform(image_list[x]).top :=  height;
161:                 end;
162:         end
163: else if (image_count > 4) and (image_count < 7) then
164:         begin
165:         height := histfrm.Height div 2;
166:         width := (histfrm.Width - 4)  div 3;
167:         for x := 1 to image_count do
168:                 begin
169:                 timageform(image_list[x]).height := height;
170:                 timageform(image_list[x]).width := width;
171:                 if x < 3 then timageform(image_list[x]).left := h↩
⇛    istfrm.width
172:                 else if (x >2) and (x <5) then timageform(image_l↩
⇛    ist[x]).left := histfrm.width + width
173:                 else  timageform(image_list[x]).left := histfrm.w↩
⇛    idth + 2*width;
174:                 if x mod 2 > 0  then timageform(image_list[x]).to↩
⇛    p := 0
175:                 else timageform(image_list[x]).top :=  height;
```

```
176:                 end;
177:         end
178: else if (image_count > 6) and (image_count <10) then
179:         begin
180:         height := histfrm.Height div 3;
181:         width := (histfrm.Width - 4)  div 3;
182:         for x := 1 to image_count do
183:                 begin
184:                 timageform(image_list[x]).height := height;
185:                 timageform(image_list[x]).width := width;
186:                 if x < 4 then timageform(image_list[x]).left := h↩
⇛    istfrm.width
187:                 else if (x >3) and (x < 7) then timageform(image_↩
⇛    list[x]).left := histfrm.width + width
188:                 else timageform(image_list[x]).left := histfrm.wi↩
⇛    dth + 2*width;
189:                 if (x-1) mod 3 = 0  then timageform(image_list[x]↩
⇛    ).top := 0
190:                 else if (x-1) mod 3 = 1 then timageform(image_lis↩
⇛    t[x]).top := height
191:                 else timageform(image_list[x]).top :=  2*height;
192:                 end;
193:         end;
194: end;
195:
196: procedure Tframeform.Use1Click(Sender: TObject);
197: begin
198: if histfrm.pixel_values then
199:         begin
200:         histfrm.pixel_values := false;
201:         use1.checked := false;
202:         end
203: else
204:         begin
205:         histfrm.pixel_values := true;
206:         use1.checked := true;
207:         end;
208: end;
209:
210: end.
```

A.2.2 Graph.pas

```
  1: unit Graph;
  2:
```

```
  3: interface
  4:
  5: uses
  6:   SysUtils, WinTypes, WinProcs, Messages, Classes, Graphics, Con↩
⇛    trols,
  7:   Forms, Dialogs, StdCtrls, OleCtrls, ChartFX, inifiles, ComCt↩
⇛    rls, Grids,
  8:   ExtCtrls, Buttons, ToolWin, Menus, RChart, math2,math,
  9:   ImgList, AdvGrid, AdvSprd,
 10:   Meter, FileCtrl, histutils, TeeProcs, TeEngine, Chart;
 11:
 12: type
 13:   tcurvemodel = (quadratic,cubic,gaussian);
 14:   tplottype = (simplestep,box,whiskers);
 15:
 16:   THISTFRM = class(TForm)
 17:     StatusBar2: TStatusBar;
 18:     MainMenu1: TMainMenu;
 19:     Log1: TMenuItem;
 20:     Run1: TMenuItem;
 21:     SaveDialog1: TSaveDialog;
 22:     OpenDialog1: TOpenDialog;
 23:     Panel2: TPanel;
 24:     ImageList1: TImageList;
 25:     datasheet: TAdvSpreadGrid;
 26:     Splitter4: TSplitter;
 27:     StatusBar1: TStatusBar;
 28:     RChart1: TRChart;
 29:     PopupMenu1: TPopupMenu;
 30:     CopySheet1: TMenuItem;
 31:     DeleteEntry1: TMenuItem;
 32:     SaveData1: TMenuItem;
 33:     FitCurve1: TMenuItem;
 34:     ProgressBar1: TProgressBar;
 35:     plottype1: TMenuItem;
 36:     SimpleStep1: TMenuItem;
 37:     Box1: TMenuItem;
 38:     Whiskers1: TMenuItem;
 39:     Type1: TMenuItem;
 40:     save1: TMenuItem;
 41:     N1: TMenuItem;
 42:     N2: TMenuItem;
 43:     N3: TMenuItem;
 44:     cubic1: TMenuItem;
 45:     quadratic1: TMenuItem;
 46:     gaussian1: TMenuItem;
 47:     PasteData1: TMenuItem;
```

```
  48:     N4: TMenuItem;
  49:     pixelsize1: TMenuItem;
  50:     procedure FormCreate(Sender: TObject);
  51:     procedure FormResize(Sender: TObject);
  52:     procedure ScrollBox2Resize(Sender: TObject);
  53:     procedure SpeedButton2Click(Sender: TObject);
  54:     procedure RadioButton1Click(Sender: TObject);
  55:     procedure RadioButton2Click(Sender: TObject);
  56:     procedure ScrollBox3Resize(Sender: TObject);
  57:     procedure SpeedButton3Click(Sender: TObject);
  58:     procedure StringGrid2MouseUp(Sender: TObject; Button: TMouse↩
⇛     Button;
  59:       Shift: TShiftState; X, Y: Integer);
  60:     procedure Save1Click(Sender: TObject);
  61:     procedure Open1Click(Sender: TObject);
  62:     procedure Run1Click(Sender: TObject);
  63:     procedure SpeedButton4Click(Sender: TObject);
  64:     procedure SpeedButton5Click(Sender: TObject);
  65:     procedure SpeedButton6Click(Sender: TObject);
  66:     procedure BitBtn1Click(Sender: TObject);
  67:     procedure RChart1MouseUp(Sender: TObject; Button: TMouseButt↩
⇛     on;
  68:       Shift: TShiftState; X, Y: Integer);
  69:     procedure ToolButton1Click(Sender: TObject);
  70:     procedure ToolButton2Click(Sender: TObject);
  71:     procedure ToolButton3Click(Sender: TObject);
  72:     procedure threaddone(sender: tobject);
  73:     procedure clear1Click(Sender: TObject);
  74:     procedure DeleteEntry1Click(Sender: TObject);
  75:     procedure datasheetMouseUp(Sender: TObject; Button: TMouseBu↩
⇛     tton;
  76:       Shift: TShiftState; X, Y: Integer);
  77:     procedure CopySheet1Click(Sender: TObject);
  78:     procedure SaveData1Click(Sender: TObject);
  79:     procedure Run;
  80:     procedure FitCurve1Click(Sender: TObject);
  81:     procedure SimpleStep1Click(Sender: TObject);
  82:     procedure Box1Click(Sender: TObject);
  83:     procedure Whiskers1Click(Sender: TObject);
  84:     procedure cubic1Click(Sender: TObject);
  85:     procedure quadratic1Click(Sender: TObject);
  86:     procedure gaussian1Click(Sender: TObject);
  87:     procedure PasteData1Click(Sender: TObject);
  88:     procedure pixelsize1Click(Sender: TObject);
  89:
  90:   private
  91:      Private declarations
```

```
 92:     stats1 : tcurvefit;
 93:   public
 94:      Public declarations
 95:   inf1, inf2, rects, logs, tx,ty,bx,by,its,image_height, image_l↩
⇒     engthh : integer;
 96:   runthreads: integer;
 97:   ts2 : boolean;
 98:   image_file : string;
 99:   data_count, current_data : integer;
100:   current_col, current_row : integer;
101:   pixel_size : single;
102:   pixel_values : boolean;
103:   model : tcurvemodel;
104:   plot : tplottype;
105:   end;
106:
107: var
108:   HISTFRM: THISTFRM;
109:   intensity_array : array[1..2,1..2000] of single;
110:
111: implementation
112:
113: uses image, rthread, Main, pix;
114:
115: $R *.DFM
116:
117: procedure THISTFRM.FormCreate(Sender: TObject);
118: var
119:     x : integer;
120: begin
121: rects := 0;
122: ts2 := false;
123: frameform.split1Click(self);
124: data_count := 0;
125: pixel_size := 0.075;
126: pixel_values := true;
127: stats1 := tcurvefit.Create;
128: model := cubic;
129: plot := whiskers;
130: end;
131:
132: procedure THISTFRM.FormResize(Sender: TObject);
133: var
134:    x : integer;
135: begin
136:
137:
```

```
138:
139:
140: end;
141:
142:
143:
144:
145: procedure THISTFRM.ScrollBox2Resize(Sender: TObject);
146: begin
147: if scrollbox2.height > 138 then
148: chartfx2.height := scrollbox2.height - 27
149: else
150: chartfx2.height := 111 ;
151: if scrollbox2.width > 549 then
152: chartfx2.width := scrollbox2.width - 43
153: else
154: chartfx2.width := 506;
155: end;
156:
157: procedure THISTFRM.SpeedButton2Click(Sender: TObject);
158: var
159:    x : integer;
160: begin
161: screen.cursor := crhourglass;
162: //speedbutton1click(sender);
163: //MCMC_curve;
164: CHARTFX3.OPENDATAex(cod_values,1,20);
165: for x := 0 to 19 do
166:     begin
167:     chartfx3.VALUE[x] := thick_array[2,(x+15)];
168:     chartfx3.legend[x] := floattostr(thick_array[1,(x+15)]/10);
169:     end;
170: CHARTFX3.CLOSEDATA(cod_values);
171:
172: screen.cursor := crdefault;
173: end;
174:
175:
176: procedure THISTFRM.RadioButton1Click(Sender: TObject);
177: var
178:    x, y : integer;
179:    mn, mx : single;
180: begin
181: mn := 256;
182: mx := 0;
183: for x := 3 to 7 do
184:     begin
```

```
185:     y := inf_val[x,4,1,1];
186:     if y < mn then mn := y;
187:     if y > mx then mx := y;
188:     end;
189: histfrm.CHARTFX2.OPENDATAex(cod_values,2,50);
190: histfrm.chartfx2.thisserie := 1;
191: for y := 1 to 5 do
192: for x := 1 to 10 do
193: begin
194: histfrm.chartfx2.VALUE[(y-1) * 10 + (x-1)] := inf_val[(y+2),1,1,↩
⇛     1];
195: end;
196: histfrm.chartfx2.thisserie := 2;
197: for x := 0 to 49 do
198: histfrm.chartfx2.VALUE[x] := graph_vals[x+1,1];
199: histfrm.CHARTFX2.CLOSEDATA(cod_values);
200:
201: histfrm.chartfx2.adm[0] :=  mn-1;
202: histfrm.chartfx2.adm[1] :=  mx + 1;
203: for x := 1 to 50 do
204:     begin
205:     y := graph_vals[x,1];
206:     if y < mn then mn := y;
207:     if y > mx then mx := y;
208:     end;
209:
210: y := strtoint(statusbar1.panels[1].text)-2;
211:
212:
213:
214:
215:
216:
217:
218:
219: end;
220:
221: procedure THISTFRM.RadioButton2Click(Sender: TObject);
222: var
223:    x, y : integer;
224:    mn, mx : single;
225: begin
226: mn := 256;
227: mx := 0;
228: for x := 3 to 7 do
229:     begin
230:     y := inf_val[x,4,2,1];
```

```
 231:     if y < mn then mn := y;
 232:     if y > mx then mx := y;
 233:     end;
 234: histfrm.CHARTFX2.OPENDATAex(cod_values,2,50);
 235: histfrm.chartfx2.thisserie := 1;
 236: histfrm.chartfx2.thisserie := 1;
 237: for y := 1 to 5 do
 238: for x := 1 to 10 do
 239: begin
 240: histfrm.chartfx2.VALUE[(y-1) * 10 + (x-1)] := regress_array[2,(y↩
⇛     +1),1,1];
 241: end;
 242: histfrm.chartfx2.thisserie := 2;
 243: for x := 0 to 49 do
 244: histfrm.chartfx2.VALUE[x] := graph_vals[x+1,2];
 245: histfrm.CHARTFX2.CLOSEDATA(cod_values);
 246:
 247: histfrm.chartfx2.adm[0] :=  mn-1;
 248: histfrm.chartfx2.adm[1] :=  mx + 1;
 249: for x := 1 to 50 do
 250:     begin
 251:     y := graph_vals[x,2];
 252:     if y < mn then mn := y;
 253:     if y > mx then mx := y;
 254:     end;
 255:
 256: y := strtoint(statusbar1.panels[3].text)-2;
 257:
 258:
 259:
 260: end;
 261:
 262: procedure THISTFRM.ScrollBox3Resize(Sender: TObject);
 263: begin
 264: if scrollbox3.height > 138 then
 265: chartfx3.height := scrollbox3.height - 27
 266: else
 267: chartfx3.height := 111 ;
 268: if scrollbox3.width > 549 then
 269: chartfx3.width := scrollbox3.width - 43
 270: else
 271: chartfx3.width := 506;
 272: end;
 273:
 274: procedure THISTFRM.SpeedButton3Click(Sender: TObject);
 275: var
 276:    inf1, inf2, x, y : integer;
```

```
277:    inf, mx, mn,correction : single;
278: begin
279: rects := rects + 1;
280: //speedbutton1click(sender);
281: //initial;
282: //thickness;
283:
284:
285: end;
286:
287:
288:
289: procedure THISTFRM.StringGrid2MouseUp(Sender: TObject;
290:   Button: TMouseButton; Shift: TShiftState; X, Y: Integer);
291: var
292:    col, row,z,xx : integer;
293:    f1 : textfile;
294: begin
295:
296: end;
297:
298: procedure THISTFRM.Save1Click(Sender: TObject);
299: var
300:    x,y,z : integer;
301:    f1 : textfile;
302:    s1 : string;
303: begin
304: if savedialog1.execute = true then
305:    begin
306:    s1 := SaveDialog1.FileName;
307:    rchart1.CopyToBMP(s1,false);
308:    end;
309: end;
310:
311: procedure THISTFRM.Open1Click(Sender: TObject);
312: var
313:    x,y,z : integer;
314:    f1 : textfile;
315:    s1 : string;
316:    dummy : string;
317: begin
318: if opendialog1.execute = true then
319:    begin
320:    s1 := OpenDialog1.FileName;
321:    assignfile(f1, s1);
322:    reset(f1);
323:    readln(f1, x);
```

```
324:    logs := x;
325:    for z := 1 to x do
326:        begin
327:        for y := 1 to 70 do
328:            begin
329:            readln(f1, dummy);
330:            end;
331:         end;
332:    closefile(f1);
333:    end;
334: end;
335:
336: procedure THISTFRM.Run1Click(Sender: TObject);
337: var
338:    count, inf, x, y,z,xx, run, pix,count_tru, line : integer;
339:    total_upper, total_lower, Lower_pos, upper_pos : integer;
340:    current_length, current_val, sum, length, dum : integer;
341:    correction, val : variant;
342:    s, dummy : string;
343:    ended : boolean;
344:    st : tstringgrid;
345:    mt, mtt : tmeter;
346:    f1, f2, f3 : textfile;
347: begin
348: run;
349: inc(runthreads);
350: frameform.caption := 'Image Lab .... Processing!!!';
351: mt := tmeter.create(self);
352: with mt do
353:      begin
354:      width := 281;
355:      height := 145;
356:      needlelayout.anchorsize := 15;
357:      colorcover := clred;
358:      caption := 'its';
359:      limwatchhighon := false;
360:      limwatchlowon := false;
361:      top := (runthreads-1)*145;
362:      meterlayout := mlcirc180;
363:      if runthreads > 4 then
364:      begin
365:      height := (runthreads - 5) *145;
366:      left := 420;
367:      end;
368:
369:      end;
370: mtt := tmeter.create(self);
```

```
371: with mtt do
372:      begin
373:      width := 137;
374:      height := 97;
375:      needlelayout.anchorsize := 15;
376:      colorcover := clred;
377:      caption := 'runs';
378:      limwatchhighon := false;
379:      limwatchlowon := false;
380:      top := (runthreads-1)*145;
381:      left := 290;
382:      if runthreads > 4 then
383:      begin
384:      height := (runthreads - 5) *145;
385:      left := 710;
386:      end;
387:
388:
389:      end;
390: st := tstringgrid.create(self);
391: with st do
392:      begin
393:      parent := self;
394:      visible := false;
395:      colcount := 101;
396:      rowcount := logs+1;
397:      for x := 1 to logs do
398:          begin
399:          for y := 1 to 100 do
400:              begin
401:              end;
402:          end;
403:      end;
404: with regmcmc.create(runthreads,logs,st,mt,mtt)do
405:      begin
406:      onterminate := threaddone;
407:      end;
408:  := 'e:\pixel\log\log.cv';
409: assignfile(f2, s);
410:  := 'e:\pixel\log\log 95.cv';
411: assignfile(f3,s);
412: rewrite(f2);
413: rewrite(f3);
414: for run := 1 to logs do
415: begin
416: progress_form.statictext1.caption := inttostr(run);
417: if stringgrid3.cells[run,1] = '1' then
```

```
 418: begin
 419:
 420:
 421: varclear(graph_vals);
 422: varclear(regress_array);
 423: varclear(inf_pts);
 424: graph_vals := vararraycreate([1,50,1,2], varsingle);
 425: with stringgrid3 do
 426: begin
 427: image_height := strtoint(cells[run,69]);
 428: inf_pts := vararraycreate([1,2,1,2,1,image_height], varsingle);
 429: regress_array := vararraycreate([1,2,1,7,1,6,1,image_height], va↩
⇒     rdouble);
 430:
 431: curve.image_height := image_height;
 432: if strtoint(cells[run,70]) = 1 then
 433:    begin
 434:    linevar := true;
 435:    load the full regress array
 436:
 437:    reset(f1);
 438:    for y := 1 to 7 do
 439:        begin
 440:        for x := 1 to image_height do
 441:            begin
 442:            for z := 1 to 5 do
 443:                begin
 444:                for xx := 1 to 2 do
 445:                    begin
 446:                    readln(f1, dummy);
 447:                    regress_array[xx,y,z,x] := strtofloat(dummy);
 448:                    end;
 449:                end;
 450:
 451:            end;
 452:        end;
 453:    closefile(f1);
 454:    end
 455: else
 456:     linevar := false;
 457:
 458: curve.its := strtoint(cells[run,2]);
 459: for y := 1 to image_height do
 460: begin
 461: inf_pts[1,1,y] := cells[run,65];
 462: inf_pts[1,2,y] := cells[run,66];
 463: inf_pts[2,1,y] := cells[run,67];
```

```
464: inf_pts[2,2,y] := cells[run,68];
465: end;
466: for y := 1 to 2 do
467:     begin
468:     for x := 1 to 7 do
469:         begin
470:         regress_array[y,x,1,1]:= cells[run,(7 + x + (y-1)*7)] ;
471:         end;
472:     end;
473: for y := 1 to 2 do
474:     begin
475:     for x := 1 to 7 do
476:         begin
477:         regress_array[y,x,3,1] := cells[run,(21 + x + (y-1)*7)];
478:         regress_array[y,x,4,1] := cells[run,(21 + x + (y-1)*7)];
479:         end;
480:     end;
481:
482: for y := 1 to 2 do
483:     begin
484:     for x := 1 to 7 do
485:         begin
486:         regress_array[y,x,5,1] := cells[run,(35 + x + (y-1)*7)];
487:         end;
488:     end;
489: for y := 1 to 2 do
490:     begin
491:     for x := 1 to 7 do
492:         begin
493:         regress_array[y,x,2,1] := cells[run,(49 + x + (y-1)*7)];
494:         end;
495:     end;
496:
497: end;
498:  randomize;
499: line := 1;
500: declare the thickness count array
501: check the update of inf_pts
502: correction := trunc(inf_pts[2,1,line]-inf_pts[1,1,line]) - 2.5;
503: for x := 1 to 50 do
504:     begin
505:     thick_array[1,x] := (x-1)/10 + correction;
506:     end;
507:    perform the mcmc analysis
508: for x := 1 to its do
509: begin
510: inf := reg_select_inf;
```

```
 511: pix := new_reg_var;
 512: regress_array[inf,pix,candidate,line] := new_reg_candidate(inf,p↩
⇒     ix,line);
 513: regression(inf);
 514: update inf_vals and inf points
 515: if reg_infs(inf, line) = true then inc(count_tru);
 516: y := trunc(10*(inf_pts[2,2,1] - inf_pts[1,2,1]-correction));
 517: thick_array[2,y] := thick_array[2,y] + 1;
 518: end;
 519: reg_mcmc;
 520:  := 'e:\pixel\log\runfile' + inttotr(run) + '.csv';
 521: assignfile(f1,s);
 522: rewrite(f1);
 523: s := stringgrid3.cells[run, 64];
 524: writeln(f1, s);
 525: for x := 1 to 100 do
 526:     begin
 527:     writeln(f1, thick_array[1,x],',', thick_array[2,x]);
 528:     end;
 529: closefile(f1);
 530: output to log
 531: writeln(f2, s);
 532: writeln(f2, curve.its);
 533: set range max and min
 534: total_lower := -1;
 535: total_upper := -1;
 536: x := 0;
 537: While total_lower = -1 do
 538:       begin
 539:       inc(x);
 540:       if thick_array[2,x] > 0 then total_lower := x;
 541:       end;
 542: x := 100;
 543: While total_upper = -1 do
 544:       begin
 545:       if thick_array[2,x] > 0 then total_upper := x;
 546:       x := x -1;
 547:       end;
 548: writeln(f2, 'Total',',',total_lower,',',total_upper);
 549: val := 0.95 * curve.its;
 550: ended := false;
 551: x := total_lower;
 552: current_length := 100;
 553: current_val := 0;
 554: sum := 0;
 555: lower_pos := total_lower;
 556: upper_pos := total_upper;
```

```
557: while ended = false do
558:       begin
559:       sum := 0;
560:       length := 0;
561:       dum := x - 1;
562:       while sum < val do
563:             begin
564:             inc(length);
565:             inc(dum);
566:             sum := sum + trunc(thick_array[2,dum]);
567:             if dum > total_upper then
568:                begin
569:                ended := true;
570:                length := 101;
571:                sum := val + 10;
572:                end;
573:             end;
574:       if length < current_length then
575:          begin
576:          current_length := length;
577:          current_val := sum;
578:          lower_pos := x;
579:          upper_pos := dum;
580:          end
581:       else if length = current_length then
582:            begin
583:            if sum > current_val then
584:               begin
585:               current_length := length;
586:               current_val := sum;
587:               lower_pos := x;
588:               upper_pos := dum;
589:               end;
590:            end;
591:       inc(x);
592:
593:       end;
594: writeln(f2, '95 % HPD',',',lower_pos,',',upper_pos,',',current_l↩
⇛     ength);
595: writeln(f3, s,',',thick_array[1,lower_pos],',',thick_array[2,upp↩
⇛     er_pos]);
596:
597: val := 0.68 * curve.its;
598: ended := false;
599: x := total_lower;
600: current_length := 100;
601: current_val := 0;
```

```
602: sum := 0;
603: lower_pos := total_lower;
604: upper_pos := total_upper;
605: while ended = false do
606:       begin
607:       sum := 0;
608:       length := 0;
609:       dum := x - 1;
610:       while sum < val do
611:             begin
612:             inc(length);
613:             inc(dum);
614:             sum := sum + trunc(thick_array[2,dum]);
615:             if dum > total_upper then
616:                begin
617:                ended := true;
618:                length := 101;
619:                sum := val + 10;
620:                end;
621:             end;
622:       if length < current_length then
623:          begin
624:          current_length := length;
625:          current_val := sum;
626:          lower_pos := x;
627:          upper_pos := dum;
628:          end
629:       else if length = current_length then
630:            begin
631:            if sum > current_val then
632:               begin
633:               current_length := length;
634:               current_val := sum;
635:               lower_pos := x;
636:               upper_pos := dum;
637:               end;
638:            end;
639:       inc(x);
640:
641:       end;
642: writeln(f2, '68 % HPD',',',lower_pos,',',upper_pos,',',current_l↩
⇒     ength);
643:
644: writeln(f2);
645: for x := 1 to 100 do
646:     begin
647:     thick_array[1,x] := 0;
```

```
 648:     thick_array[2,x] := 0;
 649:     end;
 650:
 651: end
 652: else if stringgrid3.cells[run,1] = '2' then
 653: begin
 654: correction := trunc(strtofloat(stringgrid3.cells[run,3])*10) - 3↩
⇒     5;
 655: image_height := strtoint(stringgrid3.cells[run,65]);
 656: varclear(inf_val);
 657: varclear(inf_pts);
 658: varclear(graph_vals);
 659: inf_val := vararraycreate([1,9,1,5,1,2,1,image_height], varsingl↩
⇒     e);
 660: inf_pts := vararraycreate([1,2,1,2,1,image_height], varsingle);
 661: graph_vals := vararraycreate([1,50,1,2], varsingle);
 662: for x := 1 to 9 do
 663:     begin
 664:     inf_val[#4##] is the proposed value
 665:     inf_val[x,4,1,1] := strtofloat(stringgrid3.cells[run,(7 + x↩
⇒     )]);
 666:     inf_val[x,4,2,1] := strtofloat(stringgrid3.cells[run,(16 + x↩
⇒     )]);
 667:     inf_val[#1##] is the actual values
 668:     inf_val[x,1,1,1] := strtofloat(stringgrid3.cells[run,(44 + ↩
⇒     x)]);
 669:     inf_val[x,1,2,1] := strtofloat(stringgrid3.cells[run,(53 + x↩
⇒     )]);
 670:     inf_val[#3##] is the current value
 671:     inf_val[x,3,1,1] := strtofloat(stringgrid3.cells[run,(7 + x↩
⇒     )]);
 672:     inf_val[x,3,2,1] := strtofloat(stringgrid3.cells[run,(16 + x↩
⇒     )]);
 673:     inf_val[#2##] is the intensity error
 674:     inf_val[x,2,1,1] := strtofloat(stringgrid3.cells[run,(26 + ↩
⇒     x)]);
 675:     inf_val[x,2,2,1] := strtofloat(stringgrid3.cells[run,(35 + x↩
⇒     )]);
 676:     inf_val[#5##] is the fit flag, 0 := false 1 := true
 677:     inf_val[x,5,1,1] := 0;
 678:     inf_val[x,5,2,1] := 0;
 679:     end;
 680: inf_pts[1,1,1] := strtofloat(stringgrid3.cells[run,63]);
 681: inf_pts[1,2,1] := strtofloat(stringgrid3.cells[run,64]);
 682: thickness;
 683: declare the thickness count array
 684: for x := 1 to 50 do
```

```
 685:     begin
 686:     thick_array[1,x] := (x + correction)/10;
 687:     end;
 688:    perform the mcmc analysis
 689: count := 0;
 690: testform.progressbar1.position :=0;
 691: its := strtoint(stringgrid3.cells[run,2]);
 692: for x := 1 to its do
 693: begin
 694: inc(count);
 695: if count = its/10 then
 696: begin
 697: testform.progressbar1.position := testform.progressbar1.position↩
⇒      + 10;
 698: testform.update;
 699: count := 0;
 700: end;
 701: inf := select_inf;
 702: pix := select_var;
 703: inf_val[pix,4,inf,1] := new_val(pix,inf);
 704: curve_fit(1,inf);
 705:
 706: update inf_vals and inf points
 707:
 708: if fit = true then
 709: begin
 710: inf_val[pix,3,inf,1] := inf_val[pix,4,inf,1];
 711: inf_pts[2,inf,1] := inf_pts[1,inf,1] + inflection;
 712: end;
 713: calculate the thickness and update the thickness array
 714: y := trunc(10*(inf_pts[2,2,1] - inf_pts[2,1,1]))-correction;
 715: thick_array[2,y] := thick_array[2,y] + 1;
 716:
 717: end;
 718:  := 'e:\pixel\log\runfile' + inttotr(run) + '.log';
 719: assignfile(f1,s);
 720: rewrite(f1);
 721: for x := 1 to 50 do
 722:     begin
 723:     writeln(f1, thick_array[1,x], thick_array[2,x]);
 724:     end;
 725: closefile(f1);
 726: for x := 1 to 50 do
 727:     begin
 728:     thick_array[1,x] := 0;
 729:     thick_array[2,x] := 0;
 730:     end;
```

```
731: end;
732: end;
733: closefile(f2);
734: closefile(f3);
735: testform.visible := false;
736: end;
737:
738: procedure THISTFRM.SpeedButton4Click(Sender: TObject);
739: var
740: x, y, line : integer;
741: dummy, min,max : single;
742: f1 : textfile;
743: begin
744: if ts2 = false then
745: begin
746: pagecontrol1.activepage := tabsheet2;
747: ts2 := true;
748: end;
749: min := 257;
750: max := 0;
751: inf1 := strtoint(statusbar1.panels.items[1].text);
752: inf2 := strtoint(statusbar1.panels.items[3].text);
753: varclear(graph_vals);
754: varclear(regress_array);
755: varclear(inf_pts);
756: inf_pts := vararraycreate([1,2,1,2,1,image_height], varsingle);
757: regress_array := vararraycreate([1,2,1,7,1,6,1,image_height], va↩
⇒     rdouble);
758: graph_vals := vararraycreate([1,50,1,2], varsingle);
759: for x := 1 to image_height do
760: begin
761: inf_pts[1,1,x] := inf1;
762: inf_pts[1,2,x] := inf1;
763: inf_pts[2,1,x] := inf2;
764: inf_pts[2,2,x] := inf2;
765: end;
766: for x := 1 to 7 do
767:     begin
768:
769:     end;
770: regression(1,1);
771: for x := 1 to 50 do
772: begin
773: dummy := regress_array[1,1,5,1] + regress_array[1,2,5,1]*(x+10)/↩
⇒     10
774:       + regress_array[1,3,5,1]*((x+10)/10)*((x+10)/10)
775:       + regress_array[1,4,5,1]*sin(3.141592*2*((x+10)/10)/7)
```

```
776:       + regress_array[1,5,5,1]*cos(3.141592*2*((x+10)/10)/7);
777: graph_vals[x,1]:= dummy;
778: if dummy > max then max := dummy;
779: if dummy < min then min := dummy;
780:
781: end;
782: for x := 1 to 7 do
783:     begin
784:
785:     end;
786: regression(2,1);
787: for x := 1 to 50 do
788: begin
789: dummy := regress_array[2,1,5,1] + regress_array[2,2,5,1]*(x+10)/↩
⇛     10
790:       + regress_array[2,3,5,1]*((x+10)/10)*((x+10)/10)
791:       + regress_array[2,4,5,1]*sin(3.141592*2*((x+10)/10)/7)
792:       + regress_array[2,5,5,1]*cos(3.141592*2*((x+10)/10)/7);
793: graph_vals[x,2]:= dummy;
794: end;
795:
796: histfrm.CHARTFX2.OPENDATAex(cod_values,2,50);
797: histfrm.chartfx2.thisserie := 1;
798: for y := 1 to 5 do
799: for x := 1 to 10 do
800: begin
801: histfrm.chartfx2.VALUE[(y-1) * 10 + (x-1)] := regress_array[1,(y↩
⇛     +1),1,1];
802: end;
803: histfrm.chartfx2.thisserie := 2;
804: for x := 0 to 49 do
805: begin
806: histfrm.chartfx2.VALUE[x] := graph_vals[(x+1),1];
807: end;
808: histfrm.CHARTFX2.CLOSEDATA(cod_values);
809: //y := strtoint(statusbar1.panels[1].text)-2;
810:
811:
812: end;
813:
814: procedure THISTFRM.SpeedButton5Click(Sender: TObject);
815: var
816:    x,y: integer;
817:    dummy : double;
818:    total_lower, total_upper: integer;
819:    max : single;
820: begin
```

```
821: its := 10000;
822: screen.cursor := crhourglass;
823: speedbutton4click(sender);
824: curve.image_height := image_height;
825:
826: for y := 2 to image_height do
827: begin
828: for x := 1 to 7 do
829:     begin
830:     end;
831: end;
832: for y := 2 to image_height do
833: begin
834: for x := 1 to 7 do
835:     begin
836:     end;
837: end;
838:
839: reg_MCMC;
840: total_lower := -1;
841: total_upper := -1;
842: x := 0;
843: While total_lower = -1 do
844:       begin
845:       inc(x);
846:       if thick_array[2,x] > 0 then total_lower := x;
847:       end;
848: x := 100;
849: While total_upper = -1 do
850:       begin
851:       if thick_array[2,x] > 0 then total_upper := x;
852:       x := x -1;
853:       end;
854: for x:= total_lower to total_upper do
855:     begin
856:     if thick_array[2,x] > max then max := thick_array[2,x];
857:     end;
858: end;
859:
860: procedure THISTFRM.SpeedButton6Click(Sender: TObject);
861: var
862: x, y : integer;
863: test : boolean;
864: begin
865: rects := rects + 1;
866: speedbutton4click(sender);
867: curve.image_height := image_height;
```

```
 868:
 869:
 870: reg_initial;
 871: test := reg_infs(1,1);
 872: test := reg_infs(2,1);
 873:
 874: end;
 875:
 876:
 877:
 878: procedure THISTFRM.BitBtn1Click(Sender: TObject);
 879: var
 880:    X,Y,z,count,xx: integer;
 881:    intensity, max, min, gs_int, gs_se, dummy: single;
 882:    se : double;
 883: begin
 884: statusbar1.panels.items[1].text := '';
 885: statusbar1.panels.items[3].text := '';
 886:
 887: z := 0;
 888: max := 0;
 889: min := 10000000;
 890: histfrm.CHARTFX1.OPENDATAex(cod_values,1,image_length);
 891: for z := 0 to (image_length - 1) do
 892: begin
 893: dummy := strtofloat(gridfrm.stringgrid1.cells[1,(Z + 1)]);
 894: if dummy > max then max := dummy;
 895: if dummy < min then min := dummy;
 896: histfrm.chartfx1.VALUE[Z] := dummy;
 897: end;
 898: histfrm.stringgrid1.visible := true;
 899: histfrm.CHARTFX1.CLOSEDATA(cod_values);
 900: histfrm.chartfx1.adm[0] := min;
 901: histfrm.chartfx1.adm[1] := max;
 902: edge_smooth;
 903: histfrm.visible := true;
 904: if (lf) and (rt) then
 905: begin
 906: lpos := lpos - x;
 907: rpos := rpos - x;
 908: min := 256;
 909:      for x := (lpos - 4) to (lpos + 4) do
 910:          begin
 911:               if strtofloat(gridfrm.stringgrid1.cells[1,x]) <= ↩
⇒     min then
 912:                  gridfrm.edit1.text := inttostr(x);
 913:          end;
```

```
914:
915:      min := 256;
916:      for x := (rpos - 4) to (rpos + 4) do
917:          begin
918:               if strtofloat(gridfrm.stringgrid1.cells[1,x]) < mi↩
⇛     n then
919:               gridfrm.edit2.text := inttostr(x);
920:          end;
921:
922:      gridfrm.speedbutton1.click;
923:     end;
924:
925: end;
926:
927:
928: procedure THISTFRM.RChart1MouseUp(Sender: TObject; Button: TMous↩
⇛     eButton;
929:   Shift: TShiftState; X, Y: Integer);
930: var
931:         tx,ty : integer;
932: begin
933: if shift = [ssalt] then
934: begin
935: if (button = mbleft)  then
936:         begin
937:         if datasheet.cells[3,current_data*2-1] <> '' then
938:                 begin
939:                 tx := round(rchart1.mouseposx);
940:                 ty := strtoint(datasheet.cells[3,current_data*2-↩
⇛     1]);
941:                 datasheet.cells[4,current_data*2-1] := inttostr(↩
⇛     trunc(abs(tx-ty)));
942:                 end;
943:         end
944: else if  button = mbright then
945:         begin
946:         if datasheet.cells[5,current_data*2-1] <> '' then
947:                 begin
948:                 tx := round(rchart1.mouseposx);
949:                 ty := strtoint(datasheet.cells[5,current_data*2-↩
⇛     1]);
950:                 datasheet.cells[6,current_data*2-1] := inttostr(↩
⇛     trunc(abs(tx-ty)));
951:                 end;
952:         end;
953: end
954: else
```

```
 955: begin
 956: if (button = mbleft)  then
 957:         begin
 958:         if pixel_values then statusbar1.panels[1].text := inttos↩
⇛     tr(round(rchart1.mouseposx))
 959:         else statusbar1.panels[1].text := floattostr(round(rchar↩
⇛     t1.mouseposx)*0.075);
 960:         datasheet.cells[3,current_data*2-1] := inttostr(round(rc↩
⇛     hart1.mouseposx));
 961:         datasheet.cells[4,current_data*2-1] := '3';
 962:         end
 963: else if  button = mbright then
 964:         begin
 965:         if pixel_values then statusbar1.panels[3].text := inttos↩
⇛     tr(round(rchart1.mouseposx))
 966:         else statusbar1.panels[3].text := floattostr(round(rchar↩
⇛     t1.mouseposx)*0.075);
 967:         datasheet.cells[5,current_data*2-1] := inttostr(round(rc↩
⇛     hart1.mouseposx));
 968:         datasheet.cells[6,current_data*2-1] := '3';
 969:         end;
 970: if (statusbar1.panels[1].text <> '') and (statusbar1.panels[3].t↩
⇛     ext <> '') then
 971:         begin
 972:         if pixel_values then statusbar1.panels[5].text := inttos↩
⇛     tr(strtoint(statusbar1.panels[3].text) - strtoint(↩
⇛     statusbar1.panels[1].text))
 973:         else statusbar1.panels[5].text := floattostr(strtofloat(↩
⇛     statusbar1.panels[3].text) - strtofloat(statusbar1↩
⇛     .panels[1].text));
 974:         datasheet.cells[2,current_data*2-1] := statusbar1.panels↩
⇛     [5].text;
 975:         end;
 976: end;
 977: end;
 978:
 979: procedure THISTFRM.ToolButton1Click(Sender: TObject);
 980: begin
 981: rchart1.mouseaction := mapan;
 982: end;
 983:
 984: procedure THISTFRM.ToolButton2Click(Sender: TObject);
 985: begin
 986: rchart1.mouseaction := mazoomwind;
 987: end;
 988:
 989: procedure THISTFRM.ToolButton3Click(Sender: TObject);
```

```
 990: begin
 991: rchart1.MouseAction := manone;
 992: end;
 993:
 994: procedure thistfrm.threaddone(sender :tobject);
 995: begin
 996: dec(runthreads);
 997: if runthreads = 0 then frameform.caption := 'Image Lab';
 998: end;
 999:
1000:
1001:
1002:
1003: procedure THISTFRM.clear1Click(Sender: TObject);
1004: var
1005:    x,y : integer;
1006:
1007: begin
1008: for x := 1 to 100 do
1009:     begin
1010:     for y := 1 to logs do
1011:         begin
1012:         end;
1013:     end;
1014: logs := 0;
1015: end;
1016:
1017: procedure THISTFRM.DeleteEntry1Click(Sender: TObject);
1018: var
1019:         x, data_element : integer;
1020: begin
1021: x := current_row;
1022: if x mod 2 > 0 then
1023:         begin
1024:         datasheet.RemoveRows(x,2);
1025:         end
1026: else
1027:         begin
1028:         datasheet.RemoveRows(x-1,2);
1029:         end;
1030: data_count := data_count -1;
1031: end;
1032:
1033: procedure THISTFRM.datasheetMouseUp(Sender: TObject; Button: TMo↩
⇒    useButton;
1034:   Shift: TShiftState; X, Y: Integer);
1035: var
```

```
1036:         len : integer;
1037:         xx, x_count, loc : integer;
1038:         val, min, max,z : single;
1039:         s1,s2 : string;
1040:         tl,br : tpoint;
1041:         image : timage;
1042:         run : boolean;
1043:         m,sd, dx : double;
1044: begin
1045: run := false;
1046: datasheet.MouseToCell(x,y,current_col,current_row);
1047: if (current_col = 0) and (current_row > 0) then
1048: begin
1049: if current_row mod 2 = 0 then current_row := current_row-1;
1050: current_data := (current_row + 1) div 2;
1051: statusbar1.panels[1].text := datasheet.cells[3,current_row];
1052: statusbar1.panels[3].text := datasheet.cells[5,current_row];
1053: statusbar1.panels[5].text := datasheet.cells[2,current_row];
1054: if datasheet.cells[1,current_row] <> '' then
1055:         begin
1056:         x_count := strtoint(datasheet.cells[1,current_row]);
1057:         s1 := datasheet.cells[7,current_row];
1058:         delete(s1,1,1);
1059:         loc := pos(',',s1);
1060:         s2 := s1;
1061:         delete(s1,loc,(length(s1)-loc)+1);
1062:         delete(s2,1,loc);
1063:         delete(s2,length(s2),1);
1064:         tl.x := strtoint(s1);
1065:         tl.y := strtoint(s2);
1066:         s1 := datasheet.cells[8,current_row];
1067:         delete(s1,1,1);
1068:         loc := pos(',',s1);
1069:         s2 := s1;
1070:         delete(s1,loc,(length(s1)-loc)+1);
1071:         delete(s2,1,loc);
1072:         delete(s2,length(s2),1);
1073:         br.x := strtoint(s1);
1074:         br.y := strtoint(s2);
1075:         for xx := 1 to image_count do timageform(image_list[xx])↩
⇛    .IMAGE1.Picture := timageform(image_list[xx]).IMAGE↩
⇛    2.Picture;
1076:         timageform(image_list[x_count]).DrawShape(tl,br,pmcopy);
1077:         timageform(image_list[x_count]).SetFocus;
1078:         histfrm.SetFocus;
1079:         end;
1080: if datasheet.cells[0,current_row+1] = 'Run' then run := true;
```

```
1081: len := 9;
1082: min := 258;
1083: max := -1;
1084: while (len < 1992) and (datasheet.cells[len,current_row] <> '') ↩
⇒    do
1085:         begin
1086:         val := strtofloat(datasheet.cells[len,current_row]);
1087:         if val > max then max := val;
1088:         if val < min then min := val;
1089:         intensity_array[1,len-8] := val;
1090:         val := strtofloat(datasheet.cells[len,current_row+1]);
1091:         intensity_array[2,len-8] := val;
1092:         inc(len);
1093:         end;
1094: len := len - 9;
1095: rchart1.rangelox := 0;
1096: rchart1.rangehix := len;
1097: if run then rchart1.rangeloy := min - 15
1098: else rchart1.rangeloy := min - 10;
1099: if run then rchart1.rangehiy := max + 5
1100: else rchart1.rangehiy := max + 10;
1101: rchart1.datacolor := clred;
1102: rchart1.cleargraf;
1103: if plot = simplestep then
1104:         begin
1105:         rchart1.moveto(0.5,intensity_array[1,1]);
1106:         for x := 2 to len do
1107:                 begin
1108:                 rchart1.drawto(x-0.5,intensity_array[1,x-1]);
1109:                 rchart1.drawto(x-0.5,intensity_array[1,x]);
1110:                 end;
1111:         end
1112: else if plot = box then
1113:         begin
1114:         for x := 1 to len do
1115:                 begin
1116:                 rchart1.moveto(x-0.5,intensity_array[1,x]-2*inte↩
⇒    nsity_array[2,x]);
1117:                 rchart1.drawto(x-0.5,intensity_array[1,x]+2*inte↩
⇒    nsity_array[2,x]);
1118:                 rchart1.drawto(x+0.5,intensity_array[1,x]+2*inte↩
⇒    nsity_array[2,x]);
1119:                 rchart1.drawto(x+0.5,intensity_array[1,x]-2*inte↩
⇒    nsity_array[2,x]);
1120:                 rchart1.drawto(x-0.5,intensity_array[1,x]-2*inte↩
⇒    nsity_array[2,x]);
1121:                 end;
```

```
1122:         end
1123: else if plot = whiskers then
1124:         begin
1125:         for x := 1 to len do
1126:                 begin
1127:                 rchart1.moveto(x-0.5,intensity_array[1,x]-1*inte↩
⇛    nsity_array[2,x]);
1128:                 rchart1.drawto(x-0.5,intensity_array[1,x]+1*inte↩
⇛    nsity_array[2,x]);
1129:                 rchart1.drawto(x+0.5,intensity_array[1,x]+1*inte↩
⇛    nsity_array[2,x]);
1130:                 rchart1.drawto(x+0.5,intensity_array[1,x]-1*inte↩
⇛    nsity_array[2,x]);
1131:                 rchart1.drawto(x-0.5,intensity_array[1,x]-1*inte↩
⇛    nsity_array[2,x]);
1132:                 rchart1.moveto(x,intensity_array[1,x]-2*intensit↩
⇛    y_array[2,x]);
1133:                 rchart1.drawto(x,intensity_array[1,x]-intensity_↩
⇛    array[2,x]);
1134:                 rchart1.moveto(x,intensity_array[1,x] +intensity↩
⇛    _array[2,x]);
1135:                 rchart1.drawto(x,intensity_array[1,x] +2*intensi↩
⇛    ty_array[2,x]);
1136:                 end
1137:         end;
1138: if run then
1139:         begin
1140:                 if datasheet.cells[3,current_row+1] <> '' then
1141:                         begin
1142:                         m := strtofloat(datasheet.cells[3,curren↩
⇛    t_row+1]);
1143:                         sd := strtofloat(datasheet.cells[4,curre↩
⇛    nt_row+1]) ;
1144:                         dx := rchart1.rangehix/600;
1145:                         z := rchart1.RangeLoY;
1146:                         rchart1.moveto(0,z+10*exp((-1/2)*sqr((0-↩
⇛    m)/sd)));
1147:                         for x := 0 to 600 do
1148:                                 begin
1149:                                 rchart1.drawto(x*dx,z+10*exp((-1↩
⇛    /2)*sqr((dx*x-m)/sd)));
1150:                                 end;
1151:                         end;
1152:                 if datasheet.cells[5,current_row+1] <> '' then
1153:                         begin
1154:                         m := strtofloat(datasheet.cells[5,curren↩
⇛    t_row+1]);
```

```
1155:                         sd := strtofloat(datasheet.cells[6,curre↩
⇒    nt_row+1]) ;
1156:                         dx := rchart1.rangehix/600;
1157:                         z := rchart1.RangeLoY;
1158:                         rchart1.moveto(0,z+10*exp((-1/2)*sqr((0-↩
⇒    m)/sd)));
1159:                         for x := 0 to 600 do
1160:                                 begin
1161:                                 rchart1.drawto(x*dx,z+10*exp((-1↩
⇒    /2)*sqr((dx*x-m)/sd)));
1162:                                 end;
1163:                         end;
1164:         end;
1165: rchart1.showgraf;
1166: end;
1167: end;
1168:
1169: procedure THISTFRM.CopySheet1Click(Sender: TObject);
1170: begin
1171: datasheet.CopyToClipBoard;
1172: end;
1173:
1174: procedure THISTFRM.SaveData1Click(Sender: TObject);
1175: begin
1176: datasheet.Delimiter := ',';
1177: if savedialog1.execute then
1178:         begin
1179:         datasheet.SaveToCSV(savedialog1.filename);
1180:         end;
1181: end;
1182:
1183:
1184: procedure THISTFRM.FitCurve1Click(Sender: TObject);
1185: var
1186:         x, y, inf, zone : integer;
1187:   k0, k1, k2, k3 : double;
1188:   FitQUal    : double;
1189:   dy,dx,xstep      : double;
1190:   i          : integer;
1191:   k : array[0..3] of double;
1192: begin
1193: stats1.init;
1194: inf := strtoint(datasheet.cells[3,current_data*2-1]);
1195: zone := strtoint(datasheet.cells[4,current_data*2-1]);
1196: for x := inf - zone + 8 to inf + zone + 8   do
1197:         begin
1198:         dy := strtofloat(datasheet.cells[x,current_data*2-1]);
```

```
1199:         dx := x-8;
1200:         stats1.EnterStatValue(dx,dy);
1201:         end;
1202: rchart1.datacolor := clblack;
1203: //2 fit the initial curve and generate the parameter distributio↩
⇛    ns
1204: if model = quadratic then Stats1.CalcParabolFit(k0,k1,k2,FitQual↩
⇛    )
1205: else if model = cubic then
1206:         begin
1207:         stats1.CalcPolyFit(3,k,fitqual);
1208:         k0 := k[0];
1209:         k1 := k[1];
1210:         k2 := k[2];
1211:         k3 := k[3];
1212:         end
1213: else if model = gaussian then stats1.CalcGaussFit(k0,k1,k2,fitqu↩
⇛    al);
1214: //3 plot the curve
1215: //while (RChart1.TypeOfLastItem <> tkMarkAt) and
1216: //      (RChart1.TypeOfLastItem <> tkNone) do  remove any curve↩
⇛     from graph
1217: //  RChart1.RemoveLastItem;
1218: if model = quadratic then RChart1.MoveTo(inf-zone,k0+k1*(inf-zon↩
⇛    e)+k2*sqr(inf-zone))
1219: else if model = cubic then RChart1.MoveTo(inf-zone,k0+k1*(inf-zo↩
⇛    ne)+k2*sqr(inf-zone) + k3*intpower(inf-zone,3))
1220: else if model = gaussian then rchart1.moveto(inf-zone,k0*exp(-1*↩
⇛    sqr(inf-zone-k1)/k2));
1221: xstep := 2*zone / 50;
1222: for i:=1 to 50 do
1223:   begin
1224:   dx := inf - zone +i*xstep;
1225:   if model = quadratic then RChart1.DrawTo (dx,k0+k1*dx+k2*sqr(d↩
⇛    x))
1226:   else if model = cubic then RChart1.drawTo(dx,k0+k1*(dx)+k2*sqr↩
⇛    (dx) + k3*intpower(dx,3))
1227:   else if model = gaussian then rchart1.drawto(dx,k0*exp(-1*sqr(↩
⇛    dx-k1)/k2));
1228:   end;
1229: stats1.init;
1230: inf := strtoint(datasheet.cells[5,current_data*2-1]);
1231: zone := strtoint(datasheet.cells[6,current_data*2-1]);
1232: for x := inf - zone + 8 to inf + zone + 8   do
1233:         begin
1234:         dy := strtofloat(datasheet.cells[x,current_data*2-1]);
1235:         dx := x-8;
```

```
1236:         stats1.EnterStatValue(dx,dy);
1237:         end;
1238:
1239: //2 fit the initial curve and generate the parameter distributio↩
⇒    ns
1240: if model = quadratic then Stats1.CalcParabolFit(k0,k1,k2,FitQual↩
⇒    )
1241: else if model = cubic then
1242:         begin
1243:         stats1.CalcPolyFit(3,k,fitqual);
1244:         k0 := k[0];
1245:         k1 := k[1];
1246:         k2 := k[2];
1247:         k3 := k[3];
1248:         end
1249: else if model = gaussian then stats1.CalcGaussFit(k0,k1,k2,fitqu↩
⇒    al);
1250: //3 plot the curve
1251: //while (RChart1.TypeOfLastItem <> tkMarkAt) and
1252: //      (RChart1.TypeOfLastItem <> tkNone) do  remove any curve↩
⇒     from graph
1253: //  RChart1.RemoveLastItem;
1254: if model = quadratic then RChart1.MoveTo(inf-zone,k0+k1*(inf-zon↩
⇒    e)+k2*sqr(inf-zone))
1255: else if model = cubic then RChart1.MoveTo(inf-zone,k0+k1*(inf-zo↩
⇒    ne)+k2*sqr(inf-zone) + k3*intpower(inf-zone,3))
1256: else if model = gaussian then rchart1.moveto(inf-zone,k0*exp(-1*↩
⇒    sqr(inf-zone-k1)/k2));
1257: xstep := 2*zone / 50;
1258: for i:=1 to 50 do
1259:   begin
1260:   dx := inf - zone +i*xstep;
1261:   if model = quadratic then RChart1.DrawTo (dx,k0+k1*dx+k2*sqr(d↩
⇒    x))
1262:   else if model = cubic then RChart1.drawTo(dx,k0+k1*(dx)+k2*sqr↩
⇒    (dx) + k3*intpower(dx,3))
1263:   else if model = gaussian then rchart1.drawto(dx,k0*exp(-1*sqr(↩
⇒    dx-k1)/k2));
1264:   end;
1265: rchart1.datacolor := clred;
1266:
1267: RChart1.ShowGraf;
1268: end;
1269:
1270: procedure thistfrm.run;
1271: var
1272:         x, y : integer;
```

```
1273:   zone,inf : integer;
1274:   k0, k1, k2, k3 : double;
1275:   t1,t2,t3 : double;
1276:   k : array[0..3] of double;
1277:   FitQUal    : double;
1278:   xstep      : double;
1279:   int1,int2,integral : double;
1280:   dx, dy,z : double ;
1281:   min1,min2,m1,m2 : double;
1282:   i,len,j,zz, zzz          : integer;
1283:   sample_array : array[1..2,1..100000] of double;
1284:   analysis_array1,analysis_array2 : array[1..3,1..100] of double↩
⇒    ;
1285:   analysis_length : integer;
1286:   sample_count1,sample_count2,measurement : integer;
1287:   f1, f2 : textfile;
1288:   fstats1,fstats2 : thistdata;
1289:   val, min,max : single;
1290:   fit : boolean;
1291:   gauss_x, gauss_w : array[1..5] of single;
1292:   test1, test2  : boolean;
1293:   total_count : integer;
1294: begin
1295: gauss_x[1] := 0.1488743389;
1296: gauss_x[2] := 0.4333953941;
1297: gauss_x[3] := 0.6794095682;
1298: gauss_x[4] := 0.8650633666;
1299: gauss_x[5] := 0.9739065285;
1300: gauss_w[1] := 0.2955242247;
1301: gauss_w[2] := 0.2692667193;
1302: gauss_w[3] := 0.2190863625;
1303: gauss_w[4] := 0.1494513491;
1304: gauss_w[5] := 0.0666713443;
1305: test1 := true;
1306: test2 := false;
1307: if test2 then total_count := 1
1308: else
1309: total_count := 100000;
1310: fstats1 := thistdata.create;
1311: fstats2 := thistdata.create;
1312: fstats1.initialise(100000);
1313: fstats2.initialise(100000);
1314: ssignfile(f1,'c:\rim_log.csv');\end{verb}1315: rewrite(f1);
1316: if (test1)  or (test2) then
1317:         begin
1318:ssignfile(f2,'c:\rim_test.csv');1319:         rewrite(f2);
1320:         end;
```

```
1321: for measurement := 1 to data_count do
1322:         begin
1323:
1324:         for x := 1 to 3 do
1325:         for y := 1 to 100 do
1326:                 begin
1327:                 analysis_array1[x,y] := 0;
1328:                 analysis_array2[x,y] := 0;
1329:                 end;
1330:         for x := 1 to 2 do
1331:         for y := 1 to 100000 do
1332:                 begin
1333:                 sample_array[x,y] := 0;
1334:                 end;
1335:         histfrm.Caption := 'Rim Buster ..... Analysing Measureme↩
⇒    nt ' + inttostr(measurement);
1336:         inf := strtoint(datasheet.cells[3,measurement*2-1]);
1337:         zone := strtoint(datasheet.cells[4,measurement*2-1]);
1338:         analysis_length := zone*2+1;
1339:         for x := 1 to analysis_length do //inf - zone + 8 to inf↩
⇒     + zone + 8   do
1340:                 begin
1341:                 dy := strtofloat(datasheet.cells[x+inf-zone + 8,↩
⇒    measurement*2-1]);
1342:                 analysis_array1[1,x] := dy;
1343:                 dy := strtofloat(datasheet.cells[x+inf-zone + 8,↩
⇒    measurement*2]);
1344:                 analysis_array1[2,x] := dy;
1345:                 analysis_array1[3,x] := dy*dy;
1346:                 end;
1347:         inf := strtoint(datasheet.cells[5,measurement*2-1]);
1348:         zone := strtoint(datasheet.cells[6,measurement*2-1]);
1349:         analysis_length := zone*2+1;
1350:         for x := 1 to analysis_length do //inf - zone + 8 to inf↩
⇒     + zone + 8   do
1351:                 begin
1352:                 dy := strtofloat(datasheet.cells[x+inf-zone + 8,↩
⇒    measurement*2-1]);
1353:                 analysis_array2[1,x] := dy;
1354:                 dy := strtofloat(datasheet.cells[x+inf-zone + 8,↩
⇒    measurement*2]);
1355:                 analysis_array2[2,x] := dy;
1356:                 analysis_array2[3,x] := dy*dy;
1357:                 end;
1358:
1359:         for zz := 1 to 20 do
1360:         begin
```

```
1361:         total_count := zz*5000;
1362:         for zzz := 1 to 25 do
1363:         begin
1364:         progressbar1.position := 0;
1365:         sample_count1 := 0;
1366:         sample_count2 := 0;
1367:         for y := 1 to total_count do
1368:                 begin
1369:                 if y mod 1000 = 0 then
1370:                         begin
1371:                         progressbar1.StepIt;
1372:                         frameform.Update;
1373:                         histfrm.update;
1374:                         application.ProcessMessages;
1375:                         end;
1376:                 //1 generate the candidate state and load this d↩
⇒    ata into the analysis array
1377:                 stats1.Init;
1378:                 inf := strtoint(datasheet.cells[3,measurement*2-↩
⇒    1]);
1379:                 zone := strtoint(datasheet.cells[4,measurement*2↩
⇒    -1]);
1380:                 analysis_length := zone*2+1;
1381:                 if test2 then for x := 1 to analysis_length do
1382:                         begin
1383:                         stats1.EnterStatValue(inf-zone+x+1,analy↩
⇒    sis_array1[1,x]);
1384:                        end
1385:                 else
1386:                 for x := 1 to analysis_length do
1387:                         begin
1388:                         dy := randg(analysis_array1[1,x],analysi↩
⇒    s_array1[3,x]);
1389:                         stats1.EnterStatValue(inf-zone+x-1,dy);
1390:                         end;
1391:                 //2 fit the curve and generate the parameter dis↩
⇒    tributions
1392:                 if model = quadratic then
1393:                         begin
1394:                         Stats1.CalcParabolFit(k0,k1,k2,FitQual);
1395:                         fit := true;
1396:                         for x := inf-zone to inf+zone do
1397:                                 begin
1398:                                 dx := x+0.5;
1399:                                 int1 := k0*dx + k1*dx*dx/2 + k2*↩
⇒    dx*dx*dx/3;
1400:                                 dx := x-0.5;
```

```
1401:                                   int2 := k0*dx + k1*dx*dx/2 + k2*↩
⇒    dx*dx*dx/3;
1402:                                   integral := int1-int2;
1403:                                   if (integral > analysis_array1[1↩
⇒    ,x-inf+zone+1] + 3*analysis_array1[2,x-inf+zone+1])↩
⇒     or (integral < analysis_array1[1,x-inf+zone+1] - 3↩
⇒    *analysis_array1[2,x-inf+zone+1]) then fit := false↩
⇒    ;
1404:                                   end;
1405:                           min1 := -1*k1/(2*k2);
1406:                           end
1407:                   else if model = cubic then
1408:                           begin
1409:                           for x := 0 to 3 do k[x] := 0;
1410:                           Stats1.CalcPolyFit(3,k,FitQual);
1411:                           k0 := k[0];
1412:                           k1 := k[1];
1413:                           k2 := k[2];
1414:                           k3 := k[3];
1415:                           fit := true;
1416:                           for x := inf-zone to inf+zone do
1417:                                   begin
1418:                                   dx := x+0.5;
1419:                                   int1 := k0*dx + k1*dx*dx/2 + k2*↩
⇒    dx*dx*dx/3 + k3*dx*dx*dx*dx/4;
1420:                                   dx := x-0.5;
1421:                                   int2 := k0*dx + k1*dx*dx/2 + k2*↩
⇒    dx*dx*dx/3 + k3*dx*dx*dx*dx/4;
1422:                                   integral := int1-int2;
1423:                                   if (integral > analysis_array1[1↩
⇒    ,x-inf+zone+1] + 3*analysis_array1[2,x-inf+zone+1])↩
⇒     or (integral < analysis_array1[1,x-inf+zone+1] - 3↩
⇒    *analysis_array1[2,x-inf+zone+1]) then fit := false↩
⇒    ;
1424:                                    end;
1425:                           t1 := 6*k3;
1426:                           t2 := 2*k2;
1427:                           t3 := sqr(t2) - 2*k1*t1;
1428:                           if t3 > 0 then
1429:                                   begin
1430:                                   m1 := (-1*t2 + sqrt(t3))/(t1);
1431:                                   m2 := (-1*t2 - sqrt(t3))/(t1);
1432:                                   if (k0 + k1*m1 + k2*m1*m1 + k3*m↩
⇒    1*m1*m1) > (k0 + k1*m2 + k2*m2*m2 + k3*m2*m2*m2) th↩
⇒    en min1 := m2 + 1
1433:                                   else min1 := m1 + 1;
1434:                                   end
```

```
1435:                         else min1 := inf + zone + 100;
1436:                         end
1437:                 else if model = gaussian then
1438:                         begin
1439:                         try
1440:                         Stats1.CalcGaussFit(k0,k1,k2,FitQual);
1441:                         fit := true;
1442:                         except
1443:                         fit := false;
1444:                         k0 := 1;
1445:                         k1 := 1;
1446:                         k2 := 1;
1447:                         end;
1448:                         for x := inf-zone to inf+zone do
1449:                                 begin
1450: //                                xm := x;
1451: //                                xr := 1;
1452:                                 integral := 0;
1453:                                 for j := 1 to 5 do
1454:                                         begin
1455:                                         dx := 0.5*gauss_x[j];
1456:                                         integral := integral + g↩
⇒    auss_w[j]*k0*exp(-1*sqr(x+dx-k1)/k2) + gauss_w[j]*k↩
⇒    0*exp(-1*sqr(x-dx-k1)/k2)
1457:                                         end;
1458:                                 integral := integral*0.5;
1459:                                 if (integral > analysis_array1[1↩
⇒    ,x-inf+zone+1] + 4*analysis_array1[2,x-inf+zone+1])↩
⇒     or (integral < analysis_array1[1,x-inf+zone+1] - 4↩
⇒    *analysis_array1[2,x-inf+zone+1]) then fit := false↩
⇒    ;
1460:                                 end;
1461:                         min1 := k1;
1462:                         end;
1463:                 if (min1 > inf + zone) or (min1 < inf - zone) th↩
⇒    en fit := false;
1464:                 if fit then
1465:                         begin
1466:                         inc(sample_count1);
1467:                         sample_array[1,sample_count1] := min1;
1468:                         end;
1469:                  //if test2 then write(f2,fitqual);
1470:                 //5 repeat for inf
1471:                 stats1.Init;
1472:                 inf := strtoint(datasheet.cells[5,measurement*2-↩
⇒    1]);
1473:                 zone := strtoint(datasheet.cells[6,measurement*2↩
```

```
⇒    -1]);
1474:                 analysis_length := zone*2+1;
1475:                 if test2 then for x := 1 to analysis_length do
1476:                         begin
1477:                         stats1.EnterStatValue(inf-zone+x+1,analy↩
⇒    sis_array2[1,x]);
1478:                        end
1479:                else
1480:                for x := 1 to analysis_length do
1481:                         begin
1482:                         dy := randg(analysis_array2[1,x],analysi↩
⇒    s_array2[3,x]);
1483:                         stats1.EnterStatValue(inf-zone+x-1,dy);
1484:                         end;
1485:                 if model = quadratic then
1486:                         begin
1487:                         Stats1.CalcParabolFit(k0,k1,k2,FitQual);
1488:                         fit := true;
1489:                         for x := inf-zone to inf+zone do
1490:                                 begin
1491:                                 dx := x+0.5;
1492:                                 int1 := k0*dx + k1*dx*dx/2 + k2*↩
⇒    dx*dx*dx/3;
1493:                                 dx := x-0.5;
1494:                                 int2 := k0*dx + k1*dx*dx/2 + k2*↩
⇒    dx*dx*dx/3;
1495:                                 integral := int1-int2;
1496:                                 if (integral > analysis_array2[1↩
⇒    ,x-inf+zone+1] + 3*analysis_array2[2,x-inf+zone+1])↩
⇒     or (integral < analysis_array2[1,x-inf+zone+1] - 3↩
⇒    *analysis_array2[2,x-inf+zone+1]) then fit := false↩
⇒    ;
1497:                                 end;
1498:                         min2 := -1*k1/(2*k2);
1499:                         end
1500:                 else if model = cubic then
1501:                         begin
1502:                         for x := 0 to 3 do k[x] := 0;
1503:                         Stats1.CalcPolyFit(3,k,FitQual);
1504:                         k0 := k[0];
1505:                         k1 := k[1];
1506:                         k2 := k[2];
1507:                         k3 := k[3];
1508:                         fit := true;
1509:                         for x := inf-zone to inf+zone do
1510:                                 begin
1511:                                 dx := x+0.5;
```

```
1512:                                   int1 := k0*dx + k1*dx*dx/2 + k2*↩
⇒    dx*dx*dx/3 + k3*dx*dx*dx*dx/4;
1513:                                   dx := x-0.5;
1514:                                   int2 := k0*dx + k1*dx*dx/2 + k2*↩
⇒    dx*dx*dx/3 + k3*dx*dx*dx*dx/4;
1515:                                   integral := int1-int2;
1516:                                   if (integral > analysis_array2[1↩
⇒    ,x-inf+zone+1] + 3*analysis_array2[2,x-inf+zone+1])↩
⇒     or (integral < analysis_array2[1,x-inf+zone+1] - 3↩
⇒    *analysis_array2[2,x-inf+zone+1]) then fit := false↩
⇒    ;
1517:                                    end;
1518:                           t1 := 6*k3;
1519:                           t2 := 2*k2;
1520:                           t3 := sqr(t2) - 2*k1*t1;
1521:                           if t3 > 0 then
1522:                                   begin
1523:                                   m1 := (-1*t2 + sqrt(t3))/(t1);
1524:                                   m2 := (-1*t2 - sqrt(t3))/(t1);
1525:                                   if (k0 + k1*m2 + k2*m2*m2 + k3*m↩
⇒    2*m2*m2) > (k0 + k1*m1 + k2*m1*m1 + k3*m1*m1*m1) th↩
⇒    en min2 := m1 + 1
1526:                                   else min2 := m2 + 1;
1527:                                   end
1528:                           else min2 := inf + zone + 100;
1529:                           end
1530:                   else if model = gaussian then
1531:                           begin
1532:                           try
1533:                           Stats1.CalcGaussFit(k0,k1,k2,FitQual);
1534:                           fit := true;
1535:                           except
1536:                           fit := false;
1537:                           k0 :=1;
1538:                           k1 := 1;
1539:                           k2 :=1;
1540:                           end;
1541:                           for x := inf-zone to inf+zone do
1542:                                   begin
1543: //                                  xm := x;
1544: //                                  xr := 0.5;
1545:                                   integral := 0;
1546:                                   for j := 1 to 5 do
1547:                                           begin
1548:                                           dx := 0.5*gauss_x[j];
1549:                                           integral := integral + g↩
⇒    auss_w[j]*k0*exp(-1*sqr(x+dx-k1)/k2) + gauss_w[j]*k↩
```

```
⇒    0*exp(-1*sqr(x-dx-k1)/k2)
1550:                                          end;
1551:                                integral := integral*0.5;
1552:                                if (integral > analysis_array2[1↩
⇒    ,x-inf+zone+1] + 4*analysis_array2[2,x-inf+zone+1])↩
⇒     or (integral < analysis_array2[1,x-inf+zone+1] - 4↩
⇒    *analysis_array2[2,x-inf+zone+1]) then fit := false↩
⇒    ;
1553:                                end;
1554:                          min2 := k1;
1555:                          end;
1556:                 if (min2 > inf +zone) or (min2 < inf - zone) the↩
⇒    n fit := false;
1557:                 if fit then
1558:                          begin
1559:                          inc(sample_count2);
1560:                          sample_array[2,sample_count2] := min2;
1561:                          end;
1562:                  //if test2 then writeln(f2,',',fitqual);
1563:                 end;
1564:          //6 calculate the distribution of the minima and
1565:          //hence the rim thickness in microns
1566:          //7 output the analysis results
1567:          if sample_count1 > 0 then
1568:          begin
1569:          for x := 1 to sample_count1 do fstats1.add(sample_array↩
⇒    [1,x]);
1570:          fstats1.analyse;
1571:          datasheet.cells[3,measurement*2] := format('%3.2f',[fst↩
⇒    ats1.mean]);
1572:          datasheet.cells[4,measurement*2] := format('%3.2f',[fst↩
⇒    ats1.stdev]);
1573:          //writeln(f1,'Inflection 1');
1574:          //write(f1,fstats1.mean,',',fstats1.stdev,',',fstats1.m↩
⇒    ax,',',fstats1.min);
1575:          //if test1 then write(f2,datasheet.cells[0,2*(measureme↩
⇒    nt-1)+1],',',total_count,',',fstats1.mean,',',fstat↩
⇒    s1.stdev);
1576:          //for x := 1 to fstats1.histogram.n_bins do write(f1,',↩
⇒    ',fstats1.histogram.bin[x-1]);
1577:          //writeln(f1);
1578:          //write(f1,',',',',',',');
1579:          //for x := 1 to fstats1.histogram.n_bins do write(f1,',↩
⇒    ',fstats1.histogram.hist_start + fstats1.histogram.↩
⇒    bin_width/2 + (x-1)*fstats1.histogram.bin_width);
1580:          //writeln(f1);
1581:          end
```

```
1582:          else
1583:          begin
1584:          if test1 then write(f2,datasheet.cells[0,2*(measurement↩
⇛    -1)+1],',',total_count,',',',');
1585:          end;
1586:          if sample_count2 > 0 then
1587:          begin
1588:          for x := 1 to sample_count2 do fstats2.add(sample_array↩
⇛    [2,x]);
1589:          fstats2.analyse;
1590:          datasheet.cells[5,measurement*2] := format('%3.2f',[fst↩
⇛    ats2.mean]);
1591:          datasheet.cells[6,measurement*2] := format('%3.2f',[fst↩
⇛    ats2.stdev]);
1592:          //writeln(f1,'Inflection 2');
1593:          //write(f1,fstats2.mean,',',fstats2.stdev,',',fstats2.m↩
⇛    ax,',',fstats2.min);
1594:          //if test1 then write(f2,',',fstats2.mean,',',fstats2.s↩
⇛    tdev);
1595:          //for x := 1 to fstats2.histogram.n_bins do write(f1,',↩
⇛    ',fstats2.histogram.bin[x-1]);
1596:          //writeln(f1);
1597:          //write(f1,',',',',',',');
1598:          //for x := 1 to fstats2.histogram.n_bins do write(f1,',↩
⇛    ',fstats2.histogram.hist_start + fstats2.histogram.↩
⇛    bin_width/2 + (x-1)*fstats2.histogram.bin_width);
1599:          //writeln(f1);
1600:          end
1601:          else
1602:          begin
1603:          //if test1 then write(f2,',',',');
1604:          end;
1605:          //if test1 then writeln(f2);
1606:          for x := 1 to 50000 do
1607:                 begin
1608:                 writeln(f1,sample_array[1,x],',',sample_array[2,↩
⇛    x]);
1609:                 end;
1610:         datasheet.cells[0,measurement*2] := 'Run';
1611:         if (sample_count1 > 0) and (sample_count2 > 0) then
1612:                 begin
1613:                 datasheet.cells[1,measurement*2] := format('%3.2↩
⇛    f',[(fstats2.mean -fstats1.mean)*pixel_size]);
1614:                 datasheet.cells[2,measurement*2] := format('%3.2↩
⇛    f',[sqrt(sqr(fstats1.stdev) + sqr(fstats2.stdev))*p↩
⇛    ixel_size]);
1615:                 end;
```

```
1616:         if measurement = 1 then
1617:                 begin
1618:                 current_row := measurement*2-1;
1619:                 len := 9;
1620:                 min := 258;
1621:                 max := -1;
1622:                 while (len < 1992) and (datasheet.cells[len,curr↩
⇒    ent_row] <> '') do
1623:                         begin
1624:                         val := strtofloat(datasheet.cells[len,cu↩
⇒    rrent_row]);
1625:                         if val > max then max := val;
1626:                         if val < min then min := val;
1627:                         intensity_array[1,len-8] := val;
1628:                         val := strtofloat(datasheet.cells[len,cu↩
⇒    rrent_row+1]);
1629:                         intensity_array[2,len-8] := val;
1630:                         inc(len);
1631:                         end;
1632:                 len := len - 9;
1633:                 rchart1.rangelox := 0;
1634:                 rchart1.rangehix := len;
1635:                 rchart1.rangeloy := min - 15;
1636:                 rchart1.rangehiy := max + 5;
1637:                 rchart1.datacolor := clred;
1638:                 rchart1.cleargraf;
1639:                 if plot = simplestep then
1640:                         begin
1641:                         rchart1.moveto(0.5,intensity_array[1,1])↩
⇒    ;
1642:                         for x := 2 to len do
1643:                                 begin
1644:                                 rchart1.drawto(x-0.5,intensity_a↩
⇒    rray[1,x-1]);
1645:                                 rchart1.drawto(x-0.5,intensity_a↩
⇒    rray[1,x]);
1646:                                 end;
1647:                         end
1648:                 else if plot = box then
1649:                         begin
1650:                         for x := 1 to len do
1651:                                 begin
1652:                                 rchart1.moveto(x-0.5,intensity_a↩
⇒    rray[1,x]-2*intensity_array[2,x]);
1653:                                 rchart1.drawto(x-0.5,intensity_a↩
⇒    rray[1,x]+2*intensity_array[2,x]);
1654:                                 rchart1.drawto(x+0.5,intensity_a↩
```

```
⇒    rray[1,x]+2*intensity_array[2,x]);
1655:                                rchart1.drawto(x+0.5,intensity_a↩
⇒    rray[1,x]-2*intensity_array[2,x]);
1656:                                rchart1.drawto(x-0.5,intensity_a↩
⇒    rray[1,x]-2*intensity_array[2,x]);
1657:                                end;
1658:                        end
1659:                else if plot = whiskers then
1660:                        begin
1661:                        for x := 1 to len do
1662:                                begin
1663:                                rchart1.moveto(x-0.5,intensity_a↩
⇒    rray[1,x]-1*intensity_array[2,x]);
1664:                                rchart1.drawto(x-0.5,intensity_a↩
⇒    rray[1,x]+1*intensity_array[2,x]);
1665:                                rchart1.drawto(x+0.5,intensity_a↩
⇒    rray[1,x]+1*intensity_array[2,x]);
1666:                                rchart1.drawto(x+0.5,intensity_a↩
⇒    rray[1,x]-1*intensity_array[2,x]);
1667:                                rchart1.drawto(x-0.5,intensity_a↩
⇒    rray[1,x]-1*intensity_array[2,x]);
1668:                                rchart1.moveto(x,intensity_array↩
⇒    [1,x]-2*intensity_array[2,x]);
1669:                                rchart1.drawto(x,intensity_array↩
⇒    [1,x]-intensity_array[2,x]);
1670:                                rchart1.moveto(x,intensity_array↩
⇒    [1,x] +intensity_array[2,x]);
1671:                                rchart1.drawto(x,intensity_array↩
⇒    [1,x] +2*intensity_array[2,x]);
1672:                                end
1673:                        end;
1674:                //now plot the distributions
1675:                dx := rchart1.rangehix/600;
1676:                z := rchart1.RangeLoY;
1677:                if sample_count1 > 0 then
1678:                begin
1679:                rchart1.moveto(0,z+1/(fstats1.stdev*sqrt(2*3.141↩
⇒    592))*exp((-1/2)*sqr((0-fstats1.mean)/fstats1.stdev↩
⇒    )));
1680:                for x := 0 to 600 do
1681:                        begin
1682:                        rchart1.drawto(x*dx,z+10*exp((-1/2)*sqr(↩
⇒    (dx*x-fstats1.mean)/fstats1.stdev)));
1683:                        end;
1684:                end;
1685:                if sample_count2 > 0 then
1686:                begin
```

```
1687:                 rchart1.moveto(0,z+1/(fstats2.stdev*sqrt(2*3.141↩
⇛    592))*exp((-1/2)*sqr((0-fstats2.mean)/fstats2.stdev↩
⇛    )));
1688:                 for x := 0 to 600 do
1689:                         begin
1690:                         rchart1.drawto(x*dx,z+10*exp((-1/2)*sqr(↩
⇛    (dx*x-fstats2.mean)/fstats2.stdev)));
1691:                         end;
1692:                 end;
1693:                 end;
1694:                 rchart1.showgraf;
1695:
1696:         fstats1.clear;
1697:         fstats2.clear;
1698: //        end;
1699: //        end;
1700:         end;
1701: fstats1.free;
1702: fstats2.Free;
1703: closefile(f1);
1704: //if (test1) or (test2) then closefile(f2);
1705: progressbar1.Position := 0;
1706: histfrm.Caption := 'Rim Buster';
1707: end;
1708:
1709:
1710: procedure THISTFRM.SimpleStep1Click(Sender: TObject);
1711: begin
1712: simplestep1.checked := true;
1713: box1.checked := false;
1714: whiskers1.checked := false;
1715: plot := simplestep;
1716: end;
1717:
1718: procedure THISTFRM.Box1Click(Sender: TObject);
1719: begin
1720: simplestep1.checked := false;
1721: box1.checked := true;
1722: whiskers1.checked := false;
1723: plot := box;
1724: end;
1725:
1726: procedure THISTFRM.Whiskers1Click(Sender: TObject);
1727: begin
1728: simplestep1.checked := false;
1729: box1.checked := false;
1730: whiskers1.checked := true;
```

```
1731: plot := whiskers;
1732: end;
1733:
1734: procedure THISTFRM.cubic1Click(Sender: TObject);
1735: begin
1736: model := cubic;
1737: cubic1.Checked := true;
1738: quadratic1.Checked := false;
1739: gaussian1.checked := false;
1740: end;
1741:
1742: procedure THISTFRM.quadratic1Click(Sender: TObject);
1743: begin
1744: model := quadratic;
1745: cubic1.Checked := false;
1746: quadratic1.Checked := true;
1747: gaussian1.checked := false;
1748: end;
1749:
1750: procedure THISTFRM.gaussian1Click(Sender: TObject);
1751: begin
1752: model := gaussian;
1753: cubic1.Checked := false;
1754: quadratic1.Checked := false;
1755: gaussian1.checked := true;
1756: end;
1757:
1758: procedure THISTFRM.PasteData1Click(Sender: TObject);
1759: var
1760:         x : integer;
1761: begin
1762: datasheet.Delimiter := ',';
1763: if opendialog1.execute then
1764:         begin
1765:         datasheet.LoadFromCSV(opendialog1.filename);
1766:         x := 1;
1767:         while datasheet.cells[9,2*(x-1)+1] <> '' do inc(x);
1768:         histfrm.data_count := x-1;
1769:         end;
1770: end;
1771:
1772: procedure THISTFRM.pixelsize1Click(Sender: TObject);
1773: begin
1774: form1.pixsize.value := pixel_size;
1775: form1.showmodal;
1776: end;
1777:
```

```
1778: end.
```

A.2.3 image.pas

```
  1: unit image;
  2:
  3: interface
  4:
  5: uses
  6:   Windows, Messages, SysUtils, Classes, Graphics, Controls, Forms↩
⇛    , Dialogs,
  7:   ExtCtrls, Menus, mathsutils, StdCtrls, ComCtrls, Buttons, FileC↩
⇛    trl;
  8:
  9: type
 10:   TDrawingTool = (dtRectangle, dtanrect);
 11:   Tstretch = (stfull, stupper);
 12:
 13:
 14:   Timageform = class(TForm)
 15:     ScrollBox1: TScrollBox;
 16:     Image1: TImage;
 17:     MainMenu: TMainMenu;
 18:     FileMenu: TMenuItem;
 19:     Close3: TMenuItem;
 20:     Open2: TMenuItem;
 21:     Tools1: TMenuItem;
 22:     Image2: TImage;
 23:     SaveDialog: TSaveDialog;
 24:     analyse1: TMenuItem;
 25:     Edit2: TEdit;
 26:     Edit3: TEdit;
 27:     Panel1: TPanel;
 28:     ScrollBar1: TScrollBar;
 29:     background: TImage;
 30:     loadbackground1: TMenuItem;
 31:     removebackground1: TMenuItem;
 32:     OpenDialog1: TOpenDialog;
 33:     BitBtn1: TBitBtn;
 34:     ScrollBar2: TScrollBar;
 35:     TrackBar1: TTrackBar;
 36:     TrackBar2: TTrackBar;
 37:     StaticText1: TStaticText;
 38:     StatusBar1: TStatusBar;
```

```
 39:     BitBtn2: TBitBtn;
 40:     N1: TMenuItem;
 41:     FileListBox1: TFileListBox;
 42:     averageimage1: TMenuItem;
 43:     procedure FormClose(Sender: TObject; var Action: TCloseAction↩
⇛    );
 44:     procedure Exit1Click(Sender: TObject);
 45:     procedure Close3Click(Sender: TObject);
 46:     procedure FormMouseDown(Sender: TObject; Button: TMouseButton↩
⇛    ;
 47:       Shift: TShiftState; X, Y: Integer);
 48:     procedure FormMouseUp(Sender: TObject; Button: TMouseButton;
 49:       Shift: TShiftState; X, Y: Integer);
 50:     procedure FormMouseMove(Sender: TObject; Shift: TShiftState; ↩
⇛    X,
 51:       Y: Integer);
 52:     procedure Save2Click(Sender: TObject);
 53:     procedure Open2Click(Sender: TObject);
 54:     procedure SaveAs2Click(Sender: TObject);
 55:     procedure In1Click(Sender: TObject);
 56:     procedure Out1Click(Sender: TObject);
 57:     procedure Analyse(Sender: TObject);
 58:     procedure UpDown1Click(Sender: TObject; Button: TUDBtnType);
 59:     procedure ScrollBar1Change(Sender: TObject);
 60:     procedure loadbackground1Click(Sender: TObject);
 61:     procedure removebackground1Click(Sender: TObject);
 62:     procedure BitBtn1Click(Sender: TObject);
 63:     procedure ScrollBar2Change(Sender: TObject);
 64:     procedure TrackBar2Change(Sender: TObject);
 65:     procedure count1Click(Sender: TObject);
 66:     procedure BitBtn2Click(Sender: TObject);
 67:     procedure average;
 68:     procedure averageimage1Click(Sender: TObject);
 69:   private
 70:      Private declarations
 71:     PathName: string;
 72:   public
 73:      Public declarations
 74:     zoomp, zoomm : boolean;
 75:         Drawing, con: Boolean;
 76:     REC : BOOLEAN;
 77:     MOVING, line, lf, rt, transfered: BOOLEAN;
 78:     background_intensity : integer;
 79:     zoomf : single;
 80:     LEN, analysis_height, move,lpos,rpos: INTEGER;
 81:     lorigin, rorigin, Origin, MovePt, pt, rect_end: TPoint;
 82:     lmovepoint, rmovepoint, con_origin, con_move, con_end: tpoint↩
```

```
⇒    ;
 83:     DrawingTool: TDrawingTool;
 84:     stretch: tstretch;
 85:     currentval : integer;
 86:   count_index : integer;
 87:     workarray: array[1..400,1..100] of single;
 88:     greyscale: array[0..255] of longint;
 89:     transform: array[0..255] of longint;
 90:     procedure Open(const AFileName: string);
 91:      procedure edge_smooth;
 92:     procedure DrawShape(TopLeft, BottomRight: TPoint; AMode: TPen↩
⇒    Mode);
 93:     procedure flusharray;
 94:      function GS_intensity(x,y:integer): integer;
 95:
 96:   end;
 97:
 98: var
 99:   imageform: Timageform;
100:
101:
102: const
103:   DefaultFileName = 'Untitled';
104:   crmagplus = 5;
105:
106: implementation
107:
108: uses Clipbrd, Printers, main, Graph;
109:
110: $R *.DFM
111:
112: procedure Timageform.FormClose(Sender: TObject; var Action: TClos↩
⇒    eAction);
113: var
114:         x,y : integer;
115: begin
116: for x := 1 to histfrm.data_count do
117:         begin
118:         y := strtoint(histfrm.datasheet.cells[1,(x*2)-1]);
119:         if y = count_index then histfrm.datasheet.cells[1,(x*2)-1↩
⇒    ] := ''
120:         else if y > count_index then histfrm.datasheet.cells[1,(x↩
⇒    *2)-1] := inttostr(y-1);
121:         end;
122: for x := count_index to image_count -1 do
123:         begin
124:         image_list[x] := image_list[x+1];
```

```
125:         timageform(image_list[x]).count_index := x;
126:         end;
127: //image_list[image_count] := nil;
128: image_count := image_count-1;
129: frameform.tileimages1Click(self);
130: Action := caFree;
131: end;
132:
133: procedure Timageform.Exit1Click(Sender: TObject);
134: begin
135: FrameForm.fileExit(Sender);
136: end;
137:
138:
139: procedure Timageform.Close3Click(Sender: TObject);
140: var
141:         x : integer;
142: begin
143:
144: close;
145: end;
146:
147: procedure TimageForm.Open(const AFileName: string);
148: begin
149:   PathName := AFileName;
150:   Caption := ExtractFileName(AFileName);
151:   image2.picture.loadfromfile(afilename);
152:   image1.picture := image2.picture;
153:   with imagewindow do
154:   begin
155:   imagename := afilename;
156:   copytoclipboard;
157:   end;
158:   paste;
159:
160: end;
161:
162: procedure timageform.edge_smooth;
163: var
164:    x,y,z: integer;
165:    sum: single;
166: begin
167: sum :=0;
168: for x := 1 to len do
169: begin
170:
171:      for y := 1 to (analysis_height) do
```

```
172:      begin
173:           for z:= (y) to (y) do
174:           begin
175:                sum := sum + workarray[x,z];
176:           end;
177:           sum := 0;
178:      end;
179: end;
180: for x := 1 to (analysis_height) do
181: end;
182:
183: procedure Timageform.DrawShape(TopLeft, BottomRight: TPoint; AMod↩
⇒    e: TPenMode);
184: begin
185:   with Image1.Canvas do
186:   begin
187:     PEN.WIDTH := 2;
188:     PEN.COLOR := CLRED;
189:     PEN.STYLE := PSDASH;
190:     Pen.Mode := AMode;
191:     BRUSH.STYLE := BSCLEAR;
192:     Rectangle(TopLeft.X, TopLeft.Y, BottomRight.X, BottomRight.Y)↩
⇒    ;
193:
194:  end;
195: end;
196:
197: procedure timageform.flusharray;
198: var
199:    x, y: integer;
200: begin
201:      for x := 1 to 100 do
202:      begin
203:           for y := 1 to 100 do
204:           begin
205:                workarray[x,y] :=0;
206:           end;
207:      end;
208: end;
209:
210: function Timageform.GS_intensity(x,y: integer):integer;
211: var
212:    val: longint;
213:
214: begin
215: val := colortorgb(image2.canvas.pixels[x,y]);
216: GS_intensity := val - (val div 256)*256;
```

```
217: end;
218:
219: procedure Timageform.FormMouseDown(Sender: TObject; Button: TMous↩
⇒    eButton;
220:   Shift: TShiftState; X, Y: Integer);
221: begin
222: IF BUTTON = MBRIGHT THEN
223:    BEGIN
224:
225:         IMAGE1.PICTURE := IMAGE2.PICTURE;
226:         REC := FALSE;
227:         con := false;
228:         DRAWING := FALSE;
229:    END
230: ELSE
231:   begin
232:   if  drawingtool = dtrectangle then
233:   begin
234:      Drawing := True;
235:      Image1.Canvas.MoveTo(X, Y);
236:      IF (REC = FALSE) or (zoomf > 1) THEN
237:         BEGIN
238:         Origin := Point(X, Y);
239:         MovePt := Origin;
240:         REC := TRUE;
241:         END
242:      ELSE
243:          BEGIN
244:          IMAGE1.PICTURE := IMAGE2.PICTURE;
245:          movept := point(x,y);
246:          DrawShape(Origin, movept, pmnotxor);
247:
248:          END;
249:   END
250:      else
251:         begin
252:         Drawing := True;
253:         if con then
254:            DRAWSHAPE(con_ORIGIN, Con_end, PMNOTXOR);
255:         Image1.Canvas.MoveTo(X, Y);
256:         con_origin := point(x,y);
257:         con_move := con_origin;
258:         end;
259:  end;
260: end;
261:
262: procedure Timageform.FormMouseUp(Sender: TObject; Button: TMouseB↩
```

```
⇒    utton;
263:   Shift: TShiftState; X, Y: Integer);
264: var
265:    zoomx, zoomy : single;
266: begin
267: rect_end := point(x,y);
268: if zoomp = true then
269:    begin
270:    zoomx := image1.width / abs(x - origin.x);
271:    zoomy := image1.height / abs(y - origin.y);
272:    zoomf := zoomx;
273:    DrawShape(Origin, Point(X, Y), pmnotxor);
274:    if zoomy < zoomx then zoomf := zoomy;
275:    image1.height := trunc(image1.height * zoomf);
276:    image1.width := trunc(image1.width * zoomf);
277:    zoomp := false;
278:    image1.cursor := crcross;
279:    rec := false;
280:    end
281: else if (Drawing = true) AND (MOVING = true) and (zoomp = false) ↩
⇒    then
282:     BEGIN
283:     if drawingtool = dtanrect then
284:        begin
285:             DrawShape(con_origin, Point(X, Y), pmnotxor);
286:             con := true;
287:             con_end := point(x,y);
288:             edit3.text := inttostr(con_end.x);
289:        end
290:     else
291:         begin
292:             DrawShape(Origin, Point(X, Y), pmCOPY);
293:
294:             pt := point(x, y);
295:             LEN := ABS(ORIGIN.X - PT.X);
296:             analysis_HEIGHT := ABS(ORIGIN.Y-PT.Y);
297:
298:         end;
299:     end;
300:   Drawing := False;
301:   MOVING := FALSE;
302: end;
303:
304: procedure Timageform.FormMouseMove(Sender: TObject; Shift: TShift↩
⇒    State; X,
305:   Y: Integer);
306: var
```

```
307:    start, now: tpoint;
308: begin
309:   if Drawing then
310:   begin
311:     if drawingtool = dtrectangle then
312:        begin
313:             start := origin;
314:             now := movept;
315:        end
316:     else
317:         begin
318:              start := con_origin;
319:              now := con_move;
320:         end;
321:
322:    MOVING := TRUE;
323:     DrawShape(start, now, pmnotxor);
324:
325:     if drawingtool = dtrectangle then
326:        begin
327:             MovePt := Point(X, Y);
328:             DrawShape(start, movept, pmnotxor);
329:
330:        end
331:     else
332:         begin
333:              con_move := point(x,y);
334:              DrawShape(start, con_move, pmNOTXOR);
335:         end;
336:
337:   end;
338:
339: end;
340:
341:
342: procedure Timageform.Save2Click(Sender: TObject);
343: var
344: exten : string;
345: begin
346:   if PathName = DefaultFileName then
347:     SaveAs2Click(Sender)
348:   else
349:   begin
350:   exten := extractfileext(pathname);
351:   if exten = '.BMP' then
352:    Begin
353:    imagewindow.imageinwindow.saveas(pathname,lli_disk_bmp,lli_dis↩
```

```
⇒    k_compress_auto);
354:    end
355:    else if exten = '.JPG' then
356:    begin
357:    imagewindow.imageinwindow.saveas(pathname,lli_disk_jpg,lli_dis↩
⇒    k_compress_auto);
358:    end;
359:   end;
360: end;
361:
362: procedure Timageform.Open2Click(Sender: TObject);
363: begin
364: FrameForm.fileOpen(Sender);
365: end;
366:
367: procedure Timageform.SaveAs2Click(Sender: TObject);
368: var
369: exten, temp : string;
370: xpos : variant;
371: begin
372:   SaveDialog.FileName := PathName;
373:   if SaveDialog.Execute then
374:   begin
375:     PathName := SaveDialog.FileName;
376:     temp := pathname;
377:     exten := extractfileext(pathname);
378:     if exten = '' then
379:        begin
380:        case savedialog.filterindex of
381:        1:  exten := '.BMP';
382:        2:  exten := '.JPG';
383:        end;
384:        pathname := pathname + exten;
385:        end
386:      else if exten = '.BMP' then
387:           begin
388:           case savedialog.filterindex of
389:           2:
390:           begin
391:            MessageDlg('You have tried to save a jpeg with a .bmp ↩
⇒    extension',
392:            mtInformation, [mbok], 0);
393:            exit;
394:           end;
395:           end;
396:           end
397:      else if exten = '.JPG' then
```

```
398:           begin
399:           case savedialog.filterindex of
400:           1:
401:           begin
402:            MessageDlg('You have tried to save a bitmap with a .jp↩
⇒    g extension',
403:            mtInformation, [mbok], 0);
404:            exit;
405:
406:           end;
407:           end;
408:           end;
409:     Caption := ExtractFileName(PathName);
410:     Save2Click(Sender);
411:   end;
412: end;
413:
414: procedure Timageform.In1Click(Sender: TObject);
415: begin
416: image1.cursor := crmagplus;
417: zoomp := true;
418:
419: end;
420:
421: procedure Timageform.Out1Click(Sender: TObject);
422: begin
423: if zoomf > 1 then
424:    begin
425:    image1.width := trunc(image1.width / zoomf);
426:    image1.height := trunc(image1.height / zoomf);
427:    zoomf := 1;
428:    end
429: end;
430:
431: procedure Timageform.Analyse(Sender: TObject);
432: var
433:    X,Y,z,count,xx: integer;
434:    intensity, max, min, gs_int, gs_se, dummy: single;
435:    se : double;
436:    str1 : string;
437: begin
438: inc(histfrm.data_count);
439: histfrm.current_data := histfrm.data_count;
440: histfrm.statusbar1.panels.items[1].text := '';
441: histfrm.statusbar1.panels.items[3].text := '';
442: histfrm.tx := origin.x;
443: histfrm.ty := origin.y;
```

```
444: histfrm.bx := rect_end.x;
445: histfrm.by := rect_end.y;
446: histfrm.image_file := pathname;
447: str1 := caption;
448: delete(str1,length(str1)-3,4);
449: histfrm.datasheet.cells[0,(histfrm.data_count*2) -1] := str1;
450: histfrm.datasheet.cells[1,(histfrm.data_count*2) -1] := inttostr(↩
⇒    count_index);
451: histfrm.datasheet.cells[7,(histfrm.data_count*2) -1] := '(' + int↩
⇒    tostr(origin.x) + ',' + inttostr(origin.y) + ')';
452: histfrm.datasheet.cells[8,(histfrm.data_count*2) -1] := '(' + int↩
⇒    tostr(rect_end.x) + ',' + inttostr(rect_end.y) + ')↩
⇒    ';
453: histfrm.image_length := len;
454: histfrm.image_height := analysis_height;
455: z := 0;
456: gs_int := 0;
457: X := ORIGIN.X;
458: Y := ORIGiN.Y;
459: flusharray;
460: max := 0;
461: min := 10000000;
462: while z < LEN do
463: begin
464: intensity := 0;
465: se := 0;
466: for count := 1 to analysis_height do
467:     begin
468:     xx := y+count;
469:     dummy := GS_intensity((x+z),xx);
470:     intensity := intensity + dummy;
471:     se := se + intpower(dummy,2);
472:     end;
473: se := sqrt((se-((intensity*intensity)/analysis_height))/((analysi↩
⇒    s_height-1)));
474: intensity := intensity/analysis_height;
475: histfrm.datasheet.cells[(z+9),(histfrm.data_count*2) -1] := float↩
⇒    tostr(intensity);
476: histfrm.datasheet.cells[(z+9),histfrm.data_count*2] := floattostr↩
⇒    (se);
477: if intensity >= max then
478:    max := intensity + 10;
479: if intensity <= min then
480:    min := intensity - 10;
481: intensity_array[1,z+1] := intensity;
482: intensity_array[2,z+1] := se;
483: inc(z);
```

```
484: end;
485: with histfrm do
486: begin
487: rchart1.rangelox := 0;
488: rchart1.rangehix := len;
489: rchart1.rangeloy := min - 10;
490: rchart1.rangehiy := max + 10;
491: rchart1.datacolor := clred;
492: rchart1.cleargraf;
493: if plot = simplestep then
494:         begin
495:         rchart1.moveto(0.5,intensity_array[1,1]);
496:         for x := 2 to len do
497:                 begin
498:                 rchart1.drawto(x-0.5,intensity_array[1,x-1]);
499:                 rchart1.drawto(x-0.5,intensity_array[1,x]);
500:                 end;
501:         end
502: else if plot = box then
503:         begin
504:         for x := 1 to len do
505:                 begin
506:                 rchart1.moveto(x-0.5,intensity_array[1,x]-2*inten↩
⇛    sity_array[2,x]);
507:                 rchart1.drawto(x-0.5,intensity_array[1,x]+2*inten↩
⇛    sity_array[2,x]);
508:                 rchart1.drawto(x+0.5,intensity_array[1,x]+2*inten↩
⇛    sity_array[2,x]);
509:                 rchart1.drawto(x+0.5,intensity_array[1,x]-2*inten↩
⇛    sity_array[2,x]);
510:                 rchart1.drawto(x-0.5,intensity_array[1,x]-2*inten↩
⇛    sity_array[2,x]);
511:                 end;
512:         end
513: else if plot = whiskers then
514:         begin
515:         for x := 1 to len do
516:                 begin
517:                 rchart1.moveto(x-0.5,intensity_array[1,x]-1*inten↩
⇛    sity_array[2,x]);
518:                 rchart1.drawto(x-0.5,intensity_array[1,x]+1*inten↩
⇛    sity_array[2,x]);
519:                 rchart1.drawto(x+0.5,intensity_array[1,x]+1*inten↩
⇛    sity_array[2,x]);
520:                 rchart1.drawto(x+0.5,intensity_array[1,x]-1*inten↩
⇛    sity_array[2,x]);
521:                 rchart1.drawto(x-0.5,intensity_array[1,x]-1*inten↩
```

```
⇒    sity_array[2,x]);
522:                 rchart1.moveto(x,intensity_array[1,x]-2*intensity↩
⇒    _array[2,x]);
523:                 rchart1.drawto(x,intensity_array[1,x]-intensity_a↩
⇒    rray[2,x]);
524:                 rchart1.moveto(x,intensity_array[1,x] +intensity_↩
⇒    array[2,x]);
525:                 rchart1.drawto(x,intensity_array[1,x] +2*intensit↩
⇒    y_array[2,x]);
526:                 end
527:         end;
528: rchart1.showgraf;
529: end;
530: histfrm.visible := true;
531: if (lf) and (rt) then
532: begin
533: lpos := lpos - x;
534: rpos := rpos - x;
535: min := 256;
536:      for x := (lpos - 4) to (lpos + 4) do
537:          begin
538:                if strtofloat(gridfrm.stringgrid1.cells[1,x]) <= m↩
⇒    in then
539:                   gridfrm.edit1.text := inttostr(x);
540:          end;
541:
542:      min := 256;
543:      for x := (rpos - 4) to (rpos + 4) do
544:          begin
545:               if strtofloat(gridfrm.stringgrid1.cells[1,x]) < min↩
⇒     then
546:               gridfrm.edit2.text := inttostr(x);
547:          end;
548:
549:      gridfrm.speedbutton1.click;
550:     end;
551: IMAGE1.PICTURE := IMAGE2.PICTURE;
552: REC := FALSE;
553: con := false;
554: DRAWING := FALSE;
555: end;
556:
557:
558: procedure Timageform.UpDown1Click(Sender: TObject; Button: TUDBtn↩
⇒    Type);
559: var
560:   x,y, bs, bpsl, delta : integer;
```

```
561:   BitMap : TBitMap;
562:   P : pbytearray;
563: begin
564: if button = btprev then
565: delta := -1
566: else
567: delta := 1;
568:
569:   BitMap := TBitMap.create;
570:   try
571:
572:
573:     BitMap.assign(image1.picture.bitmap);
574:     if bitmap.pixelformat = pf1bit then
575:     bs := 1
576:     else if bitmap.pixelformat = pf4bit then
577:     bs := 4
578:     else if bitmap.pixelformat = pf8bit then
579:     bs := 8
580:     else if bitmap.pixelformat = pf15bit then
581:     bs := 15
582:     else if bitmap.pixelformat = pf16bit then
583:     bs := 16
584:     else if bitmap.pixelformat = pf24bit then
585:     bs := 24
586:     else if bitmap.pixelformat = pf32bit then
587:     bs := 32;
588:     bpsl := (bitmap.width * bs)div 8;
589:         for y := 0 to BitMap.height -1 do
590:     begin
591:       P := BitMap.ScanLine[y];
592:
593:       for x := 0 to bpsl-1 do
594:           begin
595:           if (p[x]+delta) > 255 then p[x] := 255
596:           else if (p[x] + delta) < 0 then p[x] := 0
597:           else P[x] := p[x]+ delta;
598:         end;
599:     end;
600:   image1.canvas.draw(0,0,BitMap);
601:   finally
602:     BitMap.free;
603:   end;
604:  end;
605:
606: procedure Timageform.ScrollBar1Change(Sender: TObject);
607: var
```

```
608:   x,y, bs, bpsl, delta : integer;
609:   BitMap : TBitMap;
610:   P, pi : pbytearray;
611: begin
612: delta := scrollbar1.position;
613:
614:   BitMap := TBitMap.create;
615:   try
616:
617:
618:     BitMap.assign(image1.picture.bitmap);
619:     if bitmap.pixelformat = pf1bit then
620:     bs := 1
621:     else if bitmap.pixelformat = pf4bit then
622:     bs := 4
623:     else if bitmap.pixelformat = pf8bit then
624:     bs := 8
625:     else if bitmap.pixelformat = pf15bit then
626:     bs := 15
627:     else if bitmap.pixelformat = pf16bit then
628:     bs := 16
629:     else if bitmap.pixelformat = pf24bit then
630:     bs := 24
631:     else if bitmap.pixelformat = pf32bit then
632:     bs := 32;
633:     bpsl := (bitmap.width * bs)div 8;
634:         for y := 0 to BitMap.height -1 do
635:     begin
636:       P := BitMap.ScanLine[y];
637:       pi := image2.Picture.Bitmap.scanline[y];
638:       for x := 0 to bpsl-1 do
639:           begin
640:           if (pi[x]-delta) > 255 then p[x] := 255
641:           else if (pi[x] - delta) < 0 then p[x] := 0
642:           else P[x] := pi[x] - delta;
643:         end;
644:     end;
645:   image1.canvas.draw(0,0,BitMap);
646:   finally
647:     BitMap.free;
648:   end;
649: currentval := scrollbar1.position;
650: end;
651:
652: procedure Timageform.loadbackground1Click(Sender: TObject);
653: begin
654: if opendialog1.execute then
```

```
655:    begin
656:    background.picture.loadfromfile(opendialog1.filename);
657:    end;
658: end;
659:
660: procedure Timageform.removebackground1Click(Sender: TObject);
661: var
662:   x,y, bs, bpsl : integer;
663:   BitMap : TBitMap;
664:   P, pi, pb : pbytearray;
665:   dummy : byte;
666: begin
667:  BitMap := TBitMap.create;
668:   try
669:
670:
671:     BitMap.assign(image1.picture.bitmap);
672:     if bitmap.pixelformat = pf1bit then
673:     bs := 1
674:     else if bitmap.pixelformat = pf4bit then
675:     bs := 4
676:     else if bitmap.pixelformat = pf8bit then
677:     bs := 8
678:     else if bitmap.pixelformat = pf15bit then
679:     bs := 15
680:     else if bitmap.pixelformat = pf16bit then
681:     bs := 16
682:     else if bitmap.pixelformat = pf24bit then
683:     bs := 24
684:     else if bitmap.pixelformat = pf32bit then
685:     bs := 32;
686:     bpsl := (bitmap.width * bs)div 8;
687:         for y := 0 to BitMap.height -1 do
688:     begin
689:       P := BitMap.ScanLine[y];
690:       pi := image2.picture.bitmap.scanline[y];
691:       pb := background.Picture.bitmap.ScanLine[y];
692:
693:       for x := 0 to bpsl-1 do
694:           begin
695:           dummy := abs (pi[x]-pb[x] + 180);
696:           if dummy > 255 then dummy := 255
697:           else if dummy < 0 then dummy := 0;
698:           p[x] := dummy;
699:         end;
700:     end;
701:   image1.canvas.draw(0,0,BitMap);
```

```
702:   finally
703:     BitMap.free;
704:   end;
705: end;
706:
707: procedure Timageform.BitBtn1Click(Sender: TObject);
708: begin
709: image2.picture := image1.picture;
710: scrollbar1.position := 0;
711: scrollbar2.position := 0;
712: trackbar1.position := 255;
713: trackbar2.position := 0;
714: end;
715:
716: procedure Timageform.ScrollBar2Change(Sender: TObject);
717: var
718:   x,y, bs, bpsl, delta : integer;
719:   BitMap : TBitMap;
720:   P, pi : pbytearray;
721:   dummy : byte;
722:   st : boolean;
723: begin
724: st := false;
725: delta := scrollbar2.position;
726:
727:   BitMap := TBitMap.create;
728:   try
729:
730:
731:     BitMap.assign(image1.picture.bitmap);
732:     if bitmap.pixelformat = pf1bit then
733:     bs := 1
734:     else if bitmap.pixelformat = pf4bit then
735:     bs := 4
736:     else if bitmap.pixelformat = pf8bit then
737:     bs := 8
738:     else if bitmap.pixelformat = pf15bit then
739:     bs := 15
740:     else if bitmap.pixelformat = pf16bit then
741:     bs := 16
742:     else if bitmap.pixelformat = pf24bit then
743:     bs := 24
744:     else if bitmap.pixelformat = pf32bit then
745:     bs := 32;
746:     bpsl := (bitmap.width * bs)div 8;
747:         for y := 0 to BitMap.height -1 do
748:     begin
```

```
749:       P := BitMap.ScanLine[y];
750:       pi := image2.Picture.Bitmap.scanline[y];
751:       for x := 0 to bpsl-1 do
752:           begin
753:           if st = false then
754:              begin
755:              p[x] := pi[x];
756:              st := true;
757:              end
758:           else
759:               begin
760:               if (pi[x] > 255 - delta) then p[x] := 255
761:               else p[x] := pi[x];
762:               //else dummy := 255;
763:                end;
764:         end;
765:     end;
766:   image1.canvas.draw(0,0,BitMap);
767:   finally
768:     BitMap.free;
769:   end;
770:
771: end;
772:
773: procedure Timageform.TrackBar2Change(Sender: TObject);
774: var
775:   x,y, bs, bpsl, delta : integer;
776:   BitMap : TBitMap;
777:   P, pi : pbytearray;
778:   dummy, lower, upper, range : byte;
779: begin
780: upper := trackbar2.position;
781: lower := trackbar1.position;
782: range := lower - upper;
783:   BitMap := TBitMap.create;
784:   try
785:     BitMap.assign(image1.picture.bitmap);
786:     if bitmap.pixelformat = pf1bit then
787:     bs := 1
788:     else if bitmap.pixelformat = pf4bit then
789:     bs := 4
790:     else if bitmap.pixelformat = pf8bit then
791:     bs := 8
792:     else if bitmap.pixelformat = pf15bit then
793:     bs := 15
794:     else if bitmap.pixelformat = pf16bit then
795:     bs := 16
```

```
796:     else if bitmap.pixelformat = pf24bit then
797:     bs := 24
798:     else if bitmap.pixelformat = pf32bit then
799:     bs := 32;
800:     bpsl := (bitmap.width * bs)div 8;
801:         for y := 0 to BitMap.height -1 do
802:     begin
803:       P := BitMap.ScanLine[y];
804:       pi := image2.Picture.Bitmap.scanline[y];
805:       for x := 0 to bpsl-1 do
806:           begin
807:           if pi[x] > lower then dummy := 255
808:           else if pi[x] < upper then dummy := 255
809:           else dummy := 255*(pi[x] - upper) div range;
810:           P[x] := dummy;
811:         end;
812:     end;
813:   image1.canvas.draw(0,0,BitMap);
814:   finally
815:     BitMap.free;
816:   end;
817:
818: end;
819:
820: procedure Timageform.count1Click(Sender: TObject);
821: var
822:   x,y, bs, bpsl, delta, count : integer;
823:   BitMap : TBitMap;
824:   P, pi : pbytearray;
825:   dummy, lower, upper, range : byte;
826:   perc : single;
827: begin
828:   count := 0;
829:   BitMap := TBitMap.create;
830:   try
831:     BitMap.assign(image1.picture.bitmap);
832:     if bitmap.pixelformat = pf1bit then
833:     bs := 1
834:     else if bitmap.pixelformat = pf4bit then
835:     bs := 4
836:     else if bitmap.pixelformat = pf8bit then
837:     bs := 8
838:     else if bitmap.pixelformat = pf15bit then
839:     bs := 15
840:     else if bitmap.pixelformat = pf16bit then
841:     bs := 16
842:     else if bitmap.pixelformat = pf24bit then
```

```
843:     bs := 24
844:     else if bitmap.pixelformat = pf32bit then
845:     bs := 32;
846:     bpsl := (bitmap.width * bs)div 8;
847:         for y := 0 to BitMap.height -1 do
848:     begin
849:       P := BitMap.ScanLine[y];
850:       for x := 0 to bpsl-1 do
851:           begin
852:           if p[x] = 255 then count := count + 1 ;
853:           end;
854:     end;
855:   image1.canvas.draw(0,0,BitMap);
856:   perc := count / (bitmap.height*bpsl);
857:   finally
858:     BitMap.free;
859:   end;
860: statusbar1.Panels[0].text := 'count := ' + floattostr(perc) + ' %↩
⇒    ';
861: end;
862:
863: procedure Timageform.BitBtn2Click(Sender: TObject);
864: begin
865: image1.picture := image2.Picture;
866: scrollbar1.position := 0;
867: scrollbar2.position := 0;
868: trackbar1.position := 255;
869: trackbar2.position := 0;
870: end;
871:
872: procedure Timageform.average;
873: var
874:         dir : string;
875:         image,image_count, x,y, bs, bpsl : integer;
876:         BitMap : TBitMap;
877:         P, pi, pb : pbytearray;
878:         dummy : byte;
879:         image_array : array[0..8000,0..2000] of single;
880: begin
881: BitMap := TBitMap.create;
882: BitMap.assign(image1.picture.bitmap);
883:         if bitmap.pixelformat = pf1bit then
884:                 bs := 1
885:         else if bitmap.pixelformat = pf4bit then
886:             bs := 4
887:         else if bitmap.pixelformat = pf8bit then
888:             bs := 8
```

```
889:         else if bitmap.pixelformat = pf15bit then
890:             bs := 15
891:         else if bitmap.pixelformat = pf16bit then
892:             bs := 16
893:         else if bitmap.pixelformat = pf24bit then
894:             bs := 24
895:         else if bitmap.pixelformat = pf32bit then
896:             bs := 32;
897:         bpsl := (bitmap.width * bs)div 8;
898: filelistbox1.Directory :=  extractfiledir(pathname);
899: for y := 0 to BitMap.height -1 do
900:                 begin
901:                 P := BitMap.ScanLine[y];
902:                 for x := 0 to bpsl-1 do
903:                         begin
904:                         p[x] := 0;
905:                         end;
906:                 end;
907: image_count := filelistbox1.Items.Count;
908: for image := 0 to image_count-1 do
909:         begin
910:         dir := filelistbox1.Items[x];
911:         image2.picture.loadfromfile(dir);
912:         for y := 0 to BitMap.height -1 do
913:                 begin
914:                 P := BitMap.ScanLine[y];
915:                 pi := image2.picture.bitmap.scanline[y];
916:                 for x := 0 to bpsl-1 do
917:                         begin
918:                         image_array[x,y] := image_array[x,y] + pi↩
⇒    [x]/image_count;
919:                         end;
920:                 end;
921: for y := 0 to BitMap.height -1 do
922:                 begin
923:                 P := BitMap.ScanLine[y];
924:                 for x := 0 to bpsl-1 do
925:                         begin
926:                         p[x] := round(image_array[x,y]);
927:                         end;
928:                 end;
929:         image1.canvas.draw(0,0,BitMap);
930:         image2.canvas.draw(0,0,bitmap);
931:         end;
932: BitMap.free;
933:   end;
934:
```

```
935: procedure Timageform.averageimage1Click(Sender: TObject);
936: begin
937: average;
938: end;
939:
940: end.
```

Appendix B

New Zealand obsidian Data

B.1 Previously Identified Source Descriptions

Table B.1: Bibliographic References

Par	Notes
	Mayor Island
SOURCE LOCATION	Mayor Island
Map Reference	U12 - 13
Easting	2799000
Northing	6430000
Transmitted Colour	Honey, minor green-grey, green, olive green, clear yellowish-green,clear bottle green, yellow, green-black, grey, brown and black
Colour Notes	
Primary Reference	Armitage *et al.* 1972; Bird *et al.* 1981; Bollong 1983; Brothers 1957; Buck *et al.* 1981*b*; Buck 1985; Duerden *et al.* 1987; Ewart *et al.* 1968; Gold-Smith 1884; Green 1962; Duerden *et al.* 1987; Holroyd 1993; Leach 1977; Leach and Manly 1982; Leach *et al.* 1978*a*; Leach and Warren 1981; Leach 1996; Moore 1988; Neve *et al.* 1994; Pos 1961; 1965; Smith *et al.* 1977; Ward 1972; 1973; 1974*b*;*c*
Archaeological Reference	Anderson and McFadgen 1990; Armitage *et al.* 1972; Brassey 1985; Brassey and Seelenfreund 1984; Fox 1982; Fredricksen 1991; Green 1964; Harsant 1985; Leach 1973; 1977; Leach *et al.* 1986*b*; Leach and de Souza 1979; Leach and Manly 1982; Moore 1988; Reeves and Armitage 1973*b*; Ruddock 1988; Seelenfreund 1983; 1985; Seelenfreund and Bollong 1990; Ward 1974*b*
SOURCE LOCATION	Halls Pass (Aka: Ruru Pass)
Map Reference	U12 - 13
Easting	2799600
Northing	6429100
Transmitted Colour	
Colour Notes	black
Primary Reference	Holroyd 1993; Neve *et al.* 1994; Seelenfreund 1985
Archaeological Reference	
SOURCE LOCATION	Oira Bay - north (Aka: Oira Bay)
Map Reference	U12 - 13
Easting	2797200
Northing	6429400
Transmitted Colour	black through tan
Colour Notes	
Primary Reference	Ewart *et al.* 1968; Duerden *et al.* 1987; Holroyd 1993; Houghton *et al.* 1992; Neve *et al.* 1994; Pos 1965; Seelenfreund 1985; Ward 1972; 1973

continued on the next page ...

. . . continued from table D.1

Par	Notes
Archaeological Reference	
SOURCE LOCATION	Oira Bay - south (Aka: North West Bay, Te Raumata, Raumata)
Map Reference	U12 - 13
Easting	2796900
Northing	6429100
Transmitted Colour	
Colour Notes	Lower band: black; Upper band: black and green
Primary Reference	Holroyd 1993; Neve *et al.* 1994; Seelenfreund 1985; Ward 1972
Archaeological Reference	
SOURCE LOCATION	Okawa
Map Reference	U12 - 13
Easting	2700700
Northing	6430200
Transmitted Colour	
Colour Notes	black
Primary Reference	Holroyd 1993; Seelenfreund 1985; Ward 1972; 1973
Archaeological Reference	
SOURCE LOCATION	Omapu Bay
Map Reference	U12 - 13
Easting	2798600
Northing	6427600
Transmitted Colour	
Colour Notes	
Primary Reference	Ewart *et al.* 1968
Archaeological Reference	
SOURCE LOCATION	Opo Bay (Aka: South East Bay)
Map Reference	U12 - 13
Easting	2799100
Northing	6427700
Transmitted Colour	
Colour Notes	black
Primary Reference	Ewart *et al.* 1968; Holroyd 1993; Houghton *et al.* 1992; Neve *et al.* 1994; Pos 1961; Seelenfreund 1985; Ward 1972; 1973
Archaeological Reference	
SOURCE LOCATION	Opuhi Spring
Map Reference	U12 -13
Easting	2798000
Northing	6430700
Transmitted Colour	
Colour Notes	black
Primary Reference	Holroyd 1993; Neve *et al.* 1994; Seelenfreund 1985
Archaeological Reference	

continued on the next page . . .

. . . continued from table D.1

Par	Notes
SOURCE LOCATION	Orongatea Bay
Map Reference	U12 - 13
Easting	2700600
Northing	6431600
Transmitted Colour	
Colour Notes	
Primary Reference	Holroyd 1993; Houghton *et al.* 1992
Archaeological Reference	
SOURCE LOCATION	Otiora Bay - northwest (Aka: Honeymoon Bay)
Map Reference	U12 - 13
Easting	2797100
Northing	6428700
Transmitted Colour	
Colour Notes	black
Primary Reference	Holroyd 1993; Neve *et al.* 1994; Ward 1972; 1973
Archaeological Reference	
SOURCE LOCATION	Otiora Bay - southeast
Map Reference	U12 - 13
Easting	2797200
Northing	6428600
Transmitted Colour	
Colour Notes	black
Primary Reference	Holroyd 1993; Neve *et al.* 1994
Archaeological Reference	
SOURCE LOCATION	Oturu Bay
Map Reference	
Easting	
Northing	
Transmitted Colour	
Colour Notes	
Primary Reference	Ewart *et al.* 1968; Houghton *et al.* 1992
Archaeological Reference	
SOURCE LOCATION	Panui
Map Reference	U12 - 13
Easting	2799100
Northing	6427400
Transmitted Colour	
Colour Notes	
Primary Reference	Holroyd 1993
Archaeological Reference	
SOURCE LOCATION	Rangiora (Aka: Taratimi Bay)
Map Reference	U12 - 13
Easting	2700600

continued on the next page . . .

. . . continued from table D.1

Par	Notes
Northing	6425500
Transmitted Colour	
Colour Notes	black to black-green
Primary Reference	Holroyd 1993; Houghton *et al.* 1992; Seelenfreund 1985
Archaeological Reference	
SOURCE LOCATION	Raumata Point
Map Reference	U12 - 13
Easting	2796850
Northing	6429150
Transmitted Colour	
Colour Notes	black
Primary Reference	Holroyd 1993; Houghton *et al.* 1992; Neve *et al.* 1994; Ward 1972; 1973
Archaeological Reference	
SOURCE LOCATION	Staircase 'Honey'
Map Reference	U12 - 13
Easting	2700300
Northing	6429700
Transmitted Colour	honey
Colour Notes	black with occasional patches of honey, very light tan or honey.
Primary Reference	Holroyd 1993; Neve *et al.* 1994; Ward 1972; 1973
Archaeological Reference	
SOURCE LOCATION	Staircase Quarry (Aka: Taratimi, Taratimi Bay, MI/5)
Map Reference	U12 - 13
Easting	2700300
Northing	6429800
Transmitted Colour	
Colour Notes	black
Primary Reference	Holroyd 1993; Neve *et al.* 1994; Pos 1965; Seelenfreund 1985; Ward 1972; 1973
Archaeological Reference	Seelenfreund 1983
SOURCE LOCATION	Taumou
Map Reference	U12 - 13
Easting	2700500
Northing	6430500
Transmitted Colour	
Colour Notes	black
Primary Reference	Holroyd 1993; Neve *et al.* 1994; Seelenfreund 1985
Archaeological Reference	
SOURCE LOCATION	Taumou Beach (1 & 2)
Map Reference	U12 - 13
Easting	2700400

continued on the next page . . .

. . . continued from table D.1

Par	Notes
Northing	6430100
Transmitted Colour	green through black
Colour Notes	
Primary Reference	Holroyd 1993; Neve *et al.* 1994
Archaeological Reference	
SOURCE LOCATION	Taumou Pa
Map Reference	U12 - 13
Easting	2700600
Northing	6430300
Transmitted Colour	
Colour Notes	black
Primary Reference	Holroyd 1993; Neve *et al.* 1994
Archaeological Reference	
SOURCE LOCATION	Te Matawhero Point
Map Reference	U12 - 13
Easting	2799700
Northing	6427600
Transmitted Colour	
Colour Notes	black/green
Primary Reference	Holroyd 1993; Neve *et al.* 1994
Archaeological Reference	
SOURCE LOCATION	Te Paritu
Map Reference	U12 - 13
Easting	2700100
Northing	6429300
Transmitted Colour	mix of honey/yellow, and green
Colour Notes	black
Primary Reference	Holroyd 1993; Neve *et al.* 1994
Archaeological Reference	
SOURCE LOCATION	Te Ananui Flat
Map Reference	U12 - 13
Easting	2797900
Northing	6431600
Transmitted Colour	
Colour Notes	black
Primary Reference	Holroyd 1993; Neve *et al.* 1994
Archaeological Reference	
SOURCE LOCATION	Waitangi Bay (Aka: Honey Bay)
Map Reference	U12 - 13
Easting	2700100
Northing	6428800
Transmitted Colour	very light tan or honey
Colour Notes	

continued on the next page . . .

. . . continued from table D.1

Par	Notes
Primary Reference	Holroyd 1993; Ward 1972; 1973
Archaeological Reference	
	Northland
SOURCE LOCATION	Huruiki
Map Reference	Q06
Easting	2629700
Northing	6638900
Transmitted Colour	grey
Colour Notes	black with silky grey sheen in strong sunlight.
Primary Reference	Armitage *et al.* 1972; Bird *et al.* 1981; Bollong 1983; Duerden *et al.* 1987; Ferrar 1925; Green 1964; Duerden *et al.* 1987; Holroyd 1993; Leach *et al.* 1978*a*; Leach and Warren 1981; Leach 1996; Moore 1982; 1988; Neve *et al.* 1994; Ward 1972; 1973; 1974*b*;*c*
Archaeological Reference	Armitage *et al.* 1972; Brassey 1985; Brassey and Seelenfreund 1984; Fox 1982; Harsant 1985; Leach 1977; Leach and de Souza 1979; Reeves and Armitage 1973*b*; Seelenfreund 1985; Seelenfreund and Bollong 1990; Ward 1974*b*
SOURCE LOCATION	Kaeo
Map Reference	P04
Easting	2587300
Northing	6672200
Transmitted Colour	
Colour Notes	
Primary Reference	Armitage *et al.* 1972; Bird *et al.* 1981; Green 1964; Duerden *et al.* 1987; Moore and Coster 1989*b*; Smith *et al.* 1977
Archaeological Reference	Armitage *et al.* 1972; Brassey 1985; Brassey and Seelenfreund 1984; Harsant 1985; Reeves and Armitage 1973*b*; Seelenfreund 1985; Seelenfreund and Bollong 1990
SOURCE LOCATION	Pungaere (Aka: Kaeo)
Map Reference	P05
Easting	2589200
Northing	6667500
Transmitted Colour	yellow green
Colour Notes	black
Primary Reference	Bird *et al.* 1981; Bollong 1983; Duerden *et al.* 1987; Holroyd 1993; Leach 1977; Leach *et al.* 1978*a*; Leach and Warren 1981; Leach 1996; Moore 1988; Moore and Coster 1989*b*; Neve *et al.* 1994; Smith *et al.* 1977; Ward 1972; 1973; 1974*b*;*c*
Archaeological Reference	Brassey and Seelenfreund 1984; Harsant 1985; Moore 1988; Seelenfreund 1985; Seelenfreund and Bollong 1990
SOURCE LOCATION	Waiare (Aka: Kaeo, Upokorau)
Map Reference	P04

continued on the next page . . .

. . . continued from table D.1

Par	Notes
Easting	2587500
Northing	6672400
Transmitted Colour	pale green
Colour Notes	black
Primary Reference	Bird *et al.* 1981; Bollong 1983; Duerden *et al.* 1987; Holroyd 1993; Leach 1977; Leach *et al.* 1978*a*; Leach and Warren 1981; Leach 1996; Moore 1988; Moore and Coster 1989*b*; Neve *et al.* 1994; Smith *et al.* 1977; Ward 1972; 1973; 1974*b*;*c*
Archaeological Reference	Brassey and Seelenfreund 1984; Harsant 1985; Moore 1988; Seelenfreund 1985; Seelenfreund and Bollong 1990
SOURCE LOCATION	Waiarewau stream and Lake Omapere (south side)
Map Reference	P05
Easting	2583000
Northing	6650000
Transmitted Colour	
Colour Notes	typical black glass
Primary Reference	Bell and Clark 1909
Archaeological Reference	
SOURCE LOCATION	Weta (Aka: Otoroa)
Map Reference	P04
Easting	2588500
Northing	6680600
Transmitted Colour	minor dark grey and red on rare occasions.
Colour Notes	black
Primary Reference	Bird *et al.* 1981; Bollong 1983; Duerden *et al.* 1987; Holroyd 1993; Leach 1977; Leach *et al.* 1978*a*; Leach and Warren 1981; Leach 1996; Moore 1988; Ward 1972; 1973; 1974*b*;*c*
Archaeological Reference	Brassey and Seelenfreund 1984; Harsant 1985; Seelenfreund 1985; Seelenfreund and Bollong 1990
	Coromandel Arc
SOURCE LOCATION	Arid Island (Rakitu Island)
Map Reference	S08 - T08
Easting	2735500
Northing	6560100
Transmitted Colour	clear light-grey
Colour Notes	
Primary Reference	Green 1962
Archaeological Reference	
SOURCE LOCATION	Awana - Great Barrier Island (Possibly labelled under Great Barrier with Te Ahumata)
Map Reference	S08 - T08
Easting	2733100
Northing	6552000

continued on the next page . . .

. . . continued from table D.1

Par	Notes
Transmitted Colour	grey, grey to black
Colour Notes	
Primary Reference	Bird *et al.* 1981; Bollong 1983; Duerden *et al.* 1987; Holroyd 1993; Leach 1977; Leach *et al.* 1986*b*; 1978*a*; Leach and Warren 1981; Leach 1996; Neve *et al.* 1994; Spring-Rice 1963; Ward 1972; 1973
Archaeological Reference	Leach *et al.* 1986*b*; Ruddock 1988; Seelenfreund and Bollong 1990
SOURCE LOCATION	Burgess Island (Aka: Pokohinu, possibly labelled under Mokohinau with Fanal Island)
Map Reference	S07
Easting	2686100
Northing	6601500
Transmitted Colour	
Colour Notes	
Primary Reference	Duerden *et al.* 1987; Holroyd 1993; Leach and Warren 1981; Leach 1996; Neve *et al.* 1994
Archaeological Reference	Moore 1985-6
SOURCE LOCATION	Cooks Beach/Bay (Aka: Whitianga)
Map Reference	T11
Easting	2755200
Northing	6480100
Transmitted Colour	grey
Colour Notes	black with some vesicular material
Primary Reference	Bird *et al.* 1981; Bollong 1983; Duerden *et al.* 1987; Holroyd 1993; Leach *et al.* 1978*a*; Leach and Warren 1981; Leach 1977; 1996; Moore 1983; 1988; Neve *et al.* 1994; Ward 1972; 1973; 1974*b*;*c*
Archaeological Reference	Harsant 1985; Leach 1977; Leach and de Souza 1979; Seelenfreund 1985; Seelenfreund and Bollong 1990; Ward 1974*b*
SOURCE LOCATION	Fanal Island (Aka: Motukino, possibly labelled under Mokohinau with Burgess Island)
Map Reference	S07
Easting	2682650
Northing	6604350
Transmitted Colour	iridescent smoky grey, grey-black
Colour Notes	minor green-black, medium grey to black in reflected light; greenish-black
Primary Reference	Bird *et al.* 1981; Bollong 1983; Duerden *et al.* 1987; Green 1962; 1964; Holroyd 1993; Leach *et al.* 1978*a*; Leach 1996; Moore 1988; Neve *et al.* 1994; Ward 1972; 1973; 1974*b*;*c*
Archaeological Reference	Brassey 1985; Brassey and Seelenfreund 1984; Harsant 1985; Moore 1985-6; Seelenfreund 1985; Seelenfreund and Bollong 1990; Spring-Rice 1980

continued on the next page . . .

. . . continued from table D.1

Par	Notes
SOURCE LOCATION	Great Barrier
Map Reference	S08 to T08
Easting	2726000
Northing	6550000
Transmitted Colour	
Colour Notes	dark grey black
Primary Reference	Armitage *et al.* 1972; Bollong 1983; Green 1962; Duerden *et al.* 1987; Moore 1988; Spring-Rice 1962; Ward 1974*c*
Archaeological Reference	Armitage *et al.* 1972; Brassey 1985; Brassey and Seelenfreund 1984; Fox 1982; Fredricksen 1991; Harsant 1985; Leach and de Souza 1979; Reeves and Armitage 1973*b*; Ruddock 1988; Seelenfreund and Bollong 1990
SOURCE LOCATION	Hahei
Map Reference	T11
Easting	2761200
Northing	6480300
Transmitted Colour	grey
Colour Notes	black
Primary Reference	Bird *et al.* 1981; Bollong 1983; Duerden *et al.* 1987; Holroyd 1993; Leach *et al.* 1978*a*; Leach and Warren 1981; Leach 1996; Moore 1983; 1988; Neve *et al.* 1994; Ward 1972; 1973; 1974*b*;*c*
Archaeological Reference	Harsant 1985; Seelenfreund 1985; Seelenfreund and Bollong 1990
SOURCE LOCATION	Purangi
Map Reference	T11
Easting	2756200
Northing	6479500
Transmitted Colour	red-brown
Colour Notes	
Primary Reference	Bird *et al.* 1981; Bollong 1983; Duerden *et al.* 1987; Holroyd 1993; Leach *et al.* 1978*a*; Leach and Warren 1981; Leach 1996; Neve *et al.* 1994; Ward 1972; 1973; 1974*b*;*c*
Archaeological Reference	Leach 1977; Leach and de Souza 1979; Seelenfreund 1985; Seelenfreund and Bollong 1990
SOURCE LOCATION	Tairua
Map Reference	T11
Easting	2759400
Northing	6459800
Transmitted Colour	In strong sunlight a silky green or brown sheen is visible, though grey is more usual.
Colour Notes	Reflected light: black to grey-black.

continued on the next page . . .

. . . continued from table D.1

Par	Notes
Primary Reference	Bird *et al.* 1981; Bollong 1983; Duerden *et al.* 1987; Holroyd 1993; Leach *et al.* 1978*a*; Leach and Warren 1981; Leach 1996; Moore 1988; Moore and Coster 1984*b*; Neve *et al.* 1994; Ward 1972; 1973; 1974*b*;*c*
Archaeological Reference	Leach *et al.* 1986*b*; Seelenfreund 1985; Seelenfreund and Bollong 1990
SOURCE LOCATION	Te Ahumata - Great Barrier Island (Possibly labelled under Great Barrier with Awana)
Map Reference	S09
Easting	2628500
Northing	6548100
Transmitted Colour	grey, dark grey, grey-black.
Colour Notes	black
Primary Reference	Bird *et al.* 1981; Bollong 1983; Duerden *et al.* 1987; Green 1964; Holroyd 1993; Leach *et al.* 1978*a*; 1986*b*; Leach and Warren 1981; Leach 1996; Neve *et al.* 1994; Spring-Rice 1962; 1963; Ward 1972; 1973; 1974*b*;*c*
Archaeological Reference	Ruddock 1988; Seelenfreund 1985; Seelenfreund and Bollong 1990
SOURCE LOCATION	Waihi
Map Reference	T13
Easting	2762000
Northing	6411700
Transmitted Colour	red brown, grey, greyish-olive
Colour Notes	Mostly pale greyish olive to olive, also medium grey-black and minor red/brown in reflected light, red and black
Primary Reference	Bird *et al.* 1981; Bollong 1983; Duerden *et al.* 1987; Holroyd 1993; Leach 1977; Leach *et al.* 1978*a*; Leach and Warren 1981; Leach 1996; Moore 1988; Moore and Coster 1989*b*; Neve *et al.* 1994; Ward 1972; 1973; 1974*b*;*c*
Archaeological Reference	Leach *et al.* 1986*b*; Moore and Coster 1989*b*; Seelenfreund 1985; Seelenfreund and Bollong 1990
SOURCE LOCATION	Whitianga
Map Reference	T11
Easting	2751000
Northing	6481000
Transmitted Colour	
Colour Notes	
Primary Reference	Armitage *et al.* 1972; Green 1964; Duerden *et al.* 1987; Reeves and Armitage 1973*b*
Archaeological Reference	Armitage *et al.* 1972; Harsant 1985; Reeves and Armitage 1973*b*
SOURCE LOCATION	Whangamata (encompasses Whitipirorua and Onemana)
Map Reference	T12

continued on the next page . . .

. . . continued from table D.1

Par	Notes
Easting	2766200
Northing	6445600
Transmitted Colour	some brown colouring in transmitted light
Colour Notes	black
Primary Reference	Holroyd 1993; Moore 1988; Neve *et al.* 1994
Archaeological Reference	
	Taupo Volcanic Zone
SOURCE LOCATION	Ben Lomond (often referred to as Taupo)
Map Reference	T17
Easting	2767000
Northing	6284300
Transmitted Colour	
Colour Notes	medium grey to black, rare red brown
Primary Reference	Holroyd 1993; Moore 1988
Archaeological Reference	
SOURCE LOCATION	Hemo Gorge (possibly under Whakarewarewa)
Map Reference	U16
Easting	2794200
Northing	6331500
Transmitted Colour	
Colour Notes	black and white vesicular material
Primary Reference	Green 1962; Holroyd 1993; Ward 1972; 1973
Archaeological Reference	
SOURCE LOCATION	Lake Maraetai (may also be same source as Mangakino, or may have been included under Whakamaru)
Map Reference	T17
Easting	2752500
Northing	6309500
Transmitted Colour	Red
Colour Notes	red and black
Primary Reference	Armitage *et al.* 1972; Bird *et al.* 1981; Bollong 1983; Duerden *et al.* 1987; Green 1962; Duerden *et al.* 1987; Holroyd 1993; Leach *et al.* 1978*a*; Leach and Warren 1981; Leach 1977; 1996; Neve *et al.* 1994; Ward 1972; 1973; 1974*b*;*c*
Archaeological Reference	Armitage *et al.* 1972; Green 1964; Leach 1977; Seelenfreund 1985; Seelenfreund and Bollong 1990
SOURCE LOCATION	Lake Okataina
Map Reference	U16
Easting	2809000
Northing	6336000
Transmitted Colour	
Colour Notes	dark grey to black in reflected light
Primary Reference	Holroyd 1993; Moore 1988

continued on the next page . . .

. . . continued from table D.1

Par	Notes
Archaeological Reference	
SOURCE LOCATION	Lake Rotoiti (includes Rotoiti Point, Hinehopu, and Te Pohue Bay)
Map Reference	V15
Easting	2813000
Northing	6345500
Transmitted Colour	
Colour Notes	dark grey to black in reflected light
Primary Reference	Green 1962; Holroyd 1993; Moore 1988
Archaeological Reference	
SOURCE LOCATION	Lake Rotokawau
Map Reference	U16
Easting	2801300
Northing	6338100
Transmitted Colour	
Colour Notes	dark grey to black in reflected light
Primary Reference	Holroyd 1993; Moore 1988
Archaeological Reference	
SOURCE LOCATION	Lake Tarawera
Map Reference	U16
Easting	2806700
Northing	6327800
Transmitted Colour	
Colour Notes	
Primary Reference	Holroyd 1993
Archaeological Reference	
SOURCE LOCATION	Maketu
Map Reference	V14
Easting	2815800
Northing	6378600
Transmitted Colour	
Colour Notes	medium grey-black, common dark grey in reflected light
Primary Reference	Holroyd 1993; Moore 1988; Neve *et al.* 1994
Archaeological Reference	
SOURCE LOCATION	Mangakino
Map Reference	T16
Easting	2752500
Northing	6311000
Transmitted Colour	
Colour Notes	
Primary Reference	Green 1962; 1964; Neve *et al.* 1994
Archaeological Reference	
SOURCE LOCATION	Maratoto

continued on the next page . . .

. . . continued from table D.1

Par	Notes
Map Reference	T13
Easting	2755500
Northing	6428200
Transmitted Colour	
Colour Notes	black
Primary Reference	Bollong 1983; Duerden *et al.* 1987; Holroyd 1993; Leach *et al.* 1978*a*; Leach and Warren 1981; Leach 1996; Neve *et al.* 1994; Ward 1972; 1973; 1974*b*;*c*
Archaeological Reference	Seelenfreund 1985; Seelenfreund and Bollong 1990
SOURCE LOCATION	Ngongotaha
Map Reference	U16
Easting	2792200
Northing	6337400
Transmitted Colour	
Colour Notes	black
Primary Reference	Holroyd 1993; Moore 1988; Ward 1972; 1973
Archaeological Reference	
SOURCE LOCATION	Ongaroto (may have been included under Whakamaru)
Map Reference	T17
Easting	2762000
Northing	6306800
Transmitted Colour	Red-brown
Colour Notes	black
Primary Reference	Bird *et al.* 1981; Bollong 1983; Duerden *et al.* 1987; Holroyd 1993; Leach *et al.* 1978*a*; Leach and Warren 1981; Leach 1996; Neve *et al.* 1994; Ward 1972; 1973; 1974*b*;*c*
Archaeological Reference	Leach 1977; Leach *et al.* 1986*b*; Leach and de Souza 1979; Seelenfreund 1985; Seelenfreund and Bollong 1990
SOURCE LOCATION	Rotorua
Map Reference	U16
Easting	2793500
Northing	6336500
Transmitted Colour	
Colour Notes	red and black
Primary Reference	Bird *et al.* 1981; Bollong 1983; Duerden *et al.* 1987; Green 1962; 1964; Leach 1977; Leach *et al.* 1978*a*; Leach and Warren 1981; Leach 1996; Neve *et al.* 1994; Ward 1974*b*;*c*
Archaeological Reference	Fox 1982; Harsant 1985; Leach 1977; Leach and de Souza 1979; Seelenfreund 1985; Seelenfreund and Bollong 1990; Ward 1974*b*
SOURCE LOCATION	Taupo
Map Reference	U16
Easting	2793500
Northing	6336500

continued on the next page . . .

. . . continued from table D.1

Par	Notes
Transmitted Colour	Grey
Colour Notes	grey-black to black
Primary Reference	Armitage *et al.* 1972; Bird *et al.* 1981; Bollong 1983; Duerden *et al.* 1987; Green 1962; Duerden *et al.* 1987; Leach *et al.* 1978*a*; Leach and Warren 1981; Leach 1996; Neve *et al.* 1994; Ward 1972; 1974*b*;*c*
Archaeological Reference	Armitage *et al.* 1972; Fox 1982; Green 1964; Harsant 1985; Leach 1977; Leach *et al.* 1986*b*; Leach and de Souza 1979; Reeves and Armitage 1973*b*; Seelenfreund 1985; Seelenfreund and Bollong 1990; Ward 1974*b*
SOURCE LOCATION	Whakamaru (may have been regarded the same as Ongaroto)
Map Reference	T17
Easting	2762200
Northing	6306500
Transmitted Colour	red -brown
Colour Notes	dark grey to black in reflected light
Primary Reference	Holroyd 1993; Moore 1988; Neve *et al.* 1994; Ward 1972; 1973; 1974*b*
Archaeological Reference	
SOURCE LOCATION	Whakarewarewa
Map Reference	U16
Easting	2797500
Northing	6332800
Transmitted Colour	Red
Colour Notes	black, rare red brown, red flecked and red coloured
Primary Reference	Holroyd 1993; Green 1964; Moore 1988; Ward 1972; 1973
Archaeological Reference	
	Other
SOURCE LOCATION	Banks Peninsula
Map Reference	N36
Easting	2520500
Northing	5717500
Transmitted Colour	
Colour Notes	
Primary Reference	Bird *et al.* 1981; Bollong 1983; Leach 1996
Archaeological Reference	Leach *et al.* 1986*b*
SOURCE LOCATION	Otago
Map Reference	I44
Easting	2216500
Northing	5478500
Transmitted Colour	
Colour Notes	
Primary Reference	Bird *et al.* 1981; Bollong 1983

continued on the next page . . .

. . . continued from table D.1

Par	Notes
Archaeological Reference	
SOURCE LOCATION	Tamaka
Map Reference	
Easting	
Northing	
Transmitted Colour	
Colour Notes	
Primary Reference	Bird *et al.* 1981
Archaeological Reference	

B.2 Reference Collection Samples

Table B.2: Reference Samples

sample #	Location	# Samples	long	lat
1	Raumata Point			
1.1	Beach Cobble	5	2796850	6428950
1.2		3	2796850	6428950
1.3		3	2796850	6428950
1.4		4	2796850	6428950
2	Orongatea			
2.1	Seam 1	2	2800500	6431600
2.2	Seam 2	2	2800500	6431600
2.3	Seam 3	3	2800500	6431600
2.4	Internal Caldera slope	7	2800300	6431300
2.5	Inner Valley	2	2800400	6431500
2.6	Inner Valley		2800400	6431400
2.7	Internal Caldera slope	8	2800300	6431300
2.8	Internal Caldera slope	4	2800300	6431250
2.9	Internal Caldera slope	3	2800300	6431200
2.10	Internal Caldera slope	5	2800300	6431200
2.11	Internal Caldera slope	8	2800250	6431200
3	Te Ananui Flat			
3.1	Cobble Scatter 1	8	2798470	6431150
3.2	Cobble Scatter 1	2	2798470	6431150
3.3	Cobble Scatter 2	3	2798770	6431050
3.4	Cobble Scatter 2	4	2798770	6431050
3.5	Cobble Scatter 3	3	2798950	6431000
3.6	Cobble Scatter 3	3	2798950	6431000
3.7	Cobble Scatter 1	1	2798470	6431150
3.8	Cobble Scatter 2	1	2798770	6431050
3.9	Cobble Scatter 3	1	2798950	6431000

continued on the next page . . .

. . . continued from table B.2

sample #	Location	# Samples	long	lat
4	Ruawaipiro Pass			
4.1	lower flat	3	2797550	6428650
4.2	stone wall area	4	2797700	6428880
4.3	stone wall area	2	2797700	6428880
4.4	stone wall area	3	2797700	6428880
4.5	stone wall area	2	2797700	6428880
4.6	upper steep	3	2797900	6429050
4.7	stone area in upper steep	6	2797960	6429150
4.8	stone area in upper steep	5	2797960	6429150
4.9	stone area in upper steep	2	2797960	6429150
5	Te Matawhero Point			
5.1		3	2799400	6427600
5.2		4	2799400	6427600
5.3		3	2799400	6427600
5.4		3	2799400	6427600
6	Opo Bay			
6.1		4	2799120	6427150
6.2		3	2799060	6427750
6.3		6	2799150	6427720
6.4		3	2799120	6427150
7	Opuhi Springs			
7.1	C, west	5	2797970	6430700
7.2	C, west	7	2797970	6430700
7.3	B, west	4	2797970	6430620
7.4	B, west	2	2797970	6430620
7.5	B, west	5	2797970	6430620
7.6	C, west	5	2797970	6430700
7.7	C, west	3	2797970	6430700
7.8	A, west upper	7	2797900	6430600
7.9	A, west upper	6	2797900	6430600
7.10	C, Path	2	2797970	6430700
7.11	C, Path	6	2797970	6430700
7.12	C, Path	16	2797970	6430700
7.13	C, Path	7	2797970	6430700
7.14	C, Path	6	2797970	6430700
7.15	A, Path	6	2797900	6430600
7.16	D, west	50	2798150	6431050
7.17	A, east lower	5	2797900	6430600
7.18	A, east lower	6	2797900	6430600
7.19	A, east upper	6	2797900	6430600
7.20	B, west valley mouth	5	2797970	6430620
7.21	B, Path scatter	7	2797970	6430620
7.22	D, west	11	2798150	6431050
7.23	B, west	6	2797970	6430620
7.24	A,west lower	2	2797900	6430600

continued on the next page . . .

. . . continued from table B.2

sample #	Location	# Samples	long	lat
7.25	A,west lower	2	2797900	6430600
7.26	B, west valley head	3	2797970	6430620
7.27	B, west valley head	5	2797970	6430620
7.28	B, west valley head	3	2797970	6430620
8	Ohineiti			
8.1	boulder B	3	2798350	6431210
8.2	quarry 2, point 5	4	2798350	6431210
8.3	boulder E	4	2798350	6431210
8.4	boulder C	5	2798350	6431210
8.5	boulder D	6	2798350	6431210
8.6	quarry 1, point 3	4	2798350	6431210
8.7	quarry 1, point 2	4	2798350	6431210
8.8	directly above ohineiti	2	2798350	6431210
8.9	quarry 1, point 1	6	2798350	6431210
8.10	quarry 1, point 4	3	2798350	6431210
8.11	quarry 1, point 8	3	2798350	6431210
8.12	quarry 2, point 6	6	2798350	6431210
8.13	quarry 2, 9th spit 400/500	6	2798350	6431210
8.14	quarry 2, 9th spit 400/500	7	2798350	6431210
8.15	quarry 2, 9th spit flakes	13	2798350	6431210
8.16	boulder A	6	2798350	6431210
8.17	quarry 2, point 7	7	2798350	6431210
8.18	quarry 2, point 7	4	2798350	6431210
8.19	quarry 2, 8th spit 350/400	12	2798350	6431210
8.20	quarry 2, 1st spit 0-50	4	2798350	6431210
8.21	quarry 2, 2nd spit 50-100	2	2798350	6431210
8.22	quarry 2, 3rd spit 100-150	2	2798350	6431210
8.23	quarry 2, 4th spit 150-200	1	2798350	6431210
8.24	quarry 2, 5th spit 200-250	1	2798350	6431210
8.25	quarry 2, 6th spit 250-300	1	2798350	6431210
8.26	quarry 2, 7th spit 300-350	6	2798350	6431210
8.27	quarry 1, spit 1	4	2798350	6431210
8.28	quarry 1, spit 2	2	2798350	6431210
8.29	quarry 1, spit 3	2	2798350	6431210
8.30	quarry 1, spit 4	3	2798350	6431210
8.31	quarry 1, spit 5	1	2798350	6431210
8.32	quarry 1, spit 6	0	2798350	6431210
8.33	quarry 1, spit 7	4	2798350	6431210
8.34	quarry 1, spit 8	13	2798350	6431210
9	Taratimi Bay			
9.1		2	2800250	6429750
9.2		2	2800250	6429750
9.3		2	2800250	6429750
9.4		2	2800250	6429750
9.5		5	2800250	6429750

continued on the next page . . .

. . . continued from table B.2

sample #	Location	# Samples	long	lat
9.6		8	2800250	6429750
9.7	Taumou Beach South	0	2800365	6430020
9.8	Taumou Beach South	1	2800365	6430020
9.9	Taumou Beach North	1	2800480	6430095
9.10	Taumou Beach North	1	2800480	6430095
10	Young Dome			
10.1		2	2799600	6430250
10.2		1	2799600	6430250
10.3		2	2799600	6430250
11	Taumou *pā*			
11.1		4	2800630	6430260
11.2	outcrop, point 6	2	2800630	6430260
11.3	outcrop, point 4	7	2800630	6430260
11.4	outcrop, point 2	4	2800630	6430260
11.5	outcrop, point 5	5	2800630	6430260
11.6	outcrop, point 4, spit 4 (180-230mm)	24	2800630	6430260
11.7	outcrop, point 4, spit 1 (30-80mm)	30	2800630	6430260
11.8	outcrop, point 4, spit 3 (130-180mm)	32	2800630	6430260
11.9	outcrop, point 4, spit 2 (80-130mm)	44	2800630	6430260
11.10	seam	2	2800630	6430260
11.11	seam	3	2800630	6430260
11.12	seam	2	2800630	6430260
12	Otiora Bay			
12.1	South	2	2797300	6428650
12.2	South	3	2797300	6428650
12.3	North, seam and cobble samples	3	2797120	6428800
12.4	North, seam and cobble samples	3	2797120	6428800
12.5	path, seam and cobble samples	4	2797280	6428750
12.6	South	2	2797300	6428650
12.7	South	2	2797300	6428650
12.8	South	1	2797300	6428650
12.9	South	2	2797300	6428650
12.10	North	2	2797120	6428800
12.11	North	1	2797120	6428800
12.12	North	2	2797120	6428800
12.13	Central	2	2797280	6428750
12.14	Central	1	2797280	6428750
13	Upper Staircase			

continued on the next page . . .

. . . continued from table B.2

sample #	Location	# Samples	long	lat
13.1	1, top right	3	2800270	6429800
13.2	2	2	2800270	6429800
13.3	3	5	2800270	6429800
13.4	4, bottom	2	2800270	6429800
13.5	5	3	2800270	6429800
14	Halls Pass			
14.1	Layer 1	3	2799600	6429000
14.2	Layer 2	4	2799600	6429000
14.3	Layer 3	3	2799600	6429000
14.4	Layer 2	1	2799600	6429000
14.5	Layer 2	1	2799600	6429000
14.6	Layer 2	2	2799600	6429000
14.7	Layer 2	3	2799600	6429000
14.8	Layer 2	1	2799600	6429000
14.9	Layer 2	1	2799600	6429000
14.10	Layer 2	1	2799600	6429000
14.11	Layer 2, buried under 5cm humus	2	2799600	6429000
15	Staircase			
15.1	layer 2(A)	3	2800330	6429840
15.2	layer 2(B)	2	2800330	6429840
15.3	layer 2(C)	3	2800330	6429840
15.4	layer 3	3	2800330	6429840
15.5	Lower Level	3	2800330	6429840
15.6	square 1, spit 1	15	2800330	6429840
15.7	square 1, spit 2	8	2800330	6429840
15.8	square 2, spit 1	11	2800330	6429840
15.9	square 2, spit 2	6	2800330	6429840
15.10	inner northern wall	1	2800330	6429840
15.11	inner southern wall	2	2800330	6429840
15.12	mid northern wall	1	2800330	6429840
15.13	mid southern wall	2	2800330	6429840
15.14	outer northern wall	1	2800330	6429840
15.15	outer southern wall	2	2800330	6429840
15.16	mid northern wall	1	2800330	6429840
15.17	mid northern wall	2	2800330	6429840
15.18	mid southern wall	1	2800330	6429840
15.19	northern entrance	1	2800330	6429840
15.20	southern entrance	2	2800330	6429840
15.21	outside face	8	2800330	6429840
15.22	northern ceiling	2	2800330	6429840
15.23	southern ceiling	1	2800330	6429840
15.24	south entrance	1	2800330	6429840
15.25	outside face	3	2800330	6429840
16	Ruakiki Point			

continued on the next page . . .

... continued from table B.2

sample #	Location	# Samples	long	lat
16.1		5	2800050	6427700
16.2		3	2800050	6427700
16.3		3	2800050	6427700
16.4		2	2800050	6427700
16.5		3	2800050	6427700
17	Kaeo			
17.1	Caprine Road	24	2588300	6670000
17.2	Location 3, Insitu	7	2587700	6672100
17.3	Location 3, in stream	9	2587650	6672150
17.4	Location 5, sample 1	5	2586700	6673150
17.5	Location 5, sample 2	9	2586200	6673100
17.6	Location 5, sample 3	8	2585800	6673180
17.7	Location 2	1	2588600	6669850
17.8	Location 4	4	2586900	6673900
24	Whakarara	4	2592500	6682200
25	Weta	10	2587500	6682100
26	Te Paritu			
26.1	Insitu obsidian, covered in 1-2cm humus	1	2700100	6429300
26.2	Insitu obsidian, covered in 1-2cm humus	2	2700100	6429300
26.3	Insitu obsidian, covered in 1-2cm humus	4	2700100	6429300
26.4	Insitu obsidian, covered in 1-2cm humus	1	2700100	6429300
26.5	path scatter	2	2700100	6429300
26.6	path scatter	1	2700100	6429300
29	Whangamata Fault			
29.1	Ben Lomond, in situ	3	2768200	6286100
29.2	Ben Lomond, Scatter 1	4	2768200	6286100
29.3	Ben Lomond, Scatter 2	8	2768100	6285800
29.4	Otaketake, Scatter 1	6	2764200	6281200
29.5	Ben Lomond, Scatter 3	1	2767900	6285400
30	Motuapa			
30.1	Parikarangaranga Cliff flats	10	2759000	6248000
30.2	Whakamoanga Flanks	5	2759100	6247900
31	Huruiki			
31.1	Scatter	3	2629700	6638900
31.2	Scatter	1	2629700	6638900
31.3	Scatter	1	2629700	6638900
31.4	Scatter	1	2629700	6638900
31.5	Scatter	1	2629700	6638900
31.6	Scatter	1	2629700	6638900
32	Waihi			
32.1		9	2762600	6411200

continued on the next page ...

...continued from table B.2

sample #	Location	# Samples	long	lat
32.2		1	2762600	6411200
32.3		2	2762600	6411200
33	Tairua			
33.1	TA3	4	6458100	2760400
33.2	TA5	3	6457700	2760300
33.3	TA6	1	6458700	2760100
33.4	TA6	2	6458700	2760100
33.5	TA6	1	6458700	2760100
33.6	TA8	2	6459100	2759600
33.7	TA8	2	6459100	2759600
34	Onemana/Whitipirorua			
34.1	#1690	2	6445600	2766200
34.2	#1690	1	6445600	2766200
34.3	#2866	2	6445600	2766200
34.4	#34	1	6445600	2766200
37	Cook's Beach			
37.1	#2189	1	6480100	2755200
37.2	#37	1	6480100	2755200
38	Purangi			
38.1	#917	2	6479500	2756200

B.2.1 Raumata Point (Source # 1.0)

The colouring of this sample in reflected light is a combination of grey, green and black. In transmitted light, the sample is uniformly grey-green. All specimens in this sample have a dull, waxy and sometimes pitted lustre and poor translucency. There is a faint colour change in only one specimen that could be interpreted as banding, otherwise surface banding is rare. There is no internal banding, neither are there any inclusions present, except for sample 1.3. The cortex is the most distinctive feature on most of the specimens and is generally pitted and vesicular. The matrix is consistently cloudy.

Reference Sample 1.1

This sample consists of one small hand specimen and four chips

These specimens are grey-green in reflected light and grey under transmitted light. The lustre is dull and waxy. The translucency is opaque. Surface and internal banding are both absent, as are spherulites, phenocrysts and other crystal inclusions. Distinct vesicular structures are layered between crystalline, vitreous obsidian. The matrix is cloudy and the cortex vesicular.

Reference Sample 1.2

This sample consists of three flakes.

These specimens are grey-black in reflected light and greyish green under transmitted light. The lustre is waxy and pitted and the translucency moderate. Dark surface streaks are visible, although no definite banding is present. A general grey cloudiness can be observed internally. No spherulites, phenocrysts or other crystal inclusions are present and the matrix is cloudy.

Reference Sample 1.3

This sample consists of three flakes.

These specimens are green-black in reflected light and greyish green under transmitted light. The waxy lustre is accompanied by a surface texture and the translucency of the specimens is poor. Surface banding is delineated by mineral or sediment inclusions that exhibit a vague coloration change. Inclusions are composed of a welded, light grey ash that probably became attached during cooling. No spherulites, phenocrysts or other crystal inclusions are present. The matrix is cloudy.

Martin Jones 2002

Reference Sample 1.4

This sample consists of three flakes.

These specimens are grey-green in reflected and transmitted light. The waxy lustre is accompanied by a pitted texture and the translucency is moderate to poor. Surface streaking is indistinct and measures less than 1mm thick. Wavy, thinly flowing bands are also present although no internal banding can be seen. No spherulites, phenocrysts or other crystal inclusions are visible. The matrix is cloudy and the cortex grey and smooth.

B.2.2 Orongatea Valley (Source # 2.0)

Description Summary

The colour of the specimens in this sample is generally black in reflected light. The colouring under transmitted light ranges between the green vitreous samples and shades of grey seen in the duller specimens. Translucency varies from dull and waxy through to vitreous. The cortex, where present, is gritty and dull. Overall, translucency is fair to good. Surface banding is apparent on some specimens and is usually accompanied by flow banding, although some specimens display neither characteristic. Spherulites are only present in 2.9. No phenocrysts are present. Some samples show fracture lines that are probably the result of weathering. The matrix quality ranges between gritty and clear, the duller specimens also have a cloudy characteristic. The specimens generally display perfect conchoidal fracture.

Reference Sample 2.1

This sample consists of two flakes.

These specimens are black in reflected light and green under transmitted light. The lustre is vitreous and the translucency moderate. No surface or internal banding can be seen. There are also no spherulites, phenocrysts or other such inclusions. The matrix is slightly gritty.

Reference Sample 2.2

This sample consists of one small hand specimen.

This specimen is black in reflected light and green under transmitted light. The lustre is highly vitreous and the translucency moderate to good. White, surface bands occur with moderate consistency throughout the specimens. No internal banding can be seen. There are no spherulites, phenocrysts or other such inclusions. The matrix is clear.

Reference Sample 2.3

This sample consists of three small flakes.

These specimens are grey black in reflected light and grey green under transmitted light. The lustre is vitreous and the translucency poor. Distinct layers of a mineral or sediment material form plates within the obsidian, less distinct white clouds occur beside these “bands”. No internal banding can be seen. There are no spherulites, phenocrysts or other such inclusions. The matrix is clear.

Reference Sample 2.4

This sample consists of two large hand specimens, two small pieces and four flakes.

These specimens are grey black in reflected light and grey green under

transmitted light. The waxy lustre is accompanied by a pitted texture. The translucency is poor. Indistinct smoky bands can be seen on the two small pieces. The hand specimens have more definite banding in the form of mineral inclusions occurring in platy layers. No internal banding can be seen. A bulb of pumiceous material can be seen on the large hand specimen, otherwise no spherulites, phenocrysts or other such inclusions are present. The matrix is clear.

Reference Sample 2.5

This sample consists of two hand specimens.

These specimens are black in reflected light and green under transmitted light. The specimens are vitreous and have moderate to good translucency. A slight surface texture is also apparent. Surface banding is comprised of one large pale green band measuring 3 - 4 mm wide. Matrix grit is difficult to describe due to low translucency. The cortex is dull and slightly pitted.

Reference Sample 2.6

-The two largest pieces are described with matching flakes. 2.6.1 / 2.6.1a (flake) 2.6.1 / 2.6.1b (flake) *2.6.1 & 2.6.1a

These specimens are black in reflected light and green in transmitted light. It is moderately vitreous with a slight roughness when compared to the duller cortex. The sample is moderately translucent. Surface banding is faint on one section of the cortex and slight on the freshly broken section. Faint bands running through the sample give it a streaky appearance. These bands are sometimes seen on the fractured surface. Cloudy, white-grey internal banding can be seen in the flake. The consistency is difficult to determine and the sample has no detectable grit

in the matrix. There are no spherulites or phenocrysts apparent.

Reference Sample 2.6.2 & 2.6.2a

These specimens are black in reflected light and yellow-green under transmitted light. The moderately vitreous lustre is accompanied by a slight surface texture. The translucency is moderate to good. Surface banding is cloudy grey with streaks that are irregularly spaced and approximately 4 mm thick. The internal banding seen in the flakes is similar to that seen on the surface. There are no spherulites or phenocrysts, and the matrix is clear. Experimental fracturing performed on the large hand specimen revealed a greyish sheen. A weathered rind is also visible on the surface. The sheen is probably the result of water infiltration during weathering of a weakened fracture. The rind is also probably due to weathering.

Reference Sample 2.7

This sample consists of five large samples and three small flakes.

These specimens are grey-black in reflected light and grey under transmitted light. One flake is green under transmitted light. The specimens are generally quite opaque. The lustre is waxy and the surface quite textured. The cortex is quite 'dirty' and has a lighter weathered surface. The surfaces of the two largest samples have a faint cloudy appearance. Distinct bands are not apparent, however faint lineations are visible that suggest the probable orientation of banding. Flake 2.71 displays faint internal banding that can be seen in the cloudy matrix, this feature is absent in flake 2.72, which is clear. Spherulites and phenocrysts are absent. The quality of fracture is conchoidal.

Martin Jones 2002

Reference Sample 2.8

This sample consists of two hand specimens and two flakes.

These specimens are black in reflected light and grey under transmitted light. The lustre is waxy and the translucency opaque. Indistinct surface bands are welded into one another. This is probably due to the fact that the colour differentiation between these bands is not strong. This closely spaced surface banding is visible on the cortex, as well as the freshly broken surface and occurs consistently throughout the sample. There are no spherulites or phenocrysts in these samples and the matrix is very cloudy but not gritty. The fracture quality is conchoidal.

Reference Sample 2.9

This sample consists of three small hand specimens.

These specimens are black in reflected light. It is difficult to determine a colour under transmitted light as the sample is opaque and contains too many inclusions to flake. The core displays a 'blocky' structure resulting from the abundance of spherulitic and welded rock inclusions. These inclusions are composed of felsic, light grey volcanic rock (probably a welded tuff) and measure between 5 mm to 9 mm in diameter. Xenoliths consist of pumiceous material that welded during cooling. The lustre is quite vitreous and no surface or internal banding is apparent. These specimens exhibit a more amorphous fracture.

Reference Sample 2.10

This sample consists of two large hand samples and three small flakes.

These specimens are black in reflected light and grey-green under transmitted light. The highly vitreous lustre is accompanied by a slight sur-

face texture in some places. The specimens are moderately translucent. Dark grey internal banding is visible within one flake (2.10a). 2.10a has matrix grit and streaky banding concentrated regularly at a local level. The banding is very thin and measures only a fraction of a millimetre. The other flakes have neither internal banding, nor matrix grit. No spherulites, phenocrysts, or surface banding feature in this sample. The fracture quality is perfectly conchoidal.

Reference Sample 2.11

This sample consists of six hand pieces and two flakes.

These specimens are black in reflected light and green with a yellow tinge under transmitted light. This sample is highly vitreous with a dull and dirty cortex. The translucency is good. No surface or internal banding is visible and no spherulites or phenocrysts are present. Some fracture lines are defined by white mineral inclusions. This sample displays a clear, rather than gritty, matrix. The quality of fracture is perfectly conchoidal.

B.2.3 Teananui Flat (Source # 3.0)

Summary of Descriptions.

These specimens are generally black in reflected light and vary from green to grey when viewed in transmitted light. The lustre is dull and waxy and translucency low. Spherulites feature in half the specimens. Typically, these spherulites are small and quite abundant. Surface banding is composed of varied coloured streaks, although this characteristic is less common in the spherulitic specimens. Internal banding is present in only one specimen. Some weathering is visible on the spherulitic specimens. Otherwise, there are no phenocrysts or fractures in this sample.

The matrix grit is cloudy and gritty.

Reference Sample 3.1

This sample consists of four hand pieces and four small flakes.

The specimens in this sample have a greenish grey colour in reflected light and grey in transmitted light. The lustre is dull and the translucency very low. Surface banding is not easily distinguishable due to the low translucency. Banding is comprised of green-grey, 0.5 to 1mm wide streaks that occur inconsistently throughout the specimens. Neither internal nor flow banding is visible. Spherulites are abundant and occur in close proximity to each other. These inclusions vary in shape from irregular to elongate forms and measure between 1 and 2 mm in size. No phenocrysts or fracture lines are visible. The matrix grit is difficult to describe due to low translucency. The fracture quality is adversely affected by spherulitic growth.

Reference Sample 3.2

This sample consists of two flakes.

These specimens are black in reflected light and green-grey under transmitted light. Translucency is low and the vitreous lustre is accompanied by some streaking resulting from spherulitic growth. There is neither surface nor internal banding. Spherulites are abundant and measure between 0.5 and 1mm. The few striations visible are probably the result of weathering, or are ash/tuff inclusions accumulated while the obsidian cooled. The matrix grit is hard to define due to low translucency.

Reference Sample 3.3

This sample consists of one small hand specimen and two flakes.

These specimens are black in reflected light and grey-green in transmitted light. The lustre is only slightly vitreous and the translucency moderate. There is no surface or internal banding. Spherulites measure 0.5 mm in diameter and are not as abundant as samples 3.1 or 3.2. There are no phenocrysts or other crystal inclusions. The quality of fracture has been adversely affected by spherulitic growth.

Reference Sample 3.4

This sample consists of two small hand specimens and two flakes.

These specimens are black with a slight green tinge in reflected light and green in transmitted light. The waxy lustre is accompanied by slight texture and the translucency is good. Very slight surface banding is comprised of 0.25 mm green-black streaks. These streaks occur consistently throughout the specimens. There are no spherulites, phenocrysts or other crystal inclusions. The matrix grit is relatively gritty and cloudy. The fracture quality is conchoidal.

Reference Sample 3.5

This sample consists of one hand specimen and two flakes.

These specimens are green-black in reflected light and green under transmitted light. The lustre is waxy and the translucency moderate. Surface banding is comprised of greyish black streaks 0.25 mm in thickness. The banding occur consistently throughout the surface of the specimen, but not internally. There are no spherulites, phenocrysts or other crystal

inclusions. The matrix is quite cloudy and shows some grit. The quality of fracture is conchoidal.

Reference Sample 3.6

This sample consists of three labelled specimens.

These specimens are dull black in reflected light and grey in transmitted light. The lustre is textured and waxy, while the translucency is low. Surface banding measures between 2 and 5 mm in thickness. Thin streaks (0.25 mm) exist within these bands and exhibit colours ranging between green and grey. No internal banding is apparent, neither are there any spherulites, phenocrysts or other inclusions present. The matrix is cloudy.

Reference Sample 3.7

This sample consists of one specimen.

This specimen is black in reflected light and grey green under transmitted light. The waxy lustre also has a pitted texture. The translucency is poor. Surface banding occurs in two forms. First, indistinct wavy lines occur in one section and could be the result of fracture. Second, distinct sediment or mineral material occurs in a suture-like pattern. No internal banding is apparent, neither are there spherulites, phenocrysts or other inclusions. The matrix is slightly gritty.

Reference Sample 3.8

This sample consists of one specimen.

This specimen is black in reflected light and green under transmitted

light. The lustre is waxy and the translucency opaque. Surface banding is comprised of thin, white “suture-like” veins. Xenoliths consist of a light grey pumiceous material, only one small spherulite is present and measures approximately 0.25 mm in diameter.

Reference Sample 3.9

This sample consists of one specimen

This specimen is black in reflected light and green under transmitted light. The lustre is waxy and the translucency opaque. Surface banding is comprised of white mineral “suture-like” veins, as well as a 1mm thick grey line. The sample is too small to describe the consistency and intensity of the banding.

B.2.4 Ruawaipiro Pass (Source # 4.0)

The majority of these specimens are black when viewed in reflected light, however various shades of grey are also visible. There is great variation in the range of colours seen in transmitted light. Grey and green are most common. The lustre is generally vitreous, however the duller specimens also have a waxy appearance and poor translucency. Surface banding is rare, though cloudy and irregular where present. Spherulitic inclusions are also rare, but occur in moderate abundance when found. The specimens 4.1 and 4.2 each feature one xenolith. There are no phenocrysts present in this sample group. The condition of the matrix is gritty.

Reference Sample 4.1

This sample consists of one hand specimen and two flakes.

These specimens are dull, grey-brown in reflected light. It is not possible to describe the colour in transmitted light due to poor translucency. The lustre is very dull and surface and internal banding are both absent. Spherulites measure approximately 1-2 mm in diameter and occur in moderate abundance. These specimens are relatively brittle. A xenolithic inclusion is visible, which appears to be composed of one crystal. This inclusion is covered with detritus, so it is difficult to be certain about its physical characteristics. No phenocrysts are present. It is not possible to describe the matrix grit.

Reference Sample 4.2

This sample consists of one hand specimen and three flakes.

These specimens are grey-black in reflected light and grey under transmitted light. The lustre has a somewhat silky or waxy sheen and the translucency is very low. The mid-grey surface banding occurs in an irregular pattern and ranges between 1 mm and 6 mm in width. Some bands can measure upwards of 15 mm. These large dimensions are probably the result of the one or more irregular bands merging together. A mottled silvery black colour can be seen on the surface. This feature can not be defined as banding, but is interpreted here as a definite surface colour differentiation that occurs throughout a flaked section. The same feature is also suggested by the texture visible in transmitted light. Spherulites measure approximately 0.5 mm in diameter, but do not occur abundantly. Many of the features assumed to be spherulites at first examination, are in fact percussion marks. Phenocrysts are absent, but one xenolith is visible. It is possible that this latter feature is actually fracture infill of Fe. The matrix is relatively gritty.

Reference Sample 4.3

This sample consists of two specimens.

These specimens are black in reflected light and green under transmitted light. The lustre is textured and vitreous and the translucency good. The faint surface banding is comprised of indistinct, grey bands that are widely spaced. The bands are approximately 1mm in width and merge with the base black colour. Feathery, streaky internal banding is visible in the flake. This grey banding measures 0.5 mm in width, though many of the lines are smaller. In terms of appearance, the banding is wavy, moderately distinct and occurs fairly consistently throughout both specimens. No spherulites or phenocrysts. The matrix grit is clear except for the banding.

Reference Sample 4.4

This sample consists of one hand specimen and two flakes.

These specimens are black in reflected light and green under transmitted light. The vitreous lustre is accompanied by a slight surface texture and the translucency is moderate. Surface banding is rare in this sample, but cloudy internal banding can be seen in the small flake. Some linear crystal inclusions of spherulitic composition (feldspar) occur within the internal banding of the hand specimens. Spherulites are present, however no phenocrysts can be seen. The matrix is not gritty.

Reference Sample 4.5

This sample consists of two flakes.

These specimens are black in reflected light and green under transmitted light. The vitreous lustre has a slight surface texture and the translu-

cency is moderate. Internal banding is comprised of thin cloudy lines that are difficult to observe, no surface banding can be seen. Spherulites or phenocrysts are absent. The matrix grit is cloudy.

Reference Sample 4.6

This sample consists of one hand specimen and two flakes.

These specimens are black in reflected light and yellow-green in transmitted light. The lustre is vitreous has a slight surface texture, and the translucency is good. Surface banding is comprised of many thin lines that form larger, dark grey bands. No internal banding is present, neither are there any spherulites or phenocrysts. The matrix does not show any grit. The cortex is pitted and dirty.

Reference Sample 4.7

This sample consists of three hand specimens and three flakes.

These specimens are a silver grey-brown colour in reflected light and green-grey in transmitted light. The lustre is silky to waxy (very similar to 4.2). The translucency is moderate to poor. Surface banding is comprised of cloudy grey, silver-brown bands. These irregularly spaced bands are indistinct, cloudy and not well formed. There is no internal banding. Spherulites are rare. The matrix grit is cloudy.

Reference Sample 4.8

This sample consists of two hand specimens, and three flakes.

These specimens are grey-black in reflected light and green in transmitted light. The lustre is textured and slightly dull. The translucency is

best described as moderate. A more definite description is not possible as poor flake size and shape make this difficult. Neither surface nor internal banding is visible, spherulites and phenocrysts are also absent. The matrix is clear, not gritty and the cortex is dull and pitted.

Reference Sample 4.9

This sample consists of one hand specimen, and one flake.

These specimens are black in reflected light and green in transmitted light. The lustre on the flake is vitreous, but dull on the hand specimen. Welded felsic, grey, platy layers are visible on either side of an obsidian band. The translucency is moderate to poor. Surface banding on the flake is comprised of several thin wispy bands that are visible internally as well. Linear spherulitic inclusions correspond to the described banding (thin, relatively distinct, irregular internal bands). Except for this one inclusion, spherulites or phenocrysts are absent.

B.2.5 Te Matawhero Point (Source # 5.0)

This sample group is generally black in reflected light, however greyish black is also visible. In transmitted light, green is dominant throughout the sample. The lustre is vitreous, but the translucency is poor. Surface banding is present in all but one specimen and is comprised of faint grey silvery bands of varying sizes. Internal banding is seen in only one flake. Spherulitic inclusions occur abundantly throughout this sample. The distinct crystals range in size from 2 to 4 mm and are sometimes rectangular. The matrix is clear and free of grit.

Martin Jones 2002

Reference Sample 5.1

This sample consists of one hand specimen and two flakes.

These specimens are black in reflected light and grey, with a slight green tinge, in transmitted light. The lustre is vitreous and the translucency moderate to poor. Surface banding is comprised of thick and thin silvery grey bands. This banding occurs inconsistently throughout the specimen due to spherulitic content. Internal banding is visible on one of the flakes and consists of thin wispy streaks. Spherulitic inclusions are moderately abundant, the crystals typically measure 2 to 3 mm in diameter. Phenocrysts and other crystal inclusions are absent. The matrix is clear, not gritty.

Reference Sample 5.2

This sample consists of one hand specimen and three flakes.

These specimens are grey-black in reflected light and cloudy grey-green in transmitted light. The lustre is predominantly vitreous, though also slightly waxy at times. The translucency is very poor. The indistinct surface banding is comprised of cloudy grey bands with a silky texture. No internal banding can be seen. Spherulites are large and moderately abundant, ranging between 2 and 4 mm in diameter. Phenocrysts and other crystal inclusions are absent. The matrix is cloudy.

Reference Sample 5.3

This sample consists of one hand specimen and two flakes.

These specimens are black in reflected light and grey-green in transmitted light. The lustre is highly vitreous and the translucency poor to moderate. Surface banding is comprised of faint, 1mm thick lines that

are irregular. Linear inclusions, probably spherulitic material such as feldspar, occur parallel to these bands. Internal banding is hard to distinguish. Spherulites occur in moderate abundance, ranging in size from 1 to 3 mm in diameter. Phenocrysts and other crystal inclusions are absent. The matrix is clear, though the amount of crystal inclusion makes it difficult to be certain about this observation.

Reference Sample 5.4

This sample consists of one hand specimen and two flakes.

These specimens are black in reflected light and green in transmitted light. The lustre is somewhat slightly vitreous and the translucency moderate. Neither surface nor internal banding is visible, though there is a slight cloudiness to the hand specimen. Spherulites are moderately abundant and measure up to 4 mm in diameter. Phenocrysts and other crystal inclusions are absent. The matrix is clear and the cortex appears to be welded.

B.2.6 Opo Bay (Source # 6.0)

These specimens are black in reflected light, although shades of grey are also present in some pieces. In transmitted light green is the most common colour visible. The lustre exhibited by these specimens is divided between waxy and those that are fairly vitreous. Translucency is consistently poor to moderate and one specimen also displays a textured lustre. Surface banding is generally absent, although one specimen does have lines greater than 7 mm in width. No internal banding can be seen. There is a sizeable amount of spherulitic content, the crystals occur abundantly in small (1-2 mm) irregular shapes.

Martin Jones 2002

Reference Sample 6.1

This sample consists of two hand specimens and two flakes.

These specimens are black in reflected light and greyish green in transmitted light. The lustre is waxy and textured and the translucency poor. Surface banding is characterised by white lines, of greater than 7 mm, which form white mineral defined bands or "cracks". The white lines that run through the obsidian suggest internal banding. Spherulites were very abundant and are indistinct in shape, ranging between 1 and 3 mm in diameter. The combination of spherulites and linear "cracks" make these specimens very cloudy, although the matrix is not actually gritty. No phenocrysts can be seen.

Reference Sample 6.2

This sample consists of one hand specimen and two flakes.

These specimens are black in reflected light and green under transmitted light. The lustre is highly vitreous and the translucency moderate. Neither surface nor internal banding is present in these specimens. Spherulites are moderately abundant. The size of these inclusions ranges between 1 and 4 mm. Phenocrysts are absent and the matrix is clear.

Reference Sample 6.3

This sample consists of two hand specimens and four flakes.

These specimens are black in reflected light and green under transmitted light. The lustre is highly vitreous and the translucency moderate. Surface banding is easily distinguished by crystal inclusions (probably feldspar) delineating the banding. The banding itself is very thin, widely

spaced and straight. Spherulites occur in moderate abundance and measure approximately 1 to 2 mm in diameter. Phenocrysts are absent. The matrix is slightly cloudy, but is otherwise clear.

Reference Sample 6.4

This sample consists of three specimens.

These specimens are grey-black in reflected light and cloudy green under transmitted light. The lustre is waxy and the translucency poor. Neither surface nor internal banding is present in these specimens. Spherulites are very abundant. These irregularly shaped inclusions generally measure no more than 1 to 2 mm in diameter. There are no phenocrysts present. The matrix is cloudy. The sample is quite thick due to spherulitic content.

B.2.7 Opuhi Springs (Source # 7.0)

The colour of these specimens is generally black in reflected light, grey and sometimes brown are also visible. The colouring under transmitted light is mostly green, although grey is visible on rare occasions. The translucency of this sample group is quite variable. Overall, most specimens are only moderately translucent. Some dullness and texture is exhibited, but such specimens are exceptional, otherwise vitreosity is high. Banding is more common internally than on the surface, when surface banding is found it is often accompanied by mineral inclusions occurring along the flow orientation. Internal banding is faint and at times cloudy. The sample is almost entirely free of spherulitic and crystal inclusions. As already mentioned some felsic banding is occasionally visible. 7.18 is the only specimen that contains inclusions in any sort of abundance. These crystals are moderately sized and irregularly shaped.

Reference Sample 7.1

This sample consists of two hand specimens and three flakes.

These specimens are black in reflected light and green under transmitted light. The vitreous lustre has a slight texture. The translucency is moderate to good. A faint cloudiness is visible on the surface and has an appearance similar to indistinct streaky banding. Aligned streaky 'grit' clusters are visible on one of the flakes and could be interpreted as indistinct internal banding. Spherulites and phenocrysts are absent. The matrix is clear, but displays gritty areas due to the banding.

Reference Sample 7.2

This sample consists of seven flakes.

These specimens are black in reflected light and green under transmitted light. The lustre is vitreous and the translucency moderate to good. Surface banding is absent but internal banding is visible in one of the seven flakes. Areas of indistinct, but aligned grit define this banding. Spherulites and phenocrysts are absent. The matrix is generally quite clear, but some cloudiness is apparent.

Reference Sample 7.3

This sample consists of one hand specimen and three flakes.

These specimens are black in reflected light and green under transmitted light. The vitreous lustre has a slight texture and the translucency is moderate to good. Surface banding is not visible but faint internal banding, consisting of thin lines, is present in two of the flakes. There are no spherulites or phenocrysts attached to these specimens. The cortex has

dull sediment of a light yellow brown colour welded to it. The matrix is clear.

Reference Sample 7.4

This sample consists of one hand specimen and one flake.

These specimens are black in reflected light and green under transmitted light. The vitreous lustre has a slight texture and the translucency is good. Surface banding is not visible, neither are there any spherulites, phenocrysts or other crystal inclusions present. The matrix is at times slightly streaky, but generally quite clear.

Reference Sample 7.5

This sample consists of five flakes.

These specimens are black in reflected light and green under transmitted light. The lustre is vitreous and the translucency moderate to good. Surface banding is not visible. Internal banding is comprised of cloudy white streaks. Spherulites, phenocrysts or other crystal inclusions are absent. The matrix is clear, except for the banding.

Reference Sample 7.6

This sample consists of one hand specimen and four flakes.

These specimens are black in reflected light and green under transmitted light. The lustre is vitreous and the translucency moderate. Internal banding occurs in one of the four flakes. The banding is faint and has a dark streaky appearance. Surface banding is absent. Spherulites, phenocrysts and other crystal inclusions are absent. The matrix is slightly

gritty.

Reference Sample 7.7

This sample consists of three hand specimens.

These specimens are black in reflected light and green under transmitted light. The lustre is vitreous and the translucency moderate. Surface banding is not visible, nor is there any indication of internal banding. Spherulites, phenocrysts or other crystal inclusions are also absent. Matrix grit is visible, with some signs of faint, very thin dark lines.

Reference Sample 7.8

This sample consists of two hand specimens and five flakes.

These specimens are black in reflected light and grey-green under transmitted light. The lustre is waxy and somewhat silky due to the 'banding'. The translucency is poor. Surface banding is comprised of cloudy green-grey, indistinct streaks that occur throughout the specimens, no internal banding is visible. Spherulites, phenocrysts or other crystal inclusions are absent. The matrix is gritty and quite cloudy.

Reference Sample 7.9

This sample consists of three hand specimens and three flakes.

These specimens are black in reflected light and grey under transmitted light. The lustre is highly vitreous with a slightly pitted surface. The translucency is moderate. Surface banding is defined by felsic mineral inclusions that occur beside the thin white banding. The banding is irregularly spaced and indistinct. Internal banding, spherulites and

phenocrysts are absent from these specimens. The matrix is slightly gritty.

Reference Sample 7.10

This sample consists of one hand specimen and one flake.

These specimens are black in reflected light and green under transmitted light. The lustre is vitreous and the translucency moderate. Surface or internal banding is not visible, neither are there any spherulites, phenocrysts or other crystal inclusions present. The matrix is generally clear, but shows some grit. The outer surface is slightly dusty.

Reference Sample 7.11

This sample consists of one hand specimen and five flakes.

These specimens are black in reflected light and green under transmitted light. The lustre is vitreous, with a dull look on some surfaces due to a dust. The translucency is moderate. Surface banding is not visible, but the internal banding is comprised of thin, straight white lines arranged tightly together in a uniform alignment. No spherulites, phenocrysts or other crystal inclusions are present. The matrix is cloudy due to the banding.

Reference Sample 7.12

This sample consists of twelve flakes and four sundry pieces.

These specimens are black in reflected light and green and sometimes greyish green under transmitted light. The lustre is vitreous and the translucency is generally poor. Surface banding is visible in two of the

twelve flakes. Typically the banding consists of thin grey streaky lines under 1mm in size. Internal banding is not visible, neither are there any spherulites, phenocrysts or other crystal inclusions present. The matrix is clear, though slightly gritty.

Reference Sample 7.13

This sample consists of one large hand specimen and six flakes.

These specimens are grey-black in reflected light and grey under transmitted light. The vitreous lustre has a silky grey sheen. The translucency is generally quite poor. Surface banding is highly distinctive. Thin bands range between 0.5 and 2 mm in width. Bands of a light grey colour occur within the black obsidian, sometimes these lines flow together to create thicker bands. The bands also have an intense appearance and are all of a consistent width, but vary slightly in colour. The grey internal bands are comprised of white-grey, cloudy lines. No spherulites, phenocrysts or other crystal inclusions are present. The matrix is clear in the black bands, but cloudy due to the grey banding.

Reference Sample 7.14

This sample consists of one hand specimen and five flakes.

These specimens are black in reflected light and green under transmitted light. The lustre is highly vitreous and the translucency moderate to good. Surface and internal banding is not visible. No spherulites, phenocrysts or other crystal inclusions are present. The cortex is characterised by bands of lightly coloured beige crystals situated between layers of obsidian. The cortex is rough and dusty with two to three bands of welded material, followed by 1 to 3 cm of obsidian. The matrix is clear.

Reference Sample 7.15

This sample consists of one hand specimen and five flakes.

These specimens are black with a slight green tinge in reflected light and green under transmitted light. The cortex gives a dusty appearance to these specimens. Surface and internal banding is generally not visible, however one flake does have several definitely formed vitreous bands. These bands can be felt as ridges on the surface of the specimen (7.15-a). A glimpse of internal banding is seen on flake 7.15-b, this is typical of the main type of banding observed so far; that is, cloudy grey bands within a clear matrix. No spherulites, phenocrysts or other crystal inclusions are present and banding is only a minor feature in this sample. The matrix is clear, although the translucency is poor and the lustre only moderately vitreous.

Reference Sample 7.16

This sample consists of four hand specimens, sixteen labelled flakes and thirty smaller unlabelled flakes.

These specimens are grey-black in reflected light and grey-green under transmitted light. There is a fair amount of variation in this sample. The lustre is vitreous and the translucency moderate to poor. Banding is the chief factor of variance. The large hand piece (7.16a) seems to consist of welded volcanic material through which one obsidian band runs. A very thin exposed “band” of dark green glass runs on the other side of the specimen. Internal banding is only present in 7.16-d, with thin, dark linear streaks occurring within the green obsidian. No spherulites, phenocrysts or other crystal inclusions are present. In some areas the cortex is slightly vesicular and dusty and the matrix is clear.

Martin Jones 2002

Reference Sample 7.17

This sample consists of two hand specimens and three flakes.

These specimens are grey-black in reflected light and green under transmitted light. The vitreous lustre has a waxy texture and the translucency poor. Surface banding is comprised of grey streaks that look like a tiny amount of welded volcanic matter when exposed on the surface. The banding consists of thin, parallel straight lines. These lines are extremely small and faint in appearance, ranging from 1.5 mm down to only 0.1 to 0.02 mm. The banding is relatively abundant within these specimens. No internal banding is visible, due to low translucency. No spherulites, phenocrysts or other crystal inclusions are present and the matrix is gritty.

Reference Sample 7.18

This sample consists of four hand specimens and two small flakes.

These specimens are a mixture of black, brown and grey (depending on the hand specimen) in reflected light and green in reflected light. It is not possible to describe the colour under transmitted light due to the features mentioned below. The lustre is vitreous, though sometimes also dull as some specimens have a dusty cortex. The translucency is very poor due to the shape of the specimens. Surface banding is comprised of faint grey streaks that have a definite flow pattern. On 7.18, wavy suture-like lines are visible (this specimen is the only one described so far that has straight line banding). Thicker, cloudier, indistinct banding is visible on 7.18-b. No internal banding is apparent. Spherulites are present on specimens 7.18-a, b and c, but not 7.18-d, which has a pitted cortex. 7.18-a - spherulites range from 1 to 3 mm in diameter. Crystals are irregularly shaped and occur in moderate abundance. 7.18-b -

spherulites are small, 1mm in size and indistinct. They are vaguely lens shaped. 7.18-c - spherulites are very small, generally only 0.5 mm in size. They occur abundantly and can be found interspersed within the bands. It is not possible to describe the condition of the matrix.

Reference Sample 7.19

This sample consists of three hand specimens and three flakes.

These specimens are grey-black in reflected light and grey under transmitted light. The lustre is dull and waxy and the translucency very poor. Surface banding is hardly noticeable, but there are linear differentiations in colour that could be the result of either mineral inclusion banding, or cortex patterning. Internal banding is not visible, neither are there any spherulites, phenocrysts or other crystal inclusions present. It is not possible to describe the condition of the matrix.

Reference Sample 7.20

This sample consists of two hand specimens and three flakes.

These specimens are black in reflected light and green under transmitted light. Linear surface banding is comprised of thin grey streaks occurring consistently across the obsidian. Internal banding is characterised by thin, cloudy grey streaks that appear consistently throughout the glass. No spherulites, phenocrysts can be seen, but some crystal inclusions are visible in small quantities which occur along the banding as small crystal growths (felsic). The matrix is slightly gritty.

Reference Sample 7.21

This sample consists of three hand specimens and four flakes.

These specimens are black in reflected light and green under transmitted light. The lustre is waxy and textured and the translucency moderate. Some slightly wavy and indistinct surface banding is visible and varies in width from less than 1mm to 2 mm. No internal banding is present in these specimens. Crystal inclusions occur parallel to the banding. The matrix is clear.

Reference Sample 7.22

This sample consists of one hand specimen, four large and six small flakes.

These specimens are black in reflected light and green under transmitted light. The lustre is vitreous and the translucency moderate to good. Neither surface nor internal banding is present, but some cloudiness is visible on some of the flakes. Spherulites, phenocrysts and other inclusions are absent from these specimens and the matrix is clear.

Reference Sample 7.23

This sample consists of one large, three medium and two very small flakes.

These specimens are black in reflected light and green under transmitted light. The lustre is highly vitreous and the translucency good. Surface banding is visible in the medium flakes and is defined by linear inclusions running along the faint band planes. Internal banding in the larger flake is comprised of very faint, dull streaks. Spherulites, phenocrysts and other inclusions are absent from these specimens and the matrix is clear.

Reference Sample 7.24

This sample consists of two hand specimens.

These specimens are black in reflected light. It is not possible to describe the colour under transmitted light. The dull lustre is slightly textured. The translucency is also difficult to describe because specimens are too thick. Surface banding consists of lines of pale volcanic material welded to the obsidian. No internal banding, spherulites, phenocrysts or other inclusions are present in these specimens. It is not possible to describe the matrix due to poor translucency.

Reference Sample 7.25

This sample consists of one hand specimen and one flake.

These specimens are black in reflected light and green under transmitted light. The lustre is highly vitreous and the translucency moderate to poor. Surface banding is comprised of inconsistent wispy grey streaks. No internal banding is visible, neither are there any spherulites, phenocrysts or other inclusions present in these specimens. The matrix is clear.

Reference Sample 7.26

This sample consists of two hand specimens and one small flake.

These specimens are black in reflected light and green under transmitted light. The lustre is highly vitreous and the translucency moderate. Neither surface nor internal banding is present in these specimens. Spherulites, phenocrysts and other inclusions are also absent. The matrix displays some grit.

Martin Jones 2002

Reference Sample 7.27

This sample consists of one large hand specimen three flakes and one chip.

These specimens are black in reflected light. It is not possible to describe the colour under transmitted light. The lustre has a slightly dull appearance. The translucency is poor to non-existent. The cortex consists of a light brown cover akin to the texture created when obsidian has been stretched during cooling, generally the cortex looks to be welded. Neither surface nor internal banding is present in these specimens. Spherulites, phenocrysts and other inclusions are also absent. It is not possible to describe the condition of the matrix.

Reference Sample 7.28

This sample consists of one hand specimen and two chips.

These specimens are black in reflected light. It is not possible to describe the colour under transmitted light. The lustre is vitreous with a slight waxy texture and the translucency poor. Neither surface nor internal banding is present in these specimens. Spherulites, phenocrysts and other inclusions are also absent. The cortex is dull and dirty and it is not possible to describe the condition of the matrix.

Reference Sample 7.29.1

This sample consists of one hand specimen

This specimen is black in reflected light and grey-green under transmitted light. The lustre is vitreous and the translucency poor to moderate. Surface banding is characterised by distinct streaks that occur inconsistently throughout the specimen. The streaks have a grey-green, silky

sheen and do not form definite bands or lines. No internal banding, or spherulites are apparent. Crystal phenocrysts comprise the only inclusions. These translucent crystals occur at sizes less than 2 mm in diameter and are mostly short, stubby or indistinguishable. The specimen is non-vesicular. The matrix is opaque and gritty. The cortex is dull, black and has a slightly weathered rind.

Reference Sample 7.29.2

This sample consists of one hand specimen

This specimen is black in reflected light and grey-green under transmitted light. The lustre is vitreous and the translucency poor to moderate. Surface banding is characterised by distinct streaks that occur inconsistently throughout the specimen. The streaks have a grey-green, silky sheen and do not form definite bands or lines. No internal banding, or spherulites are apparent. The only inclusions present are crystal phenocrysts. These translucent crystals occur at sizes less than 2 mm in diameter and are mostly short, stubby or indistinguishable. One crystal, measuring 1.5 mm in diameter, presents an exception to this rule. This inclusion is clear and has a rectangular euhedral form. These crystals comprise one percent of the obsidian. The matrix is opaque and gritty. The cortex is dull, black and has a slightly weathered rind.

Reference Sample 7.29.3

This sample consists of one hand specimen and one small chip

These specimens are black in reflected light and grey under transmitted light. The lustre is vitreous and the translucency poor to moderate. Surface banding is characterised by continuous, distinct, silvery lines that range between 8 mm and less than 1 mm in thickness. These bands are

slightly curved, but are generally linear. The specimen is too opaque to determine the presence of internal banding. There are no spherulites present in this specimen. Translucent crystal phenocrysts range in size between 1 and 3 mm in diameter. These inclusions also occur in a variety of shapes with rounded forms dominating over larger, more elongated examples. The matrix is opaque and no cortex is attached to the sample.

Reference Sample 7.30

This sample consists of one large hand specimen and five flakes

These specimens are black in reflected light and green under transmitted light. The lustre is highly vitreous and the translucency moderate. No surface banding is apparent. Internal banding is characterised by numerous white-grey streaks. These bands are distinct, relatively continuous and measure less than 0.5 mm in width. No spherulites are present in this sample. Crystal phenocrysts are translucent and measure less than 2 mm in diameter. Other patchy clear crystal inclusions are scattered throughout the obsidian. There are no vesicles and the matrix is clear. The cortex is characterised by smooth, dull obsidian within which are imbedded pale pink-grey to brownish glassy inclusions.

B.2.8 Ohineiti Quarry (Source # 8.0)

The colour of these specimens in reflected light is black and sometimes grey or green. Likewise, grey and green is also visible at times when the specimens are viewed under transmitted light. The lustre is often vitreous and accompanied by a slight surface texture. The translucency is however only moderate at best and in most cases quite poor. Surface banding is found frequently in this sample, but is often indistinct and measures only a few millimetres thick. As seen in the Opuhi group,

surface banding is occasionally accompanied by felsic inclusions. The quality of internal banding ranges from faint, cloudy streaks to darker, more distinct lines that mimic the external banding. No spherulites or phenocrysts are found in these specimens, although 8.8 does exhibit a type of 'crushed glass' inclusion.

Reference Sample 8.1

This sample consists of two hand specimens and one flake.

These specimens are black in reflected light and green under transmitted light. The lustre is vitreous and the translucency moderate. Surface banding is faintly discernible and consists of very thin, grey, consistently spaced lines. Internal banding is comprised of very faint streaks. Spherulites, phenocrysts and other inclusions are absent from these specimens. The matrix is clear.

Reference Sample 8.2

This sample consists of one hand specimen and three flakes.

These specimens are black in reflected light and green under transmitted light. The vitreous lustre has a slight surface texture and the translucency is moderate. Surface banding is very indistinct and comprised of thin lines that occur consistently on the flaked surface of the hand specimen. These lines are typically lightly coloured and set against darker bands. Overall, they are hardly discernible. The thin internal banding is characterised by cloudy or blurry lines. The lines are a consistent width and uniform appearance throughout the specimens. Spherulites or phenocrysts are absent, although mineral-like inclusions occur parallel to the banding in the hand specimen. The matrix is cloudy.

Martin Jones 2002

Reference Sample 8.3

This sample consists of two hand specimens and two flakes.

These specimens are black in reflected light and green under transmitted light. The lustre is slightly waxy with a surface texture due to inclusions. The translucency is moderate to poor. Neither surface nor internal banding is present. The texture of the specimens is quite pitted. Lightly coloured, greyish areas within the obsidian are comprised of crushed glass, or possibly even ash. Spherulites or phenocrysts are absent and the matrix is gritty.

Reference Sample 8.4

This sample consists of three hand specimens and two chips.

These specimens are black in reflected light and green under transmitted light. The highly vitreous lustre has a surface texture and the translucency is moderate. Surface banding is emphasised by mineral inclusions (ash or pumice) bordering the bands, most look like xenolithic inclusions due to the felsic composition. Some bands have formed around these inclusions and the clear coloured grains could be crystals that precipitated when gas becoming trapped within the obsidian. Some internal banding can be seen in the smallest flake that has slight linear cloudiness. Neither spherulites nor phenocrysts are present and the matrix is cloudy.

Reference Sample 8.5

This sample consists of two hand specimens and four flakes.

These specimens are black in reflected light and green under transmitted light. The highly vitreous lustre has a slight surface texture and the translucency is moderate. Surface banding consists of thin (un-

der 0.5 mm), irregularly spaced bands of ash-like xenolithic inclusions. The inclusions occur in the hand specimen. Internal banding is absent. Spherulites or phenocrysts are also absent. The matrix is clear.

Reference Sample 8.6

This sample consists of two hand specimens and two flakes.

These specimens are black to light grey in reflected light and pale green under transmitted light. The vitreous lustre has a surface texture and the translucency is moderate. The obsidian in this sample is interbanded with a light grey, slightly vesicular, felsic rock. Banding is straight and inconsistently spaced, measuring from 0.5 to 4 mm in width. Internal banding is not apparent. Spherulites or phenocrysts are also absent. The matrix is cloudy and some obsidian surfaces have a rainbow like sheen.

Reference Sample 8.7

This sample consists of three hand specimens and one flake.

These specimens are black in reflected light and green under transmitted light. The highly vitreous lustre has a surface texture and the translucency is moderate. Surface banding is present in the largest hand specimen. The bands range from indistinct to thin, relatively distinct, streaky lines that have a noticeable texture. The internal banding is very similar, being thin and indistinct and having a cloudy, streaky appearance. Spherulites and phenocrysts are absent and the matrix is cloudy.

Reference Sample 8.8

This sample consists of one hand specimen and one flake.

These specimens are black in reflected light and green under transmitted light. The lustre is vitreous and textured and the translucency is moderate to poor. Surface and internal banding are both extremely indistinct and more prominent on the flake. These bands vary slightly in colour. White inclusions, similar to 8.3, can be seen in some places and have 'crushed glass' appearance. Spherulites and phenocrysts are absent and the matrix is clear to cloudy.

Reference Sample 8.9

This sample consists of one large hand specimen, two large and three small flakes.

These specimens are black in reflected light and green under transmitted light. The lustre has a slight waxy sheen and the translucency is moderate to poor. Surface banding consists of thin, dull grey streaks that form larger bands measuring between 1 to 5mm wide. Some mineral inclusions occur along these bands. The cortex is rough and lightly coloured. Thin internal bands have a similar appearance to the cloudy grey external bands. These bands are located in a clearer matrix, which is cloudy due to the intensity of the banding. Spherulites and phenocrysts are absent from these specimens.

Reference Sample 8.10

This sample consists of one hand specimen and two small chips.

These specimens are black in reflected light and grey-green under transmitted light. The lustre is waxy and the translucency poor. The cortex is comprised of brown, yellow and grey sediments that have a rough appearance. The obsidian beneath the cortex is streaky. The faint surface banding consists of thin, irregularly spaced, light grey streaks. No inter-

nal banding can be seen. Spherulites and phenocrysts, and other crystal inclusions are absent.

Reference Sample 8.11

This sample consists of one hand specimen and two flakes.

These specimens are black in reflected light and pale green under transmitted light. The vitreous lustre is slightly textured and the translucency is moderate. Surface banding is comprised of thin, consistently spaced, grey lines that and are of a high intensity. Internal banding is characterised by thin grey streaks, which have the effect of rendering the obsidian opaque. Spherulites and phenocrysts, or other crystal inclusions are absent from these specimens. The matrix is somewhat opaque due to banding.

Reference Sample 8.12

This sample consists of one hand specimen and five flakes.

These specimens are black in reflected light and green under transmitted light. The lustre is vitreous with a slight surface texture. The translucency is moderate to poor. The only indication of surface banding is suggested by mineral inclusions occurring beside faint lines. Some indistinct internal bands are present. Spherulites and phenocrysts are absent from these specimens and the matrix is cloudy. The cortex consists of pink pumiceous material welded in small pieces to the obsidian.

Reference Sample 8.13

This sample consists of one hand specimen and five flakes.

These specimens are black in reflected light and green under transmitted light. The lustre is vitreous and textured. The translucency is moderate to poor. Surface banding consists of pumiceous material inter-layered between obsidian and is further emphasised by mineral inclusions that occur along the banding orientation. Internal banding, spherulites and phenocrysts are absent from these specimens. The matrix is generally clear, although some grit can be seen. The cortex has a slightly scoriaceous texture. Welded bands can be seen flowing around, rather than through or truncating, the xenolithic inclusion. This material must therefore have been present before and during the cooling process for this feature to occur.

Reference Sample 8.14

This sample consists of two hand specimens and five flakes.

These specimens are black in reflected light and green under transmitted light. The lustre is vitreous with a slightly waxy surface texture. The translucency is moderate to poor. Surface banding is thin, but consistent and of a high intensity. Typically, grey lines occur against the blacker obsidian. Internal banding consists of thin, dark streaks occurring within a clear matrix. Some bands are somewhat cloudy. Spherulites and phenocrysts are absent from these specimens.

Reference Sample 8.15

This sample consists of one hand specimen and twelve flakes/chips.

These specimens are black in reflected light and green under transmitted light. The vitreous lustre has a surface texture and the translucency is poor. Surface banding is relatively distinct. The bands are only slightly wavy and are comprised of thin lines less than 0.5 mm thick. These

bands are sometimes emphasised by pumiceous inclusions. No internal banding can be seen. Spherulites and phenocrysts are also absent and the matrix is gritty.

Reference Sample 8.16

This sample consists of two hand specimens and four flakes.

These specimens are black in reflected light and grey under transmitted light. The vitreous lustre is highly textured and the translucency is very poor. Neither surface nor internal banding is present, however, some 'flow banding' can be seen and is comprised of a cream coloured pumiceous material that flows within the black obsidian. Spherulites, phenocrysts and other crystal inclusions are absent. It is not possible to describe the matrix as the specimens are too opaque. The cortex has a slight pumiceous texture.

Reference Sample 8.17

This sample consists of two hand specimens and five flakes.

These specimens are black in reflected light and green under transmitted light. The lustre is waxy and the translucency moderate to poor. Surface banding is comprised of grey lines that form larger bands ranging in size from 1mm to 1cm thick. These bands are generally straight, but sometimes have a slight wavy quality. Internal banding is the same consistency, intensity and appearance as that found on the surface. Spherulites, phenocrysts and other crystal inclusions are absent from these specimens. The matrix is cloudy due to the streaky banding.

Martin Jones 2002

Reference Sample 8.18

This sample consists of two hand specimens and two small flakes.

These specimens are black in reflected light and green under transmitted light. The slightly dull lustre is pitted and the translucency is moderate. Surface banding occurs as two distinct grey bands less than 1mm thick. Other reasonably distinct lines contribute to larger (2 to 4 mm) bands. These bands are irregularly spaced. Internal banding consists of cloudy grey streaks. Spherulites, phenocrysts and other crystal inclusions are absent and the matrix is clear.

Reference Sample 8.19

This sample consists of one large hand specimen, two large pieces and nine flakes.

These specimens are black in reflected light and green under transmitted light. The lustre is slightly pitted and quite dusty due to volcanic sediment. The translucency is poor. Surface banding occurs in two forms. First, as lines delineated by mineral inclusions (main hand specimen). Second, indistinct grey lines form cloudy bands 1mm thick. Internal banding is not visible because of the poor translucency. Spherulites and phenocrysts are absent from these specimens. The matrix is clear.

Reference Sample 8.20

This sample consists of four small flakes.

These specimens are black in reflected light and green under transmitted light. The lustre is vitreous with a slightly pitted texture. The translucency is poor. Surface banding is faint and is formed by sediment build-up falling into striations. There is no real evidence for definite sur-

face banding. No internal banding is present due to poor translucency. Spherulites, phenocrysts and other crystal inclusions are absent from these specimens. The matrix is clear.

Reference Sample 8.21

This sample consists of two flakes.

These specimens are black in reflected light and green under transmitted light. The dull lustre displays some surface texture and the translucency is poor. Surface banding is absent from these specimens, however the internal banding consists of dark streaks that vary in size throughout the matrix. Volcanic sediment is welded to one of the specimens. Spherulites, phenocrysts and other crystal inclusions are absent and the matrix is clear.

Reference Sample 8.22

This sample consists of two flakes.

These specimens are black-green in reflected light and green under transmitted light. The vitreous lustre is textured and the translucency is moderate to poor. Surface banding is absent, however internal banding is comprised of thin grey streaks that are consistent and highly intense. Spherulites, phenocrysts and other crystal inclusions are absent from these specimens. The matrix is cloudy due to streaking.

Reference Sample 8.23

This sample consists of one flake.

This specimen is black in reflected light and green under transmitted

light. The vitreous lustre is textured and the translucency poor. Surface banding is comprised of very thin, indistinct bands, that are sometimes emphasised by small linear crystal inclusions. This banding is slightly cloudy. Internal banding, spherulites and phenocrysts are all absent from this specimen. The matrix is clear.

Reference Sample 8.24

This sample consists of one flake.

This specimen is black in reflected light. It is not possible to describe the colour under transmitted light. The lustre is vitreous, though covered with sediment or welded cortex. The translucency is poor (due to the shape of the specimen). Surface banding occurs in some areas as light coloured lines (probably mineral inclusions or sediment). Internal banding, spherulites or phenocrysts are all absent from this specimen. It is not possible to describe the condition of the matrix because of the specimen size.

Reference Sample 8.25

This sample consists of one flake.

This specimen is black in reflected light and green under transmitted light. The vitreous lustre is textured and the translucency is poor. Some striation occurs on the surface. Surface and internal banding, spherulites and phenocrysts are all absent from this specimen. The matrix is probably clear judging from the extremely small position through which the transmitted colour can be seen.

Reference Sample 8.26

This sample consists of one hand specimen, two large pieces and three flakes.

These specimens are black in reflected light and green under transmitted light. The vitreous lustre is textured and the translucency is moderate to poor. The thin and irregularly spaced surface banding is accompanied by linear inclusions of volcanic sediment. Internal banding, spherulites and phenocrysts are all absent from the specimens. The matrix is clear.

Reference Sample 8.27

This sample consists of four flakes.

These specimens are black in reflected light and green under transmitted light. The lustre is dull due to volcanic sediment on the cortex and the translucency is poor. Some very small, thin, wavy lines are present; but are not considered to be surface banding. Internal banding, spherulites and phenocrysts are all absent from these specimens. The matrix is clear, though it is difficult to be certain.

Reference Sample 8.28

This sample consists of two flakes.

These specimens are a dark black-grey-green colour in reflected light and green under transmitted light. The lustre is dull due to volcanic sediment on the cortex and the translucency poor. Indistinct surface banding occurs as 1 mm thick lines. The colouring of the surface banding varies between black and grey-green. Internal banding, spherulites and phenocrysts are all absent. The matrix is clear, though it is difficult to be certain.

Martin Jones 2002

Reference Sample 8.29

This sample consists of two flakes.

These specimens are black in reflected light and green under transmitted light. The lustre is vitreous with a surface texture and the translucency poor. Surface banding is extremely thin and straight. It is grey in colour and displays a high consistency. Internal banding, spherulites and phenocrysts are all absent. It is not possible to describe the condition of the matrix.

Reference Sample 8.30

This sample consists of three flakes.

These specimens are black in reflected light and green under transmitted light. The lustre is vitreous and the translucency moderate. Some volcanic sediment is present on the surface, but no real cortex. Surface and internal banding, spherulites, phenocrysts and other crystal inclusions are all absent from these specimens. It is not possible to describe the condition of the matrix.

Reference Sample 8.31

This sample consists of one flake.

This specimen is black in reflected light and green under transmitted light. The lustre is vitreous and the translucency moderate. No surface banding is apparent. Internal banding consists of thin, dark streaks. Spherulites and phenocrysts are absent and the matrix is clear.

Reference Sample 8.32

No obsidian was found in 'H1, Spit 6' during flake collection at Ohineiti.

Reference Sample 8.33

This sample consists of one hand specimen, two small pieces and one flake.

These specimens are black to black-grey in reflected light and green under transmitted light. The lustre ranges from dull, with a surface texture, to vitreous. The translucency is moderate and the matrix is gritty. All the specimens vary in colour, lustre and surface banding: RF# 8.33-a - This specimen displays cloudy, indistinct "bands" that are more like threads. These "bands" are linear and straight throughout the entire specimen giving a streaky effect. RF# 8.33-b - This specimen displays very distinct, intense, straight lines that occur inconsistently through the rock. Minor, light grey inclusions are probably rhyolitic ash. RF# 8.33-c - No surface banding is apparent on this specimen. RF# 8.33-d - No surface banding is apparent on this specimen, though very slight internal banding (gritty) is visible.

Reference Sample 8.34

This sample consists of thirteen flakes of various sizes.

These specimens are black in reflected light and green under transmitted light. The vitreous lustre is textured and the translucency is moderate. Surface banding is comprised of thin, grey streaky bands that are generally straight, though sometimes also wavy. 8.34-a and 8.34-b display indistinct and distinct surface banding respectively. Internal banding consists of thin, dark grey streaks. Spherulites, phenocrysts and other

crystal inclusions are absent. The matrix is clear.

Reference Sample 8.35.1

This sample consists of one small chip

This specimen is black in reflected light and green under transmitted light. The lustre is waxy and the translucency poor to moderate. No surface or internal banding is visible, but there is a definite waxy texture forming streaks that occur throughout the specimen. No spherulites or other inclusions are present. The matrix is gritty and no cortex is attached to the specimen.

Reference Sample 8.35.2

This sample consists of one small chip

This specimen is black in reflected light and green under transmitted light. The lustre is waxy and the translucency poor to moderate. No surface or internal banding is visible, but there is a definite waxy texture forming streaks throughout the specimen. Spherulites are grey and occur abundantly. No other inclusions are present. The matrix is gritty and no cortex is apparent.

Reference Sample 8.36.1

This sample consists of one small flake

These specimens are black in reflected light and green under transmitted light. The lustre is vitreous and the translucency poor to moderate. Surface banding is characterised by grey streaking that becomes thicker and more consistent internally. These latter bands also have a grey col-

oration. No spherulites are present, neither are there any other inclusions or vesicles. The matrix is gritty and there is no cortex attached to the specimen.

Reference Sample 8.36.2

This sample consists of one hand specimen and one flake

These specimens are black in reflected light and green under transmitted light. The lustre is vitreous and the translucency poor to moderate. Surface banding is very faint on this specimen. No spherulites are present, however one clear crystal phenocryst measuring less than 0.5 mm in diameter can be seen. No other inclusions or vesicles are present. The matrix is moderately clear while the cortex is dull, black and shows some sign of weathering.

Reference Sample 8.37

This sample consists of one large hand specimen

This specimen is black in reflected light and green under transmitted light. The lustre is dull and the translucency poor to moderate. Surface flow banding is characterised by continuous, but inconsistent streaky bands that vary in thickness from 2 mm to 1 cm thick. No internal flow banding can be seen. Crystal phenocrysts vary in shape; both elongate and rounded forms are present in this sample. The latter measure anywhere up to 3 mm in diameter and tend to be less well formed. Clusters of these crystals occur throughout one percent of the matrix. No spherulites or vesicles can be seen and the matrix is too opaque to describe. The cortex is smooth, dull and grey.

Martin Jones 2002

Reference Sample 8.38.1

This sample consists of one hand specimen

This specimen is black in reflected light and grey under transmitted light. The lustre is vitreous and slightly textured. The translucency is poor. Surface banding is characterised by very thin, straight, continuous lines. These lines are comprised of thinly banded, layered inclusions of crystal. Indistinct greyish streaking can also be seen. Crystal phenocrysts comprise less than one percent of the matrix. There are no vesicles. The matrix is cloudy and streaky while the cortex is dull-black and slightly weathered.

Reference Sample 8.38.2

This sample consists of one hand specimen

This specimen is black in reflected light and grey under transmitted light. The lustre is vitreous and slightly textured. The translucency is poor. Surface banding is characterised by very thin, straight, continuous lines. These lines are comprised of thinly banded, layered inclusions of crystal. Indistinct greyish streaking can also be seen. Crystal phenocrysts comprise less than one percent of the matrix. No vesicles are present. The matrix is cloudy and streaky while the cortex is dull-black and slightly weathered.

Reference Sample 8.38.3

This sample consists of one hand specimen

This specimen is black in reflected light and grey under transmitted light. The lustre is vitreous and slightly textured. The translucency is poor. Surface banding is characterised by very thin, straight, continuous

lines. These lines are comprised of thinly banded, layered inclusions of crystal. Indistinct greyish streaking can also be seen. Crystal phenocrysts comprise less than one percent of the matrix. No vesicles are present. The matrix is cloudy and streaky while the cortex is dull-black and slightly weathered.

Reference Sample 8.38.4

This sample consists of one hand specimen

This specimen is black in reflected light and grey under transmitted light. The lustre is vitreous and slightly textured. The translucency is poor. Surface banding is characterised by very thin, straight, continuous lines. These lines are comprised of thinly banded, layered inclusions of crystal. Indistinct greyish streaking can also be seen. Crystal phenocrysts comprise less than one percent of the matrix. No vesicles are present. The matrix is cloudy and streaky while the cortex is dull-black and slightly weathered.

Reference Sample 8.38.5

This sample consists of one hand specimen

This specimen is black in reflected light and grey under transmitted light. The lustre is vitreous and slightly textured. The translucency is poor. Surface banding is characterised by very thin, straight, continuous lines. These lines are comprised of thinly banded, layered inclusions of crystal. Indistinct greyish streaking can also be seen. Crystal phenocrysts comprise less than one percent of the matrix. No vesicles are present. The matrix is cloudy and streaky while the cortex is dull-black and slightly weathered.

Martin Jones 2002

Reference Sample 8.39.1

This sample consists of one flake

This specimen is black in reflected light and green under transmitted light. The lustre is vitreous and the translucency poor. The pale grey surface banding is very thin and occurs continuously throughout the specimen. Some pale white crystal inclusions can be seen in these bands. The internal bands are formed similarly to those at the surface. No spherulites or phenocrysts can be seen. No vesicles are present and the matrix is clear. The cortex consists of hard, gritty sediment with a light brown colour.

Reference Sample 8.39.2

This sample consists of one flake

This specimen is black in reflected light and green under transmitted light. The lustre is vitreous and the translucency poor. The pale grey surface banding is very thin and occurs continuously throughout the specimen. Some pale white crystal inclusions can be seen in these bands. The internal bands are formed similarly to those at the surface. No spherulites or phenocrysts can be seen. No vesicles are present and the matrix is clear. There is no cortex attached to this specimen.

Reference Sample 8.40.1

This sample consists of one hand specimen and one flake

These specimens are black in reflected light and green under transmitted light. The lustre is vitreous with a slight surface texture. The translucency is moderate. Surface banding is minimal and consists of thinly layered grey-white-brown crystal inclusions. These two layers are closely

spaced, but are neither consistent nor continuous. Internal banding is only faintly visible and relatively consistently. Microscopic flecks can be seen and may be related to the surface texture. No spherulites, phenocrysts, or vesicles are present in this specimen. The cortex lacks any rind and instead consists of dull, black obsidian. The matrix is clear.

Reference Sample 8.40.2

This sample consists of one hand specimen

This specimen is black in reflected light and green under transmitted light. The lustre is vitreous with a slight surface texture. The translucency is moderate. Internal banding is only faintly visible and relatively consistent. Microscopic flecks can be seen and may be related to the surface texture. No spherulites, phenocrysts, or vesicles are present in this specimen. The cortex lacks any rind and instead consists of dull, black obsidian. The matrix is clear.

Reference Sample 8.41.1

This sample consists of one hand specimen and one small chip

This specimen is black in reflected light and green under transmitted light. The lustre is vitreous and the translucency poor to moderate. Faint surface flow banding is comprised of thin and continuous grey lines. Internal banding is absent from these specimens. Crystal inclusions occur in a variety of forms ranging from elongate to round. All display a brownish-white coloration and constitute less than one percent of the specimens. The matrix is opaque and no cortex is attached to either specimen.

Martin Jones 2002

Reference Sample 8.41.2

This sample has been destroyed.

Reference Sample 8.41.3

This sample consists of one hand specimen and one small chip

This specimen is black in reflected light and green under transmitted light. The lustre is vitreous and the translucency poor to moderate. Surface flow banding is comprised of thin, white crystal-inclusive layers that are neither continuous nor consistent. Internal banding is absent from the specimens. 3 mm elongate crystals and clear, 1 mm diameter crystal phenocrysts each form less than one percent of the specimens. There are no spherulites, vesicles or other inclusions present. The dull grey cortex is thin and shows sign of weathering. The matrix is cloudy.

Reference Sample 8.41.4

This sample consists of one hand specimen and one small chip

This specimen is black in reflected light and green under transmitted light. The lustre is vitreous and the translucency poor to moderate. No surface banding is visible. Internal banding consists of thin, grey streaks that are both consistent and continuous throughout the specimen. No spherulites or vesicles can be found. Crystal phenocrysts are the only other type of inclusion present and form less than one percent of the specimen. The phenocrysts generally measure 1 mm in diameter. The cortex is a dull, grey-black colour and shows sign of weathering. The matrix is cloudy.

Reference Sample 8.41.5

This sample consists of one hand specimen and one small chip

This specimen is black in reflected light and green under transmitted light. The lustre is vitreous and is accompanied by a slight texture. The translucency is poor to moderate. Some patchy crystal inclusions form rare and indistinct streaks. No surface or internal banding, spherulites, vesicles or other crystal inclusions are present. The matrix is opaque and the cortex is absent.

Reference Sample 8.41.6

This sample consists of one hand specimen and one small chip

This specimen is black in reflected light and green under transmitted light. The lustre is vitreous and the translucency poor to moderate. Thin lines formed by white crystal-inclusive layers define surface banding. No internal banding can be seen. There are also no spherulites, vesicles or other crystal inclusions. The dull, black cortex is weathered giving the exterior a smooth texture. The matrix is opaque.

Reference Sample 8.41.7

This sample consists of one hand specimen and one flake

This specimen is black in reflected light and green under transmitted light. The lustre is vitreous and the translucency poor to moderate. Surface banding is comprised of numerous, thin, pale grey bands. No internal banding is visible. One clear, crystal phenocryst, measuring 1 mm in diameter, is the only inclusion present. The specimen contains no spherulites or vesicles. The matrix is opaque and no cortex is attached to the specimen.

Martin Jones 2002

Reference Sample 8.42

This sample has been destroyed.

Reference Sample 8.43

This sample consists of one hand specimen and one chip

These specimens are silky-grey to black in reflected light and grey under transmitted light. The lustre is vitreous and is accompanied by a silky texture. The translucency is poor. Surface flow banding is comprised of streaky, silvery-grey bands. This banding is continuous throughout the specimen and varies in width from 1 mm to 1 cm. No internal banding, spherulites, inclusions, vesicles or phenocrysts are present. The matrix is opaque and the cortex dull and weathered. The silver-grey cortex also has a distinctive texture.

Reference Sample 8.44

This sample consists of one hand specimen and one chip

These specimens are grey-black in reflected light and grey-green under transmitted light. The lustre is vitreous with a slight waxy quality. The translucency is poor. Surface banding is indistinct and streaky. This feature occurs in a variety of colours including grey, green and black. There is no internal banding. Ovular inclusions measuring 4 mm long are comprised of a grey gritty material. This material does not occur abundantly. The matrix is cloudy and no cortex is attached to either specimen.

8.45

This sample has been destroyed.

Reference Sample 8.46

This sample consists of one hand specimen and one flake

These specimens are black in reflected light and green under transmitted light. The lustre is vitreous and the translucency poor. Surface flow banding consists of very thin, closely spaced, white-grey lines. There is no internal banding. Inclusions are grey and have a gritty texture. There is also an abundance of microscopic inclusions. There are no spherulites, vesicles or phenocrysts. The dull, grey-black cortex lacks any rind. The matrix is opaque.

Reference Sample 8.47

This sample consists of one hand specimen and one flake

These specimens are black in reflected light and green under transmitted light. The lustre is vitreous with a surface texture. The translucency is poor to moderate. Surface banding consists of thin grey-green streaks that occur continuously and consistently throughout the specimen. These bands measure less than 1 mm wide and have a slightly waxy appearance. Internal banding is very similar to that seen on the surface. The matrix has some streaking, but is generally quite clear. No cortex is attached to either specimen.

Reference Sample 8.48

This sample consists of one hand specimen and one flake

These specimens are black in reflected light and green under transmitted light. The lustre is vitreous and slightly textured. The translucency is poor. Surface banding is comprised of thin grey bands that occur inconsistently throughout the specimen. No internal banding, spherulites, or vesicles can be seen. Clear, microscopic, crystal flecks are the only visible inclusions. The matrix is opaque and the cortex dull, black and textured.

Reference Sample 8.49

This sample consists of one hand specimen and one flake

These specimens are grey-black in reflected light and grey-green under transmitted light. The lustre is vitreous and the translucency poor. Indistinct, but consistent streaking can be seen on the surface. The streaks have vague boundaries and occur in the place of definite banding. There is no internal banding, nor any spherulites, phenocrysts, or vesicles present. The only inclusions visible occur in the form of microscopic crystal flecks. The matrix is opaque and the cortex dull, black and weathered.

Reference Sample 8.50.1

This sample consists of one flake

This specimen is black in reflected light and green under transmitted light. The vitreous lustre is accompanied by a slight surface texture. The translucency is poor. Surface banding is comprised of thin, grey, wavy lines that occur continuously throughout the specimen. No internal banding, spherulites, vesicles or other inclusions present. The matrix is clear and the cortex dull, black weathered.

Reference Sample 8.50.2

This sample consists of one flake

This specimen is black in reflected light and green under transmitted light. The vitreous lustre is accompanied by a slight surface texture. The translucency is poor. Thin, light grey bands occur on the surface within which are imbedded inclusions. No internal banding is visible. There are also no spherulites or vesicles present in the matrix. The only other inclusions visible are microscopic crystalline flecks. These occur abundantly, but still comprise only 1% of the obsidian. The matrix is opaque and no cortex is attached to the specimen.

Reference Sample 8.50.3

This sample consists of one flake

This specimen is black in reflected light and green under transmitted light. The vitreous lustre is accompanied by a slight surface texture. The translucency is poor. Discontinuous and indistinct surface streaking occurs consistently throughout the specimen. No internal banding, spherulites, vesicles or other inclusions are present. The matrix is opaque and no cortex is attached to the specimen.

Reference Sample 8.50.4

This sample consists of one flake

This specimen is grey-black in reflected light. It is not possible to describe the colour under transmitted light as the obsidian is too opaque. The waxy lustre is textured and the translucency opaque. No surface or internal banding can be seen. There are also no spherulites or vesicles present in the matrix, however, silver-grey streaking is formed by

densely packed inclusions. This streaking dominates the specimen to such a great extent that the specimen takes on a rough, waxy appearance. Typical black obsidian is not present in this specimen, instead the glass has a grainy, grey-white appearance. The matrix is opaque and the specimen lacks a cortex.

Reference Sample 8.50.5

This sample consists of one hand specimen and one small chip

These specimens are black in reflected light and green under transmitted light. The vitreous lustre is accompanied by a slight surface texture. The translucency is poor. Indistinct, dark grey streaks occur in the place of definite surface banding. Crystal phenocrysts measure less than 1 mm in diameter and form one percent of the specimen. There are no spherulites or vesicles present. The matrix is opaque and the specimen lacks any cortex.

Reference Sample 8.50.6

This sample consists of one small chip

This specimen is black in reflected light and green under transmitted light. The lustre is vitreous with a slight surface texture. The translucency is poor. Surface banding is comprised of thin, discontinuously or consistently occurring layers of crystal inclusions. There is a lack of internal banding, spherulites, inclusions, vesicles and other inclusions. The matrix is opaque and the specimen lacks any cortex.

Reference Sample 8.50.7

This sample consists of one hand specimen and one small chip

This specimen is black in reflected light and green under transmitted light. The vitreous lustre is accompanied by a slight surface texture. The translucency is poor. The dark grey surface banding is indistinct and is comprised of thin lines that occur consistently and continuously throughout the specimen. No internal banding, spherulites or vesicles are present. Abundant microscopic crystalline inclusions form one percent of each specimen. The matrix is clear and the specimen lacks any cortex.

Reference Sample 8.51.1

This sample consists of one flake

This specimen is black in reflected light and grey-green under transmitted light. The lustre is vitreous with a silky surface texture. The translucency is poor. Surface flow banding is comprised of thin grey bands that occur consistently and continuously throughout the specimen. These bands are straight, closely spaced and occur in a variety of thicknesses, all less than 1 mm. Grey-white crystal inclusions are embedded within these bands. No internal banding, spherulites, vesicles or phenocrysts are present in this specimen. Microscopic crystalline flecks, while being relatively abundant, still form only 1% of the specimen. The matrix is opaque. The cortex consists of welded sediment that is thin, grey, and has a weathered appearance.

Reference Sample 8.51.2

This sample consists of one flake

This specimen is black in reflected light and grey-green under transmitted light. The vitreous lustre is accompanied by a silky surface texture. The translucency is poor. Surface flow banding is composed of thin grey

bands that occur consistently and continuously throughout the specimen. These bands are straight, closely spaced and occur in a variety of thicknesses, all less than 1 mm. Grey-white crystal inclusions are embedded within these bands. No internal banding, spherulites, vesicles or phenocrysts are present in this specimen. Microscopic crystalline flecks, while being relatively abundant, still form only 1% of the specimen. The matrix is opaque. The cortex consists of welded sediment that is thin, grey, and has a weathered appearance.

Reference Sample 8.51.3

This sample has been destroyed.

Reference Sample 8.51.4

This sample consists of one hand specimen and one chip

These specimens are black in reflected light and grey-green under transmitted light. The vitreous lustre is accompanied by a slight surface texture and the translucency is poor. Surface flow banding is comprised of thin grey bands that occur consistently and continuously throughout the specimen. These bands are straight, closely spaced and occur in a variety of thicknesses, all less than 1 mm. Grey-white crystal inclusions are embedded within these bands. No internal banding, spherulites, vesicles or phenocrysts are present in this specimen. Microscopic crystalline flecks, while being relatively abundant, still form only 1% of the specimen. The matrix is opaque. The cortex consists of welded sediment that is thin, grey, and has a weathered appearance.

Reference Sample 8.51.5

This sample consists of one small hand specimen

This specimen is black in reflected light and grey-green under transmitted light. The vitreous lustre is accompanied by a slight surface texture and the translucency is poor. Surface flow banding is composed of thin grey bands that occur consistently and continuously throughout the specimen. These bands are straight, closely spaced and occur in a variety of thicknesses, all less than 1 mm. Grey-white crystal inclusions are embedded within these bands. No internal banding, spherulites, vesicles or phenocrysts are present in this specimen. Microscopic crystalline flecks, while being relatively abundant, still form only 1% of the specimen. The matrix is opaque. The cortex consists of welded sediment that is thin, grey, and has a weathered appearance.

Reference Sample 8.51.6

This sample consists of one flake and one small chip

This specimen is black in reflected light and grey-green under transmitted light. The vitreous lustre is accompanied by a slight surface texture. The translucency is poor. Surface flow banding is characterised by thin grey bands that occur consistently and continuously throughout the specimen. These bands are straight, closely spaced and occur in a variety of thicknesses, all less than 1 mm. Grey-white crystal inclusions are embedded within these bands. No internal banding, spherulites, vesicles or phenocrysts are present in this specimen. Microscopic crystalline flecks, while being relatively abundant, still form only 1% of the specimen. The matrix is opaque. The cortex consists of welded sediment that is thin, grey, and has a weathered appearance.

Martin Jones 2002

Reference Sample 8.52.1

This sample consists of one flake

This specimen is grey-black in reflected light and grey-green under transmitted light. The lustre is vitreous and the translucency poor. Surface flow banding consists of thin bands and sometimes includes layered crystalline inclusions. These closely spaced bands occur continuously throughout the specimen.. There are no spherulites, vesicles or phenocrysts within the matrix. A grey-white crystalline material represents the only other type of inclusion present. This material forms streaks that can be seen running through the clear matrix. The dull cortex is composed of smooth welded sediment.

Reference Sample 8.52.2

This sample consists of one flake

This specimen is grey-black in reflected light and grey-green under transmitted light. The lustre is vitreous and the translucency poor. Banding is difficult to discern as the specimen is covered with coarse welded sediment. There are no spherulites, vesicles or phenocrysts within the matrix. The dull cortex consists of the coarse welded sediment mentioned above.

Reference Sample 8.52.3

This sample consists of one small hand specimen

This specimen is grey-black in reflected light and grey-green under transmitted light. The lustre is vitreous and the translucency poor. Surface flow banding consists of thin bands and includes densely layered crystalline inclusions. These closely spaced bands occur continuously

throughout the specimen. There are no spherulites, vesicles or phenocrysts within the matrix. Other inclusions consist of a pale orange-pink crystalline material that forms irregular layers within the obsidian. This feature has a rough, glassy texture and occurs inconsistently and discontinuously throughout the specimen. The dull cortex is composed of smooth welded sediment.

Reference Sample 8.52.4

This sample consists of a small hand specimen and a chip

These specimens are grey-black in reflected light and grey-green under transmitted light. The lustre is vitreous and the translucency poor. Surface flow banding consists of thin bands and sometimes includes layered crystalline inclusions. These closely spaced bands occur continuously throughout the specimen. There are no spherulites, vesicles or phenocrysts within the matrix. A grey-white crystalline material represents the only other type of inclusion present. This material forms streaks that can be seen running through the clear matrix. There is no cortex present on either specimen.

Reference Sample 8.52.5

This sample consists of one small hand specimen

This specimen is grey-black in reflected light and grey-green under transmitted light. The lustre is vitreous and the translucency poor. Surface flow banding consists of thin bands and sometimes includes layered crystalline inclusions. These closely spaced bands occur continuously throughout the specimen. There are no spherulites, vesicles or phenocrysts within the matrix. There is no cortex present.

Martin Jones 2002

Reference Sample 8.52.6

This sample consists of one hand specimen and one small chip

These specimens are grey-black in reflected light and grey-green under transmitted light. The lustre is vitreous in places, but generally quite dull. The translucency is poor. Surface flow banding consists of thin bands that sometimes include layered crystalline inclusions. These closely spaced bands occur continuously throughout the specimen. The density of these bands gives the obsidian its somewhat dull appearance. There are no spherulites, vesicles or phenocrysts within the matrix. Surface striations occur on one side of the hand specimen. These appear to have formed during the cooling process. There is no cortex present.

Reference Sample 8.52.7

This sample consists of one small hand specimen and one chip

These specimens are grey-black in reflected light and grey-green under transmitted light. The lustre is vitreous and the translucency poor. The definite surface banding consists of thin layers crystalline inclusions that, at times, completely section the hand specimen. These closely spaced bands occur continuously throughout the specimen. There are no spherulites, vesicles or phenocrysts within the matrix. An orange sediment, possibly iron oxide, is located at the edge of the most prominent 'white sediment' band. There is no cortex present.

Reference Sample 8.52.8

This sample consists of one flake

This specimen is grey-black in reflected light and grey-green under transmitted light. The lustre is vitreous and the translucency poor to mod-

erate. The thin surface banding contains small white crystalline inclusions that occur intermittently. These bands are closely spaced, but less prominent than previous examples from this group. There are no spherulites, vesicles or phenocrysts within the matrix. A grey-white crystalline material represents the only other type of inclusion present. There is no cortex present.

Reference Sample 8.52.9

This sample consists of one thin flake

This specimen is grey-black in reflected light and grey-green under transmitted light. The lustre is vitreous and the translucency moderate to good. Surface flow banding consists of thin, indefinite bands that occur continuously throughout the specimen. There are no spherulites, vesicles or phenocrysts within the matrix. A very small section of grey-white crystalline material represents the only other type of inclusion. There is no cortex present.

Reference Sample 8.52.10

This sample consists of one small hand specimen and one chip

These specimens are grey-black in reflected light and grey-green under transmitted light. The lustre is waxy and the translucency poor. Surface flow banding consists of thin bands and sometimes includes layered crystalline inclusions. These closely spaced bands occur continuously throughout the specimen. There are no spherulites, vesicles or phenocrysts within the matrix. A grey-white crystalline material represents the only other type of inclusion present. A pale cream sediment is attached to the dull cortex on both specimens.

Martin Jones 2002

Reference Sample 8.52.11

This sample consists of one small hand specimen

This specimen is grey-black in reflected light and grey-green under transmitted light. The lustre is vitreous and the translucency poor. Surface flow banding consists of thin bands and sometimes includes layered crystalline inclusions. These closely spaced bands occur continuously throughout the specimen. A pale orange-pink crystalline material also occurs in a banding type orientation. This feature forms irregular layers within the obsidian and has a rough, glassy texture. There are no spherulites, vesicles or phenocrysts within the matrix. No cortex is present.

Reference Sample 8.52.12

This sample consists of one flake

This specimen is grey-black in reflected light and grey-green under transmitted light. The lustre is vitreous and the translucency poor to moderate. Surface banding consists of thin, wavy bands, which at times include layered crystalline inclusions. These closely spaced bands occur continuously throughout the specimen. Thin grey streaks can be seen internally. There are no spherulites, vesicles or phenocrysts within the matrix. A grey-white crystalline material represents the only other type of inclusion present. This material forms streaks that can be seen running through the clear matrix. A pale yellow sediment is welded to the dull cortex.

Reference Sample 8.52.13

This sample consists of one flake

This specimen is grey-black in reflected light and grey-green under transmitted light. The lustre is vitreous and the translucency poor. Surface flow banding consists of thin bands that sometimes includes layered crystalline inclusions. These closely spaced bands occur continuously throughout the specimen. There are no spherulites, vesicles or phenocrysts within the matrix. A grey-white crystalline material represents the only other type of inclusion present. There is no cortex.

Reference Sample 8.52.14

This sample consists of one small hand specimen

This specimen is grey-black in reflected light and grey-green under transmitted light. The lustre is vitreous and the translucency poor. Surface flow banding consists of thin bands and sometimes includes layered crystalline inclusions. These closely spaced bands occur continuously throughout the specimen. There are no spherulites, vesicles or phenocrysts within the matrix. A grey-white crystalline material represents the only other type of inclusion present. There is no cortex.

Reference Sample 8.52.15

This sample consists of one small flake

This specimen is grey-black in reflected light and grey-green under transmitted light. The lustre is vitreous and the translucency poor to moderate. There is no surface or internal banding. There are also no spherulites, vesicles or phenocrysts. Streaks can be seen running through the clear matrix. There is no cortex.

Martin Jones 2002

Reference Sample 8.52.16

This sample consists of one small flake

This specimen is grey-black in reflected light and grey-green under transmitted light. The lustre is vitreous and the translucency poor. Surface flow banding consists of thin bands that sometimes includes layered crystalline inclusions. These closely spaced bands occur continuously throughout the specimen. There are no spherulites, vesicles or phenocrysts within the matrix. A grey-white crystalline material represents the only other type of inclusion present. This material forms streaks that can be seen running through the clear matrix. Smooth welded sediment is welded to the dull cortex.

Reference Sample 8.52.17

This sample consists of one small hand specimen This specimen is grey-black in reflected light and grey-green under transmitted light. The lustre is vitreous and the translucency poor. Surface flow banding consists of thin bands and sometimes includes layered crystalline inclusions. These closely spaced bands occur continuously throughout the specimen. In this example, there are two very definite layers of inclusions within the obsidian. There are no spherulites, vesicles or phenocrysts within the matrix. A grey-white crystalline material represents the only other type of inclusion present. This material forms streaks that can be seen running through the clear matrix. The cortex is dull and includes some smooth welded sediment.

Reference Sample 8.52.18

This sample consists of one chip

This specimen is grey in reflected light and grey-green under transmitted light. The waxy lustre is accompanied by a slight surface texture and the translucency is poor. Surface flow banding consists of thin bands that sometimes includes layered crystalline inclusions. These closely spaced bands occur continuously throughout the specimen. There are no spherulites, vesicles or phenocrysts within the matrix. A grey-white crystalline material represents the only other type of inclusion present. Smooth sediment is welded to the dull cortex.

Reference Sample 8.52.19

This sample consists of one small hand specimen and one chip

These specimens are grey-black in reflected light and grey-green under transmitted light. The lustre is vitreous and the translucency poor. Surface flow banding consists of thin bands and sometimes includes layered crystalline inclusions. These closely spaced bands occur continuously throughout the specimen. There are no spherulites, vesicles or phenocrysts within the matrix. A grey-white crystalline material represents the only other type of inclusion present. There is no cortex attached to either specimen.

Reference Sample 8.52.20

This sample consists of one flake and one chip

These specimens are grey-black in reflected light and grey-green under transmitted light. The lustre is vitreous and the translucency poor. Surface flow banding consists of thin bands that intermittently includes layered crystalline inclusions. These closely spaced bands occur continuously throughout the specimen. Internal banding is composed of thin grey streaks. There are no spherulites, vesicles or phenocrysts within the

matrix. A grey-white crystalline material represents the only other type of inclusion present. There is no cortex attached to either specimen.

Reference Sample 8.52.21

This sample consists of one small hand specimen and one chip

These specimens are grey-black in reflected light and grey-green under transmitted light. The waxy lustre is accompanied by a surface texture and the translucency is poor. Surface flow banding is very indistinct. There are no spherulites, vesicles or phenocrysts within the matrix. The pale orange-pink crystalline material occurs on the surface and is similar in composition to the material that forms banding within 59.11. This feature has a rough, glassy texture and occurs in localised areas over the hand specimen.

Reference Sample 8.52.22

This sample consists of one flake

This specimen is grey-black in reflected light and grey-green under transmitted light. The lustre is vitreous and the translucency poor. Surface flow banding consists of thin bands that sometimes includes layered crystalline inclusions. These closely spaced bands occur continuously throughout the specimen. There are no spherulites, vesicles or phenocrysts within the matrix. A grey-white crystalline material represents the only other type of inclusion present. Smooth sediment is welded to the dull cortex.

Reference Sample 8.52.23

This sample consists of one small hand specimen

This specimen is grey-black in reflected light and grey-green under transmitted light. The lustre is highly vitreous and the translucency poor. Surface flow banding consists of thin, closely spaced green lines that occur continuously throughout the specimen. There are no spherulites, vesicles or phenocrysts within the matrix and there is also no cortex attached to the specimen.

Reference Sample 8.52.24

This sample consists of one small hand specimen

This specimen is grey-black in reflected light and grey-green under transmitted light. The lustre is vitreous and the translucency poor. Surface flow banding consists of thin bands and sometimes includes layered crystalline inclusions. These closely spaced bands occur continuously throughout the specimen. There are no spherulites, vesicles or phenocrysts within the matrix. A pale orange-pink crystalline material also occurs in a banding type orientation. This feature forms irregular layers within the obsidian and has a rough, glassy texture.

Reference Sample 8.52.25

This sample consists of one small flake

This specimen is grey-black in reflected light and grey-green under transmitted light. The lustre is vitreous and the translucency poor. Surface flow banding consists of thin bands and sometimes includes layered crystalline inclusions. These closely spaced bands occur continuously throughout the specimen. There are no spherulites, vesicles or phenocrysts within the matrix. There is no cortex attached to the specimen.

Martin Jones 2002

Reference Sample 8.52.26

This sample consists of one hand specimen and one chip

These specimens are grey-black in reflected light and grey-green under transmitted light. The lustre is highly vitreous and the translucency poor. Surface flow banding consists of thin bands and sometimes includes layered crystalline inclusions. These closely spaced bands occur continuously throughout the specimen. There are no spherulites, vesicles or phenocrysts within the matrix. A grey-white crystalline material represents the only other type of inclusion present. This material forms streaks that can be seen running through the clear matrix. There is no cortex attached to either specimen.

Reference Sample 8.52.27

This sample consists of small flake

This specimen is grey-black in reflected light and grey-green under transmitted light. The lustre is vitreous and the translucency poor. Surface flow banding consists of thin bands and sometimes includes layered crystalline inclusions. These closely spaced bands occur continuously throughout the specimen. There are no spherulites, vesicles or phenocrysts within the matrix. A grey-white crystalline material represents the only other type of inclusion present. This material forms streaks that can be seen running through the clear matrix. Some smooth sediment is attached to the dull cortex.

Reference Sample 8.52.28

This sample consists of one small hand specimen and one chip

These specimens are grey-black in reflected light and grey-green under

transmitted light. The lustre is vitreous and the translucency poor. Surface flow banding consists of thin, wavy bands, which at times include layered crystalline inclusions. These closely spaced bands occur continuously throughout the specimen. There are no spherulites, vesicles or phenocrysts within the matrix. A grey-white crystalline material represents the only other type of inclusion present. This material forms streaks that can be seen running through the clear matrix. Some smooth sediment is attached to the dull cortex.

B.2.9 Taratimi Bay (Source # 9.0)

The following specimens are all fairly solid, amorphous and blocky. The colour visible in reflected light is black, however shades of grey and green are also visible. The colour under transmitted light is green, with a greyish green also visible in some specimens. The lustre varies between poor and highly vitreous. The vitreous specimens usually have a slight texture. The translucency is consistently moderate throughout the sample. Only specimens 9.6 and 9.10 exhibit banding of any description. Crystal inclusions are present in 9.2 and 9.6, where they occur abundantly. The matrix is generally clear and where present, the cortex is comprised of welded ash.

Reference Sample 9.1

This sample consists of one hand specimen and one flake.

These specimens are black in reflected light and green under transmitted light. The lustre is highly vitreous and translucency moderate. No surface or internal banding is present. Spherulites and other inclusions are also absent.

Reference Sample 9.2

This sample consists of one hand piece and one flake.

These specimens are black in reflected light and green under transmitted light. The lustre is highly vitreous and the translucency moderate to poor. Surface banding and internal banding as well as spherulites are all absent from these specimens. Inclusions are present in the welded volcanic sediment, as are xenoliths. The matrix is clear.

Reference Sample 9.3

This sample consists of two hand specimens.

These specimens are black in reflected light and green under transmitted light. The lustre is highly vitreous and the translucency moderate and quite opaque. No surface or internal banding is present, nor are there any spherulites or other inclusions. The matrix is clear.

Reference Sample 9.4

This sample consists of two hand specimens.

These specimens are black in reflected light and green under transmitted light. The lustre is highly vitreous and the translucency moderate to poor. No surface or internal banding is present, nor are there any spherulites or other inclusions. The matrix is clear.

Reference Sample 9.5

This sample consists of five specimens.

These specimens are black in reflected light and green under transmitted

light. The lustre is vitreous and the translucency moderate to poor. Surface banding is present on specimen 9.5a. Typically, faint grey streaky lines form bands of that range between 2 and 4 mm in width. No internal banding, spherulites, or other inclusions are noticeable. The matrix is clear.

Reference Sample 9.6

This sample consists of four hand specimens and four flakes.

- Judging from the colour, lustre, banding and spherulitic content many sub-groupings are present within this one sample.

9.6 - a.

The colour visible in reflected light is a greyish black. No colour change can be seen under transmitted light. The lustre is waxy and the translucency is opaque. Surface bands are grey-black and occur consistently throughout the specimen. These surface bands measure 1-5mm in thickness. No internal banding is visible, nor are any spherulites or inclusions. It is not possible to describe the matrix.

9.6 - b.

The colour visible in reflected light is a dark grey to a stone black. No transmitted colour is visible. The lustre has a waxy characteristic and no translucency is discernible. Surface banding is characterised by two colours flowing together. This flow pattern is typical of that found in metamorphic rocks. No internal banding, spherulites or inclusions are present. It is not possible to describe the matrix.

9.6 - c.

The colour visible in reflected light is black. No colour is visible under transmitted light. The lustre is vitreous with a slight texture. No translu-

cency is evident. Surface banding is very cloudy and indistinct, it can be described as a texture rather than definite banding. No internal bands, spherulites, or other inclusions are present. It is not possible to describe the matrix. The cortex consists of pulled or strained obsidian.

9.6 - d.

The colour visible in reflected light is black and green becomes prominent under transmitted light. The specimen is highly vitreous, but poorly translucent. Surface or internal banding is absent as are spherulites and other inclusions. The cortex has volcanic sediment welded to it. It is not possible to describe the matrix.

9.6 - e.

The colour visible in reflected light is black and green becomes prominent under transmitted light. The specimen is highly vitreous, but poorly translucent. Surface or internal banding is absent as are spherulites and other inclusions.

9.6 - f.

The colour visible in reflected light is green-grey. No colour is noticeable under transmitted light. The lustre is waxy and the translucency non-existent. Surface banding is comprised of 4 mm light grey bands. Internal banding and spherulites are both absent from the specimen. It is not possible to describe the matrix.

9.6 - g, 9.6 - h and 9.6 i.

The colours visible in these specimens are similar to that of 9.6 - f. There is a change from grey/black to grey/green, which may be part of a band, otherwise no surface banding is present. Spherulites are abundant, typically measuring 1mm in diameter. No other inclusions are present. It is not possible to describe the matrix.

Reference Sample 9.8

This sample consists of one specimen.

This specimen is black in reflected light and green under transmitted light. The slightly waxy lustre is textured and the translucency is moderate. Surface banding is absent, only an indistinct surface cloudiness can be seen. No internal banding is apparent, neither are there any spherulites, phenocrysts or other crystal inclusions. The matrix is clear.

Reference Sample 9.9

This sample consists of one specimen.

These specimens are black in reflected light and green under transmitted light. The lustre is slightly waxy and the translucency moderate. Surface and internal banding as well as spherulites, phenocrysts or other crystal inclusions are absent from this sample. The matrix is clear.

Reference Sample 9.10

This sample consists of one specimen.

These specimens are black in reflected light and green under transmitted light. The lustre is vitreous and has a slight waxy texture and the translucency is moderate to poor. Surface and internal banding is absent, there are also no spherulites, phenocrysts or other crystal inclusions. The matrix is clear.

Reference Sample 9.11

This sample consists of one hand specimen and one flake.

Martin Jones 2002

These specimens are green-grey in reflected and transmitted light. The lustre is waxy and the translucency poor to moderate. Surface banding is comprised of white to black streaks. These bands are indistinct and occur consistently throughout the obsidian. No internal banding, spherulites, phenocrysts or other crystal inclusions are present in this sample. The matrix is cloudy.

Reference Sample 9.12

This sample consists of one specimen.

These specimens are black in reflected light and green under transmitted light. The lustre is highly vitreous and the translucency moderate to poor. Surface or internal banding is absent, neither are there any spherulites, phenocrysts or other crystal inclusions. The welded cortex is comprised of a cream coloured volcanic sediment or ash. The matrix is clear.

Reference Sample 9.13

This sample consists of one specimen.

These specimens are grey-black in reflected light and green under transmitted light. The lustre is vitreous and the translucency moderate. Surface banding is distinct and grey in colour. Consistent and highly intense flow patterns occur in these specimens. Internal banding consists of straight, cloudy grey streaks. No spherulites, phenocrysts or other crystal inclusions are present. The matrix is cloudy.

B.2.10 Young Dome (Source # 10.0)

Summary of Descriptions

The specimens in this sample group are not true obsidian. The specimens are very crystalline and have a high spherulitic content. This is characterised here as a 'pseudo-crystalline', granular composition. Further, the specimens are not vitreous enough to be true obsidian, no banding is present and they are quite opaque.

Reference Sample 10.1

This sample consists of one hand specimen and one flake.

These specimens are black-grey-white in reflected light. No colour is visible under transmitted light. No translucency or lustre is discernible. No surface or internal banding is present (categories do not apply due to texture of the rock that is not ultra-crystalline or glassy, as all the other samples have been). The spherulites in this sample have grown to a size of 4 mm in diameter and the actual obsidian has taken on a pseudo-crystalline/granular texture. This texture is similar to that of plutonic rock (looks scoriaceous, but without vesicles). Spherulites are very abundant making up 30-40% of the specimen. It is not possible to describe the matrix.

Reference Sample 10.2

This sample consists of one hand specimen.

This specimen is black in reflected light, however no colour is visible under transmitted light. Translucency is also absent, as is any discernible lustre. Surface /internal banding categories do not apply (specimen similar to 10.1). This specimen is slightly shinier than 10.1 and its spherulitic

content is 'blockier' and slightly more abundant. No other inclusions were noted. Some volcanic sediment is present on the cortex. It is not possible to describe the matrix.

Reference Sample 10.3

This sample consists of two hand specimens.

10.3 - a This specimen is black and vitreous, with an abundance of phenocrysts that have no real orientation. Spherulites or phenocrysts consist of plagioclase feldspar.

10.3 - b Mid grey, low lustre obsidian with abundant phenocrysts of plagioclase feldspar, though not as many as '10.3 - a'. Vesicles occur up to 2 mm long, all of the same orientation. Spherulites range up to 2 mm in diameter.

B.2.11 Taumou Pa (Source # 11.0)

This sample is black when viewed in reflected light, although brown is also visible at times. Green or grey is visible under transmitted light. Vitreous specimens narrowly outnumber those with a dull and waxy appearance and the quality of translucency is generally moderate, but can be at times be fairly poor. Surface banding is faint and consists of either cloudy or indistinct straight lines. Internal banding is seldom present, however when this feature occurs it is comprised of thin, dark grey streaks. Only two spherulites occur in this moderately sized sample, measuring approximately 2mm. The matrix is slightly gritty and sometimes cloudy. The cortex is comprised of welded, grey volcanic sediments.

Reference Sample 11.1

This sample consists of one hand specimen and three flakes.

These specimens are black in reflected light and green under transmitted light. The lustre is vitreous and the translucency poor. Surface banding is faint and characterised by 1mm grey bands. No internal banding, spherulites, or inclusions are present. The cortex consists of welded volcanic sediments that can also seen within the surface banding. It is not possible to describe the matrix.

Reference Sample 11.2

This sample consists of two hand specimens.

These specimens are greyish black in reflected light and grey under transmitted light. The lustre is waxy and the translucency is moderate to poor. Surface banding is faint and characterised by indistinct streaks which alternate between light and dark grey. In general, banding is consistent and displays high intensity, it is assumed this feature is also present internally. One spherulite is present in each of the specimens, each inclusion measures between 1.5 mm and 3 mm in diameter.

Reference Sample 11.3

This sample consists of one hand specimen and six flakes.

These specimens are black in reflected light and grey under transmitted light. The lustre is waxy and dull and the translucency moderate. The thin surface banding is comprised of faint, inconsistently spaced, lines that differ in vitreosity from each other. Internal banding, spherulites and other such inclusions are all absent from these specimens. The matrix is cloudy, and the cortex slightly welded.

Martin Jones 2002

Reference Sample 11.4

This sample consists of two hand specimens and two flakes.

These specimens are black in reflected light and green under transmitted light. The lustre is highly vitreous and the translucency moderate to good. Consistent surface layering of the surface cortex and obsidian is likely to have occurred during the formation and cooling processes. Evidence of stretching during cooling is visible in the cortex (layering of interfaces). No spherulites or phenocrysts are noticeable and the matrix is clear.

Reference Sample 11.5

This sample consists of one hand specimen and four tiny unlabelled flakes.

These specimens are black in reflected light and green under transmitted light. The lustre is vitreous and the translucency moderate. Surface layering is similar to 11.4, with inconsistent spaces between layers and a grey cortex. Internal banding is characterised by thin dark streaks in the flakes. No spherulites or other crystal inclusions are present. The matrix is slightly gritty.

Reference Sample 11.6

This sample consists of twenty-four pieces of assorted sizes.

These specimens are black-brown in reflected light and grey under transmitted light. The lustre is dull and the translucency poor. Surface banding is present in one piece where it is delineated by volcanic sediments. No internal banding, spherulites or other inclusions are present. The cortex is welded and dirty. It is not possible to describe the matrix.

Reference Sample 11.7

This sample consists of thirty flakes of various sizes.

These specimens are black in reflected light and green under transmitted light. A mid-brown cortex covers the obsidian. The lustre is dull and the translucency moderate to poor. Surface banding can not be seen, but much surface layering is visible giving the obsidian a 'platy' appearance. 'Bands' of volcanic sediment are also visible within the specimens. Internal banding is comprised of thin dark streaks and the matrix is only slightly gritty.

Reference Sample 11.8

This sample consists thirty-two specimens of assorted sizes.

These specimens are brown in reflected light and green under transmitted light. Generally, the lustre is dull due to accompanying sediment and the translucency is moderate. Faint surface banding can be seen on only two pieces. No internal banding is visible, although some slightly gritty, dark streaks are present. No spherulites or other crystal inclusions are present and the matrix is gritty.

Reference Sample 11.9

This sample consists of forty-four specimens of assorted sizes.

These specimens are brown in reflected light and green becomes more prominent under transmitted light in some specimens. Those that do not display this green colour are opaque. Faint surface banding can be seen on some specimens and a 'platy' structure is observed in many others. Vesicles can be seen in other specimens. No spherulites or other crystal inclusions can be seen. It is not possible to describe the matrix.

Martin Jones 2002

Reference Sample 11.10

This sample consists of two hand specimens.

These specimens are black in reflected light and green under transmitted light. The vitreous lustre is slightly textured and the translucency moderate. Extremely indistinct surface cloudiness could be interpreted as surface banding. No internal banding is present in these specimens. Spherulites, phenocrysts and other crystal inclusions are also absent. The matrix is cloudy.

Reference Sample 11.11

This sample consists of one hand specimen and two flakes.

These specimens are black in reflected light and green under transmitted light. The lustre is vitreous and the translucency moderate. Some striations cross the specimens. There are no indications of any surface banding, internal banding, spherulites, phenocrysts or other crystal inclusions. The matrix is clear.

Reference Sample 11.12

This sample consists of one hand specimen and one flake.

These specimens are black in reflected light and green under transmitted light. The lustre is vitreous and the translucency moderate. Surface banding is comprised of indistinct, straight lines that occur consistently throughout the specimens. One of these lines is delineated by thin mineral or sediment inclusions. Internal banding is characterised by darker grey streaks. No spherulites, phenocrysts or other crystal inclusions are present in these specimens and the matrix is clear.

B.2.12 Otiora Bay (Source # 12.0)

This sample is black in reflected light, although one specimen is a greyish black. Green can consistently be seen under transmitted light when translucency of the specimen allows. The translucency is quite variable within this sample group. Surface banding is not generally found, though some indistinct flow banding does occur in one specimen. One specimen exhibits 4 mm thick internal banding, otherwise this feature is absent from the sample group. No spherulites or other crystal inclusions are present. The condition of the matrix varies from clear, to gritty, and finally cloudy. Where present the cortex is grey, rounded and weathered.

Reference Sample 12.1

This sample consists of one hand specimen and one flake.

These specimens are black in reflected light and green under transmitted light. The lustre is waxy and the translucency poor to opaque. No surface or internal banding, spherulites, phenocrysts or other crystal inclusions are present. The matrix is very opaque, almost cloudy.

Reference Sample 12.2

This sample consists of two hand specimens and one flake.

These specimens are black in reflected light. No colour is visible under transmitted light. The waxy lustre is textured and the translucency opaque. Indistinct flow banding is very streaky. Some sediment inclusions occur wedged in cracks. Internal banding, spherulites and other crystal inclusions are absent from these specimens. The cortex is grey, rounded and weathered. The matrix is cloudy.

Martin Jones 2002

Reference Sample 12.3

This sample consists of one hand specimen and two flakes.

These specimens are grey-black-grey in reflected light and green under transmitted light. The lustre is waxy and the translucency moderate. Surface banding is comprised of 1mm thick grey bands, which in turn contribute to wider bands of up to 15mm in thickness. Some sediment occurs parallel to the banding orientation. 4 mm thick, opaque internal bands are situated in a clear green matrix. No spherulites or other crystal inclusions are present in any of the specimens.

Reference Sample 12.4

This sample consists of one hand specimen and two flakes.

These specimens are black in reflected light and green under transmitted light. The lustre is vitreous and the translucency moderate. Neither surface nor internal banding is visible in these specimens. Spherulites and other inclusions are also absent. The matrix is clear.

Reference Sample 12.5

This sample consists of two hand specimens and two flakes.

These specimens are black in reflected light and green under transmitted light. The lustre is vitreous and pitted on specimen 12.5-a. Translucency is high in 12.5-a, but moderate in the others. Surface and internal banding is visible. No spherulites or other inclusions are present. The matrix is clear.

Reference Sample 12.6

This sample consists of one hand specimen and one flake

These specimens are black in reflected light and green under transmitted light. The lustre is vitreous with a surface texture. The translucency is poor. No surface or internal banding is visible. There are also no spherulites, vesicles or phenocrysts. Inclusions consist of abundant microscopic crystalline flecks, the presence of which creates a definite surface texture. The dull black cortex has a smooth texture. There is no sediment attached to the unweathered rind. The matrix is opaque.

Reference Sample 12.7

This sample consists of one hand specimen and one chip

These specimens are grey-black in reflected light. It is not possible to describe the colour under transmitted light due to the poor level of translucency. The lustre is waxy and the translucency opaque. Thin grey lines form thicker 3 mm wide surface bands that occur continuously throughout the specimen. Microscopic crystalline inclusions consisting of a gritty grey white material form layers within the obsidian. These abundant inclusions measure 2 mm in width and have a curved appearance. No spherulites, vesicles or phenocrysts are present in either specimen. The matrix is opaque and no cortex is attached to either specimen.

Reference Sample 12.8

This sample consists of one flake

This specimen is black in reflected light and green under transmitted light. The vitreous lustre is accompanied by a slight surface texture

and the translucency is poor. Streaking occurs in the place of definite surface banding and is neither consistent nor continuous. There is no internal banding nor are there any spherulites, vesicles or phenocrysts are present. Microscopic crystalline inclusions, while occurring abundantly, still comprise no more than 1% of the specimen; however, this abundance does give the specimen a surface texture. The cortex is composed of smooth black glass that has a slightly pitted appearance. The matrix is gritty.

Reference Sample 12.9

This sample consists of one hand specimen and one flake.

These specimens are grey-black in reflected light. It is not possible to describe the colour under transmitted light due to the poor level of translucency. The slightly vitreous lustre is accompanied by an equally slight surface texture. The translucency is opaque. Grey-white crystalline inclusions form definite grey layers or bands within the obsidian. The spacing of these bands varies throughout the specimen, the thickest bands measuring approximately 4 mm wide. All crystalline bands occur continuously throughout the hand specimen. There is no internal banding nor are there any spherulites, vesicles or phenocrysts present. The matrix is opaque and no cortex is attached to either specimen.

Reference Sample 12.10

This sample consists of one hand specimen and one chip

These specimens are grey-black in reflected light. It is not possible to describe the colour under transmitted light due to the poor level of translucency. The lustre is vitreous and the translucency opaque. Surface banding is comprised of grey lines of varying thicknesses. Bands

range between 1 and 9 mm in width and occur continuously but not consistently throughout the specimen. There is no internal banding nor are there any spherulites or phenocrysts present. Vesicles are elongate and section the specimen. Typically, these holes are 1 mm wide and some contain gritty pale yellow crystals. The matrix is opaque and the cortex smooth, with a thin rind.

Reference Sample 12.11

This sample consists of one small hand specimen

This specimen is black in reflected light and green under transmitted light. The lustre is vitreous and the translucency poor. The composition of surface banding ranges between vague, discontinuous streaks and white crystalline inclusive layers. The banding does not occur consistently throughout the specimen. Inclusions consist of a gritty, grey crystalline material. There is no internal banding nor are there any spherulites, vesicles or phenocrysts present. The matrix is opaque and no cortex is attached to the specimen.

Reference Sample 12.12.1

This sample consists of one small hand specimen

This specimen is black in reflected light and green under transmitted light. The lustre is vitreous and the translucency poor to moderate. Indistinct thin, grey streaks comprise surface banding. This feature occurs neither continuously nor consistently throughout the specimen. No internal banding is present. There are also no spherulites, vesicles, phenocrysts or other inclusions. The dull, grey-black cortex has a smooth, worn appearance. The matrix is cloudy.

Martin Jones 2002

Reference Sample 12.12.2

This sample consists of one small flake

This specimen is black in reflected light and green under transmitted light. The lustre is vitreous and the translucency poor to moderate. Indistinct thin grey streaks occur in the place of definite surface banding. There is no internal banding nor are there any spherulites, vesicles or phenocrysts present. The dull, grey-black cortex has a smooth, worn appearance. The matrix is cloudy.

Reference Sample 12.13

This sample consists of two specimens.

These specimens are black in reflected light and green under transmitted light. The lustre is waxy and the translucency poor. Surface or internal banding is not visible, neither are any spherulites, phenocrysts or other crystal inclusions. The matrix is slightly gritty.

Reference Sample 12.14

This sample consists of one specimen.

These specimens are black in reflected light and green under transmitted light. The lustre is waxy and pitted. The translucency is moderate to poor. No surface or internal banding, spherulites, phenocrysts or other crystal inclusions are present. The matrix is gritty.

B.2.13 Upper Stair Case (Source # 13.0)

This sample is black in reflected light and green or, in one instance, greyish green under transmitted light. The lustre is consistently vitreous in this small sample. The translucency is poor to moderate. Surface banding varies greatly, some specimens exhibit no banding at all and others have surface flow banding consisting of thin grey lines. The banding of the remaining specimens is delineated by mineral inclusions. Internal banding is indistinct and cloudy, but generally seldom seen. The cortex is vesicular and is comprised of rhyolitic material that has a scoriaceous or pumiceous texture. The matrix is cloudy.

Reference Sample 13.1

This sample consists of one hand specimen and two flakes.

These specimens are black in reflected light and green under transmitted light. The lustre is vitreous though somewhat masked by the cortex. The translucency is moderate to poor. The surface banding of specimen 13.1-a is comprised of thin 1mm grey lines that are slightly waxy and consistent. No internal banding, spherulites or other inclusions are present. The matrix is cloudy. The cortex is composed of welded, vesicular, rhyolitic sediment that has a scoriaceous texture.

Reference Sample 13.2

This sample consists of one hand specimen and one flake.

These specimens are black in reflected light and green under transmitted light. The lustre is vitreous and the translucency moderate to poor. Surface banding or layering is defined by mineral inclusions, which are probably representations of surface interfaces. Inclusions of what ap-

pear to be composed of white glass occur in 0.5 mm bands. The inclusions are of a high intensity and localised in the specimen 13.2-a. Some texture is visible within the banding lower down on the specimen 13.2-a, where small pitting also occurs. No internal banding is visible as the specimen is too thick. No spherulites or other inclusions are present and the matrix is slightly cloudy.

Reference Sample 13.3

This sample consists of three hand specimens and two flakes.

These specimens are black in reflected light and greyish green under transmitted light. The lustre is slightly waxy and the translucency moderate. No surface banding is visible, however there is a random inclusion on the specimen 13.3-a that is distinctly 'cloudy'. This inclusion is probably a white silica crystal. Internal banding is comprised of indistinct cloudy grey masses in the small flake. No spherulites or other inclusions are present and the matrix is cloudy.

Reference Sample 13.4

This sample consists of one hand specimen and one flake.

These specimens are black in reflected light and green under transmitted light. The lustre is vitreous and the translucency moderate. Surface flow banding is comprised of thin grey lines within which are embedded sediment inclusions . The banding varies in thickness and the lines are wavy and flow around vesicles. No internal banding, spherulites, phenocrysts or other inclusions are present in this sample. The cortex is welded and has scoriaceous and vesicular texture. The colour of the cortex varies from a creamy brown to a light grey and is reasonably thick. The matrix is clear.

Reference Sample 13.5

This sample consists of one hand specimen and two flakes.

These specimens are black in reflected light and green under transmitted light. The lustre is vitreous and the translucency moderate. No surface or internal banding is present in this specimen, neither are there any spherulites. Pumiceous inclusions are welded to the grey cortex giving it a rough texture. It also displays a brown vesicular texture that also looks like welded sediment where stretching or pulling has taken place. The matrix is clear

Reference Sample 13.6.1

This sample consists of one hand specimen

This specimen is grey black in reflected light and green under transmitted light. The lustre is vitreous and the translucency poor to moderate. There is no surface flow banding but the specimens are banded with a mid-grey welded material that has a dull, vesicular appearance. This distinct grey banding is embedded with obsidian layers and highly vesicular, paler grey lines. Spherical spherulites occur in varying sizes. Generally, these inclusions measure less than 1 mm in diameter. No crystal phenocrysts are present, only the previously described grey layers and rough vesicular material. Vesicles can only be seen within the grey material, varying in size from microscopic to 7 mm long. The matrix is opaque and the cortex consists of a dull, rough vesicular material.

Reference Sample 13.6.2

This sample consists of one hand specimen

This specimen is grey black in reflected light and green under transmit-

ted light. The lustre is vitreous and the translucency poor to moderate. There is no surface flow banding but the specimens are banded with a dull, vesicular mid-grey material. This distinct grey banding is embedded with obsidian layers and highly vesicular paler grey lines. No crystal phenocrysts are present, only the previously described grey layers and rough vesicular material. Vesicles occur only within this grey material and vary in size from microscopic to 7 mm long. The matrix is opaque and the cortex consists of a dull, rough vesicular material.

Reference Sample 13.6.3

This sample consists of one hand specimen

This specimen is grey black in reflected light and green under transmitted light. The lustre is vitreous and the translucency poor to moderate. There is no surface flow banding but the specimens are banded with a dull, vesicular mid-grey material. This distinct grey banding is embedded with obsidian layers and highly vesicular paler grey lines. Only one spherulite exists in this specimen. The 2 mm diameter inclusion is grey, radial and fragmented. No crystal phenocrysts are present, only the previously described grey layers and rough vesicular material. Vesicles occur only within the grey material and vary in size from microscopic to 7 mm long. The matrix is opaque and the cortex consists of a dull, rough vesicular material.

Reference Sample 13.6.4

This sample consists of one hand specimen

This specimen is grey black in reflected light and green under transmitted light. The lustre is vitreous and the translucency poor to moderate. There is no surface flow banding but the specimens are banded

with a dull, vesicular mid-grey material. This distinct grey banding is interspersed with obsidian layers and highly vesicular paler grey lines. Grey spherulites form less than one percent of the obsidian. No crystal phenocrysts are present, only the previously described grey layers and rough vesicular material. Vesicles occur only within the grey material and vary in size from microscopic to 7 mm long. The matrix is opaque and the cortex consists of a dull, rough vesicular material.

B.2.14 Hall's Pass (Source # 14.0)

This sample is black in reflected light and green under transmitted light. The lustre is vitreous and the translucency poor to moderate. Surface banding is comprised of xenolithic mineral inclusions. Grey bands of this material range between thin to relatively large (8mm) 'layers'. No internal banding is evident. Spherulites occur abundantly in one specimen and are roughly circular. Glassy, linear inclusions are also present in some specimens. The matrix is opaque and the cortex grey, dull and weathered.

Reference Sample 14.1

This sample consists of one hand specimen and two flakes.

These specimens are black in reflected light and green under transmitted light. The lustre is highly vitreous and the translucency poor. Surface banding is comprised of vesicular, xenolithic inclusions. These bands occur in layers 2 mm thick and flow together to form 8mm thick layers. A scoria xenolith is visible measuring 13 mm. This layer is characterised by two separate orientations occurring perpendicular to each other. No spherulites are present in this specimen. The matrix is probably cloudy, though it is difficult to be certain.

Martin Jones 2002

Reference Sample 14.2

This sample consists of three hand specimens and one flake.

These specimens are black in reflected light and green under transmitted light. The lustre is vitreous and the translucency moderate. Surface banding is comprised of very thin and inconsistently spaced sediment or mineral inclusions. This banding probably represents surface interfaces. The matrix is clear.

Reference Sample 14.3

This sample consists of two hand specimens and one flake.

These specimens are black in reflected light and green under transmitted light. The lustre is vitreous and the translucency poor. Circular spherulites occur abundantly in various sizes (0.5 to 1.5 mm in diameter). Xenoliths range between 2 mm and 1 cm in diameter and are composed of a rhyolitic/scoriaceous material. Some grey banding of variable thickness and consistency is also apparent. Linear inclusions of a translucent, glassy material are localised in one section of the specimen. The cortex is grey and dull, apparently due to weathering. The matrix is opaque.

Reference Sample 14.4

This sample has been destroyed.

Reference Sample 14.5

This sample has been destroyed.

Reference Sample 14.6

This sample consists of two hand specimens

These specimens are black under reflected light. It is not possible to describe the colour under transmitted light due to poor translucency. The lustre is vitreous. No surface or internal banding can be seen. There are many cracks on this specimen that would affect the strength and quality of fracture. No spherulites or vesicles are present. Inclusions largely consist of different forms of lithic material. The largest, measuring 6 mm in diameter, is a dull white-yellow crystal which itself has black crystal inclusions on it. Another notable inclusion has an indistinct red, brown or pink colouring. This example is irregularly shaped and measures 3 mm in diameter. In total, these types of inclusions constitute 2 percent of the proportion of the obsidian. An agglomeration of translucent phenocrysts can be seen, however this feature occurs within less the one per cent of the specimen.

Reference Sample 14.7.1

This sample consists of one flake

This specimen is black in reflected light. It is not possible to describe the colour under transmitted light due to poor translucency. The lustre is vitreous. Thin grey surface streaking occurs inconsistently. The thin, waxy-looking lines that comprise this feature interlock in an irregular flowing pattern. Conchoidal fracture would be affected by the cracks that occur across the surface of the obsidian. No spherulites or vesicles are present. Crystals measuring between 1 and 2 mm in diameter form an agglomeration of clear phenocrysts. A white quartz-like material that generally measures 3 mm in diameter is the only other type of inclusion present. The cortex is dull and thin and is to be quite worn. The matrix

is opaque.

Reference Sample 14.7.2

This sample consists of one flake

This specimen is black in reflected light. It is not possible to describe the colour under transmitted light due to poor translucency. The lustre is vitreous. Thin grey surface streaking occurs inconsistently. The thin, waxy-looking lines that comprise this feature interlock in an irregular flowing pattern. Conchoidal fracture would be affected by the cracks that occur across the surface of the obsidian. No spherulites or vesicles are present. Crystals measuring between 1 and 2 mm in diameter form an agglomeration of clear phenocrysts. A white quartz-like material that generally measures 3 mm in diameter is the only other type of inclusion present. The cortex is dull and thin and is to be quite worn. The matrix is opaque.

Reference Sample 14.7.3

This sample consists of one flake

This specimen is black in reflected light. It is not possible to describe the colour under transmitted light due to poor translucency. The lustre is vitreous. Thin grey surface streaking occurs inconsistently. The thin, waxy-looking lines that comprise this feature interlock in an irregular flowing pattern. Conchoidal fracture would be affected by the cracks that occur across the surface of the obsidian. No spherulites or vesicles are present. Crystals measuring between 1 and 2 mm in diameter form an agglomeration of clear phenocrysts. A white quartz-like material that generally measures 3 mm in diameter is the only other type of inclusion present. The cortex is dull and thin and is to be quite worn. The matrix

is opaque.

Reference Sample 14.8

This sample consists of one hand specimen.

This specimen is black in reflected light and green under transmitted light. The lustre is vitreous and the translucency poor. Surface banding consists of thin streaky flows that interlock in an irregular fashion. The thickness of this feature is inconsistent and has a gritty appearance. No spherulites can be seen. An agglomeration of clear phenocrysts, some with an orange-brown tinge is present. The component crystals measure up to 1 mm in diameter and comprise approximately five percent of the obsidian specimen. A few random vesicles also feature. Inclusions are not abundant, making up only two percent of the specimen. These yellow-white lithic pieces are probably quartz based felsic rock and measure between 1 and 4 mm in diameter. The matrix is clear with a fine-grained grit, or texture. The cortex is smooth and has a worn, dull grey appearance. No sediment or pitting is associated with this feature.

Reference Sample 14.9

This sample consists of one hand specimen.

This specimen is black in reflected light and green under transmitted light. The lustre is vitreous and the translucency poor. Surface banding consists of thin streaky flows that have a gritty appearance and interlock in an irregular fashion. No spherulites can be seen in this sample, however an agglomeration of phenocrysts is present. The component crystals are translucent, and some have an orange-brown coloration. The phenocrysts measure between 1 and 1.5 mm in diameter and form approximately five percent of the total specimen. Brownish-pink lithic in-

clusions measure approximately 2 mm in length. The matrix probably displays some degree of grit, although it is difficult to be certain due to the poor translucency. No cortex is attached to this specimen.

Reference Sample 14.10

This sample consists of one hand specimen

This specimen is black under reflected light and green under transmitted light. The lustre is vitreous and the translucency poor. Surface banding consists of thin streaky flows with a gritty appearance that interlock in an irregular fashion. No spherulites can be seen in this sample, however phenocrysts are present. These inclusions comprise approximately two percent of the obsidian and have a translucent appearance. White grainy lithics are also present, but occur in no great abundance (1measure 1 mm in diameter. No vesicles are present. The matrix is opaque making the condition difficult to describe. The cortex is comprised of smooth, grey and yellow sediments.

Reference Sample 14.11

This sample consists of one hand specimen and one chip.

These specimens area combination of grey, green and black under reflected light. It is not possible to describe the colour under transmitted light due to poor translucency. The lustre is vitreous and the translucency opaque. Surface banding is characterised by light grey streaking that flows in a non-uniform fashion and at varying degrees of thickness. No spherulites can be seen, however an agglomeration of phenocrysts, comprising approximately seven percent of the sample, is present. The component crystals measure approximately 1 mm in diameter. Lithic inclusions occur in sizes between 1 mm and 6 mm in diameter. These lithic

pieces display a variety of colours, including white, grey, red-brown and grey. The matrix is gritty. No cortex is present though some red-brown sediment has been welded to the sample.

B.2.15 Upper Staircase - Quarry (Source # 15.0)

This sample group is black in reflected light and green under transmitted light. The lustre is vitreous and the translucency poor to moderate. Surface banding is present in only a few specimens and is characterised by thin, sometimes 'streaky', grey lines that range from 2 to 10 mm in thickness. These bands are sometimes delineated by sediment inclusions. Highly intense white or grey streaks occur in two specimens, these bands vary in thickness and depth of colour. The rarely observed internal banding has a cloudy appearance. Xenoliths occur found in two specimens are comprised of a dull grey crystalline material. The cortex is also slightly dull and has a gritty texture.

Reference Sample 15.1

This sample consists of one hand specimen and two flakes.

These specimens are black in reflected light and green under transmitted light. The lustre is vitreous and the translucency moderate. Surface banding is delineated by thin sediment inclusions and thick grey lines These two features together form larger bands measuring approximately 2 mm in thickness. Cloudy bands can be seen internally. No spherulites are present in these specimens. The 3mm to 10 mm diameter xenoliths are composed of a dull grey, crystalline material. These inclusions are stretched slightly in the direction of the orientation. The matrix is clear. Inclusions measuring up to 10 mm in diameter are composed of flow banded vesicular cream-grey sediment (rhyolitic rock).

Martin Jones 2002

Reference Sample 15.2

This sample consists of one hand specimen and one flake.

These specimens are black in reflected light and green under transmitted light. The lustre is vitreous and the translucency moderate to poor. Surface banding is comprised of very thin grey streaks that form larger 10mm bands. No internal banding or spherulites are present in these specimens. Dull-white crystalline xenoliths measure between 2 and 14 mm in diameter.

Reference Sample 15.3

This sample consists of one hand specimen and two flakes.

These specimens are black in reflected light and green under transmitted light. The lustre is vitreous and the translucency moderate to poor. Surface banding is comprised of thin grey lines that form larger 5mm bands. These bands are inconsistently spaced throughout the specimens. No internal banding, spherulites, phenocrysts or other crystal inclusions are present. The matrix is clear.

Reference Sample 15.4

This sample consists of three hand specimens.

These specimens are black in reflected light and green under transmitted light. The lustre is vitreous and the translucency moderate to poor. Surface banding is comprised of thin grey lines that form larger, straight bands. These bands are concentrated, consistently spaced and of a high intensity. No internal banding is present in these specimens, neither are there any spherulites, phenocrysts or other crystal inclusions. The matrix is clear and the cortex slightly dull.

Reference Sample 15.5

This sample consists of one hand specimen and two flakes.

These specimens are black in reflected light and green under transmitted light. The lustre is vitreous and the translucency moderate. Surface or internal banding is not visible. There are also no spherulites, phenocrysts or other crystal inclusions. The matrix is clear.

Reference Sample 15.6

This sample consists of fifteen flakes.

These specimens are black in reflected light and green under transmitted light. The lustre is vitreous and the translucency moderate. Neither surface nor internal banding is visible. There are also no spherulites, phenocrysts or other crystal inclusions. The matrix is clear and the cortex dusty and gritty.

Reference Sample 15.7

This sample consists of eight flakes.

These specimens are black in reflected light and green under transmitted light. The lustre is vitreous and the translucency moderate. Neither surface nor internal banding is visible. There are also no spherulites, phenocrysts or other crystal inclusions. The matrix is clear and the cortex dusty and gritty.

Reference Sample 15.8

This sample consists of eleven flakes.

Martin Jones 2002

These specimens are black in reflected light and green under transmitted light. The lustre is vitreous and the translucency moderate to poor. No surface banding, spherulites, phenocrysts or other crystal inclusions are present in these specimens. Internal banding is characterised by high intensity, white-grey, cloudy streaks that vary in thickness. The matrix is cloudy and gritty and the cortex is dirty and gritty.

Reference Sample 15.9

This sample consists of six flakes.

These specimens are black in reflected light and green under transmitted light. The lustre is slightly dull and the translucency moderate. No surface banding, spherulites, phenocrysts or other crystal inclusions are present in these specimens. Internal banding consists of white, high intensity, slightly indistinct streaks. The matrix is slightly cloudy.

Reference Sample 15.10

This sample consists of one hand specimen

This specimen is black in reflected light and green under transmitted light. The lustre is vitreous and the translucency good to moderate. No surface banding is visible, although some surface lines create a texture on the fresh surface. Some internal banding is visible in the form of indistinct and streaky lines that occur consistently throughout the specimen. No spherulites are present, however a crystal agglomeration can be seen. This latter feature occurs in limited abundance, totalling only one percent of the specimen and the component crystals measure less than 1 mm in diameter. The matrix is clear and no cortex is attached to this specimen.

Reference Sample 15.11

This sample consists of one flake and one small chip

These specimens are black in reflected light and green under transmitted light. The lustre is vitreous and the translucency moderate to good. No surface banding can be seen. Internal banding consists of 1-2 mm wide grey streaky bands. All bands occur along the same orientation, but are not consistent in terms of spacing or width. Intensity varies greatly between the bands. No spherulites can be seen, although small amounts of other inclusions in the form of 1 mm diameter crystals occur in agglomerations. The matrix is clear and no cortex is present.

Reference Sample 15.12

This sample consists of one hand specimen

This specimen is black in reflected light and green under transmitted light. The lustre is vitreous, with a surface texture. There is some evidence for surface banding. Typically, bands are thin, linear and occur consistently across the specimen. An agglomeration of crystals contributes to one percent of the total specimen. The component crystals measure less than 1 mm in diameter, of these less than one percent have an orange-brown coloration. There is no cortex attached to either specimen.

Reference Sample 15.13

This sample consists of one hand specimen and one small chip

These specimens are black in reflected light and green under transmitted light. The lustre is vitreous and the level of translucency moderate. Surface banding is thin and linear and has a grey streaky appearance.

The spacing between these bands is inconsistent. Internal banding is assumed similar to that seen on the surface. There is one crystal agglomeration, of which the component crystals have an orange coloration. This agglomeration surrounds a vesicle, which also contains crystal growths that measure 1 mm in diameter. There is also one agglomeration of very small, less than 0.5 mm in diameter, clear phenocrysts. The matrix is clear and no cortex is attached to the specimens.

Reference Sample 15.14

This sample consists of one small hand specimen

This specimen is black in reflected light and green under transmitted light. The lustre is vitreous and the translucency poor to moderate. No surface or internal banding can be seen. Spherulites are absent, but a crystal agglomeration covering two percent of the specimen is visible. The component crystals are microscopic, measuring less than 0.25 mm in diameter and have a grey transparent appearance. The thin surface of the cortex is weathered and has a creamy yellow coloration. Translucent white encrustations are embedded in this surface layer.

Reference Sample 15.15

This sample consists of one hand specimen and one small chip

These specimens are grey-black in reflected light and green under transmitted light. The lustre is vitreous, although it is also dull in isolated areas. The translucency is moderate. Surface banding is linear and consistent. The component lines are sometimes coloured grey due to inclusions. Internal banding is faint and streaky. There are no spherulites or crystal agglomerations. There are however one or two isolated inclusions contained within vesicles. These amorphous crystals measure 17

mm long and 10 mm wide and are roughly ovular. The matrix is clear and no cortex is attached to the specimens.

Reference Sample 15.16

This sample consists of one hand specimen.

This specimen is black in reflected light. It is not possible to describe the colour of under transmitted light due to poor translucency. The lustre is vitreous, though also somewhat waxy. Inclusions to occur in the place of surface banding. These 'lines' vary in colour, from white to light grey, as does the thickness and orientation. No internal banding can be seen, there are also no spherulites or agglomerations of phenocrysts present. The cortex has a thin encrusted texture. The matrix is opaque.

Reference Sample 15.17

This sample consists of one hand specimen and one small chip

These specimens are black in reflected light and grey under transmitted light. The lustre is vitreous and the translucency poor. Surface banding is characteristically vague. Indistinct, sometimes curved, lines occur inconsistently over the specimens. Internal banding is straight, thin and closely spaced. Crystal phenocrysts occur in small concentrations, forming no more than one percent of the total area of the specimens. These inclusions measure approximately 0.5 mm in diameter. No spherulites or other inclusions are present. The matrix is clear and no cortex is attached to either of these specimens.

Reference Sample 15.18

This sample consists of one hand specimen

This specimen is black in reflected light and grey under transmitted light. The lustre is waxy and the translucency is adversely affected by the opaque nature of the specimen. Indistinct surface streaking occurs in the place of definite banding. No internal banding can be seen due to poor translucency. No spherulites or crystal phenocrysts are present, however there is a yellow grey crystalline inclusion at the end of which grey-white streaking occurs. The specimen is too opaque to determine the condition of the matrix and the cortex is absent.

Reference Sample 15.19

No specimen found

Reference Sample 15.20

This sample consists of one hand specimen and one small chip

These specimens are black in reflected light and green under transmitted light. The lustre is vitreous with a slight surface texture. The translucency is poor. The faint surface banding is composed of a mixture of thin curved and linear lines. No internal banding can be observed due to the poor translucency. Microscopic spherulites, measuring 0.1 mm in diameter, occur in moderate abundance (covering up to ten percent of the specimens). Crystal phenocrysts measure less than 1 mm in diameter, but occur more rarely (less than one percent). The matrix is clear and no cortex is attached to either specimen.

Reference Sample 15.21.1

This sample consists of one hand specimen.

This specimen is black in reflected light and green under transmitted light. The lustre is vitreous and the translucency poor. Patterned surface lineations occur in the place of definite surface banding. These microscopic white flecks have an appearance similar to pumice. A large pumiceous inclusion sections the thin flake. Shallow striations are also visible on the surface. A grey smudge effect occurs in the place of internal banding.

Reference Sample 15.21.2

This sample consists of one small chip.

This specimen is black in reflected light and green under transmitted light. The lustre is vitreous and the translucency poor. Patterned surface lineations occur in the place of definite surface banding. These microscopic white flecks have an appearance similar to pumice. Shallow striations are also visible on the surface. A grey smudge effect occurs in the place of internal banding. A 'cap' of pale yellow-green-brownish crystalline material dominates the top section of the specimen.

Reference Sample 15.21.3

This sample consists of one small hand specimen.

This specimen is black in reflected light and green under transmitted light. The lustre is vitreous and the translucency poor. Patterned surface lineations occur in the place of definite surface banding. These microscopic white flecks have an appearance similar to pumice. Shallow striations are also visible on the surface. There is a small quantity of spherulites present that measure less than 1 mm in diameter. There is also a cluster of dull red spherulites situated in an isolated location. Again, these inclusions are rare, covering just one percent of the speci-

men. The other inclusions are composed of a dull, blue-grey crystalline material. A white-yellow ash layer and a pumiceous layer are prominent.

Reference Sample 15.21.4

This sample consists of one hand specimen.

This specimen is black in reflected light and green under transmitted light. The lustre is vitreous and the translucency poor. Patterned surface lineations occur in the place of definite surface banding. These microscopic white flecks have an appearance similar to pumice. Shallow striations are also visible on the surface. A grey smudge effect occurs in the place of internal banding. Spherulites occur very rarely. These small inclusions measure less than 1 mm in diameter. Spherical microscopic inclusions occur more abundantly ($\approx$ 5%). These crystals are aligned linearly.

Reference Sample 15.21.5

This sample consists of one hand specimen.

This specimen is black in reflected light and green under transmitted light. The lustre is vitreous and the translucency poor. Patterned surface lineations occur in the place of definite surface banding. These microscopic white flecks have an appearance similar to pumice. Shallow striations are also visible on the surface. Spherical microscopic inclusions are aligned linearly. Some larger examples can be found within vesicles. These inclusions are relatively abundant ($\approx$ 2-3%)

Reference Sample 15.21.6

This sample consists of one hand specimen.

This specimen is black in reflected light and green under transmitted light. The lustre is vitreous and the translucency poor. Patterned surface lineations occur in the place of definite surface banding. These microscopic white flecks have an appearance similar to pumice. Shallow striations are also visible on the surface.

Reference Sample 15.21.7

This sample consists of one small hand specimen.

This specimen is black in reflected light and green under transmitted light. The lustre is vitreous and the translucency poor. Patterned surface lineations occur in the place of definite surface banding. These microscopic white flecks have an appearance similar to pumice. Shallow striations are also visible on the surface. This specimen has a prominent 'cap' comprising a pale yellow-green-brownish crystalline material.

Reference Sample 15.21.8

This sample consists of one small hand specimen.

This specimen is black in reflected light and green under transmitted light. The lustre is vitreous and the translucency poor. Patterned surface lineations occur in the place of definite surface banding. These microscopic white flecks have an appearance similar to pumice. Shallow striations are also visible on the surface.

Reference Sample 15.22.1

This sample consists of one hand specimen

This specimen is grey-black in reflected light. The specimen is too opaque

to describe the colour under transmitted light. The lustre is generally vitreous, however in certain areas this can become quite dull. The hand specimen is dominated by a dull grey material that varies from mid grey to a pale grey-orange. This material has a rough texture and a distinctive circular pitting on the surface. Layers of more typical black obsidian occur occasionally within this material. Mid-grey bands connect with the layers of obsidian. A pale orange, vesicular material separates these grey bands. This distinction between grey bands and the paler orange material varies throughout the specimen as the layers become less structured. No surface or internal flow banding can be seen within the obsidian layers. Vesicles are folded between the grey layering. The matrix is opaque and the cortex is comprised of a grey-orange, pitted material.

Reference Sample 15.22.2

This sample consists of one hand specimen

These specimens are black in reflected light and green under transmitted light. The lustre is vitreous and the translucency. The hand specimen is composed of a dull grey material that varies from mid grey to a pale grey-orange. The specimen has a rough texture and a distinctive circular pitting on the surface. Layers of more typical black obsidian occur occasionally within this material. The grey material forms distinctive bands that weld around the obsidian and have a consistent orientation throughout the specimen. Mid-grey bands connect with the layers of obsidian. The pale orange, vesicular material separates these grey bands. This distinction between grey bands and the paler orange material varies throughout the specimen as the layers become less structured. Flow banding is visible at a microscopic scale. The banding is very thin and characterised by lines of a pale grey material running through black obsidian. Vesicles are visible folded between the grey layering. The matrix is opaque and the cortex is comprised of a grey-orange, pitted material.

Reference Sample 15.23

This sample consists of one small hand specimen

This specimen is black in reflected light and grey under transmitted light. The lustre is vitreous and the translucency poor to moderate. Pale grey crystals combine to form curving surface banding. These bands vary in width from 1 mm to 1 cm. There is no internal banding, nor any spherulites or crystal phenocrysts present. The only other inclusions present are composed of a dull, brown-orange material. The material is too opaque to describe the condition of the matrix. The cortex lacks any rind and instead consists of dull obsidian.

Reference Sample 15.24

This sample consists of one hand specimen

This specimen is grey-black in reflected light. The specimen is too opaque to describe the colour under transmitted light. The lustre is dull. Surface flow banding is characterised by continuous thin grey streaky lines. No internal banding is visible. No spherulites or phenocrysts are present, however there exists an inclusive layer of a textured, dull grey, glassy material that bears a white coating. The specimen is too opaque to describe the condition of the matrix. No cortex is present, only dull black obsidian that lacks any rind.

Reference Sample 15.25.1

This sample consists of one hand specimen

This specimen is black in reflected light and green under transmitted light. The lustre is vitreous and the translucency poor to moderate. Folded flow structures form continuous surface bands that consist of

grey inclusive flecks. These bands are very thin and therefore more readily observed with the aid of a microscope. Internal flow banding is grey, streaky and closely spaced. One spherical mid-grey spherulite is present and displays a typical radial structure. Other slightly elongate inclusions, measuring 3 mm in diameter, occur around the spherulite. There is also an abundance of very small spherulites, most of which measure less than 1 mm in diameter. The remaining amorphous inclusions fall into two general categories. These roughly spherical, 3 mm diameter inclusions either have a pumiceous-like texture or have an orange red on white coloration. The matrix has internal flow banding, but is otherwise clear. The cortex is dull black obsidian with no rind.

Reference Sample 15.25.2

This sample consists of one hand specimen

These specimens are black in reflected light and green under transmitted light. The lustre is vitreous and the translucency poor to moderate. Folded flow structures form continuous surface bands that consist of grey inclusive flecks. These bands are very thin and therefore are more readily observed with the aid of a microscope. Internal flow banding is grey, streaky and closely spaced. Microscopic spherulites are abundant on this specimen. These inclusions are similar to spherulites, so are probably deformed examples of that type of inclusion. There are two types of inclusions present, the first are mid-grey and composed of a similar material as the spherulites. The second category consists of a cluster of elongate, slightly rounded crystal phenocrysts oriented with surface flow banding. No other inclusions are present. The matrix has internal flow banding, but is otherwise clear. The cortex is dull black obsidian with no rind.

Martin Jones 2002

Reference Sample 15.25.3

This sample consists of one hand specimen

These specimens are black in reflected light and green under transmitted light. The lustre is vitreous and the translucency poor to moderate. Folded flow structures form continuous surface bands that consist of grey inclusive flecks. These bands are very thin and therefore are more readily observed with the aid of a microscope. Internal flow banding is grey, streaky and closely spaced. Mid-grey, elongate inclusions are composed of a similar material to spherulites. These inclusions display a distinct rim and colour change from exterior to interior (mid grey to pale grey). In addition to these, other elongated, vesicular, amorphous inclusions measuring 1 cm long and 3 mm wide are present. A welded layer of pale orange brown, rough textured material with pitting is also attached to the specimen. The matrix has internal flow banding, but is otherwise clear. The cortex is dull black obsidian with no rind.

B.2.16 Ruakikini Point (Source # 16.0)

The specimens in this sample are most often black in reflected light, however one example is dark grey. The dominant colours under transmitted light are grey and green. The lustre is vitreous and the translucency variable, ranging from opaque to moderately good. Surface banding is at times emphasised by mineral or sediment inclusions. The textured banding is thick and silvery, however it is more often indistinct and discontinuous. No internal banding is present. Spherulites are abundant throughout most of the sample. The crystals measure between 1 and 6 mm in diameter and are found in a variety of shapes ranging between amorphous and elongate. Other notable features include an orange pumiceous material that occurs as banding on one specimen and

on the cortex of others. Xenoliths are welded to the gritty and cloudy matrix.

Reference Sample 16.1

This sample consists of one hand specimen, one small piece and three flakes.

These specimens are black in reflected light and green under transmitted light. The lustre is vitreous and the translucency moderate. Surface banding is comprised of mineral or sediment inclusions that define interfaces and thick, textured, silver-grey bands that vary in thickness between 1 and 2 mm. The surface interface bands are defined internally. A few random spherulites measure approximately 1 to 3 mm in diameter. The matrix is streaked by banding. The cortex is dirty and gritty.

Reference Sample 16.2

This sample consists of one hand specimen and two flakes.

These specimens are black in reflected light and grey-green under transmitted light. The lustre is vitreous and the translucency moderate to poor. Surface banding is comprised of sediment or mineral inclusions. Some faint grey lines can also be seen. No internal banding is present in these specimens. Spherulites are abundant and range between 0.5 and 3 mm in diameter. The matrix is cloudy and the cortex is comprised of a welded pumiceous material.

Reference Sample 16.3

This sample consists of one hand specimen and two flakes.

These specimens are black in reflected light and green under transmitted light. The lustre is vitreous and the translucency opaque. Surface banding is comprised of faint, 3mm thick, grey lines. This random banding occurs at a low intensity. No internal banding is apparent in these specimens. Elongated spherulites are abundant and range between 1 and 6 mm in diameter/length. A grey, 'stretched glass', vesicular, ropy texture is present on the outside of the specimens. Welded xenoliths can be seen on one specimen's cortex giving the surface a grey pumiceous appearance.

Reference Sample 16.4

This sample consists of one hand specimen and one flake

These specimens are dark grey in reflected light and grey-green under transmitted light. The lustre is dull and waxy and the translucency opaque. Surface banding is comprised of thin, indistinct, discontinuous surface streaks. This type of banding occurs throughout the specimens. No internal banding is present. Spherulites are moderately abundant and measure approximately 2 mm in diameter. There is also one 'band' of orange, pumiceous material.

Reference Sample 16.5

This sample consists of two hand specimens and one flake. - As the hand specimen differs considerably from the flake they will be described separately.

RF# 16.5-a. This specimen is black in reflected light and green under transmitted light. The lustre is highly vitreous and the translucency moderate. No surface or internal banding is apparent. Spherulites are abundant and range from 0.5 to 3 mm in diameter. These spherulites

also differ in shape, ranging from generally round, amorphous crystals to larger, blocky shapes. The matrix is slightly cloudy and no other inclusions can be seen.

RF# 16.5-b. This specimen is grey in reflected light and no colour is visible under transmitted light. The lustre is dull and the translucency opaque. The glassy cortex and inclusions are comprised of a grey, vesicular, scoriaceous material that is welded to the obsidian. No surface or internal banding is present in this specimen. Spherulites are moderately abundant and measure between 1 to 2 mm in diameter. The condition of the matrix can not be described.

B.2.17 Kaeo (Source # 17.0)

The specimens in this sample are most often black in reflected light and in one instance grey-black. The colour visible under transmitted light is green. The lustre is matt. Neither surface nor internal banding is present in these specimens. Spherulites are present in only one example. The matrix is variable, appearing clear or gritty depending on the specimen. The cortex is the most distinctive feature of this sample group. Most specimens have a cortex that covers almost all the available surface area. This outer layer is often rough, vesicular and displays colours typical of rhyolitic material. Whites, pinks, yellows and greys can occur on the same specimen. Dark grey is the most common colour, with an iron oxide stain being fairly common as well.

Reference Sample 17.1 - Caprine Road.

This sample consists of twenty-four pieces

These specimens are black in reflected light and green under transmitted light. The textured lustre is slightly waxy and the translucency poor

to opaque. Surface banding can be found on only one piece where banding is regular, but indistinct. No spherulites, phenocrysts or other crystal inclusions are present. The cortex is rough, vesicular and displays colours typical of rhyolitic material. The observed colours include between white-pink, brown, yellow and grey. Some ash or lapillae material is welded to the specimens. The matrix is presumed to be clear.

Reference Sample 17.2 - Upukarau - above river.

This sample consists of four hand specimens (one large) and three small pieces.

These specimens are black in reflected light, and grey-green under transmitted light. The surface is matt with a waxy/dull lustre and the translucency is poor. There is no evidence of surface or internal banding, spherulites, phenocrysts or other crystal inclusions in these specimens. The colour of the cortex is a combination of white, pink, beige, dark grey and finally a dull yellow grey. Some pitting or vesicularity is also visible. The cortex covers nearly the entire specimen, which is typical of the 17.0 reference group.

Reference Sample 17.3 - Urupukapuka - upper.

This sample consists of two large specimens, four hand specimens and three flakes.

These specimens are black in reflected light, and grey-green under transmitted light. The surface is matt with a waxy/dull lustre and the translucency is poor. Neither surface nor internal banding is visible, neither are any spherulites, phenocrysts or other crystal inclusions. The colour of the cortex is comprised of mid and dark grey tones and an iron oxide stain. Pits or vesicles striations also feature on the textured cortex.

Martin Jones 2002

Reference Sample 17.4 - Urupukapuka - Lower #1

This sample consists of two hand pieces and three small flakes.

These specimens are grey-black in reflected light, and grey-green under transmitted light. The matt surface has a dull lustre and translucency is poor. As with 17.3 there are no spherulites, phenocrysts or other crystal inclusions, also there is neither any surface nor internal banding. The cortex is rough and dark grey. There are no real vesicles, though some 'stretched' striations and a few vesicles are visible on 17.4-a.

Reference Sample 17.5 - Urupukapuka - Lower #2

This sample consists of five large and four small pieces.

These specimens are black in reflected light and green under transmitted light. The lustre is waxy and the translucency poor. There are no spherulites, phenocrysts or other crystal inclusions, also there is neither any surface nor internal banding. The cortex is rough, pitted and vesicular. The colour of the cortex varies from grey-yellow through to grey-brown to grey. Some white ash is present on the cortex as well.

Reference Sample 17.6 - Urupukapuka - Lower #3

This sample consists of four large and four small specimens.

These specimens are black in reflected light, and green under transmitted light. The lustre is matt/dull and the translucency poor. There are no spherulites, phenocrysts or other crystal inclusions, also there is neither is any surface nor internal banding.

Reference Sample 17.7 - Upukarau - above river.

This sample consists of one large hand specimen.

This sample is black in reflected light and Green under transmitted light. The lustre is matt and translucency is moderate. No surface or internal banding is visible.No spherulites, phenocrysts or other crystal inclusions are visible on the surface.

The cortex is rough, pitted and vesicular.

Reference Sample 17.8

This sample consists of four hand specimens.

These specimens are black in reflected light and greyish green under transmitted light. The lustre is waxy and textured and the translucency moderate to poor. No surface or internal banding is visible. One solid xenolith, 6 mm in diameter, can be seen. This feature causes no disturbance in the surrounding matrix. Spherulites are present on 17.8-a. One extremely large one, 6 mm in diameter, occurs with a mylonitic-like 'stretching' seen at each end of the inclusion. The disturbed matrix 'flows' very slightly around the spherulite. The matrix is quite gritty.

B.2.18 Whakarara(# 24)

Reference Sample 24.1

This sample consists of six hand specimens.

These specimens are black in reflected light, and light grey-Brown under transmitted light. The surface lustre is highly vitreous and translucency is good to excellent. No surface or internal banding is visible in these

samples. No spherulites are present on these samples, however crystal agglomerations approximately 1-5 mm in diameter are abundant.The fracture on these samples is conchoidal.

No cortex is present on the samples.

Reference Sample 24.2

This sample consists of one hand specimen.

This sample is black in reflected light, and dull green in transmitted light. The surface lustre is Matt due to fine pitting, and translucency is moderate. No surface or internal banding is visible on this sample. No spherulites or other crystalline inclusions are visible on this sample. The fracture on this sample is conchiodal.

No cortex is present on the sample.

B.2.19 Weta(# 25)

Reference Sample 25.1

This sample consists of three hand specimens and two flakes.

These samples are black in reflected light, and dull green in transmitted light. The surface lustre is typically matt due to fine pitting over the entire surface. Faint surface and internal banding is visible in some of the samples. No spherulites are present on any of the samples,however small rare crystal inclusions approximately 1-2 mm in diameter are present. The fracture on these samples is conchiodal.

No cortex is present on the samples.

B.2.20 Te Paritu(# 26)

Reference Sample 26.1

This sample consists of one hand specimen

This specimen is grey-black in reflected light and grey transmitted light. The lustre is dull and the translucency poor. Surface banding consists of thin linear grey-green/black bands that observe a consistent thickness and orientation. This banding has an indistinct and somewhat silky appearance. No spherulites or vesicles can be seen. Blocky and translucent crystals form an agglomeration of phenocrysts. The individual crystals measure between 1 and 2 mm in length. These inclusions comprise one percent of the specimen. The matrix is probably gritty, however it is difficult to be certain as it is only possible to view a very small edge section. The dull grey-brown cortex is thicker than most of the previous specimens, however it still shows signs of pitting and wear. Some sediment is also welded to the cortex.

Reference Sample 26.2

This sample consists of one hand specimen and one chip

These specimens are black under reflected light. It is not possible to describe the colour under transmitted due to poor translucency. No surface or internal banding is present, however the surface does have a grey-black streaky quality to it. There are no spherulites or vesicles. Phenocrysts measuring approximately 1 mm in diameter do not occur abundantly. The matrix is opaque. The cortex is thicker here than most of the other specimens, although it is still relatively thin. A combination of colours feature in the cortex, including white, yellow, brown and grey. Detailed inspection shows a degree of microscopic pitting that contains

a welded ash/sediment.

Reference Sample 26.3.1

This sample consists of 2 hand specimens.

These specimens are grey-black under reflected light and grey-green under transmitted light. The lustre is textured and vitreous. The translucency is poor. 7 mm thick surface bands are comprised of many discrete lines. Banding can be observed internally as well. In both cases, this feature is consistent, uniform and distinct. White-grey elongate crystals have developed within the banding. The average length of these orange inclusions is 10 mm. White phenocrysts measure 1 mm in diameter and comprise approximately one percent of the specimen. There are no spherulites, vesicles or lithic inclusions present. The matrix is too opaque to be described and no cortex is attached to the specimen.

Reference Sample 26.3.2

This sample consists of 2 hand specimens.

These specimens are grey-black under reflected light and grey-green under transmitted light. The lustre is textured and vitreous. The translucency is poor. 7 mm thick surface bands are comprised of many discrete lines. Banding can be observed internally as well. In both cases, this feature is consistent, uniform and distinct. White-grey elongate crystals have developed within the banding. The average length of these orange inclusions is 10 mm. White phenocrysts measure 1 mm in diameter and comprise one percent of the specimen. There are no spherulites, vesicles or lithic inclusions present. The matrix is too opaque to be described and no cortex is attached to the specimen.

Reference Sample 26.4

This sample consists of one hand specimen

This specimen is black under reflected light and grey-green under transmitted light. The lustre is vitreous and the translucency poor. Very slight surface streaking replaces any definite banding. No spherulites, vesicles, or lithic inclusions are present. An agglomeration of phenocrysts forms one percent of the specimen. The component crystals measure between 0.5 and 1 mm in diameter. The condition of the matrix is gritty. The dull grey cortex is worn and pitted.

Reference Sample 26.5.1

This sample consists of one hand specimen

This specimen is black in reflected light. It is not possible to describe to colour under transmitted light due to poor translucency. The lustre is vitreous. This specimen displays virtually no distinguishing characteristics. There is no evidence of surface or internal banding, no spherulites, crystal or lithic inclusions or vesicles. The sample is too opaque to describe the condition of the matrix and no cortex is present.

Reference Sample 26.5.2

This sample consists of one hand specimen

This specimen is black in reflected light. It is not possible to describe to colour under transmitted light due to poor translucency. The lustre is vitreous. There is surface or internal banding, but linearly oriented inclusions and light fracture lines can be seen. These light grey inclusions have a slight spherulitic appearance. No true spherulites occur in this sample. The fracture lines and inclusions affect the flaking quality

of this obsidian. The sample is too opaque to describe the condition of the matrix and the cortex is dull grey, but quite slight.

Reference Sample 26.6

This sample consists of one hand specimen

This specimen is black in reflected light and green under transmitted light. The lustre is vitreous and the translucency moderate to good. Surface and internal banding consists of definite straight lines that occur consistently throughout the specimen. These white streaky lines seem to be composed of inclusions of concentrated sediment. This feature becomes prominent when sample is chipped. No spherulites, phenocrysts or other inclusions are present. The matrix is clear and no cortex is attached to this sample.

Reference Sample 26.7.1

This sample consists of one hand specimen and one small chip

These specimens are black in reflected light and green under transmitted light. The vitreous lustre is accompanied by a definite surface texture and the translucency is poor. Surface banding is largely comprised of abundant crystalline inclusions. Consistent streaking is also apparent on these specimen. There is no internal banding nor are there any spherulites, vesicles or phenocrysts present. The dull grey-black cortex has a smooth texture. The matrix is gritty.

Reference Sample 26.7.2

This sample consists of one hand specimen

This specimen is black in reflected light and green under transmitted light. The vitreous lustre is accompanied by a definite surface texture and the translucency is poor. Surface banding is indistinct, discontinuous and largely comprised of abundant crystalline inclusions. There is no internal banding nor are there any spherulites, vesicles or phenocrysts present. The dull grey-black cortex has a smooth texture. The matrix is gritty.

Reference Sample 26.7.3

This sample consists of one flake

This specimen is black in reflected light and green under transmitted light. The vitreous lustre is accompanied by a definite surface texture and the translucency is poor. Surface banding in indistinct, discontinuous and largely comprised of abundant crystalline inclusions. Consistent streaking is also apparent on this specimen. There is no internal banding nor are there any spherulites, vesicles or phenocrysts present. The dull grey-black cortex has a smooth texture. The matrix is gritty.

Reference Sample 26.7.4

This sample consists of one hand specimen and one chip

This specimen is black in reflected light and green under transmitted light. The vitreous lustre is accompanied by a definite surface texture and the translucency is poor. Surface banding is indistinct, discontinuous and largely comprised of abundant crystalline inclusions. There is no internal banding nor are there any spherulites, vesicles or phenocrysts present. The dull grey-black cortex has a smooth texture. The matrix is gritty. A crystalline material is welded to the cortex giving it a rough appearance.

Martin Jones 2002

Reference Sample 26.7.5

This sample consists of one hand specimen and one flake

These specimens are black in reflected light and green under transmitted light. The vitreous lustre is accompanied by a definite surface texture and the translucency is poor. Surface banding is indistinct, discontinuous and largely comprised of abundant crystalline inclusions. There is no internal banding nor are there any spherulites, vesicles or phenocrysts present. The dull grey-black cortex has a smooth texture. The matrix is gritty.

Reference Sample 26.7.6

This sample consists of one hand specimen and one flake

These specimens are black in reflected light and green under transmitted light. The vitreous lustre is accompanied by a definite surface texture and the translucency is poor. Surface banding is indistinct, discontinuous and largely comprised of abundant crystalline inclusions. There is no internal banding nor are there any spherulites, vesicles or phenocrysts present. The dull grey-black cortex has a smooth texture. The matrix is gritty.

B.2.21 Lower Staircase(# 27)

Reference Sample 27.1

This sample consists of one hand specimen and one chip

These specimens are black in reflected light and green under transmitted light. The lustre is vitreous and the translucency moderate. There is no

surface banding, but sediment and agglomerations of clear phenocrysts are oriented in lines that look similar to lines of fracture. No internal banding can be seen, there are also no spherulites or vesicles. Sediments and elongate clear phenocrysts occur over approximately seven percent of each specimen. The matrix is clear and no cortex is present.

Reference Sample 27.2

This sample consists of three hand specimens

These specimens are black in reflected light. It is not possible to describe the colour under transmitted light due to poor translucency. The lustre is vitreous and the translucency opaque. Streaking is visible in the place of definite surface or internal banding. Surface fracture lines and crystal agglomerations have weakened the fabric of the obsidian. These agglomerations are oriented parallel to each other and have a dull grey appearance and a rough glassy texture. The length of these features is variable and their boundaries are at times unclear. Smaller inclusions are composed of the same grey material, but are often half the size. Some of the component crystals of the agglomerations are greyish rather then clear. No spherulites are present. The matrix is probably gritty, but it is difficult to be certain due to the poor translucency. The cortex is glassy and dull.

B.2.22 Oira Bay (Source # 28.0)

The specimens in this sample are most often black in reflected light, however grey and green are also visible. Under transmitted light grey and green are visible. The variable lustre can be either waxy or vitreous, sometimes a slight surface texture is evident as well. The translucency is poor to moderate. Surface banding is comprised of multi-coloured

(grey, green and silver) lines that occur consistently throughout two of the three specimens. These bands vary from less than 1mm up to 6 mm. Intensity also ranges from cloudy to highly intense. No internal banding is present. Spherulites are not abundant and are relatively small, measuring 0.5 to 4 mm in diameter. Other features include elongated pumiceous xenoliths that occur in one specimen and felsic minerals that are sometimes visible along banding orientation. The matrix is cloudy.

28.1.1

This sample consists of one small chip.

These specimens are black under reflected light and opaque under transmitted conditions. The lustre is vitreous and the translucency is poor. No surface or internal banding can be seen. A few phenocryst agglomerations occur with the constituent crystals measuring between 1 and 2 mm in diameter. These agglomerations cover only about 1 percent of the obsidian. Welded pumiceous/tuff sediment, similar to 28.1.2, is attached to the specimen. However the sediment seen here is harder and covers more area (30%) than the previous example. microscopic vesicles occur in elongated shapes. Again these examples are bigger than 28.1.2. The matrix is opaque.

28.1.2

This specimen is black under reflected light. It is not possible to describe the colour under transmitted light due to poor translucency. The lustre is vitreous. No surface or internal banding can be seen. There is an abundance of non-spherulitic inclusions, of which there are two main types. The first category consists of crystal phenocryst agglomerations, and the second, angular blocky euhedral inclusions of different types

of lithics. The phenocrysts occur over only one percent of the obsidian and are typically 1 mm in diameter and clear. The angular inclusions are characteristically blocky and rectangular. This type is more abundant, covering up to 35 percent of the obsidian. The inclusions themselves range in size from 1 to 15m in length and seem to be pieces of rhyolite or granite. This second category ranges in colour from green, brown to yellow. Pumiceous ash/tuff is also present. No cortex can be seen and the matrix is clear.

Reference Sample 28.2

Specimen destroyed.

Reference Sample 28.3

This sample consists of one hand specimen and one flake.

These specimens are black in reflected light and green-grey under transmitted light. The lustre is vitreous and the translucency poor. Layers of dull grey vesicular obsidian form indistinct flow banding. This feature consists of vesicular cortex material. Flow banding is formed by irregular streaks that measure between 1 and 3 mm thick. The grey streaks are associated with vesicles containing yellow sediment. These specimens are extremely vesicular. No spherulites can be seen but clear agglomerations of phenocrysts do occur in some vesicles. The average size of these inclusions is 1 mm in diameter. The cortex is a dull grey colour and the matrix gritty.

Reference Sample 28.4

This sample consists of three specimens.

Martin Jones 2002

These specimens are black in reflected light and green under transmitted light. The textured lustre is vitreous and the translucency moderate. Surface banding is comprised of alternating, silvery-greyish black bands that occur consistently at a high intensity. These bands typically measure 4 mm wide and delineated by sediment or mineral inclusions. The specimens are too thick to observe any internal bands. Spherulites do not occur in any abundance and measure between 0.5 and 4 mm in diameter.

Reference Sample 28.5

This sample consists of one hand specimen and one flake.

These specimens are green-black in reflected light and grey-green under transmitted light. The lustre is waxy and the translucency moderate to poor. Surface banding is comprised of high intensity grey/green/black bands that vary in thickness between 1 and 2 mm. The bands occur consistently throughout the specimens. Sediment or mineral inclusions delineate surface interfaces and run parallel to the banding. No internal banding or spherulites are present, however white, pumiceous xenoliths are visible. These measure approximately 3 to 4 mm in size and have an elongated shape. Like the sediment inclusions, the xenoliths run parallel to the orientation of the banding. The matrix is cloudy.

Reference Sample 28.6

This sample consists of two hand specimens and one flake.

These specimens are grey-black in reflected light and green-grey under transmitted light. The lustre is waxy and the translucency poor. Surface banding is indistinct and cloudy and the component lines are thin and only visible in one area. No internal banding or spherulites are present,

although small white inclusions of felsic minerals can be seen parallel to the banding orientation. The matrix is cloudy

B.2.23 Whangamata Fault (Source # 29.0)

The specimens in this sample are most often grey-black in reflected light, under transmitted light grey and sometimes green is visible. The lustre is vitreous and the translucency variable, ranging from poor to good. Surface banding is best described as a faint surface cloudiness rather than definite banding. Typically, these faint 'bands' are grey in colour and occur at a low intensity. No internal banding is present. Specimens sometimes include no spherulites while others display extremely large (up to 1 cm) globular crystals arranged in a roughly concentric pattern. The matrix is clear to gritty. The cortex is generally smooth, although sometimes it can be gritty.

Reference Sample 29.1

This sample consists of one hand specimen and two flakes.

These specimens are light grey in reflected light and grey under transmitted light. The lustre is vitreous with surface texturing and the translucency poor. A surface cloudiness, rather than definite banding, is apparent. Distinct mineral or sediment inclusions define the orientation of the 'banding' with thin pink-white lines. A distinctive 'broken glass' texture can be seen on the surface. No internal banding or spherulites are present in these specimens. The matrix is cloudy. The cortex has a smooth surface, although some striations do occur.

Martin Jones 2002

Reference Sample 29.2

This sample consists of three hand specimens and one flake - One the specimens, 29.2-a, is markedly different from the rest of the sample and will be described separately.

RF# 29.2-a - The cortex completely covers the obsidian. This cortex is smooth and dark grey in colour. Some small vesicles and striations are visible, as well as a yellow volcanic sediment.

RF# 29.2 - Balance of the Sample. These specimens are black in reflected light and grey under transmitted light. The lustre is highly vitreous and the translucency moderate. Surface banding is comprised of faint, grey bands that are widely spaced and occur at a low intensity. Mineral or sediment inclusions delineate surface interfaces. No internal banding is present in these specimens. The tiny white spherulites differ in colour and crystal composition from other samples in this group. These 1mm diameter spherulites occur in a concentric structure and at a low abundance. The matrix is clear.

Reference Sample 29.3

This sample consists of eight flakes of various sizes.

These specimens are black in reflected light and green under transmitted light. The textured lustre is vitreous, but also slightly waxy. The translucency is moderate to good. A surface cloudiness occurs in the pace of definite banding. No internal banding is visible. Orange and grey spherical/globular 'spherulites' occur in a similar pattern to 29.2. These inclusions measure up to 1 cm in diameter. No other crystal inclusions are present. The matrix is gritty and the cortex pumiceous.

Reference Sample 29.4

This sample consists of one hand specimen and five flakes.

These specimens are black in reflected light and grey under transmitted light. The lustre is slightly waxy and the translucency moderate to poor. A surface texture, or cloudiness occurs in the place of definite banding. Specimens are too thick to see any internal banding. 'Spherulites' are comprised of globular, grey crystals arranged in a concentric pattern. These inclusions measure between 3 and 15 mm in diameter. Generally, these spherulites are round, but can be grouped and elongated. The matrix is clear and the cortex dull and dusty.

Reference Sample 29.5

This sample consists of one hand specimen.

These specimens are grey-black in reflected light and grey under transmitted light. The lustre is vitreous and the translucency moderate. Definite surface banding is absent, but grey inclusions surrounded by a cloudiness occur in a linear arrangement. No internal banding is present, neither are there any spherulites, phenocrysts or other crystal inclusions. The matrix is gritty and the cortex is generally smooth, though sometimes gritty.

B.2.24 Motuapa (Source # 30)

Reference Sample 30.1

This sample consists of 10 small hand specimens.

The samples are typically black in reflected light, however one sample

is red in reflected light. In general the translucency is too opaque to allow colour under transmitted light to be ascertained, however the samples sufficiently translucent to transmit light are all grey under transmitted light. The surface lustre varies between dull and vitreous. No flow banding is visible on these samples. No spherulites are visible, however abundant crystal inclusions approximately 1 to 2 mm in diameter are present.These samples have a very poor sub-conchiodal to perlitic fracture.

No cortex is present on any these samples.

Reference Sample 30.2

This sample consists of five large hand specimens.

These samples are typically black in reflected light with an extremely high level of crystalline inclusion, appearing to be more similar to a conglomerate or plutonic rock, however some portions of samples contain glassy material that is red in reflected light. The glassy component of the rock has a highly vitreous surface lustre, however the samples are too opaque to allow colour in transmitted light to be ascertained. No flow banding is visible on the surface or internally on any of these samples. There are extremely abundant crystalline inclusions approximately 0.5-20 mm in diameter throughout these samples. In total these would comprise something of the order 25-50 percent of the total volume.

No cortex is present on any of these samples.

B.2.25 Huruiki (Source # 31)

Reference Sample 31.1

This sample consists of one hand specimen and two chips

These specimens are black in reflected light and grey-black in transmitted light. The lustre is vitreous and the translucency poor. No surface or internal banding can be seen, although there is some faint and irregular streaking. No spherulites or inclusions are present in this specimen and the matrix is gritty. Rough sediments are welded to the cortex, sometimes forming shallow layers. The sediments occur in a variety of colours dominated by yellows and pinks

Reference Sample 31.2

This sample consists of one hand specimen.

The specimen is black in reflected light, however the translucency as too opaque for transmitted colour to be ascertained. The lustre is waxy to vitreous. Indistinct surface banding can be seen as a slight change in surface colouration from black to grey. The specimen is too opaque for any internal banding to be seen. There are very few crystal agglomerations on the surface, less than 1%. There is one large vesicle approximately 11 mm long on the surface with white ashy sediments in it. The matrix is opaque.

Reference Sample 31.3

This sample consists of 1 hand specimen.

The reflected colour of the sample is black, however translucency is too low to ascertain transmitted colour. The surface lustre is vitreous, and

translucency opaque. There is no visible flow banding on the surface or internally. No spherulites or other crystal inclusions are visible.

There is a thin cortex present. This is pitted and dull grey in colour.

Reference Sample 31.4

This sample consists of one hand specimen.

The sample is black in reflected light, however translucency is too opaque to ascertain transmitted colour. The surface has a vitreous lustre. No surface or internal banding is visible. no spherulites or other crystal inclusions are visible.

The cortex is rough and pitted, with an orange/Brown ash welded to the surface.

Reference Sample 31.5

The sample consists of one hand specimen.

The sample is black in reflected light, however translucency is too opaque to ascertain transmitted colour. The surface lustre is vitreous. Faint surface flow banding can be seen in cortex and surface lineations, however no internal flow banding can be seen as the sample is opaque. No spherulites can be seen on the sample, however crystal agglomerations of about 0.5-1 mm in diameter occur over about 1% of the surface area.

The sample has a thin grey pitted cortex.

Reference Sample 31.6

This sample consists of 1 hand specimen.

The sample is black in reflected light, however translucency is too opaque to ascertain transmitted colour. The surface lustre is waxy and slightly pitted in a pattern which suggests banding. No spherulites are present on the surface,however crystal agglomerations less than 7 mm in diameter occur over about 1% of the surface area.

The sample has a thin grey cortex.

B.2.26 Waihi (Source # 32.0)

Reference Sample 32.1

This sample consists of five large hand specimens and four flakes.

These specimens are grey in reflected and transmitted light. The textured lustre is vitreous and the translucency moderate to poor. Surface banding is comprised of high intensity, consistent light to dark grey bands. These colours flow into each other, but are oriented straight and relatively streaky. These bands measure between 1 to 6mm thick. Internal banding is not visible, but is assumed present in the specimens. There are no spherulites, however yellow/orange oxidised crystals can be seen in a few vesicles (only on 32.1-a). The yellow-grey cortex is smooth and weathered and the matrix cloudy.

Reference Sample 32.2

This sample consists of 1 hand specimen.

The sample is grey in reflected and transmitted light, the surface lustre is vitreous and translucency is moderate. Surface flow banding is wavy, irregular and looks very “flowy” (similar to metamorphic e.g. gneiss/marble). Colour differentiation is from light grey-dark grey-black. This is also ap-

parent internally. Bands are thick (2-30 mm) and have distinct colour differentiation. One 2mm diameter inclusion of white crystals round in shape is seen, and the banding flows around it very slightly so it must have formed before the obsidian solidified.

The dull grey cortex is very thin and worn, covered with tiny holes as well as larger pits.

Reference Sample 32.3

This sample consists of 1 hand specimen and 1 small piece.

The reflected colour of this sample is mid-dark grey, the transmitted colour is grey. The surface lustre is waxy-vitreous, and translucency is poor. Indistinct surface banding is present as a grey/green waxy bands approximately 1.2 mm thick. These bands are not continuous. No spherulites are present, however crystal agglomerations 1-1.5 mm in diameter cover approximately 1% of the surface.

No cortex on sample.

B.2.27 Tairua (Source # 33.0)

Reference Sample 33.1

This sample consists of four hand specimens.

These specimens are black in reflected light. The translucency is opaque and the lustre vitreous. No surface or internal banding is present in this sample, spherulites, phenocrysts or other crystal inclusions are also absent. The grey cortex has a covering of pale brown-orange volcanic sediment. Yellow, slightly elongate, pits or holes are visible, as are striations that may be the result of cortex stretching during cooling.

Reference Sample 33.2

This samples consists of 1 hand specimen and 2 flakes.

The reflected colour of the sample is black, and colour under transmitted light is pale-mid grey. The surface lustre is vitreous and translucency is low. Surface banding is present in both the cortex and exposed surface. The bands consist of thin $> 1mm$ waxy flowbands that are occur as dark grey cloudy streaks in the black obsidian. These are also seen internally, as a layer of about 2 cm thick consisting of tiny cloudy bands. The matrix is generally clear, though cloudy where bands are located.

Reference Sample 33.3

This sample consists of one hand specimen.

The reflected colour of the sample is black, and it is grey under transmitted light. The surface lustre is highly vitreous, and sample translucency is low. No surface banding is visible, however internal banding is present as faint cloudy streaks. Spherulites of about 1 mm in diameter are moderately abundant, however no other inclusions are present.

The black-dull grey cortex has a wide-yellow ash welded to the surface.

Reference Sample 33.4

This sample consists of one hand specimen and one small piece.

The sample is black in reflected light, and transmitted under grey light. The surface lustre is vitreous, and translucency is poor. No surface or internal banding can be seen. Crystal inclusions approximately 1 mm in diameter are present however not abundant.A single spherulite approximately 5 mm in diameter is present on the surface.

Martin Jones 2002

The dull grey cortex has a rough pitted surface with thin, small, linear vesicles. A brown-yellow ash appears to be welded to the surface.

Reference Sample 33.5

The sample consists of one hand specimen.

The reflected colour of the sample is black, however the translucency is too opaque to enable the transmitted colour to be ascertained. The surface lustre is vitreous. No surface or internal banding is visible. There are occasional crystal inclusions present ranging in size from 1 to 25 mm in diameter.

The thin dull grey cortex is worn and pitted, with some white fine ash sediment welded to it.

Reference Sample 33.6

This sample consists of 1 hand specimen plus 1 small piece.

The sample is black in reflected light and grey under transmitted light. The surface lustre is vitreous and translucency is poor. Streaky, irregular grey flow banding is present on both the surface and internally. This banding is variable in thickness but continuous. Small spherulites are present over approximately 1% of the surface.

The thin grey cortex exhibits banding.

Reference Sample 33.7

This sample consists of one hand specimen plus one small piece.

The reflected colour of this sample is black, and it is grey under trans-

mitted light. The surface lustre is vitreous, and translucency is poor. Irregular, variable thickness, banding is present on the surface and internally. Small crystal agglomerations less than about 0.5 mm in diameter cover approximately 1% of the surface area. A single spherulite approximately 3 mm in diameter is also present.

The thin, worn, grey-brown cortex is pitted.

B.2.28 Onemana/Whitipirorua (Source # 34)

Reference Sample 34.1

This sample consists of 1 hand specimen and 1 small flake.

Reflected colour is black, transmitted is pale grey. Lustre is highly vitreous, translucency is good. No surface banding is seen, internal banding is indistinct, consisting of vague streaks of slightly gritty/cloudy material. No sperulites or inclusions are present. The matrix is slightly gritty. Cortex is dull grey-black, rough pitted, vesicular, with a yellow-orange ashy sediment welded to it.

Reference Sample 34.2

This sample consists of one hand specimen.

The reflected colour of the sample is black, however the translucency is too opaque to ascertain the colour under transmitted light. The surface lustre is highly vitreous. No surface or internal banding is visible.No crystal inclusions or spherulites are visible.

The cortex is dull grey, with occasional vesicles and pits. The presence of some banding is indicated by linear striations etched in the cortex. At one location an orange-yellow sediment (volcanic, tuff?) with small

particles less than about 4 mm in diameter is welded to the cortex.

Reference Sample 34.3

This sample consists of two hand specimens.

The sample is black in reflected light, and grey under transmitted light. The surface lustre is highly vitreous, and translucency is poor to moderate. No banding is visible on the surface or internally. No spherulites or other crystal inclusions are visible.

The cortex is mid-grey, with some linear striations on one specimen. The cortex surface is pitted with large irregular ovular depressions 1-2 cm in size, plus small circular pits approximately 2-5 mm in diameter. At occasional points an orange-yellow sediment (tuff?) with small particles less than about 4 mm in diameter is welded to the cortex.

Reference Sample 34.4

This sample consists of one hand specimen.

This sample is black in reflected light, and grey under transmitted light. The surface lustre is highly vitreous, and translucency is poor to moderate. No surface or internal banding is visible. No spherulites are present, however occasional small crystal agglomerations approximately 1 mm in diameter are present. Predominant elongate vesicules are apparent, the occasional small one at 2mm long, usually 5-24 mm long. Tiny light grey crystals have grown inside the vesicles. These are too small to see the individual crystals with the naked eye. Inclusions of yellow-orange ashy sediment is present in some vesicles near the outer cortex surface of the rock.

The cortex is thin, worn, lineated and pitted. It displays distinct layers

defined by lineations which may correspond to surface/internal banding, however the rock is too opaque to see evidence of this.

B.2.29 Cook's Beach (Source # 37)

Reference Sample 37.1

This sample consists of one hand specimen.

The reflected colour of the sample is black, and grey under transmitted light. The surface lustre is vitreous, and translucency is poor. Faint surface banding is present as thin straight grey lines. Rare spherulites are present ranging in size from approximately 1-4 mm in diameter. No other inclusions are present.

The cortex is grey and rough with occasional vesicles.

Reference Sample 37.2

This sample consists of one hand specimen.

The sample is black in reflected light, and grey under transmitted light. The surface lustre is highly vitreous, and translucency is poor to moderate. Surface bands are present, consisting of thin (approximately < 0.5 mm wide) grey linear bands through the specimen. The sample is too opaque to establish whether internal banding is also present. Spherulites are moderately abundant, consisting of 1-4 mm diameter feldspar. No other inclusions a visible.

The cortex is mid grey and rough with linear striations corresponding to the banding pattern.

Martin Jones 2002

B.2.30 Purangi (Source # 38)

Reference Sample 38.1

This sample consists of one hand specimen plus one small flake.

The sample is black in reflected light, and grey under transmitted light. The surface lustre is vitreous, and the translucency is poor to moderate. Faint linear flow banding is present both internally and on the surface. Both small crystal agglomerations and spherulites (0.5-1 mm in diameter) are present, in combination these cover approximately 2% the surface area.

The cortex is thin and light grey in colour.

Appendix C

Hydration Rate data

C.1 Ambrose Inductions

Hydration thicknesses have been measured for four samples of Mayor Island obsidian that have been hydrated for approximately 13 years at 40 ^{0}C in a vapour atmosphere by Wal Ambrose (Table C.1).

Table C.1: Mayor Island samples hydrated at 40 ^{0}C by Wal Ambrose

Sample #	Hydration Duration (days)
ANU 5092	4853
12	5131
16	5131
30	5131

C.2 Finite Difference Diffusion Models

Diffusion in one dimension is modelled by the 1-D partial differential model

$$\frac{\partial c}{\partial t} = \frac{\partial}{\partial x}\left(D\frac{\partial c}{\partial x}\right) \tag{C.1}$$

if D is a constant then Equation C.1 simplifies to

$$\frac{\partial c}{\partial t} = D\frac{\partial^2 c}{\partial x^2} \tag{C.2}$$

This can be solved in a number of ways. Probably the most approachable is to use finite difference schemes, either implicit or explicit. The explicit or Forward time centred finite difference solution to Equation C.2 is

$$C_x^{t+1} = C_x^t + D\Delta t\left[\frac{c_{x+1}^t - 2c_x^t + c_{x-1}^t}{(\Delta x)^2}\right] \tag{C.3}$$

which is stable as long as

$$\frac{2D\Delta t}{(\Delta x)^2} \leq 1 \tag{C.4}$$

A second approach is to use a backward time or fully implicit finite differencing scheme, in this case Equation C.2 can be solved as

$$C_x^{t+1} = C_x^t + D\Delta t \left[\frac{c_{x+1}^{t+1} - 2c_x^{t+1} + c_{x-1}^{t+1}}{(\Delta x)^2} \right] \tag{C.5}$$

which requires the solution of a set of simultaneous equations at each time step. This is straight forward as the problem is tridiagonal requiring the solution

$$-\alpha c_{x-1}^{t+1} + (1 + 2\alpha)c_x^{t+1} - \alpha c_{j+1}^{t+1} = c_x^t$$

where

$$\alpha \equiv \frac{2D\Delta t}{(\Delta x)^2}$$

In contrast to the explicit method this scheme is stable for any stepsize Δt, though it is not second order accurate in both space and time.

An alternative approach that combines the stability of the implicit scheme and the accuracy of the explicit scheme is simply to form the average of the two methods as

$$C_x^{t+1} = C_x^t + \frac{D\Delta t}{2} \left[\frac{(c_{x+1}^{t+1} - 2c_x^{t+1} + (c_{x-1}^{t+1}) + c_{x+1}^t - 2c_x^t + c_{x-1}^t)}{(\Delta x)^2} \right] \tag{C.6}$$

This is known as the Crank-Nicholson scheme.

The three schemes just presented offer numerical solution to Equation C.2 where D is constant. In this thesis two situations may be encountered where D is non-constant; where D is a function of location (*i.e.* $D = D(x)$) or where D is a function of concentration (*i.e.* D=D(c)).

In the case where D is a function of concentration the solution is fairly simple for the explicit scheme, though less simple for the implicit and

Crank-Nicholson schemes. In the explicit case Equation C.1 becomes

$$\frac{\partial c}{\partial t} = \frac{\partial}{\partial x} D(x) \frac{\partial c}{\partial x} \tag{C.7}$$

here the explicit finite difference solution is

$$F_x^{t+1} = c_x^{t+1}) = c_x^t + \frac{\Delta t}{(\Delta x)^2} \left(D_{x+1/2}(c_{x+1}^t - c_x^t) - D_{x-1/2}(c_x^t - c_{x-1}^t) \right) \tag{C.8}$$

where

$$D_{x\pm 1/2} \equiv Dx \pm 1/2 = \frac{1}{2} \left[D(c_x^t) + D(c_{x\pm 1}^t) \right] \tag{C.9}$$

The implicit schemes are more difficult as the replacement of t with $t+1$ in dc requires the solution of coupled nonlinear equations at each time step. The problem is easier if the form of $D(u)$ allows the analytic integration of

$$dz = D(u)du$$

to evaluate $z(u)$. In this case Equation C.7 becomes

$$\frac{\partial c}{\partial t} = D \frac{\partial^2 z}{\partial x^2} \tag{C.10}$$

which can be differenced implicitly as

$$C_x^{t+1} = C_x^t + D\Delta t \left[\frac{z_{x+1}^{t+1} - 2z_x^{t+1} + z_{x-1}^{t+1}}{(\Delta x)^2} \right]$$

Each term in Equation C.2 can be linearised as follows

$$\begin{aligned} z_{x+1}^{t+1} &\equiv z(c_{x+1}^{t+1} = z(c_{x+1}^t) + (c_{x+1}^{t+1} - c_{x+1}^t) D(c_{x+1}^t) \\ z_x^{t+1} &\equiv z(c_x^{t+1} = z(c_x^t) + (c_x^{t+1} - c_x^t) D(c_x^t) \\ z_{x-1}^{t+1} &\equiv z(c_{x-1}^{t+1} = z(c_{x-1}^t) + (c_{x-1}^{t+1} - c_{x-1}^t) D(c_{x-1}^t) \end{aligned} \tag{C.11}$$

Thus the problem can be finite differenced as

$$\begin{aligned} c_x^{t+1} = \frac{\Delta t}{(\Delta x)^2} (z_{x+1}^t + D_{x+1}^t (c_{x+1}^{t+1} - c_{x+1}^t) \\ -2(z_x^t + D_x^t (C_x^{t+1} - c_x^t)) + z_{x-1}^t + D_{x-1}^t (C_{x-1}^{t+1} - c_{x-1}^t)) \end{aligned} \tag{C.12}$$

which can be arranged to give

$$\begin{aligned}
\alpha c_{x+1}^{t+1} - \beta c_x^{t+1} + \gamma c_{x-1}^{t+1} &= (\Delta x)^2[D_{x+1}^t c_{x+1}^t - (2D_x^t - 1)c_x^t + D_{x-1}^t c_{x-1}^t - z_{x+1}^t + 2z_x^t - z_{x-1}^t] \\
\alpha &= \Delta t D_{x+1}^t \\
\beta &= 2\Delta t D_x^t + (\Delta x)^2 \\
\gamma &= \Delta t D_{x-1}^t
\end{aligned} \tag{C.13}$$

Thus the solution again involves a set of simultaneous equations in tridiagonal form, which can be efficiently solved. Again a Crank-Nicholson scheme can be produced by averaging the explicit and implicit solutions.

In the case that D is a function of location (*i.e.* $D = D(x)$) the schemes presented above can be reworked accordingly. In this case the implicit schemes do not involve coupled non-linear equations and the solution is less complicated than where $D = D(c)$ as the diffusion estimate can be directly calculated. thus the estimates become

$$\begin{aligned}
F_x^{t+1} &= c_x^{t+1} = c_x^t + \frac{\Delta t}{(\Delta x)^2}\left(D_{x+1/2}(c_{x+1}^t - c_x^t) - D_{x-1/2}(c_x^t - c_{x-1}^t)\right) \\
B_x^{t+1} &= c_x^{t+1} = c_x^t + \frac{\Delta t}{(\Delta x)^2}\left(D_{x+1/2}(c_{x+1}^{t+1} - c_x^{t+1}) - D_{x-1/2}(c_x^{t+1} - c_{x-1}^{t+1})\right) \\
C_x^{t+1} &= c_x^{t+1} = \frac{F_x^{t+1} + B_x^{t+1}}{2}
\end{aligned} \tag{C.14}$$

where

$$D_{x\pm1/2} \equiv Dx \pm 1/2 = \frac{1}{2}\left[Dx + Dx \pm 1\right]$$

C.3 Diffusion Simulation Results

Table C.2: Model 1 results

time	0.90%	0.50%	0.10%	$max\left(\frac{dc}{dx}\right)$	$max\left(\frac{d^2c}{dx^2}\right)$
0	0	0	0	0	0

continued on the next page

Table C.2: *continued from Table C.2*

time	0.90%	0.50%	0.10%	$max\left(\frac{dc}{dx}\right)$	$max\left(\frac{d^2c}{dx^2}\right)$
50	0.34	0.26	0.12	0.29	0.35
100	0.48	0.37	0.17	0.41	0.49
150	0.59	0.45	0.20	0.51	0.61
200	0.69	0.52	0.24	0.59	0.70
250	0.77	0.58	0.26	0.66	0.78
300	0.84	0.64	0.29	0.72	0.86
350	0.91	0.69	0.31	0.78	0.92
400	0.97	0.74	0.33	0.83	0.99
450	1.03	0.78	0.35	0.88	1.05
500	1.08	0.82	0.37	0.93	1.11
550	1.14	0.86	0.39	0.97	1.16
600	1.19	0.90	0.41	1.02	1.21
650	1.24	0.94	0.43	1.06	1.26
700	1.28	0.97	0.44	1.10	1.31
750	1.33	1.01	0.46	1.14	1.35
800	1.37	1.04	0.47	1.17	1.40
850	1.41	1.07	0.49	1.21	1.44
900	1.45	1.10	0.50	1.24	1.48
950	1.49	1.14	0.51	1.28	1.52
1000	1.53	1.16	0.53	1.31	1.56
1050	1.57	1.19	0.54	1.34	1.60
1100	1.61	1.22	0.55	1.38	1.64
1150	1.64	1.25	0.57	1.41	1.68
1200	1.68	1.28	0.58	1.44	1.71
1250	1.71	1.30	0.59	1.47	1.75
1300	1.75	1.33	0.60	1.49	1.78
1350	1.78	1.35	0.61	1.52	1.82

continued on the next page

Table C.2: *continued from Table C.2*

time	0.90%	0.50%	0.10%	$max\left(\frac{dc}{dx}\right)$	$max\left(\frac{d^2c}{dx^2}\right)$
1400	1.81	1.38	0.62	1.55	1.85
1450	1.85	1.40	0.64	1.58	1.88
1500	1.88	1.43	0.65	1.61	1.91
1550	1.91	1.45	0.66	1.63	1.95
1600	1.94	1.47	0.67	1.66	1.98
1650	1.97	1.50	0.68	1.68	2.01
1700	2.00	1.52	0.69	1.71	2.04
1750	2.03	1.54	0.70	1.73	2.07
1800	2.06	1.56	0.71	1.76	2.10
1850	2.09	1.58	0.72	1.78	2.13
1900	2.11	1.61	0.73	1.81	2.16
1950	2.14	1.63	0.74	1.83	2.18
2000	2.17	1.65	0.75	1.85	2.21
2050	2.20	1.67	0.76	1.88	2.24
2100	2.22	1.69	0.77	1.90	2.27
2150	2.25	1.71	0.77	1.92	2.29
2200	2.27	1.73	0.78	1.94	2.32
2250	2.30	1.75	0.79	1.97	2.35
2300	2.33	1.77	0.80	1.99	2.37
2350	2.35	1.79	0.81	2.01	2.40
2400	2.38	1.80	0.82	2.03	2.42
2450	2.40	1.82	0.83	2.05	2.45
2500	2.42	1.84	0.83	2.07	2.47
2550	2.45	1.86	0.84	2.09	2.50
2600	2.47	1.88	0.85	2.11	2.52
2650	2.50	1.90	0.86	2.13	2.55
2700	2.52	1.91	0.87	2.15	2.57

continued on the next page

Table C.2: *continued from Table C.2*

time	0.90%	0.50%	0.10%	$max\left(\frac{dc}{dx}\right)$	$max\left(\frac{d^2c}{dx^2}\right)$
2750	2.54	1.93	0.88	2.17	2.59
2800	2.57	1.95	0.88	2.19	2.62
2850	2.59	1.97	0.89	2.21	2.64
2900	2.61	1.98	0.90	2.23	2.66
2950	2.63	2.00	0.91	2.25	2.69
3000	2.66	2.02	0.91	2.27	2.71
3050	2.68	2.03	0.92	2.29	2.73
3100	2.70	2.05	0.93	2.31	2.75
3150	2.72	2.07	0.94	2.33	2.77
3200	2.74	2.08	0.94	2.35	2.80
3250	2.76	2.10	0.95	2.36	2.82
3300	2.79	2.12	0.96	2.38	2.84
3350	2.81	2.13	0.97	2.40	2.86
3400	2.83	2.15	0.97	2.42	2.88
3450	2.85	2.16	0.98	2.44	2.90
3500	2.87	2.18	0.99	2.45	2.93
3550	2.89	2.19	0.99	2.47	2.95
3600	2.91	2.21	1.00	2.49	2.97
3650	2.93	2.23	1.01	2.50	2.99
3700	2.95	2.24	1.02	2.52	3.01
3750	2.97	2.26	1.02	2.54	3.03
3800	2.99	2.27	1.03	2.56	3.05
3850	3.01	2.29	1.04	2.57	3.07
3900	3.03	2.30	1.04	2.59	3.09
3950	3.05	2.31	1.05	2.61	3.11
4000	3.07	2.33	1.06	2.62	3.13
4050	3.09	2.34	1.06	2.64	3.15

continued on the next page

Table C.2: *continued from Table C.2*

time	0.90%	0.50%	0.10%	$max\left(\frac{dc}{dx}\right)$	$max\left(\frac{d^2c}{dx^2}\right)$
4100	3.11	2.36	1.07	2.65	3.17
4150	3.12	2.37	1.08	2.67	3.19
4200	3.14	2.39	1.08	2.69	3.20
4250	3.16	2.40	1.09	2.70	3.22
4300	3.18	2.42	1.09	2.72	3.24
4350	3.20	2.43	1.10	2.73	3.26
4400	3.22	2.44	1.11	2.75	3.28
4450	3.24	2.46	1.11	2.77	3.30
4500	3.25	2.47	1.12	2.78	3.32
4550	3.27	2.48	1.13	2.80	3.34
4600	3.29	2.50	1.13	2.81	3.35
4650	3.31	2.51	1.14	2.83	3.37
4700	3.32	2.53	1.14	2.84	3.39
4750	3.34	2.54	1.15	2.86	3.41
4800	3.36	2.55	1.16	2.87	3.43
4850	3.38	2.57	1.16	2.89	3.44
4900	3.39	2.58	1.17	2.90	3.46
4950	3.41	2.59	1.17	2.92	3.48
5000	3.43	2.60	1.18	2.93	3.50
Model 2 Results					
50	0.24	0.17	0.08	0.18	0.16
100	0.34	0.24	0.11	0.25	0.23
150	0.41	0.29	0.13	0.31	0.28
200	0.48	0.34	0.15	0.35	0.33
250	0.54	0.38	0.17	0.40	0.37
300	0.59	0.41	0.19	0.43	0.40
350	0.63	0.45	0.20	0.47	0.43

continued on the next page

Table C.2: *continued from Table C.2*

time	0.90%	0.50%	0.10%	$max\left(\frac{dc}{dx}\right)$	$max\left(\frac{d^2c}{dx^2}\right)$
400	0.68	0.48	0.22	0.50	0.46
450	0.72	0.51	0.23	0.53	0.49
500	0.76	0.53	0.24	0.56	0.52
550	0.79	0.56	0.25	0.59	0.54
600	0.83	0.59	0.27	0.61	0.57
650	0.86	0.61	0.28	0.64	0.59
700	0.90	0.63	0.29	0.66	0.61
750	0.93	0.65	0.30	0.69	0.63
800	0.96	0.68	0.31	0.71	0.65
850	0.99	0.70	0.32	0.73	0.67
900	1.02	0.72	0.33	0.75	0.69
950	1.04	0.74	0.33	0.77	0.71
1000	1.07	0.76	0.34	0.79	0.73
1050	1.10	0.77	0.35	0.81	0.75
1100	1.12	0.79	0.36	0.83	0.77
1150	1.15	0.81	0.37	0.85	0.78
1200	1.17	0.83	0.38	0.87	0.80
1250	1.20	0.84	0.38	0.89	0.82
1300	1.22	0.86	0.39	0.90	0.83
1350	1.24	0.88	0.40	0.92	0.85
1400	1.27	0.89	0.41	0.94	0.87
1450	1.29	0.91	0.41	0.95	0.88
1500	1.31	0.93	0.42	0.97	0.90
1550	1.33	0.94	0.43	0.99	0.91
1600	1.35	0.96	0.43	1.00	0.93
1650	1.38	0.97	0.44	1.02	0.94
1700	1.40	0.99	0.45	1.03	0.95

continued on the next page

Table C.2: *continued from Table C.2*

time	0.90%	0.50%	0.10%	$max\left(\frac{dc}{dx}\right)$	$max\left(\frac{d^2c}{dx^2}\right)$
1750	1.42	1.00	0.45	1.05	0.97
1800	1.44	1.01	0.46	1.06	0.98
1850	1.46	1.03	0.47	1.08	1.00
1900	1.48	1.04	0.47	1.09	1.01
1950	1.49	1.06	0.48	1.11	1.02
2000	1.51	1.07	0.49	1.12	1.04
2050	1.53	1.08	0.49	1.13	1.05
2100	1.55	1.10	0.50	1.15	1.06
2150	1.57	1.11	0.50	1.16	1.07
2200	1.59	1.12	0.51	1.18	1.09
2250	1.61	1.13	0.52	1.19	1.10
2300	1.62	1.15	0.52	1.20	1.11
2350	1.64	1.16	0.53	1.21	1.12
2400	1.66	1.17	0.53	1.23	1.13
2450	1.68	1.18	0.54	1.24	1.15
2500	1.69	1.19	0.54	1.25	1.16
2550	1.71	1.21	0.55	1.27	1.17
2600	1.73	1.22	0.55	1.28	1.18
2650	1.74	1.23	0.56	1.29	1.19
2700	1.76	1.24	0.56	1.30	1.20
2750	1.78	1.25	0.57	1.31	1.21
2800	1.79	1.26	0.57	1.33	1.22
2850	1.81	1.28	0.58	1.34	1.24
2900	1.82	1.29	0.58	1.35	1.25
2950	1.84	1.30	0.59	1.36	1.26
3000	1.85	1.31	0.59	1.37	1.27
3050	1.87	1.32	0.60	1.38	1.28

continued on the next page

Table C.2: *continued from Table C.2*

time	0.90%	0.50%	0.10%	$max\left(\frac{dc}{dx}\right)$	$max\left(\frac{d^2c}{dx^2}\right)$
3100	1.88	1.33	0.60	1.40	1.29
3150	1.90	1.34	0.61	1.41	1.30
3200	1.92	1.35	0.61	1.42	1.31
3250	1.93	1.36	0.62	1.43	1.32
3300	1.94	1.37	0.62	1.44	1.33
3350	1.96	1.38	0.63	1.45	1.34
3400	1.97	1.39	0.63	1.46	1.35
3450	1.99	1.40	0.64	1.47	1.36
3500	2.00	1.41	0.64	1.48	1.37
3550	2.02	1.42	0.65	1.49	1.38
3600	2.03	1.43	0.65	1.50	1.39
3650	2.05	1.44	0.66	1.51	1.40
3700	2.06	1.45	0.66	1.52	1.41
3750	2.07	1.46	0.66	1.53	1.42
3800	2.09	1.47	0.67	1.54	1.43
3850	2.10	1.48	0.67	1.55	1.44
3900	2.11	1.49	0.68	1.56	1.45
3950	2.13	1.50	0.68	1.57	1.45
4000	2.14	1.51	0.69	1.58	1.46
4050	2.15	1.52	0.69	1.59	1.47
4100	2.17	1.53	0.70	1.60	1.48
4150	2.18	1.54	0.70	1.61	1.49
4200	2.19	1.55	0.70	1.62	1.50
4250	2.21	1.56	0.71	1.63	1.51
4300	2.22	1.57	0.71	1.64	1.52
4350	2.23	1.58	0.72	1.65	1.53
4400	2.25	1.59	0.72	1.66	1.54

continued on the next page

Table C.2: *continued from Table C.2*

time	0.90%	0.50%	0.10%	$max\left(\frac{dc}{dx}\right)$	$max\left(\frac{d^2c}{dx^2}\right)$
4450	2.26	1.59	0.72	1.67	1.54
4500	2.27	1.60	0.73	1.68	1.55
4550	2.28	1.61	0.73	1.69	1.56
4600	2.30	1.62	0.74	1.70	1.57
4650	2.31	1.63	0.74	1.71	1.58
4700	2.32	1.64	0.74	1.72	1.59
4750	2.33	1.65	0.75	1.73	1.60
4800	2.35	1.66	0.75	1.74	1.60
4850	2.36	1.66	0.76	1.75	1.61
4900	2.37	1.67	0.76	1.75	1.62
4950	2.38	1.68	0.76	1.76	1.63
5000	2.39	1.69	0.77	1.77	1.64
Model 3 Results					
50	0.35	0.25	0.08	0.31	0.37
100	0.50	0.35	0.11	0.43	0.53
150	0.61	0.43	0.13	0.53	0.65
200	0.71	0.49	0.15	0.61	0.75
250	0.79	0.55	0.17	0.69	0.83
300	0.86	0.61	0.18	0.75	0.91
350	0.93	0.65	0.20	0.81	0.99
400	1.00	0.70	0.21	0.87	1.06
450	1.06	0.74	0.23	0.92	1.12
500	1.12	0.78	0.24	0.97	1.18
550	1.17	0.82	0.25	1.02	1.24
600	1.22	0.86	0.26	1.06	1.29
650	1.27	0.89	0.27	1.11	1.35
700	1.32	0.93	0.28	1.15	1.40

continued on the next page

Table C.2: *continued from Table C.2*

time	0.90%	0.50%	0.10%	$max\left(\frac{dc}{dx}\right)$	$max\left(\frac{d^2c}{dx^2}\right)$
750	1.37	0.96	0.29	1.19	1.45
800	1.41	0.99	0.30	1.23	1.49
850	1.46	1.02	0.31	1.27	1.54
900	1.50	1.05	0.32	1.30	1.58
950	1.54	1.08	0.33	1.34	1.63
1000	1.58	1.11	0.34	1.37	1.67
1050	1.62	1.13	0.35	1.41	1.71
1100	1.66	1.16	0.35	1.44	1.75
1150	1.69	1.19	0.36	1.47	1.79
1200	1.73	1.21	0.37	1.50	1.83
1250	1.76	1.24	0.38	1.54	1.87
1300	1.80	1.26	0.39	1.57	1.90
1350	1.83	1.29	0.39	1.60	1.94
1400	1.87	1.31	0.40	1.63	1.97
1450	1.90	1.33	0.41	1.65	2.01
1500	1.93	1.36	0.41	1.68	2.04
1550	1.97	1.38	0.42	1.71	2.08
1600	2.00	1.40	0.43	1.74	2.11
1650	2.03	1.42	0.43	1.76	2.14
1700	2.06	1.44	0.44	1.79	2.18
1750	2.09	1.46	0.45	1.82	2.21
1800	2.12	1.48	0.45	1.84	2.24
1850	2.15	1.50	0.46	1.87	2.27
1900	2.18	1.53	0.47	1.89	2.30
1950	2.20	1.55	0.47	1.92	2.33
2000	2.23	1.56	0.48	1.94	2.36
2050	2.26	1.58	0.48	1.97	2.39

continued on the next page

Table C.2: *continued from Table C.2*

time	0.90%	0.50%	0.10%	$max\left(\frac{dc}{dx}\right)$	$max\left(\frac{d^2c}{dx^2}\right)$
2100	2.29	1.60	0.49	1.99	2.42
2150	2.31	1.62	0.50	2.01	2.45
2200	2.34	1.64	0.50	2.04	2.48
2250	2.37	1.66	0.51	2.06	2.50
2300	2.39	1.68	0.51	2.08	2.53
2350	2.42	1.70	0.52	2.11	2.56
2400	2.45	1.71	0.52	2.13	2.59
2450	2.47	1.73	0.53	2.15	2.61
2500	2.50	1.75	0.53	2.17	2.64
2550	2.52	1.77	0.54	2.19	2.66
2600	2.55	1.78	0.54	2.22	2.69
2650	2.57	1.80	0.55	2.24	2.72
2700	2.59	1.82	0.55	2.26	2.74
2750	2.62	1.83	0.56	2.28	2.77
2800	2.64	1.85	0.57	2.30	2.79
2850	2.66	1.87	0.57	2.32	2.82
2900	2.69	1.88	0.58	2.34	2.84
2950	2.71	1.90	0.58	2.36	2.87
3000	2.73	1.92	0.58	2.38	2.89
3050	2.76	1.93	0.59	2.40	2.91
3100	2.78	1.95	0.59	2.42	2.94
3150	2.80	1.96	0.60	2.44	2.96
3200	2.82	1.98	0.60	2.46	2.99
3250	2.85	1.99	0.61	2.48	3.01
3300	2.87	2.01	0.61	2.50	3.03
3350	2.89	2.03	0.62	2.51	3.05
3400	2.91	2.04	0.62	2.53	3.08

continued on the next page

Table C.2: *continued from Table C.2*

time	0.90%	0.50%	0.10%	$max\left(\frac{dc}{dx}\right)$	$max\left(\frac{d^2c}{dx^2}\right)$
3450	2.93	2.06	0.63	2.55	3.10
3500	2.95	2.07	0.63	2.57	3.12
3550	2.97	2.08	0.64	2.59	3.14
3600	2.99	2.10	0.64	2.61	3.17
3650	3.02	2.11	0.65	2.62	3.19
3700	3.04	2.13	0.65	2.64	3.21
3750	3.06	2.14	0.65	2.66	3.23
3800	3.08	2.16	0.66	2.68	3.25
3850	3.10	2.17	0.66	2.70	3.27
3900	3.12	2.19	0.67	2.71	3.30
3950	3.14	2.20	0.67	2.73	3.32
4000	3.16	2.21	0.68	2.75	3.34
4050	3.18	2.23	0.68	2.76	3.36
4100	3.20	2.24	0.68	2.78	3.38
4150	3.22	2.25	0.69	2.80	3.40
4200	3.23	2.27	0.69	2.82	3.42
4250	3.25	2.28	0.70	2.83	3.44
4300	3.27	2.29	0.70	2.85	3.46
4350	3.29	2.31	0.70	2.87	3.48
4400	3.31	2.32	0.71	2.88	3.50
4450	3.33	2.33	0.71	2.90	3.52
4500	3.35	2.35	0.72	2.91	3.54
4550	3.37	2.36	0.72	2.93	3.56
4600	3.39	2.37	0.72	2.95	3.58
4650	3.40	2.39	0.73	2.96	3.60
4700	3.42	2.40	0.73	2.98	3.62
4750	3.44	2.41	0.74	2.99	3.64

continued on the next page

Table C.2: *continued from Table C.2*

time	0.90%	0.50%	0.10%	$max\left(\frac{dc}{dx}\right)$	$max\left(\frac{d^2c}{dx^2}\right)$
4800	3.46	2.42	0.74	3.01	3.66
4850	3.48	2.44	0.74	3.03	3.67
4900	3.49	2.45	0.75	3.04	3.69
4950	3.51	2.46	0.75	3.06	3.71
5000	3.53	2.47	0.76	3.07	3.73

Table C.3: Rate of diffusant uptake for concentration dependant diffusion functions

$\sqrt{years}$	Model 1	Model 2	Model 3
0.00	0.00	0.00	0.00
7.07	3.53	4.63	4.06
10.00	4.99	6.55	5.75
12.25	6.11	8.02	7.04
14.14	7.06	9.26	8.13
15.81	7.89	10.35	9.09
17.32	8.64	11.34	9.95
18.71	9.34	12.25	10.75
20.00	9.98	13.10	11.49
21.21	10.59	13.89	12.19
22.36	11.16	14.64	12.85
23.45	11.70	15.36	13.48
24.49	12.22	16.04	14.08
25.50	12.72	16.70	14.65
26.46	13.20	17.33	15.20
27.39	13.67	17.94	15.74
28.28	14.12	18.52	16.25
29.15	14.55	19.09	16.75
30.00	14.97	19.65	17.24
30.82	15.38	20.19	17.71
31.62	15.78	20.71	18.17

C.4 Experimental Structure

Table C.4: Obsidian sources used in the experimental induction program

Source #	Source Name	Provenance
4	Raumata Pt , Tuhua	*infra vide*:§B.2
5	Hall's Pass, Tuhua	*infra vide*:§B.2
6	Staircase, Tuhua	*infra vide*:§B.2
7	Ben Lomond,	*infra vide*:§B.2
8	Waihi	*infra vide*:§B.2
9	Huruiki	*infra vide*:§B.2
10	Te Ahumata	#680/6, Dept. Anthropology Auckland University
11	Kaeo	*infra vide*:§B.2
12	Kaeo	*infra vide*:§B.2
13	Mayor Island, generic	*infra vide*:§B.2
14	Huruiki	*infra vide*:§B.2
15	Kaeo	*infra vide*:§B.2
16	Kaeo	*infra vide*:§B.2
17	Tairua	*infra vide*:§B.2
18	Tairua	*infra vide*:§B.2
19	waihi	*infra vide*:§B.2
20	Fanal	*infra vide*:§B.2
21	Fanal	*infra vide*:§B.2
22	onemana	*infra vide*:§B.2
23	Awana	*infra vide*:§B.2
24	Awana	*infra vide*:§B.2
25	Kaeo	*infra vide*:§B.2
26	Cook's Beach	*infra vide*:§B.2

continued on the next page

Table C.4: *continued from Table C.4*

Source #	Source Name	Provenance
27	Purangi	*infra vide*:§B.2
28	Whitiporua	*infra vide*:§B.2
29	Taumou beach	*infra vide*:§B.2
30	Taumou beach	*infra vide*:§B.2
31	Taumou beach	*infra vide*:§B.2
32	Taumou beach	*infra vide*:§B.2
33	Staircase Quarry, Layer 2c	*infra vide*:§B.2
34	Staircase Quarry, Layer 2b	*infra vide*:§B.2
35	Staircase Quarry, Layer 3	*infra vide*:§B.2
36	Staircase Quarry, Layer 2a	*infra vide*:§B.2
37	Staircase Quarry. Lower level	*infra vide*:§B.2
38	Taumou Point 4	*infra vide*:§B.2
39	Taumou Point 9	*infra vide*:§B.2
40	Taumou Point 6	*infra vide*:§B.2
41	Hall's pass Layer 2	*infra vide*:§B.2
42	Taratimi	*infra vide*:§B.2
43	Taratimi 2	*infra vide*:§B.2
44	Taratimi 3	*infra vide*:§B.2
45	Taratimi 4	*infra vide*:§B.2
46	Ruawaipiro pass	*infra vide*:§B.2
47	Ruawaipiro pass	*infra vide*:§B.2
48	Raumata Point, Beach cobble	*infra vide*:§B.2
49	Raumata Point, seam #1	*infra vide*:§B.2
50	Raumata Point, seam #2	*infra vide*:§B.2
51	Raumata Point, Seam #3	*infra vide*:§B.2
52	Orongatea upper cliff seam #1	*infra vide*:§B.2
53	Orongatea upper cliff seam #2	*infra vide*:§B.2

continued on the next page

Table C.4: *continued from Table C.4*

Source #	Source Name	Provenance
54	Orongatea upper cliff seam #3	*infra vide*:§B.2
55	Orongatea inner valley	*infra vide*:§B.2
56	Orongatea inner valley	*infra vide*:§B.2
57	Orongatea ridge, crater side	*infra vide*:§B.2
58	Orongatea ridge, crater side	*infra vide*:§B.2
59	Oira South	*infra vide*:§B.2
60	Oira North	*infra vide*:§B.2
61	Oira North	*infra vide*:§B.2
62	Oira North	*infra vide*:§B.2
63	Otiora South	*infra vide*:§B.2
64	Otiora North, Seam	*infra vide*:§B.2
65	Otiora North, cobble #1	*infra vide*:§B.2
66	Otiora North, cobble #2	*infra vide*:§B.2
67	Te Matawhero Point	*infra vide*:§B.2
68	Te Matawhero Point	*infra vide*:§B.2
69	Te Matawhero Point	*infra vide*:§B.2
70	Ruakiki	*infra vide*:§B.2
71	Ruakiki	*infra vide*:§B.2
72	Opo East	*infra vide*:§B.2
73	Opo East	*infra vide*:§B.2
74	Te Ananui Flat	*infra vide*:§B.2
75	Te ananui Flat	*infra vide*:§B.2
76	Opuhi Springs A, West Lower	*infra vide*:§B.2
77	Opuhi Springs B, West Valley Mouth	*infra vide*:§B.2
78	Opuhi Springs B, West Valley Head	*infra vide*:§B.2
79	Opuhi Springs C, East Side	*infra vide*:§B.2
80	Opuhi Springs C, West Side	*infra vide*:§B.2

continued on the next page

Table C.4: *continued from Table C.4*

Source #	Source Name	Provenance
81	Opuhi Springs C, West Side	*infra vide*:§B.2
82	Opuhi Springs D, West Side	*infra vide*:§B.2
83	OH , #1 pt 1	*infra vide*:§B.2
84	OH quarry pt 4	*infra vide*:§B.2
85	OH quarry pt 8	*infra vide*:§B.2
86	OH quarry pt 7	*infra vide*:§B.2
87	OH quarry pt 5	*infra vide*:§B.2
88	OH quarry pt 6	*infra vide*:§B.2
89	OH quarry boulder B	*infra vide*:§B.2
90	OH quarry boulder D	*infra vide*:§B.2
91	OH quarry boulder E	*infra vide*:§B.2
92	Above OH quarry	*infra vide*:§B.2

Run 1

The first run was carried out at 100 ^{0}C in the incubation oven. This run was conducted over the following time frame:

Table C.5: Induction 1 run time

Run Begin	Run End	Run Time
4/3/96 3:00 PM	15/3/96 3:00 PM	11 Days

Using the following experimental structure:

Table C.6: Run 1 structure

Glass #	Environments†
1	D
2	D
4	D, S, V, Sl, Sd
5	D, S, V
6	D, S, V
7	D, S, V
8	D, S, V
9	D, S, V, Sl, Sd
10	D, S, V
11	D, S, V, Sl, Sd

† Note: Letters refer to the induction environments employed and to which the glasses where exposed in any experiment, codes are as follows:
D= distilled water
S= saturated water
V = water vapour
Sl = soil
Sd = sand

Each experimental condition in this run contained two replicates. In addition to the structure outlined above samples prepared by cutting and polishing were also run as comparisons to the flake samples. These were run in the following conditions

Being the first experimental run this set was an exploration of the induction technique. The general process of conducting inductions had been explored prior to the run, but as the first “real” run this experimental set provided most of the “field testing” of the induction process in use. In

Table C.7: Flake preparation comparison experiment

Glass #	Condition
1	D
4	V
5	V
6	D
7	D
8	D

particular the temperature variation of this run was closely monitored to evaluate the temperature variability of the oven.

Runs 2-6

The set of runs at 95 ^{0}C followed after the initial run had demonstrated that the induction technique worked (ie produced an induced rim) and could maintain a stable induction environment that would ensure that the results were valid. These runs were conducted initially as they would be of most use in determining experimental precision, and as they are the lowest temperature that could be induced in a reasonable time frame (ultimately the 95 ^{0}C runs have involved seven months continuous induction time).

The following hydration structure was employed in Runs 2-6 at 95 ^{0}C.

Table C.8: Inductions 2-6 structure

Glass #	Run 2	Run 3	Run 4	Run 5	Run 6
4	V	D, S, V	D, S, V		
5	V	D, S, V	D, S, V		
6	V	V			
7	D, S, V	D, S, V, Sl, Sd	D, S, V	D, S, V	D
8		D, S, V	D, S, V		
9		D, S, V	D, S, V		
10	D, S, V	D, S, V, Sl, Sd	D, S, V		
11	D, S, V	D, S, V, Sl, Sd	D, S, V	V	V
12	D, S, V	D, S, V, Sl, Sd	D, S, V	V	V
13	D, S, V	D, S, V, Sl, Sd	D, S, V	D, S, V	V

The run times where as follows

Table C.9: Induction2-6 run durations

Run	Begin	End	Run length
2	5/04/96 20:21	6/05/96 15:00	30.8 Days
3	5/04/96 20:00	30/05/96 12:30	54.6 Days
4	5/04/96 20:21	30/05/96 12:30	54.6 Days
5	12/06/96 14:21	12/07/96 16:21	30.1 Days
6	12/06/96 14:31	12/07/96 16:21	30.1 Days

Runs 7-9

The 112.5 ^{0}C induction runs were carried out to reproduce the results of Runs 2-6 at a higher temperature. This would serve to validate the fixed condition conclusions drawn from the runs and would additionally allow

the temperature dependance of the hydration process to be explored. An additional part of the 112.5 ^{0}C induction was to provide a rate (k) for a suite of NZ obsidian at this temperature as part of a program to provide hydration controls for NZ obsidian.

In this set of runs and intensive experiment to observe the effects of solution chemistry was carried out during Run 8. The placement of this experiment in Run 8 was arbitrary.

The following structure was employed in Runs 7-9:

Table C.10: Runs 7-9 induction structure

Glass #	Run 7	Run 8	Run 9
1	D		
2	D		
4	V		
7	V	V,E†	V
8	V		
9	V		
10	V		
11	V		
12	D,S,V		
13	V		
14	V	V,E	V
15	V		
16	V	V,E	V
17	V		
18	V		
19	V		
21	V		
22	V		
25	D,S,V		
27	V		
28	V		
29	V		
30	V	V,E	V
31	V		

† E stands for the experimental suite of conditions 6-11.

The time frame of runs 7-9 were as follows:

Table C.11: Run 7-9 induction durations

Run #	Run Start	Run End	Run Duration
7	30/08/96 13:00	13/09/96 17:00	14.2 Days
8	11/09/96 22:30	20/09/96 10:00	8.5 Days
9	15/09/96 13:00	19/09/96 13:00	4 Days

Run 10

Run 10 was conducted at 107 ^{0}C in the oven primarily to provide another dataset for examining the temperature response of obsidian hydration rates, and for producing working rate estimates for New Zealand obsidian. In this run an additional set of experiments comparing induction sample preparation was conducted. Each sample induced was prepared as a flake and also as a polished section after the process outlined in Mazer *et al.* (1991), to provide another comparison of the validity of using polished sections as analogues of flake surfaces.

Table C.12: Run 10 induction structure

Glass #	Condition
9	V
10	V
13	V
15	V
16	V
25	V
28	V
29	V

Table C.13: Run 10 induction duration

Run #	Run Start	Run End	Run Duration
10	26/9/96 1:00 PM	5/11/96 1:00 PM	41 Days

Run 11

The Run 11 inductions were run at 125 ^{0}C to provide a comparison of a wide suite of representative New Zealand obsidian. This was done to provide further data for the examination of the temperature response of obsidian hydration rates and as part of an effort to define useful hydration rate controls for dating purposes. The Run 11 inductions were conducted in the oven.

Table C.14: Induction 11 structure

Glass #	Condition
5	V
7	V
9	V
10	V
11	V
14	V
15	V
16	V
17	V
18	V
25	V
26	V
27	V
28	V

continued on the next page

Table C.14: *continued from Table C.14*

Glass #	Condition
33	V
34	V
35	V
36	V
37	V
38	V
39	V
41	V
43	V
44	V
45	V
47	V
48	V
49	V
50	V
52	V
53	V
56	V
57	V
58	V
60	V
64	V
66	V
71	V
73	V
75	V
77	V

continued on the next page

Table C.14: *continued from Table C.14*

Glass #	Condition
78	V
81	V
82	V
84	V
85	V
86	V
87	V
88	V
89	V
92	V

Table C.15: induction 11 run duration

Run #	Run Start	Run End	Run Duration
11	6/12/96 1:00 PM	10/1/97 1:00 PM	35 Days

Runs 12,14 & 15

The run 12,14& 15 inductions were run at 160 ^{0}C to provide comparative data for modelling $t(x)$ and $k(T)$. These data allow the influence of temperature on $T(x)$ model form to be explored, as well as the temperature dependance of hydration rate parameters. These inductions were conducted in Parr reaction vessels in the oven.

Martin Jones 2002

Table C.16: Runs 12,14,15 induction structure

Glass #	Run 12	Run 14	Run 15
7	V	V	V
10	V	V	V
12	V	V	V
13	V	V	V
34	V	V	V

Table C.17: Induction 12,14,15 run durations

Run #	Run Start	Run End	Run Duration (hours)
12	1/10/97 8:00 PM	2/10/97 8:00 AM	12
14	1/10/97 8:00 PM	2/10/97 12:00 PM	16
15	2/10/97 9:00 AM	3/10/97 9:00 AM	24

C.5 Induced Hydration Results

Table C.18: Ben Lomond induction results

Glass #	Run	Run Length (days)	Temp (^oK)	Condition	Rim (μm)	error
7	2	30.00	368.15	D	0.675	0.075
7	2	30.00	368.15	D	0.713	0.075
7	2	30.00	368.15	S	0.675	0.075
7	2	30.00	368.15	S	0.713	0.075
7	2	30.00	368.15	V	0.675	0.075
7	2	30.00	368.15	V	0.713	0.075

continued on the next page

Table C.18: *continued from Table C.18*

Glass #	Run	Run Length (days)	Temp (^oK)	Condition	Rim (μm)	error
7	3	54.00	368.15	D	0.900	0.075
7	3	54.00	368.15	D	0.863	0.075
7	3	54.00	368.15	S	0.863	0.075
7	3	54.00	368.15	S	0.900	0.075
7	3	54.00	368.15	V	0.863	0.075
7	3	54.00	368.15	V	0.938	0.075
7	3	54.00	368.15	Sl	0.863	0.075
7	3	54.00	368.15	Sd	0.863	0.075
7	4	54.00	368.15	D	0.863	0.075
7	4	54.00	368.15	D	0.863	0.075
7	4	54.00	368.15	S	0.863	0.075
7	4	54.00	368.15	S	0.863	0.075
7	4	54.00	368.15	V	0.900	0.075
7	4	54.00	368.15	V	0.863	0.075
7	5	30.00	368.15	V	0.675	0.075
7	5	30.00	368.15	V	0.638	0.075
7	5	30.00	368.15	S	0.713	0.075
7	5	30.00	368.15	S	0.675	0.075
7	5	30.00	368.15	D	0.638	0.075
7	5	30.00	368.15	D	0.713	0.075
7	6	30.00	368.15	V	0.675	0.075
7	6	30.00	368.15	V	0.675	0.075
7	7	14.20	385.65	V	0.863	0.075
7	8	8.50	385.65	.5 M NaCl	0.675	0.075
7	8	8.50	385.65	0.1 M NaCl	0.675	0.075
7	8	8.50	385.65	2 M NaCl	0.563	0.075

continued on the next page

Table C.18: *continued from Table C.18*

Glass #	Run	Run Length (days)	Temp (^oK)	Condition	Rim (μm)	error
7	8	8.50	385.65	pH 8	0.675	0.075
7	8	8.50	385.65	pH 10.5	0.675	0.075
7	8	8.50	385.65	pH 3.5	0.713	0.075
7	8	8.50	385.65	pH 6.2	0.675	0.075
7	8	8.50	385.65	pH 7	0.713	0.075
7	8	8.50	385.65	V	0.675	0.075
7	9	4.00	385.65	V	0.488	0.075
7	11	35.00	398.15	V	2.066	0.146
7	12	0.50	433.15	V	0.660	0.015
7	14	0.67	433.15	V	0.806	0.052
7	15	1.00	433.15	V	0.977	0.054

Table C.19: Cook's Beach induction results

Glass #	Run	Run Length (days)	Temp (^oK)	Condition	Rim (μm)	error
26	11	35.00	398.16	V	1.946	0.229

Table C.20: Halls Pass induction results

Glass #	Run	Run Length (days)	Temp (^oK)	Condition	Rim (μm)	error
5	2	30.00	368.15	V	0.563	0.075
5	3	54.00	368.16	D	0.750	0.075
5	3	54.00	368.16	D	0.675	0.075
5	3	54.00	368.16	S	0.675	0.075
5	3	54.00	368.16	S	0.713	0.075
5	3	54.00	368.16	V	0.750	0.075
5	3	54.00	368.16	V	0.750	0.075
5	4	54.00	368.16	D	0.750	0.075
5	4	54.00	368.16	D	0.675	0.075
5	4	54.00	368.16	S	0.675	0.075
5	4	54.00	368.16	S	0.713	0.075
5	4	54.00	368.16	V	0.750	0.075
5	4	54.00	368.16	V	0.713	0.075
5	11	35.00	398.16	V	1.578	0.105
41	11	35.00	398.16	V	1.609	0.109

Table C.21: Huruiki induction results

Glass #	Run	Run Length (days)	Temp (^oK)	Condition	Rim (μm)	error
9	10	41.00	380.16	V	1.230	0.135
9	11	35.00	398.16	V	1.946	0.191
14	11	35.00	398.16	V	2.020	0.205
9	3	54.00	368.16	D	0.863	0.075
9	3	54.00	368.16	D	0.788	0.075
9	3	54.00	368.16	S	0.863	0.075
9	3	54.00	368.16	S	0.788	0.075
9	3	54.00	368.16	V	0.863	0.075
9	3	54.00	368.16	V	0.900	0.075
9	4	54.00	368.16	D	0.863	0.075
9	4	54.00	368.16	D	0.938	0.075
9	4	54.00	368.16	S	0.863	0.075
9	4	54.00	368.16	S	0.825	0.075
9	4	54.00	368.16	V	0.863	0.075
9	4	54.00	368.16	V	0.825	0.075
14	7	14.20	385.66	V	0.825	0.075
9	7	14.20	385.66	V	0.825	0.075
14	8	8.50	385.66	.5 M NaCl	0.713	0.075
14	8	8.50	385.66	0.1 M NaCl	0.675	0.075
14	8	8.50	385.66	2 M NaCl	0.713	0.075
14	8	8.50	385.66	pH 10.5	0.638	0.075
14	8	8.50	385.66	pH 3.5	0.750	0.075
14	8	8.50	385.66	pH 6.2	0.675	0.075
14	8	8.50	385.66	pH 8	0.675	0.075
14	8	8.50	385.66	pH 7	0.713	0.075
14	8	8.50	385.66	V	0.713	0.075
14	9	4.00	385.66	V	0.488	0.075

Table C.22: Source Kaeo induction results

Glass #	Run	Run Length (days)	Temp (^oK)	Condition	Rim (μm)	error
16	8	8.50	385.66	.5 M NaCl	0.675	0.075
16	8	8.50	385.66	0.1 M NaCl	0.638	0.075
16	8	8.50	385.66	2 M NaCl	0.675	0.075
11	2	30.00	368.16	D	0.675	0.075
11	2	30.00	368.16	D	0.675	0.075
11	3	54.00	368.16	D	0.863	0.075
11	3	54.00	368.16	D	0.788	0.075
11	4	54.00	368.16	D	0.863	0.075
11	4	54.00	368.16	D	0.863	0.075
12	2	30.00	368.16	D	0.675	0.075
12	2	30.00	368.16	D	0.713	0.075
12	3	54.00	368.16	D	0.863	0.075
12	3	54.00	368.16	D	0.788	0.075
12	4	54.00	368.16	D	0.825	0.075
12	4	54.00	368.16	D	0.863	0.075
12	7	14.20	385.66	D	0.825	0.075
25	7	14.20	385.66	D	0.863	0.075
16	8	8.50	385.66	pH 10.5	0.675	0.075
16	8	8.50	385.66	pH 3.5	0.713	0.075
16	8	8.50	385.66	pH 6.2	0.675	0.075
16	8	8.50	385.66	pH 7	0.675	0.075
16	8	8.50	385.66	pH 8	0.675	0.075
11	2	30.00	368.16	S	0.675	0.075
11	2	30.00	368.16	S	0.713	0.075
11	3	54.00	368.16	S	0.825	0.075
11	3	54.00	368.16	S	0.863	0.075

continued on the next page

Table C.22: *continued from Table C.22*

Glass #	Run	Run Length (days)	Temp (^oK)	Condition	Rim (μm)	error
11	4	54.00	368.16	S	0.825	0.075
11	4	54.00	368.16	S	0.825	0.075
12	2	30.00	368.16	S	0.675	0.075
12	2	30.00	368.16	S	0.713	0.075
12	3	54.00	368.16	S	0.788	0.075
12	3	54.00	368.16	S	0.788	0.075
12	4	54.00	368.16	S	0.825	0.075
12	4	54.00	368.16	S	0.788	0.075
12	7	14.20	385.66	S	0.863	0.075
25	7	14.20	385.66	S	0.863	0.075
11	3	54.00	368.16	Sd	0.863	0.075
12	3	54.00	368.16	Sd	0.825	0.075
11	3	54.00	368.16	Sl	0.863	0.075
12	3	54.00	368.16	Sl	0.788	0.075
11	2	30.00	368.16	V	0.638	0.075
11	2	30.00	368.16	V	0.638	0.075
11	5	30.00	368.16	V	0.675	0.075
11	5	30.00	368.16	V	0.638	0.075
11	6	30.00	368.16	V	0.638	0.075
11	6	30.00	368.16	V	0.600	0.075
12	2	30.00	368.16	V	0.638	0.075
12	2	30.00	368.16	V	0.638	0.075
12	5	30.00	368.16	V	0.638	0.075
12	5	30.00	368.16	V	0.638	0.075
12	6	30.00	368.16	V	0.638	0.075
12	6	30.00	368.16	V	0.638	0.075

continued on the next page

Table C.22: *continued from Table C.22*

Glass #	Run	Run Length (days)	Temp (^oK)	Condition	Rim (μm)	error
11	3	54.00	368.16	V	0.825	0.075
11	3	54.00	368.16	V	0.825	0.075
11	4	54.00	368.16	V	0.825	0.075
11	4	54.00	368.16	V	0.863	0.075
12	3	54.00	368.16	V	0.863	0.075
12	3	54.00	368.16	V	0.788	0.075
12	4	54.00	368.16	V	0.863	0.075
12	4	54.00	368.16	V	0.863	0.075
16	10	41.00	380.16	V	1.110	0.105
16	10	41.00	380.16	V	1.181	0.131
25	10	41.00	380.16	V	1.159	0.041
16	9	4.00	385.66	V	0.450	0.075
16	8	8.50	385.66	V	0.675	0.075
11	7	14.20	385.66	V	0.863	0.075
12	7	14.20	385.66	V	0.825	0.075
15	7	14.20	385.66	V	0.825	0.075
16	7	14.20	385.66	V	0.863	0.075
25	7	14.20	385.66	V	0.825	0.075
11	11	35.00	398.16	V	1.999	0.199
12	11	35.00	398.16	V	1.946	0.139
16	11	35.00	398.16	V	2.014	0.101
25	11	35.00	398.16	V	2.033	0.090
12	12	0.50	433.15	V	0.606	0.036
12	14	0.67	433.15	V	0.709	0.068
12	15	1.00	433.15	V	0.919	0.056

Table C.23: Mayor Island (generic) induction results

Glass #	Run	Run Length (days)	Temp (^oK)	Condition	Rim (μm)	error
13	2	30.00	368.16	D	0.563	0.075
13	2	30.00	368.16	D	0.600	0.075
13	2	30.00	368.16	S	0.563	0.075
13	2	30.00	368.16	S	0.638	0.075
13	2	30.00	368.16	V	0.525	0.075
13	2	30.00	368.16	V	0.600	0.075
13	3	54.00	368.16	D	0.675	0.075
13	3	54.00	368.16	D	0.713	0.075
13	3	54.00	368.16	S	0.750	0.075
13	3	54.00	368.16	S	0.713	0.075
13	3	54.00	368.16	V	0.750	0.075
13	3	54.00	368.16	V	0.675	0.075
13	3	54.00	368.16	Sl	0.750	0.075
13	3	54.00	368.16	Sd	0.750	0.075
13	4	54.00	368.16	D	0.675	0.075
13	4	54.00	368.16	D	0.750	0.075
13	4	54.00	368.16	S	0.675	0.075
13	4	54.00	368.16	S	0.675	0.075
13	4	54.00	368.16	V	0.713	0.075
13	4	54.00	368.16	V	0.675	0.075
13	5	30.00	368.16	D	0.563	0.075
13	5	30.00	368.16	D	0.600	0.075
13	5	30.00	368.16	S	0.525	0.075
13	5	30.00	368.16	S	0.563	0.075
13	5	30.00	368.16	V	0.600	0.075
13	5	30.00	368.16	V	0.525	0.075
13	6	30.00	368.16	V	0.600	0.075
13	6	30.00	368.16	V	0.600	0.075
13	7	14.20	385.66	V	0.713	0.075
13	10	41.00	380.16	V	1.005	0.105
13	12	0.50	433.15	V	0.503	0.077
13	14	0.67	433.15	V	0.598	0.065
13	15	1.00	433.15	V	0.809	0.054

Table C.24: OH Quarry induction results

Glass #	Run	Run Length (days)	Temp (^oK)	Condition	Rim (μm)	error
84	11	35.00	398.16	V	1.515	0.173
85	11	35.00	398.16	V	1.549	0.191
86	11	35.00	398.16	V	1.583	0.083
87	11	35.00	398.16	V	1.586	0.131
88	11	35.00	398.16	V	1.604	0.066
89	11	35.00	398.16	V	1.628	0.188
92	11	35.00	398.16	V	1.659	0.149

Table C.25: Oira North induction results

Run	Run Length (days)	Temp (^oK)	Condition	Rim (μm)	error	
60	11	35.00	398.16	V	1.931	0.124

Table C.26: Onemana induction results

Glass #	Run	Run Length (days)	Temp (^oK)	Condition	Rim (μm)	error
22	7	14.20	385.66	V	?	0.075

Table C.27: Opo East induction results

Glass #	Run	Run Length (days)	Temp (^oK)	Condition	Rim (μm)	error
73	11	35.00	398.16	V	1.706	0.169

Table C.28: Opuhi Springs Induction Results

Glass #	Run	Run Length (days)	Temp (^oK)	Condition	Rim (μm)	error
77	11	35.00	398.16	V	1.575	0.090
78	11	35.00	398.16	V	1.590	0.135
81	11	35.00	398.16	V	1.616	0.176
82	11	35.00	398.16	V	1.650	0.225

Table C.29: Orongatea induction results

Glass #	Run	Run Length (days)	Temp (^oK)	Condition	Rim (μm)	error
52	11	35.00	398.16	V	1.549	0.176
53	11	35.00	398.16	V	1.581	0.086
56	11	35.00	398.16	V	1.590	0.080
57	11	35.00	398.16	V	1.594	0.079
58	11	35.00	398.16	V	1.650	0.098

Table C.30: Otiora North induction results

Glass #	Run	Run Length (days)	Temp (^oK)	Condition	Rim (μm)	error
64	11	35.00	398.16	V	1.789	0.154
66	11	35.00	398.16	V	1.643	0.037

Table C.31: Purangi induction results

Glass #	Run	Run Length (days)	Temp (^oK)	Condition	Rim (μm)	error
27	7	14.20	385.66	V	?	0.075
27	11	35.00	398.16	V	1.888	0.038

Table C.32: Raumata Pt induction results

Glass #	Run	Run Length (days)	Temp (^oK)	Condition	Rim (μm)	error
4	2	30.00	368.16	V	0.563	0.075
4	3	54.00	368.16	D	0.788	0.075
4	3	54.00	368.16	D	0.713	0.075
4	3	54.00	368.16	S	0.713	0.075
4	3	54.00	368.16	S	0.675	0.075
4	3	54.00	368.16	V	0.750	0.075
4	3	54.00	368.16	V	0.713	0.075
4	4	54.00	368.16	D	0.750	0.075
4	4	54.00	368.16	D	0.675	0.075
4	4	54.00	368.16	S	0.788	0.075
4	4	54.00	368.16	S	0.675	0.075
4	4	54.00	368.16	V	0.713	0.075
4	4	54.00	368.16	V	0.750	0.075
4	7	14.20	385.66	V	0.713	0.075
48	11	35.00	398.16	V	1.598	0.082
49	11	35.00	398.16	V	1.646	0.259
50	11	35.00	398.16	V	1.650	0.053

Table C.33: Ruakiki induction results

Glass #	Run	Run Length (days)	Temp (^oK)	Condition	Rim (μm)	error
71	11	35.00	398.16	V	1.634	0.131

Table C.34: Ruawaipiro induction results

Glass #	Run	Run Length (days)	Temp (^oK)	Condition	Rim (μm)	error
47	11	35.00	398.16	V	1.710	0.180

Table C.35: Staircase induction results

Glass #	Run	Run Length (days)	Temp (^oK)	Condition	Rim (μm)	error
6	2	30.00	368.16	V	0.563	0.075
6	3	54.00	368.16	V	0.750	0.075
33	11	35.00	398.16	V	1.553	0.188
34	11	35.00	398.16	V	1.613	0.058
35	11	35.00	398.16	V	1.613	0.075
36	11	35.00	398.16	V	1.644	0.134
37	11	35.00	398.16	V	1.661	0.079
34	12	0.50	433.15	V	0.544	0.077
34	14	0.67	433.15	V	0.633	0.045
34	15	1.00	433.15	V	0.774	0.066

Table C.36: Source Tairua induction results

Glass #	Run	Run Length (days)	Temp (^oK)	Condition	Rim (μm)	error
18	7	14.20	385.66	V	0.790	0.075
17	7	14.20	385.66	V	0.830	0.075
17	11	35.00	398.16	V	1.898	0.105
18	11	35.00	398.16	V	1.935	0.143

Table C.37: Taratimi induction results

Glass #	Run	Run Length (days)	Temp (^oK)	Condition	Rim (μm)	error
42	8	8.50	385.66	.5 M NaCl	0.525	0.075
42	8	8.50	385.66	0.1 M NaCl	0.638	0.075
42	8	8.50	385.66	2 M NaCl	0.600	0.075
42	8	8.50	385.66	pH 8	0.638	0.075
42	8	8.50	385.66	pH 10.5	0.525	0.075
42	8	8.50	385.66	pH 3.5	0.600	0.075
42	8	8.50	385.66	pH 6.2	0.563	0.075
42	8	8.50	385.66	pH 7	0.600	0.075
42	8	8.50	385.66	V	0.565	0.075
43	11	35.00	398.16	V	1.620	0.082
44	11	35.00	398.16	V	1.627	0.135
45	11	35.00	398.16	V	1.691	0.131

Table C.38: Toumau Beach induction results

Glass #	Run	Run Length (days)	Temp (^oK)	Condition	Rim (μm)	error
29	7	14.20	385.66	V	0.713	0.075
31	7	14.20	385.66	V	0.713	0.075
30	7	14.20	385.66	V	0.938	0.075
30	8	8.50	385.66	.5 M NaCl	0.750	0.075
30	8	8.50	385.66	1 M NaCl	0.713	0.075
30	8	8.50	385.66	2 M NaCl	0.788	0.075
30	8	8.50	385.66	D	0.713	0.075
30	8	8.50	385.66	pH 10.5	0.750	0.075
30	8	8.50	385.66	pH 3.5	0.900	0.075
30	8	8.50	385.66	pH 6.8	0.713	0.075
30	8	8.50	385.66	V	0.750	0.075
30	9	4.00	385.66	V	0.450	0.075
29	10	41.00	380.16	V	1.309	0.146
38	11	35.00	398.16	V	1.736	0.049
39	11	35.00	398.16	V	2.093	0.090

Table C.39: Te Ahumata induction results

Glass #	Run	Run Length (days)	Temp (^oK)	Condition	Rim (μm)	error
10	2	30.00	368.16	D	0.788	0.075
10	2	30.00	368.16	D	0.750	0.075
10	2	30.00	368.16	S	0.750	0.075
10	2	30.00	368.16	S	0.788	0.075
10	2	30.00	368.16	V	0.750	0.075
10	2	30.00	368.16	V	0.713	0.075
10	3	54.00	368.16	D	1.050	0.075
10	3	54.00	368.16	D	0.975	0.075
10	3	54.00	368.16	S	1.013	0.075
10	3	54.00	368.16	S	1.088	0.075
10	3	54.00	368.16	V	1.013	0.075
10	3	54.00	368.16	V	1.050	0.075
10	3	54.00	368.16	Sl	0.975	0.075
10	3	54.00	368.16	Sd	0.975	0.075
10	4	54.00	368.16	D	0.975	0.075
10	4	54.00	368.16	D	1.050	0.075
10	4	54.00	368.16	S	1.013	0.075
10	4	54.00	368.16	S	1.088	0.075
10	4	54.00	368.16	V	1.050	0.075
10	4	54.00	368.16	V	1.013	0.075
10	7	14.20	385.66	V	0.975	0.075
10	10	41.00	380.16	V	1.373	0.173
10	11	35.00	398.16	V	2.333	0.305
10	12	0.50	433.15	V	0.772	0.032
10	14	0.67	433.15	V	0.913	0.063
10	15	1.00	433.15	V	1.063	0.039

Table C.40: Te Ananui Flat induction results

Glass #	Run	Run Length (days)	Temp (^oK)	Condition	Rim (μm)	error
75	11	35.00	398.16	V	1.586	0.139

Table C.41: Waihi induction results

Glass #	Run	Run Length (days)	Temp (^oK)	Condition	Rim (μm)	error
8	3	54.00	368.16	D	0.975	0.075
8	3	54.00	368.16	D	0.788	0.075
8	4	54.00	368.16	D	0.825	0.075
8	4	54.00	368.16	D	0.863	0.075
8	3	54.00	368.16	S	0.825	0.075
8	3	54.00	368.16	S	0.938	0.075
8	4	54.00	368.16	S	0.825	0.075
8	4	54.00	368.16	S	0.938	0.075
8	3	54.00	368.16	V	0.900	0.075
8	3	54.00	368.16	V	0.825	0.075
8	4	54.00	368.16	V	0.900	0.075
8	4	54.00	368.16	V	0.788	0.075
8	7	14.20	385.66	V	0.750	0.075
19	7	14.20	385.66	V	0.863	0.075

Table C.42: Whitiporua induction results

Glass #	Run	Run Length (days)	Temp (^oK)	Condition	Rim (μm)	error
28	7	14.20	385.66	V	1.088	0.075
28	10	41.00	380.16	V	1.481	0.041
28	11	35.00	398.16	V	2.456	0.146

C.6 Regressions

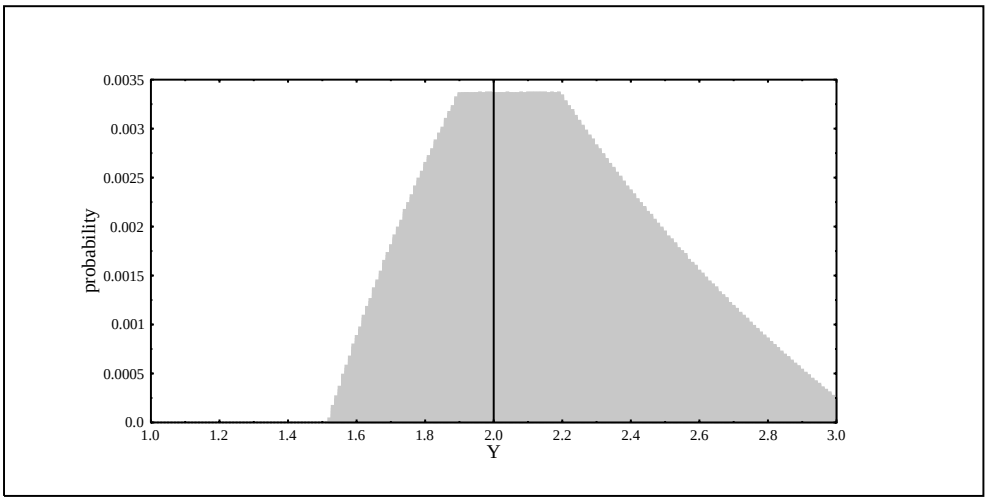

Figure C.1: Probability distribution of y for the 95 ^{0}C Ben Lomond vapour induction data

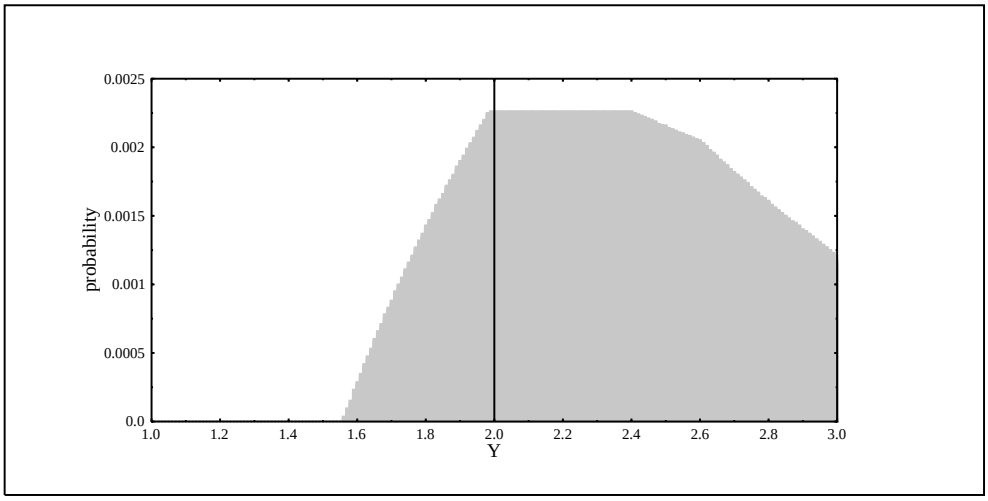

Figure C.2: Probability distribution of y for the 112.5 ^{0}C Ben Lomond vapour induction data

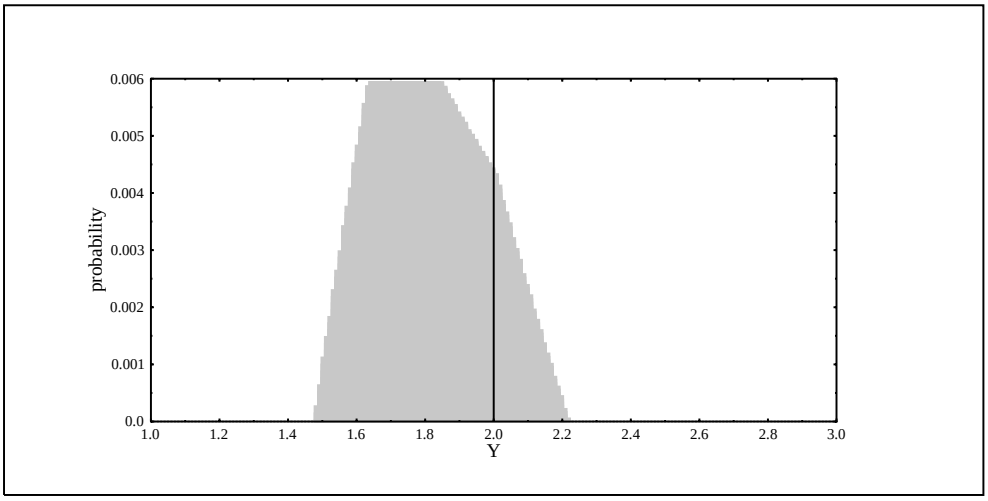

Figure C.3: Probability distribution of y for the 160 ^{0}C Ben Lomond vapour induction data

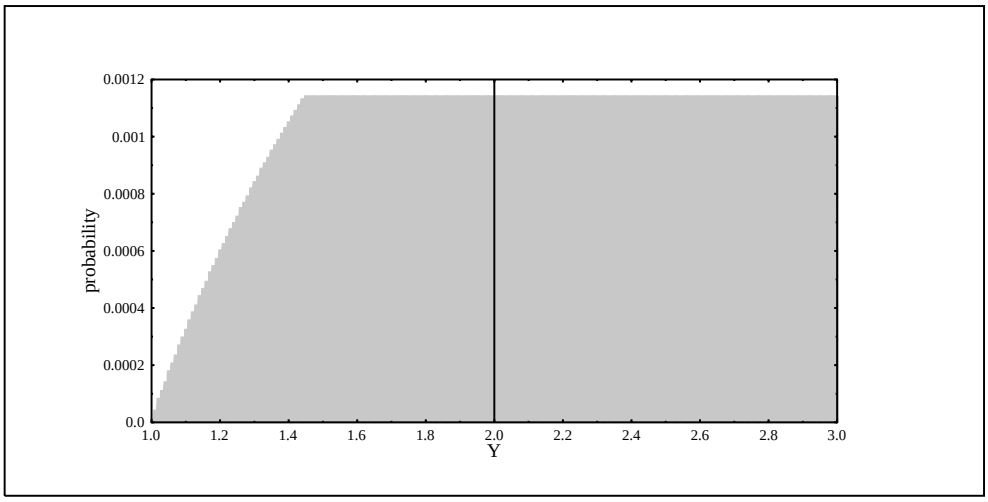

Figure C.4: Probability distribution of y for the 95 ^{0}C Hall's Pass vapour induction data

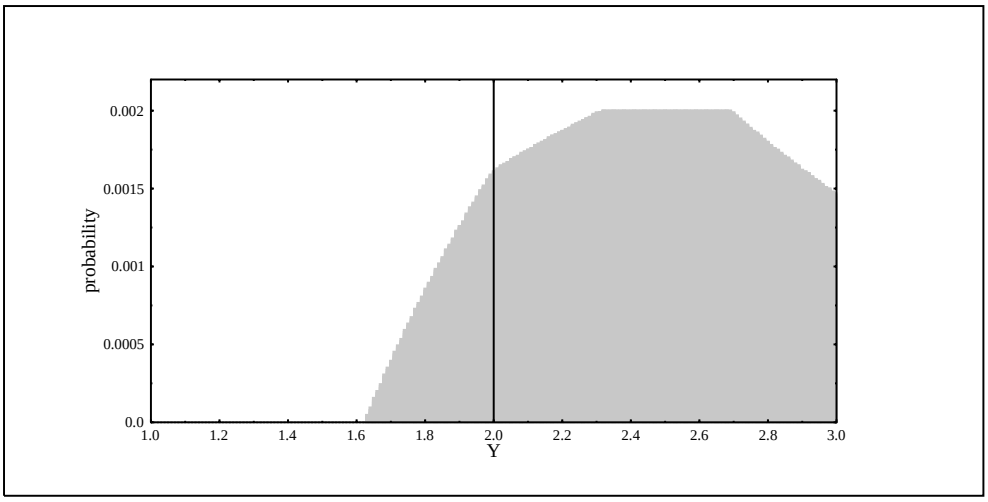

Figure C.5: Probability distribution of y for the 112.5 ^{0}C Huruiki vapour induction data

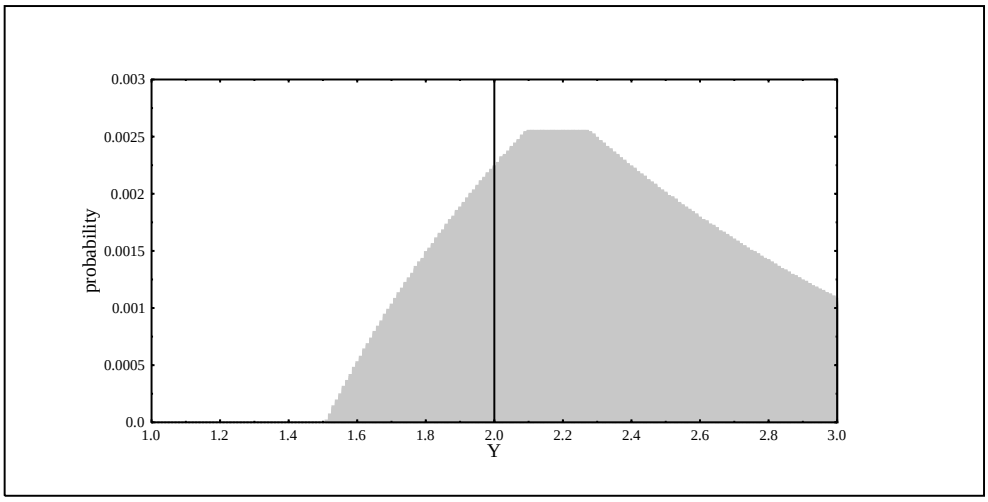

Figure C.6: Probability distribution of y for the 95 ^{0}C Kaeo (# 11) vapour induction data

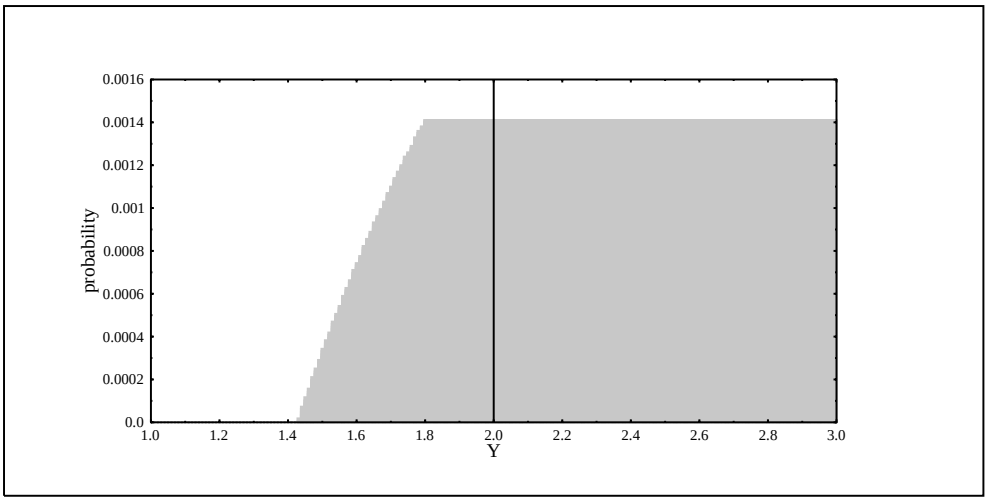

Figure C.7: Probability distribution of y for the 95 ^{0}C Kaeo (# 12) vapour induction data

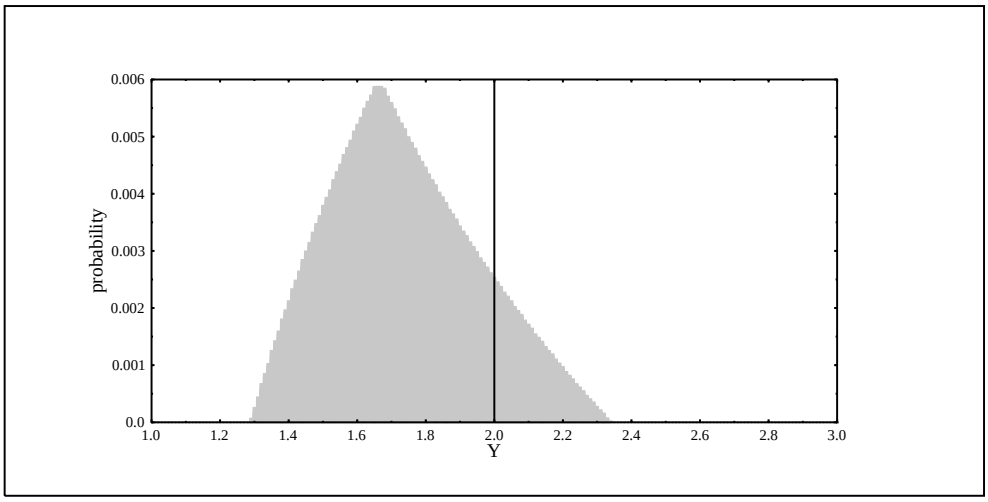

Figure C.8: Probability distribution of y for the 160 ^{0}C Kaeo vapour induction data

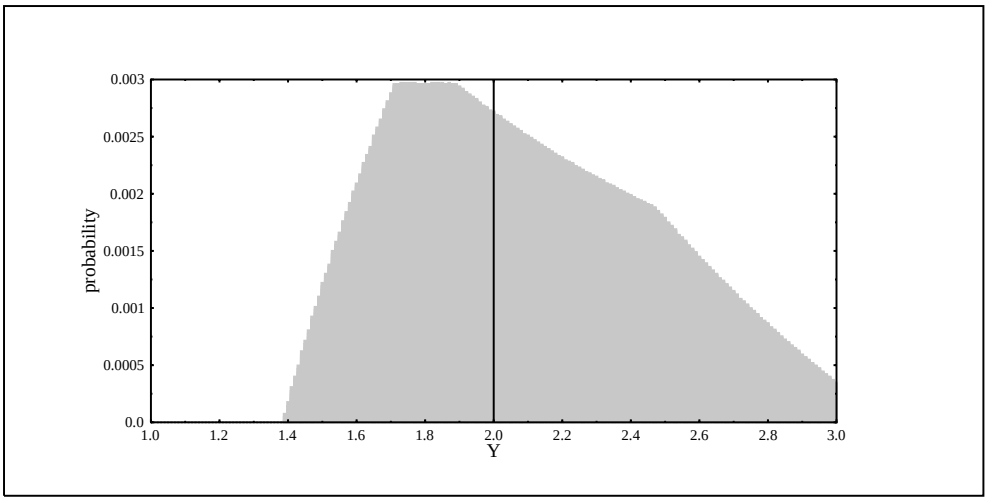

Figure C.9: Probability distribution of y for the 112.5 ^{0}C Kaeo vapour induction data

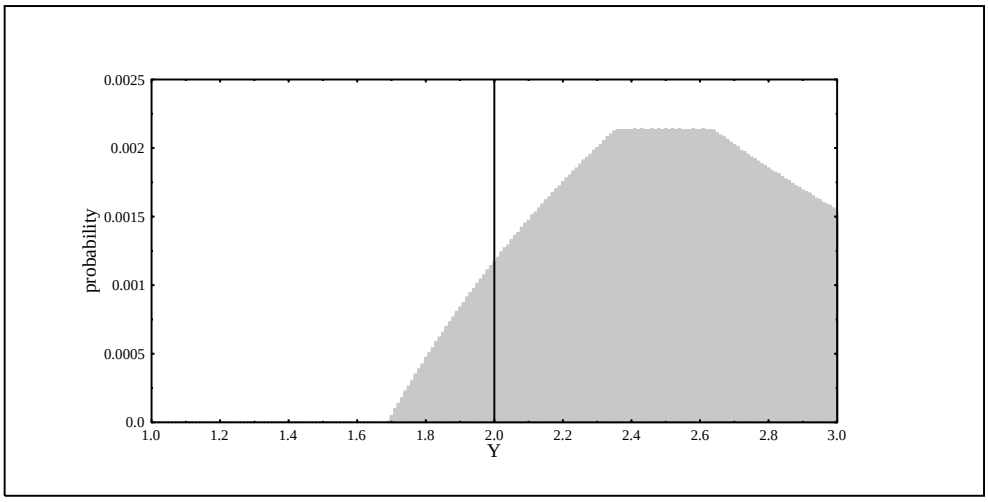

Figure C.10: Probability distribution of y for the 95 ^{0}C M.I. vapour induction data

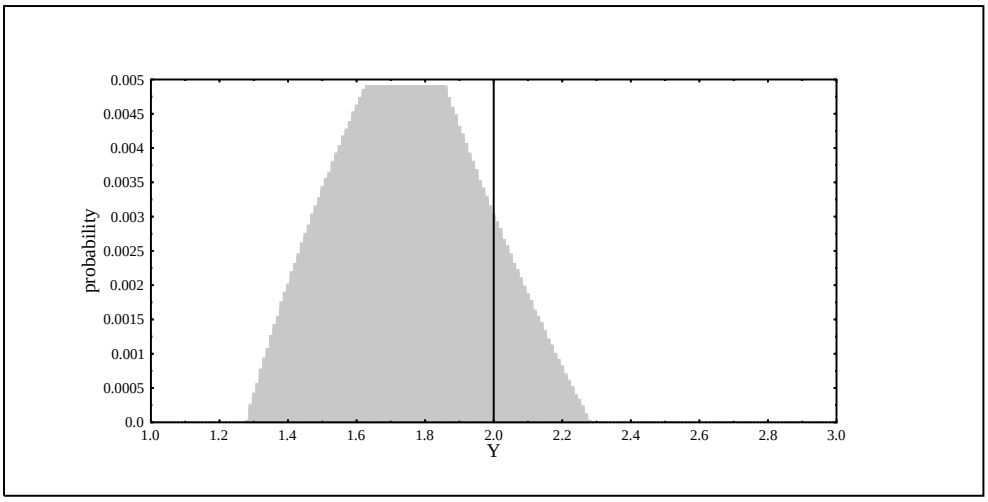

Figure C.11: Probability distribution of y for the 160 ^{0}C M.I. vapour induction data

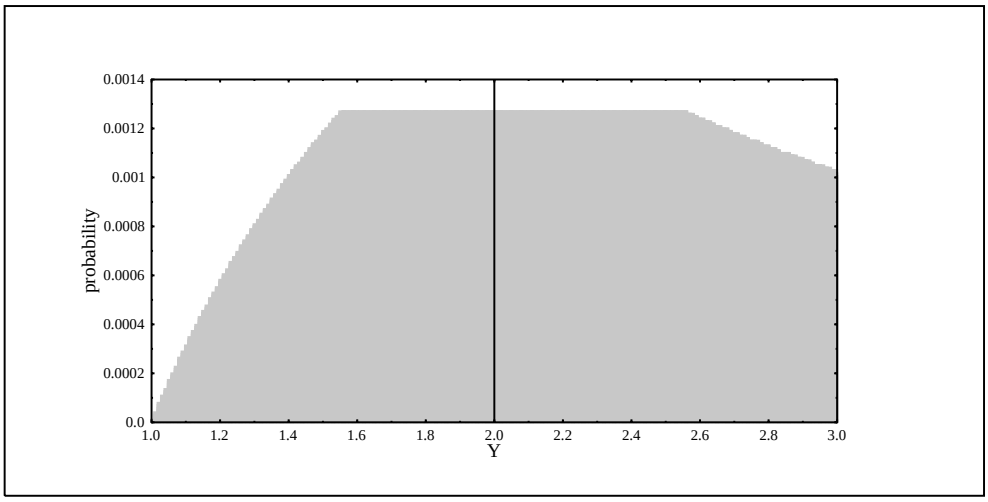

Figure C.12: Probability distribution of y for the 95 ^{0}C Raumata vapour induction data

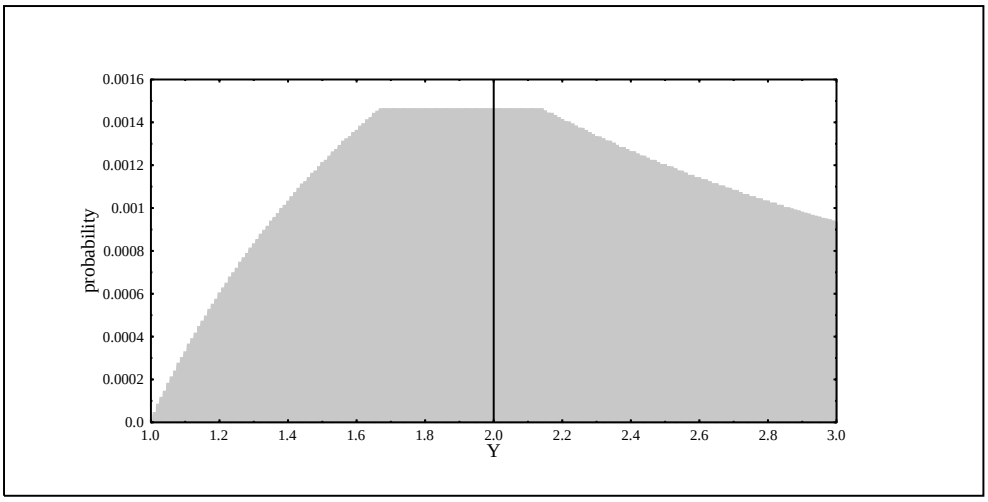

Figure C.13: Probability distribution of y for the 95 ^{0}C Staircase vapour induction data

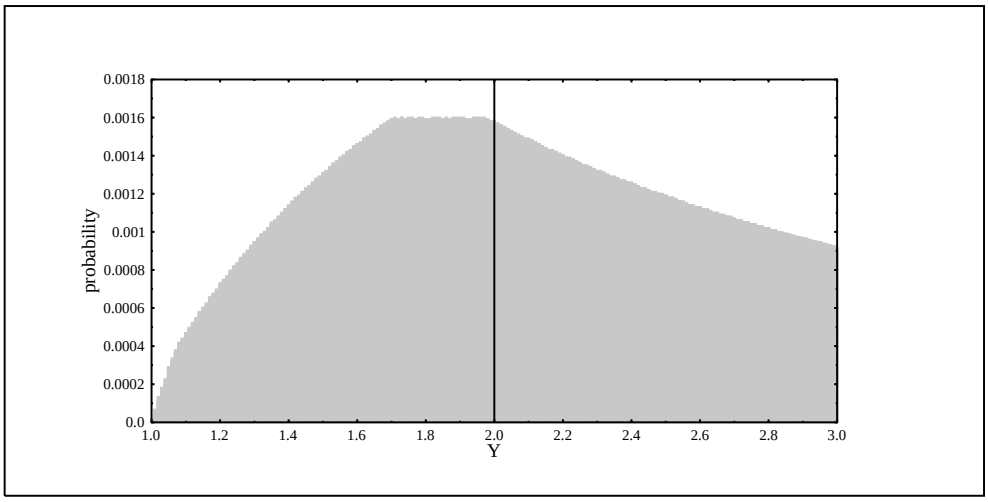

Figure C.14: Probability distribution of y for the 160 ^{0}C Staircase vapour induction data

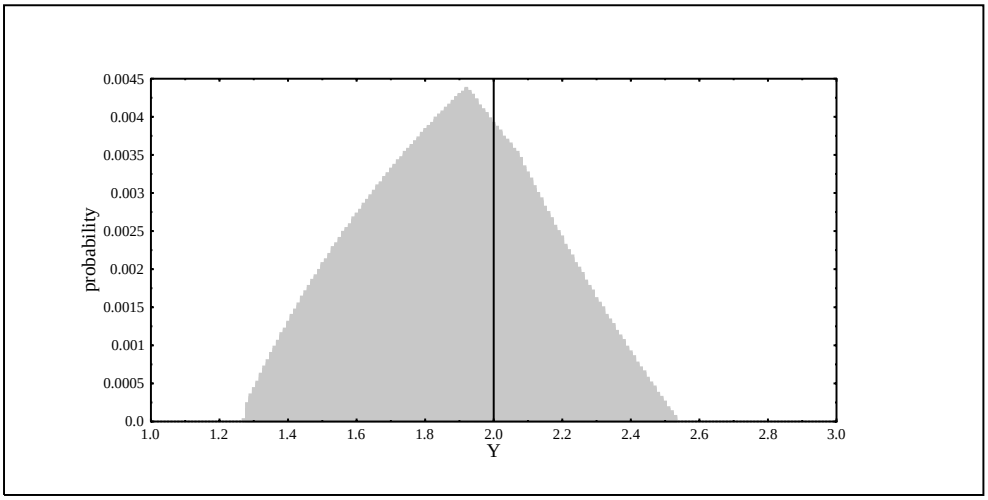

Figure C.15: Probability distribution of y for the 112.5 ^{0}C Taumou vapour induction data

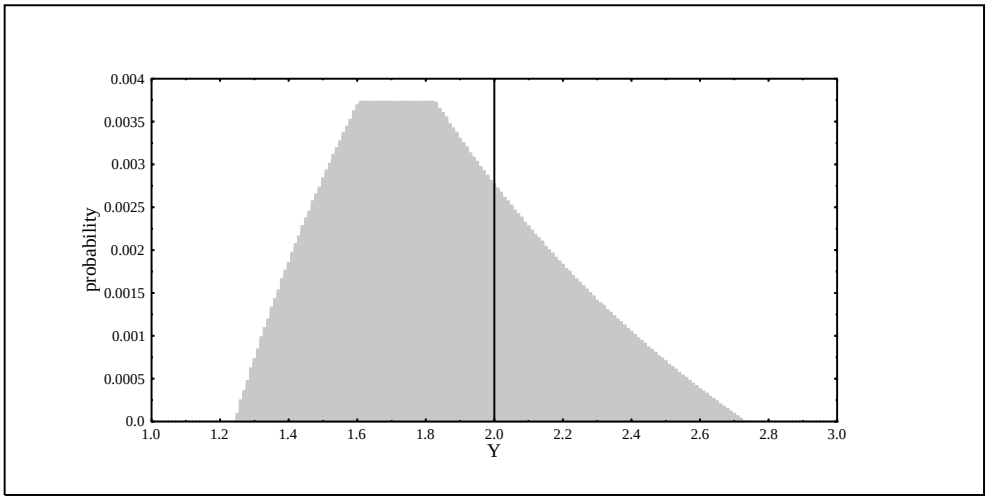

Figure C.16: Probability distribution of y for the 95 ^{0}C Te Ahumata vapour induction data

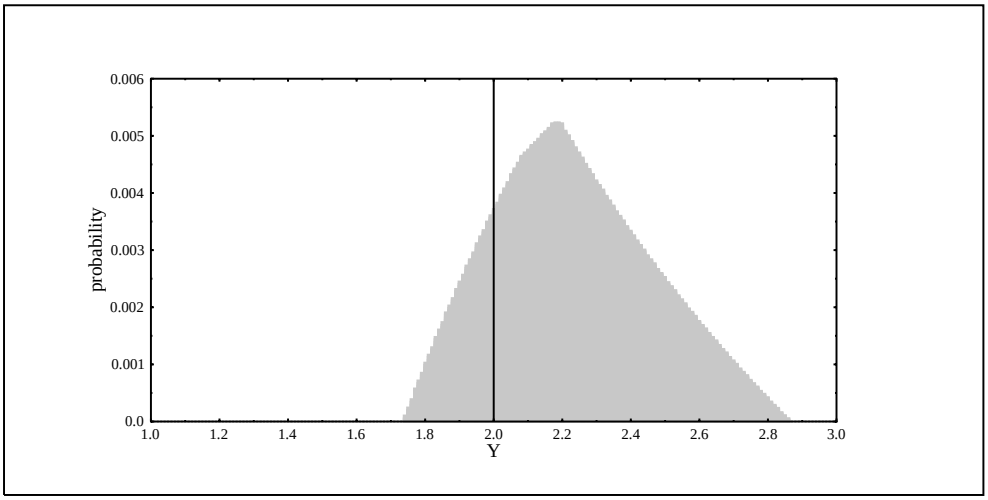

Figure C.17: Probability distribution of y for the 160 ^{0}C Te Ahumata vapour induction data

C.7 Other Results

Table C.43: Ambrose (1976) powder induction results: Taupo $< 44\mu m$

Duration (days)	Weight		
	T=40 ^{0}C	T=30 ^{0}C	T=20 ^{0}C
1.66	0.055	0.0414	0.0339
5.52	0.095	0.0614	0.0503
12.46	0.1389	0.0985	0.0666
22.00	0.179	0.1242	0.0843
32.95	0.2098	0.1456	0.0969
36.00	0.2175	0.1513	0.1019
49.00	0.251	0.1742	0.1132

Table C.44: Ambrose (1976) powder induction results: Taupo $44-63\mu m$

Duration (days)	Weight	
	T=40 ^{0}C	T=20 ^{0}C
1.66	0.0187	0.0016
5.52	0.034	0.0161
12.46	0.0493	0.0306
22.00	0.0657	0.0338
32.95	0.0798	0.0419
36.00	0.081	0.0435
49.00	0.0532	0.0974

Table C.45: Ambrose (1976) powder induction results: Mayor Island 38 – 63μm

Duration	Weight	
(days)	T=45 ^{0}C	T=25 ^{0}C
1.1236	0.0267	0.0146
3.8416	0.0486	0.0243
6.7081	0.0607	0.034
10.5625	0.0752	0.0411
17.4724	0.0897	0.0484
26.2144	0.1079	0.0557
32.0356	0.1237	

Table C.46: Ambrose (1976) powder induction results: Mayor Island 44 – 63μm

Duration	Weight	
(days)	T=45 ^{0}C	T=20 ^{0}C
0.915849	0.027	0.01
2.4964	0.0404	0.0151
4.4944	0.0472	0.0125
8.2369	0.0674	0.0226
12.1104	0.0763	0.0276
16	0.0875	0.0325
22.9441	0.1054	0.04

Table C.47: Ericson (1989) induction results: 180 ^{0}C

Flow	Duration (days)	$x(\mu m)$
2 1	3.67	3.72
2 1	5.71	4.92
2 1	10.00	6.49
2 2	3.67	3.32
2 2	5.71	4.68
2 2	10.00	6.2
2 3	3.67	5.12
2 3	5.71	6.4
2 3	10.00	9.24
2 4	3.67	4.12
2 4	5.71	5.51
2 4	10.00	6.77
2 5	3.67	5.04
2 5	5.71	6.97
2 5	10.00	8.63
2 6	3.67	4.34
2 6	5.71	6.28
2 6	10.00	7.15

Table C.48: Friedman (1976) induction results: 100 ^{0}C

Hydration Duration (days)	Rim Thickness (μm)
1460	7
870	4.216965034
800	4.216965034
730	3.945970609
600	4
470	3.595582274
365	3.09303344
300	2.95906051
240	2.424462017
182	1.5
115	1.5
88	1

Table C.49: Friedman (1976) induction results: Iceland Obsidian 95 ^{0}C

Hydration Duration (days)	Rim Thickness (μm)
94	0.86
206	2.017
393	2.30
571	2.61
730	3.08

Table C.50: Friedman (1976) induction results: Iceland Obsidian 150 ^{0}C

Hydration Duration (days)	Rim Thickness (μm)
9	2.31
20	3.10
23	3.56
31	3.87
34	4.02
54	5.15
61	5.30

Table C.51: Friedman (1976) induction results: Iceland Obsidian 195 ^{0}C

Hydration Duration (days)	Rim Thickness (μm)
2	2.94
8	6.46
20	9.38
26	11.70

Table C.52: Mazer *et al.* (1991) induction results: coso 4-1 obsidian at 175 ^{0}C

Hydration Duration (days)	Rim Thickness (μm)
4	7
4	7.5
7.84	11
16	14.7

Table C.53: Michels *et al.* (1983) induction results: Cerro de las navajas Obsidian

Temperature	Hydration Duration (days)	x (μm)	sd
200	0.5	2	0.05
200	1	3	0.19
200	2	4	0.11
200	4	5.88	0.12
200	6	7.1	0.09
250	4	16.18	0.26
225	4	11.16	0.39
175	4	3.61	0.05
150	4	1.9	0.11

Table C.54: (Michels 1989) induction results: 200 ^{0}C

Source	Duration (days)	x (μm)
Napa Glass Mountain	1	2.66
Napa Glass Mountain	2	3.8
Napa Glass Mountain	4	5.33
Napa Glass Mountain	6	6.62
Annadel Farms	1	2.47
Annadel Farms	2	3.52
Annadel Farms	4	5.01
Annadel Farms	6	6.21
Casa Diablo	1	2.66
Casa Diablo	2	3.81
Casa Diablo	4	5.46
Casa Diablo	6	6.62
Otumba	1	2.89
Otumba	2	3.99
Otumba	4	5.71
Otumba	6	6.98
Hawkins-Malad	1	2.46
Hawkins-Malad	2	3.36
Hawkins-Malad	4	4.89
Hawkins-Malad	6	6.02

Table C.55: Stevenson *et al.* (1987) induction results

Source	Temperature (^{0}C)	Duration (days)	x (μm)	error
government Mountain	200	0.5	1.78	0.04
government Mountain	200	1	2.36	0.03
government Mountain	200	2	5.44	0.09
government Mountain	200	4	3.44	0.04
government Mountain	175	4	4.08	0.06
government Mountain	150	4	1.82	0.04
rio grande gravel group II	200	0.5	2.13	0.07
rio grande gravel group II	200	1	2.34	0.04
rio grande gravel group II	200	2	3.73	0.04
rio grande gravel group II	200	4	5.18	0.04
rio grande gravel group II	175	4	3.26	0.05
rio grande gravel group II	150	4	1.86	0.05
Vulture	200	0.5	1.65	0.04
Vulture	200	1	2.09	0.03
Vulture	200	2	3.91	0.03
Vulture	200	4	4.52	0.04
Vulture	200	6	2.53	0.04
Vulture	250	4	2.14	0.05
Vulture	225	4	2.54	0.07
Vulture	175	4	3.58	0.04
Vulture	150	4	1.75	0.04
antelope wells	150	2	1.56	0.03
antelope wells	150	4	2.29	0.03
antelope wells	150	6	2.76	0.03
antelope wells	150	8	3.06	0.06
antelope wells	150	12	3.62	0.03
antelope wells	130	6	1.39	0.04
antelope wells	170	6	4.35	0.03
antelope wells	190	6	7.06	0.05
antelope wells	210	6	10.47	0.06
antelope wells	230	6	17.06	0.06

Table C.56: Stevenson and Scheetz (1989*b*) induction results: 160 ^{0}C

source	Duration (days)	$x(\mu m)$
sugar loaf	3	3.72
sugar loaf	6	5.05
sugar loaf	12	6.9
sugar loaf	18	8.9
West sugar loaf	3	2.38
West sugar loaf	6	3.58
West sugar loaf	12	5.02
West sugar loaf	18	5.34

Table C.57: Tremaine and Fredrickson (1988) induction results: 200 ^{0}C

Source	Duration (days)	x (μm)
Borax Lake	1	3.49
Borax Lake	2	4.08
Borax Lake	4	5.59
Borax Lake	6	5.92
Napa Glass mountain	1	2.77
Napa Glass mountain	2	3.12
Napa Glass mountain	4	4.68
Napa Glass mountain	6	5.11
Konociti	1	2.74
Konociti	2	3.15
Konociti	4	4.62
Konociti	6	5.21
Annadel	1	2.36
Annadel	2	2.52
Annadel	4	3.74
Annadel	6	3.85

Table C.58: Tsong *et al.* (1981) induction results: 90 ^{0}C

Duration (hrs)	x (μm)
8	0.092
12	0.115
24	0.146
48	0.192
72	0.255

Appendix D

Hydration Rate Estimation Data

D.1 Comparative Reference Data

Table D.1: Reference data set: chemical data

Glass	Rate μm	Density g/cm^3	Si	Al	Fe	Mn	Mg	Ca Mol %	Na	K	Ti	P	H_2O+
7	2.066	2.342	71.965	13.76	0.994	0.039	0.255	1.121	7.534	4.128	0.13	0.019	0.057
5	1.578	2.411	68.196	10.662	4.265	0.104	0.035	0.244	11.247	5.03	0.164	0.015	0.038
41	1.609	2.409	68.02	10.601	4.256	0.103	0.031	0.237	11.354	5.108	0.166	0.014	0.111
9	1.946	2.358	70.716	14.39	0.958	0.022	0.106	0.771	8.26	4.658	0.068	0.013	0.038
14	2.02	2.363	70.684	14.397	0.954	0.023	0.1	0.777	8.284	4.654	0.067	0.012	0.046
11	1.999	2.41	69.544	11.1	3.254	0.061	0.02	0.137	10.675	5.037	0.1	0.009	0.063
12	2.014	2.405	69.571	11.086	3.245	0.061	0.024	0.136	10.719	4.952	0.1	0.008	0.096
25	2.033	2.401	69.523	11.1	3.252	0.063	0.022	0.135	10.72	4.956	0.103	0.008	0.12
60	1.931	2.411	69.906	11.111	3.232	0.074	0.024	0.177	10.147	5.104	0.154	0.009	0.062
73	1.706	2.405	69.164	11.435	3.316	0.076	0.028	0.211	10.361	5.159	0.167	0.01	0.073
77	1.575	2.408	69.616	11.402	3.178	0.072	0.028	0.195	10.162	5.153	0.161	0.009	0.025
78	1.59	2.399	69.579	11.359	3.191	0.074	0.021	0.195	10.197	5.182	0.161	0.009	0.03
53	1.581	2.42	69.787	11.355	3.145	0.07	0.026	0.19	10.066	5.168	0.154	0.009	0.029
56	1.59	2.415	69.812	11.372	3.15	0.072	0.03	0.191	10.045	5.162	0.157	0.01	0
52	1.549	2.403	69.728	11.35	3.147	0.071	0.026	0.192	10.067	5.251	0.158	0.01	0
27	1.888	2.352	71.675	13.926	0.982	0.045	0.167	0.92	7.874	4.237	0.081	0.015	0.077
48	1.598	2.406	69.206	10.532	3.935	0.094	0.027	0.199	10.724	5.059	0.149	0.011	0.064
49	1.646	2.41	69.131	10.502	3.933	0.094	0.026	0.196	10.739	5.102	0.148	0.011	0.118
50	1.65	2.409	69.101	10.509	3.943	0.094	0.022	0.203	10.748	5.112	0.149	0.011	0.108
47	1.71	2.402	69.461	10.453	3.891	0.09	0.026	0.193	10.698	5.023	0.146	0.01	0.008
33	1.553	2.393	69.522	11.39	3.194	0.074	0.027	0.195	10.133	5.244	0.159	0.01	0.05
34	1.613	2.389	69.464	11.383	3.178	0.073	0.03	0.196	10.194	5.229	0.16	0.01	0.082
36	1.644	2.4	69.552	11.358	3.186	0.072	0.027	0.196	10.053	5.274	0.159	0.009	0.115
35	1.613	2.396	69.562	11.379	3.178	0.072	0.025	0.193	10.115	5.224	0.158	0.009	0.084
37	1.661	2.391	69.378	11.365	3.181	0.072	0.025	0.195	10.264	5.16	0.16	0.009	0.191
45	1.691	2.402	69.545	11.402	3.198	0.074	0.026	0.195	10.218	5.168	0.159	0.009	0.004

continued on the next page ...

...continued from table D.1

Glass	Rate	Density	Si	Al	Fe	Mn	Mg	Ca	Na	K	Ti	P	H_2O+
	μm	g/cm^3						Mol %					
44	1.627	2.405	69.543	11.403	3.178	0.072	0.028	0.195	10.143	5.192	0.16	0.009	0.077
43	1.62	2.398	69.471	11.342	3.172	0.071	0.027	0.193	10.193	5.198	0.161	0.009	0.164
10	2.333	2.346	71.525	13.993	0.955	0.021	0.156	0.759	6.888	5.604	0.078	0.017	0.004
16	1.946	2.41	69.512	11.089	3.257	0.06	0.021	0.137	10.67	5.016	0.101	0.008	0.131
28	2.456	2.342	71.95	13.617	0.964	0.035	0.094	0.735	7.752	4.612	0.064	0.008	0.167

Table D.2: Index reference data set

Glass	Rate μm	Density g/cm^3	C	M	zeta	CI	MI 1	MI 2
7	2.066	2.342	0.005	0.058	3.683	8.914	1.154	0.154
5	1.578	2.411	0.001	0.001	-21.552	54.891	0.904	0.096
41	1.609	2.409	0.002	0	-22.334	53.76	0.89	0.11
9	1.946	2.358	0.052	0.052	2.495	30.497	1.121	0.121
14	2.02	2.363	0.054	0.052	2.423	30.274	1.119	0.119
11	1.999	2.41	0.036	0.008	-17.622	61.214	0.906	0.094
12	2.014	2.405	0.036	0.006	-17.555	60.428	0.907	0.093
25	2.033	2.401	0.035	0.007	-17.505	60.083	0.908	0.092
60	1.931	2.411	0.003	0.002	-16.266	59.649	0.93	0.07
73	1.706	2.405	0.001	0.017	-15.81	56.949	0.938	0.062
77	1.575	2.408	0.016	0.006	-15.265	59.088	0.94	0.06
78	1.59	2.399	0.016	0.006	-15.649	59.271	0.934	0.066
53	1.581	2.42	0.002	0.001	-15.193	59.465	0.94	0.06
56	1.59	2.415	0.002	0.001	-15.038	59.856	0.943	0.057
52	1.549	2.403	0.002	0.001	-15.488	59.918	0.935	0.065
27	1.888	2.352	0.001	0.023	3.319	21.219	1.144	0.144
48	1.598	2.406	0.049	0.021	-20.558	57.729	0.905	0.095
49	1.646	2.41	0.046	0.022	-20.855	56.748	0.9	0.1
50	1.65	2.409	0.044	0.022	-20.9	56.82	0.9	0.1
47	1.71	2.402	0.018	0.001	-20.71	59.431	0.901	0.099
33	1.553	2.393	0.008	0.01	-15.51	58.528	0.937	0.063
34	1.613	2.389	0.009	0.01	-15.689	57.65	0.932	0.068
36	1.644	2.4	0.007	0.01	-15.492	57.248	0.937	0.063
35	1.613	2.396	0.007	0.01	-15.433	58.061	0.937	0.063
37	1.661	2.391	0.007	0.01	-15.769	55.675	0.931	0.069
45	1.691	2.402	0.004	0.001	-15.487	59.523	0.937	0.063

continued on the next page ...

...continued from table D.2

Glass	Rate μm	Density g/cm^3	C	M	zeta	CI	MI 1	MI 2
44	1.627	2.405	0.003	0.001	-15.325	57.972	0.939	0.061
43	1.62	2.398	0.003	0.001	-15.754	56.326	0.931	0.069
10	2.333	2.346	0.01	0.003	2.724	30.249	1.128	0.128
16	1.946	2.41	0.034	0.007	-17.592	59.797	0.907	0.093
28	2.456	2.342	0.004	0.014	1.938	31.3	1.113	0.113

D.2 Rate Comparison Graphs

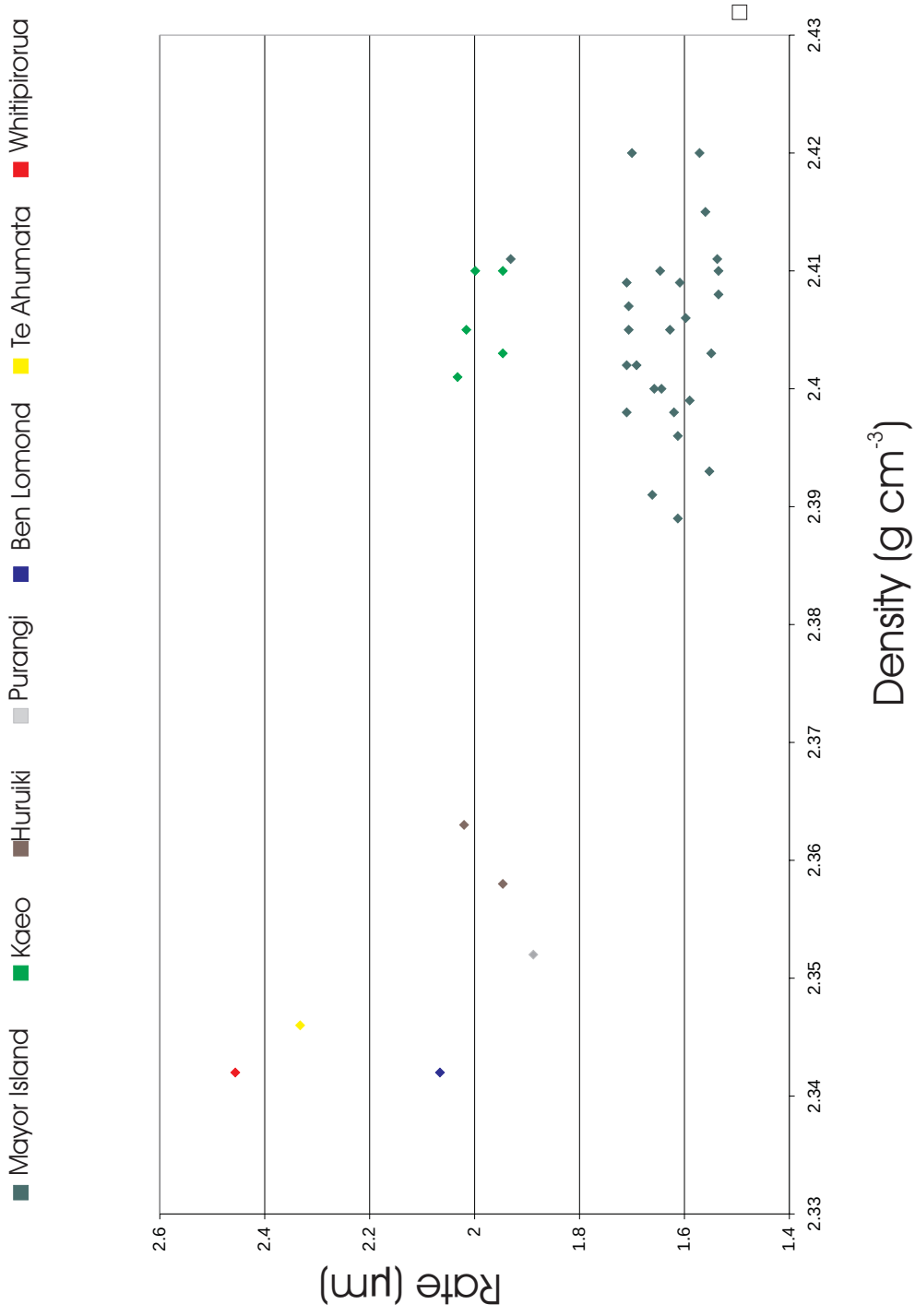

Figure D.1: Density versus hydration rate for reference samples

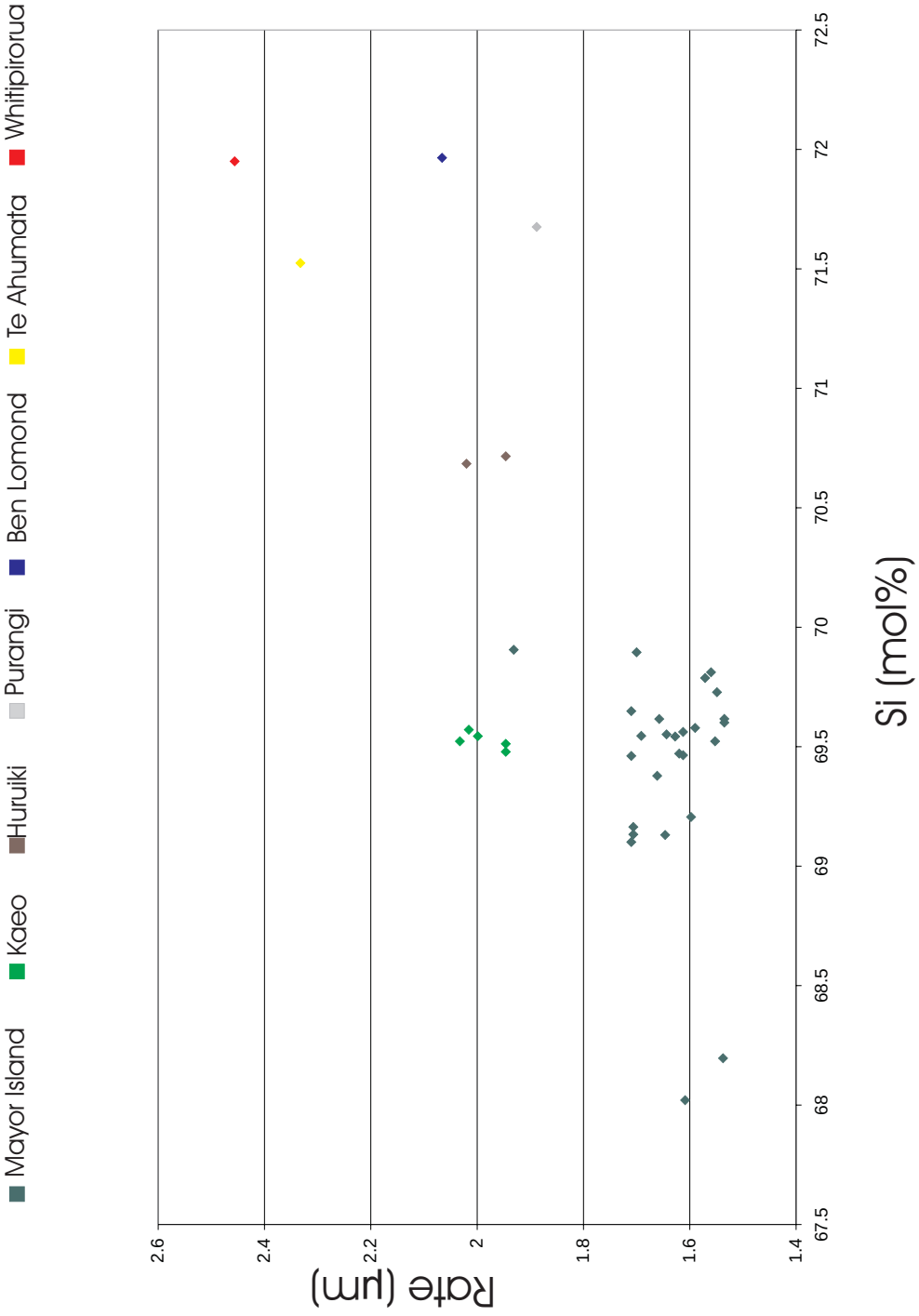

Figure D.2: Si (Molar %) versus hydration rate for reference samples

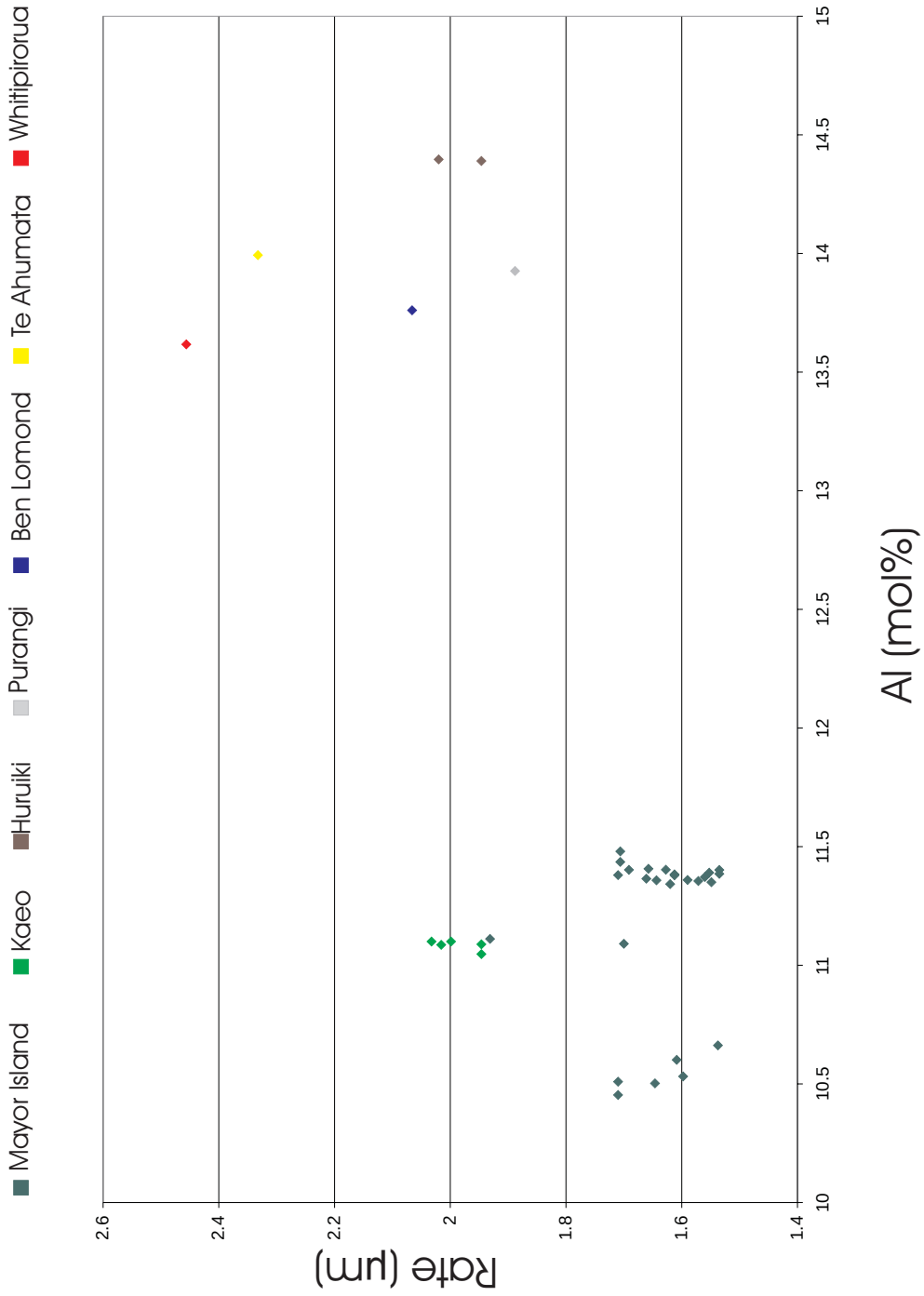

Figure D.3: Al(Molar %) versus hydration rate for reference samples

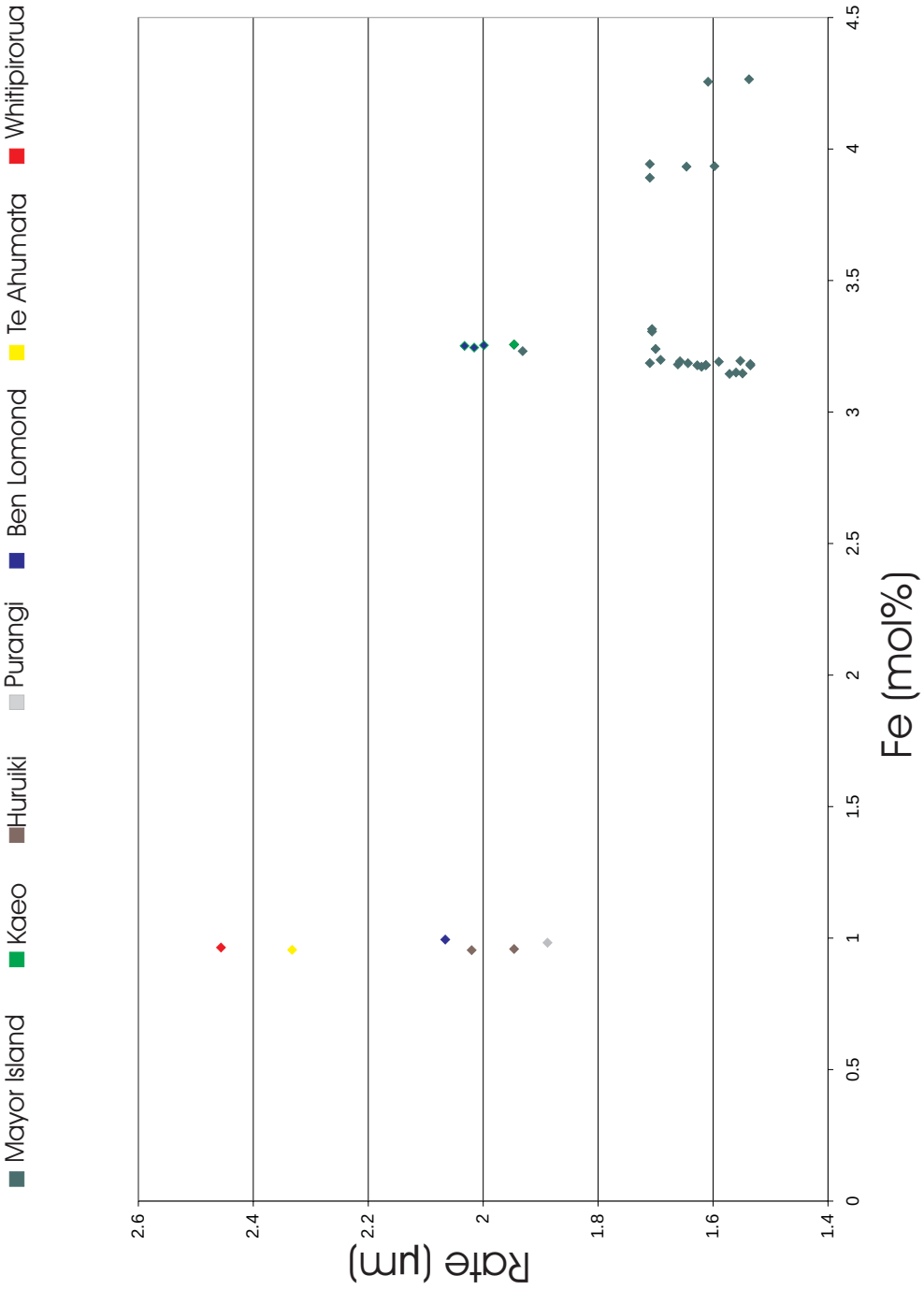

Figure D.4: Fe (Molar%) versus hydration rate for reference samples

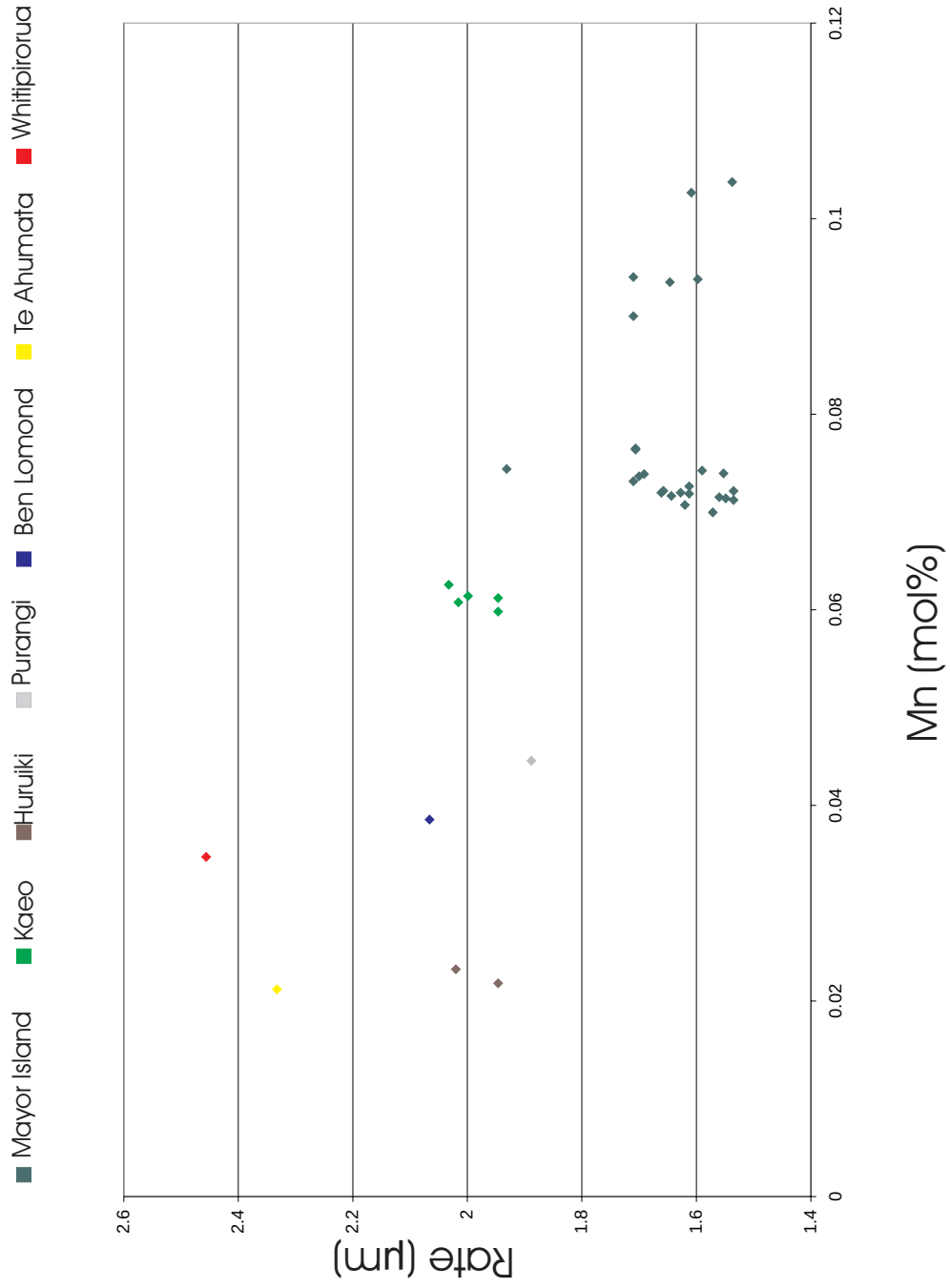

Figure D.5: Mn (Molar %) versus hydration rate for reference samples

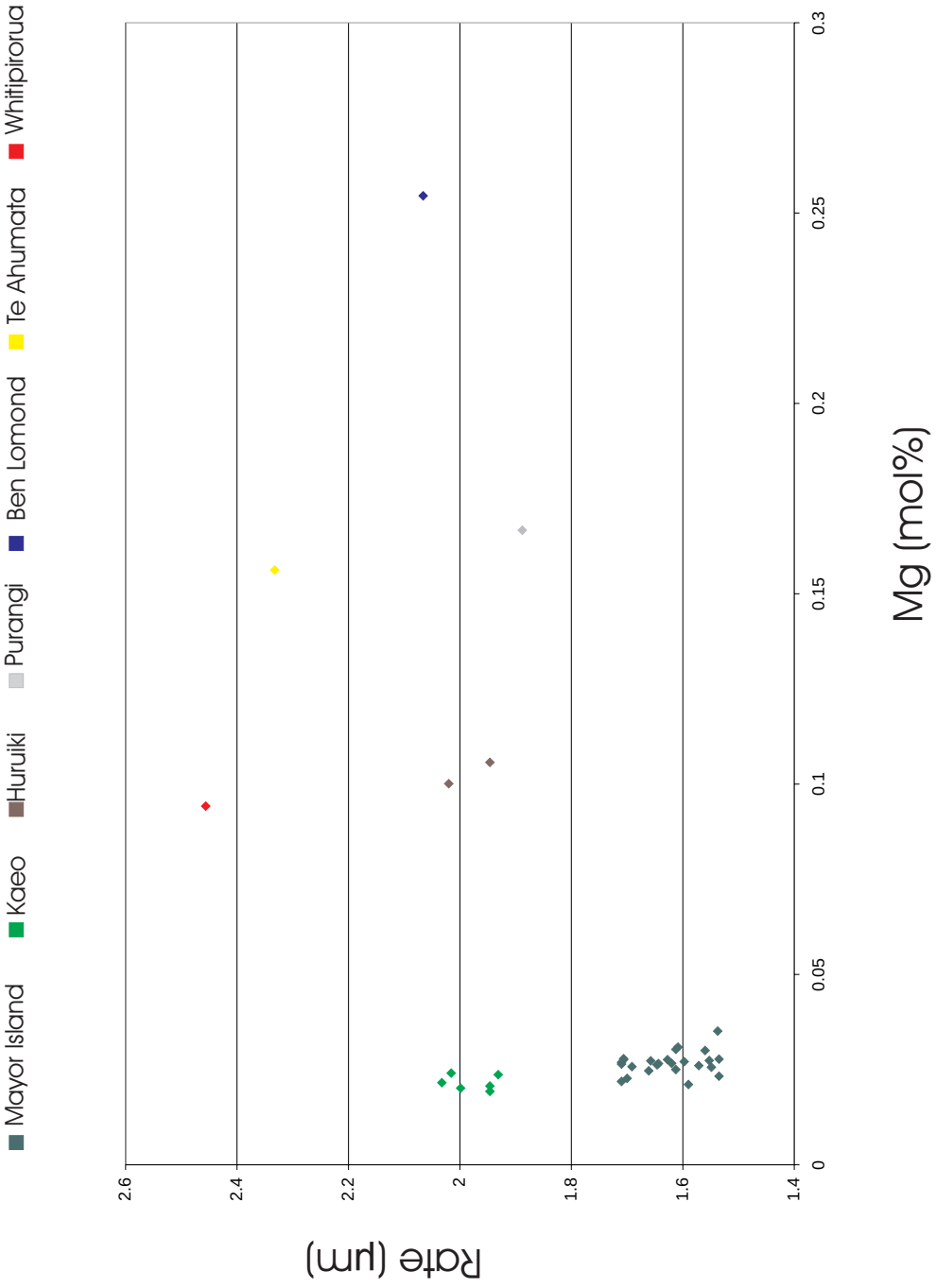

Figure D.6: Mg (Molar%) versus hydration rate for reference samples

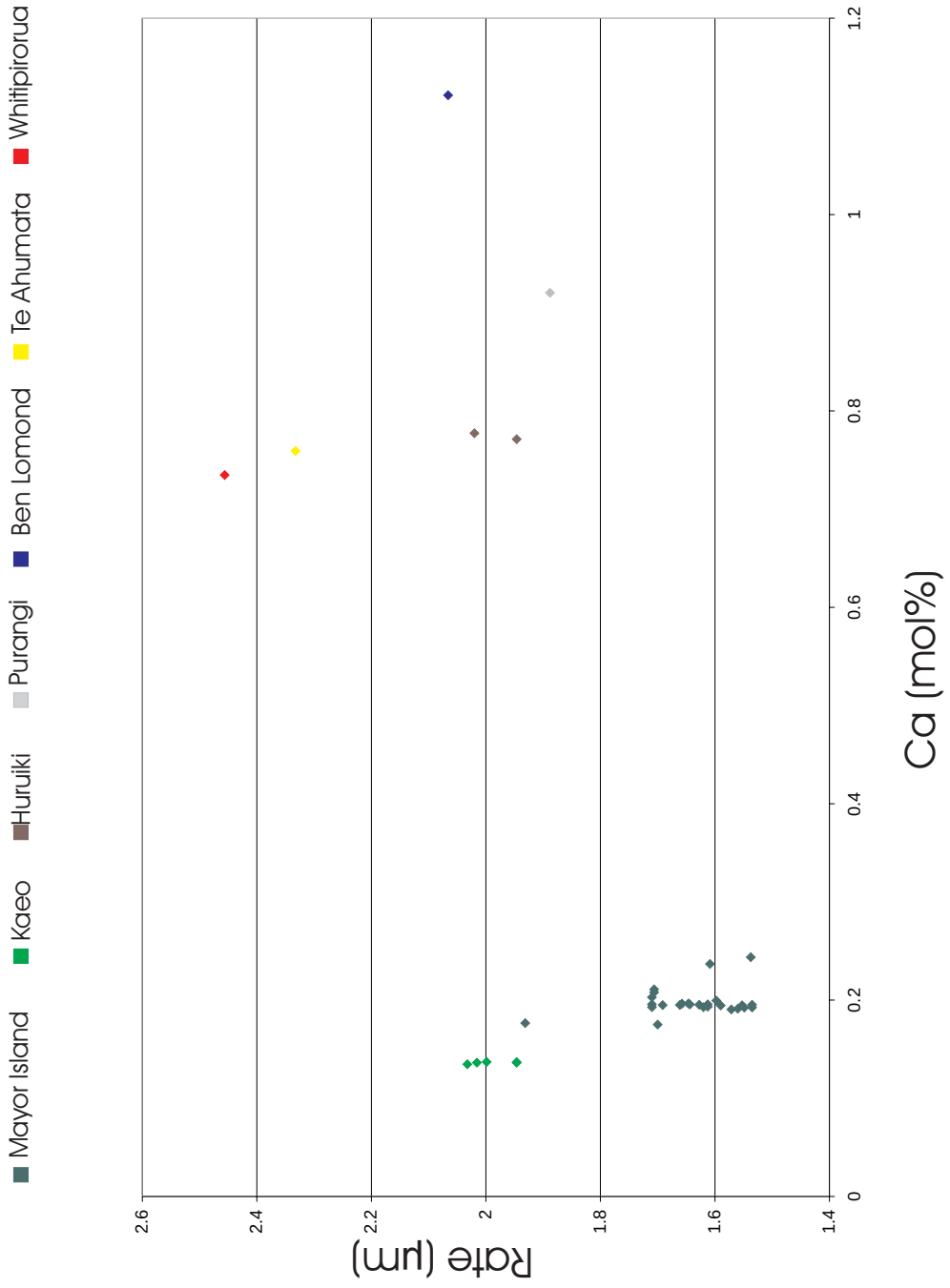

Figure D.7: Ca (Molar%) versus hydration rate for reference samples

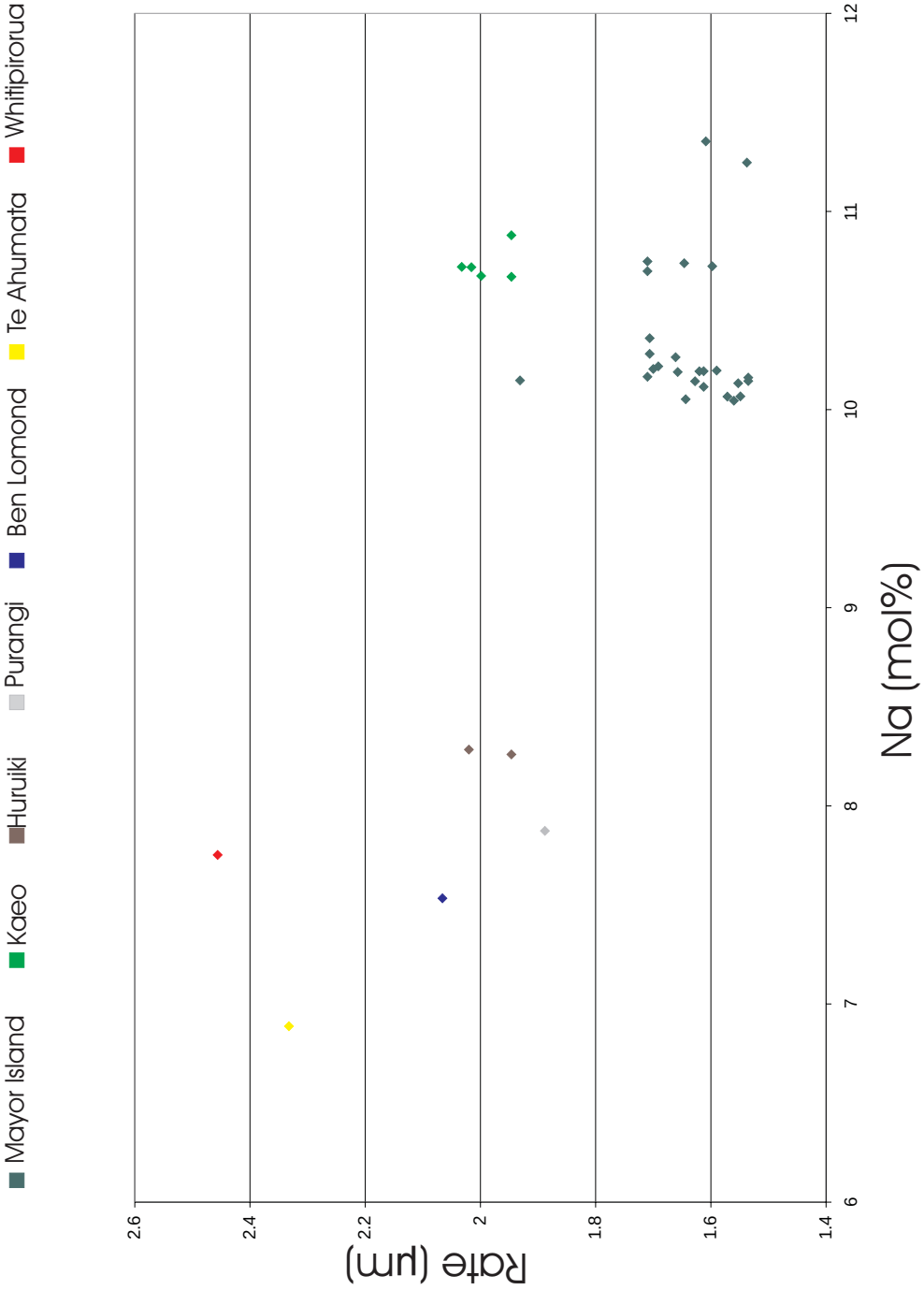

Figure D.8: Na (Molar %) versus hydration rate for reference samples

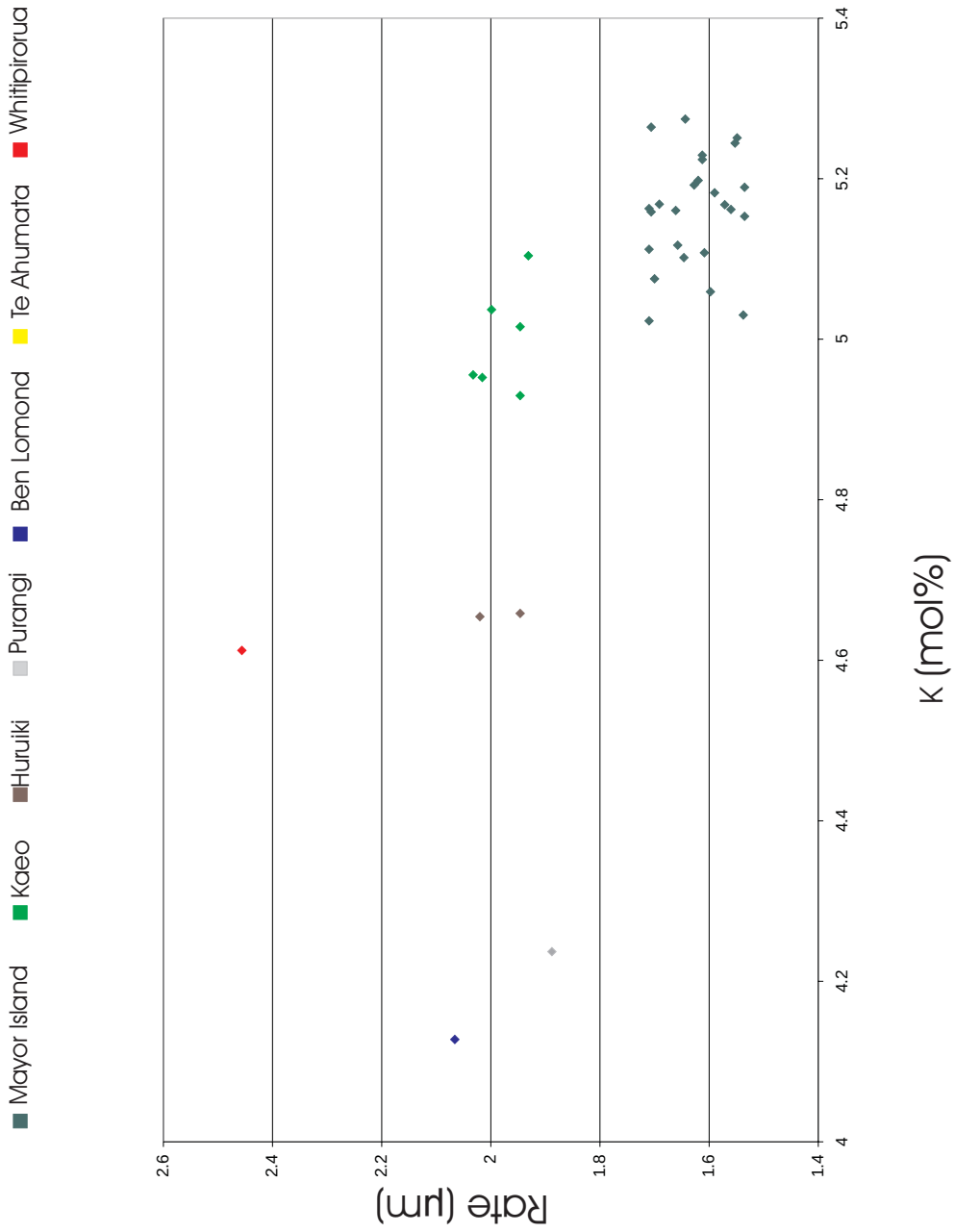

Figure D.9: K (Molar%) versus hydration rate for reference samples

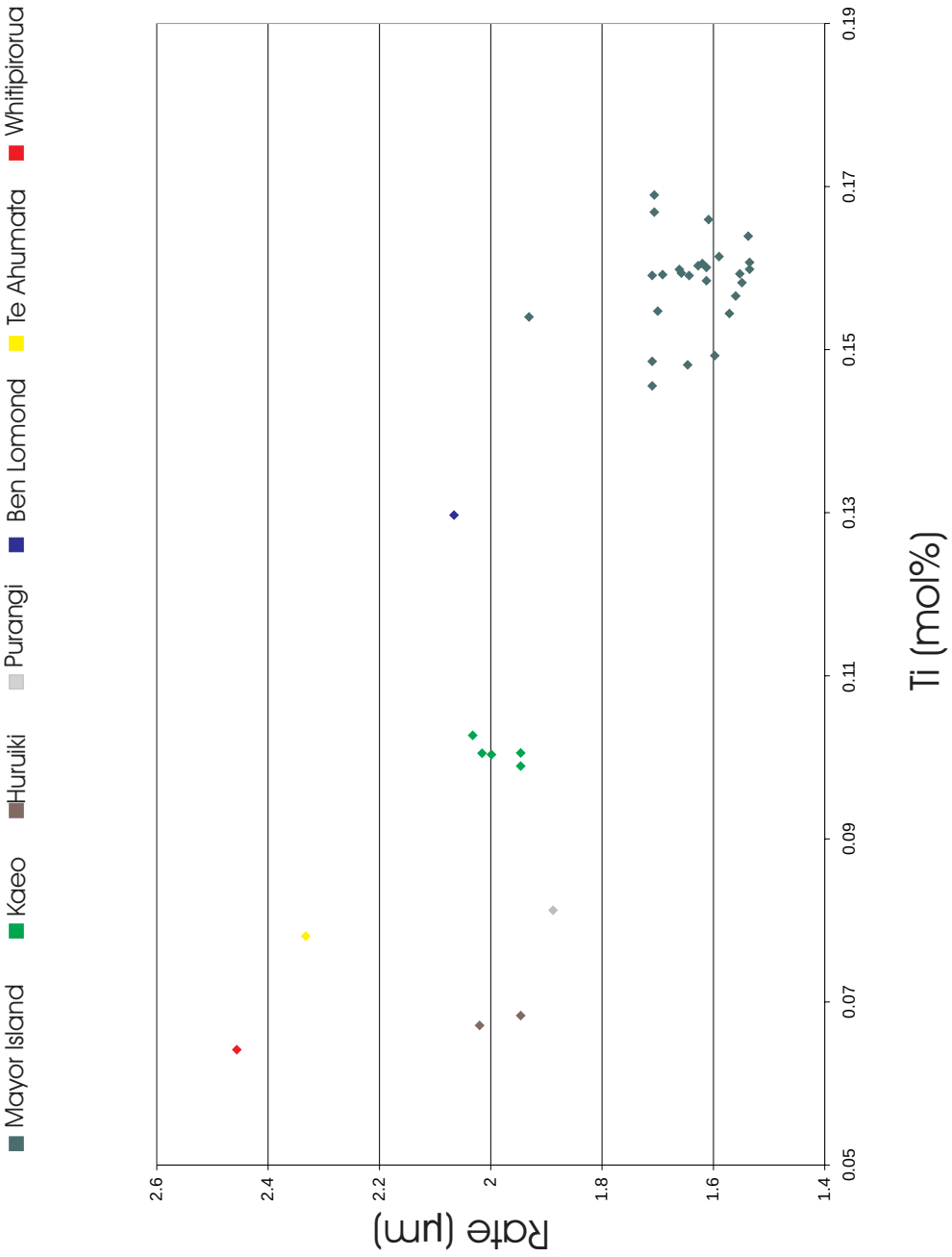

Figure D.10: Ti (Molar %) versus hydration rate for reference samples

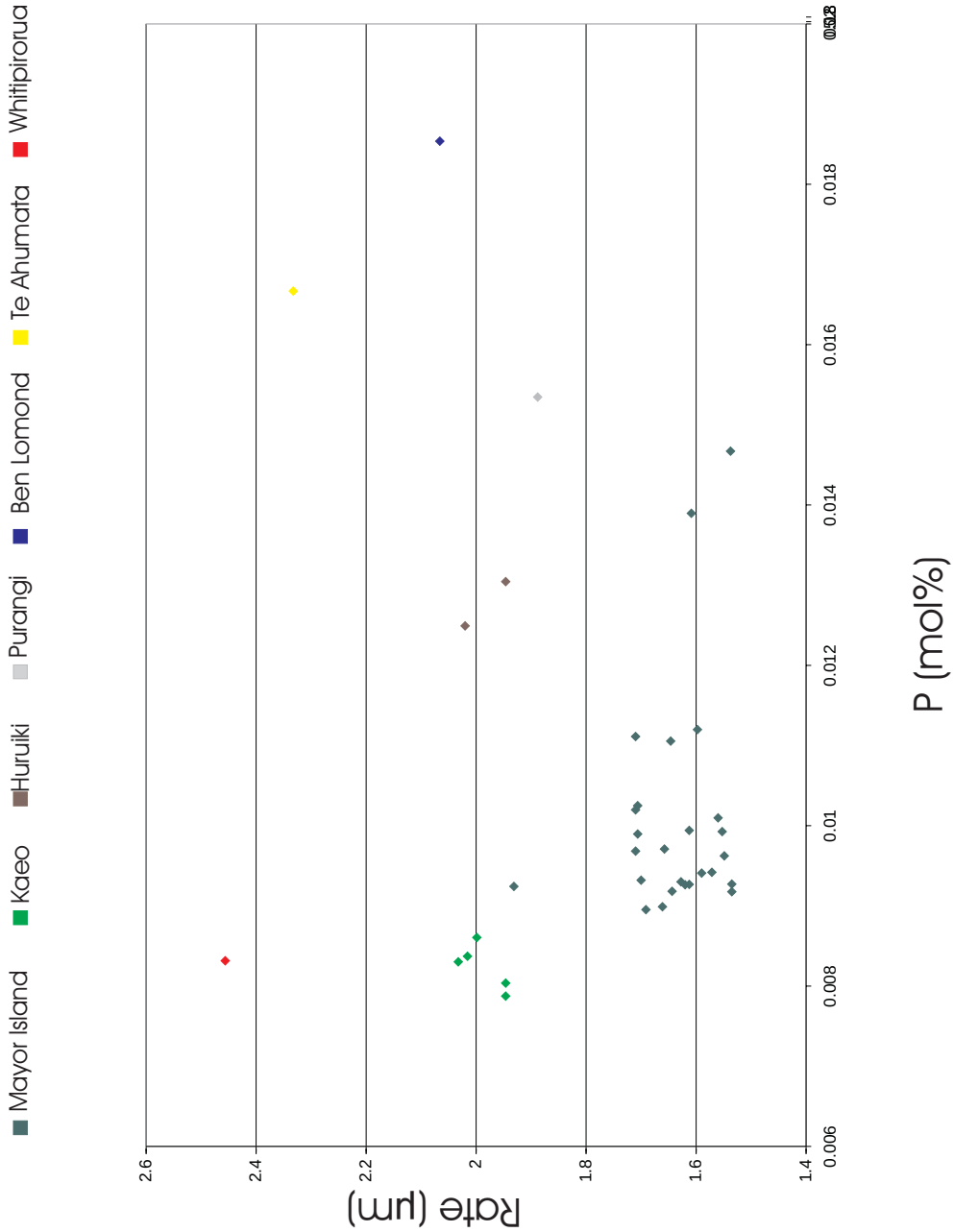

Figure D.11: P (Molar%) versus hydration rate for reference samples

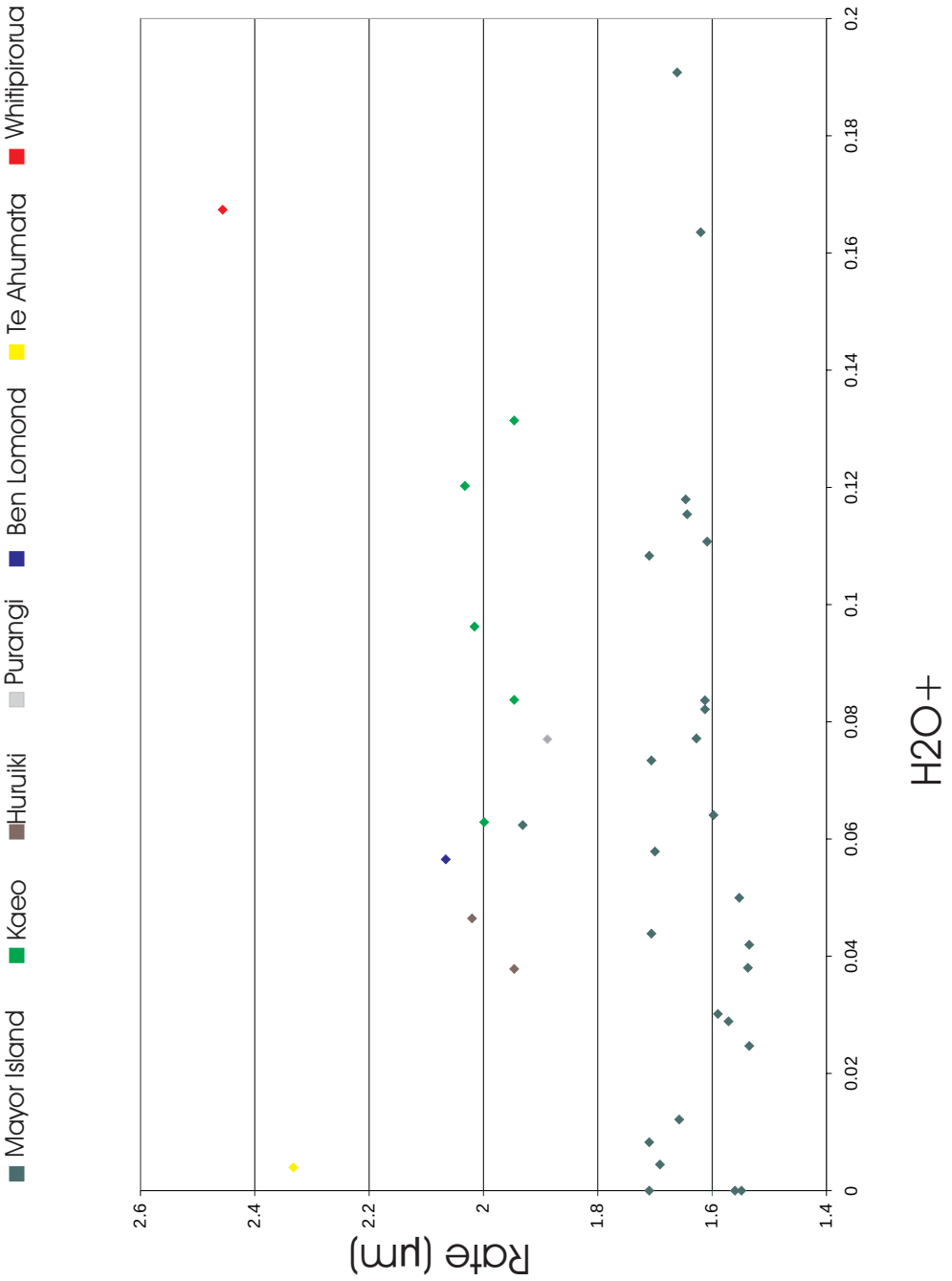

Figure D.12: H_2O+ versus hydration rate for reference samples

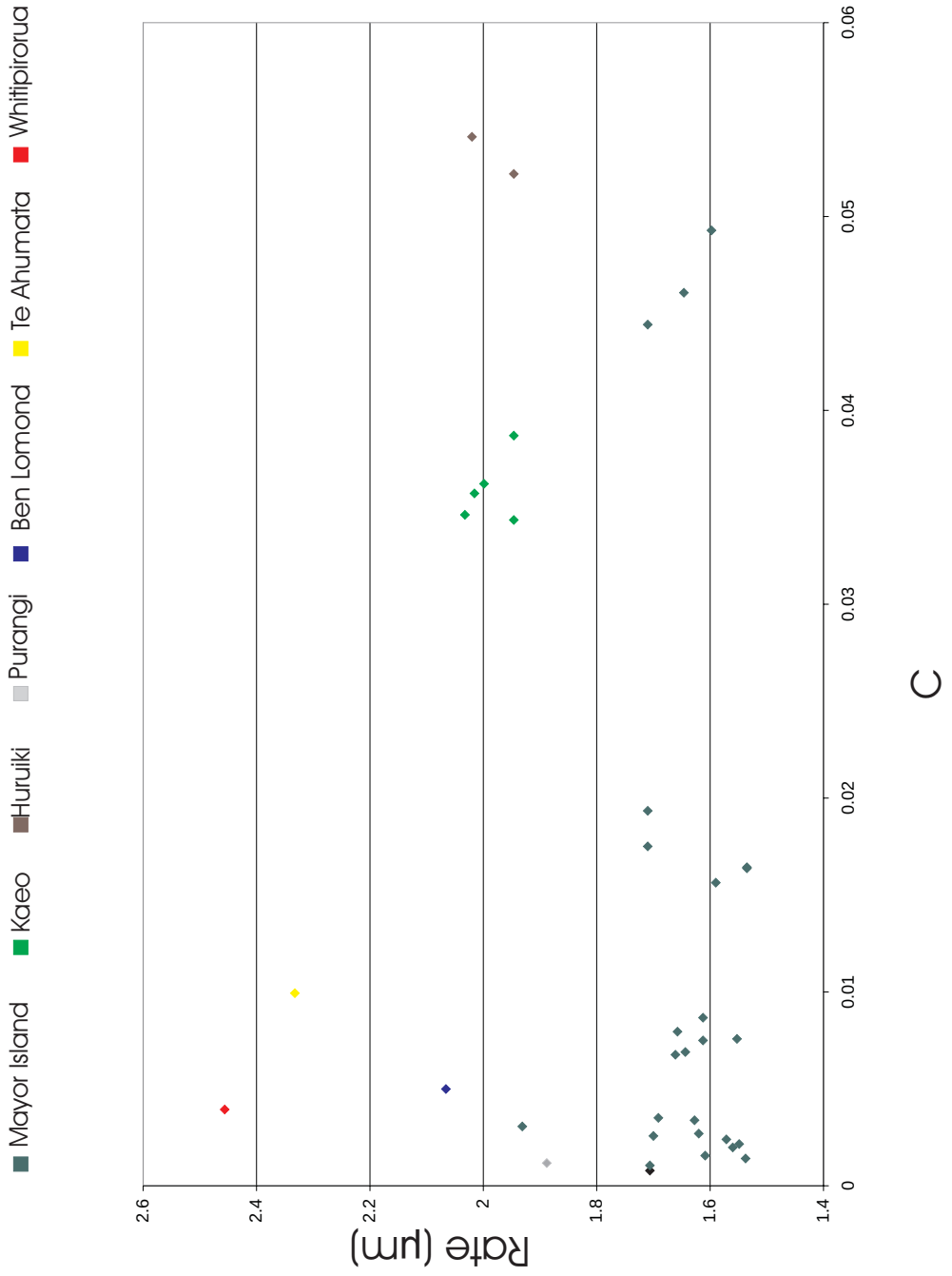

Figure D.13: C versus hydration rate for reference samples

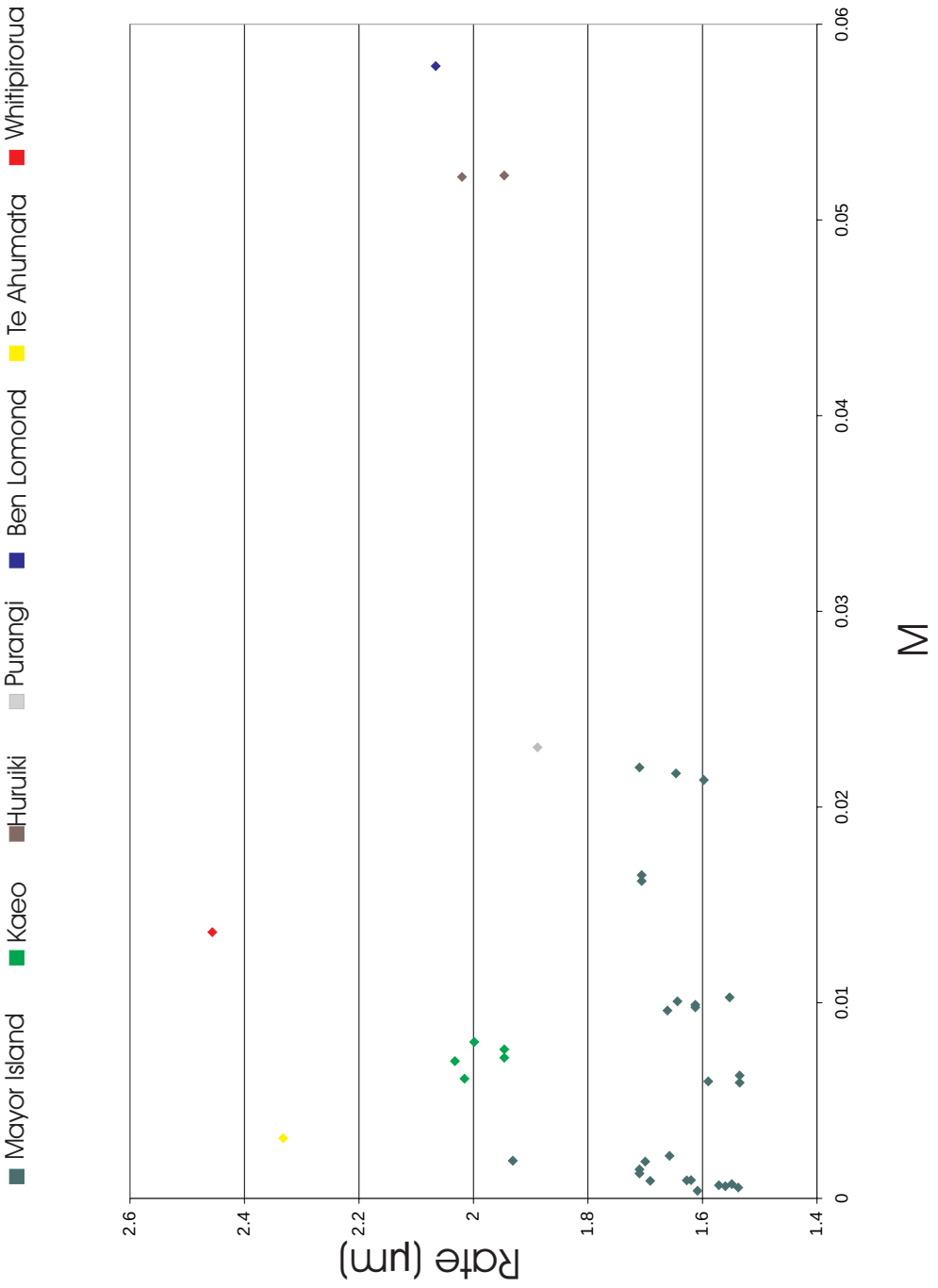

Figure D.14: M versus hydration rate for reference samples

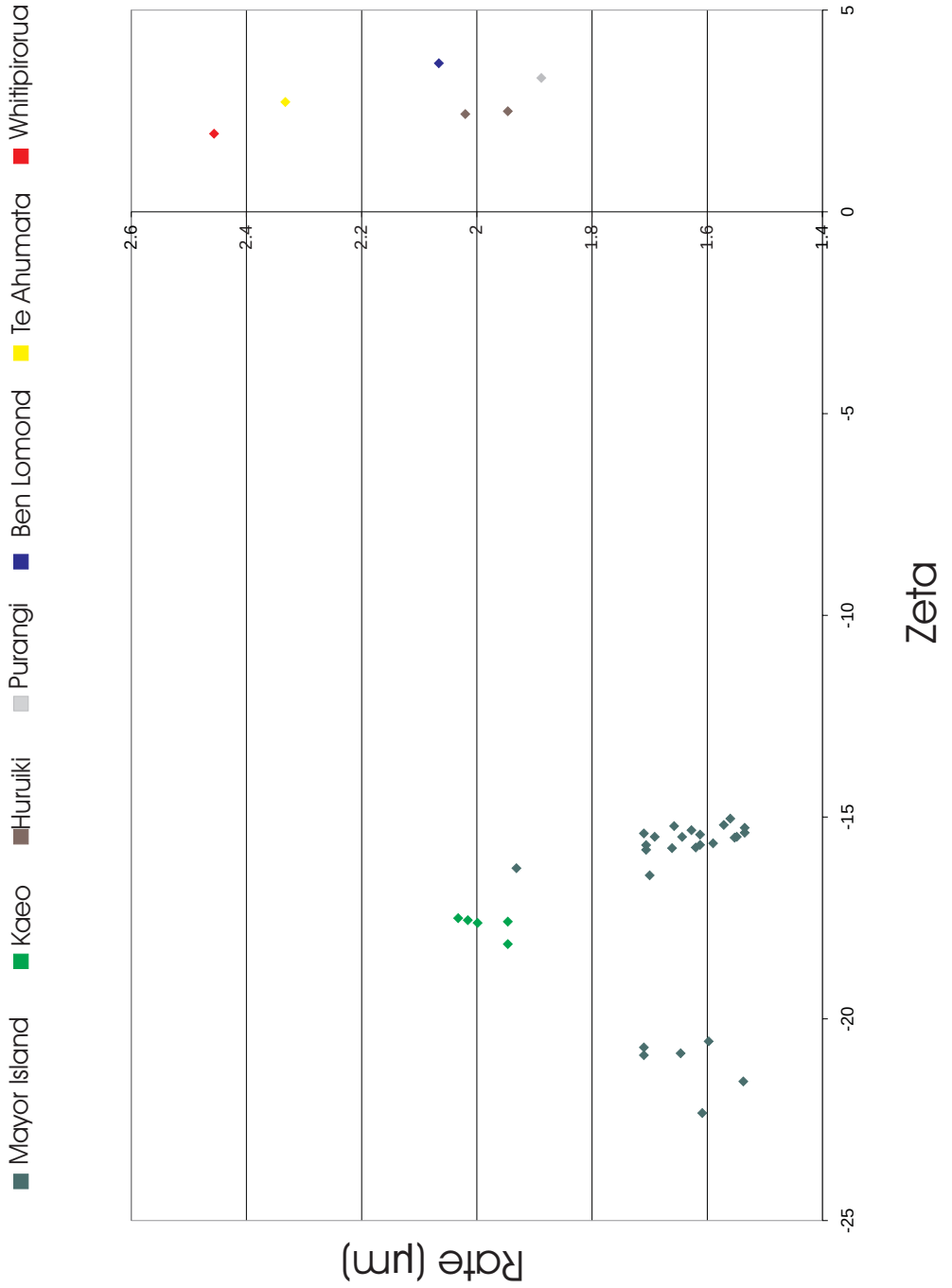

Figure D.15: Zeta versus hydration rate for reference samples

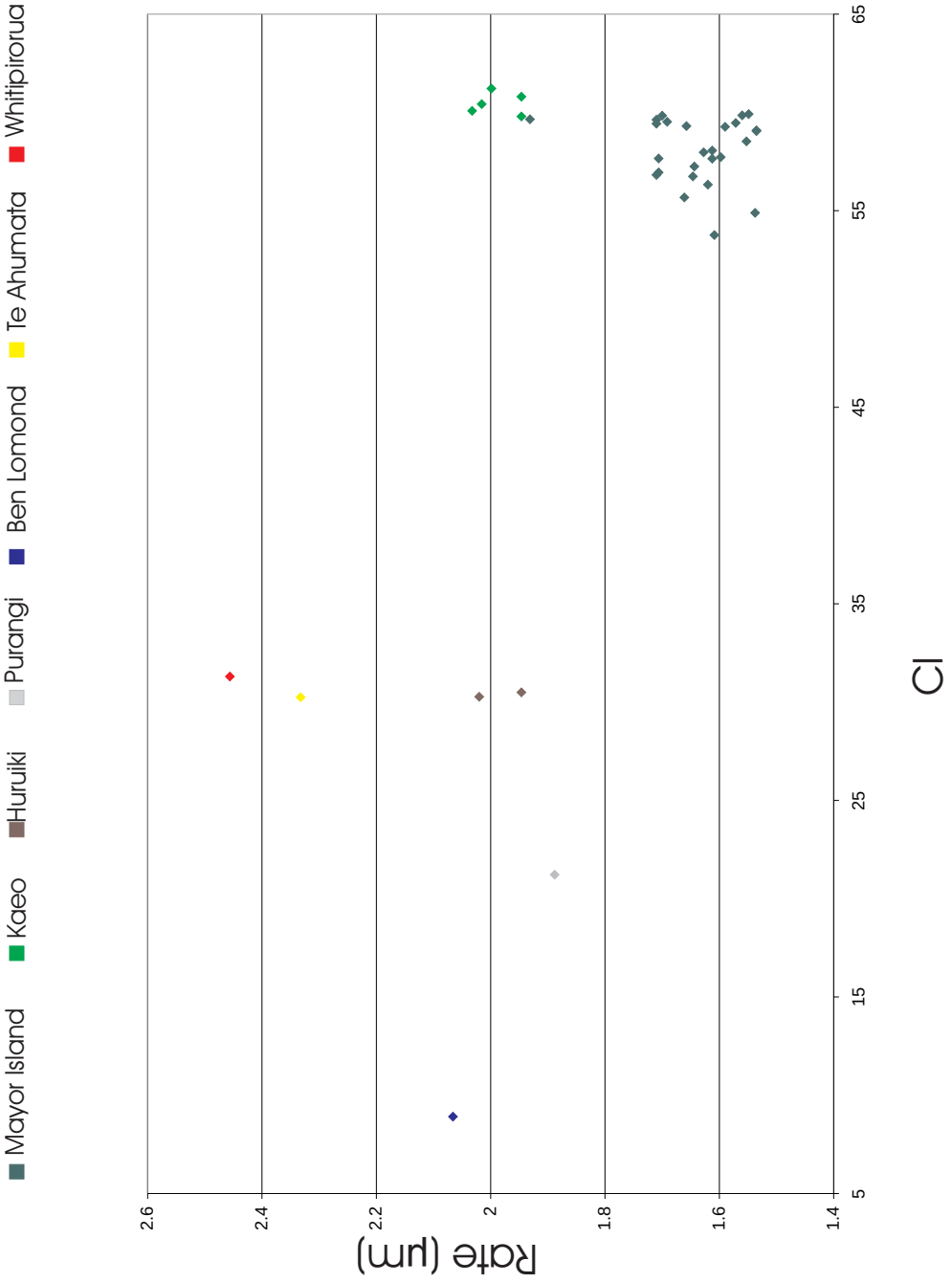

Figure D.16: CI versus hydration rate for reference samples

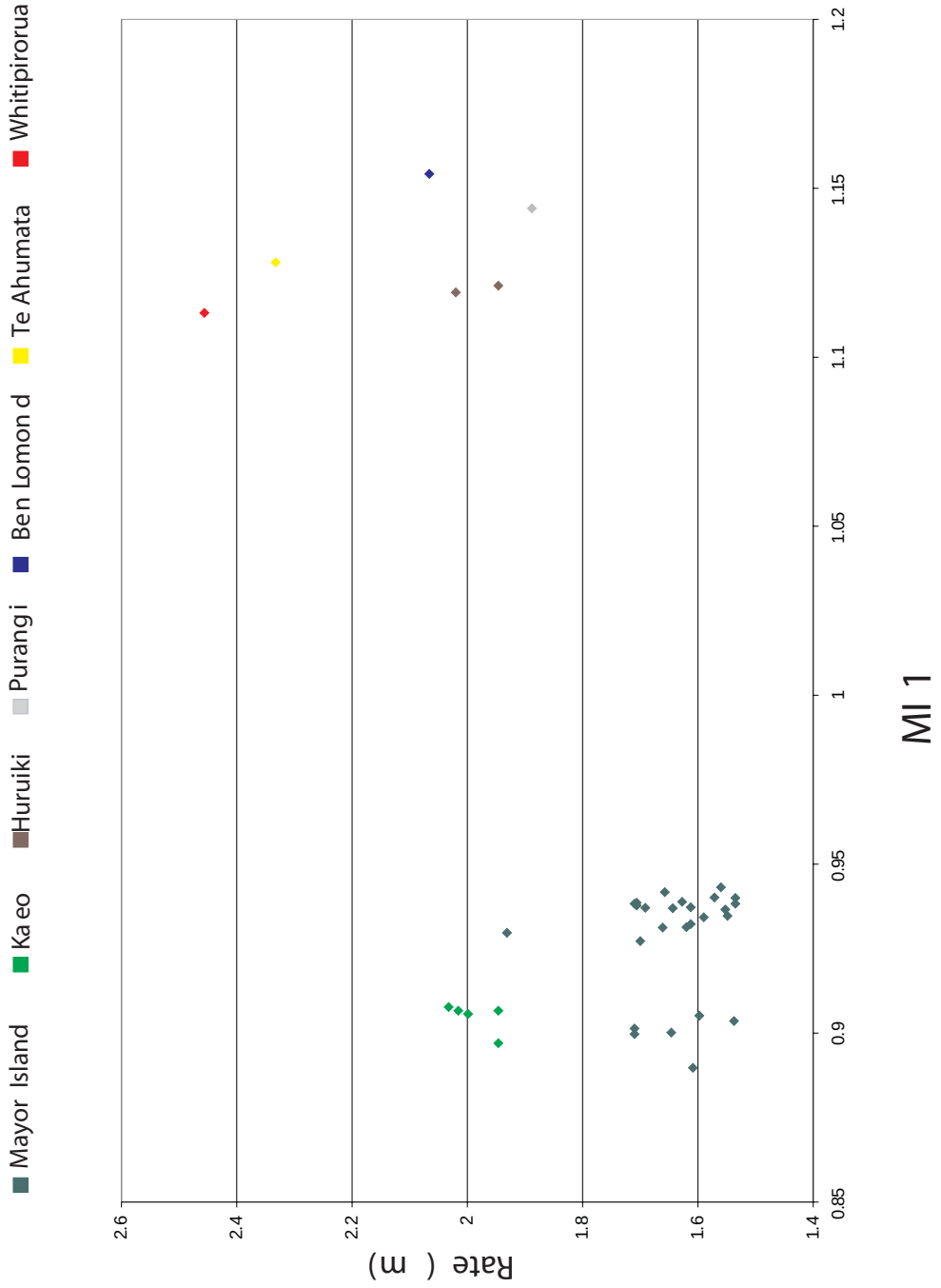

Figure D.17: M1 versus hydration rate for reference samples

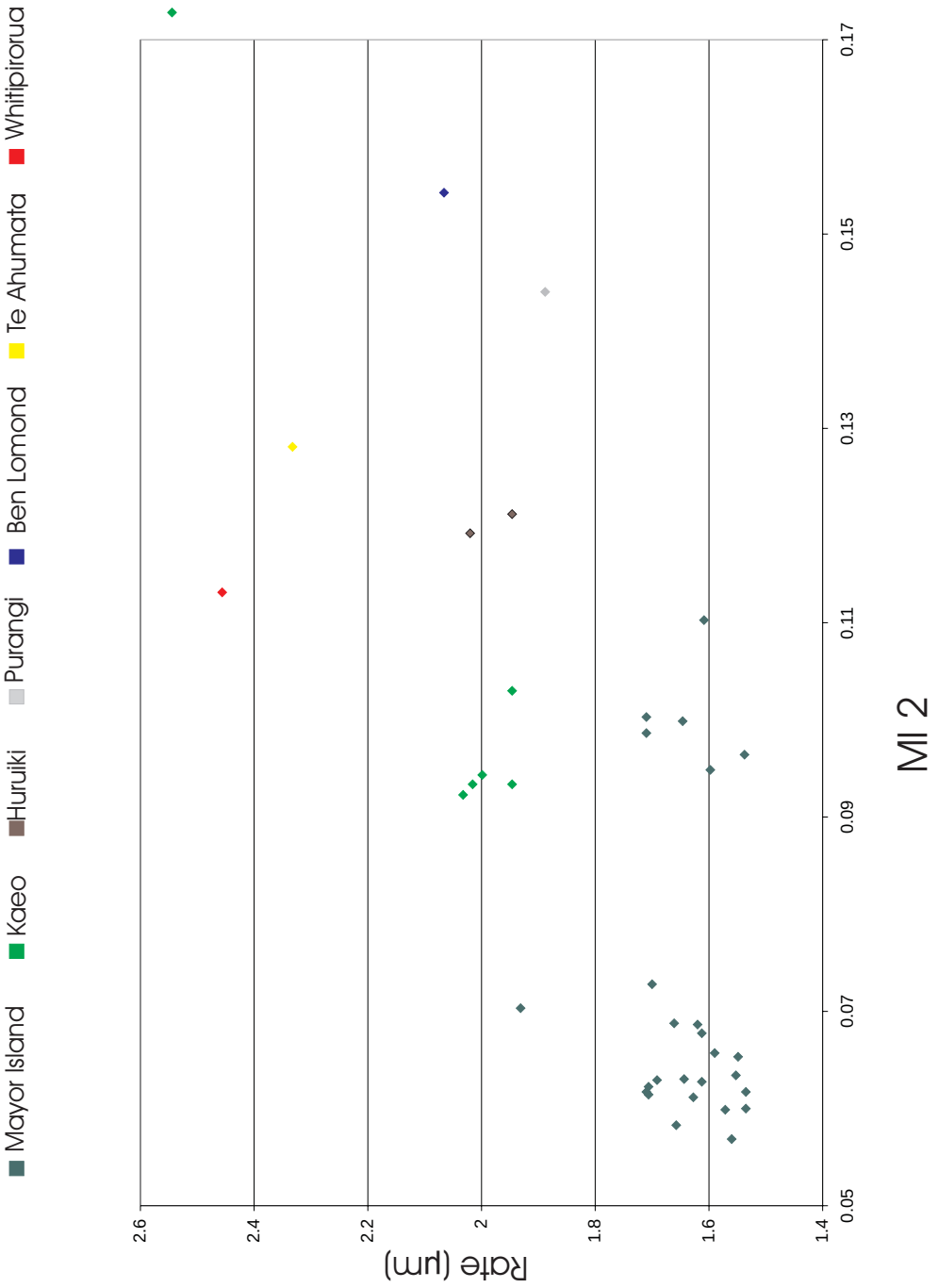

Figure D.18: M2 versus hydration rate for reference samples

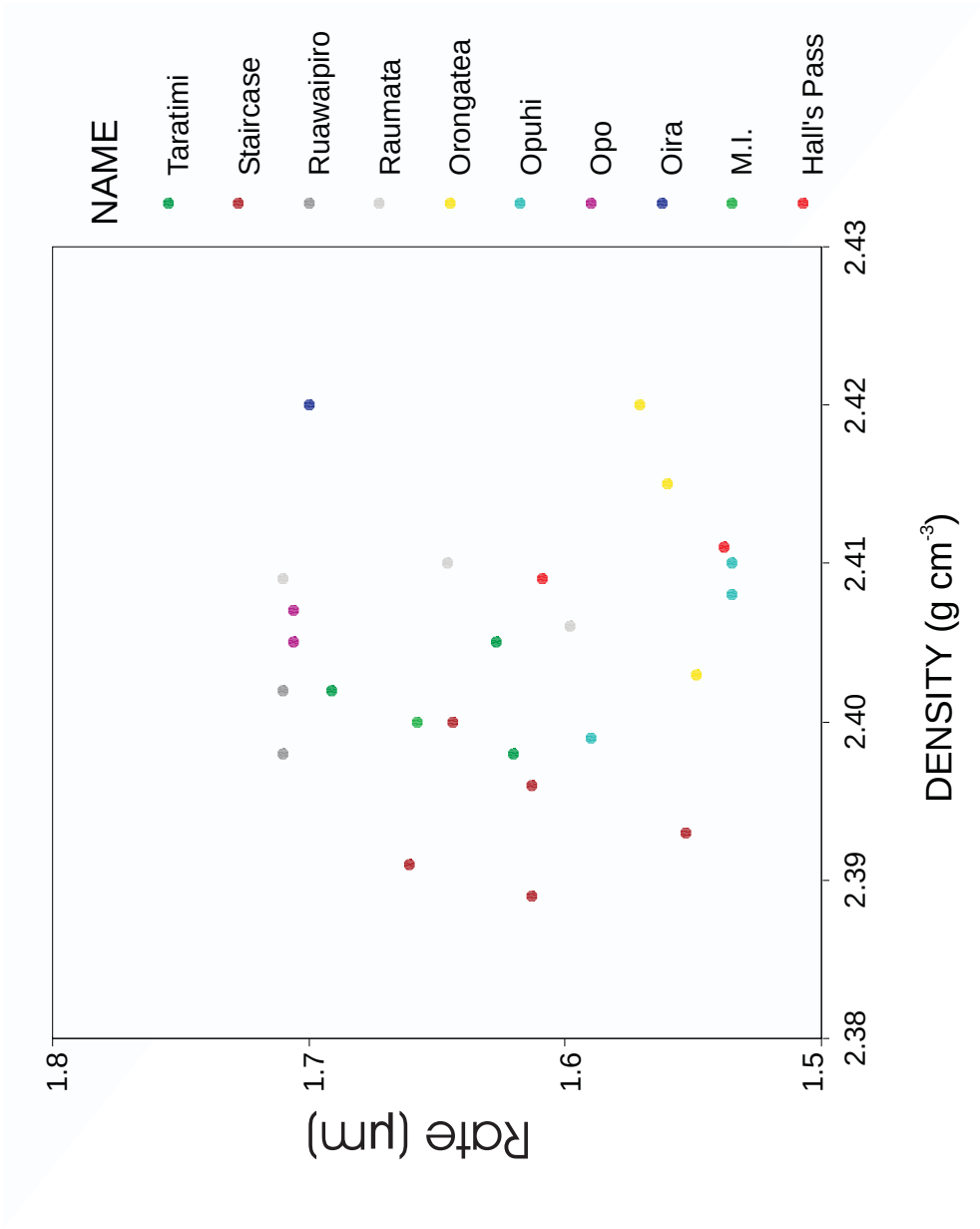

Figure D.19: Density versus hydration rate for Mayor Island reference samples

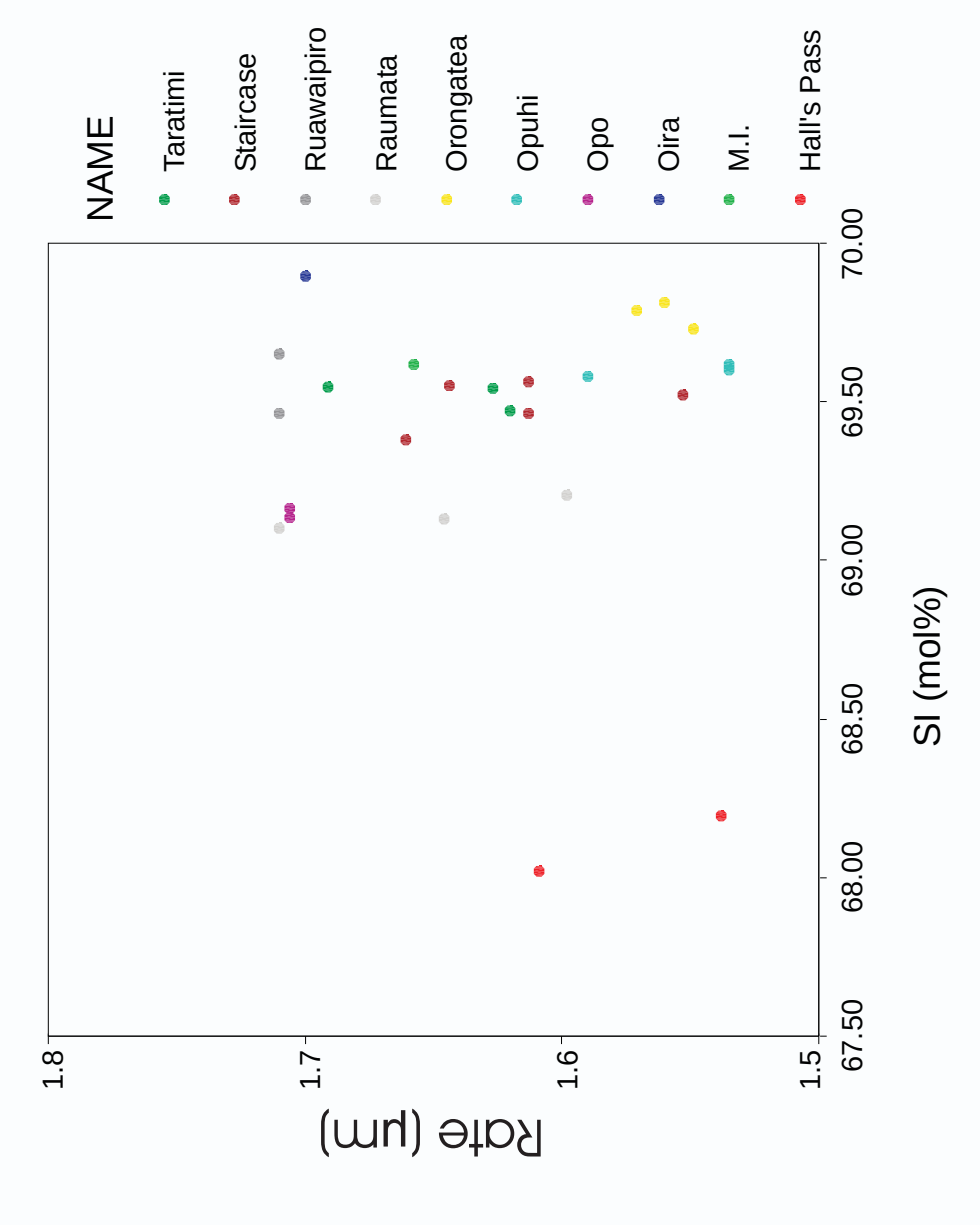

Figure D.20: Si (Molar %) versus hydration rate for Mayor Island reference samples

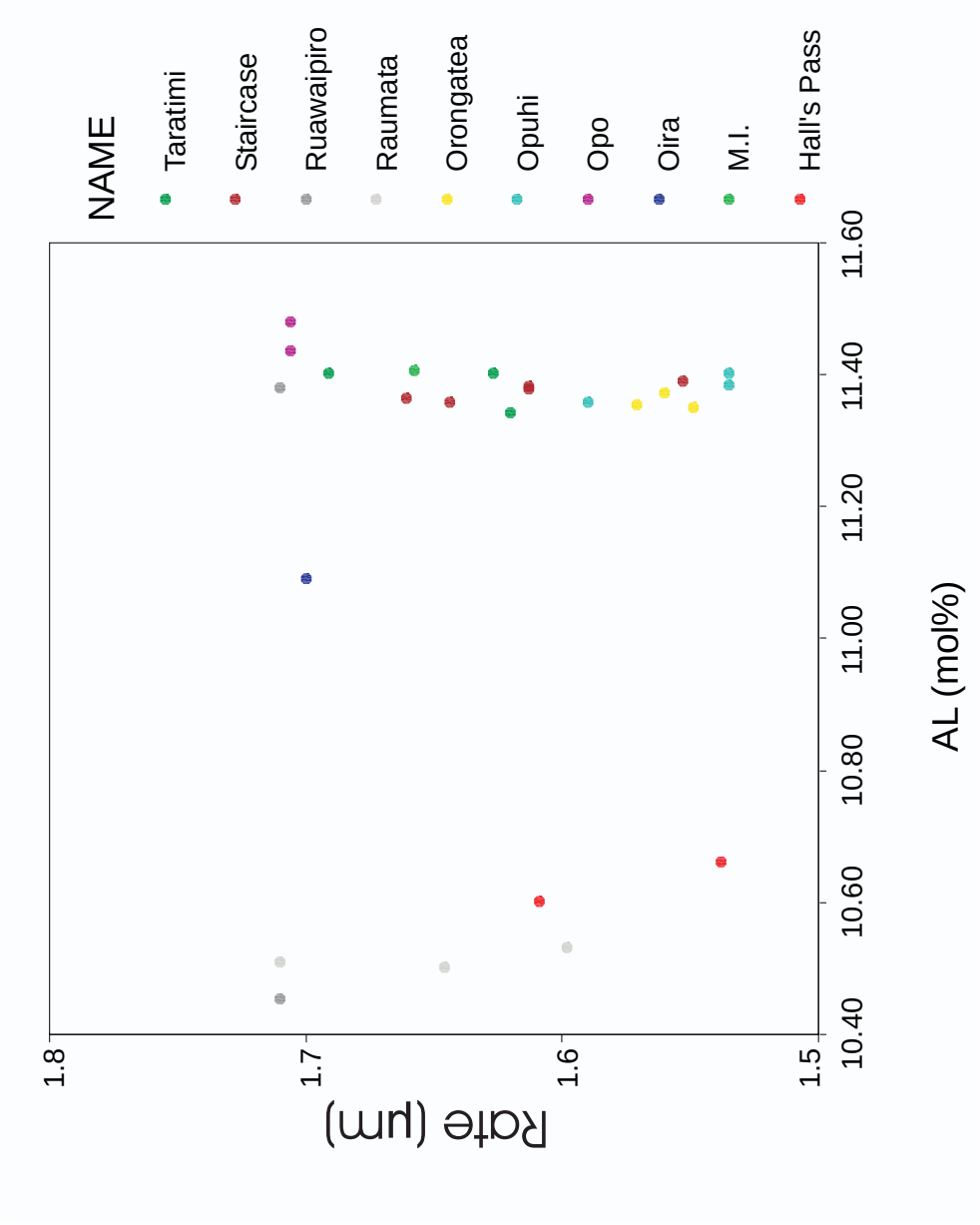

Figure D.21: Al(Molar %) versus hydration rate for Mayor Island reference samples

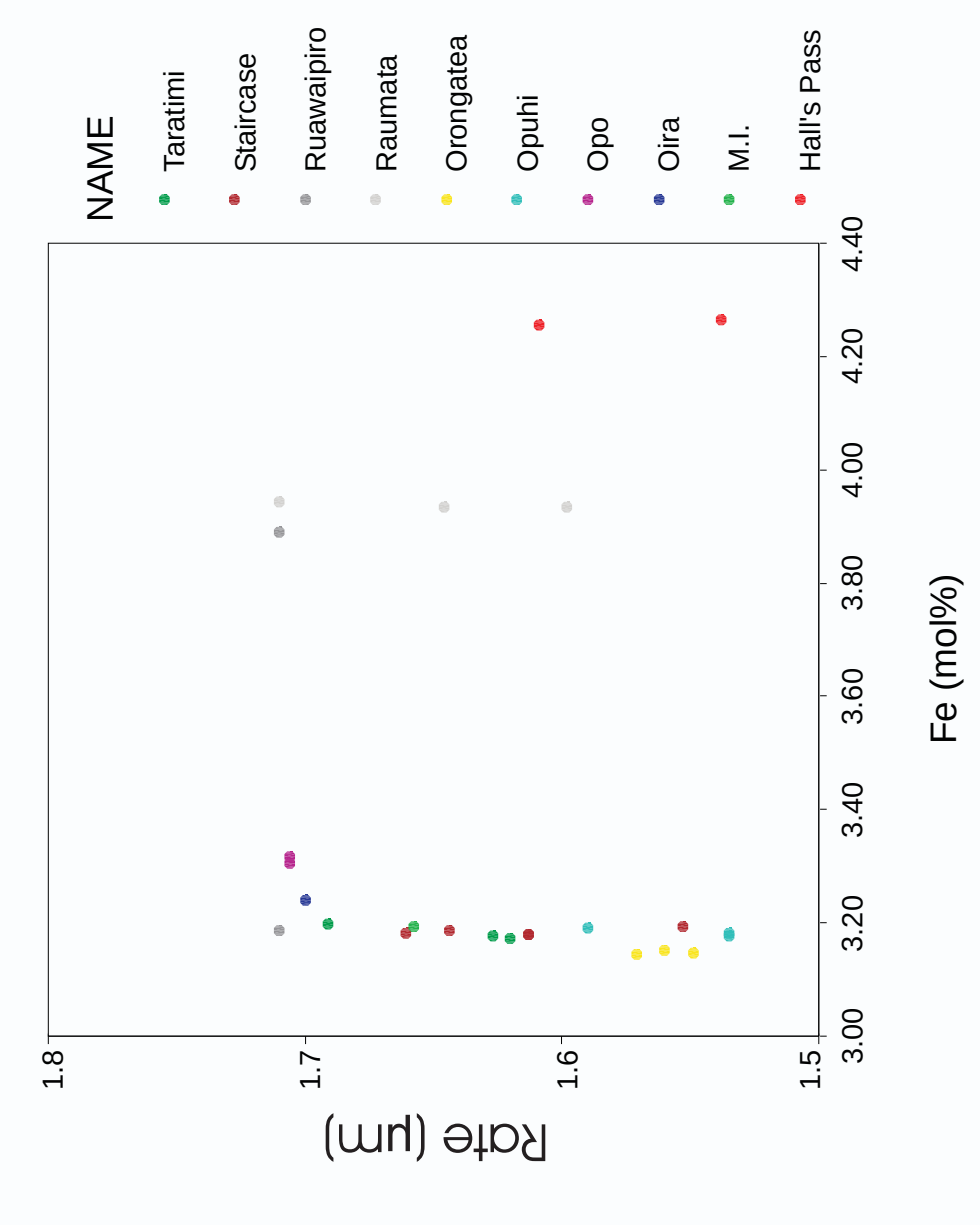

Figure D.22: Fe (Molar%) versus hydration rate for Mayor Island reference samples

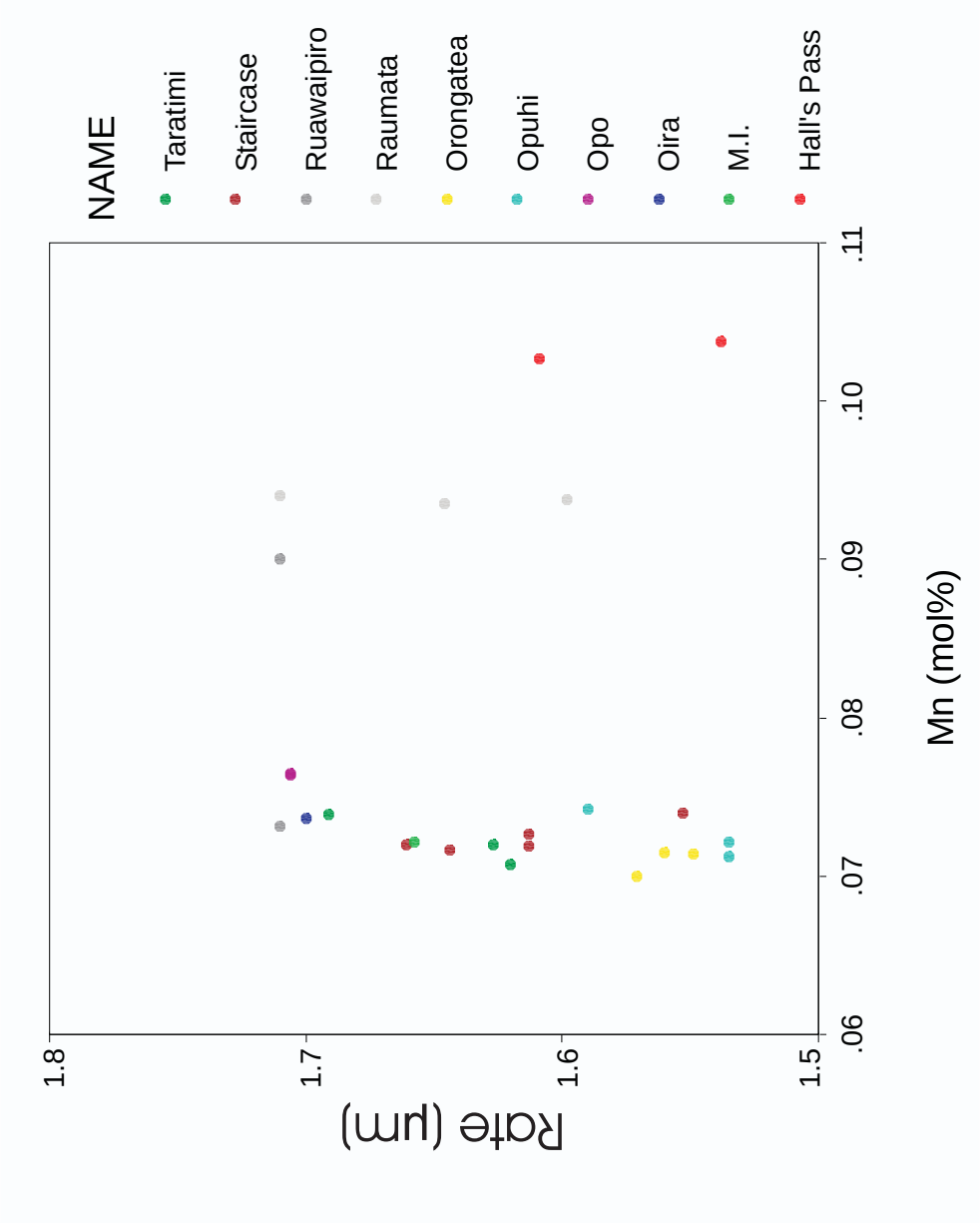

Figure D.23: Mn (Molar %) versus hydration rate for Mayor Island reference samples

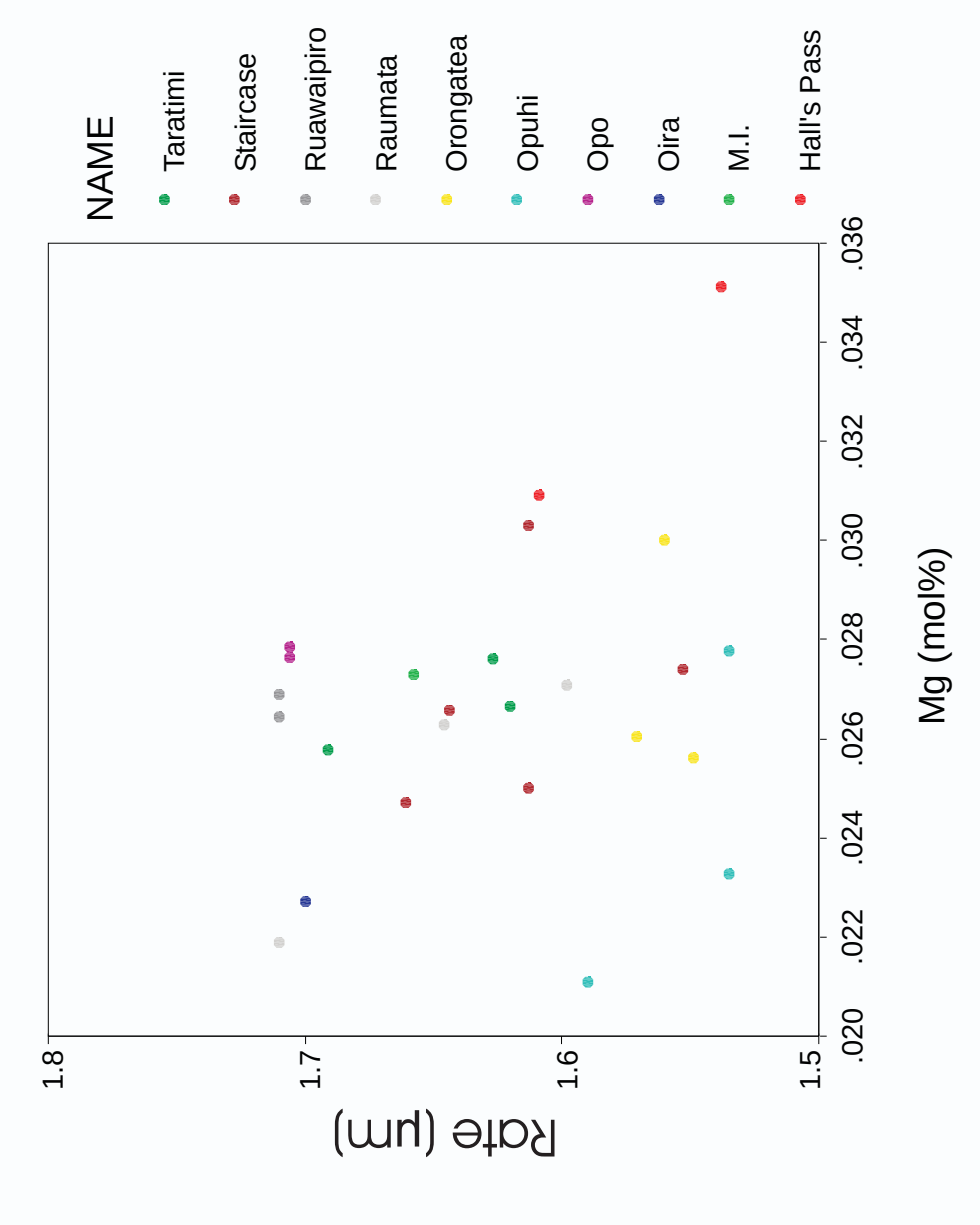

Figure D.24: Mg (Molar%) versus hydration rate for Mayor Island reference samples

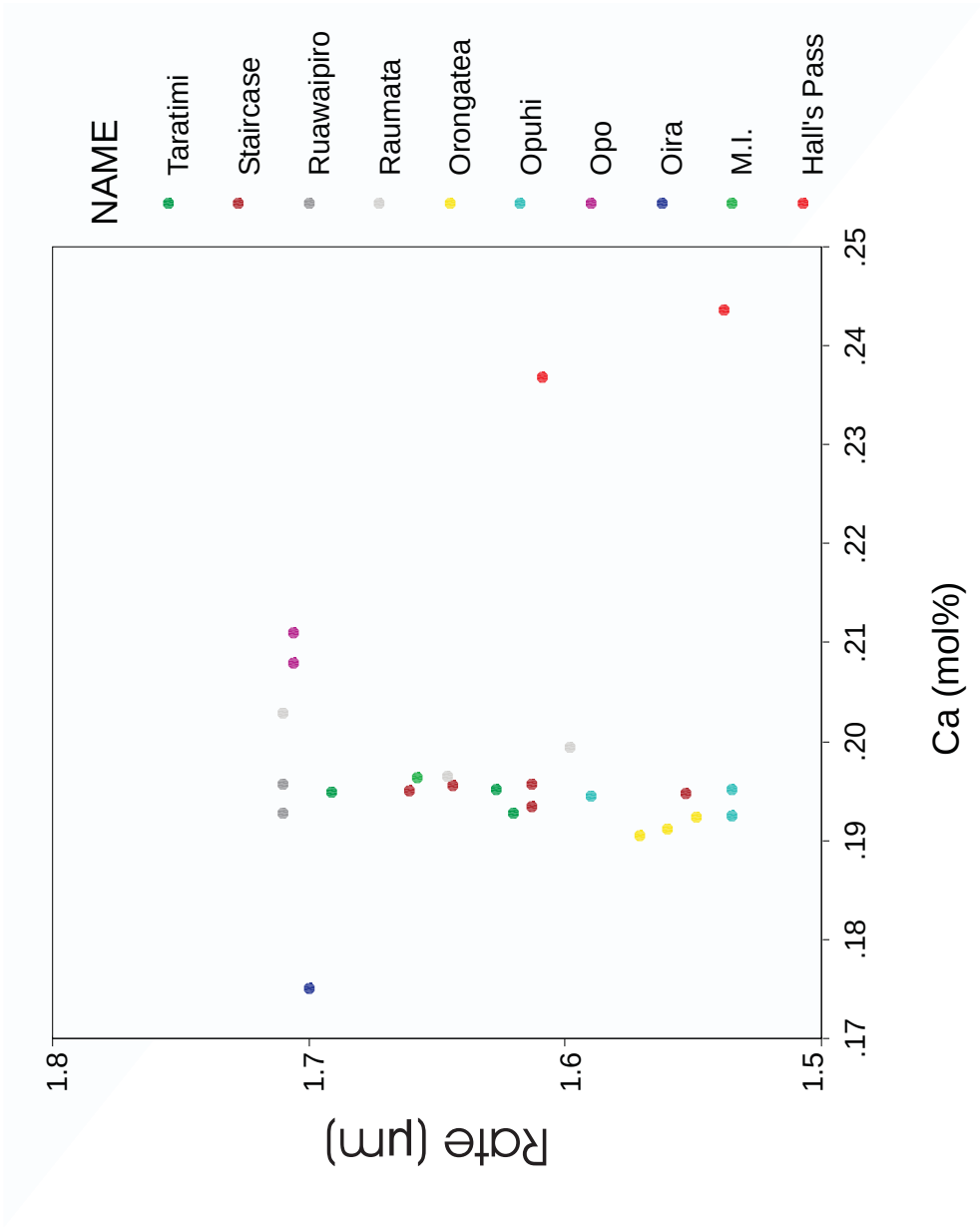

Figure D.25: Ca (Molar%) versus hydration rate for Mayor Island reference samples

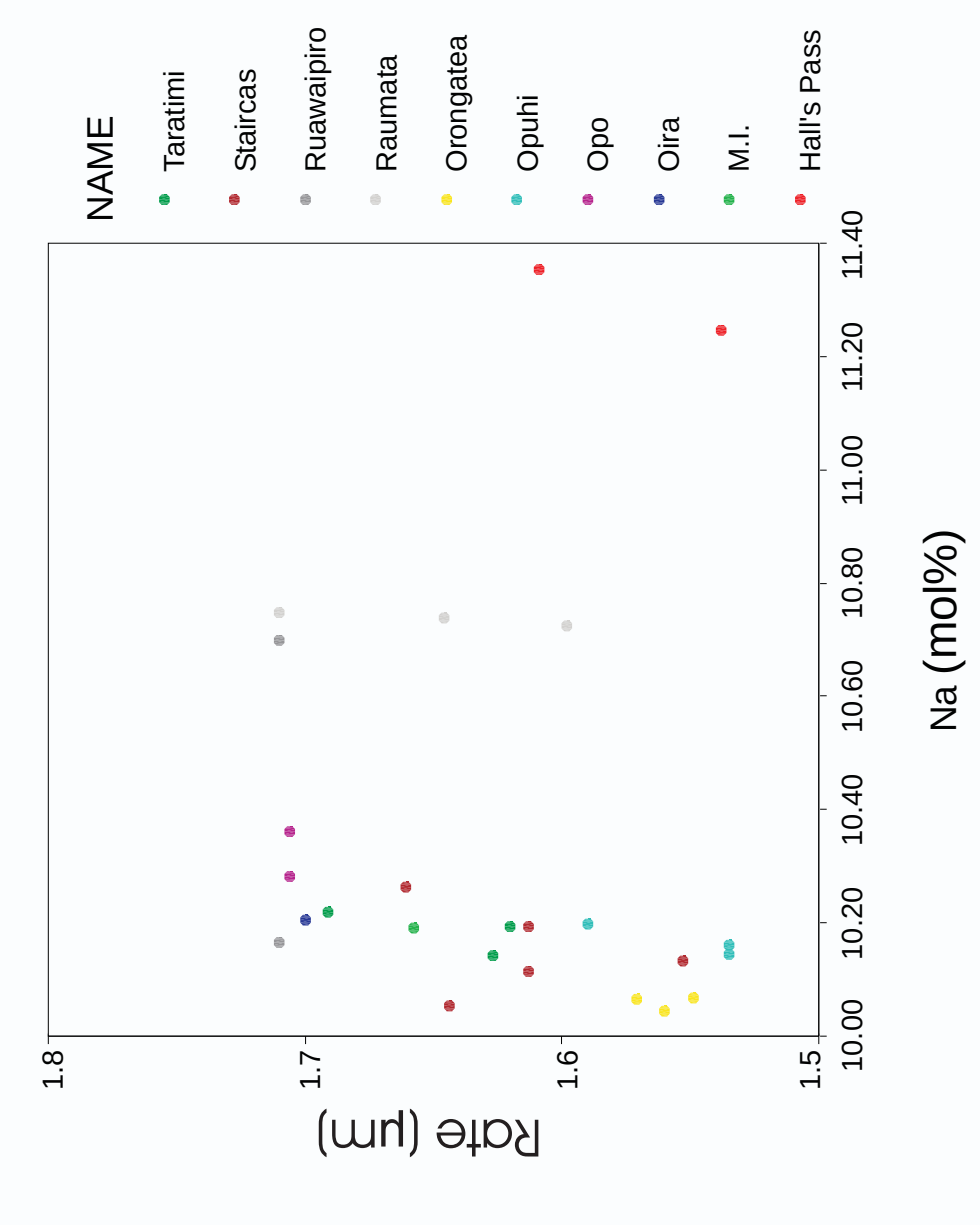

Figure D.26: Na (Molar %) versus hydration rate for Mayor Island reference samples

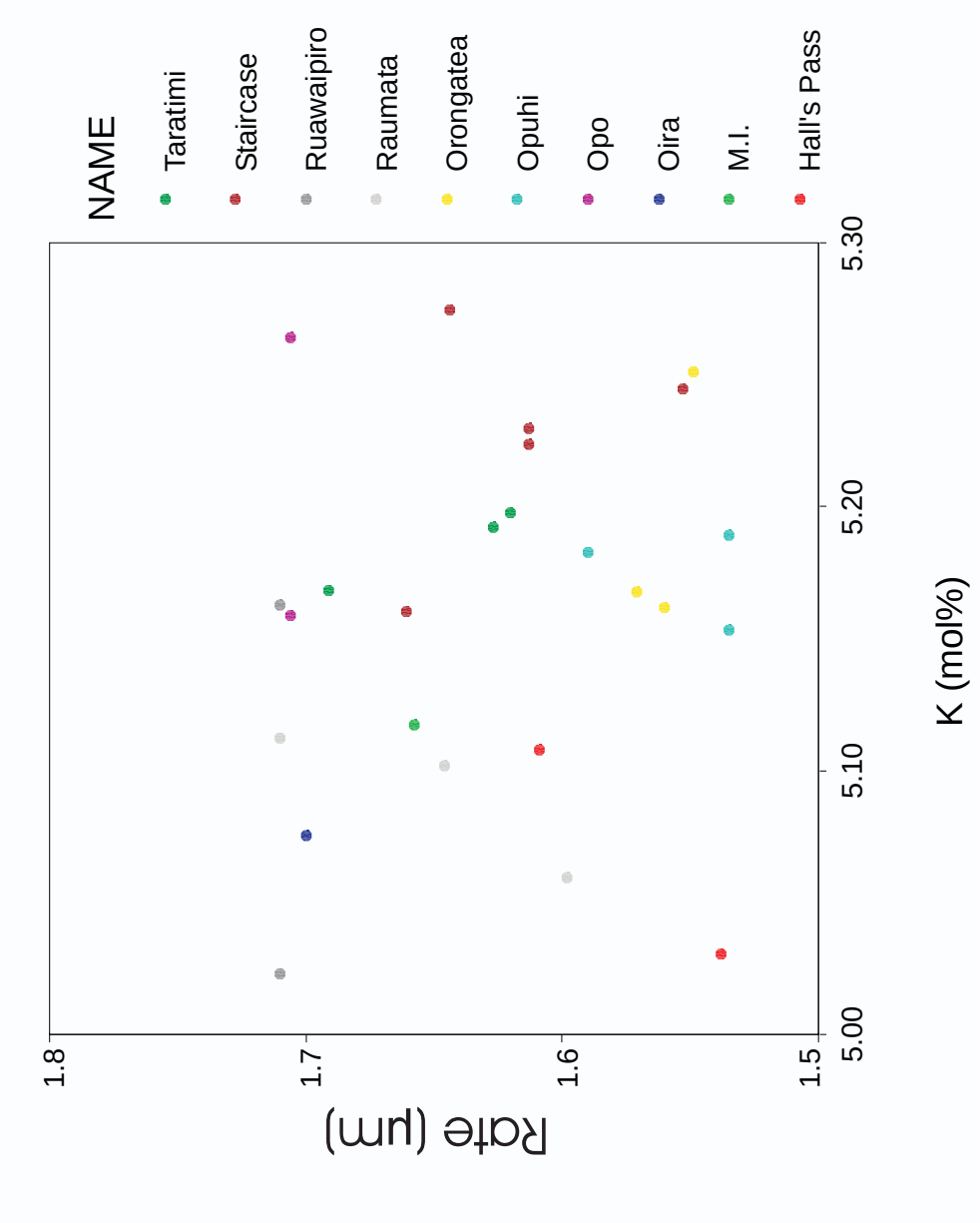

Figure D.27: K (Molar%) versus hydration rate for Mayor Island reference samples

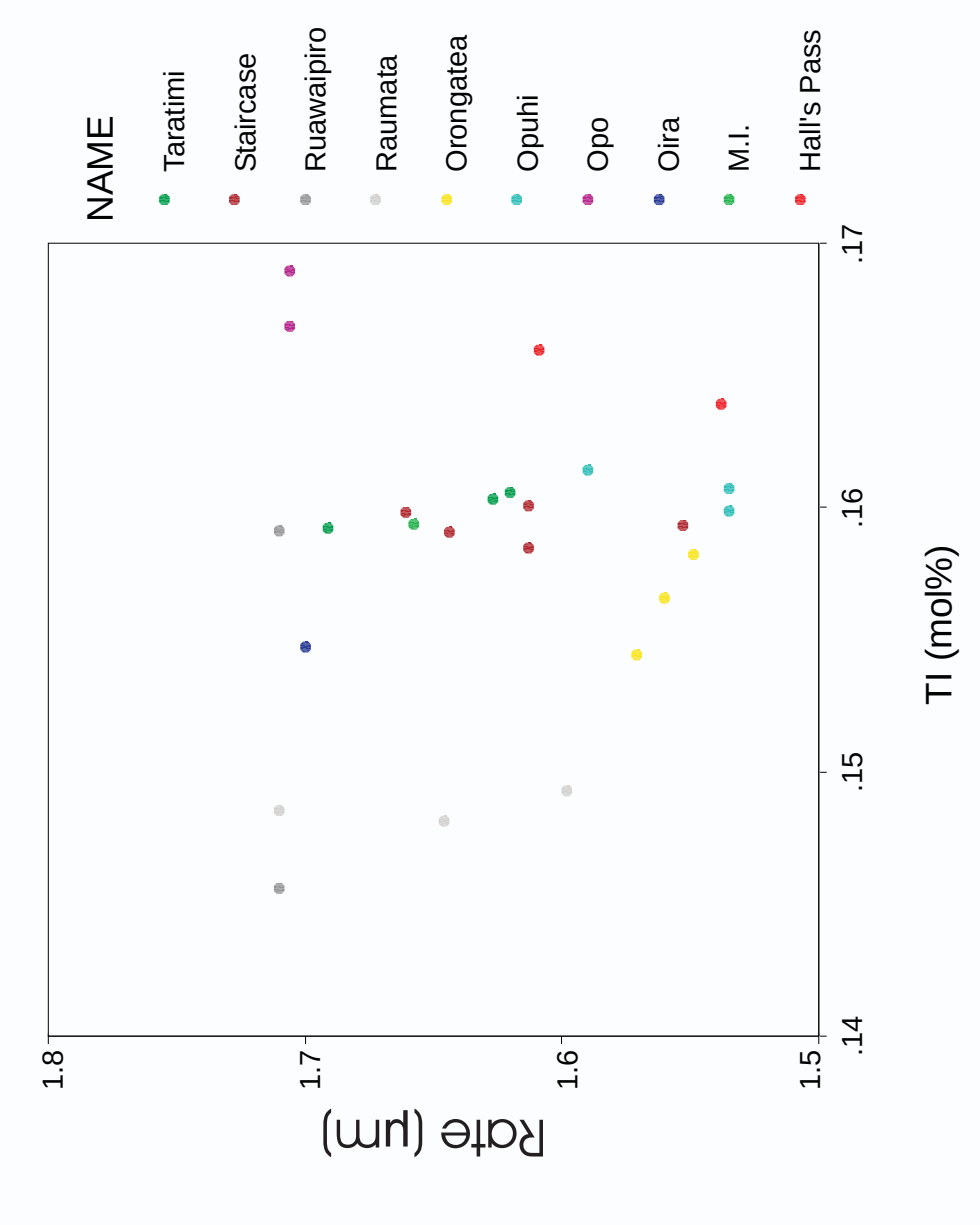

Figure D.28: Ti (Molar %) versus hydration rate for Mayor Island reference samples

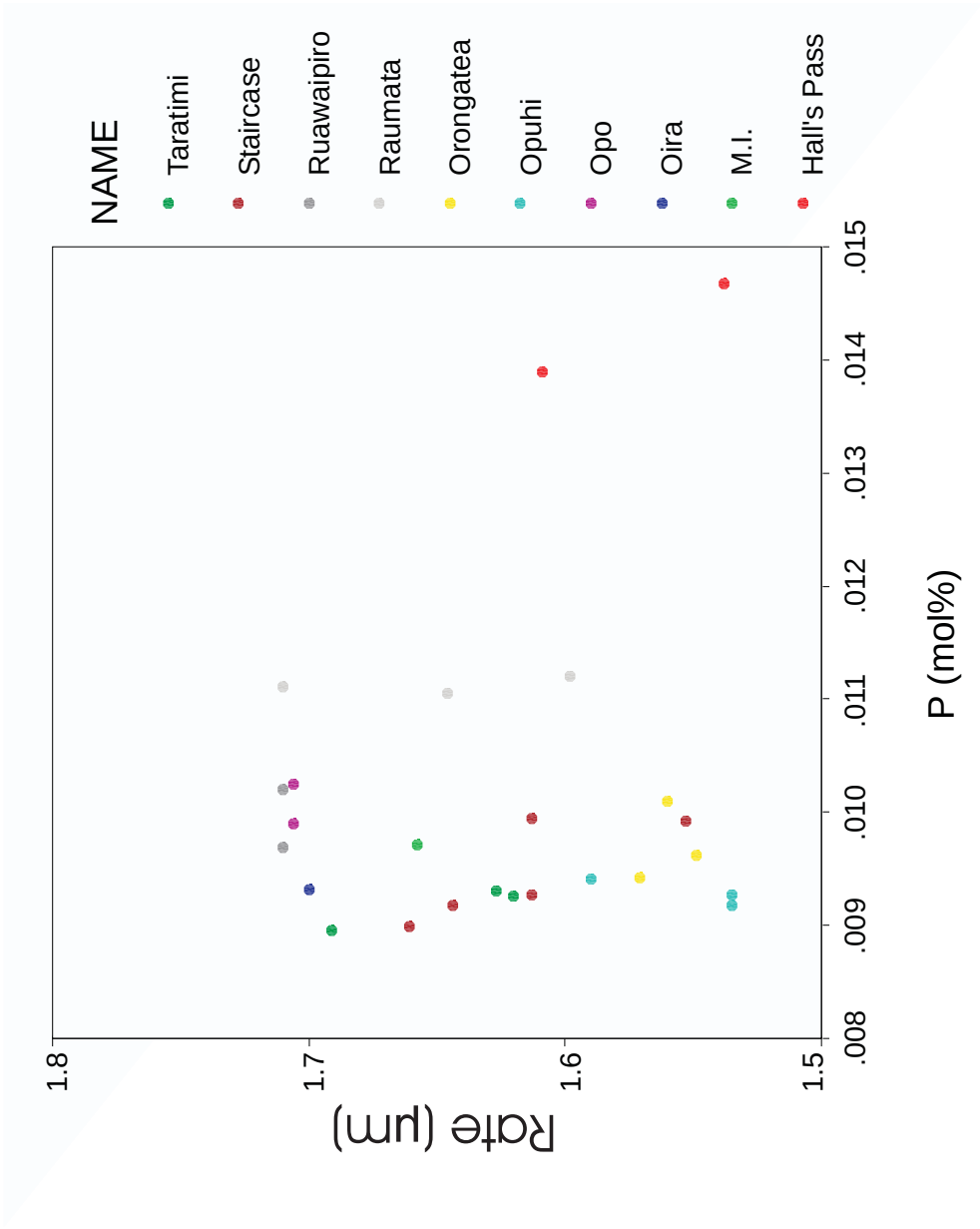

Figure D.29: P (Molar%) versus hydration rate for Mayor Island reference samples

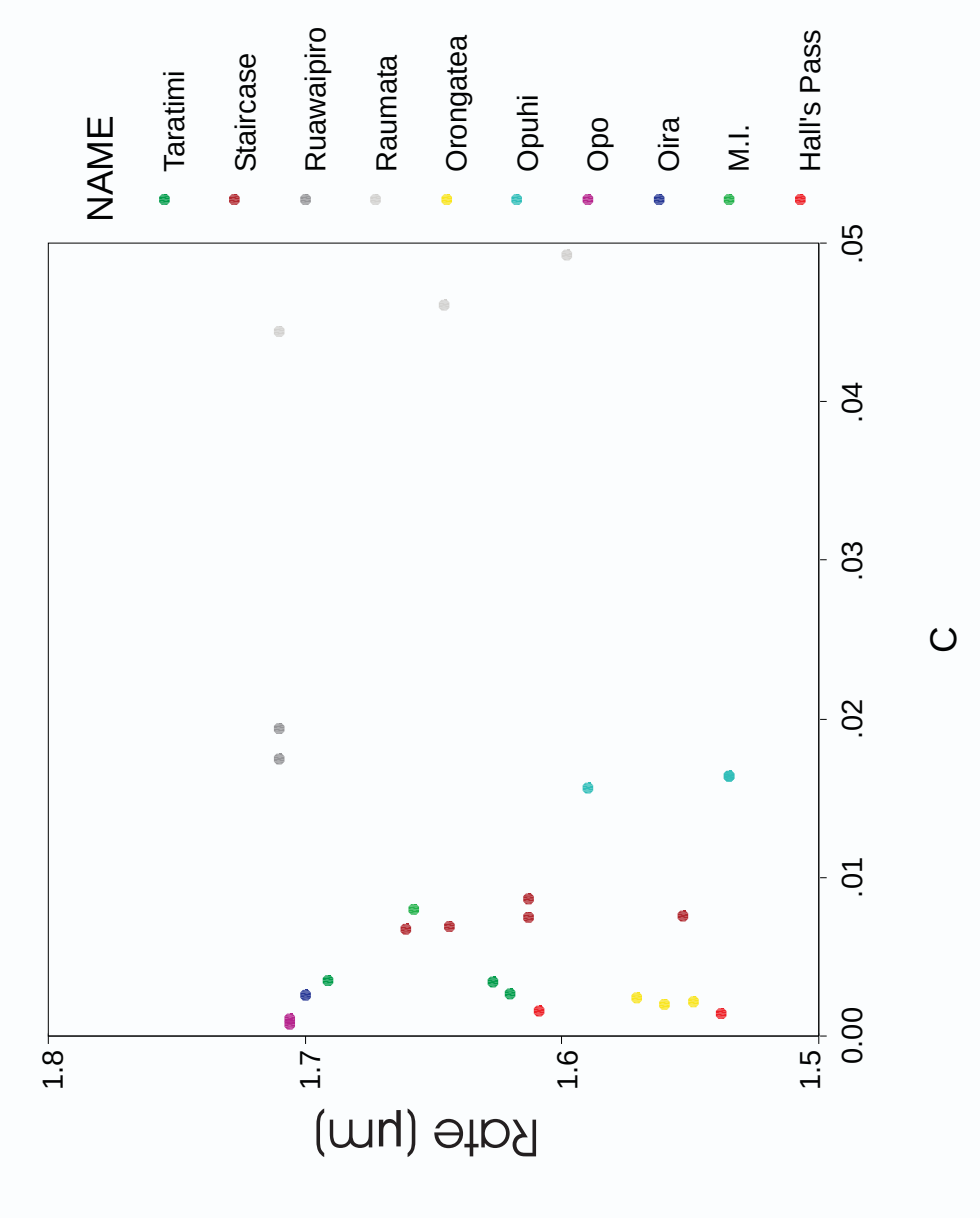

Figure D.30: C versus hydration rate for Mayor Island reference samples

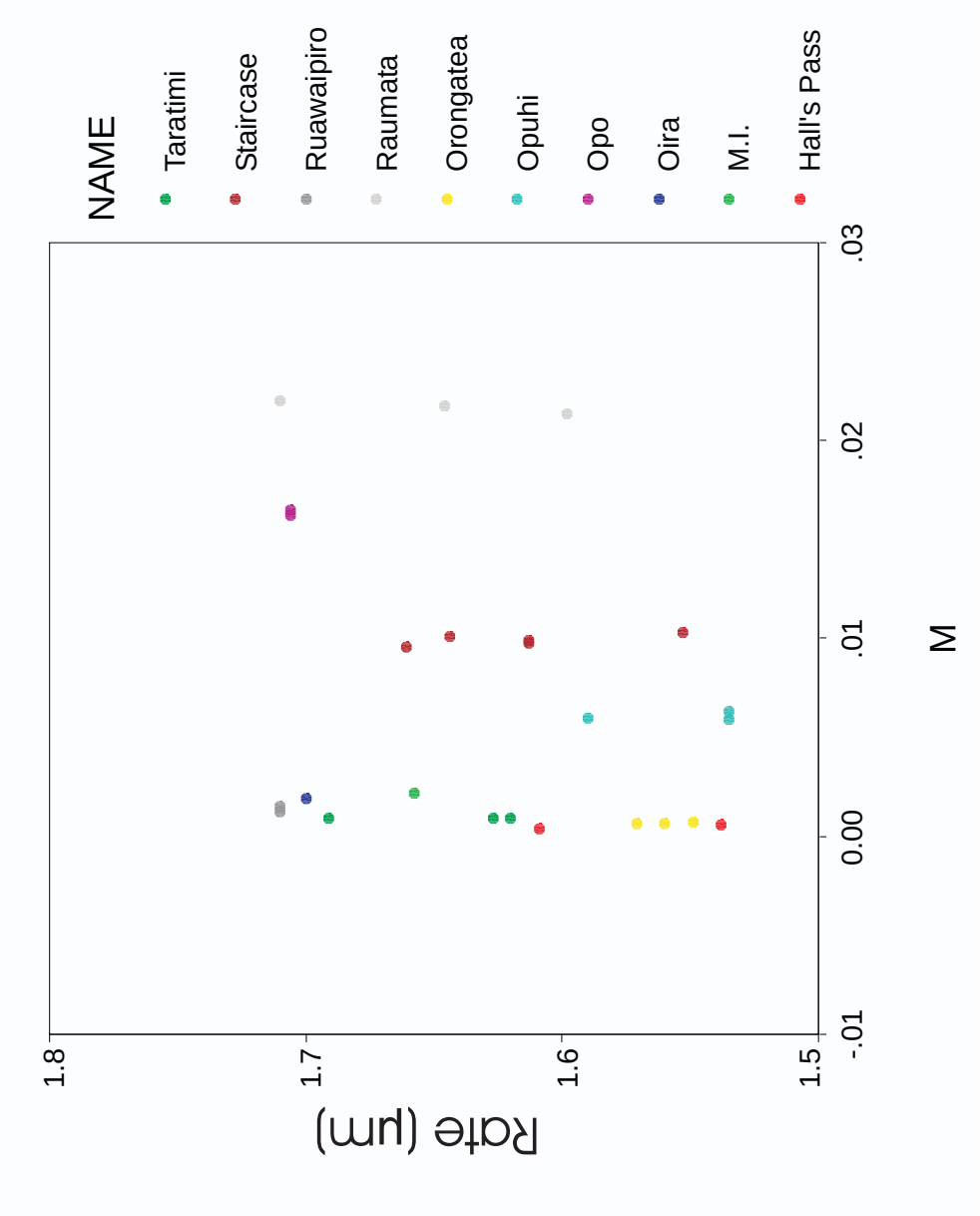

Figure D.31: M versus hydration rate for Mayor Island reference samples

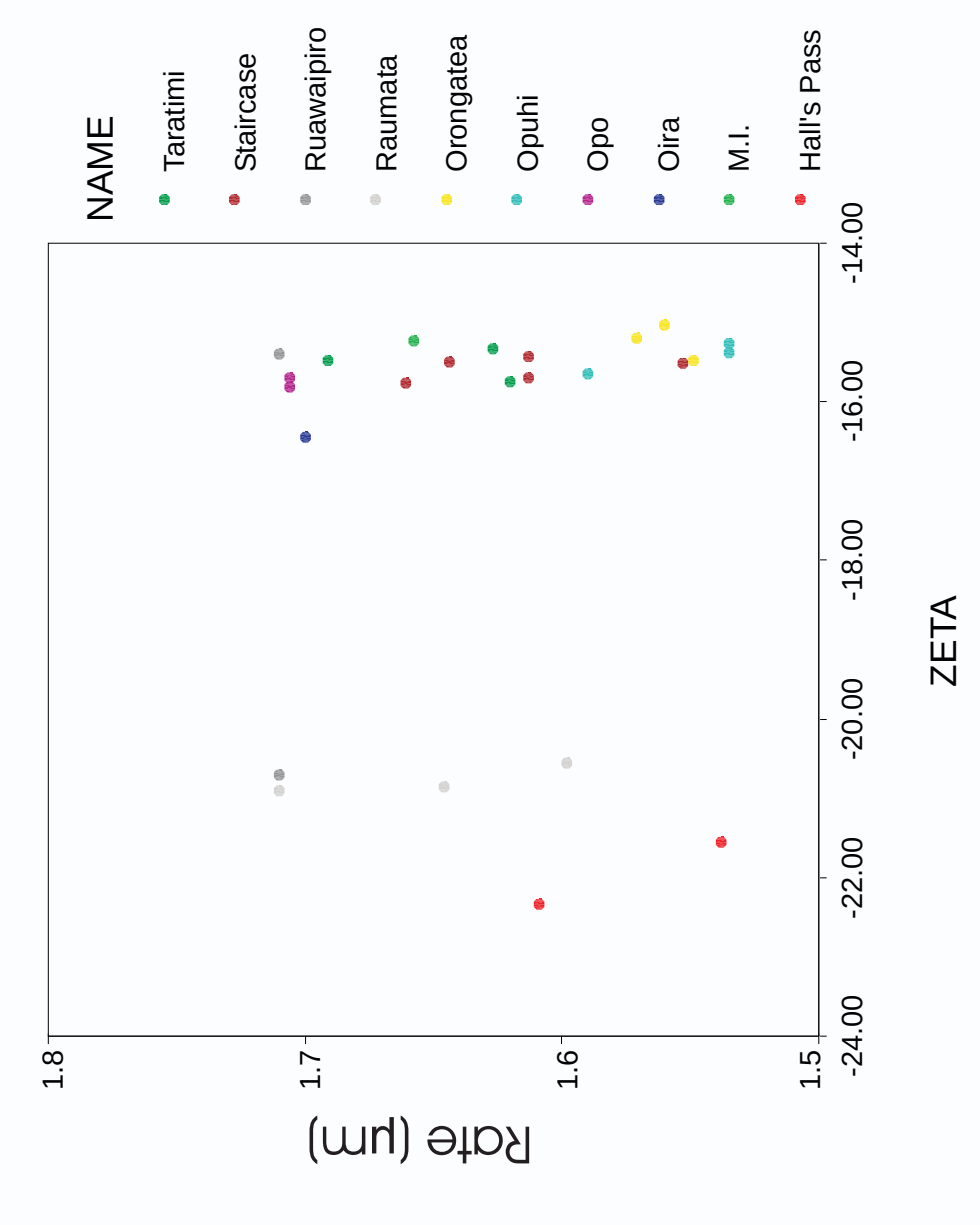

Figure D.32: Zeta versus hydration rate for Mayor Island reference samples

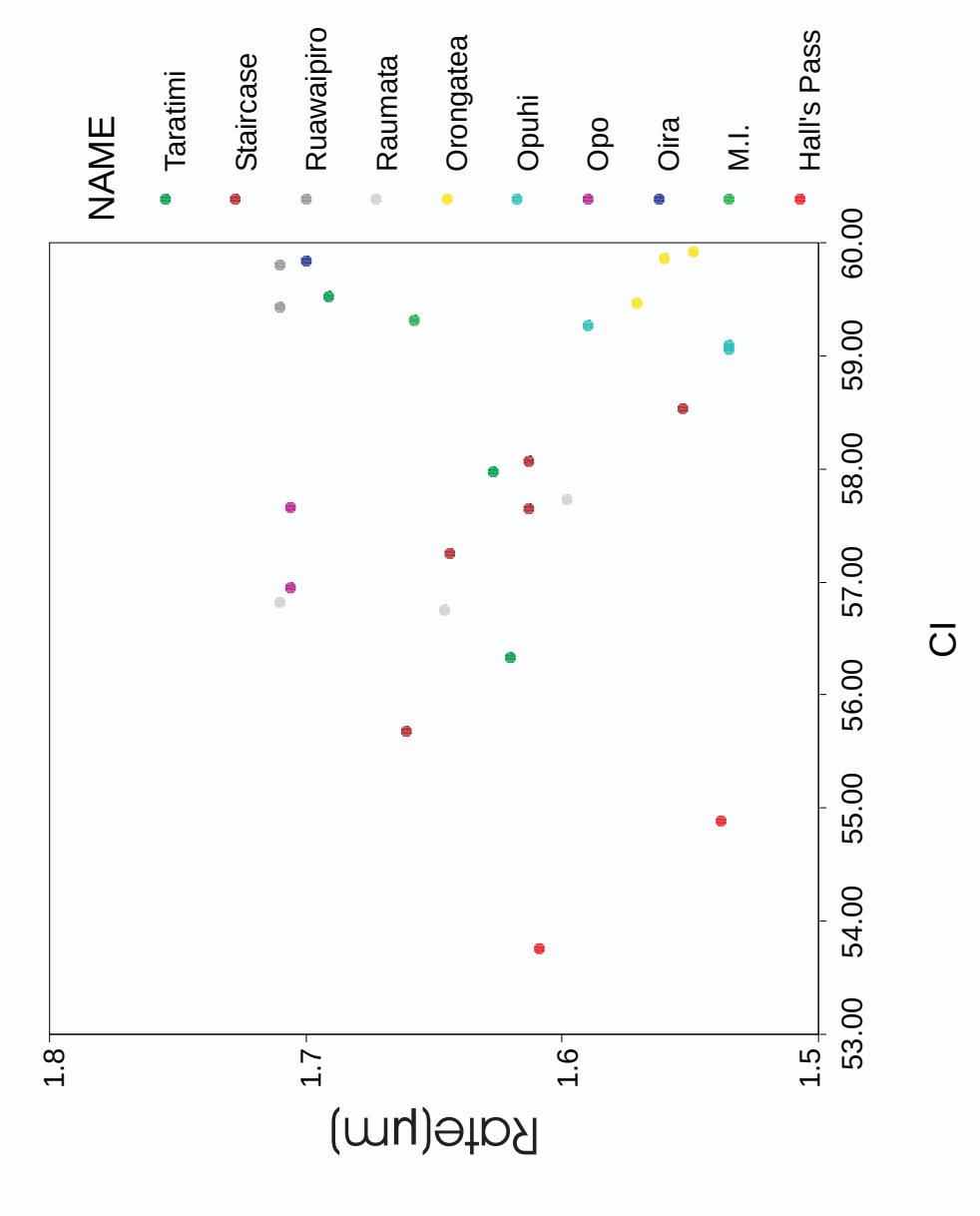

Figure D.33: CI versus hydration rate for Mayor Island reference samples

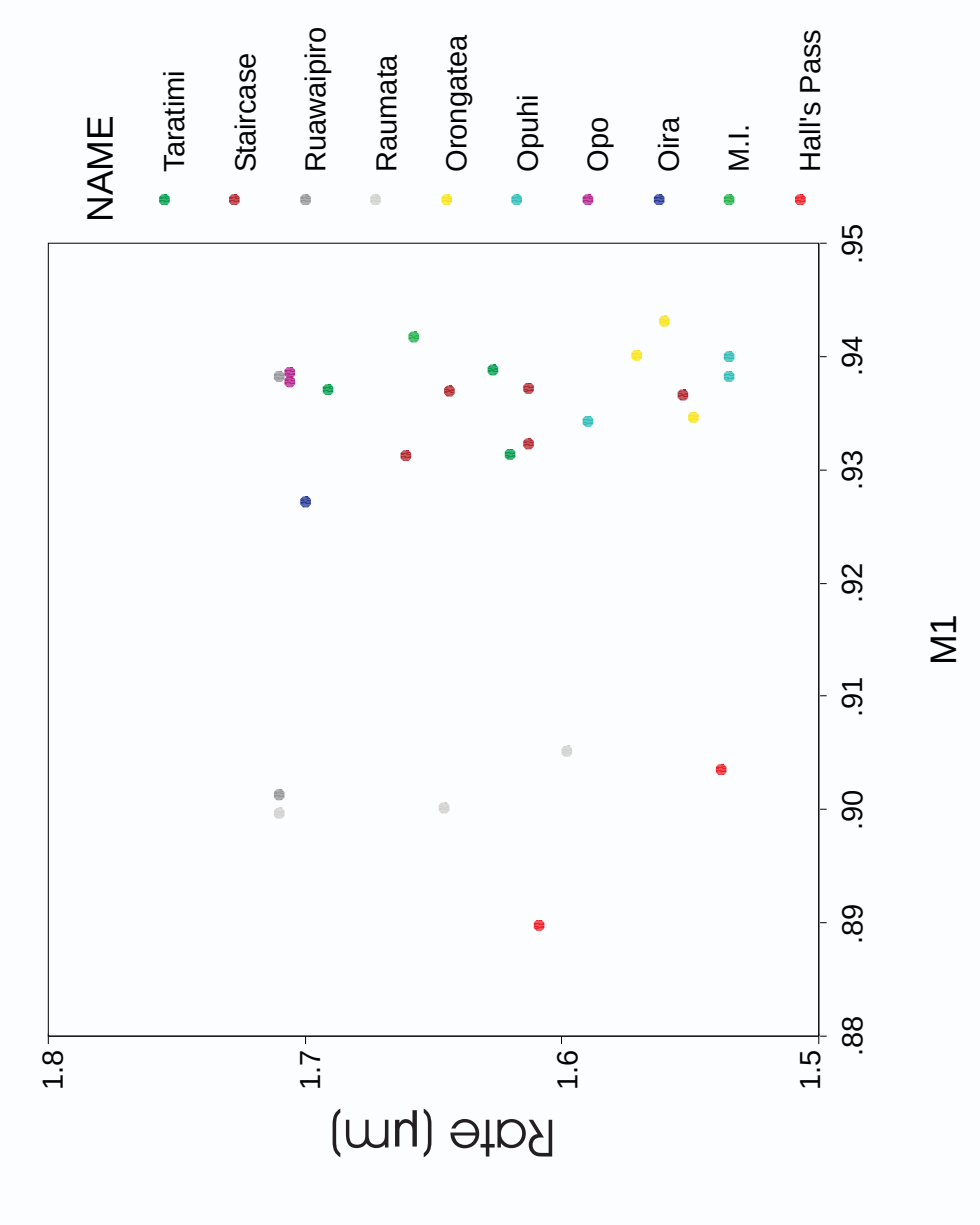

Figure D.34: M1 versus hydration rate for Mayor Island reference samples

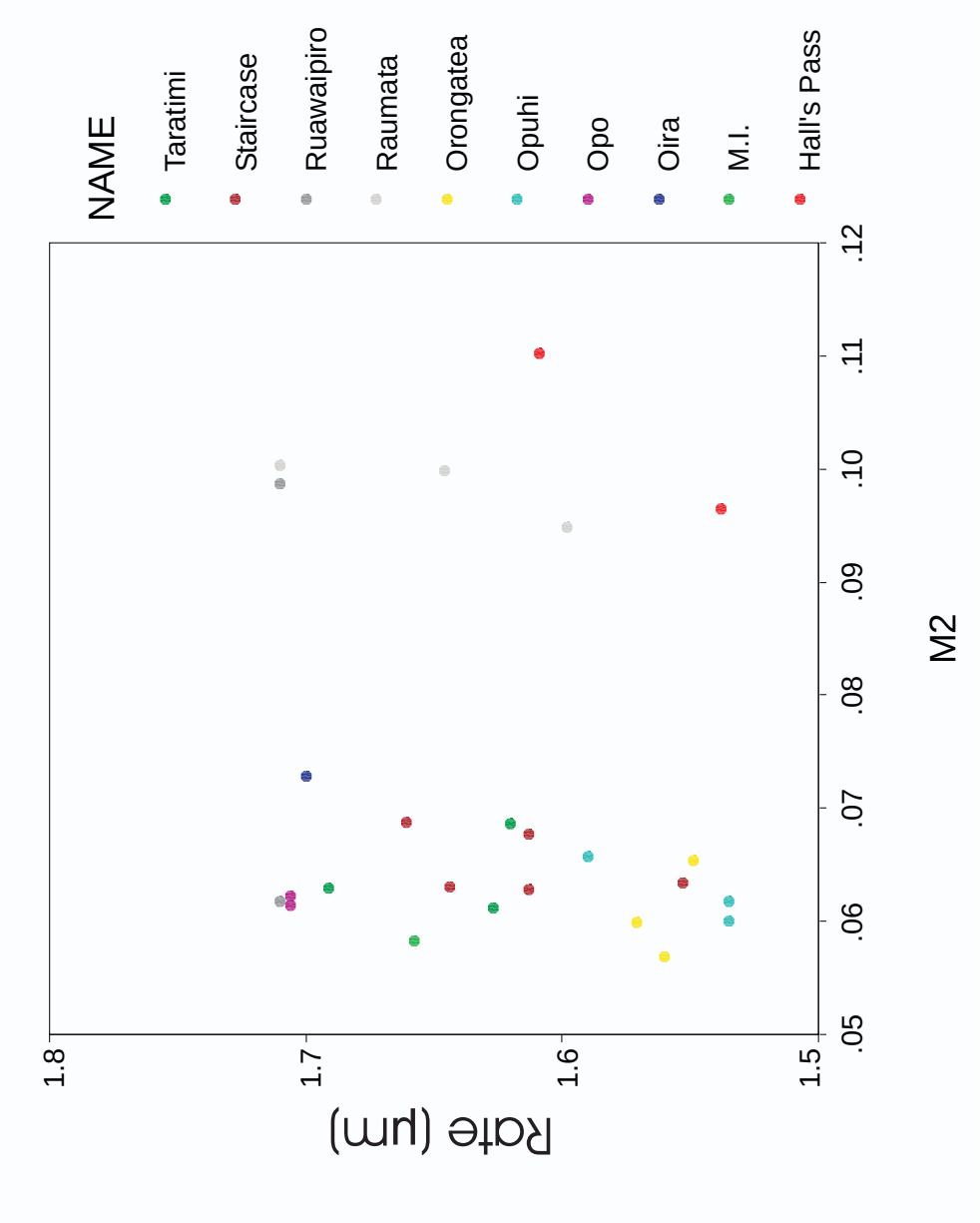

Figure D.35: M2 versus hydration rate for Mayor Island reference samples

Appendix E

New Zealand Rate Data

E.1 Source Rate Results

E.1.1 Mayor Island

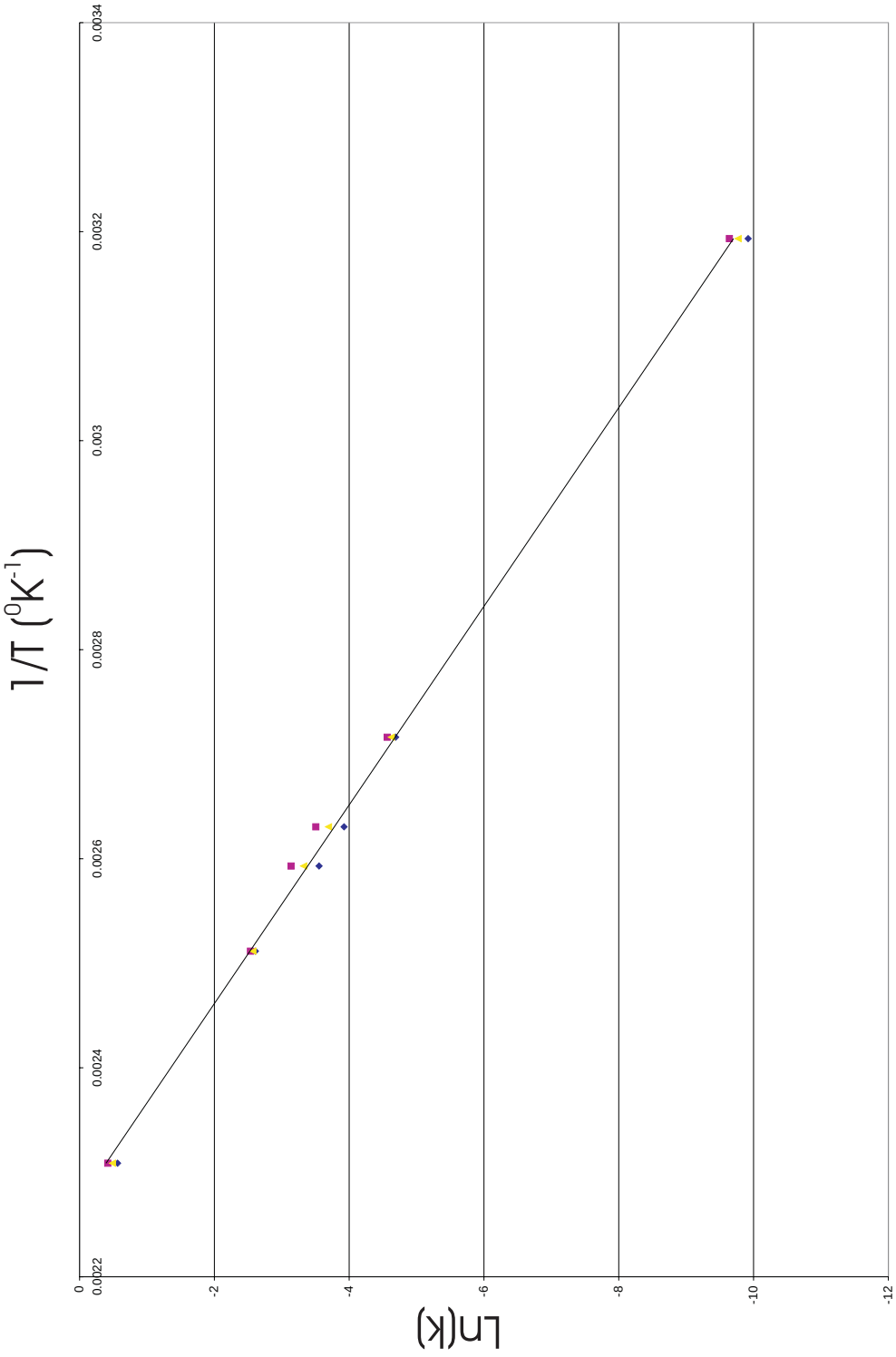

Figure E.1: Mayor Island hydration rate data

Martin Jones 2002

Table E.1: Mayor Island primary hydration rate data

Source	Source #	Temperature	k_{lower}	k_{upper}	$\bar{k}$
MI (Ambrose)		40	4.92119E-05	6.49983E-05	5.71051E-05
HP		95	0.0084375	0.011411574	0.009924537
MI		95	0.0091875	0.010416667	0.009802083
RAUMATA	4	95	0.0084375	0.011411574	0.009924537
SC	6	95	0.0084375	0.012604167	0.010520833
Pooled		95	0.0091875	0.010416667	0.010520833
MI		107	0.019756098	0.03005122	0.024903659
TAUMOU	29	107	0.032961128	0.051634754	0.042297941
MI		112.5	0.028396127	0.043396127	0.035896127
RAUMATA	4	112.5	0.028396127	0.043396127	0.035896127
Taratimi	42	112.5	0.028247059	0.048188235	0.038217647
TAUMOU	29	112.5	0.028620158	0.043672975	0.036146567
TAUMOU	31	112.5	0.028620158	0.043672975	0.036146567
Pooled		112.5	0.028620158	0.043396127	0.036146567
TAUMOU	30	112.5	0.053602941	0.06890625	0.061254596
Te Ananui	75	125	0.059864463	0.085017859	0.072441161
HP		125	0.064285718	0.080880183	0.072582951
OH	84	125	0.051494462	0.081361607	0.066428035
OH	85	125	0.052651613	0.086502858	0.069577236
OH	86	125	0.064285714	0.079206434	0.071746074
OH	87	125	0.060486422	0.084280176	0.072383299
OH	88	125	0.067540186	0.079682854	0.07361152
OH	89	125	0.059245719	0.09412072	0.07668322
OH	92	125	0.065145714	0.093344465	0.07924509
Orongatea	52	125	0.053821603	0.085017859	0.069419731
Orongatea	53	125	0.063857852	0.079444467	0.07165116
Orongatea	56	125	0.065145714	0.079682857	0.072414286
Orongatea	57	125	0.065577857	0.079921607	0.072749732
Orongatea	58	125	0.068864464	0.087250179	0.078057321
Opuhi Springs	77	125	0.063006429	0.079206424	0.071106427
Opuhi Springs	78	125	0.060486422	0.085017859	0.072752141
Opuhi Springs	81	125	0.059245714	0.091801607	0.075523661
Opuhi Springs	82	125	0.058017853	0.100446429	0.079232141
sc	33	125	0.053235	0.086502857	0.069868929
sc	34	125	0.069086429	0.079682857	0.074384643
sc	35	125	0.067540181	0.081361607	0.074450894
sc	36	125	0.065145712	0.090271611	0.077708661
sc	37	125	0.071551607	0.086502857	0.079027232
Ruakiki	71	125	0.064500188	0.089006432	0.07675331
RAUMATA	48	125	0.065577866	0.080639995	0.073108931
RAUMATA	49	125	0.055004464	0.103686429	0.079345446
RAUMATA	50	125	0.072914467	0.082814469	0.077864468
Otiora seam	66	125	0.073600714	0.08064	0.077120357

continued on the next page

Table E.1: *continued* from table E.1

Source	Source #	Temperature	k_{lower}	k_{upper}	$\bar{k}$
Taratimi	43	125	0.067540179	0.082814464	0.075177321
Taratimi	44	125	0.06364446	0.088754469	0.076199464
Taratimi	45	125	0.069531423	0.094900178	0.082215801
Opo	73	125	0.067540181	0.100446429	0.083993305
Pooled		125	0.073600714	0.079206424	0.083993305
Otiora cobble	64	125	0.076377857	0.10780875	0.092093304
TAUMOU	38	125	0.081361607	0.091034997	0.086198302
TAUMOU	39	125	0.114571614	0.136094468	0.125333041
Oira	60	125	0.093344465	0.120657865	0.107001165
MI		160	0.569081641	0.658359375	0.613720508
SC160	34	160	0.517734375	0.688509375	0.603121875
Pooled		160	0.569081641	0.658359375	0.603121875

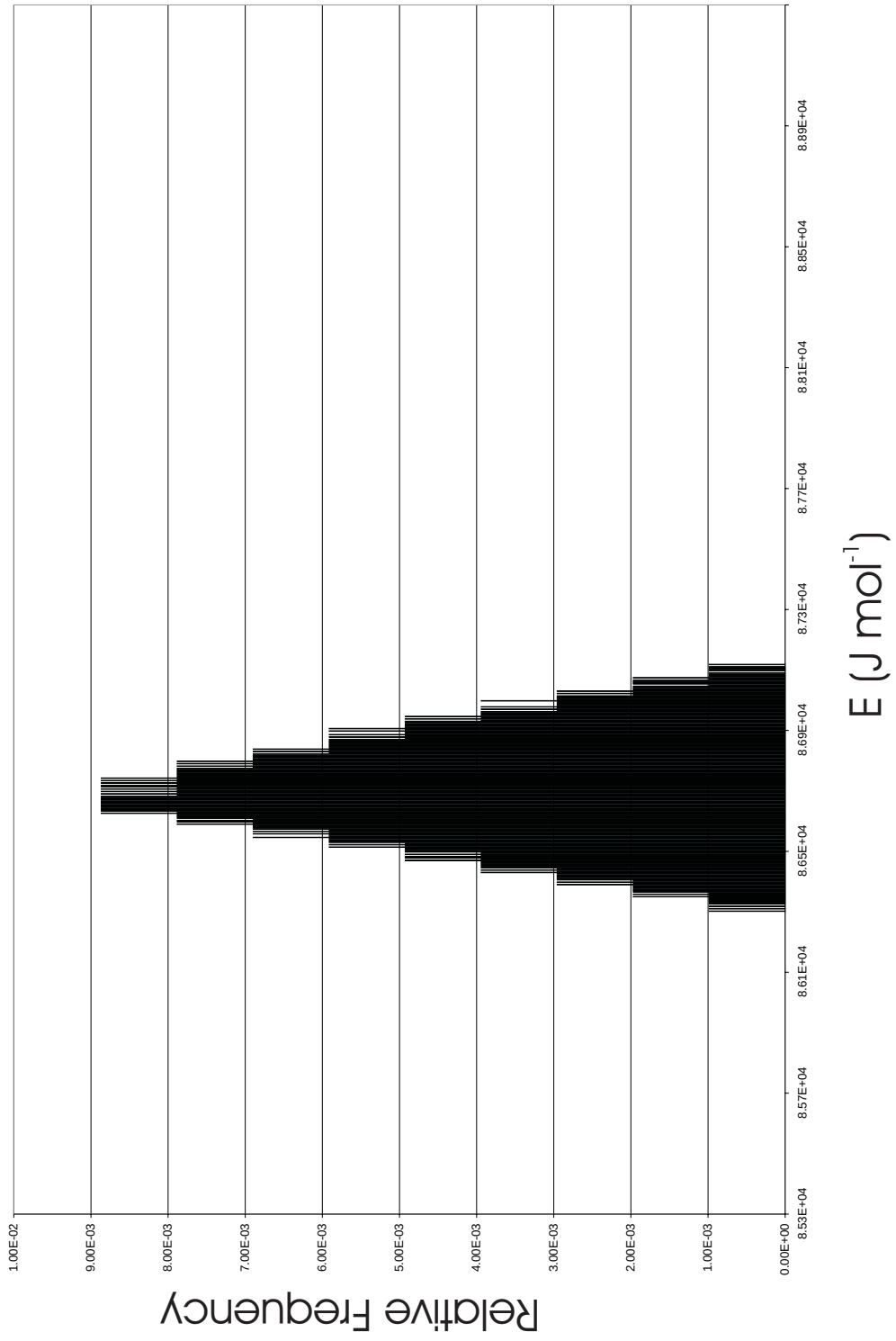

Figure E.2: Probability distribution of E for obsidian associated with the Mayor Island rhyolites

Martin Jones 2002

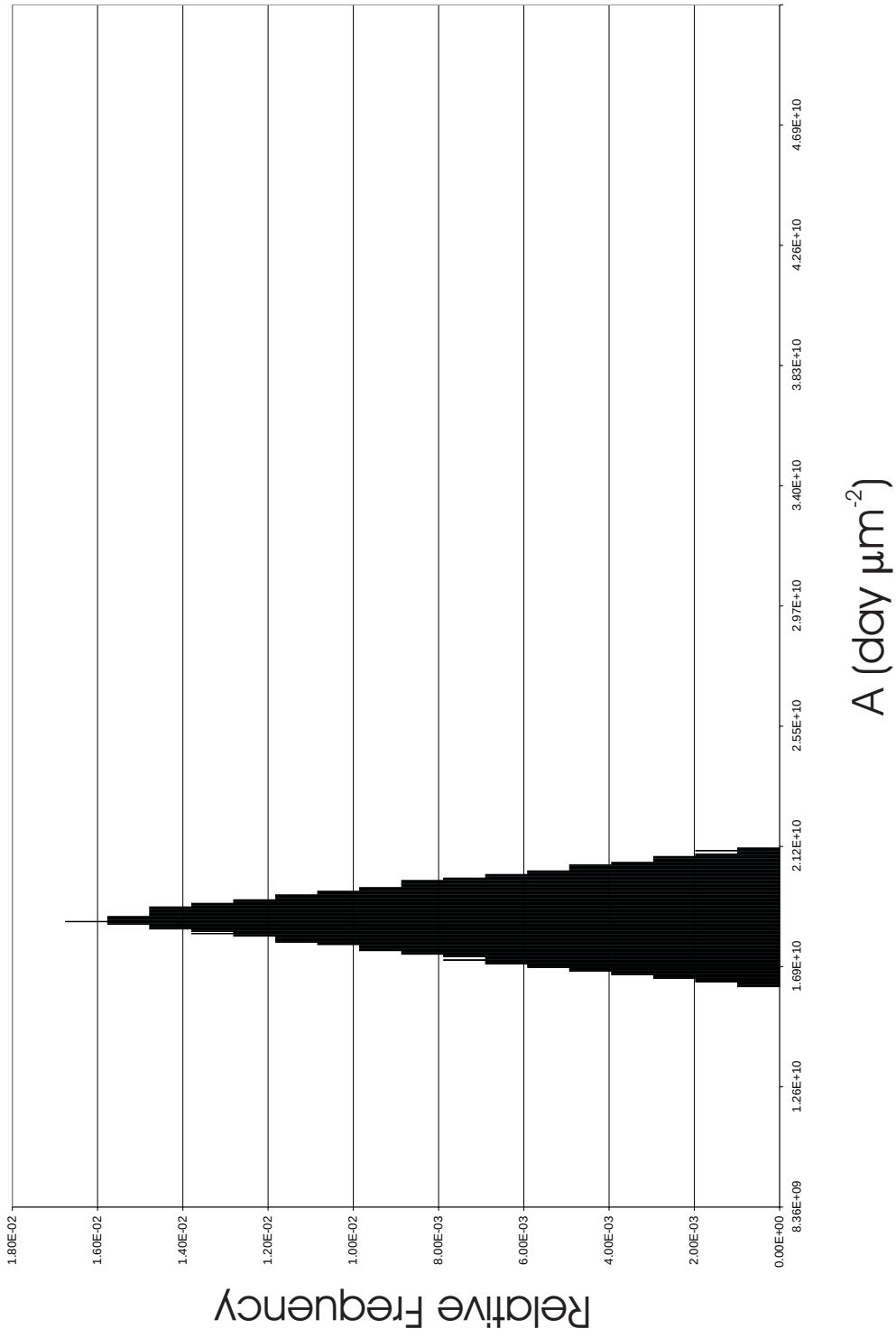

Figure E.3: Probability distribution of A for obsidian associated with the Mayor Island rhyolites

Martin Jones 2002

E.1.2 Northland

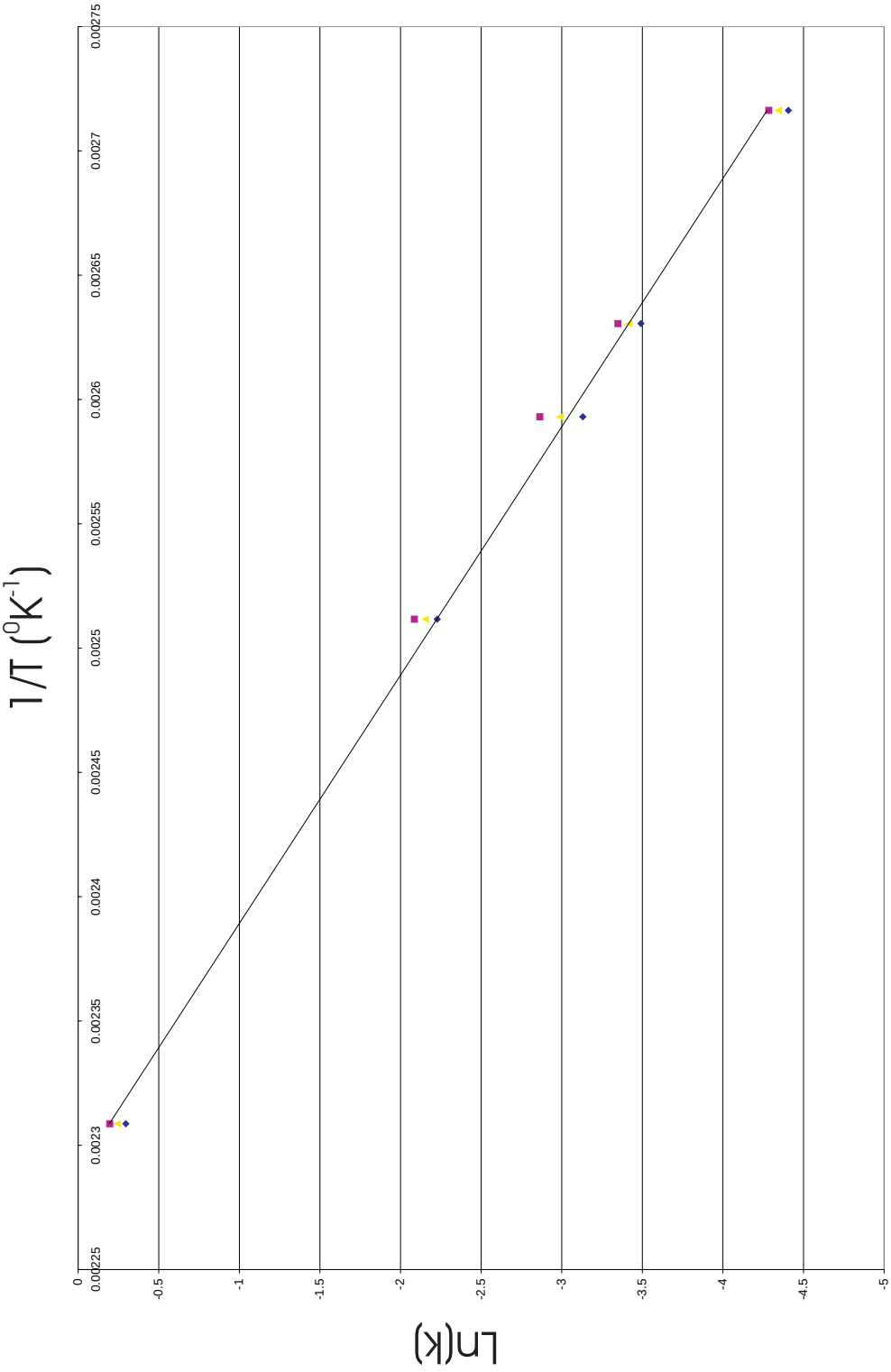

Figure E.4: Kaeo hydration rate data

Martin Jones 2002

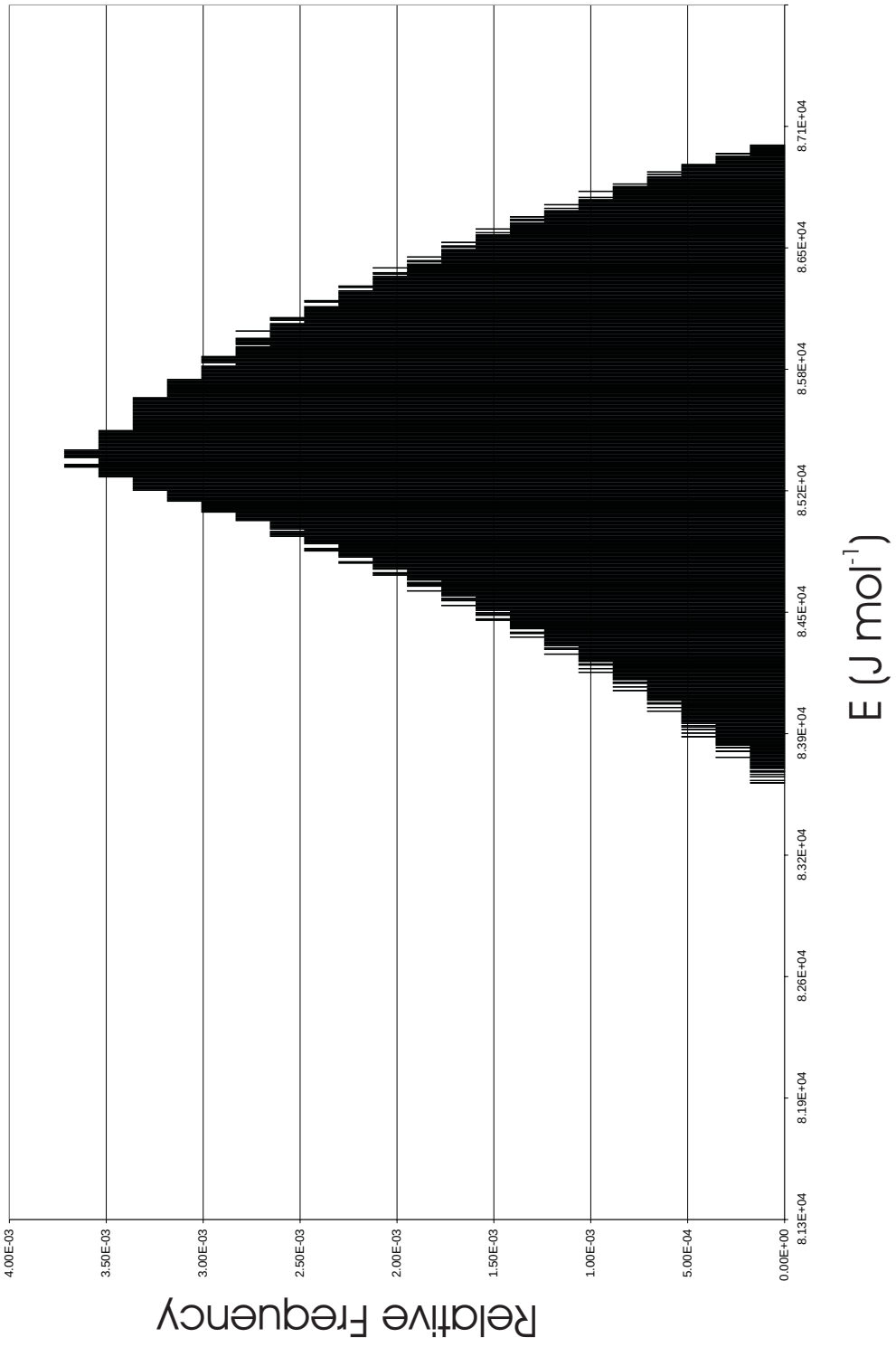

Figure E.5: Probability distribution of E for Kaeo obsidian

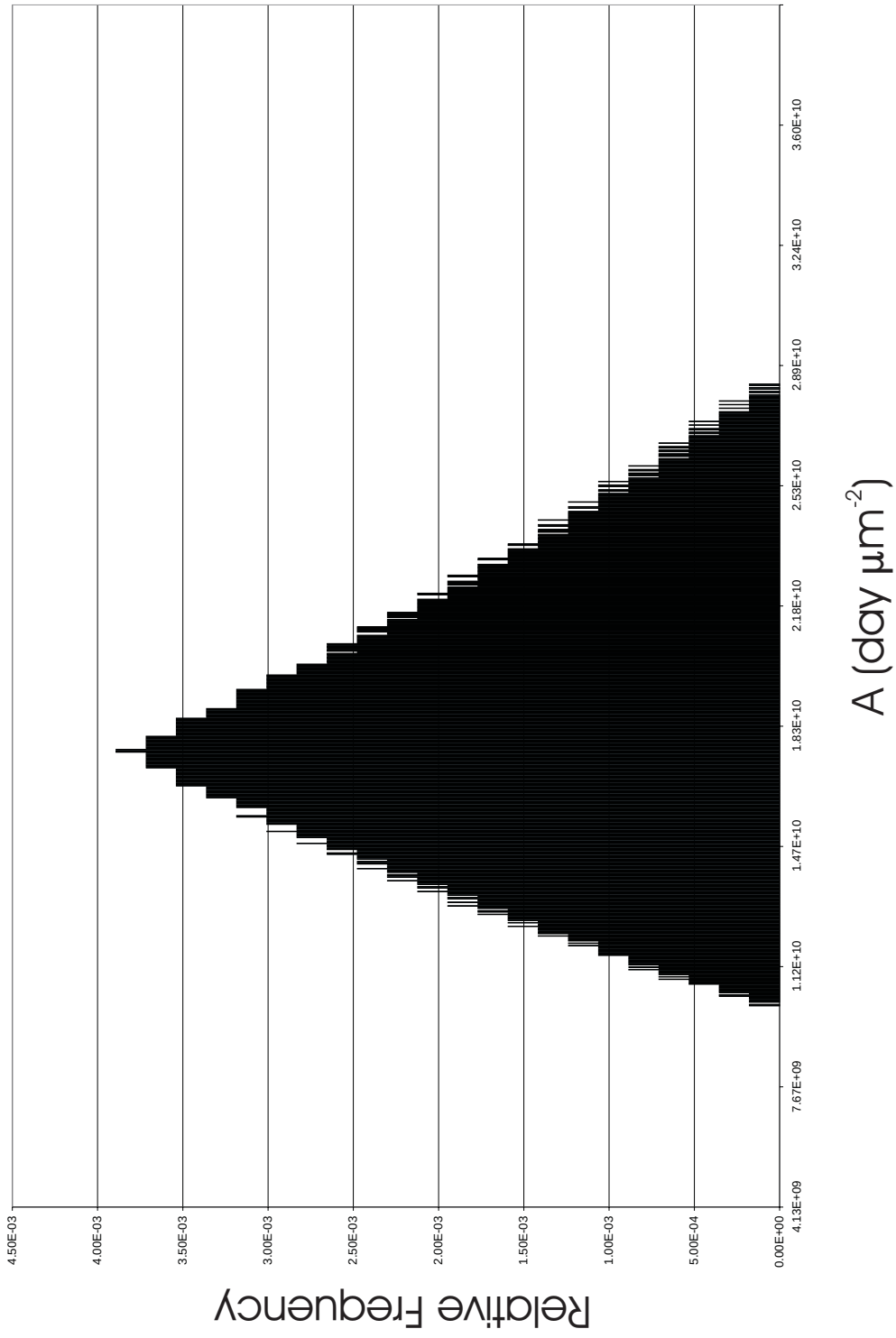

Figure E.6: Probability distribution of A for Kaeo obsidian

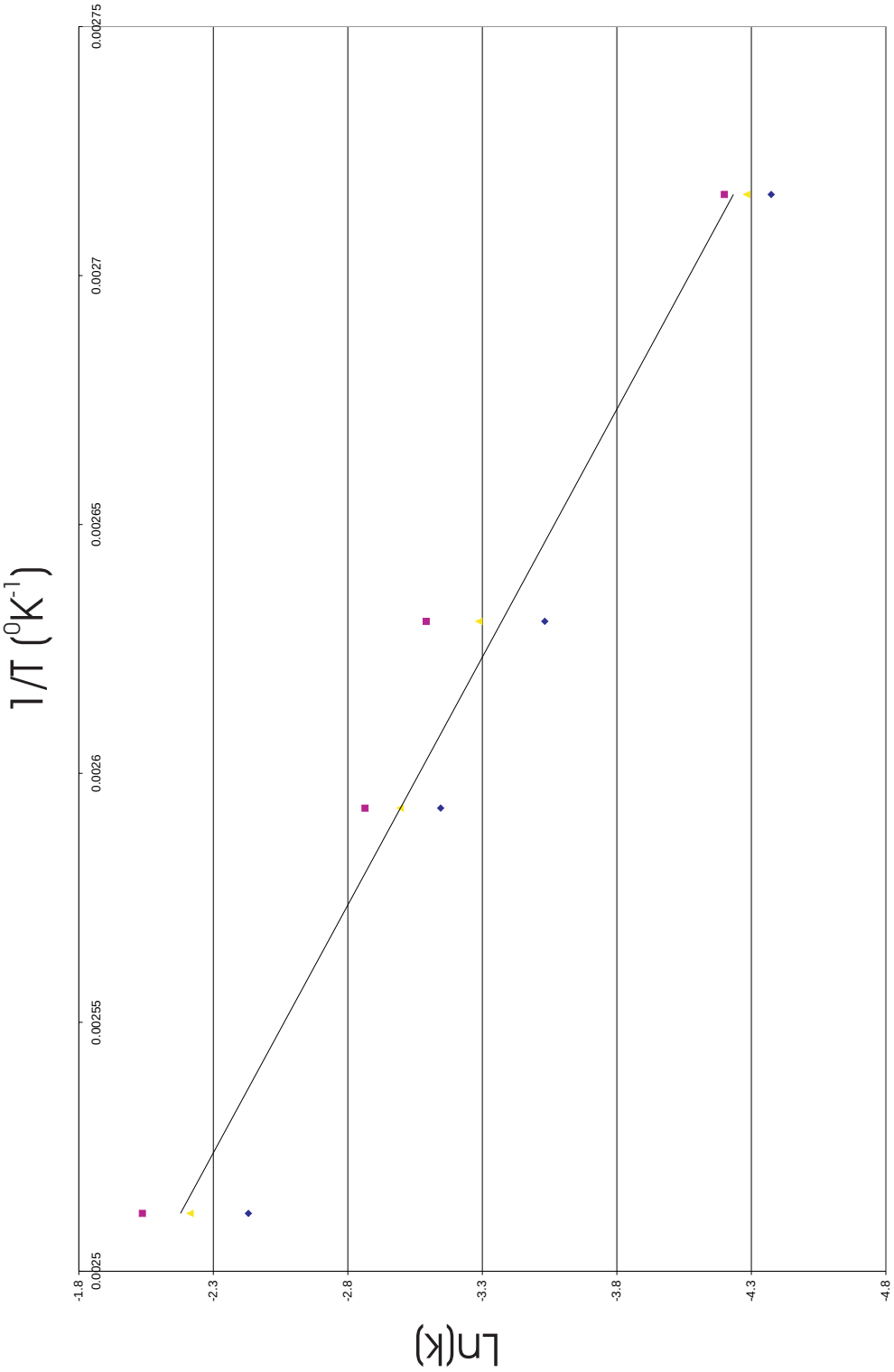

Figure E.7: Huruiki hydration rate data

Martin Jones 2002

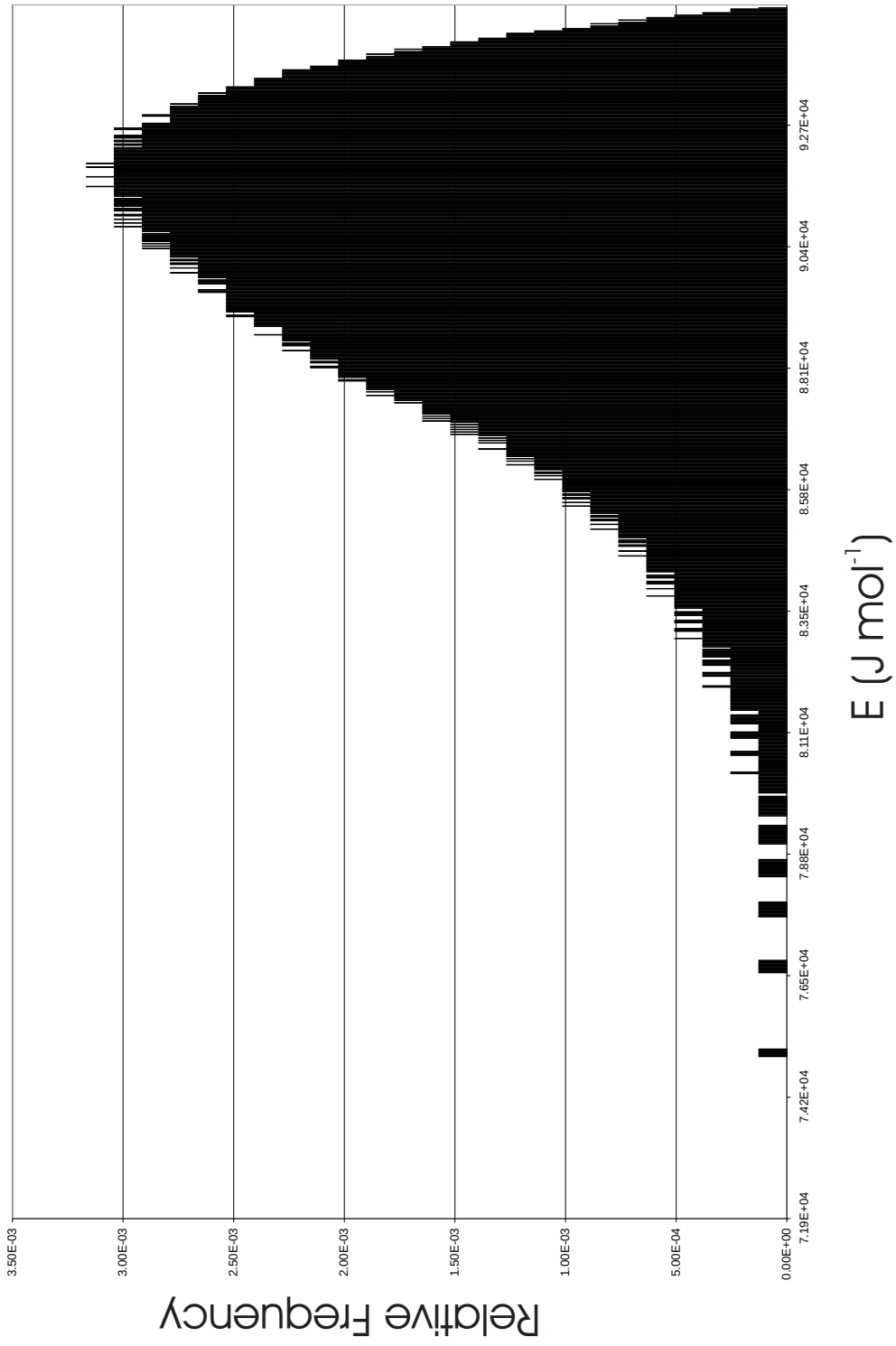

Figure E.8: Probability distribution of E for Huruiki obsidian

Martin Jones 2002

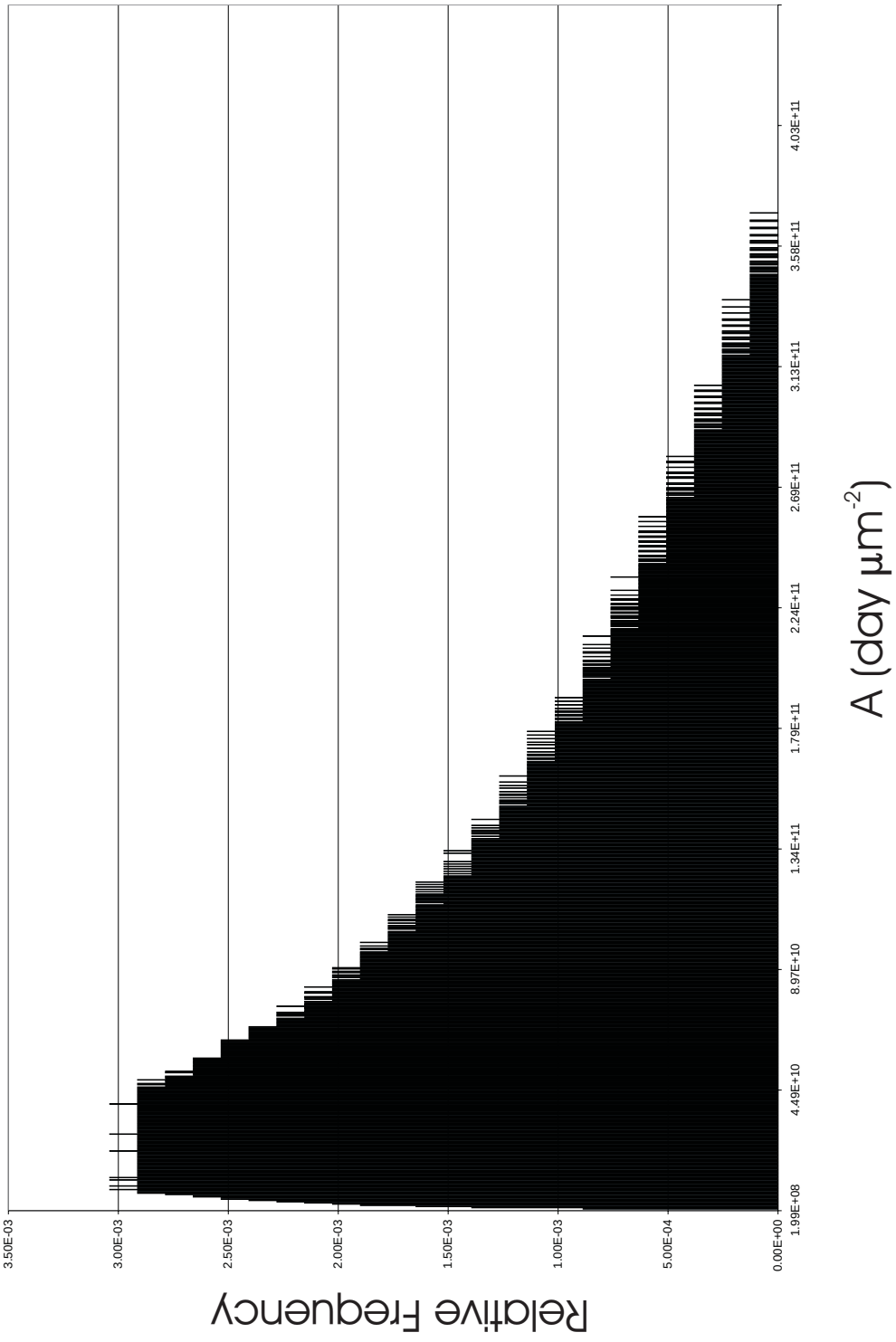

Figure E.9: Probability distribution of A for Huruiki obsidian

Table E.2: Northland primary hydration rate data

Huruiki				
9	95	0.012604167	0.015	0.013802083
9	107	0.029244514	0.045444516	0.037344515
9	112.5	0.043061765	0.057677817	0.050369791
14	112.5	0.039612676	0.057042254	0.048327465
9	125	0.088000714	0.130540184	0.109270449
Kaeo				
11	95	0.012	0.015	0.0135
12	95	0.011484375	0.013776042	0.012630208
g	95	0.012200833	0.013776042	0.012988438
25	107	0.030458687	0.035121951	0.032790319
16	107	0.026890244	0.036005491	0.031447868
g	107	0.030458687	0.035121951	0.032790319
11	112.5	0.043672975	0.061894806	0.052783891
12	112.5	0.039612676	0.057042254	0.048327465
15	112.5	0.039612676	0.057042254	0.048327465
16	112.5	0.043672975	0.061894806	0.052783891
25	112.5	0.039612676	0.057042254	0.048327465
g	112.5	0.043672975	0.057042254	0.050357614
11	125	0.092571429	0.137971607	0.115271518
16	125	0.104504464	0.124206433	0.114355449
25	125	0.10780875	0.128714464	0.118261607
g	125	0.10780875	0.124206433	0.116007592
12	160	0.74390625	0.822403125	0.783154688

E.1.3 TVZ

Table E.3: Ben Lomond primary hydration rate data

Temperature ^{0}C	k_{max}	k_{min}	$\bar{k}$
95	0.01386	0.01619	0.01502
112.5	0.04340	0.06157	0.05248
125	0.10533	0.13986	0.12259
160	0.85101	0.91125	0.88113

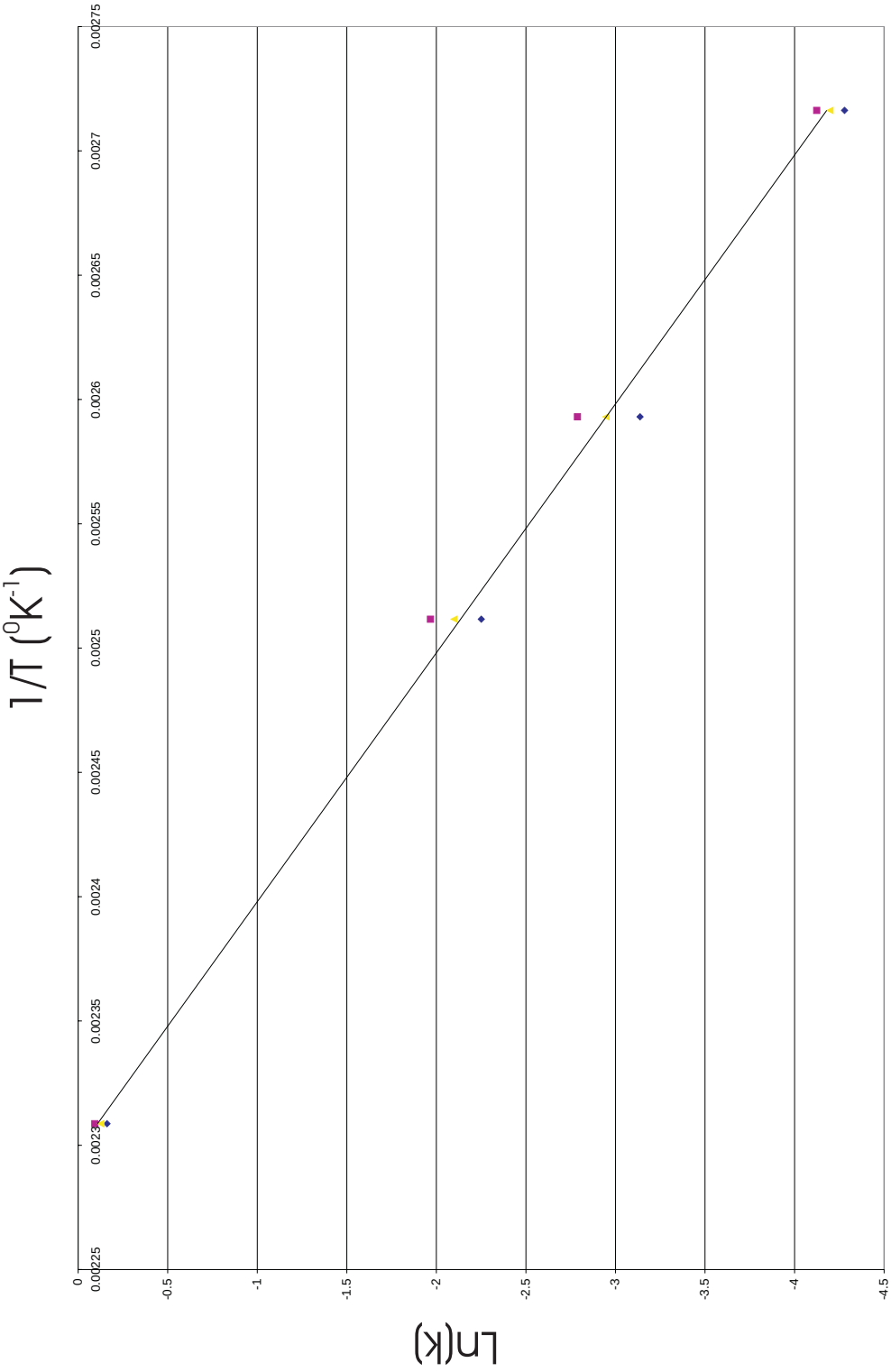

Figure E.10: Ben Lomond source rate data

Martin Jones 2002

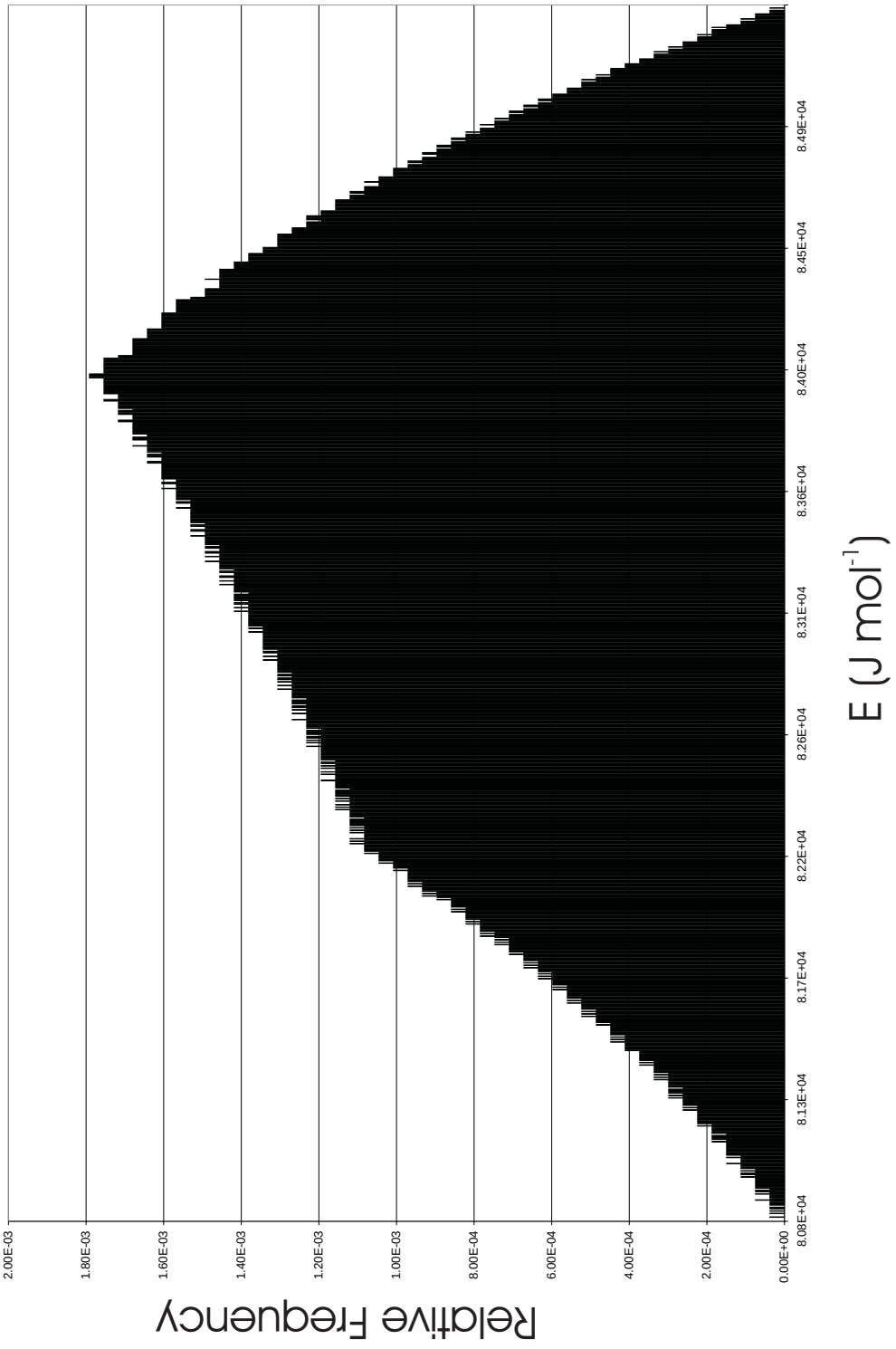

Figure E.11: Probability distribution of E for Ben Lomond obsidian

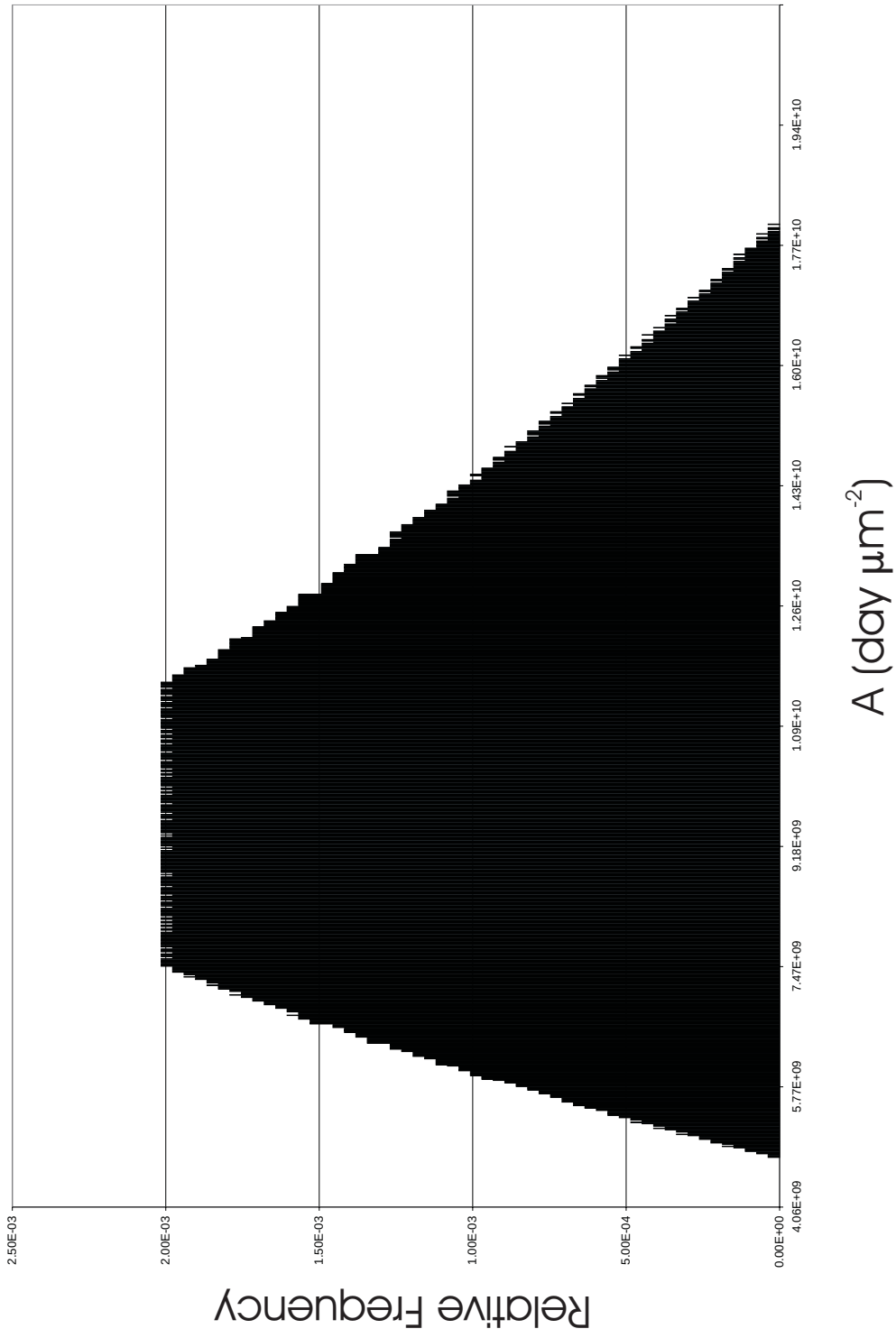

Figure E.12: Probability distribution of A for Ben Lomond obsidian

E.1.4 Coromandel

Table E.4: Coromandel primary hydration rate data

Cook's Beach		125	0.084280179	0.135160714	0.109720446
Purangi	27	125	0.0978518	0.105943765	0.101897782
TAIRUA	17	112.5	0.040142606	0.057677817	0.048910211
TAIRUA	18	112.5	0.036001761	0.052691901	0.044346831
TAIRUA	g	112.5	0.040142606	0.052691901	0.046417254
TAIRUA	17	125	0.091801607	0.114571607	0.103186607
TAIRUA	18	125	0.091801607	0.123314464	0.107558036
TAIRUA	g	125	0.091801607	0.114571607	0.103186607
TA		95	0.017604167	0.020671875	0.019138021
TA		107	0.035121951	0.058220122	0.046671037
TA		112.5	0.056410211	0.076903169	0.06665669
TA		125	0.117450191	0.198754479	0.158102335
TA		160	1.0952	1.21550625	1.155353125
Waihi	8	95	0.012604167	0.013776042	0.013190104
Waihi	8	112.5	0.032086268	0.047931338	0.040008803
Waihi	19	112.5	0.043672975	0.061894806	0.052783891
Waihi	g	112.5	0.043672975	0.047931338	0.045802157
WHITI		107	0.050575614	0.056536734	0.053556174
WHITI		112.5	0.072551056	0.095579225	0.084065141
WHITI		125	0.15246	0.193514466	0.172987233

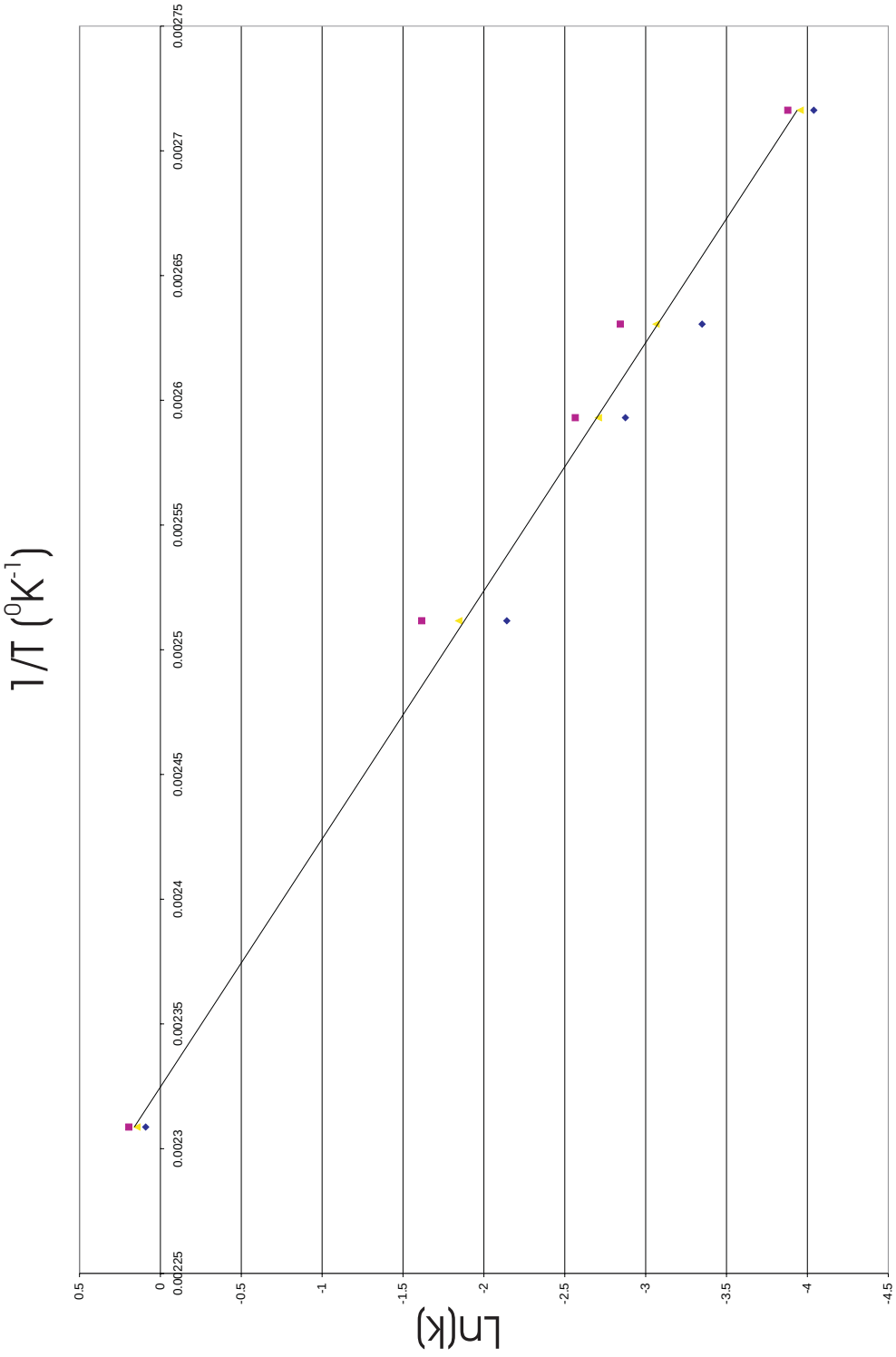

Figure E.13: Te Ahumata hydration rate data

Martin Jones 2002

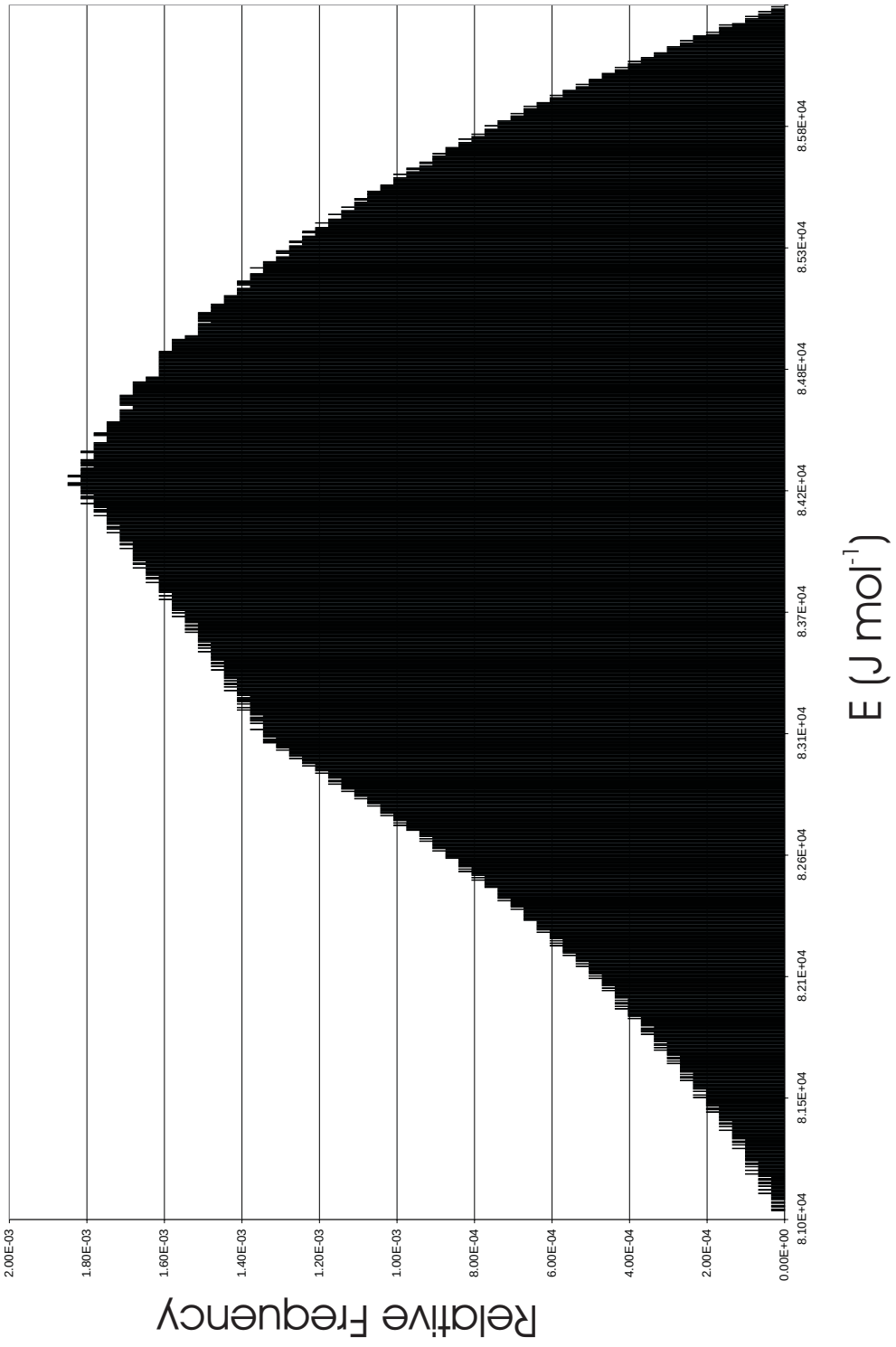

Figure E.14: Probability distribution of E for Te Ahumata obsidian

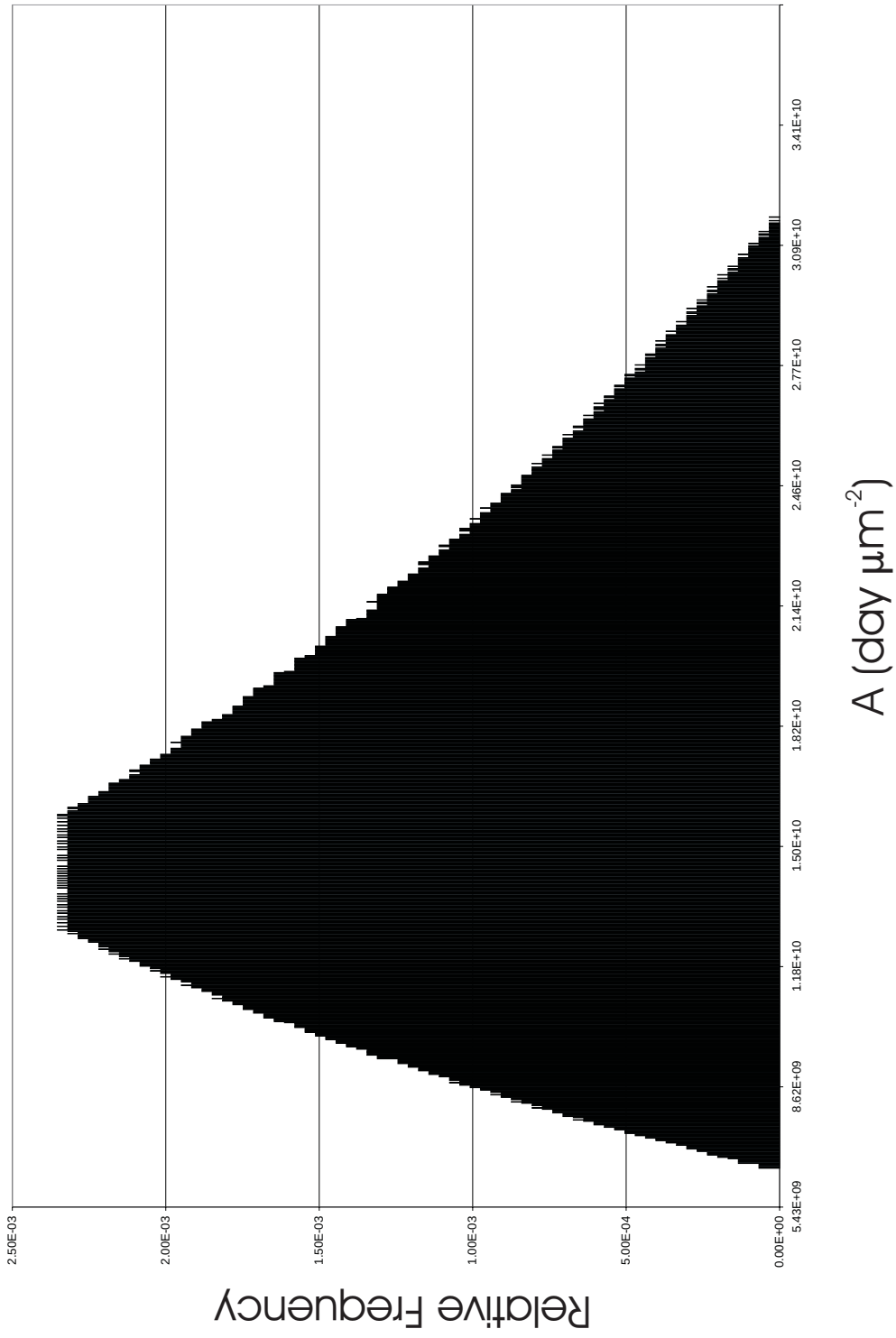

Figure E.15: Probability distribution of A for Te Ahumata obsidian

E.2 Source Hydration Rate Comparisons

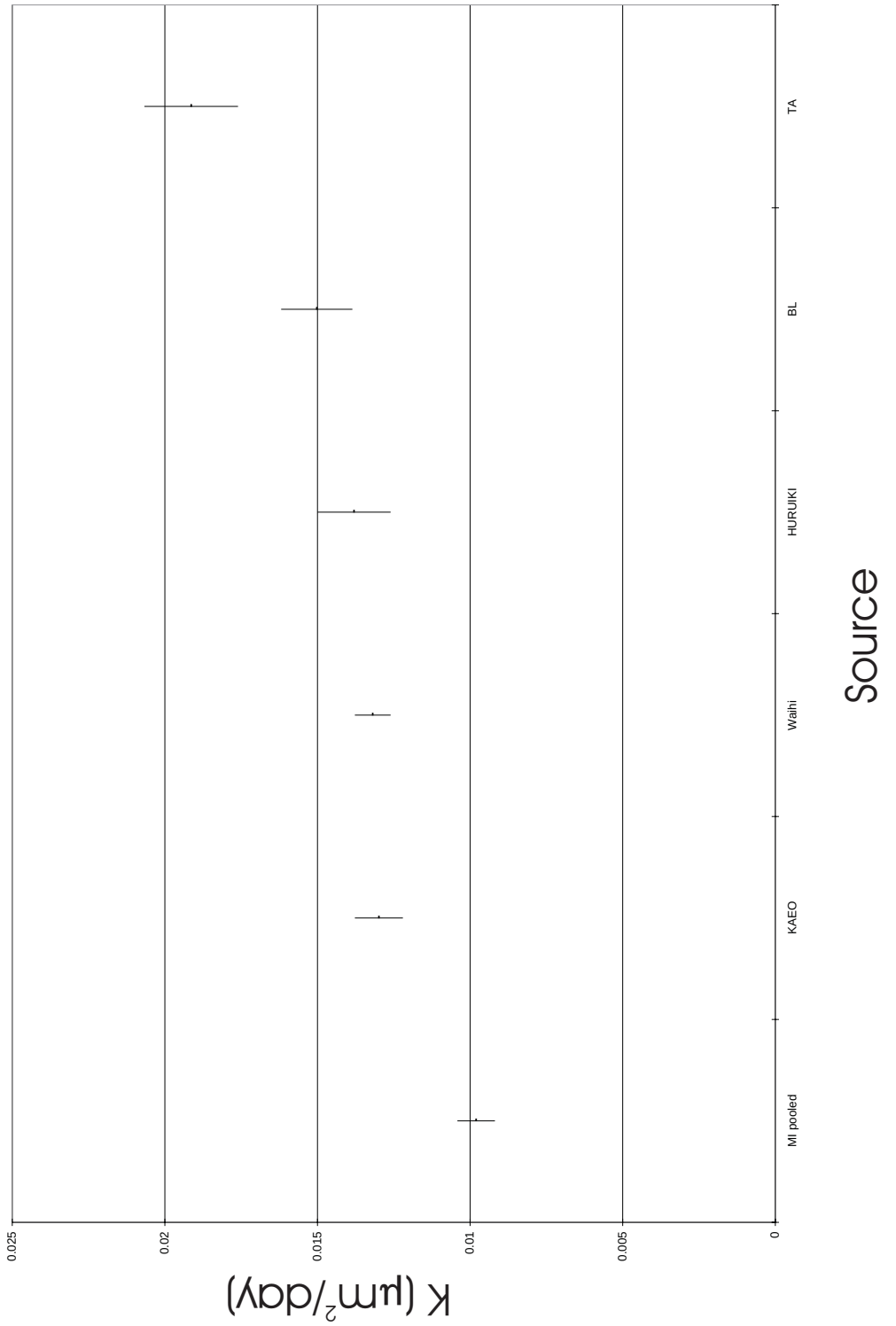

Figure E.16: 95 ^{0}C Source rate comparison data

Martin Jones 2002

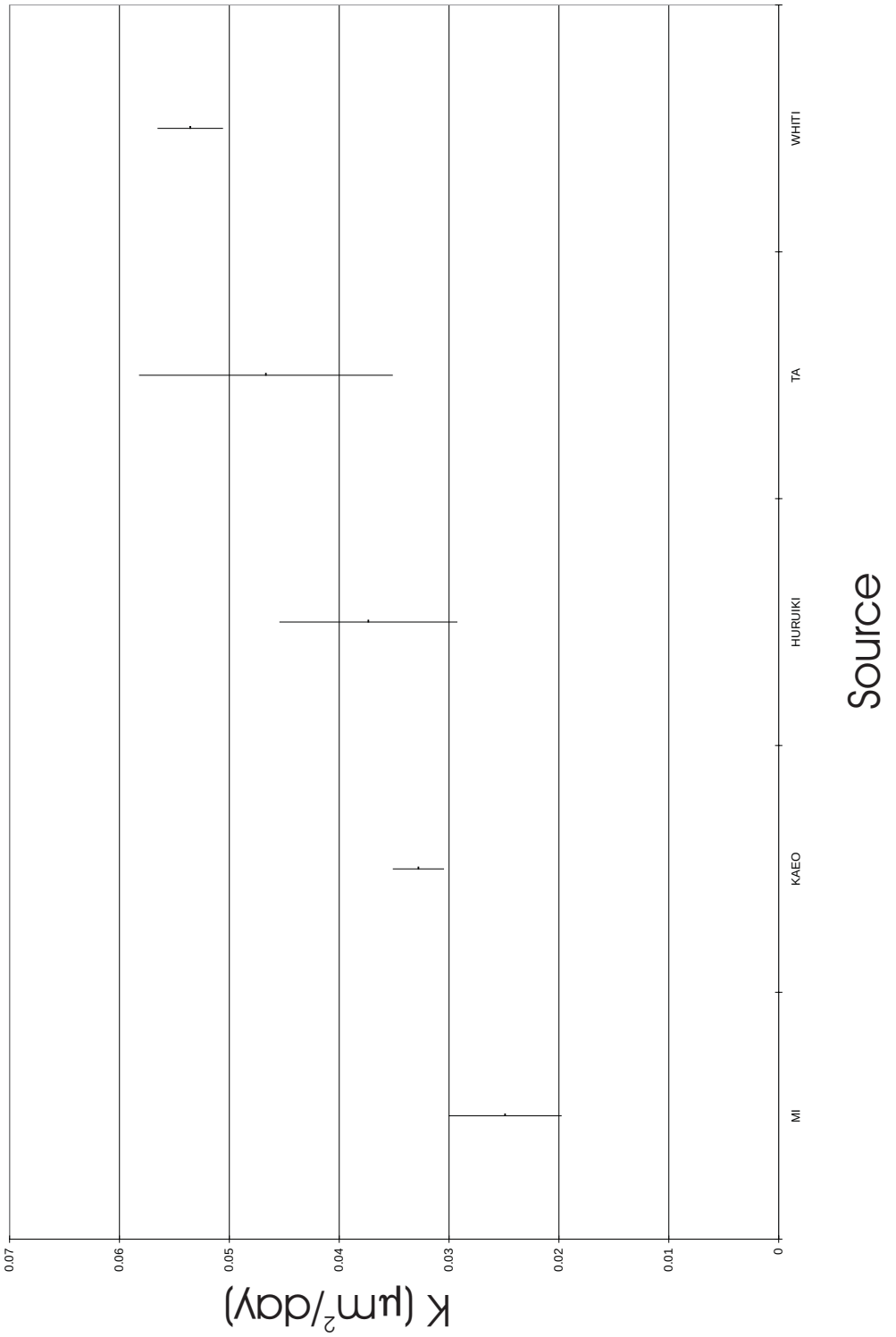

Figure E.17: 107 ^{0}C Source rate comparison data

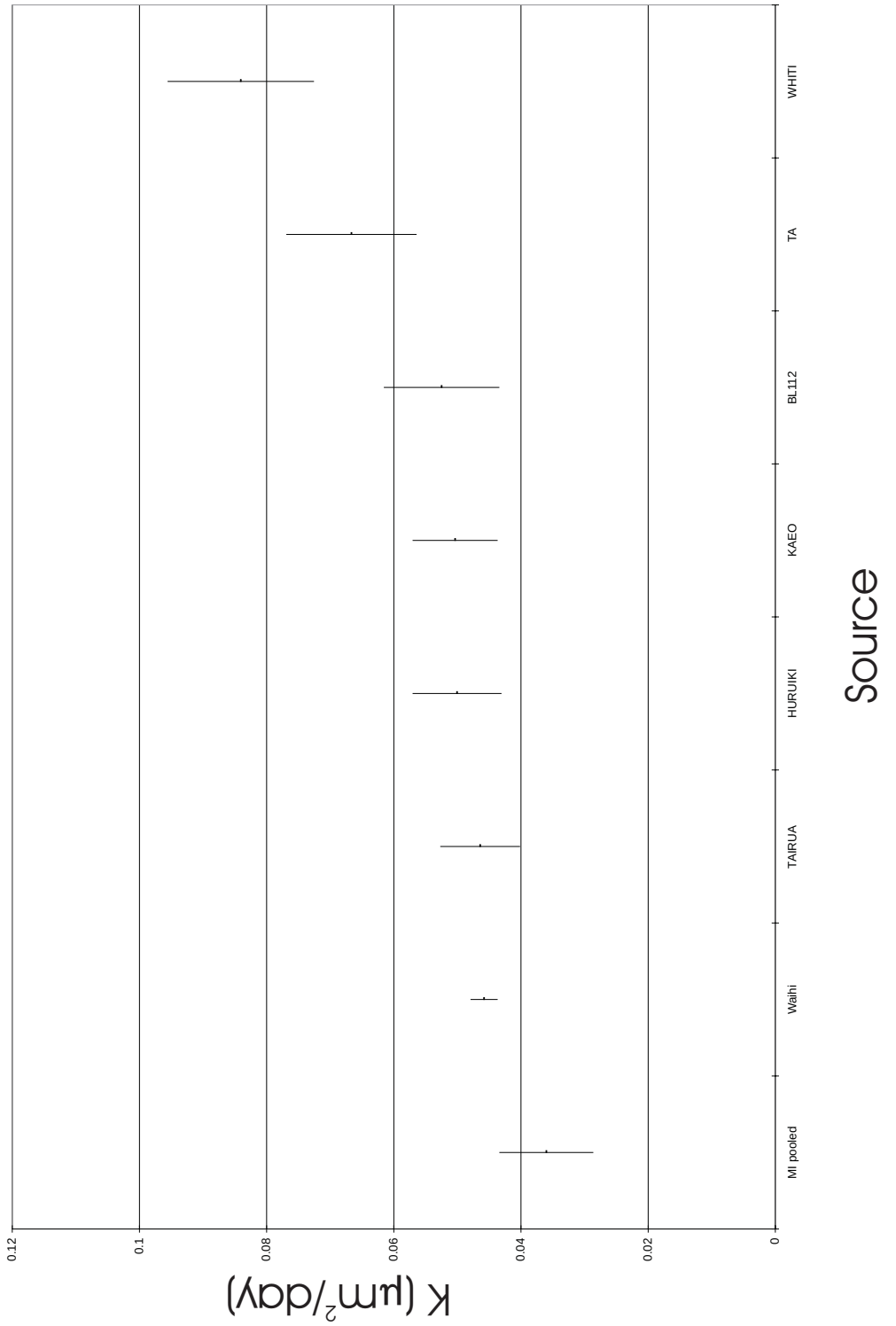

Figure E.18: 112.5 ^{0}C source rate comparison data

Martin Jones 2002

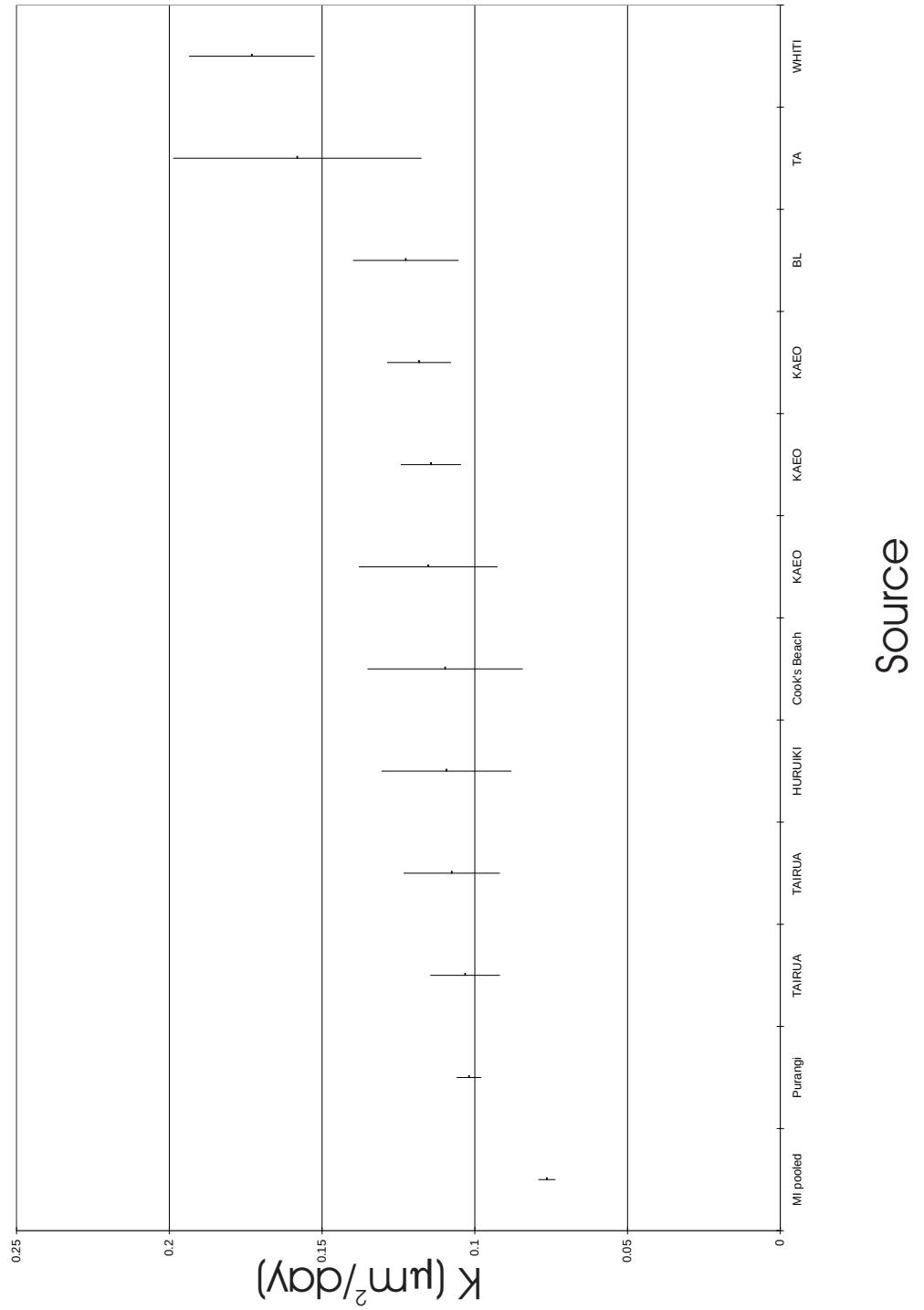

Figure E.19: 125^0C source rate comparison data

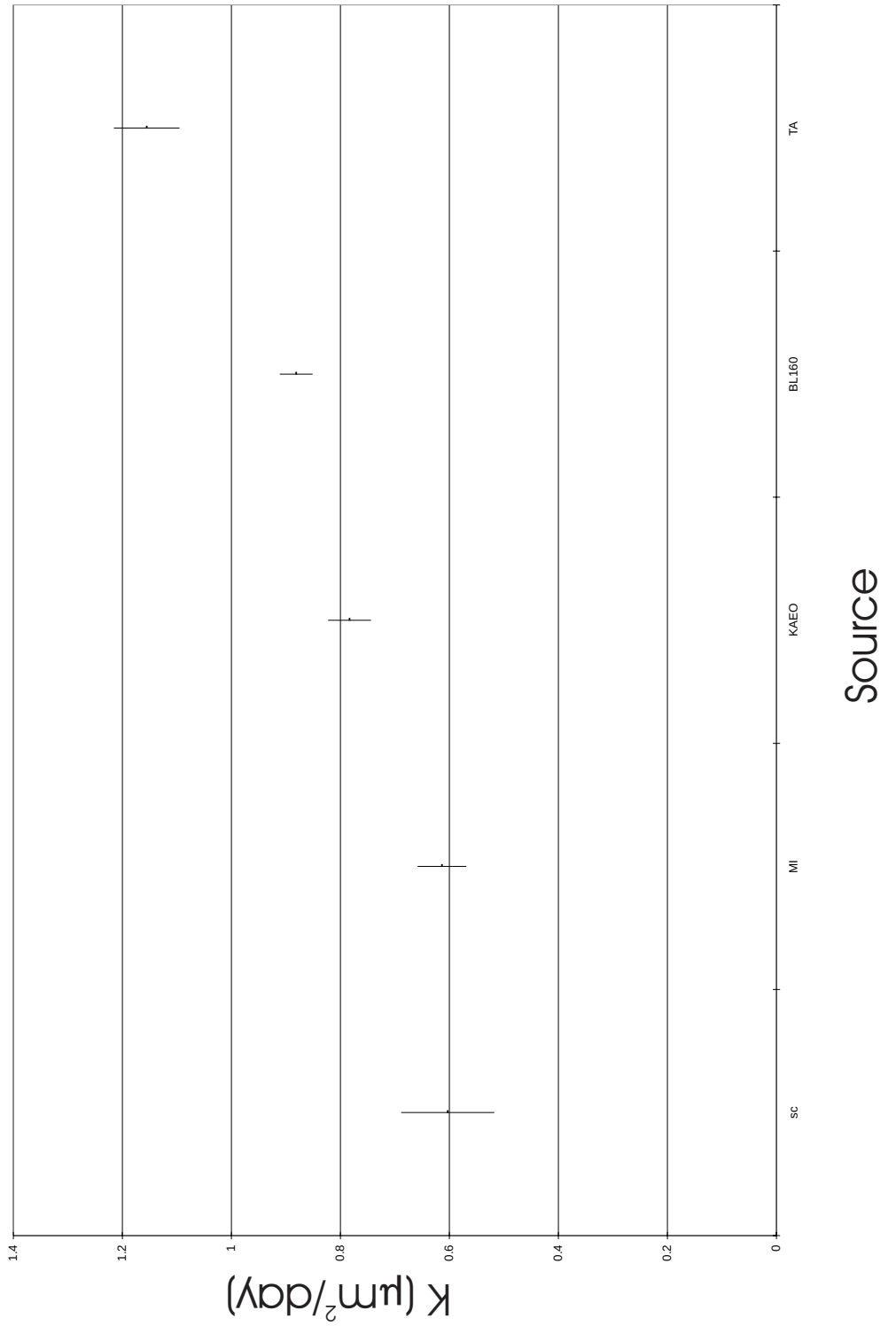

Figure E.20: 160 ^{0}C source rate comparison data

Martin Jones 2002

Appendix F

New Zealand Meteorological Database

F.1 Daily Meteorological Data

Martin Jones 2002

Table F.1: Station details for the daily meteorological database

station	name	Type	alt	map	Easting	Northing
A42462	CAPE REINGA AWS	AWS	191	M02816525	2481600	6752500
A53125	KAITAIA OBSERVATORY	Climatological	85	O04348742	2534800	6674200
A53191	KERIKERI EWS	EDR Research/EWS	79	P05952684	2595200	6668400
A53487	KAIKOHE EDR	EDR/EDL	204	P05854418	2585400	6641800
A53982	DARGAVILLE	Climat/Synop	15	P07860841	2586000	6584100
A54737	WHANGAREI AERO AWS	AWS	37	Q07340028	2634000	6602800
A55912	MOKOHINAU AWS	AWS	60	S07016864	2701600	6586400
A64282	LEIGH 2	Climatological	27	R09719462	2671900	6546200
A64463	WARKWORTH	Climat/Synop	72	R09601285	2660100	6528500
A64863	WHANGAPARAOA AWS	AWS	89	R10746092	2674600	6509200
A6487A	AUCKLAND CITY EDR	EDR/EDL	75	R11665810	2666500	6481000
A64971	AUCKLAND,OWAIRAKA	Climatological	41	R11642775	2664200	64777500

Table F.2: Daily data variables recorded at each station

Station	C	V	DIR	SPD	Dry bulb temp	Wet bulb temp	Rh	5CM	10CM	20CM	30CM	100CM	Air Pressure	SUN	RAD	MAXDIR	gustspeed	EVAP
A42462			✓	✓	✓	✓	✓						✓					
A53125	✓	✓	✓	✓	✓	✓	✓	✓	✓	✓	✓	✓	✓	✓	✓	✓	✓	✓
A53191	✓	✓	✓	✓	✓	✓	✓	✓	✓	✓	✓	✓	✓		✓	✓		✓
A53487			✓	✓	✓	✓	✓		✓	✓	✓	✓			✓	✓	✓	
A53982	✓	✓	✓	✓	✓	✓	✓						✓	✓				
A54737			✓	✓	✓	✓	✓						✓		✓	✓	✓	
A55912			✓	✓	✓	✓	✓						✓			✓	✓	
A64282	✓	✓	✓	✓	✓	✓	✓			✓	✓	✓	✓		✓	✓	✓	✓
A64463	✓	✓	✓	✓	✓	✓	✓		✓				✓			✓	✓	
A64863	✓	✓	✓	✓	✓	✓	✓											
A6487A			✓	✓	✓	✓	✓				✓					✓	✓	
A64971	✓	✓	✓	✓	✓	✓	✓		✓	✓	✓							

F.2 Long-Term Meteotological Data

Martin Jones 2002

Table F.3: Station details for the long-term meteorological database

station	name	Type	alt	map	Easting	Northing	recording start	recording finish
A42461	CAPE REINGA	Climat/Synop	68.2	M02816525	2481600	6752500	7/1/1919	9/1/1987
A42581	TE PAKI STN, TE HAPUA	Climatological	42.2	N02922440	2492200	6744000	7/1/1931	9/1/1973
A53021	KAITAIA AERO	Climat/Synop	37.1	O04343773	2543400	6677300	12/1/1948	1/1/1986
A53125	KAITAIA OBSERVATORY	Climatological	12.8	O04348742	2543400	6674200	4/1/1985	1/1/1998
A53191	KERIKERI EWS	EDR Research/EWS	16.4	P05952684	2595200	6668400	8/1/1981	1/1/1998
A53193	KERIKERI DOWNS 2	Climatological	2.8	P05960688	2596000	6668800	7/1/1984	5/1/1987
A53291	KERIKERI 1	Climatological	38.4	P05971632	2597100	6663200	8/1/1935	12/1/1973
A53482	KAIKOHE D.S.I.R.	Climatological	13.3	P05855418	2585500	6641800	12/1/1972	4/1/1986
A53487	KAIKOHE EDR	EDR/EDL	12.3	P05854418	2585400	6641800	10/1/1985	1/1/1998
A53982	DARGAVILLE	Climat/Synop	55.0	P07860841	2586000	6584100	1/1/1943	1/1/1998
A54601	PUKETURUA NORTHLAND	Climatological	11.0	P06085138	2608500	6613800	12/1/1964	12/1/1975
A55911	MOKOHINAU	Climat/Synop	45.7	.	2701752.12	6586902.97	11/1/1934	7/1/1980
A64741	WOODHILL FOREST	Climatological	46.0	Q10382940	2638200	6494000	1/1/1948	1/1/1994
A64751	RIVERHEAD FOREST	Climatological	59.0	R10514919	2651400	6491900	4/1/1928	3/1/1987
A64761	KUMEU	Climatological	.	.			2/1/1978	12/1/1989
A64863	HENDERSON, RIVER PK	Climatological	25.4	R11552820	2655200	6482000	9/1/1972	1/1/1998
A64865	AUCKLAND REGIONAL COUNCIL, HENDERSON	EDR Research/EWS	3.2	R11559810	2655900	6481000	11/1/1994	1/1/1998
A64871	AUCKLAND REGIONAL COUNCIL, HENDERSON	EDR Research/EWS	.	.			11/1/1994	1/1/1998
A64872	MECHANICS BAY	Climat/Synop	14.6	R11698823	2669800	6482300	1/1/1948	8/1/1962

continued on the next page

Table F.3: *continued*

station	name	Type	alt	map	Easting	Northing	recording start	recording finish
A64878	AUCKLAND CITY	Climat/Synop	28.3	R11665810	2666500	6481000	9/1/1962	12/1/1990
A64971	AUCKLAND,OWAIRAKA	Climatological	49.0	R11642775	2664200	6477500	1/1/1949	1/1/1998
A74052	MANUKAU HEADS 2	Climat/Synop	62.2	Q12477599	2647700	6459900	11/1/1935	1/1/1998
B75152	THAMES 2	Climatological	40.3	T12369463	2736900	6446300	10/1/1957	1/1/1998
B75182	TAIRUA FOREST	Climatological	41.0	T12637440	2763700	6444000	1/1/1953	1/1/1994
B75252	NGATEA 1	Climat/Synop	14.0	T12341348	2734100	6434800	1/1/1961	1/1/1975
B75361	PAEROA	Climatological	79.8	T13462216	2746200	6421600	4/1/1914	1/1/1994
B75362	PAEROA AWS	AWS	7.4	T13480221	2748000	6422100	8/1/1990	1/1/1998
B75381	WAIHI	Climatological	91.0	T13618194	2761800	6419400	10/1898	12/1/1989
B75382	WAIHI, BARRY ROAD EWS	EDR Research/EWS	14.3	T13623198	2762300	6419800	10/1/1983	1/1/1998
B75571	TE AROHA	Climatological	109.0	T13502027	2750200	6402700	01/1889	1/1/1998
B75592	KATIKATI	Climatological	18.2	U13705020	2770500	6402000	11/1/1979	1/1/1998
B76611	TAURANGA	Climatological	24.0	U14894870	2789400	6387000	1/1/1970	1/1/1994
B76621	TAURANGA	Climatological	.	.			1/1/1970	1/1/1994
B76624	TAURANGA AERO AWS	AWS	7.9	U14921874	2792100	6387400	2/1/1990	1/1/1998
B76835	TE PUKE	Climatological	16.8	U14026706	2802600	6370600	1/1/1973	10/1/1989
B76836	TE PUKE EDR	EDR/EDL	10.6	U14026706	2802600	6370600	1/1/1986	8/1/1996
B76984	EDGECUMBE DAIRY CO	Climatological	16.7	V15469511	2846900	6351100	7/1/1970	3/1/1987
B76995	WHAKATANE AERO AWS	AWS	7.4	W15546568	2854600	6356800	8/1/1990	1/1/1998
B85284	TOKOROA	Climat/Synop	8.9	T16618271	2761800	6327100	8/1/1958	7/1/1967
B85285	KINLEITH 2	Climat/Synop	22.7	T16628210	2762800	6321000	7/1/1967	3/1/1990
B86124	WHAKAREWAREWA	Climatological	83.0	U16960327	2796000	6332700	01/1899	1/1/1982
B86131	ROTORUA AERO 2	Climat/Synop	34.2	U16010384	2801000	6338400	11/1/1963	1/1/1998
B86133	ROTORUA AERO AWS	AWS	16.6	U16009388	2800900	6338800	6/1/1981	1/1/1998

continued on the next page

Table F.3: *continued*

station	name	Type	alt	map	Easting	Northing	recording start	recording finish
B86602	TAUPO N.Z.E.D.	Climatological	44.1	U18773759	2777300	6275900	12/1/1949	1/1/1994
B86611	WAIRAKEI POWER STN	Climat/Synop	37.4	U17802817	2780200	6281700	7/1/1951	12/1/1988
B86612	WAIRAKEI RESEARCH STN	Climatological	25.5	U17809829	2780900	6282900	12/1/1961	6/1/1987
B87103	WAIMANA	Climatological	42.6	W16676318	2867600	6331800	6/1/1955	1/1/1998
C64971	AUCKLAND,MANGERE	Climatological	38.9	R11685689	2668500	6468900	2/1/1959	1/1/1998
C64981	AUCKLAND,OTARA	Climatological	34.5	R11771702	2677100	6470200	1/1/1952	7/1/1986
C74082	AUCKLAND AERO	AWS	35.7	R11696647	2669600	6464700	5/1/1962	1/1/1998
C74091	ARDMORE	Climatological	53.5	R11852614	2685200	6461400	7/1/1944	1/1/1998
C74191	PAERATA	Climatological	35.3	R12782487	2678200	6448700	3/1/1924	6/1/1959
C74282	PUKEKOHE M.A.F.	Climatological	19.9	R12757423	2675700	6442300	10/1/1969	9/1/1989
C74283	PUKEKOHE EWS	EDR Research/EWS	11.9	R12757423	2675700	6442300	2/1/1986	1/1/1998
C74371	WAIUKU FOREST	Climatological	56.0	R13626273	2662600	6427300	1/1/1940	12/1/1995
C75731	RUAKURA	Climatological	91.9	S14140779	2714000	6377900	7/1/1905	5/1/1997
C75733	RUAKURA EWS	EDR Research/EWS	1.3	S14140779	2714000	6377900	10/1/1996	1/1/1998
C75801	WHATAWHATA	Climatological	45.4	S14940749	2694000	6374900	9/1/1952	1/1/1998
C75831	RUKUHIA	Climatological	38.0	S14127724	2712700	6372400	9/1/1946	9/1/1984
C75842	CAMBRIDGE	Climatological	13.0	1/0/1900	2727202.31	6366102.16	7/1/1928	7/1/1941
C75953	CAMBRIDGE	Climatological	15.0	S15298620	2729800	6362000	3/1/1975	3/1/1990
C85132	WAIKERIA	Climatological	20.8	S15196431	2719600	6343100	4/1/1977	1/1/1998
C85141	WAIKERIA	Climatological	55.7	S15203400	2720300	6340000	7/1/1921	3/1/1977
C85314	TE KUITI	Climat/Synop	38.9	S16983169	2698300	6316900	3/1/1959	1/1/1998
C94001	NEW PLYMOUTH	Climatological	109.0	P19037367	2603700	6237178.29	1/1/1864	12/1/1973
C94002	OMATA	Climatological	18.7	P19968345	2596593.68	6234500	10/1/1970	6/1/1989
C94003	NEW PLYMOUTH	Climatological	19.5	P19037367	2603700	6236700	1/1/1974	7/1/1993
C94011	NEW PLYMOUTH AERO	Climat/Synop	54.0	Q19124432	2612400	6243200	1/1/1944	1/1/1998
C94012	NEW PLYMOUTH AWS	AWS	16.1	Q19121436	2612100	6243600	12/1/1981	1/1/1998

continued on the next page

Table F.3: *continued*

station	name	Type	alt	map	Easting	Northing	recording start	recording finish
C95022	LOWER RETARUKE	Climatological	31.6	S19001342	2700100	6234200	6/1/1966	1/1/1998
D05964	WAINGAWA	Climat/Synop	65.1	S26297221	2729700	6022100	2/1/1926	3/1/1991
D05973	MASTERTON, TE ORE	Climatological	5.3	T26378245	2737800	6024500	9/1/1992	1/1/1998
D06022	KOPUA	Climatological	35.5	U23892202	2789200	6120200	7/1/1962	1/1/1998
D06051	WAIPUKURAU AERO	Climatological	51.0	V23116286	2811600	6128600	1/1/1945	1/1/1996
D06212	DANNEVIRKE	Climatological	47.0	U23746062	2774600	6106200	1/1/1951	1/1/1998
D15253	MARTINBOROUGH,CANNOCK	Climatological	4.6	1/0/1900	2726409.21	5990299.7	1/1/1954	8/1/1958
D78931	RUATORIA	Climatological	36.4	Z15775536	2977500	6353600	7/1/1960	12/1/1996
D87683	GISBORNE, MANUTUKE	Climatological	48.4	Y18351690	2935100	6269000	2/1/1945	6/1/1993
D87692	GISBORNE AERO	Climat/Synop	60.7	Y18438707	2943800	6270700	5/1/1937	1/1/1998
D87695	GISBORNE AWS	AWS	8.2	Y18437708	2943700	6270800	11/1/1989	1/1/1998
D96241	MAKAHU SADDLE	Climatological	9.3	U20037075	2803700	6207500	1/1/1966	4/1/1975
D96484	NAPIER AERO AWS	AWS	7.3	V21420868	2842000	6186800	9/1/1990	1/1/1998
D96491	NAPIER	Climatological	104.0	1/0/1900	2846900.8	6184108.01	07/1862	1/1/1966
D96591	NAPIER NELSON PK	Climatological	136.0	V21463821	2846300	6182100	07/1862	1/1/1998
D96680	HASTINGS FIRE STATION	Climatological	8.2	V21386679	2838600	6167900	10/1/1981	12/1/1989
D96681	HASTINGS	Climatological	74.0	V21400677	2840000	6167700	01/1892	8/1/1966
D96688	HASTINGS	Climatological	16.1	V21397662	2839700	6166200	10/1/1965	11/1/1981
D96689	HAVELOCK NTH D.S.I.R. 1	Climatological	33.0	V21429640	2842900	6164000	9/1/1950	9/1/1983
D9668A	HAVELOCK NTH D.S.I.R. 2	Climatological	7.3	V21429640	2842900	6164000	6/1/1982	9/1/1989
D9668B	HAVELOCK NTH EDR	EDR/EDL	8.4	V21429640	2842900	6164000	12/1/1985	5/1/1994
D96696	WHAKATU EWS	EDR Research/EWS	0.3	V21459700	2845900	6170000	9/1/1997	1/1/1998
D96931	MAKARETU	Climatological	22.8	U22937343	2793700	6134300	8/1/1967	5/1/1990
E05041	MARTON,M.A.F.	Climatological	19.5	S23137224	2713700	6122400	7/1/1947	1/1/1967

continued on the next page

Table F.3: *continued*

station	name	Type	alt	map	Easting	Northing	recording start	recording finish
E05221	BULLS,FLOCKHOUSE	Climatological	63.0	S23041039	2704100	6103900	9/1/1926	9/1/1989
E05231	BULLS,FLOCKHOUSE	Climatological	.	.			9/1/1926	9/1/1989
E05343	PALMERSTON N KAIRANGA	Climatological	20.8	S24197933	2719700	6093300	12/1/1969	9/1/1990
E05363	PALMERSTON N	Climatological	69.7	T24317885	2731700	6088500	5/1/1928	1/1/1998
E05368	PALMERSTON NORTH AWS	AWS	6.6	T24319948	2731900	6094800	6/1/1991	1/1/1998
E05620	LEVIN AWS	AWS	7.3	S25009626	2700900	6062600	10/1/1990	1/1/1998
E05622	LEVIN M.A.F.	Climatological	96.0	S25019595	2701900	6059500	07/1895	2/1/1991
E14272	WELLINGTON,KELBURN	Climatological	70.0	R27580899	2658000	5989900	1/1/1928	1/1/1998
E14273	MAKARA	Climatological	20.3	R27520937	2652474.2	5993999.6	5/1/1955	8/1/1975
E15102	WALLACEVILLE	Climatological	74.1	R27823061	2682300	6006100	1/1/1924	1/1/1998
E94313	STRATFORD MTN HOUSE	Climatological	23.7	P20068101	2606800	6210100	1/1/1963	9/1/1986
E94333	STRATFORD DEM FARM	Climatological	37.6	Q20224068	2622400	6206800	6/1/1960	1/1/1998
E94512	MANAIA DEM FARM	Climatological	31.0	P21085857	2608500	6185700	1/1/1959	1/1/1990
E9452A	NORMANBY EDR	EDR/EDL	11.7	Q21177878	2617700	6187800	5/1/1986	1/1/1998
E95902	WANGANUI,SPRIGGENS PARK EWS	EDR Research/EWS	126.0	R22847389	2684700	6138900	01/1872	1/1/1998
F03501	FAREWELL SPIT	Climat/Synop	110.0	N24107732	2510700	6073200	01/1874	6/1/1984
F03502	FAREWELL SPIT AWS	AWS	20.3	N24107732	2510700	6073200	10/1/1977	1/1/1998
F20791	HOKITIKA SOUTH	Climat/Synop	98.0	J33427290	2342700	5829000	01/1866	12/1/1964
F20793	HOKITIKA AERO	Climat/Synop	34.1	J32452306	2345200	5830600	12/1/1963	1/1/1998
F20794	HOKITIKA AWS	AWS	17.3	J32448306	2344800	5830600	9/1/1980	1/1/1998
F21182	REEFTON EWS	EDR Research/EWS	37.4	L30156984	2415600	5898400	8/1/1960	1/1/1998
F66161	PUYSEGUR POINT	Climat/Synop	106.0	B46168310	2016800	5431000	06/1880	4/1/1987
F66162	PUYSEGUR POINT AWS	AWS	17.1	B46168310	2016800	5431000	12/1/1980	1/1/1998

continued on the next page

Table F.3: *continued*

station	name	Type	alt	map	Easting	Northing	recording start	recording finish
G12581	GOLDEN DOWNS FOREST	Climatological	51.0	N28002623	2500200	5962300	5/1/1929	4/1/1980
G13211	APPLEBY	Climatological	65.0	N27183906	2518300	5990600	1/1/1932	12/1/1996
G13212	APPLEBY EWS	EDR Research/EWS	1.3	N27183906	2518300	5990600	9/1/1996	1/1/1998
G13222	NELSON AERO	Climat/Synop	57.5	N27289899	2528900	5989900	7/1/1940	1/1/1998
G13231	NELSON	Climatological	90.0	O27347926	2534700	5992600	07/1862	1/1/1952
G13301	MOUTERE HILLS	Climatological	25.8	N27163833	2516300	5983300	8/1/1960	5/1/1986
G13322	NELSON AWS	AWS	17.3	N27283896	2528300	5989600	9/1/1980	1/1/1998
G13494	BLENHEIM RESEARCH	Climatological	12.4	P28904673	2590400	5967300	8/1/1985	1/1/1998
G13495	BLENHEIM RESEARCH EWS	EDR Research/EWS	2.0	P28904673	2590400	5967300	1/1/1996	1/1/1998
G13592	BLENHEIM	Climatological	58.5	P28896660	2589600	5966000	4/1/1927	9/1/1985
G14711	GRASSMERE SALT WORKS	Climatological	54.5	P29053416	2605300	5941600	8/1/1943	1/1/1998
G14721	CAPE CAMPBELL	Climat/Synop	113.0	Q29160412	2616000	5941200	10/1873	9/1/1986
H21951	ARTHURS PASS	Climat/Synop	91.9	K33926063	2392600	5806300	3/1/1906	1/1/1998
H22783	ARTHURS PASS	Climat/Synop	.	.			3/1/1906	1/1/1998
H22871	BALMORAL FOREST	Climatological	70.1	M33895159	2489500	5815900	6/1/1921	7/1/1991
H30711	MT COOK,THE HERMITAGE	Climatological	96.7	H36759154	2275900	5715400	6/1/1901	1/1/1998
H30841	GODLEY PEAKS, TEKAPO	Climatological	62.4	I37068018	2306800	5701800	1/1/1914	5/1/1976
H31241	HARPER RIVER	Climatological	74.1	K34850762	2385000	5776200	1/1/1924	1/1/1998
H31352	LAKE COLERIDGE	Climatological	83.2	K35908594	2390800	5759400	9/1/1913	11/1/1996
H31562	RUDSTONE	Climatological	40.4	K36049396	2404900	5739600	5/1/1913	10/1/1953
H31572	RUDSTONE	Climatological	.	.			5/1/1913	10/1/1953
H31883	WINCHMORE EWS	EDR Research/EWS	51.0	L36129121	2412900	5712100	1/1/1947	1/1/1998

continued on the next page

Table F.3: *continued*

station	name	Type	alt	map	Easting	Northing	recording start	recording finish
H31971	ASHBURTON COUNCIL	Climatological	88.7	K37093004	2409300	5700400	5/1/1909	1/1/1998
H32252	ASHLEY FOREST 1	Climatological	48.2	M34767737	2476700	5773700	11/1/1941	1/1/1990
H32352	RANGIORA	Climatological	33.3	M35752664	2475200	5766400	1/1/1965	4/1/1998
H32412	DARFIELD	Climatological	78.2	L35402459	2440200	5745900	11/1/1919	1/1/1998
H32424	EYREWELL FOREST	Climatological	47.9	M35515566	2451500	5756600	1/1/1942	12/1/1989
H32451	CHRISTCHURCH AERO	AWS	54.3	M35726461	2472600	5746100	10/1/1943	1/1/1998
H32561	CHRISTCHURCH GARDENS	Climatological	134.0	M35792419	2479200	5741900	1/1/1864	1/1/1998
H32641	LINCOLN	Climatological	106.0	M36667289	2466700	5728900	01/1881	12/1/1987
H32642	LINCOLN, BROADFIELD EDL	Climatological	25.9	M36671311	2467100	5731100	3/1/1972	1/1/1998
H40041	LAKE TEKAPO, AIR SAFARIS	Climatological	71.3	I37048862	2304800	5686200	10/1/1926	1/1/1998
H40182	FAIRLIE	Climatological	53.2	J38358760	2335800	5676000	5/1/1925	7/1/1978
H40892	IKAWAI	Climatological	24.8	J40471909	2347100	5590900	4/1/1969	1/1/1994
H41131	ORARI ESTATE	Climatological	101.0	K38746744	2374600	5674400	10/1897	1/1/1998
H41323	TEMUKA	Climatological	.	.			1/1/1961	1/1/1994
H41325	TIMARU AERO AWS	AWS	7.7	J38684545	2368400	5654500	5/1/1990	1/1/1998
H41411	ADAIR	Climatological	36.6	J39639402	2363900	5640200	11/1/1949	6/1/1986
H41421	TIMARU GARDENS	Climatological	88.0	K39706428	2370600	5642800	01/1897	11/1/1985
H41424	TIMARU 2	Climatological	101.0	K39709427	2370900	5642700	01/1897	1/1/1998
H41701	WAIMATE	Climatological	100.0	J40544056	2354400	5605600	01/1898	1/1/1998
I41901	OAMARU AIRPORT	Climat/Synop	42.9	J41586801	2358600	5580100	12/1/1942	11/1/1985
I49591	OMARAMA,TARA HILLS	Climatological	36.1	H39627265	2262700	5626500	11/1/1949	12/1/1985
I49592	TARA HILLS EDR	EDR/EDL	12.8	H39628266	2262800	5626600	4/1/1985	1/1/1998

continued on the next page

Table F.3: *continued*

station	name	Type	alt	map	Easting	Northing	recording start	recording finish
I49711	WANAKA	Climat/Synop	60.5	F40047045	2204700	5604500	2/1/1930	8/1/1990
I50012	NASEBY FOREST 1	Climatological	60.3	H41807712	2280700	5571200	1/1/1923	4/1/1983
I50102	GIMMERBURN EDL	EDR/EDL	4.2	H42781539	2278100	5553900	1/1/1982	3/1/1986
I50113	RANFURLY MANIOTOTO	Climatological	14.8	H41817608	2281700	5560800	3/1/1975	12/1/1989
I50212	WAIPIATA	Climatological	41.7	H42858484	2285800	5548400	1/1/1925	9/1/1966
I50471	PALMERSTON	Climatological	28.9	J43311234	2331100	5523400	2/1/1969	1/1/1998
I50771	TAIAROA HEAD	Climat/Synop	62.8	J44332900	2333200	5490000	4/1/1935	1/1/1998
I50831	INVERMAY, TAIERI	Climatological	37.9	I44049802	2304900	5480200	5/1/1939	3/1/1977
I50835	INVERMAY, TAIERI	Climatological	9.8	I44068798	2306800	5479800	3/1/1976	12/1/1985
I50836	INVERMAY EDR	EDR/EDL	9.5	I44068798	2306800	5479800	4/1/1985	10/1/1994
I50951	DUNEDIN,MUSSELBURGH	Climat/Synop	79.7	I44169754	2316900	5475891.94	1/1/1918	9/1/1997
I50954	DUNEDIN, MUSSELBURGH EWS	EDR Research/EWS	0.4	I44169754	2317180.31	5475400	8/1/1997	1/1/1998
I58061	QUEENSTOWN	Climatological	127.0	E41684657	2168400	5565700	09/1871	1/1/1998
I58075	QUEENSTOWN AWS	AWS	20.4	F41741675	2174100	5567500	8/1/1977	1/1/1998
I59065	LAUDER EWS	EDR Research/EWS	12.5	G41489690	2248900	5569000	7/1/1985	1/1/1998
I59161	OPHIR 2	Climatological	73.8	G41433614	2243300	5561400	4/1/1924	1/1/1998
I59162	MOA CREEK	Climatological	70.9	G42471522	2247100	5552200	6/1/1913	4/1/1984
I59232	EARNSCLEUGH D.S.I.R.	Climatological	35.9	G42220461	2222000	5546100	5/1/1947	4/1/1983
I59234	ALEXANDRA	Climat/Synop	61.7	G42266440	2226600	5544000	1/1/1922	9/1/1983
I59235	CLYDE	Climatological	13.4	G42204494	2220400	5549400	1/1/1983	6/1/1996
I59238	ALEXANDRA, THEYERS ST	Climatological	10.3	G42259444	2225900	5544400	10/1/1983	1/1/1994
I59239	CLYDE EWS	EDR Research/EWS	1.8	G42204494	2220400	5549400	4/1/1996	1/1/1998
I59722	MOA FLAT	Climatological	44.7	G44207877	2220700	5487700	1/1/1936	9/1/1980
I59842	BEAUMONT N.Z.F.S.	Climatological	47.4	G44369770	2236900	5477000	12/1/1939	4/1/1987
I59891	MAHINERANGI DAM	Climatological	46.8	H44751764	2275100	5476400	6/1/1943	3/1/1990

continued on the next page

Table F.3: *continued*

station	name	Type	alt	map	Easting	Northing	recording start	recording finish
I59921	TAPANUI	Climatological	101.0	G45197674	2219700	5467400	05/1897	1/1/1998
I68093	EAST GORE	Climatological	59.0	F45970500	2197000	5450000	1/1/1907	12/1/1965
I68182	GORE EDR	EDR/EDL	11.5	F45920470	2192000	5447000	7/1/1986	1/1/1998
I68191	GORE	Climatological	28.6	F45958482	2195800	5448200	1/1/1943	8/1/1971
I68192	GORE,GRASSLANDS D.S.I.R.	Climatological	15.4	F45924470	2192400	5447000	9/1/1971	2/1/1987
I68252	HOKONUI FOREST	Climatological	51.7	E46691352	2169100	543200	7/1/1935	3/1/1987
I68362	WOODLANDS	Climatological	15.4	F46709174	2170900	5417400	3/1/1971	8/1/1986
I68431	INVERCARGILL	Climatological	62.0	1/0/1900	2153625.53	5413238.08	04/1890	6/1/1952
I68433	INVERCARGILL AERO	Climat/Synop	58.4	E46508110	2150800	5411000	9/1/1939	1/1/1998
I68435	INVERCARGILL AERO AWS	AWS	2.9	E46498116	2149800	5411600	2/1/1995	1/1/1998
I69191	MILTON	Climatological	56.0	H45757507	2275700	5450700	12/1/1929	12/1/1985
I69481	NUGGET POINT	Climat/Synop	59.2	H46647131	2264700	5413100	1/1/1930	3/1/1989

Table F.4: Long-term data variables recorded at each station

STATION	Air Max	Air Min	Grass Min	Extreme Air Max	Extreme Air Min	Extreme Grass Min	Min Air Max	Max Air Min	5cm	10cm	20cm	30cm	50cm	100cm	Global Radiation	Total Sun	Max Wind Run	Wind Run	VPRESS	Mean Rh	Sunken Pan Evap	Penman
A42461	✓	✓		✓	✓		✓	✓												✓		
A42581	✓	✓	✓	✓	✓	✓	✓	✓				✓				✓				✓		
A53021	✓	✓	✓	✓	✓	✓	✓	✓		✓	✓	✓			✓	✓				✓		✓
A53125																						✓
A53191																						✓
A53193																						✓
A53291	✓	✓	✓	✓	✓	✓	✓	✓		✓	✓	✓				✓				✓		
A53482	✓	✓	✓	✓	✓	✓	✓	✓		✓	✓	✓		✓		✓		✓		✓		✓
A53487									✓				✓									✓
A53982	✓	✓	✓	✓	✓	✓	✓	✓		✓	✓	✓				✓		✓		✓		✓
A54601	✓	✓	✓	✓	✓		✓	✓		✓	✓	✓		✓	✓			✓		✓		
A55911	✓	✓	✓	✓	✓		✓	✓														
A64741	✓	✓	✓	✓	✓	✓	✓	✓				✓		✓			✓	✓		✓		
A64751	✓	✓	✓	✓	✓	✓	✓	✓														
A64761																						✓
A64863	✓	✓	✓	✓	✓	✓	✓	✓												✓		
A64865	✓	✓		✓	✓		✓	✓							✓		✓	✓				
A64871																						✓
A64872																						✓
A64878																						✓
A64971	✓	✓	✓	✓	✓	✓	✓	✓		✓	✓	✓								✓		
A74052	✓	✓	✓	✓	✓	✓	✓	✓												✓		

continued on the next page

Table F.4: *continued*

STATION	Air Max	Air Min	Grass Min	Extreme Air Max	Extreme Air Min	Extreme Grass Min	Min Air Max	Max Air Min	5cm	10cm	20cm	30cm	50cm	100cm	Global Radiation	Total Sun	Max Wind Run	Wind Run	VPRESS	Mean Rh	Sunken Pan Evap	Penman
B75152	✓	✓	✓	✓	✓	✓	✓	✓								✓	✓	✓	✓	✓		✓
B75182	✓	✓	✓	✓	✓	✓	✓	✓											✓	✓		
B75252	✓	✓	✓	✓	✓	✓	✓	✓		✓	✓	✓		✓			✓	✓	✓	✓		
B75361	✓	✓	✓	✓	✓	✓	✓	✓		✓	✓	✓							✓	✓		
B75362																				✓		✓
B75381	✓	✓	✓	✓	✓	✓	✓	✓		✓		✓				✓	✓	✓	✓	✓		✓
B75382																				✓		✓
B75571	✓	✓	✓	✓	✓	✓	✓	✓				✓							✓	✓		
B75592	✓	✓	✓	✓	✓	✓	✓	✓											✓	✓		
B76611	✓	✓	✓	✓	✓	✓	✓	✓								✓			✓	✓		
B76621																				✓		✓
B76624																				✓		✓
B76835	✓	✓	✓	✓	✓	✓	✓	✓		✓	✓	✓		✓		✓	✓	✓	✓	✓		✓
B76836													✓							✓		✓
B76984	✓	✓	✓	✓	✓	✓	✓	✓		✓	✓	✓							✓	✓		
B76995																				✓		✓
B85284	✓	✓	✓	✓	✓	✓	✓			✓	✓	✓		✓								
B85285	✓	✓	✓	✓	✓	✓	✓	✓	✓	✓	✓	✓		✓					✓	✓		
B86124	✓	✓	✓	✓	✓	✓	✓	✓		✓	✓	✓				✓	✓	✓	✓	✓		✓
B86131	✓	✓	✓	✓	✓	✓	✓	✓							✓	✓			✓	✓		
B86133	✓	✓	✓	✓	✓	✓	✓	✓							✓		✓	✓	✓	✓		
B86602	✓	✓	✓	✓	✓	✓	✓	✓	✓	✓	✓	✓		✓		✓	✓	✓	✓	✓	✓	✓
B86611	✓	✓	✓	✓	✓	✓	✓	✓											✓	✓		

continued on the next page

Table F.4: *continued*

STATION	Air Max	Air Min	Grass Min	Extreme Air Max	Extreme Air Min	Extreme Grass Min	Min Air Max	Max Air Min	5cm	10cm	20cm	30cm	50cm	100cm	Global Radiation	Total Sun	Max Wind Run	Wind Run	VPRESS	Mean Rh	Sunken Pan Evap	Penman
B86612	✓	✓	✓	✓	✓	✓	✓	✓		✓	✓	✓		✓						✓		
B87103	✓	✓	✓	✓	✓	✓	✓	✓		✓	✓	✓		✓		✓	✓	✓	✓	✓		✓
C64971									✓													✓
C64981	✓	✓	✓	✓	✓	✓	✓	✓		✓	✓	✓		✓			✓	✓	✓	✓		
C74082	✓	✓	✓	✓	✓	✓	✓	✓		✓	✓	✓		✓	✓	✓	✓	✓	✓	✓		✓
C74091	✓	✓	✓	✓	✓	✓	✓	✓												✓		
C74191	✓	✓	✓	✓	✓	✓			✓	✓												
C74282	✓	✓	✓	✓	✓	✓	✓	✓	✓	✓	✓	✓				✓	✓	✓	✓	✓		✓
C74283	✓	✓	✓	✓	✓	✓	✓	✓	✓	✓	✓	✓	✓	✓	✓	✓	✓	✓	✓	✓	✓	✓
C74371	✓	✓	✓	✓	✓	✓	✓	✓				✓		✓								
C75731	✓	✓	✓	✓	✓	✓	✓	✓	✓	✓	✓	✓		✓	✓	✓	✓	✓	✓	✓		✓
C75733													✓									
C75801	✓	✓	✓	✓	✓	✓	✓	✓	✓	✓	✓	✓		✓	✓	✓	✓	✓	✓	✓	✓	✓
C75831	✓	✓	✓	✓	✓	✓	✓	✓		✓	✓	✓		✓	✓	✓	✓	✓	✓	✓		✓
C75842																✓						
C75953	✓	✓	✓	✓	✓	✓	✓	✓		✓	✓	✓		✓			✓	✓	✓	✓		
C85132	✓	✓	✓	✓	✓	✓	✓	✓		✓	✓	✓		✓					✓	✓		
C85141	✓	✓	✓	✓	✓	✓	✓	✓		✓	✓	✓		✓			✓		✓	✓		
C85314	✓	✓	✓	✓	✓	✓	✓	✓		✓	✓	✓				✓	✓	✓	✓	✓		✓
C94001	✓	✓	✓	✓	✓	✓	✓	✓			✓	✓				✓		✓	✓	✓		
C94002	✓	✓	✓	✓	✓	✓	✓	✓		✓	✓	✓							✓	✓		
C94003	✓	✓	✓	✓	✓	✓	✓	✓		✓	✓	✓		✓					✓	✓		
C94011	✓	✓	✓	✓	✓	✓	✓	✓		✓	✓	✓		✓	✓	✓				✓		✓

continued on the next page

Table F.4: *continued*

STATION	Air Max	Air Min	Grass Min	Extreme Air Max	Extreme Air Min	Extreme Grass Min	Min Air Max	Max Air Min	5cm	10cm	20cm	30cm	50cm	100cm	Global Radiation	Total Sun	Max Wind Run	Wind Run	VPRESS	Mean Rh	Sunken Pan Evap	Penman
C94012	✓	✓	✓	✓	✓	✓	✓	✓							✓		✓	✓	✓	✓		✓
C95022	✓	✓	✓	✓	✓	✓	✓	✓	✓	✓	✓	✓		✓					✓	✓		
D05964	✓	✓	✓	✓	✓	✓	✓	✓		✓	✓	✓			✓	✓	✓	✓	✓	✓		✓
D05973																						✓
D06022	✓	✓	✓	✓	✓	✓	✓	✓		✓	✓	✓		✓					✓	✓		
D06051	✓	✓	✓	✓	✓	✓	✓	✓		✓	✓	✓				✓			✓	✓		
D06212	✓	✓	✓	✓	✓	✓	✓	✓		✓	✓	✓		✓		✓			✓	✓		✓
D15253											✓	✓		✓								
D78931	✓	✓	✓	✓	✓	✓	✓	✓		✓	✓	✓				✓			✓	✓		✓
D87683	✓	✓	✓	✓	✓	✓	✓	✓	✓	✓	✓					✓		✓	✓	✓	✓	✓
D87692	✓	✓	✓	✓	✓	✓	✓	✓		✓	✓	✓		✓	✓	✓		✓	✓	✓		✓
D87695	✓	✓	✓	✓	✓	✓	✓	✓		✓					✓		✓	✓	✓	✓		✓
D96241	✓	✓	✓	✓	✓	✓	✓	✓		✓	✓	✓		✓	✓	✓	✓	✓	✓	✓		✓
D96484																		✓				✓
D96491	✓	✓	✓	✓	✓	✓	✓	✓									✓	✓				
D96591	✓	✓	✓	✓	✓	✓	✓	✓	✓	✓	✓	✓		✓		✓	✓	✓	✓	✓		✓
D96680	✓	✓	✓	✓	✓	✓	✓	✓		✓	✓	✓		✓					✓	✓		
D96681	✓	✓	✓	✓	✓	✓	✓	✓		✓	✓	✓										
D96688	✓	✓	✓	✓	✓	✓	✓	✓		✓	✓	✓		✓		✓			✓	✓		✓
D96689	✓	✓	✓	✓	✓	✓	✓	✓	✓	✓	✓	✓		✓		✓	✓	✓	✓	✓		✓
D9668A	✓	✓	✓	✓	✓	✓	✓	✓	✓	✓	✓	✓		✓	✓		✓	✓	✓	✓		✓
D9668B	✓	✓	✓	✓	✓	✓	✓	✓	✓	✓	✓	✓	✓	✓	✓		✓	✓	✓	✓		✓
D96696													✓									

continued on the next page

Table F.4: *continued*

STATION	Air Max	Air Min	Grass Min	Extreme Air Max	Extreme Air Min	Extreme Grass Min	Min Air Max	Max Air Min	5cm	10cm	20cm	30cm	50cm	100cm	Global Radiation	Total Sun	Max Wind Run	Wind Run	VPRESS	Mean Rh	Sunken Pan Evap	Penman
D96931	✓	✓	✓	✓	✓	✓	✓	✓			✓						✓	✓	✓	✓		
E05041	✓	✓	✓	✓	✓	✓	✓	✓			✓											
E05221	✓	✓	✓	✓	✓	✓	✓	✓			✓						✓	✓	✓	✓		
E05231																						✓
E05343	✓	✓	✓	✓	✓	✓	✓	✓			✓	✓				✓	✓	✓	✓	✓		✓
E05363	✓	✓	✓	✓	✓	✓	✓	✓			✓	✓		✓		✓	✓	✓	✓	✓	✓	✓
E05368	✓	✓	✓	✓	✓		✓	✓							✓		✓	✓	✓	✓		✓
E05620	✓	✓	✓	✓	✓	✓	✓	✓			✓	✓		✓	✓		✓	✓	✓	✓		✓
E05622	✓	✓	✓	✓	✓	✓	✓	✓			✓	✓		✓	✓	✓	✓	✓	✓	✓		✓
E14272	✓	✓	✓	✓	✓	✓	✓	✓			✓	✓		✓	✓	✓	✓	✓	✓	✓	✓	✓
E14273	✓	✓	✓	✓	✓	✓	✓	✓			✓	✓				✓	✓	✓	✓	✓		✓
E15102	✓	✓	✓	✓	✓	✓	✓	✓			✓	✓		✓		✓	✓	✓	✓	✓		✓
E94313	✓	✓	✓	✓	✓	✓	✓	✓			✓	✓		✓		✓	✓	✓	✓	✓		✓
E94333	✓	✓	✓	✓	✓	✓	✓	✓			✓	✓		✓		✓	✓	✓	✓	✓		✓
E94512	✓	✓	✓	✓	✓	✓	✓	✓	✓		✓	✓		✓		✓	✓	✓	✓	✓		✓
E9452A													✓									
E95902	✓	✓	✓	✓	✓	✓	✓	✓			✓	✓		✓	✓	✓	✓	✓	✓	✓		✓
F03501	✓	✓	✓	✓	✓	✓	✓	✓			✓						✓	✓	✓	✓		✓
F03502	✓	✓	✓	✓	✓		✓	✓			✓						✓	✓	✓	✓		✓
F20791	✓	✓	✓	✓	✓	✓	✓	✓			✓	✓				✓		✓				✓
F20793	✓	✓	✓	✓	✓	✓	✓	✓			✓	✓		✓	✓	✓		✓	✓	✓		✓
F20794	✓	✓	✓	✓	✓	✓	✓	✓			✓				✓		✓		✓	✓		✓
F21182	✓	✓	✓	✓	✓	✓	✓	✓			✓	✓		✓					✓	✓		✓

continued on the next page

Table F.4: *continued*

STATION	Air Max	Air Min	Grass Min	Extreme Air Max	Extreme Air Min	Extreme Grass Min	Min Air Max	Max Air Min	5cm	10cm	20cm	30cm	50cm	100cm	Global Radiation	Total Sun	Max Wind Run	Wind Run	VPRESS	Mean Rh	Sunken Pan Evap	Penman
F66161	✓	✓	✓	✓	✓	✓	✓	✓												✓		
F66162	✓	✓		✓	✓		✓	✓									✓	✓	✓	✓		
G12581	✓	✓	✓	✓	✓	✓	✓	✓		✓	✓	✓					✓	✓	✓	✓		
G13211	✓	✓	✓	✓	✓	✓	✓	✓		✓	✓	✓		✓		✓	✓	✓	✓	✓	✓	
G13212	✓	✓	✓	✓	✓	✓	✓	✓		✓	✓	✓		✓	✓		✓	✓	✓			
G13222	✓	✓	✓	✓	✓	✓	✓	✓	✓	✓	✓	✓		✓	✓	✓	✓		✓	✓		✓
G13231	✓	✓	✓	✓	✓	✓	✓	✓		✓	✓	✓		✓		✓						
G13301	✓	✓	✓	✓	✓	✓	✓	✓		✓	✓	✓		✓			✓	✓	✓	✓		
G13322	✓	✓	✓	✓	✓	✓	✓	✓		✓	✓	✓			✓		✓	✓	✓	✓		✓
G13494																				✓		✓
G13495																				✓		✓
G13592	✓	✓	✓	✓	✓	✓	✓	✓		✓	✓	✓				✓			✓	✓		✓
G14711																						
G14721	✓	✓		✓	✓		✓	✓											✓	✓		
H21951	✓	✓	✓	✓	✓	✓	✓	✓											✓	✓		
H22783																				✓		✓
H22871	✓	✓	✓	✓	✓	✓	✓	✓									✓	✓	✓	✓		
H30711	✓	✓	✓	✓	✓	✓	✓	✓								✓	✓	✓	✓	✓		
H30841	✓	✓	✓	✓	✓	✓	✓	✓											✓	✓		
H31241	✓	✓	✓	✓	✓	✓	✓	✓											✓	✓		
H31352	✓	✓	✓	✓	✓	✓	✓	✓											✓	✓		
H31562	✓	✓	✓	✓	✓	✓										✓		✓	✓			✓
H31572																						✓

continued on the next page

Table F.4: *continued*

STATION	Air Max	Air Min	Grass Min	Extreme Air Max	Extreme Air Min	Extreme Grass Min	Min Air Max	Max Air Min	5cm	10cm	20cm	30cm	50cm	100cm	Global Radiation	Total Sun	Max Wind Run	Wind Run	VPRESS	Mean Rh	Sunken Pan Evap	Penman
H31883	✓	✓	✓	✓	✓	✓	✓	✓		✓	✓	✓		✓	✓		✓	✓	✓	✓	✓	✓
H31971	✓	✓	✓	✓	✓	✓	✓	✓		✓	✓	✓				✓			✓	✓		
H32252	✓	✓	✓	✓	✓	✓	✓	✓								✓	✓	✓	✓	✓		✓
H32352	✓	✓	✓	✓	✓	✓	✓	✓	✓	✓	✓	✓		✓			✓	✓	✓	✓	✓	
H32412	✓	✓	✓	✓	✓	✓	✓	✓											✓	✓		
H32424	✓	✓	✓	✓	✓	✓	✓	✓											✓	✓		
H32451	✓	✓	✓	✓	✓	✓	✓	✓		✓	✓	✓		✓	✓	✓	✓	✓	✓	✓	✓	✓
H32561	✓	✓	✓	✓	✓	✓	✓	✓		✓	✓	✓		✓		✓			✓	✓		
H32641	✓	✓	✓	✓	✓	✓	✓	✓		✓	✓	✓		✓	✓	✓	✓	✓	✓	✓	✓	✓
H32642	✓	✓	✓	✓	✓	✓	✓	✓	✓	✓	✓	✓		✓	✓		✓	✓	✓	✓		✓
H40041	✓	✓	✓	✓	✓	✓	✓	✓		✓	✓	✓		✓		✓	✓	✓	✓	✓	✓	✓
H40182	✓	✓	✓	✓	✓	✓	✓	✓		✓	✓	✓		✓		✓	✓	✓	✓	✓	✓	✓
H40892	✓	✓	✓	✓	✓	✓	✓	✓		✓	✓	✓		✓	✓	✓	✓	✓	✓	✓	✓	✓
H41131	✓	✓	✓	✓	✓	✓	✓	✓		✓	✓	✓		✓	✓	✓	✓	✓	✓	✓	✓	✓
H41323																						
H41325																						
H41411	✓	✓	✓	✓	✓	✓	✓	✓		✓	✓	✓		✓	✓	✓	✓	✓	✓	✓	✓	✓
H41421	✓	✓	✓	✓	✓	✓	✓	✓		✓	✓					✓			✓	✓		
H41424	✓	✓	✓	✓	✓	✓	✓	✓		✓	✓					✓			✓	✓		
H41701	✓	✓	✓	✓	✓	✓	✓	✓								✓	✓	✓	✓	✓		✓
I41901	✓	✓	✓	✓	✓	✓	✓	✓								✓			✓	✓	✓	
I49591	✓	✓	✓	✓	✓	✓	✓	✓		✓	✓	✓				✓	✓	✓	✓	✓		✓
I49592	✓	✓	✓	✓	✓	✓	✓	✓		✓	✓	✓	✓	✓	✓		✓	✓	✓	✓		

continued on the next page

Table F.4: *continued*

STATION	Air Max	Air Min	Grass Min	Extreme Air Max	Extreme Air Min	Extreme Grass Min	Min Air Max	Max Air Min	5cm	10cm	20cm	30cm	50cm	100cm	Global Radiation	Total Sun	Max Wind Run	Wind Run	VPRESS	Mean Rh	Sunken Pan Evap	Penman
I49711	✓	✓	✓	✓	✓	✓	✓	✓											✓	✓		
I50012	✓	✓	✓	✓	✓	✓	✓	✓											✓	✓		
I50102																						✓
I50113																						✓
I50212	✓	✓	✓	✓	✓	✓	✓	✓				✓				✓						
I50471	✓	✓	✓	✓	✓	✓	✓	✓		✓	✓	✓				✓		✓	✓	✓		✓
I50771	✓	✓	✓	✓	✓	✓	✓	✓											✓	✓		
I50831	✓	✓	✓	✓	✓	✓	✓	✓		✓	✓	✓		✓		✓			✓	✓	✓	
I50835	✓	✓	✓	✓	✓	✓	✓	✓		✓	✓	✓		✓		✓			✓	✓		✓
I50836	✓	✓	✓	✓	✓	✓	✓	✓	✓	✓	✓	✓	✓	✓	✓		✓	✓	✓	✓		✓
I50951	✓	✓	✓	✓	✓	✓	✓	✓	✓	✓	✓	✓		✓		✓	✓		✓	✓		✓
I50954													✓									
I58061	✓	✓	✓	✓	✓	✓	✓	✓								✓	✓	✓	✓	✓		✓
I58075																						✓
I59065													✓									
I59161	✓	✓	✓	✓	✓	✓	✓	✓											✓	✓		
I59162	✓	✓	✓	✓	✓	✓	✓	✓		✓	✓								✓	✓		
I59232	✓	✓	✓	✓	✓	✓	✓	✓		✓	✓	✓		✓					✓	✓		
I59234	✓	✓	✓	✓	✓	✓	✓	✓		✓	✓	✓		✓		✓	✓	✓	✓	✓		✓
I59235																						✓
I59238	✓	✓	✓	✓	✓	✓	✓	✓								✓			✓	✓		
I59239	✓	✓	✓	✓	✓	✓	✓	✓		✓	✓	✓		✓			✓	✓				
I59722	✓	✓	✓	✓	✓	✓	✓	✓		✓	✓						✓	✓	✓	✓		

continued on the next page

Table F.4: *continued*

STATION	Air Max	Air Min	Grass Min	Extreme Air Max	Extreme Air Min	Extreme Grass Min	Min Air Max	Max Air Min	5cm	10cm	20cm	30cm	50cm	100cm	Global Radiation	Total Sun	Max Wind Run	Wind Run	VPRESS	Mean Rh	Sunken Pan Evap	Penman
I59842	✓	✓	✓	✓	✓	✓	✓	✓											✓	✓		
I59891	✓	✓	✓	✓	✓	✓	✓	✓									✓	✓	✓	✓	✓	
I59921	✓	✓	✓	✓	✓	✓	✓	✓											✓	✓		
I68093	✓	✓	✓	✓	✓	✓																
I68182	✓	✓	✓	✓	✓	✓	✓	✓		✓	✓	✓	✓	✓	✓		✓	✓	✓	✓		✓
I68191	✓	✓	✓	✓	✓	✓				✓	✓	✓				✓	✓	✓	✓			✓
I68192	✓	✓	✓	✓	✓	✓	✓	✓		✓	✓	✓			✓	✓	✓	✓	✓	✓		✓
I68252	✓	✓	✓	✓	✓	✓	✓	✓											✓	✓		
I68362	✓	✓	✓	✓	✓	✓	✓	✓	✓	✓	✓	✓							✓	✓		
I68431	✓	✓		✓	✓	✓										✓						
I68433	✓	✓	✓	✓	✓	✓	✓	✓		✓	✓	✓		✓	✓	✓			✓	✓	✓	✓
I68435																					✓	✓
I69191	✓	✓	✓	✓	✓	✓	✓	✓											✓	✓		

F.3 Fitted Model

Table F.5: Parameters for fit of Equations refeq:spatehtmod to monthly soil temperature data

Coeff	5cm		10cm		20cm		30cm		50cm		100cm	
	B	Std. Error	B	Std. Error	B	Std. Error	B	Std. Error	B	Std. Error	B	Std. Error
(Constant)	6.798E+01	4.147E+00	-1.069E+01	3.465E+00	-4.067E+01	3.524E+00	-6.291E+00	2.572E+00	-4.594E+01	7.018E+00	6.317E+01	3.359E+00
ALT12	-1.824E-01	8.049E-02	3.239E-02	1.363E-02	6.589E-02	7.480E-03	2.938E-02	5.251E-03	-8.341E-02	9.112E-03	-2.188E-01	1.700E-02
ALT2	-3.572E-04	4.848E-05	-2.682E-05	3.991E-06							-7.673E-05	6.625E-06
ALT2SLAT	-7.123E-04	9.162E-05			1.635E-05	2.296E-06	-2.537E-05	2.231E-06	4.628E-04	5.027E-05		
ALT3LL			-6.755E-12	6.821E-13	-1.892E-12	1.615E-13					-1.134E-11	1.100E-12
ALT3SLAT									-1.011E-06	1.022E-07	-8.677E-08	6.638E-09
ALTITUDE			-1.770E-02	4.997E-03								
ALTLAT					3.646E-04	5.331E-05						
ALTLATLO	-7.350E-06	1.543E-06					-5.203E-06	3.304E-07				
ALTLONG			8.422E-05	3.090E-05	4.209E-05	1.377E-05	-2.635E-04	1.563E-05			1.381E-04	1.186E-05
ALTSLAT	7.459E-02	9.143E-03							-3.544E-02	8.084E-03	1.701E-02	8.731E-04
CM							1.656E+00	2.606E-01				
CM2	-3.038E-01	3.477E-02	-2.795E-01	9.419E-03								
CMA2LL	1.726E-08	3.309E-09	1.764E-09	4.858E-10	3.874E-09	4.528E-10			-1.537E-09	9.662E-11	5.771E-08	2.315E-09
CMA3LL			-4.461E-12	7.801E-13	5.717E-11	3.025E-12	8.494E-11	2.872E-12			-3.757E-12	1.030E-12
CMALT			7.471E-02	5.965E-03	7.322E-03	5.984E-04	6.410E-03	3.071E-04			1.208E-02	7.492E-04
CMALT2											4.109E-04	1.489E-05
CMALT3	2.591E-07	4.328E-08			4.805E-07	2.275E-08	6.356E-07	2.116E-08				
CMALTLON			-4.281E-04	3.444E-05								
CMALTLT2	1.112E-05	1.705E-06										
CMALTSLT	2.667E-02	4.119E-03			2.289E-02	1.024E-03	3.421E-02	1.019E-03			5.849E-02	1.489E-03
CMCLAT	-3.346E+01	1.763E+00	-8.512E+00	6.203E-01	-7.066E+00	5.525E-01	-2.673E+00	5.782E-01	8.584E+00	1.186E+00	-7.703E+00	5.548E-01
CML2L2			1.542E-07	9.327E-09			1.522E-07	1.518E-08	8.095E-07	8.116E-08		
CMLAT2							-4.187E-03	3.025E-04	-1.754E-02	1.835E-03		
CMLAT3											3.572E-05	4.123E-06
CMLON3			6.994E-07	5.442E-08	1.040E-06	9.125E-08					-3.139E-07	1.063E-07
CMSLAT					2.026E+00	2.235E-01					9.083E-01	3.756E-01
LAT2LON3	3.365E-09	5.218E-10										
LAT3									-6.269E-04	7.631E-05	4.167E-04	2.164E-05
LAT3LON3											-8.504E-11	6.826E-12
LAT3LONG					-3.981E-07	8.461E-08						
LATCM	6.173E-01	4.058E-02	3.479E-01	1.523E-02	1.621E-01	1.022E-02						
LATCM2					8.827E-03	2.115E-04	9.026E-03	2.028E-04	6.694E-03	1.084E-03	5.464E-03	2.215E-04
LATITUDE			-4.453E-01	7.681E-02	-9.957E-01	6.767E-02	-3.852E-01	5.706E-02				
LATLONG	1.208E-02	1.223E-03									4.120E-03	4.951E-04
LATSM											-6.810E-02	1.418E-02
LATSM2	2.207E-03	8.689E-04									1.556E-02	2.884E-03
LONG3											-4.065E-06	2.865E-07

continued on the next page

Table F.5: *continued*

Coeff	5cm		10cm		20cm		30cm		50cm		100cm	
	B	Std. Error	B	Std. Error	B	Std. Error	B	Std. Error	B	Std. Error	B	Std. Error
LONGSM			1.924E-02	6.739E-05	4.555E-02	4.763E-03						
LONGSM2			2.132E-02	3.828E-03	2.593E-02	3.508E-03					2.637E-03	6.749E-04
SLAT			-1.521E+01	1.164E+00	-2.853E+01	1.598E+00	-1.509E+01	8.607E-01	-5.875E+01	6.129E+00		
SM					-4.370E+00	8.300E-01	2.005E+00	2.319E-01				
SM2			-3.677E+00	6.660E-01	-4.452E+00	6.104E-01						
SMA2LL			5.612E-10	1.366E-10	2.133E-09	4.479E-10					1.947E-09	6.209E-10
SMA3LL			-1.782E-12	3.167E-13	1.517E-11	2.591E-12	2.951E-11	2.865E-12			6.665E-11	3.427E-12
SMALLL									-5.083E-06	7.959E-07		
SMALT	-7.729E-04	3.175E-04			3.451E-03	5.929E-04						
SMALT3					1.419E-07	2.018E-08	2.225E-07	2.111E-08			5.202E-07	2.580E-08
SMALTLON									-2.025E-04	3.442E-05		
SMALTLT2							1.170E-06	1.490E-07			3.010E-06	3.283E-07
SMALTSLT					6.741E-03	8.396E-04	1.061E-02	8.683E-04			2.155E-02	9.706E-04
SMCLAT							-3.153E+00	3.200E-01	3.410E+00	8.662E-01	-6.230E+00	4.526E-01
SML2L2											-9.746E-08	6.031E-09
SMLAT3							1.855E-05	1.450E-06				
SMLON2	1.065E-04	1.424E-06										
SMLON3									1.262E-06	1.578E-07		

Appendix G

New Zealand Specific Environmental Models for RADLAB Simulation

G.1 Air Humidity

Air humidity is an environmental variable that we should explicitly model for **RADLAB** as this variable influences processes such as the latent heat flux and water vapour flux both of which are major elements of the surface energy exchange process (*infra vide*:§8).

The model that will be adopted here is identical to that outlined in §12.3.1 and illustrated with the Air Temperature model in §12.3.2 for the variables $MAIRMAX$ and $MAIRMIN$. No further model development is required beyond developing a spatially indexed model for rH series data from the 142 sites given in Table F.4.

G.1.1 rH Deterministic Seasonal Model

The stationary seasonal data for rH were extracted using the seasonal average given in Equation 11.2. This seasonal series was then modelled using a spatially indexed harmonic series as discussed previously (§12.3.1). The regression has been conducted with no constant as we have defined the constant to be equal to zero through the normalisation procedure which produced the stationary series.

A summary of the fitted model for rH is given in Table G.1. This shows that while the analysis is significant only about 45 % of the observed structure for the seasonal component can be described in terms of a regular seasonal variation.

Following this analysis we can model the deterministic seasonal component of rH as

$$
\begin{aligned}
rH_{detseasonal} := \\
&1.068E-09CMLL4 + 1.1556SM2 + 2.114E-06SMLAT4 \\
&0.5493CM2 - 3.118E-14CMALT3L4 - 1.563E-07CMLL3
\end{aligned}
$$

Table G.1: Fitted model for the deterministic seasonal component of rH

Model Summary

R	R Square	Adjusted R Square	Std. Error of the Estimate
0.6813	0.4642	0.4639	4.3265

ANOVA

	Sum of Squares	df	Mean Square	F	Sig.
Regression	422848.6360	12	35237.3863	1882.4749	0
Residual	488163.6391	26079	18.7186		
Total	911012.2751	26091			

Coefficients

	Unstandardized Coefficients		Standardized Coefficients	t	Sig.
	B	Std. Error	Beta		
CMLL4	1.068E-09	7.283E-11	4.7531	14.6619	0.0000
SM2	1.1556	0.0379	0.1381	30.4628	0.0000
SMLAT4	2.114E-06	3.637E-07	0.7687	5.8123	0.0000
CM2	0.5493	0.0378	0.0658	14.5225	0.0000
CMALT3L4	-3.118E-14	3.163E-15	-1.1153	-9.8559	0.0000
CMLL3	-1.563E-07	1.263E-08	-4.0115	-12.3829	0.0000
CMALT3L3	-6.614E-12	4.989E-13	-5.5069	-13.2568	0.0000
SMLAT3	1.278E-04	3.257E-05	1.0941	3.9256	0.0001
CMALT	0.0334	0.0019	0.8153	17.2943	0.0000
CMA2L2L	-6.641E-10	4.477E-11	-3.0086	-14.8340	0.0000
CMALT4L4	-7.845E-17	7.448E-18	-2.1543	-10.5333	0.0000
SML3L4	-5.360E-14	2.049E-14	-0.4080	-2.6163	0.0089

Residuals Statistics

	Minimum	Maximum	Mean	Std. Deviation	N
Predicted Value	-11.574	12.673	8.247E-03	4.026	26091
Residual	-23.680	26.780	0.241	4.319	26091

$$-6.614E-12CMALT3L3+1.278E-04SMLAT3$$
$$+0.0334CMALT-6.641E-10CMA2L2L-7.845E-17CMALT4L4$$
$$-5.360E-14SML3L4 \quad \text{(G.1)}$$

G.1.2 Stochastic Seasonal Model for rH

Following the modelling approach defined previously (§12.3.1 & §12.3.2) we will use an ARIMA(1,0,0) model to describe the stochastic structure of the rH seasonal component. A Summary of this analysis is presented in Table G.2.

Table G.2: ARIMA(1,0,0) model for rH stochastic seasonal component

Analysis of Variance

	DF	Adj. Sum of Squares	Residual Variance
Residuals	26090	468184.78	17.930231

Coefficients

	B	SEB	T-RATIO	APPROX. PROB.
AR1	.21607071	.00626813	34.471291	.0000000

Residual Statistics

	N	Minimum	Maximum	Mean	Std. Deviation
Residual	26091	-23.95084	26.77979	.2148934	4.2364327

From this analysis we can describe the stochastic seasonal component of rH as:

$$r_{rH}(x) := 0.216 r_{rH}(x-1) + z^{dsrH} \quad \text{(G.2)}$$

where $z^{dsrH} \sim N(0, 4.236)$

G.1.3 Spatial Model

Following the approach described in §12.3.1, the spatial model has been fitted by regressing the locational mean rH data against fully crossed

fourth order spatial polynomial model of longitude, latitude and altitude, using a stepwise regression. A Summary of this analysis for locational mean rH values is presented in Table G.3 with summary residual statistics in Table G.4.

Table G.3: Regression model summary for the rH spatial model fit

Model Summary

Model	R	R Square	Adjusted R Square	Std. Error of the Estimate
1	0.4962	0.2462	0.1631	3.7879

ANOVA

Model		Sum of Squares	df	Mean Square	F	Sig.
1	Regression	595.1443	14	42.5103	2.9628	6.125E-04
	Residual	1822.2056	127	14.3481		
	Total	2417.3499	141			

Coefficients

		Unstandardized		Standardized	t	Sig.
Model		B	Std. Error	Beta		
1	(Constant)	53.8040	19.7579		2.7232	0.0074
	ALTITUDE	-0.1328	0.1600	-5.9765	-0.8299	0.4081
	LONG	0.0638	0.1064	0.2057	0.5993	0.5500
	LAT5	-4.062E-07	1.751E-07	-4.8407	-2.3199	0.0219
	LONG5	-2.656E-10	2.664E-10	-0.7684	-0.9969	0.3207
	ALT2	-1.345E-04	1.858E-04	-4.4313	-0.7241	0.4704
	LATLONG5	-1.228E-11	8.553E-12	-0.9301	-1.4358	0.1535
	LAT5LON5	3.846E-18	1.637E-18	5.7810	2.3493	0.0204
	ALTLON5	8.819E-13	7.728E-13	6.1206	1.1411	0.2560
	ALTLAT5	-1.690E-10	3.252E-10	-1.1061	-0.5196	0.6043
	ALT3LON5	1.931E-18	1.651E-18	8.4046	1.1696	0.2444
	ALT3LAT5	-3.903E-16	1.615E-15	-1.2869	-0.2416	0.8095
	ALT5LON5	-1.104E-24	1.433E-24	-3.9116	-0.7710	0.4421
	ALT2L5L5	2.640E-24	7.514E-24	1.7261	0.3514	0.7259
	ALT5L5L5	3.028E-33	1.126E-32	1.1146	0.2690	0.7884

Table G.4: Residual statistics for the spatial regression model fitted to the rH data

N	Min	Max	Mean	σ
142	-17.95	7.52	-5.67E-14	3.59

Following these analyses we can describe the location mean values for rH as:

$$
\begin{aligned}
rH_{spatial}(latitude, longtitude, altitude) := \\
&53.8040 - 0.1328ALTITUDE + 0.0638LONG - 4.062E-07LAT5 \\
&-2.656E-10LONG5 - 1.345E-04ALT2 - 1.228E-11LATLONG5 \\
&+3.846E-18LAT5LON5 + 8.819E-13ALTLON5 - 1.690E-10ALTLAT5 \\
&+1.931E-18ALT3LON5 - 3.903E-16ALT3LAT5 - 1.104E-24ALT5LON5 \\
&+2.640E-24ALT2L5L5 + 3.028E-33ALT5L5L5 + z^{sprh}
\end{aligned} \tag{G.3}
$$

where $z^{sprh} = 3.59$

G.1.4 Long-Term Trend

To model the long term stochastic structure for rH any apparent long term trend over the duration of the recording period was removed. This was achieved by regressing the trend data against a cubic model of year. This model treats any apparent long-term trend as an additive effect that is global to New Zealand as a whole. A summary of this analysis is given in Figure G.1. As discussed previously, the regression residuals are the most important aspect of this analysis as we need to describe the stochastic structure of the residuals in order to model realistic long term sequence data. Following the modelling approach defined above we will use an ARIMA(3,0,0) model (§12.3.2; lag from Table 12.10) for the stochastic structure of the residuals. A summary of this analysis is presented in Table G.5.

Table G.5: Fitted parameters for the rH stochastic model

	B	SEB	T-RATIO	APPROX. PROB.
AR1	.81949654	.03431928	23.878607	.00000000
AR2	.13837069	.04764687	2.904088	.00375561
AR3	-.00246973	.03607279	-.068465	.94542765

For the purposes of the **RADLAB** simulation we will not use the fitted long-term trend equations given in Figure G.1 as we cannot extrapolate

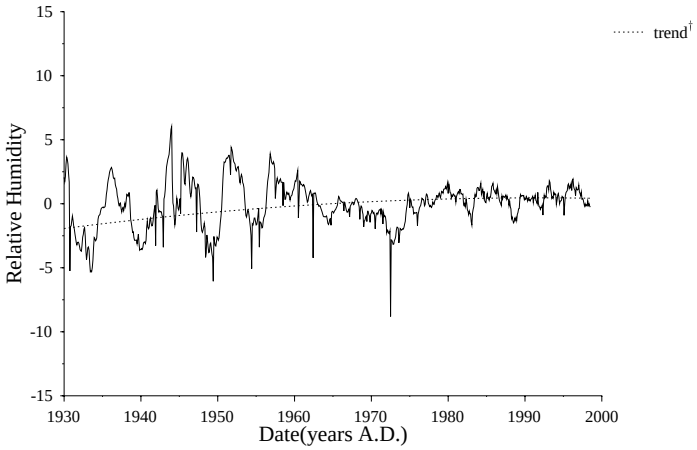

Figure G.1: Long-term trend for monthly mean relative humidity

† $x = -1680.819 + 1.266x - 1.064E - 07x^3$ $R^2 = 0.275$ Sig. = 0

these trends beyond the recording period. The model applied will be that there has been no long-term trend other than the variations observed as a function of long-term stochastic variation such as that illustrated in Figure 12.8. Thus we model the long-term trend component of rH as:

$$rH_{trend}(x) := 0.8195(x-1) + 0.1384(x-2) - 0.0025(x-3) + z \tag{G.4}$$

where $z \sim N(0, 1.4)$ (Table 12.12)

G.1.5 rH Model

For the purposes of the **RADLAB** simulations in New Zealand rH series data can be modelled by the summation of Equations G.3, G.4, G.1 and G.2after Equation 12.11.

G.2 Windspeed

Windspeed is an important environmental variable as it influences mass transfer processes involved in the latent and sensible heat fluxes. The variable modelled here is the monthly wind run in km at each of the 72 monitoring locations given in Table F.4. The wind run is simply the wind velocity integrated over the month. Thus the mean windspeed in km/hr is simply the windrun divided by the number of hours in the particular month. The mean wind speed in Metres per second follows naturally. In the following we will develop a model for the Windrun variable, however we will then use this to estimate locational windspeeds in ms^{-1}.

G.2.1 Wind Speed Deterministic Seasonal Model

The stationary seasonal data for Windrun were extracted using the seasonal average given in Equation 11.2. This seasonal series was then modelled using a spatially indexed harmonic series as discussed in §12.3.1. The regression has been conducted with no constant as we have defined the constant to be equal to zero through the normalisation procedure which produced the stationary series.

A summary of the fitted model for Windrun is given in Table G.6. This shows that while the analysis is significant only about 35 % of the observed structure for the seasonal component can be described in terms of a regular seasonal variation.

Following this analysis we can model the deterministic seasonal component of monthly Windrun as

$$\begin{aligned} WR_{detseasonal} := & \\ & -3.566E-09SMLL4 - 5.7308SM2 + 1.904E-10CMALT2L4 \\ & -1.876E-03CMLAT3 - 3.284E-13SMALT3L4 - 4.564E-03SMLON2 \\ & +6.952E-23SMA4L4L3 - 2.497E-16SMAL4L4 + 1.716E-06SMALT3 \\ & +1.996E-07SMALTL41.445E-15SMA4LL2 - 1.562E-13CMALT3L4 \\ & -3.269E-14CML4L4 - 8.172E-09CMLON4 - 9.657E-05CMALTL2 \end{aligned} \tag{G.5}$$

G.2.2 Stochastic Seasonal Model for Wind Speed

There are no significant autocorrelations for the residuals from the monthly windrun seasonal data. Accordingly we will simply describe the stochastic component of the monthly windrun season component as a purely random variable distributed according to the residual parameters given

Table G.6: Fitted model for the deterministic seasonal component of Wind Run

Model Summary

R	R Square	Adjusted R Square	Std. Error of the Estimate
0.5920	0.3504	0.3496	33.7641

ANOVA

	Sum of Squares	df	Mean Square	F	Sig.
Regression	7678301.9083	15	511886.7939	449.0171	0
Residual	14234243.6777	12486	1140.0163		
Total	21912545.5860	12501			

Coefficients

	Unstandardized Coefficients		Standardized Coefficients	t	Sig.
	B	Std. Error	Beta		
SMLL4	-3.566E-09	3.023E-10	-2.2607	-11.7977	0.0000
SM2	-5.7308	0.4272	-0.0968	-13.4160	0.0000
CMALT2L4	1.904E-10	1.204E-11	1.5439	15.8148	0.0000
CMLAT3	-1.876E-03	2.593E-04	-2.2101	-7.2325	0.0000
SMALT3L4	-3.284E-13	8.925E-14	-2.0322	-3.6793	0.0002
SMLON2	-4.564E-03	3.692E-04	-2.3448	-12.3637	0.0000
SMA4L4L3	6.952E-23	2.628E-23	1.6901	2.6449	0.0082
SMAL4L4	-2.497E-16	3.932E-17	-2.7305	-6.3517	0.0000
SMALT3	1.716E-06	2.984E-07	3.1373	5.7503	0.0000
SMALTL4	1.996E-07	3.394E-08	2.5476	5.8808	0.0000
SMA4LL2	1.445E-15	3.311E-16	2.6738	4.3646	0.0000
CMALT3L4	-1.562E-13	1.110E-14	-0.9461	-14.0807	0.0000
CML4L4	-3.269E-14	6.480E-15	-1.4502	-5.0450	0.0000
CMLON4	-8.172E-09	2.190E-09	-0.1269	-3.7320	0.0002
CMALTL2	-9.657E-05	6.345E-06	-0.6535	-15.2201	0.0000

Residuals Statistics

	Minimum	Maximum	Mean	Std. Deviation	N
Predicted Value	-65.1724	65.1724	0.3083	24.7824	12501
Residual	-130.4993	235.3284	1.1274	33.7264	12501

in Table G.6. That is we will describe the stochastic seasonal component of monthly windrun as:

$$r_{wr}(x) := z^{dsWR} \tag{G.6}$$

where $z^{dsWR} \sim N(0, 33.74)$

G.2.3 Spatial Model

Following the approach used above, a spatial model has been fitted to the mean monthly windspeed data by regressing the monitored data against fully crossed fifth order spatial polynomial model of longitude, latitude and altitude, using a stepwise regression. A Summary of this analysis for locational mean windrun values is presented in Table G.7. This shows that around 25% of the observed structure in the data can be

Table G.7: Regression model summary for the windrun spatial model fit

Model Summary

R	R Square	Adjusted R Square	Std. Error of the Estimate
0.5449	0.2969	0.2659	14.3038

ANOVA

	Sum of Squares	df	Mean Square	F	Sig.
Regression	5875.3170	3	1958.4390	9.5721	0.0000
Residual	13912.6529	68	204.5978		
Total	19787.9699	71			

Coefficients

	Unstandardized		Standardized	t	Sig.
	B	Std. Error	Beta		
(Constant)	349.7479	134.6632		2.5972	0.0115
LAT5	7.579E-06	2.376E-06	22.0038	3.1894	0.0022
LAT4	4.235E-04	1.399E-04	23.5749	3.0266	0.0035
LATLONG	0.0696	0.0346	2.0285	2.0114	0.0483

Residuals Statistics

	Minimum	Maximum	Mean	Std. Deviation	N
Predicted Value	138.8025	173.6332	163.1804	9.0968	72
Residual	-40.3060	33.4671	0.0000	13.9983	72

described through systematic spatial variation.

Following this analysis we can describe the location mean values for mean monthly windrun as:

$$\begin{aligned} windrun_{spatial}(latitude, longtitude, altitude) := \\ 349.7479 + 7.579E-06LAT5 + 4.235E-04LAT4 \\ +0.0696LATLONG + z^{spwr} \end{aligned} \quad \text{(G.7)}$$

where $z^{spwr} = 14.0$

G.2.4 Long-Term Trend

To model the long term stochastic structure for Monthly Windrun any apparent long term trend over the duration of the recording period was removed. This was achieved by regressing the data against a cubic model of year. This model treats any apparent long-term trend as an additive effect that is global to New Zealand as a whole. A summary of this analysis is given in Figure G.2.

As discussed previously, the regression residuals are the most important aspect of this analysis as we need to describe the stochastic structure of the residuals in order to model realistic long term sequence data. Following the modelling approach defined above we will use an ARIMA(3,0,0) model (§12.3.2; lag from Table 12.10) for the stochastic structure of the residuals. A summary of this analysis is presented in Table G.8. For

Table G.8: Fitted parameters for the windrun long-term stochastic model

	B	SEB	T-RATIO	APPROX. PROB.
AR1	.97603465	.00552958	176.51161	.0000000

the purposes of the **RADLAB** simulation we will not use the fitted long-term trend equations given in Figure G.2 as we cannot extrapolate these trends beyond the recording period. The model applied will be that there has been no long-term trend other than the variations observed

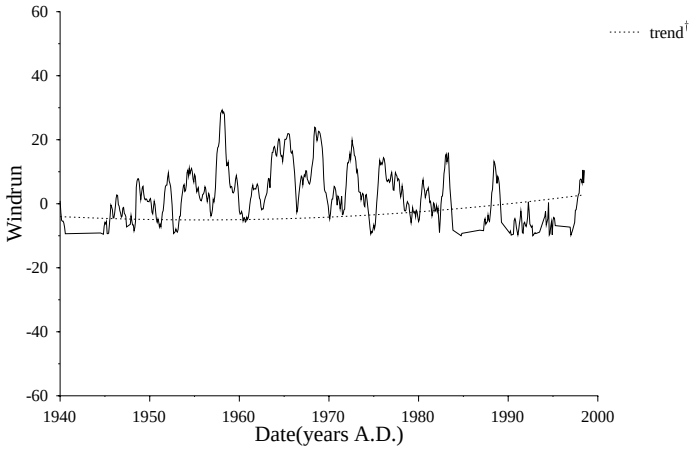

Figure G.2: Long-term trend for monthly windrun

† $x = 41.826 - 5.084E-09x^3$ $R^2 = 0.011$ Sig. = 0.012

as a function of long-term stochastic variation such as that illustrated in Figure 12.8. Thus we model the long-term stochastic component of Windrun as:

$$WR_{trend}(x) := 0.976(x-1) + z \tag{G.8}$$

where $z \sim N(0, 9.47)$ (Table 12.12)

G.2.5 Windspeed Model

For the purposes of the **RADLAB** simulations in New Zealand, monthly Windrun series data can be modelled by the summation of Equations G.7, G.8, G.5 and G.6after Equation 12.11. From this we will model the mean monthly wind speed (ms^{-1}) as

$$\frac{\text{Windrun}}{\text{n\_days}} \times \frac{1}{86.4} \tag{G.9}$$

G.3 Rainfall

Here we will model the monthly rainfall totals data given in the database (§11.2). This variable records the total rainfall received for each month in mm. In total data are recorded for 158 locations as given in Table F.4. In order to convert this into an estimated rain intensity series we will also model the mean number of rainfall events (N) per month at each location. From this we can calculate the mean rainfall per event as being

$$\frac{\text{rainfalltotal}}{\text{N}}$$

and by making the (admittedly arbitrary) assumption that the duration of each event is 24 hrs we can calculate the rate as being equal to the mean rain per day. Thus at the start of any given day the probability of rain is N/30 after which rain falls at rate R for the day. In the following we will model the Rain Total variable and develop a spatial model for N. From this we will produce a rainfall model.

G.3.1 Deterministic Seasonal Model Raintot

The stationary seasonal data for Windrun were extracted using the seasonal average given in Equation 11.2. This seasonal series was then modelled using a spatially indexed harmonic series as discussed previously (§12.3.1). The regression has been conducted with no constant as we have defined the constant to be equal to zero through the normalisation procedure which produced the stationary series.

A summary of the fitted model for Windrun is given in Table G.6. This shows that while the analysis is significant only about 35 % of the observed structure for the seasonal component can be described in terms of a regular seasonal variation.

Following this analysis we can model the deterministic seasonal component of monthly Raintotal as

$$\begin{aligned} RT_{detseasonal} := & \\ & -1.624E-07CMLON4 - 3.672E-09CMLL4 + 4.0424CM2 \\ & -2.747E-10CMALT2L4 + 1.279E-07SMLON4 + 7.584E-05SMLAT4 \\ & -0.1761SMLAT2 - 3.868E-09CMALT4 - 3.052E-15CMA4LL2 \\ & -1.233E-08CMALT2L3 - 2.874E-12SML4L3 - 0.7970SM2 \end{aligned} \quad \text{(G.10)}$$

G.3.2 Stochastic Seasonal Model for Monthly Raintotal

There are no significant autocorrelations for the residuals from the monthly mraintotal seasonal data. Accordingly we will simply describe the stochastic component of the monthly raintotal season component as a purely random variable distributed according to the residual parameters given in Table G.9. That is we will describe the stochastic seasonal component

Table G.9: Fitted model for the deterministic seasonal component of monthly rain total

Model Summary

R	R Square	Adjusted R Square	Std. Error of the Estimate
0.2104	0.0443	0.0441	54.7024

ANOVA

	Sum of Squares	df	Mean Square	F	Sig.
Regression	11326931.5400	12	943910.9617	315.4412	0
Residual	244448175.2332	81691	2992.3514		
Total	255775106.7732	81703			

Coefficients

	Unstandardized Coefficients		Standardized Coefficients	t	Sig.
	B	Std. Error	Beta		
CMLON4	-1.624E-07	4.422E-09	-1.8482	-36.7249	0.0000
CMLL4	-3.672E-09	1.080E-10	-1.7238	-34.0085	0.0000
CM2	4.0424	0.2705	0.0511	14.9417	0.0000
CMALT2L4	-2.747E-10	3.390E-11	-1.5684	-8.1032	0.0000
SMLON4	1.279E-07	1.297E-08	1.4542	9.8674	0.0000
SMLAT4	7.584E-05	7.103E-06	3.0611	10.6766	0.0000
SMLAT2	-0.1761	0.0155	-3.8907	-11.3823	0.0000
CMALT4	-3.868E-09	3.045E-10	-3.4015	-12.7039	0.0000
CMA4LL2	-3.052E-15	2.441E-16	-3.3670	-12.5033	0.0000
CMALT2L3	-1.233E-08	1.489E-09	-1.6154	-8.2795	0.0000
SML4L3	-2.874E-12	7.978E-13	-0.5885	-3.6024	0.0003
SM2	-0.7970	0.2708	-0.0101	-2.9434	0.0032

Residuals Statistics

	Minimum	Maximum	Mean	Std. Deviation	N
Predicted Value	-64.6305	72.7154	0.1581	11.7734	81703
Residual	-154.8238	1035.9460	3.2352	54.6029	81703

of monthly raintotal as:

$$r_{rt}(x) := z^{dsRT} \tag{G.11}$$

where $z^{dsRT} \sim N(0, 54.6)$

G.3.3 Spatial Model for Raintot

Following the approach used above, a spatial model has been fitted to the mean monthly windspeed data by regressing the monitored data against fully crossed fourth order spatial polynomial model of longitude, latitude and altitude, using a stepwise regression. A Summary of this analysis for locational mean windrun values is presented in Table G.7. This shows that around 68% of the observed structure in the data can be described through systematic spatial variation.

Following this analysis we can describe the location mean values for Monthly Raintotal as:

$$\begin{aligned} &RT_{spatial}(latitude, longtitude, altitude) := \\ &\quad -32.6238 + 0.0078LONG - 7.286E-06LAT5 \\ &\quad -1.658E-08LONG5 + 1.392E-03ALT2 - 6.568E-10LATLONG5 \\ &\quad -5.268E-15LAT4LON5 - 1.019E-11ALTLON5 + 1.417E-08ALTLAT5 \\ &\quad -4.181E-18ALT3LON5 - 4.145E-14ALT3LAT5 + 1.797E-23ALT5LON5 \\ &\quad -5.657E-14ALTL3L4 + 1.847E-22ALT2L5L5 \\ &\quad +3.037E-31ALT5L5L5 + z^{spRT} \end{aligned} \tag{G.12}$$

where $z^{spwr} = 34$

G.3.4 Long-Term Trend

To model the long term stochastic structure for Monthly Rain total any apparent long term trend over the duration of the recording period was removed. This was achieved by regressing the data against a cubic model

Table G.10: Regression model summary for the rainfall spatial model fit

Model Summary

Model	R	R Square	Adjusted R Square	Std. Error of the Estimate
1	0.8211	0.6742	0.6423	35.6534

ANOVA

Model		Sum of Squares	df	Mean Square	F	Sig.
1	Regression	376180.7894	14	26870.0564	21.1381	3.612E-28
	Residual	181776.5114	143	1271.1644		
	Total	557957.3008	157			

Coefficients

		Unstandardized		Standardized	t	Sig.
Model		B	Std. Error	Beta		
1	(Constant)	-32.6238	169.4203		-0.1926	0.8476
	LONG	0.0078	0.2681	0.0017	0.0291	0.9768
	LAT5	-7.286E-06	1.465E-06	-6.0654	-4.9739	0.0000
	LONG5	-1.658E-08	3.712E-09	-3.3875	-4.4664	0.0000
	ALT2	1.392E-03	1.451E-03	3.2092	0.9595	0.3389
	LATLONG5	-6.568E-10	1.385E-10	-3.3795	-4.7431	0.0000
	LAT4LON5	-5.268E-15	9.492E-16	-10.0878	-5.5502	0.0000
	ALTLON5	-1.019E-11	4.609E-12	-4.9398	-2.2100	0.0287
	ALTLAT5	1.417E-08	5.624E-09	6.6608	2.5189	0.0129
	ALT3LON5	-4.181E-18	1.505E-17	-1.2471	-0.2778	0.7815
	ALT3LAT5	-4.145E-14	1.381E-14	-9.8203	-3.0013	0.0032
	ALT5LON5	1.797E-23	1.391E-23	4.2771	1.2919	0.1985
	ALTL3L4	-5.657E-14	2.160E-14	-12.1168	-2.6190	0.0098
	ALT2L5L5	1.847E-22	5.297E-23	8.6658	3.4873	0.0006
	ALT5L5L5	3.037E-31	1.049E-31	7.7270	2.8941	0.0044

Residuals Statistics

N	Min	Max	Mean	σ
158	-99.91	130.12	2.14E-12	34.03

of year. This model treats any apparent long-term trend as an additive effect that is global to New Zealand as a whole. A summary of this analysis is given in Figure G.3.

As discussed previously, the regression residuals are the most important aspect of this analysis as we need to describe the stochastic structure of the residuals in order to model realistic long term sequence data. Following the modelling approach defined above we will use an ARIMA(4,0,0) model (§12.3.2; lag from Table 12.10) for the stochastic structure of the residuals. A summary of this analysis is presented in Table G.11. For

Table G.11: Fitted parameters for the rain total stochastic model

	B	SEB	T-RATIO	APPROX. PROB.
AR1	1.4618162	.02460338	59.415266	.00000000
AR2	-.7334760	.04306397	-17.032243	.00000000
AR3	.3269614	.04306264	7.592693	.00000000
AR4	-.1204140	.02461709	-4.891481	.00000110

the purposes of the **RADLAB** simulation we will not use the fitted long-term trend equations given in Figure G.2 as we cannot extrapolate these trends beyond the recording period. The model applied will be that there has been no long-term trend other than the variations observed as a function of long-term stochastic variation such as that illustrated in Figure 12.8. Thus we model the long-term stochastic component of Monthly total rainfall as:

$$Rainfall_{trend}(x) := 1.4618162(x-1) - .7334760(x-2) + 0.3269614(x-3) - 0.1204140(x-4) + z \quad \text{(G.13)}$$

where $z \sim N(0, 2.54)$ (Table 12.12)

G.3.5 Spatial Model for N_r

Following the approach used above, a spatial model has been fitted to the mean monthly number of rainfall days (N_r) by regressing the moni-

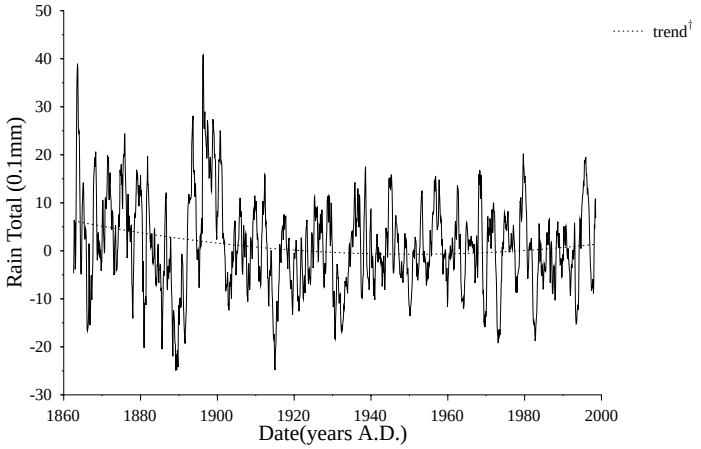

Figure G.3: Long-term trend for monthly mean rain total

† $x = 2298.984 - 1.768x + 1.549E - 07x^3$ $R^2 = 0.038$ Sig. = 0

tored data against fully crossed fifth order spatial polynomial model of longitude, latitude and altitude, using a stepwise regression. A Summary of this analysis for locational mean N_r values is presented in Table G.12. This shows that around 56% of the observed structure in the data can be

Table G.12: Regression model summary for the number of rainfall days (N_r) spatial model fit

Model Summary

R	R Square	Adjusted R Square	Std. Error of the Estimate
0.7496	0.5618	0.5532	1.8033

ANOVA

	Sum of Squares	df	Mean Square	F	Sig.
Regression	3823.6042	18	212.4225	65.3257	0.0000
Residual	2981.8513	917	3.2517		
Total	6805.4554	935			

Coefficients

	Unstandardized		Standardized	t	Sig.
	B	Std. Error	Beta		
(Constant)	0.6873	2.1750		0.3160	0.7521
SMLON5	1.004E-10	2.320E-11	4.1168	4.3303	0.0000
SMLAT5	-8.537E-08	1.163E-08	-3.0308	-7.3373	0.0000
LATLONG5	8.879E-12	8.538E-13	1.0836	10.3994	0.0000
CMCLAT	-7.325E+00	5.962E-01	-1.4457	-12.2849	0.0000
CML2L2	1.252E-07	1.427E-08	1.6870	8.7748	0.0000
LONG	1.826E-01	1.681E-02	1.1985	10.8630	0.0000
SMLL	3.586E-03	7.067E-04	6.7076	5.0736	0.0000
ALTLAT3	7.812E-07	3.439E-07	4.8612	2.2719	0.0233
LATLONG3	-6.932E-08	1.495E-08	-0.2983	-4.6358	0.0000
CMALT4	-3.184E-12	9.888E-13	-0.0739	-3.2204	0.0013
ALTLAT4	3.121E-08	5.933E-09	8.5423	5.2610	0.0000
ALTLON5	1.383E-12	1.301E-13	15.6162	10.6341	0.0000
ALTITUDE	-2.644E-01	2.821E-02	-20.1206	-9.3709	0.0000
ALT2LON5	2.113E-16	3.040E-17	1.6968	6.9507	0.0000
ALT3L5L5	9.618E-28	1.846E-28	0.8079	5.2091	0.0000
LATLONG4	-4.719E-10	1.560E-10	-0.3313	-3.0253	0.0026
SMLONG	-1.268E-02	5.110E-03	-0.5720	-2.4809	0.0133
CMLAT	3.576E-02	1.662E-02	0.3856	2.1523	0.0316

Residuals Statistics

Minimum	Maximum	Mean	Std. Deviation	N
3.239484072	14.70323944	7.259508557	2.02223051	936

described through systematic spatial variation.

Following this analysis we can describe the mean values for Monthly N_r:

$$
\begin{aligned}
&N_r(latitude, longtitude, altitude) := \\
&\quad 0.6873 + 1.004E-10SMLON5 - 8.537E-08SMLAT5 \\
&\quad 8.879E-12LATLONG5 - 7.325E+00CMCLAT1.252E-07CML2L2 \\
&\quad 1.826E-01LONG + 3.586E-03SMLL + 7.812E-07ALTLAT3 \\
&\quad -6.932E-08LATLONG3 - 3.184E-12CMALT4 + 3.121E-08ALTLAT4 \\
&\quad 1.383E-12ALTLON5 - 2.644E-01ALTITUDE + 2.113E-16ALT2LON5 \\
&\quad 9.618E-28ALT3L5L5 - 4.719E-10LATLONG4 - 1.268E-02SMLONG \\
&\quad 3.576E-02CMLAT + z^{spRT}
\end{aligned} \tag{G.14}
$$

where $z^{spRT} = 2$

G.3.6 Rainfall Model

For the purposes of the **RADLAB** simulations in New Zealand, mean monthly rainfall total (RT) data can be modelled by the summation of Equations G.12, G.13, G.10 and G.11after Equation 12.11. From this we will model the probability of rain on any given day as equal to

$$\mathrm{P(rain)} = \frac{N}{30} \tag{G.15}$$

where N is given by Equation G.14, and the rate (R mm hr^{-1}) is equal to

$$R = \frac{RT}{N * 24} \tag{G.16}$$

G.4 Cloudiness

The percentage cloud cover is a variable that needs to be estimated for the purposes of longwave and shortwave surface energy exchange balances (§8.2.1,8.2.2). In order to calculate the cloud cover we will compare the measured monthly total sunshine hours (ST) to the calculated maximum total monthly sunshine hours (SM). In the absence of any cloud

cover ST will equal SM. Thus the cloud index value (CI)value given by

$$CI = 1 - \frac{ST}{SM} \tag{G.17}$$

will give a measure of the monthly average proportion of cloud cover. CI data have been calculated from the available monthly suntotal data and this variable analysed in an identical manner to that outlined in §12.3.1 and illustrated with the Air Temperature model in §12.3.2 for the variables $MAIRMAX$ and $MAIRMIN$. No further model development is required beyond developing a spatially indexed model for CI series data.

G.4.1 Cloud Index Deterministic Seasonal Model

The stationary seasonal data for CI were extracted using the seasonal average given in Equation 11.2. This seasonal series was then modelled using a spatially indexed harmonic series as discussed in §12.3.1. The regression has been conducted with no constant as we have defined the constant to be equal to zero through the normalisation procedure which produced the stationary series.

A summary of the fitted seasonal model for CI is given in Table G.13. This shows that while the analysis is significant only about 16 % of the observed structure for the seasonal component can be described in terms of a regular seasonal variation.

Following this analysis we can model the deterministic seasonal component of CI as

$$\begin{aligned} CI_{detseasonal} := \\ & -2.862E-10CMLON4 + 3.933E-10SMLON4 + 1.616E-02CM2 \\ & 1.147E-07SMLAT4 - 8.604E-03SM21.343E-03CMALT \\ & -4.203E-12CMLL4 - 2.593E-04SMLAT2 + 3.206E-05CMALTLAT \end{aligned}$$

Martin Jones 2002

Table G.13: Fitted model for the deterministic seasonal component of CI

Model Summary

R	R Square	Adjusted R Square	Std. Error of the Estimate
0.3994	0.1595	0.1590	0.0733

ANOVA

	Sum of Squares	df	Mean Square	F	Sig.
Regression	29.1180	17	1.7128	319.0952	0
Residual	153.3997	28578	0.0054		
Total	182.5177	28595			

Coefficients

	Unstandardized Coefficients		Standardized Coefficients	t	Sig.
	B	Std. Error	Beta		
CMLON4	-2.862E-10	3.087E-11	-2.2916	-9.2713	0.0000
SMLON4	3.933E-10	4.653E-11	3.1500	8.4522	0.0000
CM2	1.616E-02	6.128E-04	0.1430	26.3662	0.0000
SMLAT4	1.147E-07	1.201E-08	3.1842	9.5547	0.0000
SM2	-8.604E-03	6.126E-04	-0.0762	-14.0436	0.0000
CMALT	1.343E-03	1.487E-04	2.5963	9.0286	0.0000
CMLL4	-4.203E-12	4.007E-13	-1.3832	-10.4890	0.0000
SMLAT2	-2.593E-04	3.452E-05	-3.9805	-7.5106	0.0000
CMALTLAT	3.206E-05	3.720E-06	2.6669	8.6169	0.0000
CMA2L4L4	5.863E-22	1.097E-22	2.1737	5.3431	0.0000
CMALT4L4	-1.361E-18	1.225E-19	-3.3581	-11.1091	0.0000
CMA3L3L2	-2.468E-18	2.350E-19	-5.3200	-10.5004	0.0000
CMALT2L2	-1.815E-09	2.089E-10	-4.1738	-8.6898	0.0000
SMLL4	7.270E-12	1.080E-12	2.3937	6.7333	0.0000
SMALL	8.012E-09	1.398E-09	0.1144	5.7295	0.0000
SMALT2	5.985E-08	1.456E-08	0.0729	4.1117	0.0000
CMLON2	2.604E-06	1.142E-06	0.6924	2.2798	0.0226

Residuals Statistics

	Minimum	Maximum	Mean	Std. Deviation	N
Predicted Value	-0.0725	0.0845	0.0000	0.0319	28595
Residual	-0.2774	0.3421	0.0000	0.0732	28595

$$+5.863E-22CMA2L4L4-1.361E-18CMALT4L4-2.468E-18CMA3L3L2$$
$$-1.815E-09CMALT2L2+7.270E-12SMLL4+8.012E-09SMALL$$
$$5.985E-08SMALT2+2.604E-06CMLON2 \quad \text{(G.18)}$$

G.4.2 Stochastic Seasonal Model for Cloud Index

Following the modelling approach defined previously (§12.3.1 & §12.3.2) we will use an ARIMA(1,0,0) model to describe the stochastic structure of the rH seasonal component. A Summary of this analysis is presented in Table G.14. This shows that the ARIMA analysis is not significant.

Table G.14: ARIMA(1,0,0) model for CI stochastic seasonal component

Analysis of Variance

	DF	Adj. Sum of Squares	Residual Variance
Residuals	28594	153.39539	.00536460

Coefficients

	B	SEB	T-RATIO	APPROX. PROB.
AR1	-.00529578	.00591375	-.89550272	.37052595

Accordingly we will describe the stochastic seasonal component of CI as a purely random variable according to the residual statistics given in Table G.13. Thus we describe the stochastic seasonal component of CI as:

$$r_{CI}(x) := z^{dsCI} \quad \text{(G.19)}$$

where $z^{dsCI} \sim N(0, 0.07)$

G.4.3 Spatial Model

Following the approach described above, the spatial model has been fitted by regressing the monitored rH data against fully crossed fourth order spatial polynomial model of longitude, latitude and altitude, using

a stepwise regression. However the regression model is not significant with an ANOVA p. value of 0.599. Accordingly we will describe the locational mean CI value as a Normally distributed random value with the parameters given in Table G.15. Thus we will model the spatial compo-

Table G.15: Descriptive statistics for the cloud index over New Zealand

N	Minimum	Maximum	Mean	Std. Deviation
72	-.95	.62	.4575	.1977

nent of the CI variable as:

$$CI(lat, long, alt) := z \tag{G.20}$$

where $z \sim N(0.4575, 0.2)$

G.4.4 Long-Term Trend

To model the long term stochastic structure for CI any apparent long term trend over the duration of the recording period was removed. This was achieved by regressing the data against a cubic model of year. This model treats any apparent long-term trend as an additive effect that is global to New Zealand as a whole. A summary of this analysis is given in Figure G.4.

As discussed previously, the regression residuals are the most important aspect of this analysis as we need to describe the stochastic structure of the residuals in order to model realistic long term sequence data. There are no significant autocorrelations for the residuals from the long-term CI data. Accordingly we will simply describe the stochastic component of the long-term CI component as a purely random variable distributed according to the residual parameters given in Table G.16. That is we will describe the long-term stochastic seasonal component of CI as:

$$r_{ci}(x) := z \tag{G.21}$$

where $z \sim N(0, 0.049)$ (Table G.16)

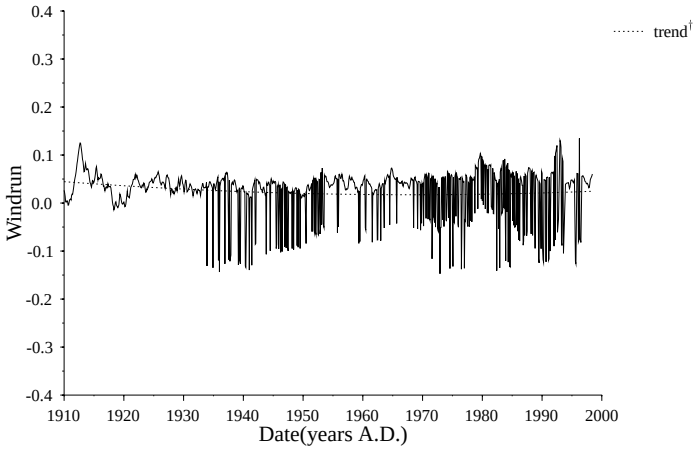

Figure G.4: Long-term trend for monthly mean rain total

† $x = 20.844 - 1.587E-02x + 1.365E-09x^3$ $R^2 = 0.03$ Sig. = 0

Table G.16: Descriptive statistics for the long term trend data for *CI*

	N	Minimum	Maximum	Mean	Std. Deviation
CI	24832	-0.15	0.35	0	4.866E-02

G.4.5 Cloud Index Model

For the purposes of the **RADLAB** simulations in New Zealand *CI* series data can be modelled by the summation of Equations G.20, G.21, G.18 and G.19after Equation 12.11.

G.5 Linke t

The Linke t value for New Zealand is required for the calculation of the shortwave radiation flux (§8.2.1). Here we will use Equation 8.29 to calculate the Line t value, thus we need to establish an appropriate value for Linke t at $m = 2$(*infravide* : §8.2.1).

To calculate this value we can make use of the measured shortwave radiation data in the available database (§11.2). If we compare the clear sky radiation measurements to the predicted shortwave maximum flux it is possible to calculate the Linke t value from Equations 8.22 and 8.28 and a reworking of 8.27 as

$$T_L = -\frac{\ln\left(\frac{S_b}{\hat{S}_i}\right)}{\delta_R m} \tag{G.22}$$

The necessary data is available for two location Kaitia and Paraparaumu which are separated by half the longitudinal range of New Zealand. Thus these two locations can be used to asses whether we would expect significant longitudinal variation in the $T_L(\beta)$ function for New Zealand. The data return the following values for clear sky Linke t at $m = 2$

Location	Linke t	
	$\bar{x}$	σ
Kaitia	4.0	2.7
Paraparaumu	3.8	2.6

These are not significantly different and we an estimate a New Zealand specific Linke t at $m = 2$ as 3.9 ± 3.7.

Thus we can model $L_T(\beta)$ in New Zealand following Equation 8.29 with Linke t at $m = 2$ given as:

$$L_T(m = 2) \sim N(3.9, 3.7^2) \tag{G.23}$$

G.6 New Zealand Environmental Code Module

To enable New Zealand specific soil temperature regime estimates the environmental models described in §12.3.1 above have been coded in a module **nz_env.pas** within **RADLAB** . This module is a straight implementation of the models described in §12.3.1 and provides a new implementation of some of the variables defined in the **RADLAB** module **env.pas**.

To allow these new variables to be coded a simple flag has been inserted into the **env.pas** code. This requires the value of an environmental variable to be called from the nz_env.pas module if the location is within New Zealand (this is indicated by the boolean flag **nz**). So for example the function `air_temp` within **env.pas** is recoded as

```
function air_temp : double;
begin
if nz then result := nz_airtemp
else
result := 13 + 5*cos(2*pi*(months + days/31 + hours/(31*24) $...$
end;
```

G.7 Micro-Scale Δ_{EHT} Simulation Results

Table G.17: Bethells micro-scale Δ_{EHT} simulation results

	beth1-1	beth2-1	beth3-1	beth4-1	beth5-1	beth1-2	beth2-2	beth3-2	beth4-2	beth5-2
beth1-1		-0.022	-0.143	0.301	0.225	0.622	0.612	0.509	0.86	0.81
beth2-1			-0.12	0.323	0.248	0.644	0.634	0.532	0.883	0.832
beth3-1				0.443	0.368	0.765	0.755	0.652	1.003	0.953
beth4-1					-0.075	0.321	0.311	0.209	0.56	0.51
beth5-1						0.397	0.387	0.284	0.635	0.585
beth1-2							-0.01	-0.113	0.238	0.188
beth2-2								-0.102	0.248	0.198
beth3-2									0.351	0.301
beth4-2										-0.05
beth5-2										
beth1-3										
beth2-3										
beth3-3										
beth4-3										
beth5-3										
beth1-4										
beth2-4										
beth3-4										
beth4-4										
beth5-4										

	beth1-3	beth2-3	beth3-3	beth4-3	beth5-3	beth1-4	beth2-4	beth3-4	beth4-4	beth5-4
beth1-1	0.757	0.749	0.654	0.97	0.929	0.766	0.758	0.667	0.963	0.926
beth2-1	0.779	0.772	0.676	0.992	0.951	0.788	0.781	0.69	0.986	0.949
beth3-1	0.9	0.892	0.797	1.113	1.072	0.909	0.901	0.81	1.106	1.069
beth4-1	0.457	0.449	0.353	0.67	0.628	0.465	0.458	0.367	0.663	0.626
beth5-1	0.532	0.524	0.429	0.745	0.703	0.541	0.533	0.442	0.738	0.701
beth1-2	0.135	0.127	0.032	0.348	0.307	0.144	0.136	0.045	0.341	0.304
beth2-2	0.145	0.137	0.042	0.358	0.317	0.154	0.147	0.055	0.351	0.314
beth3-2	0.248	0.24	0.144	0.461	0.419	0.256	0.249	0.158	0.454	0.417
beth4-2	-0.103	-0.111	-0.206	0.11	0.069	-0.094	-0.102	-0.193	0.103	0.066
beth5-2	-0.053	-0.061	-0.156	0.16	0.119	-0.044	-0.052	-0.143	0.153	0.116
beth1-3		-0.008	-0.103	0.213	0.172	0.009	0.001	-0.09	0.206	0.169
beth2-3			-0.095	0.221	0.179	0.016	0.009	-0.082	0.214	0.177
beth3-3				0.316	0.275	0.112	0.104	0.013	0.309	0.272
beth4-3					-0.041	-0.204	-0.212	-0.303	-0.007	-0.044
beth5-3						-0.163	-0.17	-0.261	0.034	-0.003
beth1-4							-0.007	-0.098	0.197	0.16
beth2-4								-0.091	0.205	0.168
beth3-4									0.296	0.259
beth4-4										-0.037
beth5-4										

Table G.18: Hot Water Beach micro-scale Δ_{EHT} simulation results

	hwb1-1	hwb2-1	hwb3-1	hwb4-1	hwb5-1	hwb1-2	hwb2-2	hwb3-2	hwb4-2	hwb5-2
hwb1-1		0.136	0.688	0.267	0.035	0.629	0.731	1.2	0.846	0.652
hwb2-1			0.552	0.131	-0.101	0.493	0.595	1.064	0.71	0.516
hwb3-1				-0.421	-0.653	-0.059	0.043	0.512	0.158	-0.036
hwb4-1					-0.232	0.362	0.464	0.933	0.579	0.385
hwb5-1						0.594	0.696	1.165	0.811	0.617
hwb1-2							0.102	0.571	0.217	0.022
hwb2-2								0.469	0.115	-0.079
hwb3-2									-0.354	-0.548
hwb4-2										-0.194
hwb5-2										
hwb1-3										
hwb2-3										
hwb3-3										
hwb4-3										
hwb5-3										
hwb1-4										
hwb2-4										
hwb3-4										
hwb4-4										
hwb5-4										

	hwb1-3	hwb2-3	hwb3-3	hwb4-3	hwb5-3	hwb1-4	hwb2-4	hwb3-4	hwb4-4	hwb5-4
hwb1-1	0.761	0.851	1.281	0.958	0.78	0.765	0.848	1.249	0.948	0.782
hwb2-1	0.625	0.715	1.145	0.821	0.644	0.629	0.711	1.113	0.811	0.646
hwb3-1	0.073	0.163	0.593	0.27	0.092	0.077	0.16	0.561	0.26	0.094
hwb4-1	0.494	0.584	1.014	0.69	0.513	0.498	0.58	0.982	0.68	0.515
hwb5-1	0.726	0.816	1.246	0.922	0.745	0.73	0.812	1.214	0.912	0.747
hwb1-2	0.132	0.222	0.651	0.328	0.151	0.135	0.218	0.62	0.318	0.152
hwb2-2	0.03	0.12	0.55	0.226	0.049	0.033	0.116	0.518	0.216	0.051
hwb3-2	-0.439	-0.349	0.081	-0.243	-0.42	-0.435	-0.353	0.049	-0.253	-0.418
hwb4-2	-0.085	0.005	0.435	0.111	-0.066	-0.082	0.001	0.403	0.101	-0.064
hwb5-2	0.11	0.199	0.629	0.306	0.128	0.113	0.196	0.597	0.296	0.13
hwb1-3		0.09	0.519	0.196	0.019	0.003	0.086	0.488	0.186	0.021
hwb2-3			0.43	0.107	-0.071	-0.086	-0.003	0.398	0.097	-0.069
hwb3-3				-0.323	-0.501	-0.516	-0.433	-0.032	-0.333	-0.499
hwb4-3					-0.177	-0.193	-0.11	0.292	-0.01	-0.176
hwb5-3						-0.015	0.067	0.469	0.167	0.002
hwb1-4							0.083	0.485	0.183	0.017
hwb2-4								0.402	0.1	-0.066
hwb3-4									-0.302	-0.467
hwb4-4										-0.166
hwb5-4										

Table G.19: Leigh micro-scale Δ_{EHT} simulation results

	l1-1	l1-2	l1-3	l1-4
l1-1		0.628	0.764	0.773
l1-2			0.136	0.146
l1-3				0.010
l1-4				

Table G.20: Pakiri micro-scale Δ_{EHT} simulation results

	pak2-1	pak3-1	pak4-1	pak5-1	pak1-2	pak2-2	pak3-2	pak4-2	pak5-2
pak1-1	3.46E-01	1.74E-01	1.84E-02	6.63E-02	6.25E-01	9.04E-01	7.79E-01	6.45E-01	6.88E-01
pak2-1		-1.72E-01	-3.28E-01	-2.80E-01	2.79E-01	5.58E-01	4.33E-01	2.99E-01	3.42E-01
pak3-1			-1.56E-01	-1.08E-01	4.51E-01	7.30E-01	6.04E-01	4.70E-01	5.13E-01
pak4-1				4.80E-02	6.07E-01	8.86E-01	7.61E-01	6.26E-01	6.69E-01
pak5-1					5.59E-01	8.38E-01	7.13E-01	5.78E-01	6.22E-01
pak1-2						2.79E-01	1.54E-01	1.96E-02	6.26E-02
pak2-2							-1.25E-01	-2.59E-01	-2.16E-01
pak3-2								-1.34E-01	-9.11E-02
pak4-2									4.30E-02
pak5-2									
pak1-3									
pak2-3									
pak3-3									
pak4-3									
pak5-3									

	pak1-3	pak2-3	pak3-3	pak4-3	pak5-3
pak1-1	7.63E-01	1.01E+00	9.04E-01	7.82E-01	8.21E-01
pak2-1	4.16E-01	6.68E-01	5.58E-01	4.35E-01	4.75E-01
pak3-1	5.88E-01	8.39E-01	7.30E-01	6.07E-01	6.47E-01
pak4-1	7.44E-01	9.95E-01	8.86E-01	7.63E-01	8.03E-01
pak5-1	6.96E-01	9.48E-01	8.38E-01	7.15E-01	7.55E-01
pak1-2	1.37E-01	3.89E-01	2.79E-01	1.56E-01	1.96E-01
pak2-2	-1.42E-01	1.10E-01	1.14E-05	-1.23E-01	-8.29E-02
pak3-2	-1.64E-02	2.35E-01	1.25E-01	2.61E-03	4.25E-02
pak4-2	1.18E-01	3.69E-01	2.59E-01	1.37E-01	1.77E-01
pak5-2	7.47E-02	3.26E-01	2.16E-01	9.37E-02	1.34E-01
pak1-3		2.51E-01	1.42E-01	1.90E-02	5.88E-02
pak2-3			-1.10E-01	-2.32E-01	-1.92E-01
pak3-3				-1.23E-01	-8.29E-02
pak4-3					3.99E-02
pak5-3					

Table G.21: Pukekohe micro-scale Δ_{EHT} simulation results

	p1-1	p1-2	p1-3	p1-4
p1-1		0.628	0.764	0.773
p1-2			0.136	0.146
p1-3				0.010
p1-4				

Table G.22: Tapharanui micro-scale Δ_{EHT} simulation results

	taph1-1	taph2-1	taph3-1	taph4-1	taph1-2	taph2-2	taph3-2	taph4-2
taph1-1		7.91E-01	-1.75E-01	2.56E-01	6.25E-01	1.29E+00	4.79E-01	8.44E-01
taph2-1			-9.66E-01	-5.35E-01	-1.66E-01	4.99E-01	-3.12E-01	5.29E-02
taph3-1				4.31E-01	8.00E-01	1.46E+00	6.54E-01	1.02E+00
taph4-1					3.69E-01	1.03E+00	2.23E-01	5.88E-01
taph1-2						6.65E-01	-1.46E-01	2.19E-01
taph2-2							-8.11E-01	-4.46E-01
taph3-2								3.65E-01
taph4-2								
taph1-3								
taph2-3								
taph3-3								
taph4-3								
taph1-4								
taph2-4								
taph3-4								
taph4-4								

	taph1-3	taph2-3	taph3-3	taph4-3	taph1-4	taph2-4	taph3-4	taph4-4
taph1-1	7.63E-01	1.37E+00	6.29E-01	9.61E-01	7.73E-01	1.34E+00	6.49E-01	9.58E-01
taph2-1	-2.86E-02	5.79E-01	-1.62E-01	1.70E-01	-1.79E-02	5.50E-01	-1.43E-01	1.66E-01
taph3-1	9.37E-01	1.55E+00	8.04E-01	1.14E+00	9.48E-01	1.52E+00	8.23E-01	1.13E+00
taph4-1	5.06E-01	1.11E+00	3.73E-01	7.05E-01	5.17E-01	1.08E+00	3.92E-01	7.01E-01
taph1-2	1.37E-01	7.45E-01	4.13E-03	3.36E-01	1.48E-01	7.16E-01	2.34E-02	3.32E-01
taph2-2	-5.28E-01	8.00E-02	-6.61E-01	-3.29E-01	-5.17E-01	5.05E-02	-6.42E-01	-3.33E-01
taph3-2	2.83E-01	8.91E-01	1.50E-01	4.82E-01	2.94E-01	8.61E-01	1.69E-01	4.78E-01
taph4-2	-8.15E-02	5.26E-01	-2.15E-01	1.17E-01	-7.08E-02	4.97E-01	-1.95E-01	1.13E-01
taph1-3		6.08E-01	-1.33E-01	1.99E-01	1.07E-02	5.78E-01	-1.14E-01	1.95E-01
taph2-3			-7.41E-01	-4.09E-01	-5.97E-01	-2.95E-02	-7.22E-01	-4.13E-01
taph3-3				3.32E-01	1.44E-01	7.11E-01	1.93E-02	3.28E-01
taph4-3					-1.88E-01	3.80E-01	-3.13E-01	-3.66E-03
taph1-4						5.68E-01	-1.25E-01	1.84E-01
taph2-4							-6.92E-01	-3.83E-01
taph3-4								3.09E-01
taph4-4								

Table G.23: Tramvalley Road micro-scale Δ_{EHT} simulation results

	tvr1-2	tvr2-2	tvr3-2	tvr4-2	tvr5-2
tvr1-2		0.006	0.012	0.010	0.011
tvr2-2			0.006	0.003	0.004
tvr3-2				-0.002	-0.001
tvr4-2					0.001
tvr5-2					

Table G.24: Comparisons between simulated and observed Δ_{EHT} results for the Bethells depth profile

	beth1-1	beth1-2	beth1-3
beth1-1		-0.037931595	-0.453
beth1-2			-0.415
beth1-3			

Table G.25: Comparisons between simulated and observed Δ_{EHT} results for the Bethells spatial results

	beth1-2	beth2-2	beth3-2	beth4-2	beth5-2
beth1-2		-0.180	0.064	-0.136	-0.293
beth2-2			0.243	0.043	-0.113
beth3-2				-0.200	-0.357
beth4-2					-0.157
beth5-2					

Table G.26: Comparisons between simulated and observed Δ_{EHT} results for the Hot Water Beach depth profile

	hwb5-1	hwb5-2	hwb5-3	hwb5-4
hwb5-1		-0.138	-2.396	-0.182
hwb5-2			-2.258	-0.045
hwb5-3				2.213
hwb5-4				

Table G.27: Comparisons Between Simulated and Observed Δ_{EHT} Results for the Hot Water Beach spatial results

	hwb2-3	hwb3-3	hwb4-3	hwb5-3
hwb2-3		0.450	0.549855311	-0.036
hwb3-3			0.100013188	-0.486
hwb4-3				-0.586156015
hwb5-3				

Table G.28: Comparisons between simulated and observed Δ_{EHT} results for the Leigh depth profile

	l1-1	l1-2	l1-3	l1-4
l1-1		-0.178514856	3.130	0.07876055
l1-2			3.309	0.257275406
l1-3				-3.05171128
l1-4				

Table G.29: Comparisons between simulated and observed Δ_{EHT} results for the Pakiri depth profiles

	pak1-1	pak1-2	pak1-3
pak1-1		0.053	-0.192
pak1-2			-0.245
pak1-3			
	pak2-1	pak2-2	pak2-3
pak2-1		0.123	0.475
pak2-2			0.352
pak2-3			
	pak3-1	pak3-2	pak3-3
pak3-1		-0.033	0.118
pak3-2			0.150
pak3-3			
	pak4-1	pak4-2	pak4-3
pak4-1		0.074	0.347
pak4-2			0.274
pak4-3			
	pak5-1	pak5-2	pak5-3
pak5-1		0.166	-0.170
pak5-2			-0.337
pak5-3			

Table G.30: Comparisons between simulated and observed Δ_{EHT} results for the Pakiri spatial results

	pak1-1	pak2-1	pak3-1	pak4-1	pak5-1	pak1-2	pak2-2	pak3-2	pak4-2	pak5-2	pak1-3	pak2-3	pak3-3	pak4-3	pak5-3
pak1-1		-0.226	-0.780	-2.207	-2.594	-1.793	-0.609	-1.371	-1.480	0.038	-0.440	-0.051	0.137	-0.441	-0.871
pak2-1			-0.554	-1.981	-2.368	-1.567	-0.383	-1.145	-1.254	0.264	-0.214	0.175	0.363	-0.215	-0.645
pak3-1				-1.427	-1.814	-1.013	0.172	-0.591	-0.700	0.819	0.341	0.729	0.917	0.339	-0.091
pak4-1					-0.387	0.414	1.598	0.836	0.727	2.245	1.767	2.156	2.344	1.766	1.336
pak5-1						0.801	1.985	1.223	1.114	2.632	2.154	2.543	2.731	2.153	1.723
pak1-2							1.184	0.422	0.313	1.831	1.353	1.741	1.930	1.352	0.922
pak2-2								-0.762	-0.871	0.647	0.169	0.557	0.746	0.168	-0.263
pak3-2									-0.109	1.410	0.931	1.320	1.508	0.930	0.500
pak4-2										1.519	1.040	1.429	1.617	1.039	0.609
pak5-2											-0.478	-0.090	0.099	-0.479	-0.910
pak1-3												0.388	0.577	-0.001	-0.432
pak2-3													0.188	-0.390	-0.820
pak3-3														-0.578	-1.008
pak4-3															-0.430
pak5-3															

Table G.31: Comparisons between simulated and observed Δ_{EHT} results for the Tapharanui depth profiles

	taph1-1	taph1-2	taph1-3	taph1-4
taph1-1		-4.186	0.144	-0.274
taph1-2			4.330	3.912
taph1-3				-0.418
taph1-4				

	taph4-1	taph4-2	taph4-3
taph4-1		-0.188	-0.245
taph4-2			-0.057
taph4-3			

Table G.32: Comparisons between simulated and observed Δ_{EHT} results for the Tapharanui spatial results

	taph1-1	taph1-3	taph2-3	taph3-3	taph4-1	taph4-2	taph4-3	taph5-3
taph1-1		0.144	0.858	-0.758	-0.148	-0.337	-0.394	-0.108
taph1-3			0.714	-0.902	-0.292	-0.480	-0.537	-0.252
taph2-3				-1.616	-1.006	-1.195	-1.252	-0.966
taph3-3					0.610	0.422	0.365	0.650
taph4-1						-0.188	-0.245	0.040
taph4-2							-0.057	0.229
taph4-3								0.286
taph5-3								

Loc1

	taph1-1	taph1-3	taph2-3
taph1-1		0.144	0.858
taph1-3			0.714
taph2-3			

Loc2

	taph3-3	taph4-1	taph4-2	taph4-3	taph5-3
taph3-3		0.610	0.422	0.365	0.650
taph4-1			-0.188	-0.245	0.040
taph4-2				-0.057	0.229
taph4-3					0.286
taph5-3					

Table G.33: Comparisons between simulated and observed Δ_{EHT} results for the Tramvalley Road results

	tvr1-1	tvr2-1	tvr3-1	tvr4-1	tvr5-1
tvr1-1		-0.409	-0.300	-0.085	-0.696
tvr2-1			0.108	0.323	-0.288
tvr3-1				0.215	-0.396
tvr4-1					-0.611
tvr5-1					

Appendix H

MCMC sampler updates for Date Lab 1.1

H.1 The Date Lab 1.1 MCMC sampler

Nicholls and Jones (2001) define an algorithm generating a Markov chain sample $\{\psi^{(j)}, \theta^{(j)}\}_{j=0}^{J}$ from the posterior $h_{\Psi,\Theta}(\psi, \theta|\mathcal{Y})$. We need to extend this to allow sampling from the posterior defined in Equations 13.1 and 13.14. Following Nicholls and Jones (2001) we define a Markov chain via a stochastic update rule that determines a transition density from v to v' which preserves the posterior. In order to get an efficient sampler Nicholls and Jones (2001) define several transition rules labelled $v = 1, 2 \ldots$. Each rule is made up of a generation step, in which a candidate state (v') is generated according to a density q_u for rule u, and an acceptance step, in which the candidate state is accepted with probability $\alpha_u(v'|v)$, or rejected. Precise details of the sampling algorithm are given by Nicholls and Jones (2001) and they define four updates for the sampling process:

- Update a single θ variable, $u = 1$, $(\psi, \theta \rightarrow \psi, \theta')$.
- Update a single ψ variable, $u = 2$, $(\psi, \theta \rightarrow \psi', \theta)$.
- Shift all dates, $u = 3$, $(\psi, \theta \rightarrow \psi', \theta')$.
- Expand the dates about their mean, $u = 4$, $(\psi, \theta \rightarrow \psi', \theta')$.

These steps define the transition from $\psi, \theta, A, E, \bar{T}, \Delta_T$ to $\psi', \theta', A, E, \bar{T}, \Delta_T$. In order to sample the posterior distributions given in Equations 13.1 and 13.14 we need to define four additional update steps to take account of the variables $A, E, \bar{T}, \Delta_T$ and enable the full transition from v to v'. These update steps are:

- Update a single A variable, $u = 5$,
- Update a single E variable, $u = 6$,

- Update $\bar{T}$, $u = 7$,
- Update a single Δ_T variable, $u = 8$,

In each case a random walk update is used. So, for example, with update 5 a parameter A_i is chosen uniformly at random (UAR) from the set $\{_1 \ldots A_{N_A}\}$. A shift variable S is chosen uniformly at random in the interval $[-1E-8, 1E+8]$ and added to A_i; *i.e.* $A'_i = A_i + S$. In this case $q_5(\psi, \theta, A', E, \bar{T}, \Delta_T | \psi, \theta, A, E, \bar{T}, \Delta_T) = q_5(\psi, \theta, A, E, \bar{T}, \Delta_T | \psi, \theta, A', E, \bar{T}, \Delta_T)$, since the probabilities to choose the forward and reverse shifts are equal. Here

$$\alpha_5(\psi, \theta, A', E, \bar{T}, \Delta_T | \psi, \theta, A, E, \bar{T}, \Delta_T) = \min \left\{ 1, \frac{L(\mathcal{Y} | \theta, A', E, \bar{T}, \Delta_T) f_A(A')}{L(\mathcal{Y} | \theta, A, E, \bar{T}, \Delta_T) f_A(A)} \right\}$$

The updates for the other variables follow in an identical manner, except that the interval for the shift variable S is set to an appropriate value for each update type.